THE PHYSICS OF CHROMOSPHERIC PLASMAS

COVER ILLUSTRATION: Spectroheliogram taken in Ca II K_3 by Francisco Miranda Costa Lobo with the Coimbra spectroheliograph at 10:52 UT on 19 October 1926 (courtesy of Adriana Garcia).

ASTRONOMICAL SOCIETY OF THE PACIFIC CONFERENCE SERIES

A SERIES OF BOOKS ON RECENT DEVELOPMENTS IN ASTRONOMY AND ASTROPHYSICS

VOLUME 368

Beginning 2004, ASP-CS Volumes may be found as e-books with color images at:
http://www.aspbooks.org

A listing of all IAU Volumes published
and the ASP Conference Series published during the past one year
may be found at teh back of this volume.

For all ASP-CS Volumes published see: http://www.astrosociety.org/pubs.html

ASTRONOMICAL SOCIETY OF THE PACIFIC
CONFERENCE SERIES

VOLUME 368

THE PHYSICS OF CHROMOSPHERIC PLASMAS

Proceedings of the Coimbra Solar Physics Meeting held at
The University of Coimbra, Coimbra, Portugal
9–13 October 2006

Edited by

Petr Heinzel
Astronomical Institute, Academy of Sciences of the Czech Republic, Ondřejov, Czech Republic

Ivan Dorotovič
Slovak Central Observatory, Hurbanovo, Slovak Republic
Observatório Astronómico da Universidade de Coimbra, Coimbra, Portugal

Robert J. Rutten
Sterrekundig Instituut, Utrecht University, Utrecht, The Netherlands
Institute of Theoretical Astrophysics, University of Oslo, Norway

SAN FRANCISCO

ASTRONOMICAL SOCIETY OF THE PACIFIC
390 Ashton Avenue
San Francisco, California, 94112-1722, USA

Phone: 415-337-1100
Fax: 415-337-5205
E-mail: service@astrosociety.org
Web site: www.astrosociety.org
E-books: www.aspbooks.org

ASP Conference Series – First Edition

ISBN: 978-1-583812-36-5

Library of Congress (LOC) Cataloging in Publication (CIP) Data:
Main entry under title
Library of Congress Control Number (LCCN): **LCCN number**

Printed in the United States of America by Sheridan Books, Ann Arbor, Michigan

Dedication

This book contains the proceedings of the Coimbra Solar Physics Meeting held at the occasion of the 80^{th} anniversary of the first spectroheliogram taken at Coimbra by Francisco Miranda Costa Lobo (1864 – 1945).

Contents

Part 4. Prominences and Filaments

Part 5. Chromospheric Flares

Part 6. Long-term Solar Variations

Preface

The Coimbra Solar Physics Meeting 2006 entitled "The Physics of Chromospheric Plasmas" was held in Coimbra, Portugal from 9 to 13 October, 2006. In that year the Astronomical Observatory of the University of Coimbra in Portugal – Observatório Astronómico da Universidade de Coimbra (OAUC) – celebrated the 80th anniversary of the first spectroheliographic observations in Coimbra. The instrument was built as a twin of the spectroheliograph at the Observatoire de Paris in Meudon. Full-disk spectroheliograms have been routinely taken in the Ca II K line since then, and in 1990 regular observation in Hα started as well.

This anniversary was an excellent opportunity to organize an international solar physics meeting, including a historical session commemorating the life and work of Prof. Francisco Costa Lobo (1864–1945) who installed the spectroheliograph in Coimbra during the 1920s, and reviewing the subsequent eighty years of solar physics in Coimbra. Coimbra University, which hosted the meeting, was founded in 1290 as one of the oldest European universities.

The content of the meeting was defined to fill a scientific gap by addressing chromospheric plasmas, covering various aspects which are particularly well observed in the traditionally used Hα and Ca II lines, but also in a variety of other lines including the UV and EUV spectral ranges. These aspects included the structure and dynamics of the chromosphere (cell interior, network, spicules etc.) as well as other features seen at the chromospheric level or having the properties of plasmas at chromospheric temperatures: sunspot chromospheres, plages, chromospheric flares, filaments etc. The relation of such plasmas to other atmospheric layers and/or processes was also discussed, in particular using the UV and EUV data from SOHO (ESA/NASA) and other space telescopes. The long-term (cyclic) evolution of the chromosphere and its activity, including solar irradiation variability and effects on space weather, were included, in particular with respect to the long-term observations made in Coimbra. Finally, since this meeting was organized around the Coimbra spectroheliograph anniversary, a session devoted to new solar instruments capable of observing chromospheric plasmas was included as well. About 100 scientists from 24 countries participated in the meeting.

New developments also occur at the Coimbra spectroheliograph itself. CCD technology has recently replaced the classical registration on photographic plates (achieved with the assistance of the Ondřejov Observatory). The large archive of spectroheliographic plates is currently being digitized with the support of the Ministerio da Ciência, da Technologia e do Ensino Superior, and the Coimbra Solar Information System is being constructed in a collaboration with UNINOVA. The meeting was also the final conclusion meeting of the European

Solar Magnetism Network (ESMN) funded by the European Community in the Fifth Framework program.

We are indebted to the Scientific Organizing Committee for defining the excellent scientific program and to the participants to make it a very worthwile and lively conference. The SOC consisted of Mats Carlsson, Werner Curdt, Carsten Denker, Ivan Dorotovič, Lyndsay Fletcher, Petr Heinzel (Chair), Robert Rutten, Brigitte Schmieder, Javier Trujillo Bueno, Georgia Tsiropoula, Han Uitenbroek, and Jean-Claude Vial. In addition, we are most grateful to the Local Organizing Committee consisting of Sandro Batista (webmaster of the meeting's website, `http://www.mat.uc.pt/~cspm2006/`), Ivan Dorotovič, João Fernandes (Chair), and Adriana Garcia for their effort to make of our meeting pleasant and scientifically successful. The meeting was jointly organized by Observatório Astronómico da Universidade de Coimbra and Grupo de Astrofísica da Universidade de Coimbra. The local Host Committee of Artur Soares Alves, Helmut Malonek, and João Fernandes organized the historical session. We also acknowledge the professional efforts in the logistics and the excursions by travel agency Viagens Abreu (Carmen Ramalhão and Sofia Lapo) and the cheerful technical and touristic assistance by hostesses Joana Rebocho and Joana Morais.

The meeting benefited from significant financial support of the following institutions to which we express our sincere gratitude: Fundação Para a Ciência e Tecnologia, Fundação Luso-Americana, Fundação Calouste Gulbenkian, Gabinete de Relações Internacionais da Ciência e do Ensino Superior, British Council, European Space Agency, European Physical Society, Caixa Geral de Depositos, Reitoria da Universidade de Coimbra, Departamento de Matemática da Universidade de Coimbra, the Astronomical Institute of the Academy of Sciences of the Czech Republic, and the EC–RTN European Solar Magnetism Network.

Finally, we thank John Leibacher and the ASP-CS editors for advice on editing, Július Koza for careful proof checking, and the authors for providing the content and worth of this book.

Petr Heinzel, Ivan Dorotovič, Rob Rutten Ondřejov, February 2007

Participants

Jean Aboudarham, Observatoire de Paris, LESIA, 5 Place Janssen, Batiment 14, F-92190 Meudon, France ⟨ Jean.Aboudarham@obspm.fr ⟩

Ali Ajabshirizadeh, Dept. of Theoretical & Astrophysics, University of Tabriz, 51666 Tabriz, Iran, and Research Institute for Astronomy & Astrophysics, 55134-441, Maragha, Iran ⟨ a-adjab@tabrizu.ac.ir, ali_ajabshir@yahoo.com ⟩

Vincenzo Andretta, INAF-Osservatorio Astronomico di Capodimonte, Salita Moiariello 16, 80131 Napoli, Italy ⟨ andretta@oacn.inaf.it ⟩

Andrés Asensio Ramos, Instituto de Astrofísica de Canarias, C/ Via Láctea s/n, E–38205 La Laguna, Tenerife, Spain ⟨ aasensio@iac.es ⟩

Eugene H. Avrett, Harvard-Smithsonian Center for Astrophysics, 60 Garden Street, Cambridge, MA 02138, USA ⟨ avrett@cfa.harvard.edu ⟩

Horst Balthasar, Astrophysikalisches Institut Potsdam, An der Sternwarte 16, D–14482 Potsdam, Germany ⟨ hbalthasar@aip.de ⟩

Luca Belluzzi, INAF/Osservatorio Astrofisico di Arcetri, Largo Enrico Fermi 5, 50125 Firenze, Italy ⟨ belluzzi@arcetri.astro.it ⟩

Arkadiusz Berlicki, Astronomical Institute, Wroclaw University, ul. Kopernika 11, 51–622 Wroclaw, Poland ⟨ berlicki@astro.uni.wroc.pl ⟩

D. Shaun Bloomfield, Max-Planck-Institut für Sonnensystemforschung, Max-Planck-Str. 2, 37191 Katlenburg-Lindau, Germany ⟨ bloomfield@mps.mpg.de ⟩

Z. Funda Bostasncı, Istanbul University, Department of Astronomy and Space Sciences, TR-34119 University, Istanbul, Turkey ⟨ bostanci@istanbul.edu.tr ⟩

Václav Bumba, Astronomical Institute AS CR, Fričova 298, CZ-251 65 Ondřejov, Czech Republic ⟨ bumba@asu.cas.cz ⟩

Jérôme Bureau, Université Pierre et Marie Curie, Case 76, 4, Place Jussieu, 75252 Paris Cedex 05 - France ⟨ jbureau@lpma.jussieu.fr ⟩

Dirk Callebaut, Physics Dept., CGB, University of Antwerp, B-2020 Antwerp, Belgium ⟨ Dirk.Callebaut@ua.ac.be ⟩

Mats Carlsson, Institute of Theoretical Astrophysics, University of Oslo, P.O. Box 1029 Blindern, N-0315 Oslo, Norway ⟨ mats.carlsson@astro.uio.no ⟩

Gianna Cauzzi, INAF/Osservatorio Astrofisico di Arcetri, Largo Enrico Fermi 5, 50125 Firenze, Italy ⟨ gcauzzi@arcetri.astro.it ⟩

Werner Curdt, Max-Planck-Institut für Sonnensystemforschung, Max-Planck-Str. 2, 37191 Katlenburg-Lindau, Germany ⟨ curdt@mps.mpg.de ⟩

Carsten Denker, New Jersey Institute of Technology, Center for Solar-Terrestrial Research, 323 Martin Luther King Blvd, Newark, NJ 07102, USA ⟨cdenker@adm.njit.edu⟩

Mingde Ding, Department of Astronomy, Nanjing University, Nanjing 210093, P. R. China ⟨dmd@nju.edu.cn⟩

Ivan Dorotovič, Slovak Central Observatory, P.O. Box 42, SK-94701 Hurbanovo, Slovakia ⟨dorotovic@suh.sk⟩

Elena Dzifčáková, Dept. of Astronomy, Physics of the Earth and Meteorology, Faculty of Mathematics, Physics and Informatics, Comenius University, Mlynská dolina F2, SK-84248 Bratislava, Slovak Republic ⟨dzifcakova@fmph.uniba.sk⟩

Hossein Ebadi, Institut d'Astrophysique Spatiale, Batiment 121, CNRS-Université Paris-Sud, 91405 Orsay Cedex, France ⟨h_ebadie@yahoo.com⟩

Robertus Erdélyi, The University of Sheffield, Dept. of Applied Mathematics, Hicks Building, Hounsfield Road, Sheffield, S3 7RH, UK ⟨robertus@sheffield.ac.uk⟩

Ilaria Ermolli, INAF Osservatorio Astronomico di Roma, via Frascati 33, 00040 Monte Porzio Catone, Italy ⟨ermolli@oaroma.inaf.it⟩

Netzach Farbiash, Physics Department, Ben-Gurion University, P.O.B. 653, Beer-Sheva 84105, Israel ⟨farbiash@bgu.ac.il⟩

João Fernandes, Observatório Astronómico da Universidade de Coimbra, Santa Clara, 3040 Coimbra, Portugal ⟨jmfernan@mat.uc.pt⟩

Boris Filippov, IZMIRAN, Troitsk, Moscow Region, 142190, Russia ⟨bfilip@izmiran.ru⟩

Bernhard Fleck, NASA/GSFC, Mailcode 671.1, Greenbelt, MD 20771, USA ⟨bfleck@esa.nascom.nasa.gov⟩

Lyndsay Fletcher, Department of Physics and Astronomy, University of Glasgow, Glasgow G12 8QQ, UK ⟨lyndsay@astro.gla.ac.uk⟩

Juan Fontenla, LASP, Univ. of Colorado, Boulder, CO 80303, USA ⟨juan.fontenla@lasp.colorado.edu⟩

Adriana Garcia, Observatório Astronómico da Universidade de Coimbra, Almas de Freire, Santa Clara, 3040-004 Coimbra, Portugal ⟨adriana@mat.uc.pt⟩

Bernard Gelly, Instituto de Astrofísica de Canarias, C/ Via Láctea s/n, E-38205 La Laguna, Tenerife, Spain ⟨bgelly@themis.iac.es⟩

Peter Gömöry, Astronomical Institute, Slovak Academy of Sciences, SK 059 60 Tatranská Lomnica, Slovak Republic ⟨gomory@astro.sk⟩

Asuman Gültekin, Istanbul University, Department of Astronomy and Space Sciences, TR-34119 University, Istanbul, Turkey ⟨al@istanbul.edu.tr⟩

Stanislav Gunár, Astronomical Institute AS CR, Fričova 298, CZ-251 01 Ondřejov, Czech Republic ⟨gunar@asu.cas.cz⟩

Robert Hammerschlag, Astronomical Institute University Utrecht, Princetonplein 5, NL-3584CC Utrecht, The Netherlands ⟨R.H.Hammerschlag@astro.uu.nl⟩

Viggo Hansteen, Institute of Theoretical Astrophysics, University of Oslo, P.O. Box 1029 Blindern, N-0315 Oslo, Norway ⟨viggoh@astro.uio.no⟩

Petr Heinzel, Astronomical Institute AS CR, Fričova 298, CZ-251 65 Ondřejov, Czech Republic ⟨pheinzel@asu.cas.cz⟩

Axel Hofmann, Astrophysikalisches Institut Potsdam, An der Sternwarte 16, D–14482 Potsdam, Germany ⟨ahofmann@aip.de⟩

Hugh Hudson, SSL/UC Berkeley, 7 Gauss Way, Berkeley CA,94720-1450, USA ⟨hhudson@ssl.berkeley.edu⟩

Boris Ioshpa, IZMIRAN, Troitsk, 142190, Moscow Reg., Russia ⟨ioshpa@ttk.ru⟩

Sonja Jejčič, University of Ljubljana, Department of Physics, Jadranska 19, 1000 Ljubljana, Slovenia ⟨sonja.jejcic@guest.arnes.si⟩

Stuart D. Jordan, NASA Goddard Space Flight Center, Solar Physics Branch, Code 612.1, Greenbelt, MD 20771, USA ⟨sjordanpop600@gsfc.nasa.gov⟩

Bhuwan Joshi, Ayrabhatta Research Institute of Observational Sciences (ARIES), Manora Peak, Nainital 263 129, India ⟨bhuwan@aries.ernet.in, bhuwan.joshi@yahoo.com⟩

Larisa Kashapova, Institute of Solar-Terrestrial Physics, P.O. box 291, Irkutsk, 664033, Russia ⟨lkk@iszf.irk.ru⟩

Jana Kašparová, Astronomical Institute AS CR, Fričova 298, CZ-251 01 Ondřejov, Czech Republic ⟨kasparov@asu.cas.cz⟩

Jan Klimeš, Observatory Úpice, U lipek 160, 542 32 Úpice, Czech Republic ⟨klimes.ml@obsupice.cz⟩

Pavel Kotrč, Astronomical Institute AS CR, Fričova 298, CZ-251 01 Ondřejov, Czech Republic ⟨pkotrc@asu.cas.cz⟩

Serge Koutchmy, Institut d'Astrophysique de Paris CNRS and UPMC, 98 Bis Bd Arago, F-75014 Paris, France ⟨koutchmy@iap.fr⟩

Július Koza, Astronomical Institute, Slovak Academy of Sciences, SK-059 60 Tatranská Lomnica, Slovakia ⟨koza@astro.sk⟩

Alena Kulinová, Dept. of Astronomy, Physics of the Earth and Meteorology, Comenius University, Mlynská dolina F2, SK-84248 Bratislava, Slovak Republic ⟨kulinova@fmph.uniba.sk⟩

Nicolas Labrosse, Institute of Mathematical and Physical Sciences, The University of Wales, Aberystwyth, Ceredigion SY23 3BZ, United Kingdom ⟨nll@aber.ac.uk⟩

Philippe Lamy, Laboratoire d'Astrophysique de Marseille, B.P.8, 13376 Marseille Cecex 12, France ⟨philippe.lamy@oamp.fr⟩

Egidio Landi Degl'Innocenti, Dipartimento di Astronomia e Scienza dello Spazio, Largo E. Fermi 5, 50125 Firenze, Italy ⟨landie@arcetri.astro.it⟩

Øystein Langangen, Institute of Theoretical Astrophysics, University of Oslo, P.O. Box 1029 Blindern, N-0315 Oslo, Norway ⟨oysteol@astro.uio.no⟩

Jorrit Leenaarts, Sterrekundig Instituut Utrecht - Universitaat Utrecht, P.O. Box 80000, 3508 TA Utrecht, The Netherlands ⟨j.leenaarts@astro.uu.nl⟩

Torben Leifsen, Institute of Theoretical Astrophysics, University of Oslo, P.O. Box 1029 Blindern, N-0315 Oslo, Norway ⟨torben.leifsen@astro.uio.no⟩

Hui Li, Purple Mountain Observatory, 2 West Beijing Road, Nanjing 210008, P.R. China ⟨lihui@mail.pmo.ac.cn⟩

Jianping Li, Purple Mountain Observatory, 2 West Beijing Road, Nanjing 210008, P.R. China ⟨jpli@pmo.ac.cn⟩

Arturo López Ariste, Instituto de Astrofísica de Canarias, C/ Via Láctea s/n, E- 38205 La Laguna, Tenerife, Spain ⟨arturo@themis.iac.es⟩

Duncan Mackay, School of Mathematics and Statistics, University of St. Andrews, North Haugh, St. Andrews, Fife KY16 9SS, UK ⟨duncan@mcs.st-and.ac.uk⟩

Rafael Manso Sainz, Instituto de Astrofísica de Canarias, C/ Via Láctea s/n, E- 38205 La Laguna, Tenerife, Spain ⟨rsainz@iac.es⟩

Eva Marková, Observatory Úpice, U lipek 160, 542 32 Úpice, Czech Republic ⟨markova@obsupice.cz⟩

Pablo Mauas, Instituto de Astronomía y Física del Espacio, CC 67 Suc 28, 1428 Buenos Aires, Argentina ⟨pablo@iafe.uba.ar⟩

Radek Melich, Institute of Plasma Physics, Department of Optical Diagnostics, Skálova 89, 51101 Turnov, Czech Republic ⟨RMelich@centrum.cz⟩

Laura Merenda, Instituto de Astrofísica de Canarias, C/ Via Láctea s/n, E-38205 La Laguna, Tenerife, Spain ⟨merenda@iac.es⟩

Zadig Mouradian, Observatoire de Paris-Meudon - LESIA, 5 Place Janssen, Bat. 14 92195 Meudon Pl. CEDEX, France ⟨zadig.mouradian@obspm.fr⟩

Daniel Yu. Myachin, Institute of Solar-Terrestrial Physics, RAS SD, P.O.Box 4026, Irkutsk, 664033, Russia ⟨myachin@iszf.irk.ru⟩

Diane B. Paulson, NASA Goddard Space Flight Center, Solar Physics Branch, Code 612.1, Greenbelt, MD 20771, USA ⟨diane.b.paulson@gsfc.nasa.gov⟩

Anna Pietarila, National Center for Atmospheric Research, P.O.Box 3000, Boulder, Co, 80307-3000, USA ⟨annap@ucar.edu⟩

Teodor Pintér, Slovak Central Observatory, P.O. Box 42, SK-94701 Hurbanovo, Slovakia ⟨pinter@suh.sk⟩

Bart de Pontieu, Lockheed Martin Solar & Astrophysics Lab, 3251 Hanover Street, Org. ADBS, Bldg. 252 Palo Alto, CA 94304, USA ⟨bdp@lmsal.com⟩

Tomáš Prosecký, Astronomical Institute AS CR, Fričova 298, CZ-251 01 Ondřejov, Czech Republic ⟨tomas.proso@post.cz⟩

Renzo Ramelli, IRSOL, Via Patocchi, CH-6605 Locarno-Monti, Switzerland ⟨ramelli@irsol.ch⟩

Wolfgang Rammacher, Kiepenheuer Institut für Sonnenphysik, Schoeneckstrasse 6, 79104 Freiburg, Germany ⟨wrammacher@kis.uni-freiburg.de⟩

Marta Rovira, Instituto de Astronomía y Física del Espacio, CC 67 Suc 28, 1428 Buenos Aires, Argentina ⟨rovira@iafe.uba.ar⟩

Günther Rüdiger, Astrophysikalisches Institut Potsdam, An der Sternwarte 16, D–14482 Potsdam, Germany ⟨gruediger@aip.de⟩

Robert J. Rutten, Sterrekundig Instituut Utrecht, Postbus 80 000, NL–3508 TA Utrecht, The Netherlands ⟨R.J.Rutten@astro.uu.nl⟩

Clementina Sasso, Max-Planck-Institut für Sonnensystemforschung, Max-Planck-Strasse 2, 37191 Katlenburg-Lindau, Germany ⟨sasso@mps.mpg.de⟩

Brigitte Schmieder, Observatoire de Paris-Meudon - LESIA, 5 Place Janssen, Bat. 14, Meudon Cedex 92195, France ⟨brigitte.schmieder@obspm.fr⟩

Pavol Schwartz, Astronomical Institute AS CR, Fričova 298, CZ-251 01 Ondřejov, Czech Republic ⟨schwartz@asu.cas.cz⟩

Giuseppe Severino, INAF-Osservatorio Astronomico di Capodimonte, Salita Moiariello 16, 80131 - Napoli, Italy ⟨severino@na.astro.it⟩

Artur Soares Alves, Observatório Astronómico da Universidade de Coimbra, Almas de Freire, Santa Clara, 3040-004 Coimbra, Portugal ⟨asalves@mat.uc.pt⟩

Michal Sobotka, Astronomical Institute AS CR, Fričova 298, CZ-251 01 Ondřejov, Czech Republic ⟨msobotka@asu.cas.cz⟩

Sami K. Solanki, Max-Planck-Institut für Sonnensystemforschung, Max-Planck-Strasse 2, 37191 Katlenburg-Lindau, Germany ⟨solanki@mps.mpg.de⟩

Oskar Steiner, Kiepenheuer-Institut für Sonnenphysik, Schöneckstrasse 6, D–79104 Freiburg, Germany ⟨steiner@kis.uni-freiburg.de⟩

Pieter Thijssen, Financial Department, Department of Physics and Astronomy, Princetonplein 5, NL-3584 CC Utrecht, The Netherlands ⟨P.M.A.Thijssen@phys.uu.nl⟩

Alan Title, Lockheed Martin Solar & Astrophysics Lab, 3251 Hanover Street, Org. ADBS, Bldg. 252 Palo Alto, CA 94304, USA ⟨title@lmsal.com⟩

Javier Trujillo Bueno, Instituto de Astrofísica de Canarias, C/ Via Láctea s/n, E-38205 La Laguna, Tenerife, Spain ⟨jtb@iac.es⟩

Georgia Tsiropoula, Institute for Space Applications and Remote Sensing, National Observatory of Athens, Lofos Koufos, 15236 Palea Penteli, Greece ⟨georgia@space.noa.gr⟩

Kostas Tziotziou, Institute for Space Applications and Remote Sensing, National Observatory of Athens, Lofos Koufos, 15236 Palea Penteli, Greece ⟨kostas@space.noa.gr⟩

Han Uitenbroek, National Solar Observatory, Sacramento Peak Observatory, 1 Loop Drive, Sunspot NM 88349, USA ⟨huitenbroek@nso.edu⟩

José M. Vaquero, Departamento de Física Aplicada, Escuela Politécnica, Universidad de Extremadura, Avda. de la Universidad s/n, 10071 Cáceres, Spain ⟨ jvaquero@unex.es ⟩

Michal Varady, Astronomical Institute AS CR, Fričova 298, CZ-251 01 Ondřejov, Czech Republic ⟨ varady@asu.cas.cz ⟩

Jean-Claude Vial, Institut d'Astrophysique Spatiale, CNRS-Université Paris-Sud, Batiment 121, 91405 Orsay Cedex, France ⟨ jean-claude.vial@ias.u-psud.fr ⟩

Jaime Vilinga, Institut d'Astrophysique de Paris CNRS and UPMC, 98 Bis Bd Arago, F-75014 Paris, France ⟨ vilinga@iap.fr ⟩

Nikola Vitas, Dept. of Astronomy, Faculty of Mathematics, University of Belgrade, Studentski trg 16, 11001 Belgrade, Republic of Serbia; Sterrekundig Instituut, Universiteit Utrecht, P.O. Box 80000, NL-3508 TA Utrecht, The Netherlands ⟨ nikola@matf.bg.ac.yu, N.Vitas@phys.uu.nl ⟩

Angelos Vourlidas, Naval Research Laboratory, Code 7663V, 4555 Overlook Ave SW, Washington DC 20375, USA ⟨ vourlidas@nrl.navy.mil ⟩

Eberhard Wiehr, Ewaldstr. 75, D–37075 Göttingen, Germany, ⟨ ewiehr@astro.physik.uni-goettingen.de ⟩

Alfred de Wijn, c/o UCAR/HAO, P.O. Box 3000, Boulder, CO 80307-3000, USA ⟨ A.G.deWijn@astro.uu.nl, dwijn@ucar.edu ⟩

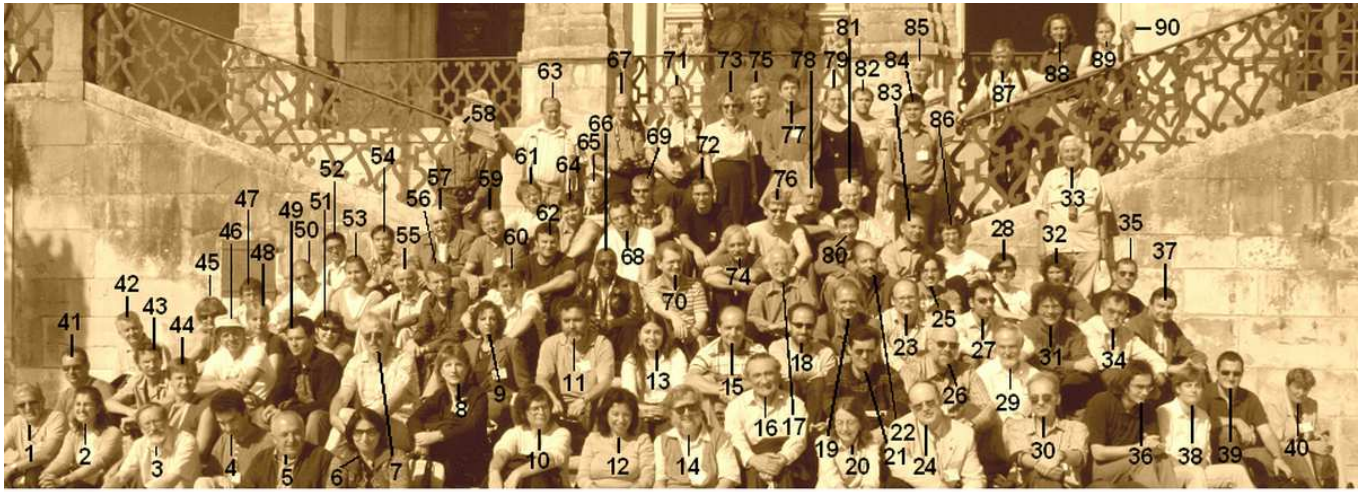

1. Jean-Claude Vial
2. Funda Bostanci
3. Petr Heinzel
4. Július Koza
5. Ali Ajabshirizadeh
6. Mrs. Ajabshirizadeh
7. Werner Curdt
8. Marta Rovira
9. Adriana Garcia
10. Georgia Tsiropoula
11. Pablo Mauas
12. Albina Severino
13. Clementina Sasso
14. Giuseppe Severino
15. Vincenzo Andretta
16. Zadig Mouradian
17. Rob Rutten
18. Nicolas Labrosse
19. Han Uitenbroek
20. Ilaria Ermolli
21. Hossein Ebadi
22. Boris Filippov
23. Carsten Denker
24. Daniel Myachin
25. Andrés Asensio Ramos
26. Angelos Vourlidas
27. Luca Belluzzi
28. Laura Merenda
29. Stuart Jordan
30. Juan Fontenla
31. Renzo Ramelli
32. Sonja Jejčić
33. Václav Bumba
34. Javier Trujillo Bueno
35. Ivan Dorotović
36. Jerome Bureau
37. Michal Sobotka
38. Gianna Cauzzi
39. Rafael Manso Sainz
40. Eva Marková
41. Kostas Tziotziou
42. Axel Hofmann
43. Pavol Schwartz
44. Arkadiusz Berlicki
45. Elena Dzifčáková
46. Pavel Kotrč
47. Felix Bettonvil
48. Alena Kulinová
49. Stanislav Gunár
50. Nikola Vitas
51. Larisa Kashapova
52. Hui Li
53. Asuman Gültekin
54. Jianping Li
55. Philippe Lamy
56. Alfred de Wijn
57. Serge Koutchmy
58. Boris Ioshpa
59. Hugh Hudson
60. Jorrit Leenaarts
61. Oskar Steiner
62. Bart de Pontieu
63. Teodor Pintér
64. Duncan Mackay
65. Jan Klimeš
66. Jaime Vilinga
67. Jean Aboudarham
68. Viggo Hansteen
69. Radek Melich
70. Pieter Thijssen
71. Netzach Farbiash
72. Øystein Langangen
73. Brigitte Schmieder
74. Mats Carlsson
75. Wolfgang Rammacher
76. Torben Leifsen
77. Arturo López Ariste
78. Egidio Landi Degl'Innocenti
79. Anna Pietarila
80. Mingde Ding
81. Alan Title
82. Peter Gömöry
83. Sami Solanki
84. Bhuwan Joshi
85. Eberhard Wiehr
86. Ruth Peterson
87. Horst Balthasar
88. Michal Varady
89. Jana Kašparová
90. Dirk Callebaut

Not present:
Eugene Avrett
Róbert Erdélyi
João Fernandes
Bernhard Fleck
Lyndsay Fletcher
Bernard Gelly
Robert Hammerschlag
Diane Paulson
Tomáš Prosecký
Günther Rüdiger
Artur Soares Alves
José Vaquero

Photo by João Fernandes, OAUC

The tower of Coimbra University

Part I

History

The Physics of Chromospheric Plasmas
ASP Conference Series, Vol. 368, 2007
Petr Heinzel, Ivan Dorotovič and Robert J. Rutten, eds.

Eightieth Anniversary of Solar Physics at Coimbra

Zadig Mouradian[1] and Adriana Garcia[2]

[1] *Paris-Meudon Observatory, France*
[2] *Coimbra Observatory, Portugal*

Abstract. A few years after the invention of the spectroheliograph by G. E. Hale and H. Deslandres, Prof. F. M. da Costa Lobo from the University of Coimbra decided to construct a spectroheliograph, among the first ones in the world, at the beginning of the twentieth century (1907). Prof. da Costa Lobo got in touch with solar astronomers in Meudon. With their help and in order to study the structure of the solar chromosphere, he built in Coimbra a spectroheliograph identical to that in Meudon. In turn, French astronomers asked to complete their own collection of observations with that of Coimbra. Thus a cooperative program between both institutions started, the French partners being H. Deslandres and L. d'Azambuja. Since then, the processing of observations and drawings of synoptic maps of solar activity have mainly been based on Meudon and Coimbra observational material. This collaboration is certainly among one of the longest in astronomical studies, and marked the beginning of European scientific collaborations, at least between Portugal and France.

1. About the Invention of the Spectroheliograph

The nineteenth century marks the real beginning of astrophysics. Contributing elements include the progress in laboratory and theoretical physics, the discovery of solar spectroscopy by Joseph Fraunhofer in 1814 and the invention of photography by Nicéphore Joseph Niepce in 1826.

Contemporary to these, the discovery of solar prominences during the total solar eclipses, is of utmost importance. Jules Janssen – the future founder of Meudon Astrophysical Observatory – decided to study the chemical composition of solar prominences during the total solar eclipse of August 18$^{\text{th}}$, 1868 at Guntoor (India). For this observation, Janssen used a direct vision spectroscope (Fig. 1) manufactured by the Parisian optician Hofmann (Janssen 1862). During the eclipse, Janssen discovered that the prominence spectrum showed bright lines of the Ballmer series of hydrogen. Stimulated by the view of prominences, Janssen observed until October 4$^{\text{th}}$ and showed the possibility of observation of solar structures without solar eclipes, by scanning the limb and the disk with the slit of his spectroscope (Janssen 1868). For a better view of the intensity variation of spectral lines, he isolated these with a second slit parallel to the spectral lines. Moreover, he made possible the rotation of the spectroscope all around the solar limb, for an easier search of prominences. Janssen gave the principle of what will be the spectrohelioscope, in a report to the French Academy of Sciences (Janssen 1869). We note that during the IGY (1957–58), Janssen's type spectrohelioscope, a Zeiss Co. production, was in use (Fig. 2). About Janssen's invention, G. E. Hale wrote: *"The establishment of a national*

Figure 1. J. Janssen's direct-vision spectroscope (courtesy F. Launay).

astrophysical observatory by the French government was a natural sequel to the able work of M. Janssen at the total solar eclipse of 1868. The discovery in that year of a method by which the spectrum of the chromosphere could be observed in full sunlight created the greatest enthusiasm, and the spectroscopic study of the Sun was undertaken in many European and American observatories" (Hale 1899). Later on, from this idea emerged the construction of the first spectroheliograph independently by G. E. Hale from Kenwood Observatory in 1891 and by Henri Deslandres from Meudon Observatory in 1892. They introduced a linear scan of the solar image and of the photographic plate settled behind the second slit. In connection to this, H. Deslanders wrote: *"...chaque jour, dans plusieurs Observatoires, on reléve par la méthode de M. Janssen, la chromospère et les protubérances, mais avec l'oeil seulement"*, and continued: *"Or j'ai appliqué la même méthode dans une région du spectre, qui est ou peu visible ou invisible, mais facile à photographier, et qui comprend le bleu, le violet et une partie de l'ultraviolet invisible jusqu'à* λ 380*"* (Deslandres 1891) (Fig. 3).

Consequently, solar physics was provided with a basic and powerful instrument providing the possibilities for new and important discoveries in the field of physical constitution of the solar atmosphere.

One can say that at the beginning of the twentieth century systematic observations of the chromosphere started, whereas coronal observations still remained in the domain of total solar eclipses, until the invention of the coronograph by B. Lyot (Lyot 1932). The importance of the spectroheliograph is revealed by the construction of at least 16 units, in the first half of the twentieth century (Table 1).

Figure 2. Janssen type spectrohelioscope for prominence observation (courtesy Bucharest Observatory).

At the same time, solar astronomers initiated the international collaboration. G. E. Hale mentioned: *"At the congress held in Paris, in 1887, ... there was some discussion of inaugurating co-operative investigations of an astrophysical nature..."* and added: *"More recently, a solar commission ... recommended that a general plan of solar research be undertaken"* (Hale 1904).

2. Solar Astrophysics in Coimbra

In 1907, after visiting some of the most important European observatories, Prof. da Costa Lobo from Coimbra University decided to build a spectroheliograph in Coimbra. H. Deslandres offered his assistance and offered the layout of the new spectroheliograph under construction in Meudon. At that time, he was finishing the settling of his new instrument, which is still in operation today. In 1912 started the construction of the elements of the Coimbra spectroheliograph, identical to that of Meudon.
The First World War stopped the efforts in astronomy and all possible collaborations. After the end of this big human disaster, the construction of the spectroheliograph resumed and finally finished after an interruption of 11 years. At that time, at Meudon Observatory, the young assistant of H. Deslandres, L. d'Azambuja became his main collaborator and, shortly after, the chief of Solar Department (Fig. 4).

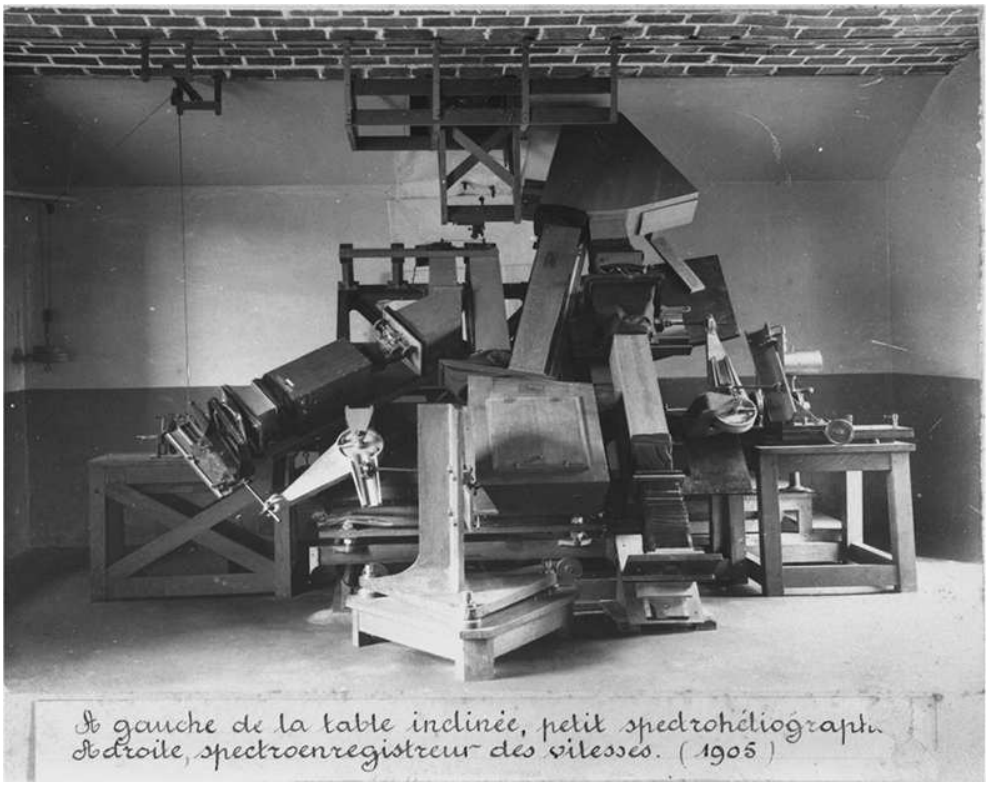

Figure 3. The "Petit Siderostat" solar laboratory at Meudon Observatory in 1905. On the left side the spectroheliograph, on the right the velocity recorder.

Table 1. Spectroheliographs in the world before 1950, compiled from R. Coutrez in *"The Sun"* by G. Kuiper (ed.), 1953.

		Observatory	Country
1	1904	Kodaikanal	India
2	1908	Meudon	France
3	1908	Mt. Wilson	USA
4	1908	Ebro	Spain
5	1911	Arosa	Switzerland
6	1911	Kodaikanal	India
7	1911	Madrid	Spain
8	1920	Mitaka	Japan
9	1925	Arcetri	Italy
10	*1907-26*	*Coimbra*	*Portugal*
11	1935	McMath-Hulbert	USA
12	1942	Wendelstein	Germany
13	1943	Freibrug	Germany
14	1944	Ikomasan	Japan
15	1948	Simei	Ukraine
16	1948	Stockholm	Sweden

Figure 4. H. Deslandres and L. d'Azambuja, about 1903.

Lucien d'Azambuja's (1884–1970) grandfather Diego was a native of Azambuja, a town north of Lisbon. L. d'Azambuja started to work in the Meudon Observatory at 15, as a "cleaner of spectroheliograms". Simultaneously, he continued to study till he obtained his doctorate degree from Paris University (1930) and finished his carrier as head of the Meudon Observatory, which had meanwhile been attached to the Paris Observatory.

Different firms contributed to the construction of Coimbra's spectroheliograph. For instance, the coelostat was built in France by engineer Prin, the objective of the telescope by the optician Jobin and the power units by Carpentier Co. Germany's Zeiss Co furnished the dispersing prisms for K line observation. The Institute of Superior Technique in Coimbra and the observatory workshop also manufactured some other pieces of the spectrograph. Finally, the components were assembled and the hopes became reality on April 12^{th}, 1925

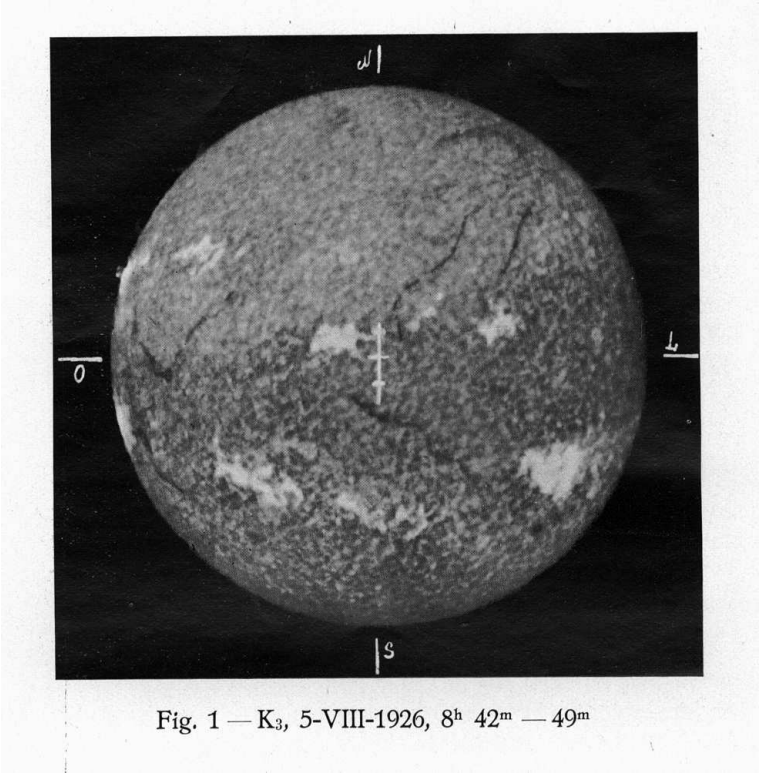

Figure 5. The K_3 spectroheligram is showing plages and filaments, as well as a small flare on east limb.

when the first spectroheliogram was obtained. On January 1st, 1926 started the program of solar chromospheric observations at Coimbra Observatory, using the Ca II K_3 line. Shortly after, K_{1V} and later on the Hα images were added to the program. Figure 5 shows one of the K_3 images from the beginning of observations. An important characteristic of Meudon and Coimbra instruments is the large dimension of solar images (85 mm diameter), which favors high spatial resolution.

The Coimbra and Meudon spectroheliographs being built with the same plans, all components are identical and interchangeable and this characteristic was used to improve one or the other instrument.

At the beginning the spectroheliograph was located within the Geophysical Institute of the University of Coimbra. In 1966, Prof. Dr. Simoes da Silva, the Director, decided to move the spectroheliograph to Santa Clara, where the observations started on April 10th, 1968 (da Silva 1968).

We can probably say that the collaboration between Coimbra and Meudon Observatories is among the first and longest scientific programs, long before the birth of the idea of a European union.

3. The Use of Spectroheliograms

What were the scientific programs of observation? Once more Coimbra and Meudon were in agreement; they decided to follow the solar activity through the physics of active regions and of filaments from a complementary point of view. Coimbra opted for short time (daily and monthly) and Meudon for long time (cyclic) evolution studies of solar activity parameters.

The observations cannot always be performed on a daily basis, principally on account of meteorological conditions; consequently the days off must be filled. The best solution is to mutually complete the collection of spectroheliograms. Coimbra and Meudon Observatories are not far in longitude, therefore they have almost the same window of observation, but they are not close enough to have the same type of weather at the same time. In the last years, around 20 to 25% of Meudon collection of solar images are complements from Coimbra. In the end, less than 10% of the days are left without data. The observation instruments being identical, the spectroheliograms can by immediately used, without adjustment. Each staff use both these collections of solar images in its proper way.

3.1. Solar activity analysis at Coimbra

The important parameters of solar activity were measured on daily spectroheliograms: as position, dimension, number of structures, type and evolution of four principal structures: sunspots, plages, filaments and prominences. They were tabulated and graphically represented accompanied by some geophysical parameters, Coimbra staff being always sensitive to solar–terrestrial relationships (da Costa Lobo 1929b).

Towards the limb of the sun, the shape of structures changes by foreshortening. Consequently the images must be corrected to follow in good condition the development of features during the passage over the solar disk, from East limb to West. This means that the spherical surface of the sun must be transformed into a flat surface in rectangular coordinates. Prof. da Costa Lobo proposed an original solution: to divide the solar chromospheric image in 36 equal-angle sectors in a radial disposed belt, which peaks are in the center of the solar disk, where image distortion is zero (da Costa Lobo 1929a). The width of each sector is so that the inside latitude variation is negligible. In this way the sphere is brought to a flat surface; the result resembles to the shape of a rose window from gothic churches (Fig. 6). This method was also temporarily adopted for the Meudon Observatory analysis (Deslandres 1929).

The daily parameters of solar activity measured on spectroheliograms were published in the volume I of "Annais do Observatório", starting from 1929. This contains data of the same year and continues until Volume XVI. This constitutes a complete and homogeneous summary of solar activity for this period. Data publication was initiated by Prof. da Costa Lobo and continued by Dr. M. dos Reis, the next director.

Prof. da Costa Lobo invented a second device for the reading of the position of solar structures on spectroheliograms, giving higher precision (0.1°) and ease of use. The device is a sphere provided with a metallic spherical triangle, with two mobile sides, in order to measure directly the solar heliographic coordinates (Fig. 7).

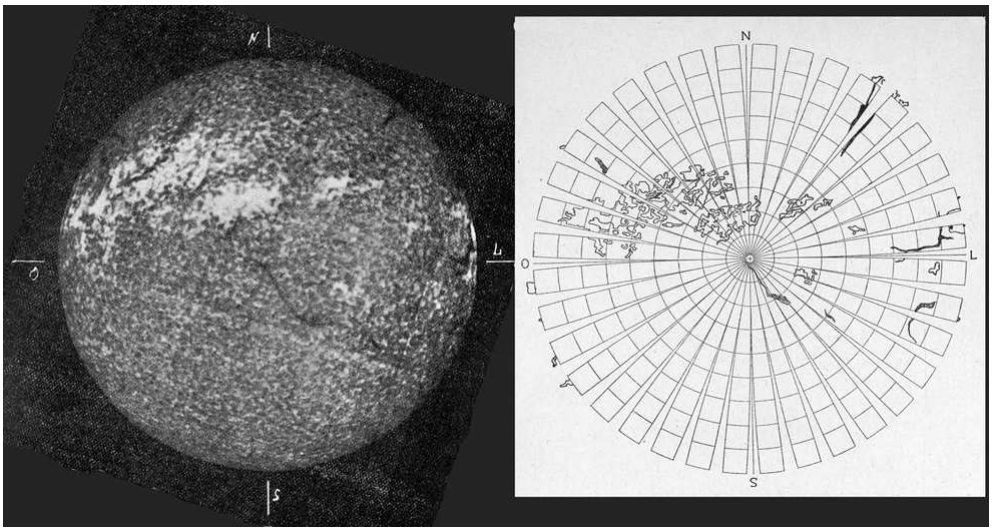

Figure 6. Hα spectroheliogram and corresponding plane transformation.

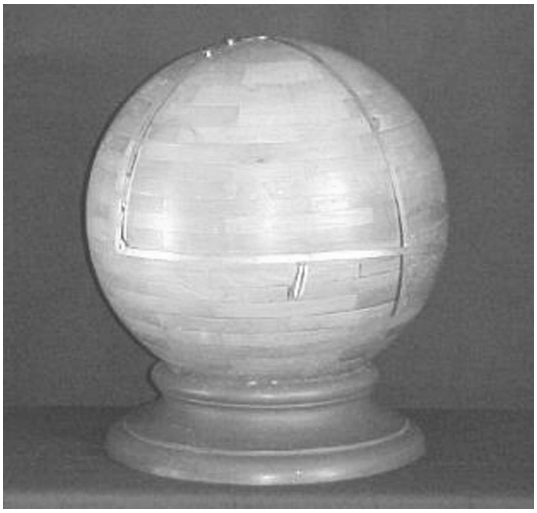

Figure 7. A sphere used for the measurement of Solar coordinates.

3.2. Solar activity analysis at Meudon

In 1908 began in Meudon Observatory the systematic daily observations of the Sun by the spectroheliograph. The three well known series of Meudon chromospheric images in the Hα, K_3 and K_{1V} features, only started in 1919, after the end of the First World War, by d'Azambuja and his assistants. These observations are still continuing with the same instrument, in order to keep the homogeneity of the solar image collection. The Meudon spectroheliograms, completed with those from Coimbra, form the Meudon collection of solar chromospheric

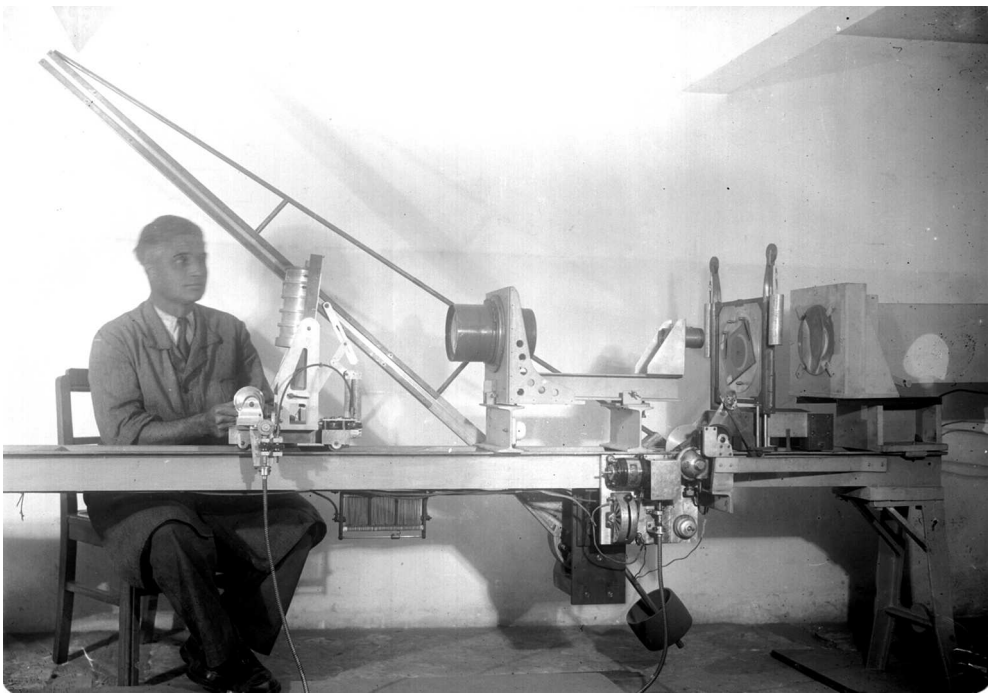

Figure 8. R. Servajean's optical anamorphoser with M. Brebion, the mechanic in charge of building the device.

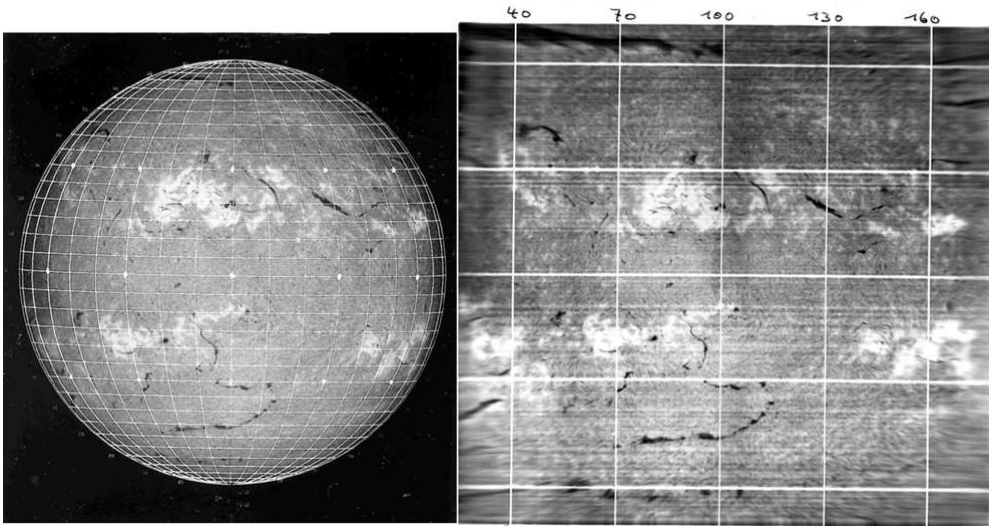

Figure 9. A Hα spectroheliogram and its anamorphosed image.

images. During the periods when the Coimbra spectroheliograph was not in operation, complements were asked to other observatories, but this introduced

additional adjustments that damaged the quality of images. During the Second World War, the observations were not interrupted in Meudon, thanks to K. O. Kiepenheuer, who provided the necessary photographic plates for spectroheliograph, allowing solar watching to continue.

In 1928, L. d'Azambuja started publishing synoptic maps (Deslandres & d'Azambuja 1913; d'Azambuja 1921) in order to give a general and condensed view of solar activity for each Carrington rotation. These maps were in cylindrical coordinates (d'Azambuja 1928). At the beginning, the positions and contours of structures on the solar images were read with a coordinate diagram. In 1950, R. Servajean invented the "anamorphoser" (Fig. 8), a unique instrument which transforms the image of a spherical surface into a flat one (Fig. 9) (Mouradian 1998). The anamorphoser was basically a photographic differential enlarger. By using this device, the solar structures were directly drawn from the anamorphosed image, which really simplified the production of synoptic maps. In the case of use of Coimbra photographic plates, these were introduced in the anamorphoser without any adjustment, contrary to those of other origin.

4. International Collaboration of Coimbra Observatory

Coimbra Observatory collaborations with other astronomical institutions take many aspects:

- Coimbra Observatory publication of solar data was in *"Annais do Observatório Astronómico da Universidade de Coimbra – Fenómenos Solares", Imprensa da Universidade, Coimbra*, from 1929 to 1943.
- In 1953 started the publications of *"Comuicações do Observatório Astronómico da Universidade de Coimbra", Seção de Impressão do Obervatório Astronómico de Universidade de Coimbra*. This issue is composed of a series of scientific articles in different domains of astrophysics. Here one can also find also some papers by Belgian and French authors.
- Beginning from 1931, Coimbra contributed to *"Bulletin for character figures of solar phenomena"* published by the Eidgenössische Sternwarte (Zürich).
- From January 1st, 1980 complementary observations were systematically exchanged between Coimbra and Meudon which improved the making of *"Synoptic Maps of Solar Activity"*.
- Another form of collaboration is the publication of numerous co-author articles.

We note that, in order to honor Prof. da Costa Lobo, the French Academy of Sciences invited him as a guest to the July 11th, 1927 session. Through H. Deslandres, Prof. da Costa Lobo presented to French Academy of Sciences a number of scientific reports on his contributions to solar physics, between 1912 and 1927. All these reports are printed in *"Comptes Rendus de l'Academie des Sciences de Paris"*.

5. The Present and the Near Future

Coimbra and Meudon spectroheliographs were built with the best techniques and material of that time, but in 1980 it became urgent to renovate them without changing the optical layout, in order to maintain the homogeneity of the collections of spectroheliograms. The renewing was undertaken under the direction of G. Olivieri helped by A. Garcia and I. Bualé. After the renewing of scanning components, new optical pieces (especially computed lenses, made with modern glass) replaced the old ones. For instance, the lenses were computed in order to have the same focal length in Hα and K lines. New dispersion grating and higher quality slits were set up. The observation process is now completely under computer control and all these changes contribute to producing images of higher quality and in a much shorter time. In the same, human cooperation resumed. In 1972 M. Pinheiro and later on A. Garcia stayed in Meudon Observatory and I. Bualé and G. Olivieri went to Coimbra Observatory several times (see on this issue the paper of I. Bualé et al.).

The last instrumental improvement was the change of receivers, by the use of a CCD camera with computer control, storage and processing of data. A. S. Alves, the present director of Coimbra Observatory, in collaboration with Ondřejov Observatory (Czech Republic), provided the spectroheliograph with digital devices in order to record observations. These constitute the digital archives of Coimbra. M. Klvaňa leads all these operations. An equivalent initiative was made for the Meudon spectroheliograph. These improvements simplify the image exchange. In Coimbra and in Meudon Observatories a real effort is now placed on digitalizing the whole collection of old photographic plates of solar images. Solar observations being digitalized, number of previous problems finds new solutions.

In 1990 in Meudon Observatory, a semi-digital processing method started for the analysis and drawing of synoptic maps of solar activity (Mouradian 1998), which continue the synoptic maps started by d'Azambuja. Once repetitive and tiring, these operations are now made by computer, under the supervision of an operator in case different options are available. This method furnished maps of each structure of solar activity (spot, plage, filament, prominence), which can be used separately or assembled. Using this process, digital maps of solar activity from 1998 to 2003 (`http://bass2000.obspm.fr/home.php`; Mouradian et al. 1998) have been published. A group of astronomers and computer engineers are now working on making a complete automatic program for reading and analyzing spectroheliograms and drawing the synoptic maps of solar activity (see on this issue the paper of Aboudarham et al.). As in the past, the new process will need to continue the collaboration between Coimbra and Meudon Observatories.

Acknowledgments. The authors are indebted to G. Olivieri, J. Fernandes, G. Servajean, I. Bualé, F. Launay as well as the Bucharest Observatory staff for important information and documents.

References

da Costa Lobo, F.M. 1929a, Comptes Rendus Acad. Sci. Paris, 189, 277
da Costa Lobo, F.M. 1929b, Annais do Observatório Astronómico da Universidade de Coimbra, Coimbra, Universidade de Coimbra, Tomo I

da Silva, A.S. 1968, Pub. Obser. Astro. Univ. Coimbra, Nr. 4
d'Azambuja, L. 1921, Comptes Rendus Acad. Sci. Paris, 173, 1450
d'Azambuja, L. 1928, Annales de l'Observatoire de Paris, Section d'Astrophysique de Meudon, 6, Fasc. 1.
Deslandres, H. 1891, Comptes Rendus Acad. Sci. Paris, 131, 307
Deslandres, H. 1929, Comptes Rendus Acad. Sci. Paris, 189, 277
Deslandres, H., & d'Azambuja, L. 1913, Comptes Rendus Acad. Sci. Paris, 157, 413
Hale G. E. 1899, ApJ, 10, 369
Hale, G. E. 1904, ApJ, 15, 306
Janssen, J. 1862, Comptes Rendus Acad. Sci. Paris, 55, 576
Janssen, J. 1868, Comptes Rendus Acad. Sci. Paris, 67, 838
Janssen, J. 1869, Comptes Rendus Acad. Sci. Paris, 68, 93
Lyot, B. 1932, Z. für Astroph., 5, 73
Mouradian, Z. 1998, in ASP Conf. Series, 140, ed. K. S. Balasubramaniam, J. W. Harvey & D. M. Rabin, Univ. Arizona, Tucson, 197
Mouradian, Z., Renié, C., & Zlicaric, G. 1998; 2000; 2003 Cartes Synoptiques de l'Activité Solaire, Publ. Obs. Paris, 8; 9; 10

The Physics of Chromospheric Plasmas
ASP Conference Series, Vol. 368, 2007
Petr Heinzel, Ivan Dorotovič and Robert J. Rutten, eds.

Improvement of the Coimbra Spectroheliograph (1988 – 1992)

I. Bualé, Z. Mouradian and B. Schmieder

LESIA, Observatoire de Paris, Meudon

Abstract. We summarize the parallel modernization of the identical spectroheliographs at Coimbra and Meudon.

The Coimbra and Meudon Observatories' spectroheliographs are identical. They were constructed with the same optical layout thanks to the scientific collaboration between F. da Costa Lobo of Coimbra University and H. Deslandre and L. d'Azambuja of Meudon Observatory. This collaboration started at the beginning of the twentieth century with the construction of the spectroheliograph of the Coimbra Observatory and still continues in taking daily solar observations (see the preceding paper by Mouradian & Garcia).

This long and continuous monitoring of solar activity through spectroheliograms in Ca II K_3, K_{1V} and Hα provides solid archives of solar activity for research. These three spectral lines cover the whole chromosphere. The spectroheliogram archives are very useful for studies of long-term evolution of solar activity and solar-terrestrial relationships.

Figure 1. *Left*: solar laboratory at Coimbra. *Right*: spectroheliograph building at Meudon.

After intensive use for over 80 years, both the Coimbra and Meudon spectroheliographs needed revision and improvement of all key components, both optical and mechanical. They were replaced with modern units during 1988–1992 by G. Olivieri and I. Bualé from Meudon, and A. Garcia and M. M. Pinheiro from Coimbra. The coelostat, telescope and spectroheliograph optics were replaced with new modern material. Thus, the coelostat mirrors are now of low-expansion Zerodur glass, from the Schott Co. The telescope objective, the collimator and the spectrograph objective are specifically computed lenses, with the same focal length for Hα and Ca II K. This advance in the design of spectroheliographs

Figure 2. *Left*: The solar group of Coimbra Observatory. *Right*: time off – M. Pinhiero offering figs from the Coimbra observatory garden.

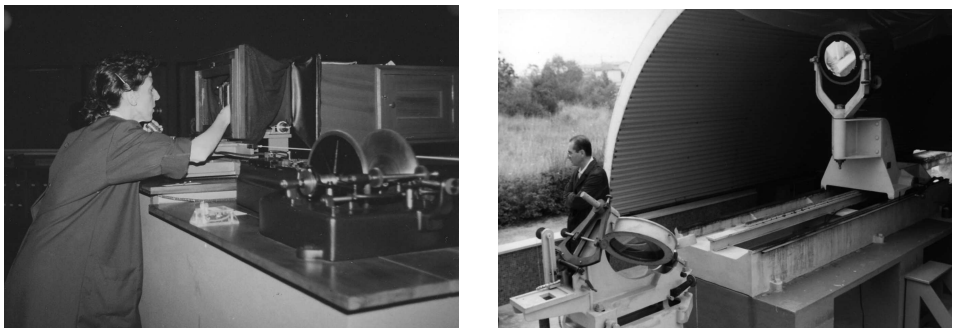

Figure 3. *Left*: A. Garcia adjusting Hα. *Right*: G. Olivieri near the primary coelostat mirror.

eliminates the need for focal length adjustments during the observing. It also substitutes the old three-prism-plus-grating dispersion system by a single new blazed grating for the entire spectral domain. Of course the mechanical mechanism of the spectroheliograph for the rotation of the primary mirror of the coelostat, solar-image scanning, and the movement of the photographic plate were also renewed. Recently, the recording system at Coimbra was also updated with a computer-guided CCD camera. This improvement was undertaken by M. Klvaňa of the Ondřejov Observatory.

Also in the Meudon Observatory the spectroheliograph was entirely revised and a system of digital recording camera came into action from 2000, due to G. Olivieri.

The Coimbra–Meudon collaboration is also very important in order to complete the archive of solar activity at Meudon. It is planned to archive all Coimbra observations into the Meudon webserver Bass2000.

The Physics of Chromospheric Plasmas
ASP Conference Series, Vol. 368, 2007
Petr Heinzel, Ivan Dorotovič and Robert J. Rutten, eds.

Spectroheliographic Observations in Madrid (1912 – 1917)

J. M. Vaquero, M. C. Gallego, F. J. Acero and J. A. García

Departamento de Física, Universidad de Extremadura, Spain

Abstract. We have compiled information and data on solar spectroheliographic observations in Madrid during 1912–1917. We have created a database with information on 829 flocculi specifying heliographic position, dates of observation, angular velocity, and typology. We analyze the reliability of the data by reconstructing the butterfly diagram, active longitudes, and flocculi typology.

1. Introduction

The Madrid Astronomical Observatory was founded in the 18th century. During the first years of the 20th century, this observatory made an active program of solar observations (sunspots, prominences, solar corona during eclipses, solar spectroscopy, etc.). In 1911, the observatory bought a spectroheliograph (Ascarza 1912). The installation of this spectroheliograph was completed during the first months of 1912 (Ascarza & Tinoco 1915).

In this work we provide some information about the spectroheliograph of the Observatory of Madrid, and aim to show the reliability of the data obtained from 1912 until 1917. Wwe have constructed a database of the flocculi observed in Madrid described in Section 2. In Section 3 some final comments are given.

The spectrohelioscope of the Observatory of Madrid consisted of three fundamental parts (Fig. 1). The first is a polar heliostate with two flat mirrors of 0.2 m diameter. The second is a lens of 0.25 m diameter and 6.8 m focal length. The third part is the spectrohelioscope, with two slits of 75 mm length, twin collimator and camera lenses of 0.1 m diameter and 2.18 m focal length, and a flint prism of 90 degrees and 20 cm height. The solar image has a diameter of 64 mm. A detailed description is given in Iñiguez & Ascarza (1911).

At the end of 1910, the work on the installation of the spectroheliograph started. The pillars and the base to support and shelter the device were constructed. At the beginning of 1911 the installation of the instrument was started. The first photographs were obtained in June 1911. Nevertheless, until December 1911 the observations were not begun regularly. The largest problems of the installation were related to the convective currents that formed near the spectroheliograph mount and its surroundings.

The observing program consisted of photography of the Sun in the calcium K line and of analyzing the flocculi appearing on the photographs by calculating their heliographic positions and analyzing their aspect.

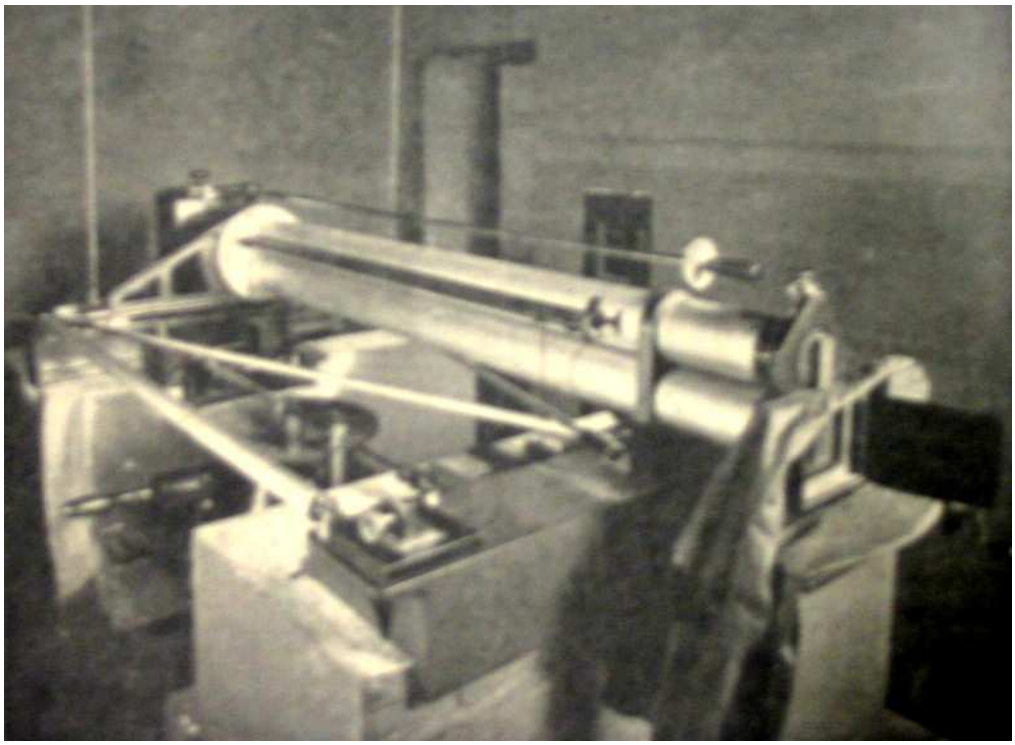

Figure 1. The Madrid spectroheliograph installed in 1911.

2. Database

We have created a database with information on 829 flocculi (heliographic position, dates of observation, angular velocity, and typology) from the spectroheliographic observations in Madrid during the years 1912-1917. This database is available by request to the authors.

3. Results

Figure 2 shows the butterfly diagram for the observed flocculi. During the years 1912 and 1913 one sees flocculi in very low latitudes, corresponding to solar cycle 15. In Fig. 2 flocculi appear also at high latitudes, getting down in latitude during the advance of solar cycle 16.

Figure 3 shows a histogram of the number of flocculi with respect to their solar longitude. During 1912–1917 the maximum number of focculi occurred around longitude 180°, the minimum around longitude 0°.

The observers in Madrid classified the flocculi according to condensation and intensity. For condensation they judged whether the flocculus was observed as a single, continuous, and compact surface or, on the contrary, whether the flocculus appeared fragmented, in several grouped areas, etc. With respect to condensation, they established the following categories: (cc) very condensed, (c)

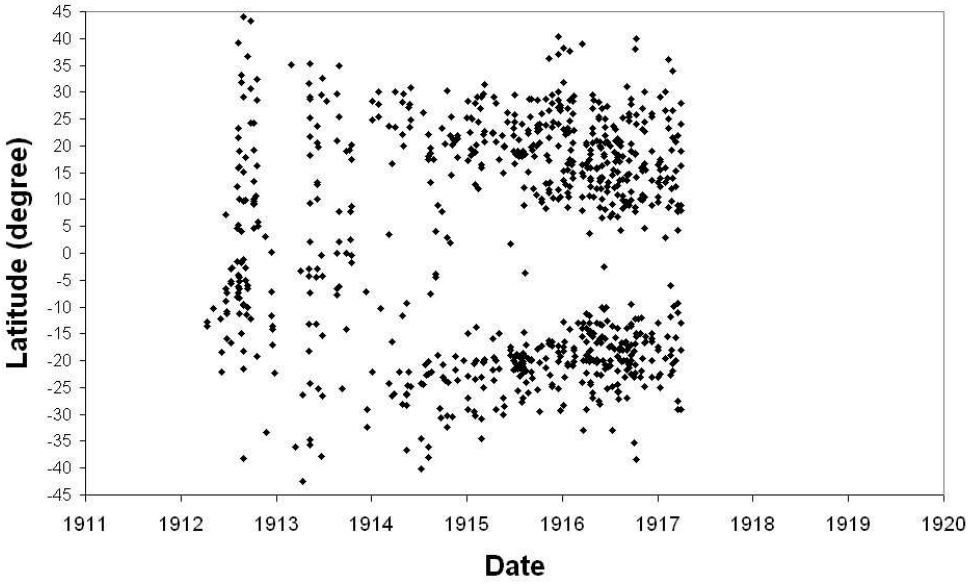

Figure 2. Butterfly diagram for 829 flocculi during 1912–1917.

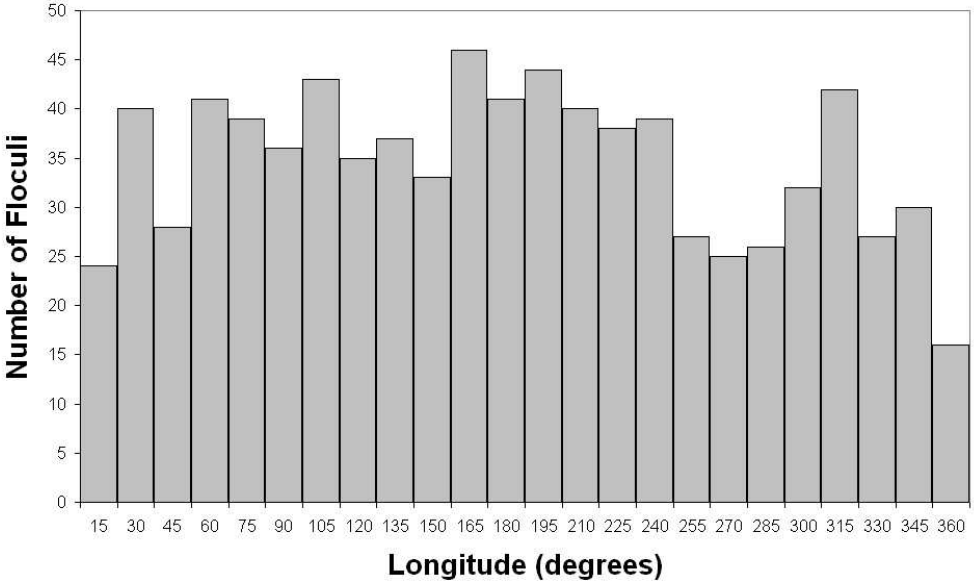

Figure 3. Histogram of the number of flocculi with respect to heliographical longitude during 1912–1917.

condensed, (s) subdivided, and (ss) very subdivided. With regard to the intensity of the flocculi, the observers established the following categories: (f) strong intensity, (ff) very strong intensity, (d) weak, and (dd) very weak. Figure 4 shows

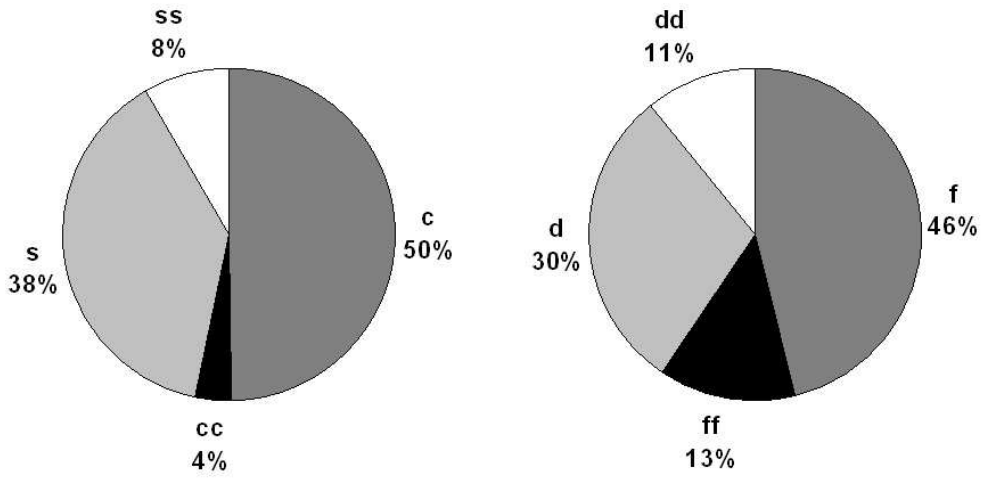

Figure 4. Distribution of floccular typology during 1912–1917 according to (left) their condensation and (right) their intensity.

the distribution of the different typologies of flocculi observed during 1912–1917. Flocculi with strong intensity and condensed are the most numerous.

4. Final Comments

In this work, we have tried to recover the observations carried out with the spectrohelioscope of the Observatory of Madrid during the beginning of the 20th century. So far we have processed the information from March, 1912 up to March, 1917. However, we have original observations until the year 1920. These observations can be useful to compare with observations of other spectroheliographs of this epoch and to fill gaps in the available time sequences of spectroheliographic observations during this decade.

Acknowledgments. This research has made use of the Astrophysics Data System (NASA). Support from the Universidad de Extremadura is gratefully acknowledged.

References

Ascarza, F., & Tinoco, J. 1915, Asociacion Española para el Progreso de las Ciencias, III, 155

Iñiguez, F., & Ascarza, F. 1911, Anuario del Observatorio de Madrid, 1912, 269

Ascarza, F. 1912, Anuario del Observatorio de Madrid, 1913, 441

The Physics of Chromospheric Plasmas
ASP Conference Series, Vol. 368, 2007
Petr Heinzel, Ivan Dorotovič and Robert J. Rutten, eds.

ESMN in Memoriam (1998 – 2006)

Robert J. Rutten
Sterrekundig Instituut, Utrecht University, The Netherlands
Institutt for Teoretisk Astrofysikk, University of Oslo, Norway

Abstract. The EC-FP5 *European Solar Magnetism Network* (ESMN) was terminated during this conference. Together with its FP4 predecessor, the *European Solar Magnetometry Network* (ESMN), it funded 22 postdoc and 9 graduate-student appointments at nine solar physics groups in Western Europe, it enhanced Europe-wide collaboration in solar physics, and it contributed to the integration of East-European groups in West-European enterprises. Its unfortunate demise results from lack of further fortune in the FP6 lottery. The FP6-funded Utrecht-Stockholm-Oslo graduate school in solar physics represents offspring, the FP6 Solaire network is a partial replacement, and the EAST undertaking and pledge to build an EST is a most worthy FP7 stake. The EC's policy shifts from postdoc to predoc funding and from requiring (too) small to requiring (too) large consortia are criticized.

1. ESMN Start

The ESMN mission was "to integrate the development and usage of the European solar telescopes on the Canary Islands with space observation and data interpretation and theoretical analysis". In both proposals nice pictures of (not from) solar telescopes sold the message "exploit these investments". Both proposals adhered to, in what I regard as EC-speak writing contest plus political lottery rather than meritocratic peer-review selection (Rutten 2001):

> *"Parent birds preferentially feed those fledglings that open beaks widest, scream loudest, have the brightest throat marks, shake wings most frantic — because their own parental genes are biologically coded for long-term survival. Any money-dispensing authority in the EC is politically coded to support those endeavors that promise most advertisable successes, feathers in their cap. In this feeding dance the EC calls the steps; we have to shake and scream and paint our throats the way they like it. Hard-coded facts of life that lead to hard questions. In parlance: how to strategize priorities, facilitate empowerment, implement visioning? In plainer language: who does what where to maximize our take?"*

The size and constitution of the ESMN were dictated by the EC program constraints. In FP4 and FP5 these required that a network proposed to divide a limited amount (about 1.5 million Euro) during four years over a maximum number of groups from a maximum number of EC nations including "less favored regions", and do so in the form of postdoc salaries and interpartner travel. No money for computers or other hardware. The ESMN-2 partners were:

- Sterrekundig Instituut Utrecht
- IAC, La Laguna
- OAA, Florence
- Institute of Theoretical Astrophysics, Oslo
- Institute for Solar Physics, Stockholm
- Astrophysikalisches Institut Potsdam
- Observatoire de Paris, Meudon
- ESA Solar and Solar-Terrestrial Missions Division, Noordwijk
- Astronomical Institute, Ondřejov
- Astronomical Institute, Tatranská Lomnica
- Department of Astronomy, Eötvös University, Budapest,

whereas the ESMN-1 consisted of only the West-European groups above, with the OAC at Naples instead of the OAA at Florence.

These ESMN groups together represent a sizable part of groundbased European solar physics but obviously incompletely. Glaring absentees were the Kiepenheuer Institute and the Göttingen, Zürich, Toulouse (Pic du Midi), Sicilian and Greek solar physics groups within the original EC, and other Eastern-European groups than the three ESMN-2 ones. A network tying groundbased European solar physics together should have about two dozen partner groups.

In addition, there is no clear distinction between groundbased and space-based solar physics; the ESMN was strongly oriented to the Canary Island telescopes but also a large user of SOHO and TRACE. Adding space-oriented groups (Lindau, Orsay, Culham, Ukkel, etc.) would bring the group total to about thirty. Complete solar physics coverage would then add theory-oriented groups (St Andrews and other UK groups, Leuven, etc) as well. Thus, the "European solar physics research area" encompasses roughly 40 groups.

2. ESMN Feats

The ESMN-1 hired as "Fellows": Pit Sütterlin, Olaf Dittmann, Cristina Gabellieri, Laura Merenda, Klaus Pushmann, Regina Aznar Cuadrado, Carla Gil, Jack Ireland (twice), Etienne Vogt, Colin Rosenthal, Bertil Dorch, Boris Gudiksen, Karin Muglach, Marcelo Lopez Fuentes, Kostas Tziotziou, Eoghan O'Shea, and Axel Settele.

In the second round, the ESMN-2 fellows were Kostas Tziotziou (again), Arek Berlicki (twice), Moncef Derouich, Laura Merenda (again), Katja Janssen, Andrés Asensio Ramos, Luc Rouppe van der Voort, Kai Langhans, Monica Sánchez Cuberes, Peter Gömöry, Jaroslav Dudík, and Stéphane Régnier.

The ESMN produced over 350 ESMN-acknowledging papers, met all over the world in some official and many more non-official meetings, was involved in many dozens of multi-telescope observing campaigns, and ran or participated in six schools (the photograph in Fig. 1 is from the last one). Of course, many of these activities would also have taken place without an ESMN, but it is fair to claim that the ESMN funding indeed contributed to the intensification of solar-physics collaborations across Europe.

Figure 1. The ESMN at Tatranská Lomnica in November 2004. The attire, custom-designed by Kostas Tziotziou and Frans Snik, is inspected by schoolmasters Aleš Kučera (leftmost) and myself (rightmost). Jacques Beckers is rightfully at the center: he proposed and orchestrated the final session in which all students were split into four observatories, directed by Katja Janssen, Kai Langhans, Monica Sánchez Cuberes, and Andrés Asensio Ramos (for example the KAI = Kai's Astronomical Institute). They got the task to compete for EC funding with detailed plans for the future. Mats Carlsson and Bernhard Fleck were the stern EC evaluators and complained conformally about over-optimistic budgets and gender aspects. I was the EC but behaved non-conformally by funding all four because their plans were so good. Photograph: Jaroslav Ambróz.

3. ESMN End

Unfortunately, our ESMN-3 proposal did not make it through the EC's last-call FP6 network selection. Fortunately, our friendly-competitor Solaire did. To some extent this is a descendant of the earlier PLATON network which targeted MHD theory more than observation and overlapped partially with ESMN-1 (we ran a joint school at Dwingeloo). Five ESMN partners are now Solaire partners.

Can we try again? No, since FP7 targets much larger research consortia, at the size where these become only bureaucratically existing rather than as true research collaboration. As noted above, our "research area" is about 40 teams, each characteristically made up by 2-6 tenured researchers located at or near a university, a national research institution, or ESA. Ours is a relatively small field but the ESMN covered only about a quarter of it; the same holds for Solaire. Now, in FP7, the EC desires research conglomerates covering complete disciplines via national institutions (ASTRONET). Our research area was too large for FP4 through FP6 but is too small as an FP7 entity. The EC prefers that all the fish it should hatch or catch is of a single measure.

The fish that we should catch from the EC is funding for EAST to build the EST, better sooner than later. However, sweeping this sweepstake is not easy. The question is again: *who does what where to maximize our take?*

A direct descendant spawned by the ESMN is USO–SP, the "Utrecht–Stockholm–Oslo collaboration in Solar Physics" which was formally established

by these three ESMN groups and then cornered an FP6 EST grant for graduate student training, the "USO graduate school in solar physics" coordinated by Dan Kiselman. It funds only predoc training, no postdocs.

FP7 caps this post-to-predoc trend with its "Initial Training Networks", much more like FP6 EST than FP6 RTN networks. The obvious political choice for "the younger the better" in migrating the next generation into non-nationalistic Europeans is easily made by Brussels bureaucrats, but they forget that recruiting abroad with promise of quality as principal criterion is much harder for fresh graduates. Europe should adopt the practices through which the better US graduate schools select and attract the best PhD students: centralized GRE or comprehensive physics examinations and in-depth interviews. The US does not only spend more on higher education but also migrates the best students, including from Asia, to the best universities. In Europe only the most famous UK universities have similar attractivity and apply similar weeding. Across much of Europe, the quality of high-school math and physics deteriorates to the American level, requiring remedial teaching at universities. The EU's quest for a knowledge economy needs much better mechanisms than what FP7 offers now.

4. ESMN Epitaph

So was it worth it? The claim has been made that the best to come out of the ESMN was Boris Gudiksen's thesis. For me, the motivation to start the ESMN was that I desperately needed outside success to enhance my local standing in battling for DOT survival, fighting imminent DOT bankruptcy right after its inauguration by Crown Prince Willem Alexander (1997). It worked, but in addition the ESMN enabled me to bring Pit Sütterlin into the DOT team. Pit not only brought his version of the Göttingen speckle code but then used it to turn the DOT from open-principle demonstrator into a prolific producer of tomographic solar movies in which seeing no longer kills the viewing. Without exception, all observations in the DOT database at `http://dotdb.phys.uu.nl/DOT` have been taken by him. Thus, the DOT became a productive telescope thanks to the ESMN[1]. *Yes, it was worth it.*

Acknowledgments. The ESMN was funded by the EC in contracts ERBFMRXCT980190 and HPRN-CT-2002-00313. I am grateful to my ESMN partners for making the ESMN a productive undertaking (excepting some re yearly reporting). Pieter Thijssen has been an invaluable source of advice next to his efficient and expert ESMN administratorship. It was a pleasure to work with Stephen Davies as EC program officer. Horst Balthasar suggested to conclude the ESMN during this conference.

References

Rutten R. J., 2001, in Solar Encounter, Procs. First Solar Orbiter Workshop, ESA SP-493, Estec, Noordwijk, 353

[1]DOT bankruptcy is imminent again, see Hammerschlag et al. on p. 573 ff in these proceedings.

Part II

Structure and Dynamics of the Solar Chromosphere

The Physics of Chromospheric Plasmas
ASP Conference Series, Vol. 368, 2007
Petr Heinzel, Ivan Dorotovič and Robert J. Rutten, eds.

Observing the Solar Chromosphere

Robert J. Rutten
Sterrekundig Instituut, Utrecht University, The Netherlands
Institutt for Teoretisk Astrofysikk, University of Oslo, Norway

Abstract. This review is split into two parts: one on chromospheric line formation in answer to the frequent question "where is my line formed", and one presenting state-of-the-art imagery of the chromosphere. In the first part I specifically treat the formation of the Na D lines, Ca II H&K, and Hα. In the second I show DOT, IBIS, VAULT, and TRACE images as evidence that the chromosphere consists of fibrils of intrinsically different types. The straight-up ones are hottest. The slanted ones are filled by shocks and likely possess thin transition sheaths to coronal plasma. The ones hovering horizontally over "clapotispheric" cell interiors outline magnetic canopies and are buffeted by shocks, most violently in the quietest regions.

In the absence of integral-field ultraviolet spectrometry, Hα remains the principal chromosphere diagnostic. The required fast-cadence profile-sampling imaging is an important quest for new telescope technology.

1. Introduction

An excellent review of observational chromospheric issues and research is given by Philip G. Judge in the 2005 NSO/Sacramento Peak workshop proceedings (Judge 2007; `http://download.hao.ucar.edu/pub/judge/judge_ws23.pdf`). His major conclusion is that while chromospheric magnetism smoothes out with height, its thermal fine structuring remains tremendous. Here, I tread less wide by concentrating on diagnostics of this fine structure, in particular those in the visible. Long-duration observing with Hinode's SOT and higher-resolution observing exploiting adaptive optics at existing telescopes (DST, VTT, SST) and hopefully at upcoming telescopes (GREGOR, NST, EST, ATST) employing Ca II H&K, the Ca II infrared lines, and above all the H I Balmer lines are likely to provide new high-resolution vistas and understanding of the chromosphere the coming years while, unfortunately, ultraviolet spectrometry lags behind. I split the discussion into a didactic part on chromospheric line formation and a morphological part on chromospheric scenes, concluded by a list of speculations and a brief discussion of research approaches.

2. Chromospheric Line Formation

As author of lecture notes on radiative transfer (Rutten 2003a) I am often asked how high some line is formed. In this section I follow the inspiring "Fads and Fallacies" example of Athay (1976) to illustrate that the question is only answerable for numerical models or simulations, not for observations.

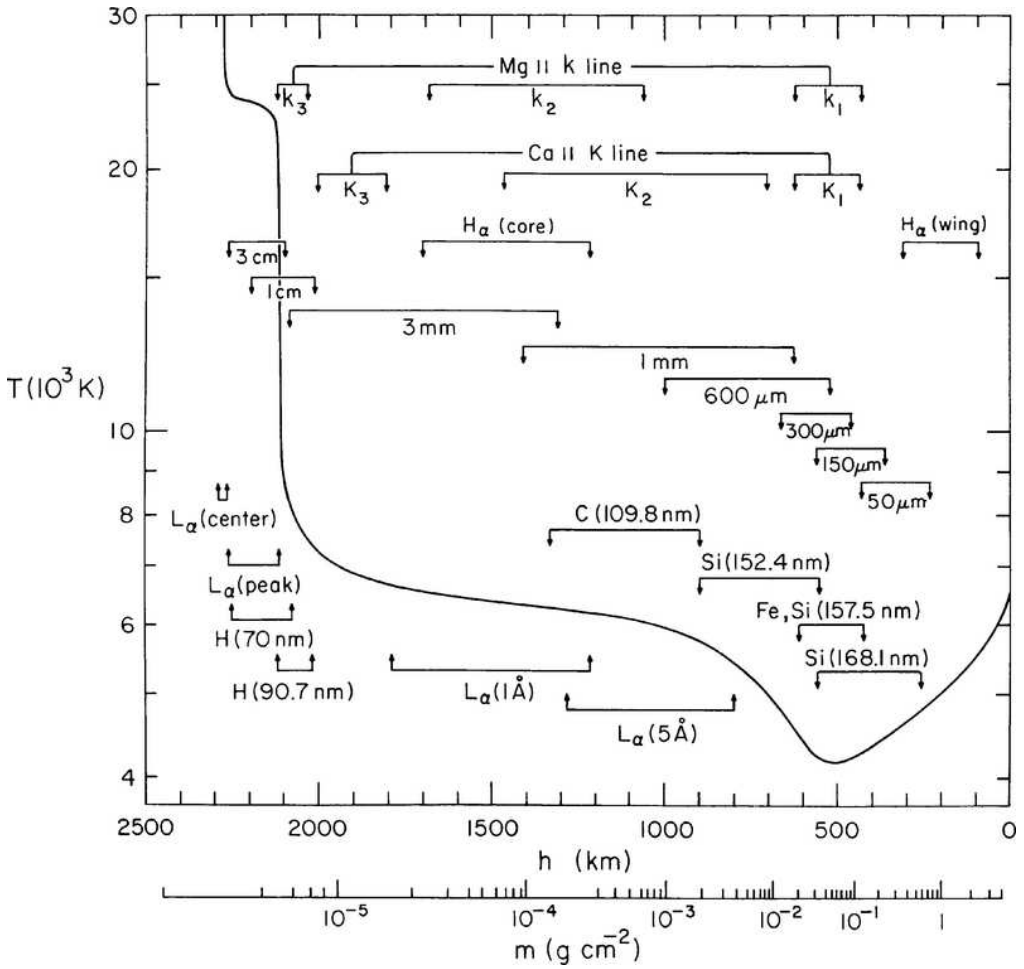

Figure 1. Classic VAL3C height-of-formation graph from Vernazza et al. (1981). The bars span 90% of the area under the intensity contribution functions $\mathrm{d}I/\mathrm{d}h$ plotted for many wavelengths in Fig. 36 of the same paper.

The answer evolved over the years from "weighting functions" (e.g., Pecker 1951, Unsöld 1955) through "line-depression contribution functions" (e.g., Edmonds 1967; Gurtovenko & Ratnikova 1974; Magain 1986; Kucera et al. 1998) to "response functions" (e.g., Mein 1971; Beckers & Milkey 1975; Caccin et al. 1977) which became the backbone of least-square-fit inversions with the SIR code of Ruiz-Cobo et al. (1990, 1992) and its companions (see del Toro Iniesta 2003; Cabrera Solana et al. 2005). I discuss the answer first in the context of solar-atmosphere model evolution, and then for some specific lines.

2.1. HOLMUL, SIR, VAL3C, RADYN, CO^{5}BOLD chromospheres

For decades already, stellar abundance determiners prefer the HOLMUL model of Holweger & Müller (1974) in the classical Unsöld "fine analysis" recipe of computing stellar line formation as plane-parallel hydrostatic LTE with best-fit microturbulence and van der Waals damping enhancement but no other pa-

rameters (cf. Rutten 1998, 2002). The HOLMUL temperature stratification is essentially Holweger's (1967) empirical fit to many observed optical lines, from iron in particular, assuming LTE excitation and ionization. Actual iron-line NLTE departures (mainly smaller opacity due to overionization for weaker Fe I lines, source function deficit due to scattering for the strongest Fe I lines, and source function excess for pumped subordinate Fe II lines) happen to largely cancel in this procedure over much of the optical spectrum (Rutten & Kostik 1982), so that the model performs very well in reproducing any line similar to the ones from which it was made, under the same assumptions. It does not possess a chromospheric temperature rise because iron lines exhibit no self-reversals.

The Holweger technique of empirically establishing a temperature-height stratification by fitting excitation temperatures and optical depth scales to observed lines assuming LTE is automated in the SIR code for Stokes evaluation. It effectively constructs such Holweger models per pixel. They won't have chromospheres either, except when inverting the Mg I 12-micron lines which do show conspicuous reversals – but then wrongly because their emission peaks are actually photospheric NLTE ones (Carlsson et al. 1992). Another key inversion assumption is that solar stratifications vary smoothly with height, as cubic splines through only a few sampling nodes. This is a dangerous assumption when large fluctuations occur, such as the shocks making up umbral flashes (cf. Socas-Navarro et al. 2001).

The VAL3C model of Vernazza et al. (1981) differs from the Holweger approach in primarily fitting continua rather than lines but extends much higher by including the full ultraviolet, necessitating detailed NLTE evaluation of many bound-free edges and PRD evaluation of Ly-α. This model is elevated to stellar status ("the star VAL3C") in my lecture notes because it represents a complete self-consistent numerical simulation of the radiation from a time-invariant plane-parallel star which strictly obeys all standard equations in my course (plus some more, because the latter do not yet treat PRD whereas the Avrett-Loeser PANDORA code does) while resembling the sun (at least spectrally) in having a chromosphere and some sort of transition region to a coronal regime. The magnificent VAL3 paper adds a superb collection of informative graphs diagnosing for many frequencies how this star radiates, where its radiation originates, and breaking down its radiative energy budget. The FALC model of Fontenla et al. (1993) and more recent ones by e.g., Fontenla et al. (2006) represent updates of the approach with a similar code. Figure 1, perhaps the best-known graph of solar physics, shows heights of formation for many VAL3C diagnostics. In the star VAL3C these are rigorously correct. Are they in the sun?

For example, the chromospheric dynamics analysis of Bloomfield et al. (2004) relied on the VAL3C height difference between Hα and Ca II K core formation, the latter higher than the former, to estimate upward propagation speeds and so assign particular MHD wave modes and appropriate mode conversions to a few observed oscillation wave trains through wavelet analysis of network bright points in filtergrams. The approach is interesting but the reliance on VAL3C formation heights, with Ca II K higher up than Hα, is naïve even if purely radial structures were indeed observed in both lines (see Fig. 6). I feel that numerical wave simulation comparing detailed Hα and Ca II K line synthesis using a detailed model of such a structure is a sine-qua-non step in such mode identification.

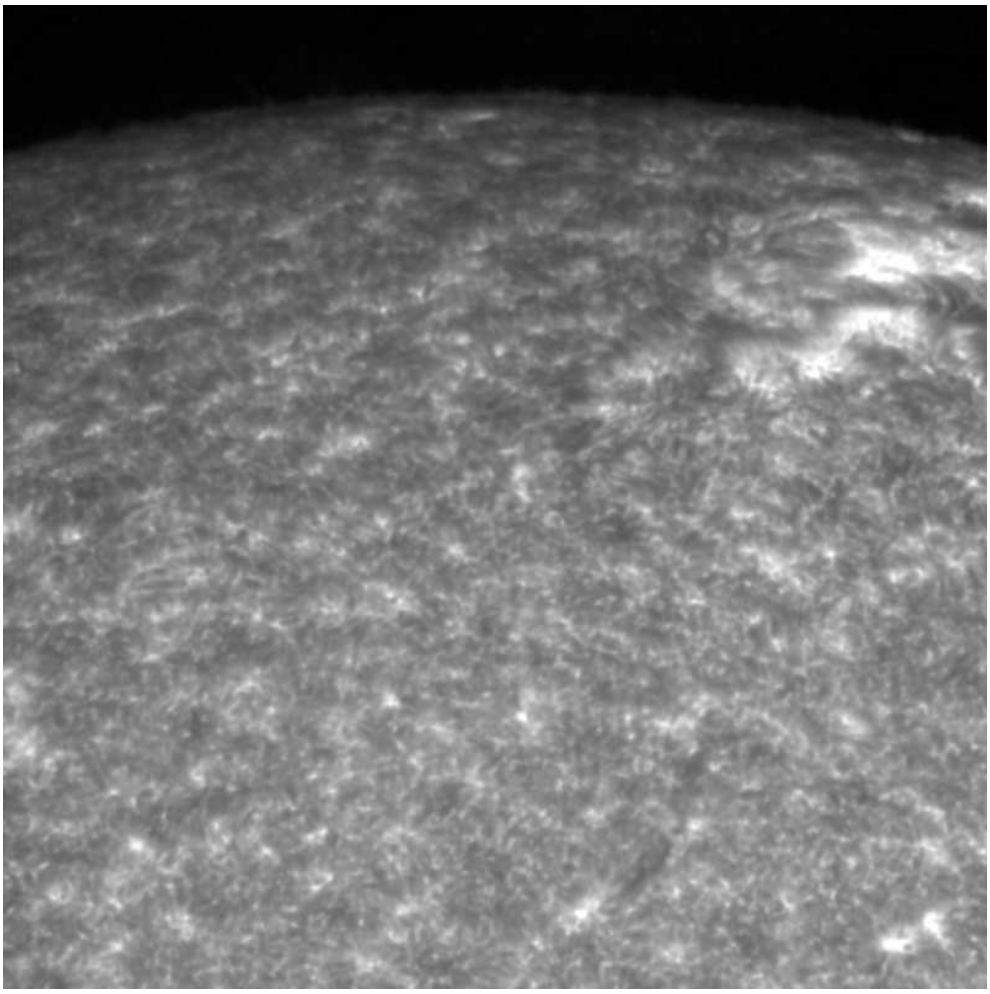

Figure 2. Another classic: part of a Ca II K_{2V} spectroheliogram taken by B. Gillespie at Kitt Peak thirty years ago. Other cutouts appeared on the cover of Lites (1985), in Zirin (1988), in Rutten & Uitenbroek (1991b), as frontispiece to Solar Phys. 134, and elsewhere. Outside active areas this image displays the solar clapotisphere rather than the solar chromosphere. Courtesy K. P. Reardon.

Detailed wave simulation was undertaken for the much easier case of purely acoustic waves sampled by the 170 nm and 160 nm bandpasses of TRACE by Fossum & Carlsson (2005a, 2005b, 2006) using the RADYN code of Carlsson & Stein (e.g., 1992, 1997). These ultraviolet continua suffer considerable NLTE Si I bound-free scattering, as is obvious in the pertinent Fig. 36 *B*-*J*-*S* panels of VAL3, but at least this scattering obeys complete frequency redistribution over the ionization edge. Fossum & Carlsson included it in evaluating brightness response to acoustic-wave perturbations. They first explained the puzzling high-frequency phase-difference behavior observed by De Wijn et al. (2005) as due to doubly-peaked 170 nm response, and they then evaluated the amount of observed high-frequency power as not enough to heat the chromosphere.

The latter result is questioned on p. 93 ff of this book by Wedemeyer-Böhm et al. (2007) who compute synthetic 160 nm images from CO^{5}BOLD simulations in LTE, without and with magnetic fields, to claim that the RADYN code by being only one-dimensional severely underestimates acoustic heating through the small-scale high-frequency acoustic interference patterns found in the 3D CO^{5}BOLD atmosphere at about $h = 500$ km. I have called such a quiet-sun regime where wave interference acts as the dominant structuring agent, above the overshooting convection but still below a magnetic canopy, a "*clapotisphere*" (Rutten 1995), inspired by Carlsson (1994) and the reference in Rutten & Uitenbroek (1991a) to Dowd (1981). While the grey CO^{5}BOLD star does not (yet) possess a fibrilar magnetism-dominated chromosphere as the solar one displayed in Section 3 below, it surely has a violent clapotisphere, even in excess of RADYN's.

Does the sun possess a clapotisphere? Yes, see the much-published spectroheliogram in Fig. 2. Selecting the special Ca II K_{2V} passband emphasizes acoustic shocks as "cell grains" in internetwork areas (Rutten & Uitenbroek 1991a). They are brightest in H_{2V} and K_{2V} through intricate vertical shock interference explained beautifully in Figs. 4–7 of Carlsson & Stein (1997), but remain visible through wider passbands (Fig. 10 of Krijger et al. 2001).

Which of the VAL3C, RADYN, and CO^{5}BOLD chromospheres resembles the solar one the best? In the VAL3C star the resonance lines of Mg II and Ca II are the major chromospheric cooling agents and require NLTE–PRD synthesis. RADYN neglects h&k and assumes CRD for H&K (perhaps mutually corrective since line cooling is too large in CRD due to deeper photon escape through the wings) but adds the virtue of computing time-dependent ionization. CO^{5}BOLD has the virtue of being 3D but unrealistically assumes grey LTE radiative transfer at all heights, ignoring actual strong-line cooling, lack of surface cooling through scattering, and fast-versus-slow asymmetry between ionization and recombination in and behind shocks (Carlsson & Stein 2002). It may so overestimate the occurrence of fine structure (Leenaarts & Wedemeyer-Böhm 2006).

The verdict is not in. Let us regard VAL3C, RADYN, and CO^{5}BOLD as interesting stars with sun-like photospheres but chromospheres that exist only computationally. VAL3C assumes that temperature fluctuations around the mean are small enough to be meaningfully averageable. RADYN's shocks deny such averaging but do not generate ultraviolet line emission. CO^{5}BOLD has more acoustic heating but its grey-LTE-instantaneous radiative cooling is very non-solar.

My feeling remains that the actual solar chromosphere is hot where the field points up or fans out from network and plage, that the internetwork is cool below the canopy except within shocks, that the latter clapotispheric domain represents a wide radial gap in H&K emissivity and Hα opacity, and that chromospheric internetwork radiation in Hα, the Ca II infrared lines and all ultraviolet lines including Ly-α comes from canopy-constituting mottles/fibrils/spicules and their sheath-like boundary layers. I gave some evidence in Rutten (2007) and give some more in Section 3 below.

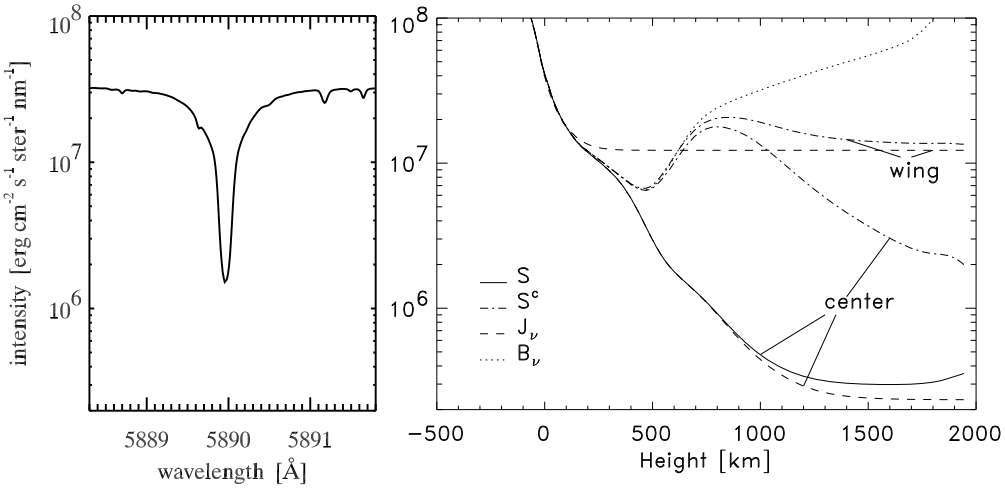

Figure 3. Formation of the Na D$_2$ line. Lefthand panel: disk-center line profile from the Kitt Peak FTS atlas (Neckel 1999) plotted on the same logarithmic scale as the S,B,J line-formation graph at right from Uitenbroek & Bruls (1992). The Na D$_2$ line is deep because its source function sinks deep, far below the temperature minimum. The model shown by the dotted B_ν curve is actually FALC of Fontenla et al. (1993), whose photosphere copied the VAL3C update of Maltby et al. (1986) which effectively brought the significantly-cooler-than-HOLMUL upper photosphere of VAL3C back to HOLMUL (and to near-radiative-equilibrium and near-LTE iron ionization) through the inclusion of a great many NLTE-scattered ultraviolet line haze lines in PANDORA (cf. Avrett 1985; Rutten 1990), but Uitenbroek & Bruls maintained the name VALC. At line center, the total source function equals the line source function which closely mimics a two-level atom dominated by scattering with complete redistribution. You may refresh your grasp of line formation by estimating ε and working out why the background continuum source function differs between line center and wing (hint: why does $S^c_{\rm wing} \Rightarrow J_{\rm wing}$ at right?).

2.2. Na I D in VAL3C

Figure 3 diagnoses Na I D formation in VAL3C didactically. The Eddington-Barbier relation $I_\nu \approx S_\nu(\tau_\nu = 1)$ suggests, through simply drawing a horizontal line from line center at left to the solid curve at right, that Na D$_2$ line center originates at $h \approx 600$ km. It is more like $h \approx 800$ km in Bruls et al. (1992) but in any case $\tau_\nu = 1$ lies in the VAL3C chromosphere, i.e. above the temperature minimum. Contribution functions to the emergent intensity or to the line depression will put the core formation there too. However, the intensity is obviously dominated by scattered photons originating much deeper: the line-center source function doesn't appreciate that VAL3C possesses a chromosphere. The Na D lines are often called chromospheric but their VAL3C brightness response is photospheric. Only when studying Na D Dopplershift may one call these lines chromospheric (assuming a VAL3C-like chromosphere) because the Dopplershift is encoded at the last photon scattering towards the observer. Thus, the "magnetoacoustic portals" analysis of Jefferies et al. (2006) comparing Na I to K I

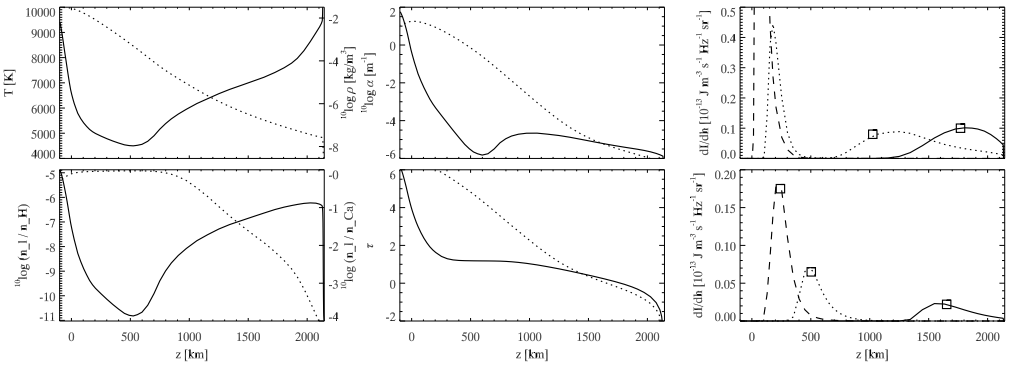

Figure 4. Didactic explanation of the difference between Hα and Ca II H formation assuming LTE, taken from Leenaarts et al. (2006). *Top left*: FALC temperature (lefthand scale, solid) and density (righthand scale, dotted). *Bottom left*: population fraction of the lower level relative to the total species density, respectively for Hα (lefthand scale, solid) and for Ca II H (righthand scale, dotted). *Top center*: line-center extinction coefficient for Hα (solid) and Ca II H (dotted). *Bottom center*: line-center optical depth for Hα (solid) and Ca II H (dotted). *Top right*: Hα intensity contribution functions for $\Delta\lambda = 0$ (solid), -0.038 (dotted), and -0.084 nm (dashed) from line center. Squares mark $\tau = 1$ locations. *Bottom right*: the same for Ca II H, at $\Delta\lambda = 0$ (solid), -0.024 (dotted), and -0.116 nm (dashed) from line center.

Dopplershifts rightfully claims measurement at the bottom of the chromosphere, whatever that may be.

Let me ask you some examination questions. Where is $\tau_\nu = 1$ for the weak blend at $\lambda = 5888.6$ Å in the lefthand panel of Fig. 3? Should you compute an intensity or a line depression contribution function for it? Is Milne-Eddington or Schuster-Schwarzschild the better approximation for inversion? Well, drawing the Eddington-Barbier connecting line locates $\tau_\nu = 1$ at about $h = 100$ km, right? Fitting a Milne-Eddington line-depression contribution would be your first bet in modeling such a weak line, right? Wrong! And not a little either. The line is due to water vapor in our own atmosphere, a million times higher up than your estimate, and Schuster-Schwarzschild is the better description.

2.3. Ca II H and Hα in FALC

Figure 4 compares Hα formation to Ca II H formation in FALC assuming LTE which holds reasonably well in the wings of these lines. The difference is enormous!

Ca II H originates from the ground state of the dominant ionization stage, containing virtually all calcium particles out to $h \approx 800$ km where ionization (taking only 11.9 eV) to Ca III sets in (row 2 panel 1), and so has smooth sampling throughout the lower atmosphere with near-constant inward τ_ν build-up, resulting in nice single-peaked intensity contribution functions which smoothly shift outward closer to line center. The extended Ca II H&K wings present an ideal probe to step smoothly through the lower atmosphere, also furnishing blends for Doppler and Zeeman sampling as diagnostics ripe for SIR inversions.

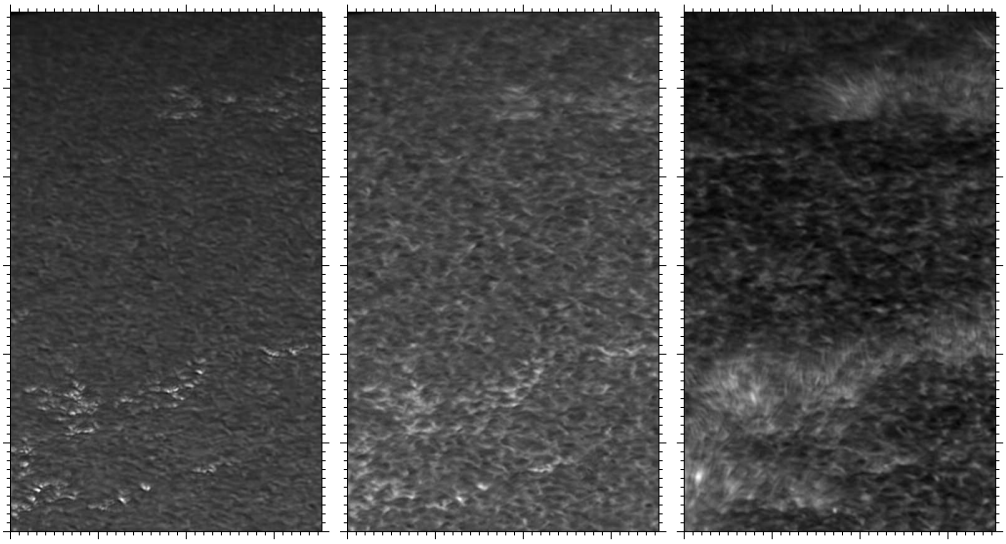

Figure 5. Three partial near-limb images taken with the DOT on June 18, 2003. Ticks at arcsec intervals. *Left*: G band. *Center*: Ca II H wing. *Right*: Ca II H line center. From Rutten (2007).

In contrast, Hα originates from the extremely temperature-sensitive $n = 2$ level at 10.2 eV, and so has a pronounced formation gap around the temperature minimum, no τ_ν buildup there, and double-peaked contribution functions as already shown by Schoolman (1972): in Hα one either observes the deep photosphere or the overlying chromosphere.

3. Chromospheric Scenes

In this section I insert images from the DOT[1], IBIS, and VAULT to demonstrate that the chromosphere is intrinsically fibrilar (with the term "fibrils" encompassing quiet-sun "mottles" and off-limb "spicules"). This message is far from new (e.g., Zirin 1988) but the state-of-the-art images in Figs. 5–12 deliver it beyond any wishful 1D thinking.

3.1. Ca II H&K and Hα chromosphere

Figure 5 shows at left the onset of reversed granulation and "faculae", the latter as short bright stalks where our slanted G-band view penetrates through relatively empty network fluxtubes into hot granule tops as sketched in Fig. 7 of Rutten (1999a) and more recently in Fig. 4 of Keller et al. (2004). The center panel shows a similar scene sampled slightly higher up. The third panel shows a dark wing-contributed background of reversed granulation with some shock interference wherever there is insignificant magnetic-feature emission in

[1] All available at `ftp://dotdb.phys.uu.nl` with a convenient search interface at `http://dotdb.phys.uu.nl/DOT`.

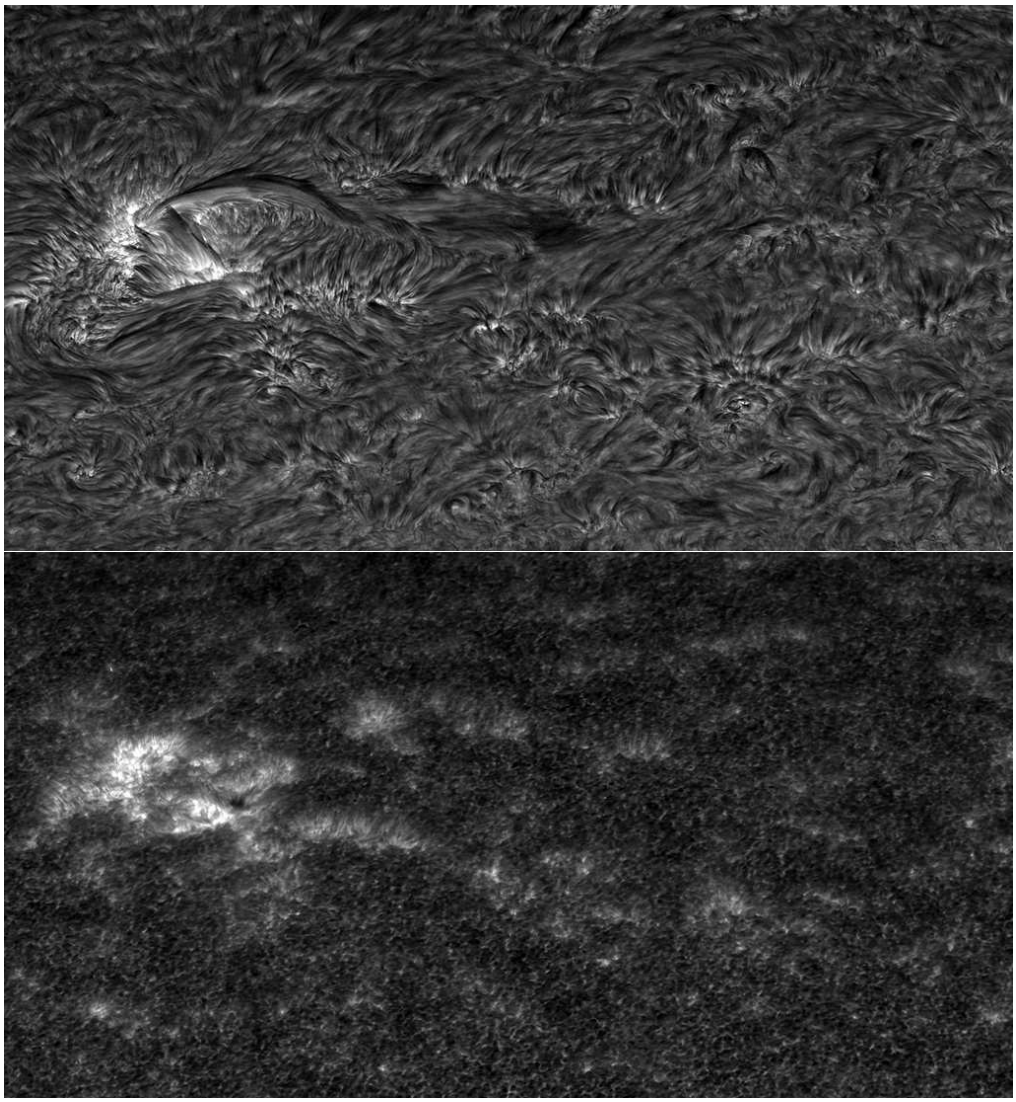

Figure 6. Simultaneous image mosaics taken with the DOT on October 4, 2005, respectively in Hα and Ca II H. The field of view is close to the limb (off the top) and measures about 265×143 arcsec^2.

the Ca II H core. The active network shows up through clusters of long, thin, bright features added by the line core. They start at photospheric faculae, are sharply delineated from the dark background in their foreground, appear to be optically thin, and stand rather upright causing overall hedge-row appearance. They make up the bright patches in the narrower-band image in Fig. 2. The movie from which this frame is taken shows that they are very dynamic. I called them "straws" in Rutten (2007). They are only seen at high resolution, meaning angular rather than spectral resolution. In fact, it is better to use a fairly wide passband to catch the emission peak whatever its Dopplershift. Adding inner-

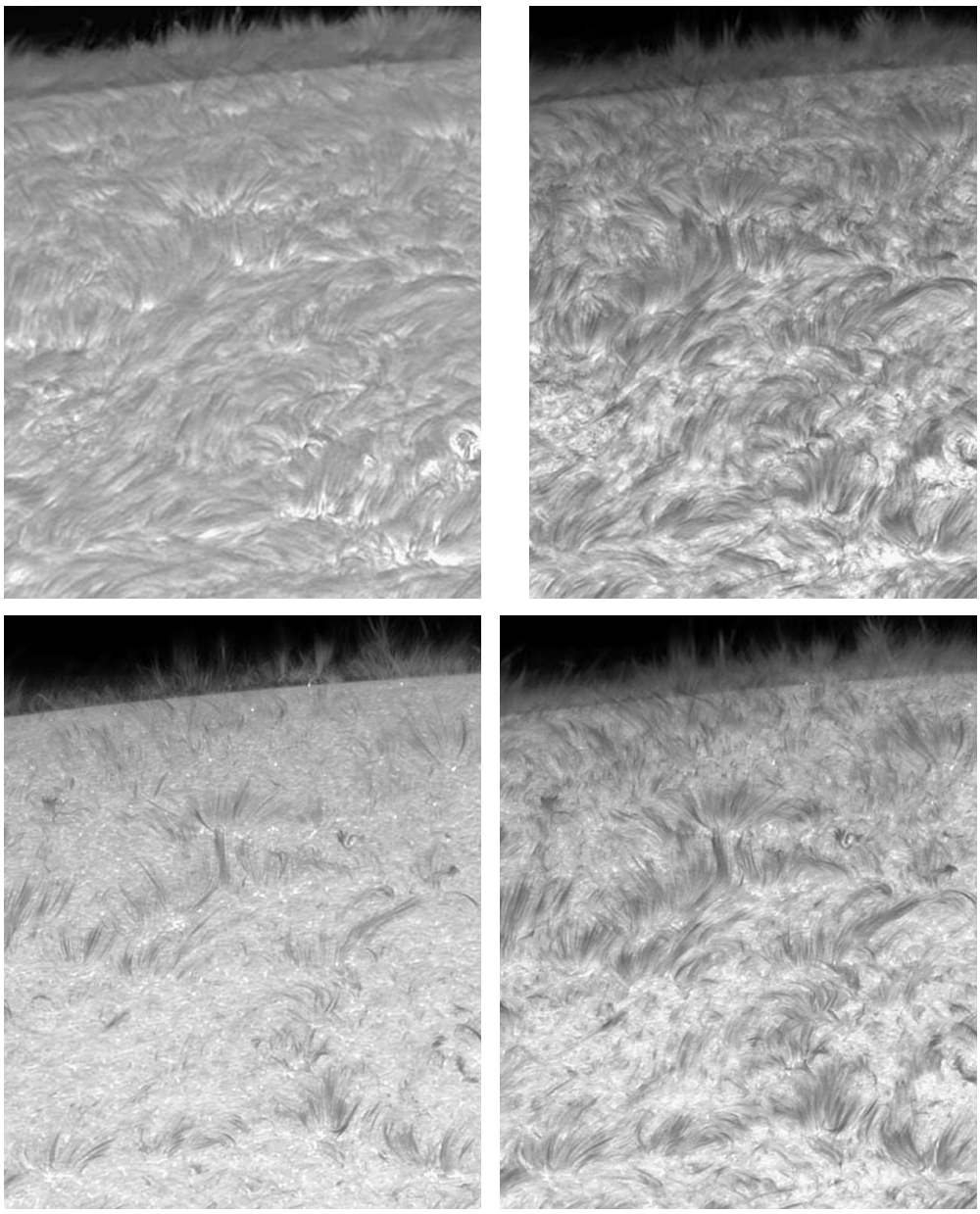

Figure 7. Profile-sampled Hα fine structure near and at the limb, taken with the DOT on October 4, 2005. Clockwise: line center, $\Delta\lambda = -400$, -600, -800 mÅ, not simultaneous but all four taken within one minute. Field of view about 70×85 arcsec^2.

wing reversed-granulation background poses no problem because this is quite dark.

Figure 6 is a similar but higher-up near-limb scene comparison, between Ca II H and Hα. The Ca II H image again shows much dark photospheric background with bright network hedges and straw crowding in the small active region.

In contrast, Hα is chromospheric nearly everywhere, with fibrils covering internetwork cells in a fibrilar canopy. The comparison immediately repudiates the notion that Ca II H is formed higher than Hα. The lower panel shows only the onset of the chromosphere, the upper one the full monty.

Figure 7 samples the limb part of this field while stepping the DOT Hα filter through the line. The line-center image again shows a mass of cell-spanning fibrils as a flattened carpet, with upright ones jutting out from network. I doubt that the double limb is caused by parasitic light (continuum leak outside the Hα passband): the lower limb is bumpy (zoom in with a viewer) and seems to mark the top of the carpet, the upper limb the end of hedge-row visibility. We have no DOT movie yet of off-limb spicules, but many are bound to bounce up and down with 3–5 min periodicity – perhaps fading on their return to convey the classical notion that spicules send up much more mass then comes down. Their upper ends correspond to the tops of "dynamic fibrils" as those observed on-disk with the SST on the same glorious day and analyzed in detail in the beautiful paper of De Pontieu et al. (2007).

The off-limb line-center fibrils constitute the authentic "chromosphere" because this name comes from their Hα emission during totality. Since there is no intrinsic difference between off-limb fibrils and on-disk fibrils (they don't care about our location in their sky), the proper definition of "chromosphere" is simply the mass of fibrils observed in Hα.

The other panels show the same scene progressively further out into the blue Hα wing. At decreasing line opacity one sees more and more photospheric background (not even granularly reversed) between the hedge rows. In the outer wing only rather upright fibrils in network hedge rows remain, appearing as dark to very dark strands against the deep-photosphere background and across the continuum limb. J. Leenaarts has pointed out that the latter is much brighter than the high-photosphere background seen in Ca II H, making straws dark in Hα while bright in Ca II H&K. In addition, Doppler shifts may darken them further by shifting the line core into the passband. A. G. de Wijn has suggested that Hα outer-wing darkness may also result from excessive Hα line width due to high temperature.

Let us now move to disk center. Figure 8 shows an area containing active network in Ca II H center and H$\alpha - 0.3$ Å. The slender bright stalks jutting out from the network, seen in Ca II H but only at high angular resolution, are the on-disk representation of the near-limb straws. Blinking shows that they usually coincide with the lower ends of bright Hα fibrils. Many of the latter span much further out across the internetwork. In Ca II H the latter is dark with reversed granulation and therefore photospheric or clapotispheric but not chromospheric. Hα shows fibrils over much longer lengths than Ca II H, implying large heights since Ca II H straws are preferentially upright. However, in the upper-right corner of this cut-out field the Hα wing shows short and grainy fine structure in a very quiet area, possibly as chromospheric transparency into either the top of the clapotisphere or the deep photosphere.

Figure 9 display an extremely quiet region. The Hα line-center scene shows much less large-scale organization than for more active areas. Most fibrils are short and strongly curved. In many places the Hα chromosphere appears optically thin. The two summed-wing images (second row) confirm this: the $\Delta\lambda = -700$ mÅ one shows only parts of fibrils close to the scarce and sparse

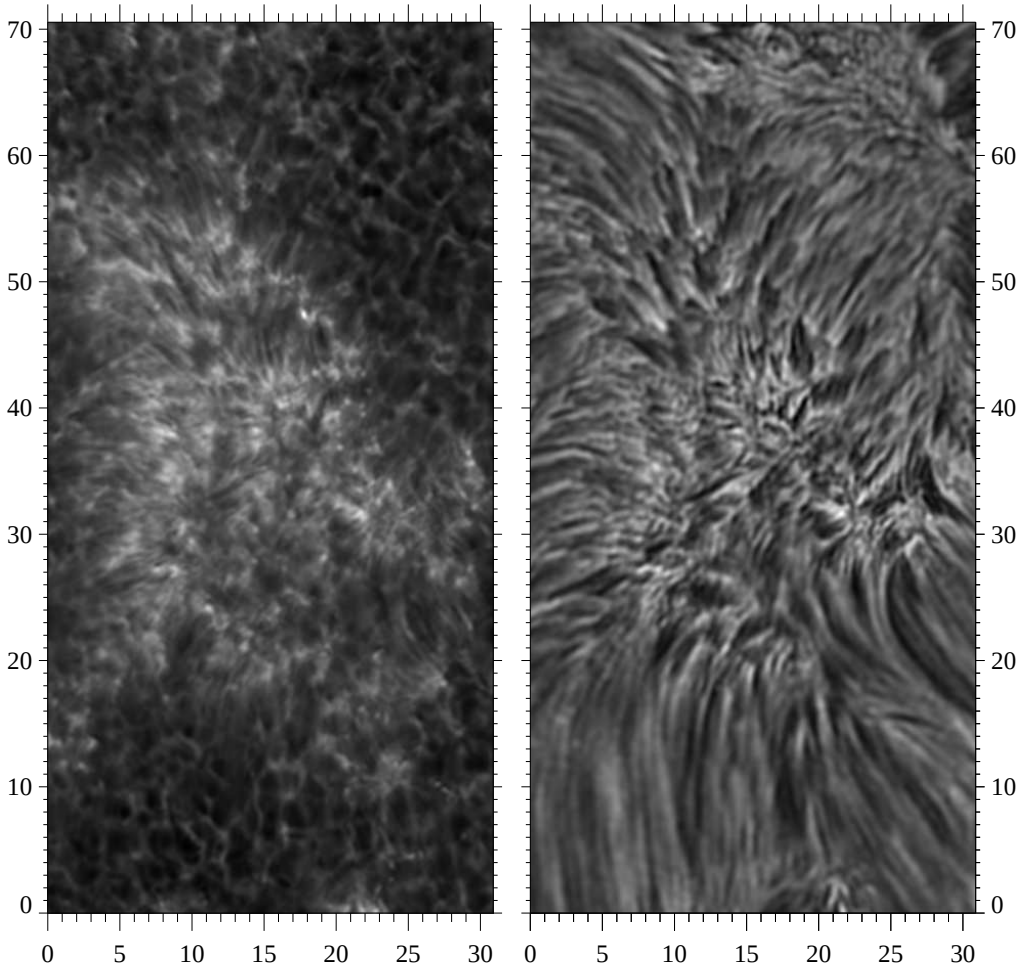

Figure 8. Two partial on-disk images taken with the DOT on April 24, 2006. Scales in arcsec. *Left*: Ca II H. *Right*: Hα − 350 mÅ. Courtesy P. Sütterlin.

network. The $\Delta\lambda = -350$ mÅ Dopplergram (third row) shows as much confusion as the line-center image. These samples come from a 71-minute multi-wavelength DOT sequence with half-minute cadence (one minute for the Hα wing wavelengths between which the filter switched alternatively). Movies from these data show that this cadence is much too slow. The quietest areas on the solar surface are least stable in Hα.

Figure 10 indicates why. The occurrence of an "acoustic event" is diagnosed by the sudden appearance of a bright repetitive grain in Ca II H. It follows on the squeezing away of a small granular shard by converging large granules, just as the "collapsars" of Skartlien et al. (2000). The Hα line-center brightness does not react markedly but there is large response in both Doppler samplings, most clearly seen in the time slices: sudden onset of oscillation wave trains with upward increasing amplitude. Their spatial extent, 4 arcsec, is much wider than the piston or the Ca II H grain, suggesting that an extended piece of elastic canopy responds to the shock buffeting from below. This area is also quiet,

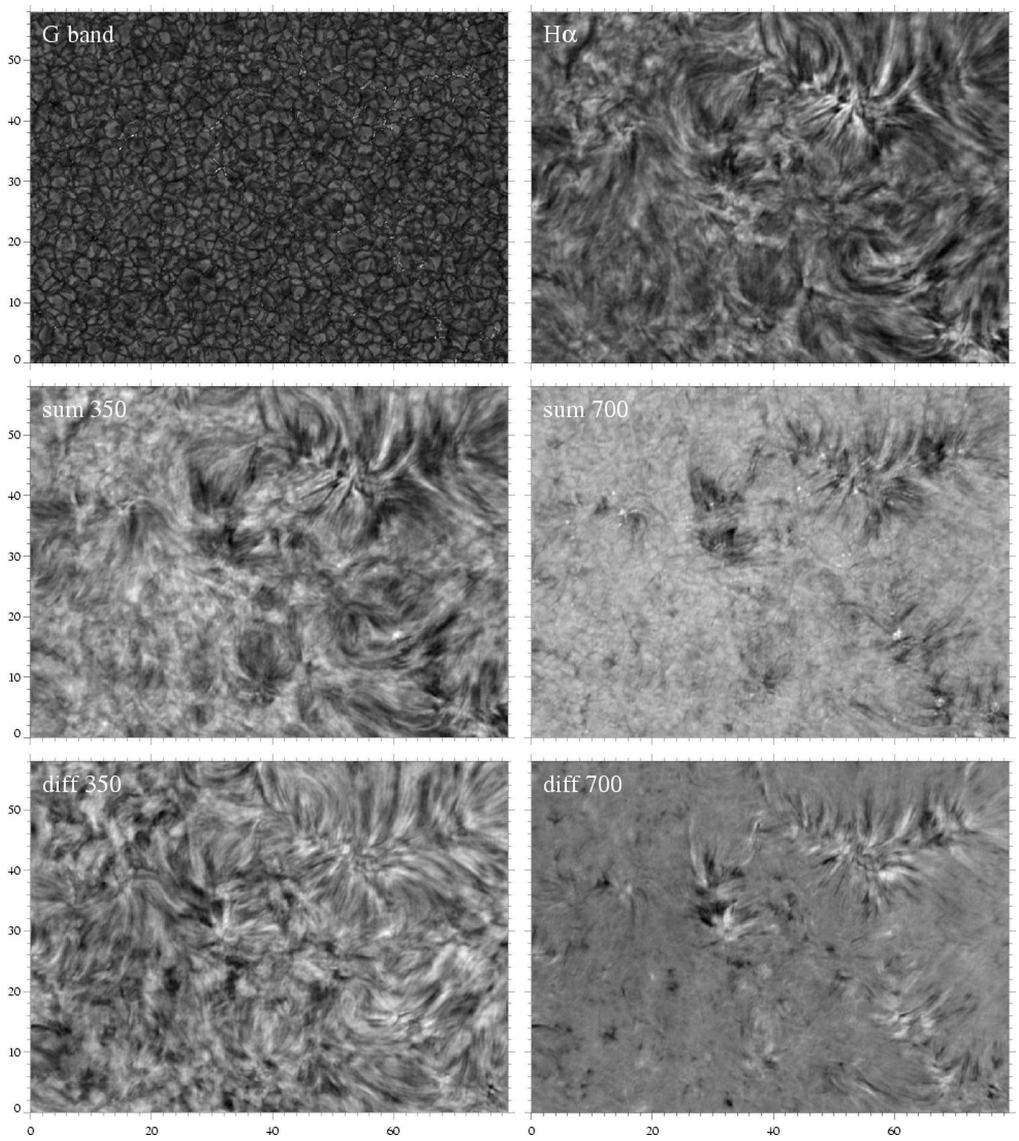

Figure 9. Very quiet disk-center scene taken with the DOT on October 19, 2005. *Upper row*: G band and Hα center. *Middle row*: sums of Hα wing brightness at $\Delta\lambda = \pm 350$ and ± 700 mÅ. *Bottom row*: differences of these wing pairs (Dopplergrams, blueshift dark). Scales in arcsec. Courtesy P. Sütterlin.

indeed without evident fibrilar structuring. The time slices indicate that most of the small-scale Hα brightness patterning is of oscillatory nature.

3.2. Ca II IR chromosphere

Figure 11 shows the chromosphere as it appears in Ca II 8542 Å. The bottom panels resemble Hα rather than Ca II H in Fig. 8. At various occasions I have wondered how this subordinate calcium line can be more chromospheric than its

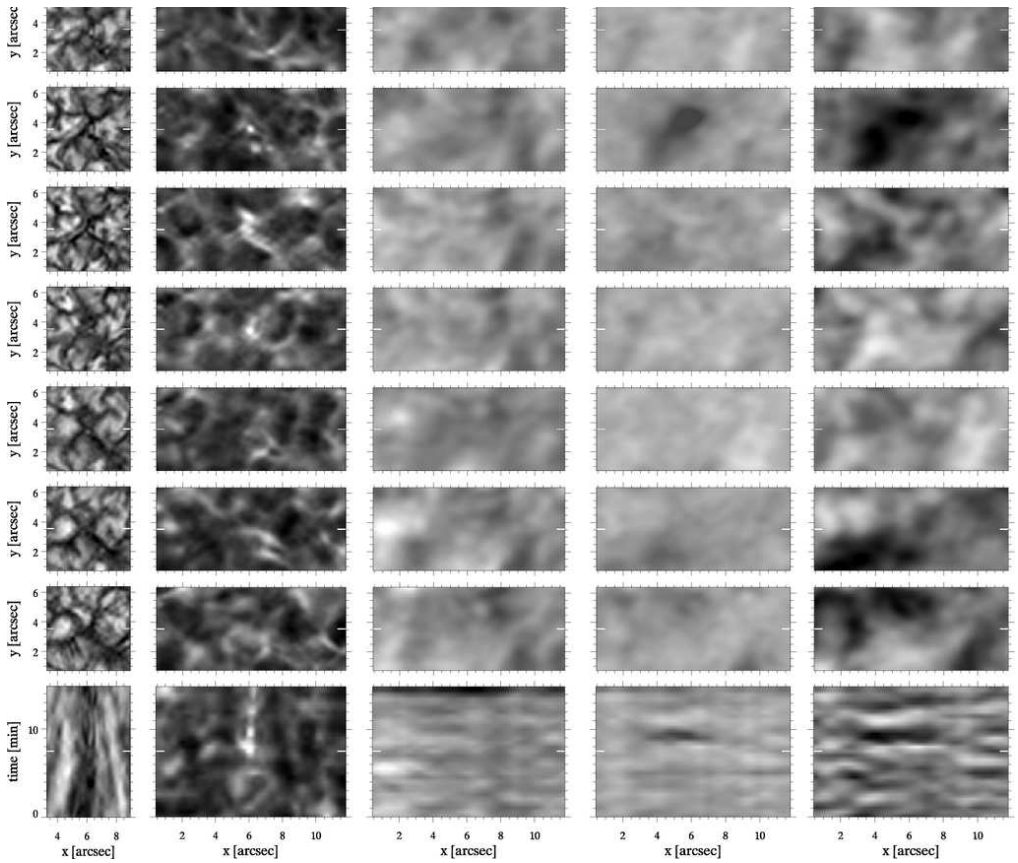

Figure 10. Hα response to an acoustic event, from DOT images taken on October 14, 2005. The first seven rows are small image cutouts, respectively G band, Ca II H center, Hα center, and Hα Dopplergrams from $\Delta\lambda = \pm 700$ mÅ wing pairs and from $\Delta\lambda = \pm 350$ mÅ wing pairs. Bright implies blueshift in the latter two. The cutouts are wider for Ca II H and Hα in order to show more context in the $x-t$ time slices in the bottom panels. The latter show the brightness evolution along the horizontal cut through the center of the subfield defined by the white markers in each image cutout. The time step between consecutive image rows is one minute, with time increasing from bottom to top in correspondence with the time direction in the slices. The image sequence is centered in time (fourth row, white markers in the slices) on the first appearance of a bright Ca II H grain. Courtesy B. van Veelen.

resonant H&K siblings with larger opacity. The habitual answer of G. Cauzzi, H. Uitenbroek and M. Carlsson is that the sizable excitation energy of its lower level gives larger temperature sensitivity and that the steep flanks of its narrower line profile give larger Doppler sensitivity, and that these combine to pick up fibril signatures that are less evident in H&K filtergrams. Reardon et al. illustrate the point further on p. 151 ff in these proceedings.

In large active regions one can often trace dark fibrils in Ca II H if one knows where they are from Hα, but they appear much clearer in Ca II 8542, with enhanced small-scale contrast in the inner-wing panel of Fig. 11, presumably

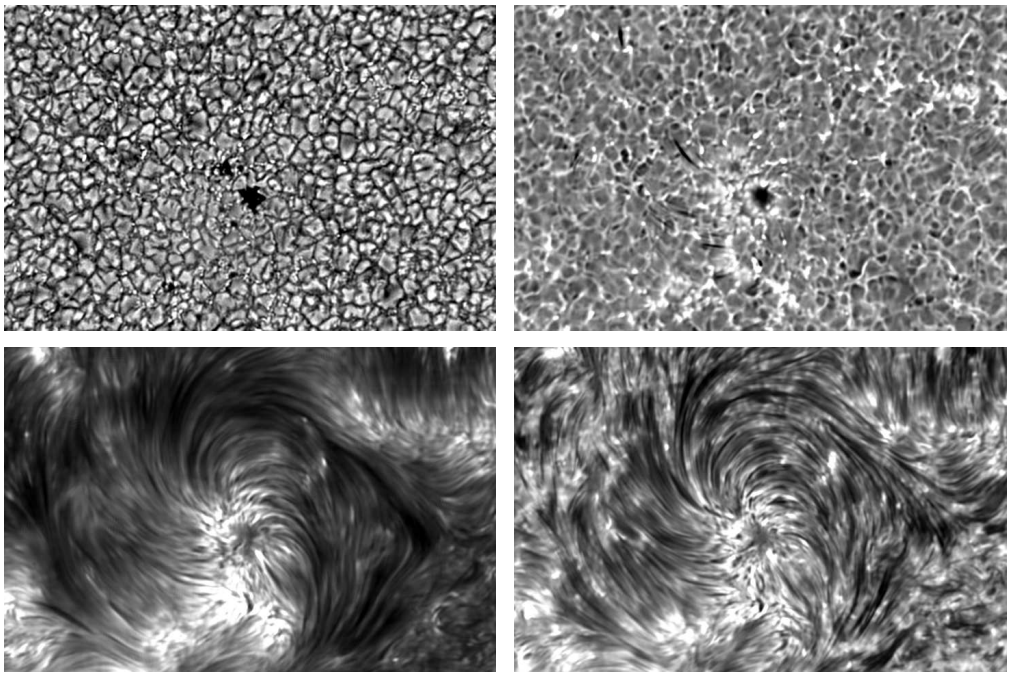

Figure 11. Near-simultaneous images taken with IBIS at the DST on October 1, 2005 using adaptive optics and speckle reconstruction, clockwise in white light and in Ca II 8542 Å at $\Delta\lambda = -600$, -200, and 0 mÅ from line center. Field about 60×40 arcsec^2. Courtesy G. Cauzzi.

from Dopplershifts (cf. Cauzzi et al. on p. 127 ff). The outer-wing panel shows the upper-photospheric mesh of reversed granulation with acoustic brightenings (cf. Rutten 2003b) very markedly, suggesting that the temperature sensitivity does not cause as wide a formation gap as the Hα jump from normal (or flattened, see Leenaarts & Wedemeyer-Böhm 2006) granulation to chromospheric fibrils.

Combining Hα and Ca II 8542 with full profile sampling may permit disentangling Dopplershift, thermal line broadening, and source function variation since their atomic mass difference produces large difference in thermal Dopplerwidth. Dopplerwidth measurement may provide a more direct handle on fibrilar temperature than fibril brightness, most awkwardly set by NLTE opacity and source function complexities for Hα.

3.3. Ly-α chromosphere

Figure 12 shows a beautiful Ly-α image. Towards the limb it is remarkably similar to the outer-wing Hα scene (Fig. 7) but with reversed contrast: bright hedge rows of short upright fibrils jut out at network borders of cells; the latter are covered by flatter and darker extended-fibril canopies. The rows of stubby fibrils appear similar to oscillation-loaded dynamic fibrils in Hα. They seem optically thick so that their brightness implies enhanced source function, either through $S = (1-\varepsilon)J + \varepsilon B$ resonance-scattering with small ε or through Balmer and higher recombination adding an ηB^* term. Both mechanisms suggest high

Figure 12. Ly-α image from the second flight of the VAULT rocket telescope (Korendyke et al. 2001; Vourlidas et al. 2001; `http://wwwsolar.nrl.navy.mil/rockets/vault`). Field 246×384 arcsec^2. The passband contains the full line. Courtesy A. Vourlidas.

temperature. The probable identity of Hα and Ly-α fibrils implies that the latter are thin hot sheaths around the former.

The extended active-region plage towards the bottom of the image appears very grainy, suggestive of mossy plage in TRACE 171 Å movies (e.g., Berger et al. 1999; Fletcher & de Pontieu 1999; de Pontieu et al. 1999).

3.4. Hα and Fe 171 chromosphere

Finally, Fig. 13 compares the appearance of an active region in Hα images from the DOT and in Fe 171 Å images from TRACE (movie: `http://dot.astro.uu.nl/movies`). The G-band image illustrates that granulation remains visible even in one-hour averaging. The Ca II H wing image represents an unsigned magnetogram because reversed granulation vanishes better through temporal averaging. This was done here to emphasize the overall bright-dark patterns in the remaining images. They are strikingly similar between Hα line-center brightness and Fe 171 brightness. The first should sample 10^4 K gas, the latter 10^6 K gas; the close similarity therefore needs consideration.

Hα is bright either due to large chromospheric emissivity or due to sufficiently small chromospheric opacity that one sees into the underlying deep photosphere. Note that the latter is certainly the case in umbrae since they display umbral dots even at Hα line center (also in this figure), implying absence of chromospheric opacity. Bright-dark contrast between otherwise similar fibrils may come from larger thickness of the darker ones, having lower scattering source functions at their surface. Excess emissivity may result from excess excitation and from excess recombination. The latter may arise in steep-gradient neutral-to-coronal interfaces or through the Zanstra mechanism as for planetary-nebulae Balmer emission.

Fe 171 is bright solely through thermal photon creation but is dark in two ways: either through absence of emissivity along the line of sight into the black photospheric or sky background[2], or through blocking of thermal background brightness by foreground bound-free out-of-the-passband scattering in the H I, He I and/or He II continua as explained in Fig. 10 of Rutten (1999a).

The bright blob at image center appears similarly in Fe 171, at Hα line center, and in the Hα wing summation. The Fe 171 blob suggests a relatively dense cloud of 10^6 K gas. The Hα brightness either results from chromospheric transparency or from chromospheric emissivity. Whichever of the two, it must correlate with the presence of very hot gas. Hydrogen ionization may explain excess transparency, recombination excess emissivity.

4. Speculations

My impressions from the images in the previous section are:

- the chromosphere consists of the mass (or mess) of fibrils observed in Hα;
- cell-spanning fibrils outline magnetic canopies. Above quiet cell centers they are jostled and kicked up by upward-propagating shocks, producing an extended cool clapotisphere underneath;

[2]The term "volume blocking" is nonsensical since a volume doesn't block by itself. It is used to express lack of emissivity along a line of sight through some volume, an "emissivity void" – but a void doesn't block either; lack of emissivity cannot be expressed as opaqueness.

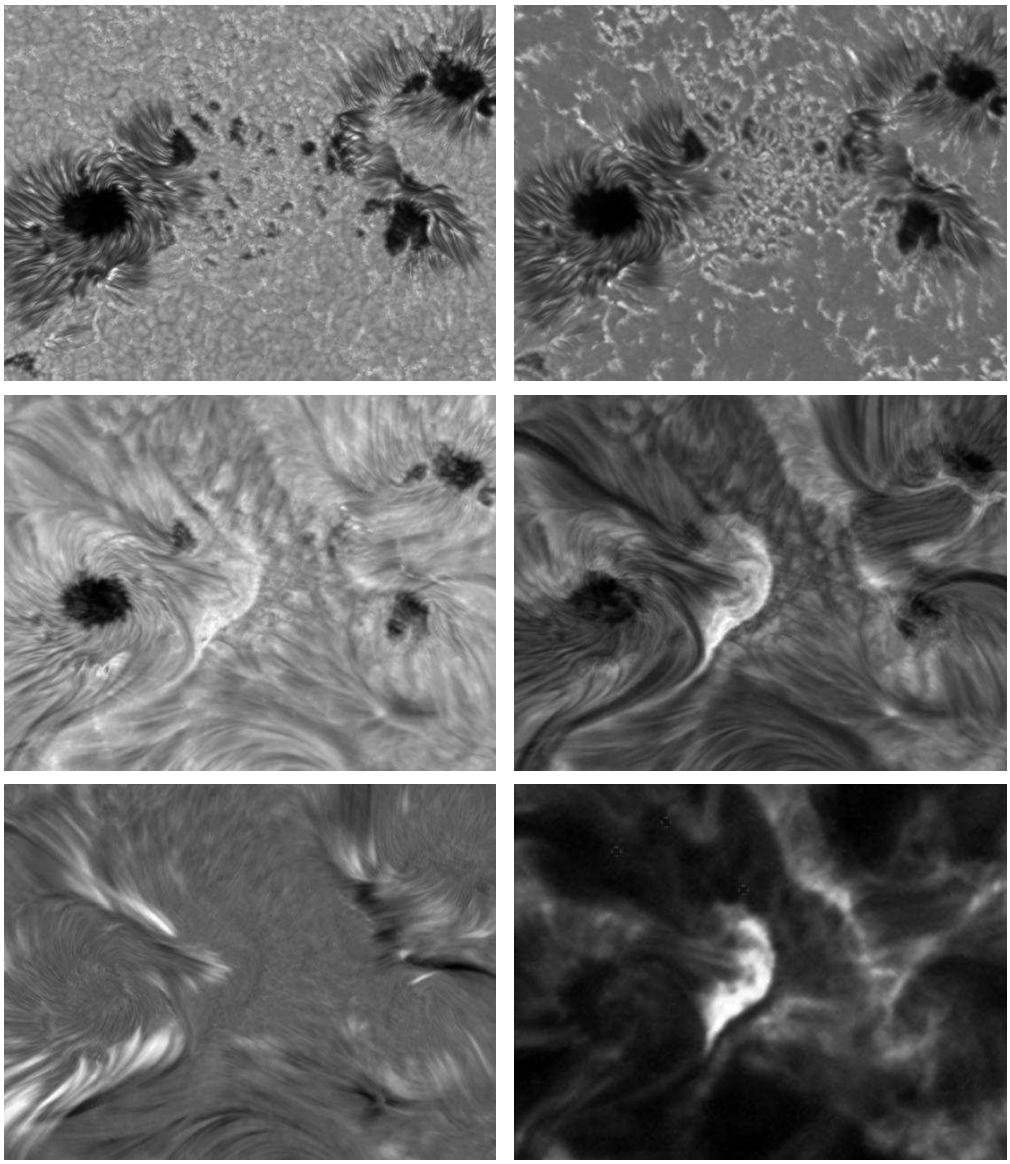

Figure 13. One-hour temporal averages of co-aligned DOT and TRACE image sequences taken on July 9, 2005. *Top*: G band; Ca II H at $\Delta\lambda = -2.35$ Å from line center. *Middle*: sum of Hα at $\Delta\lambda = \pm 500$ mÅ; Hα line center. *Bottom*: difference of Hα at $\Delta\lambda = \pm 500$ mÅ (Dopplershift, upward dark); TRACE 171 Å. Field size 78×60 arcsec^2. The bright blob in Hα and Fe 171 is sharply delineated at right, presumably at the neutral line through this active region. The Hα wing difference indicates marked absence of large Dopplershifts in this area, without fibrilar structuring (best seen by zooming in with a pdf viewer). Courtesy A. G. de Wijn.

– slanted fields jutting out from network and plage suffer oscillatory cool-gas loading to become dynamic fibrils (De Pontieu et al. 2007) and EUV shutters

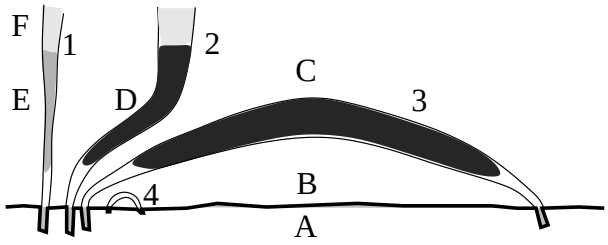

Figure 14. Different types of fibrils together constituting the chromosphere. Rough temperatures: D$\sim 10^4$ K, E$\sim 10^5$ K, F$\sim 10^6$ K. Outside regimes: A = photosphere with normal/reversed granulation and relatively empty magnetic elements, B = subcanopy "clapotisphere" pervaded by acoustic shocks but otherwise cool, C = coronally transparent in H&K, Hα, and Ly-α. Type 1: bright upright network straws opening into coronal plasma. Type 2: dark Hα fibrils bending upward into hot plasma from unipolar crowding. Type 3: dark Hα fibrils spanning across cell interiors in bipolar network outling magnetic canopies. Type 4: short weak-field near-network loops postulated by Schrijver & Title (2003). From Rutten (2007).

(De Wijn et al. 2007). These possess transition-interface sheaths that are optically thick in Ly-α;

- more straight-up fields above network and plage show up as bright Ca II straws and bright Hα fibril feet, likely through recombination emissivity. Near the limb they appear as hedge rows that are bright in Ca II and Ly-α but dark in the outer Hα wings from bright background, large Dopplershift, and/or large thermal broadening.
- near-vertical fields in active regions produce graininess in Ly-α, mossy plage, and brightness correspondence between Hα and Fe 171. They provide locations where hot gas comes very close to the photosphere, presumably through downward conduction and lack of upward kicking.

These impressions are cartoonized in Fig. 14, copied from Rutten (2007) where I summarized them without showing so many tell-tale images.

5. Suggestions

We obviously need improved Hα imaging. Combination with Hβ and one or more of the Ca II IR lines is desirable. Yet better is multi-line chromospheric imaging with synchronous co-spatial Dopplergrams and magnetograms of the underlying photosphere and with TRACE/SDO EUV imaging of the higher-temperature scenes. All this in long-duration movie sequences. Unfortunately, Hinode's tunable filter seems not fulfilling its intended Hα capability (but would anyhow deliver only slow cadence due to telemetry limitations).

The Hα images in Figs. 6–10 illustrate the necessity of high angular resolution. Because Hα fibrils appear as high-lying Schuster-Schwarzschild clouds which may be optically thin, there is no smallest-scale limit set by mean-free photon paths or scattering lengths. In addition, their dynamical behavior necessitates taking sustained-quality image sequences at fast cadence. The DOT does so admirably, but the twice larger SST yields not only higher resolution

but also better signal-to-noise through better cameras, better alignment through MOMFBD restoration (Van Noort et al. 2005), and especially faster cadence because MOMFBD requires fewer frames than speckle reconstruction. Van Noort & Rouppe van der Voort (2006) demonstrated that imaging cadence as fast as 1 fps is needed for some Hα dynamics, well beyond the traditional estimate of soundspeed travel across a resolution element.

In addition, one should add line-profile sampling to disentangle the complex cross-talk between opacity, source function, and Dopplershift variations. Chromospheric imaging at high resolution so becomes just as photon-starved as photospheric spectropolarimetry at high resolution, making fast-cadence profile-sampling narrow-band imaging a second motivation for telescope aperture beyond the angular resolution in reach of AO and post-detection processing. Post-focus light handling is presently done best by rapid-scan Fabry-Pérot imaging. Fiber field reformatting may enable 2D MOMFBD spectrometry in the future (Rutten 1999b).

The obvious desire to add ultraviolet spectrometry at high angular resolution to sample hot fibril sheaths is presently unanswered: no HRTS- or SUMER-like spectrometer is available for regular co-pointing. Even better would be integral-field ultraviolet profile sampling because slits, whether scanning or sitting-and-staring, tend to be at the wrong place at the wrong time. The lack of such ultraviolet instrumentation is the major longer-term deficiency in chromospheric observing, making Hα the key diagnostic by default.

The simple question "where is this line formed?" discussed in Section 2 is a naïve way of asking "how well does my interpretation fit reality?", a question well beyond observation. So let me end by addressing modeling options.

The SIR technique thanks its large success in its main application, photospheric Stokes profile inversion, to the same reasons why Holweger's line fitting made HOLMUL such a success in abundance determination: LTE and smooth radial behavior are good assumptions for photospheric iron lines. Extension to scattering and sinusoidal waves around $h = 500$ km is doable (outside sunspots) within such inversion approaches, but already the shocked clapotisphere below the canopy needs forward modeling based on numerical simulations.

The fibrilar chromosphere surely requires simulation physics to diagnose its structural and dynamical physics; the breakthrough example is Hansteen's simulation in De Pontieu et al. (2007). The chromosphere cannot be treated by inversion before its physics is understood, and then only if all fibrils are so similar in geometry, temperature, density, etc., that multi-cloud modeling (with some sort of NLTE radiative transfer in and between each) remains realistically limited in parameter space. The interpretational path to follow is forward modeling based on 2D and 3D simulations. However, PANDORA-style 1D modeling suits to study radiative transfer in and between fibrils with transition sheaths in full detail for working out and testing simpler recipes for multi-D codes. This step is similar to studying transition-sheath radiation in and from prominences as by Schwartz et al. (2006).

Shortcutting through untested tractability assumptions is dangerous even though it may produce intrinsically interesting "code-as-a-star" papers.

Acknowledgments. I thank the CSPM organizers for a very good meeting and for inviting me to both speakership and editorship. My participation was funded by the Leids Kerkhoven-Bosscha Fonds and the EC-RTN European Solar Magnetism Network.

References

Athay R. G., 1976, in C. J. Cannon (ed.), Interpretation of Atmospheric Structure in the Presence of Inhomogeneities, Comm. 12, General Assembly IAU, Grenoble, Univ. Sydney, Sydney, 69
Avrett E. H., 1985, in B. W. Lites (ed.), Chromospheric Diagnostics and Modeling, NSO/SP Summer Conference, Sunspot, 67
Beckers J. M., Milkey R. W., 1975, Solar Phys. 43, 289
Berger T. E., de Pontieu B., Schrijver C. J., Title A. M., 1999, ApJ 519, L97
Bloomfield D. S., McAteer R. T. J., Mathioudakis M., Williams D. R., Keenan F. P., 2004, ApJ 604, 936
Bruls J. H. M. J., Rutten R. J., Shchukina N. G., 1992, A&A 265, 237
Cabrera Solana D., Bellot Rubio L. R., del Toro Iniesta J. C., 2005, A&A 439, 687
Caccin B., Gomez M. T., Marmolino C., Severino G., 1977, A&A 54, 227
Carlsson M. (ed.), 1994, Chromospheric Dynamics, Proc. Mini-workshop, Inst. Theor. Astrophys., Oslo
Carlsson M., Rutten R. J., Shchukina N. G., 1992, A&A 253, 567
Carlsson M., Stein R. F., 1992, 397, L59
Carlsson M., Stein R. F., 1997, ApJ 481, 500
Carlsson M., Stein R. F., 2002, ApJ 572, 626
de Pontieu B., Berger T. E., Schrijver C. J., Title A. M., 1999, Solar Phys. 190, 419
De Pontieu B., Hansteen V. H., Rouppe van der Voort L., van Noort M., Carlsson M., 2007, ApJ 655, 624
De Wijn A. G., De Pontieu B., Rutten R. J., 2007, ApJ 654, 1128
De Wijn A. G., Rutten R. J., Tarbell T. D., 2005, A&A 430, 1119
del Toro Iniesta J. C., 2003, Astronomische Nachrichten 324, 383
Dowd J., 1981, Sea Kayaking, Univ. Washington Press, Seattle
Edmonds, Jr. F. N., 1967, AJ 72, 793
Fletcher L., de Pontieu B., 1999, ApJ 520, L135
Fontenla J. M., Avrett E., Thuillier G., Harder J., 2006, ApJ 639, 441
Fontenla J. M., Avrett E. H., Loeser R., 1993, ApJ 406, 319
Fossum A., Carlsson M., 2005a, Nat 435, 919
Fossum A., Carlsson M., 2005b, ApJ 625, 556
Fossum A., Carlsson M., 2006, ApJ 646, 579
Gurtovenko E. A., Ratnikova V. A., 1974, AZh 51, 1032
Holweger H., 1967, Z. f. Astrophysik 65, 365
Holweger H., Müller E. A., 1974, Solar Phys. 39, 19
Jefferies S. M., McIntosh S. W., Armstrong J. D., Bogdan T. J., Cacciani A., Fleck B., 2006, ApJ 648, L151
Judge P. G., 2007, in H. Uitenbroek, J. Leibacher, R. F. Stein (eds.), Solar MHD: Theory and Observations, Procs. 23rd NSO workshop, ASP Conf. Ser. 354, 265
Keller C. U., Schüssler M., Vögler A., Zakharov V., 2004, ApJ 607, L59
Korendyke C. M., Vourlidas A., Cook J. W., Dere K. P., Howard R. A., Morrill J. S., Moses J. D., Moulton N. E., Socker D. G., 2001, Solar Phys. 200, 63
Krijger J. M., Rutten R. J., Lites B. W., Straus T., Shine R. A., Tarbell T. D., 2001, A&A 379, 1052
Kucera A., Balthasar H., Rybak J., Wöhl H., 1998, A&A 332, 1069
Leenaarts J., Rutten R. J., Sütterlin P., Carlsson M., Uitenbroek H., 2006, A&A 449, 1209
Leenaarts J., Wedemeyer-Böhm S., 2006, A&A 460, 301

Lites B. W. (ed.), 1985, Chromospheric Diagnostics and Modeling, Proceedings NSO Summer Conference, Sunspot
Magain P., 1986, A&A 163, 135
Maltby P., Avrett E. H., Carlsson M., Kjeldseth-Moe O., Kurucz R. L., Loeser R., 1986, ApJ 306, 284
Mein P., 1971, Solar Phys. 20, 3
Neckel H., 1999, 184, 421
Pecker J.-C., 1951, Annales d'Astrophysique 14, 115
Ruiz Cobo B., del Toro Iniesta J. C., 1992, ApJ 398, 375
Ruiz Cobo B., del Toro Iniesta J. C., Collados M., Sánchez Almeida J., 1990, Ap&SS 170, 113
Rutten R. J., 1990, in G. Wallerstein (ed.), Cool Stars, Stellar Systems and the Sun, Proc. Sixth Cambridge Workshop, ASP Conf. Ser. 9, 91
Rutten R. J., 1995, in J. T. Hoeksema, V. Domingo, B. Fleck, B. Battrick (eds.), Helioseismology, Proc. Fourth SOHO Workshop, ESA SP–376 Vol. 1, ESA Publ. Div., ESTEC, Noordwijk, 151
Rutten R. J., 1998, in C. Fröhlich, M. C. E. Huber, S. Solanki, R. von Steiger (eds.), Solar Composition and its Evolution – from Core to Corona, Procs. ISSI Workshop, Space Sci. Rev. 85, 269
Rutten R. J., 1999a, in B. Schmieder, A. Hofmann, J. Staude (eds.), Magnetic Fields and Oscillations, Procs. Third Adv. in Solar Physics Euroconf., ASP Conf. Ser. 184, 181
Rutten R. J., 1999b, in T. R. Rimmele, K. S. Balasubramaniam, R. R. Radick (eds.), High Resolution Solar Physics: Theory, Observations, and Techniques, Procs. 19th NSO/Sacramento Peak Summer Workshop, ASP Conf. Ser. 183, 296
Rutten R. J., 2002, Jour. Astron. Data 8, 8
Rutten R. J., 2003a, Radiative Transfer in Stellar Atmospheres, Lecture Notes Utrecht University, 8th Edition, `http://www.astro.uu.nl/~rutten`
Rutten R. J., 2003b, in R. von Fay-Siebenbürgen, K. Petrovay, J.-L. Ballester, M. Aschwanden (eds.), Turbulence, Waves and Instabilities in the Solar Plasma, NATO ASI Series II 124, Kluwer, Dordrecht, 137
Rutten R. J., 2007, in H. Uitenbroek, J. Leibacher, R. F. Stein (eds.), Solar MHD: Theory and Observations, Procs. 23rd NSO workshop, ASP Conf. Ser. 354, 282
Rutten R. J., Kostik R. I., 1982, A&A 115, 104
Rutten R. J., Uitenbroek H., 1991a, Solar Phys. 134, 15
Rutten R. J., Uitenbroek H., 1991b, in P. Ulmschneider, E. R. Priest, R. Rosner (eds.), Mechanisms of Chromospheric and Coronal Heating, Proc. Heidelberg Conf., Springer, Berlin, 48
Schoolman S. A., 1972, Solar Phys. 22, 344
Schrijver C. J., Title A. M., 2003, ApJ 597, L165
Schwartz P., Heinzel P., Schmieder B., Anzer U., 2006, A&A 459, 651
Skartlien R., Stein R. F., Nordlund Å., 2000, ApJ 541, 468
Socas-Navarro H., Trujillo Bueno J., Ruiz Cobo B., 2001, ApJ 550, 1102
Uitenbroek H., Bruls J. H. M. J., 1992, A&A 265, 268
Unsöld A., 1955, Physik der Sternatmosphären, Springer, Berlin
van Noort M., Rouppe van der Voort L., Löfdahl M. G., 2005, Solar Phys. 228, 191
van Noort M. J., Rouppe van der Voort L. H. M., 2006, ApJ 648, L67
Vernazza J. E., Avrett E. H., Loeser R., 1981, ApJS 45, 635
Vourlidas A., Klimchuk J. A., Korendyke C. M., Tarbell T. D., Handy B. N., 2001, ApJ 563, 374
Wedemeyer-Böhm S., Steiner O., Bruls J., Rammacher W., 2007, in P. Heinzel, I. Dorotovič, R. J. Rutten (eds.), The Physics of Chromospheric Plasmas, Coimbra Solar Physics Meeting, ASP Conf. Ser. 368, 93
Zirin H., 1988, Astrophysics of the Sun, Cambridge Univ. Press, Cambridge UK

The Physics of Chromospheric Plasmas
ASP Conference Series, Vol. 368, 2007
Petr Heinzel, Ivan Dorotovič and Robert J. Rutten, eds.

Modeling the Solar Chromosphere

Mats Carlsson

Institute of Theoretical Astrophysics, University of Oslo, Norway

Abstract. Spectral diagnostic features formed in the solar chromosphere are few and difficult to interpret — they are neither formed in the optically thin regime nor in local thermodynamic equilibrium (LTE). To probe the state of the chromosphere, both from observations and theory, it is therefore necessary with modeling. I discuss both traditional semi-empirical modeling, numerical experiments illustrating important ingredients necessary for a self-consistent theoretical modeling of the solar chromosphere and the first results of such models.

1. Introduction

My keynote talk was similar in content to a recent talk at a Sacramento Peak workshop celebrating the 70th birthday of Robert F. Stein. This written version builds to a large extent on that writeup (Carlsson 2006), but it is updated and some sections have been expanded.

Before discussing models of the solar chromosphere it is worthwhile discussing the very definition of the term "chromosphere". The name comes from the Greek words "$\chi\rho\omega\mu\alpha$" (color) and "$\sigma\varphi\alpha\iota\rho\alpha$" (ball) alluding to the colored thin rim seen above the lunar limb at a solar eclipse. The color comes mainly from emission in the Balmer Hα line. This is thus one possible definition — the chromosphere is where this radiation originates. At an eclipse this region has a sharp lower edge, the visible limb, but a fuzzy upper end with prominences protruding into the corona. The nature of this region is difficult to deduce from eclipse observations since we see this region edge on during a very short time span and we have no way of telling whether it is homogeneous along the line of sight or very inhomogeneous in space and time. It was early clear that the emission in Hα must mean an atmosphere out of radiative equilibrium — without extra heating the temperature will not be high enough to have enough hydrogen atoms excited to the lower or upper levels of the transition. Early models were constructed to explain observations in Hα and in resonance lines from other abundant elements with opacity high enough to place the formation in these regions even in center-of-disk observations (lines like the H and K resonance lines from singly ionized calcium). These early models were constructed assuming one dimensional plane-parallel geometry and they resulted in a temperature falling to a minimum around 4000 K about 500 km above the visible surface, a temperature rise to 8000 K at a height of about 2000 km and then a very rapid temperature rise to a million degree corona. These plane-parallel models have

[1] also at Center of Mathematics for Applications, University of Oslo, Norway

led to a common notion that there is a more or less homogeneous, plane-parallel region between these heights that is hotter than the temperature minimum. In such a picture the chromosphere may be defined as a region occupying a given height range (e.g. between 500 and 2000 km height over the visible surface) or a given temperature range. We may also use physical processes for our definition: the chromosphere is the region above the photosphere where radiative equilibrium breaks down and hydrogen is predominantly neutral (the latter condition giving the transition to the corona). This discussion shows that there is no unique definition of the term "chromosphere", not even in a one-dimensional, static world. It is even more difficult to agree on a definition of the "chromosphere" that also encompasses an inhomogeneous, dynamic atmosphere.

As mentioned above, the first models of the chromosphere were constructed with a large number of free parameters to match a set of observational constraints. Since some equations are used to restrict the number of free parameters (not all hydrodynamical variables at all points in space and time are determined empirically) we call this class of models *semi-empirical* models. Typically one assumes hydrostatic equilibrium and charge conservation but no energy equation. The temperature as function of height is treated as a free function to be determined from observations. In the other main class of models one tries to minimize the number of free parameters by including an energy equation. Such theoretical models have been very successful in explaining radiation from stellar photospheres with only the effective temperature, acceleration of gravity and abundances as free parameters. In the chromosphere, an additional term is needed in the energy equation — e.g. energy deposition by acoustic shocks or energy input in connection with magnetic fields (e.g. currents or reconnection).

It is thus clear from observations that the chromosphere is not in radiative equilibrium — there is a net radiative loss. This loss has to be balanced by an energy deposition, at least averaged over a long enough time span, if the atmosphere is to be in equilibrium. This is often called the problem of chromospheric "heating". It is important to bear in mind, though, that the radiative losses may be balanced by a non-radiative energy input without an increase in the average temperature. The term "chromospheric heating" may thus be misleading since it may be interpreted as implying that the average temperature is higher than what is the case in a radiative equilibrium atmosphere. In the following we will use the term "heating" in a more general sense: a source term in the energy equation, not necessarily leading to an increased temperature.

Chromospheric heating is needed not only for the quiet or average Sun but also in active regions, sunspots and in the outer atmospheres of many other stars. I will in the following mainly discuss the quiet Sun case.

The outline of this paper is as follows: In Section 2 we discuss semi-empirical models of the chromosphere. In Section 3 we discuss theoretical models; first we elaborate on 1D hydrodynamical models, then we discuss the role of high frequency acoustic waves for the heating of the chromosphere and finally we describe recent attempts to model the chromosphere in 3D including the effects of magnetic fields.

2. Semi-empirical Models

Semi-empirical models can be characterized by the set of observations used to constrain the model, the set of physical approximations employed and the set of free parameters to be determined. Spectral diagnostics used to constrain chromospheric models must have high enough opacity to place the formation above the photosphere. The continuum in the optical part of the spectrum is formed in the photosphere so the only hope for chromospheric diagnostics lies in strong spectral lines in this region of the spectrum. Candidates are resonance lines of dominant ionization states of abundant elements and lines from excited levels of the most abundant elements (hydrogen and helium). Most resonance lines are in the UV but the resonance lines of singly ionized calcium (Ca II), called the H and K lines, fulfill our criteria. These lines originate from the ground state of Ca II, the dominant ionization stage under solar chromospheric conditions, and the opacity is therefore given by the density directly and the optical depth is directly proportional to the column mass (i.e. to the total pressure in hydrostatic equilibrium). Also the source function has some coupling to local conditions even at quite low densities (in contrast to the strongly scattering resonance lines of neutral sodium). Other chromospheric diagnostic lines in the optical region are the hydrogen Balmer lines and the helium 1083 nm line. They all originate from highly excited levels and thus have very temperature sensitive opacity. The population of He 1083 is also set by recombination such that its diagnostic potential is very difficult to exploit. With the advent of space based observatories, the full UV spectral range was opened up. Continua shortward of the opacity edge from the ground state of neutral silicon at 152 nm are formed above the photosphere and can be used to constrain chromospheric models. Together with observations in Ly-α, such UV continuum observations were used by Vernazza et al. (1973, 1976, 1981) in their seminal series of papers on the solar chromosphere. The VAL3 paper (Vernazza et al. 1981) is one of the most cited papers in solar physics (1072 citations in ADS at the time of writing) and the abstract gives a very concise description of the models and the principles behind their construction: "The described investigation is concerned with the solution of the non-LTE optically thick transfer equations for hydrogen, carbon, and other constituents to determine semi-empirical models for six components of the quiet solar chromosphere. For a given temperature-height distribution, the solution is obtained of the equations of statistical equilibrium, radiative transfer for lines and continua, and hydrostatic equilibrium to find the ionization and excitation conditions for each atomic constituent. The emergent spectrum is calculated, and a trial and error approach is used to adjust the temperature distribution so that the emergent spectrum is in best agreement with the observed one. The relationship between semi-empirical models determined in this way and theoretical models based on radiative equilibrium is discussed by Avrett (1977). Harvard Skylab EUV observations are used to determine models for a number of quiet-sun regions."

The VAL3 models are thus characterized by them using Ly-α and UV-continuum observations for observational constraint, hydrostatic equilibrium and non-LTE statistical equilibrium in 1D as physical description and temperature as function of height as free function. To get a match with observed line-strengths, a depth-dependent microturbulence was also determined and a

corresponding turbulent pressure was added. The number of free parameters to be determined by observations is thus large — in principle the number of depth-points per depth-dependent free function (temperature and microturbulence). In practice the fitting was made by trial and error and only rather smooth functions of depth were tried thus decreasing the degrees of freedom in the optimization procedure.

The models have a minimum temperature around 500 km above the visible surface (optical depth unity at 500 nm), a rapid temperature rise outwards to about 6000 K at 1000 km height and thereafter a gradual temperature increase to 7000 K at 2000 km height with a very rapid increase from there to coronal temperatures.

The Ca II lines were not used in constraining the VAL3 models and the agreement between the model representing the average quiet Sun, VAL3C, and observations of these lines was not good. An updated model with a different structure in the temperature minimum region was published in Maltby et al. (1986) (where the main emphasis was on similarly constructed semi-empirical models for sunspot atmospheres).

A peculiar feature with the VAL models was a temperature plateau introduced between 20000 and 30000 K in order to reproduce the total flux in the Lyman lines. This plateau was no longer necessary in the FAL models where the semi-empirical description of the transition region temperature rise was replaced by the balance between energy flowing down from the corona (conduction and ambipolar diffusion) and radiative losses (Fontenla et al. 1990, 1991, 1993).

One goal of semi-empirical models is to obtain clues as to the non-radiative heating process. From the models it is possible to calculate the amount of non-radiative heating that is needed to sustain the model structure. For the VAL3C model this number is 4.2 kW m^{-2} with the dominant radiative losses in lines from Ca II and Mg II, with Ly-α taking over in the topmost part.

The models described so far do not take into account the effect of the very many iron lines. This was done in modeling by Anderson & Athay (1989). Instead of using the temperature as a free parameter and observations as the constraints, they adjusted the non-radiative heating function until they obtained the same temperature structure as in the VAL3C model (arguing that they would then have an equally good fit to the observational constraints as the VAL3C model). The difference in the physical approximations is that they included line blanketing in non-LTE from millions of spectral lines. The radiation losses are dominated by Fe II, with Ca II, Mg II, and H playing important, but secondary, roles. The total non-radiative input needed to balance the radiative losses is three times higher than in the VAL3C model, 14 kW m^{-2}.

The VAL3 and FAL models show a good fit to the average (spatial and temporal) UV spectrum but fail to reproduce the strong lines from CO. These lines show very low intensities in the line center when observed close to the solar limb, the radiation temperature is as low as 3700 K (Noyes & Hall 1972; Ayres & Testerman 1981; Ayres et al. 1986; Ayres & Wiedemann 1989; Ayres & Brault 1990). If the formation is in LTE this translates directly to a temperature of 3700 K in layers where the inner wings of the H and K lines indicate a temperature of 4400 K. The obvious solution to the problem is that the CO lines are formed in non-LTE with scattering giving a source function below the Planck-function. Several studies have shown that this is not the solution — the

CO lines are formed in LTE (e.g. Ayres & Wiedemann 1989; Uitenbroek 2000). The model M_CO constructed to fit the CO-lines (Avrett 1995) give too low UV intensities. One way out is to increase the number of free parameters by abandoning the 1D, one-component, framework and construct a two component semi-empirical atmosphere. The COOLC and FLUXT atmospheric models of Ayres et al. (1986) was such an attempt where a filling factor of 7.5% of the hot flux tube atmosphere FLUXT and 92.5% of the COOLC atmosphere reproduced both the H and K lines and the CO-lines. The UV continua, however, are overestimated by a factor of 20 (Avrett 1995). A combination of 60% of a slightly cooler model than M_CO and 40% of a hot F model provides a better fit (Avrett 1995). Another way of providing enough free parameters for a better fit is to introduce an extra force in the hydrostatic equilibrium equation providing additional support making possible a more extended atmosphere. With this extra free parameter it is possible to construct a 1D temperature structure with a low temperature in the right place to reproduce the near-limb observations of the CO lines and a sharp temperature increase to give enough intensity in the UV continua (Fontenla 2007).

A word of caution is needed here. Semi-empirical models are often impressive in how well they can reproduce observations. This is, however, not a proper test of the realism of the models since the observations have been used to constrain the free parameters. The large number of free parameters (e.g., temperature as function of height, microturbulence as function of height and angle, non-gravitational forces) may hide fundamental shortcomings of the underlying assumptions (e.g., ionization equilibrium, lateral homogeneity, static solution). It is not obvious that the energy input required to sustain a model that reproduces time-averaged intensities is the same as the mean energy input needed in a model that reproduces the time-dependent intensities in a dynamic atmosphere. Semi-empirical modeling may give clues as to what processes may be important but we also need to study these underlying physical processes with fewer free parameters. This is the focus of theoretical models.

3. Theoretical Models

In contrast to semi-empirical models theoretical models include an energy equation. To model the full 3D system with all physical ingredients we know are important for chromospheric conditions is still computationally prohibitive — various approximations have to be made. In one class of modeling one tries to illustrate basic physical processes without the ambition of being realistic enough to allow detailed comparison with observations. Instead the aim is to fashion a basic physical foundation upon which to build our understanding. The other approach is to start with as much realism as can be afforded. Once the models compare favourably with observations, the system is simplified in order to enable an understanding of the most important processes. I here comment on both types of approaches.

3.1. 1D radiation hydrodynamic simulations

Acoustic waves were suggested to be the agent of non-radiative energy input already by Biermann (1948) and Schwarzschild (1948). Such waves are inevitably

excited by the turbulent motions in the convection zone and propagate outwards, transporting mechanical energy through the photospheric layers into the chromosphere and corona. Due to the exponential decrease of density with height, the amplitude of the waves increases and they steepen into shocks. The theory that the dissipation of shocks heats the outer atmosphere was further investigated by various authors, see reviews by Schrijver (1995); Narain & Ulmschneider (1996).

In a series of papers, Carlsson & Stein (1992, 1994, 1995, 1997, 2002a) have explored the effect of acoustic waves on chromospheric structure and dynamics. The emphasis of this modeling was on a very detailed description of the radiative processes and on the direct comparison with observations. The full non-LTE rate equations for the most important species in the energy balance (hydrogen, helium and calcium) were included thus including the effects of non-equilibrium ionization, excitation, and radiative energy exchange on fluid motions and the effect of motion on the emitted radiation from these species. To make the calculations computationally tractable, the simulations were performed in 1D and magnetic fields were neglected. To enable a direct comparison with observations, acoustic waves were sent in through the bottom boundary with amplitudes and phases that matched observations of Doppler shifts in a photospheric iron line.

These numerical simulations of the response of the chromosphere to acoustic waves show that the Ca II profiles can be explained by acoustic waves close to the acoustic cut-off period of the atmosphere. The simulations of the behaviour of the Ca II H line reproduce the observed features to remarkable detail. The simulations show that the three minute waves are already present at photospheric heights and the dominant photospheric disturbances of five minute period only play a minor modulating role (Carlsson & Stein 1997). The waves grow to large amplitude already at 0.5 Mm height and have a profound effect on the atmosphere. The simulations show that in such a dynamic situation it is misleading to construct a mean static model (Carlsson & Stein 1994, 1995). It was even questioned whether the Sun has an average temperature rise at chromospheric heights in non-magnetic regions (Carlsson & Stein 1995). The simulations also confirmed the result of Kneer (1980) that ionization/recombination timescales in hydrogen are longer than typical hydrodynamical timescales under solar chromospheric conditions. The hydrogen ionization balance is therefore out of equilibrium and depends on the previous history of the atmosphere. Since the hydrogen ionization energy is an important part of the internal energy equation, this non-equilibrium ionization balance also has a very important effect on the energetics and temperature profile of the shocks (Carlsson & Stein 1992, 2002a). Kneer (1980) formulated this result as strongly as "Unless confirmed by consistent dynamical calculations, chromospheric models based on the assumption of statistical steady state should be taken as rough estimates of chromospheric structure."

Are observations in other chromospheric diagnostics than the Ca II lines consistent with the above mentioned radiation-hydrodynamic simulations of the propagation of acoustic waves? The answer is "No". The continuum observations around 130 nm are well matched by the simulations (Judge et al. 2003) but continua formed higher in the chromosphere have higher intensity in the observations than in the simulations (Carlsson & Stein 2002c). The chromospheric lines from neutral elements in the UV range are formed in the mid to

upper chromosphere. They are in emission at all times and at all positions in the observations, and they show stronger emission than in the simulations.

The failure of the simulations to reproduce diagnostics formed in the middle to upper chromosphere gives us information on the energy balance of these regions. The main candidates for an explanation are the absence of magnetic fields in the simulations and the fact that the acoustic waves fed into the computational domain at the bottom boundary do not include waves with frequencies above 20 mHz.

The reason for the latter shortcoming is that the bottom boundary is determined by an observed wave-field and high frequency waves are not well determined observationally. I first explore the possibility that high frequency acoustic waves may account for the increased input and address the issue of magnetic fields in the next section.

3.2. High frequency waves

Observationally it is difficult to detect high frequency acoustic waves for two reasons: First, the seeing blurs the ground based observations and makes these waves hard to observe. Second, for both ground based and space based observations the signal we get from high frequency waves is weakened by the width of the response function. Wunnenberg et al. (2002) have summarized the various attempts at detecting high frequency waves, and we refer to them for further background.

Theoretically it is also non-trivial to determine the spectrum of generated acoustic waves from convective motions. Analytic studies indicate that there is a peak in the acoustic spectrum around periods of 50 s (Musielak et al. 1994; Fawzy et al. 2002) while results from high-resolution numerical simulations of convection indicate decreasing power as a function of frequency (Goldreich et al. 1994; Stein & Nordlund 2001).

Recently, Fossum & Carlsson (2005b) & Fossum & Carlsson (2006) analyzed observations from the Transition Region And Coronal Explorer (TRACE) satellite in the 1600 Å passband. Simulations were used to get the width of the response function (Fossum & Carlsson 2005a) and to calibrate the observed intensity fluctuations in terms of acoustic energy flux as function of frequency at the response height (about 430 km). It was found that the acoustic energy flux at 430 km is dominated by waves close to the acoustic cut-off frequency and the high frequency waves do not contribute enough to be a significant contributor to the heating of the chromosphere. Waves are detected up to 28 mHz frequency, and even assuming that all the signal at higher frequencies is signal rather than noise, still gives an integrated energy flux of less than 500 $\mathrm{W\,m^{-2}}$, too small by a factor of ten to account for the losses in the VAL3C model. For the field free internetwork regions used in the TRACE observations it is more appropriate to use the VAL3A model that was constructed to fit the lowest intensities observed with Skylab. It has about 2.2 times lower radiative losses than VAL3C (Avrett 1981) so there is still a major discrepancy. One should also remember that Anderson & Athay (1989) found three times higher energy requirement than in the VAL3C model when they included the radiative losses in millions of spectral lines, dominated by lines from Fe II. As pointed out by Fossum & Carlsson (2006), the main uncertainty in the results is the limited spatial resolution of the

TRACE instrument (0.5″ pixels corresponding to 1″ resolution with a possible additional smearing from the little known instrument PDF): "There is possibly undetected wave power because of the limited spatial resolution of the TRACE instrument. The wavelength of a 40 mHz acoustic wave is 180 km and the horizontal extent may be smaller than the TRACE resolution of 700 km. Several arguments can be made as to why this effect is probably not drastic. Firstly, 5 minute waves are typically 10–20″ in coherence, 3 minute waves 5–10″. In both cases 3–6 times the vertical wavelength. This would correspond to close to the resolution element for a 40 mHz wave. Secondly, even a point source excitation will give a spherical wave that will travel faster in the deeper parts (because of the higher temperature) and therefore the spherical wavefront will be refracted to a more planar wave. With a distance of at least 500 km from the excitation level it is hard to imagine waves of much smaller extent than that at a height of 400 km. There is likely hidden power in the subresolution scales, especially at high frequencies. Given the dominance of the low frequencies in the integrated power, the effect on the total power should be small. It is possible to quantify the missing power by making artificial observations of 3D hydrodynamical simulations with different resolution. This is not trivial since the results will be dependent on how well the simuation describes the excitation of high frequency waves and their subsequent propagation. Preliminary tests in a 3D hydrodynamical simulation extending from the convection zone to the corona (Hansteen 2004) indicate that the effect of the limited spatial resolution of TRACE on the total derived acoustic power is below a factor of two. Although it is thus unlikely that there is enough hidden subresolution acoustic power to provide the heating for the chromosphere, the effect of limited spatial resolution is the major uncertainty in the determination of the *shape* of the acoustic spectrum at high frequencies."

Another effect that goes in the opposite direction is that the analysis assumes that *all* observed power above 5 mHz corresponds to propagating acoustic waves. Especially at lower frequencies we will also have a signal from the temporal evolotion of small scale structures that in this analysis is mistakenly attributed to wave power.

In a restrictive interpretation the result of Fossum & Carlsson (2005b) is that acoustic heating can not sustain a temperature structure like that in static, semi-empirical models of the Sun. Whether a dynamic model of the chromosphere can explain the observations with acoustic heating alone has to be answered by comparing observables from the hydrodynamic simulation with observations. This was done by Wedemeyer-Böhm et al. (2007). They come to the conclusion that their dynamic model (Wedemeyer et al. 2004) is compatible with the TRACE observations (the limited spatial resolution of the TRACE instrument severly affects the synthetic observations) and that acoustic waves could provide enough heating of the chromosphere. The synthetic TRACE images do not take into account non-LTE effects or line opacities. It is also worth noting that the model of Wedemeyer et al. (2004) does not have an average temperature rise in the chromosphere and the dominant wave power is at low frequencies close to the acoustic cut-off and not in the high frequency part of the spectrum. Their study, however, is a major step forward — the question will have to be resolved by more realistic modeling and synthesis of observations paired with high quality observations.

The results by Fossum & Carlsson also show that the neglect of high-frequency waves in the simulations by Carlsson & Stein is not an important omission. Comparing their simulations with observations shows that the agreement is good in the lower chromosphere (Carlsson & Stein 1997; Judge et al. 2003) but lines and continua formed above about 0.8 Mm height have much too low mean intensities. This is probably also true for the Wedemeyer et al. (2004) model (since it has similar mean temperature) but this needs to be checked by proper calculations. It thus seems inevitable that the energy balance in the middle and upper chromosphere is dominated by processes related to the magnetic field. This is consistent with the fact that the concept of a non-magnetic chromosphere is at best valid in the low chromosphere — in the middle to upper chromosphere, the magnetic fields have spread and fill the volume. Even in the photosphere, most of the area may be filled with weak fields or with stronger fields with smaller filling factor (Sanchez Almeida 2005; Trujillo Bueno et al. 2004).

3.3. Comprehensive models in 3D

3D hydrodynamic simulations of solar convection have been very successful in reproducing observations (e.g. Nordlund 1982; Stein & Nordlund 1998; Asplund et al. 2000; Vögler et al. 2005). It would be very natural to extend these simulations to chromospheric layers to study the effect of acoustic waves on the structure, dynamics and energetics of the chromosphere. This approach would then include both the excitation of the waves by the turbulent motions in the convection zone and their subsequent damping and dissipation in chromospheric shocks. For a realistic treatment there are several complications. First, the approximation of LTE that works nicely in the photosphere will overestimate the local coupling in chromospheric layers. The strong lines that dominate the radiative coupling have a source function that is dominated by scattering. Second, shock formation in the chromosphere makes it necessary to have a fine grid or describe sub-grid physics with some shock capturing scheme. Third, it is important to take into account the long timescales for hydrogen ionization/recombination for the proper evaluation of the energy balance in the chromosphere (Kneer 1980; Carlsson & Stein 1992, 2002a).

Skartlien (2000) addressed the first issue by extending the multi-group opacity scheme of Nordlund to include the effects of coherent scattering. This modification made it possible to make the first consistent 3D hydrodynamic simulations extending from the convection zone to the chromosphere (Skartlien et al. 2000). Due to the limited spatial resolution, the emphasis was on the excitation of chromospheric wave transients by collapsing granules and not on the detailed structure and dynamics of the chromosphere.

3D hydrodynamic simulations extending into the chromosphere with higher spatial resolution were performed by Wedemeyer et al. (2004). They employed a much more schematic description of the radiation (gray radiation) and did not include the effect of scattering. This shortcoming will surely affect the amount of radiative damping the waves undergo in the photosphere. The neglect of strong lines avoids the problem of too strong coupling with the local conditions induced by the LTE approximation so in a way two shortcomings partly balance out. The chromosphere in their simulations is very dynamic and filamentary.

Hot gas coexists with cool gas at all heights and the gas is in the cool state a large fraction of the time. As was the case in Carlsson & Stein (1995) they find that the average gas temperature shows very little increase with height while the radiation temperature does have a chromospheric rise similar to the VAL3C model. The temperature variations are very large, with temperatures as low as 2000 K and as high as 7000 K at a height of 800 km. It is likely that the approximate treatment of the radiation underestimates the amount of radiative damping thus leading to too large an amplitude.

The low temperatures in the simulations allow for a large amount of CO to be present at chromospheric heights, consistent with observations. For a proper calculation of CO concentrations it is important to take into account the detailed chemistry of CO formation, including the timescales of the reactions. This was done in 1D radiation hydrodynamic models by Asensio Ramos et al. (2003) and in 2D models by Wedemeyer-Böhm et al. (2005). The dynamic formation of CO was also included in the 3D models and it was shown that CO-cooling does *not* play an important role for the dynamic energy balance at chromospheric heights (Wedemeyer-Böhm & Steffen 2007).

Including long timescales for hydrogen ionization/recombination is non-trivial. In a 1D simulation it is still computationally feasible to treat the full non-LTE problem in an implicit scheme (avoiding the problem of stiff equations) as was shown by Carlsson & Stein. The same approach is not possible at present in 3D; the non-local coupling is too expensive to calculate. Fortunately, the hydrogen ionization is dominated by collisional excitation to the first excited level (local process) followed by photo-ionization in the Balmer continuum. Since the radiation field in the Balmer continuum is set in the photosphere, it is possible to describe the photoionization in the chromospheric problem with a fixed radiation field (thus non-local but as a given rate that does not change with the solution). This was shown to work nicely in a 1D setting by Sollum (1999). Leenaarts & Wedemeyer-Böhm (2006) implemented the rate equations in 3D but without the coupling back to the energy equation. The non-equilibrium ionization of hydrogen has a dramatic effect on the ionization balance of hydrogen in the chromosphere in their simulation.

Magnetic fields start to dominate over the plasma somehere in the chromosphere. Chromospheric plasma as seen in the center Hα (e.g., Rutten (2007), De Pontieu et al. (2007)) is very clearly organized along the magnetic structures. It is very likely that acoustic heating alone is not sufficient to account for the radiative losses in the chromosphere. It is thus of paramount importance to include magnetic fields in chromospheric modeling but unfortunetely the inclusion of magnetic fields increase the level of complexity enormously. As was the case with acoustic waves, it is necessary to perform numerical experiments and modeling in simplified cases in order to fashion a basic physical foundation upon which to build our understanding. A number of authors have studied various magnetic wave modes and how they couple, see Bogdan et al. (2003) and Khomenko & Collados (2006) for references. Rosenthal et al. (2002) and Bogdan et al. (2003) reported on 2D simulations in various magnetic field configurations in a gravitationally stratified isothermal atmosphere, assuming an adiabatic equation of state. Carlsson & Stein (2002b) and Carlsson & Bogdan (2006) reported on similar calculations in the same isothermal atmosphere but this time in 3D and also studying the effect of radiative damping of the shocks.

Hasan et al. (2005) studied the dynamics of the solar magnetic network in two dimensions and Khomenko & Collados (2006) studied the propagation of waves in and close to a structure similar to a small sunspot.

The picture that emerges from these studies is that waves undergo mode conversion, refraction and reflection at the height where the sound speed equals the Alfvén speed (which is typically some place in the chromosphere). The critical quantity for mode conversion is the angle between the magnetic field and the k-vector: the attack angle. At angles smaller than 30 degrees much of the acoustic, fast mode from the photosphere is transmitted as an acoustic, slow mode propagating along the field lines. At larger angles, most of the energy is refracted/reflected and returns as a fast mode creating an interference pattern between the upward and downward propagating waves. When damping from shock dissipation and radiation is taken into account, the waves in the low-mid chromosphere have mostly the character of upward propagating acoustic waves and it is only close to the reflecting layer we get similar amplitudes for the upward propagating and refracted/reflected waves. It is clear that even simple magnetic field geometries and simple incident waves create very intricate interference patterns. In the chromosphere, where the wave amplitude is expected to be large, it is crucial to include the effects of the magnetic fields to understand the structure, dynamics and energetics of the atmosphere. This is true even in areas comparably free of magnetic field (such regions *may* exist in the lower chromosphere).

The fact that wave propagation is much affected by the magnetic field topology in the chromosphere can be used for "seismology" of the chromosphere. Observational clues have been obtained by McIntosch and co-workers: McIntosh et al. (2001) & McIntosh & Judge (2001) find a clear correlation between observations of wave power in SOHO/SUMER observations and the magnetic field topology as extrapolated from SOHO/MDI observations. These results were extended to the finding of a direct correlation between reduced oscillatory power in the 2D TRACE UV continuum observations and the height of the magnetic canopy (McIntosh et al. 2003) and the authors suggest using TRACE time-series data as a diagnostic of the plasma topography and conditions in the mid-chromosphere through the signatures of the wave modes present. Such helioseismic mapping of the magnetic canopy in the solar chromosphere was performed by Finsterle et al. (2004) and in a coronal hole by McIntosh et al. (2004).

The chromosphere is very inhomogeneous and dynamic. There is no simple way of inverting the above observations to a consistent picture of the chromospheric conditions. One will have to rely on comparisons with full 3D Radiation-Magneto-Hydrodynamic forward modeling. Steiner et al. (2007) tracked a plane-parallel, monochromatic wave propagating through a non-stationary, realistic atmosphere, from the convection-zone through the photosphere into the magnetically dominated chromosphere. They find that a travel time analysis, like the ones mentioned above, indeed is correlated with the magnetic topography and that high frequency waves can be used to extract information on the magnetic canopy.

Including not only 3D hydrodynamics but in addition the magnetic field, and extending the computational domain to include the corona is a daunting task. However, the development of modern codes and computational power is

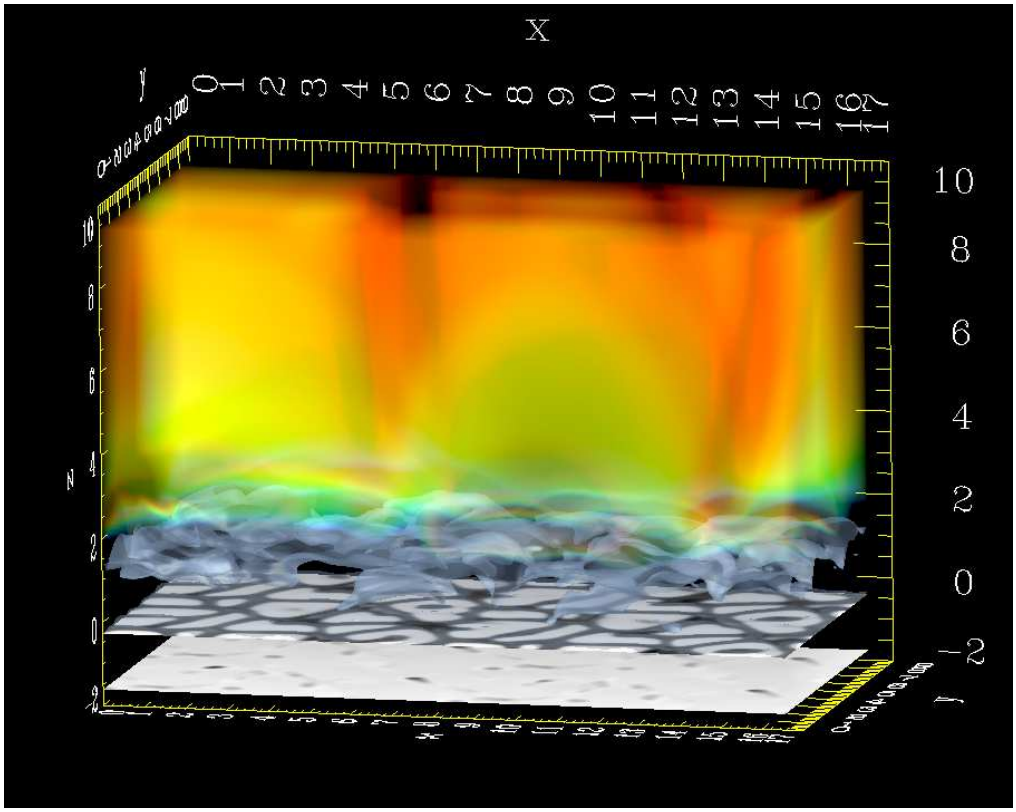

Figure 1. Temperature structure in a 3D simulation box. The bottom plane shows the temperature at 1.5 Mm below τ_{500}=1 ranging from 15 700 K in down-flowing plumes to 16 500 in the gas flowing into the simulation domain. The next plane is in the photosphere and shows hot granules and cool intergranular lanes. In the chromosphere the isothermal surfaces show pronounced small scall structures and corrugated shock fronts. The upper 8 Mm is filled with plasma at transition region and coronal temperatures up to 1 MK.

such that it is a task that is within reach of fulfillment. Hansteen (2004) reported on the first results from such comprehensive modeling. The 3D computational box is $16 \times 8 \times 12$ Mm in size extending 2 Mm below and 10 Mm above the photosphere. Radiation is treated in detail, using multi-group opacities including the effect of scattering (Skartlien 2000), conduction along field-lines is solved for implicitly and optically thin losses are included in the transition region and corona. For a snapshot of such a simulation, see Fig.1.

After a relaxation phase from the initial conditions, coronal temperatures are maintained self-consistently by the injection of Pointing flux from the convective buffeting of the magnetic field, much as in the seminal simulations by Gudiksen & Nordlund (2002, 2005a, 2005b).

It is clear from these simulations that the presence of the magnetic field has fundamental importance for chromospheric dynamics and the propagation of waves through the chromosphere. It is also clear that magnetic fields play a role in the heating of the chromosphere (Hansteen et al. 2007).

There are several hotly debated topics in chromospheric modeling today: Is the internetwork chromosphere wholly dynamic in nature or are the dynamic variations only minor perturbations on a semi-static state similar to the state in semi-empirical models (e.g., Kalkofen et al. 1999)? Is there a semi-permanent cold chromosphere (where CO lines originate) or is the CO just formed in the cool phases of a dynamic atmosphere? Is there enough chromospheric heating in high frequency waves of small enough spatial extent that they are not detected by the limited spatial resolution of TRACE? What is the role of the magnetic field (mode conversion of waves, reconection, currents, channeling of waves)? A reason for conflicting results is the incompleteness of the physical description in the modeling and the lack of details (spatial and temporal resolution) in the observations. We are rapidly progressing towards the resolution of this situation. New exciting observations at high temporal and spatial resolution (especially from the Swedish 1-m Solar Telescope on La Palma) are changing our view of the chromosphere. New observing facilities are on the verge of coming on line (GREGOR, Hinode). On the modeling side, several groups have developed codes that start to include the most important ingredients for a comprehensive modeling of the dynamic chromosphere (e.g., Hansteen 2004; Schaffenberger et al. 2006). There is still more work to do with simulations of idealized cases to build up a foundation for our understanding and this is also a field with several groups active at present. The future for chromospheric modeling thus looks both promising and exciting.

Acknowledgments. This work was supported by the Research Council of Norway grant 146467/420 and a grant of computing time from the Program for Supercomputing.

References

Anderson L. S., Athay R. G., 1989, ApJ 336, 1089
Asensio Ramos A., Trujillo Bueno J., Carlsson M., Cernicharo J., 2003, ApJ 588, L61
Asplund M., Nordlund Å., Trampedach R., Allende Prieto C., Stein R. F., 2000, A&A 359, 729
Avrett E., 1981, in R.M.Bonnet, A.K.Dupree (eds.), Solar Phenomena in Stars and Stellar Systems, Dordrecht, 173
Avrett E. H., 1995, in J. R. Kuhn, M. J. Penn (eds.), Infrared tools for solar astrophysics: What's next?, 303
Ayres T. R., Brault J. W., 1990, ApJ 363, 705
Ayres T. R., Testerman L., 1981, ApJ245, 1124
Ayres T. R., Testerman L., Brault J. W., 1986, ApJ304, 542
Ayres T. R., Wiedemann G. R., 1989, ApJ338, 1033
Biermann L., 1948, Zs. f. Astrophys. 25, 161
Bogdan T. J., Carlsson M., Hansteen V., McMurry A., Rosenthal C., Johnson M., Petty-Powell S., Zita E., Stein R., McIntosh S., Nordlund Å., 2003, ApJ 599, 626
Carlsson M., 2006, in H.Uitenbroek, J.Leibacher, R.F.Stein (eds.), Solar MHD: Theory and Observations - a High Spatial Resolution Perspective, ASP Conf. Ser. 354, 291
Carlsson M., Bogdan T. J., 2006, Phil. Trans. R. Soc. A 364, 395
Carlsson M., Stein R. F., 1992, ApJ 397, L59
Carlsson M., Stein R. F., 1994, in M. Carlsson (ed.), Proc. Mini-Workshop on Chromospheric Dynamics, Institute of Theoretical Astrophysics, Oslo, 47
Carlsson M., Stein R. F., 1995, ApJ 440, L29

Carlsson M., Stein R. F., 1997, ApJ 481, 500
Carlsson M., Stein R. F., 2002a, ApJ 572, 626
Carlsson M., Stein R. F., 2002b, in H. Sawaya-Lacoste (ed.), Magnetic Coupling of the Solar Atmosphere, ESA SP-505, 293
Carlsson M., Stein R. F., 2002c, in A.Wilson (ed.), SOHO-11: From Solar Minimum to Maximum, ESA SP-508, 245
Fawzy D., Rammacher W., Ulmschneider P., Musielak Z. E., Stępień K., 2002, A&A 386, 971
Finsterle W., Jefferies S. M., Cacciani A., Rapex P., McIntosh S. W., 2004, ApJ 613, L185
Fontenla J., 2007, in P. Heinzel, I. Dorotovič, R.J. Rutten (eds.), The Physics of the Chromospheric Plasmas, ASP Conf. Ser. 368, 499
Fontenla J. M., Avrett E. H., Loeser R., 1990, ApJ 355, 700
Fontenla J. M., Avrett E. H., Loeser R., 1991, ApJ 377, 712
Fontenla J. M., Avrett E. H., Loeser R., 1993, ApJ 406, 319
Fossum A., Carlsson M., 2005a, ApJ 625, 556
Fossum A., Carlsson M., 2005b, Nature 435, 919
Fossum A., Carlsson M., 2006, ApJ 646, 579
Goldreich P., Murray N., Kumar P., 1994, ApJ 424, 466
Gudiksen B. V., Nordlund Å., 2002, ApJ 572, L113
Gudiksen B. V., Nordlund Å., 2005a, ApJ 618, 1031
Gudiksen B. V., Nordlund Å., 2005b, ApJ 618, 1020
Hansteen V., Carlsson M., Gudiksen B., 2007, in P. Heinzel, I. Dorotovič, R.J. Rutten (eds.), The Physics of the Chromospheric Plasmas, ASP Conf. Ser. 368, 107
Hansteen V. H., 2004, in A.V.Stepanov, E.E.Benevolenskaya, E.G.Kosovichev (eds.), IAU Symp. 223: Multi Wavelength Investigations of Solar Activity, 385
Hasan S. S., van Ballegooijen A. A., Kalkofen W., Steiner O., 2005, ApJ 631, 1270
Judge P. G., Carlsson M., Stein R. F., 2003, ApJ 597, 1158
Kalkofen W., Ulmschneider P., Avrett E. H., 1999, ApJ 521, L141
Khomenko E., Collados M., 2006, ApJ653, 739
Kneer F., 1980, A&A87, 229
Leenaarts J., Wedemeyer-Böhm S., 2006, A&A460, 301
Maltby P., Avrett E. H., Carlsson M., Kjeldseth-Moe O., Kurucz R. L., Loeser R., 1986, ApJ 306, 284
McIntosh S. W., Bogdan T. J., Cally P. S., Carlsson M., Hansteen V. H., Judge P. G., Lites B. W., Peter H., Rosenthal C. S., Tarbell T. D., 2001, ApJ 548, L237
McIntosh S. W., Fleck B., Judge P. G., 2003, A&A 405, 769
McIntosh S. W., Fleck B., Tarbell T. D., 2004, ApJ 609, L95
McIntosh S. W., Judge P. G., 2001, ApJ 561, 420
Musielak Z. E., Rosner R., Stein R. F., Ulmschneider P., 1994, ApJ 423, 474
Narain U., Ulmschneider P., 1996, Space Sc. Rev. 75, 453
Nordlund Å., 1982, A&A 107, 1
Noyes R. W., Hall D. N. B., 1972, ApJ 176, L89
De Pontieu B., Hansteen V., van der Voort L. R., van Noort M., Carlsson M., 2007, in P. Heinzel, I. Dorotovič, R.J. Rutten (eds.), The Physics of the Chromospheric Plasmas, ASP Conf. Ser. 368, 65
Rosenthal C., Bogdan T., Carlsson M., Dorch S., Hansteen V., McIntosh S., McMurry A., Nordlund Å., Stein R. F., 2002, ApJ 564, 508
Rutten R., 2007, in P. Heinzel, I. Dorotovič, R.J. Rutten (eds.), The Physics of the Chromospheric Plasmas, ASP Conf. Ser. 368, 27
Sanchez Almeida J., 2005, A&A 438, 727
Schaffenberger W., Wedemeyer-Böhm S., Steiner O., Freytag B., 2006, in H.Uitenbroek, J.Leibacher, R.F.Stein (eds.), Theory and Observations - a High Spatial Resolution Perspective, ASP Conf. Ser. 354, 351
Schrijver C., 1995, A&A Rev.6, 181

Schwarzschild M., 1948, ApJ 107, 1
Skartlien R., 2000, ApJ 536, 465
Skartlien R., Stein R. F., Nordlund Å., 2000, ApJ 541, 468
Sollum E., 1999, Hydrogen Ionization in the Solar Atmosphere: Exact and Simplified Treatments, MSc Thesis, Institute of Theoretical Astrophysics, University of Oslo, Norway
Stein R. F., Nordlund A., 1998, ApJ 499, 914
Stein R. F., Nordlund Å., 2001, ApJ 546, 585
Steiner O., Vigeesh G., Krieger L., Wedemeyer-Böhm S., Schaffenberger W., Freytag B., 2007, ArXiv Astrophysics e-prints
Trujillo Bueno J., Shchukina N., Asensio Ramos A., 2004, Nature 430, 326
Uitenbroek H., 2000, ApJ536, 481
Vernazza J. E., Avrett E. H., Loeser R., 1973, ApJ 184, 605
Vernazza J. E., Avrett E. H., Loeser R., 1976, ApJS 30, 1
Vernazza J. E., Avrett E. H., Loeser R., 1981, ApJS 45, 635
Vögler A., Shelyag S., Schüssler M., Cattaneo F., Emonet T., Linde T., 2005, A&A429, 335
Wedemeyer S., Freytag B., Steffen M., Ludwig H.-G., Holweger H., 2004, A&A 414, 1121
Wedemeyer-Böhm S., Kamp I., Bruls J., Freytag B., 2005, A&A 438, 1043
Wedemeyer-Böhm S., Steffen M., 2007, A&A, in press
Wedemeyer-Böhm S., Steiner O., Bruls J., Ramacher W., 2007, in P. Heinzel, I. Dorotovič, R.J. Rutten (eds.), The Physics of the Chromospheric Plasmas, ASP Conf. Ser. 368, 93
Wunnenberg M., Kneer F., Hirzberger J., 2002, A&A 395, L51

Opening ceremony: Artur Soares Alves (Observatory Director), Petr Heinzel, Fernando Seabra Santos (University Rector), Joaquim Júdice (Head Mathematics Dept.), João Fernandes

Gianna Cauzzi

The Physics of Chromospheric Plasmas
ASP Conference Series, Vol. 368, 2007
Petr Heinzel, Ivan Dorotovič and Robert J. Rutten, eds.

High-Resolution Observations and Numerical Simulations of Chromospheric Fibrils and Mottles

Bart De Pontieu[1], Viggo H. Hansteen[2], Luc Rouppe van der Voort[2], Michiel van Noort[3] and Mats Carlsson[2]

[1]*Lockheed Martin Solar and Astrophysics Lab, Palo Alto, CA, USA*
[2]*Institute of Theoretical Astrophysics, University of Oslo, Norway*
[3]*Institute for Solar Physics of the Royal Swedish Academy of Sciences, Stockholm, Sweden*

Abstract. With the recent advent of the Swedish 1-m Solar Telescope (SST), advanced image processing techniques, as well as numerical simulations that provide a more realistic view of the chromosphere, a comprehensive understanding of chromospheric jets such as spicules, mottles and fibrils is now within reach. In this paper, we briefly summarize results from a recent analysis of dynamic fibrils, short-lived jet-like features that dominate the chromosphere (as imaged in Hα) above and about active region plage. Using extremely high-resolution observations obtained at the SST, and advanced numerical 2D radiative MHD simulations, we show that fibrils are most likely formed by chromospheric shock waves that occur when convective flows and global oscillations leak into the chromosphere along the field lines of magnetic flux concentrations.

In addition, we present some preliminary observations of quiet Sun jets or mottles. We find that the mechanism that produces fibrils in active regions is most likely also at work in quiet Sun regions, although it is modified by the weaker magnetic field and the presence of more mixed-polarity. A comparison with numerical simulations suggests that the weaker magnetic field in quiet Sun allows for significantly stronger (than in active regions) transverse motions that are superposed on the field-aligned, shock-driven motions. This leads to a more dynamic, and much more complex environment than in active region plage. In addition, our observations of the mixed polarity environment in quiet Sun regions suggest that other mechanisms, such as reconnection, may well play a significant role in the formation of some quiet Sun jets. Simultaneous high-resolution magnetograms (such as those provided by Hinode), as well as numerical simulations that take into account a whole variety of different magnetic configurations, will be necessary to determine the relative importance in quiet Sun of, respectively, the fibril-mechanism and reconnection.

1. Introduction

Spicules and related flows such as mottles and fibrils dominate the highly dynamic chromosphere (Rutten 2007, p. 27 ff in this volume), a region in which over 90% of the non-radiative energy going into the outer atmosphere to drive solar activity and space weather is deposited. Spicules are relatively thin, elongated structures, best seen at the limb in Hα. They are but one form of the many "spicular" features that dominate the chromosphere, such as quiet Sun mottles, or active region (AR) fibrils, both observed on the disk (Beckers 1968).

Even though it is not clear how all of these "spicular features" are related, it seems that all represent real mass motion of chromospheric plasma to coronal heights (see, e.g., the many EUV absorbing features in images taken with the Transition Region and Coronal Explorer, TRACE, Handy et al. 1999).

Spicules (at the limb), mottles (on the quiet Sun disk) and fibrils (in active regions) have been studied for many decades, but until recently they have remained poorly understood, because of a lack of high quality observations: their diameters of a few hundred km and lifetimes of a few minutes were too close to observational limits. In addition, theoretical models were usually highly simplified (1D) and focused mainly on spicule-like jets in isolation from the surrounding, driving atmosphere. Several recent advances have now enabled major breakthroughs in our understanding of at least some of these dynamic chromospheric jets.

On the observational side, new telescopes such as the Swedish 1-m Solar Telescope (SST, Scharmer et al. 2003) in La Palma, as well as advanced image processing techniques, such as the Multi-Object Multi-Frame Blind Deconvolution method (MOMFBD, van Noort et al. 2005), have allowed diffraction-limited ($\sim$120 km) time series in chromospheric lines (e.g., Hα) at extremely high temporal resolution (1 second). These datasets have, for the first time, resolved the dominant temporal and spatial evolution of active region fibrils and quiet Sun mottles (Hansteen et al. 2006; De Pontieu et al. 2007).

Parallel to these observational advances, theoretical efforts have also made significant progress. Several papers have explored, for the first time, the intricate relationship between the formation of fibrils and the photospheric magnetoconvective flowfield. De Pontieu et al. (2004) used a synthesis of idealized 1D modeling and observations to propose that photospheric oscillations can leak into the chromosphere, where they form shocks to drive fibrils upwards. This idea was based on the close connection between oscillations in upper transition region moss (De Pontieu et al. 1999) and the presence of quasi-periodic jets or fibrils in the chromosphere above active region plage (De Pontieu et al. 2003a). These ideas have now been confirmed and expanded by Hansteen et al. (2006) and De Pontieu et al. (2007) who analyzed a diffraction-limited time series of Hα fibrils, and directly compared them to advanced radiative MHD simulations. They find excellent agreement between observations and simulations.

In this paper, we will very briefly summarize the analysis of Hansteen et al. (2006) and De Pontieu et al. (2007) in Section 2. While this analysis explains the formation of fibrils above active region plage, it is not yet fully clear what role this mechanism plays in quiet Sun. To explore this issue, we show (in Section 3) some very preliminary results of an analysis of very recent SST observations of the quiet Sun chromosphere.

2. Active Region Fibrils

Hansteen et al. (2006) and De Pontieu et al. (2007) use Hα observations with 120 km spatial resolution and 1 s temporal resolution to study the evolution of so-called dynamic fibrils (DFs). These fibrils are relatively short (1,250 km on average), thin (120-700 km) and jet-like features that occur above or in the direct vicinity of active region plage. They are the same jets that dominate the

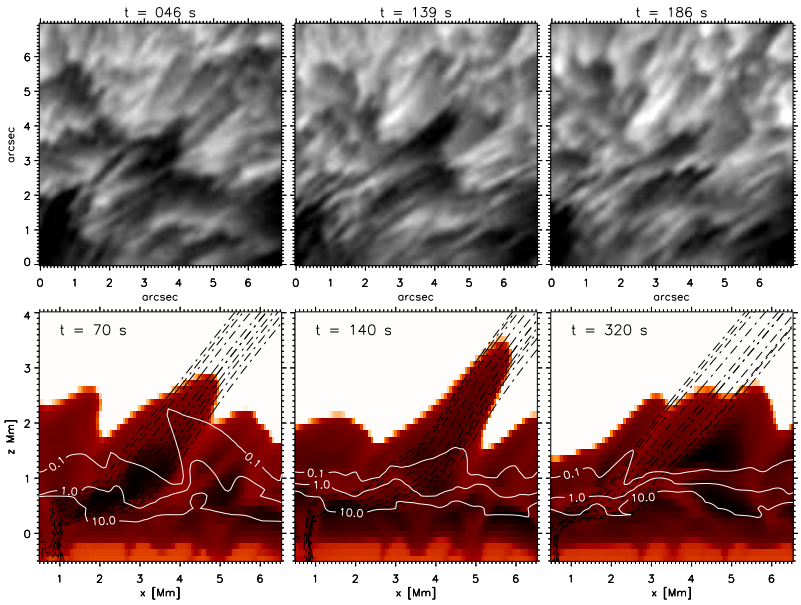

Figure 1. Taken from Hansteen et al. (2006). Temporal evolution of dynamic fibrils from Hα line-center observations at the SST (top panels), and from numerical simulations (bottom panels). The observations show a dark elongated feature with an upper chromospheric temperature of less than 10 000 K rise and fall within 4 minutes. Its maximum length is about $2''$. The bottom panels show the logarithm of the plasma temperature T, which is set to saturate at $\log T = 4.5$, from numerical simulations covering the upper convection zone ($z < 0$) up through the corona (white region at the top). The vertical scale has its origin at the photosphere (where the optical depth $\tau_{500} = 1$). Contours of plasma β are drawn in white where $\beta = 0.1, 1, 10$. The simulations show that dynamic fibrils ascend as a result of upwardly propagating shock waves. These shock waves seem to preferentially enter the corona where the magnetic field lines (dotted black curves) also enter the corona.

dynamics on timescales of minutes of the upper TR moss emission (De Pontieu et al. 2003b). Extensive statistical analysis of the Hα time series reveals that most dynamic fibrils have short lifetimes of 3 to 6 minutes, with clear differences in lifetimes depending on the magnetic topology of the plage region. Plage regions with more vertically oriented field are dominated by DFs with lifetimes of 3 minutes, whereas less dense plage region or plage where the field is more inclined from the vertical typically show DF lifetimes of order 5 minutes. Note that what are traditionally called Hα fibrils typically includes a large subset of almost horizontal loops that form a canopy-like structure that connects neighboring plage regions or sunspots. This subset of usually much longer fibrils is clearly more stable (in time) than the DFs. Wavelet analysis shows that whereas the DFs are dominated by quasi-period oscillations with periods that are identical to the DF lifetimes (i.e., 3 and 5 min), the horizontal fibrils show quasi-periodicity with periods longer than 10 minutes (Hansteen et al. 2006; De Pontieu et al. 2007).

One of the major findings of Hansteen et al. (2006) and De Pontieu et al. (2007) is that almost all fibrils that can be nicely isolated from the background or

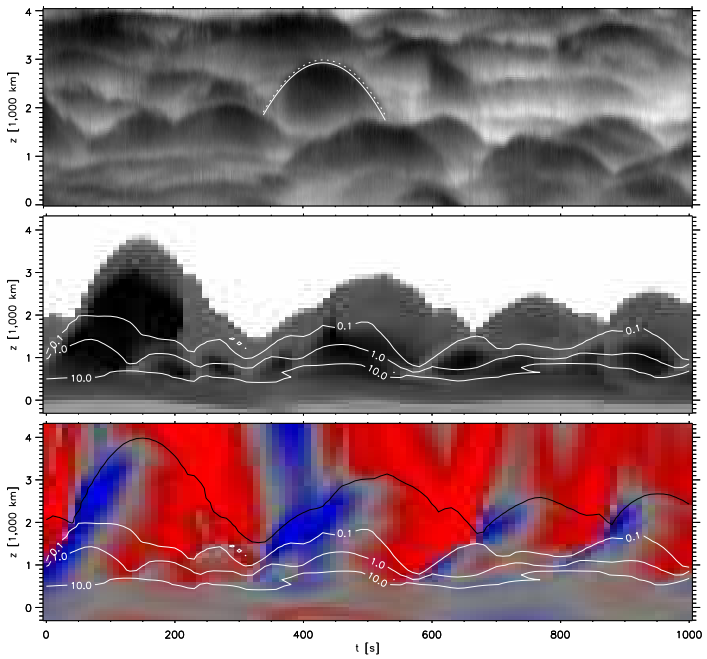

Figure 2. Taken from Hansteen et al. (2006). Space-time plots of: the height of dynamic fibrils for Hα line-center observations (top panel), the logarithm of the plasma temperature in numerical simulations (middle panel), and simultaneous plasma velocity from the same simulation (bottom panel). Most of the dynamic fibrils in the top panel follow a near perfect parabolic path in their rise and descent from the lower atmosphere. Parabolic paths with similar parameters are traced by fibril-like features in the 2D numerical simulations (middle panel). Contours of plasma β are drawn in white where $\beta = 0.1, 1, 10$. Upward plasma velocities (blue in the bottom panel) show the upward propagation of the shocks that drive the fibril-like features along their parabolic path. This initial upward impulse is followed by a constant deceleration which leads to downward velocities (red) of roughly equal magnitude as the initial upward velocities. The black line in the bottom panel outlines the top or transition region of the simulated chromospheric fibrils.

foreground of other fibrils, follow an almost perfect parabolic path in their ascent and descent (Figs. 1, 2). The sharp delineation of the fibril tops is presumably related to the fact that these fibrils have sharp transition regions at their top end. The measurements thus trace the path of the transition region. The velocity of the TR at the beginning of a fibril's life is between 10 and 35 km/s (projected), i.e., supersonic speeds. The velocity then linearly decreases with time, reverses sign and, at the end of the fibril's life, reaches a maximum speed that is similar in magnitude as the initial speed. The deceleration fibrils undergo is significantly less than solar gravity, ranging from 50 to 300 m/s^2. Fibrils typically have internal structure, with various parts rising and falling with slightly different speeds and decelerations. The widths mentioned above were defined as the width over which the parabolic paths still look similar in lifetime and speed.

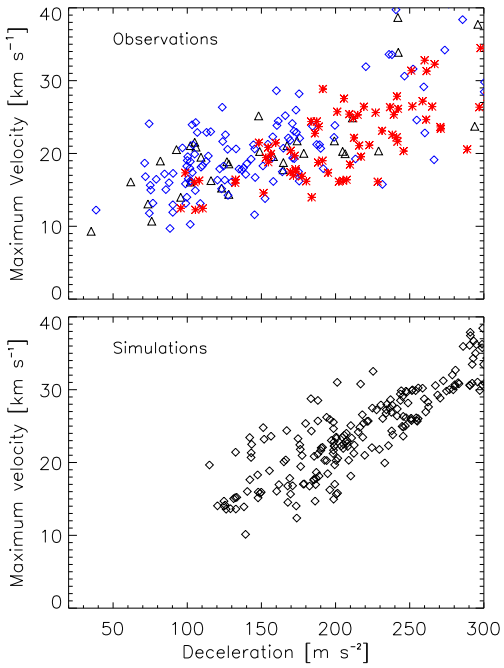

Figure 3. Adapted from Hansteen et al. (2006). Decelerations have been corrected by a factor of 2 (see De Pontieu et al. (2007) for details). Maximum velocities versus decelerations from 257 observed dynamic fibrils (top panel). The maximum velocity and deceleration have been corrected for line-of-sight projection, assuming that the fibril is aligned with the local magnetic field as deduced from potential field calculations. Red stars indicate fibrils from the dense plage region, whereas blue diamonds indicate fibrils in the inclined field region. The same scatterplot (lower panel), made from analyzing fibril-like features in the numerical simulations, reveals that the simulations reproduce the observed correlation between these parameters, as well as reproducing the range in deceleration and maximum velocity.

The numerical simulations described in Hansteen et al. (2006) and De Pontieu et al. (2007) show that fibril-like features occur in a natural fashion in the proximity of flux concentrations, as a result of chromospheric shocks. These shocks form when convective flows and oscillations leak into the chromosphere along magnetic field lines. Figure 1 shows that the jet-like features formed in the simulations have lengths and lifetimes that are similar to the observed fibrils. The simulations also show that the parabolic paths observed in Hα fibrils are a clear sign that these jets are caused by single slow-mode magneto-acoustic shocks. This is evident from Fig. 2, where the shocks are clearly seen in the xt-plot of the velocity in the simulations (bottom panel). One of the most striking results is that the jet-like features in the simulation not only reproduce the parabolic paths, but also the observed correlations between the deceleration and maximum velocity (Fig. 3).

This correlation can be understood in terms of shock wave physics, as illustrated in Fig. 4. Preliminary results of a parameter study of detailed numerical

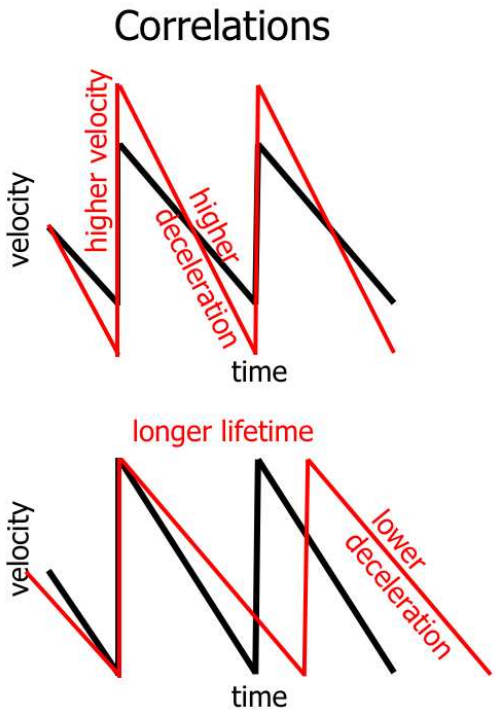

Figure 4. Cartoon illustrating the cause for the correlations between the deceleration and maximum velocity of fibrils (see Fig. 3), and between lifetime and maximum velocity of fibrils (see De Pontieu et al. 2007). Given a fixed lifetime (or shock wave period), higher velocity amplitudes automatically lead to higher decelerations. For a fixed velocity amplitude, longer wave periods lead to lower decelerations.

simulations indicate that this intuitive explanation does indeed dominate the observed correlation between velocity and deceleration (Heggland, De Pontieu, Hansteen, in preparation).

Hansteen et al. (2006) and De Pontieu et al. (2007) find clear differences in fibril properties for two different plage regions. They find higher decelerations, slightly lower velocities, shorter lifetimes and shorter lengths for a dense plage region where the magnetic field is inclined more vertically. In a neighboring plage region, where the field is more inclined from the vertical they find fibrils with lower decelerations, slightly higher velocities, longer lifetimes and longer lengths. All of these measurements are of course projected onto the plane of the sky, which potentially leaves the possibility that these differences are caused by projection effects. While Hansteen et al. (2006) and De Pontieu et al. (2007) use magnetic field extrapolations to exclude this possibility, a more straightforward consideration directly shows that the regional differences are not caused by projection effects, but are rather a sign of real physical differences between the two regions. Let us consider whether there exists a viewing angle that would cause all differences to disappear between both regions. This is clearly impossible, for two reasons. Firstly, the lifetimes are very different between both regions. Lifetimes are very well defined, and independent of viewing angle. Secondly, let

us assume a difference in viewing angle is causing the other differences. Assume that the dense plage region is more tilted towards the observer than the other plage region. In such a case the projected lengths, velocities and decelerations would be lower than those measured along the axis of the fibril. In other words, such a viewing angle difference could resolve the difference in lengths and velocity, but would render the difference in deceleration even worse than it already is. This shows that projection effects cannot explain these differences. In addition, the correlations between various parameters that were found are also independent of projection angle, since both parameters would be corrected by the same factor.

The fact that fibrils are caused by single shock waves is apparently confirmed by the work of Langangen et al. (p. 145 ff in this volume), who use Hα spectra from the SST to determine velocities and decelerations of dynamic fibril features. Similar shock-like features also seem to be present in the data presented by Cauzzi et al. (p. 127 ff in this volume), although further analysis is necessary to confirm this.

Future work will need to involve more advanced radiative transfer calculations for Hα in the numerical simulations. Such calculations could provide insight into why the horizontal fibrils are generally not as dynamic as the DFs, and whether the fact that those fibrils are along loops that most often do not have a transition region plays an important role in its more stable behavior.

3. Quiet Sun Mottles

Preliminary analysis of data from June 18, 2006 shows that the quiet Sun chromosphere as imaged in a diffraction-limited, 5 s cadence Hα line-center time series, is much more complex than similar time series for active regions. The more complex topology of the quiet Sun with its predominantly mixed polarity magnetic fields leads to a much more diverse appearance of dark and bright features (see Fig. 5). Active regions are dominated by long horizontal fibrils and short dynamic fibrils. Quiet Sun has equivalent features: long horizontal dark mottles and short dynamic mottles, that both connect to network regions. In addition, quiet Sun shows many short, highly curved and highly dynamic features that do not seem to be associated with network, but mostly appear in the internetwork (see the area around $21''$, $4''$ in Fig. 5). These internetwork features can often be seen underneath the canopy-like long horizontal mottles, so they seem to be formed at lower heights than the "canopy". The internetwork features seem to be associated with the underlying granular dynamics. In this section we will focus on the network-associated features.

Contrary to active regions, it is generally extremely difficult to track single QS mottles during their lifetime. One reason for this difficulty is that many mottles lack the sharp "top" end that dominates the appearance of dynamic fibrils in active regions. More importantly, most mottles undergo not only up and downward motions along the direction of the magnetic field, but also significant motions transverse to the magnetic field, as well as fading or dimming during their lifetime. The transverse motions are often well organized or coherent over several arcseconds, so that a whole batch of almost parallel mottles seem to undergo rocking or rotating motions during their lifetime. The appar-

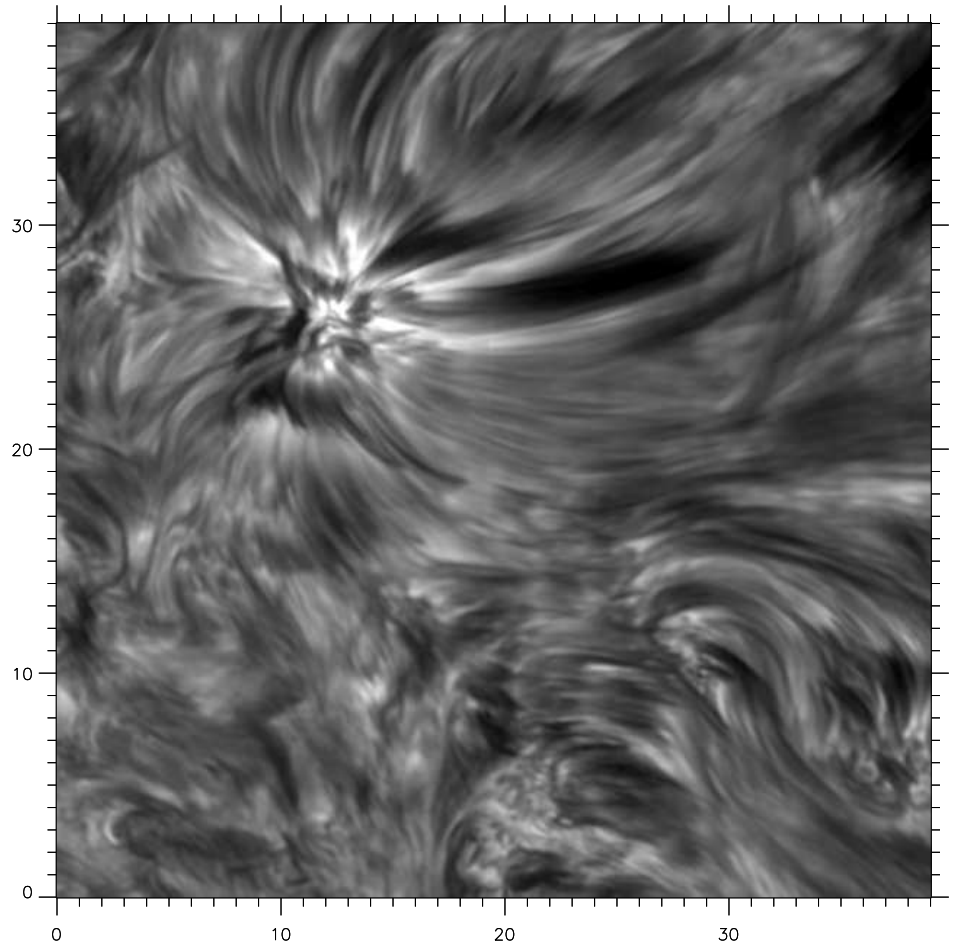

Figure 5. Diffraction-limited image taken at the SST on June 18, 2006 showing Hα line-center brightness of a quiet region. Note the long and curved dark mottles emanating from a network region around (10″, 25″). When tracing loops from the network region to the upper right, a pattern below the loops becomes visible because of lower opacity in the loops. This is the same pattern that is visible in the internetwork regions that are visible in the lower left of the image.

ently changing (with time) opacity as well as the transverse motions often lead to line-of-sight superposition, which renders unique identification throughout the lifetime of the mottle often quite challenging. Figure 6 shows an example of the transverse motion a short mottle (associated with network) undergoes. While its top end is initially at (1″, 1.7″), the whole mottle moves to the lower right, and the top ends at (1.7″, 1.1″) after 51 seconds. The average speed transverse to the mottle axis is of order 13 km/s. Many mottles generally undergo some transverse motion, with typical velocities between 5 and 30 km/s, although larger apparent velocities are also present. It is interesting to note that

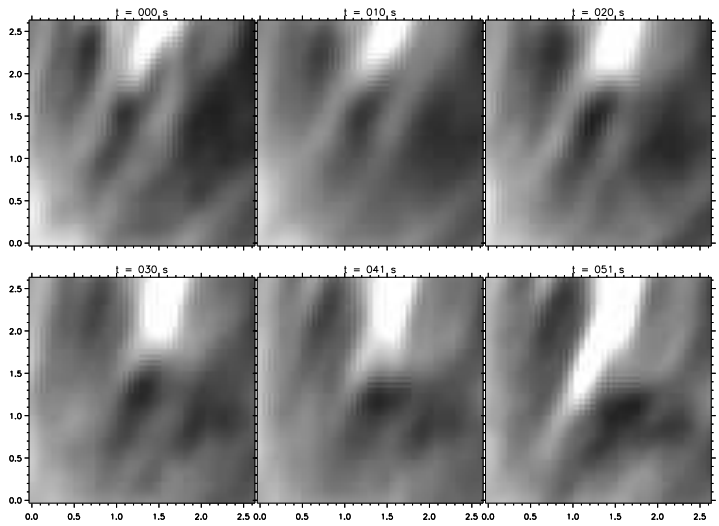

Figure 6. Temporal evolution of a dark mottle that undergoes transverse motions from uper left to lower right. The average velocity with which the mottle is shifted in the direction transverse to its own axis is of order 13 km/s. Units of x and y: arcseconds.

turning or rotating motions have also been observed in active region fibrils by Koza et al. (p. 115 ff in this volume). We should also note that visual inspection of movies indicates that what appears as a transverse motion may sometimes be an artefact of complicated radiative transfer effects combined with coherent wave-driven motion with phase delay between different (parallel) field lines. For example, it is possible that some apparently transverse motion occurs because brightening and darkening of neighboring field lines is coherent, but with phase delays between neighboring field lines. Such coherence and phase delays would not be surprising, since it has also been observed in active region fibrils (Hansteen et al. 2006; De Pontieu et al. 2007).

Despite the general difficulty with tracing individual mottles, some mottles have a sharply-defined top end and do not show as much transverse motion, so that xt cuts along the mottle axis can be drawn. In such cases, we find that the mottle top often undergoes a parabolic path, similar to active region fibrils. Several examples are shown in Fig. 7. Why don't all mottles show such parabolic paths? As mentioned, many mottles are not well-defined enough, or move too much in the transverse direction to show a parabolic path in xt plots. The lack of a well-defined top in many QS mottles is most probably because much of the quiet Sun chromosphere is not in direct thermal contact (along the field line) with a hot transition region. Such contact does occur for dynamic fibrils in active region, so that they do have sharply defined top-ends. It is not a coincidence that most of the well-defined parabolas of Fig. 7 are found in the region directly above or close to the strong network region, where the field is not quite as inclined from the vertical, and coronal loops end. On heavily inclined (i.e., almost horizontal) loops, the mottle tops are not as well defined, presumably because there is no plasma of coronal/TR temperatures anywhere

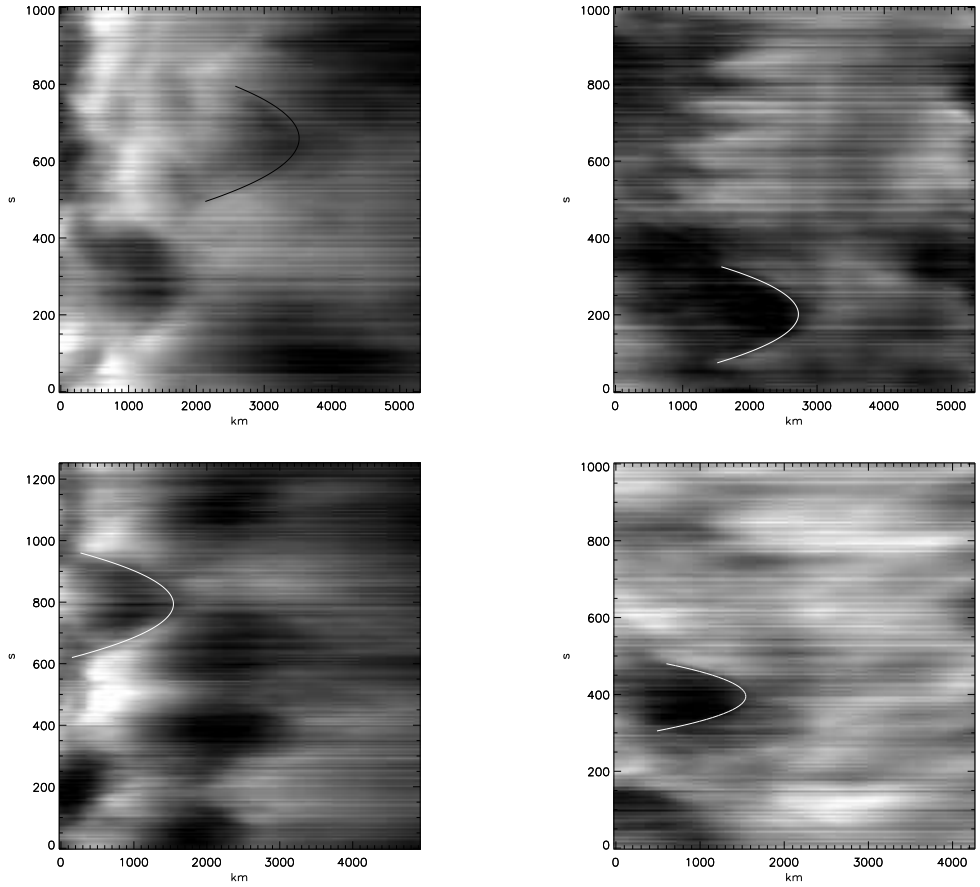

Figure 7. Space-time ("*xt*") plots of mottles in four different areas, all closely associated with the network at (10″, 25″) of Fig. 5. To mitigate the effects of transverse motion, the *xt* plot has been averaged over 10 pixels (0.53″) in the direction perpendicular to the mottle axis. While most of the parabolas are not quite as clearly defined as those of fibrils above active region plage, it is clear that parabolic paths occur often for mottles that do not show much transverse motion, and that have a well-defined top. x-axis in km, y-axis in seconds.

along such loops. Preliminary comparisons with the numerical simulations of Hansteen et al. (2006) indicate that heavily inclined loops with apex heights less than 2 Mm typically remain chromospheric in temperature from one end to the other end. It is tempting to speculate that on such loops the definition of a mottle top (or end) is no longer determined by the steep temperature increase of the TR (and accompanying steep decrease in opacity), but directly related to the complicated non-LTE line formation of the Hα line. Comparisons with detailed Hα non-LTE radiative transfer calculations will be necssary to confirm this suspicion.

Regardless of the difficulties of tracking individual mottles, it is clear that many of those that can be tracked follow parabolic paths similar to the paths

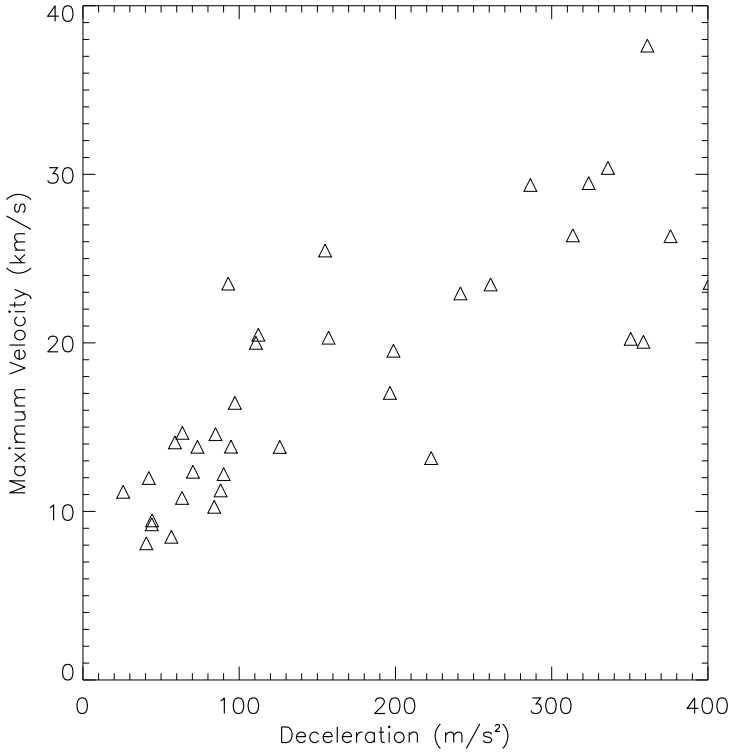

Figure 8. Scatterplot of maximum velocity versus deceleration for 37 quiet Sun mottles. Despite the relatively low statistics, it is clear that a linear correlation similar to the one found for active region fibrils (Fig. 3) is present. A comparison with a similar correlation plot for fibril-like jets in numerical simulations of the chromosphere (bottom panel of Fig. 3) strongly suggests that the fibril-mechanism is also important in the formation of quiet Sun mottles.

of active region fibrils. In addition, a preliminary analysis of the correlation between deceleration and maximum velocity of the parabolic paths of quiet Sun mottles (Fig. 8) shows that the deceleration and maximum velocity is linearly correlated. Comparison with Fig. 3 shows that the linear correlation found for quiet Sun mottles is very similar to the one found for active region fibrils, as well as the one found for jets in the numerical simulations. This strongly suggests that the fibril mechanism, i.e., leakage of convective flows and global oscillations into the chromosphere along magnetic field lines, is also important in the formation of jets or mottles in quiet Sun. Note that the minimum velocities are, just like for active region fibrils, around 8 km/s, which is compatible with the chromospheric speed of sound. Such a lower cutoff can be expected since the mottles/fibrils are driven by chromospheric shocks.

Since these results suggest that leakage of global oscillations plays an important role in the dynamics of the quiet Sun chromosphere, we performed a wavelet-based oscillation analysis of two different quiet Sun datasets. The first

dataset is a diffraction-limited Hα line-center time series taken on June 18, 2006 between 11:54 and 12:42 UT (at 5.15 s cadence). The second dataset is also diffraction-limited, but consists of Hα wing images ($\pm$300 mÅ) at 18.4 s cadence, taken on June 21,2006 between 16:34 UT and 17:28 UT.

A preliminary analysis of the dominant oscillatory behavior of the quiet Sun chromosphere, as imaged in high-resolution Hα line-center time series, is shown in Fig. 9. This is a map of the dominant wave period for each location of the quiet Sun chromosphere (Hα line-center) that shows significant wavelet power for at least two wave periods. The mottles and loops emanating from the network region around (25″, 30″) are all dominated by oscillatory behaviour with periods around 5–7 minutes, with some of the longer and lower-lying loops dominated by periods of up to 10 minutes. This finding is compatible with the idea that leakage of global oscillations from the photosphere (with dominant periods around 5 minutes) are important in the formation and dynamics of network-associated mottles. The internetwork regions, such as the lower left region, show periods that are closer to 3 minutes. This suggests that internetwork regions (where the field is not as dominant) are dominated by waves with periods around the chromospheric acoustic cutoff period of 3 minutes. It is interesting to note that the 3-min power is also often visible in regions where the long, low-lying loops, e.g., around (45″, 45″), that are typically dominated by longer periods, start to become transparent. This suggests that in such regions lower opacity of the overlying loops allows glimpses of the internetwork dynamics and oscillations underneath.

A similar picture emerges from the H$\alpha \pm 300$ mÅ summed time series shown in the upper panels of Fig. 10. The network-associated loops are dominated by periods of 5 min or longer (e.g., around 35″, 35″), whereas the internetwork regions (e.g., around 15″, 25 ″) are dominated by 3-min oscillations. This again strongly suggests that leakage of photospheric oscillations into the chromosphere dominates much of the dynamics of the quiet network chromosphere. There is a hint that right at the center of the network regions, periods closer to 3 minutes appear to occur more often (e.g., at 33″, 28″). This is presumably where the field is more vertical, so that the acoustic cutoff period reverts to its nominal 3 min value (similar to the dense plage region in Hansteen et al. (2006)). We also see slightly longer periods dominating the loops connecting two opposite polarity network regions (one centered at 35″, 30″, and one at 30″, 45″). These longer periods are reminiscent of the periods that are seen in low-lying long fibrils that originate in sunspots or strong plage (De Pontieu et al. 2007). This may not be a coincidence, as the quiet network regions shown here actually contain a stronger than usual amount of magnetic flux (some tiny pores are even visible in the continuum images, not shown).

The dominant periods in the Doppler signal are generally significantly lower than those in the summed signal (bottom panel of Fig. 10). Generally, the areas dominated by 3-min oscillations are a bit more extended in the Doppler signal than in the summed signal, so that the "internetwork" regions cover a larger fraction of the field of view. This may be partially caused by the fact that the overlying canopy is continuously buffeted and impinged by 3-min shocks in the internetwork (similar to the shocks described by Carlsson & Stein 1992, 1994, 1997), an effect which perhaps starts to dominate the velocity signal at those locations where the canopy becomes more transparent? This could explain why

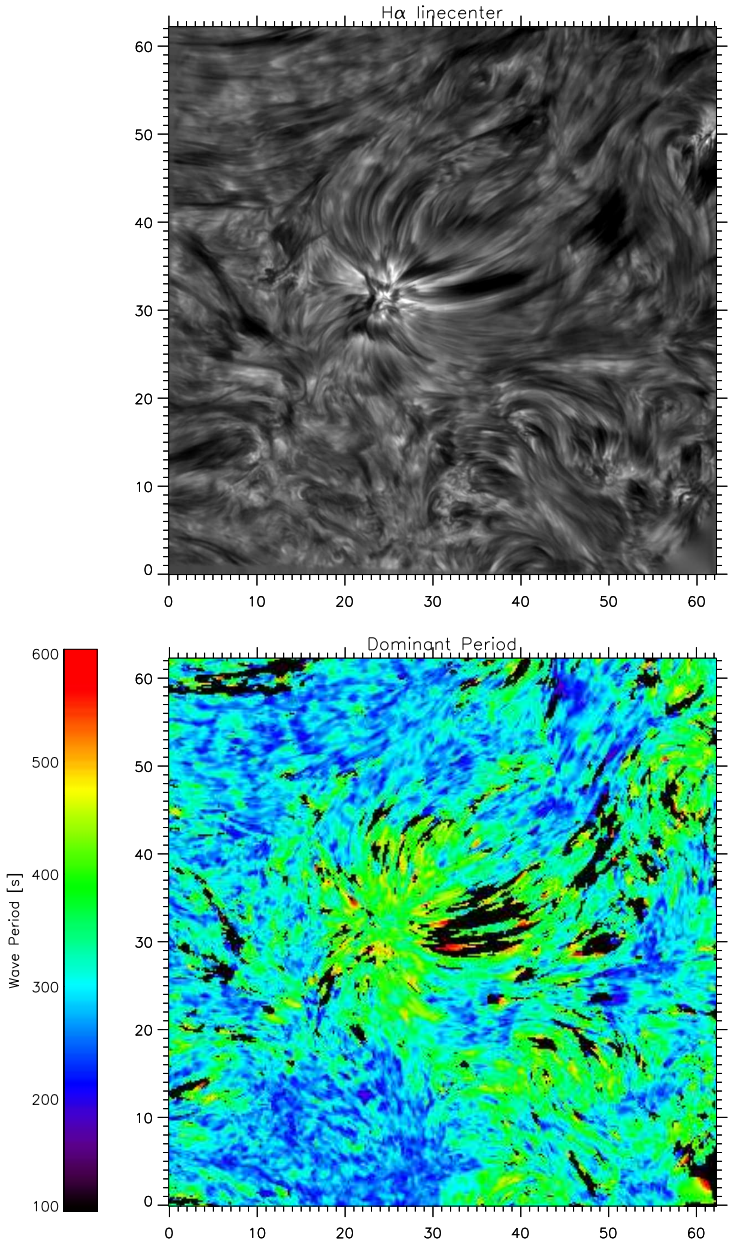

Figure 9. Results from a wavelet analysis of a 48-minute long Hα line-center time series of quiet Sun taken on June 18, 2006. The upper panel shows a snapshot of the region, whereas the lower panel illustrates for each location which wave period dominates, i.e., contains the highest number of wavepackets with significant power.

the influence of the "network" (i.e., 5-min signal) is less spatially extended in the velocity signal than in the intensity signal? Or perhaps the dominant effect is that the velocity signal inherently contains higher frequencies than the intensity

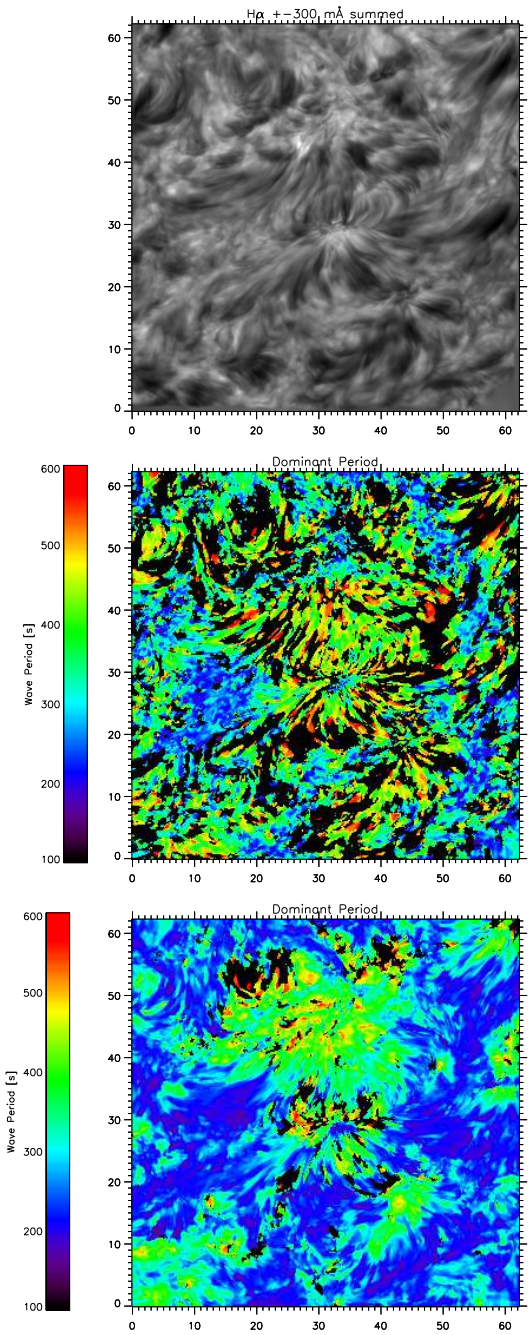

Figure 10. Results from a wavelet analysis of a 54-minute long H$\alpha\pm$300 mÅ time series of quiet Sun taken on June 21, 2006. The top panel shows a snapshot of the region, the middle panel illustrates for each location which wave period dominates in the summed wing images, whereas the bottom panel shows the same for the Doppler signal.

signal? The latter is perhaps not surprising since fast-mode magnetoacoustic waves (propagating perpendicular to the field), which predominantly appear in the velocity signal, are ubiquitous in the numerical simulations of Hansteen et al. (2006) and De Pontieu et al. (2007). For example, if fast modes lift a fibril towards the observer along the line-of-sight, such a velocity signal would be completely absent in the intensity signal (which defines the dark mottle). Detailed comparisons with numerical simulations will be necessary to resolve this issue. Such simulations will perhaps also be able to explain why the region around (30″, 50″) is dominated by 3–5 min signals in intensity, and 5–7 min signals in velocity. The region in question is an internetwork region, with little opacity from the overlying canopy (which may be absent altogether at that location). Perhaps the amplitudes in velocity are quite low in this region, so that more long term evolution dominates the signal compared to other internetwork regions?

In concluding, the parabolic paths, correlation between deceleration and maximum velocity and oscillatory properties of quiet Sun mottles strongly suggest that the mechanism that drives active region fibrils is also responsible for the formation of at least a subset of quiet Sun mottles. This is not surprising, since all of the ingredients of the fibril mechanism are also present in quiet Sun: global oscillations and convective flows that are guided into the chromosphere along magnetic field lines. How is this mechanism modified under quiet Sun conditions? The generally weaker magnetic fields of the quiet Sun imply that the height of the plasma $\beta = 1$ surface is generally higher than in active region plage. That implies that the field is less rigid: flows and waves can influence the motion of magnetic field lines up to larger heights. A less rigid field would lead to a much more dynamic magnetic field at upper chromospheric heights, with significantly more transverse motions. This is exactly what we observe in our quiet Sun data. Mode coupling between different wave modes at the plasma $\beta = 1$ surface can also be expected to play a large role in this magnetic environment (Bogdan et al. 2003). In fact, the numerical simulations of Hansteen et al. (2006) and De Pontieu et al. (2007) clearly show that fast-mode magnetoacoustic waves play a significant role in the dynamics of fibril-like jets (under weaker field conditions). These fast modes propagate perpendicular to the fibril-axis, and can lead to a significant transverse motion of the whole fibril-like jet. Our model thus nicely explains the qualitative differences between fibril and mottle dynamics.

Our observations also show many examples where significant reorganizations of the magnetic field occur, with apparent (un?)twisting and motions at Alfvénic speeds. Such reorganizations are most probably signs of magnetic reconnection caused by the dynamic magneto-convective driving of mixed polarity fields in the quiet Sun. While reconnection clearly occurs often in quiet Sun, it is unclear how much of a role reconnection plays in the formation of Hα mottles. Taken together with the evidence presented here for a fibril-like mechanism in quiet Sun, it seems quite possible that both reconnection and the shockwave-driven mechanism play a role in jet-formation in quiet Sun. It is possible that one of the reasons the spicule problem has been so difficult to resolve is that there are indeed multiple mechanisms at play, with perhaps a different dominant player for jets observed in different wavelengths (e.g., visual vs. UV). To determine which mechanism dominates where, new datasets (that include si-

multaneous high resolution magnetograms) and more advanced (3D) numerical simulations will be necessary. With the maturing of advanced optics and post-processing techniques, the advent of larger ground-based telescopes and satellite missions (Hinode), as well as more advanced 3D radiative MHD simulations, a solution to these issues is now within reach.

Acknowledgments. BDP thanks the organizers of the meeting for the opportunity to present this work. BDP was supported by NASA grants NAG5-11917, NNG04-GC08G and NAS5-38099 (TRACE), and thanks the ITA/Oslo group for excellent hospitality. VHH thanks LMSAL for excellent hospitality during the spring of 2006. This research was supported by the European Community through the European Solar Magnetism Network (ESMN, contract HPRN-CT-2002-00313) and the Theory, Observation and Simulation of Turbulence in Space network (TOSTISP, contract HPRN-CT-2002-00310) programs, by The Research Council of Norway through grant 146467/420 and through grants of computing time from the Programme for Supercomputing. The Swedish 1-m Solar Telescope is operated on the island of La Palma by the Institute for Solar Physics of the Royal Swedish Academy of Sciences in the Spanish Observatorio del Roque de los Muchachos of the Instituto de Astrofísica de Canarias.

References

Beckers J. M., 1968, Sol. Phys. 3, 367

Bogdan T. J., Carlsson M., Hansteen V. H., McMurry A., Rosenthal C. S., Johnson M., Petty-Powell S., Zita E. J., Stein R. F., McIntosh S. W., Nordlund Å., 2003, ApJ 599, 626

Carlsson M., Stein R. F., 1992, ApJ 397, L59

Carlsson M., Stein R. F., 1994, in M. Carlsson (ed.), Chromospheric Dynamics, 47

Carlsson M., Stein R. F., 1997, ApJ 481, 500

De Pontieu B., Berger T. E., Schrijver C. J., Title A. M., 1999, Sol. Phys. 190, 419

De Pontieu B., Erdélyi R., de Wijn A. G., 2003a, ApJ 595, L63

De Pontieu B., Erdélyi R., James S. P., 2004, Nature 430, 536

De Pontieu B., Hansteen V. H., Rouppe van der Voort L., van Noort M., Carlsson M., 2007, ApJ 655, 624

De Pontieu B., Tarbell T., Erdélyi R., 2003b, ApJ 590, 502

Handy B. N., Acton L. W., Kankelborg C. C., Wolfson C. J., Akin D. J., Bruner M. E., Caravalho R., Catura R. C., Chevalier R., Duncan D. W., Edwards C. G., Feinstein C. N., Freeland S. L., Friedlaender F. M., Hoffmann C. H., Hurlburt N. E., Jurcevich B. K., Katz N. L., Kelly G. A., Lemen J. R., Levay M., Lindgren R. W., Mathur D. P., Meyer S. B., Morrison S. J., Morrison M. D., Nightingale R. W., Pope T. P., Rehse R. A., Schrijver C. J., Shine R. A., Shing L., Strong K. T., Tarbell T. D., Title A. M., Torgerson D. D., Golub L., Bookbinder J. A., Caldwell D., Cheimets P. N., Davis W. N., Deluca E. E., McMullen R. A., Warren H. P., Amato D., Fisher R., Maldonado H., Parkinson C., 1999, Sol. Phys. 187, 229

Hansteen V. H., De Pontieu B., Rouppe van der Voort L., van Noort M., Carlsson M., 2006, ApJ 647, L73

Scharmer G. B., Bjelksjö K., Korhonen T. K., Lindberg B., Petterson B., 2003, in Innovative Telescopes and Instrumentation for Solar Astrophysics. eds. S.L. Keil & S.V. Avakyan. Proc. SPIE 4853, 341

van Noort M., Rouppe van der Voort L., Löfdahl M. G., 2005, Sol. Phys. 228, 191

The Physics of Chromospheric Plasmas
ASP Conference Series, Vol. 368, 2007
Petr Heinzel, Ivan Dorotovič and Robert J. Rutten, eds.

New Models of the Solar Chromosphere and Transition Region from SUMER Observations

Eugene H. Avrett

Harvard-Smithsonian Center for Astrophysics, Cambridge, U.S.A.

Abstract. The SUMER atlas of the disk-center spectrum of the average quiet Sun between 67 and 161 nm, together with HRTS spectra to 173 nm, provide valuable observational data that can be used to determine the structure of the chromosphere, transition region, and low corona. The Pandora atmospheric modeling program is being used to determine atmospheric models and calculated spectra consistent with these observations, resulting in a new model of the average quiet chromosphere and transition region in better agreement with observations than before. We find that temperature variations of 400 K cause the computed chromospheric intensities, both in lines and the continuum, to change by a factor of about 4. This is greater than the observed intensity variations at chromospheric wavelengths 1) with time in quiet regions, and 2) with position from cell centers to bright network. These results appear to conflict with dynamical models that predict time variations of 1000 K or more in the chromosphere. Also, we demonstrate that the optically-thin or coronal approximation that is often used to analyze observed line intensities from high stages of ionization is reasonably accurate only: 1) for C IV and higher carbon ions, and C III for $T > 50,000$ K, and 2) for O V and higher oxygen ions, and O IV for $T > 150,000$ K..

This paper summarizes progress so far in attempting to interpret the EUV spectrum of the average quiet Sun from the SUMER atlas of Curdt et al. (2001) by means of a semi-empirical average-quiet-Sun model atmosphere. The continuum and the many emission lines in the spectrum are emitted from a broad range of heights in the solar atmosphere, from the temperature minimum region through the chromosphere and transition region into the corona. This paper shows that a single distribution of temperature with height in the atmosphere can generally account for most of the SUMER average-quiet-Sun spectrum formed in the chromosphere and transition region.

The overall SUMER atlas spectrum is plotted as a solid curve in Fig. 1 (green in the pdf version). The SUMER spectrum extends to 161 nm, but longward of about 147 nm there is a contribution from the hydrogen Lyman continuum in second order. To avoid this complication we plot (in brown) the HRTS spectrum, from Brekke (1973), between 147 and 173 nm.

The plot near the top of Fig. 1 shows the bright-network to cell-center intensity ratio given in the SUMER atlas. The corresponding Skylab ratio (see caption) is roughly the same, but somewhat larger at the long wavelength end. These spatial variations give an indication of the range of intensities contributing to the quiet-Sun average. Here we attempt to match the average spectrum with an average model. SUMER spectra for network and cell regions are available (W. Curdt, private communication). Models for the separate regions will be given in a subsequent paper.

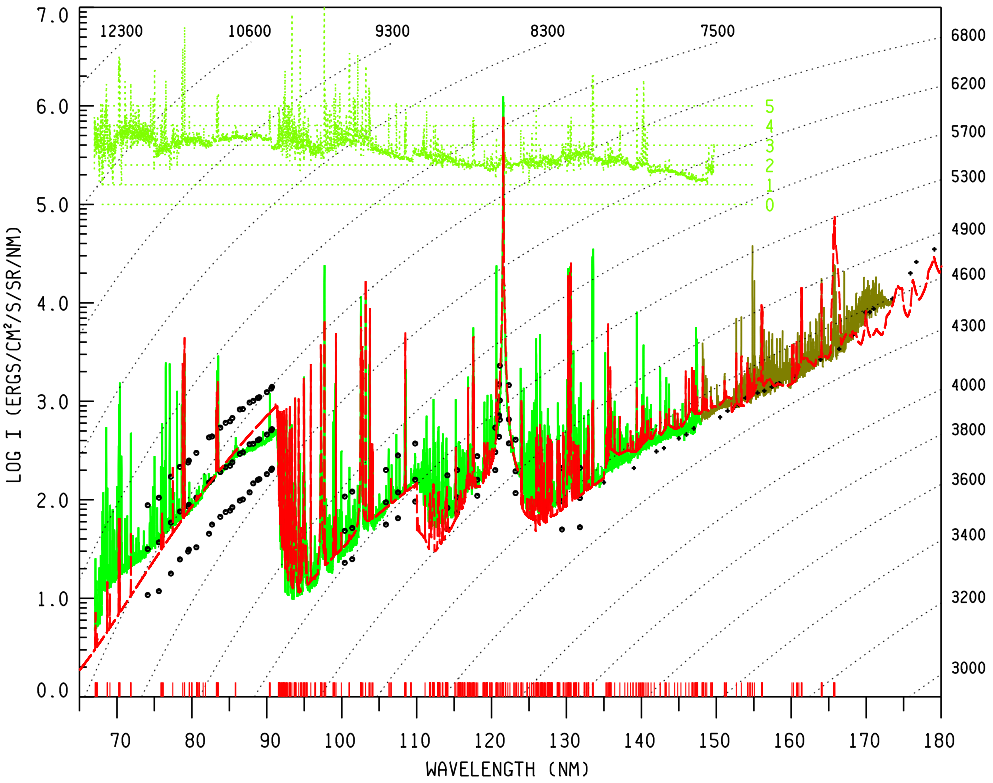

Figure 1. The SUMER disk-center spectrum (green) of the average quiet Sun between 67 and 147 nm is plotted with the corresponding HRTS spectrum (brown) between 147 and 173 nm, along with the calculated spectrum (red long dashes), continuum rocket observations between 134 and 180 nm from Samain (1978) and Samain (1980) (crosses), and Skylab observations of cell-center, average, and bright-network intensities from Vernazza et al. (1981) (open circles) at shorter wavelengths. Note that the average (middle) values agree reasonably well with the average-quiet-Sun SUMER observations. The lefthand scale gives the disk-center intensity, and the corresponding brightness temperatures are shown on the right (and across the top). The plot near the top shows the bright-network to cell-center intensity ratio in the SUMER atlas.

The calculated spectrum is based on the current atmospheric model discussed here: a one-dimensional, time-independent semi-empirical model with an assumed temperature stratification in the photosphere and chromosphere. The temperature distribution in the transition region is determined theoretically, using lower boundary conditions established at the top of the semi-empirical chromosphere, and from a balance between the net energy lost by radiation and the energy transported from the corona by thermal conduction and particle diffusion (see Fontenla et al. 1990, 1991, 1993, 2002).

The photospheric temperature distribution is taken from Fontenla et al. (2006). The chromospheric distribution has been adjusted by trial and error to obtain the best fit to the continuum distribution between the many emission lines in Fig. 1. The model is not determined to fit the emission lines, with the

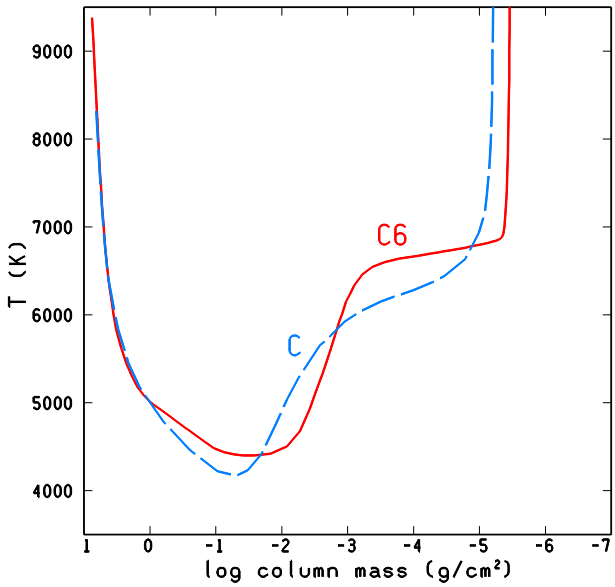

Figure 2. The model C6 temperature distribution compared with that for model C of Vernazza et al. 1981

.

exception of the hydrogen Ly-α line which is formed in the transition region. The extent of agreement between the calculated and observed emission lines, formed at different heights, is a measure of the overall consistency of the model as a representation of the average quiet solar atmosphere.

Further changes are needed to obtain a better fit to the observed slope of the Lyman continuum shortward of 91.1 nm. We find that this slope is sensitive to the temperature and density variations where the base of the transition region is joined to the top of the chromosphere.

Our current (2006) best-fit temperature distribution is shown in Fig. 2, labeled C6, compared with the average-quiet-Sun model C from Vernazza et al. (1981). The two distributions are shown vs. column mass (the inward integral of the mass density) rather than vs. height, since temperature changes cause changes in the relationship between height and density, and the spectrum is better related to temperature as a function of column mass.

For model C6 we have chosen a minimum temperature of 4400 K simply to match the observations in Fig. 1 in the minimum region near 160 nm. Fontenla, Balasubramanian & Harder in recent work summarized here on p. 499 ff specify a much lower minimum temperature to account for the low-temperature CO lines, but their model still agrees with the 160 nm observations (and those at 150 μm) since their low-temperature region contributes very little to the continuum intensities. We do not expect the chromospheric modeling discussed here to be substantially affected by these differences in the minimum region.

In addition to assuming a temperature distribution, we specify a turbulent-pressure velocity distribution $v_{\rm tp}$ which, for simplicity, we assume is equal to the microturbulent or non-thermal velocity distribution $v_{\rm nt}$ derived from the observed doppler line widths that exceed thermal values. The balance between

pressure and gravity for a given temperature distribution gives the total density variation with height. Using $v_{\rm tp} = v_{\rm nt}$ to obtain a total pressure, which exceeds the gas pressure, causes the upper chromosphere to be more extended, and in better agreement with heights of the transition region observed at the limb; these velocities do not greatly affect the lower chromosphere. Fontenla, Balasubramanian & Harder suggest that the buoyant forces needed to extend the chromosphere are better represented by the use of an effective gravity, smaller than the solar surface value. Such buoyant forces can affect the lower chromosphere, and can accomodate a lower minimum temperature to account for the strong CO lines while maintaining agreement with the minimum brightness temperatures near 160 nm, and near 150 μm. We agree with this new approach but here continue to use $v_{\rm tp} = v_{\rm nt}$ as in earlier studies, with $v_{\rm nt}$ as in Vernazza et al. (1981).

Table 1. C I–IV Line Formation Temperatures. For each wavelength in nm of the line or strongest multiplet line component we give the temperature where the maximum contribution to the central line intensity occurs.

T (K)	C I	C II	C III	C IV
69190				154.8
65300			69.1, 97.7	
			117.6, 124.7	
46210		68.7		
31940		85.8, 101.0		
28540		103.6		
8665		90.4		
7422		78.6, 80.7		
		81.0, 106.6,		
		109.2, 133.5		
6845	165.7			
6815	156.0			
6803	94.5, 114.0			
	119.3, 128.0			
6793	132.9			
6750		132.4		
6735	112.2, 115.6			
	147.2			
6718	113.9			
6665	112.8, 131.1			
	135.8			
6640	128.8			
6600	127.5, 143.2			
6545	160.8			
6335	126.6			
5280	161.3			
4500	149.3, 151.2			
4420	148.1			

Given temperature T and $v_{\rm tp}$ as functions of height, we balance pressure and gravity to obtain density vs. height, and solve the full set of equations of a) radiative transfer, for all relevant lines and continua, b) statistical equilibrium for

all relevant atomic levels, and c) ionization equilibrium for all relevant ionization stages (thus obaining the electron number density from charge balance).

We calculate the emergent continuum and line spectrum, compare with the observed spectrum, use the differences to redetermine the temperature distribution to improve the fit, and continue until a satisfactory match is obtained.

While not shown here, we can finally use the model to calculate the total net radiative losses vs. depth, which should represent the non-radiative energy input needed to produce our observation-based atmospheric model.

Table 2. O I–VI Line Formation Temperatures. For each wavelength in nm of the line or strongest multiplet line component we give the temperature where the maximum contribution to the central line intensity occurs.

T (K)	O I	O II	O III	O IV	O V	O VI
432900						103.2
227800					76.0, 77.5, 137.1	
212000				121.8		
92020			78.7, 139.7			
81470			70.2			
69190			83.3			
33640		67.3				
31940		71.9				
23150		83.4				
21260	102.6					
11420	93.7					
7995	92.6					
7422		79.7				
6845	130.2					
6830	130.5					
6818	92.5, 99.0					
6805	97.4					
6782	97.6, 99.1, 102.7, 103.9, 130.6					
6767	95.1					
6753	93.8, 102.8, 104.1, 115.2					
6720	92.3, 95.3, 99.9, 104.2					
6695	92.7, 93.9, 95.2, 97.6					
6544	98.9, 135.6, 135.9					
6335	164.1					

The atoms and ions included in the present model calculation are H, H^-, He I–II, C I–IV, N I–II, O I–VI, Ne I–VIII, Na I–II, Mg I–II, Al I–II, Si I–IV, S I–IV, Ca I–II, and Fe I. The SUMER atlas contains the following subset of these atoms and ions: H, He I–II, C I–IV, N I–IV, O I–IV, Ne I, IV–VIII, Mg II, Si I–IV,

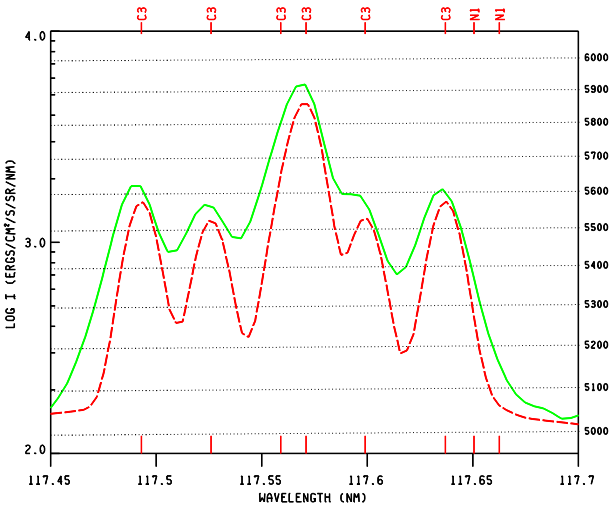

Figure 3. Comparison between the observed (solid) and calculated (dashed) C III multiplet line near 117.6 nm. The lefthand and righthand scales show intensity and brightness temperature as in Fig. 1.

S I–IV (and a weak Ca II line at 128.72 nm). Some of the lines appear in second order, e.g., the He I 58.433 nm resonance line from the second-order spectrum appears in the mainly first-order spectrum at 116.867 nm. In the present paper we show results mainly for C I–IV and O I–VI. The abundances we use in the calculation are from Asplund (2005), Asplund et al. (2004, 2005a,b) and Grevesse & Sauval (2000).

We now indicate the depths and temperatures at which the lines of C I–IV and O I–VI are formed. Table 1 shows the results for the carbon lines. The C IV and C III lines and the stronger C II lines are formed in the transition region while the weaker C II and the C I lines are formed in the chromosphere. The weakest C I lines are formed just above the temperature minimum region.

Table 2 shows the results for the oxygen lines. The O III–VI lines are formed in the transition region, while the lines of O II and O I originate both in the transition region and chromosphere.

Figure 3 shows the calculated 6-component C III multiplet near 117.6 nm compared with the SUMER quiet-Sun atlas profile. The atlas profiles are averages over cell and network structures that have a small range of atmospheric motions within the field of view, while our calculations are from a single model without any flow velocities. For the comparison we have convolved the calculated intensity distribution with a gaussian that has a FWHM of 0.015 nm to change the deep calculated minimum between the peaks at 117.57 and 117.6 nm to only a slight minimum. While this comparison suggests that we could choose a larger value for the convolved width, comparisons at other wavelengths show 0.015 nm to be a reasonable choice.

Figure 4 shows the comparison with a group of C I line components around 128 nm, while Fig. 5 shows the hydrogen Ly-β line at 102.572 nm and lines of O I, C II, and O VI. The calculated He II line emission at 102.527 nm is much larger than observed. This line transition, between He II levels 2 and 6, is much

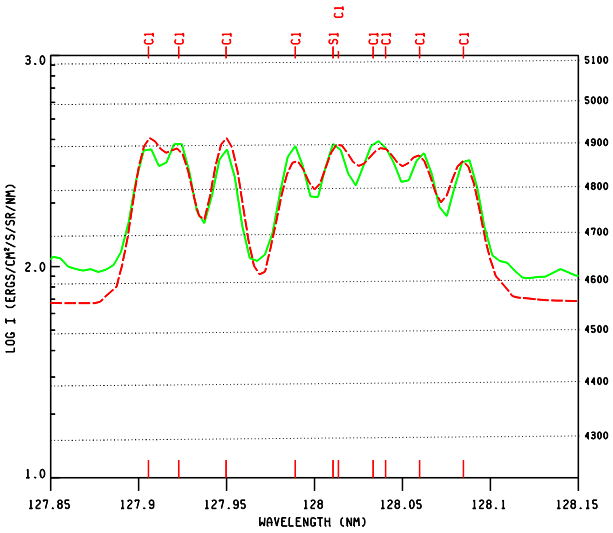

Figure 4. Observed and calculated C I component profiles near 128 nm.

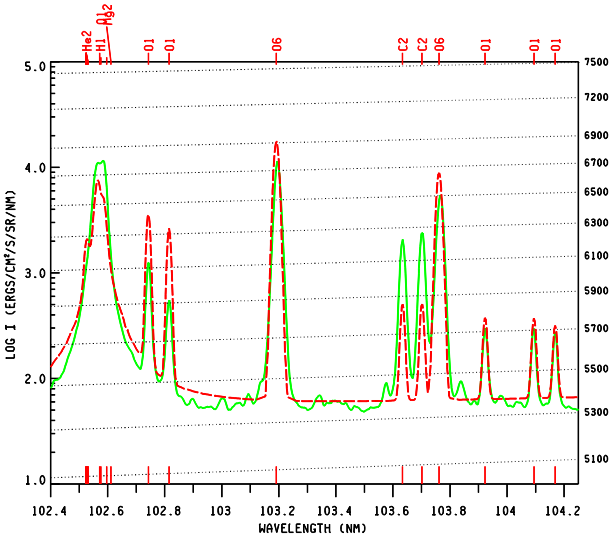

Figure 5. The H I Ly-β line profile and lines of O I, C II, O VI, and He II.

weaker than Ly-β, implying formation in the chromosphere, but the interaction between the two lines needs further examination. One of the O I triplet lines, at 102.576 nm is also blended with Ly-β. We calculate in detail the radiative interactions among these three lines of different elements.

The O I triplet lines near 104 nm agree with the observed ones, but those in the wing of Ly-β are too strong. The calculated O VI doublet lines at 103.19 and 103.76 nm match the observations reasonably well, but the calculated C II doublet lines at 103.62 and 103.7 nm are too weak. All of these lines are sensitive to the collisional excitation rates used in the calculation, and we are still searching for the best available values. Given the lack of consistency in match-

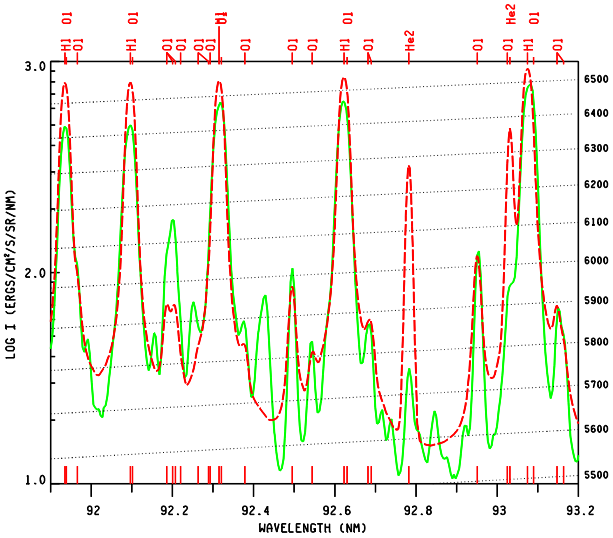

Figure 6. Lines of H, O I, and He II.

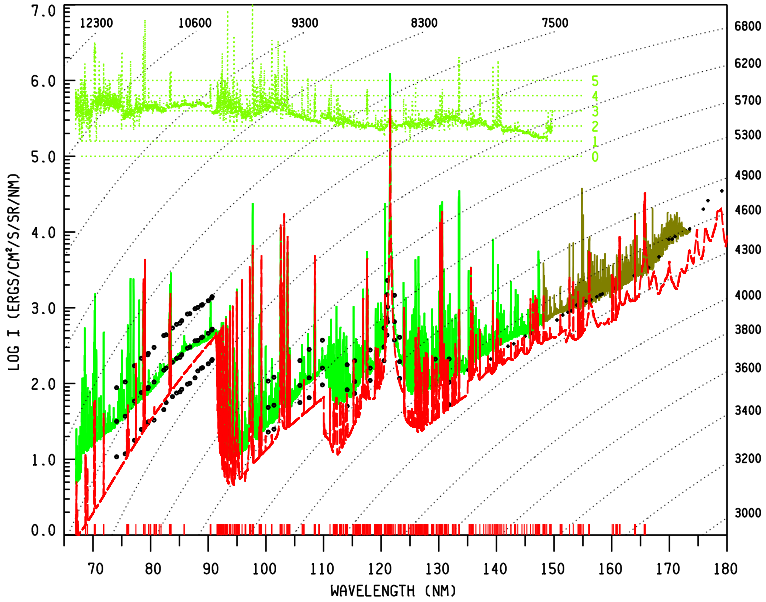

Figure 7. The same observations as in Fig. 1, but with intensities calculated from a model with temperatures 200 K lower than those of the C6 model throughout the chromosphere and temperature-minimum region.

ing the calculated and observed O I lines shown in this figure, it is premature to attempt to use these results to determine solar abundances. However, if better rates and cross sections lead to improved consistency, we should be able to determine abundances from the many prominent chromospheric emission lines in this wavelength region.

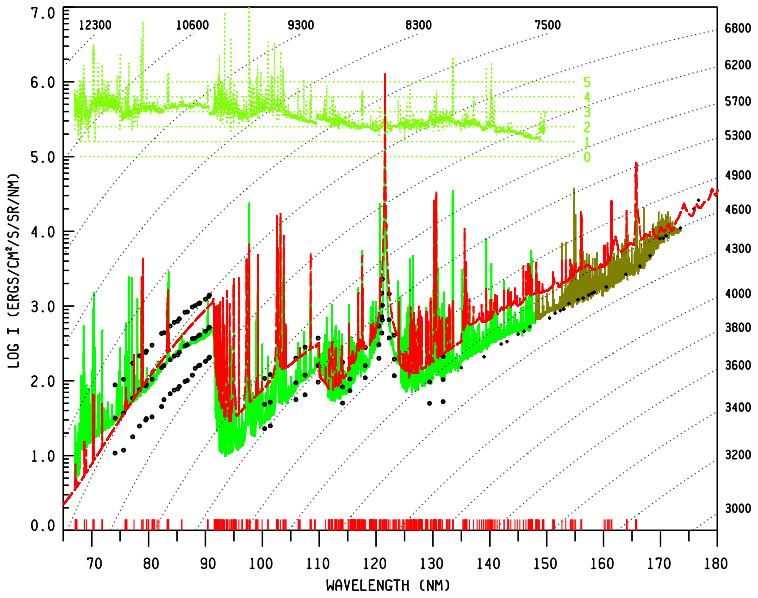

Figure 8. The same observations as in Fig. 1, but with intensities calculated from a model with temperatures 200 K higher than those of the C6 model throughout the chromosphere and temperature-minimum region.

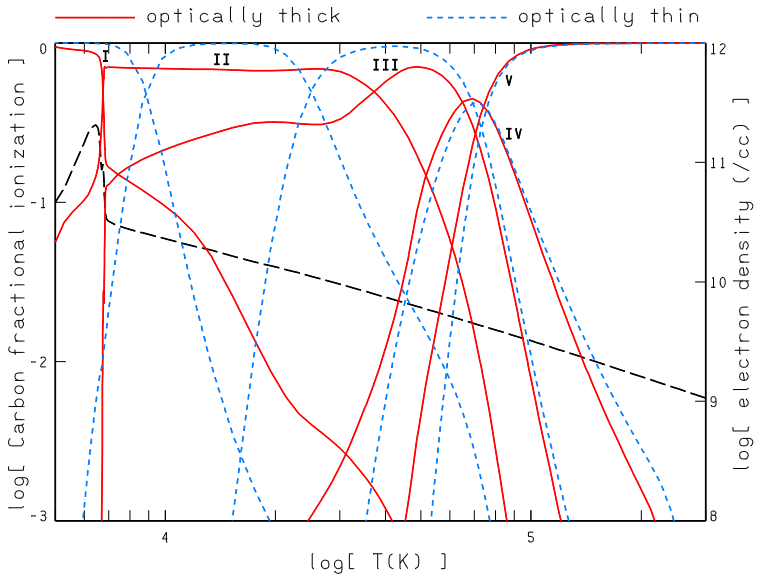

Figure 9. Calculated C I–IV ion fractions (contiuous red lines) and electron density (long-dashed black) from model C6 compared with the results obtained by setting all photoionization and photoexcitation rates equal to zero (short-dashed blue).

Figure 6 shows further O I lines in the vicinity of the hydrogen Lyman lines with upper levels 11, 10, 9, 8, and 7 from 919.35 to 930.75 nm. Again, the calculated He II lines are too strong.

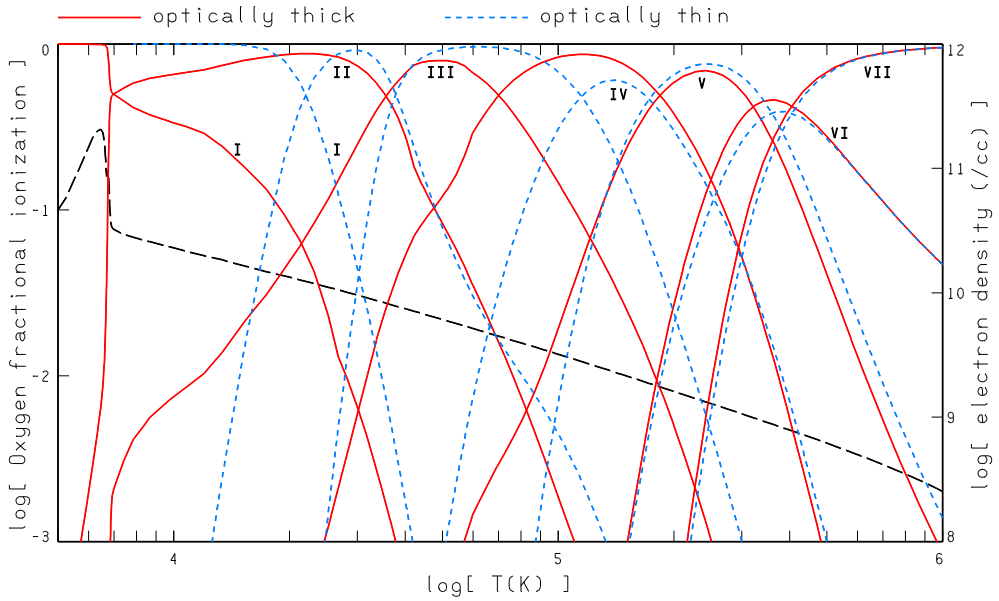

Figure 10. Calculated O I–VI ion fractions (continuous red lines) and electron density (long-dashed black) from model C6 compared with the results obtained by setting all photoionization and photoexcitation rates equal to zero (short-dashed blue).

This sampling of results shows the general correspondence between the observations and our calculations based on the model C6 temperature distribution shown in Fig. 2.

We now illustrate the sensitivity of the calculated spectrum to changes in temperature. Figure 7 shows the overall spectrum calculated from a model with temperatures 200 K lower than those of the C6 model throughout the chromosphere and temperature-minimum region. Figure 8 shows the corresponding results for temperatures 200 K higher.

These are arbitrary temperature changes, but the resulting spectra are roughly similar to cell-center and network regions, respectively, based on the Skylab data points for brightness components A and F, and the SUMER network to cell-center ratio plotted at the top of these figures. These results suggest that the spatial temperature variations for the quiet Sun do not exceed roughly $\pm$ 200 K. We have not carefully reviewed the available studies of temporal variations in quiet chromospheric regions, but Wilhelm et al. (2005), e.g., found that the temporal variations in the 116-118 nm band for both lines and the continuum were smaller than the variations between cell and network.

The final results in this paper concern the optically thin or coronal approximation, often used to analyze emission lines of high stages of ionization formed in the transition region and corona. This approximation assumes that photoionization is negligible compared with collisional ionization, and that photoexcitation is negligible compared with collisional excitation. Thus, the line-forming region is assumed to be optically thin to the extent that every photon emitted by an atom escapes from the region rather than being absorbed by another atom, caus-

ing an ionization or excitation. We test this approximation simply by setting all photoionization and photoexcitation rates equal to zero.

Figure 9 shows the results we obtain for C I–IV. Note that while we may not be using the best available atomic data, we are using the same collision rates, radiative recombination rates, dielectronic recombination rates, and Einstein A coefficients in the two cases. We conclude from this comparison that the optically thin or coronal approximation is valid for C IV and higher carbon ions, and for C III for $T > 50,000$ K, but is otherwise unreliable.

Figure 10 shows the corresponding results for O I–VI. From these results we conclude that the optically thin approximation is valid for O V and higher oxygen ions, and O IV for $T > 150,000$ K, but is otherwise unreliable.

Acknowledgments. I am indebted to Rudolf Loeser for his programming assistance over the last 40 years that has made this research possible. I am also indebted to Juan Fontenla for his essential contributions to the photospheric and transition-region modeling, described here only briefly.

References

Asplund, M. 2005, ARAA, 43, 481
Asplund, M., Grevesse, N., Sauval, A. J., Allende Prieto, C., & Kiselman, D. 2004, A&A, 417, 751
Asplund, M., Grevesse, N., & Sauval, A. J. 2005a, in Cosmic Abundances as Records of Stellar Evolution and Nucleosynthesis, ed. T. B. Barnes & F. N. Bash, ASP Conf. Ser. 336, 25
Asplund, M., Grevesse, N., Sauval, A. J., Allende Prieto, C., & Blomme, R. 2005b, A&A, 431. 693
Brekke, P. 1973, ApJS, 87, 443
Curdt, W., Brekke, P., Feldman, U., Wilhelm, K., Dwivedi, B. N., Schühle, U., & Lemaire, P. 2001, A&A, 591, 613
Fontenla, J. M., Avrett, E. H., & Loeser, R. 1990, ApJ, 355, 700
Fontenla, J. M., Avrett, E. H., & Loeser, R. 1991, ApJ, 377, 712
Fontenla, J. M., Avrett, E. H., & Loeser, R. 1993, ApJ, 406, 319
Fontenla, J. M., Avrett, E. H., & Loeser, R. 2002, ApJ, 572, 636
Fontenla, J. M., Avrett, E., Thuillier, G., & Harder, J. 2006, ApJ, 639, 441
Grevesse, N., & Sauval, A. J. 2000, in Origin of Elements in the Solar System: Implications of Post-1957 observations, ed. O. Manuel, Kluwer, 261
Samain, D. 1978, Ph.D. Thesis, Univ. of Paris
Samain, D. 1980, ApJS, 44, 273
Vernazza, J. E., Avrett, E. H., & Loeser, R. 1981, ApJS, 45, 635
Wilhelm, K., Schühle, U., Curdt, W., Hilchenbach, M., Marsch, E., Lemaire, P., Bertaux, J.-L., Jordan, S. D., & Feldman, U. 2005 A&A, 439, 701

Nicolas Labrosse, Pavol Schwartz, Jean-Claude Vial, Brigitte Schmieder

Viggo Hansteen, Horst Balthasar, Sami Solanki, Bernhard Fleck

The Physics of Chromospheric Plasmas
ASP Conference Series, Vol. 368, 2007
Petr Heinzel, Ivan Dorotovič and Robert J. Rutten, eds.

What is Heating the Quiet-Sun Chromosphere?

S. Wedemeyer-Böhm[1,2], O. Steiner[1], J. Bruls[1] and W. Rammacher[1]

[1]*Kiepenheuer-Institut für Sonnenphysik, Freiburg, Germany*
[2]*Institute of Theoretical Astrophysics, University of Oslo, Norway*

Abstract. It is widely believed that the heating of the chromosphere in quiet-Sun internetwork regions is provided by dissipation of acoustic waves that are excited by the convective motions close to the top of the convection zone and in the photospheric overshoot layer. This view lately became challenged by observations suggesting that the acoustic energy flux into the chromosphere is too low, by a factor of at least ten. Based on a comparison of TRACE data with synthetic image sequences for a three-dimensional simulation extending from the top layers of the convection zone to the middle chromosphere, we come to the contradicting conclusion that the acoustic flux in the model provides sufficient energy for heating the solar chromosphere of internetwork regions. The role of a weak magnetic field and associated electric current sheets is also discussed.

1. Introduction

In two recent papers Fossum & Carlsson (2005, 2006, hereafter FC05 and FC06) come to the conclusion that 'high-frequency acoustic waves are not sufficient to heat the solar chromosphere'. This conclusion is based on a study of image sequences from the 1600 Å channel of TRACE (Transition Region and Coronal Explorer). The continuum intensity at the wavelength of 160 nm originates from the upper photosphere. There, acoustic waves suffer no longer strong radiative damping and have not yet become strongly non-linear. Hence, the TRACE images seem to be an excellent means for measuring the total mechanical flux entering the chromosphere at its base. However, the mechanical flux cannot be measured directly but must be inferred from the measured intensity fluctuation $(\Delta I/I)_{160\,\mathrm{nm}}$. FC05 do this by comparing the average spectral power density for $(\Delta I/I)^{\mathrm{obs}}_{160\,\mathrm{nm}}$ with those for corresponding synthetic intensity fluctuations $(\Delta I/I)^{\mathrm{synth}}_{160\,\mathrm{nm}}$ from simulations with the one-dimensional radiation hydrodynamics code RADYN (e.g., Carlsson & Stein 1997). They find that the power spectra fit best for simulation runs that yield a mechanical flux at a height of 400 km (integrated over 5 to 50 mHz) of merely $438\,\mathrm{W\,m^{-2}}$ — ten times less than is needed to compensate the radiative losses of approximately $4300\,\mathrm{Wm^{-2}}$ (excluding Lyman α) in the semi-empirical model of the chromosphere by Vernazza et al. (1981, hereafter VAL).

Here, we present new calculations based on the three-dimensional radiation hydrodynamic simulation by Wedemeyer et al. (2004, hereafter W04), which exhibit a dynamic pattern on a spatial scale too small to be resolved with TRACE. We discuss potential implications for the heating of the solar chromosphere.

2. Acoustic Heating on Small Spatial Scales

2.1. Three-dimensional non-magnetic simulations

The three-dimensional radiation hydrodynamics simulations by W04 were carried out with the computer code CO^{5}BOLD (Freytag et al. 2002) and cover a horizontal region of $7\farcs7 \times 7\farcs7$ and extend from the upper convection zone at a depth of 1400 km to the middle chromosphere at a height of 1710 km. The spatial resolution is 40 km in the horizontal directions and 12 km vertically in the atmosphere. Magnetic fields are not included so that this model represents very quiet internetwork regions only.

In order to keep the computations feasible, the radiative transfer is treated grey (i.e. frequency-independent) and under the assumption of local thermodynamic equilibrium (LTE). These are severe assumptions for the upper photosphere and the chromosphere above but are reasonable for the low photosphere in the framework of time-dependent three-dimensional simulations. The model chromosphere is – in sharp contrast to semi-empirical static models like, e.g., those by VAL – highly intermittent in time and space, consisting of a dynamic mesh-work like pattern of hot shock wave fronts and cool post-shock regions in between. The assumptions made for the radiative transfer affect the temperature amplitudes and the chromospheric energy balance but are reasonable for the low photosphere, where the acoustic waves are excited. The model provides sufficient acoustic energy to counterbalance the radiative losses in the internetwork chromosphere without need for further contributions from processes related to magnetic fields (Wedemeyer 2003).

2.2. Intensity synthesis

The general procedure for our analysis can be summarised like this: (i) synthesis of the continuum intensity at relevant ultra-violet (UV) wavelengths, (ii) integration of the intensity over wavelength to a synthetic TRACE channel, (iii) image degradation to the spatial resolution due to the instrument's optics, (iv) spatial intensity integration for mimicking the TRACE detector (pixels), and finally (v) calculation of (average) power spectra from the intensity sequences resulting from step (i) to (iv).

We use a short simulation sequence from W04 with a duration of 10 min and a cadence of 10 s. For each snapshot we calculate continuum intensity maps with the radiative transfer code Linfor3D (`http://www.aip.de/~msteffen/`) at wavelengths from 150 nm to 180 nm with an increment of 5 nm, covering the wavelength range relevant for the TRACE 160 nm channel. With increasing wavelength the intensity fluctuations become smaller, whereas the absolute intensity level grows strongly. Including longer wavelengths thus effectively reduces the signal $I/ < I >$ and the resulting spectral power density. The intensity sequences for different wavelengths (150 nm – 180 nm) are now integrated according to the instrument's transmission curve (Handy et al. 1999, see also `http://www.lmsal.com/solarsoft`), resulting in a short sequence for the synthetic TRACE channel. A typical intensity image is shown in Fig. 1a.

In the next step the synthetic intensity images are convolved with a point-spread function (PSF) in order to mimic the instrument's UV optics (Fig. 1b). Unfortunately, the PSF of TRACE is poorly known but might be represented

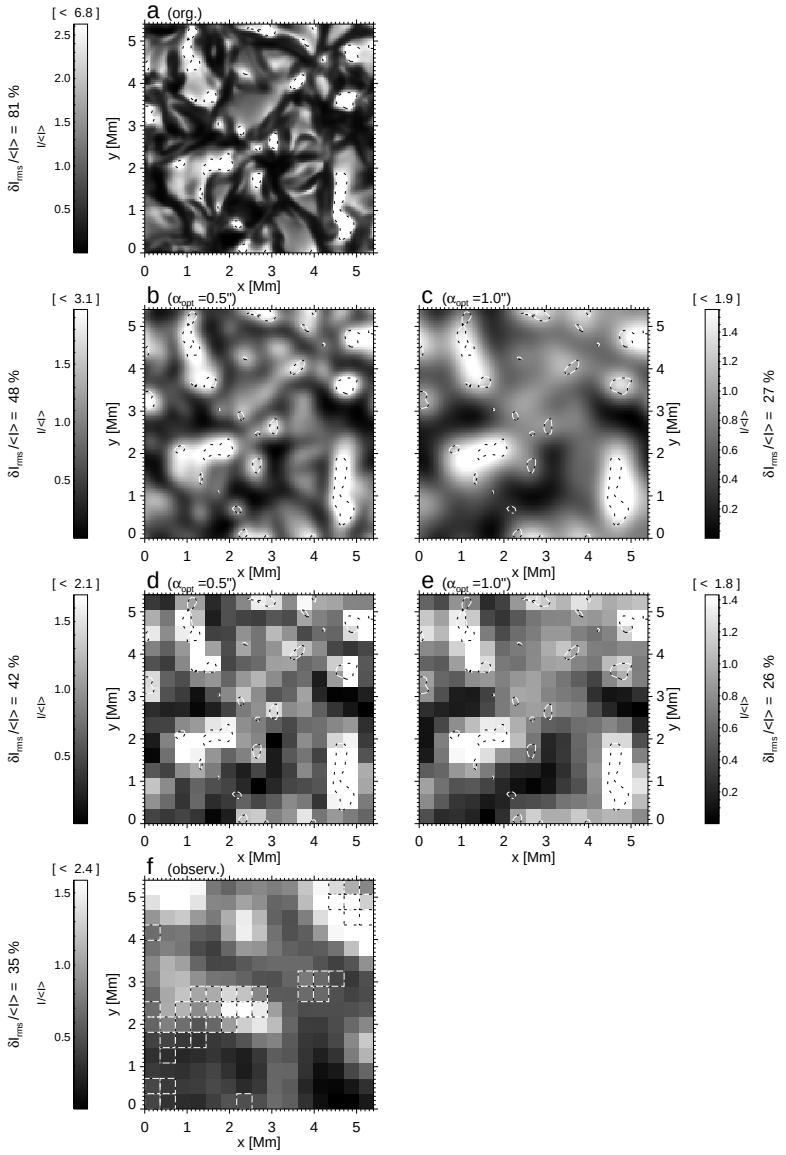

Figure 1. Synthetic intensity images for 160 nm passband of TRACE: **a)** original image, **b)** degraded to a spatial resolution of $0\farcs5$, and **d)** after integration on TRACE $0\farcs5$ pixels. The image degradation is repeated for a coarser resolution of $1\farcs0$ in panel **c)** but with the same pixel size in panel **e)**. The dashed contours for the original intensity in panel a help to identify the enclosed regions in the other panels. Panel **f)** shows observed TRACE data from September $28^{\rm th}$, 2005, taken from a data set kindly provided by Fossum & Carlsson. The dashed squares mark pixels that would be disregarded according to the pixel selection method by FC06. The grey scale ranges of the panels are clipped individually. The maximum value is given in brackets above each legend. The intensity contrast is noted on the side of each panel.

best by a Gaussian kernel of width (FWHM) larger than $0\farcs5$ but not more than $1''$ (Krijger et al. 2001; Schneider et al. 2004; Schrijver 2006). The detector of TRACE has a pixel-scale of $0.5\,''$/px. A synthetic pixel thus corresponds to spatial integration over (square) regions of 9×9 model grid cells (Fig. 1c). Note that FC05 additionally apply a binning of 2×2 pixels but FC06 use no binning. An example of observational data from FC06 is shown in Fig. 1d for comparison.

Figure 1 clearly demonstrates that the pattern on small spatial scales is lost and only the brightest features are still visible in the synthetic image. Consequently the intensity contrast decreases from 81 % to 42 % for the displayed snapshot (89 % and 33 %, respectively, for the whole sequence). The lower intensity contrast of the observational data (35 % for the displayed region, 30 % for the whole time series for that region, and 26 % for the time series of all pixels according to the mask by FC06) suggests that the true resolution of TRACE might be coarser than the $0\farcs5$ shown in Fig. 1c, which represents a lower limit only. A resolution of $1\,''$, on the other hand, might indeed be considered an upper limit as it reduces the contrast of the synthetic images to 33 % for the displayed snapshot and only 26 % for the whole time series.

2.3. Spectral power density

We derive the temporal spectral power density (one-sided) for each spatial position in the synthetic image sequences separately. The horizontally averaged power spectra are shown in Fig. 2 for the sequence with the original spatial resolution of the input model and also for the two sequences degraded to lower resolution ($0\farcs5$ and $1\,''$). For comparison we plot the power spectra that we calculate from the observed TRACE sequence from September $28^{\rm th}$, 2005 (FC05), (i) for the pixel sample of FC06 and (ii) for the small region shown in Fig. 1d. Image degradation obviously suppresses power on small spatial scales. The average power is reduced by a factor of 10 at 12 mHz for the degraded sequence with a resolution of $0\farcs5$, with respect to the original image sequence, whereas a resolution of $1''$ results in a factor of 27 for the same frequency (see Fig. 2). The reduction in power increases with frequency up to ~ 20 mHz as higher frequencies are connected to smaller wavelengths (of acoustic waves) that are more severely affected by a limited resolution than large-scale fluctuations. The power when using a PSF of $1''$ width agrees well with the observational results in the range 3 mHz to ~ 12 mHz.

The discrepancy at low frequencies is due to the short sequence duration, which results in a frequency resolution (see solid circles) that is too small to resolve the local minimum at $\nu \approx 2.5$ mHz. A longer synthetic image sequence at 160 nm with a duration of 76 min and a cadence of 30 s, that we calculated in addition, shows results similar to those for the short sequence at 160 nm with respect to absolute magnitude of power and the relative effect of degrading the spatial resolution. The longer duration provides much finer frequency sampling so that the average power spectrum indeed exhibits a local minimum at low frequencies.

The increasing difference at higher frequencies is most likely connected to the assumption of LTE that had to be made in order to keep the calculations computationally tractable. The assumption is validated by comparison with a more detailed calculation with the RH code (see, e.g., Uitenbroek 2000) for

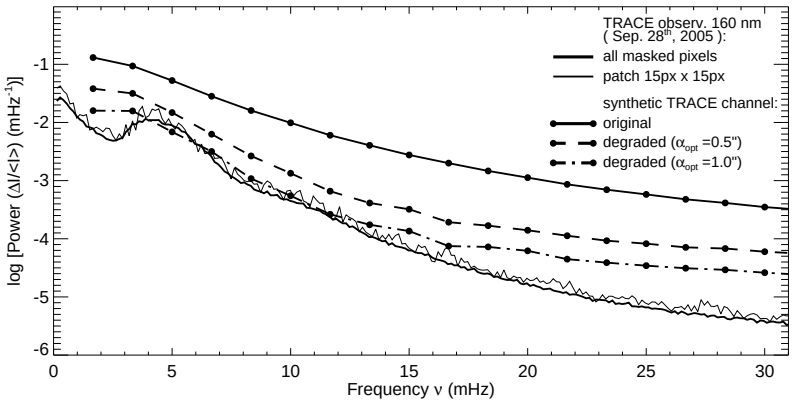

Figure 2. Average one-sided power density spectra for the short sequence of synthetic TRACE images (lines with dots) for original spatial resolution (solid), degradation to $0\farcs5$ (dashed) and $1''$ (dot-dashed) without pixel-binning. The solid dots mark the data points. The two other curves are calculated from observational data from September $28^{\rm th}$, 2005, in the same way as done for the synthetic sequences. The thick curve includes all pixels according to the mask by FC06, whereas the thin one is for the region displayed in Fig. 1d only.

eight 2D slices from the model for a wavelength of 160 nm, taking into account deviations from LTE. The rms fluctuations of the resulting intensity samples are 150.8 % for Linfor3D (LTE), 199.3 % for RH in LTE, and 134.9 % for RH in NLTE. The difference for the LTE samples must be attributed to (i) the assumption of 2D for our application of RH in contrast to full 3D with Linfor3D, (ii) differences in opacity data (in particular concerning photoionization cross-sections of silicon), and (iii) the neglect of continuum scattering in Linfor3D. The latter, however, is expected to be of minor importance as there are few continuum scattering processes that are relevant at wavelengths around 160 nm. More important is the correct treatment of bound-free transitions of silicon (taken into account in RH). They can be regarded as bound-free "two-level" resonance scatterers and effectively smooth out fluctuations. Nevertheless this qualitative comparison demonstrates that neglecting non-LTE effects tends to produce too large relative intensity fluctuations and with that an excess in average power for higher frequencies as visible in Fig. 2.

In addition, a simulation sequence with non-grey radiative transfer (Wedemeyer 2003) was used for intensity synthesis at 160 nm. The resulting power spectra at original and lowered resolution are very similar to the grey sequence used here.

3. Ohmic Dissipation of Chromospheric Current Sheets

3.1. Three-dimensional MHD simulation

We have also carried out a three-dimensional simulation including magnetic fields. The computational domain extends from a depth of 1400 km below the

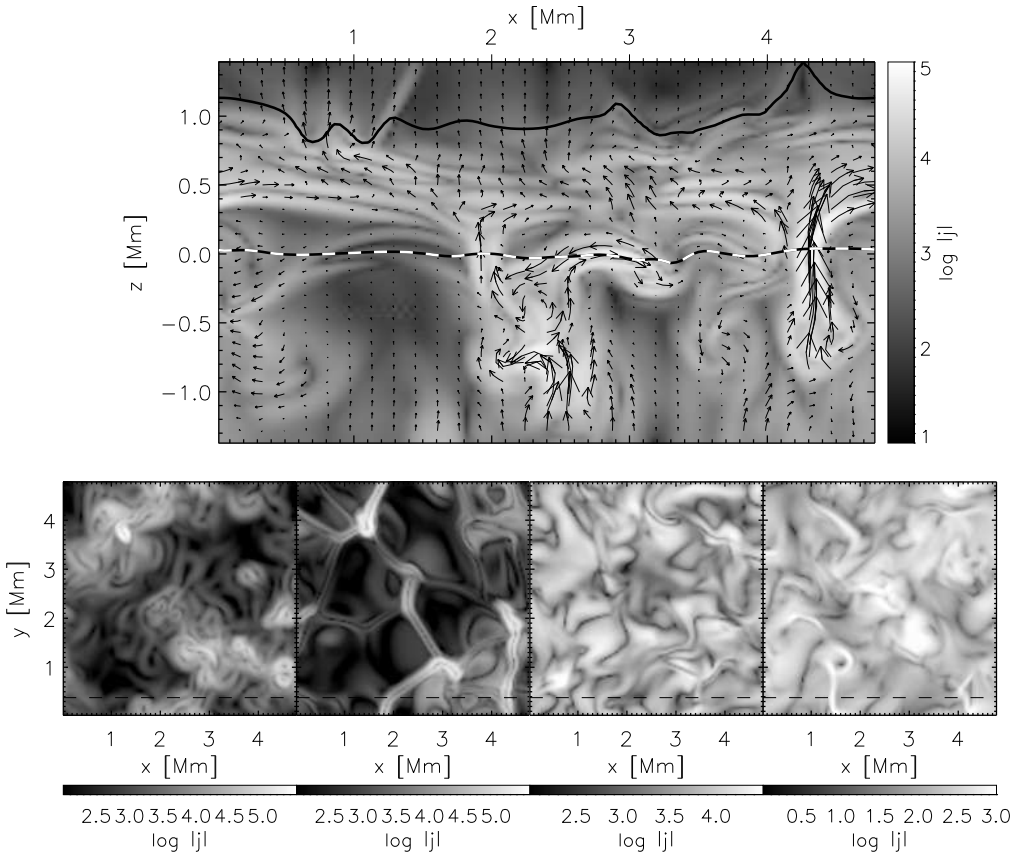

Figure 3. Logarithmic current density, $\log |j|$, in a vertical cross section (top panel) and in four horizontal cross sections in a depth of 1180 km below, and at heights of 90 km, 610 km, and 1310 km above the mean surface of optical depth unity from left to right, respectively. The arrows in the top panel indicate the magnetic field strength and direction. The dashed line indicates the position of the vertical section. $[j] = 3 \times 10^5$ A m^{-2}.

mean surface of optical depth unity to 1400 km above it well into the chromospheric layers. The horizontal extent is only slightly smaller than for the model by W04. See Schaffenberger et al. (2005, 2006) for details.

The MHD simulation starts with a homogeneous, vertical, unipolar magnetic field of a flux density of 10 G superposed on a previously computed, relaxed model of thermal convection. This flux density is thought to represent magneto-convection in a very quiet network-cell interior. The magnetic field is constrained to have vanishing horizontal components at the top and bottom boundary but lines of force can freely move in the horizontal direction. Because the top boundary is located in the chromosphere, the magnetic field can freely expand with height through the photospheric layers into the more or less homogeneous chromospheric field, different from conventional simulations that extend to a height of typically 600 km only.

A very common phenomenon in this simulation is the formation of a 'magnetic canopy field' that extends in a more or less horizontal direction over expanding granules and between photospheric flux concentrations. The formation of such canopy fields proceeds by the action of the expanding flow above granule centres. This flow transports 'shells' of horizontal magnetic field to the upper photosphere and lower chromosphere, where shells of different field directions may be pushed close together, leading to a complicated network of current sheets in a height range from approximately 400 to 900 km.

This network can be seen in Fig. 3 (top), which shows, for a typical snapshot of the simulation, the logarithmic current density, $\log|j|$, together with arrows indicating the magnetic field strength and direction. Figure 3 (bottom) shows from left to right $\log|j|$ in four horizontal cross sections in a depth of 1180 km below, and at heights of 90 km, 610 km, and 1310 km above the mean surface of optical depth unity. Higher up in the chromosphere (rightmost panel), thin current sheets form along shock fronts, e.g., in the lower left corner near $x = 1.4$ Mm.

3.2. Ohmic dissipation

In this simulation we have not taken an explicit magnetic diffusion into account so that the effective electrical conductivity is determined by the inherent artificial diffusion of the numerical scheme. Therefore, due to lack of a realistic electric conductivity, we here use molecular values when computing the ohmic dissipation of the chromospheric current sheets. Although the values might be orders of magnitude too high, they still can be employed for the following calculation, which gives a rough idea about the significance of ohmic dissipation for chromospheric heating. The typical current density in the height range from 400 to 900 km of Fig. 3 (top) is $j = 0.03\,\mathrm{A\,m^{-2}}$. The electrical conductivity, σ, in the photosphere and the lower chromosphere is about 10 to 100 A/Vm (Stix 2002). Using this value, the ohmic dissipation is

$$P_j = \frac{1}{\sigma} j^2 \approx \frac{1}{10 \ldots 100}\, 0.03^2 \approx 10^{-5} \ldots 10^{-4}\,\mathrm{W\,m^{-3}}\,. \tag{1}$$

When integrating over a height range of 500 km this heat deposition leads to an energy flux of 5 to 50 $\mathrm{W\,m^{-2}}$. This value is about two orders of magnitude short of being relevant for chromospheric heating. However, the amplitude and width of the current sheets in the simulation is determined by the spatial resolution of the computational grid rather than by the molecular conductivity. The effective conductivity in the simulation may easily be two orders of magnitude lower so that magnetic heating by ohmic dissipation must be seriously taken into account as a chromospheric heating agent. Further simulations, taking explicit ohmic diffusion into account will clarify this issue.

4. Discussion

The photosphere of the model by W04 can account for many aspects of observations of internetwork regions (see, e.g., Leenaarts & Wedemeyer-Böhm 2005). Here we provide evidence that the UV intensity in the TRACE 160 nm channel is matched reasonably well, too. When degraded to the spatial resolution of the

instrument, the synthetic intensity images presented here have similar contrasts and also result in average spectral power densities similar to the TRACE observations. The power spectra exhibit an enhancement around periods of 5 min and otherwise a decrease with frequency as it was found by FC05 and FC06 both from observations and their 1D simulations.

At higher frequencies, however, we derive too much power from the synthetic image series. This discrepancy is most likely due to the LTE assumption made for the intensity synthesis with Linfor3D. The test calculations with the RH code show that taking into account deviations from LTE reduces the intensity contrast by $\sim 60\,\%$ compared to the LTE case for a wavelength of 160 nm. The deviation from LTE at the shorter wavelengths is mostly due to the strong over-ionization of Si I, which affects the continuum forming bound-free transitions. Similar to true continuum scattering, this effect smoothes out fluctuations, so that the LTE assumption used here actually tends to produce too large fluctuations and thus an excess in power. We argue that the derived reduction of $\sim 60\,\%$ in intensity contrast can be considered as an upper limit for the influence of this scattering-like process. In contrast, the deviations from LTE are much smaller for the longer wavelengths. For a rough estimate we derive an average ratio of LTE and NLTE intensities based on the RH calculations and use it to scale the LTE intensities of the whole synthetic 160 nm sequence. This "pseudo-NLTE" time series leads to a further reduction in power by approximately a factor of two around periods close to 5 min to four for higher frequencies. The tendency of larger power reduction with increasing frequency might be even more enhanced by non-LTE effects being more important on time scales too short for relaxation to equilibrium conditions. The "pseudo-NLTE" estimate is of course an order of magnitude approximation only and needs to be replaced with detailed NLTE calculations that include not only 160 nm but the whole wavelength range relevant for the TRACE channel. Taking into account line blanketing acts in the opposite direction by reducing the intensity at the longer wavelengths and thus increasing the relative fluctuations. A comparison of the spectra calculated with MULTI for the VAL model A results in a reduction of integrated intensity by a factor of ~ 2 (Carlsson 2006). But whether it really counterbalances the expected NLTE effects and if so by how much and for which frequencies remains subject to detailed radiative transfer calculations.

The computational box of the hydrodynamical simulation is small (5.6 Mm $\times$ 5.6 Mm). Consequently, the number of possible oscillation modes is much smaller than in the real Sun so that the power in the model is distributed over a smaller number of modes. The total energy content of the modes, however, remains the same. Also the finite grid resolution limits the treatment of high-frequency waves but FC06 state that the neglect of frequency beyond 20 mHz is not an important omission.

When computing the mechanical energy flux from the intensity fluctuations, FC05 and FC06 assume that the resolution of TRACE is sufficient to fully capture the energy carrying waves. FC06 state that tests with 2D models related to the hydrodynamic simulations by Hansteen (2004) imply that only a factor of two in acoustic flux is missed due to insufficient spatial resolution. In contrast our 3D study presented here shows that the unresolved small-scale pattern provides more power by an order of magnitude or even more.

At this stage we cannot exactly determine how much of the additional power hidden on small spatial scales is indeed transported to the chromosphere and how much remains in the photosphere and therefore does not contribute to chromospheric heating. Separating the acoustic flux from the total mechanical flux is not easy for our 3D model the latter gets on average even negative in the middle photosphere as a consequence of convective overshooting. There is a local maximum of the radiative flux divergence in the low chromosphere and a mechanical counterpart of opposite sign that we interpret as evidence for the conversion of mechanical energy provided by acoustic waves into thermal energy, which is subsequently emitted in form of radiation (Wedemeyer 2003). Integration of the mechanical flux divergence over the height range from 570 km to 1710 km results in an acoustic energy flux of $7.9\,\mathrm{kW\,m^{-2}}$ which is sufficient to counterbalance the (semi-)empirically determined radiative energy losses from the chromosphere (see, e.g, VAL). Moreover, the total mechanical flux at a height of 800 km (which approaches the pure accoustic flux there) amounts to $3.8\,\mathrm{kW\,m^{-2}}$ and is thus in line with the 1D models by Rammacher (2005).

On the other hand, the energy flux due to Ohmic dissipation of current sheets in the MHD model chromosphere is only of the order of 5 to $50\,\mathrm{W\,m^{-2}}$. This value must be considered as a lower limit only because of the uncertainty in the electrical conductivity. It can thus not be ruled out that the magnetic heating contribution might be underestimated by even two orders of magnitude.

Although the energy balance of the model chromosphere is affected by a too simple treatment of the radiative transfer, the calculations presented here suggest that the acoustic contribution to chromospheric heating cannot be neglected. Magnetic fields may also play an indirect role for guiding acoustic waves and for mode conversion (Suematsu 1990; Ulmschneider et al. 1991; Jefferies et al. 2006).

5. Conclusions

Based on the analysis presented here we conclude that TRACE might miss acoustic power by at least one order of magnitude due to its limited spatial resolution. Horizontal flows, as they are clearly seen within the reversed granulation pattern, contribute to the intensity variations although their relevance for the energy transport to the upper layers is not clear yet.

Matching the empirical power spectra with a model that has enough acoustic power to counterbalance the observed chromospheric emission should not be interpreted such that high-frequency waves alone are sufficient to heat the chromosphere. It is not clear from this study how important the small relative power contribution of high-frequency waves is for chromospheric heating. Moreover, the model used here exhibits a chromosphere with pronounced dynamics and a highly inhomogeneous structure – in sharp contrast to static and one-dimensional semi-empirical VAL-like models. The ubiquitous shock waves, which produce our model chromosphere's characteristic structure, play certainly an important role for the energy balance of our model chromosphere.

It must be emphasised that – owing to simplifications that are necessary in order to keep the problem computationally tractable – the topic should be addressed again with detailed NLTE calculations. Nevertheless, the presented

study clearly demonstrates that three-dimensional radiation hydrodynamics simulations in principle can reproduce the TRACE observations of internetwork regions without strong need for magnetic fields, although weak fields are most likely an integral part of those regions. We conclude that an acoustic "basal flux" (Schrijver 1987) must still be considered a possible option for heating the chromosphere of internetwork regions.

Acknowledgments. We thank the CSPM organisers for a very good meeting and M. Carlsson, K. Muglach, C. Schrijver, R. Rutten, V. Hansteen, and H. Uitenbroek for discussion and helpful comments. We are grateful to A. Fossum for kindly providing observational data and useful remarks regarding data reduction. Thanks go also to M. Steffen, H.-G. Ludwig, and B. Freytag for their support for Linfor3D and CO^{5}BOLD. H. Uitenbroek friendly provided his RH code. This work was supported by the *Deutsche Forschungsgemeinschaft (DFG)*, grant Ste 615/5.

References

Carlsson M., & Stein R. F., 1997, ApJ481, 500
Carlsson, M. 2006, priv. comm.
Fossum, A. & Carlsson, M. 2005, Nat, 435, 919 (FC05)
Fossum, A. & Carlsson, M. 2006, ApJ, 646, 579 (FC06)
Freytag, B., Steffen, M., & Dorch, B. 2002, Astron. Nachr., 323, 213
Handy, B. N., Acton, L. W., Kankelborg, C. C., et al. 1999, Solar Phys. , 187, 229
Hansteen, V. H. 2004, in Multi-Wavelength Investigations of Solar Activity, A. V. Stepanov, E. E. Benevolenskaya, & A. G. Kosovichev (eds.), IAU Symposium 223, 385
Jefferies, S. M., McIntosh, S. W., Armstrong, J. D., et al. 2006, ApJ, 648, L151
Krijger, J. M., Rutten, R. J., Lites, B. W., et al. 2001, A&A, 379, 1052
Leenaarts, J. & Wedemeyer-Böhm, S. 2005, A&A, 431, 687
Rammacher, W. 2005, in Chromospheric and Coronal Magnetic Fields, D. E. Innes, A. Lagg, & S. A. Solanki (eds.), ESA SP-596, (CD-ROM)
Schaffenberger, W., Wedemeyer-Böhm, S., Steiner, O., & Freytag, B. 2005, in Chromospheric and Coronal Magnetic Fields, D. Innes, A. Lagg, S. Solanki, & D. Danesy (eds.), ESA SP-596, (CD-ROM)
Schaffenberger, W., Wedemeyer-Böhm, S., Steiner, O., & Freytag, B. 2006, in Solar MHD Theory and Observation: A High Spatial Resolution Perspective, H. Uitenbroek, J. Leibacher, & R.F. Stein (eds.), ASP Conf. Series 354, 351
Schneider, G., Pasachoff, J. M., & Golub, L. 2004, Icarus, 168, 249
Schrijver, C. J. 1987, A&A, 172, 111
Schrijver, C. J. 2006, priv. comm.
Stix, M. 2002, The Sun, 2nd edition, Springer
Suematsu, Y. 1990, in LNP Vol. 367: Progress of Seismology of the Sun and Stars, ed. Y. Osaki & H. Shibahashi, 211
Uitenbroek, H. 2000, ApJ, 536, 481
Ulmschneider, P., Zaehringer, K., & Musielak, Z. E. 1991, A&A, 241, 625
Vernazza, J. E., Avrett, E. H., & Loeser, R. 1981, ApJS, 45, 635 (VAL)
Wedemeyer, S. 2003, PhD thesis, University of Kiel, http://e-diss.uni-kiel.de/diss_764/
Wedemeyer, S., Freytag, B., Steffen, M., Ludwig, H.-G., & Holweger, H. 2004, A&A, 414, 1121 (W04)

The Physics of Chromospheric Plasmas
ASP Conference Series, Vol. 368, 2007
Petr Heinzel, Ivan Dorotovič and Robert J. Rutten, eds.

Non-equilibrium Hydrogen Ionization in the Solar Atmosphere

Jorrit Leenaarts[1,2], Sven Wedemeyer-Böhm[2], Mats Carlsson[2,3] and Viggo H. Hansteen[2,3]

[1] *Sterrekundig Instituut, Utrecht University, The Netherlands*
[2] *Institutt for Teoretisk Astrofysikk, University of Oslo, Norway*
[3] *Center of Mathematics for Applications, University of Oslo, Norway*

Abstract. The assumption of statistical equilibrium for atomic level populations of hydrogen does not hold under the conditions of the chromosphere due to the low density and the short dynamic timescale. In order to calculate the hydrogen ionization balance and the electron density one has to solve the time-dependent rate equations. We present results from 2D and 3D radiation-magneto-hydrodynamics simulations of the solar atmosphere incorporating the time-dependent rate equations for hydrogen. Both the hydrogen ionization degree and the electron density in our models are much more constant than LTE and statistical equilibrium theory predict. These simulations provide multi-dimensional model atmospheres with realistic electron densities and hydrogen level populations that can be used in detailed radiative transfer modeling.

1. Introduction

The one-dimensional (1D) simulations of Kneer (1980) have shown that non-equilibrium hydrogen ionization is an essential ingredient of solar atmospheric dynamics. The density in the solar chromosphere and transition region is so low that the hydrogen populations will not relax towards their equilibrium values on the timescale that the atmosphere changes. Carlsson & Stein (2002) have published a detailed analysis of non-equilibrium hydrogen ionization, with a 1D simulation spanning from the convection zone to the corona, incorporating fully-fledged time-dependent radiation transport.

Two and three-dimensional models have so far not incorporated this non-equilibrium ionization, instead relying on LTE (Wedemeyer et al. 2004) or statistical equilibrium ionization (Skartlien 2000) for reasons of limited computing power and algorithm stability.

Sollum (1999) showed that the radiation field for hydrogen can be approximated by fixed radiative rates in 1D simulations, thus reducing the complex time-dependent radiative transfer to a relatively simple problem of advection of populations with local sources and sinks. We have implemented this method in two multi-dimensional radiation-magneto-hydrodynamics codes.

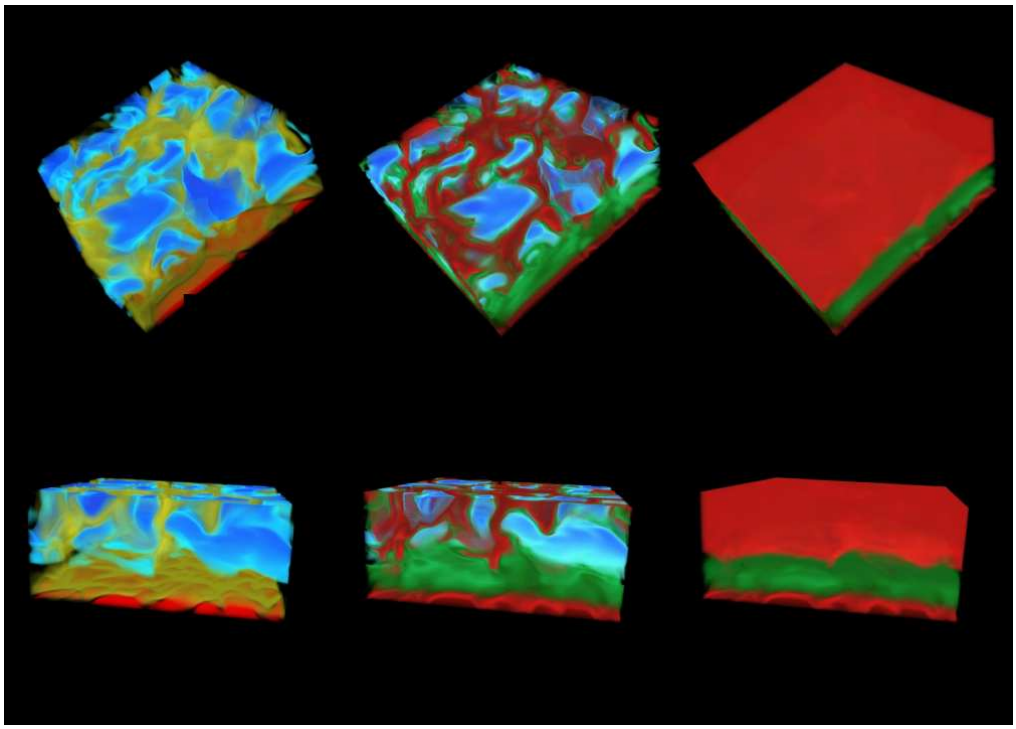

Figure 1. A 3D visualisation of the results of the CO^{5}BOLD simulation. The left-hand cubes show the temperature, with the high temperature granulation pattern below (red), the cool chromospheric inter-shock regions (blue) interspersed with shock waves (yellowish) at the top. The middle and right-hand panels show the LTE and non-equilibrium ionization degree, with low (blue), middle (green) and high ionization degree (red). The non-equilibrium case shows an almost constant ionization degree throughout the chromosphere, in stark contrast with the LTE case. See Leenaarts & Wedemeyer-Böhm (2006) for details.

2. Results

The method by Sollum (1999) has been implemented in the CO^{5}BOLD code (Freytag et al. 2002), but without taking into account the effect of the hydrogen ionization on the equation of state of the gas. With this code we have performed a 3D simulation from the convection zone up to the chromosphere, without magnetic fields. Figure 1 shows the temperature and ionization degree of a snapshot of the simulation. The ionization degree in the non-equilibrium case (right-hand panels) is rather constant, whereas the LTE case (middle panels) shows strong fluctuations reflecting the temperature structure (left-hand panels). See Leenaarts & Wedemeyer-Böhm (2006) for more details on this model.

The method of fixed rates has also been implemented in the radiation-magneto-hydrodynamics code developed in Oslo (Hansteen 2004) based on the

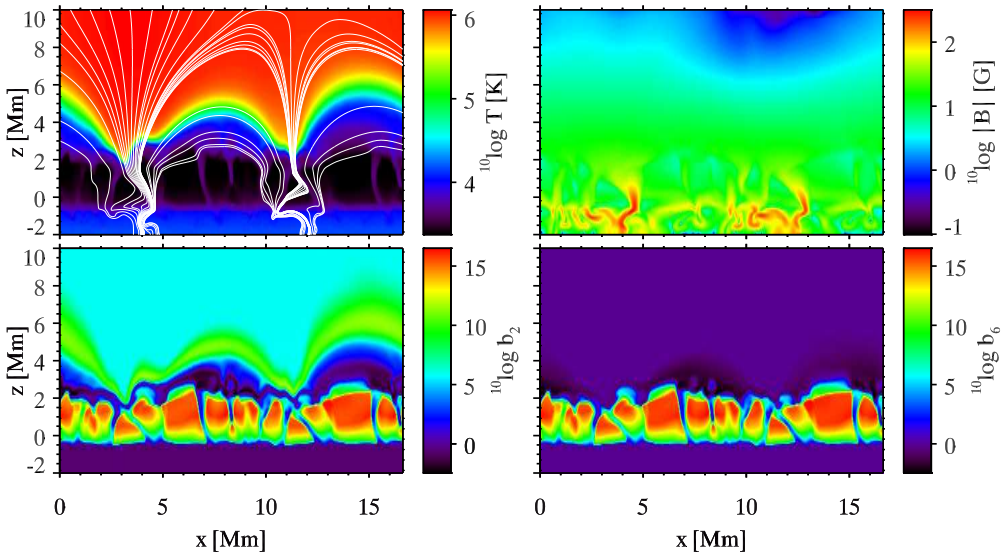

Figure 2. Results from the simulation with the Oslo code. The photosphere is just below $z = 0$ Mm. *Top left*: temperature, with some magnetic field lines overplotted in white. *Top right*: magnetic field strength. *Bottom left*: departure coefficient of the $n = 2$ level of hydrogen. *Bottom right*: departure coefficient of the proton density (ionised hydrogen). The excited and ionised states of hydrogen are hugely overpopulated in the chromospheric inter-shock region. Interestingly, the $n = 2$ level is more overpopulated in the transition region (the green arcs around $z = 5$ Mm) than in coronal equilibrium.

staggered grid code by Galsgaard & Nordlund[1]. Here we also implemented the feedback of the ionization on the equation of state, thereby replacing the often used equation of state tables by an explicitly computed equation of state. With this code we performed a 2D simulation from the convection zone up into the corona, including the transition region (see Fig. 2). The same model setup has recently been used to explain dynamic fibrils (Hansteen et al. 2006). We intend to show synthetic Hα spectra from this simulation in a forthcoming publication.

3. Conclusions

We have shown results from two radiation-magneto-hydrodynamics codes which incorporate non-equilibrium hydrogen ionization. The degree of hydrogen ionization in the chromosphere is much more constant in the non-quilibrium case than equilibrium theory predicts. The results from these simulations can be directly used to synthesise Hα spectra, and the realistic electron densities that the simulations provide can be used for spectral synthesis of other chromospheric diagnostics as the Ca II H line and the Ca infrared triplet.

[1]See `http://www.astro.ku.dk/~kg/`.

References

Carlsson M., Stein R. F., 2002, ApJ 572, 626
Freytag B., Steffen M., Dorch B., 2002, Astronomische Nachrichten 323, 213
Hansteen V. H., 2004, in A. V. Stepanov, E. E. Benevolenskaya, A. G. Kosovichev (eds.), IAU Symposium, p. 385
Hansteen V. H., De Pontieu B., Rouppe van der Voort L., van Noort M., Carlsson M., 2006, ApJ 647, L73
Kneer F., 1980, A&A 87, 229
Leenaarts J., Wedemeyer-Böhm S., 2006, A&A 460, 301
Skartlien R., 2000, ApJ 536, 465
Sollum E., 1999, Master's thesis, University of Oslo
Wedemeyer S., Freytag B., Steffen M., Ludwig H.-G., Holweger H., 2004, A&A 414, 1121

The Physics of Chromospheric Plasmas
ASP Conference Series, Vol. 368, 2007
Petr Heinzel, Ivan Dorotovič and Robert J. Rutten, eds.

3D Numerical Models of the Chromosphere, Transition Region, and Corona

Viggo H. Hansteen, Mats Carlsson and Boris Gudiksen

Institute of Theoretical Astrophysics, University of Oslo, Norway

Abstract. A major goal in solar physics has during the last five decades been to find how energy flux generated in the solar convection zone is transported and dissipated in the outer solar layers. Progress in this field has been slow and painstaking. However, advances in computer hardware and numerical methods, vastly increased observational capabilities and growing physical insight seem finally to be leading towards understanding. Here we present exploratory numerical MHD models that span the entire solar atmosphere from the upper convection zone to the lower corona. These models include non-grey, non-LTE radiative transport in the photosphere and chromosphere, optically thin radiative losses as well as magnetic field-aligned heat conduction in the transition region and corona.

1. Introduction

The notion that chromospheric and coronal heating in some way follow from excess "mechanical" energy flux as a result of convective motions has been clear since the mid-1940's. Even so, it is only recently that computer power and algorithmic developments have allowed one to even consider taking on the daunting task of modeling the entire system from convection zone to corona in a single model.

Several of these challenges were met during the last few years in the work of Gudiksen & Nordlund (Gudiksen & Nordlund 2002), where it was shown that it is possible to model the photosphere to corona system. In their model a scaled down longitudinal magnetic field taken from an SOHO/MDI magnetogram of an active region is used to produce a potential magnetic field in the computational domain that covers $50\times50\times30$ Mm^3. This magnetic field is subjected to a parameterization of horizontal photospheric flow based on observations and, at smaller scales, on numerical convection simulations as a driver at the lower boundary.

In this paper we will consider a similar model, but one which simulates a smaller region of the Sun; at a higher resolution and in which convection is included. The smaller geometrical region implies that several coronal phenomena cannot be modeled. On the other hand the greater resolution and the inclusion of convection (and the associated non-grey radiative transfer) should allow the model described here to give a somewhat more satisfactory description of the chromosphere and, perhaps, the transition region and lower corona.

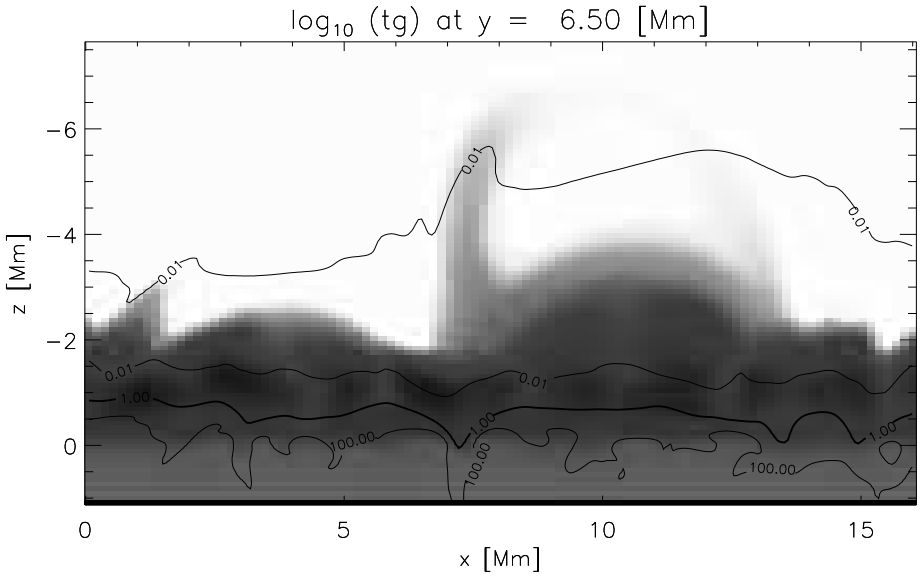

Figure 1. Temperature structure in one plane of the simulation box. At $z = 0$ Mm temperatures span 5000 K to 10 000 K, at the bottom of the computational domain, 1.5 Mm into the convection zone, we find temperatures ranging from 15 700 K in down-flowing plumes to 16 500 K in the gas flowing into the simulation domain. Above the photosphere, the chromosphere extends 2–4 Mm (see also Fig. 4) with temperatures from 2000 K to 8000 K. The upper 10 Mm of the model is filled with plasma at transition region and coronal temperatures of up to some 1 MK, though even at great heights there are intrusions of cooler gas. Also plotted are contours of plasma $\beta = p_g/p_B$; $\beta = 1$ is found in the mid to lower chromosphere, occasionally almost reaching the photosphere. β is much greater than one in the convection zone, much smaller than one in the transtion region and corona. Note that we find high intensity "bright points" in the photosphere where the magnetic field is strong. High intensity in the chromosphere is due both hydrodynamic shocks and magnetic heating.

2. Method

There are several reasons that the attempt to construct forward models of the convection zone or photosphere to corona system has been so long in coming. We will mention only a few:

The magnetic field will tend to reach heights of approximately the same as the distance between the sources of the field. Thus if one wishes to model the corona to a height of, say, 10 Mm this requires a horizontal size close to the double, or 20 Mm in order to form closed field regions up to the upper boundary. On the other hand, resolving photospheric scale heights of 100 km or smaller and transition region scales of some few tens of kilometers will require minimum grid sizes of less than 50 km, preferably smaller. (Numerical "tricks" can perhaps ease some of this difficulty, but will not help by much more than a factor two). Putting these requirements together means that it is difficult to get away with

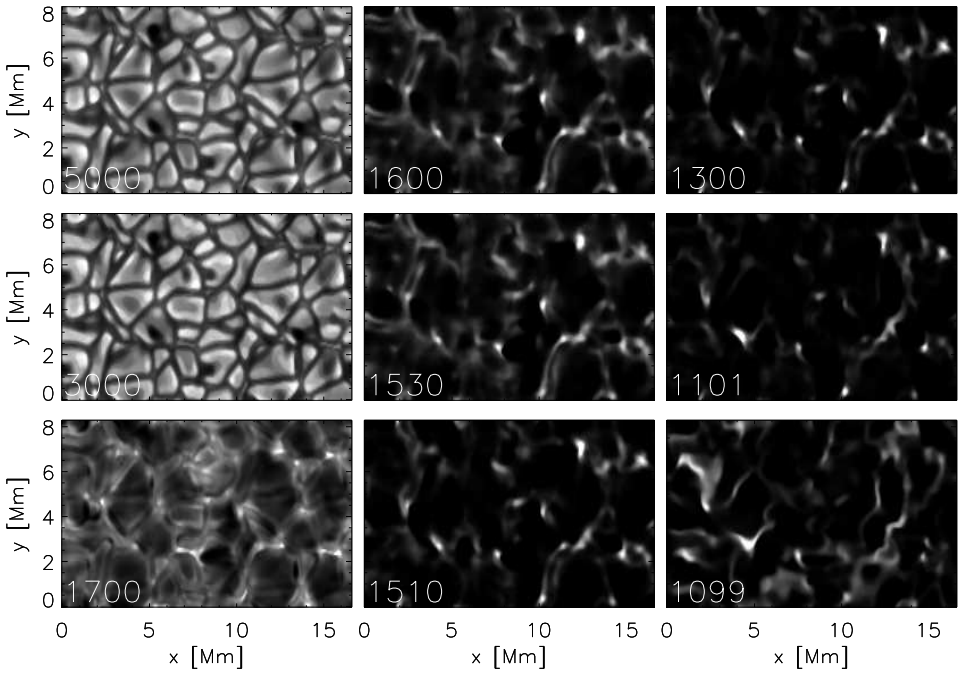

Figure 2. Emergent intensities in various continua (wavelength in Å in each panel) as seen from above. The continua at 5000 and 3000 Å show photospheric granulation, the continuum at 1700 is formed a few hunderd kilometers higher and shows reverse granulation, at 1600 and 1530 Å we sample the the upper photosphere. The 1510 continuum is just shortward of the bound-free edge of neutral silicon, carrying the formation to the lower chromosphere. The 1300 and 1101 continua are formed in the lower-mid chromosphere and the 1099 continuum is just shortward of the bound-free edge of neutral carbon and is formed in the upper chromosphere.

computational domains of much less than 150^3 — a non-trivial exercise even on todays systems.

The "Courant condition" for a diffusive operator such as that describing thermal conduction scales with the grid size Δz^2 instead of with Δz for the magneto-hydrodynamic operator. This severely limits the time step Δt the code can be stably run at. One solution is to vary the magnitude of the coefficient of thermal conduction when needed. Another, used in this work, is to proceed by operator splitting, such that the operator advancing the variables in time is $L = L_{\rm hydro} + L_{\rm conduction}$, then solving the conduction operator implicitly, for example using the multigrid method.

Radiative losses from the photosphere and chromosphere are optically thick and require the solution of the transport equation. A sophisticated treatment of this difficult problem was devised by (Nordlund 1982) in which opacities are binned according to their magnitude; in effect one is constructing wavelength bins that represent stronger and weaker lines and the continuum so that radiation in all atmospheric regions is treated to a certain approximation. If one

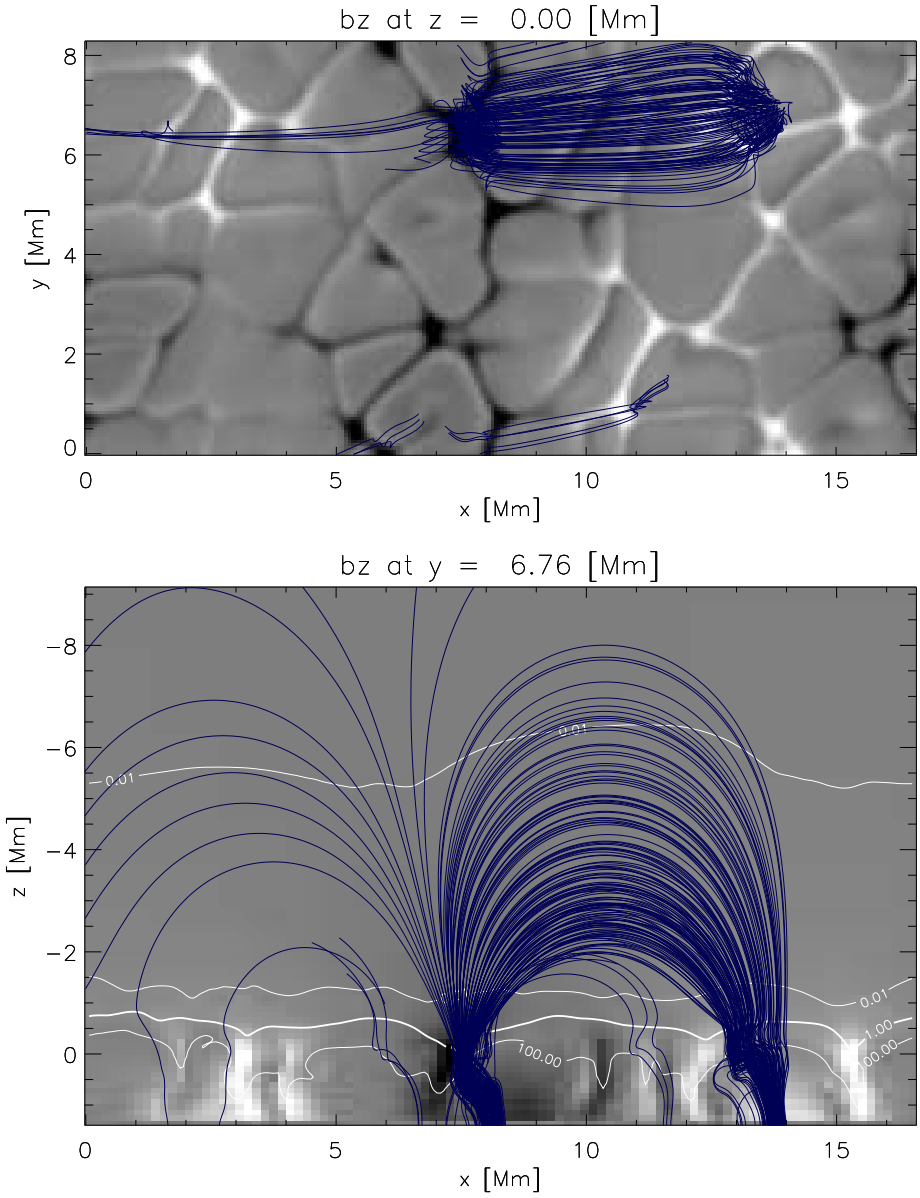

Figure 3. The $\mathbf{B}_z$ component of the magnetic field in the photosphere, $z = 0$ Mm is shown in the upper panel. A subset of magnetic field lines – a semi-random selection based on the strongest magnetic field at the height where $\beta \approx 1$ is drawn. The lower panel shows the same, projected from side. In addition countours of constant β are drawn in white. Note that the field lines identified fit well with the location of maximum emission in the Ne VIII and Mg X lines as evident in Fig. 6.

further assumes that opacities are in LTE the radiation from the photosphere can be modeled. Modeling the chromosphere requires that the scattering of photons is treated with greater care (Skartlien 2000), or in addition that one uses

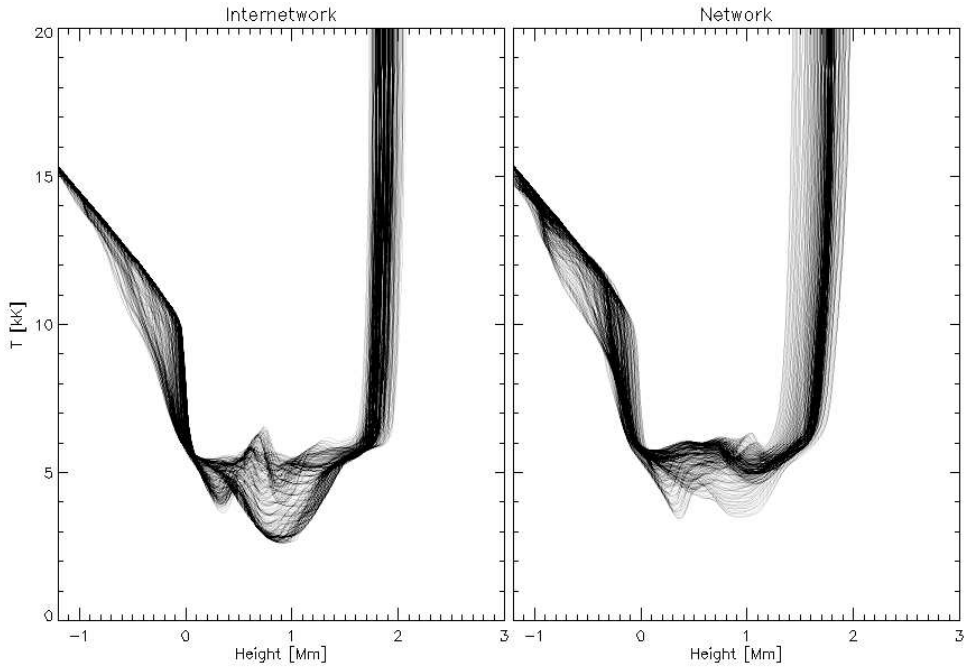

Figure 4. *Left*: temperature structure in the chromosphere as found above a region of very weak photospheric field. *Right*: temperature above a region with stronger magnetic field. Note that the average chromospheric temperature is higher and that the transition region extends further down towards the photosphere in the "network". Note also the evidence of shock propagation in the "internetwork" panel at left.

methods assuming that chromospheric radiation can be tabulated as a function of local thermodynamic variables *a priori*.

In this paper we have used the methods mentioned to solve the MHD equations, including thermal conduction and non-grey non-LTE radiative transfer. The numerical scheme used is an extended version of the numerical code described in Dorch & Nordlund 1998; Mackay & Galsgaard 2001 and in more detail by Nordlund & Galsgaard at `http://www.astro.ku.dk/kg/`. In short, the code functions as follows: The variables are represented on staggered meshes, such that the density ρ and the internal energy e are volume centered, the magnetic field components $\mathbf{B}$ and the momentum densities $\rho\mathbf{u}$ are face centered, while the electric field $\mathbf{E}$ and the current $\mathbf{J}$ are edge centered. A sixth order accurate method involving the three nearest neighbor points on each side is used for determining the partial spatial derivatives. In the cases where variables are needed at positions other than their defined positions a fifth order interpolation scheme is used. The equations are stepped forward in time using the explicit 3rd order predictor-corrector procedure by Hyman 1979, modified for variable time steps. In order to suppress numerical noise, high-order artificial diffusion is added both in the forms of a viscosity and in the form of a magnetic diffusivity.

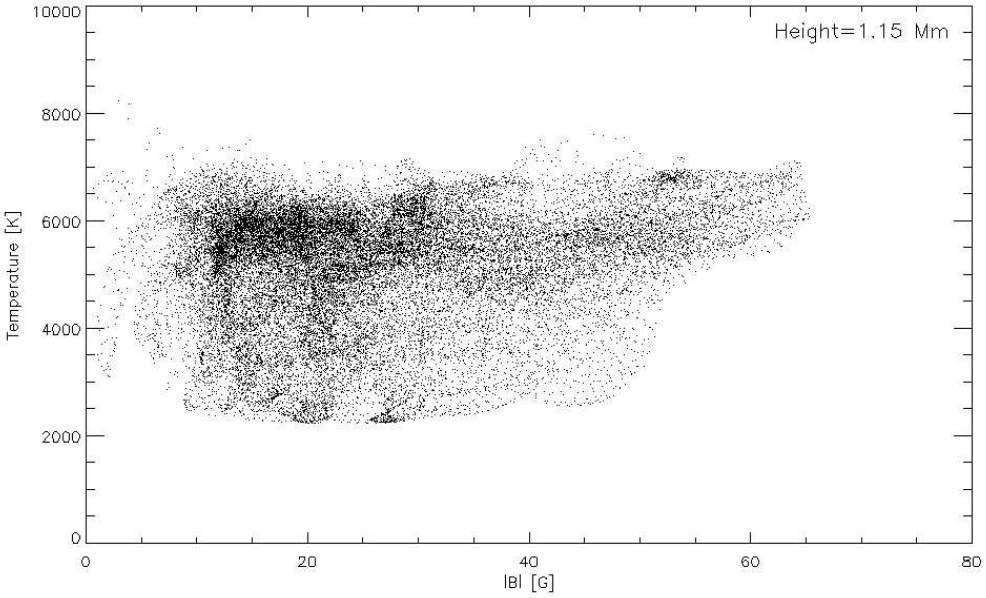

Figure 5. Relation between the magnetic field strength and temperature in the chromosphere 1.15 Mm above the photosphere.

3. 3d Models

The models described here are run on a box of dimension $16{\times}8{\times}16$ Mm^3 resolved on a grid of $256 \times 128 \times 160$ points, equidistant in x and y but with increasing grid size with height in the z direction. At this resolution the model has been run a few minutes solar time starting from an earlier simulation with half the resolution presented here. The lower resolution simulation had run some 20 minutes solar time, starting from a (partially) relaxed convective atmosphere in which a potential field with field strengths of order 1 kG at the lower boundary and an average unsigned field strength of 100 G in the photosphere was added. The convective atmosphere has been built up from successively larger models, and has run of order an hour solar time; some periodicities are still apparent at lower heights where the time scales are longer (of order several hours near the lower boundary).

The initial potential magnetic field was designed to have properties similar to those observed in the solar photosphere. The average temperature at the bottom boundary is maintained by setting the entropy of the fluid entering through the bottom boundary. The bottom boundary, based on characteristic extrapolation, is otherwise open, allowing fluid to enter and leave the computational domain as required. The magnetic field at the lower boundary is advected with the fluid. As the simulation progresses the field is advected with the fluid flow in the convection zone and photosphere and individual field lines quickly attain quite complex paths throughout the model.

A vertical cut of the temperature structure in the model is shown in Fig. 1. In Fig. 2 we show the emergent intensity in various continua as calculated *a*

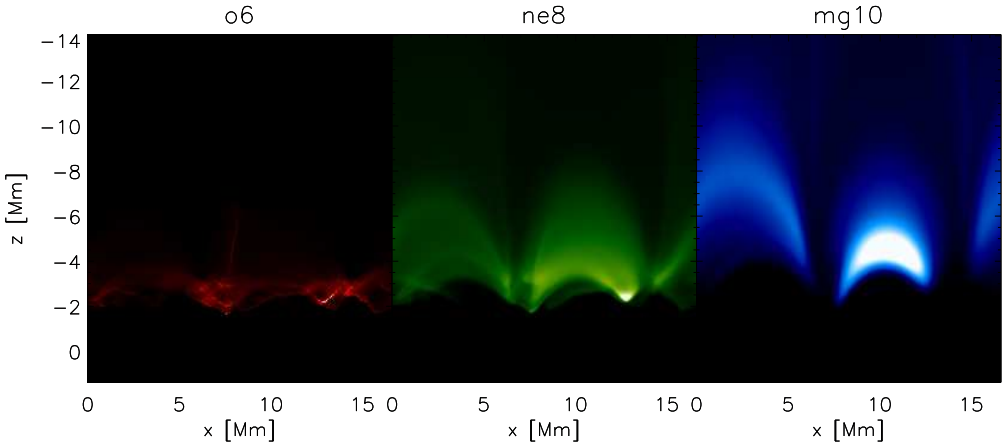

Figure 6. Line emission from the O VI, 300 kK formation temperature, Ne VIII line, formed at roughly 700 kK, and Mg X formed at some 1 MK, all seen seen from the side. Note the ray of O VI emission near $x = 7$ Mm that extends to some $z = -6$ Mm.

posteriori from a data cube some minutes into the simulation run. Though the analysis of these intensities is far from complete (the model is still in some need of further relaxation) a number of observed solar characteristics are recognized. Solar granulation seems faithfully reproduced in the 300 nm and 500 nm bands including bright patches/points in intergranular lanes where the magnetic field is strong. Reverse granulation is evident in the 170 nm band as is enhanced emission where the magnetic field is strong. Bright emission in the bands formed higher in the chromosphere is a result of both strong magnetic fields as well as hydrodynamic shocks propagating through the chromosphere.

The field in the models described here was originally potential. However, it is rapidly deformed by convective motions in the photosphere and below and becomes concentrated in down-flowing granulation plumes on a granulation timescale. In regions below where $\beta \equiv p_g/p_B = 1$ the magnetic field is at the mercy of plasma motions, above the field expands, attempts to fill all space, and forms loop-like structures. The B_z component of the magnetic field in the photosphere is shown in the upper panel of Fig. 3, also plotted are magnetic field lines chosen on the basis of their strength at the surface where $\beta = 1$. The same field lines seen from the side are plotted in the lower panel of Fig. 3 overplotted the vertical magnetic field B_z.

Chromospheric energetics and dynamics are set by a number of factors. Among the most important of these are acoustic waves generated in the photosphere and convection zone impinging on the chromosphere from below; the topology of the magnetic field and the location of the plasma $\beta = 1$ surface; the amount of chromospheric heating due the dissipation of magnetic energy; non-LTE radiative losses and related phenomena such as time dependent ionization and recombination. Most of these phenomena with the exception of time dependent ionization is accounted for (to various degrees of accuracy) in the models presented here. The latter is currently under implementation (Leenaarts et al. 2007). Examples of the chromospheric temperature structure and its relation to the magnetic field are shown in Figs. 4 and 5.

As the stresses in the coronal field grow so does the energy density of the field. This energy must eventually be dissipated; at a rate commensurate with the rate at which energy flux is pumped in. This will depend on the strength of the magnetic field and on the amplitude of convective forcing. On the Sun the magnetic diffusivity η is very small and gradients must become very large before dissipation occurs; in the models presented here we operate with an η many orders of magnitude larger than on the Sun and dissipation starts at much smaller magnetic field gradients. Even so, it seems the model is able to reproduce diagnostics that resemble those observed in the solar transition region and corona as shown in Fig. 6. (It is also interesting to note that we find emission from O VI 103.7 nm in a narrow ray up to 6 Mm above the photosphere, much higher than it should be found in a hydrostatically stratified model.)

4. Conclusions

The model presented here seems a very promising starting point and tool for achieving an understanding of the outer solar layers. But perhaps a word or two of caution is in order before we celebrate our successes. Are the tests we are subjecting the model to — e.g., the comparison of synthetic observations with actual observations actually capable of separating a correct description of the sun from an incorrect one? Conduction along field lines will naturally make loop like structures. This implies that reproducing TRACE-like "images" is perhaps not so difficult after all, and possible for a wide spectrum of coronal heating models. The transition region diagnostics are a more discerning test, but clearly it is still too early to say that the only possible coronal model has been identified. It will be very interesting to see how these forward coronal heating models stand up in the face of questions such as: How does the corona react to variations in the total field strength, or the total field topology, and what observable diagnostic signatures do these variations cause? One could also wonder about the role of emerging flux in coronal heating: How much new magnetic flux must be brought up from below in order to replenish the dissipation of field heating the chromosphere and corona?

Acknowledgments. This work was supported by the Research Council of Norway grant 146467/420 and a grant of computing time from the Program for Supercomputing.

References

Dorch S. B. F., Nordlund A., 1998, A&A 338, 329
Gudiksen B. V., Nordlund Å., 2002, ApJ 572, L113
Hyman J., 1979, in R. Vichnevetsky, R. Stepleman (eds.), Adv. in Comp. Meth. for PDE's—III, 313
Leenaarts J., Wedemeyer-Böhm S., Carlsson M., Hansteen V. H., 2007, in P. Heinzel, I. Dorotovič, R. J. Rutten (eds.), The Physics of Chromospheric Plasmas, ASP Conf. Ser. 368, 103
Mackay D. H., Galsgaard K., 2001, Solar Phys. 198, 289
Nordlund Å., 1982, A&A 107, 1
Skartlien R., 2000, ApJ 536, 465

The Physics of Chromospheric Plasmas
ASP Conference Series, Vol. 368, 2007
Petr Heinzel, Ivan Dorotovič and Robert J. Rutten, eds.

Temporal Variations in Fibril Orientation

J. Koza[1,2], P. Sütterlin[1], A. Kučera[2] and J. Rybák[2]

[1]*Sterrekundig Instituut, Utrecht University, The Netherlands*
[2]*Astronomical Institute, SAS, Tatranská Lomnica, Slovakia*

Abstract. We measure variations in orientation of fourteen dynamic fibrils as a function of time in a small isolated plage and nearby network using a 10-min time sequence of Hα filtergrams obtained by the Dutch Open Telescope. We found motions with average angular velocities of the order of $1\,\mathrm{deg\,min^{-1}}$ suggesting systematic turning from one limit position to another, particularly apparent in the case of fibrils with lifetimes of a few minutes. Shorter fibrils tend to turn faster than longer ones, which we interpret as due to vortex flows in the underlying granulation that twist magnetic fields.

1. Introduction

The solar chromosphere is filled with fibrils in plages and mottles in network seen on the disk and with spicules seen at the limb. Although the mutual correspondence of fibrils, mottles, and spicules has not yet been established directly, we believe that they represent the same feature seen under different circumstances (cf. Christopoulou et al. 2001). Their ubiquity is especially evident in images taken at the center of strong spectral lines. So far most effort has been directed towards understanding their nature, internal structure (De Pontieu et al. 2004; Tziotziou et al. 2003, 2004), and drivers (Hansteen et al. 2006; De Pontieu et al. 2007). Less attention has been paid to their less obvious tangential motions (i.e., perpendicular to the axis) which may betray braiding of chromospheric magnetic fields due to vortex granular flows underneath (Brandt et al. 1988). The first spectroscopic observation of spicule motions parallel to the limb was made by Pasachoff et al. (1968). Nikolsky & Platova (1971) reported on the quasi-periodic motion of spicules along the limb with tangential velocities of 10–15 $\mathrm{km\,s^{-1}}$ and amplitudes about 1 arcsec. Mamedov & Orudzhev (1983a,b) pointed out the similarity between radial (i.e., along the line-of-sight) and tangential velocities of spicules along the limb and speculated on the motion of spicules as a whole.

In this paper, we study tangential motions of fibrils in a small isolated plage and nearby network using a 10-min time sequence of Hα filtergrams obtained with the Dutch Open Telescope (DOT). We concentrate on relatively short-lived straight dynamic fibrils (henceforth DFs, de Wijn & de Pontieu 2006) exhibiting conspicuous elongation and/or retraction within a few minutes. Longer, more static or more curved fibrils are not considered here. We for the first time present measurements of temporal variations in DF orientations. They suggest a relation between angular velocity and DF length.

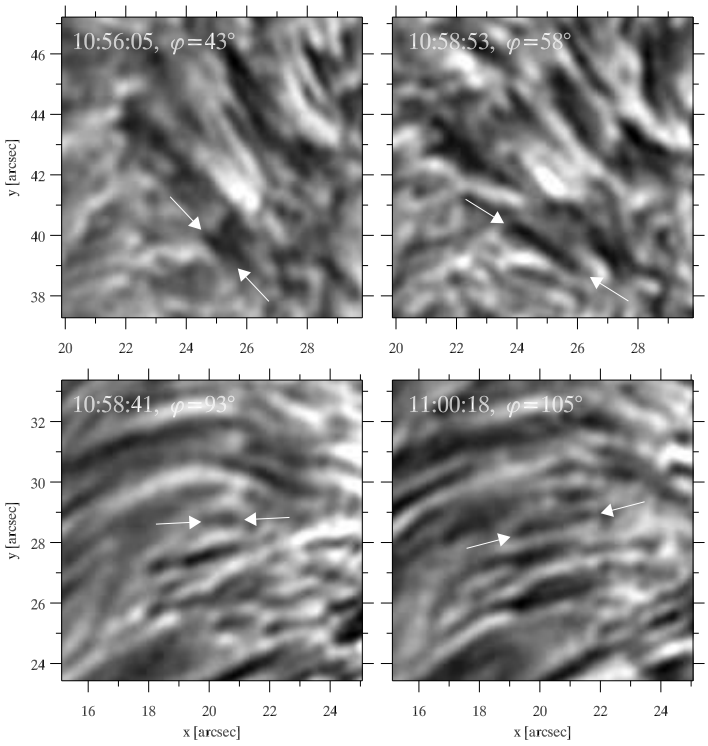

Figure 1. The orientations and lengths of two fibrils highlighted by arrows at intervals of 2.8 min (upper panels) and 1.6 min (lower panels). The angle φ is measured clockwise from the fibril to the righthand y-axis.

2. Observations and Measurements

We use data from the DOT obtained on April 24, 2006 for an isolated plage at $\mu = 0.768$. A tomographic multiwavelength image sequence was recorded during excellent seeing from 10:53:05 UT until 11:02:54 UT. The seeing quality measured at the G band by the average, maximum, and minimum Fried parameter r_0 was 13.0, 16.2, 8.6, respectively. The processed data and movies are available at `http://dotdb.phys.uu.nl/DOT/`. The burst cadence was 12 s. The resulting time sequence was reconstructed by speckle masking and other steps as summarized in Rutten et al. (2004). In this study, we analyse the 10-min sequence of Hα filtergrams taken by the DOT Lyot filter (Gaizauskas 1976) with a FWHM passband of 0.025 nm at $\Delta\lambda = -0.03$ nm from line center.

Inspecting the Hα movie frame-by-frame we focused on relatively short-lived ($\approx$5 min), straight DFs exhibiting apparent elongation or/and retraction. We identified fourteen such DFs and measured the image coordinates of the apparent feet and tops per individual frame. Because the feet locations also vary with time we used the time-averaged feet positions as references. We measured the DF orientations with respect to the y-axis (terrestrial north) and the DF lengths along lines connecting their tops and reference foot locations. Figure 1 shows two examples.

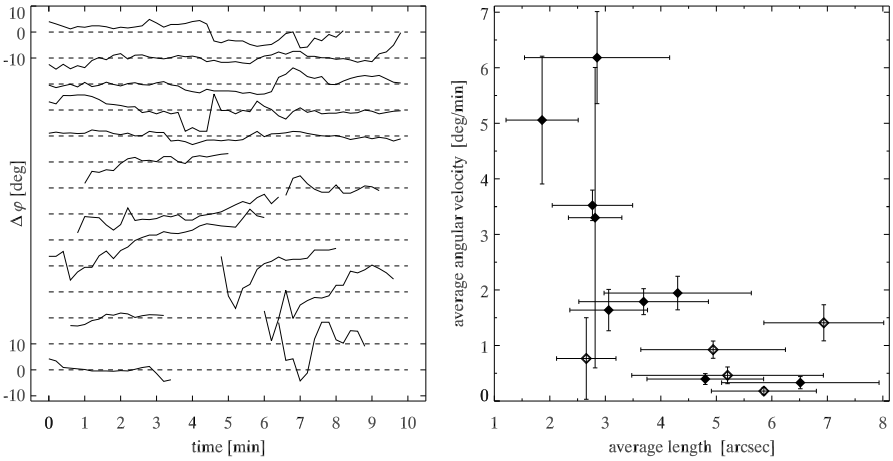

Figure 2. *Left:* Temporal variations in fibril orientation $\Delta\varphi$ measured as difference with the average value represented by dashed lines. The shifts of the curves in time correspond to the fibril occurrence within the image sequence. *Right:* Average angular velocities of the orientation variation versus average fibril length. The filled and empty diamonds represent fibrils turning counterclockwise and clockwise, respectively.

3. Results

Figure 2 shows the measured variations in orientation for the fourteen selected DFs and the rate of change in orientation inferred from linear fits to the curves at left plotted against average DF length. Although the measurements suffer from uncertainty and subjectivity, systematic trends appear. The orientation variations of some short-lived DFs can be characterised as a progression between sign changes, i.e., orientation change from one limit position to another. In contrast, the DFs present during the whole time sequence show stable orientation with only episodic deviations from the average value. Figure 2 suggests that the angular turning speed may be related to DF length, and that shorter DFs turn faster than longer ones. The average fibril lengths and angular velocities yield an estimate of centrifugal acceleration of $1\,\mathrm{m\,s^{-2}}$.

4. Discussion

Because of projection and the magnetic nature of DFs (De Pontieu et al. 2004, 2007; Hansteen et al. 2006), we interpret the temporal variation of the measured fibril orientation as a sum of variations in azimuth and inclination of magnetic flux tubes with respect to the local vertical. In the context of force-free fields (e.g. Lüst & Schlüter 1954), the phenomenon may indicate field twisting and braiding by vortex granular flows beneath (Brandt et al. 1988), injection of twist into the corona, and twisted coronal fans seen in TRACE EUV movies. On the basis of the indicated relation between angular velocity and length (Fig. 2) we suggest that granulation with larger vortical flows produce more upright flux tubes, i.e., faster turning and shorter in projection on the disk, but better seen as long spicules at the limb with conspicuous tangential motions as reported in Pasachoff

et al. (1968), Nikolsky & Platova (1971), and Mamedov & Orudzhev (1983a,b). In contrast, granulation with smaller or no vortical flows permits more slanted flux tubes with smaller angular velocities, longer in on-disk projection but hardly observable on the limb because of crowding. Measurements of the horizontal flow fields in the photosphere and elimination of the projection effects are needed to test this scenario. The observed angular velocity of $\approx 1\,\mathrm{deg\,min^{-1}}$ implies more intensive twisting of the field lines than in sunspots which have typical rotation velocities of about $1\,\mathrm{deg\,h^{-1}}$ (Kucera 1982; Brown et al. 2003).

5. Summary

Using a time sequence of high-resolution Hα filtergrams obtained by the DOT we have searched for temporal variation in the azimuthal orientation of fourteen dynamic fibrils. They show significant variation, for shorter-lived fibrils indicating turning motions at about $1\,\mathrm{deg\,min^{-1}}$. Shorter DFs turn faster than longer ones, which may indicate difference in granulation vorticity. This conjecture suggests measurements of horizontal flow fields in the photosphere together with elimination of the projection effects in fibril imaging.

Acknowledgments. We thank Rob Rutten for improvements to the text. J. Koza's research is supported by an EC Marie Curie Intra European Fellowship. This research was part of the European Solar Magnetism Network and is supported by Slovak agency VEGA (2/6195/26).

References

Brandt P. N., Scharmer G. B., Ferguson S., Shine R. A., Tarbell T. D., 1988, Nature 335, 238
Brown D. S., Nightingale R. W., Alexander D., Schrijver C. J., Metcalf T. R., Shine R. A., Title A. M., Wolfson C. J., 2003, Solar Phys. 216, 79
Christopoulou E. B., Georgakilas A. A., Koutchmy S., 2001, Solar Phys. 199, 61
De Pontieu B., Erdélyi R., James S. P., 2004, Nature 430, 536
De Pontieu B., Hansteen V. H., Rouppe van der Voort L., van Noort M., Carlsson M., 2007, ApJ 655, 624
de Wijn A. G., de Pontieu B., 2006, A&A 460, 309
Gaizauskas V., 1976, JRASC 70, 1
Hansteen V. H., De Pontieu B., Rouppe van der Voort L., van Noort M., Carlsson M., 2006, ApJ 647, L73
Kucera A., 1982, Bulletin of the Astronomical Institutes of Czechoslovakia 33, 345
Lüst R., Schlüter A., 1954, Zeitschrift f. Astrophys. 34, 263
Mamedov S. G., Orudzhev E. S., 1983a, Soviet Astronomy 27, 692
Mamedov S. G., Orudzhev E. S., 1983b, AZh 60, 1192
Nikolsky G. M., Platova A. G., 1971, Solar Phys. 18, 403
Pasachoff J. M., Noyes R. W., Beckers J. M., 1968, Solar Phys. 5, 131
Rutten R. J., Hammerschlag R. H., Bettonvil F. C. M., Sütterlin P., de Wijn A. G., 2004, A&A 413, 1183
Tziotziou K., Tsiropoula G., Mein P., 2003, A&A 402, 361
Tziotziou K., Tsiropoula G., Mein P., 2004, A&A 423, 1133

The Physics of Chromospheric Plasmas
ASP Conference Series, Vol. 368, 2007
Petr Heinzel, Ivan Dorotovič and Robert J. Rutten, eds.

2D Observation of a Small Active Region in Hα

Asuman Gültekin, Z. Funda Bostancı and Nurol Al Erdoğan

Istanbul University, Faculty of Science, Istanbul, Turkey

Abstract. A small active region on the solar chromosphere was observed with high spatial and spectral resolution in Hα. The data were obtained with the Göttingen Fabry-Pérot Spectrometer mounted in the Vacuum Tower Telescope at the Observatorio del Teide in May 2002. Intensity and velocity maps for different line widths were derived over the two-dimensional field of view by applying the Lambdameter method. Some physical parameters like the source function, the line-of-sight velocity, the Doppler width, and the optical depth of fibril-like structures were determined using Beckers' cloud model. First results of this study are presented.

1. Introduction

Some of the basic fine structures of an active region of the solar chromosphere are facular granules, moustaches, and details of flares and fibrils. In high-resolution Hα images, fibrils are seen to occur near sunspots and facular areas. They appear as dark elongated elements and have a lifetime of 10–20 minutes. Their apparent widths and lengths are of order of 1–3″ and 15–20″, respectively (Bray & Loughhead 1974). In this work, the Lambdameter method (Tsiropoula et al. 1993) and the cloud model (Beckers 1964) are applied to a two-dimensional field of view which includes fibrils around the facular area within an small active region.

2. Observation and Data Reduction

In May 2002, a time series of 60 wavelength scans was taken with the Göttingen Fabry-Pérot spectrometer in the Hα line including a small active region near the solar disk center. The spectrometer is based on two Fabry-Pérot interferometers. It is installed in the Vacuum Tower Telescope (Bendlin et al. 1992; Bendlin & Volkmer 1995; Koschinsky et al. 2001). Steps of 125 mÅ between adjacent wavelength positions were chosen for the spectral scans. The narrow-band images were taken at 18 wavelength positions which gives a wavelength coverage of approximately 2.125 Å. The exposure time was 30 ms and the time interval between the start of two consecutive spectral scans was 49 s. During the observations, which were obtained under very good seeing conditions, broad-band images were taken simultaneously with the narrow-band images. Our best scan chosen for this study reached a Fried parameter of r_0=17.1 cm. After usual correction procedures (for dark signal, flat field, and image motion) the broad-band images were restored by using the spectral ratio (von der Lühe 1984) and the speckle masking technique (Weigelt 1977), while the narrow-band images were

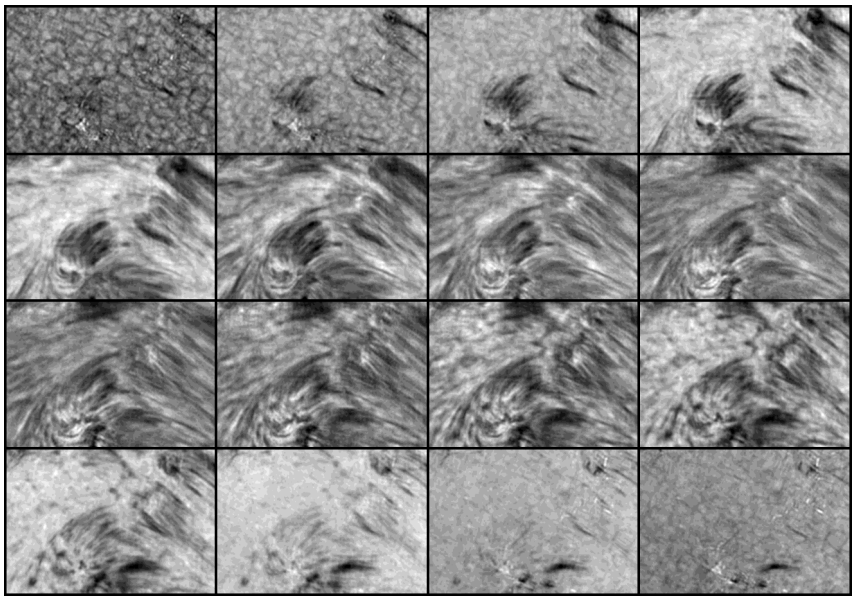

Figure 1. Reconstructed narrow-band images through the best scan. The wavelength decreases row by row from the left to the right by a value of 0.125 Å. The first image in the third row corresponds to the spectral position of the center of the mean line profile. The field of view is $33\farcs0 \times 23\farcs0$.

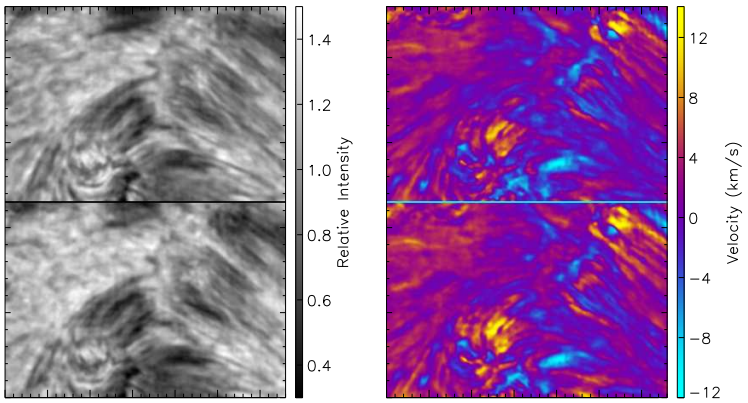

Figure 2. Intensity (left panel) and line-of-sight velocity (right panel) images obtained by the Lambdameter method for profile widths of 0.51 Å and 0.765 Å (upper and lower panels). Positive and negative values indicate upflows and downflows, respectively.

reconstructed by using a method which is presented by Keller & von der Lühe (1992). As a result, we obtained a reconstructed narrow-band image for each wavelength position of the Hα line profile, see Fig. 1.

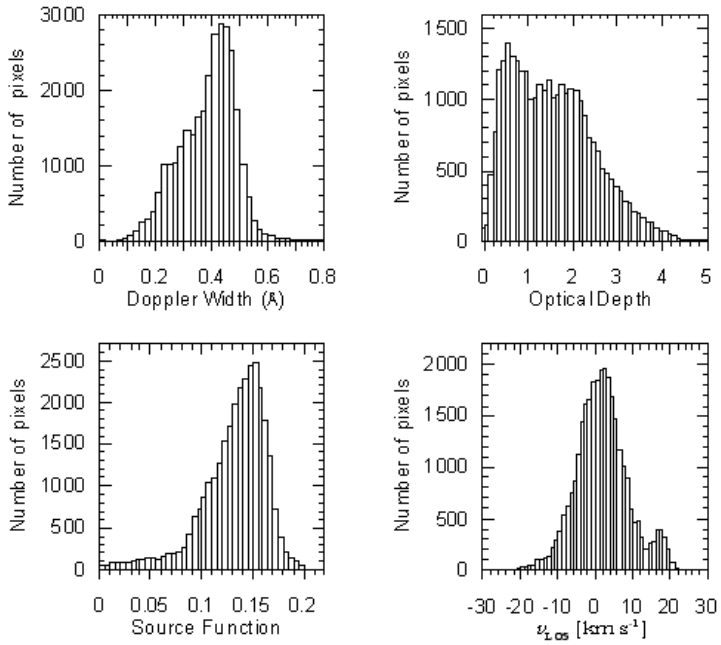

Figure 3. Histograms of Doppler width, optical depth, source function and cloud velocity.

3. Results

3.1. Lambdameter method

The Lambdameter method is used for the derivation of intensity and velocity images for different profile widths. Figure 2 shows the intensity and velocity images for widths of 0.51 Å and 0.765 Å. The maximum and minimum velocities in the Doppler images of this figure (right panel) are 14.06 and -11.77 km s^{-1} for the upper image, 11.26 and -8.74 km s^{-1} for the lower image. The corresponding mean values are 1.30 and -0.8 km s^{-1}, respectively.

3.2. Cloud model

The cloud model is extensively used for the deduction of different physical parameters of chromospheric fine structures seen in Balmer lines (Al et al. 2004; Tsiropoula 2000; Tsiropoula et al. 1993; Alissandrakis et al. 1990). These parameters are the source function, the optical depth at the line center, the line-of-sight velocity and the Doppler width. The model is based on the assumption that the source function, the velocity, and the Doppler width are constant within the cloud along the line of sight. In this study, it was employed within the limits discussed by Alissandrakis (1990).

Figure 3 shows the histograms of Doppler width, optical depth, source function, and the cloud velocity. The average values for these parameters found in this work are 0.38 Å, 1.54, 0.13, and 1.8 km s^{-1}, respectively. The image of the cloud velocity for the two-dimensional field of view resulting from this model is presented in Fig. 4.

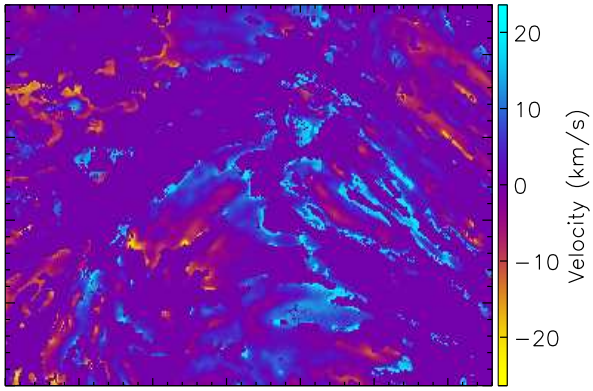

Figure 4. The velocity image obtained with the cloud model.

3.3. Number densities and temperature

The number density of the second level in hydrogen (N_2), the electron density (N_e), and the temperature (T) are estimated as presented by Bostancı (2005):

$$\tau_0 = 1.38 \times 10^{-21} \frac{N_2 L}{\Delta\lambda_D} \quad N_e = 3 \times 10^8 \sqrt{N_2} \qquad \Delta\lambda_D = \frac{\lambda_0}{c} \sqrt{\frac{2kT}{m_H} + \xi_t^2}. \qquad (1)$$

Here, L and ξ_t are the geometrical width of the structure under investigation and the microturbulence velocity. Using the average values of τ_0 and $\Delta\lambda_D$ and taking L in a range between 725–2200 km (Bray & Loughhead 1974), we find values for N_2 and N_e in the range of $5.91 - 1.95 \times 10^4$ cm^{-3} and $7.8 - 4.5 \times 10^{10}$ cm^{-3}, respectively. Assuming ξ_t equal to 5, 10, and 15 km s^{-1}, we find temperatures of 17075, 12575, and 5075 K, respectively.

Acknowledgments. The Vacuum Tower Telescope is operated by the Kiepenheuer Institut für Sonnenphysik, Freiburg, at the Spanish Observatorio del Teide of the Instituto de Astrofísica de Canarias.

References

Al, N., Bendlin, C., Hirzberger, J., Kneer, F., & Trujillo Bueno, J. 2004, A&A, 418, 1131
Alissandrakis, C. E., Tsiropoula, G., & Mein, P. 1990, A&A, 230, 200
Beckers, J.M. 1964, Ph.D. Thesis, Utrecht
Bendlin, C., Volkmer, R., & Kneer, F. 1992, A&A, 257, 817
Bendlin, C. & Volkmer, R., 1995, A&AS, 112, 371
Bostanci, Z. F. 2005, CCMF Conf.(ESA SP-596): Chromospheric and Coronal Magnetic Fields, (eds. Innes D. E., Lagg A. & Solanki S. K.), 53
Bray, R.J. & Loughhead, R. E. 1974, The Solar Chromosphere
Keller C. & von der Lühe O. 1992, A&A, 261, 321
Koschinsky, M., Kneer, F., & Hirzberger, J. 2001, A&A, 365, 588
Tsiropoula, G., Alissandrakis, C. E., & Schmieder, B. 1993, A&A, 271, 574
Tsiropoula, G. 2000, A&A, 357,735
von der Lühe, O. 1984, J. Opt. Soc. Am. A, 1, 510
Weigelt, G. P. 1977, Optics Comm., 21, 55

The Physics of Chromospheric Plasmas
ASP Conference Series, Vol. 368, 2007
Petr Heinzel, Ivan Dorotovič and Robert J. Rutten, eds.

Temporal Evolution of Mottles in Hα

Z. Funda Bostancı and Nurol Al Erdoğan

Istanbul University, Faculty of Science, Istanbul, Turkey

Abstract. In April 2002, Hα observations of the solar chromosphere with high spatial and spectral resolution were obtained with the Göttingen Fabry-Pérot Spectrometer mounted in the Vacuum Tower Telescope (VTT) at the Observatorio del Teide. In this work, we analyze a short time sequence of a quiet region with chains of mottles. Some physical parameters of dark mottles are determined by using Beckers' cloud model which takes the source function, the Doppler width, and the velocity to be constant within the cloud along the line of sight. Here, we present the results of our study.

1. Introduction

Two dimensional Hα observations of network regions on the solar disk center with high spatial resolution show dark elongated structures, the so-called "dark mottles". These structures usually form two groups, which are called chains of mottles or rosettes (Beckers, 1963). In a chain, mottles point in the same direction while rosettes have a more or less circular shape with a bright center, which is surrounded by a number of mottles aligned radially outwards (Tziotziou et al. 2003).

Beckers' cloud model (Beckers 1964) is widely used for the determination of physical quantities of mottles such as the line-of-sight velocity, the source function, the optical depth, and Doppler width (Tsiropoula et al. 1994; Lee et al. 2000; Tziotziou et al. 2003; Al et al. 2004; Bostanci 2005). Here, we applied this model to a short time series of a two-dimensional field of view which includes chains of mottles.

2. Observations and Data Analysis

The observation of a network region near disk center was done in Hα using the Göttingen Fabry-Pérot Spectrometer at the VTT (Bendlin & Volkmer 1995; Koschinsky et al. 2001). Two-dimensional broad-band and narrow-band images were taken simultaneously at 18 wavelength positions by scanning through Hα. The wavelength settings of two consecutive positions differed by 125 m$\mathring{\text{A}}$ and the time interval between two consecutive scans was 49 s. The broad-band images were restored by spectral ratio (von der Lühe 1984) and speckle masking (Weigelt 1977) methods while the narrow-band images were reconstructed by using a method given by Keller & von der Lühe (1992). The Hα line profile for each pixel of the field of view was produced from intensity values of narrow-band images belonging to 18 wavelength positions.

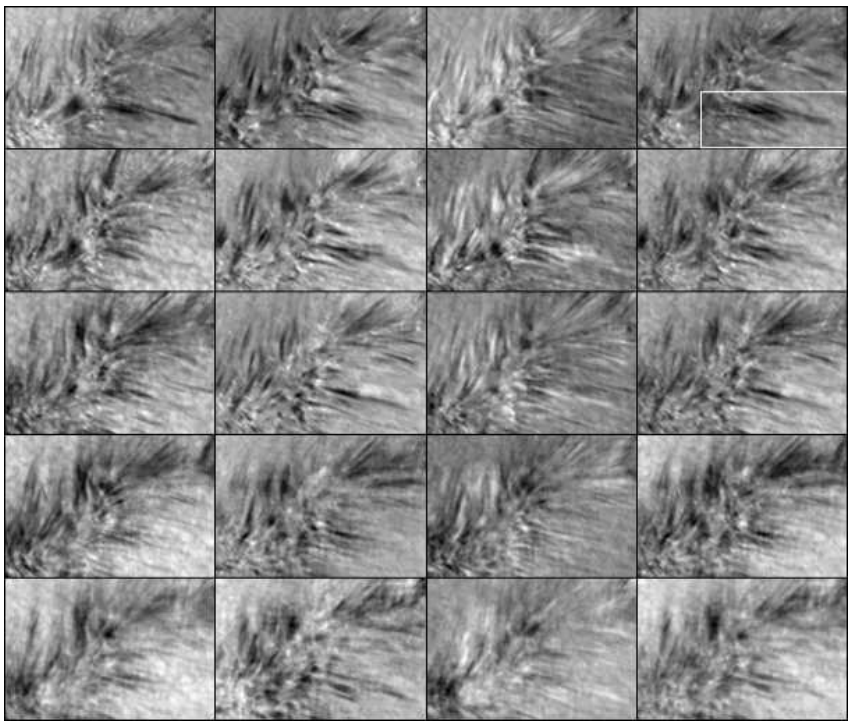

Figure 1. A short time sequence of the entire FOV (30.″3×20.″5) at +0.650 Å (first column) and −0.650 Å (second column) from the Hα line center with corresponding Doppler and intensity images (third and fourth column, respectively). The time cadence is 49 s.

3. Cloud Model

The observed contrast profiles were matched with theoretical contrast profiles by using the cloud model (Beckers 1964). This model assumes the source function, the Doppler width, and the LOS velocity to be constant within the cloud along the line of sight. The contrast profile is given by

$$C(\lambda) = \frac{I(\lambda) - I_0(\lambda)}{I_0(\lambda)} = \left(\frac{S}{I_0(\lambda)} - 1\right)\left(1 - \mathrm{e}^{-\tau(\lambda)}\right) \tag{1}$$

where $I_0(\lambda)$ is the reference profile emitted by the background. S denotes the source function and $\tau(\lambda)$ the optical thickness. The wavelength dependence of the optical thickness is given by

$$\tau(\lambda) = \tau_0 \exp\left[-\left(\frac{\lambda - \lambda_\mathrm{c}(1 - \upsilon_\mathrm{LOS}/\mathrm{c})}{\Delta\lambda_\mathrm{D}}\right)^2\right] \tag{2}$$

where τ_0 is the optical depth at the line center, $\lambda_\mathrm{c}(\upsilon_\mathrm{LOS}/c)$ the shift due to the velocity υ_LOS and λ_c the line center wavelength.

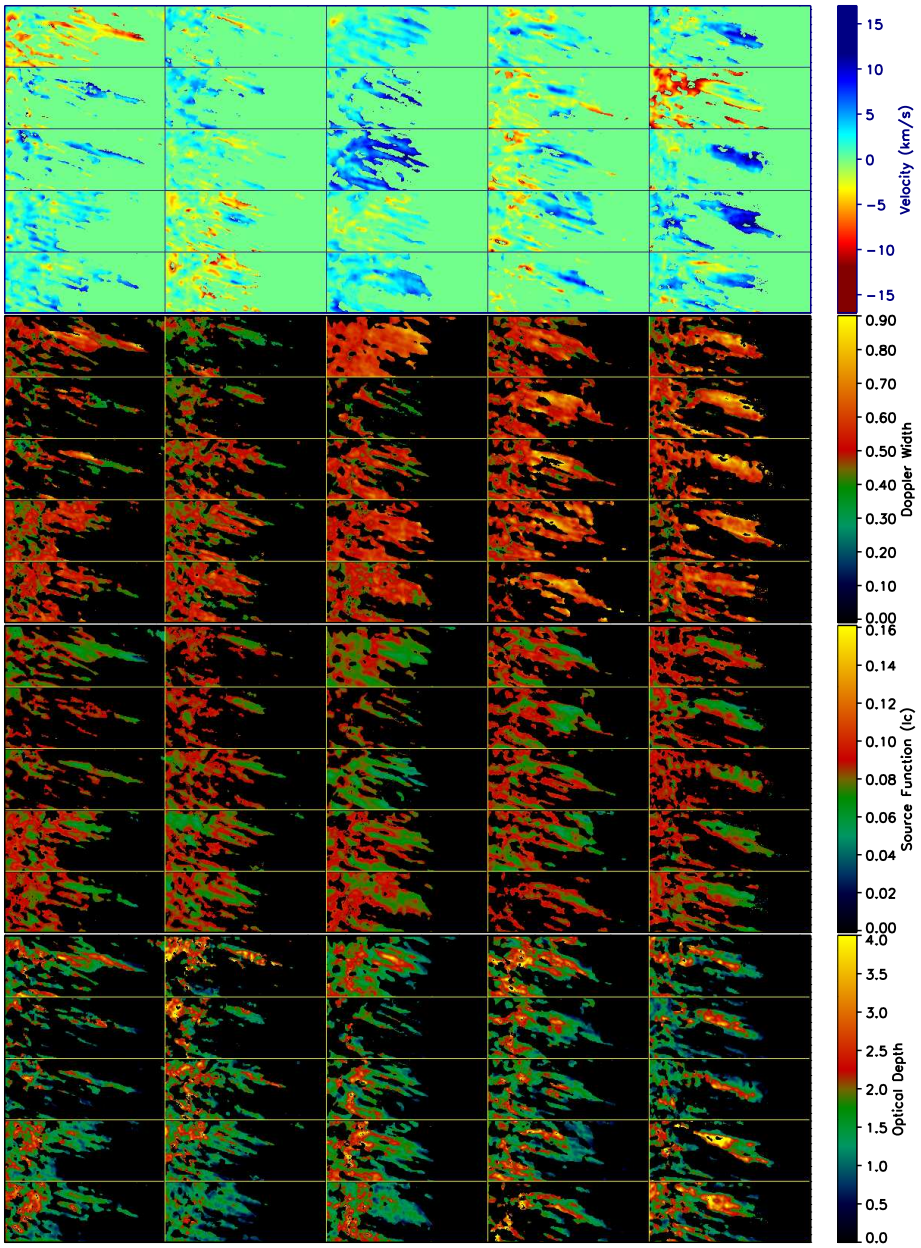

Figure 2. Short time sequences of velocity, Doppler width, source function, and optical depth for the region marked by the white frame in Fig. 1 (21.″3×8.″1). Time proceeds row by row from top to bottom in 49 s steps. In the top images, blue and red indicate upward and downward motion, respectively.

4. Results

In this study, we found the average thickness of the mottles to be 0.″7 ranging between 0.″3 and 1.″1 and the average length to be 9.″8 ranging between 6.″7

and 13.″4. Their lifetime is close to 10 minutes. Their inclination appears more horizontal than vertical with respect to the solar surface, while their orientation slightly changes in some frames. Sometimes nearby mottles seem to merge forming a single structure or they split in two parts. Their shape and length clearly change from frame to frame as can be seen in Fig. 1.

The optical depth at the line center varies from 0 to 4 with a mean value of 1.7 which is in agreement with the mean value found by Lee et al. (2000). The center parts of the structures under investigation show higher values, while their boundaries correspond to lower ones. The source function varies between 0 and 0.15. For this parameter we found a mean value of 0.08, which is below the values found by other authors (Tziotziou et al. 2003; Lee et al. 2000). The highest values occur close to the footpoints of the mottles. The Doppler width ranges between 0 and 0.88 Å with a mean value of 0.52 Å. Lee et al. (2000) found a mean value of 0.55 Å for this parameter. The velocity takes values between -25 and 25 km/s indicating the presence of both downward and upward motion as seen in some frames of our time series (see Fig. 2). During our observation, the footpoints of dark mottles mostly showed red-shift while their upper parts showed both blue and red shift. The dominant motion is an upflow with a mean value of 1.64 km/s.

Acknowledgments. The Vacuum Tower Telescope is operated by the Kiepenheuer Institut für Sonnenphysik, Freiburg, at the Spanish Observatorio del Teide of the Instituto de Astrofísica de Canarias.

References

Al N., Bendlin C., Hirzberger J., Kneer F. & Trujillo Bueno J. 2004, A&A, 418, 1131
Beckers J.M. 1963, ApJ 138, 648
Beckers J.M. 1964, Ph.D. Thesis, Utrecht
Bendlin C. & Volkmer R. 1995, A&AS, 112, 371
Bostanci Z. F. 2005, CCMF Conf. (ESA SP-596): Chromospheric and Coronal Magnetic Fields, (eds. Innes D. E., Lagg A. & Solanki S. K.), 53
Keller C. & von der Lühe O. 1992, A&A, 261, 321
Koschinsky M., Kneer F. & Hirzberger J. 2001, A&A, 365, 588
Lee C. Y., Chae J. & Wang H. 2000, ApJ, 545, 1124
Tsiropoula G., Alissandrakis C. E. & Schmieder B. 1994, A&A, 290, 285
Tziotziou K., Tsiropoula G. & Mein P. 2003, A&A, 402, 361
von der Lühe, O. 1984, J. Opt. Soc. Am., A 1, 510
Weigelt G. P. 1977, Optics Comm., 21, 55

The Physics of Chromospheric Plasmas
ASP Conference Series, Vol. 368, 2007
Petr Heinzel, Ivan Dorotovič and Robert J. Rutten, eds.

Acoustic Shocks in the Quiet Solar Chromosphere

G. Cauzzi[1], K. P. Reardon[1], A. Vecchio[1], K. Janssen[1] and T. Rimmele[2]

[1]*INAF–Osservatorio Astrofisico di Arcetri, Firenze, Italy*
[2]*National Solar Observatory, Sunspot, USA*

Abstract. We exploit the two-dimensional spectroscopic capabilities of the Interferometric BIdimensional Spectrometer (IBIS) to study the chromospheric Ca II 854.2 nm line and its temporal evolution in a quiet region at the center of the solar disk. The Ca II 854.2 profiles in the internetwork portion of the field of view clearly indicate the presence of hydrodynamic shocks, occurring at frequencies above the acoustic cut-off. The location and strength of such shocks perfectly map the areas where large velocity power is found at frequencies of 5.5–8 mHz in a standard Fourier analysis. The shocks locations evidence a sharp partition of the quiet area in regions of very distinct dynamical behavior, highlighting the role of the local magnetic topology in structuring the lower chromosphere. The portions of the field of view where the photospheric field is very weak, and that are presumably connected to distant magnetic structures (or open to the interplanetary field), are the site of frequent shock occurrence. On the contrary, in regions neighboring the magnetic network and harboring a more horizontal configuration of the chromospheric magnetic field, shocks are heavily suppressed, even if the photospheric field is essentially absent in these areas as well. These latter regions, with much reduced velocity power at frequencies of 5.5–8 mHz (the "magnetic shadows" first described in Judge et al. 2001), are spatially coincident with fibrilar structures visible in the Ca II 854.2 line core intensity maps. We finally argue that areas within and immediately surrounding the magnetic network also display evidence of chromospheric shocks, but occurring at periodicities of 4–6 minutes. Such slow shocks are stronger than those occurring in field-free areas, as evidenced by the strong emission in the inner blue-wing of the line. This is in agreement with recent results claiming that magneto-acoustic shocks can develop in inclined magnetic structures, acting as 'portals' through which the powerful low-frequency photospheric oscillations can leak into the chromosphere.

1. Introduction

The dynamics and energetics of the solar chromosphere are still subject to intense study, as this very meeting testifies. Even for a "simple" case such as the non-magnetic lower chromosphere, a strong debate is still underway as to what exact contribution is provided by the dissipation of high-frequency ($\nu \geq 10$ mHz) vs. low-frequency acoustic waves, or what might be the role of magnetic phenomena at small scales (e.g. Fossum & Carlsson 2006; Wedemeyer-Böhm et al. 2006).

We present in this paper new ground-based observations of the chromospheric Ca II 854.2 nm line, obtained with the 2-D spectrometer IBIS (Cavallini 2006). This high performance instrument allowed us to combine in a single dataset a full spectroscopic information on atmospheric fluctuations, usually

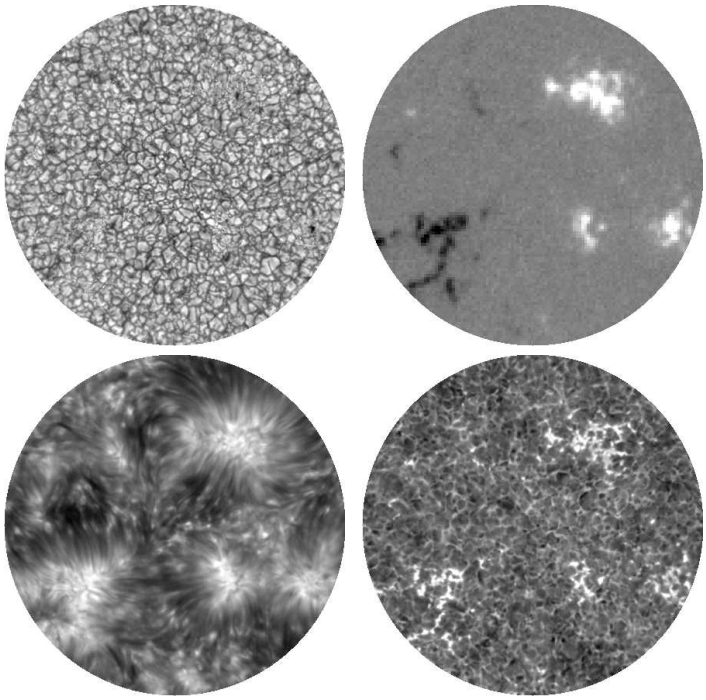

Figure 1. Full field of view of the observations described in this paper (80 arcsec in diameter). *Top left*: white light image of the quiet area, covering a full supergranular cell. Some abnormal granulation is visible in correspondence of the magnetic network elements. *Top right*: HR MDI co-spatial and co-temporal line-of-sight magnetic field (±200 G), outlining the enhanced network. *Bottom right*: IBIS image acquired in the blue wing of the Ca II 854.2 line, at about 0.1 nm from core. The bright elements clearly indicate magnetic structures, over a mesh of reversed granulation. *Bottom left*: IBIS Ca II 854.2 line core intensity image. Of particular interest are the fibrilar structures fanning out around the network into the surrounding internetwork regions (see text).

performed with single-slit spectrographs, with the high spatial resolution and large FOV typical of filter instruments.

2. Data

IBIS is installed at the Dunn Solar Telescope (DST) of the US National Solar Observatory, and takes advantage of the resident high-order adaptive optics system (Rimmele 2004). By using two Fabry-Pérot interferometers in series, the instrument provides narrow-band images at high spatial resolution in the range 580–860 nm (FWHM = 2.5–4.5 pm). Through sequential stepping of the spectral passband, one can rapidly acquire full spectral information over an extended field of view (80" in diameter) in a set of selected lines. The data presented here were obtained on June 2nd, 2004, in a quiet region at disk center. The Ca II 854.2 nm line, formed in the low chromosphere (Pietarila et al. 2006), was sampled in 27 spectral positions in about 7 s. A 54-minute sequence was obtained under

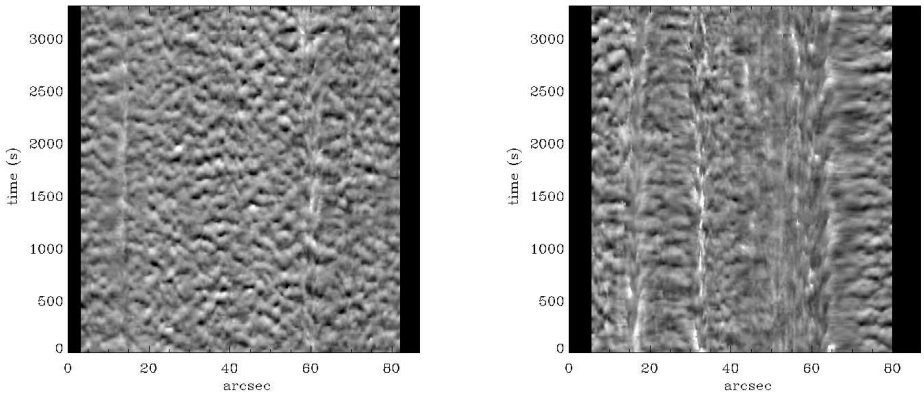

Figure 2. Temporal evolution of Ca II 854.2 nm core vertical velocity, for the whole course of the observations, for two "slices" within the FOV (i.e. as we were using a single-slit spectrograph). Values are scaled between ± 5 km/s. *Left*: quiet area, slicing horizontally through the center of the FOV of Fig. 1. The 3-minute chromospheric oscillations are readily visible in the middle section of the slice, while two weak magnetic elements show up as vertical stripes at positions 15″ and 60″. *Right*: slice crossing several magnetic network elements. Note the longer periodicities as well as the regions of reduced velocities around some magnetic elements (e.g., position 65–70 arcsec), that coincide with the fibrilar structures seen in the core intensity images.

excellent seeing conditions, with a repetition rate of 19 s and a pixel scale of 0.165″ per pixel. Fig. 1 provides an example of the data. After the spectral profile of the line(s) is recovered for each pixel within the FOV, usually by means of interpolation, a whole host of line parameters can be calculated. We display in Fig. 2 an example of the temporal evolution of the Ca II 854.2 nm core vertical velocity for two horizontal slices through the FOV. For further details on the data and their reduction, we refer to Janssen & Cauzzi (2006) and Vecchio et al. (2007).

3. Results

Hydrodynamical shocks in internetwork regions. The first two panels of Fig. 3 display the temporal evolution of the Ca II 854.2 nm spectral profiles, in two pixels around the center of the FOV. Their position was chosen so to avoid both photospheric magnetic fields and the fibrilar structures visible in the line core intensity images. The profiles clearly display a recurrent, saw-tooth behavior, with periodicity of 200 s or less ($\nu > \nu_{\rm cutoff)}$), that is highly evocative of the occurrence of shocks. This is qualitatively demonstrated by the remarkably similar temporal series of Ca II 854.2 nm profiles displayed in the rightmost panel. These profiles result from the hydrodynamical simulations of Carlsson & Stein (1997, calculations courtesy of A. Pietarila), which include the occurrence of weak shocks at the height of formation of the Ca II line (Pietarila et al. 2006). One intriguing detail in Fig. 3 is the relative lack of "extreme" downward velocities (red-shifts) in the observations with respect to the simulations. We

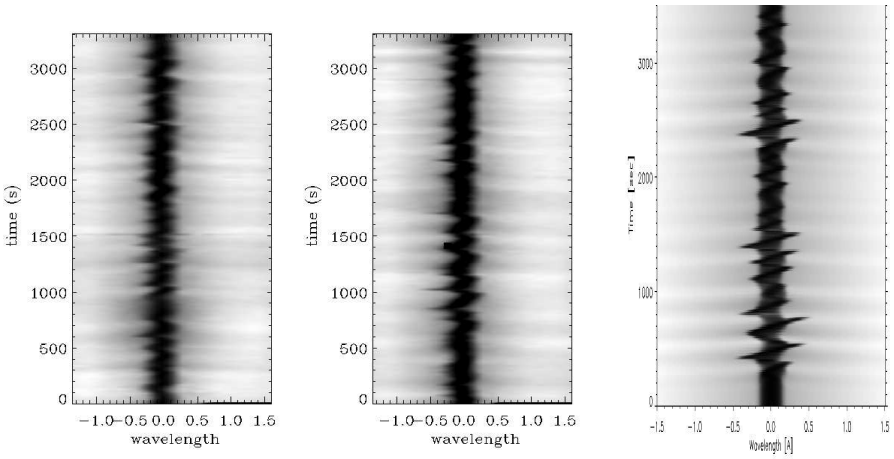

Figure 3. *Left and center*: Ca II 854.2 nm spectral profiles vs. time, for two positions within the central, quiet part of the FOV. Wavelength is in Å from the average position of line center; time is in seconds. Note the distinctive saw-tooth appearance. The line center shifts correspond to Doppler velocities as high as 8–10 km/s. *Right*: spectral profiles resulting from hydrodynamical simulations (no magnetic fields, courtesy of A. Pietarila). The driving piston in this case is taken from a sequence of MDI vertical velocities. The spectral profiles are sharper because not degraded by any instrumental profile, but the similarity is impressive.

are currently working on a quantitative comparison of our observations with results of such simulations, using a piston derived from the photospheric velocities obtained by IBIS in conjunction with the Ca II 854.2 nm data.

Magnetic shadows. Where do these hydrodynamical shocks occur? Analyzing the temporal sequences of the spectral profiles for all pixels within the FOV, we derived a series of spatial maps displaying the occurrence of shocks at periodicity (P) of 200 s or less. The left panel of Fig. 4 shows a typical instantaneous shock map: the shocks have a coherence length of a few arcsec, and are more common in regions quite distant from the magnetic network. This latter fact becomes most evident in the cumulative shock map (middle panel) that shows how shocks concentrate in a limited fraction of the field of view, much smaller than what would be defined as "internetwork" on the basis of photospheric signatures (cf. Fig. 1). The very conspicuous features where shocks are absent spatially coincide with the fibrilar structures visible in the Ca II line core intensity. We argue that these fibrils trace horizontal field lines at middle-chromospheric heights and act to suppress, or somehow divert through mode conversion, the purely acoustic oscillations originating underneath, that would otherwise propagate vertically and eventually develop into shocks. This hypothesis is supported by the results of a classical Fourier analysis on the Ca II 854.2 nm line core velocities. In the rightmost panel of Fig. 4 we show the map of the Fourier velocity power integrated over frequencies above the acoustic cut-off (5.5–8.0 mHz, the "classic" 3-minute power studied in the literature), that perfectly reproduces

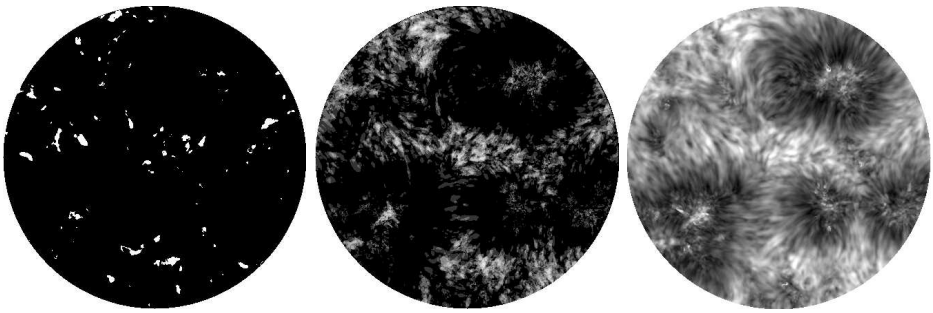

Figure 4. *Left*: "Instantaneous" map of shocks with $P < 180\,\mathrm{s}$, for a time around the middle of the observed sequence and the whole FOV. A pixel was defined as undergoing a shock at a certain time if the core velocity between that time and the next one or two time steps ($\Delta t = 19 - 38\,\mathrm{s}$) changed from positive (downward) to negative (upward) by a Δv of at least 8 km/s. A running window of 3 minutes width was used to discriminate the shocks at short periodicity from other events. *Center*: cumulative shock map, constructed by summing over the occurrence of shocks in any given pixel, weighted by the amplitude of the shocks as defined above. Note the location of the shocks, that not only avoid most of the magnetic network area, but also their surrounding, giving rise to the "magnetic shadows". *Right*: map of the Fourier power of vertical velocity, in the frequency interval $\nu = 5.5 - 8$ mHz. See Vecchio et al. (2007) for more details.

the shock map. As discussed in more details in Vecchio et al. (2007), the large dark features around the network in the Fourier map correspond to the magnetic shadows first described in Judge et al. (2001) and further analyzed by McIntosh & Judge (2001) and McIntosh et al. (2003). The shadows signal the presence of the magnetic canopy (layer where the plasma-β is approximately unity) below the region of formation of the diagnostic employed, and highlight the fact that even the quiet solar atmosphere can be sharply partitioned into regions of different connectivity between the lower photosphere and higher layers. This strongly depends on the local magnetic topology – we expect for example that the extension and shape of the shadows would be quite different in the case of unipolar or weak network fields, with many consequences on the amount of shocks (heating?) developing in the higher atmosphere.

Magnetoacoustic shocks within the network points. Several recent papers have addressed the possibility of 'leakage' of the powerful 5-minute photospheric oscillations into the chromosphere in presence of inclined magnetic fields (De Pontieu et al. 2004; Hansteen et al. 2006; McIntosh & Jefferies 2006). This is a topic that can be thouroughly investigated with the dataset described in this paper. Without entering in detail, we offer in Fig. 5 tantalizing evidence that within magnetic structures originating in network points, the chromospheric plasma undergoes shocks at periodicities of 4–6 minutes. They seem to occur preferentially on the edges of photospheric network points (see also the analysis in Vecchio et al. 2007), lending support to the possible role of inclined magnetic structures. Further, these shocks are stronger than those occurring in the internetwork, as evidenced by the strong emission in the inner blue-wing of the line

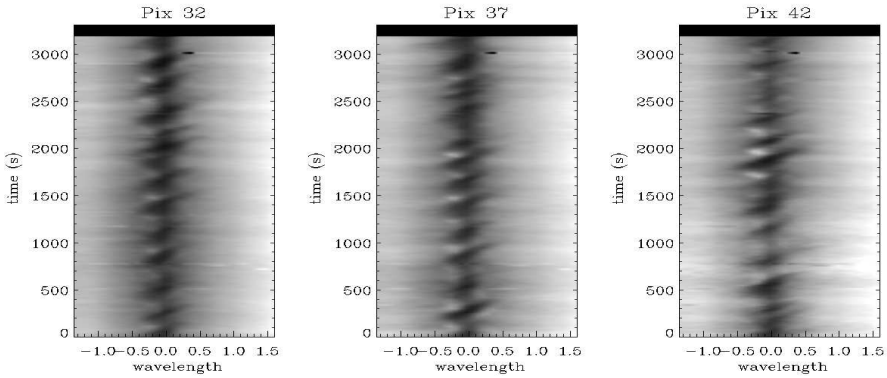

Figure 5. Ca II 854.2 nm spectral profiles vs. time, for three pixels within the magnetic network area. Pixels are less than 1 arcsec apart one from another. The temporal evolution is very suggestive of presence of strong shocks, that cause emission in the inner blue wing of the line, at periodicities of 4–6 minutes.

that give the spectral profiles an appearance very reminiscent of the "grains" in the Ca II H&K lines. A full analysis of this phenomenon is currently underway.

Acknowledgments. We thank A. Pietarila for the hydrodynamical calculations. IBIS was built with contributions from INAF/Arcetri Observatory, the University of Florence, the University of Rome Tor Vergata, and MIUR. NSO is operated by the Association of Universities for Research in Astronomy, Inc. (AURA), under cooperative agreement with the National Science Foundation. This research was partially funded through the European Solar Magnetism Network (ESMN, contract HPRN-CT- 2002-00313), PRIN-MIUR 2004 and the Italian Ministry of Foreign Affairs (MAE).

References

Carlsson M., Stein R. F., 1997, ApJ 481, 500
Cavallini F., 2006, Solar Phys. 236, 415
De Pontieu B., Erdélyi R., James S. P., 2004, Nat 430, 536
Fossum A., Carlsson M., 2006, ApJ 646, 579
Hansteen V. H., De Pontieu B., Rouppe van der Voort L., van Noort M., Carlsson M., 2006, ApJ 647, L73
Janssen K., Cauzzi G., 2006, A&A 450, 365
Judge P. G., Tarbell T. D., Wilhelm K., 2001, ApJ 554, 424
McIntosh S. W., Fleck B., Judge P. G., 2003, A&A 405, 769
McIntosh S. W., Jefferies S. M., 2006, ApJ 647, L77
McIntosh S. W., Judge P. G., 2001, ApJ 561, 420
Pietarila A., Socas-Navarro H., Bogdan T., Carlsson M., Stein R. F., 2006, ApJ 640, 1142
Rimmele T. R., 2004, in D. Bonaccini Calia, B. L. Ellerbroek, R. Ragazzoni (eds.), Advancements in Adaptive Optics. Proceedings of the SPIE, Volume 5490, p. 34
Vecchio A., Cauzzi G., Reardon K. P., Janssen K., Rimmele T., 2007, A&A 461, L1
Wedemeyer-Böhm S., Steiner O., Bruls J., Rammacher W., 2006, ArXiv Astrophysics e-prints

The Physics of Chromospheric Plasmas
ASP Conference Series, Vol. 368, 2007
Petr Heinzel, Ivan Dorotovič and Robert J. Rutten, eds.

Propagating Waves in the Chromospheric Network

P. Gömöry[1,2], J. Rybák[1], A. Kučera[1], W. Curdt[3] and H. Wöhl[4]

[1]*Astronomical Institute, SAS, Tatranská Lomnica, Slovakia*
[2]*Astrophysikalishes Institut, Potsdam, Germany*
[3]*MPI für Sonnensystemforschung, Katlenburg-Lindau, Germany*
[4]*Kiepenheuer-Institut für Sonnenphysik, Freiburg, Germany*

Abstract. Wave modulation of ultraviolet emissions originated in and above quiet chromospheric network is studied. In particular, cross-correlation, wavelet analysis and phase difference analysis of the intensities as well as the Doppler shifts of emission lines of He I 584.33 Å (chromosphere), O V 629.73 Å (transition region) and Mg IX 368.07 Å (corona) are employed to study waves at different heights and their direction of propagation. The results are interpreted as evidence of compressive waves that propagate downward from the transition region to the chromosphere in the observed chromospheric network. Different scenarios regarding the origin and source localization of these waves are discussed.

1. Introduction

Turbulent motions in the convective zone and the lower photosphere create conditions for the existence of acoustic waves in the solar atmosphere. Moreover, the photospheric plasma motion continually affects footpoints of the magnetic field lines and excites Alfvén waves and magneto-acoustic waves (Narain & Ulmschneider 1996). Such waves propagate upward along the magnetic field lines and transfer energy from the photosphere to the corona where it may get dissipated and consequently heat the corona (Walsh & Ireland 2003). But the high temperature of the corona can be also explained as a result of the cumulative energy input released during many small-scale reconnection events (nanoflares) in the corona (Parker 1988). However, a nanoflare should also create strong stress in magnetic field lines which may afterwards propagate down as a magnetic body wave (Hansteen 1993). Detection of the magnetic body waves in the chromospheric network and determination of their direction may therefore help to discriminate between the proposed mechanisms to heat the solar corona above. This contribution sumarizes results determined using the SOHO/CDS spectrometer already reported by Gömöry et al. (2005, 2006) and it discusses possible scenarios regarding origin and source localization of the proposed waves.

2. Data and Data Reduction

The SOHO/CDS (Harrison et al. 1995) data taken on May 14, 1998 between 23:25 UT and 23:53 UT are used. A quiet solar atmosphere near disk center was observed with the normal incidence (NIS) part of CDS using the 2 arcsec

wide and 141 arcsec long slit in the He I 584.33 Å ($\log T = 4.5$), O V 629.73 Å ($\log T = 5.3$) and Mg IX 368.07 Å ($\log T = 6.0$) spectral lines. A dataset of 190 spectral images with an exposure time of 5 s and cadence of 9.1 s was obtained using the "sit-and-stare" observation mode (solar rotation was compensated).

Using standard CDS software, the raw measurements were corrected for instrumental effects of the CDS/NIS instrument and the measurements were then converted to physical units. For the Mg IX line, binning of 2 pixels along the slit and 5 exposures in time was performed to increase the signal-to-noise ratio. A single Gaussian with a linear background and Poisson statistics were used for fitting of each spectral line profile. The fitted data product consists of the intensities (i.e. amplitudes of the Gaussian profiles) and the Doppler shifts per spatial pixel per exposure.

3. Results and Discussion

The following results were determined from cross-correlation, wavelet and phase difference analysis of the temporal variations of the intensities and Doppler shifts in the He I, O V, and Mg IX emission (for more details see Gömöry et al. 2005, 2006):

- There is significant correlation between the He I and O V modulations, with O V intensity leading He I intensity by $27.3\,\mathrm{s} \pm 4.6\,\mathrm{s}$ but with no significant time delay in the Doppler shifts.
- Cross-correlation between the O V and Mg IX intensities reveals multiple maxima without correlation between their Doppler shifts.
- Wavelet power analysis gives evidence for intermittent chromospheric and transition-region oscillations with periodicities in the $250-450$ s range and for coronal oscillations in the $110-300$ s range.
- Wavelet phase difference analysis shows that the determined time delay between variations of the He I and O V intensities is dominated by waves with about 300 s periodicity.
- There is no significant phase difference between the oscillations detected in the temporal variations of the O V and Mg IX intensities and Doppler shifts.

The results determined from the cross-corelation function and from the wavelet analysis of the He I and O V intensities demonstrate that the intensity changes start at first in the transition region and appear only later in the chromosphere. On the other hand, we revealed that the cross-correlation function of the Doppler shifts of these lines reaches its maximum for a time delay of 0 s. This implies simultaneous macroscopic plasma motion. Following these results we can assume that the non-radiative energy had to be transferred from the transition region downward to the chromosphere without any significant bulk mass motion. Assuming a magnetic nature of the chromospheric network which creates conditions for the existence of magneto-acoustic waves our results can be explained by downward propagating compressive waves taking place in this part of the solar atmosphere.

The ambiguous interpretation of the cross-correlation function of the O V and Mg IX intensities (multiple maximum) does not allow to determine if the

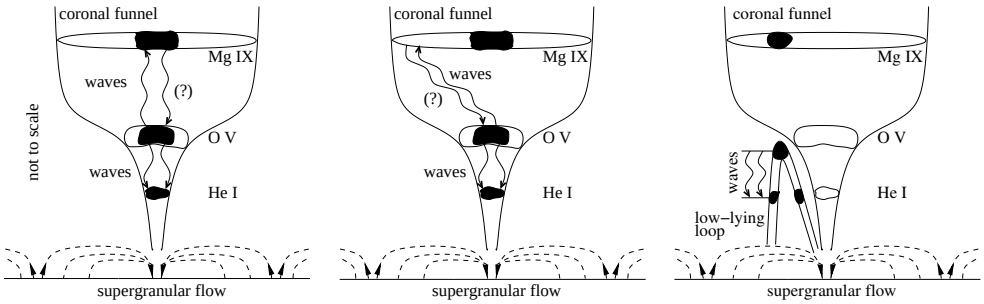

Figure 1. Topological models of the quiet solar atmosphere above chromospheric network adopted after Gabriel (1976) (left and middle) and after Dowdy et al. (1986) (right) supplemented by the proposed alternative scenarios of the propagating waves. The black areas correspond to the observed parts of the atmospheric layers while the white contoured areas show the whole layers where the He I, O V, and Mg IX line radiation can be generated. The wavelike arrows of different orientations describe the propagating waves.

proposed waves originate in the corona and then spread down to lower parts of the solar atmosphere or if they originate in the transition region and later affect the chromosphere and corona (Fig. 1, left). Hansteen (1993) studied numerically nanoflares in the corona and he found that the excited waves reach the transition region approximately 30 s earlier than the chromosphere what is in good agreement with our determined time delay between the He I and O V intensities. This agreement probably points to the coronal origin of the proposed waves.

Moreover, if we follow Gabriel's model of the transition region (Gabriel 1976) then it is also possible that the observed parts of the transition region and the corona were not magnetically coupled. In this case the waves could be magnetically driven from an unobserved part of the corona to the observed part of the transition region but also vice versa (Fig. 1, middle).

On the other hand, low cross-correlation of the O V and Mg IX intensities and no cross-correlation between their Doppler shifts could predict that the signals discussed here originated in different magnetic structures (Fig. 1, right). The multicomponent model of the chromospheric network (Dowdy et al. 1986; Peter 2001) predicts the existence of small low-lying loops next to the magnetic canopies. Following this model it can be alternatively assumed that the observed downward propagating waves occur only in low-lying loops and do not affect the corona above the particular chromospheric network.

Summarizing our results we can state that these findings clearly show the presence of the downward propagating waves spreading from the transition region to the chromosphere. On the other hand, ambiguous results derived from the coronal spectral line Mg IX does not allow to localize the original source of the proposed waves. This ambiguity finally led to the suggestion of the three possible scenarios of the waves source localization (Fig. 1). To clarify which of the proposed scenarios is the most relevant, a new Joint Observing Program (JOP 171) of the SOHO instruments (i.e. CDS, MDI, and EIT) and the TRACE satellite was proposed. This observing program provides statistically more significant data comparing to the JOP 78 program (i.e. longer time series taken in

more spectral lines)[1]. Moreover, the JOP 171 observing program was supported also by the high resolution photospheric observations provided by the Dutch Open Telescope (DOT) or German Vacuum Tower Telescope (VTT).

Acknowledgments. CDS is part of the Solar and Heliospheric Observatory, which is a mission of international cooperation between ESA and NASA. P. G., J. R. and A. K. are grateful to the Slovak grant agency VEGA for support of this work (grant No. 2/6195/26). J. R., A. K. and H. W. are grateful to the German DFG Project grant Nr. 436 SLK 113/7 for support of this work. This research was part of the European Solar Magnetism Network (EC/RTN contract HPRN-CT-2002-00313). Wavelet software was provided by C. Torrence and G. Compo (`http://paos.colorado.edu/research/wavelets/`).

References

Dowdy J. F., Rabin D., Moore R. L., 1986, Solar Phys. 105, 35
Gabriel A. H., 1976, Phil. Trans. Roy. Soc. Lond. A. 281, 339
Gömöry P., Rybák J., Kučera A., Curdt W., Wöhl H., 2005, Hvar Obs. Bull. 29, 71
Gömöry P., Rybák J., Kučera A., Curdt W., Wöhl H., 2006, A&A 448, 1169
Hansteen V. H., 1993, ApJ 402, 741
Harrison R. A., Sawyer E. C., Carter M. K., et al., 1995, Solar Phys. 162, 233
Narain U., Ulmschneider P., 1996, Space Science Reviews 75, 453
Parker E. N., 1988, ApJ 330, 474
Peter H., 2001, A&A 374, 1108
Walsh R. W., Ireland J., 2003, A&A Review 12, 1

[1]Details at `http://sohowww.nascom.nasa.gov/soc/JOPs/jop171`

The Physics of Chromospheric Plasmas
ASP Conference Series, Vol. 368, 2007
Petr Heinzel, Ivan Dorotovič and Robert J. Rutten, eds.

Chromospheric and Transition-Region Dynamics in Plage

A. G. de Wijn[1], B. De Pontieu[2] and R. J. Rutten[1,3]

[1]*Sterrekundig Instituut, Utrecht University, The Netherlands*
[2]*Lockheed Martin Solar and Astrophysics Laboratory, USA*
[3]*Institutt for Teoretisk Astrofysikk, University of Oslo, Norway*

Abstract. We study the dynamical interaction of the solar chromosphere with the transition region in mossy and non-mossy active-region plage. We carefully align image sequences taken with the Transition Region And Coronal Explorer (TRACE) in the ultraviolet passbands around 1550, 1600, and 1700 Å and the extreme ultraviolet passbands at 171 and 195 Å. We compute Fourier phase-difference spectra that are spatially averaged separately over mossy and non-mossy plage to study temporal modulations as a function of temporal frequency. The 1550 versus 171 Å comparison shows zero phase difference in non-mossy plage. In mossy plage, the phase differences between all UV and EUV passbands show pronounced upward trends with increasing frequency, which abruptly changes into zero phase difference beyond 4 – 6 mHz. The phase difference between the 171 and 195 Å sequences exhibits a shallow dip below 3 mHz and then also turns to zero phase difference beyond this value. We attribute the various similarities between the UV and EUV diagnostics that are evident in the phase-difference diagrams to the contribution of the C IV resonance lines in the 1550 and 1600 Å passbands. The strong upward trend at the lower frequencies indicates the presence of upward-traveling disturbances. It points to correspondence between the lower chromosphere and the upper transition region, perhaps by slow-mode magnetosonic disturbances, or by a connection between chromospheric and coronal heating mechanisms. The transition from this upward trend to zero phase difference at higher frequencies is due to the intermittent obscuration by fibrils that occult the foot points of hot loops, which are bright in the EUV and C IV lines, in oscillatory manner.

1. Introduction

The above abstract is copied from the journal paper describing the research presented by the first author at the meeting. In the meantime this paper has appeared as de Wijn et al. (2007). We summarize the most important results here.

This research concerns Fourier analysis of image sequences recorded with TRACE in its UV and EUV passbands. The three UV passbands at 1550, 1600, and 1700 Å sample the low chromosphere in the continuum. The 1550 and 1600 Å passbands also contain the C IV lines around 1548 Å sampling the transition region at temperatures of about 10^5 K. The EUV passbands at 171 and 195 Å sample the upper transition region ($\sim 10^6$ K). The latter images contain "moss", a highly dynamic transition-region structure. Its emission originates from the footpoints of hot, dense loops, that are intermittently obscured by chromospheric fibrils in quasi-periodic fashion (e.g., Berger et al. 1999; De Pontieu et al. 2003).

We computed Fourier power, coherence, and phase-difference spectra averaged seprately over regions of non-mossy and mossy plage, respectively.

2. Results and Conclusions

In non-mossy plage, the 1700–171 Å phase-difference spectrum show noise without indication of a particular signal. The 1550–171 Å spectrum, however, shows near-constant zero-degree phase difference. The 1600–171 Å spectrum is again very noisy, but hints at the presence of some signal. We conclude that there is common modulation in the C IV lines and the 171 Å passband, possibly through small-scale energy deposition such as reconnection, from O VI contamination in the 171 Å passband, or from coronal rain in overlying loops.

All UV–EUV phase-difference spectra show a linear trend up to about 4 mHz that corresponds to a time delay of about 7 minutes. This trend at low frequencies indicates the presence of upward traveling disturbances with periods longer than 5 minutes that cause brightness changes in the low chromosphere, and similar brightness changes in the high transition region about 400 s later. We consider that this relationship may be caused by slow-mode magnetosonic waves that travel upward. While true waves with such long periods cannot propagate, the initial or an impulsive disturbance can. We find a propagation speed of 3.5 to 11 km/s, assuming a vertical wave guide and reasonable formation heights of the moss emission. These speeds are low, but perhaps possible for slow-mode waves. Alternatively, the relationship may be caused by a connection between chromospheric and coronal heating mechanisms. In such a scenario, heating in the chromosphere would be followed by heating in the corona which would then lead to subsequent heating of the transition region through thermal conduction.

Beyond 4 mHz, the trend in mossy plage suddenly turns to zero-degree phase difference in the 1600–171 Å and 1550–171 Å spectrum. We interpret this as the result of the "shutter" action by dynamic fibrils that intermittently obscure the loop footpoints in C IV emission. The shutter instantaneously blocks both the C IV and EUV emission, thus causing zero-degree phase difference. The EUV obscuration comes from scattering out of the passband by photoionization plus subsequent recombination of hydrogen. We suspect that the C IV obscuration results from resonance-line scattering.

Acknowledgments. AdW and RJR acknowledge travel support from the Leids Kerkhoven-Bosscha Fonds and from the European Solar Magnetism Network. AdW is grateful for hospitality at LMSAL and Montana State University. BDP was supported by NASA grants NAG5-11917, NNG04-GC08G, and NAS5-38099 (TRACE).

References

Berger T. E., de Pontieu B., Fletcher L., Schrijver C. J., Tarbell T. D., Title A. M., 1999, Solar Phys. 190, 409

De Pontieu B., Erdélyi R., de Wijn A. G., 2003, ApJ 595, L63

de Wijn A. G., De Pontieu B., Rutten R. J., 2007, ApJ 654, 1128

The Physics of Chromospheric Plasmas
ASP Conference Series, Vol. 368, 2007
Petr Heinzel, Ivan Dorotovič and Robert J. Rutten, eds.

The Ca II Infrared Triplet Lines as Diagnostics of Chromospheric Magnetism

Anna Pietarila[1,2], Hector Socas-Navarro[1] and Tom Bogdan[3]

[1] *HAO, National Center for Atmospheric Research, USA*
[2] *Institute for Theoretical Astrophysics, University of Oslo, Norway*
[3] *Space Environment Center, NCEP/NWS/NOAA, USA*

Abstract. The Ca II infrared (IR) triplet lines are a promising candidate for studying chromospheric magnetism and dynamics. To study how good of a diagnostic the lines are for chromospheric magnetism in the quiet Sun we have constructed a MHD simulation in the high plasma-β regime, analyzed quiet Sun spectropolarimetric data of the lines and used a non-local thermodynamic equilibrium (nLTE) inversion code on the observations. In the simulation, where shocking acoustic waves dominate the dynamics, the Ca lines show a time-varying pattern of disappearing and reappearing Stokes V lobes. Waves are seen in the observations as well, but the dynamics are more complex. Unlike in the simulation, the observed Ca lines do not have similar shapes and the Stokes V asymmetries are determined by the local magnetic topology, not the phase of the wave. The fundamental differences between the observations and the simulation lead one to conclude that a 1D plane parallel atmosphere is not a valid approximation for the chromosphere. Nor can the effects of magnetic fields on the dynamics be neglected. This is further supported by the inversions failure to reproduce line profile asymmetries caused by gradients in the velocity and/or magnetic field. To explain the asymmetries, 3D structures and strongly localized gradients need to be included. The work presented here will be published in more detail elsewhere.

1. Introduction

The study of magnetic fields, especially outside of active regions, has to a large degree focused on the photosphere. However, magnetic fields in the chromosphere are of great importance, not least because of their possible connection to heating the solar atmosphere. The Ca II infrared triplet lines at around 8500 Å are a good candidate for studying the magnetic chromosphere. The lines are magnetically sensitive and their formation regions cover the upper photosphere and lower chromosphere. In this contribution a brief summary of a study of the Ca IR triplet lines as a diagnostic for chromospheric magnetism is presented. The study consists of three parts: a numerical simulation of the line formation in a high-β regime, spectropolarimetric observations of the lines in a quiet Sun region and nLTE inversions of the observations.

2. Results

The formation of the Ca II IR triplet lines was studied in a 2-dimensional high plasma-β simulation (Pietarila et al. 2006). In a high-β regime the effects of the magnetic field on the atmospheric dynamics can be neglected and the dynamics are entirely controlled by the plasma. The nLTE radiative transfer and hydrodynamics were solved self-consistently using the radiation hydrodynamic code of Carlsson & Stein (1997), while the time evolution of the magnetic field is governed by the time evolution of the column mass. The magnetic field varies both in the vertical and horizontal direction whereas the radiation hydrodynamics only vary in the vertical direction. Snapshots of the simulation were used to synthesize the full Stokes profiles of the Ca lines.

In the simulation, waves propagating through and forming shocks in the formation regions of the Ca lines cause a time-varying pattern in the line profiles (two left-most panels in Fig. 1). As the local fluid velocity changes with the changing phase of the propagating wave, the line absorption profile is shifted away from the line core. Combined with atmospheric velocity gradients this leads to a repeated pattern of disappearing and reappearing lobes in the Stokes V profiles. Except for the differences due to the lines' formation heights (since 8542 Å is formed slightly higher, where the gradients are larger, it is more asymmetric), the shapes and time evolution of the Ca lines are very similar. The Stokes V profiles at a given time have similar shapes along the horizontal direction: in the high-β regime, the effect of the magnetic topology on the formation of asymmetries is not as strong as the effect of velocity gradients. This is also shown by the strong correlation between the Stokes V asymmetries and the atmospheric velocity gradients and the insignificant correlation between the asymmetries and magnetic field gradients.

The simulation results were compared with spectropolarimetric data of the Ca IR triplet lines in a quiet Sun region near disk center taken with the Spectropolarimeter for Infrared and Optical Regions (SPINOR, Socas-Navarro et al. 2006) on May 19, 2005 at 14:14 UT.

The observed Stokes I and V profiles in the network are very dynamic and large self-reversals, especially in 8542 Å, are common (two right-most panels in Fig. 1). There is some similarity between the observations and the simulation, e.g., clear indications of upward propagating, shocking waves are seen in both. However, closer inspection reveals significant differences. Strong correlations between the 8498 Å and 8542 Å lines and the Stokes V area and amplitude asymmetries, found in the simulation, are missing in the observations. Instead, despite being formed fairly close, the 8498 Å and 8542 Å Stokes V profiles often exhibit different shapes. In general, the observed profiles have more complex shapes with asymmetries and multiple lobes being common. Also the spatial and temporal patterns of observed Stokes V profiles are more complex. In contrast to the simulation, in the observed network (which is likely to be a low-β regime) the magnetic topology, not the phase of the waves, is the determining factor for the shapes of the Stokes V profiles.

Lastly, a nLTE inversion code (Socas-Navarro et al. 2000) was used on the observed profiles. The inversion code is successful in reproducing large scale features, such as general shapes and amplitudes of the profiles, but not more detailed measures, such as Stokes V asymmetries (Fig. 2). Asymmetries in Stokes

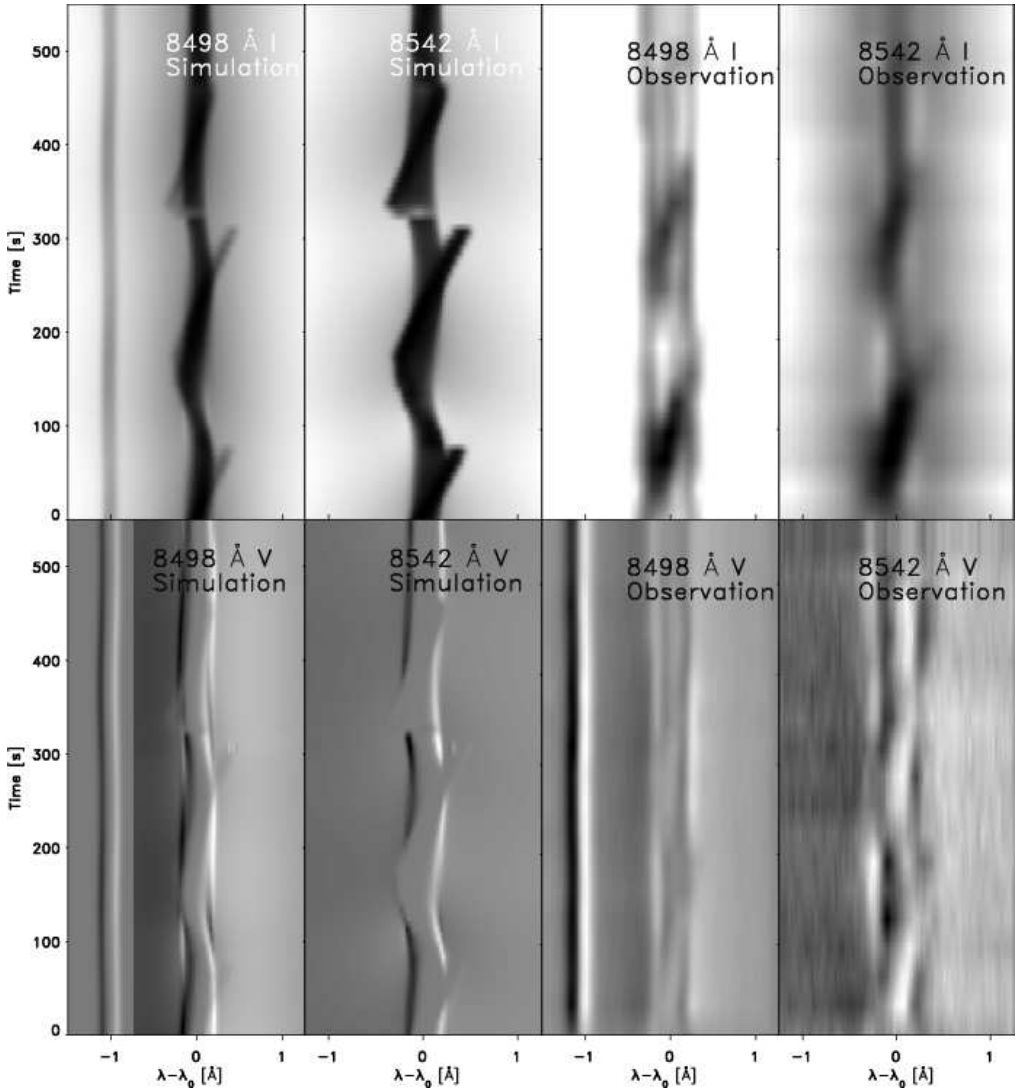

Figure 1. Simulated and observed time evolution of the Ca II 8498 Å and 8542 Å line Stokes I and V profiles.

V profiles are caused by gradients in the atmospheric velocity and/or magnetic field. The inversions code allows for gradients, but since spline interpolation is used for regions between the nodes of the atmospheric variables, no strongly localized gradients or dicontinuities are produced. The inversions retrieve known characteristics of the atmosphere, e.g., the network appears hotter and has a stronger magnetic flux than the internetwork. The expansion of the network with height is seen in the temperature and magnetic flux.

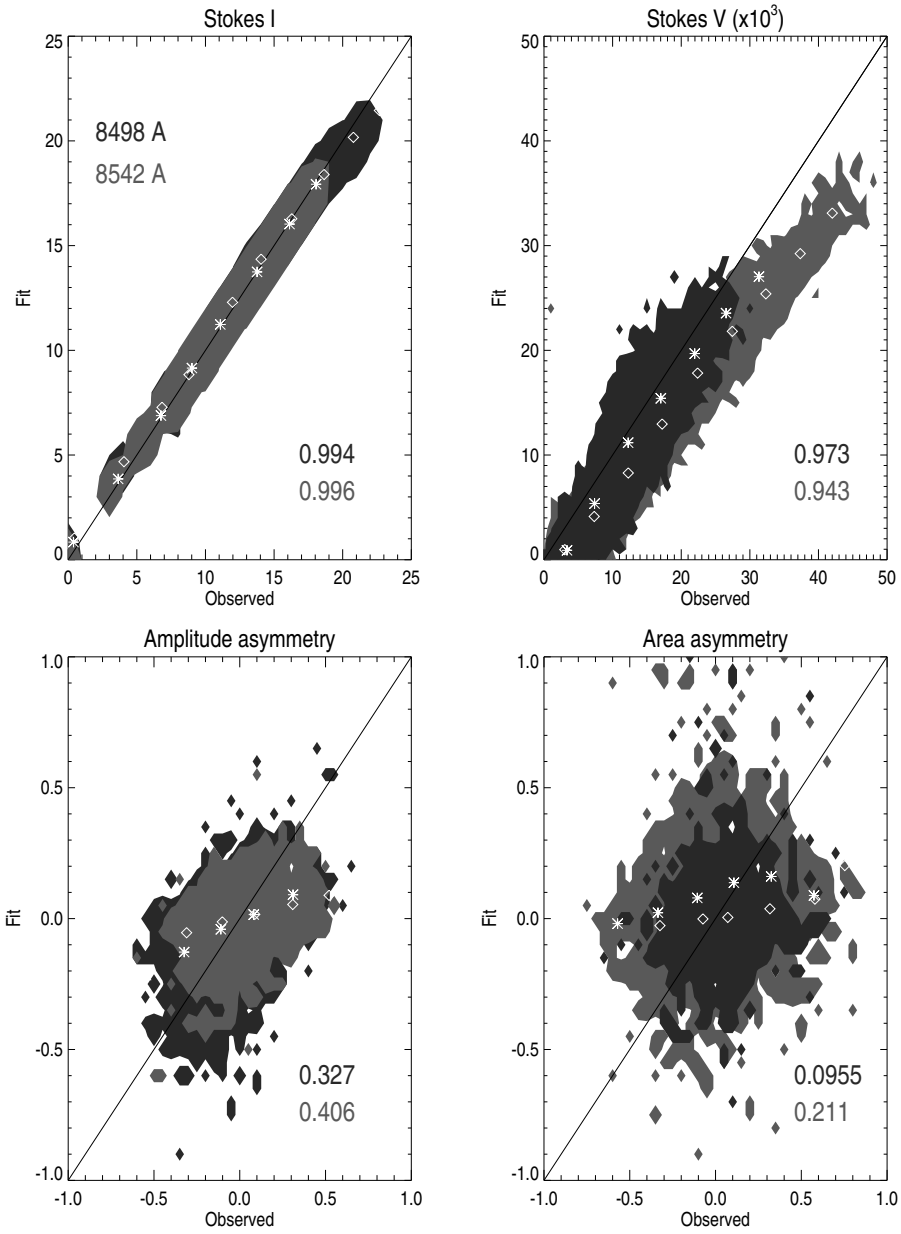

Figure 2. Scatter plots of observed and fitted values of Stokes I and V amplitudes and Stokes V amplitude and area asymmetries for 8498 Å (dark gray) and 8542 Å (light gray) lines. Shown in the lower right corner of each plot is the cross correlation coefficient for the observed and fitted values. The asterisk and diamond symbols show the means of the 8498 Å and 8542 Å fits, respectively.

3. Discussion

The comparison of the high-β simulation and the observations reveals some similarities, e.g., the presence of upward propagating shocking waves. However,

some main features of the observations are not seen in the simulation. In the observations, the two Ca lines often exhibit different Stokes V profile shapes, whereas in the simulation the two lines strongly resembled each other and the differences could be understood in terms of slight differences in formation height. The observed Stokes I profiles exhibit much larger self-reversals than what is seen in the simulation, and also the Stokes V profiles are more complex. In the simulation the time evolution and shape of the line profiles is determined by the upward propagating waves, but the local magnetic topology is the most important factor in the observations.

Large velocity gradients are more common in the chromosphere than in the photosphere and it is likely that variation in the vertical direction plays a more important role than variation in the horizontal direction. Taking into account these two factors and the two Ca lines different Stokes V profile shapes and asymmetries in the observations, indicates that the chromospheric asymmetries reflect the line-of-sight inhomogeneities, and not so much variations in the horizontal direction as is thought to be the case in the photosphere (Khomenko et al. 2005). Strongly localized gradients and discontinuities are likely to contribute to the observed chromospheric asymmetries. This remains a challenge for current nLTE inversion codes.

Because of multiple lobes and strong signal in the wings of the observed Stokes V profiles, the asymmetries are difficult to interpret, and not necessarily good proxies for the complexity of the Stokes V profiles or for atmospheric gradients. This is especially true if the two, area and amplitude, asymmetries are viewed separately.

The combination of the simulation, observations and inversions shows that the Ca II IR triplet lines are formed in a very interesting region where the effects of magnetic fields can no longer be neglected . The differences between the two observed Ca lines make it clear that a plane parallel atmosphere dominated by acoustic waves does not provide an accurate description of the magnetic chromosphere. Instead, in order to explain the formation of the lines and their asymmetries, we have to extend the simulation into 3D, consider more complex magnetic structures, and include magnetic fields in the dynamics.

References

Carlsson, M., & Stein, R. F. 1997, ApJ, 481, 500
Khomenko, E. V., Shelyag, S., Solanki, S. K., & Vögler, A. 2005, A&A, 442, 1059
Pietarila, A., Socas-Navarro, H., Bogdan, T., Carlsson, M., & Stein, R. F. 2006, ApJ, 640, 1142
Socas-Navarro, H. et al. 2006, Solar Phys., 235(1-2), 55
Socas-Navarro, H., Trujillo Bueno, J., & Ruiz Cobo, B. 2000, ApJ, 530, 977

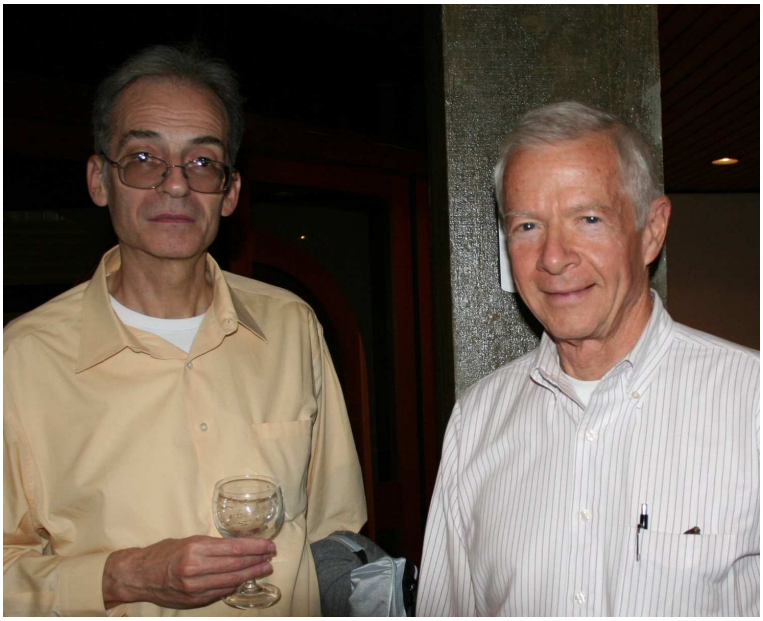

Juan Fontenla and Eugene Avrett

Sonja Jejčič and Jana Kašparová

The Physics of Chromospheric Plasmas
ASP Conference Series, Vol. 368, 2007
Petr Heinzel, Ivan Dorotovič and Robert J. Rutten, eds.

Chromospheric Spectrometry at High Spatial Resolution

Ø. Langangen, M. Carlsson, L. Rouppe van der Voort, V. H. Hansteen

Institute of Theoretical Astrophysics, University of Oslo, Norway

B. De Pontieu

Lockheed Martin Solar and Astrophysics Lab, Palo Alto, CA, USA

Abstract. In this summary we present spectrograms and images of the chromosphere obtained in a co-observation campaign with the SST and the DOT. The data are used to identify and measure the Doppler shifts of dynamic fibrils. Quantitative comparison with the results of (Hansteen et al. 2006) requires compensation for several observational issues.

1. Observations

The data briefly presented here were obtained in a co-observation campaign using the Swedish 1-m Solar Telescope (SST) (Scharmer et al. 2003) and the Dutch Open Telescope (DOT) (Rutten et al. 2004). Spectrograms were obtained with the SST, its adaptive optics system, and the TRI-Port Polarimetric Echelle-Littrow (TRIPPEL) spectrograph. To put the spectrograms into context we obtained narrow-band Hα images with the DOT. The wide band slit-jaw images obtained together with the spectrograms were used to co-align the spectrograms and the DOT images. The data presented here are from NOAA AR 10878 on May 04 2006 (08:22:03-09:00:48 UT), see Fig. 1.

2. Dynamic Fibrils

This data set is used to identify dynamic fibrils (DFs), see Fig. 2. We identify a DF when a co-spatial signature is seen in both the SST spectrogram and in the narrow-band DOT image. In this way we identify 32 DFs. The DF velocities are quite successfully fitted with first-order polynomials, see the righthand panels in Fig. 2. This gives us a deceleration of 85 ± 25 m/s^2, a maximum velocity of 10.8 ± 4.4 km/s and a lifetime of 209 ± 39 seconds. None of these results were corrected for line-of-sight projection effects. This is one of the reasons why these results are lower than what was reported by (Hansteen et al. 2006). Furthermore, the fact that we only observe along a one-dimensional slit can result in lower lifetimes and lower maximum velocities. Atmospheric seeing can also result in lower velocities and decelerations. A more thorough analysis of these effects will be given in a paper to be submitted to the ApJ.

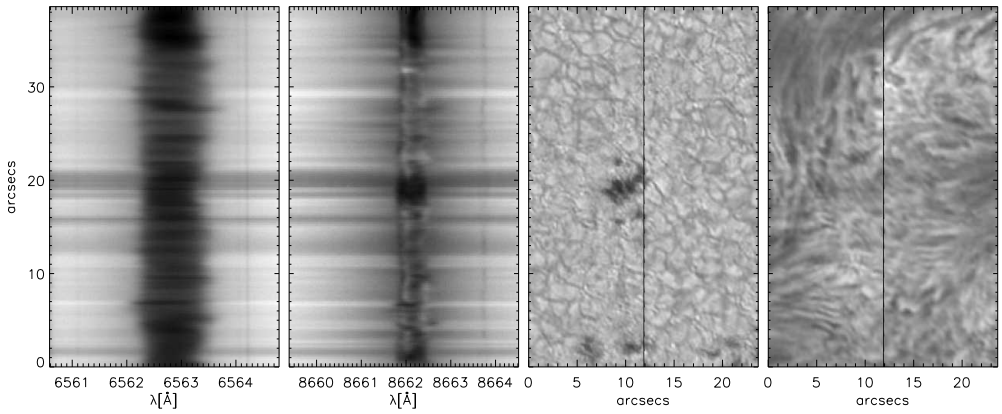

Figure 1. The aligned spectrograms and DOT images. This unique data set enables identification of chromospheric features such as dynamic fibrils.

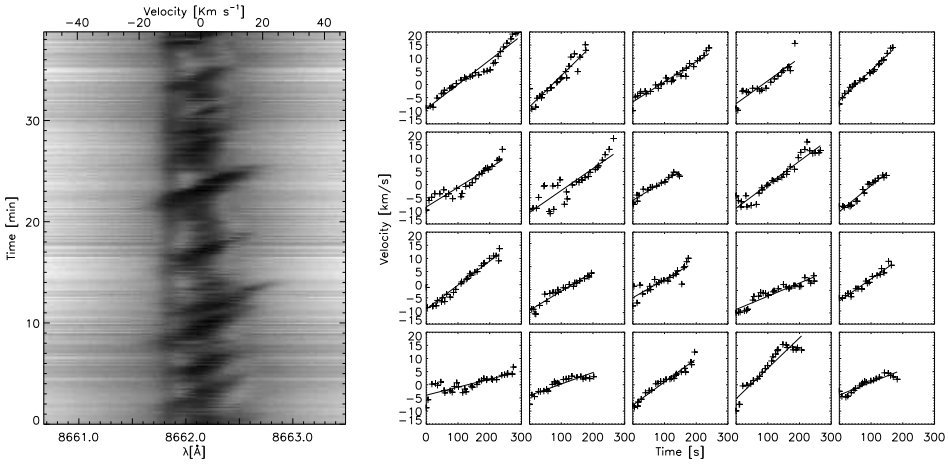

Figure 2. The lefthand panel shows the time evolution of one super-pixel (triple-binned pixel, 0.″12) in the Ca II 8662 Å line. Several DFs are seen as dark components moving across the spectral line. The 20 panels to the right show some examples of DF velocities and how well they are approximated with linear polynomials.

References

Hansteen V. H., De Pontieu B., Rouppe van der Voort L., van Noort M., Carlsson M., 2006, ApJ 647, L73

Rutten R. J., Hammerschlag R. H., Bettonvil F. C. M., Sütterlin P., de Wijn A. G., 2004, A&A 413, 1183

Scharmer G. B., Bjelksjo K., Korhonen T. K., Lindberg B., Petterson B., 2003, in S. L. Keil, S. V. Avakyan (eds.), Innovative Telescopes and Instrumentation for Solar Astrophysics, SPIE 4853, 341

The Physics of Chromospheric Plasmas
ASP Conference Series, Vol. 368, 2007
Petr Heinzel, Ivan Dorotovič and Robert J. Rutten, eds.

Observations and Simulations of Ca II H and Ca II 8662

W. Rammacher, W. Schmidt and R. Hammer

Kiepenheuer-Institut für Sonnenphysik, Freiburg, Germany

Abstract. We study chromospheric dynamics by analyzing long high spatial resolution time series of spectra of the Ca II H line and the Ca II infrared line at 8662 Å, recorded simultaneously near disk center of the sun. The observations were made at the VTT, Tenerife. The time series have a temporal resolution of 3 (8662) and 6 s (H), respectively. After the statistical analysis of the observation results, we used 1-D chromosphere simulation codes to make a series of computations with purely acoustic waves to obtain a time series of synthetic line profiles for Ca II H. A comparison of observational and theoretical results shows profound differences between these model calculations and the observations. A more detailed description of this work is in preparation and will be published in a main astronomy journal.

1. Observations

We study chromospheric dynamics by analyzing long (5000 s) high spatial resolution time series of slit spectra of the Ca II H line and the Ca II infrared line at 8662 Å, recorded simultaneously near disk center of the sun. The observations were made at the Vacuum Tower Telescope, Tenerife, in August 2005. The time series have a temporal resolution of 3 (8662) and 6 s (H), respectively. For Ca II H, the spatial resolution is $0.34''$ ($0.68''$ after binning) and the spectral resolution is 0.005 Å. For Ca II 8662, the corresponding values are $0.25''$ ($0.5''$) and 0.008 Å. The entrance slit covered more than 100 Mm on the sun.

Time variations of the intensity can be found for both lines and all wavelengths. The H line shows two regions with enhanced intensities, presumably network areas cut the entrance slit. In the IR line, only one of these two network areas is perceptible. To get spatially normalized fluctuations, we have calculated for every pixel of the slit the time averaged intensity; these mean values are then subtracted from the measured intensities. The so obtained fluctuation patterns for both lines look relatively homogeneous along the whole slit and the network regions are no longer predominant. A two-component-model could explain these structures: component 1 are acoustic and magnetoacoustic waves, which permeate the whole atmosphere and cause intensity fluctuations of comparable amplitudes; component 2 causes an overall enhancement of intensities in the active regions. It is obvious to assume that magnetic effects are responsible for this second component.

One of the most remarkable results of the observation analysis is the high degree of intensity correlations for different wavelengths of the same line. The temporal intensity fluctuations of the blue wing core profiles (0 - 0.3 Å distance from the line center) of the line are nearly synchronous, and the same is true for

the red wing core profiles. But there is only a low correlation between blue and red wing, and the blue and red emission peaks around ±0.1 Å are anti-correlated. This is a typical characteristic of shock fronts with their strong Doppler-shifted line profiles before and behind the front.

The upper part of Fig. 1 shows the correlation matrix R for the core profile of Ca II H derived from the first 4200 s of the VTT Tenerife time series. We have calculated this matrix R for every single pixel of the slit and then averaged over all pixels excluding those pixels that are part of the chromospheric network. The R variations along the slit are only moderate, also for the network pixels: here, the correlation degree is even a little bit higher. The resulting matrix can be considered as a "fingerprint" of all the chromospheric dynamic action for the observed time interval. Every line produces such a fingerprint, and additional fingerprints can be derived by a cross-correlation of two lines.

Mainly vertically propagating waves should generate intensity fluctuations that successively wander from the wings (radiation comes from the photosphere or lower chromosphere) to the core of the line (radiation comes from the middle or high chromosphere). When a wave needs n seconds to propagate from the lower into the higher chromosphere, the wing intensities at $t = 0$ should show a good correlation with the core intensities at $t = n$. We have therefore also varied this time lag n between 5 and 300 s. But neither the Ca II H nor the Ca II 8662 line shows at any time higher correlations than the correlation matrices at $t = 0$. We will emphasize that individual bright points can show different behaviour, but these are exceptions to the rule.

2. Simulations

Every realistic numerical model should be able to reproduce such fingerprints with sufficient accuracy. We have therefore used our 1-D chromosphere simulation code WAVE (Rammacher,W. & Ulmschneider, P., 2003) to make a series of computations with purely acoustic plane parallel waves to obtain a time series of synthetic line profiles for Ca II H. The waves are generated in the photosphere at level $\tau_{5000} = 0$ by a piston. Considering recent publications of Fossum & Carlsson (2005, 2006), we have chosen as a velocity driver for the piston the same acoustic power spectrum as used by these authors (see also Fig. 4 in Rammacher 2005). However, we use higher frequency integrated mechanical fluxes in our calculations: our model with the lowest flux has $F_{\rm mech} = 5.0 \times 10^7$ erg/cm^2 s – this is the minimum value to get the observed emission peaks in the time averaged core profiles of Ca II H (Rammacher, 2005) and also the theoretical lower limit of generated mechanical flux as proposed by Musielak et al. (1994).

We have also treated several additional models with the same power spectrum form, but different integrated mechanical fluxes (range from $F_{\rm mech} = 5.0 \times 10^7$ to 2.0×10^8 erg/cm^2 s) and several models with purely monochromatic waves, varying the wave period between 30 and 90 s. All these synthetic time series were used to derive correlation matrices for the Ca II H line. Fig. 1 compares one of these model correlation matrices with the observed matrix for the H line. Large differences can be seen. None of our 1-D models can reproduce the observed fingerprint: the differences to the observed values are rather large, especially for the models which use power spectra. (The exact form of the used

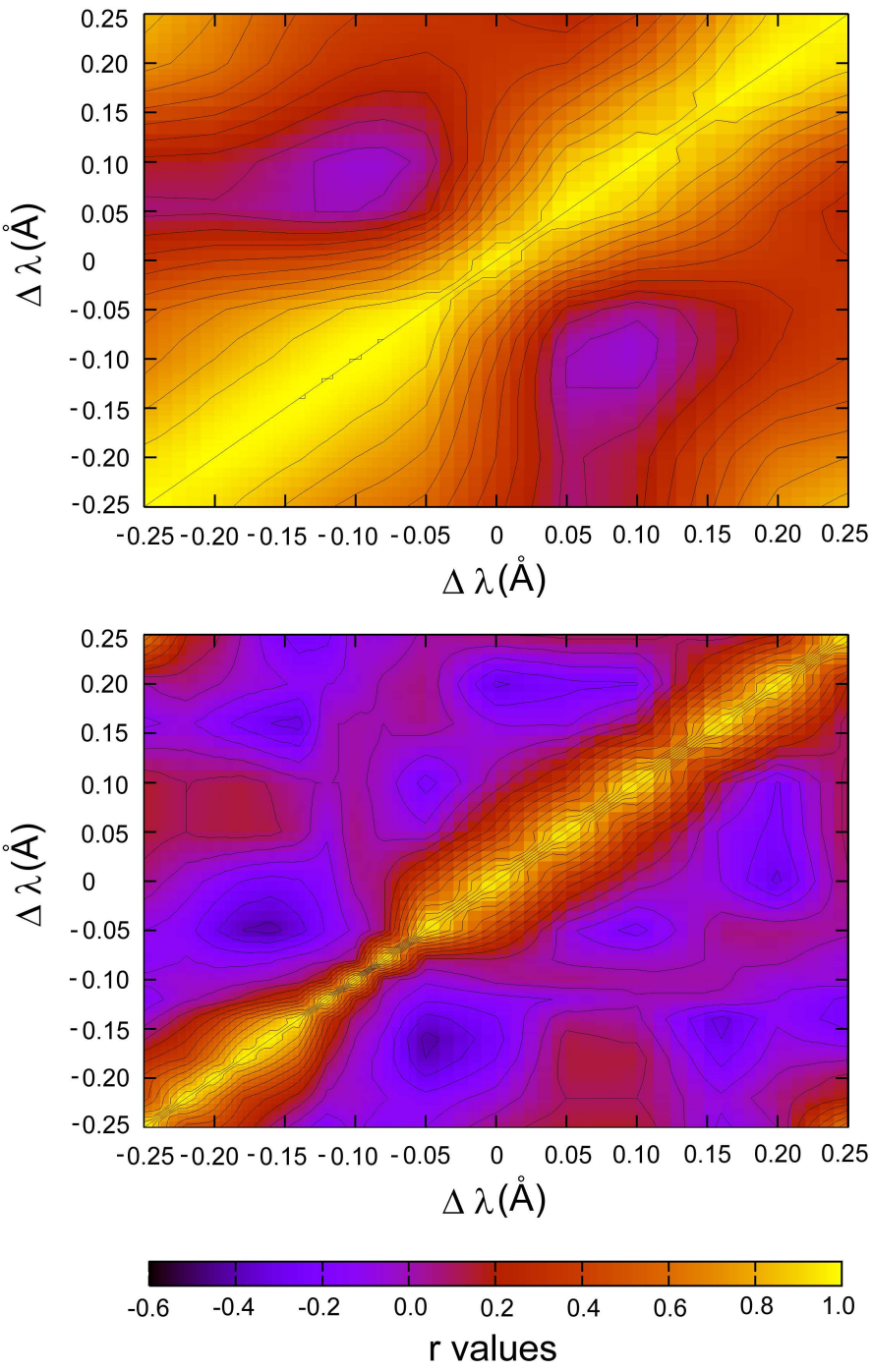

Figure 1. Ca II H correlation matrices derived from the VTT observations (top panel, internetwork pixels only) and from a 1-D model simulation using a power spectrum with $F_{\rm mech} = 5.0 \times 10^7$ erg/cm^2 s (bottom panel). Distance of adjacent contour lines is 0.1; the r value on the diagonal is 1.

power spectra is of minor relevance for the temperature structure and the Ca II line emissions of the chromosphere, see Rammacher 2005)

Simple plane parallel shock waves propagating nearly vertically through the atmosphere can therefore not explain the dynamics of the chromosphere. But oblique acoustic shock fronts could possibly generate such high correlations: in such a case, the observer looks at the same time at different layers of the shock front. The deepest layers are relatively cool, the higher layers however hot but all layers as part of the same moving shock front change synchronously their temperatures and therefore also their intensities. Existing 3D-models (Wedemeyer et al. 2004, 2005) show clearly the existence of oblique shock fronts, but the needed computer power (3D-NLTE radiation transport) for the calculation of 3D fingerprints is currently not available. However it seems possible to simulate oblique shock fronts with the aid of 1-D plane parallel waves, at least very roughly. Such simulations are in preparation.

Acknowledgments. We thank the CSPM organisers for a very good meeting and R. J. Rutten and H. Uitenbroek for discussion and helpful comments. This work has been supported by the German Research Foundation under grant Schm 1168/6-1.

References

Fossum, A. & Carlsson, M. 2005, ApJ, 625, 556
Fossum, A. & Carlsson, M. 2005, Nature, 435, 919
Fossum, A. & Carlsson, M. 2006, ApJ, 646, 579
Musielak, Z.E., Rosner, R., Stein, R.F., & Ulmschneider, P. 1994, ApJ, 423, 474
Rammacher, W. & Ulmschneider, P. 2003, ApJ, 589, 988
Rammacher, W. 2005, in ESA SP-596, Chromospheric and Coronal Magnetic Fields, ed. D. E. Innes, A. Lagg, D. Danesy, & S. Solanki
Wedemeyer, S., Freytag, B., Steffen, M., Ludwig, H.-G., & Holweger, H. 2004, A&A, 414, 1121
Wedemeyer, S., Kamp, I., Bruls, J., & Freytag, B. 2005, A&A, 438, 1043

The Physics of Chromospheric Plasmas
ASP Conference Series, Vol. 368, 2007
Petr Heinzel, Ivan Dorotovič and Robert J. Rutten, eds.

Comparison of Ca II K and Ca II 8542 Å Images

Kevin P. Reardon[1], Gianna Cauzzi[1] and Thomas Rimmele[2]

[1]*INAF, Arcetri Astrophysical Observatory, Florence, Italy*
[2]*National Solar Observatory, Sunspot, USA*

Abstract. We compare a time sequence of filtergrams obtained in the Ca II K line with a series of spectrally resolved images obtained simultaneously with the IBIS instrument in the Ca II 8542 Å line. Using the narrowband IBIS images and a synthetic filter profile, we construct simulated 8542 filtergrams that mimic the observed K_{2V} filtergrams. We observe that these filtergrams appear to contain elements corresponding to both photospheric and chromospheric structures. Intermediate scale patterns seen in the filtergrams may simply be the result of the combination of a variety of structures from different atmospheric levels. We analyze the Fourier power spectra of the filtergrams and note that at frequencies well above the acoustic cut-off value the observed power in the K_{2V} filtergrams seems to be predominantly photospheric in origin. The use of Ca II H and K filtergrams to study the chromospheric behavior thus may be inherently problematic. Narrowband images in the Ca II 8542 Å line might provide a better source of information about chromospheric behavior with little loss in spatial or temporal resolution.

1. Introduction

The Ca II H and K lines have long been used to study the solar atmosphere, using both slit-based grating spectrographs as well as narrow band filters isolating a portion of the spectral line, usually near the line center. The latter approach has seen extensive use in the more recent past because of the information it provides about the spatial distribution and temporal evolution of structures in the 2-D field of view (e.g. Wöger et al. 2006, Tritschler et al. 2007). This filtergram approach has the drawback that even the narrowest available filters (0.3-0.6 Å FWHM) result in the mixing of information from a substantial range of wavelengths within the line. Therefore, it is not clear how observed intensity patterns and fluctuations relate to physical structures in the solar atmosphere.

Singlely ionized Calcium also produces three strong lines near 8600 Å, the "infrared triplet", which provide several observational advantages with respect to the H and K lines, including a generally better response of the detectors and the reduced effect of the atmospheric turbulence at longer wavelengths, as well as a higher photon flux. We present here an analysis of quiet-Sun data obtained with IBIS, a dual Fabry-Pérot imaging spectrometer (Cavallini 2006), that can obtain narrowband images in the Ca II 8542 Å line with a tunable 45 mÅ passband. These spectrally resolved images provide us with the opportunity to examine the composition of the Ca II K-line filtergrams.

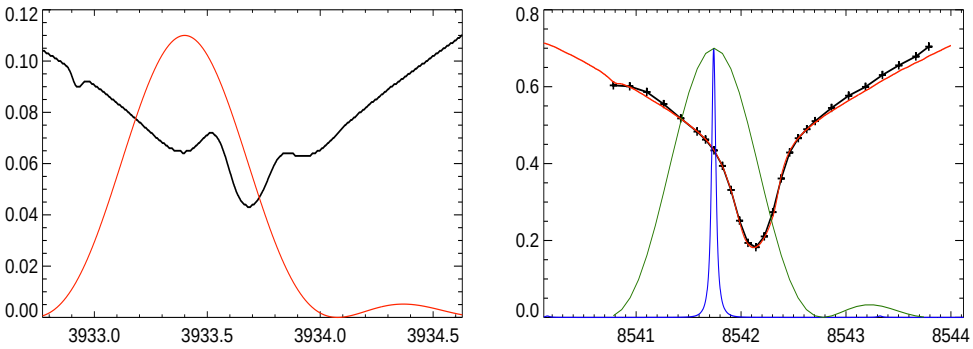

Figure 1. *Left:* atlas profile of the Ca II K line with the theoretical profile of a Lyot filter (FWHM = 0.6 Å) positioned at 0.3 Å from line center. *Right:* atlas profile of the Ca II 8542 Å line with crosses showing the individual wavelengths of the IBIS observations. The narrow profile represents the instrumental profile of IBIS, while the broader profile is the synthetic filter profile used to construct the simulated filtergrams. The transmission of the filter profiles have been arbitrarily scaled to fit the plot.

2. Data and Analysis

We employ a sequence of quiet Sun Ca II 8542 Å data, acquired with IBIS at 27 separate wavelength positions within the line ($t_{\rm exp}$ = 25 ms; image scale = 0.165 ″/ pixel). Each scan took about 7 s, and the repetition rate was 19 s. We obtained a total of 175 scans, covering a period of approximately one hour. Simultaneous and cospatial Ca II K_{2V} images were obtained through a Halle filter (0.6 Å FWHM) with a $t_{\rm exp}$ of 1.2 s, and image scale of 0.08 ″/ pixel. Their cadence was 2 s/image, but for this study we only selected the 175 images obtained closest in time to the image at the core of the 8542 Å line.

The observations were obtained during a period of excellent seeing with adaptive optics using as a reference the quiet Sun granulation at the center of the field. The data were further destretched using images in a whitelight reference channel obtained strictly simultaneously with the IBIS narrowband images. The two datasets were co-aligned and the Ca II K data masked to select the same area as the circular aperture of the IBIS data.

Using the images obtained at multiple wavelengths with IBIS, we then created a synthetic 8542 Å "filtergram" by applying a theoretical filter profile, defined as a sinc funtion, to the spectra observed at each position in the field of view. The formation of the 8542 Å is strictly coupled with that of the K-line, resulting in very similar source functions for the two lines, that are located however at approximately twice the relative distance from the line center for the 8542 Å line compared to the K line (Uitenbroek 1989). Given the limited range of the IBIS spectral scan, as a first approximation we applied a theoretical profile with a FWHM of 0.9 Å, centered 0.4 Å to the blue of the line center (compared to the 0.6 Å FWHM for the K_{2V} filter, see Fig. 1). We remark however that the appearance of the simulated filtergram is not strongly dependent on the width of the synthetic filter profile. We also applied a spatial smearing of five pixels (0.8″) to the IBIS data to mimic the degradation of the image quality due to changes in the atmosphere during the long exposure of the K data.

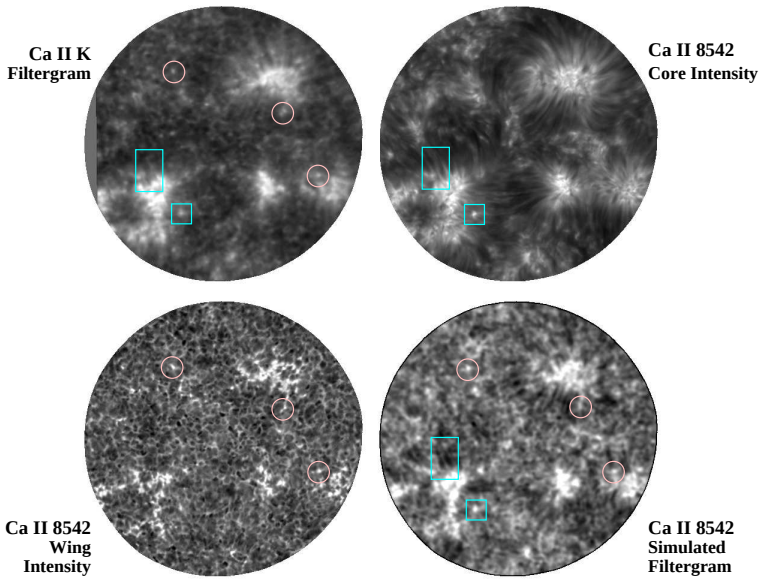

Figure 2. Images obtained on 02 June 2004 of a quiet Sun region at disk center. *Upper left*: Ca II K filtergram. *Upper right*: Ca II 8542 Å line core intensity. *Lower left*: Ca II 8542 Å line wing. *Lower right*: Ca II 8542 Å simulated filtergram (see text). The circles indicate examples of photospheric features that appear in the 8542 Å line wing image as well as in the two filtergrams. The rectangles surround examples of features of chromospheric origin appearing in the 8542 Å line core intensity as well as in the two filtegrams.

3. Simulated Filtergrams and Intensity Power Spectra

A first result is shown in Fig. 2 for one of the 175 sequences. The Ca II K filtergram shows the typical bright network regions surrounding more diffuse structures in the internetwork. The synthetic 8542 filtergram well resembles the K-line filtergram, something that is even more striking when watching the timeseries of the K-line and simulated filtergrams. The figure also shows two of the 8542 Å individual images: one is the core intensity, clearly showing a wealth of chromospheric fibrils, and one is from a position in the broad wings with a typical formation height in the mid photosphere (Uitenbroek 1989). Both the K-line and synthetic 8542 filtergrams display features present in one or another of the narrowband images, indicating a mix of both photospheric and chromospheric elements. It is also interesting to note that the simulated filtergram shows patterns, especially in the internetwork, that are not present in any of the individual narrowband images but rather result from the combination of the disparate images at the different wavelengths. The remaining differences are probably due to a combination of the increased relevance of the Doppler shifts and decreased temperature sensitivity at the longer wavelength.

We perform an additional comparison by computing the Fourier power spectrum of the intensity fluctuations at each position in the field of view. We generate power maps (Fig. 3) by averaging the measured power spectrum over three

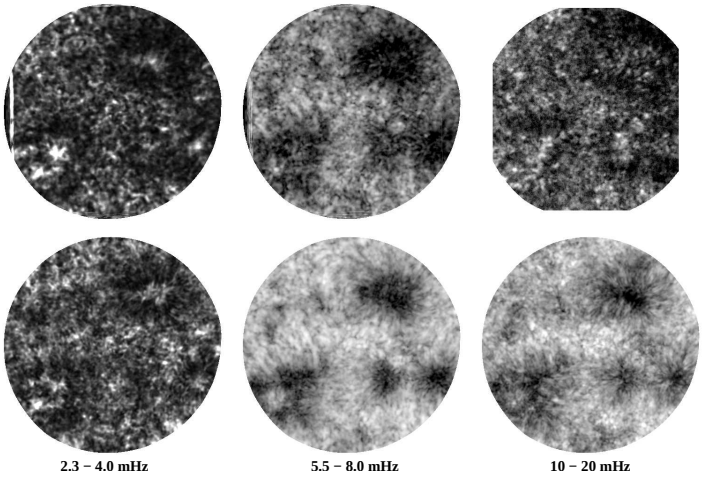

Figure 3. Maps of the intensity power averaged over three distinct frequency bands for the Ca II K_{2V} filtergrams (top row) and the 8542 Å simulated filtergrams (bottom row). The low power regions near the network patches are the chromospheric "magnetic shadows", which are not visibile in the maps of the high frequency power in the Ca II K_{2V} data. The clipping at the edges of the field is due to the intrusion of the edge of the observed field into the masked area.

bands: 2.3-4.0 mHz (five minutes); 5.5-8.0 mHz (three minutes); 10-20 mHz (high frequency). The power maps are rather similar for the five-minute and three-minute frequency bands. However, in the high-frequency band the two power maps are quite different, with only the simulated filtergram continuing to show some trace of the "magnetic shadows" seen in the three-minute band (Vecchio et al. 2007). The K_{2V} filtergram power maps instead appear very simular to the power maps from the wings of the 8542 Å line (not shown in the figure), indicating that intensity fluctuations at higher frequencies in the K_{2V} filtergrams may be predominantly photospheric in origin.

Our results hence show that by properly combining high spectral resolution Ca II 8542 Å data we can reproduce many of the features observed in the Ca II K_{2V} filtergrams, as well as their temporal behavior. We thus confirm that the Ca II K_{2V} filtergrams contain structures of both chromospheric and photospheric origin, as well some patterns that seem to arise from the combination of the vastly different structures visible at multiple wavelengths. One must take care to interpret the features seen in such filtergrams as corresponding directly to chromospheric structures.

References

Cavallini, F., 2006, Solar Phys. 236, 415
Tritschler, A., Schmidt, W., Uitenbroek, H., Wedemeyer-Böhm, S., 2007, A&A 462, 303
Uitenbroek, H., 1989, A&A 213, 360
Vecchio, A., Cauzzi, G., Reardon, K. P., Janssen, K., Rimmele, T., 2007, A&A 461, L1
Wöger, F., Wedemeyer-Böhm, S., Schmidt, W., von der Lühe, O., 2006, A&A 459, L9

The Physics of Chromospheric Plasmas
ASP Conference Series, Vol. 368, 2007
Petr Heinzel, Ivan Dorotovič and Robert J. Rutten, eds.

Scattering Polarization of the Ca II Infrared Triplet as Diagnostic of the Quiet Solar Chromosphere

Rafael Manso Sainz[1] and Javier Trujillo Bueno[1,2]

[1] *Instituto de Astrofísica de Canarias, La Laguna, Spain*
[2] *Consejo Superior de Investigaciones Científicas, Spain*

Abstract. In observations close to the edge of the solar disk, the Ca II infrared triplet has a scattering polarization pattern at the level of 10^{-3} in its two strongest lines and at the 10^{-4} level in the weakest. This polarimetric sensitivity is now accessible with modern spectropolarimeters and scattering polarization has been observed by several authors in the Ca II infrared triplet. We discuss here the interest of observing these lines for the detection and mapping of magnetic fields in the quiet solar chromosphere. To this end, we investigate theoretically the sensitivity of the polarization pattern to the presence of magnetic fields through the Hanle effect. We find that the Ca II 8542 Å and 8662 Å lines are mostly sensitive to fields between 0.001 and 0.1 G, the former is also weakly sensitive to fields between 1 and 10 G. Otherwise the polarization signals are dependent only on the magnetic field geometry, but not on its intensity. The 8498 Å line is highly sensitive in the whole regime 0.001-10 G, but its polarization signal is much lower. Diagnostic diagrams giving the Q/I vs. U/I values at the line core for several magnetic field configurations and intensities are presented. We also discuss the sensitivity of the scattering polarization signals to the temperature gradient of the atmospheric model.

1. Introduction

The detection and measurement of magnetic fields in the quiet solar chromosphere – whose very definition is the apparent absence of fields – is rather difficult for two reasons. First, the chromosphere is quite tenuous; hence, only resonant lines of relatively abundant elements have oscillator strengths large enough to form in such a rarefied medium. Unfortunately, most of those lines lie in the blue and UV regions of the spectrum and only a handful of chromospheric spectral lines are accessible for observation from the ground. Second, chromospheric magnetic fields are intrinsically weak and unable to generate sizable Zeeman signals. Those two reasons justify this research. We report a study on scattering line polarization and the Hanle effect in the Ca II infrared triplet and we explore the possibility of using these lines to diagnose weak fields in the quietest regions of the solar chromosphere.

The scattering polarization pattern of the Ca II infrared triplet has been detected in the solar spectrum by Stenflo et al. (1983), and more clearly by Stenflo, Keller & Gandorfer (2000), and also by Dittmann et al. (2001). The formation of the observed polarization pattern is now well understood (Manso Sainz, 2002; Manso Sainz & Trujillo Bueno 2001, 2003a). The Q/I signal of the strongest lines is produced by selective *absorption* of polarization components

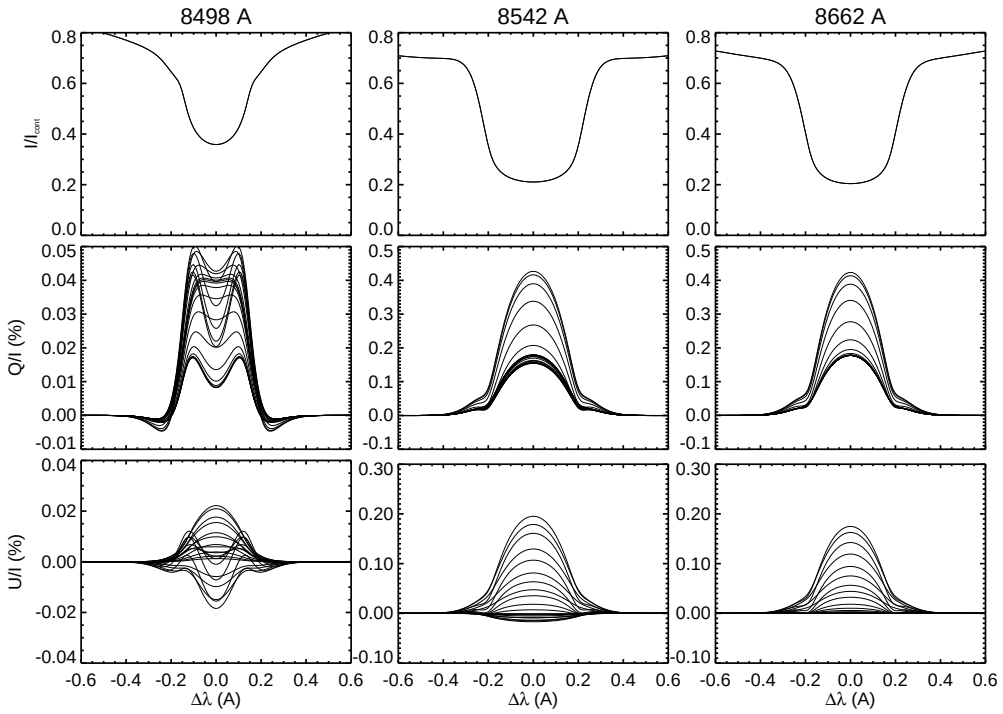

Figure 1. This figure illustrates the scattering line polarization and the Hanle effect in the 8498, 8542 and 8662 Å lines of the Ca II infrared triplet in the FAL-C solar model atmosphere (Fontenla, Avrett & Loeser 1991). Close to the limb ($\mu = 0.1$) observations are assumed. Uppermost panels show the normalized intensity profiles, which are independent of the magnetic field. The central and lower panels show the fractional Stokes parameters Q/I and U/I, respectively. The calculations assume a constant magnetic field inclined 30° with respect to the vertical and tilted towards the observer. Several magnetic field intensities have been assumed: 10^{-3}, 1.7×10^{-3}, 3.1×10^{-3}, 5.6×10^{-3}, 10^{-2}, 1.7×10^{-2}, 3.1×10^{-2}, 5.6×10^{-2}, ..., 100 G. These configurations appear in the lower panels of Fig. 2.

(dichroism) in the solar chromosphere which is due to imbalances between the populations of the magnetic sublevels of the metastable levels of Ca II that the anisotropic radiation field of the solar atmosphere induces (Manso Sainz, 2002; Manso Sainz & Trujillo Bueno 2001, 2003a). The observed Q/I in the λ8662 line is exclusively produced by this mechanism (its upper level with $J = 1/2$ cannot be polarized by radiation pumping unless a net amount of circular polarization is present in the atmosphere); the Q/I signal in the λ8542 line has also a contribution coming from its polarizable ($J = 3/2$), upper level. This contribution is negligible, because the level's excitation is dictated by the strong Ca II K line, which imposes a quasi-isotropic radiation field at the height of formation of the infrared triplet lines.

A magnetic field in the chromospheric plasma manifests itself by removing the degeneracy of the magnetic sublevels of the atomic levels (Zeeman splitting), which changes the atomic polarization of the metastable levels and hence the

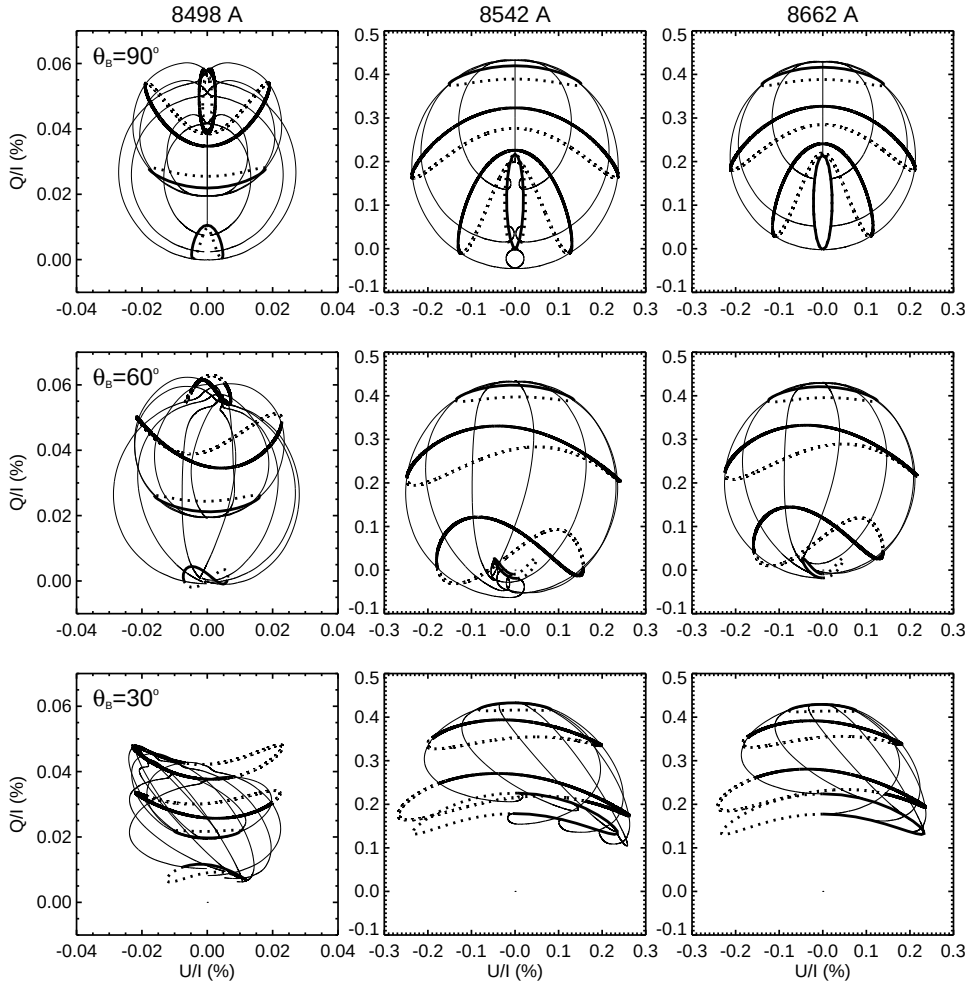

Figure 2. These diagrams show the Q/I and U/I signal at the line core of the Ca II infrared triplet lines for several line-of-sight and magnetic field configurations in the FAL-C atmospheric model. The observation is always close-to-the-limb ($\mu = 0.1$). Thick lines correspond to constant strength magnetic fields of 1.8×10^{-3}, 5.6×10^{-3}, 1.8×10^{-2}, and 18 G when observed with $0^\circ < \chi - \chi_B < 180^\circ$ (solid line) and $180^\circ < \chi - \chi_B < 360^\circ$ (dotted line), where $\chi - \chi_B$ is the azimuth between the line-of-sight and the magnetic field. (These two tracks do not coincide in the $\theta_B = 90^\circ$ case because we are not in the 90°-scattering or tangential observation limit, but at $\mu = 0.1$). The thin solid lines correspond to $\chi - \chi_B = 0^\circ, 30^\circ, 60^\circ, 90^\circ, 120^\circ, 150^\circ$, and 180°. Upper panels correspond to a magnetic field inclined $\theta_B = 90^\circ$ with respect to the vertical (i.e., horizontal magnetic field), central and lower panels correspond to inclinations of $\theta_B = 60^\circ$ and $\theta_B = 30^\circ$, respectively.

emergent polarization signal due to dichroism. If the removal of degeneracy is only partial (i.e., the Zeeman splitting is of the order of the natural width of the sublevels – the sublevels still *overlap*), the linear polarization signal gradually changes with the magnetic field intensity (and geometry); the effect is illustrated in Fig. 1. It can be seen that the 8542 and 8662 Å lines have a strong dependence

on the magnetic field strength in the regime $\nu_{\rm L} \sim B_{\ell u} J$ ($\nu_{\rm L}$ being the Larmor frequency), which is when the Zeeman splitting is of the order of the inverse of the mean life time of the lower levels of those transitions (lower-level Hanle effect regime). The 8542 Å line has an additional upper-level Hanle effect regime for $\nu_{\rm L} \approx A_{u\ell}$ with a much lower signal for the reasons explained above. When the degeneracy is completely removed ($\nu_{\rm L} \gg 1/\tau_{\rm life}$) the Hanle effect *saturates*, and the emergent polarization signals depend only on the magnetic field geometry, not on the strength.

Figure 2 shows the emergent Q/I and U/I signals at the line core of the Ca II infrared triplet lines for different magnetic field configurations and strengths in the FAL-C model solar atmosphere for a close-to-the-limb ($\mu = 0.1$) observation. Each of the four thick lines in a given panel correspond to a fixed magnetic field strength for an observation with azimuth ranging $0^\circ \leq \chi - \chi_B \leq 180^\circ$ (i.e., from *along* the magnetic field to *away from* the magnetic field; solid line), and azimuthal angles $180^\circ \leq \chi - \chi_B \leq 360^\circ$ (dashed line). Thin lines correspond to magnetic fields ranging between 0 G and 1000 G and a fixed value of $\chi - \chi_B$. They show the pattern of depolarization (Q/I decreases) and rotation of the polarization plane (U/I appears) characteristic of the Hanle effect in a 90° scattering geometry. However, it is important to recall that this is not always the case; an important example of this is the forward scattering case.

The chromosphere is a highly dynamic medium and it is difficult to resolve the structure of its magnetic field, especially with the low spatio-temporal resolution required for high sensitivity spectropolarimetric observations using current instrumentation and telescopes. Figure 3 shows the emergent fractional polarization in a close-to-the-limb observation in two different thermal models of the solar atmosphere in which the magnetic field azimuth has been averaged between 0 and 2π. This simulates the case of an unresolved magnetic fields with a random distribution of azimuths within the resolution element. The figure shows Q/I (U vanishes due to the symmetric distribution of fields), for fields of 0.3 G (dashed lines) that correspond to the saturation regime of the lower-level Hanle effect and 100 G (solid lines), when the upper-level Hanle effect saturates. It is evident that λ8662 does not show two different regimes (dashed and solid-line profiles coincide), since its upper level is intrinsically unpolarized.

Two interesting conclusions can be reached from a simple inspection of this figure. First, a simple qualitative interpretation of the observations reported by Stenflo et al. (2000) can be given. They find significant signals in both lines, 8542 and 8662 Å, which is incompatible with field inclinations of the order of 60° in these models. On the other hand, the reported Q/I signals are of the same amplitude, which makes them incompatible with predominantly horizontal fields in the 0.1–1 G regime. Actually, Stenflo's et al. (2000) observations of such two lines would be compatible with a magnetized FAL-C model and a field inclination of 30° with unresolved azimuth in the saturated Hanle effect regime.

Second, it is also interesting to observe that the calculated polarization amplitudes are very sensitive to the assumed thermal model of the solar chromosphere (see also Fig. 4 of Manso Sainz & Trujillo Bueno 2001). For this and the above-mentioned reasons we think that systematic observations of the scattering polarization in the Ca II infrared triplet should be carried out in order to

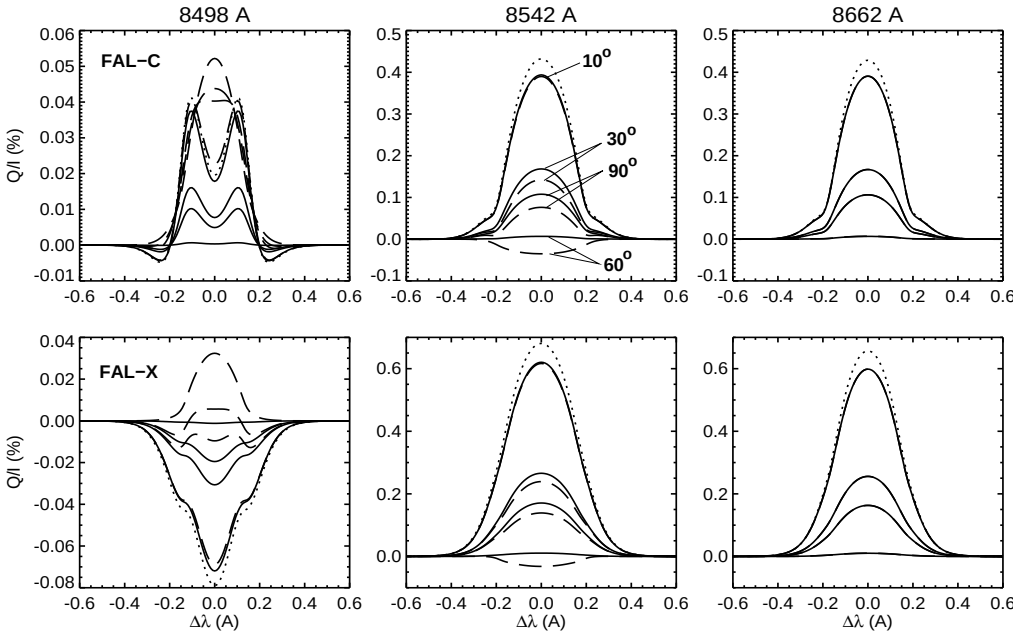

Figure 3. Averaging over a random distribution of magnetic field azimuths for a fixed inclination (labels), the Stokes parameter U cancels out and the emergent polarization is given only by Q/I. The three upper panels show Q/I in a simulation of a close-to-the-limb observation ($\mu = 0.1$) of the Ca II infrared triplet in the FAL-C model for four magnetic field inclinations (labels) and averaging over the azimuth. Dashed and solid lines correspond to 0.3 and 100 G, respectively, which correspond to the saturation regime for the lower-level and upper-level Hanle effect. Dotted lines show the non-magnetic pure scattering regime. The lower panels correspond to the FAL-X atmospheric model, which has a cool chromosphere.

use them as a sensitive thermometer and magnetometer of the quiet regions of the solar chromosphere .

2. Methods

We consider a 5-level atomic model of Ca II including the ground level, the metastable $^2D_{3/2,5/2}$ levels and the $^2P_{1/2,3/2}$ upper levels of the Ca II H and K lines; the excitation state in such a model is given by 29 statistical tensor elements ρ^K_Q ($K = 0$, 2, or 4, $Q = -K, ..., K$), including the total populations of the five levels. The radiative transition probabilities are those of Edlén & Risberg (1956) compiled at the NIST database[1]. (This transition probabilities for the infrared triplet are larger than those used in Manso Sainz & Trujillo Bueno (2003a); correspondingly, the Q/I values for the zero-field case are slightly larger here than in our previous work.) Inelastic collisional rates and line broadening

[1] `http://physics.nist.gov/PhysRefData/ASD`

parameters have been taken from Shine & Linsky (1974); elastic depolarizing collisions are treated according to Lamb & ter Haar (1971). The collisional pumping of statistical tensors is treated following Landi degl'Innocenti & Landolfi (2004). The reference model atmosphere is either the FAL-C model of Fontenla, Avrett & Loeser (1991), or the FAL-X (or M_{CO}) model of Avrett (1995). The number density of Ca II has been computed in Non-LTE. At each point in the atmosphere we solve 28 statistical equilibrium equations plus the conservation of particles equation to calculate the excitation state of the atomic system. Then we calculate the radiation field at each point in the model atmosphere for each of the five radiative transitions by formal integration of the radiative transfer equations for the Stokes parameters applying a parabolic improvement of the DELO method (Socas-Navarro, Trujillo Bueno & Ruiz Cobo, 2000; Trujillo Bueno, 2003). Then, radiation field tensors J^K_Q are calculated and used to work out the new excitation state of the atomic system and so on, iteratively. The convergence of the iterative process is guaranteed by a generalization of the method developed by Trujillo Bueno (1999); see Manso Sainz (2002) and Manso Sainz & Trujillo Bueno (2003b) for details.

Acknowledgments. This research has been funded by the Spanish Ministerio de Educación y Ciencia through project AYA2004-05792.

References

Avrett, E. H. 1995, in J. R. Kuhn, M. J. Penn (eds.), Infrared Tools for Solar Astrophysics: What's next?, World Scientific, Singapore, 303

Dittmann, O., Trujillo Bueno, J., Semel, M., & López Ariste, A. 2001, in M. Sigwarth (ed.), ASP Conf. Series 236, Advanced Solar Polarimetry: Theory, Observation and Instrumentation, 125

Edlén, B. & Risberg, P. 1956, Ark. Fys., 10, 553

Fontenla, J. M., Avrett, E. H., & Loeser, R. 1991, ApJ, 377, 712

Lamb, F. K. & ter Haar, D. 1971, Phys. Rep., 2, 253

Landi degl'Innocenti, E. & Landolfi, M. 2004, Polarization in Spectral Lines, Kluwer Academic Publ., Dordrecht

Manso Sainz, R. 2002, PhD Thesis, Scattering Line Polarization and the Hanle Effect in Weakly Magnetized Stellar Atmospheres, Universidad de la Laguna, Spain

Manso Sainz, R. & Trujillo Bueno, J. 2001, in M. Sigwarth (ed.), ASP Conf. Series 236, Advanced Solar Polarimetry: Theory, Observation and Instrumentation, 213

Manso Sainz, R. & Trujillo Bueno, J. 2003a, Phys. Rev. Lett., 91, 111102

Manso Sainz, R. & Trujillo Bueno, J. 2003b, in J. Trujillo Bueno, J. Sánchez Almeida (eds.), ASP Conf. Ser. 307, Solar Polarization 3, 251

Shine, R. A. & Linsky, J. L. 1974, Solar Phys., 39, 49

Socas-Navarro, H., Trujillo Bueno, J., & Ruiz Cobo, B. 2000, ApJ, 530, 977

Stenflo, J.O., Keller, C.U., & Gandorfer, A. 2000, A&A, 355, 789

Stenflo, J.O., Twerenbold, D., Harvey, J. W., & Brault, J. W. 1983, A&AS, 54, 505

Trujillo Bueno, J. 1999, in K.N. Nagendra, J.O. Stenflo (eds.), Kluwer Astrophys. Space Sci. Library 243, Solar Polarization 2, 73

Trujillo Bueno, J. 2003, in I.Hubeny, D. Mihalas, & K. Werner (eds.), ASP Conf. Series 288, Stellar Atmospheres Modeling, 551

The Physics of Chromospheric Plasmas
ASP Conference Series, Vol. 368, 2007
Petr Heinzel, Ivan Dorotovič and Robert J. Rutten, eds.

The Magnetic Field of Solar Chromospheric Spicules

J. Trujillo Bueno[1,2], R. Ramelli[3], L. Merenda[1] and M. Bianda[3]

[1] *Instituto de Astrofísica de Canarias, La Laguna, Tenerife, Spain*
[2] *Consejo Superior de Investigaciones Científicas, Spain*
[3] *Istituto Ricerche Solari Locarno, Locarno Monti, Switzerland*

Abstract. A suitable diagnostic tool for investigating the magnetism of the solar chromosphere is the observation and theoretical modeling of the Hanle and Zeeman effects in solar spicules. In our presentation we highlighted the great scientific interest of this new diagnostic window by showing how the magnetic field vector can be inferred from spectropolarimetric observations of solar chromospheric spicules in several spectral lines, such as those of the 10830 Å and 5876 Å multiplets of neutral helium. Our off-limb spectropolarimetric observations of the He I 10830 Å multiplet were obtained with the Tenerife Infrared Polarimeter (TIP) attached to the Vacuum Tower Telescope at the Observatorio del Teide (Tenerife), while those of the 5876 Å multiplet resulted from observations with the Zurich Imaging Polarimeter (ZIMPOL) at the Gregory Coudé Telescope of the Istituto Ricerche Solari Locarno. The application of a Stokes profiles inversion technique led to the following conclusion. In quiet Sun spicules the magnetic field vector at a height of about 2000 km above the solar visible "surface" has a typical strength of the order to 10 G and is inclined by approximately 35° with respect to the solar local vertical direction. In spicules observed close to active regions the strength of the magnetic field was of the order of 50 G. The two figures below show the off-limb Stokes profiles of the He I 5876 Å multiplet observed in a quiet region (upper figure) and close to an active region (lower figure). Note that in both cases Stokes U is non-zero, which is the observational signature of the Hanle effect of an inclined magnetic field. The change of sign in Stokes U along the spatial direction of the spectrograph's slit can be explained by variations in the azimuth of the magnetic field vector. Interestingly, while the Stokes V profiles corresponding to the observed quiet region are caused by the alignment-to-orientation transfer mechanism (see, e.g., page 607 of Landi Degl'Innocenti & Landolfi 2004), that observed in the spicules close to the active region is dominated by the longitudinal Zeeman effect. The interested reader will find more information in the papers by Trujillo Bueno et al. (2005) and by Ramelli et al. (2006).

References

Landi Degl'Innocenti E., Landolfi M., 2004, Polarization in Spectral Lines, Kluwer Academic Publishers

Ramelli R., Bianda, M., Merenda, L., Trujillo Bueno, J. 2006, in R. Casini, B. W. Lites (eds.), Solar Polarization 4, ASP Conf. Series, Vol. 358, in press

Trujillo Bueno J., Merenda L., Centeno R., Collados M., Landi Degl'Innocenti E., 2005, ApJ 619, L191

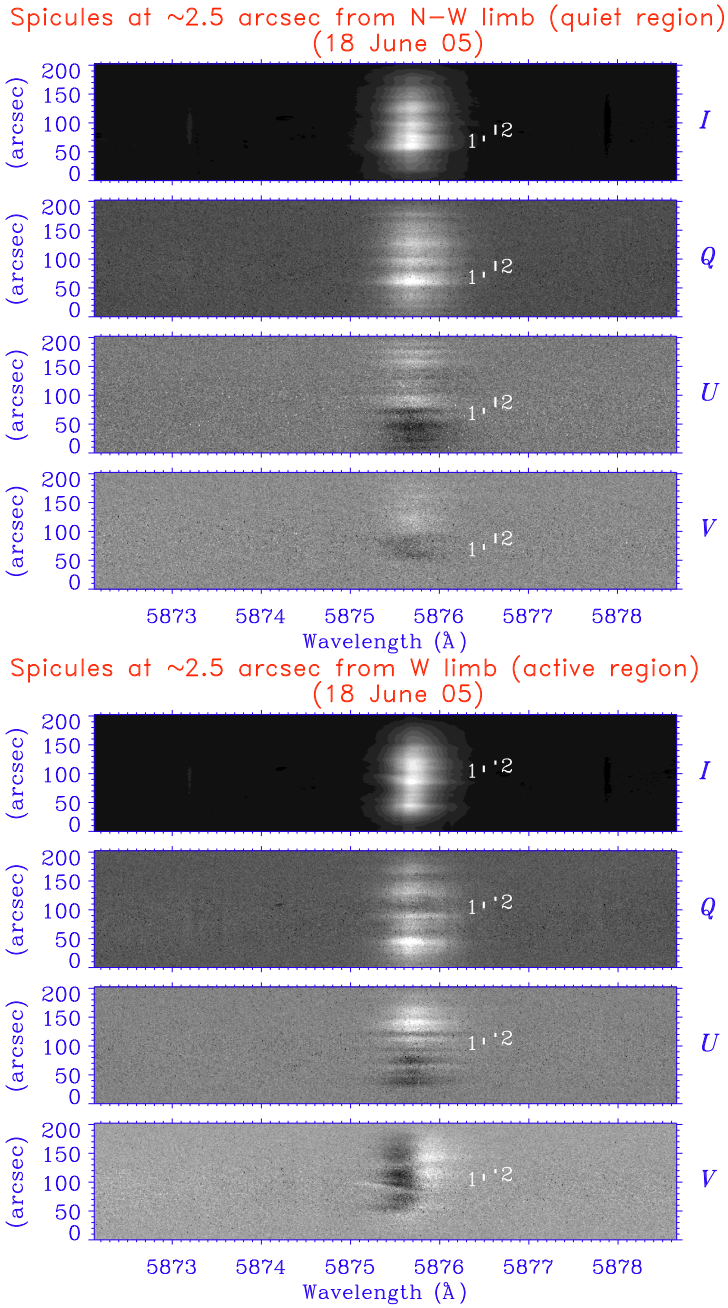

Figure 1. Illustrative examples of the off-limb Stokes profiles of the He I 5876 Å multiplet observed in a quiet region (upper four panels) and close to an active region (lower four panels). The slit was parallel to the solar limb, at 2.5 arcsec from the visible limb (as seen in the slit-jaw image). Note the fine structure along the slit. The reference direction for Stokes Q is the parallel to the solar limb.

The Physics of Chromospheric Plasmas
ASP Conference Series, Vol. 368, 2007
Petr Heinzel, Ivan Dorotovič and Robert J. Rutten, eds.

A User-Friendly Code to Diagnose Chromospheric Plasmas

A. Asensio Ramos[1] and J. Trujillo Bueno[1,2]

[1] *Instituto de Astrofísica de Canarias, La Laguna, Spain*
[2] *Consejo Superior de Investigaciones Científicas, Spain*

Abstract. The physical interpretation of spectropolarimetric observations of lines of neutral helium, such as those of the 10830 Å multiplet, represents an excellent opportunity for investigating the magnetism of plasma structures in the solar chromosphere. Here we present a powerful forward modeling and inversion code that permits either to calculate the emergent intensity and polarization for any given magnetic field vector or to infer the dynamical and magnetic properties from the observed Stokes profiles. This diagnostic tool is based on the quantum theory of spectral line polarization, which self-consistently accounts for the Hanle and Zeeman effects in the most general case of the incomplete Paschen-Back effect regime. We also take into account radiative transfer effects. An efficient numerical scheme based on global optimization methods has been applied. Our Stokes inversion code permits a fast and reliable determination of the global minimum.

1. Introduction

The quality of spectropolarimetric observations of solar chromospheric plasmas is steadily increasing. However, in order to obtain reliable empirical information on the strength and geometry of the magnetic field vector we also need to develop and apply suitable diagnostic tools within the framework of the quantum theory of spectral line polarization (e.g., the recent monograph by Landi Degl'Innocenti & Landolfi 2004). In particular, the development of a forward modeling and inversion code of Stokes profiles is of great importance because it would facilitate the investigation of a variety of problems of great astrophysical interest. For such a diagnostic tool to be reliable, it has to include all the important physical mechanisms that induce spectral line polarization in stellar atmospheres (e.g., the recent review by Trujillo Bueno 2006). Not only the Zeeman effect, but also the atomic level polarization induced by anisotropic radiation pumping and its modification by the Hanle effect have to be taken into account. For a remarkable example of a pioneering work in this field see Landi Degl'Innocenti (1982).

One of the main motivations of our investigation has been to develop a robust but user-friendly computer program for facilitating the analysis of the polarization signals induced by the above-mentioned physical mechanisms in the spectral lines of the He I 10830 Å multiplet, which are sensitive to both the Zeeman effect and to the presence of atomic level polarization (Trujillo Bueno et al. 2002; Trujillo Bueno & Asensio Ramos 2007). Spectro-polarimetric observations of this multiplet have been carried out in a variety of plasma structures of the solar chromosphere and corona, such as sunpots (Harvey & Hall

1971; Rüedi et al. 1995; Centeno et al. 2006), coronal filaments (Lin et al. 1998; Trujillo Bueno et al. 2002), prominences (Trujillo Bueno et al. 2002; Merenda et al. 2006), emerging magnetic flux regions (Solanki et al. 2003; Lagg et al. 2004), chromospheric spicules (Trujillo Bueno et al. 2005), active region filaments (Martínez Pillet et al. 2007; in preparation) and flaring regions (Sasso et al. on p. 467 ff of these proceedings).

2. The Forward Modeling Option

The adopted atomic model includes the following five terms of the triplet system of He I: $2s^3S$, $2p^3P$, $3s^3S$, $3s^3P$ and $3d^3D$. It has been concluded that this 11 J-levels model with 6 radiative transitions between the terms is enough for a satisfactory modeling of the polarization properties of the spectral lines of the He I D_3 multiplet at 5876 Å (Bommier 1977; Landi Degl'Innocenti 1982), and it should be also a reasonable approximation for those of the He I 10830 Å multiplet which result from transitions between the terms $2s^3S$ and $2p^3P$.

It is well-known that the He I atom can be correctly described by the L-S coupling scheme (e.g., Condon & Shortley 1935). The different J-levels are grouped in terms with well defined values of the electronic angular momentum L and the spin S. The energy separation between the J-levels inside each term is very small in comparison with the energy difference between different terms. Therefore, in addition to the atomic polarization of each J-level (population imbalances and coherences between its magnetic substates), it turns out to be fundamental to allow for coherences between different J-levels pertaining to the same term. However, coherences between different J-levels pertaining to different terms can be safely neglected. In conclusion, we can describe the atom via the formalism of the multi-term atom (see Sections 7.5 and 7.6 of Landi Degl'Innocenti & Landolfi 2004).

The atomic level polarization is quantified by the multipole components, $\rho^K_Q(J, J')$, of the atomic density matrix (Landi Degl'Innocenti & Landolfi 2004). The number of real quantities required to describe the excitation state of our multi-term model atom is 405. The helium atoms are illuminated by the (given) anisotropic radiation field coming from the underlying solar photosphere (Pierce 2000), whose properties are quantified by two spherical tensors: J^0_0 and J^2_0 (see Eq. 5.164 in Landi Degl'Innocenti & Landolfi 2004). They describe the mean intensity and the "degree of anisotropy" of the radiation field, respectively. We also consider that a magnetic field $\mathbf{B}$ is present, with strength B, inclination θ_B with respect to the local vertical and azimuth χ_B. The density matrix elements are obtained by solving the statistical equilibrium equations (see Section 7.6a of Landi Degl'Innocenti & Landolfi 2004), which take into account the effect of the radiative transitions in the presence of the Zeeman splittings produced by the assumed magnetic field vector.

Once the elements of the atomic density matrix are known, the coefficients of the emission vector and of the propagation matrix of the Stokes-vector transfer equation can be directly calculated (see Section 7.6b of Landi Degl'Innocenti & Landolfi 2004). The next step is to compute the emergent Stokes profiles by solving the Stokes-vector transfer equation. To this aim, our code includes several options. The simplest one assumes that the emergent Stokes profiles are

simply proportional to the corresponding emissivity. This optically-thin case is representative of the conditions found in some prominences. The second option assumes that the He I atoms are located in a slab of constant physical properties characterized by a non-negligible optical depth $\Delta\tau$ and that magneto-optical effects are negligible (see Trujillo Bueno et al. 2005 for the analytical expressions of the emergent Stokes profiles). Finally, the most general radiative transfer option is accomplished by using the DELOPAR method (Trujillo Bueno 2003).

Following the previously described approach, we have developed an efficient computer program that we have combined with an easy-to-use interactive front-end. It allows to interactively select the physical effects to be taken into account, thus helping to achieve a fast and reliable investigation of the influence of various physical parameters on the emergent Stokes parameters (for a first application, see Trujillo Bueno & Asensio Ramos 2007). For instance, our code allows to include or discard the effect of the magneto-optical terms and/or stimulated emission processes. Furthermore, it is possible to carry out the forward modeling including or neglecting the presence of atomic polarization. When atomic polarization is not taken into account, the problem reduces to the simplified case of the Zeeman effect, but with the positions and strengths of the σ and π components calculated within the framework of the incomplete Paschen-Back effect theory. This is important for the He I 10830 Å multiplet because the linear Zeeman effect theory underestimates the inferred magnetic field strength (Socas-Navarro et al. 2004). In the absence of atomic level polarization, the emergent spectral line radiation is polarized due to the non-zero magnetic splitting produced by the presence of the magnetic field. For completeness, the Milne-Eddington solution of the radiative transfer equation can also be used in this case. By default, the total Hamiltonian (including the fine structure and magnetic contributions) is diagonalized numerically. However, our code also permits to calculate the emergent Stokes profiles assuming the linear Zeeman regime, which is useful in order to compare with those calculated within the framework of incomplete Paschen-Back theory.

3. The Stokes Inversion Option

The previously described forward modeling code has been also combined with a robust inversion scheme. The inversion algorithm is based on the minimization of a merit function that describes how well our model reproduces the observed Stokes profiles. This merit function is chosen to be the standard χ^2–function (least square method). The minimization algorithm tries to find the value of the model's parameters that lead to synthetic Stokes profiles in closest agreement with the observed ones (i.e., to those that imply the smallest value of the merit function). The model's parameters are the magnetic field vector $\mathbf{B}$, the thermal velocity $v_{\rm th}$, the macroscopic velocity $v_{\rm mac}$ and the damping of the line a. If radiative transfer effects are taken into account, this set is augmented with the optical depth of the slab ($\Delta\tau$).

The standard Levenberg-Marquardt (LM) procedure for the minimization of the χ^2 function has been used. The LM method is one of the fastest and simplest available methods when the initial estimation of the parameters is close to the correct minimum. On the contrary, like with the majority of the standard

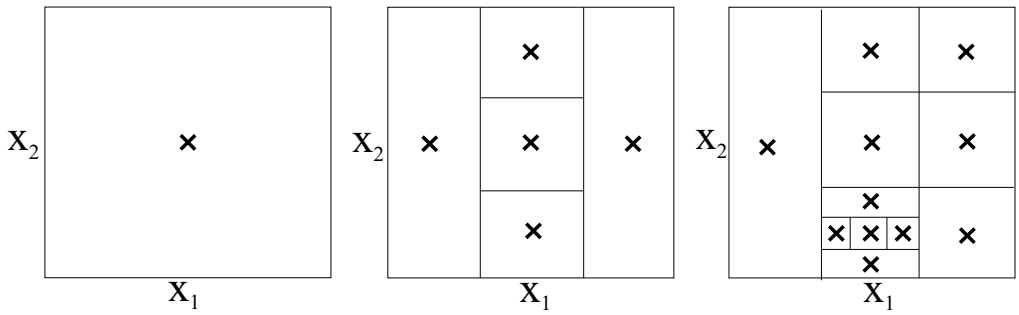

Figure 1. This figure illustrates the philosophy of the DIRECT method for searching for the region where the global minimum is located. In this case, we illustrate a case in two dimensions. After the evaluation of the function at some selected points inside each region, the DIRECT algorithm decides, using the Lipschitz condition, which rectangles can be further subdivided because they are potentially interesting. The method rapidly locates the region where the minimum is located.

numerical methods for function minimization, its main drawback is that it can easily get trapped in a local minimum of the χ^2 function. A straightforward but time consuming strategy to overcome this difficulty is to restart the minimization process with different values of the initial parameters.

In our case, this difficulty has been overcome by using global optimization methods (GOM) that provide a good starting point. The majority of this type of methods are based on stochastic optimization techniques. The key idea is to efficiently sample the whole space of parameters to find the global minimum of a given function. One of the most promising methods is genetic optimization. In spite of the lack of a convergence theorem, they perform quite well in practice (e.g., Lagg et al. 2004). In our case, we propose to apply instead the DIRECT deterministic method that relies on a strong mathematical basis. The name stands for "DIviding RECTangles" (Jones et al. 1993) and the idea is to recursively sample parts of the space of parameters, locating in each iteration the part of the space where the global minimum is potentially located. The decision algorithm is based on the assumption that the function is Lipschitz continuous. For clarifying purposes, consider the case of a one-dimensional function $f : M \rightarrow R$. It is said to be Lipschitz continuous with constant α in an interval $M = [a, b]$ if:

$$|f(x) - f(x')| \leq \alpha |x - x'|, \qquad \forall x, x' \in M. \tag{1}$$

In particular, a consequence of the previous equation is that the two following equations have to be fulfilled $\forall x \in M$:

$$f(x) \geq f(a) - \alpha(x - a) \tag{2}$$
$$f(x) \geq f(b) + \alpha(x - b). \tag{3}$$

These two straight lines form a V-shape below the function $f(x)$ whose intersection provides a first estimation x_1 of the minimum of the function. Repetition of this procedure in the two new subintervals $[a, x_1]$ and $[x_1, b]$ leads to new estimations x_i that converge to the global minimum. Severe problems arise when

Step	Method	Free parameters	Stokes profiles
1	DIRECT	$v_{\rm th}$, $v_{\rm mac}$, $\Delta\tau$, a	I
2	LM	$v_{\rm th}$, $v_{\rm mac}$, $\Delta\tau$, a	I
3	DIRECT	B, θ_B, χ_B	I, Q, U, V
4	LM	B, θ_B, χ_B	I, Q, U, V

Table 1. Scheme applied for the inversion of the Stokes profiles. The two DIRECT cycles are used for obtaining an initial value of the parameters as close to the global minimum as possible. This is accomplished by the fast global convergence of DIRECT. Then, a few LM iterations are sufficient to rapidly refine the value of the minimum.

generalizing this method to higher dimensions because of the difficulty in estimating the Lipschitz constant. Actually, the function is often not Lipschitz continuous. The DIRECT algorithm overcomes these problems because it does not require knowledge of the Lipschitz constant. It uses all possible values of such a constant to determine if a region of the space of parameters should be broken into subregions because of its potential interest. Fig. 1 shows a schematic illustration of the subdivision process for a function of two parameters.

One of the main drawbacks of deterministic global optimization methods is that they present a very good global convergence but a poor local convergence. Therefore, they quickly locate the region of the space of parameters where the global minimum is located, but the refinement of this solution takes a very long time. Consequently, the DIRECT method is a perfect candidate for its application as an estimator of the initial value of the parameters that are then rapidly refined by the LM algorithm. Since the initial point is very close to the minimum, the LM method, thanks to the quadratic convergence behavior, takes a few iterations to rapidly converge towards the global minimum. We have confirmed that this scheme reduces the number of evaluations of the merit function. It is important to point out that, because the most time-consuming part of the optimization procedure is the evaluation of the complex forward problem (with the solution of the statistical equilibrium equations and the radiative transfer), it is fundamental to minimize the number of merit function evaluations.

A critical and fundamental point in the optimization of functions is the stopping criterion. In the few (unrealistic) cases where the value of the function at the global minimum is known (noise-free cases), it is possible to stop the convergence process when the relative error is smaller than a fixed value. In the general case with DIRECT, very good results are obtained when the hypervolume (in the parameter space) where the algorithm is looking for the global minimum has been reduced by a given factor, $f \approx 0.001$, with respect to the original hypervolume. Another possible option is to stop after a fixed number of evaluations of the merit function.

The full inversion scheme, shown schematically in Table 1, is started with the DIRECT method to obtain a first estimation of the thermodynamical parameters by using only Stokes I. After this initialization, some iterations of the LM method are carried out to refine the initial values of the thermodynamical parameters obtained in the previous step. Once the LM method has converged, the inferred values of $v_{\rm th}$, $v_{\rm mac}$, and a (and $\Delta\tau$ when it applies) are kept fixed.

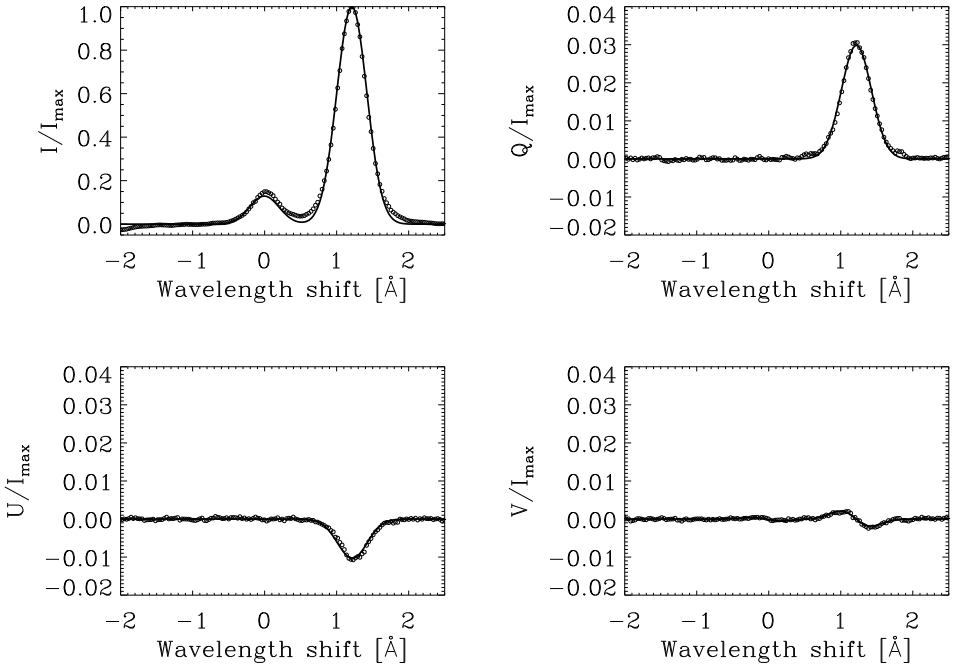

Figure 2. Example of the best theoretical fit obtained with the inversion code to the observed profiles presented in Merenda et al. (2006). The emergent Stokes profiles have been obtained by assuming an optically thin plasma. The inferred magnetic field vector is given by $B = 26.8\,\mathrm{G}$, $\theta_B = 25.5°$ and $\chi_B = 161°$. Furthermore, the inferred thermal velocity is $v_{\mathrm{th}} = 7.97$ km s^{-1}. All these values are in close agreement with the results obtained by Merenda et al. (2006). The positive direction of Stokes Q is the one parallel to the solar limb.

In a next step, the DIRECT method is used again for the initialization of the magnetic field vector (B, θ_B and χ_B). According to our experience, the first estimation of the magnetic field vector given by the DIRECT algorithm is typically very close to the final solution. As a final step, some iterations of the LM method are performed to refine the value of the magnetic field strength, inclination and azimuth until reaching the global optimum. Obviously, if any parameter is known in advance, we can keep it fixed during the whole inversion process.

4. Illustrative Applications

Here we have only space to demonstrate the application of this new plasma diagnostic tool to the case of a prominence and to that of an emerging magnetic flux region. For more details and applications see Asensio Ramos & Trujillo Bueno (in preparation).

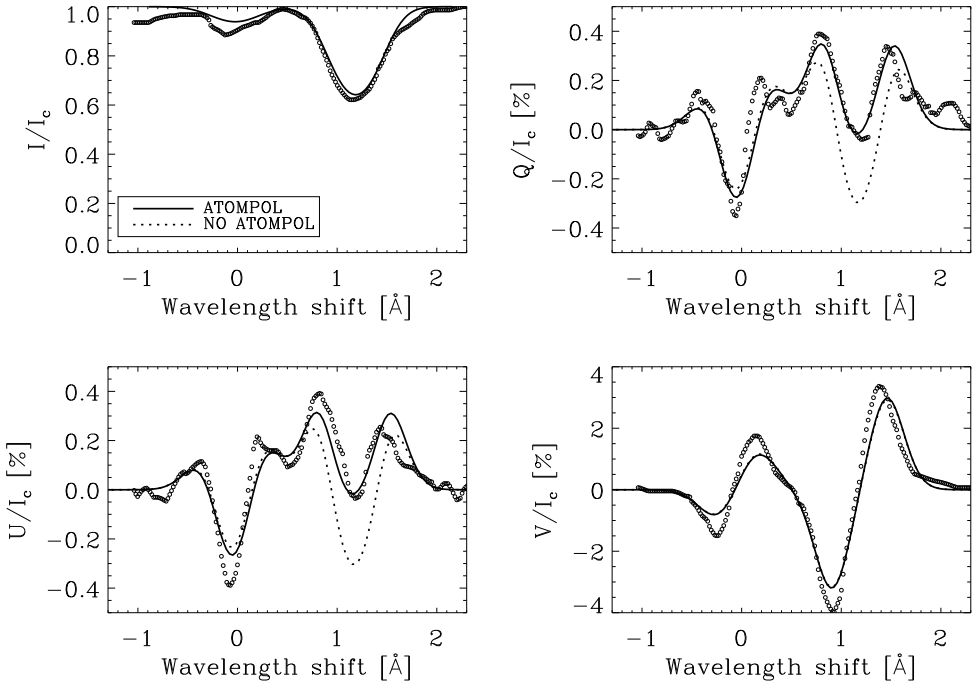

Figure 3. Emergent Stokes profiles of the He I 10830 Å multiplet in an emerging flux region. The circles represent the observations shown by Lagg et al. (2004) in their Fig. 2. The dotted lines present the best theoretical fit obtained neglecting the influence of atomic level polarization, which corresponds to $B = 1070\,\mathrm{G}$, $\theta_B = 86°$ and $\chi_B = -160°$. On the contrary, the solid lines show the best fit when the effect of atomic level polarization is included, giving $B = 1009\,\mathrm{G}$, $\theta_B = 91°$ and $\chi_B = -161°$. The best fit to the observations is provided by the solid lines, which indicates the presence of atomic level polarization in a relatively strong field region.

4.1. A polar crown prominence

For illustrative purposes, we have applied our inversion code to infer the magnetic field vector of the polar crown prominence that generated the Stokes profiles presented in Fig. 9 of Merenda et al. (2006). We have assumed that the prominence plasma was optically thin. Our inversion code was used to infer the value of the thermal velocity $v_{\rm th}$ and the magnetic field vector (B, θ_B, χ_B). The height of the prominence atoms was fixed at $h = 20''$, the same value used by Merenda et al. (2006). After the four steps summarized in Table 1, we ended up with a thermal velocity of $v_{\rm th} = 7.97$ km s^{-1} and a magnetic field vector characterized by $B = 26.8\,\mathrm{G}$, $\theta_B = 25.5°$, and $\chi_B = 161.0°$. The inferred magnetic field vector is in very good agreement with that obtained by Merenda et al. (2006), namely $B = 26\,\mathrm{G}$, $\theta_B = 25°$, and $\chi_B = 160.5°$. Therefore, we fully support their conclusion of nearly-vertical fields in the observed polar-crown prominence.

4.2. An emerging Magnetic flux region

As pointed out by Trujillo Bueno & Asensio Ramos (2007), the modeling of the emergent Stokes Q and U profiles of the He I 10830 Å multiplet should be done by taking into account the possible presence of atomic level polarization, even for magnetic field strengths as large as 1000 G. An example of a spectropolarimetric observation of an emerging magnetic flux region is shown by the circles of Fig. 3. The solid lines show the best theoretical fit to these observations of Lagg et al. (2004). Here, in addition to the Zeeman effect, we took into account the influence of atomic level polarization. The dotted lines neglect the atomic level polarization that is induced by anisotropic radiation pumping in the solar atmosphere. Our results indicate the presence of atomic level polarization in a relatively strong field region ($\sim$1000 G). However, it may be tranquilizing to point out that both inversions of the observed profiles yield a similar magnetic field vector, in spite of the fact that the corresponding theoretical fit is much better for the case that includes atomic level polarization.

Acknowledgments. We would like to thank Egidio Landi Degl'Innocenti for sharing with us his deep knowledge on the physics of spectral line polarization. This research has been funded by the Spanish Ministerio de Educación y Ciencia through project AYA2004-05792.

References

Bommier V., 1977, Thèse de 3ème Cycle, Université de Paris VI
Centeno R., Collados M., Trujillo Bueno J., 2006, ApJ 640, 1153
Condon E. U., Shortley G. H., 1935, The Theory of Atomic Spectra, Cambridge University Press, Cambridge
Harvey J., Hall D., 1971, in R. Howard (ed.), IAU Symp. 43: Solar Magnetic Fields, 279
Jones D. R., Perttunen C. D., Stuckmann B. E., 1993, Journal of Optimization Theory and Applications 79, 157
Lagg A., Woch J., Krupp N., Solanki S. K., 2004, A&A 414, 1109
Landi Degl'Innocenti E., 1982, Solar Phys. 79, 291
Landi Degl'Innocenti E., Landolfi M., 2004, Polarization in Spectral Lines, Kluwer, Dordrecht
Lin H., Penn M. J., Kuhn J. R., 1998, ApJ 493, 978
Merenda L., Trujillo Bueno J., Landi Degl'Innocenti E., Collados M., 2006, ApJ 642, 554
Pierce K., 2000, in Allen's Astrophysical Quantities, ed. A. N. Cox, Springer Verlag and AIP Press, New York
Rüedi I., Solanki S. K., Livingston W., Harvey J., 1995, A&AS 113, 91
Socas-Navarro H., Trujillo Bueno J., Landi Degl'Innocenti E., 2004, ApJ 612, 1175
Solanki S. K., Lagg A., Woch J., Krupp N., Collados M., 2003, Nat 425, 692
Trujillo Bueno J., 2003, in I. Hubeny, D. Mihalas, K. Werner (eds.), Stellar Atmosphere Modeling, ASP Conf. Ser. 288, 551
Trujillo Bueno J., 2007, in R. Ramelli, O. Shalabiea, I. M. Saleh, J. O. Stenflo (eds.), Int. Symp. on Solar Physics and Solar Eclipses, Sebha University Publ., Sebha, Libya, 77
Trujillo Bueno J., Asensio Ramos A., 2007, ApJ 655, 642
Trujillo Bueno J., Landi degl'Innocenti E., Collados M., Merenda L., Manso Sainz R., 2002, Nat 415, 403
Trujillo Bueno J., Merenda L., Centeno R., Collados M., Landi Degl'Innocenti E., 2005, ApJ 619, L191

The Physics of Chromospheric Plasmas
ASP Conference Series, Vol. 368, 2007
Petr Heinzel, Ivan Dorotovič and Robert J. Rutten, eds.

Multi-wavelength Analysis of a Quiet Solar Region

G. Tsiropoula[1], K. Tziotziou[1], J. Giannikakis[1], P. Young[2], U. Schühle[3] and P. Heinzel[4]

[1]*Institute for Space Applications and Remote Sensing, Athens, Greece*
[2]*CCLRC Rutherford Appleton Laboratory, United Kingdom*
[3]*MPI für Sonnensystemforschung, Katlenburg-Lindau, Germany*
[4]*Astronomical Institute AS, Ondřejov, Czech Republic*

Abstract. We present observations of a solar quiet region obtained by the ground-based Dutch Open Telescope (DOT), and by instruments on the spacecraft SOHO and TRACE. The observations were obtained during a coordinated observing campaign on October 2005. The aim of this work is to present the rich diversity of fine-scale structures that are found at the network boundaries and their appearance in different instruments and different spectral lines that span the photosphere to the corona. Detailed studies of these structures are crucial to understanding their dynamics in different solar layers, as well as the role such structures play in the mass balance and heating of the solar atmosphere.

1. Introduction

In the quiet regions of the solar surface the magnetic field is mainly concentrated at the boundaries of the network cells. Over the past decade, apart from the well-known mottles and spicules, several other structures residing at the network boundaries such as explosive events, blinkers, network flares, upflow events have been mentioned in the literature. However, their interpretation, inter-relationship and their relation to the underlying photospheric magnetic concentrations remain ambiguous, because the same feature has a different appearance when observed in different spectral lines and by different instruments. For most of the events mentioned above magnetic reconnection is suggested as the driving mechanism. This is not surprising, since it is now well established from investigations of high resolution magnetograms, that new bipolar elements emerge continuously inside the cell interiors and are, subsequently, swept at the network boundaries by the supergranular flow (Wang et al. 2006; Schrijver et al. 1997). Interactions of the magnetic fields have as a result either the enhancement of the flux concentration in the case of same polarities or its cancellation in the case of opposite polarities. Observations support the idea that flux cancellation most likely invokes magnetic reconnection. In this context, the study and comprehension of the dynamical behaviour of the different fine-scale structures is crucial to the understanding of the dynamics of the solar atmosphere.

In this work we present observations of a solar quiet region and some of the properties of several different structures appearing at the network boundaries and observed in different wavelengths by the different instruments involved in a coordinated campaign.

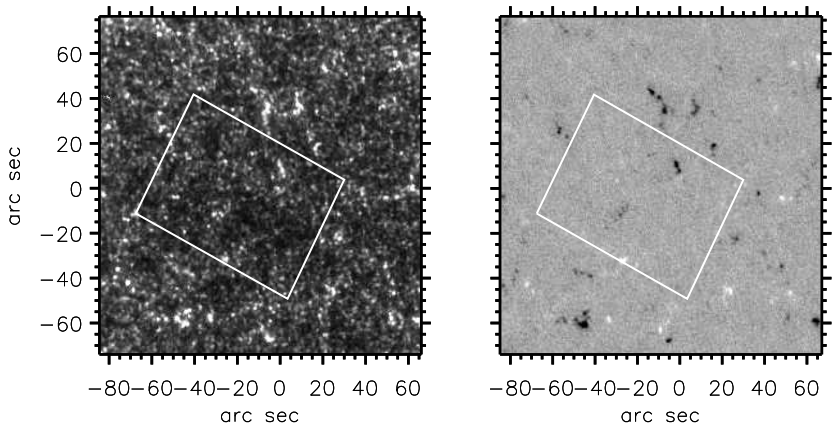

Figure 1. *Left*: C IV TRACE image. *Right*: MDI magnetogram. The white rectangle inside the images marks the DOT's field-of-view.

2. Observations and Data Reduction

In October 2005 we ran a 12 days observational campaign. The aim of that campaign was the collection of multi-wavelength observations both from the ground and space that could be used for the study of the dynamical behaviour of mottles/spicules and other fine structures, observed in different layers of the solar atmosphere.

Three ground-based telescopes were involved in that campaign: DOT on La Palma, THEMIS on Tenerife and SOLIS at Kitt Peak. From space telescopes two spacecraft were involved: SOHO (with CDS, SUMER, and MDI) and TRACE.

The analysed data were obtained on October 14 and consist of time sequences of observations of a quiet region found at the solar disk center recorded by different instruments. Sequences recorded by the DOT were obtained between 10:15:43 – 10:30:42 UT and consist of 26 speckle reconstructed images taken simultaneously at a cadence of 35 s with a pixel size of 0.071″ in 5 wavelengths along the Hα line profile (i.e. at -0.7 Å, -0.35 Å, line centre, 0.35 Å and 0.7 Å), in the G band with a 10 Å filter, in the Ca II H line taken with a narrow band filter and in the blue and red continuum. TRACE obtained high cadence filter images at 1550 Å, 1600 Å and 1700 Å. SUMER obtained raster scans and sit-and-stare observations from 8:15 to 10:30 UT. CDS obtained sit-and-stare observations from 6:44 to 10:46 UT and six 154″ × 240″ raster scans (each one having a duration of 30 min) from 10:46 to 13:52 UT. Both SOHO instruments (i.e., CDS and SUMER) observed in several spectral lines spanning the upper solar atmosphere. Using the standard software the raw measurements were corrected for flat field, cosmic rays and other instrumental effects. A single Gaussian with a linear background and Poisson statistics were used for fitting each spectral line profile. MDI obtained high cadence images at its high resolution mode.

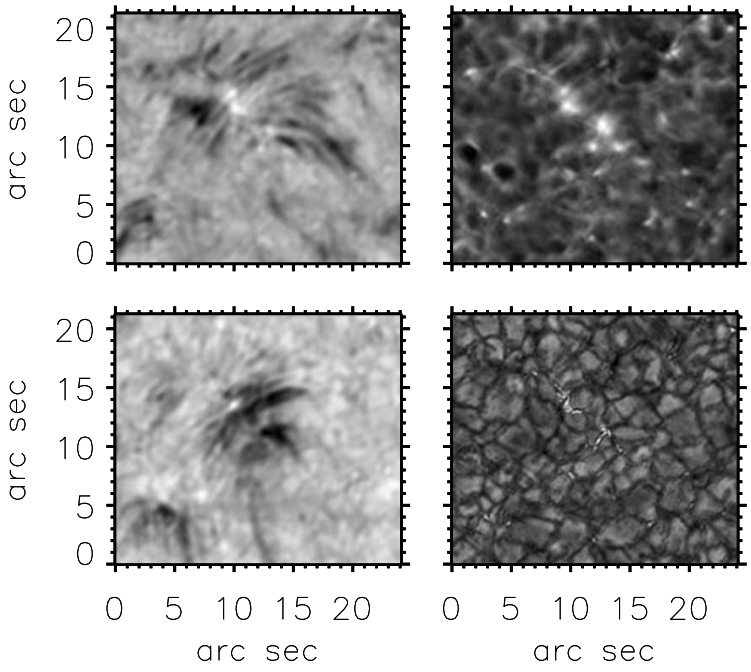

Figure 2. DOT images of a rosette region. *Left*: Hα -0.7 Å (*first row*), Hα +0.7 Å (*second row*). *Right*: Ca II H (*first row*), G band (*second row*).

Extensive work went into collecting, scaling and co-aligning the various data sets to a common coordinate system (see Fig. 1 showing the coalignment of TRACE, MDI, and DOT images).

3. Analysis and Results

3.1. DOT observations

DOT's field-of-view (FOV) is 80″ in the X direction and 63″ in the Y direction. For the present study we selected a smaller region which contains a rosette with several mottles pointing to a common center (see Fig. 2) and is found at the middle upper part of the DOT's FOV. In the G-band image (Fig. 2, *right, second row*) isolated bright points show up in the regions of strong magnetic field as can be seen in the MDI image. These seem to be passively advected with the general granular flow field in the intergranular lanes. While we have not conducted an exhaustive study of bright point lifetimes we find that bright points can be visible from some minutes up to almost the entire length of the time series. In the contemporal Ca II H images (Fig. 2, *right, first row* bright points are less sharp due to strong scattering in this line and possibly due to increasing flux tube with height. Reversed granulation caused by convection reversal is obvious in this image.

In the H$\alpha - 0.7$ Å (Fig. 2, *left, first row*) the dark streaks are part of the elongated Hα mottles seen better at Hα line center. Some mottle endings appear

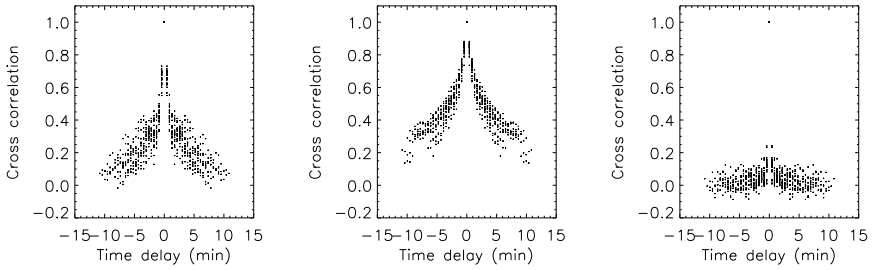

Figure 3. Cross correlation function vs time for *Left*: the intensity at H$\alpha -$ 0.7 Å, *Middle*: the intensity at Hα line center. *Right*: the velocity at H$\alpha -$ 0.7 Å.

extra dark in the blue wing image through Doppler blueshift. Near the mottle endings one can see bright points. These are sharper in the G-band but stand out much clearer in the Hα wing. Thus Hα wing represents a promising proxy magnetometer to locate and track isolated intermittent magnetic elements. This is because the Hα wing has a strong photospheric contribution, as it is shown by Leenaarts et al. (2006) who arrived to this conclusion by using radiative transfer calculations and convective simulations. In the H$\alpha + 0.7$ Å (Fig. 2, *left, second row*) dark streaks around the rosette's center are signatures of redshifts. Blueshifts in the outer endings and redshifts in the inner endings of mottles provide evidence for the presence of bi-directional flows along these structures.

An important parameter for the study of the dynamics of mottles is their velocity. For its determination, when filtergrams at two wavelengths of equal intensity at the blue and the red side of the line are available, a technique based on the subtraction of images can be used. In this technique, by using the well known representation of the line intensity profile and assuming a Gaussian wavelength dependence of the optical thickness, we can define the parameter DS:

$$DS = \frac{\Delta I}{\Sigma I - 2I_{0\lambda}}, \tag{1}$$

where $\Delta I = I(-\Delta\lambda) - I(+\Delta\lambda)$, $\Sigma I = I(-\Delta\lambda) + I(+\Delta\lambda)$ and $I_0(\Delta\lambda)$ is the reference profile emitted by the background. DS is called Doppler signal, has the same sign as the velocity and can be used for a qualitative description of the velocity field (for a description of the method see Tsiropoula 2000). When an optical depth less than one is assumed then quantitative values of the velocity can be obtained from the relation:

$$v = \frac{{\Delta\lambda_{\rm D}}^2}{4\Delta\lambda}\frac{c}{\lambda}\ln\frac{1+DS}{1-DS}, \tag{2}$$

since in that case the velocity depends only on DS (obtained from the observations) and the Doppler width, $\Delta\lambda_{\rm D}$ (obtained from the literature). By using these relations we have constructed 2-D intensity and velocity images for the whole time series. We found out that it is difficult to follow each one mottle for more than two or three frames and that the general appearance of the region

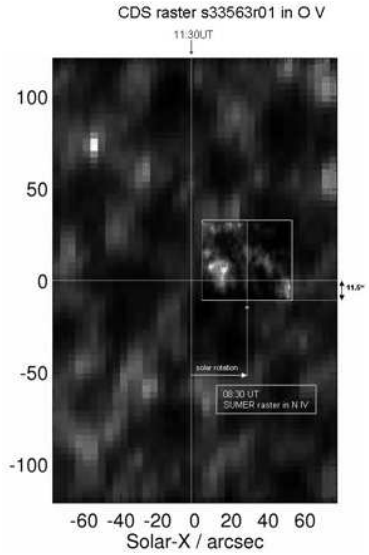

Figure 4. CDS raster image obtained at the O V 629.7 Å line with an overplotted SUMER image at Ne VIII 770 Å.

seems to change quite rapidly with time. For a quantitative estimate of the temporal changes we computed the value of the cross correlation (CC) function over the 2-D FOV both for the intensity and velocity. Figure 3 shows the intensity CC curve at H$\alpha - 0.7$ Å *(left)* and Hα line center *(middle)* and the velocity CC curve at H$\alpha \pm 0.7$ Å *(right)*. The decay of the CC curve is a measure of the lifetime of the structures. The e-folding time for the left curve is found equal to 2 min, the middle curve equal to 5 min and the right curve is of the order of the cadence.

3.2. CDS and SUMER observations

In Fig. 4 we show the CDS raster image obtained in the O V 629.7 Å line with the SUMER image at Ne VIII 770 Å overplotted. Although there is a time difference of 3 hours between the two images the network is constant enough to allowed the coalignement of the two images. In CDS intensity maps several brightenings are observed which are called blinkers (Harrison et al. 1999). These events are best observed in transition region lines and show an intensity increase of 60 - 80%. Most of them have a repetitive character and reappear at the same position several times.

In Fig. 5 (*left, up)* we show an integrated (over the spectral line with the background included) intensity image in the Ne VIII 770 Å line produced by sit-and-stare observations of a network region. The image is produced by binning over 6 spectra in order to improve the signal-to-noise ratio. The Doppler shift map was derived by applying a single Gaussian fitting (Fig. 5, *left, bottom*). The Doppler shift map and the spectral line profiles were visually inspected for any non-Gaussian profiles with enhancements in both the blue and red wings that are the main characteristics of the presence of bi-directional jets. Large numbers of such profiles were found at the network boundaries (Fig. 5, *right*).

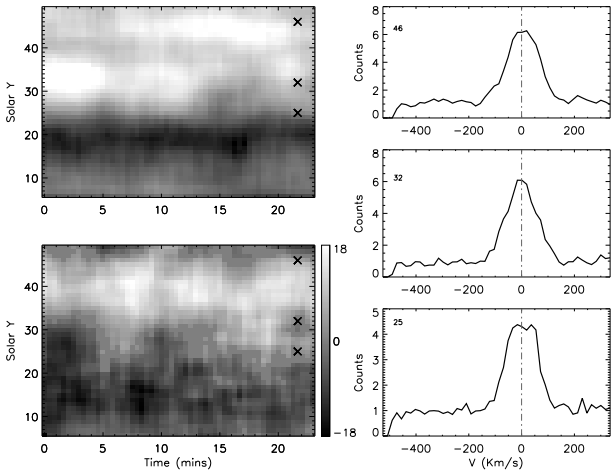

Figure 5. SUMER sit-and-stare observations in the Ne VIII line. *Left*: intensities (*up*), Doppler velocities (*bottom*) (network boundaries are bright in the intensity image). *Right*: non-Gaussian profiles in the positions marked by "x" inside the images in the left.

4. Conclusions

In this work we present observations of a quiet solar region obtained by different instruments in different spectral lines. Network boundaries are found to be the locus of several structures which have different appearances when observed by different instruments e.g., blinkers (when observed with CDS), mottles (when observed with DOT), jets (when observed with SUMER). Their interrelationship is to be further explored.

Regarding flows no-clear pattern is found in blinkers, while bi-directional flows are found in jets. In dark mottles downward velocities are found at their footpoints and upwards velocities at their upper parts and very fast changes in their appearance.

The network shows a remarkable constancy when observed in low resolution images. However when seen in high resolution images several fine structures are observed which change so fast that it is very hard to follow.

Acknowledgments. K. Tziotziou acknowledges support by Marie Curie European Reintegration Grant MERG-CT-2004-021626. This work has been partly supported by a Greek-Czech programme of cooperation.

References

Harrison, A., Lang, J., Brooks, D.H., & Innes, D.E. 1999, A&A, 351, 1115
Leenarts, J., Rutten, R.J., Sütterlin, P., Carlsson, M., & Uitenbroek H. 2006, A&A, 449, 1209
Schrijver, C.J., Title, A.M., Van Ballegooijen, A.A., Hagenaar, H.J., & Shine, R.A. 1997, ApJ, 487, 424
Tsiropoula, G. 2000, New Astronomy, 5, 1
Wang, H., Tang, F., Zirin, H., & Wang, J. 1996, Solar Phys. , 165, 223

The Physics of Chromospheric Plasmas
ASP Conference Series, Vol. 368, 2007
Petr Heinzel, Ivan Dorotovič and Robert J. Rutten, eds.

On the Dynamic Nature of the Prolate Chromosphere

Boris Filippov[1,2], Serge Koutchmy[2] and Jaime Vilinga[2]

[1]*IZMIRAN, Troitsk, Moscow Region, Russia*
[2]*Institut d'Astrophysique de Paris, CNRS and Univ. P.M.C., France*

Abstract. The upper edge of the solar chromosphere looks not like a perfect circle in some spectral lines. It is prolate in the South-North direction at the epoch of minimum solar activity and nearly spherically symmetrical at the maximum phase. We attribute the effect to the dynamical nature of the upper chromosphere, which consists of a large number of small cool jets (jetlets) ascending into the corona. A proposed simple geometric model can explain the effect of the prolateness of the solar chromosphere. Due to the dynamic nature of the solar atmosphere above the 2 Mm level, the magnetic field is considered to play a very important role in the density distribution with the height, guiding the mass flows along the field lines. The difference of the magnetic field topology in the polar and the equatorial regions leads to different heights of the chromospheric limb. We could not resolve a source region of an individual jetlet, however similar but larger structures are visible in EUV coronal lines. We present an example of the jet formation obtained by TRACE in the 171 Å channel. Field aligned motion arises above the null point created in the corona by the emerging magnetic bipole. The scale of bipole is large enough to recognize the saddle structure around the 3D null point in the TRACE images. We believe that similar but smaller processes could happen very often at smaller scale in the chromosphere near emerging magnetic ephemeral regions forming numerous jetlets of the upper chromosphere.

1. Introduction

Many past observations showed that at the epoch of solar minimum the extension of the chomosphere near the poles is systematically higher than at the equator (Secchi 1877; Fracastoro 1948) and modern precise measurements (Fig. 1) confirmed and substantiated these early suggestions (Johannesson & Zirin 2000; Auchere et al. 1998; Vilinga & Koutchmy 2005). The amount of prolateness depends on the amount of plasma that emits at the observed light. In the transition region (TR) resonance line of He II at 304 Å, the effect seems more prominent than in a chromospheric cool Balmer line like Hα of H I ($\sim$ 8000 K), because additional structures appear at TR temperatures higher up, especially over coronal holes (CH).

The upper part of the chromosphere is far from the static state. It consists of numerous thin jet-like structures filling magnetic flux tubes. High resolution images of the solar limb in Hα shows a "forest" of spike-like features. The highest of them are more straight and tilted to the vertical within the angle of 20-30°. In the lower part one can see a number of arches. We assume that the dynamical part of the solar atmosphere, being a mixture of moving up and down

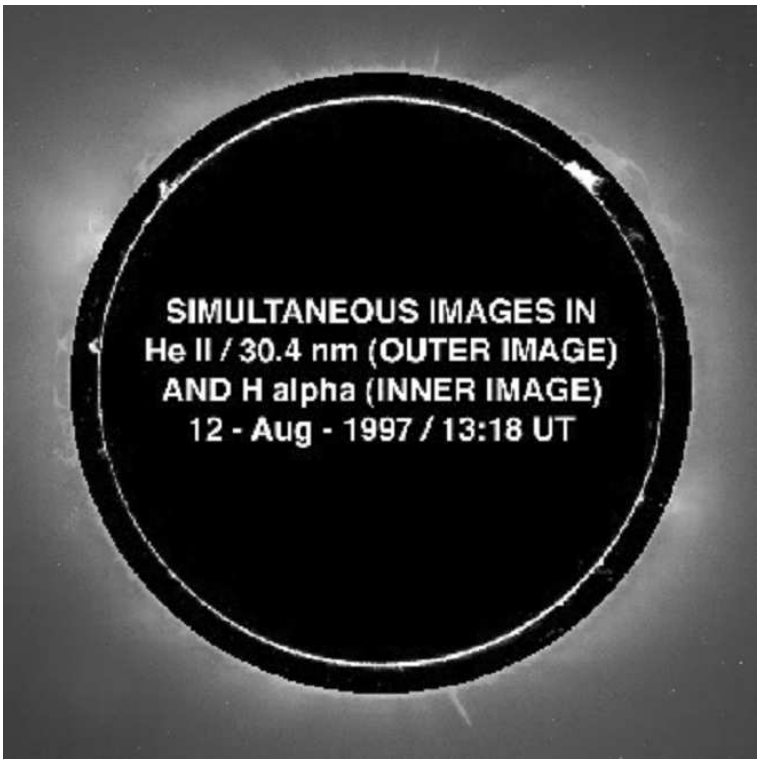

Figure 1. The shape of the solar chromosphere as observed in Hα and in He II emission (Koutchmy et al. 1998). A scale of the inner Hα image is a little bit smaller for an illustrative correlation of the images.

jets of chromospheric matter and coronal plasma between them, is responsible for the solar prolateness. Due to the dynamic nature of this layer, the magnetic field plays a very important role in the density distribution with respect to the height, guiding the mass flows along the field lines.

Network magnetic elements in polar regions are predominantly of the same polarity. In the quiet solar equatorial regions, they are of mixed polarity (Varsik et al. 1999; Belenko 2001). For ballistic jet motion (which is not exact for a large part of spicules but can be assumed as a first approximation), the maximal height of a spicule would be the same for all trajectories along the curved field lines if a line reaches this height. In the polar region all jets are able to ascend up to a gravitationally limited height. The mean density distribution in the upper polar chromosphere is determined by i) the scale height in an individual spicule and ii) the distribution of the number of spicules versus the height. In the equatorial region some jets will be forced to come down after they reach the apex of a relatively low arch. When considering the average over time heights reached by spicules, this factor will reduce the mean chromosphere density at a given height proportionally to the fall of the magnetic flux of one polarity:

$$\rho(z) = \rho_0 \left(\frac{\Phi(z)}{\Phi_0} \right) \exp\left(-\frac{z}{h} \right), \qquad (1)$$

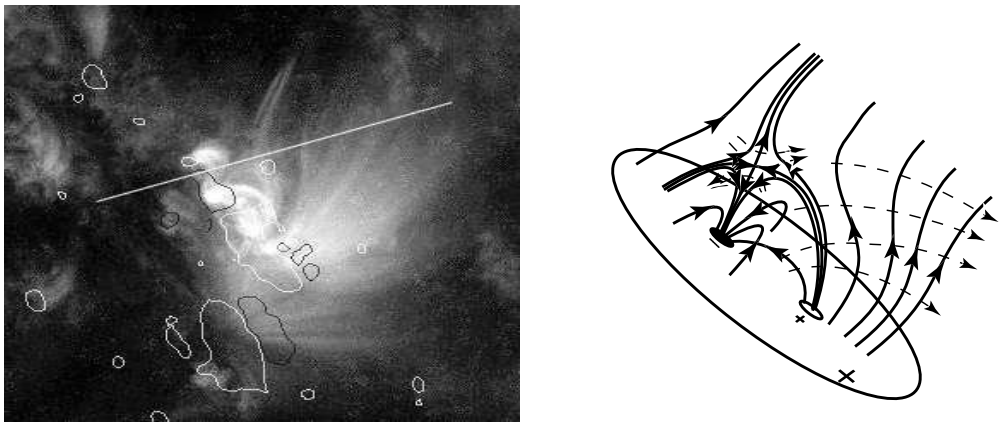

Figure 2. Magnetic field level +50 G contours overlapped on the 171 Å TRACE image. Positive polarities are shown by red areas and negative polarities are shown by blue areas. A straight white line shows the projection of the local vertical direction (left). A sketch of the 3D geometry of the magnetic field in the region of the jet formation. The dashed lines show the plasma displacement during the growth of the bipole (right).

where h is the effective scale height which is considerably larger than the 0.2 Mm hydrostatic scale height (Filippov & Koutchmy 2000).

2. A Small Jet in the Corona

Many jets are associated with emerging small flux regions that manifest themselves also as brightenings in chromospheric and coronal spectral lines. Such a new patch of parasitic polarity within a large-scale unipolar area, inevitably leads to the appearance of a new null point (X-point) in the chromosphere or corona (Filippov 1999). It is not trivial task to find real null points in the solar magnetic field. One can measure the magnetic field only on the photosphere level and only the line-of-sight component can be measured with satisfactory sensitivity and spatial resolution. These data are used to calculate the field above the photosphere by solving the boundary problem under current-free or force-free approximation. However, chromospheric and coronal plasmas filling the magnetic tubes visualise the magnetic field and one can find the specific saddle structures corresponding to the singular points.

We selected a clear observation of a jet formation above an X-point in the corona (Fig. 2). The event was observed by the Transition Region and Coronal Explorer (TRACE) camera on 3 October 2001. The cadence of TRACE images was about 20 s and all temporal changes within the saddle structure were clearly visible. A movie of the event can be found at the TRACE Web site in the collection of movies as the movie Nr. 50 from `http://vestige.lmsal.com/TRACE/Public/Gallery/Images/TRACEpod.html`.

The null point was created by an emerging nearly horizontal bipole and the ambient vertical magnetic field. The growth of the bipole leads to a reconnection of the field lines and to a specific plasma motion in the vicinity of the null point

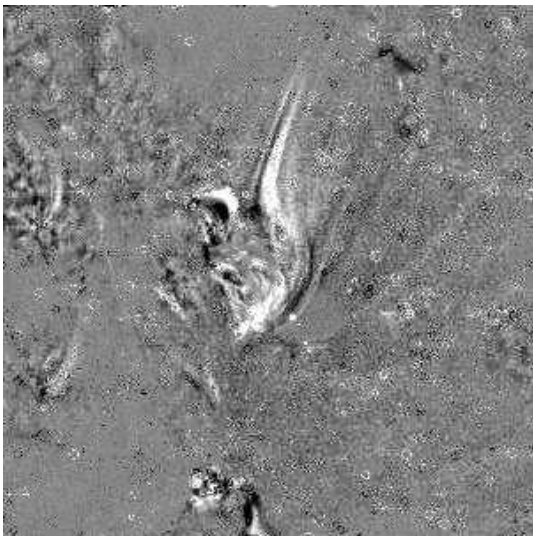

Figure 3. TRACE difference image (03:04:10 UT - 02:57:26 UT) showing the displacement in coronal loops and the formation of new ones.

that results in a plasma flow along the spine line of the 3D null. During the growth of the emerging bipole, nearly vertical field lines of the unipolar region should be rearranged coming from the left side of the bipole to the right side. Frozen-in plasma motion is shown by dashed lines in a sketch of the 3D geometry of the magnetic field in the right-hand part of Fig. 2. Some field lines pass through the reconnection in the X-point while most of them are able simply to flow around the null point (fan reconnection), what is impossible to represent in a 2D geometry (Priest & Titov 1996). Difference image (Fig. 3) obtained by subtracting the image at 02:57:26 UT from the image at 03:04:10 UT shows the changes in the location of the coronal loops and the formation of new ones.

The frozen-in plasma motion will evolve in accordance with the expression

$$\mathbf{v}_d = c\frac{\mathbf{E}\times\mathbf{B}}{B^2}, \tag{2}$$

where

$$\mathbf{E} = -\frac{1}{c}\frac{\partial \mathbf{A}}{\partial t} \tag{3}$$

is the induction electric field, and $\mathbf{A}$ is the vector potential of the magnetic field $\mathbf{B}$. Transient inhomogeneities of the velocity field inevitably result in the formation of regions with plasma compression and rarefaction, in agreement with the equation of continuity

$$\frac{\partial \rho}{\partial t} + \mathrm{div}\rho\mathbf{v} = 0. \tag{4}$$

Hyperbolic shape of field lines leads to plasma compression within two diametrically opposed quadrants, where flows converge, and rarefaction within two other quadrants, where flows diverge. The action of this geometrical factor is enhanced by the effect of acceleration of plasma approaching to null point, as B

is decreasing (div $\mathbf{v} > 0$). Plasma that outflows from the null point decelerates (div $\mathbf{v} < 0$). So, regions of enhanced density (and enhanced pressure) should appear right-and-above the center of the saddle structure in the TRACE images and left-and-down of it during the growth of the bipole. It is two bright features in the difference image that are located just in these two quadrants, namely, a small arch to the left of the saddle, both end of which are anchored in the photosphere, and to the right of it, a jet-like structure along the spine. Enhanced gas pressure initiates field aligned motion that forms the jet.

For a smaller scale emerging magnetic bipole we would not be able to see a saddle structure created by its interaction with the background magnetic field but would still observe the field-aligned jet-like motion. A lot of small jets could be created by very small magnetic elements that have been found everywhere on the solar surface. These small jets could be identified as spicules, dark mottles, macrospicules, surges. Their shapes and direction are defined by the geometry of the larger-scale ambient magnetic field and the orientation of the magnetic moment of emerging ephemeral magnetic regions. A host of jet-like structures (jetlets) forms the dynamic upper chromospheric shell that shows the prolateness at the epoch of low activity. Although it is still difficult to observe the null points and the small-scale saddle structures within the low chromosphere, we believe that the physics is the same as in the processes in the larger-scale saddle structures in the corona where plasma motion is visible more clearly. Hopefully, the new observations planned in space with Solar-B and SDO will permit to resolve this issue.

3. Conclusions

We analyzed a jet-like event observed by TRACE on 3 October 2001 above a structure that could be recognized as a saddle structure around a null (X-type) point. This null point was created by an emerging nearly horizontal bipole and the ambient vertical magnetic field. The growth of the bipole leads to a reconnection of the field lines and to a specific plasma motion in the vicinity of the null point that results in a plasma flow along the spine line of the 3D null. We believe that similar but smaller processes could happen very often at smaller scale in the heart of the chromosphere, near emerging magnetic ephemeral regions, producing numerous jet-like structures (jetlets) in the upper chromosphere such as spicules, dark mottles, giant spicules, macrospicules, spikes, and surges (see also Yamauchi et al. 2004). Assuming that this structure is "universal" and exists at very small scale, the geometry of the ambient magnetic field influences the jet trajectories and should determine the average density distribution in the upper chromosphere. At the epoch of low activity, the difference in the large-scale structure of the polar magnetic field and the one of the low latitude quite regions magnetic field results in a natural explanation of the prolateness of the chromospheric dynamic shell overlying the quasi-hydrostatic atmospheric layers.

Acknowledgments. B. F. is grateful to the CSPM organizers for financial support. This work was supported in part by the Russian Foundation for Basic Research (grant 06-02-16424) and in part by NATO CRG 940291.

References

Auchere F., Boulade S., Koutchmy S., Smartt R. N., Delaboudiniere J. P., Georgakilas A., Gurman, J. B., Artzner G. E., 1998, A&A 366, L57
Belenko I. A., 2001, Solar Phys. 199, 23
Filippov B. P., 1999, Solar Phys. 185, 297
Filippov B., Koutchmy S., 2000, Solar Phys. 196, 311
Fracastoro M. G., 1948, Pub. R. Oss. Arcetri 64, 44
Johannesson A., Zirin H., 1996, ApJ 471, 510
Koutchmy S., Smartt R. N., Auchere F., 1998, NOAO Newsletters 56, 7
Priest E. R., Titov V. S., 1996, Phil. Trans. Roy. Soc. Lond. A. 354, 2951.
Secchi S. J., 1877, Le Soleil, Gauthier-Villars, 38
Varsik J. R., Wilson P. R., Li Y., 1999, Solar Phys. 184, 223
Vilinga J., Koutchmy S., 2005, in K. Sankarasubramanian, M. Penn, A. Pevtsov (eds.), ASP Conf. Ser. 346: Large-Scale Structures and Their Role in Solar Activity, 269
Yamauchi Y., Wang H., Jiang Y., Schwandron N., Moore R. L., 2005, ApJ 629, 572

The Physics of Chromospheric Plasmas
ASP Conference Series, Vol. 368, 2007
Petr Heinzel, Ivan Dorotovič and Robert J. Rutten, eds.

EUNIS Results on He II 304 Å Line Formation

Stuart D. Jordan[1] and Jeffrey W. Brosius[1,2]

[1] *NASA's Goddard Space Flight Center, Greenbelt, MD, USA*
[2] *The Catholic University of America, Washington, DC, USA*

Abstract. The first flight of the Goddard Extreme Ultraviolet Normal Incidence Spectrograph (EUNIS) took place from White Sands Missile Range at 18:10 UT on April 12, 2006. Observations of the He II 304 Å principal resonance line were obtained with a cadence of $\sim$ 2 seconds along an eleven arc-minute slit. Corresponding EIT images of this line, and additional EUNIS observations of the strong coronal line of Fe XVI at 335.4 Å, were used to assess the role of the photoionizing coronal flux in the formation of the He II line. In agreement with previous work of these authors and others, the results support formation by the collisional excitation mechanism by thermal electrons in the quiet Sun.

1. Introduction

The EUNIS sounding rocket experiment was designed largely by Roger Thomas and developed under the direction of Principal Investigator Douglas Rabin at NASA's Goddard Space Flight Center (Thomas & Davila 2001, Rabin 2006). It was launched for the first time on April 12, 2006, and obtained data that permit us to reassess the atomic line-formation mechanism for the He II 304 Å line.

The He II 304 Å line is the strongest spectral line in the solar transition region, and is critical to understanding the transition region's structure, heating, and dynamics. Earlier work showed that thermal-electron collisional excitation is almost certainly the dominant atomic mechanism for the formation of this line in the quiet Sun (Jordan et al. 1993, Falconer et al. 1998, Andretta et al. 2003). The EUNIS observations confirm this assessment. Nevertheless, several problems remain. The atomic line-formation mechanism in solar active regions remains poorly understood, and the possibility that photoionization-recombination (P-R) of He II by strong coronal radiation may dominate there, as argued by Zirin (1998), cannot be ruled out. In addition, there remains the further problem of reproducing the observed flux in the line with semi-empirical models. These last two issues will be discussed in Section 4, along with how future flights of EUNIS can address them.

2. Observations

Figure 1 shows one exposure of the 304 Å slit spectrum and the location of the EUNIS slit on a 304 Å image of the solar area taken with the SOHO/EIT instrument. The spectra exhibited in the lower part of the figure have been smoothed over three adjacent one-arc-second spatial pixels. Also plotted with the same smoothing are the simultaneous spectra of the Fe XVI 335.4 Å line.

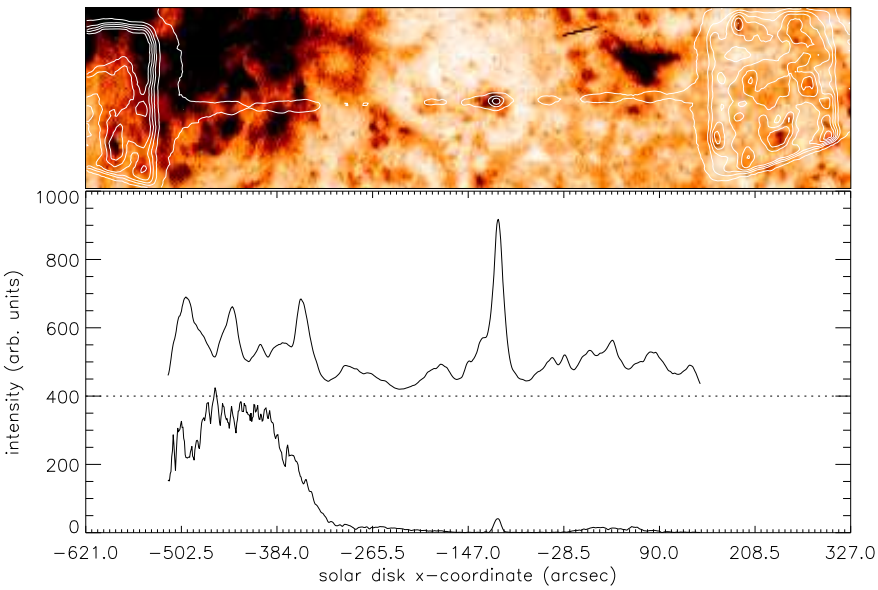

Figure 1. Top frame shows the He II 304 Å image obtained with EIT at 18:12 UT, displayed as a negative intensity image, with EUNIS He II intensity contours. Solar north is up and west is to the right. Coalignment was achieved by matching features in the EUNIS "lobes" (the wide areas at the ends of the slit) with those in the EIT full disk image. The bottom frame shows integrated line intensities of He II at 304 Å and Fe XVI at 335 Å (in arbitrary units) as functions of position (solar disk x-coordinate in arcsec, at 1 AU) along the slit. The He II intensity is displaced upward 400 units for clarity; its zero level is plotted as a dotted line. NOAA Active Region 10871 appears toward the left of the figure, and AR 10870 toward the right.

EUNIS obtained 75 such exposures in its "stare mode" (no rastering) over a duration of 171 s, with a cadence of ~ 2 s and an exposure time of one second. Note that the He II intensity is shifted upward 400 units for clarity. Intensities are in arbitrary units as the final instrumental calibration has not been derived as of this writing.

3. Analysis

Pending absolute calibration of the spectra, we have applied the same technique used for the SERTS-89 analysis (Jordan et al. 1993) to estimate the absolute fluxes in the He II and Fe XVI lines. That is, we assume the quiet-Sun flux values for the Fe XVI 335.4 Å line from Chapman and Neupert (1974) are identical to the quiet-Sun flux values we have observed for quiet-Sun spatial slit positions for which the relative count rate in the 335.4 Å line is less than 100. We have also averaged all relative count rates over the first ten stare exposures. Using this and a preliminary relative calibration curve provided by Roger Thomas, we obtain the relative count-rate efficiency of the detected photons for the two lines used in this analysis, which permits us to obtain estimates of the fluxes in these

two lines, both for the quiet Sun and in the active region spatial pixels. For the active region flux estimates, we have averaged over those spatial pixels with a relative count rate above 100. These results are given in Table 1. A comparison is also provided in Table 1 with results from SERTS-91, SERTS-93 (Brosius *et al.* 1996) and SERTS-97 (Brosius et al. 2000a, 2000b), when the observed solar regions were generally quieter, especially the active regions that were observed on those flights.

Table 1. Average spectral line fluxes ($\mathrm{erg\,cm^{-2}\,s^{-1}}$) in the quiet Sun (QS) and observed active regions (AR) measured along the SERTS-89 (Thomas & Neupert 1994), SERTS-91 and SERTS-93 (Brosius et al. 1996), SERTS-97 (Brosius et al. 2000a, 2000b), and EUNIS-06 slit for He II 304 Å and Fe XVI 335 Å. Results for SERTS-97 are based on an absolute calibration performed at Rutherford-Appleton Laboratory, UK.

Observation	He II in QS	He II in AR	Fe XVI in QS	Fe XVI in AR
EUNIS-06	7.34×10^4	1.37×10^5	1.24×10^3	3.53×10^4
SERTS-89	NA	1.95×10^5	1.24×10^3	3.84×10^4
SERTS-91	2.44×10^4	5.37×10^4	3.18×10^2	1.06×10^4
SERTS-93	2.18×10^4	1.05×10^5	5.12×10^2	1.28×10^4
SERTS-97	2.60×10^4	8.70×10^4	7.51×10^2	1.58×10^4

These flux estimates remain very approximate, pending final absolute calibration. However, they lie well within the range of uncertainty for using the Fe XVI 335.4 Å flux, in particular, as a proxy for estimating the coronal radiation that contributes to the formation of the 304 Å line. The estimate we obtain for the 335.4 Å flux corresponds to a total ionizing coronal flux below 228 Å smaller by more than one order of magnitude in the quiet Sun than the amount needed to equal the effect of thermal- electron collisional excitation (Jordan et al. 1993).

4. Conclusion and Discussion

EUNIS has reconfirmed three previous studies of the atomic line-formation mechanism for the He II 304 Å line, demonstrating again that collisional excitation by thermal electrons in the quiet Sun dominates the atomic line-formation process. The overall performance of EUNIS was quite good for the first flight of a sounding rocket payload, especially in view of the excellent new, still-to-be-exploited diagnostic data it has provided.

However, the full potential of EUNIS has yet to be realized for investigating the problem of the He II 304 Å line formation. What was not achieved on this first flight was a precise coalignment of the two spectrographs. Although the operations plan for the April 2006 flight did provide for rastering the payload through a 40 arc-second range centered on the stare-mode position of the slit, the alignment of the two instruments was not sufficient to achieve coregistration of the slit spectra. Consequently, we did not obtain simultaneous short-wavelength spectra over 170-205 Å that would have provided a direct measurement of the

P-R radiation. Thus we had to use the longer-wavelength Fe XVI 335.4 Å line as a proxy for the photoionizing coronal flux. In addition, the spectral resolution did not achieve the desired 70 mÅ in the long-wavelength spectra. With both proper coalignment and the higher spectral resolution, we should be in a position to investigate two additional problems these data could not address: (1) the atomic mechanism of line formation in active regions, where the rough method based on proxies has been shown to be inadequate (Jordan et al. 1993); and (2) the role of what has been called "velocity redistribution" and of better models of the line-formation region in producing agreement between semi-empirical models and actual observed fluxes, a long-standing problem still not solved. For the nature and role of velocity redistribution, see Andretta et al. (2000). For the impact of improved models, see Fontenla et al. (2002).

Acknowledgments. We thank the CSPM organisers for a very good meeting.

References

Andretta V., Del Zanna G., & Jordan S. D., 2003, A&A 400, 737
Andretta V., Jordan S. D., Brosius J. W., Davila J. M., Thomas R. J., Behring W. E., Thompson W. T., & Garcia A., 2000, ApJ 535, 438
Brosius J. W., Davila J. M., Thomas R. J., & Monsignori-Fossi B. C., 1996, ApJS 106, 143
Brosius J. W., Thomas R. J., Davila J. M., & Landi E., 2000a, ApJ 543, 1016
Brosius J. W., Thomas R. J., Davila J. M., & Thompson W. T., 2000b, Solar Phys. 193, 117
Chapman R. D., & Neupert W. M., 1974, *JGR* 79, 4138
Falconer D. A., Jordan S. D., Brosius J. W., Davila J. M., Thomas R. J., Andretta V. & Hara H., 1998, Solar Phys. 180, 179
Fontenla J. M., Avrett E. H. & Loeser R., 2002, ApJ 572, 636
Jordan S. D., Thompson W. T., Thomas R. J., & Neupert W. M., 1993, ApJ 406, 346
Rabin D. M., 2006, `http://eunis.gsfc.nasa.gov/`
Thomas R. J., & Davila J. M., 2001, Proc. SPIE 4498, 161
Thomas R. J., & Neupert W. M., 1994, ApJS 91, 461
Zirin H., 1988, Astrophysics of the Sun, Cambridge University Press

The Physics of Chromospheric Plasmas
ASP Conference Series, Vol. 368, 2007
Petr Heinzel, Ivan Dorotovič and Robert J. Rutten, eds.

Trapped Eigenoscillations in the Lower Solar Atmosphere: Is there a Resonant Coupling?

Robert Erdélyi[1], Viktor Fedun[1], Chris Malins[1] and Balázs Pintér[2]

[1]*SP²RC, University of Sheffield, Sheffield, UK*
[2]*Institute of Mathematical and Physical Sciences, Ceredigion, UK*

Abstract. Magnetic coupling through MHD waves and oscillations at the solar interior - lower corona interface is studied here. First, the effect of a magnetic solar atmosphere on solar global oscillations is investigated. Frequency shifts of acoustic eigenmodes are found due to the presence of the chromospheric and coronal magnetic fields. Potential application to local magneto-seismology is highlighted.

Next, the propagation and leakage of global acoustic waves is studied in a multi-dimensional realistic model of the lower solar magnetized atmosphere with temperature, pressure and density profiles based on the VAL IIIc model. The higher atmosphere, on the other hand, is the McWhirter atmospheric model. Acoustic waves, mainly identified by solar global oscillations, manifest at photospheric heights. Their leakage into the lower atmosphere is approximated by a harmonic point velocity driver at a range of realistic driver periods measured at photospheric heights, positioned just above the temperature minimum in the photosphere. Convective instability may thus be ignored.

The excited high-frequency waves are seen to propagate through the lower atmosphere to the transition region, and, dependant on the wave period, are transmitted into the lower corona. It was found that for periods close to the lower atmospheric resonant cavity period, reflection from the transition region and trapping in the cavity formed right below the transition region is manifested in the form of chromospheric standing waves. We urge observers to justify these standing waves in the region between the photosphere and transition region by carrying out space or ground-based high-resolution and high-cadence observations.

Further, it is observed in the simulations that waves driven below the cut-off period propagate through into the higher atmosphere with only a slight reflected component. Waves driven at a higher period, in contrast, are largely trapped in the lower atmosphere, with some leakage through the transition region. For specific drivers of around 5 minutes, clear evidence of standing waves being set up in the lower atmospheric cavity is found, and the formation of surface waves travelling outwards *along* the transition region is demonstrated.

When the lower atmospheric magnetic canopy is also considered, global oscillations can resonantly interact at a much wider range of frequencies as opposed to quiet Sun regions. The properties of this interaction allow us to carry out local magneto-seismology, i.e. to derive diagnostic information about the chromospheric magnetic field. This technique can be further used to improve the missing details of wave leakage, spicule and chromospheric jet formation.

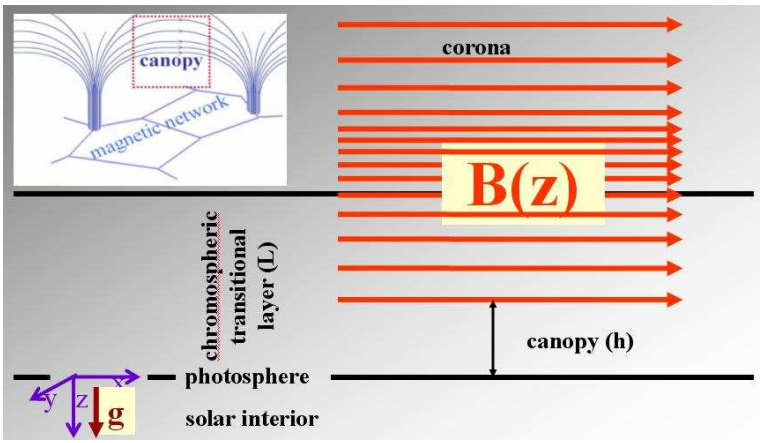

Figure 1. Simple minded working solar model including a politrop interior, partially magnetized transitional layer (from photosphere to the top of the transition zone), and a fully magnetic corona.

1. Introduction

There is now plenty of evidence that the solar photosphere, chromosphere, transition zone and the corona are magnetically coupled. If one would make a hypothetic vertical journey from the visible surface of the Sun to the corona, and at various consecutive heights (where each height roughly corresponds to a given temperature from about 5,000 K at photospheric levels to 4-6 MK X-ray corona) in the solar atmosphere one would take a horizontal snapshot, the obtained images would contain numerous bright and very inhomogeneous patches. Overlaying these images above a magnetogram taken at the visible photosphere would indicate that the locii of these bright patches correspond well to the locii of magnetic field concentrations of the magnetogram. The manifestation of this magnetic coupling has at least two exciting aspects:

- What is the influence of the magnetic solar atmosphere on solar global coherent motions (i.e. on the acoustic p/f or possibly even g mode oscillations)?
- What is the role -if any- of the solar global oscillations in the dynamics of the solar atmosphere?

In the present paper we briefly address these two complementary questions by highlighting some key points of the magnetic coupling. We shall use a working toy-model of the solar atmosphere (see Fig. 1) and will demonstrate how magnetic coupling is manifested. Some observational predictions will be made, in order to encourage the closure of gap between modeling (analytical and numerical) and observational efforts. The methodology implemented here will be magneto-seismology, i.e. using MHD waves and oscillations in order to obtain information about the physical conditions (geometry, shape, temperature, density, magnetic field diagnostics, transport coefficients, etc.) of the wave guides these periodic motions take place.

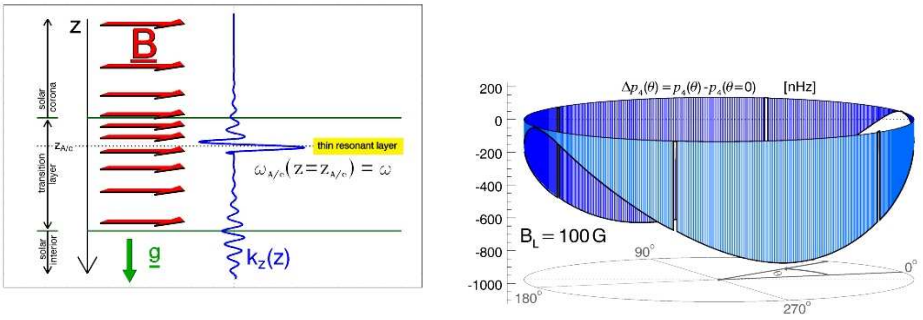

Figure 2. (a) Schematic view of resonant interaction of solar global oscillations with the magnetized atmosphere. (b) Dependence of frequency shift as function of angle between the propagation vector of global oscillations and the horizontal magnetic field.

2. Magnetic Coupling

Coupling between the solar interior and magnetic atmosphere can occur at various scales (local or random vs. global or coherent) and can involve various coupling elements (flow fields or magnetic fields). The transitional layer between the solar interior and the corona (also called as solar boundary layer), that includes the photosphere, chromosphere and TR, is around 2-3 Mm thick and contains both coherent and random magnetic and velocity fields making it a very difficult task to describe wave perturbations even in approximate terms. Random flows (e.g., turbulent granular motion), coherent flows (meridional flows or the near-surface component of the differential rotation), random magnetic fields (e.g., the continuously emerging tiny magnetic fluxes or magnetic carpet) and coherent fields (large loops and their magnetic canopy region) each have their own effect on wave perturbations. Some of these effects may be more important than the others. The magnitude of these corrections has to be estimated one by one and it is suspected that, unfortunately, they all may contribute to line widths or frequency shifts of the global acoustic oscillations on a rather equal basis (for a review, see Erdélyi 2006). In helioseismology, corrections from this boundary layer are called the surface term (Basu 2002), and in many helioseismologic modelings the surface term is taken in some ad-hoc functional form.

Here we shall only demonstrate one particular aspect of the effect of the transitional layer on global oscillations. No background flow fields will be considered (for that see e.g. Erdélyi & Taroyan 2001a; Erdélyi & Taroyan 2001b), neither random magnetic fields are allowed (see e.g. Erdélyi et al. 2005). We solve the eigenvalue problem of the model atmosphere (Fig. 1) subject to boundary conditions that at $\pm\infty$ the energy density drops to zero. In this plain-parallel model, $-\infty$ represents the solar center and $+\infty$ is the outer corona. The spatial eigensolutions indicate that global oscillations penetrate into the magnetized solar atmosphere and interact resonantly with local Alfvénic and/or slow MHD oscillations (see Fig. 2a). The result of this resonant interaction is that the eigenfrequencies of global oscillations will be shifted of the order of μHz when compared to their non-magnetic counterparts, and, the eigenfrequencies will also

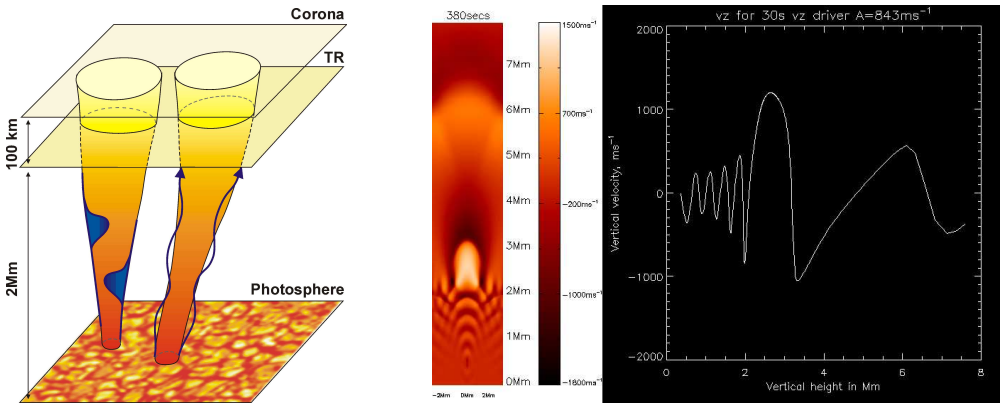

Figure 3. (a) Schematic view of magnetic coupling along thin and intensive flux tubes in the form of solitons (left tube) and progressive waves (right tube). (b) Snapshot of high-frequency photospheric perturbations propagating into the solar corona.

have an imaginary part referring to dissipation. Dissipation will occur at the resonant layer and will result in damping of global oscillations. Changing e.g., the strength of the equilibrium magnetic field (that may for instance mimic the global solar cycle variations) or the direction of propagation of the global p/f modes will influence the derived frequency shifts and/or line widths (the latter is directly linked to the complex part of the global acoustic eigenfrequency, $\Im(\omega)$). Figure 2b shows how, for example, the direction of propagation vector will influence the frequencies of the resonant coupling of the global modes to the magnetized atmosphere. The example shows the frequency shift for the p_4 mode. Note, that there is a maximum shift when global oscillations propagate perpendicular to the coherent atmospheric magnetic field. We strongly suggest that, this feature can be fully exploited when carrying out local seismology, e.g., ring analysis, and the method will provide an additional information about the direction of the magnetic field!

3. Dynamical Coupling

Next, we try to briefly investigate the answer to the second question raised above in the Introduction. (Un)fortunately, the solar atmosphere is not a time-independent static environment. Dynamical phenomena occur at almost all time scales (from very short lived surges, explosive events to dynamical jets, spicules and variations in solar wind). Here we shall demonstrate only one particular aspect: the consequence of leakage of global oscillations into the magnetized solar atmosphere.

A great deal of work has been carried out on examining the propagation of photospheric signals in regions of strong magnetic fields where waves are to some extent guided by field lines (Bogdan et al. 2003; De Pontieu et al. 2004; Hasan et al. 2005). Photospheric motions (e.g., p modes or granular buffeting) perturb the flux tubes and these motions can, depending on the relation of their periods to the acoustic cut-off frequency, propagate along the field lines up in

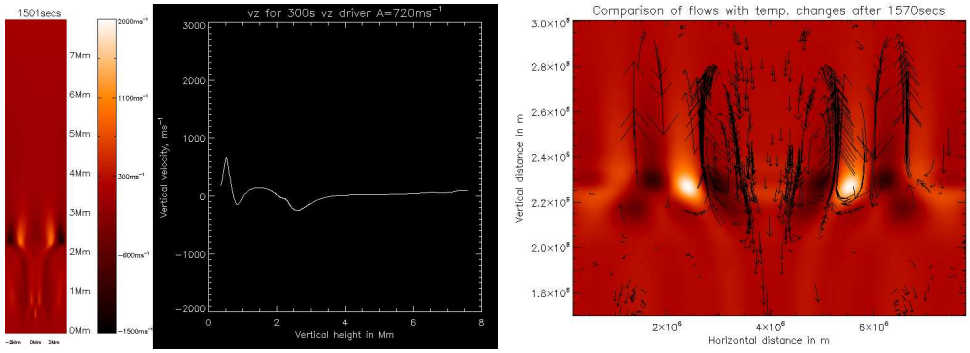

Figure 4. (a) Snapshot of low-frequency standing waves trapped between the photosphere and transition region of the solar atmosphere. (b) Zoom in of a snapshot of the transition region, showing the propagation of surface gravity waves *along* the thin transition zone. Local velocity vectors are over-plotted.

the stratified atmosphere. For a schematic view of thin flux tubes supporting wave leakage (harmonic and solitary) see Fig. 3a. High frequency foot-point perturbations leak rather easily into the upper atmosphere, as it is shown on a snapshot for a photospheric velocity driver with a period of 30 s in Fig. 3b. However, acoustic waves with periods of around 300 s will resonantly interact with the photosphere - transition region cavity. These low-frequency perturbations are reflected from the strong temperature gradient at the transition region and are trapped in the lower solar atmosphere. A typical snapshot of the vertical velocity component of such trapped perturbations is shown in Fig. 4a. These low-frequency trapped (standing or resonant) oscillations also perturb the transition region and disturbances in form of surface gravity waves will propagate *along* the thin transition zone (see a zoomed in snapshot in Fig. 4b).

Of course, the real advancement in numerical modeling of leakage of global acoustic motions, and, in understanding the dynamical role of photospheric - coronal coupling would be if studies were carried out in the framework of full 3-dimensional radiative MHD. Initial steps in the direction of 3D modeling have very recently taken. Numerical simulations of a vertical magnetic flux tube embedded in VAL IIIc model (Vernazza et al. 1981) combined with a McWhirter higher atmosphere (McWhirter et al. 1975) confirm the one- and two-dimensional findings presented above. In Fig. 5a, the visualization of such 3D equilibrium state is shown, while Fig. 5b is a snapshot of photospheric p-mode leakage into the 3-D solar VAL IIIc atmosphere. The horizontal plane indicates the transition region. Observe the extensive surface wave propagation along the transition region.

This paper is a short progress report of where we are now with the numerical and analytical modeling of MHD wave coupling of the solar interior - atmosphere. Reasonable advancement is already made in one- and two-dimensional modeling. Simulations show fine scale structures (spicules) that can be observationally tested and with impetus from space and ground-based data modeling efforts can be refined. Various photospheric drivers have been investigated (point source, harmonic 2-D driver with fundamental, 1st harmonic and broad-band spectra,

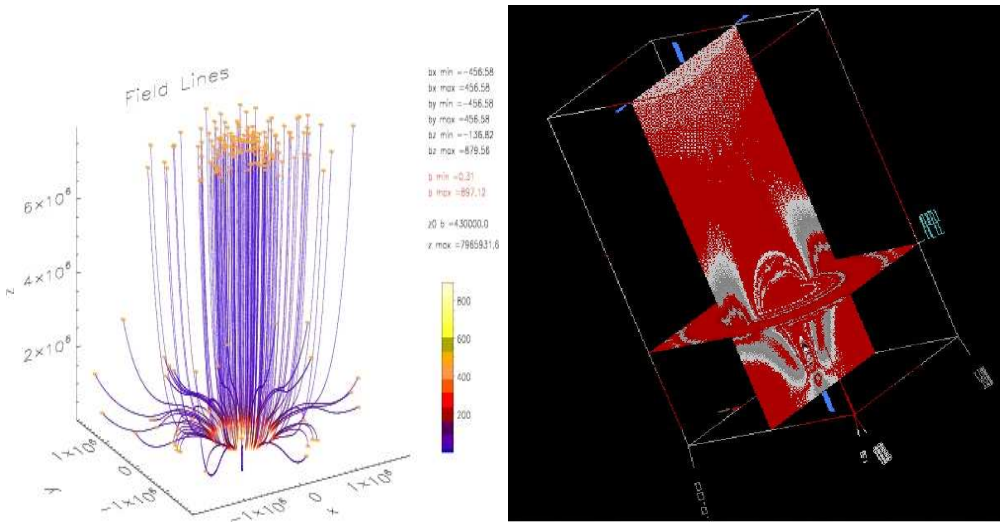

Figure 5. (a) Schematic view of magnetic coupling along thin and intensive 3-dimenasional magnetic flux tube. (b) Snapshot of p-mode wave leakage into a 3-dimensional VAL IIIc atmosphere.

etc.). Advanced 3-D MHD simulations, however, are still in their infancy state and it is anticipated that major progress will be achieved in the near future.

Acknowledgments. We thank the CSPM organisers for a very good and stimulating meeting. R. E. acknowledges M. Kéray for patient encouragement and is also grateful to the NSF, Hungary (OTKA, Ref. No. TO43741). The authors thank Drs. B. De Pontieu and Y. Taroyan for their comments and for the fruitful discussions that helped us to make the recent progress.

References

Basu, S. 2002, ESA SP-508: From Solar Min to Max: Half a Solar Cycle with SOHO, 11, 7
Bogdan, T. J. et al. 2003, ApJ, 599, 626
De Pontieu, B., Erdélyi, R., & James, S. P. 2004, Nat, 430, 536
Erdélyi, R. 2006, Royal Society of London Philosophical Transactions Series A, 364, 351
Erdélyi, R., Kerekes, A., & Mole, N. 2005, A&A, 431, 1083
Erdélyi, R. & Taroyan, Y. 2001, IAU Symposium, 203, 208
Erdélyi, R. & Taroyan, Y. 2001, ESA SP-464: SOHO 10/GONG 2000 Workshop: Helio- and Asteroseismology at the Dawn of the Millennium, 10, 203
Hasan, S. S., van Ballegooijen, A. A., Kalkofen, W., & Steiner, O. 2005, ApJ, 631, 1270
McWhirter, R. W. P., Thonemann, P. C., & Wilson, R. 1975, A&A, 40, 63
Vernazza, J. E., Avrett, E. H., & Loeser, R. 1981, ApJS, 45, 635

The Physics of Chromospheric Plasmas
ASP Conference Series, Vol. 368, 2007
Petr Heinzel, Ivan Dorotovič and Robert J. Rutten, eds.

A Post-MHD for the Solar Atmosphere

D. K. Callebaut

Physics Deptartment, CGB, University of Antwerp, Belgium

Abstract. In magnetohydrodynamics (MHD) one neglects the displacement current, which is usually an excellent approximation. However, when dealing with fast phenomena (often small ones) this displacement current plays a role. Using Callebaut's exact solution of the MHD evolution equation, one may verify the approximation by using Maxwell's equations to calculate the displacement current and the charges associated with it. An example is given. An iteration may yield a further improvement.

This post-MHD may be particularly relevant in connection with work by Callebaut and Karugila, showing that the accumulation of some small *oscillations* (however, including the nonlinear terms) may lead, in narrow strips to very large, even divergent, velocities leading to turbulence and thus reducing the MHD dissipation time. This may explain the short explosion times for flares, CMEs, etc.

1. Introduction

MHD is an excellent approximation for electromagnetism in conducting fluids. There results one equation of evolution for the magnetic field **H**, however still linked to the set of (hydro)dynamic equations through the velocity **v**:

$$\partial_t \mathbf{H} = \mathrm{rot}(\mathbf{v}\times\mathbf{H}) - \mathrm{rot}\,(\eta\,\mathrm{rot}\mathbf{H}), \tag{1}$$

in which $\eta = 1/\mu\sigma$ is the resistivity ($\mu = 4\pi \times 10^{-7}$ Henry/m or kgm/C^2, the magnetic permeability, taken to be constant; σ is the conductivity; SI units). Putting $\eta = 0$, Callebaut & Makarov (2005), Callebaut & Khater (2006a) succeeded in solving the resulting equation exactly in spherical coordinates (r, ϑ, φ), provided **v** has only an azimuthal component v_φ which depends only on r and ϑ. With a straightforward explicit solution the question arises how good the MHD approximation is and when a post-MHD should be considered. It may be noted that Veselovsky (2006a,b) too drew attention, in general terms, to the importance of the space charge, which is neglected in MHD, but represents an extra variable. An example of the calculation of the space charge was developed by Callebaut & Khater (2006b): we shall use it here, at least formally, although it is not yet as general as desired.

The plan of the paper is as follows: in Section 2 we reproduce briefly the results of Callebaut & Khater (2006b). Section 3 gives the results of Callebaut & Karugila (2006a,b) and considers the application to flares, CMEs, etc. Section 4 gives the conclusion.

2. Net Space Charge and Displacement Current

The resistivity is supposed to vanish. The solution of Eq. (1), which is independent of φ, and generated by an initially bipolar field (H_r, H_ϑ, 0) reads

$$H_r = \frac{H_b \cos\vartheta}{r^3},\ \ H_\vartheta = \frac{H_b \sin\vartheta}{2r^3},\ \ H_\varphi = -\frac{t\,\partial(\omega,\Phi)}{r\,\partial(r,\vartheta)}, \tag{2}$$

where H_b is a constant, where $\omega(r,\,\vartheta)$ is the angular frequency and where Φ is the stream function generating H_r, H_ϑ:

$$\Phi = -\frac{H_b \sin^2\vartheta}{2r}. \tag{3}$$

We obtained for the electric field $\mathbf{E}$

$$\mathbf{E} = \frac{\mu H_b\,\omega}{2r^2}(\sin^2\vartheta,\,-2\sin\vartheta\cos\vartheta,\,0), \tag{4}$$

and for the space charge density ρ

$$\rho = \operatorname{div}\mathbf{D} = \epsilon\,(\frac{\partial_r(r^2\,E_r)}{r^2} + \frac{\partial_\vartheta(\sin\vartheta\,E_\vartheta)}{r\sin\vartheta}), \tag{5}$$

or

$$\rho = \frac{\epsilon\mu\,H_b}{2r^3}(r\sin^2\vartheta\,\partial_r\omega - \sin 2\vartheta\,\partial_\vartheta\omega + 2\omega\,(\sin^2\vartheta - 2\cos^2\vartheta)). \tag{6}$$

The displacement current is

$$\partial_t\mathbf{D} = \epsilon\partial_t\mathbf{E} = \frac{\epsilon\mu H_b\,\partial_t\omega}{2r^2}(\sin^2\vartheta,\,-\sin 2\vartheta,\,0). \tag{7}$$

As foreseen the charge density and the displacement current are proportional to $\epsilon\mu = c^{-2}$ which is very small indeed. The MHD current density is

$$\mathbf{j} = \operatorname{rot}\mathbf{H} = [\frac{tH_b\,\partial_\vartheta(\sin^2\vartheta\,(2r\cos\vartheta\,\partial_r\omega + \sin\vartheta\,\partial_\vartheta\omega))}{2r^4\sin\vartheta},$$

$$\frac{-tH_b\sin\vartheta\,\partial_r(r^{-2}(2r\cos\vartheta\,\partial_r\omega + \sin\theta\,\partial_\vartheta\omega))}{2r},\,0] \tag{8}$$

The φ-component of the current vanishes here as H_r and H_ϑ form a gradient. Thus the MHD current is zero at $t = 0$, but grows linearly with time. The initial field had no azimuthal component at $t = 0$, which explains the special time interval. Taking 100 G for the field, i.e. $\mu H_b/r^3$ about 0.01 T, requires ω of the order of 10^{10} cycles/s to generate a charge density of 10^{-3} C/m^3, which is quite large. However, it is difficult to say what is small and what is large with respect to charge: one needs a comparison. For the currents we have the possibility to compare the displacement current with the MHD current: we have then to compare $\partial_t\,\omega/c^2$ with $(t/r)\,\partial^2_{r\vartheta}\,\omega$ and $t\,\partial^2_{rr}\,\omega$ or similar expressions. Hence, we can say that the displacement current may exceed the MHD current, at least at the start, if the time variation of ω, i.e. of the velocity, is very fast and

the space variation is very slow. If we consider the radius of the Sun (7×10^8 m) and a time variation of 1 cycle/s the displacement current may exceed the MHD current during a few seconds. Considering a phenomenon of 1 km and a time variation of 1 megacycle/s, then the displacement current may exceed the MHD current during the first microseconds. An intermediate case is a structure like a prominence (the average current density may be a milli-ampere per square meter cross-section; yet, because of the huge volumes involved the total current may be 10^{11} A). Taking 10^4 km as diameter of the flux tube the time variation should be 10^4 cycles for the displacement current to be comparable to the MHD current during some seconds. Hence rapid motions in slowly varying spaces may require the post-MHD approach. It may be noted that these conditions do not easily go together, but they often do for instabilities. We expect this behavior to be of a general nature, although we studied a specific case.

3. Triggering of Instability by Accumulation of a Few Small Oscillations

Callebaut and Karugila (2003, 2006a,b) developed a nonlinear theory by considering first a single first order perturbation. They calculated (computer algebra) many higher order terms. They showed in some cases analytically and in many cases numerically that the total sum of all the higher order terms can become divergent for a certain value of the amplitude of the first order term. E.g. for a cold infinite plasma the limit of convergence is reached when the first order density amplitude equals e^{-1} (37 per cent) of the equilibrium density. Next they have considered several first order perturbations of moderate amplitude occurring together. Each separately leads to a family of higher order terms which may total a somewhat larger amplitude. The interference terms between the various families may easily be obtained from a combinatorial rule once the family of a single first order term is obtained. All the non-linear terms of all first order perturbations may lead for a certain phase to a very large and even a divergent result. This may be delayed according to the initial amplitudes and the commensurability of the phases. However, a kind of bunching, concentration of the energy in small periodic phase intervals, occurs sooner or later. This gives an instability or rather an explosion, even if all the initial perturbations are *oscillations*. The critical phase and corresponding strip in space is repeated periodically; moreover these strips move in space as the critical phase moves, so that the whole plasma is wiped periodically by the "divergent strip", causing the instability of the whole plasma and the corresponding dissipation of energy. Indeed, as the velocities in such a strip become very large (infinite), turbulence may develop in it. This turbulence may increase the resistivity by 4 to 5 orders of magnitude. This allows the magnetic energy to be dissipated much faster. Moreover, runaway electrons are created which may explain (at least partially) the high energy electrons and radiation.

Moreover, this may act as a trigger for neighboring configurations which have much more stored energy and thus cause gigantic explosions. In fact a chain reaction may occur: a combination of small oscillations (e.g., sound waves) at the solar surface may thus cause an instability corresponding to a bright point. The (larger) waves generated by several bright points may cause the flashing of

a prominence or a solar flare or a CME. This may explain some other sudden outbursts which occur on Earth (interruption of power generators) and in the laboratory as well.

Inducing several moderate perturbations in a quiet plasma (e.g., in a Q-machine) may allow experimental verification of the theoretical convergence limit. This convergence limit lowers when the thermal motions of the electrons and/or ions are taken into account.

4. Conclusion

We have investigated a post-MHD approach in the solar context. Clearly fairly high frequencies are required (often above 1 Mcycle/s). One possibility may come from small waves which interfere (including their higher order terms) and thus cause "divergent strips", which are periodic in space and time, thus moving and wiping over the whole plasma and making it unstable. As turbulence is expected to be generated the dissipation times may be shortened by 4 or 5 orders of magnitude, allowing flashes. Moreover, chain reactions may occur: e.g. starting from sound waves, yielding bright points and next prominences and/or flares.

Acknowledgments. I am grateful to C. de Jager (previously Utrecht University, now NIOZ, Texel, The Netherlands) for discussions.

References

Callebaut, D. K., & Karugila, G. K. 2003, Physica Scripta, 68 (1), 7

Callebaut, D. K., & Karugila, G. K. 2006a, in Sec. Int. Symp. Unconv. Plasmas, ed. D. K. Callebaut, G. C. Dijkhuis and H. Kikuchi, Eindhoven Univ. of Techn., Eindhoven, the Netherlands, 23

Callebaut, D. K., & Karugila, G. K. 2006b, Canadian J. of Physics, submitted

Callebaut, D. K. & Khater, A. H. 2006a, in Solar Activity and its Magnetic Origin, ed. V. Bothmer and A. A. Hady, Proc. IAU Symposium 233, Cairo, Egypt

Callebaut, D. K. & Khater, A. H. 2006b, in Proc. ISUP, Sec. Int. Symp. Unconv. Plasmas, ed. D. K. Callebaut, G. C. Dijkhuis and H. Kikuchi, Eindhoven Univ. of Techn., Eindhoven, the Netherlands, 36

Callebaut, D. K. & Makarov, V. I. 2005, in Solar Activity as a Factor of Cosmic Weather, ed. A. V. Stepanov, A. A. Solovév and V. A. Dergachev, Proc. IX Pulkovo Int. Conf. on Solar Phys., Pulkovo Astr. Obs., 196140 St. Petersburg, Russia, 379

Veselovsky, I.S. 2006a, in Solar Activity and its Magnetic Origin, ed. V. Bothmer and A. A. Hady, Proc. IAU Symposium 233, Cairo, Egypt

Veselovsky, I.S. 2006b, in Proc. ISUP, Sec. Int. Symp. Unconv. Plasmas, ed. D. K. Callebaut, G. C. Dijkhuis and H. Kikuchi, Eindhoven Univ. of Techn., Eindhoven, the Netherlands, 172

The Physics of Chromospheric Plasmas
ASP Conference Series, Vol. 368, 2007
Petr Heinzel, Ivan Dorotovič and Robert J. Rutten, eds.

Stellar Atmospheres and the Diamagnetic Effect

Netzach Farbiash and Raphael Steinitz

Ben-Gurion University, Beer-Sheva, Israel

Abstract. The structure of stellar atmospheres is modified when they include embedded diverging magnetic fields. Diamagnetic Effects (DME) combined with gravity result in speed filters. These, in turn, modify the hydrostatic and thermal structure. Using numerical simulations of charged particle motion, we examine the relevant effects. The run of temperature and pressure is the result of the modified effective gravity for the faster particles of the thermal distribution.

1. Introduction

It is well known that magnetic fields play a major role in stellar atmospheric phenomena such as stellar winds, corona, and stellar spots. While several mechanisms have been suggested to account for them, there is yet no consensus as to which one, or combination of, is actually responsible.

We are motivated by two facts: Motion of charged particles in the presence of magnetic fields is a fundamental problem in astrophysics; magnetic fields play significant roles in stellar atmospheres.

Diverging magnetic fields are abundant: in sunspots, coronas, and in outer space. They cause the diamagnetic effect. Although its presence is independent of waves or other processes, current studies of cooling sunspots, coronal heating, and acceleration of the solar wind have not been taken it into account. In the following we present a *single mechanism* responsible for the mentioned stellar phenomena.

2. The Model

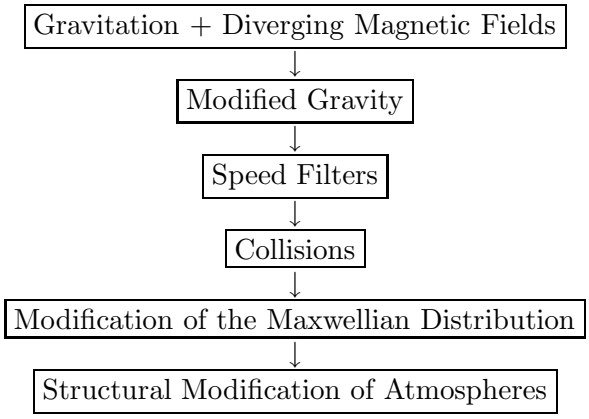

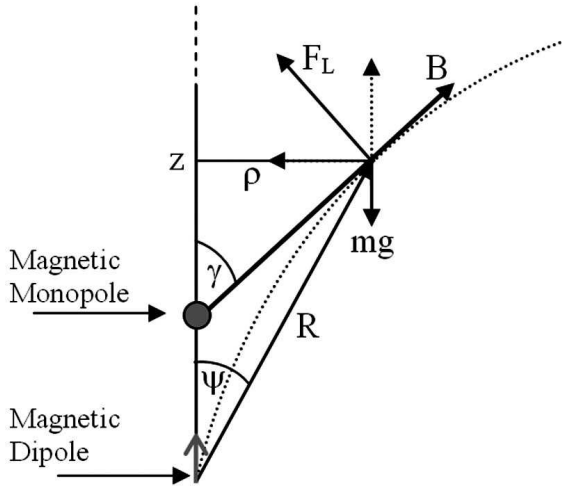

Figure 1. Dipole field approximated locally by a magnetic monopole.

This flowchart describes the stages the diamagnetic effect, combined with gravity, modifies the atmospheric structure. In this section we describe each of the processes of our model.

For sufficiently small regions, a monopole field is a reasonable approximation to the true diverging field (Fig. 1). For simplicity and analytic solutions, we mimic the true magnetic field by local monopoles: $\overrightarrow{B} = (\beta/R^3)\,\overrightarrow{R}$, where β is a constant. The equation of motion of a charged particle with mass m and charge q in the presence of this magnetic field combined with gravity is therefore

$$\ddot{\vec{R}} = \left(\frac{q\beta}{m}\right)\frac{1}{R^3}\left(\dot{\vec{R}} \times \vec{R}\right) + \vec{g} \tag{1}$$

We explore the motion of a charged particle, located at a height z_0 above the monopole using Eq. 1. The height z_0 is chosen so that the **vertical** component of the Lorentz force is equal and opposite to the gravitational force ($\sum F_z = 0$). This choice ensures that the particle is floating.
We now have (see Fig. 2):

$$|F_{\text{Lorentz}}| \sin\alpha = mg, \tag{2}$$

and

$$|F_{\text{Lorentz}}| \cos\alpha = \frac{mv_\perp^2}{r}. \tag{3}$$

Combining 2 and 3, and remembering that $\tan\alpha = r/z_0$, (see Fig. 2), we obtain

$$z_0 = \frac{v_\perp^2}{g}. \tag{4}$$

Equation (4) demonstrates that the floating height z_0 depends on $v_\perp^2$. If the particle has also a velocity component along the field, it will oscillate about z_0.

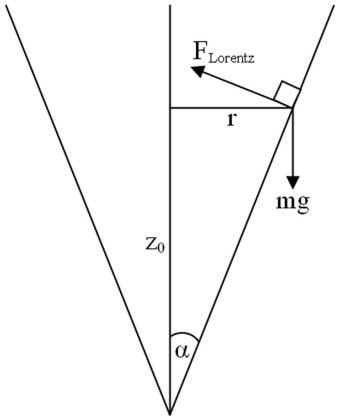

Figure 2. Speed filter.

For $v_\perp^2 < gz_0$ the particle falls and the diamagnetic effect (DME) increases until the vertical component of the Lorentz force is equal to the gravitational one. In this case, we have $z_{\text{down}} < z_0$. For $v_\perp^2 > gz_0$ the particle rises and the DME decreases until the the vertical component of the Lorentz force is equal to the gravitational force. In that case, we have $z_{\text{up}} > z_0$. We define the combination of the DME and gravity as a **speed filter**.

Consider a collisionless plasma in the presence of a static diverging magnetic field and gravity. Since the magnetic field is energy preserver, the total energy of the system is constant. However, speed filters exchange the energy distribution; slow particles (cold) sink due to the DME, while fast (hot) ones rise. Thus, we expect a cold plasma (cold spots?) near the magnetic monopole, and hot plasma high above it (hot corona?).

3. The Role of Collisions

Although speed filters can explain the exchange between the perpendicular component of the kinetic energy and the parallel one (Farbiash and Steinitz, 2005), it cannot explain energy transfer from one atmospheric "layer" to the others. On the other hand, collisions may be the mechanism that allow fast particles to transfer their energy to the slower ones in the layer above. When taking collisions into account, it is important to distinguish between two possible plasma states: fully ionized plasma (relevant for coronas and fast stellar winds), and low ionized plasma (relevant for cold spots). In the first case Coulomb collisions are the dominant ones, while for a cold plasma, mechanical collisions dominate. For the last case, mechanical collisions can transfer energy to faster particles, accelerating the speed filter process.

For Coulomb collisions we study the following equation combining DME, gravity and collisions:

$$\ddot{\vec{r}} = \frac{q}{m}\left(\dot{\vec{r}} \times \vec{B}\right) + \vec{g} + \frac{\vec{F}_c}{m} \tag{5}$$

and explicitly,

$$\begin{pmatrix} \ddot{x}_i \\ \ddot{y}_i \\ \ddot{z}_i \end{pmatrix} = \frac{q\beta}{m}\left(x_i^2+y_i^2+z_i^2\right)^{-3/2}\begin{pmatrix} \dot{y}_i z_i - y_i \dot{z}_i \\ x_i \dot{z}_i - \dot{x}_i z_i \\ \dot{x}_i y_i - x_i \dot{y}_i \end{pmatrix} - \begin{pmatrix} 0 \\ 0 \\ g \end{pmatrix} + \tag{6}$$

$$+\frac{kq_iq_j}{m}\left((x_i-x_j)^2+(y_i-y_j)^2+(z_i-z_j)^2\right)^{-3/2}\begin{pmatrix} x_i-x_j \\ y_i-y_j \\ z_i-z_j \end{pmatrix}$$

4. Conclusions

We have demonstrated (Farbiash and Steinitz 2005) that in the presence of DME and gravitation, particles fall slower than in a gravitation field alone, or can even rise. Thus, the DME results in "*modified gravity*", which provides a "*speed filter*".

Although here we investigate only DME's caused by monopoles, the fundamental physics should be the same also for magnetic dipoles. In that case, when the dipole magnetic fields are the sources of diverging field lines, we expect cold spots close to the dipole poles, and hot plasmas in loops connecting the poles. If magnetic lines are "open", fast particles are moving along them, creating "stellar winds".

Planned future work will include calculation for Coulomb collisions as well as mechanical ones and follow the evolution of a Maxwellian distribution into a non-Maxwellian one, as required for the initial conditions in the theory discussed by Scudder (1992a, 1992b, 1994), and Anderson (1994).

References

Anderson S. W., 1994, ApJ 437, 860
Farbiash N., Steinitz R., 2005, in C. Sterken, C. Aerts (eds.), ASP Conf. Ser. 349: Astrophysics of Variable Stars, 237
Scudder J. D., 1992, ApJ 398, 299
Scudder J. D., 1992, ApJ 398, 319
Scudder J. D., 1994, ApJ 427, 446

Part III

Active Regions and Sunspots

The Physics of Chromospheric Plasmas
ASP Conference Series, Vol. 368, 2007
Petr Heinzel, Ivan Dorotovič and Robert J. Rutten, eds.

Semiempirical Models of Solar and Stellar Active Chromospheres

Pablo Mauas

Instituto de Astronomía y Física del Espacio, Buenos Aires, Argentina

Abstract. Semiempirical models have been used for decades to study the chromospheres of the Sun and of stars of different spectral types. These models are built to match the observations in different spectral features, and make no assumption about the physical processes responsible for the heating of the chromosphere, but can be used to constrain these processes. In this paper we review some of the work done in the modeling of solar and stellar atmospheres, in particular to study active phenomena: solar and stellar flares and chromospheres of stars of different activity levels. We also review an application to RGB stars, where this technique allowed the detection of a stellar wind.

1. Introduction

Semiempirical models have been used for decades to study the structure of the solar chromosphere, and of the chromospheres of stars of different spectral types. These models describe the variations of the essential physical parameters, in particular the temperature, across the chromosphere. Starting from a distribution of temperature vs. height (or column mass), the spectra in a set of features (continua or line profiles) is computed and compared to the observations. Then, the model is iterated until a satisfactory match is found.

Therefore, to build a semiempirical model there is no assumption *a priori* about the physical process responsible for the heating of the chromosphere, but the results of the models can be used to constrain these processes.

To build the model, it is usually assumed a homogeneous atmosphere, in static or quasi static equilibrium. Regarding the homogeneity, it refers to different scales when different features are modeled. In the solar case, the scale is usually fixed by the resolution of the observations under study, and it is different for models of the mean solar chromosphere, of active regions, or for particular flare kernels. In the stellar case, on the other hand, observations do not allow to separate different stellar structures, and therefore it is usually assumed a homogeneous chromosphere covering all the star. However, in a few cases two components were assumed. For example, when studying a flare on the dMe star Ad Leo, Mauas & Falchi (1996) modeled the flaring kernel assuming different filling factors, and used for the atmosphere of the quiet star a model previously obtained to match observations taken during the quiescent state (Mauas & Falchi 1994).

Therefore, these models give information on a "mean" state of the atmosphere, both temporally and spatially. For example, Fontenla et al. (2006) built "semiempirical models of the solar photosphere at spatial resolution of a few

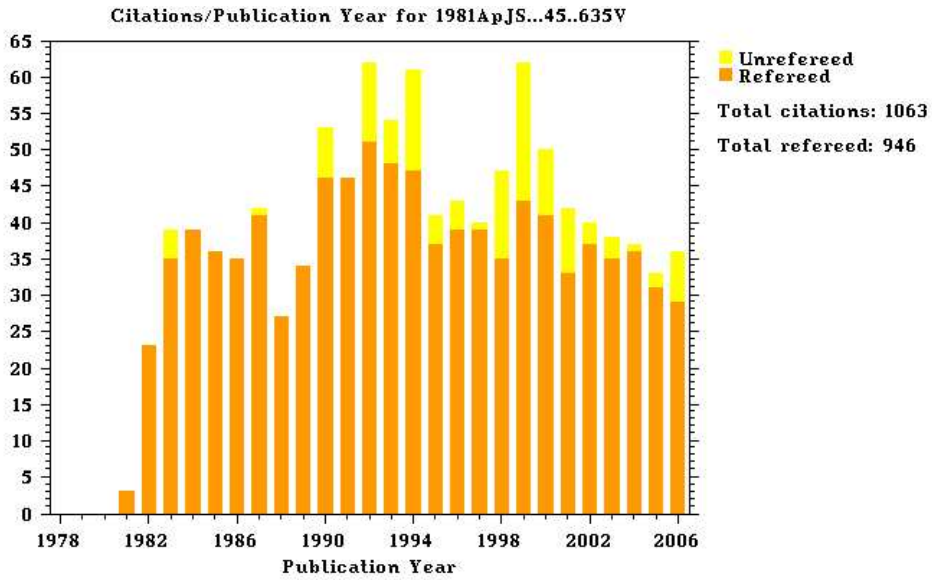

Figure 1. Citation history of the paper by Vernazza et al. (1981), obtained from the ADS in December 2006.

arcseconds and temporally averaged over several p-mode oscillation periods". It is important to keep in mind that the "mean" structure obtained is weighted by the effect on the emitted radiation, in particular on the features under study.

The most important problem of this approach lies in the uniqueness of the models computed in this way. In fact, knowing that a particular atmosphere would emit a line profile like the one we observe for a given star does not imply that the star has indeed this atmospheric structure, since we do not know whether some other atmosphere would produce the same profile. To solve, or at least to reduce, this problem, the modeling has to be based in several spectral features, with different regions of formation. Usually, Ca II K and Hα (or another Balmer line) are used. However, in this case the higher part of the chromosphere is left undefined, except in very active situations (for a thorough discussion of this problem, see Mauas 2000).

2. Solar Models

Certainly the best known semiempirical model is the one for the average Quiet-Sun, Model C by Vernazza et al. (1981). In fact, this is one of the most cited papers in solar physics, as can be seen in Fig. 1 which shows its citation history obtained from the ADS.

In that work, the authors used EUV Skylab observations to determine separate chromospheric models for six brightness components, ranging from a dark cell center to a very bright network element. These models were built to match Ly-α, Ly-β, the Lyman continuum, and other continua.

Later on, this model was modified, in particular in the temperature minimum region, by Maltby et al. (1986), who computed semiempirical models for

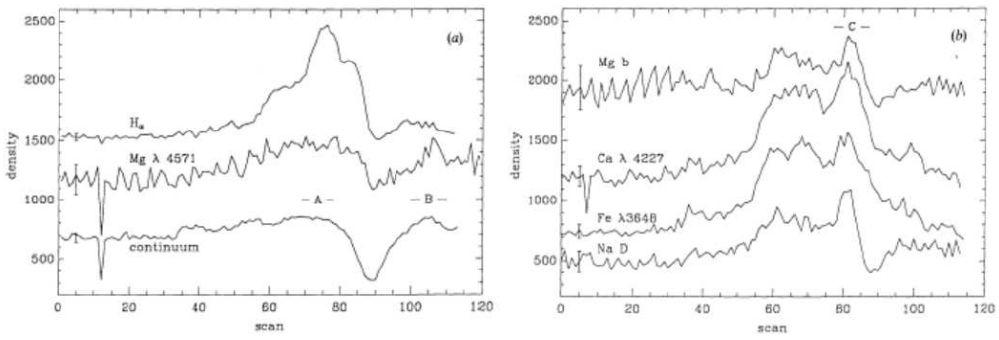

Figure 2. Microdensitometer scans made in the direction across the dispersion, for a continuum window and several spectral lines (Mauas et al. 1990).

sunspot umbrae. More recently, this model has been updated in a series of papers by Fontenla et al. (1990, 1991, 1993, 2002).

Fontenla et al. (1999) built models for different solar features, including sunspots, plage, network, and the quiet atmosphere. This kind of work provides an understanding of the sources of variability arising from solar-activity surface structures. In fact, the output of these models was used to study variations of the solar irradiance, a subject of particular interest for solar-terrestrial studies.

More details about ongoing work in the modeling of different features of the solar atmosphere can be found in the presentations by Avrett and Fontenla et al. in these proceedings.

3. Solar Flare Models

The first semiempirical models of solar flares were constructed by Machado & Linsky (1975), to approximately simulate observations of flares. They studied in particular the Ca II lines, using their wings to derive models of the upper photosphere of the flare. Later, Lites & Cook (1979) built a semiempirical model of the chromosphere between 5500 and 100,000 K during a flare, based on its ultraviolet spectrum.

Perhaps the best known semiempirical flare models are the ones by Machado et al. (1980), who built two models representative of bright and fainter flares, and not for specific events. Their models reproduced observations in lines and continua of H I, Si I, C I, Ca II, and Mg II. They found that the minimum temperature is located deeper and it is higher than in the quiet-sun and active-region models. They concluded that substantial Ly-α radiative back-heating occurs in the upper chromosphere, resulting from the conductive energy flux in the transition zone where the Ly-α line cools the gas.

Gan & Fang (1987) started a series of semiempirical models to study the influence of the chromospheric condensation in the energy balance of the flaring atmosphere (see also Gan et al. 1993). In particular, Gan & Mauas (1994) found that the back-warming of the atmosphere is enhanced by the condensation, and may be very effective to heat the region of the temperature minimum and the

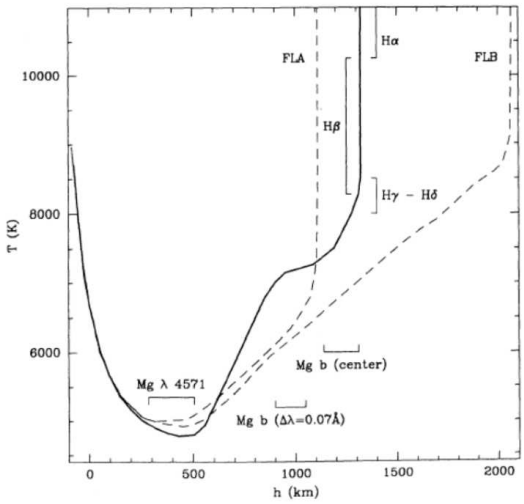

Figure 3. Models for the three kernels of the white light flare studied by Mauas et al. (1990), and the height of formation of different lines.

upper photosphere, as deep as $h = 0$ km, resulting in an enhancement of the continuum emission.

Later, Mauas et al. (1990) and Mauas (1990, 1993) studied different regions of a white light flare (WLF), and built the first semiempirical models of a WLF which are consistent not only with observations of the continuum emission level but also with a set of spectral lines having heights of formation which span the chromosphere and the upper photosphere. In particular, they used as diagnostics the Balmer lines, and the lines of Mg I.

The regions studied can be seen in Fig. 2, which shows microdensitometer scans made in the direction across the dispersion, in spectral features formed at different heights in the atmosphere. In the figure, three distinct kernels can be seen: Kernel A is the brightest in Hα, and one of the brightest in the continuum. Kernel B, on the other hand, is bright in white light but not in Hα. Finally, kernel C is the brightest in the lines which are formed in the mid-chromosphere, but it is not the brightest in Hα, and is even darker in the continuum.

In Fig. 3 the models for the three kernels are shown. Finally, Fig. 4 shows a comparison, for one kernel, of the computed emission for the continuum and the two first Balmer lines with the observations.

Regarding the two white-light kernels, A and B, the models are not compatible with the hypothesis that the continuum emission is caused by enhanced Balmer and Paschen hydrogen continua, and they present strong evidence instead that the emission is of photospheric origin and that its source is due to H^-. The observation and the models derived from them showed that white-light emission can occur in areas of the active region where there is no chromospheric emission and in particular no Hα emission. This fact seems to rule out the viability of downward transport mechanisms as the source of the energy required for the WLF.

One of the results that can be derived from this kind of models, is the cooling rate Φ, which is the net energy radiated by the main spectral features. This

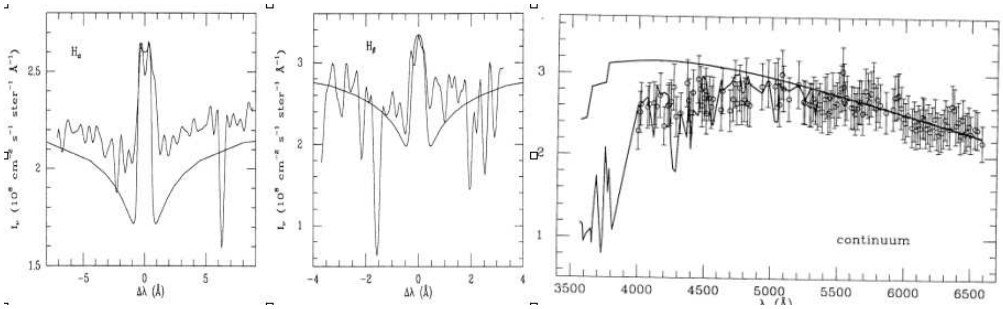

Figure 4. Computed and observed emission in Hα, Hβ and the continuum for Kernel A. In the continuum window, the lower and upper curves show the emission computed with and without line-blanketing, respectively (Mauas et al. 1990).

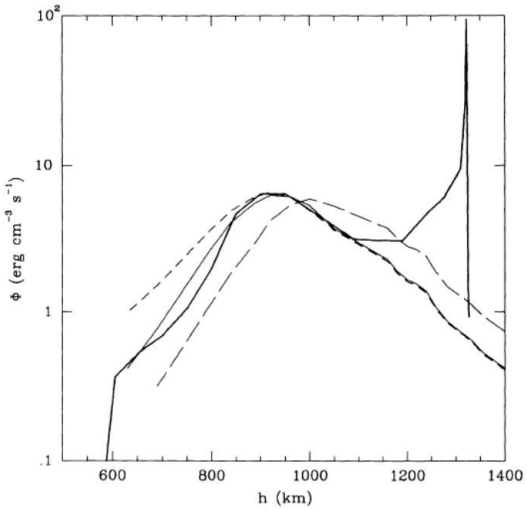

Figure 5. The cooling rate for the mid-chromospheric kernel, compared with the energy deposited by different electron beams (Mauas 1993).

cooling rate can be used to constrain the energy needed to heat the atmosphere. In Fig. 5 a detail of Φ for the model for the mid-chromospheric kernel is compared to the energy deposited by different electron beams (which was computed using the method developed by Gomez & Mauas 1992; Mauas & Gomez 1997). It can be seen that the match is very good for a particular beam, and therefore that this method can be used to effectively constrain the heating mechanism in this region.

Another application of this kind of modeling is to include velocity fields, trying to reproduce the observed line asymmetries, and in this way to further constrain the processes that take place during flares. To do so, Falchi & Mauas (2002) studied the chromospheric structure of a small flare, before, during and after the fist hard X-ray spike. They constructed 5 semiempirical models for different times, to reproduce the profiles of the Hα, Ca II K and Si I 3905 lines

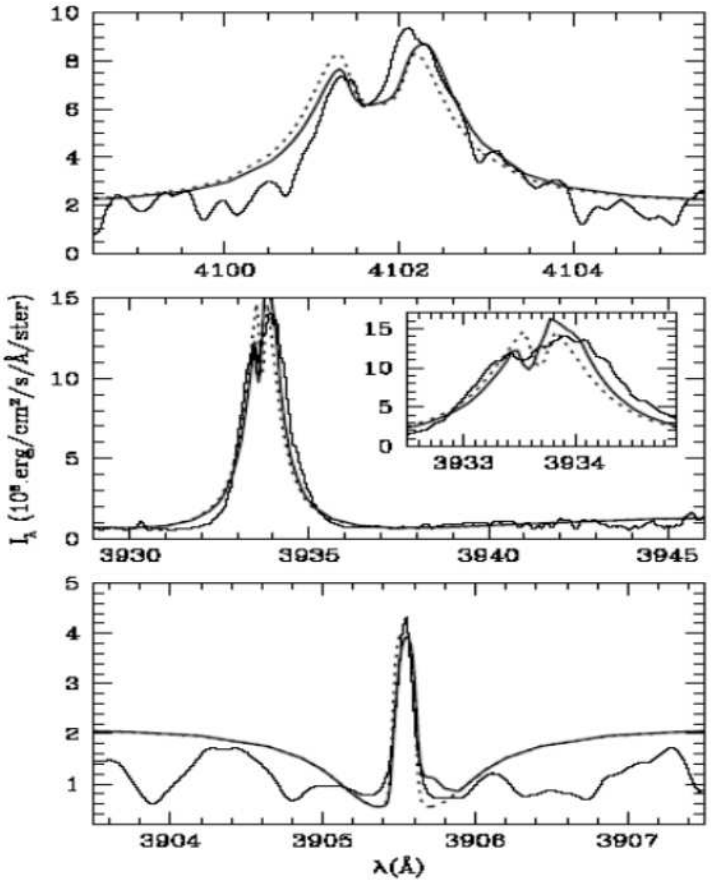

Figure 6. An example of the match obtained between computed and observed profiles, with a velocity field to reproduce the line asymmetries. Upper panel: Hα. Mid panel: Ca II K. Lower panel: Si I (Falchi & Mauas 2002).

during the flare evolution. The lines were chosen because their heights of formations span the whole atmosphere, to avoid indetermination in the deduced chromospheric structure and in the velocity field.

In Fig. 6 a comparison between observed and computed profiles can be seen, and shown in Fig. 7 are the evolution in time of the temperature T, of the electron density $n_{\rm e}$, and of the velocity v at two points in the atmosphere, one in the mid chromosphere, at ≈ 900, and another one at the base of the transition region, at ≈ 1400 km. Also shown is the evolution of the coronal pressure $P_{\rm cor}$.

It can be seen that that the whole chromosphere undergoes a strong upward motion within 1 s of the maximum of the first hard X-ray spike, when the temperature and the density begin to rapidly increase. This seems the first chromospheric response to the energy deposition and/or release. Only 6 s after the hard X-ray peak, a strong downflow begins in the low chromosphere and its velocity continues to increase even during the cooling phase.

Another study of the evolution of chromospheric velocity fields during solar flares was done by Berlicki et al. (2005), who built a grid of models and fitted

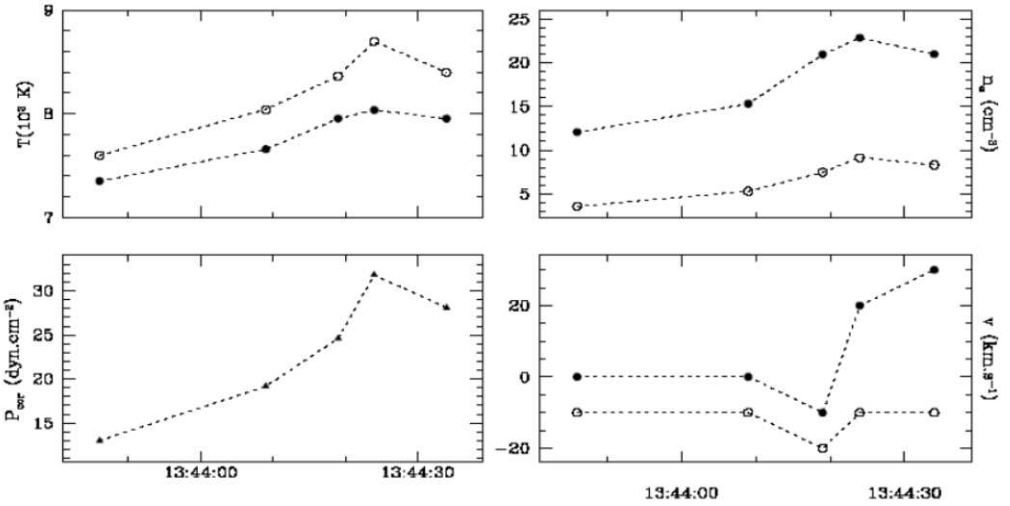

Figure 7. Evolution of temperature, electron density and velocity in two points of the atmosphere, one in the mid-chromosphere (full dots), and another at the base of the transition region (empty dots). Also shown is the evolution of the coronal pressure (Falchi & Mauas 2002).

the observed profiles of the Hα line (see also the paper by Berlicki on p. 387 ff in these proceedings).

4. Models for Solar Analogues

The same technique was successfully applied to the modeling of the atmospheres of cool stars. Specifically, there has been extensive modeling of dM stars, starting perhaps with the work by Cram & Mullan (1979). In particular, modeling of the quiescent state of dM stars was done by the Armagh group (see Short & Doyle 1998, and references therein), and by Mauas & Falchi (1994), and Mauas et al. (1997). Also, flares in these stars were studied by the same groups (Mauas & Falchi 1996; García-Alvarez et al. 2002).

More recently, Vieytes et al. (2005) built models for the Sun as a star and 9 stars with the same color than the Sun and, therefore, the same photosphere, and different levels of activity, which implies different chromospheric structures. The models were built to match the Hβ, Ca II K, Na D and Mg b line profiles, and a velocity field was added when needed to match the asymmetry in the K line.

In Fig. 8 the resulting models are shown, and in Fig. 9 the profiles for two stars, a very inactive and a very active one, are compared to the observations. Note that in the second case, an asymmetry in the K line is observed, and a velocity field was included to match it.

This model was later complemented with a similar one, where K stars of different activity levels were modeled (Vieytes et al, A&A submitted). The main result of both papers is shown in Fig. 10, where the cooling rate Φ, computed from the models, was integrated over all the chromosphere and normalized by

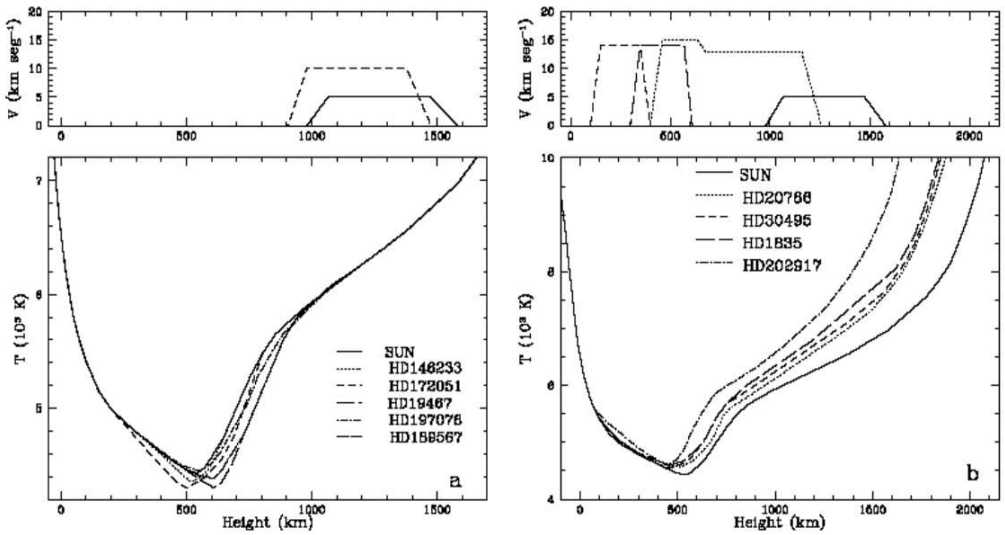

Figure 8. Models of the least active stars (left) and of the most active stars. Top: macroscopic velocity fields for the corresponding star (Vieytes et al. 2005).

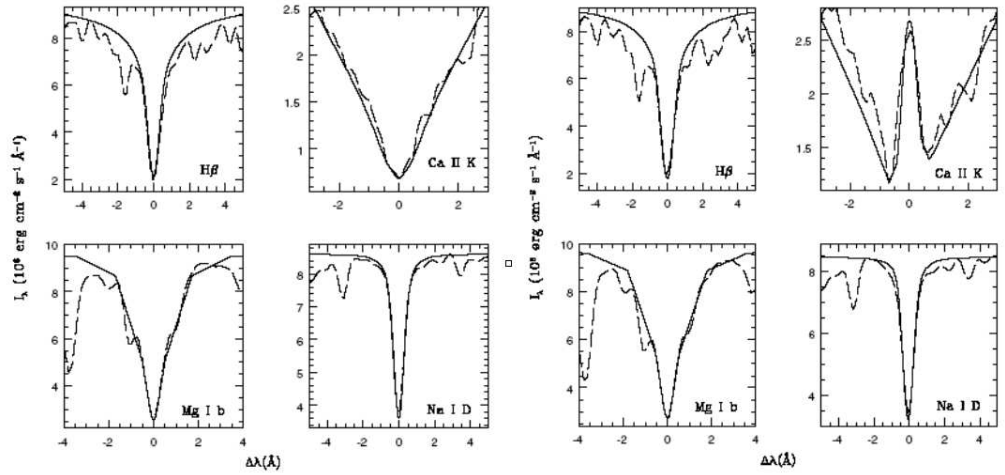

Figure 9. Observed (dashed line) and synthetic (full line) profiles for two stars. *Left*: HD19467. *Right*: HD 1835.

the bolometric luminosity $L = \sigma T_{\rm eff}^4$. The resulting quantity is plotted against S in Fig. 10. S is the most usual index of stellar chromospheric activity, which is essentially the flux in the Ca II H+K lines normalized by the continuum nearby. From the figure, it can be seen that this index is, indeed, a good proxy for chromospheric activity, since it is a good indicator of the ratio between the energy radiated in the chromosphere and the total luminosity.

This S index was first defined for the largest observational study of stellar chromospheric activity, which is the one started in 1966 at the Mount Wilson

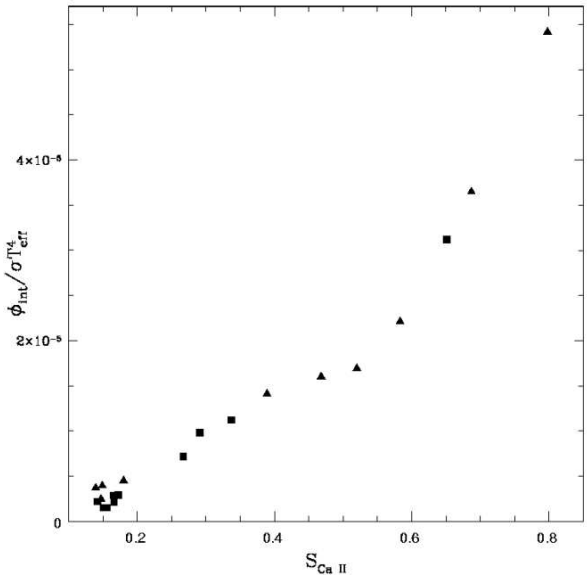

Figure 10. $\Phi_{int}/\sigma\, T_{\rm eff}^4$ vs. S for K (triangles) and G stars (squares).

Observatory. This index is computed using a four channel spectrometer to measure the emission in the core of the H and K lines of Ca II and in two continuum windows nearby. Emission in these lines, by analogy with the Sun, is assumed to be well correlated with surface magnetic fields and, therefore, with chromospheric activity.

Qualitative studies of this data by Vaughan & Preston (1980) suggested that a "gap" in chromospheric emission exists for stars in the range $0.45 \leq B - V \leq 1.0$. Their results are shown in the left panel of Fig. 11, where it can be seen that there are relatively large numbers of stars in this color range with either strong or weak chromospheric emission, but relatively few with moderate emission.

In a survey of Ca II emission in southern solar-type stars, Henry et al. (1996) also found a bimodal distribution, although they considered it "more of a transition zone than a gap", and that "there is not a complete absence of stars" in it. In fact, the right panel of Fig. 11 shows their results. It can be seen that there is a large number of stars with $0.1 < S < 0.2$, and a lower number of stars with $S > 0.2$.

Much has been speculated on the origin of this gap, usually called the Vaughan-Preston (VP) gap in the literature. For example, since chromospheric activity decreases with increasing stellar age, the VP gap could represent a change in the nature of activity at a certain stellar age (Knobloch et al. 1981; Soderblom 1983). Similarly, Hartmann et al. (1984) interpreted the break in chromospheric activity as a fluctuation in the local stellar birthrate.

Alternatively, since activity is closely related to stellar rotation through the stellar dynamo generating the surface magnetic fields, Durney et al. (1981) suggested that the VP gap can be due either to a rapid spindown at some point of stellar evolution, or to an abrupt change of the efficiency of the dynamo for a

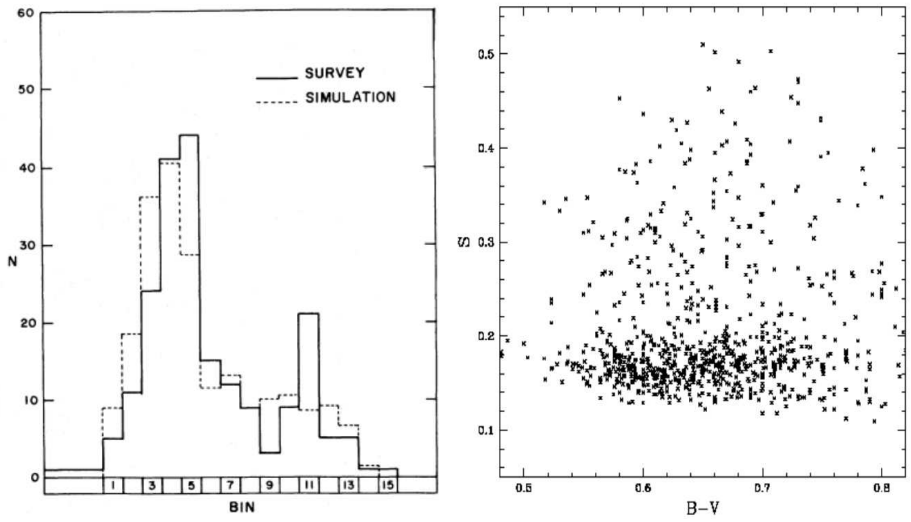

Figure 11. *Left*: Distribution of stars with different levels of activity. A gap for $0.2 \leq S \leq 0.3$ is evident (Vaughan & Preston 1980). *Right*: The results of the survey by Henry et al. (1996), for southern stars.

given rotation period. Other interpretations in terms of dynamo theory can be found in Soon et al. (1993) and Baliunas et al. (1996). Brandenburg et al. (1998) also proposed a break in the rotation period around age 2-3 Gyr, roughly at the VP gap. Rocha-Pinto & Maciel (1998) suggested that the VP gap is related to an abrupt change in the metallicity distribution of these stars.

To investigate the response of the Ca II lines to the changes in the chromospheric structure induced by stellar activity, Vieytes & Mauas (2004) built a set of chromospheric models for stars with the same photospheric structure than the Sun and different activity levels. To do so, active stellar chromospheres were generated starting from the solar model C (Fontenla et al. 1993), and shifting inwards the T vs. $\log(m)$ structure in the chromosphere by a fixed $\Delta \log(m)$, down to the height below T_{min} where the original temperature is higher. Some of these models are shown in Fig. 12.

From the computed models, the values of S were obtained integrating the Ca II profiles. These S values are shown in Fig. 13 as a function of $\Delta \log(m)$. It can be seen that the activity index has a bimodal behavior, changing slope at about $\Delta \log(m) = 0.7$, where $S \approx 0.2$.

This change in behavior can explain why there is a much larger number of stars with $S < 0.2$, since all stars having $\Delta \log(m) < 0.7$ are in this region, and stars having $\Delta \log(m) > 0.8$ are already well above this value.

To further check this assumption, the distribution of the values of S was computed, under the assumption that all models have the same probability to occur in nature. In the right panel of Fig. 13 this distribution is compared with the distribution of the sample by Henry et al. (1996) shown in the right panel of Fig. 11, which has more than 900 observations. It can be seen that the agreement between both distributions is remarkable.

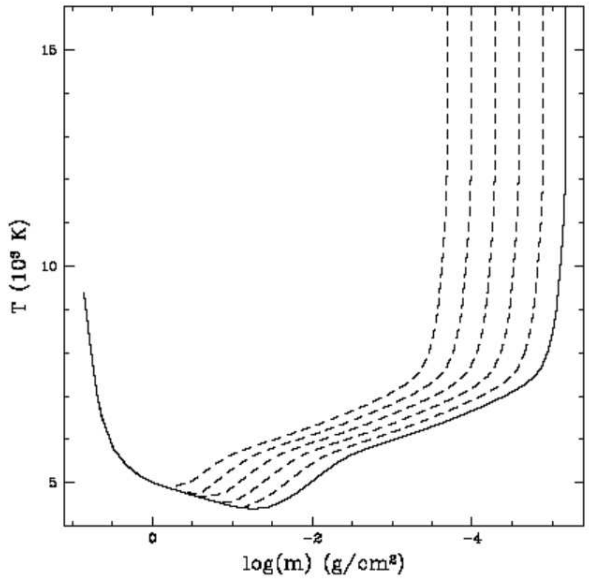

Figure 12. Some of the atmospheric models used by Vieytes & Mauas (2004). The full line is the quiet Sun model C by Fontenla et al. (1993) and the dashed lines are the models built by shifting this model by $\Delta \log(m) = 0.3$, 0.6, 0.9, 1.2 and 1.5.

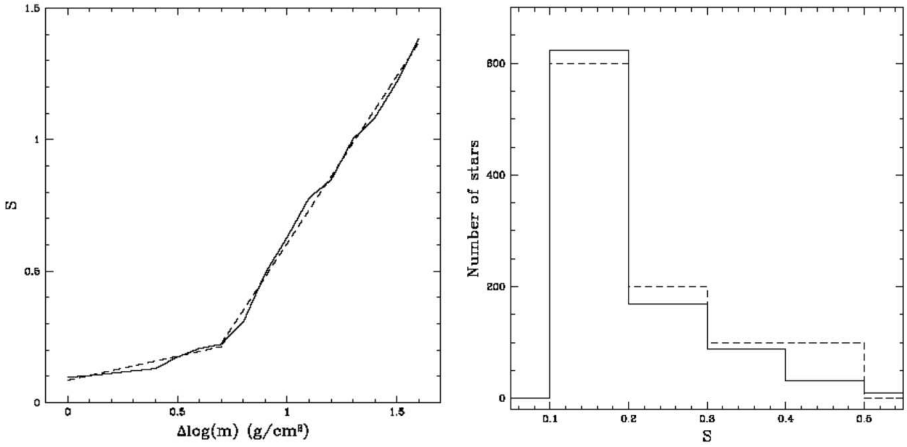

Figure 13. *Left*: The response of the Ca II S index to the different atmospheric models of Fig. 12. Also shown as dashed lines are the linear fits to the two different regimes (see text). *Right*: The full line is the histogram of S values for the survey by Henry et al. (1996) and the dashed line is the histogram of the computations by Vieytes & Mauas (2004), conveniently scaled.

5. Chromospheres and Mass Loss in Red Giant Stars

Stellar evolution theory requires some mass loss by Population II stars during the evolutionary phases preceding the horizontal branch phase, in order to ac-

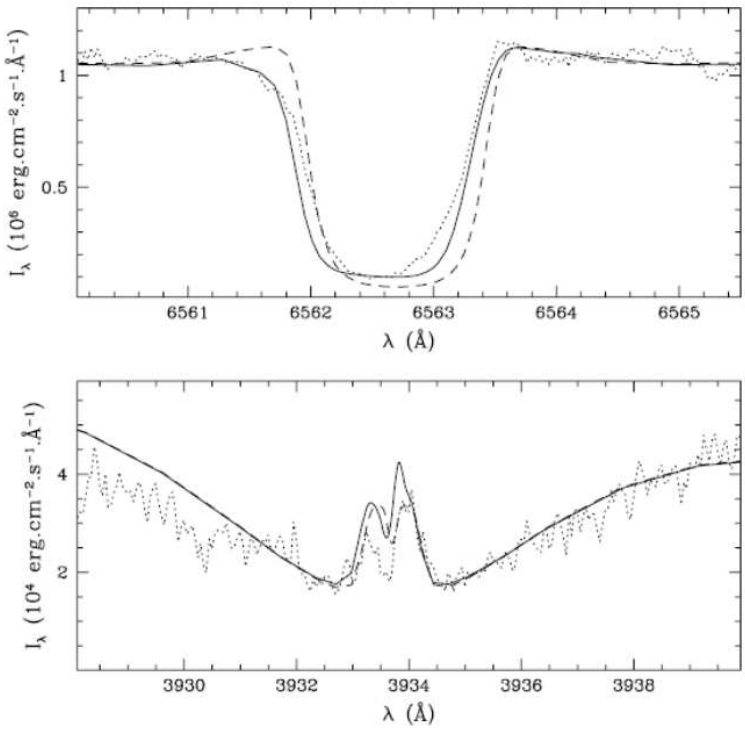

Figure 14. Observed (dotted) and computed (full) profiles for one of the red giant stars studied by Mauas et al. (2006). Also shown for reference are the profiles computed without any velocity field.

count for (1) the observed morphologies of the horizontal branch in globular clusters, and (2) the maximum luminosity reached by stars on the asymptotic giant branch. However, direct evidence for mass loss in these stars has been quite elusive.

In these stars, usually the profiles of the main chromospheric lines (Ca II and Hα) show asymmetric emission peaks, which is an evidence of mass motions. Dupree et al. (1984) built semiempirical models to reproduce the Hα profile, and concluded that the Hα line alone provides no evidence for a steady mass loss that can significantly affect the evolution of stars on the red giant branch of globular clusters.

Recently, Mauas et al. (2006) modeled 5 stars with clear evidence of emission in the Hα wings and at the bottom of the Ca II K absorption core (K_2 reversal). To reproduce the observed asymmetries, the models included the appropriate velocity fields.

Since the observed profiles for the stars were very similar, and differed mainly in the amount of asymmetry in the K_2 and Hα emission wings, it was possible to fit all the profiles with only two T vs. $\log(m)$ distributions, and different velocity fields. The computed profiles for one of the stars are compared with the observations in Fig. 14. Also shown are the profiles computed for the corresponding model without including the velocity field, as a reference for clarity.

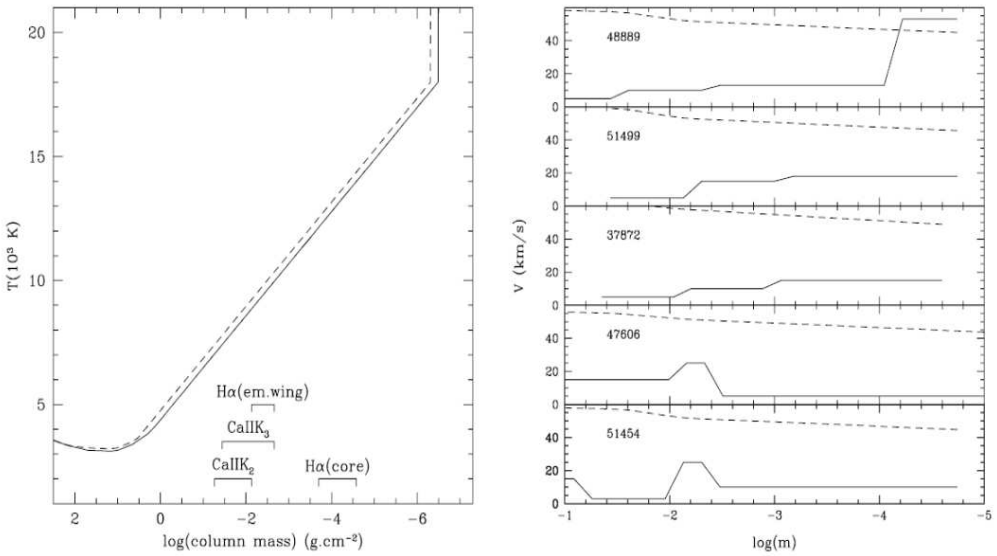

Figure 15. *Left*: The chromospheric models for the red giant stars. The approximate depth of formation of the Hα core and wings, and of the Ca II K_2 and K_3 line components are also indicated. *Right*: The velocity as a function of depth (solid line), derived from the best match with the Ca K and Hα lines, compared to the corresponding escape velocity (dashed line) (Mauas et al. 2006).

The models and the velocity fields are shown in Fig. 15. For comparison, the corresponding escape velocity is also shown. It can be seen that for one of the stars (star 48889) the expansion velocity at the most external point that can be modeled is larger than the escape velocity. This implies that, at least for this star, the material above this level is escaping from the atmosphere.

For the other stars, the expansion velocities estimated for the outermost modeled point are smaller than the escape velocity at that depth. However, there is a mass outflow at this height, and the velocity is increasing in all cases, while, of course, the escape velocity is decreasing. Furthermore, there are no signs of a reversal in the velocity field, i.e. there is no material falling back in. Therefore, the most probable situation is that the velocity continues to increase, until eventually it reaches the escape velocity.

Therefore, these models confirm the existence of the stellar wind required by the theory, at least in some of the stars under study. Furthermore, from the estimated velocity, and the column mass at the outermost point, the mass-loss rate can be estimated. It turns out that these rates are in agreement with the ones expected from stellar evolution theory.

Acknowledgments. I would like to thank Marcos Machado, Gene Avrett, and Ambretta Falchi. Without them, this work would not have been possible. I would also like to thank the organizers of the CSPM, for the wonderful meeting. In particular, Petr Heinzel for the invitation, and João Fernandes for his patience, and the University of Coimbra for financing my participation.

References

Baliunas S. L., Nesme-Ribes E., Sokoloff D., Soon W. H., 1996, ApJ 460, 848
Berlicki A., Heinzel P., Schmieder B., Mein P., Mein N., 2005, A&A 430, 679
Brandenburg A., Saar S. H., Turpin C. R., 1998, ApJ 498, L51
Cram L. E., Mullan D. J., 1979, ApJ 234, 579
Dupree A. K., Hartmann L., Avrett E. H., 1984, ApJ 281, L37
Durney B. R., Mihalas D., Robinson R. D., 1981, PASP 93, 537
Falchi A., Mauas P. J. D., 2002, A&A 387, 678
Fontenla J., White O. R., Fox P. A., Avrett E. H., Kurucz R. L., 1999, ApJ 518, 480
Fontenla J. M., Avrett E., Thuillier G., Harder J., 2006, ApJ 639, 441
Fontenla J. M., Avrett E. H., Loeser R., 1990, ApJ 355, 700
Fontenla J. M., Avrett E. H., Loeser R., 1991, ApJ 377, 712
Fontenla J. M., Avrett E. H., Loeser R., 1993, ApJ 406, 319
Fontenla J. M., Avrett E. H., Loeser R., 2002, ApJ 572, 636
Gan W. Q., Fang C., 1987, Solar Phys. 107, 311
Gan W. Q., Mauas P. J. D., 1994, ApJ 430, 891
Gan W. Q., Rieger E., Fang C., 1993, ApJ 416, 886
García-Alvarez D., Jevremović D., Doyle J. G., Butler C. J., 2002, A&A 383, 548
Gomez D. O., Mauas P. J., 1992, ApJ 398, 682
Hartmann L., Soderblom D. R., Noyes R. W., Burnham N., Vaughan A. H., 1984, ApJ 276, 254
Henry T. J., Soderblom D. R., Donahue R. A., Baliunas S. L., 1996, AJ 111, 439
Knobloch E., Rosner R., Weiss N. O., 1981, MNRAS 197, 45P
Lites B. W., Cook J. W., 1979, ApJ 228, 598
Machado M. E., Avrett E. H., Vernazza J. E., Noyes R. W., 1980, ApJ 242, 336
Machado M. E., Linsky J. L., 1975, Solar Phys. 42, 395
Maltby P., Avrett E. H., Carlsson M., Kjeldseth-Moe O., Kurucz R. L., Loeser R., 1986, ApJ 306, 284
Mauas P. J. D., 1990, ApJS 74, 609
Mauas P. J. D., 1993, ApJ 414, 928
Mauas P. J. D., 2000, ApJ 539, 858
Mauas P. J. D., Cacciari C., Pasquini L., 2006, A&A 454, 609
Mauas P. J. D., Falchi A., 1994, A&A 281, 129
Mauas P. J. D., Falchi A., 1996, A&A 310, 245
Mauas P. J. D., Falchi A., Pasquini L., Pallavicini R., 1997, A&A 326, 249
Mauas P. J. D., Gomez D. O., 1997, ApJ 483, 496
Mauas P. J. D., Machado M. E., Avrett E. H., 1990, ApJ 360, 715
Rocha-Pinto H. J., Maciel W. J., 1998, MNRAS 298, 332
Short C. I., Doyle J. G., 1998, A&A 336, 613
Soderblom D. R., 1983, in J. O. Stenflo (ed.), IAU Symp. 102: Solar and Stellar Magnetic Fields: Origins and Coronal Effects, 439
Soon W. H., Baliunas S. L., Zhang Q., 1993, ApJ 414, L33
Vaughan A. H., Preston G. W., 1980, PASP 92, 385
Vernazza J. E., Avrett E. H., Loeser R., 1981, ApJS 45, 635
Vieytes M., Mauas P., Cincunegui C., 2005, A&A 441, 701
Vieytes M., Mauas P. J. D., 2004, Ap&SS 290, 311

The Physics of Chromospheric Plasmas
ASP Conference Series, Vol. 368, 2007
Petr Heinzel, Ivan Dorotovič and Robert J. Rutten, eds.

Chromospheric Cloud-Model Inversion Techniques

Kostas Tziotziou
National Observatory of Athens, Institute for Space Applications and Remote Sensing, Greece

Abstract. Spectral inversion techniques based on the cloud model are extremely useful for the study of properties and dynamics of various chromospheric cloud-like structures. Several inversion techniques are reviewed based on simple (constant source function) and more elaborated cloud models, as well as on grids of synthetic line profiles produced for a wide range of physical parameters by different NLTE codes. Several examples are shown of how such techniques can be used in different chromospheric lines, for the study of structures of the quiet chromosphere, such as mottles/spicules, as well as for active region structures such as fibrils, arch filament systems (AFS), filaments and flares.

1. Introduction

Observed intensity line profiles are a function of several parameters describing the three-dimensional solar atmosphere, such as chemical abundance, density, temperature, velocity, magnetic field, microturbulence etc (which one would like to determine), as well as of wavelength, space (solar coordinates) and time. However, due to the large number of parameters that an observed profile depends on, as well as data noise, model atmospheres have to be assumed in order to restrict the number of these unknown parameters. The term "inversion techniques" refers to the procedures used for inferring these model parameters from observed profiles. We refer the reader to Mein (2000) for an extended overview of inversion techniques. In this paper, we will review only a class of such inversion techniques known in the solar community as "cloud models".

Cloud models refer to models describing the transfer of radiation through structures located higher up from the solar photosphere, which represents the solar surface, resembling clouds on earth's sky (see Fig. 1). Such cloud-like structures, when observed from above, would seem to mostly absorb the radiation coming from below, an absorption which mostly depends on the optical thickness of the cloud, that is the "transparency" of the cloud to the incident radiation and also on the physical parameters that describe it. The possibility of observed emission from such structures cannot, of course, be excluded when the radiation produced by the cloud-like structure is higher than the absorbed one. The aforementioned processes are described by the radiative transfer equation

$$I(\Delta\lambda) = I_0(\Delta\lambda)\ \mathrm{e}^{-\tau(\Delta\lambda)} + \int_0^{\tau(\Delta\lambda)} S_t\ \mathrm{e}^{-t(\Delta\lambda)}\ \mathrm{d}t\,, \qquad (1)$$

where $I(\Delta\lambda)$ is the observed intensity, $I_0(\Delta\lambda)$ is the reference profile emitted by the background (the incident radiation to the cloud from below), $\tau(\Delta\lambda)$ is the

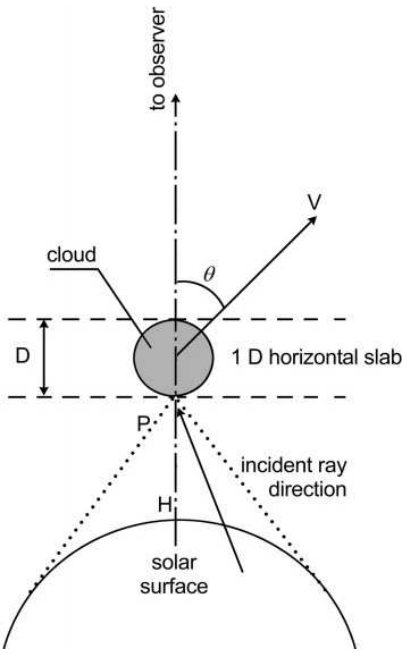

Figure 1. Geometry of the cloud model. D is the geometrical thickness of the cloud at height H above the solar surface and V its velocity. From Heinzel et al. (1999).

optical thickness and S the source function which is a function of optical depth along the cloud. The first term of the right hand part of the equation represents the absorption of the incident radiation by the cloud, while the second term represents emission by the cloud itself.

The simple cloud model method introduced by Beckers (1964) arose from the need to solve fast the radiation transfer equation and deduce the physical parameters that describe the observed structure. Beckers assumed that a) the structure is fully separated from the underlying chromosphere, b) the source function, radial velocity, Doppler width and the absorption coefficient are constant along the line-of-sight (hereafter LOS) and c) the background intensity is the same below the structure and the surrounding atmosphere; hence it can be extrapolated from a neighboring to the structure under study region. Under the above assumptions the radiative transfer equation is simplified to

$$I(\Delta\lambda) = I_0(\Delta\lambda)\ \mathrm{e}^{-\tau(\Delta\lambda)} + S(1 - \mathrm{e}^{-\tau(\Delta\lambda)}) \tag{2}$$

and can be rewritten as

$$C(\Delta\lambda) = \frac{I(\Delta\lambda) - I_0(\Delta\lambda)}{I_0(\Delta\lambda)} = \left(\frac{S}{I_0(\Delta\lambda)} - 1\right)(1 - \mathrm{e}^{-\tau(\Delta\lambda)}), \tag{3}$$

where $C(\Delta\lambda)$ defines the contrast profile. A Gaussian wavelength dependence is usually assumed for the optical depth as follows

$$\tau(\Delta\lambda) = \tau_0\ \mathrm{e}^{-\left(\frac{\Delta\lambda - \Delta\lambda_I}{\Delta\lambda_\mathrm{D}}\right)^2}, \tag{4}$$

where τ_0 is the line center optical thickness, $\Delta\lambda_I = \lambda_0 v/c$ is the Doppler shift with λ_0 being the line center wavelength, c the speed of light and $\Delta\lambda_\mathrm{D}$ is the Doppler width. The latter depends on temperature T and microturbulent velocity ξ_t through the relationship

$$\Delta\lambda_\mathrm{D} = \frac{\lambda_0}{c}\sqrt{\xi_\mathrm{t}^2 + \frac{2kT}{m}}\,, \tag{5}$$

where m is the atom rest mass. Other wavelength dependent profiles than the Gaussian one can also be assumed for the optical depth, e.g., a Voigt profile (Tsiropoula et al. 1999).

The four adjustable parameters of the model are the source function S, the Doppler width $\Delta\lambda_\mathrm{D}$, the optical thickness τ_0 and the LOS velocity v. All these parameters are assumed to be constant through the structure. There are some crucial assumptions concerning Beckers' cloud model (hereafter BCM):

- the uniform background radiation assumption, which is not always true especially for cloud-like structures that do not reside above quiet Sun regions. Moreover, the background radiation plays an important role in the correct quantitative determination of the physical parameters.
- the neglect of incident radiation, the effects of which are of course not directly considered in BCM, but does play an important role in non-Local Thermodynamic Equilibrium (hereafter NLTE) modeling, since it determines the radiation field within the structure, that is the excitation and ionization conditions and hence the source function.
- the constant source function assumption which is not realistic especially in the optically thick case or not valid in the presence of large velocity gradients.

However, the cloud model works quite well for a large number of optically thin structures and can provide useful, reasonable estimates for the physical parameters that describe them. We refer the reader to Alissandrakis et al. (1990) for a detailed discussion on the validity conditions of BCM for different types of contrast profiles.

2. Cloud Model Variants

Since the introduction of the BCM method several improvements have been suggested in the literature. When looking at the radiative transfer equation (Eq. 1), it is obvious that all efforts concentrate on a better description of the source function S which in BCM is considered to be constant. In the following subsections some of these suggested improvements are described.

2.1. Variable source function

Mein et al. (1996a) considered a source function that is a function of optical depth and is approximated by a second-order polynomial

$$S_\mathrm{t} = S_0 + S_1\frac{\tau_0}{\tau_{0,\max}} + S_2\left(\frac{\tau_0}{\tau_{0,\max}}\right)^2 \tag{6}$$

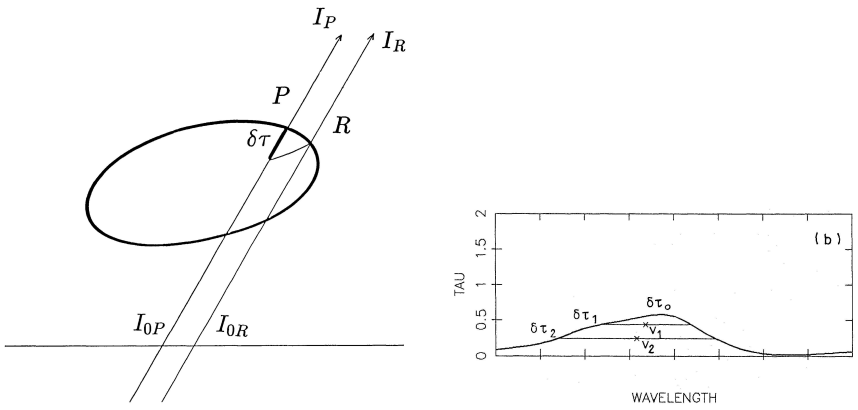

Figure 2. *Left:* Geometry of the cloud model in the case of first-order differential cloud model. From Heinzel et al. (1992). *Right:* The "3-optical depths" procedure for solving the differential cloud model case which is described in Sect. 3.5 (from Mein & Mein (1988)).

with the optical depth at the center of the line τ_0 taking values between 0 and the total optical thickness at line center $\tau_{0,\max}$, while S_0, S_1 and S_2 are functions of $\tau_{0,\max}$. This formulation was further improved by Heinzel et al. (1999), who included also the effect of cloud motion by assuming that S_0, S_1 and S_2 are now not only functions of $\tau_{0,\max}$, but also depend on the velocity v of the structure.

Tsiropoula et al. (1999) assumed the parabolic formula

$$S_t = S_0 \left(1 + \alpha \left(t - \frac{\tau_0}{2}\right)^2\right) \tag{7}$$

as an initial condition for the variation of the source function with optical depth, where S_0 is the source function at the middle of the structure, τ_0 the optical depth at line center, and α a constant expressing the variation of the source function. However, their final results on the dependence of the source on optical depth were in good agreement with the results of Mein et al. (1996a).

2.2. Differential cloud models

First and second order differential cloud models (hereafter DCM1 and DCM2) were introduced by Mein & Mein (1988) to account for fast mass flows observed on the disc, where BCM is not valid due to fluctuations of the background and strong velocity gradients along the LOS. DCM1 assumes that the source function S, temperature T and velocity v are constant within a small volume contained between two close lines of sight P and R (see Fig. 2, left panel). If we assume that the variation of the background profile is negligible ($I_{0\mathrm{P}} \simeq I_{0\mathrm{R}}$) for such close points then the differential cloud contrast profile can be written as

$$C(P,R,\lambda) = \frac{I_P(\lambda) - I_{\mathrm{R}}(\lambda)}{I_R(\lambda)} = \left(\frac{S}{I_{\mathrm{R}}(\lambda)} - 1\right)\left(1 - \mathrm{e}^{-\delta\tau(\lambda)}\right) \tag{8}$$

with

$$\delta\tau(\lambda) = \delta\tau_0 \, \mathrm{e}^{-\left(\frac{\lambda - \lambda_0 - v\lambda_0/c}{\Delta\lambda_\mathrm{D}}\right)^2}, \tag{9}$$

where $\Delta\lambda_\mathrm{D}$ is the Doppler width. The zero velocity reference wavelength λ_0 is obtained by averaging over the whole field of view. DCM1 is a method for suppressing the use of the background radiation. If velocity shears are present between neighboring LOS then DCM2 can be used instead which requires the use of three neighboring LOS. We refer the reader to Mein & Mein (1988) for the precise formulation of DCM2 and to Table 1 of the same paper which summarizes the validity conditions, constrains and results of the two models in comparison to the classical BCM.

2.3. Multi-cloud models

The multi-cloud model (Gu et al. 1992, 1996) – hereafter MCM – was introduced for the study of asymmetric, non-Gaussian profiles, such as line profiles of post-flare loops, prominences and surges and was based on the BCM and DCMs models. These asymmetric line profiles are assumed to be the result of overlapping of several symmetric Gaussian profiles along the LOS, formed in small radiative elements (clouds) which have a) different or identical physical properties and b) a source function and velocity independent of depth. The profile asymmetry mostly results from the relative Doppler shifts of the different clouds. The total intensity I_λ emitted by m clouds is then given by the relation

$$I_\lambda = I_{0,\lambda}\,\mathrm{e}^{-\tau_\lambda} + \sum_{j=1}^{m} S_j(1 - \mathrm{e}^{-\tau_{\lambda,j}}) \exp\left(-\sum_{i=0}^{j-1}\tau_{\lambda,i}\right), \tag{10}$$

where $\tau_{\lambda,0} = 0$, $I_{0,\lambda}$ is the background intensity, $\tau_\lambda = \sum_{j=1}^{m}\tau_{\lambda,j}$ is the total optical depth of the m clouds and

$$\tau_{\lambda,j} = \tau_{0,j} \, \mathrm{e}^{-\left(\frac{\lambda - \lambda_0 - \Delta\lambda_{0,j}}{\Delta\lambda_{\mathrm{D},j}}\right)^2} \tag{11}$$

$\Delta\lambda_{0,j} = \lambda_0 v_j/c$, S_j, $\tau_{0,j}$, v_j, $\Delta\lambda_{\mathrm{D},j}$ are respectively the optical depth, Doppler shift, source function, line-center thickness, velocity and Doppler width of the j^{th} cloud.

A somewhat similar in philosophy, two-cloud model method was used by Heinzel & Schmieder (1994) in their study of black and white mottles. It was assumed that the LOS intersects two mottles treated as two different clouds $c1$ and $c2$ with optical depths τ_1 and τ_2 respectively. Hence the emerging intensity from the lower mottle I_1 is assumed to be the background incident intensity for the second upper mottle. Then, the equations describing the radiation transfer through the two mottles are

$$\begin{aligned} I_2(\Delta\lambda) &= I_1 \, \mathrm{e}^{-\tau_2(\Delta\lambda)} + I_{c2}(\Delta\lambda) \\ I_1(\Delta\lambda) &= I_0 \, \mathrm{e}^{-\tau_1(\Delta\lambda)} + I_{c1}(\Delta\lambda), \end{aligned} \tag{12}$$

where I_0 is the background chromospheric intensity and I_{c1}, I_{c2} the intensity emitted by the two clouds respectively. The novelty of the method is that for the emitted by the clouds intensity, a grid of 140 NLTE models was used which was computed for prominence-like structures by Gouttebroze et al. (1993). So this method is a combination of MCM with NLTE source function calculations which will be further discussed in Section 2.6.

2.4. The Doppler signal method

The Doppler signal method (Georgakilas et al. 1990; Tsiropoula 2000) can be used when filtergrams at two wavelengths $-\Delta\lambda$ and $+\Delta\lambda$ (blue and red side of the line) are available and a fast determination of mass motions is needed. Then the Doppler signal DS can be defined from the BCM equations as

$$DS = \frac{\Delta I}{\sum I - 2I_0} = \frac{\mathrm{e}^{-\tau^+} - \mathrm{e}^{-\tau^-}}{2 - \mathrm{e}^{-\tau^+} - \mathrm{e}^{-\tau^-}}\,, \tag{13}$$

where $\Delta I = I(-\Delta\lambda) - I(+\Delta\lambda)$, $\sum I = I(-\Delta\lambda) + I(+\Delta\lambda)$ and $\tau^{\pm} = \tau(\pm\Delta\lambda)$. The Doppler signal DS has the same sign as velocity and can be used for a qualitative description of the velocity field. The left hand side of the above equation can be determined by the observations while the right hand clearly does not depend on the source function. Quantitative values for the velocity can be obtained when $\tau_0 < 1$; then the Doppler signal equation reduces to

$$DS = \frac{\tau^- - \tau^+}{\tau^- + \tau^+} \tag{14}$$

and the velocity v – once DS is calculated from the observations and a value of the Doppler width $\Delta\lambda_{\mathrm{D}}$ is obtained from the literature or assumed – is given by the equation

$$v = \frac{\Delta\lambda_{\mathrm{D}}^2}{4\Delta\lambda}\frac{c}{\lambda}\ln\left(\frac{1+DS}{1-DS}\right)\,. \tag{15}$$

2.5. Avoiding the background profile

Liu & Ding (2001) in order to avoid the use of the background profile needed in BCM assumed that it is symmetric, that is $I_0(\Delta\lambda) = I_0(-\Delta\lambda)$. Then it can easily be shown that we can obtain the relationship

$$\Delta I(\Delta\lambda) = I(\Delta\lambda) - I(-\Delta\lambda) = [I(\Delta\lambda) - S][1 - \mathrm{e}^{\tau(\Delta\lambda)-\tau(-\Delta\lambda)}]\,, \tag{16}$$

which does not require the use of the background for the derivation of the physical parameters.

2.6. NLTE methods

As Eq. 1 shows, in the general case, the source function S within a cloud-like structure is not constant, but usually depends on optical depth. In order to calculate this dependence, the NLTE radiative transfer problem within the structure has to be solved, taking into account all excitation and ionization conditions within the structure. Several efforts have been undertaken in the past for

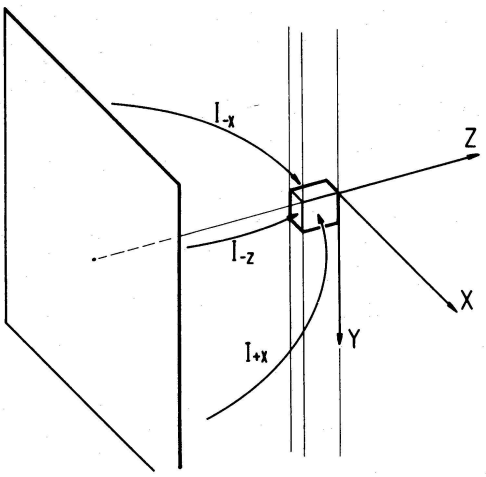

Figure 3. Geometry of a two-dimensional cloud model slab. The incident radiation comes not only from below, but also from the sides of the structure. From Vial (1982).

such NLTE calculations, usually for the case of filaments or prominences. Such NLTE calculations started from the one-dimensional regime, where the cloud-like structure is approximated by an infinite one-dimensional slab (see Fig. 1) or a cylinder. We refer the reader to the works of Heasley et al. (1974), Heasley & Mihalas (1976), Heasley & Milkey (1976), Mozozhenko (1978), Fontenla & Rovira (1985), Heinzel et al. (1987), Gouttebroze et al. (1993), Heinzel (1995), Gouttebroze (2004) for an overview of such one-dimensional NLTE models. The philosophy of two-dimensional NLTE models is similar to the one-dimensional models, but now the cloud-like structure is replaced by a two-dimensional slab or cylinder which is infinite in the third dimension, allowing both vertical, as well as horizontal radiation transport (see Fig. 3). Furthermore, the incident radiation is treated as anisotropic and comes now not only from below, but also from the sides of the structure. We refer the reader to the works of Mihalas et al. (1978), Vial (1982), Paletou et al. (1993), Auer & Paletou (1994), Heinzel & Anzer (2001), Gouttebroze (2005) for an overview of such two-dimensional NLTE models.

A general recipe for such NLTE models, which is modified according to the specific needs, i.e. the line profile used and the structure observed, has as follows:

- The cloud-like structure is assumed to be a 1-D or 2-D slab or cylinder at a height H above the photosphere. This slab/cylinder can be considered to be either isothermal (e.g., Heinzel 1995) or isothermal and isobaric (e.g., Paletou et al. 1993).
- The incident radiation comes in the case of 1-D models only from below and in the case of 2-D models also from the sides and determines the radiation field within the structure, that is all excitation and ionization conditions.
- A multi-level atom plus continuum is assumed. The larger the number of atomic levels used, the more computationally demanding the method is.

Complete or partial redistribution effects (CRD or PRD) are also assumed depending on the formation properties of the line. Methods with CRD are computationally much faster so sometimes CRD is used but with simulated PRD effects taken into account (e.g., Heinzel 1995).

- Some physical parameters are assigned to the slab/cylinder, like temperature T, bulk velocity v, geometrical thickness Z, electronic density $N_{\rm e}$ or pressure p. Calculations with electronic density are usually faster than calculations with pressure.
- The radiative transfer statistical equilibrium equations are numerically solved and the population levels are found and hence the source function as a function of optical depth for a set of selected physical parameters.

Once the source function S is obtained as a function of optical depth, Eq. 1 can be solved in order to calculate the emerging observed profile from the structure which is going to be compared to the observed one.

3. Solving the Cloud Model Equations

In the following subsections some of the methods used to solve the cloud model equations are reviewed. We remind the reader that whenever the background profile is needed, either the average profile of a quiet Sun region is taken or the average profile of a region close to the structure under study.

3.1. Solving the constant-S case with the "5-point" method

Mein et al. (1996a) introduced the "5-point method" for solving the BCM equation with constant S. According to this method five intensities of the observed and the background profile at wavelengths λ_1, λ_2 (blue wing of the observed profile), λ_3, λ_4 (red wing of the the observed profile) and the line-center wavelength λ_0 are used for solving Eqs. 3 and 4. It is an iterative method that works as follows:

- The line-center wavelength λ_0 profile and background intensities are used for calculating S, where τ_0, $\Delta\lambda_{\rm D}$ and v are determined in a previous iteration. At the first step of the iteration some values can be assumed and S can be taken as equal to zero.
- Profile and background intensities at wavelengths λ_1 and λ_3 are used for calculating a new τ_0.
- Afterwards a new $\Delta\lambda_{\rm D}$ is calculated using the other two remaining wavelengths λ_2 and λ_4.
- Finally a new velocity is calculated from wavelengths λ_1, λ_2, λ_3, and λ_4 and then a reconstructed profile obtained using the derived parameters which is compared to the observed one. If any of the departures between the reconstructed and the observed profile is higher than an assumed small threshold value (i.e. 10^{-4}) then the aforementioned procedure is repeated until convergence is achieved. If no convergence is gained after a certain number of iterations then it is assumed that no solution exists.

We refer the reader to Mein et al. (1996a) for a detailed description of the analytical equations described above.

3.2. Solving the constant-S case with an iterative least-square fit

This method which was used by Alissandrakis et al. (1990) and further described in Tsiropoula et al. (1999) and Tziotziou et al. (2003) fits the observed contrast profile with a curve that results from an iterative least-square procedure for non-linear functions which is repeated until the departures between computed and observed profiles are minimized. The coefficients of the fitted curve are functions of the free parameters of the cloud model. At the beginning of the iteration procedure initial values have to be assumed for the free parameters and especially for the source function S which is usually estimated from some empirical approximate expressions that relate it to the line-center contrast. This method is very accurate and usually converges within a few iterations. The more observed wavelengths used within the profile, the better the determination of the ohysical parameters is. However, as Tziotziou et al. (2003) have reported, the velocity calculation can overshoot producing very high values, if the wings of the profile are not sufficiently covered by observed wavelengths. The suggested way to overcome the problem is to artificially add two extra contrast points near the continuum of the observed profile where the contrast should be in theory equal to zero.

This iterative method can also be successfully used not only in the case of a constant source function S, but also for cases with a prescribed expression for the source function, such as the parabolic expression of Eq. 7 used by Tsiropoula et al. (1999).

3.3. Solving the constant-S case with a constrained nonlinear least-square fitting technique

The constrained nonlinear least-square fitting technique, used by Chae et al. (2006) for the inversion of a filament with BCM, was introduced by Chae et al. (1998). According to the method a) expectation values p_i^e of the ith free parameters, b) their uncertainties ε_i, as well as c) the data to fit are provided (M wavelengths along the profile) and then a set of N free parameters $\mathbf{p} = (p_0, p_1, ...p_{N-1})$ are sought, i.e. $\mathbf{p} = (S, \tau_0, \lambda_0, \Delta\lambda_{\rm D})$, that minimize the function

$$H(\mathbf{p}) = \sum_{j=0}^{M-1} \left(\frac{C_j^{\rm obs} - C_j^{\rm mod}(\mathbf{p})}{\sigma_j} \right)^2 + \sum_{i=0}^{N-1} \left(\frac{p_i - p_i^e}{\varepsilon_i} \right)^2 , \qquad (17)$$

where $C_j^{\rm obs}$ and $C_j^{\rm mod}$ are respectively the observed and calculated with the expectation values contrasts and σ_j the noise in the data. The first term of the sum H represents the data χ^2, while the second term the expectation χ^2 which regularizes the solution by constraining the probable range of free parameters. For very small values of ε_i the solution will not be much constrained by the data and will be close to the chosen set of expectation values p_i^e, while for large values of ε_i it will be mostly constrained by the data and not by the expectation values. We refer the reader to Chae et al. (2006) for a detailed discussion of the effects of constrained fitting.

3.4. Solving the variable-S case

Apart from the iterative least-square procedure described above which can be used when the source function varies in a prescribed way, Mein et al. (1996a) have

introduced also the "4-point method" for solving the case of a source function that is described by the second order polynomial of Eq. 6. According to the method an intensity $I'(\Delta\lambda)$ can be defined as follows

$$\begin{aligned} I'(\Delta\lambda) &= I(\Delta\lambda) - \frac{1-[\tau(\Delta\lambda)+1]\ \mathrm{e}^{-\tau(\Delta\lambda)}}{\tau(\Delta\lambda)}\ S_1 + \\ &\quad \frac{2-[\tau^2(\Delta\lambda)+2\tau(\Delta\lambda)+2]\ \mathrm{e}^{-\tau(\Delta\lambda)}}{\tau^2(\Delta\lambda)}\ S_2 \end{aligned} \tag{18}$$

and then the radiative transfer equation reduces to

$$I'(\Delta\lambda) = S_0 + (I_0 - S_0)\ \mathrm{e}^{-\tau(\Delta\lambda)}\,. \tag{19}$$

This equation can be solved now using the iteration procedure described in Sect. 3.1, with the modification that $I(\Delta\lambda)$ is now replaced by $I'(\Delta\lambda)$ and that the source function calculation in the first step is replaced by the assumed theoretical relation for S given by Eq. 6.

3.5. Solving the DCM cases

A method for solving the differential cloud model cases is the "3-optical depths" procedure introduced by Mein & Mein (1988). According to this procedure:

- the zero velocity reference is obtained from the average profile over the whole field of view;
- a value S is assumed between zero and the line-center intensity (in principle it could even work also for emitting clouds) and a function $\delta\tau(\lambda)$ is derived from Eq. 8. The latter is characterized by the maximum value $\delta\tau_0$ and $\delta\tau_1$, and the values $\delta\tau_2$ (see right panel of Fig. 2) which correspond to the half widths $\Delta\lambda_1$ and $\Delta\lambda_2$ respectively and are given by the following relations

$$\begin{aligned} \delta\tau_1 &= \delta\tau_0\ \mathrm{e}^{-(\Delta\lambda_1/\Delta\lambda_\mathrm{D})^2} \\ \delta\tau_2 &= \delta\tau_0\ \mathrm{e}^{-(\Delta\lambda_2/\Delta\lambda_\mathrm{D})^2}\,; \end{aligned} \tag{20}$$

- the code fits S and $\Delta\lambda_\mathrm{D}$ by the conditions of Eq. 20 coupled with Eq. 8 and the solutions are assumed to be acceptable when the radial velocities v_1 and v_2, which correspond to widths $\Delta\lambda_1$ and $\Delta\lambda_2$ respectively and are defined as the displacement of the middle of these chords compared with the zero reference position, are not that different. When convergence is achieved the $\delta\tau(\lambda)$ curve is well represented by a Gaussian and the Doppler width $\Delta\lambda_\mathrm{D}$ is independent of the chord $\Delta\lambda$.

3.6. Solving the MCM case

We refer the reader to the papers by Li & Ding (1992) and Li et al. (1993, 1994) for a detailed description of the methods and mathematical manipulations used for fitting observed profiles with the multi-cloud method, which unfortunately are not easy to concisely describe within a few lines.

3.7. Using NLTE Methods

The most straightforward method for deriving the parameters of an observed structure with NLTE calculations would be the calculation of a grid of models for a wide range of the physical parameters used to describe the structure. However, the calculation of such a grid is computationally demanding, especially in the case when a) a large number of atomic levels is assumed and/or b) partial redistribution effects (PRD) are taken into account and/or c) a two-dimensional geometry is considered. For such cases, either a very small grid of models is constructed and thus only approximate values for the observed structure are derived or "test and try" methods are used where the user makes a "good guess" for the physical parameter values, proceeds to the respective NLTE calculations, compares the derived profile(s) with the observed one(s) and applies the necessary adjustments to the model parameters according to the derived results.

However, nowadays the construction of a large grid of models, although time-demanding, becomes more of a common practice with the extended capabilities of modern computers. We refer the reader to Molowny-Horas et al. (2001) and Tziotziou et al. (2001) for two such examples, both considering a one-dimensional isothermal slab for a cloud-like structure, which is the same filament observed and studied in the Hα in Ca II 8542 Å lines respectively. The general methodology used in the case of grids of models is the following:

- a grid of synthetic line profiles for a wide range of model parameters is computed using NLTE calculations for the source function, as described in Sect. 2.6;
- these synthetic profiles are convolved with the characteristics of the instrument used for the observations in order to simulate its effects on the observed profiles;
- each observed profile is compared with the whole library of convolved synthetic profiles and the best fit is derived, that is the synthetic profile with the smallest departure, and hence the physical parameters that describe it;
- an interpolation (linear or parabolic) between neighboring points in the parameter space can also be used, for a more accurate quantitative determination of the physical parameters that best describe the observed profile.

Grid models based on NLTE calculations have many advantages since preferred geometries, temperature structures, etc can be used, no iterations are required, errors can be easily defined from the parameter space and inversions are nowadays becoming faster with modern computers.

4. Validity of the Cloud Models

The validity of the cloud model used for an inversion obviously strongly depends on a) the method used, b) the assumptions that were made for the model atmosphere describing the structure and c) the specific characteristics of the structure under study. Most of the reviewed papers in Sect. 5, concerning applications of different cloud models, have extended discussions on the validity of the cloud model method and the results obtained, as well as the limitations

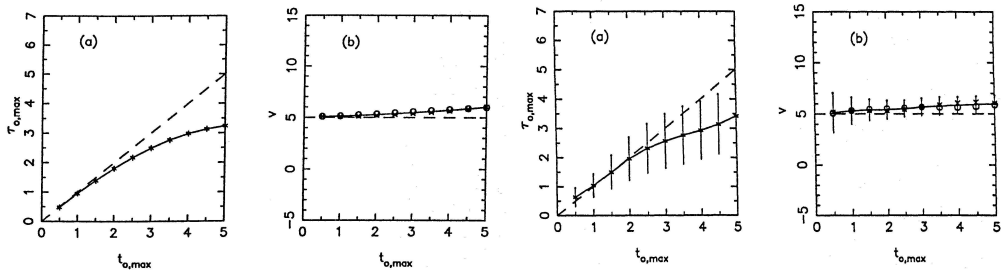

Figure 4. *Two left panels:* The calculated optical depth $\tau_{0,\max}$ and velocity v with BCM (constant source function) versus the assumed optical thickness. The dashed curve is the model, the solid curve the inversion. *Two right panels:* Same plots but with added Gaussian noise. From Mein et al. (1996a).

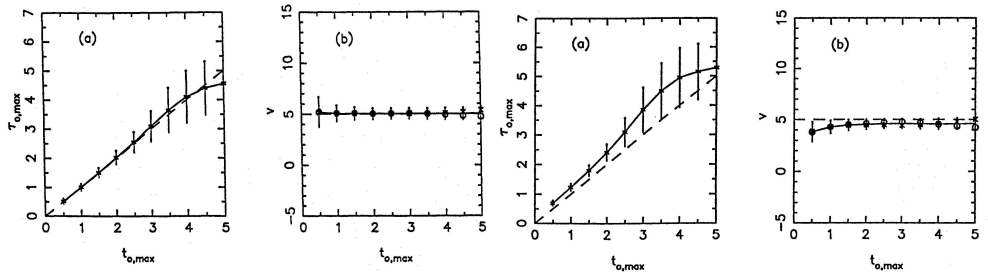

Figure 5. *Two left panels:* The calculated optical depth $\tau_{0,\max}$ and velocity v using a cloud model with variable source function (see Eq. 6) depending only on line-center optical thickness versus the assumed optical thickness. Gaussian noise has also been taken into account. *Two right panels:* Same plots but for an over-estimated chromospheric background profile. From Mein et al. (1996a).

of the method for the specific structure. However, below, some studies found in literature about the validity of cloud models are presented.

Mein et al. (1996a) presented a rather detailed study about the validity of BCM (constant source function), as well as of cloud models with a variable source function as described in Eq. 6 (depending only on line-center optical thickness) by inverting theoretical profiles produced with a NLTE code and comparing the resulting model parameters from the inversion with the assumed ones. Figure 4 (two left panels) shows the results of the inversion versus the assumed model optical thickness for the BCM inversion (constant source function). The calculated optical thickness is smaller, with the difference increasing with the thickness of the cloud, while the difference in velocity is no more than 20% and only for high values of the thickness. The figure shows that for optically thin structures there is practically no difference in the obtained results. When noise is included (Fig. 4, two right panels) the error increases for increasing thickness but the mean values stay almost the same. Again for optically thin structures the difference in the results is very small.

Figure 5 (two left panels) shows the results of the inversion versus the assumed model optical thickness for a cloud model with variable source function

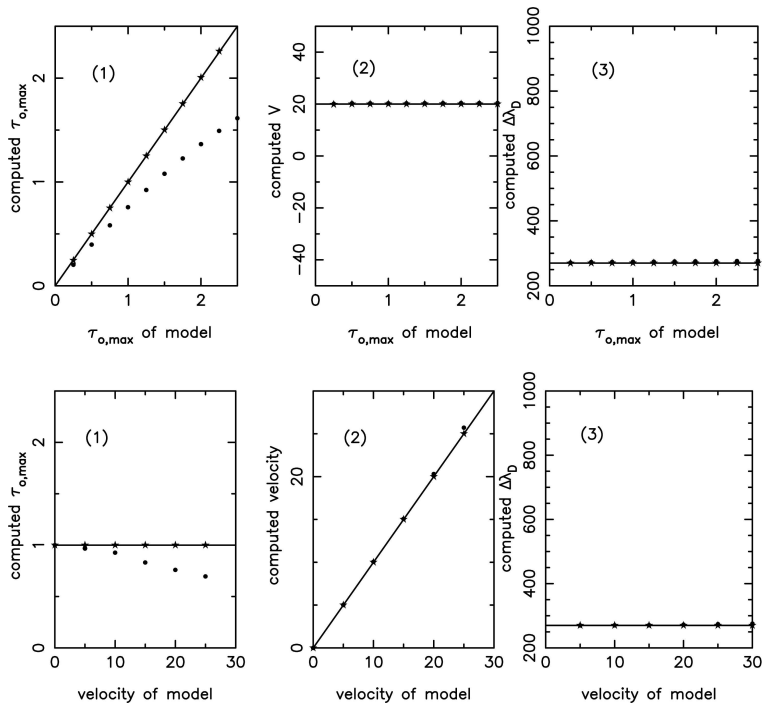

Figure 6. Comparison of the results obtained with method (a) represented by dots and with method (b) represented by asterisks (see text for details of the methods) with the assumed model values (solid curve). From Heinzel et al. (1999).

according to Eq. 6 depending only on line-center optical thickness with an added Gaussian noise; without noise the results are perfectly reproduced. We see that the differences are now almost negligible for a large range of the assumed optical thickness and the parameters are better determined. However, when taking a slightly brighter background (Fig. 5, two right panels) we see that the calculated values of the optical thickness are larger than the assumed ones, while the estimation of velocity is still rather good. This shows the importance of a correct background profile choice in cloud model calculations.

Heinzel et al. (1999) has repeated the same exercise (inversion of NLTE synthetic profiles) for a cloud model with a variable source function according to Eq. 6 depending a) only on line-center optical thickness (method a) and b) on line-center optical thickness and velocity (method b). Some of their results are shown in Fig. 6. We see that although with method (a) there are some differences in the calculation of optical thickness, similarly to Mein et al. (1996a), method (b) gives exact solutions. Heinzel et al. (1999) have also applied the two methods in observed profiles of a dark arch filament. Figure 7 shows the comparison of the results obtained with the two methods.

We refer also the reader selectively to a) Molowny-Horas et al. (2001) (Fig. 12 of their paper) for a comparison of inversion results for a filament with a NLTE method and a cloud model with a parabolic S, b) Schmieder et al. (2003) (Fig. 16 of their paper) for a comparison of inversion results for a filament with

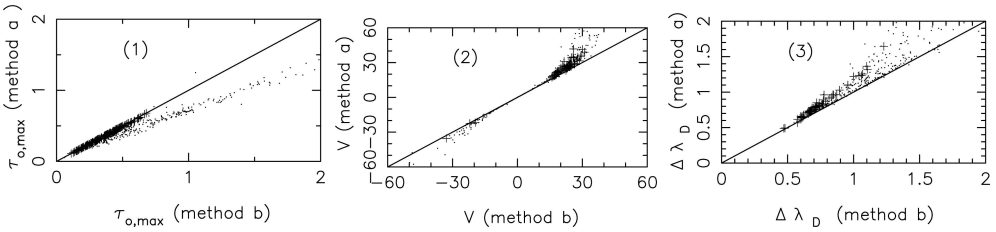

Figure 7. Comparison of the results obtained with the two methods (a) and (b) (see text for details) from the inversion of observed profiles of a dark arch filament. Scatter plots are shown for (1) optical thickness, (2) velocity (in km s^{-1}), and (3) Doppler width (in Å). From Heinzel et al. (1999).

a NLTE method and a constant source function cloud model, c) Tsiropoula et al. (1999) (Fig. 5 of their paper) for a comparison of inversion results for mottles for cloud models with a constant and parabolic S, and d) Alissandrakis et al. (1990) (Fig. 8 to 11 of their paper) for a comparison of inversion results for an arch filament system with Beckers' cloud model, the Doppler signal method and the differential cloud model.

5. Examples of Cloud Model Inversions

Cloud models have been so far successfully applied for the derivation of the parameters of several cloud-like solar structures of the quiet Sun, such as mottles/spicules, as well of active region structures, such as arch filament systems (AFS), filaments, fibrils, flaring regions, surges etc. Below, some examples of such cloud model inversions are presented.

5.1. Application to filaments

Filaments are commonly observed features that appear on the solar disc as dark long structures, lying along longitudinal magnetic field inversion lines. When observed on the limb they are bright and are called prominences. Filaments were some of the first solar structures to be studied with cloud models (see for example Maltby 1976, and references therein). Since then several authors used different cloud models to infer the dynamics and physical parameters of filaments. Mein, Mein & Wiik (1994), for example, studied the dynamical fine structure (threads) of a quiescent filament assuming a number of identical – except for the velocity – threads seen over the chromosphere and using a variant of BCM, while Schmieder et al. (1991) performed a similar study for threads by using the DCM. Morimoto & Kurokawa (2003) developed an interesting method applying BCM to determine the three-dimensional velocity fields of disappearing filaments.

Molowny-Horas et al. (2001) and Tziotziou et al. (2001) studied the same filament observed in Hα and Ca II 8542 Å respectively with the Multichannel Subtractive Double Pass (MSDP) spectrograph (Mein 1991, 2002) mounted on the German solar telescope VTT in Tenerife. The filament was studied by using two very large grids of models in Hα and Ca II 8542 Å respectively which were constructed with the NLTE one-dimensional code MALI (Heinzel 1995), as

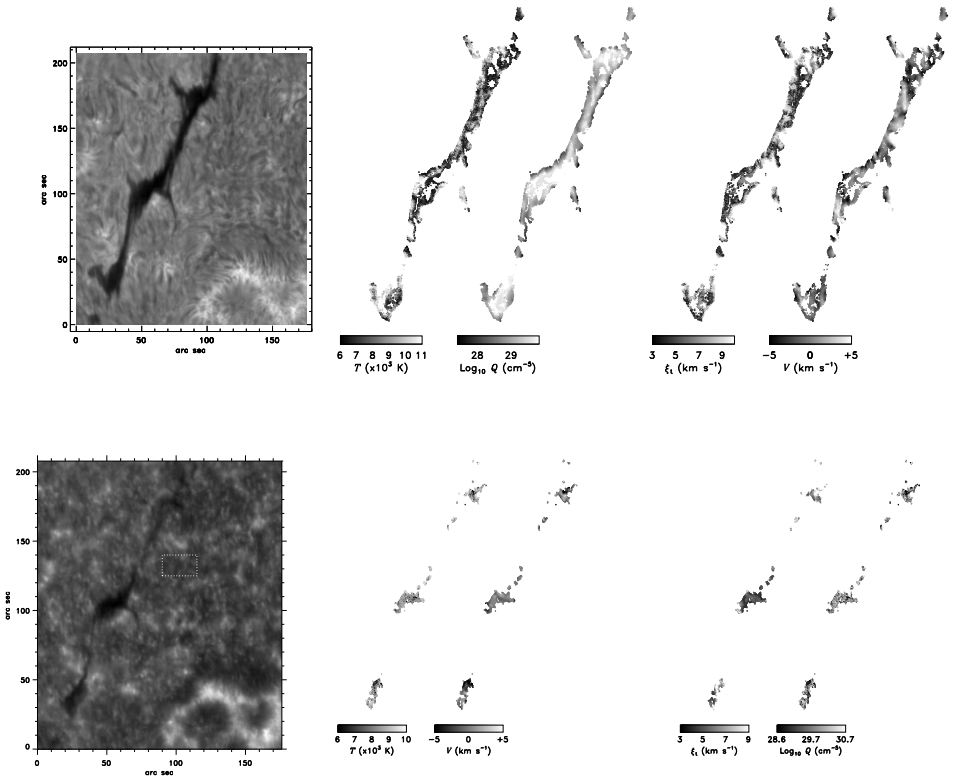

Figure 8. *Top row:* A filament observed in Hα and the two-dimensional parameter distributions derived with a Hα NLTE inversion using a grid of models. From Molowny-Horas et al. (2001). *Bottom row:* Same filament observed in Ca II 8542 Å and the two-dimensional parameter distributions derived with a Ca II 8542 Å NLTE grid model inversion. From Tziotziou et al. (2001).

described in Sect. 2.6 Two-dimensional distributions of the physical parameters were obtained (see Fig. 8) which are not that similar due to the different physical formation properties and formation heights of the two lines. Schmieder et al. (2003) performed a similar NLTE grid inversion of a filament combined with a classical BCM inversion in a multi-wavelength study of filament channels. More recently, Chae et al. (2006) used Hα images obtained with a tunable filter and a BCM inversion to obtain detailed two-dimensional distributions of the physical parameters describing a quiescent filament.

5.2. Application to arch filaments (AFS)

Arch filaments systems (AFSs) are low-lying dark loop-like structures formed during the emergence of solar magnetic flux in active regions. Georgakilas et al. (1990) have used the Doppler signal method described in Sect. 2.4 to study mass motions in AFSs observed in Hα, while Alissandrakis et al. (1990) and Tsiropoula et al. (1992) used the standard BCM to obtain the physical parameters describing arch filament regions observed in the same line (see Fig. 9). An example of the use of the differential cloud model described in Sect. 2.2 for the

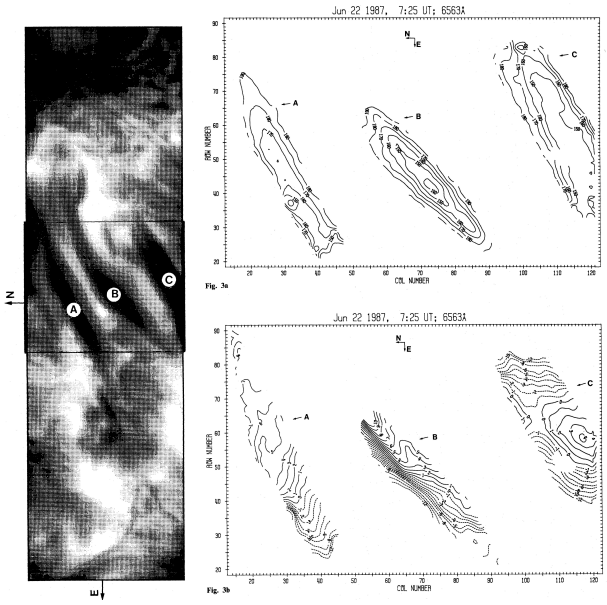

Figure 9. Contours maps of source function (*top right panel*) and the velocity (*bottom right panel*) derived with the cloud model for the AFS shown in Hα in the left panel of the figure. From Alissandrakis et al. (1990).

study of the dynamics of AFSs can be found in Mein et al. (1996b) who applied the method to Hα observations from a two-telescope coordinated campaign. Finally Mein et al. (2000) present a study of AFSs in Ca II 8542 Å using a fitting done with NLTE synthetic profile calculations – as described in Sect. 2.6 – with the one-dimensional MALI code (Heinzel 1995).

5.3. Application to fibrils

Fibrils are small dark structures, belonging to the family of "chromospheric fine structures", found in active regions surrounding plages or sunspots (penumbral fibrils). One of the first studies of fibrils was conducted by Bray (1974) who compared observed profiles of fibrils with profiles calculated with BCM. Alissandrakis et al. (1990) used the standard BCM to obtain two-dimensional maps of several physical parameters distributions describing fibrils using Hα observations obtained at Pic du Midi Observatory. Georgakilas et al. (2003) used filtergrams obtained at nine wavelengths along the Hα to study the Evershed flow in sunspots and reconstruct the three-dimensional velocity vector using the Doppler signal method (see Fig. 10), while Tsiropoula (2000) used also the Doppler signal method to determine LOS velocities of dark penumbral fibrils.

5.4. Application to mottles

Mottles are small-scale structures (appearing both bright and dark) belonging also to the family of "chromospheric fine structures" and occurring at quiet Sun regions at the boundaries of supergranular cells. Mottles are believed to be the counterparts of limb spicules. They form groups called chains (when they are almost parallel to each other) or rosettes (when they are more or less

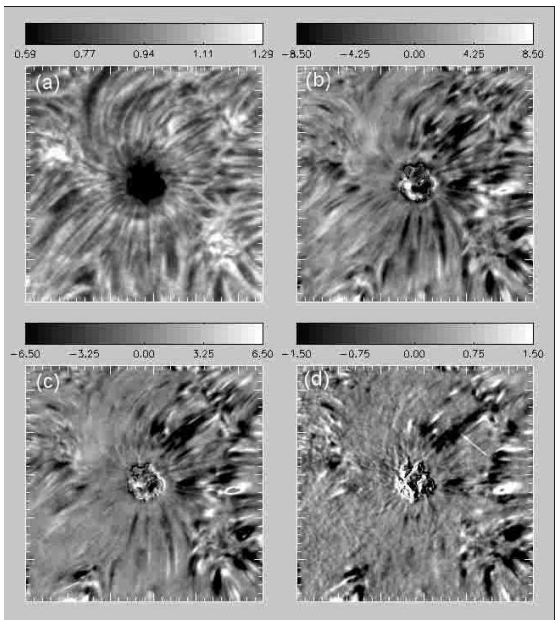

Figure 10. Image of a sunspot observed in Hα (a) and Doppler velocity maps computed with the Doppler signal method from filtergrams in H$\alpha\pm$0.35Å (b), in H$\alpha\pm$0.5Å (c) and in H$\alpha\pm$0.75Å (d). The intensity gray scale bar corresponds to normalized intensities while the Doppler velocity gray scale bars to velocities in km s^{-1}. From Georgakilas et al. (2003).

circularly aligned, pointing radially outwards from a central core) depending on their location at the chromospheric network.

First cloud studies of mottles started with a controversy about the ability of BCM to explain their contrast profiles. Bray (1973) and Loughhead (1973) who studied bright and dark mottles found that their contrast profiles are in good agreement with BCM. However, Loughhead (1973) used also BCM to deduce that it could not explain the contrast of individual bright and dark mottles observed in Hα near the limb, while Cram (1975) claimed that the parameters inferred from an application of BCM to contrast profiles of chromospheric fine structures are unreliable.

Since then cloud models have been established as a reliable method for the study of physical parameters of mottles. Tsiropoula et al. (1999) studied several bright and dark mottles to derive physical parameters assuming a constant as well as a varying source function according to Eq. 7. Tsiropoula & Schmieder (1997) applied Beckers' cloud model to determine physical parameters in Hα dark mottles of a rosette region, while Tsiropoula et al. (1993, 1994) studied the time evolution and fine structure of a rosette with BCM and first showed an alternating behaviour with time for velocity along mottles (see Fig. 11, *left panel*). A similar behaviour has also been found by Tziotziou et al. (2003) using BCM for a chain of mottles (see Fig. 11, *right panel*), while the dynamics of an enhanced network region were also explored in high resolution Hα images by Al et al. (2004).

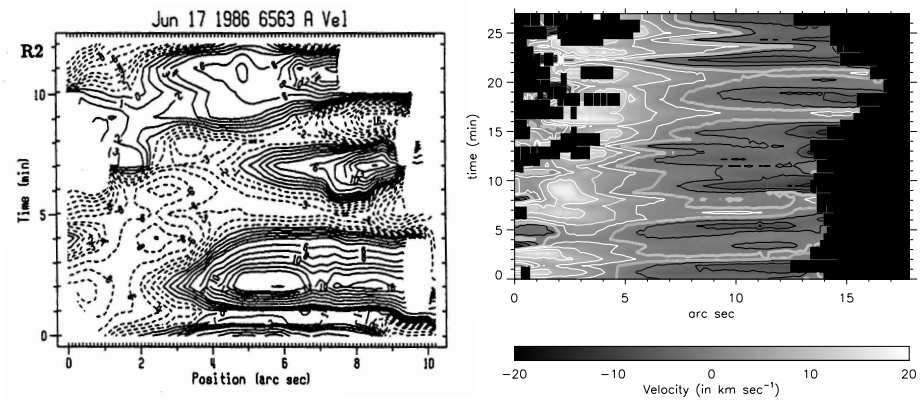

Figure 11. *Left panel:* Cloud velocity as a function of position and time along the axis of a dark mottle belonging to a rosette. From Tsiropoula et al. (1994). *Right panel:* Cloud velocity as a function of position and time along the axis of a dark mottle belonging to a chain of mottles. White contours denote downward velocities, black upward velocities, while the thick gray curve is the zero velocity contour. From Tziotziou et al. (2003).

5.5. Application to post-flare loops

Post-flare loops are loops generally observed between two-ribbon flares. We refer the reader to Bray & Loughhead (1983) for one of the first post-flare loop studies, who constructed theoretical curves based on the cloud model to fit observed contrast profiles of active region loops. Later Schmieder et al. (1988) and Heinzel et al. (1992) used a differential cloud model to study the structure and dynamics of post-flare loops. Heinzel et al. (1992) also constructed several isobaric and isothermal NLTE models of post-flare loops. Their results were compared by Gu et al. (1997) with two-dimensional maps of Hα post-flare loop cloud parameters obtained using a two-cloud model. Multi-cloud models like the ones described in Sect. 2.3 were used by Liang et al. (2004) to study Hα post-flare loops at the limb (see Fig. 12), by Gu & Ding (2002) for the study of Hα and Ca II 8542 Å post-flare loops and by Dun et al. (2000) for the study of Hβ post-flare loops. Liu & Ding (2001) obtained parameters of Hα post-flare loops using the modified cloud model method presented in Sect. 2.5 that eliminates the use of the background profile while Gu et al. (1992) presented an extensive study using BCM, the differential cloud model and a two-cloud model to study the time evolution of post-flare loops in two-ribbon flares. Finally, we refer the reader to Berlicki et al. (2005) who studied Hα ribbons during the gradual phase of a flare by comparing observed Hα profiles with a grid of synthetic Hα profiles calculated with the NLTE code MALI (Heinzel 1995) which was modified to account for flare conditions.

5.6. Application to surges

Surges are large jet-like structures observed in opposite polarity flux emergence areas in active regions believed to be supported by magnetic reconnection. Gu et al. (1994) studied a surge on the limb observed in Hα, using a two-cloud model inversion as described in Sect. 2.3 (see Fig 13). The inversion result was

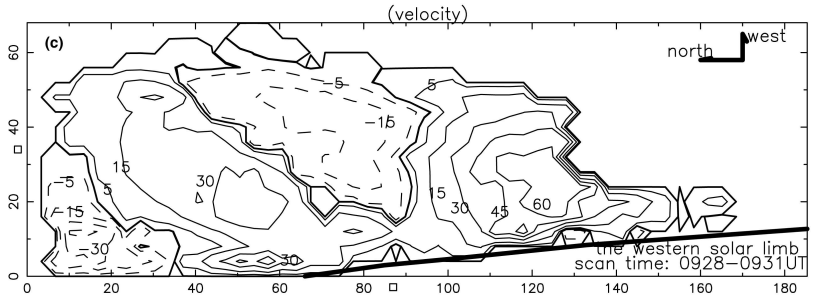

Figure 12. The distributions of Doppler velocity (in km s^{-1}) derived with a multi-cloud method for Hα limb post-flare loops. Coordinates are in units of arcsec, dashed curves show red-shifted mass motions, while solid curves indicate blue-shifted ones. From Liang et al. (2004).

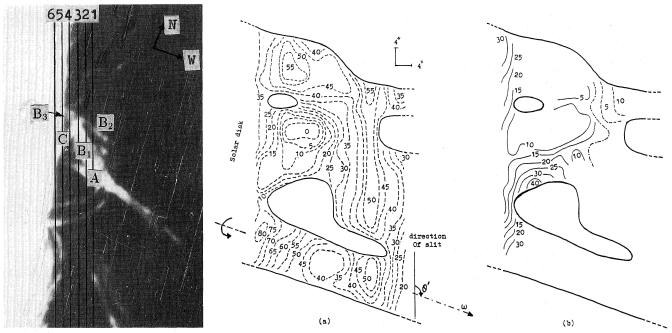

Figure 13. An Hα filtergram of a surge (*left panle*) and the two-dimensional isocontours of Doppler velocity derived with a two-cloud model. Dashed curves refer to blue-shifted velocities (*middle panel*), solid curves red-shifted ones (*right panel*), while the unit of velocity is in km s^{-1}. From Gu et al. (1994).

detailed two-dimensional maps of the blue-shifted and red-shifted LOS velocity distributions.

6. Conclusions

Several inversion techniques for chromospheric structures based on the cloud model have been reviewed. Cloud models are fast, quite reliable tools for inferring the physical parameters describing cloud-like chromospheric structures located above the solar photosphere and being illuminated by a background radiation. Cloud model techniques usually provide unique solutions and the results do not differ – in principle – qualitatively, especially for velocity, when using different cloud model techniques. However there can be quantitative differences arising from a) the selection of the background intensity, b) the physical conditions and especially the behaviour of the source function within the structure under study, and c) the particular model assumptions. Cloud models are mainly used for absorbing structures, however most of the techniques do work also for

line-center contrasts that are slightly higher than zero, indicating an important emission by the structure itself.

Several different variants for cloud modeling have been proposed in literature so far that mainly deal with different assumptions or calculations for the source functions and span from the simple BCM that assumes a constant source function to more complicated NLTE calculations of the radiation transfer and hence the source function within the structure. Accordingly, several different techniques – most of them iterative – have been proposed for solving cloud model equations. The latest and more accurate inversion techniques involve the construction of large grids of synthetic profiles, for different geometries and physical conditions, which are used for comparison with observed profiles.

Cloud models can be applied with success to several, different in geometry and physical conditions, solar structures both of the quiet Sun, as well as of active regions. The resulting parameter inversions has shed light to several problems involving the physics and dynamics of chromospheric structures.

The future of cloud modeling looks even more brighter. New high resolution data from telescopes combined with an always increasing computer power and the continuous development of new, state of the art, NLTE one-dimensional and two-dimensional cloud model codes will provide further detailed insights to the physics and dynamics that govern chromospheric structures.

Acknowledgments. KT thanks G. Tsiropoula for constructive comments on the manuscript and acknowledges support by the organizers of the meeting and by Marie Curie European Reintegration Grant MERG-CT-2004-021626.

References

Al N., Bendlin C., Hirzberger J., Kneer F., Trujillo Bueno J., 2004, A&A 418, 1131
Alissandrakis C. E., Tsiropoula G., Mein P., 1990, A&A 230, 200
Auer L. H., Paletou F., 1994, A&A 284, 675
Beckers J. M., 1964, A study of the fine structures in the solar chromosphere, Ph.D. Thesis, Utrecht
Berlicki A., Heinzel P., Schmieder B., Mein P., Mein N., 2005, A&A 430, 679
Bray R. J., 1973, Solar Phys. 29, 317
Bray R. J., 1974, Solar Phys. 38, 377
Bray R. J., Loughhead R. E., 1983, Solar Phys. 85, 131
Chae, J., Yun, H.S., Poland, A.I., 1998, ApJS 114, 151
Chae, J., Park, Y.-D., Park, H.-M., 2006, Solar Phys. 234, 115
Cram L. E., 1975, Solar Phys. 42, 53
Dun J.P., Gu X.M., Zhong S.H., 2000, Ap&SS 274, 473
Fontenla J. M., Rovira M., 1985, Solar Phys. 96, 53
Georgakilas A. A., Alissandrakis C. E., Zachariadis Th. G., 1990, Solar Phys. 129, 277
Georgakilas A. A., Christopoulou E. B., Skodras A., Koutchmy S., 2003, A&A 403, 1123
Gouttebroze P., 2004, A&A 413, 733
Gouttebroze P., 2005, A&A 434, 1165
Gouttebroze P., Heinzel P., Vial J.-C., 1993, A&AS 99, 513
Grossmann-Doerth U., Uexküll M., 1971, Solar Phys. 20, 31
Gu X. M., Ding M. D., 2002, Chin. J. Astron. Astrophys. 2, 92
Gu X. M., Lin J., Luan T., Schmieder B., 1992, A&A 259, 649
Gu X. M., Lin J., Li K. J., Xuan J. Y., Luan T., Li Z. K., 1994, A&A 282, 240
Gu X. M., Lin J., Li K. J., Dun J. P., 1996, Ap&SS 240, 263

Gu X. M., Ding Y. J., Luo Z., Schmieder B., 1997, A&A 324, 289
Heasley J. N., Mihalas D., 1976, ApJ 205, 273
Heasley J. N., Milkey R. W., 1976, ApJ 210, 827
Heasley J. N., Mihalas D., Poland A., 1974, ApJ 192, 181
Heinzel P., 1995, A&A 299, 563
Heinzel P., Anzer U., 2001, A&A 375, 1082
Heinzel P., Schmieder B., 1994, A&A 282, 939
Heinzel P., Gouttebroze P., Vial J.-C., 1987, A&A 183, 351
Heinzel P., Mein N., Mein P., 1999, A&A 346, 322
Heinzel P., Schmieder B., Mein P., 1992, Solar Phys. 139, 81
Liang H., Zhan L., Xiang F., Zhao H., 2004, New Astron. 10, 121
Li K. J., Ding Y. J., 1992, Acta Astron. Sin. 33, 171
Li K. J., Ding Y. J., Gu X. M., Li Q. S., Zhong S. H., Li Q. Y., 1993, A&A 269, 496
Li K. J., Ding Y. J., Bai J. M., Zhong S. H., Xuan J. Y., Li Q. Y., 1994, Solar Phys. 150, 87
Liu Y., Ding M. D., 2001, Solar Phys. 200, 127
Loughhead R. E., 1973, Solar Phys. 29, 327
Maltby P., 1976, Solar Phys. 46, 149
Mein P., 1991, A&A 248, 669
Mein P., 2000, in J.-P. Zahn, M. Stavinschi (eds.), NATO ASIC Proc. 558: Advances in Solar Research at Eclipses from Ground and from Space, 221
Mein P., 2002, A&A 381, 271
Mein P., Mein N., 1988, A&A 203, 162
Mein N., Mein P., Wiik, J. E., 1994, Solar Phys. 151, 75
Mein N., Mein P., Heinzel, P., Vial, J.-C., Malherbe, J. M., Staiger, J., 1996a, A&A 309, 275
Mein P., Démoulin P., Mein N., Engvold O., Molowny-Horas R., Heinzel, P., Gontikakis, C., 1996b, A&A 305, 343
Mein P., Briand C., Heinzel, P., Mein, N., 2000, A&A 355, 1146
Mihalas D., Auer L. H., Mihalas B. R., 1978, ApJ 220, 1001
Molowny-Horas R., Heinzel P., Mein P., Mein N., 1999, A&A 345, 618
Morimoto T., Kurokawa H., 2003, PASJ 55, 503
Mozozhenko N. N., 1978, Solar Phys. 58, 47
Paletou F., Vial, J.-C., Auer L. H., 1993, A&A 274, 571
Schmieder B., Mein P., Malherbe J.-M., Forbes T. G., 1988, Advances in Space Research 8, 145
Schmieder B., Raadu M. A., Wiik, J. E., 1991, A&A 252, 353
Schmieder B., Tziotziou K., Heinzel, P., 2003, A&A 401, 361
Tsiropoula G., 2000, New Astron. 5, 1
Tsiropoula G., Schmieder B., 1997, A&A 324, 1183
Tsiropoula G., Georgakilas A. A., Alissandrakis C. E., Mein P., 1992, A&A 262, 587
Tsiropoula G., Alissandrakis C. E., Schmieder B., 1993, A&A 271, 574
Tsiropoula G., Alissandrakis C. E., Schmieder B., 1994, A&A 290, 285
Tsiropoula G., Madi C., Schmieder B., 1999, Solar Phys. 187, 11
Tziotziou K., Heinzel P., Mein P., Mein N., 2001, A&A 366, 686
Tziotziou K., Tsiropoula G., Mein P., 2003, A&A 402, 361
Vial J.-C., 1982, ApJ 254, 780

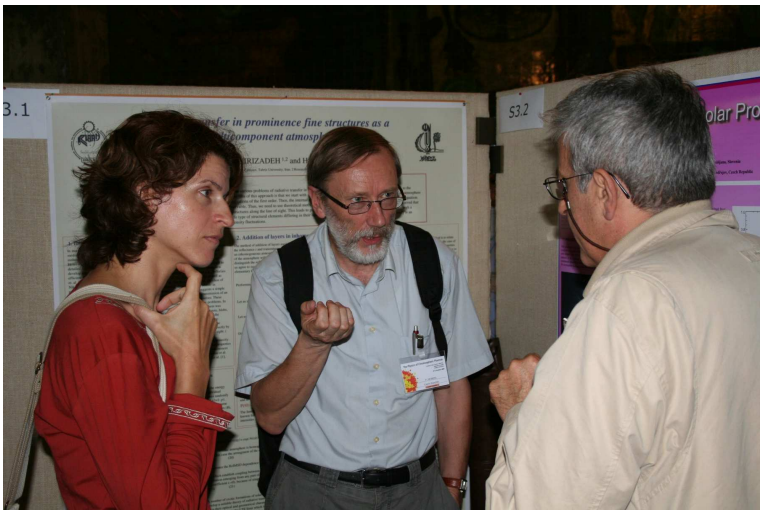

Sonja Jejčič, Petr Heinzel, Jean-Claude Vial

Pavel Kotrč, Elena Dzifčáková, Alena Kulinová

The Physics of Chromospheric Plasmas
ASP Conference Series, Vol. 368, 2007
Petr Heinzel, Ivan Dorotovič and Robert J. Rutten, eds.

Observations of Running Waves in a Sunspot Chromosphere

D. Shaun Bloomfield, Andreas Lagg and Sami K. Solanki

MPI für Sonnensystemforschung, Katlenburg-Lindau, Germany

Abstract. Spectropolarimetric time series data of the primary spot of active region NOAA 9448 were obtained in the Si I 10827 Å line and the He I 10830 Å multiplet with the Tenerife Infrared Polarimeter. Throughout the time series the spectrograph slit was fixed over a region covering umbra, a light bridge, penumbra, and quiet sun. We present speeds of running penumbral waves in the chromosphere, their relation to both photospheric and chromospheric umbral oscillations, and their dependence on the magnetic field topology.

1. Introduction

Running penumbral waves (RPWs), which exist in sunspot chromospheres, were first observed by Zirin & Stein (1972) and more recently studied though various imaging observations (e.g., the series of papers by Christopoulou et al. 2000; Georgakilas et al. 2000; Christopoulou et al. 2001). Although this phenomenon has been investigated in detail, the origin of these moving disturbances and their relation to other phenomena occurring within sunspots remains unclear. In particular, a comparative study by Tziotziou et al. (2006) between the possibility of RPWs being a trans-sunspot wave in the chromosphere or a visual pattern of upward-propagating waves was unable to conclude one way or the other.

The work presented here will attempt to finally address the true origin of these waves using full Stokes time series observations of a sunspot obtained at high cadence. The benefit of observing the full Stokes polarization profiles is the retrieval of the complete magnetic field vector, circumventing the need for any assumptions of the field topology in our conclusions of possible wave propagation.

2. Observations

The data used here were obtained on 2001 May 9 with the Tenerife Infrared Polarimeter (Martínez Pillet et al. 1999) attached to the German VTT. The full Stokes (I, Q, U, V) vector was measured by a slit fixed across active region NOAA 9448. The slit sampled sunspot umbra, a light bridge, penumbra and neighboring quiet Sun at a rate of one exposure every 2.1 s over the period 09:10–10:20 UT. The recorded data from inside the sunspot umbra were previously presented by Centeno et al. (2006), who found vertically propagating, slow-mode waves in a stratified isothermal atmosphere to reliably fit the observed temporal Fourier behavior when radiative cooling was taken into account.

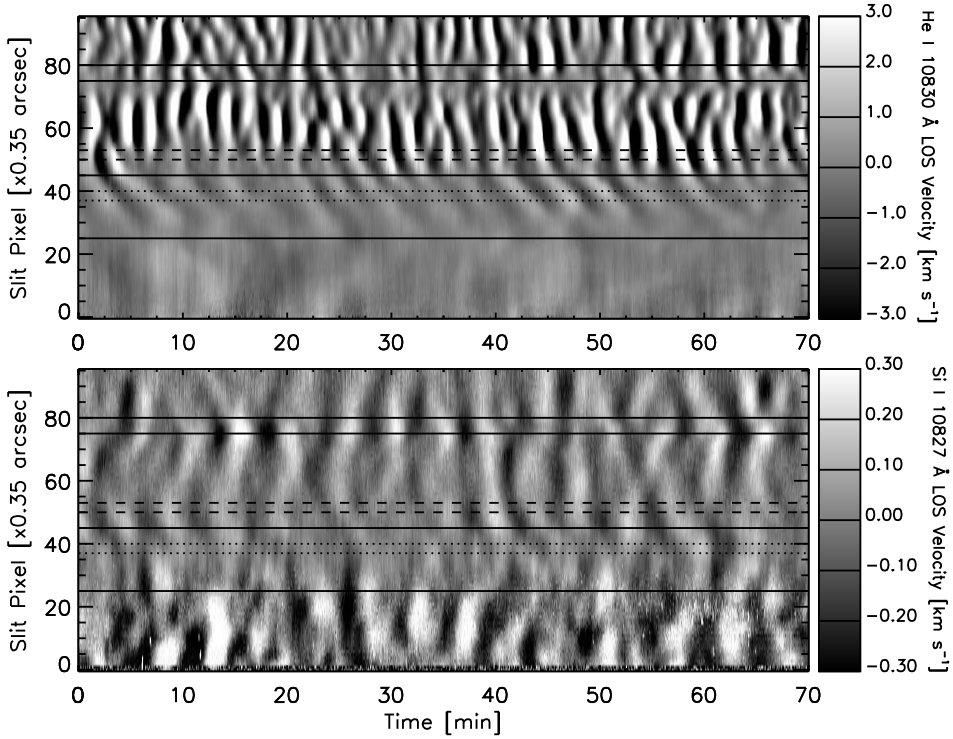

Figure 1. Space-time plots of LOS velocity in the photospheric Si I 10827 Å line (bottom) and upper-chromospheric He I 10830 Å multiplet (top).

The Stokes profiles of the photospheric Si I 10827 Å and high-chromospheric He I 10830 Å lines were individually inverted using the inversion code of Lagg et al. (2004). Atmospheres containing a single magnetic component were used in both cases, while the Si I inversion included an additional non-magnetic, stray-light component. The resulting line-of-sight (LOS) velocities from the inversion are displayed in Fig. 1, where solid horizontal lines mark boundaries between different regions of the sunspot: quiet Sun ($y = 0 - 25$); penumbra ($y = 25 - 45/50$); umbra ($y = 45/50 - 95$); a light bridge ($y = 75 - 80$). It is evident that whereas the umbral oscillations in He I have a period of 3 min, in Si I the umbra oscillates at around 5 min. Note, the RPWs also show a period close to 5 min.

3. Horizontal Motions

Initially, raw He I velocities were studied to determine the apparent horizontal propagation speed of the RPW disturbances through the penumbra. Simple spatial tracking of a number of the velocity maxima in Fig. 2a yielded values $\approx$16 km s^{-1}. Time lags between all of the penumbral He I velocity signals and an averaged, mid-penumbral He I signal (region of averaging marked by dotted lines in Fig. 1) were found by cross-correlating the velocity profiles in time and are presented in Fig. 2b. Spatial tracking of the peak correlation yielded an apparent speed of $\approx$18 km s^{-1}. The same spatial correlation approach was also

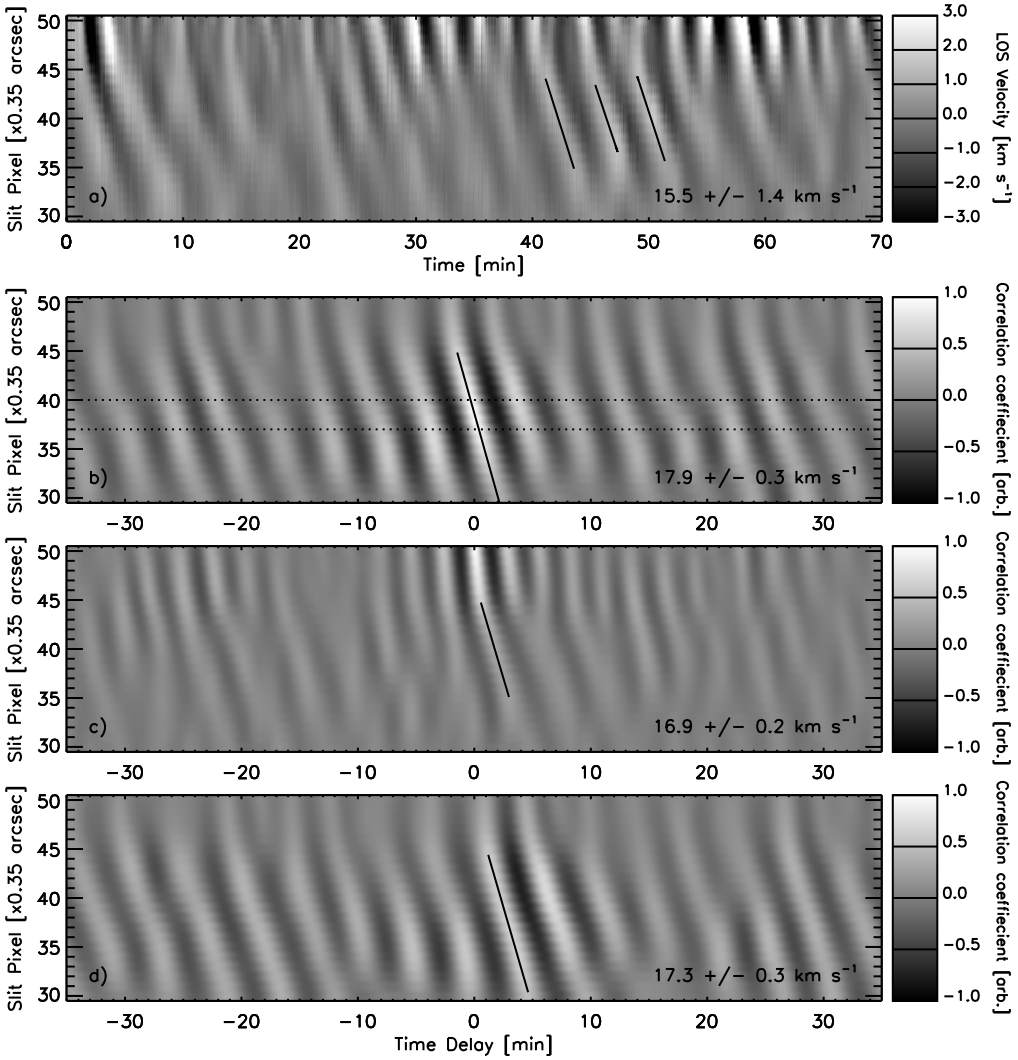

Figure 2. a) Space-time plot of penumbral LOS velocity in the He I multiplet. Variation of temporal cross correlation between individual spatial He I velocity profiles and b) an average, central penumbral He I profile, c) an average, outer umbral He I profile, and d) an average, outer umbral Si I profile.

performed between all of the penumbral He I velocity signals and both an averaged, outer-umbral He I signal (Fig. 2c; region of averaging marked by dashed lines in Fig. 1) and an averaged, outer-umbral Si I signal (Fig. 2d, each yielding apparent speeds of $\approx$17 km s^{-1}. These values are in good agreement with the previous literature (see, e.g., the recent review of Bogdan & Judge 2006). Note that values of correlation coefficient in the umbral He I case diminish rapidly through the penumbra since attempting to correlate a signal with a dominant 3-min period to one with a 5-min period. The correlation with the umbral Si I displays the opposite behavior, being strong throughout the penumbra but petering out at the umbra/penumbra boundary for the same reason.

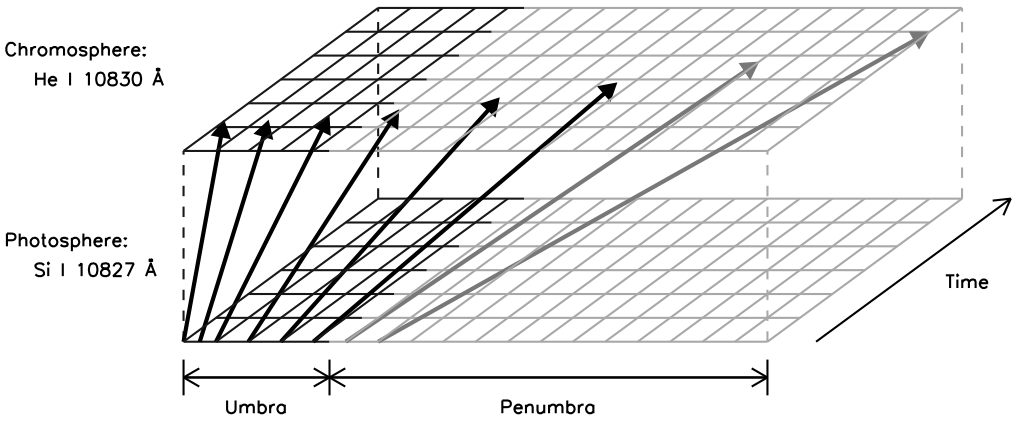

Figure 3. Cartoon schematic of the proposed field geometry linking pixels in the umbra (dark grid) to those in the penumbra (light grid) at photospheric and chromospheric sampling heights through increasingly inclined field lines.

4. Upward Propagation

The scenario proposed here for the generation of these running disturbances in the penumbral chromosphere is shown in Fig. 3 as a cartoon schematic. Although assuming vertical fields in the umbra of this sunspot was sufficient for the work of Centeno et al. (2006), pixels toward the outer edge of the umbra show somewhat inclined fields ($35 - 45°$; which may account for the spread of phase difference points with frequency in Centeno et al. 2006). These inclinations mean that some field lines originating from the photospheric umbra can pass through the chromospheric penumbra. From the values of inclination retrieved here, most chromospheric penumbral pixels can be traced back to the outer umbra/inner penumbra, all of which show photospheric velocity signatures of similar phase. If waves which travel along the field are indeed excited at the photospheric level within the umbral region (as shown by Centeno et al. 2006), those waves propagating along more inclined paths will have larger distances to traverse before showing their presence at the He I sampling height in the upper chromosphere. The increased path lengths that are experienced with increasing distance through the chromospheric penumbra mean that initially similar velocity signals in the Si I line have increasing temporal delay in the He I signal, resulting in an apparent horizontal motion outward from the umbra as proposed by Rouppe van der Voort et al. (2003).

Photospheric and chromospheric spatial pixels were paired using the values of local solar inclination recorded in the Si I and He I lines to determine the expected spatial offset between the two sampling heights in the atmosphere. The subsequent LOS velocity pairings between the photosphere and chromosphere were subjected to Fourier phase difference analysis following Krijger et al. (2001). Phase difference spectra from several neighboring spatial pixels were overplotted in each of the panels of Fig. 4 to heighten the clarity of any relation which may exist. These phase difference diagrams are comparable to Fig. 6 of Centeno et al. (2006), although they differ slightly as the shade and size of data points here denote the Fourier coherence and cross-spectral power, respectively.

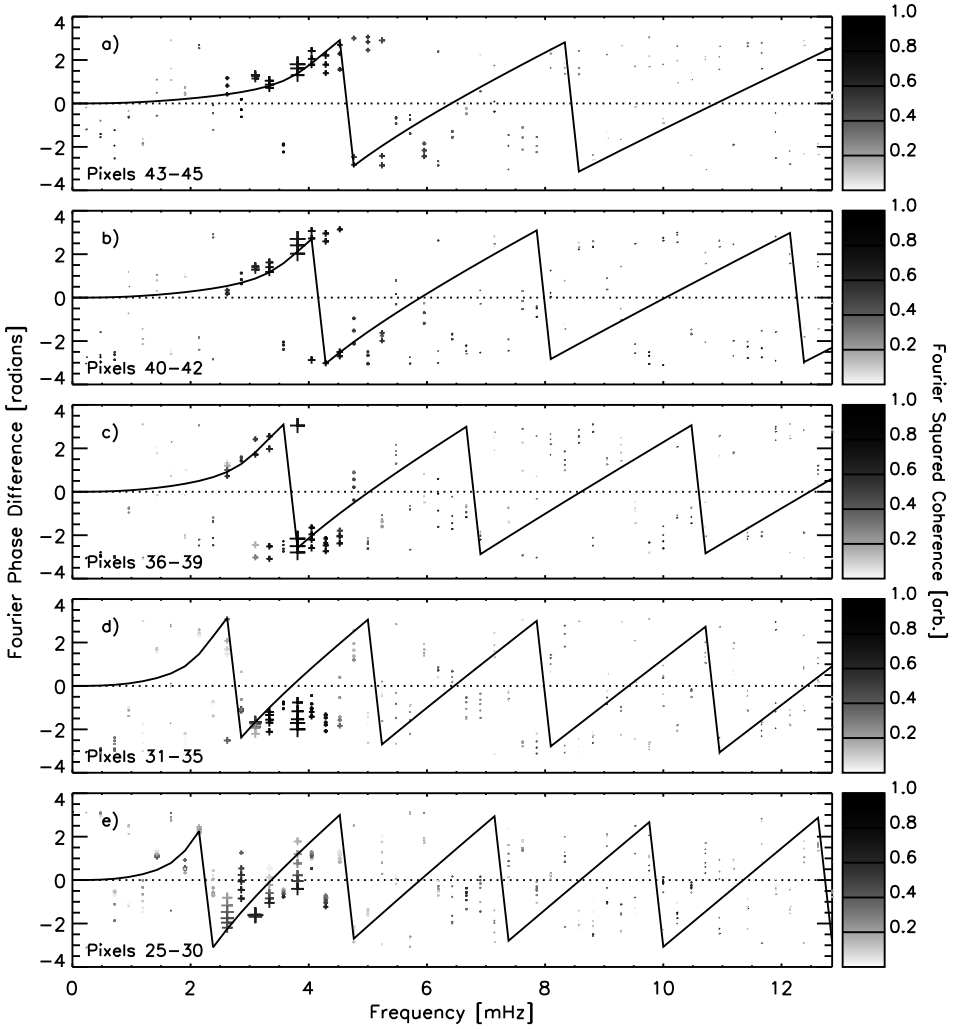

Figure 4. Phase differences between spatially offset pairings of photospheric and chromospheric LOS velocities. Panels show phase difference relations moving from those chromospheric pixels closest to the umbra/penumbra boundary (top) toward those at the penumbra/quiet-sun boundary (bottom).

It is clear when moving from the chromospheric umbra/penumbra boundary (top panel) toward the penumbra/quiet sun boundary (bottom panel) that the phase difference relations show deviation from the classical acoustic cutoff ($\approx$ 5.2 mHz) which can be explained by the reduced gravity experienced by waves propagating non-vertically. Solid curves plotted in Fig. 4 show the expected phase difference relations achieved using the equations provided by Centeno et al. (2006) for field-aligned waves in an isothermal atmosphere with radiative cooling, when the reduced gravity and increased path length from inclinated fields are taken into account, and the values of temperature, height separation, and cooling time scale which they determined for the umbra of this sunspot ($T = 4000\,\mathrm{K}$, $\Delta z = 1000\,\mathrm{km}$, and $\tau_\mathrm{R} = 55\,\mathrm{s}$, respectively). Although only

arbitrarily chosen and not reached by any form of fitting, good comparison is found with the observations for field inclinations of 40°, 45°, 53°, 63°, and 65° when moving from top to bottom panels of Fig. 4: these values are also in good agreement with the local solar inclinations determined by the Stokes inversion.

5. Future Work

Given that the work presented here is incomplete, the initial results are very promising. Fourier analysis confirms that RPWs are indeed the visual pattern of low-β slow magneto-acoustic waves that are generated at very similar phase at the photosphere but propagate along field lines of increasing inclination, hence showing increased time delays at (roughly) the same chromospheric altitude.

Improvements that are still required include least-squares fitting of the phase difference relation to the data to retrieve the spatial variation of the physical parameters T, Δz, and $\tau_{\rm R}$. In addition, refinement of the Si I inversion to include fine structure in the photospheric penumbra (e.g., a second magnetic component to account for known highly inclined filament or flux tube fields) will provide better linkage between velocity signals in the inner-penumbral photosphere and those in the outer-penumbral chromosphere. Observations of a small pore region will also be investigated for such running waves since the findings of this work indicate that the existence of a penumbra is not neccessary for their production: only sufficiently inclined fields in the umbra (or pore) are required to guide the waves outside this region.

Acknowledgments. The authors wish to extend their thanks to Rebecca Centeno, Manuel Collados, and Javier Trujillo Bueno for providing this excellent data set for our analysis. We are also grateful to the conference organisers for the opportunity to upgrade this presentation from a poster to a talk.

References

Bogdan T. J., Judge P. G., 2006, Royal Society of London Philosophical Transactions Series A 364, 313

Centeno R., Collados M., Trujillo Bueno J., 2006, ApJ 640, 1153

Christopoulou E. B., Georgakilas A. A., Koutchmy S., 2000, A&A 354, 305

Christopoulou E. B., Georgakilas A. A., Koutchmy S., 2001, A&A 375, 617

Georgakilas A. A., Christopoulou E. B., Koutchmy S., 2000, A&A 363, 306

Krijger J. M., Rutten R. J., Lites B. W., Straus T., Shine R. A., Tarbell T. D., 2001, A&A 379, 1052

Lagg A., Woch J., Krupp N., Solanki S. K., 2004, A&A 414, 1109

Martínez Pillet V., Collados M., Sánchez Almeida J., González V., Cruz-Lopez A., Manescau A., Joven E., Paez E., Diaz J., Feeney O., Sánchez V., Scharmer G., Soltau D., 1999, in T. R. Rimmele, K. S. Balasubramaniam, R. R. Radick (eds.), ASP Conf. Ser. 183: High Resolution Solar Physics: Theory, Observations, and Techniques, p. 264

Rouppe van der Voort L. H. M., Rutten R. J., Sütterlin P., Sloover P. J., Krijger J. M., 2003, A&A 403, 277

Tziotziou K., Tsiropoula G., Mein N., Mein P., 2006, A&A 456, 689

Zirin H., Stein A., 1972, ApJ 178, L85

The Physics of Chromospheric Plasmas
ASP Conference Series, Vol. 368, 2007
Petr Heinzel, Ivan Dorotovič and Robert J. Rutten, eds.

Some Structural Properties of Solar Magnetic Fields

B. Ioshpa, E. Mogilevskii and V. Obridko

IZMIRAN, Troitsk, Moscow Region, Russia

Abstract. We discuss some results of the study of spatial characteristics of solar magnetic fields. The analysis is based on the magnetic field data obtained with a new spectromagnetograph installed on the IZMIRAN Tower Telescope (Fe I 6302.5 Å) (Kozhevatov et al., 2002), the data of the MSFC solar vector magnetograph (Fe I 5250.2 Å) and the data of longitudinal magnetic 96 m daily maps of SOHO/MDI magnetograph (Ni I 6768 Å) downloaded through Internet. Our study was directed in some different ways: the fractal properties of sunspots; fractal properties of space distribution of the magnetic fields along great distances comparable with the size of active regions or active complexes; fractal properties of active and quiet regions as global entities. To do it we used some different methods, particularly, the well known method using the relation between the area and the perimeter of magnetic field lines (see (Feder, 1988; Meunier, 1999; Nesme-Ribes at al., 1996; Balke et al., 1993)) and technique developed by Higuchi (1988), who applied it to the investigation of long time series. Note also that magnetic structure in terms of the fractal models was developed earlier in (Zelenyi & Milovanov, 1991; Milovanov & Zelenyi, 1993; Mogilevskii, 1994; Mogilevskii, 2001; Abramenko et al., 2002; Abramenko, 2005; Salakhudinova & Golovko, 2005).

The main results are:

1. Fractal analysis of sunspot magnetic field indicated the existence of three families of self-similar contour lines roughly belonging to the umbra, penumbra and the ambient photosphere correspondingly. The greatest fractal dimension corresponds to the regions of weakest fields (ambient photosphere), the least one corresponds to the intermediate region (penumbra).

2. More detailed analysis shows that the fractal coefficient has a maximum (about 1.50) near the umbra–penumbra interface.

3. The global fractal numbers of space distribution of magnetic field on solar surface is closely connected with the mean absolute values of the longitudinal magnetic field for this surface. The fractal numbers diminish with the rising of mean magnetic field (from values about 2.0 for the relatively quiet region to 1-1.2 for very active regions).

4. The dependences of fractal numbers of the space distribution of longitudinal and transversal fields versus mean longitudinal field are similar by their character but the fractal values for transversal field are higher than the corresponding factor values for longitudinal field by factor about 1.5. This means that the distribution of transversal field along the space is more chaotic than the distribution of longitudinal field.

Acknowledgments. The authors are grateful to the staff of the MSFC vector magnetograph and SOHO/MDI for the data supplied. The work was supported by the RFFI grant 04-02-17007.

References

Abramenko, V.I., Yurchyshyn, V.B., Wang, H., Spirock, T.J., & Goode, P.R. 2002, ApJ, 577, 487
Abramenko, V.I. 2005, Solar Phys., 228, 29
Balke, A.C., Schrijver, C.J., Zwaan, C., & Tarbell, T.D. 1993, Solar Phys., 143, 215
Feder, J. 1988, Fractals, Plenum, New York
Higuchi, T. 1988, Phisica D, 31, 277
Kozhevatov, I.E., Rudenchik, E.A., Cheragin, N.P., Obridko, V.N., & Kulikova, E.H. 2002, Instruments and Experimental Techniques, 45, No 1, 98
Mandelbrot, B.B. 1983, The Fractal Geometry of Nature, Freeman, New York
Meunier, N. 1999, ApJ, 515, 801
Milovanov, A.V., & Zelenyi, L.M. 1992, Phys. Fluids, 5(7), 1406
Mogilevskii, E.I. 1994, Sov. Astron. Lett., 20, N8, 607
Mogilevskii, E.I. 2001, Fractals on the Sun, Fizmatlit
Nesme-Ribes, E., Meunier, N., & Collin, D. 1996, A&A, 308, 213
Salakhudinova, I.L., & Golovko, A.A. 2005, Solar Phys., 225, 59
Zelenyi, L.M., & Milovanov, A.V. 1991, Astr. Lett., 17, 425

The Physics of Chromospheric Plasmas
ASP Conference Series, Vol. 368, 2007
Petr Heinzel, Ivan Dorotovič and Robert J. Rutten, eds.

O VI and H_2 Lines in Sunspots

Nicolas Labrosse[1], Huw Morgan[2], Shadia Rifai Habbal[2]
and Daniel Brown[1]

[1]*Institute of Mathematical and Physical Sciences, Aberystwyth, UK*
[2]*Institute for Astronomy, University of Hawaii, USA*

Abstract. Sunspots are locations on the Sun where unique atmospheric conditions prevail. In particular, the very low temperatures found above sunspots allow the emission of H_2 lines. In this study we are interested in the radiation emitted by sunspots in the O VI lines at 1031.96 Å and 1037.60 Å. We use SOHO/SUMER observations of a sunspot performed in March 1999 and investigate the interaction between the O VI lines and a H_2 line at 1031.87 Å found in the Werner band. The unique features of sunspots atmospheres may very well have important implications regarding the illumination of coronal O^{+5} ions in the low corona, affecting our interpretation of Doppler dimming diagnostics.

1. Introduction

The O VI lines at 1031.96 Å and 1037.60 Å are far more intense in sunspots than in the Quiet Sun (Foukal et al. 1974; Curdt et al. 2001). The contribution of sunspots to the total integrated disk spectrum seen by O^{+5} ions in the corona is therefore non negligible. This has important consequences on the interpretation of observed O VI lines in the corona (Morgan & Habbal 2005). Our goal is to understand the formation mechanisms of these lines in sunspots. We present an analysis of SUMER observations of a sunspot from March 18, 1999. We discuss the interaction between the O VI lines and the emission line of molecular hydrogen H_2 at 1031.87 Å.

2. Observations

We use the reference spectrum obtained by the SUMER spectrometer onboard the SOHO spacecraft on March 18, 1999 (Schühle et al. 1999). These observations were made with the detector B and lasted for 7 hours. The spectrometer slit ($0.3'' \times 120''$) was kept at a fixed position centered on the sunspot (Fig. 1, left) and compensation for the solar rotation was turned on. From the MDI continuum intensity we estimate the location of the sunspot umbra to be between $364''$ and $382''$ on the SUMER slit (Fig. 1, right). The surrounding penumbra is between $344''$ and $364''$, and between $382''$ and $392''$. The upper and lower parts of the slit are on the quiet sun. These features will now be denoted U, P, and QS, respectively.

The two panels of Fig. 2 show how the intensities of the O VI lines are affected by the different physical conditions in the quiet sun, in the penumbra, and in the umbra. The integrated intensities have been determined by a simple

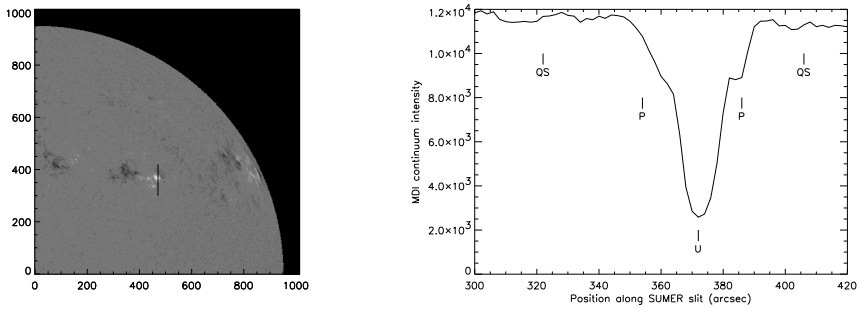

Figure 1. *Left:* MDI image of sunspot with SUMER slit. *Right:* MDI continuum intensity along SUMER slit.

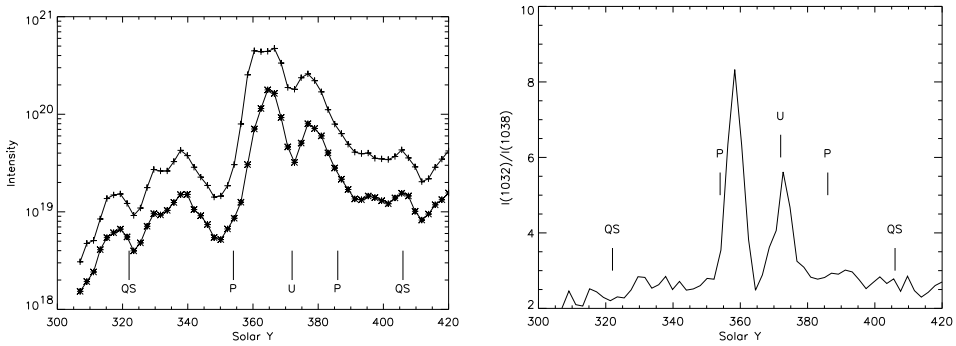

Figure 2. *Left:* Integrated intensity of O VI 1032 Å (+) and 1038 Å (*) lines. The line intensities are enhanced in the sunspot region compared to the quiet sun, particularly in the penumbra/umbra interface. *Right:* Intensity ratio of O VI lines along SUMER slit.

integration over the line profiles. The intensity profile of the O VI lines is similar to what has been observed by, e.g., Foukal et al. (1974).

An interesting and important feature is that the ratio between the two lines significantly deviates from its average value. While it is around 2 on QS, it reaches values greater than 8 in the southern umbra/penumbra interface. This implies that the coronal O^{5+} ions, which are sensitive to the disk radiation, are illuminated by a radiation field which may very well be different from the averaged one (QS) that is usually assumed. Doppler dimming diagnostic techniques using the O VI doublet line ratios, are sensitive to the value of the ratio on the disk. Adopting a value of 2 for the line ratio and a homogeneous disk could lead to spurious results of ion speeds in the corona considering the impact that sunspots can have on the disk radiation field. This is due to the presence of H_2 emission at 1031.87 Å (Bartoe et al. 1979) in the 1–1 Werner band. This molecular line is excited by resonance fluorescence from the O VI line.

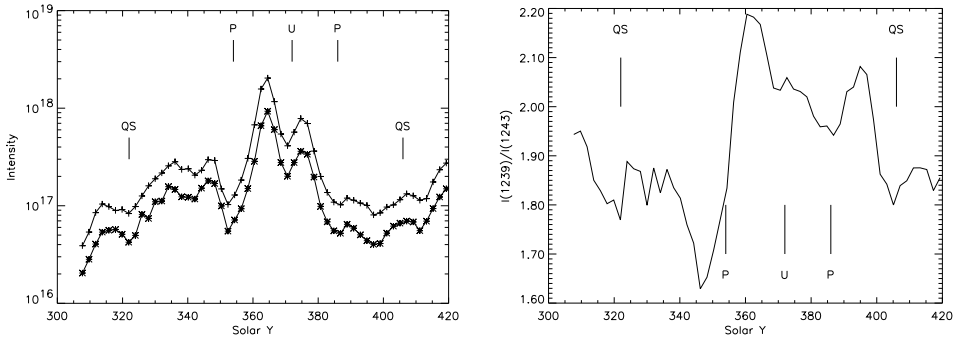

Figure 3. *Left:* Integrated intensities of N V 1239 (+) and 1243 (*) lines. *Right:* Intensity ratio of N V lines along SUMER slit.

3. Line Formation

The two panels in Fig. 3 present the integrated intensities and intensity ratio of the two N V lines at 1239 and 1243 Å from the same data set as O VI. The N V and O VI doublets are in the lithium-like sequence. The N V doublet is very similar to O VI (same collisional excitation coefficient ratio and similar temperature of formation), so the N V 1239/1243 intensity ratio should be close to 2 at all temperatures, even accross the sunspot. This proves the special case of O VI due to its interaction with the H_2 lines in the Q3 band.

Furthermore, the SUMER data shows that the C II lines at 1036.3 and 1037 Å are fainter in the sunspot region. This is expected as the lines of first ions are reduced in intensity over sunspots (Bartoe et al. 1979). This may in turn have implications for the pumping of the coronal O VI 1037 Å line at speeds above ∼100 km/s.

Figure 4 helps us to quantify the amount of H_2 molecular emission present in the SUMER sunspot observations by assuming that the integrated intensity at 1032 Å is normally the double of the intensity at 1038 Å. This figure also presents the normalized intensity profiles of four H_2 Werner band lines across the sunspot. These lines are not blended with other UV lines, therefore they predict what the 1031.87 Å 1–1 line would look like in the absence of interaction with O VI. The relative intensity of all these lines agree closely with the calculated emission transition probabilities (see Schühle et al. 1999). We can see that H_2 and O^{5+} interaction is significant in the sunspot area only.

4. Conclusion

The sunspot's molecular H_2 line interacting with the O VI lines is one of many in the H_2 Werner band. Theory gives relative intensities for each line, and this theory has been tested by Schühle et al. (1999) on the SUMER sunspot data. This means that we can know very closely the H_2 emission in the 1–1 band at 1031.87 Å, which is the one that pumps the O VI 1031.9 Å, just by looking at a clean line (e.g., the 1–3 band at 1119 Å) and multiplying by the theoretical intensity ratio between the two given in Bartoe et al. (1979).

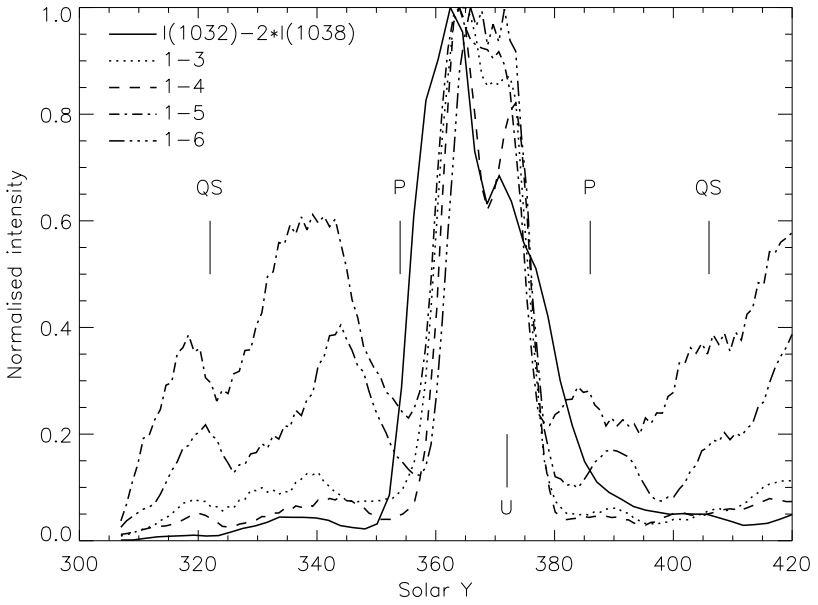

Figure 4. Normalized intensity profiles of four unblended H_2 Werner band lines across the sunspot. The solid line shows the difference I(O VI 1032)-2×I(O VI 1038). The enhancement of intensity at the sides of the sunspot is interesting, and is possible evidence of ambipolar diffusion of H_2 from the umbra, that is, H_2 and other neutrals can diffuse across the near-vertical magnetic field of the sunspot umbra (Kuhn & Morgan 2006).

In a future work we will model a slab of oxygen ions in the transition region above a sunspot and calculate the 1032 and 1038 line intensities emitted by the slab purely by collisions. Then, using a radiative transfer code, we will add the H_2 line intensity at the bottom of the slab, and study the pumping of O VI 1032 Å that ensues.

Acknowledgments. N. L. acknowledges financial support from the organisers of the Coimbra Solar Physics Meeting, the University of Wales through the Gooding Fund, and PPARC through grant PPA/G/O/2003/00017.

References

Bartoe J.-D. F., Brueckner G. E., Nicolas K. R., Sandlin G. D., Vanhoosier M. E., Jordan C., 1979, MNRAS 187, 463

Curdt W., Brekke P., Feldman U., Wilhelm K., Dwivedi B. N., Schühle U., Lemaire P., 2001, A&A 375, 591

Foukal P. V., Noyes R. W., Reeves E. M., Schmahl E. J., Timothy J. G., Vernazza J. E., Wilhbroe G. L., Huber M. C. E., 1974, ApJ 193, L143

Kuhn J., Morgan H., 2006, in Uitenbroek, Leibacher, Stein (eds.), Solar MHD Theory and Observations: A High Spatial Resolution Perspective, ASP Conf. Series, in press

Morgan H., Habbal S. R., 2005, ApJ 630, L189

Schühle U., Brown C. M., Curdt W., Feldman U., 1999, in J.-C. Vial, B. Kaldeich-Schürmann (eds.), 8th SOHO Workshop: Plasma Dynamics and Diagnostics in the Solar Transition Region and Corona, ESA SP-446, 617

The Physics of Chromospheric Plasmas
ASP Conference Series, Vol. 368, 2007
Petr Heinzel, Ivan Dorotovič and Robert J. Rutten, eds.

Models of the Large-Scale Corona: Formation, Evolution and Lift-Off of Magnetic Flux Ropes

D. H. Mackay[1] and A. A. van Ballegooijen[2]

[1]*School of Mathematics and Statistics, St. Andrews, Scotland*
[2]*Harvard-Smithsonian Centre for Astrophysics, Cambridge, USA*

1. Summary of Work

We investigate the response of the large-scale coronal magnetic field to the transport of magnetic flux in the photosphere (Mackay & van Ballegooijen 2006a,b). In order to follow the evolution on long time scales, the coronal plasma velocity is assumed to be proportional to the Lorentz force (magnetofriction), causing the coronal field to evolve through a series of non-linear force-free states (van Ballegooijen et al. 2000). Magnetofrictional simulations are used to study the formation and evolution of coronal flux ropes, highly sheared and/or twisted magnetic fields located above polarity inversion lines on the photosphere. As in our earlier studies, the 3D numerical model includes the effects of solar differential rotation, meridional circulation and small-scale convective flows; the latter are described in terms of surface diffusion. The model is extended to include the effects of coronal magnetic diffusion, which limits the degree of twist of coronal flux ropes, and the solar wind, which opens up the field at large height.

The interaction of two bipolar magnetic regions is considered (Mackay & van Ballegooijen 2005). A key element in the formation of the flux ropes, is the reconnection of magnetic fields associated with photospheric flux cancellation at the polarity inversion lines. Flux ropes are shown to form both above the external inversion line between bipoles (representing Type-B filaments) and above the internal inversion line of each bipole in a sigmoid shape. It is found that once a flux rope has formed the coronal field may diverge from equilibrium with the ejection of the flux rope (Fig. 1).

During the ejection, the changing connectivity of the coronal magnetic field is considered (Mackay & van Ballegooijen 2006b). Reconnections occurring above the flux ropes slowly strip away coronal arcades overlying the flux ropes and allow the flux ropes to be ejected. In contrast those below help to push the flux ropes out. It is found that the reconnection occurring below each flux rope may result in significant skew being maintained within the coronal field above the PIL after the flux rope is ejected. In addition, after the eruption, as the coronal field closes down the large scale transport of open flux across the bipoles takes place through the process of "interchange reconnection". As a result, new photospheric domains of open flux are created within the centres of the bipoles where field lines were previously closed. The net open flux in the simulation may be split into two distinct contributions; the non-potential equilibrium coronal fields of the bipoles and the temporary enhancement to this during the ejection of the flux ropes where previously closed field lines become open. These results suggest that the non-potential nature of coronal magnetic

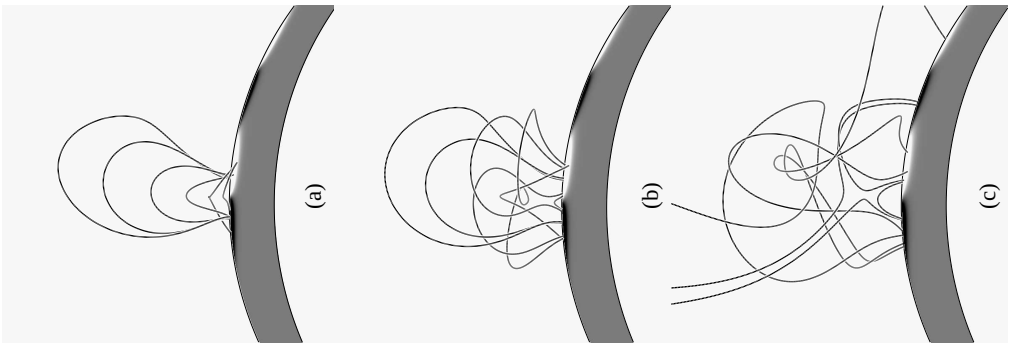

Figure 1. Example of the lift off of the flux rope lying above the internal PIL of the trailing bipole on (a) day 17, (b) day 22 and (c) day 25. In (b) and (c) the formation of a quasi-separatrix layer occurs below the flux rope in the form of an X-line when viewed in 2D. This quasi-separatrix layer is seen to rise as the flux rope rises.

fields may effect the variation of the Sun's open flux during periods of high solar activity and should be considered in future simulations. After the flux rope is ejected the coronal field once again relaxes down to an equilibrium. This ability to follow the evolution of the coronal field through eruptions is essential for future full-Sun simulations in which multiple bipoles are evolved for many months or years.

Acknowledgments. D. H. M. would like to thank the UK Particle Physics and Astronomy Research Council for financial support. The simulations were carried out on a SHRIF/PPARC funded supercomputer located in St. Andrews.

References

Mackay, D. H. & van Ballegooijen, A. A. 2005, ApJ, 621, L77
Mackay, D. H. & van Ballegooijen, A. A. 2006, ApJ, 641, 577
Mackay, D. H. & van Ballegooijen, A. A. 2006, ApJ, 642, 1193
van Ballegooijen, A. A., Priest, E. R., & Mackay, D. H. 2000, ApJ, 539, 983

The Physics of Chromospheric Plasmas
ASP Conference Series, Vol. 368, 2007
Petr Heinzel, Ivan Dorotovič and Robert J. Rutten, eds.

Spectrophotometry of Ellerman Bombs with THEMIS

Etienne Pariat[1], Brigitte Schmieder[1], Arkadiusz Berlicki[1,2] and Arturo López Ariste[3]

[1] *Observatoire de Paris, Meudon, France*
[2] *Astronomical Institute, Wrocław University, Wrocław, Poland*
[3] *THEMIS-CNRS UPS 833, La Laguna, Tenerife, Spain*

Abstract. During coordinated campaigns with THEMIS and space missions (TRACE, SOHO) emerging flux was observed in multi-wavelengths. Ellerman bombs (EBs) have been identified in TRACE 1600 Å and in chromospheric lines. The Hα and Ca II 8542 Å lines present two enhanced emission peaks respectively at 1 Å and at 0.35 Å which are signatures of EBs. Vector magnetic field measured in the photosphere are consistent with previous results indicating the presence of bald-patches under the EBs and consequently the emergence of horizontal flux tubes from below the photosphere.

1. Introduction

Ellerman (1917) discovered bright emission kernels in both Hα wings in several locations of the low chromosphere. These small scale events are called Ellerman Bombs (EB). For decades, they were frequently observed in areas of flux emergence and strong fields, such as the vicinity of the penumbra around isolated sunspots and the interspot areas of new and dynamic emerging flux regions (see the extensive review of Georgoulis et al. 2002). The typical size of EBs is of the order of $1''$ and their lifetime 10 to 14 minutes. They are observed in other wavelengths indicating their presence in temperature minimum layers (Qui et al. 2000). Several models have been proposed to explain EB characteristics, mainly thermal models with a hotter layer (Fang et al. 2006) or magnetic reconnection with or without bombardment of the low chromosphere by energetic particles (Hénoux et al. 1998).

Progress on this topics has been made recently using the Flare Genesis Experiment (FGE) observations (Bernasconi et al. 2002) and THEMIS (Fang et al. 2006). EBs would be due to magnetic reconnection of sections of flux tube during its emergence from the sub-photosphere. High-resolution chromospheric Hα filtergrams (spatial resolution $0.8''$), as well as photospheric vector magnetograms (spatial resolution $0.5''$) and Dopplergrams, have been acquired by FGE in January 2000 during the emergence of a new active region (NOAA 8844).

Ellerman bombs (EBs) and Arch Filament System (AFS) have been observed in Hα and statistical properties have been investigated (Georgoulis et al 2002). EBs are small elongated events ($1.8'' \times 1''$) but their size depends on the instrument resolution. Their energy is estimated to 10^{28} erg with a temperature enhancement of 2×10^3 K and the timescale radiative cooling is short of the order of few seconds. The distribution function of the energies of EBs exhibits

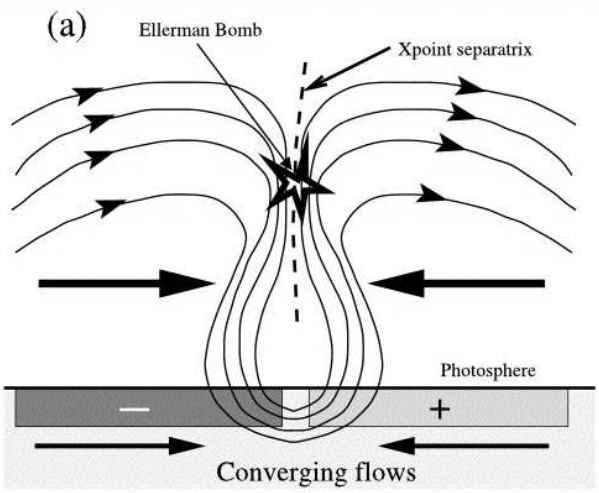

Figure 1. Example of magnetic reconnection in bipolar magnetic field region by horizontal flows proposed as a mechanism of Ellerman bomb triggering (Georgoulis et al. 2002).

a power-law shape with an index (−2.1), suggesting that EBs could be due to heating of the chromosphere during magnetic reconnection. They occur preferentially above magnetic field inversion lines or above separatrices. Cartoons of magnetic reconnection were proposed by Georgoulis et al. 2002 (Fig. 1). Pariat et al (2004) extended this work by using a linear-force-free extrapolation code developed by Démoulin et al. (1997). The magnetic topology of the small scale EBs reveals that they are linked by a hierarchy of elongated flux tubes showing aperiodic spatial undulations, whose wavelengths are typically above the threshold of the Parker instability. This study suggested that arch filament systems result from the rise of undulated flux tubes whose upper parts emerge because of the Parker instability and whose dipped lower parts emerge because of magnetic reconnection (Fig. 2).

2. THEMIS Observations

During a coordinated campaign with space and ground based instruments a new emerging flux was observed in the central part of the active region NOAA 10655 in August 2004. This campaign was organized in the frame of the Joint Observing Program JOP 157 involving SOHO, TRACE 1600 Å, and THEMIS.

THEMIS is a polarization-free telescope working in different modes. On August 3 2004, THEMIS worked successively with the MSDP spectrograph and the MTR spectro-polarimeter (Mein 2002, López Ariste et al. 2006). The MSDP provided observations in Na D1 and in Ca II 8542 Å lines leading to longitudinal magnetograms and images of the chromosphere at different wavelengths in the Ca II line (Fig. 3). The MTR provided multi-lines observations and particularly the four Stokes parameters in the Fe I lines after computations with the THEMIS software (SQUV of Sainz Dalda and the PCA code of López Ariste et al. (2006).

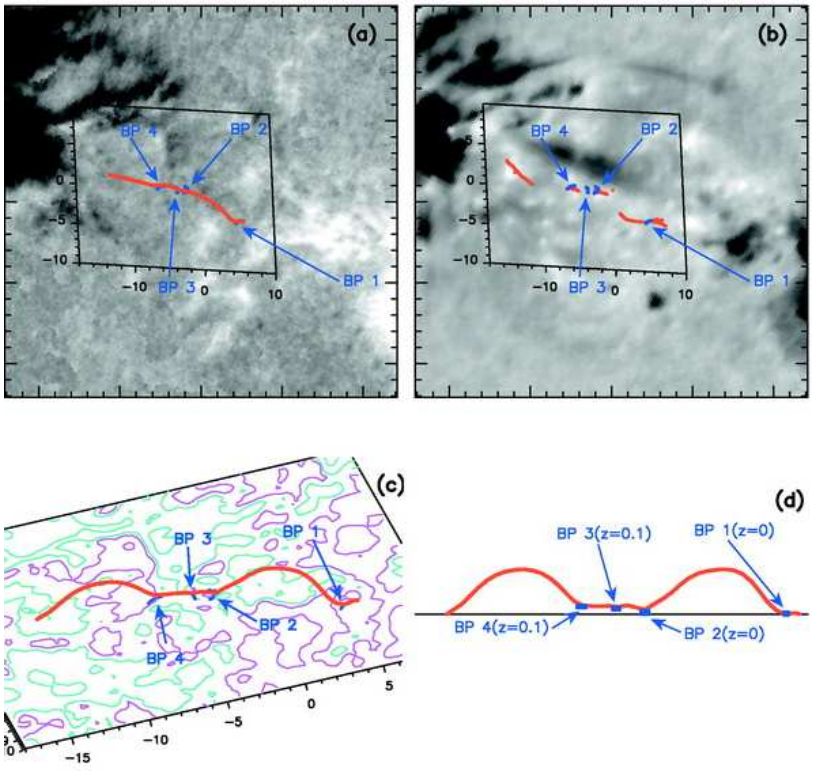

Figure 2. Flare Genesis experiment observations: (a) longitudinal photospheric magnetogram, (b) filtergram at Hα -0.8 Å, (c) and (d) projection view of an undulated flux tube computed by extrapolation of the photospheric magnetogram. BPs are the "bald patch" regions, where magnetic field lines are tangent to the photosphere (Pariat et al. 2004).

The MTR provided also simultaneously the profiles of Hα line in each point of the field-of-view of Fe I magnetograms.

In the central part of the active region, new emerging mixed polarities were observed in the box of Fig. 3. The corresponding images of Ca II obtained in the wings show typical bright points corresponding to Ellerman bombs well visible in TRACE 1600 Å images. The profiles of Ca II after subtraction of a neigboring point's profile (without EB) , confirm the existence of such enhancements in emission in both wings of the line profiles at $\pm$ 0.35 Å (Fig. 4). Similar bright points are observed in Hα images corresponding to enhancements of emission in the wings at $\pm$1 Å (Fig. 4).

3. Magnetic Topology of Ellerman Bombs

The extrapolation made from the FGE magnetograms had shown the existence of EBs in preferential locations corresponding to Bald Patches (Pariat et al.

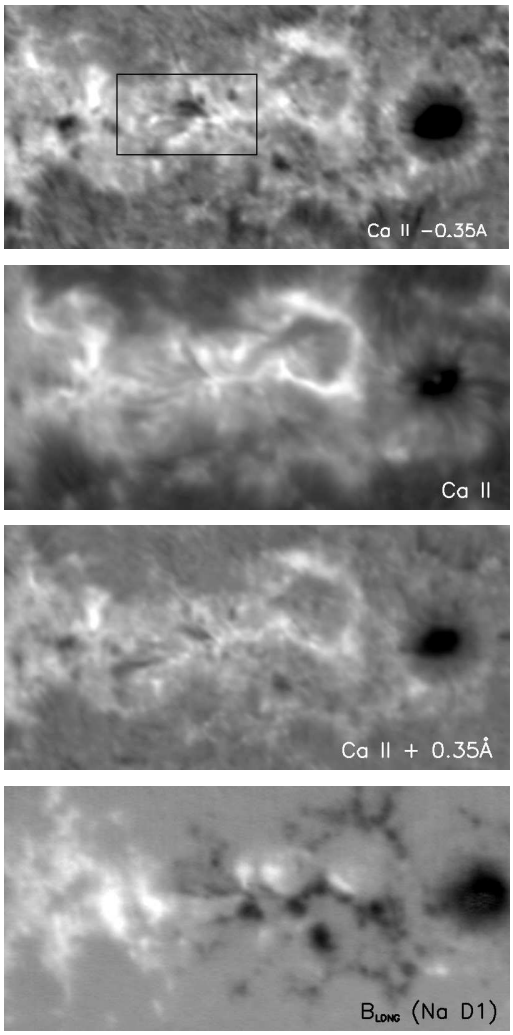

Figure 3. Observations of the Active Region NOAA 10655 on August 3 2004, with THEMIS/MSDP spectrograph, from top to bottom panels: image in the blue wing -0.35 Å, in the center, in the red wing $+0.35$ Å of Ca II line, magnetogram in the Na D1 line ($205'' \times 95''$). The box indicates the new emerging flux area where arch filaments are observed. Bright points in the wing images indicate the presence of Ellerman bombs.

2004). This indicates that the magnetic field lines are tangent to the solar surface at the locations of EBs.

Using MTR observations, it was possible to get maps of the Stokes parameter V indicating the topology of the longitudinal component of the magnetic field and maps of the transverse field. Figure 5 presents a zoom of the emerg-

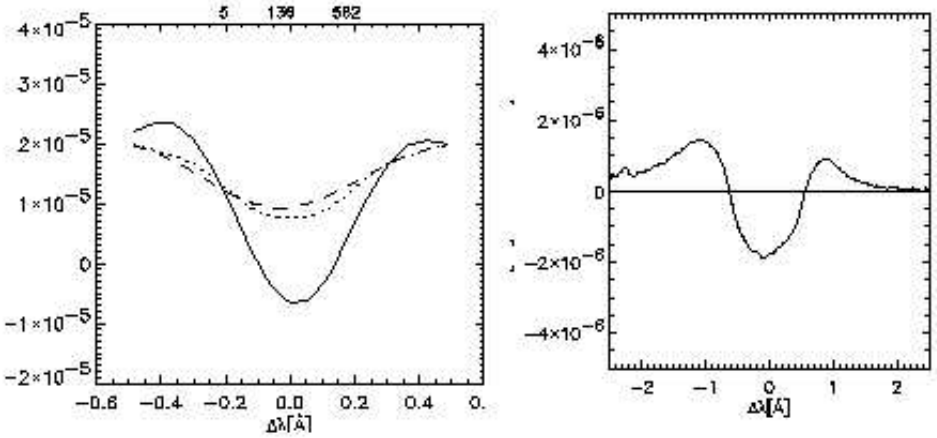

Figure 4. Typical differential profiles of Ellerman bombs. A neigboring point profile has been substracted from the EB profile: in Ca II 8542 Å (solid, lefthand panel) and in Hα (solid, righthand panel).

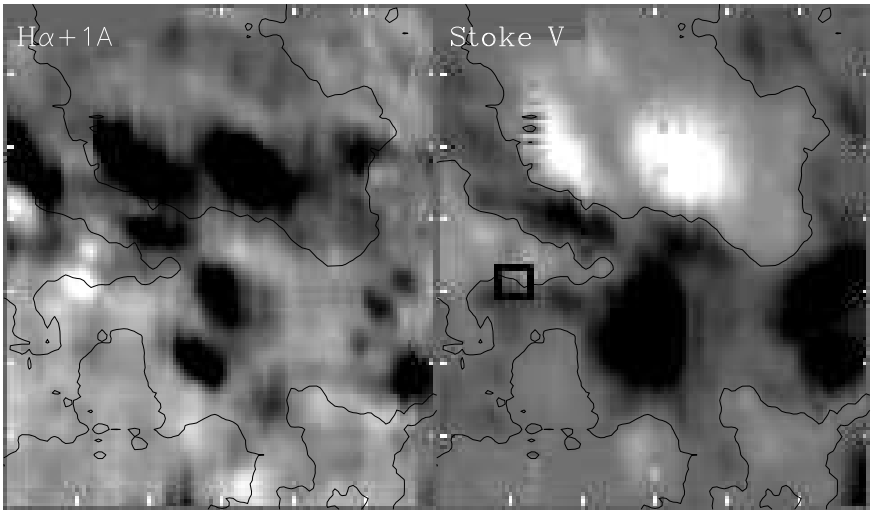

Figure 5. *Left*: Partial Hα +1 Å image ($40'' \times 47''$) obtained from THEMIS/MTR showing bright points, so called Ellerman bombs. *Right*: The corresponding Stokes V image. The black box points out an inversion line under an Hα EB visible in the Stokes V image.

ing flux region corresponding approximatively to the field-of-view of the box in Fig. 3. We observed that EBs were located over magnetic inversion lines between two opposite polarities (magnetic bipole). The transverse field vectors join the negative polarity to the positive polarity. The 180° ambiguity was not resolved. But the global magnetic characteristics of the active region was the following: a negative leading polarity and a positive following polarity. The small bipoles under the EBs were of reversed sign, indicating that probably the magnetic field

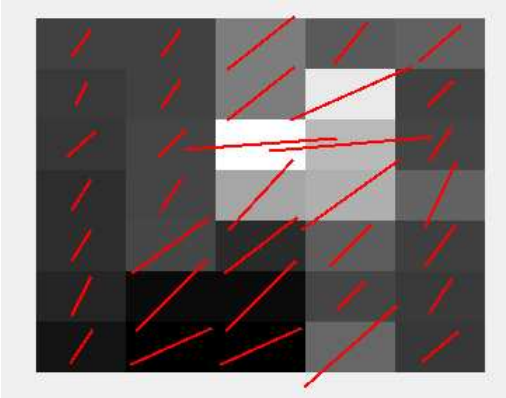

Figure 6. Longitudinal magnetogram of a bipole under an EB overlaid by vectors representing the transverse field. The ambiguity is not resolved. The field-of-view corresponds to the black box in Fig. 5.

was going from negative to positive polarity (Fig. 6). This would suggest loops rather than Ω loops (going from positive to negative polarities).

4. Conclusion

THEMIS spectro-polarimeter allowed us to observe Ellerman bombs in chromospheric lines during flux emergence. The investigations of the magnetic photospheric topology in Ellerman bomb regions show the existence of small bipoles linked with transverse field. This confirms previous results concerning the emergence of flux tubes resulting of successive magnetic reconnections (Pariat et al. 2004).

Acknowledgments. We thank the CSPM organizers for a very good meeting. This work was supported by the European Commission through the RTN program (European Solar Magnetism Network, contract HPRN-CT-2002-00313).

References

Bernasconi, P.N., Rust, D.M., Georgoulis, M.K. , & Labonte, B.J. 2002, Solar Phys. 209, 119
Démoulin, P., Bagala, L.G., Mandrini, C.H., Hénoux, J.C., & Rovira, M.G. 1997, A&A 325, 305
Ellerman, F. 1917, ApJ 46, 298
Fang, C., Tang, Y.H., Xu, Z., Ding, M.D., & Chen, P.F. 2006, ApJ 643, 1325
Georgoulis, M.K., Rust, D.M., Bernasconi, P.N., & Schmieder, B. 2002, ApJ 575, 506
Hénoux, J.C., Fang, C., & Ding, M.D. 1998, A&A 337, 294
López Ariste, A., Aulanier, G., Schmieder, B., & Sainz Dalda, A. 2006, A&A 456, 725
Mein, P. 2002, A&A 381, 271
Pariat, E., Aulanier, G., Schmieder, B., Rust, D.M., Georgoulis, M.K., & Bernasconi, P.N. 2004, ApJ 614, 1099
Qiu, J., Ding, M.D., Wang, H., Denker, C., & Goode P.R. 2000, ApJ 544, L157

The Physics of Chromospheric Plasmas
ASP Conference Series, Vol. 368, 2007
Petr Heinzel, Ivan Dorotovič and Robert J. Rutten, eds.

Horizontal Motions in the Vicinity of Sunspots

Michal Sobotka[1] and Thierry Roudier[2]

[1]*Astronomical Institute AS, Ondřejov, Czech Republic*
[2]*Laboratoire d' Astrophysique de l'Observatoire Midi-Pyrénées, France*

Abstract. Many sunspots in late phases of evolution are surrounded by an annular "moat", where systematic horizontal flows radially away from the sunspot are observed. Applying the local correlation tracking technique to series of white-light and 1600 Å images acquired by the satellite TRACE, we use photospheric granules and C IV emission structures to track horizontal motions in the vicinity of sunspots of different sizes, shapes, and phases of evolution. We define the moat regions on the basis of horizontal motions. We present preliminary results about the relations between the sunspot types and the occurrence, areas, and velocities of the moats in the photosphere and chromosphere. Further we analyze observed asymmetries in moat shapes and velocities and their relation to the sunspot age and proper motion.

1. Introduction

Sunspots are dynamical systems accompanied by specific motions of plasma in the convection zone, photosphere, and chromosphere. The existence of an annular region around a sunspot, where magnetic fields are not static, was first reported by Sheeley (1969). He termed this region *a moat*. From Doppler measurements, Sheeley & Bhatnagar (1971) found radially oriented outflows in moats. Time series of spectroheliograms, magnetograms, white-light and G-band images show that magnetic elements, G-band bright points, and granules in moats move predominantly away from sunspot border with speeds of about 0.5–1 $\mathrm{km\,s^{-1}}$ (Muller & Mena 1987; Shine et al. 1987; Brickhouse & Labonte 1988; Bonet et al. 2005). These speeds are about twice as large as the supergranular ones (Brickhouse & Labonte 1988). Moats were observed mainly around old, well-developed spots.

Meyer et al. (1974), attempted to associate the radial outflow in moats with convective flows assumed in their theoretical sunspot model: The heat excess below a sunspot causes upflows around the spot's flux tube in the convection zone and diverging flows in the photosphere. So, the moat outflow is similar to supergranular convection with the sunspot at the center of the cell. Convergent flows deep in the convection zone contribute to mechanical stability of the spot. An alternative explanation is provided by numerical simulations of compressible convection around magnetic flux tubes. Hurlburt & Rucklidge (2000) found that plasma cooling in the vicinity of a cold flux tube causes downflows around the tube, creating a convective "collar" with convergent flows near the surface – just in the opposite direction compared with the model by Meyer et al. (1974). This

"collar", however, is hidden below a shallow sunspot penumbra and the moat outflow is a manifestation of a counter-cell that surrounds the "collar".

In this paper we utilize time series of images acquired by the Transition Region and Coronal Explorer (TRACE) to study sunspot moats, defining them by means of horizontal motions of photospheric and chromospheric structures.

2. Data Processing and Analysis

From the TRACE data base (`http://trace.lmsal.com/trace_cat.html`) we extracted time series of white light and ultraviolet 1600 Å frames, each lasting approximately 1 hour, with temporal and spatial resolutions of 0.5–1 minute and $1''$. The characteristics of TRACE white-light and 1600 Å channels are described by Handy el al. (1999). The first channel probes low photospheric layers, while the second one contains a mixture of a UV continuum, originating in upper photosphere near the temperature minimum (Fossum & Carlsson 2005), and of C IV emission lines (1548 and 1551 Å) from the transition region, formed in magnetic features.

We analyzed time series of 32 sunspots in white-light and 26 in 1600 Å channels observed during the years 2000 – 2004. The selection criteria of sunspots were the location in the central part of the solar disk and the representation of a broad range of morphological types and evolutionary phases, disregarding the presence and development of moats. We divided our sample in two groups, growing *young* spots before reaching the maximum area (14 in white light and 12 in 1600 Å) and *old* spots in the maximum or decay phase of evolution (18 in white light and 14 in 1600 Å).

The frames in the series were aligned, so that sunspots are static in the field of view, and a Fourier 3D k–ω filter was applied to remove 5-min oscillations. Horizontal motions of granules and other features were measured using the Local Correlation Tracking technique (LCT, November & Simon 1988). The FWHM of the Gaussian correlation window was $3''$ and the computed velocities were averaged over the duration of each series, i.e., about 1 hour. As a result we obtained maps of horizontal velocities with field of view $3'12''\times3'12''$.

Our definition of the moat region is based on horizontal velocities of granules (white light) or C IV emission and UV continuum features (1600 Å). We use two criteria: (1) The speed must be higher than 250 m s^{-1} and (2) the deviation of velocity vector from the radial direction with respect to the spot center must be less than $\pm30^\circ$. When the moat is defined, we can measure its area and asymmetry, velocities inside and outside it, and azimuthal asymmetry of velocity magnitudes. Using average velocities in distant quiet regions as a reference, we also measure the proper motion of a sunspot with respect to quiet granulation.

3. Results

A visual inspection of velocity maps with identified moat regions (an example is shown in Fig. 1) reveals that moats, or at least their parts, are detected in white light and 1600 Å around all sunspots, both old and young. A similar conclusion was already made by Brickhouse & Labonte (1988). Further, moats have mostly

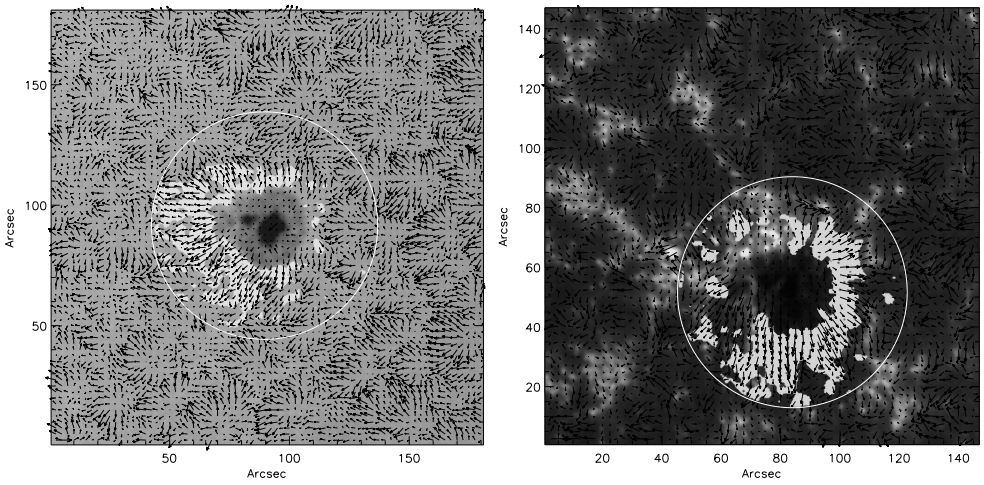

Figure 1. Horizontal velocity maps around the old spot NOAA 9339, computed for white light (*left*) and 1600 Å (*right*). Moat regions are white. Length of the horizontal arrow in the bottom-left corner corresponds to $1\,\mathrm{km\,s^{-1}}$. White circles delimit the regions of interest. East is at left and north at top.

asymmetric, sectored shapes. The asymmetry is independent on the position on the solar disc, so that we can exclude a projection effect.

Comparing moat areas A_m with areas of sunspots A_s in white light, we find that $A_\mathrm{m}/A_\mathrm{s} \simeq 1$ for young and 2 for old spots. Old spots have larger moats, probably because the convective flows around them are better developed. The correlation between moat areas observed in 1600 Å and those in white light is very high (correlation coefficient = 0.88). This means that the size of a moat is practically independent on the height in the atmosphere.

Let us define the maximum moat radius $R_\mathrm{max} = \sqrt{(A_\mathrm{max} + A_\mathrm{s})/\pi}$ as an effective radius of a hypothetical moat with area A_max obtained by azimuthal extrapolation of the area of the best-developed moat sector to all directions. We find that in white light the relation between the maximum moat radius and the effective radius of the sunspot $r_\mathrm{s} = \sqrt{A_\mathrm{s}/\pi}$ is approximately linear: $R_\mathrm{max} = 9\farcs8 + 1.1\,r_\mathrm{s}$ for young spots and $R_\mathrm{max} = 15\farcs5 + 1.1\,r_\mathrm{s}$ for old spots. Since the linear coefficient is close to 1, the maximum moat width $R_\mathrm{max} - r_\mathrm{s}$ does not practically change with the spot radius but it depends on the evolutionary phase: it is equal to $10''$ for young and $16''$ for old spots. These values are comparable with the typical radius of a supergranule ($14''$–$20''$).

To study the asymmetry of moat area, we divided the moat region into 18 sectors of 20°, where 0° is oriented to east and 90° to south. Moat areas were calculated for each sector separately and averaged for all spots. The result is shown in the left panel of Fig. 2. In white light, moats are asymmetrical in the east-west direction. While the eastern part of the moat area is large, the western part is very small and sometimes is even missing (see Fig. 1). This area asymmetry is particularly strong for old spots with well-developed moats. The situation is different in the 1600 Å channel. Moat areas around young spots do not show any east-west asymmetry and those around old spots have a minimum in the eastern sectors, conversely to the white-light case.

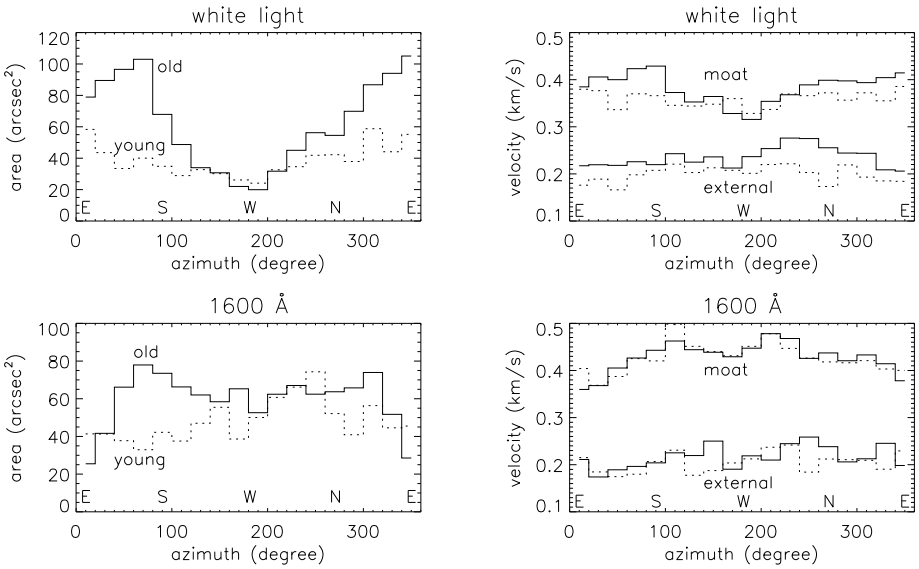

Figure 2. *Left:* Average azimuthal distribution of moat area. *Right:* Average azimuthal distribution of velocities inside the moat and outside (external). Solid line – old spots, dotted line – young spots.

Horizontal velocities measured in regions of interest (outlined by white circles in Fig. 1, to show an example) and averaged for young and old spots separately are summarized in Table 1, together with standard deviations that characterize the dispersion of speeds of individual sunspots. We can see that inside the moat, speeds of granules in white light are higher around old spots than around young ones. This might indicate that the sub-photospheric convective flows are faster in case of old spots. In the 1600 Å channel, speeds in the moat are generally higher than in white light. Velocities outside the moat are substantially smaller than inside. They are more reduced in the vicinity of young spots, possibly due to dispersed magnetic field in developing active regions.

Like the moat areas, magnitudes of horizontal velocities in moats also show the azimuthal asymmetry. This is illustrated in the right panel of Fig. 2, where we plot average azimuthal distributions of velocity magnitudes inside and outside the moat. While there is no east-west asymmetry of speeds outside the moat region, the moat velocities in white light are higher in eastern and lower in

Table 1. Average horizontal velocities [m s^{-1}]

Position	Channel	Young spots	Old spots
Inside moat	White light	380 ± 30	410 ± 30
	1600 Å	450 ± 70	450 ± 40
Outside moat	White light	200 ± 40	240 ± 40
	1600 Å	200 ± 40	210 ± 50

western sectors. In the 1600 Å channel, the asymmetry is reverse to that in white light, with a minimum at east and a maximum at west, both for young and old spots. The difference between the maxima and minima is $\sim$ 100 m s^{-1}. We can conclude that the asymmetry of speeds is consistent with the asymmetry of areas: at low photospheric layers (white light), both areas and speeds are larger in the eastern parts of moats, while higher in the atmosphere (1600 Å), areas are larger and horizontal motions are faster in the western parts.

Since the reference frame of all series of images is always connected with a sunspot, we can determine the spot's proper motion (drift) with respect to the photosphere from average motions of quiet-granulation areas distant from the spot. Average drift velocities from east to west are shown in Table 2, together with numbers of sunspots. Leading and following parts of spot groups are considered separately. The north-south drift velocities are very close to zero. We see that young spots, both leading and following, drift to west with a speed of approximately 100 m s^{-1}. Old leading spots drift with a similar speed, while old following spots are practically without motion. This results in a separation of leading and following parts of sunspot groups. Such kinds of motions were derived in the past e.g. by Gilman & Howard (1985) and van Driel-Gesztelyi & Petrovay (1990) from positional observations of sunspots.

An interesting question is how the east-west asymmetry of moat areas and velocities is related to the proper motion of sunspots. We characterize the asymmetry by the normalized difference of areas $(A_{\rm e}-A_{\rm w})/(A_{\rm e}+A_{\rm w})$ integrated over 8 eastern (e) and 8 western (w) sectors of the moat or by the normalized difference of average velocities $(v_{\rm e}-v_{\rm w})/(v_{\rm e}+v_{\rm w})$ in these sectors. No correlation was found between the drift speeds and the asymmetry of moat velocities. Also the moat area asymmetry observed in the 1600 Å channel is independent on the proper motion. Nevertheless, in white light we detect a weak positive correlation with a coefficient of 0.6 between the moat area asymmetry and the drift speed of old spots. The east-west asymmetry of white-light moat areas around old spots tends to increase with the increasing speed of proper motion. No such correlation was observed for young spots with less developed moats. If we admit that the moat shape in white light, defined by granular motions, depends on sub-photospheric convective flows around the spot, we may speculate that these flows are deformed by the spot's proper motion through the convection zone. Moats shapes in 1600 Å may be influenced by other mechanisms, because they are mostly determined by moving magnetic features (seen in the C IV emission), connected rather with the sunspot than with the sub-photospheric convective cells in its neighbourhood.

Table 2. Average east-to-west drift velocities of sunspots with respect to quiet granulation [m s^{-1}]. Numbers of spots are in parenthesis.

Sunspots	Young	Old
Leading	110 (9)	120 (13)
Following	90 (5)	40 (4)

4. Conclusions

Moats observed in the white-light channel. Moat regions were defined on the basis of horizontal motions of granules, directed radially away from the spot. Moats are found both around old and young spots. Old spots have larger moats with faster granular motions compared to young spots. The maximum moat width, defined in Sect. 3, depends on the evolutionary phase but it is almost independent on the spot radius. Its value is comparable with the typical radius of supergranules. Moat regions are asymmetric, elongated toward east. This asymmetry is stronger for old spots, where moats are better developed. Velocities of granules in moats are higher at east than at west. In case of old sunspots, the moat area asymmetry increases with increasing speed of spot's proper motion with respect to quiet granulation.
Moats observed in the 1600 Å channel. Moat regions were defined on the basis of horizontal motions of intensity structures in the upper photosphere (temperature minimum) and of C IV emission structures representing magnetic features in the transition region. Moat areas in 1600 Å are well correlated with those observed in white light. Eastern parts of moats of old spots are small, i.e., the area asymmetry is opposite to that in white light. Horizontal velocities in moats observed in 1600 Å are higher on average and have an opposite east-west asymmetry compared to those measured in white light.

While the moats observed in white light may be related to sub-photospheric flows around sunspots, the properties of moats in 1600 Å are mostly determined by moving magnetic features (C IV emission) that are connected directly with spots. This may explain the observed differences between the two channels.

Acknowledgments. Thanks to the TRACE team and to the solar database BASS 2000 for kind use of their data. M. S. appreciates the hospitality of the Paul Sabatier University in Toulouse. This work was supported by the Grant Agency of the Academy of Sciences of the Czech Republic (grant IAA 3003404) and the European Solar Magnetism Network (contract HRPN-CT-2002-00313).

References

Bonet, J. A., Márquez, I., Muller, R., Sobotka, M., & Roudier, Th. 2005, A&A, 430, 1089
Brickhouse, N. S. & Labonte, B. J. 1988, Solar Phys. , 115, 43
van Driel-Gesztelyi, L. & Petrovay, K. 1990, Solar Phys. , 126, 285
Fossum, A. & Carlsson, M. 2005, ApJ, 625, 556
Gilman, P. A. & Howard, R. 1985, ApJ, 295, 233
Handy, B. N., et al. 1999, Solar Phys. , 187, 229
Hurlburt, N. E. & Rucklidge, A. M. 2000, MNRAS, 314, 793
Meyer, F., Schmidt, H. U., Weiss, N. O., & Wilson, P. R. 1974, MNRAS, 169, 35
Muller, R. & Mena, B. 1987, Solar Phys. , 112, 295
November, L. J. & Simon, G. W. 1988, ApJ, 333, 427
Sheeley, N. R. 1969, Solar Phys. , 9, 347
Sheeley, N. R. & Bhatnagar A. 1971, Solar Phys. , 19, 338
Shine, R. A., Title, A. M., Tarbell, T. D., & Topka, K. P. 1987, Science, 238, 1203

The Physics of Chromospheric Plasmas
ASP Conference Series, Vol. 368, 2007
Petr Heinzel, Ivan Dorotovič and Robert J. Rutten, eds.

Chromospheric Activity in K Stars

M. Vieytes, P. Mauas, C. Cincunegui and R. Diaz

Instituto de Astronomía y Física del Espacio (IAFE), Buenos Aires

Abstract. We computed chromospheric models for six stars of spectral type K, in most cases in two different moments of activity. The stars were chosen with $0.82 < B-V < 0.90$ including the widely studied star ε Eridani. The stars in the sample have a wide variety of magnetic activity levels, which allows us to study the differences in structures induced by stellar activity, and expand our previous work for G stars including the Sun as a star. The models were constructed to obtain the best possible match with the Ca II K and Hβ observed profiles. We also computed the net radiative losses for each model to constrain the heating mechanism to maintain the structure in the atmosphere predicted by the models. We find a strong correlation between these losses and $S_{\rm Ca\,II}$, the index generally used as a proxy for activity, as we found for G stars.

1. The Models

We select the stars in our sample with $0.82 < B-V < 0.90$, a colour similar to ε Eri, and with different magnetic activity levels. The stellar parameters of the stars in our sample are listed in Table 1. In the second column we list the spectral type, in the third and fourth columns we indicate the colour indexes $B-V$ and $U-B$ and the metallicity is included in the fifth column. In columns 5 to 7 of Table 1 we show the mean values of the $S_{\rm Ca\,II}$ index obtained at the Cerro Tololo InterAmerican Observatory (Henry et al. 1996), and the maximum and minimum $S_{\rm Ca\,II}$ from our spectra.

HD	Sp. type	$B-V$	$U-B$	[Fe/H]	$S_{\rm CTIO}$	$S_{\rm CMmax}$	$S_{\rm CMmin}$
26965	K1 V	0.82	0.43	-0.25	0.185	0.149	0.138
128621	K1 V	0.90	0.63	0.24	0.209	0.247	0.164
22049	K2 V	0.88	1.47	-0.14	0.483	0.555	0.440
17925	K1 V	0.86	1.41	0.10	0.662	0.792	0.566
37572	K0 V	0.85	—	—	0.952	0.703	0.691
177996	K1 V	0.86	0.518	—	0.861	0.821	0.613

Table 1. The first four columns list the stellar parameters (from Hipparcos 1997, and from Cincunegui & Mauas, 2004). The next three columns give the $S_{\rm Ca\,II}$ measured by Henry et al. (1996) at CTIO and by Cincunegui & Mauas (2004) at CASLEO, both converted to Mount Wilson S.

A different chromospheric model was built in each case, assuming one-dimensional, plane-parallel atmospheres, using the code Pandora. For a given temperature distribution with height, we self-consistently computed non-LTE population for H and 11 other ions. A description of this code can be found

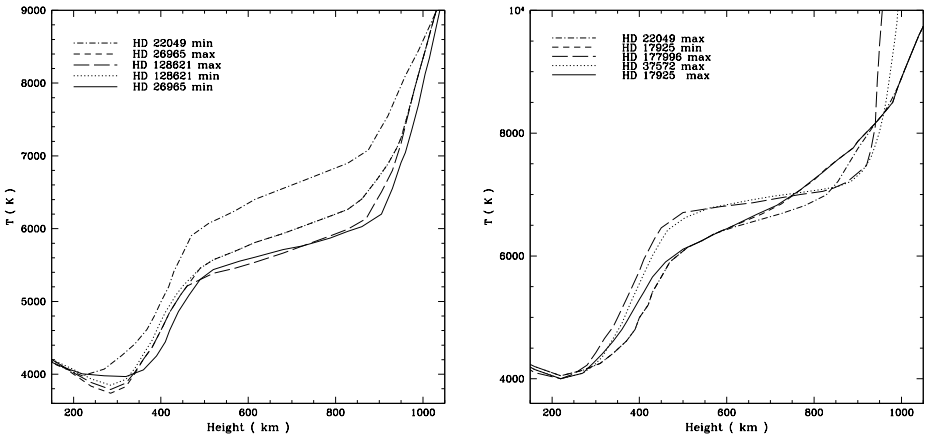

Figure 1. *Left:* Models for the less active group. *Right:* Models for the more active group. All the models have the same structure before 150 km.

in Avrett & Loeser (2003). From the finished model, we computed the emitted profiles of Hβ and of the Ca II K lines, and modified the model until we found a satisfactory match with the observations. The K line profile was computed using Partial Redistribution. We also check the models comparing the computed and observed profiles of the Mg I b and the Na I D lines.

2. Results

The differences between models for different activity levels of the same star can be larger than for different stars. Models for stars less active than ε Eridani (Fig. 1, left) have their minimum temperature $T_{\rm min}$ cooler and higher in the atmosphere, and the temperature increases with activity everywhere in the chromosphere, from the temperature-minimum zone to the transition region. This behavior is different than G stars, for which the changes with activity are practically limited to the $T_{\rm min}$ region. For the most active models (Fig. 1, right), on the other hand, the $T_{\rm min}$ has almost the same value and position, and the changes in the chromospheric structure affects mainly the chromospheric plateau and the rise to the transition region. In Fig. 2 we show the comparison between the observed and synthetic profiles for ε Eridani.

To constrain the amount of chromospheric heating required to sustain the atmosphere of the stars, we computed the radiative cooling rate ϕ (erg cm^{-3} sec^{-1}) for H, H$^-$, H$_{\rm ff}$, Mg I, Mg II, Fe I, Na I, Si I, Ca II, and CO. As we did in Vieytes et al. (2005), to quantify the amount of energy deposited in the chromosphere, we integrated the cooling rate ($\phi_{\rm int}$) from the depth in the chromosphere where cooling rate is positive to the region where the temperature reaches 10^4 K. Figure 3 shows a graphic of $\phi_{\rm int}$ versus $S_{\rm Ca\,II}$ index calculated from models, the triangles are the K star models, and the squares are the G star models from Vieytes et al. (2005). The figure shows that the amount of non-radiative energy

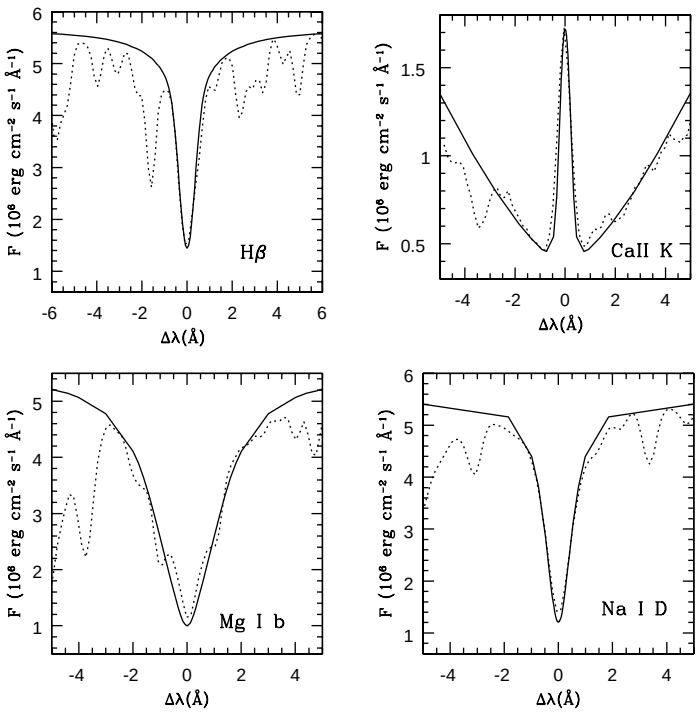

Figure 2. Integrated cooling rate versus $S_{\rm Ca\,II}$ index. The square are the K star models from this work and the triangle are G star models from Vieytes et al. (2005).

needed to heat the chromosphere for the same range of stellar activity, is higher in G stars than in K stars.

To investigate the possibility of different physical processes to heat the stellar atmosphere depending on spectral type, we normalized $\phi_{\rm int}$ to the surface luminosity ($\sigma T_{\rm eff}^4$). For G stars we used the solar $T_{\rm eff}$, and for K star we used the value of ε Eridani. The result is shown in Fig. 4. There is a unique trend for all the stars independently of spectral type, as we suspected if the physical processes that supply the energy to sustain the atmospheric structure were the same in both cases.

References

Avrett E., & Loeser R. 2003, in Modeling of Stellar Atmospheres, IAU Symp. No. 210, ed. W. Weiss & N. Piskunov (Dordrecht: Kluwer), A-21

Cincunegui C., & Mauas P. 2004, A&A, 414, 699

Henry T., Soderblom D., Donahue R., & Baliunas S. 1996, AJ, 111, 439

Hipparcos, Perryman, M. A. C., Lindegren, L., Kovalevsky, J., et al. 1997, A&A, 323, L49

Vieytes, M., Mauas, P., & Cincunegui, C. 2005 A& A, 441, 701

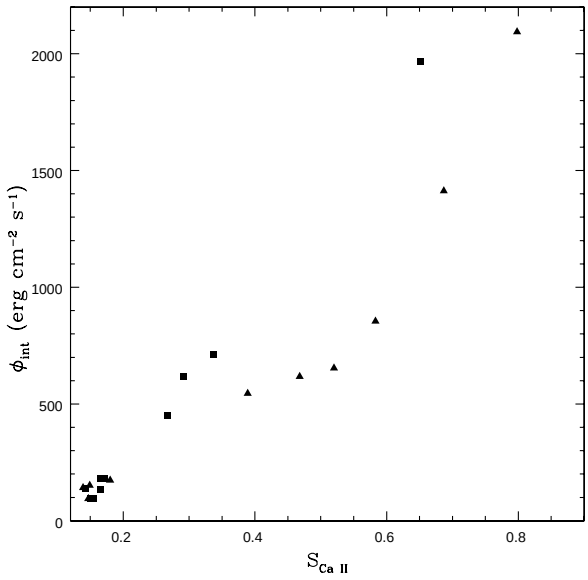

Figure 3. Integrated cooling rate versus $S_{\mathrm{Ca\,II}}$ index. The square are the K star models from this work and the triangle are G star models from Vieytes et al. (2005).

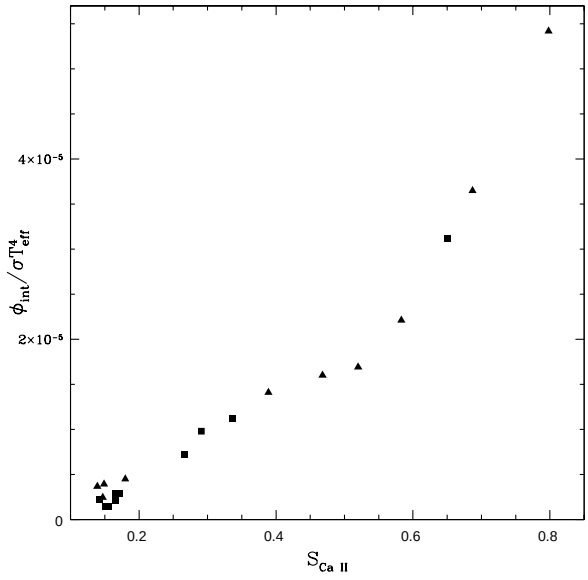

Figure 4. Normalized ϕ_{int} versus $S_{\mathrm{Ca\,II}}$ index. The square are the K star models from this work and the triangle are G star models from Vieytes et al. (2005).

Part IV

Prominences and Filaments

The Physics of Chromospheric Plasmas
ASP Conference Series, Vol. 368, 2007
Petr Heinzel, Ivan Dorotovič and Robert J. Rutten, eds.

The Fine Structure of Solar Prominences

Petr Heinzel

Astronomical Institute AS, Ondřejov, Czech Republic

Abstract. Solar prominences and filaments (prominences projected against the solar disk) exhibit a large variety of fine structures which are well observed down to the resolution limit of ground-based telescopes. We describe the morphological aspects of these fine structures which basically depend on the type of a prominence (quiescent or active-region). Then we review current theoretical scenarios which are aimed at explaining the nature of these structures. In particular we discuss in detail the relative roles of magnetic pressure and gas pressure (i.e., the value of the plasma-β), as well as the dynamical aspects of the fine structures. Special attention is paid to recent numerical simulations which include a complex magnetic topology, energy balance (heating and cooling processes), as well as the multidimensional radiative transfer. Finally, we also show how new ground-based and space observations can reveal various physical aspects of the fine structures including their prominence-corona transition regions in relation to the orientation of the magnetic field.

1. Introduction

Solar prominences have been observed since the invention of the spectrohelioscope and as an example one can see well-known Hα drawings by Secchi (1877) (one can be found in the textbook of Tandberg-Hanssen (1995)). Although these pioneering observations were rather simple, they already indicate that prominences consist of many complicated structures having seemingly chaotic behaviour. Prominence fine structures have then been frequently observed with better and better resolution, reaching today a hundred of km. However, although the fine structure was known, the prominences have been modeled for decades *as a whole*, using simplified one-dimensional (1D) slab models. Their magnetohydrostatic (MHS) structure was first derived by Kippenhahn & Schlüter (1957) (hereafter referred to as KS-model) and their radiative properties were studied in a 1D-slab approximation by many authors. Such models reproduced rather well the spectral properties of prominences as observed with lower resolution. The aim of this review is to discuss various aspects of current investigations of prominence fine structures. This topic was thoroughly reviewed by Heinzel & Vial (1992), while Engvold (2004) summarized the latest observational results achieved with the highest resolution. Some aspects of prominence fine structures related to space research were briefly discussed by Vial (2006). For a more general description of the prominence physics the reader is referred to the monograph of Tandberg-Hanssen (1995).

2. Morphology of Prominence Fine Structures

Prominence fine-structure morphology manifests itself rather differently in case of the limb observations and in case of disk filaments. Moreover, one has to clearly distinguish between typical quiescent and active-region prominences or filaments. Generally speaking, a prominence seen on the limb has appeared before or will appear later as a filament on the disk. In case of quiescent prominences larger-scale structures remain fixed while the fine structure changes rather rapidly. However, it seems to be very difficult to identify the same structures as seen on the limb and on the disk – this makes a lot of confusion and we will discuss this later.

Our information about the fine structure morphology and dynamics comes from currently available high-resolution ground-based observations mostly made in the Hα line. With the instruments like the new SST (Swedish 1-m Solar Telescope) or DOT (Dutch Open Telescope), one can see fine structures down to the resolution limit ($0.15''$ for SST or around 100 km). Homogeneous time series are now expected with a similar spatial resolution from the Solar Optical Telescope (SOT) onboard the Hinode satellite. A large variety of fine structures and their dynamics is also seen on TRACE movies, although the spatial resolution is lower, around $1''$ (see e.g., TRACE filament movies on DVD provided by LMSAL). These images are usually taken with a 171 or 195 Å filter where the hot coronal structures appear simultaneously with cool ones – see Fig. 1. Cool prominences or filaments are dark against the bright background which is due to the absorption of the background coronal radiation emitted in these lines by the hydrogen and helium resonance continua (see cartoon in Rutten 1999) and partially due to lack of emissivity of the TRACE lines within a volume occupied by cool prominence plasmas. At 171 or 195 Å, the He I and He II absorption dominates over the H I and it was shown theoretically that this opacity is quite comparable to that of the Hα line (Anzer & Heinzel 2005).

A large quiescent prominence observed at Big Bear Solar Observatory (see Fig. 2) exhibits many vertically oriented threads of the cool plasma which are a few hundred kilometers wide (from Low & Petrie 2005). On a larger scale, one can identify a few vertical plasma sheets which, using a lower spatial resolution, would appear as more-or-less homogeneous slabs with the thickness typically smaller compared to the other two spatial dimensions. Such a kind of low-resolution images led modelers to use a vertical 1D slab approximation to a real prominence geometry which completely neglected the fine structure. In case of MHS models we already mentioned the classical KS solution. To handle the non-LTE radiative transfer, 1D slab models were extensively used starting from Poland & Anzer (1971), Yakovkin & Zel'dina (1975) and others. We will not detail these models here but rather discuss their recent generalizations to fine-structure modeling.

On the disk, the high-resolution Hα images or movies show fine-structure fibrils of different lengths, the thinnest visible down to the resolution limit of SST or DOT. Very thin dark fibrils (we call them "fibrils" to distinguish them from vertical "threads" seen on the limb) visible along the spine of a quiescent filament are rather short and inclined to the filament axis due to the shear of the magnetic field lines (Fig. 3). On the other hand, much longer fibrils can be seen within the barbs or connecting various parts of the filament main body (Fig. 4). The fact

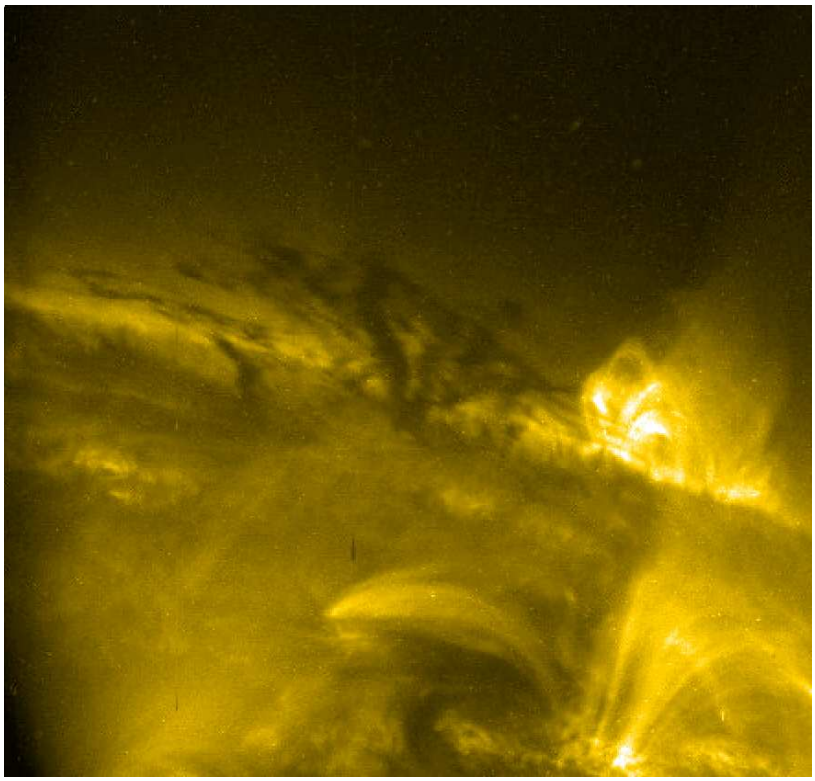

Figure 1. TRACE image of a limb prominence taken in the 195 Å line. Note the fine structures which appear very dynamic on the respective TRACE movies.

that densely packed fibrils seen along the spine are rather short compared to a large-scale magnetic arcade in which the prominence/filament sits indicates that these fibrils are locations of cool plasma condensations in a presumably dipped magnetic field.

3. Dynamics of Prominence Fine Structures

While the large-scale quiescent prominence structure is rather stable, the fine structures described above exhibit a strongly dynamical behaviour. Their shape and brightness change on time scales of minutes which was already noticed by Engvold (1976) using the Hα prominence observations made at the Dunn VTT at Sacramento Peak. Today one can study the fine-structure dynamics and prominence evolution on prominence/filament movies taken by TRACE in the 195 Å line or on high-resolution Hα images or movies. Within the disk filaments, individual fibrils move sideways with velocities up to 3 km s^{-1} which seems to be consistent with limb observations of Zirker & Koutchmy (1990, 1991). A qualitatively new observation was reported by Zirker et al. (1998) who identified a kind of streaming and counter-streaming in a filament in both spines and barbs, having flow velocities around 15 ± 10 km s^{-1}. Dark Hα knots were tracked for

Figure 2. Big Bear Solar Observatory (BBSO) image of a typical quiescent prominence. Quasi-vertical plasma threads are well visible (from Low & Petrie 2005).

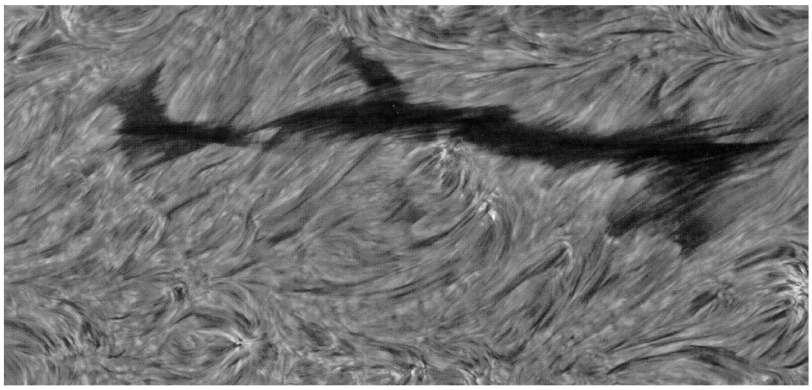

Figure 3. Dutch Open Telescope (DOT) image of a disk filament. Many dark fibrils are seen along the filament spine and elsewhere (courtesy of R.J. Rutten).

distances of 10^4 to 10^5 km at these speeds – see long arrows in Fig. 2 of Zirker et al. (1998).

The same counter-streaming was further observed by Lin et al. (2003) using the high-resolution SST Hα images and Dopplergrams. Both Zirker et al. (1998) and Lin et al. (2003) interpret these motions as plasma flows along the magnetic flux tubes which are not dipped. We have an evidence that these high-resolution Hα images show fine structures which are well coaligned with dark features

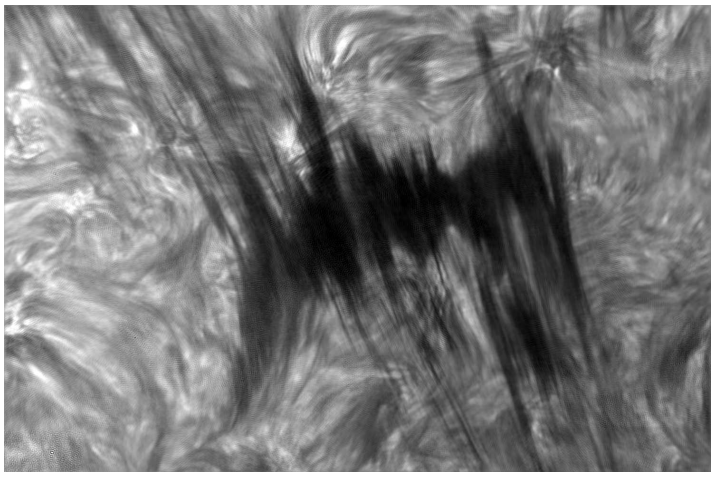

Figure 4. Swedish 1-m Solar Telescope (SST) image of a disk filament. Here we can see long dark fibrils which resemble rather thin flux-tubes (courtesy of O. Engvold).

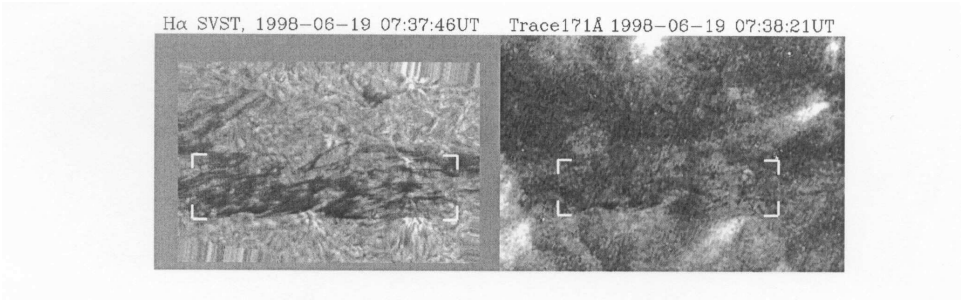

Figure 5. Hα and TRACE fine-structure fibrils. The spatial resolution of TRACE is lower, but same dark fibrils can be well identified on both images (from Schmieder et al. 2004).

visible in the same filament on TRACE 195 Å images – see Fig. 5 from Schmieder et al. (2004). These authors have studied the same filament as Lin et al. (2003).

4. Thermodynamic Properties from Spectral Diagnostics

Spectral diagnostics of prominence fine structures is a difficult task for several reasons. First, one has to distinguish between optically-thin and optically-thick fine structures. In the former case several fine-structure elements (FSE) are seen along the line of sight and their radiation output is thus integrated. On the other hand, in case of thick structures, we mostly see only one FSE, most probably located closer to the border of a prominence rather than in its central parts. The situation is actually more complex, because an optically-thick FSE is thick in the line core but becomes thin in the line wings, where we again see many FSE along the line of sight. This situation largely complicates the analysis of spectral data. Second reason is that, as already mentioned above, FSE are highly dynamical

and thus any multi-wavelength observation has to be made simultaneously or at least quasi-simultaneously (this means within time shorter than the life-time of the FSE) in all wavelength bands of interest. Another complication arises from the lack of our detailed knowledge about the internal structure of FSE and their distributions within a prominence – even their elementary geometry is subject of a controversial debate (vertical threads, horizotal fibrils with flows, blobs etc.). For spectroscopic work, two basic models are usually considered: (i) Each FSE has its own prominence-corona transition region (PCTR), its 3D shape will then depend on the magnetic field threading the FSE because of principally different thermal conductivity along and across the field lines, (ii) FSE are more-or-less isothermal, but their temperature increases towards the prominence boundaries and this forms another kind of PCTR on a larger scale. A combination of (i) and (ii) is also possible. For further details and references see the review by Vial (1998) and his recent summary at the SOHO-17 workshop (Vial 2006). The scenario (i) was corroborated by various authors, while the second one (ii) was suggested e.g., by Poland & Tandberg-Hanssen (1983) who analyzed the spectral data from SMM/UVSP. Here it is worth mentioning that the scenario (ii) allows one to use a 1D slab model with a relevant PCTR on each side as a first approximation (see Anzer & Heinzel 1999), while the effect of a fine-structure PCTR (case (i)) has to be modeled by considering a superposition of several FSE (each of them, however, can be again modeled by a simple 1D slab which describes, contrary to (ii), only one FSE) – see Vial et al. (1989), Heinzel (1989) or Fontenla et al. (1996). Finally, a principal difficulty in our understanding of the thermodynamical properties of prominence plasmas comes from the nature of radiation processes involved. The prominence spectral lines are mostly formed, namely in cooler parts, by the scattering of the incident radiation coming from the solar surface (photosphere, chromosphere, or even PCTR, depending on the spectral line under consideration). This leads to strong departures from LTE and thus the non-LTE theory of radiative transfer must be applied to prominences and filaments. This is known for a long time, here we can mention pioneering works by Poland & Anzer (1971), by an HAO group in the seventies (see Heasley & Milkey (1978) and references therein) or by Kiev groups (Yakovkin & Zel'dina 1975, Morozhenko 1984). For a recent summary of modern non-LTE techniques see Heinzel & Anzer (2005). The use of these transfer methods for 1D slabs is almost routine today and several 1D non-LTE codes do exist: the IAS code (Gouttebroze & Labrosse 2000), the Ondřejov code (Heinzel 1995), PANDORA is now also being modified to prominence slabs (Heinzel & Avrett 2007). 2D slab models were considered first by Vial (1982) using the MAM code of Mihalas et al. (1978), then by Auer & Paletou (1994) and Paletou (1995) and finally by Heinzel & Anzer (2001). All these codes can be or have been used to model either the prominence or filament as a whole (note: for prominences one uses slabs standing vertically above the solar surface, while in case of filaments the slabs are horizontal, i.e., parallel to the solar surface) or individual FSE. However, in case of several FSE, the situation becomes much more complex because of their mutual radiative interaction. This was treated in simplified ways by Zharkova (1989) and by Heinzel (1989), but in most other cases the radiative interaction was neglected, all FSE were considered the be identical (as 1D slabs) and simply superimposed along the line of sight (Fontenla

et al. 1996; Heinzel et al. 2001). This interaction could, however, be tackled using todays high-performance parallel machines.

In the above summary we have tried to give the reader an idea how complex the spectral diagnostics of prominence fine structure is. However, we still completely neglected the dynamics or temporal variations of thermodynamic properties. The actual values of thermodynamic parameters like the kinetic temperature (T), gas pressure (p), plasma density (ρ), electron density ($n_{\rm e}$), but also the number of FSE along the line of sight or their geometrical dimensions, derived from prominence/filament spectra, have been summarized e.g., by Tandberg-Hanssen (1995), Vial (1998) or recently, using SOHO/SUMER data, by Patsourakos & Vial (2002). One approach is to study in detail the properties at a given prominence location, where we see – as discussed above – one or more FSE along the line of sight, or to perform a statistical analysis of the raster data to get the information about a global distribution of such parameters. Here we can mention the recent work by Wiehr et al. (2007) (see also López Ariste & Aulanier 2007 on p. 291 ff in this volume), where the line ratio technique (He D_3 over Hβ) was used. The results based on high-resolution filtrograms taken on VTT at Tenerife do indicate distinct situations: The case when for example the gas pressure would be almost constant over the prominence region (see also Stellmacher & Wiehr (2005)) is of a particular interest since it indicates an almost linear decrease of the magnetic field intensity with height and a statistical homogeneity of the spatial distribution of FSE.

4.1. Spectral diagnostics with SOHO

A few months before this Coimbra meeting solar physicists celebrated 10 years of successful observations with the Solar and Heliospheric Observatory (SOHO), which is a joint ESA/NASA mission (see proceedings from SOHO 17 Workshop held in Sicily, May 2006 – ESA SP-617). During this period, SOHO was frequently used to observe solar prominences and filaments in UV and EUV spectral bands. In particular SUMER and CDS spectrometers provided us with a wealth of unique data. The use of SUMER for prominence physics was reviewed by Patsourakos & Vial (2002), prominence spectroscopy with SUMER was also summarized by Heinzel et al. (2006). Concerning the prominence fine structure, Wiik et al. (1999) and Cirigliano et al. (2004) have studied the behaviour of lines formed in PCTR, while Heinzel et al. (2006) give a summary of their work on the hydrogen Lyman spectrum. The Lyman lines of hydrogen were also studied by Aznar Cuadrado et al. (2003). Finally, let us mention that Parenti et al. (2004) and Parenti et al. (2005) have produced an atlas of the prominence EUV spectrum observed by SOHO/SUMER.

5. Magnetic Field Determinations

Magnetic fields in solar prominences were measured since several decades, using first the Zeeman technique and later on the Hanle effect. This is summarized in the review by López Ariste & Aulanier (2007) on p. 291 ff in this volume. Older polarimetric observations made with the coronagraph led, in the case of quiescent prominences, to magnetic fields typically below 20 G. For latitudes larger than 35° one obtains a mean value of B equal to 8 G, while at lower

latitudes the mean field is around 10 G (Bommier et al. 1994). Leroy et al. (1983) analyzed data for a large number of polar-crown filaments and found B in the range 2 – 15 G, while Athay et al. (1983) arrived at values 6 – 27 G for a sample of 13 prominences (however, they didn't distinguish between quiescent and eruptive prominences). Practically all these measurements have indicated the predominance of horizontal fields which naturally posses the question why the fine-structure threads appear quasi-vertical and not aligned along the field lines like the magnetic flux-tubes (Leroy 1989).

More recent measurements seem to indicate higher fields, reaching values of a few tens of Gauss (López Ariste & Aulanier 2007). However, the respective observations concern only a rather restricted sample of prominences which may not always be of a quiescent type or are restricted to low parts of prominences (including their feets). Higher fields also follow from the analysis of the Stokes V – signal which was not used in earlier studies. The actual intensity of the magnetic field is critical for our understanding of the prominence support and we will discuss this in the next Section.

6. Magnetic Models of Fine Structures

Since the fine-structure magnetic fields have not yet been detected (not because of lack of the spatial resolution, but due to still a low signal-to-noise ratio in polarimetric signals), most of our current knowledge or ideas come from data-driven modeling. Either one can use the detailed distribution of surface magnetic fields (like the SOHO/MDI maps) and perform coronal extrapolations of various degrees of sophistication (see review by López Ariste & Aulanier (2007) in this volume), or use indirect spectroscopic methods and modeling to infer the fine structure of the magnetic field (like that suggested in Heinzel et al. (2001) and recently used in Schmieder et al. (2007)). Here we are mainly interested in the topology of the field inside and in the surroundings of FSE (for a recent summary see also Anzer (2002)).

Two different magnetic configurations are considered in relation to prominence fine structures. The first one, also discussed by López Ariste & Aulanier (2007), is based on the assumption that the plasma-β (ratio of gas to magnetic pressure) is always very low, of the order of 10^{-2} or lower. In that case, the plasma itself has negligible effect on the topology of magnetic fields related to FSE. If, however, the plasma-β is larger, of the order of 0.1 – 1.0 or even higher, the weight of the plasma will produce what we call "gravity-induced magnetic dips". Let us discuss these two situations in more detail (see also Anzer 2002).

6.1. Low-β models

The topology of the prominence magnetic fields at low β is discussed by López Ariste & Aulanier (2007) on p. 291 ff so that we give only a brief overview here. Today various authors try to model the prominence magnetic field by linear or non-linear force-free-field ("fff") extrapolations of the measured photospheric field. Aulanier & Démoulin (1998) show that the prominence may consist of many rather shallow magnetic dips which can be filled by the cool material visible e.g., in the Hα line. The presence of such dips was further demonstrated by Aulanier & Schmieder (2002) and by Aulanier & Démoulin (2003). In the latter

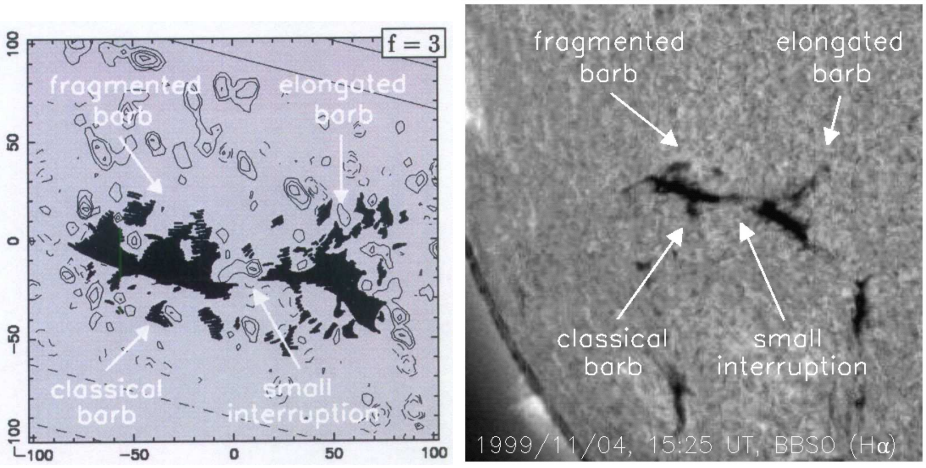

Figure 6. Computed dark-fibril pattern from linear fff extrapolations (left) and the corresponding filament observed in the Hα line (right). See the text where this "blind" test is described. From Aulanier et al. (2000).

paper the authors studied several prominences and found that the extrapolated field strength is rather low for typically quiescent prominence (less that 10 G), higher than 10 G for a plage filament and can reach 30-40 G for active-region prominences. This clearly shows how important the knowledge of the prominence type is: when we speak about the fine structure of quiescent prominences (as in this review), we cannot use measurements obtained for other types of structures. Some of the recent measurements which indicate rather strong fields seem to be related to more active structures. Moreover, these new measurements were not obtained using the coronagraphs and thus, because of scattered light higher above the limb, the measurements are more restricted to lower heights where the prominences appear brighter and where the polarization signal/noise ratio is sufficient (López Ariste – private communication). The usefulness of the filament modeling with linear fff was rather convincingly demonstrated by Aulanier et al. (2000) who performed a kind of "blind test": magnetic dips obtained from numerical extrapolation were marked by black bars schematically indicating the location of the absorbing Hα material – see Fig. 6. The shape of the filament and its various parts were then compared with the true shape as observed on the disk in Hα and the agreement is quite reasonable. Non-linear fff models were considered e.g., by van Ballegooijen (2004).

For a given curvature of the magnetic dip, Aulanier & Schmieder (2002) assumed that the dip is filled by cool plasma up to one pressure scale-height $H = kT/g\mu$, where μ is the mean molecular mass (Fig. 7). For typical prominence conditions H is of the order of 200 km. With the computed curvature of the fff dips one can draw the bars which indicate the presence of the absorbing material and have the length $2l$ as indicated in Fig. 7. However, the real distribution of the opacity will depend on the actual dip configuration, mass loading in it and on various plasma parameters including the hydrogen excitation/ionization conditions. This was not so far considered in the context of fff models.

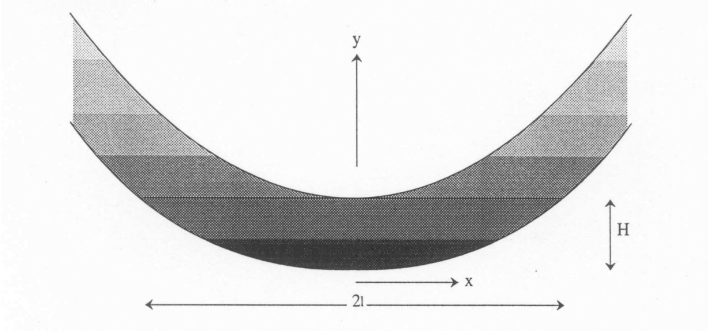

Figure 7. A schematic model showing how the magnetic dip is filled by the plasma up to one pressure scale-height H. A corresponding horizontal extension of the mass loading is $2l$. From Priest (1990).

6.2. Gravity-induced dip models

Spectroscopic determinations of the plasma density and its ionization degree, together with spectro-polarimetric determinations of the magnetic field lead in many cases to rather high values of the plasma-β. This is for example the case of a sample of 14 prominences studied by Bommier et al. (1994), where the plasma-β reaches unity in several cases (see also the non-LTE analysis of these prominences by Heinzel & Anzer (1998)). Using a simple 1D MHS configuration for a vertical fine-structure slab (representing vertical threads as seen in Fig. 2), one can easily derive a relation between the plasma-β and the angle ψ of the magnetic-field inclination at the border of the dip (e.g., Heinzel & Anzer 1999), $\beta \simeq \cot^2 \psi$.

Construction of equilibrium configurations in which the weight of the plasma inside the magnetic dip is balanced against the solar gravity by the Lorentz force is a difficult task. An analytical solution to this problem, assuming that the whole prominence is represented by a 1D vertical plasma slab hanging in a dipped magnetic field, was proposed already in 1957 by Kippenhahn and Schlüter (so-called "normal" polarity model), while Kuperus & Raadu (1974) have suggested a similar model but with an "inverse" polarity. Based on the idea of Poland & Mariska (1988) that the fine-structure threads are in fact vertically-aligned magnetic dips loaded with mass, Anzer & Heinzel (1999) and Heinzel & Anzer (2001) started to model such gravity-induced dips using general 1D or 2D MHS equilibria, respectively. Such local solutions within the magnetic dip are sometimes called KS-type models (according to Kippenhahn and Schlüter) because they use the KS-type analytical solution of the pressure equilibrium (see Section 8). However, they have nothing to do with the global magnetic topology of the whole prominence so that the inverse-polarity prominences can be treated in the same way. A comprehensive description of the gravity-induced dip models is given in the lecture notes by Heinzel & Anzer (2005) to which the reader is referred for further details. Here we will only mention one important result, namely the dependence of the plasma-β on the mass loading M and the field strength B, which can be derived for 1D vertical slab in MHS equilibrium (Anzer & Heinzel 2007)

$$\beta = \left(\frac{2\pi g M}{B^2}\right)^2 . \quad (1)$$

Using the results of Gouttebroze et al. (1993), one can relate this M to optical parameters like the Hα line-center optical thickness or Hα integrated intensity.

Recently, Low & Petrie (2005) have also considered a series of 1D gravity-induced dips aligned along the prominence spine and being in MHS equilibrium of the KS-type (Fig. 8). However, these authors did not consider the radiative transfer in these structures and thus could not predict their optical properties like the Hα contrast against the disk. They only draw the black bars as other authors do in case of low-β dips.

6.3. Other scenarios

Finally, we should also mention that some authors considered waves propagating vertically within a flux-tube and aimed at supporting the cool plasma against the gravity. For example, Pécseli & Engvold (2000) have suggested MHD waves. They show an illustratory example (see their Fig. 1) of such "vertical flux-tubes" in a quiescent prominence with presumably vertical field in which the waves are propagating. However, this example rather resembles the situation discussed by Leroy (1989), i.e., quasi-vertical fine-structure threads which are threaded by horizontal field lines. There is also an ongoing debate whether the field in barbs is more inclined or quasi-vertical (Zirker et al. 1998) or made of dips (Aulanier & Schmieder 2002, Chae et al. 2005). In the former case, for flows which do not correspond to a free fall, one would need a special support.

7. Fine-Structure Energetics

The energetics of quiescent prominences is still an unsolved problem. Although mutually connected, we can divide this problem in two aspects: the energetics of central cool cores of the FSE and the energetics of their PCTRs.

The basic question is whether the incident radiation which almost fully determines the radiation properties of cool cores can also determine the kinetic temperature in these regions. In other words, is the cool core of FSE in a radiative equilibrium or do we need some extra heating to achieve the observed values of temperatures which are typically between 6000 to 9000 K. The computation of the radiative equilibrium under the non-LTE conditions is a rather difficult task, moreover, the result will strongly depend on the incident radiation fields used as boundary conditions for the solution of the radiation transfer problem. Radiation-equilibrium models in 1D slabs, for a mixture of hydrogen and helium plasma, were first constructed by Heasly & Mihalas (1976) who arrived at relatively low temperatures, down to 4600 K. By adding some extra energy input via a heating function, higher temperatures were obtained in accordance with typical observations. Since the thermal conductivity is not efficient in these central cool parts, several other mechanisms were considered during the last few decades. Among them, we can mention mainly the wave dissipation or enthalpy transport. However, a surprisingly new result was recently obtained by Gouttebroze (2007), who computed a set of fine-structure models in radiation equilibrium. 1D axially-symmetric cylinders represent vertically standing threads illuminated

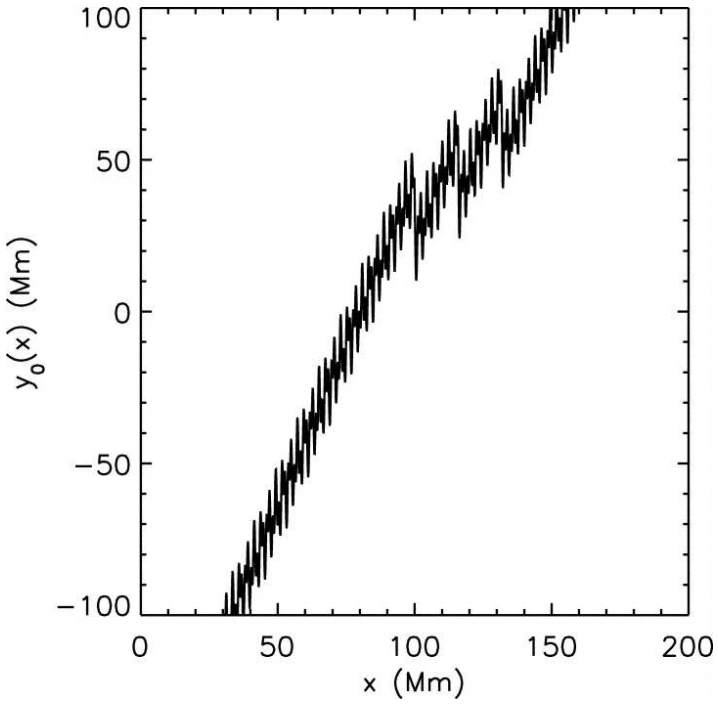

Figure 8. Gravity-induced magnetic dips as projected onto the disk. Each black bar corresponds to a vertical 1D dip model. From Low & Petrie (2005).

by the disk radiation. With currently used incident radiation fields (Gouttebroze 2004), Gouttebroze (2007) arrived at much higher radiation-equilibrium temperatures as compared to the results of Heasly & Mihalas (1976) – we show this in Fig. 9. Namely thinner cylinders which are of interest for the fine-structure modeling (plots in Fig. 9a) reveal temperatures between 7000 and 9500 K for gas pressures between 0.5 to 0.01 dyn cm^{-2}, respectively. This would then mean that no extra heating is required for cool central parts of fine-strucure threads. In these models only the radiative losses due to the hydrogen were considered, which nevertheless can be compared with results of Heasly & Mihalas (1976) because the helium does not contribute much. However, there is still an open question concerning the importance of other species like calcium, magnesium or other optically-thin losses (see e.g., discussion by Anzer & Heinzel (1999)).

Concerning the energetics of the PCTR, our knowledge is also rather incomplete. At lower temperatures, say up to 10^5 K, the conduction along the magnetic field already plays a role (Fontenla & Rovira 1984). Moreover, in analogy to CCTR (Fontenla et al. 1990), the ambipolar diffusion was also considered for fine-structure prominence threads by Fontenla et al. (1996). Quite recently, Vial et al. (2007) tested various kinds of 1D models against the SOHO/SUMER observations of hydrogen Lyman line intensities and found that all models with the ambipolar diffusion predict unrealistically high integrated intensities of the Lyman β line. This can be related to the relative orientation of the line of sight and the magnetic field as discussed in Heinzel et al. (2005). At still higher temperatures, most of the work was restricted to the analysis of the differen-

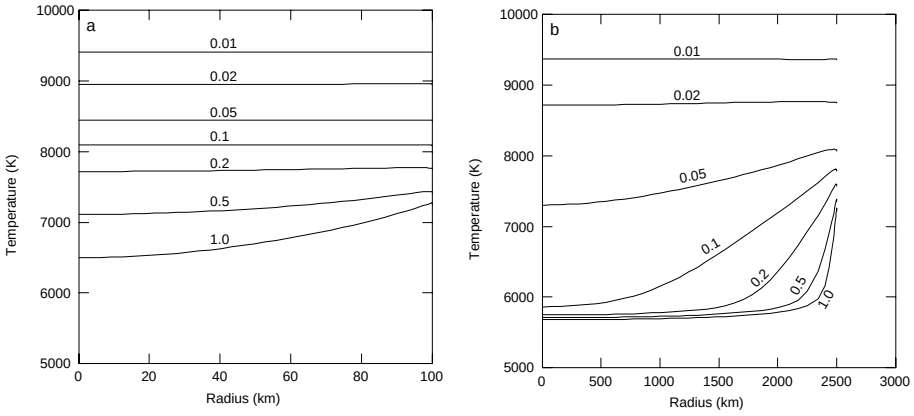

Figure 9. Temperature variation along the radius of vertical cylindrical threads in radiative equilibrium, for two diameters and various pressures. Pressures (in dyn cm^{-2}) are indicated as curve labels. Left: for cylinders with the width of 200 km; right: for a width of 5000 km. From Gouttebroze (2007).

tial emission measure (DEM) – see e.g., Engvold (1998). However, this analysis is usually based on the so-called coronal approximation and thus the question arises whether the departures from this approximation, due to radiative excitations, can play any important role. For chromospheric conditions, this issue is discussed in this book by Avrett (2007). At temperatures higher than 30000 K, dynamical models of flux-tubes with prominence condensations were studied using extensive numerical simulations of the time-dependent loop energetics and plasma dynamics (see Karpen et al. (2006) and references therein).

8. RMHS Simulations

The equations of magneto-hydrostatic equilibrium originally derived by KS become considerably simpler if one uses instead of the Cartesian coordinate x the column-mass coordinate m, defined by the relation

$$\mathrm{d}m = -\rho\,\mathrm{d}x\,, \tag{2}$$

where ρ is the the plasma density. $m = 0$ at one surface of the prominence slab and $m = M$ at the opposite. Loading of such mass into an initially horizontal magnetic field leads to a formation of a gravity-induced dip as we will demonstrate in the next Section. The pressure-balance equation for such a 1D equilibrium dip configuration is governed by the equation

$$p(m) = 4p_{\mathrm{c}}\frac{m}{M}\left(1 - \frac{m}{M}\right) + p_0\,, \tag{3}$$

where p is the gas and turbulent pressure and p_0 is the coronal pressure at the surfaces. This equation was first derived by Heasly & Mihalas (1976) and used to model prominences as a whole. At the slab surface one has the vertical

component of the field vector $B_z \equiv B_{z1}$ which gives, together with the horizontal component B_x =const.

$$M = \frac{B_x B_{z1}}{2\pi g} \,. \tag{4}$$

Using this formula, we obtain for $p_{\rm c}$

$$p_{\rm c} = \frac{\pi g^2}{B_x^2} \frac{M^2}{2} = \frac{B_{z1}^2}{8\pi} \,. \tag{5}$$

The quantity $p_{\rm c}$ can be interpreted in the following way: at the slab center we have the pressure

$$p_{\rm cen} = p(M/2) = p_{\rm c} + p_0 \,. \tag{6}$$

If p_0 would be zero, then $p_{\rm cen} = p_{\rm c} = B_{z1}^2/8\pi$, which is the magnetic pressure. Therefore, in this case the gas pressure at the slab centre will be equal to the magnetic pressure calculated with $B = B_{z1}$. This formulation with the column mass has a great advantage of a simple analytical integration which is valid for any (i.e., non-constant) temperature and ionization-degree distribution. To get the density $\rho(m)$ we use the state equation with the mean molecular mass

$$\mu = \frac{1 + 4\alpha}{1 + \alpha + i} m_{\rm H} \,, \tag{7}$$

where i is the ionization degree of hydrogen $i = n_{\rm p}/n_{\rm H}$ ($n_{\rm p}$ and $n_{\rm H}$ are the proton and hydrogen densities, respectively), α the helium abundance relative to hydrogen and $m_{\rm H}$ the hydrogen atom mass. i varies between zero (neutral gas) and unity (fully-ionized plasma). Inside the prominence and its PCTR, one can consider some schematic variation of i with depth but for a given prominence model the true ionization-degree structure results from rather complex non-LTE radiative-transfer calculations.

The 1D-slab MHS equilibrium of this type was first used by Heasly & Mihalas (1976), who combined it with the full set of non-LTE equations. Their models were aimed at describing the whole prominence. A similar study was repeated recently by Anzer & Heinzel (1999) who have considered a grid of models and studied their energetics. In the latter work, new incident radiation fields and the partial-redistribution in hydrogen Lyman lines were used. As a next step, Heinzel & Anzer (2001) have generalized these 1D models to two dimensions and developed fully 2D MHS models coupled to the radiation field. The latter were computed using the 2D radiative-transfer technique similar to that of Auer & Paletou (1994). In this way, all quantities including the ionization structure were consistently evaluated in the frame of such a 2D Radiation-MHS (RMHS) approach. However, contrary to previous work, these 2D models were aimed at representing the vertical fine-structure threads frequently observed in quiescent prominences. The only drawback of this kind of modeling is that Heinzel & Anzer (2001) didn't consider the energy-balance problem and, instead, used some kind of empirical temperature structure. Their PCTR *along* the magnetic field lines is much more extended as compared to that *across* the lines, which corresponds to different thermal conductivities. Since these 2D models allow us to look at the fine-structure threads in various directions, we see that the respective synthetic spectra reflect very well the different structure of PCTR's.

Namely the hydrogen Lyman lines appear quite reversed when we look across the field lines and much less reversed or even unreversed when looking along the field lines. This quite interesting behaviour was discovered already in Heinzel et al. (2001) on basis of SOHO/SUMER spectra.

In subsequent papers, Heinzel et al. (2005) and Gunár et al. (2007) extended this 2D modeling of vertical threads to a 12-level plus continuum hydrogen model atom and studied in detail the formation of hydrogen Lyman lines and Lyman continuum. In Fig. 10 we show one of their results, and namely the 2D contribution functions which illustrate the formation of hydrogen Lyman lines along and across the field lines, in a 2D vertical thread with PCTR temperatures ranging up to 50 000 K in this numerical box. This pattern is quite complex but leads to synthetic line profiles which are in good agreement with SOHO/SUMER observations (see also the paper by Gunár et al. on p. 317 ff in this volume). The sensitivity of Lyman-line profiles to orientation of the magnetic field with respect to the line of sight has been also proven recently by Schmieder et al. (2007) who studied a kind of "round-shape filament" approaching the solar limb and consecutively showing its different parts above the limb having different orientations of the field lines.

Finally, let us note that these 2D threads which can be anisotropically irradiated represent the basic ingredient of a more realistic multi-thread modeling. Several such threads distributed in space will be illuminated by the solar radiation penetrating through this "forest" of threads and the mutual radiative interaction between all those threads can be consistently taken into account. Another important aspect of this 2D MHS modeling is that such threads or their clusters can represents prototypes of realistic models used to synthesize the Stokes profiles and thus study the influence of the fine structure on the polarization signals.

9. RMHD Simulations

Equation (3) gives the 1D MHS equilibrium of the KS-type. In order to see how the cool and dense plasma structure can evolve in the magnetic field under the action of Lorentz and gravity forces, Bárta et al. (2007) solved numerically the system of compressible one-fluid MHD equations in a 2D vertical plane, starting with the dense and cool blob (a thread in 3D) representing a thread of the filament fine structure surrounded by the gravitationally stratified, constant-temperature hot corona. The initial magnetic field has only a horizontal component. At the very beginning the plasma blob starts to fall down, the internal electric current is induced inside it which generates the restoring Lorenz force. Due to the inertial mass the blob overshoots the (global) equilibrium point and an upward-directed Lorentz force prevails over the gravity turning the movement of the blob up. The system starts to oscillate but due to the numerical viscous term the oscillations are damped. After several oscillations the system is practically relaxed and in the MHS equilibrium. The evolution of the system at four subsequent times is shown in Fig. 11. These first simulations will now be replaced by fully 3D modeling which will also include the 3D radiative transfer. The latter is necessary to determine the ionization state of the plasma and its radiation losses.

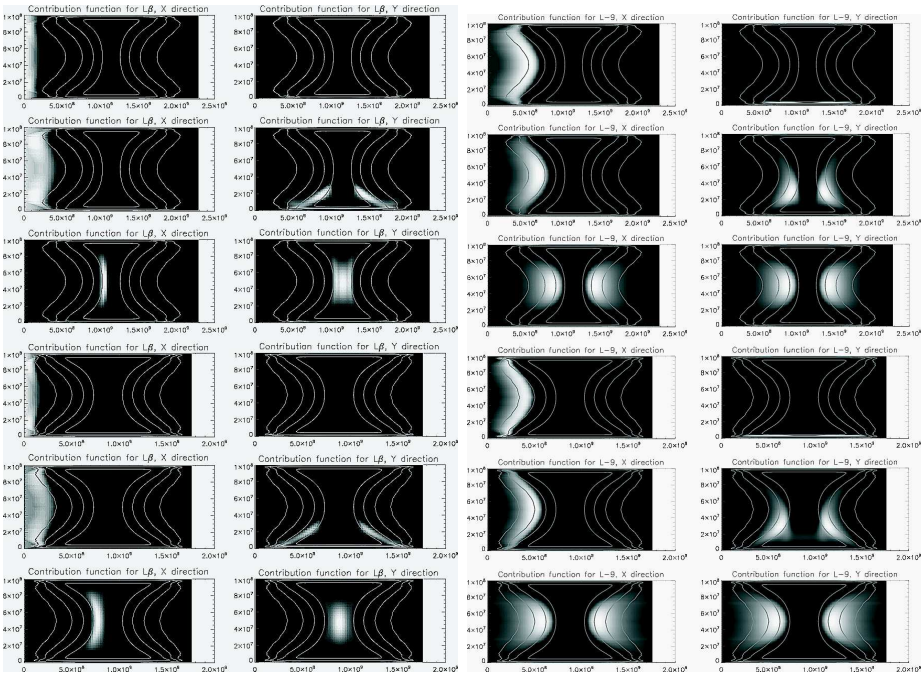

Figure 10. Contribution functions along and across the field lines showing the formation depths of the hydrogen Lyman β (left two columns) and Lyman 9 (right two columns). Two different models are displayed (twice three rows). In each part, the first row corresponds to the line center, the second one to the peak wavelength and the third one to the wing. Left columns refer to the direction along the field lines (x-direction), while right columns to the direction across the field (y-direction). The temperature contours are also drawn showing two quite different PCTR's. The line core of Lyman β is formed at the surface of the 2D thread (at the highest temperatures), the peaks deeper and in the line wing we can see the central parts of the structure. The Lyman 9 line is optically thinner and thus the thread more transparent in all wavelengths allowing the diagnostics of deeper layers. Note the different scales in both directions, in reality the "fibril" projected onto solar disk is much more stretched.

10. Comments on Magnetic Dips

Any analysis of 2D images or movies can lead to misinterpretations just due to the lack of information on fully 3D structural and dynamical pattern. As an example we will mention here again the scenario of counter-streaming (Zirker et al. 1998 or Lin et al. 2003). A close inspection of high-resolution Hα movies (see them on CD enclosed to the Solar Physics Vol. 216) reveals that dark fine-strucure blobs (rather than long threads) move on relatively short paths, although sometimes in opposite directions. These motions don't resemble at all flows along long magnetic fluxtubes, but rather a kind of oscillations. Quite interestingly, when watching the TRACE movies of similar prominences, one clearly sees sideway oscillations of small blobs which, projected on the disk, would probably resemble the kind of motions seen on SST movies (projected

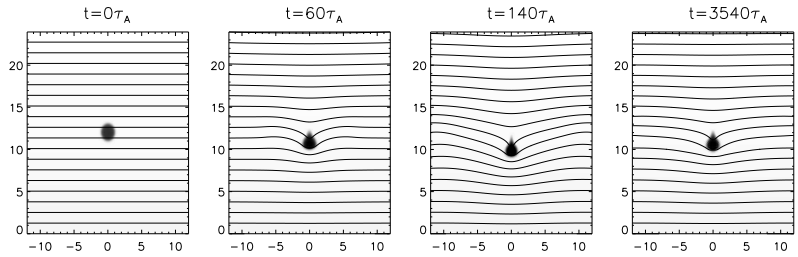

Figure 11. A sequence of four snapshots of the prominence fine-structure evolution according to the MHD system of equations. The simulation is carried out in the dimensionless units; lengths are expressed in the initial thread half-width $L_{\rm t}$, times in the units of Alfvén transit time $\tau_{\rm A} = L_{\rm t}/v_{\rm A}$. Recalculated for reasonable coronal conditions (coronal temperature $T_{\rm c} = 2 \times 10^6$K, coronal gravitation length scale $L_{\rm g} = 6 \times 10^9$ cm) we get $L_{\rm t} \approx 1200$ km, $\tau_{\rm A} \approx 20$ s. Thus the thread characteristic dimension is ≈ 2500 km and the final (relaxed) state in the last frame is reached after almost 20 hours.

blobs seen in Hα and TRACE 195 Å are shown in Fig. 5). However, these blobs visible on TRACE movies form very frequently the quasi-vertical threads also shown in Fig. 1 and Fig. 2 and thus, according to our discussion above, they should represent plasma condensations hanging in a dipped magnetic field which seems to oscillate in the corona. This scenario is, however, quite different from that of Lin et al. (2003) (flows along long fluxtubes without any dips).

Another observational support for dips being located along the prominence spine is the fact that the Hα absorbing fibrils are concentrated along the spine and we typically don't see any significant absorption further away from the spine. This seems to indicate that there are no such flows which could be detected along the whole magnetic arcade which is of course much wider than the width of the spine. Even Hα images or movies taken out of the line center don't show such a pattern.

Actually there should be no principal controversy between low-β dip models and gravity-induced dip models. Yet there are no time-dependent simulations of how the plasma is condensed in a dipped field and how this may evolve leading to an enhancement of the plasma density and thus its weight which, eventually, will modify the magnetic structure of the dip. Existing time-dependent simulations of prominence condensations assume an initial shape of the magnetic loop and this is not changed during simulations even when the mass loading at the loop top increases. Static models of dips which neglect the prominence weight (fff extrapolations) can reasonably well reproduce the large-scale distribution of dips and this has proven to be a quite novel approach. On the other hand, static models of gravity-induced dips have been developed to understand the *local* magnetic topology of a dip and its thermodynamic and radiative properties. These two approaches should not be in conflict, but rather complementary: provided that the plasma-β is large enough, the weight effects should be added to initially fff-dips. This is a challenge for future prominence modeling. As discussed above, today the actual values of plasma beta are still very uncertain and thus various configurations are possible. An important diagnostics test would be the quantitative modeling of the Hα contrast of fine-structure fibrils

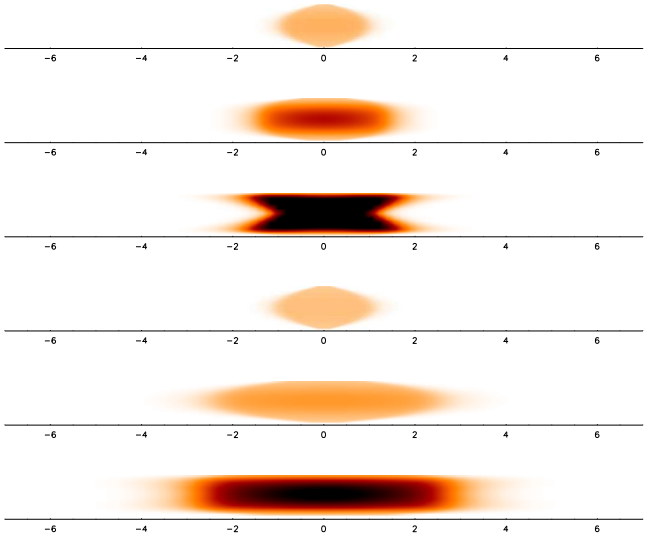

Figure 12. (2+1)D models of Hα fibrils. Six 2D thread models are shown with different mass loadings and magnetic-field strengths. From Heinzel & Anzer (2006).

located along the filament spines. This contrast, which certainly increases with increasing spatial resolution of new telescopes, is due to the absorption of the background radiation in the Hα line (the scattering contribution to the source function is typically small). It has to be modeled in 3D fibril geometry which requires realistic estimate of the mass loading. An example of how this can be handled was given recently by Heinzel & Anzer (2006), who used some kind of (2+1)D models to demonstrate the theoretical Hα contrast of gravity-induced magnetic dips as projected against the solar disk. A few examples are shown in Fig. 12, where the fibril models do exhibit a significant stretching in the direction of the magnetic field and this resembles real dark fibrils as seen e.g., in Fig. 3.

11. Conclusions

To conclude this review, let us go again back to Secchi (1877). In his book *Le Soleil* one can read: *"Les protubérances se présentent sous des aspects si bizarres et si capricieux qu'il est absolument impossible de les décrire avec quelque exactitude."* After 130 years, this still seems to be the case.

Acknowledgments. I am very grateful to my colleagues and collaborators for many useful discussions which helped me to prepare this review and to others from SOC and LOC for a nice meeting. In particular, I am indebted to Uli Anzer and Rob Rutten for reading the manuscript and suggesting several improvements. This work was done in the frame of the ESA-PECS project No. 98030. I also acknowledge travel support from the ESMN.

References

Anzer, U. 2002, in Proc. 10th Solar Physics Meeting, ESA SP-506, 389
Anzer, U., & Heinzel, P. 1999, A&A, 349, 974
Anzer, U., & Heinzel, P. 2005, ApJ, 622, 714
Anzer, U., & Heinzel, P. 2007, A&A, in press
Athay, R.G., Querfeld, C., Smartt, R., Landi Degl'Innocenti, E., & Bommier, V. 1983, Solar Phys., 89, 3
Auer, L.H., & Paletou, F. 1994, A&A, 285,675
Aulanier, G., & Démoulin, P. 1998, A&A, 329, 1125
Aulanier, G., & Démoulin, P. 2003, A&A, 402, 769
Aulanier, G., & Schmieder, B. 2002, A&A, 386, 1106
Aulanier, G., Srivastava, N., & Martin, S. 2000, ApJ, 543, 447
Avrett, E.H., 2007, in P. Heinzel, I. Dorotovič, R. J. Rutten (eds.), The Physics of Chromospheric Plasmas, ASP Conf. Ser. 368, 81
Aznar Cuadrado, R., Andretta, V., Teriaca, L., & Kucera, T.A. 2003, Mem. S. A. It., 74, 611
Bárta, M., Anzer, U., Heinzel, P., & Karlický, M. 2007, in preparation
Bommier, V., Leroy, J.-L., Landi Degl'Innocenti, E., & Sahal-Bréchot, S. 1994, Solar Phys., 154, 231
Chae, J., Moon, Y.J., & Park, Y.D. 2005, ApJ., 626, 574
Cirigliano, D., Vial, J.-C., & Rovira, M. 2004, Solar Phys., 223, 95
Engvold, O. 1976, Solar Phys., 49, 283
Engvold, O. 1976, in Proc. IAU Coll. 167, New Perspectives on Solar Prominences, ed. D. Webb, D. Rust & B. Schmieder, ASP Conf. Ser., 150, 23
Engvold, O. 2004, in Proc. IAU Symp. No. 223, ed. A.V. Stepanov & E. Benevolenskaya, (Cambridge: Cambridge Univ. Press), 187
Fontenla, J.M., & Rovira, M. 1985, Solar Phys. 96, 53
Fontenla, J., Avrett, G., Loeser, R. 1990, ApJ, 355, 700
Fontenla, J., Rovira, M., Vial, J.-C., & Gouttebroze, P. 1996, ApJ, 466, 496
Gouttebroze, P. 2004, A&A, 413, 733
Gouttebroze, P. 2007, A&A, in press
Gouttebroze, P., & Labrosse, N. 2000, Solar Phys., 196, 349
Gouttebroze, P., Heinzel, P., & Vial, J.-C. 1993, A&AS, 99, 513
Gunár, S., Heinzel, P., & Anzer, U. 2007, A&A, 463, 737
Heasley, J.N., & Mihalas, D. 1978, ApJ, 205, 273
Heasley, J.N. & Milkey, R.W. 1978, ApJ, 221, 677
Heinzel, P. 1989, in Proc. IAU Coll. 117, Hvar Obs. Bull. 13, 279
Heinzel, P. 1995, A&A, 299, 563
Heinzel, P., & Anzer, U. 1998, Solar Phys., 179, 75
Heinzel, P., & Anzer, U. 1999, Solar Phys., 184, 103
Heinzel, P., & Anzer, U. 2001, A&A, 375, 1082
Heinzel, P., & Anzer, U. 2005, in Solar Magnetic Phenomena, ed. A. Hanslmeier, A. Veronig & M. Messerotti, Astrophys. Space Sci. Lib., 320 (Springer: Dordrecht), 115
Heinzel, P., & Anzer, U. 2006, ApJ, 643, L65
Heinzel, P. & Avrett, G. 2007, in preparation
Heinzel, P., & Vial, J.-C. 1992, Proc. ESA Workshop on Solar Physics and Astrophysics at Interferometry Resolution, ESA SP-348, 57
Heinzel, P., Anzer, U., & Gunár, S. 2005, A&A, 442, 331
Heinzel, P., Schmieder, B., & Vial, J.-C. 2006, Proc. SOHO 17 – 10 years of SOHO and Beyond, ESA SP-617 (CD-ROM)
Heinzel, P., Schmieder, B., Vial, J.-C., & Kotrč, P. 2001, A&A, 370, 281
Karpen, J.T., Antiochos, S.K., & Klimchuk, J.A. 2006, ApJ, 637, 531
Kippenhahn, R., & Schlüter, A. 1957, Z. Astrophys., 43, 36

Kuperus, M., & Raadu, M.A. 1974, A&A, 31, 189
Leroy, J.-L. 1989, in Dynamics and Structure of Quiescent Solar Prominences, ed. E.R. Priest, Astrophys. Space Sci. Lib., 150, 77
Leroy, J.-L., Sahal-Bréchot, S., & Bommier, V. 1983, Solar Phys., 83, 135
Lin, Y., Engvold, O., & Wiik, J.E. 2003, Solar Phys. 216, 109
López Ariste, A., & Aulanier, G. 2007, in P. Heinzel, I. Dorotovič, R. J. Rutten (eds.), The Physics of Chromospheric Plasmas, ASP Conf. Ser. 368, 291
Low, B.C., & Petrie, G.J.D. 2005, ApJ, 626, 551
Mihalas, D., Auer, L.H., & Mihalas, B.W. 1978, ApJ, 220, 1001
Morozhenko, N. N. 1984, Spectrophotometric investigations of quiescent solar prominences (Naukova dumka: Kiev)
Paletou, F. 1995, A&A, 302, 587
Parenti, S., Vial, J.-C., & Lemaire, P. 2004, Solar Phys., 220, 61
Parenti, S., Vial, J.-C., & Lemaire, P. 2005, A&A, 443, 685
Patsourakos, S., & Vial, J.-C. 2002, Solar Phys., 208, 253
Pécseli, H., & Engvold, O. 2000, Solar Phys., 194, 73
Poland, A.I., & Anzer, U. 1971, Solar Phys., 19, 401
Poland, A.I., & Mariska, J.T. 1988, in Dynamics and Structure of Solar Prominences, ed. J.L. Ballester & E.R. Priest (Université des Illes Baléares), 133
Poland, A.I., & Tandberg-Hanssen, E. 1983, Solar Phys., 84, 63
Priest, E.R. 1990, in Proc. IAU Coll. 117, ed. V. Ruždjak & E. Tandberg-Hanssen, Lecture Notes in Physics, 363 (Springer-Verlag: Berlin), 150
Rutten, R.J. 1999, in Proc. 3rd Advances in Solar Physics Euroconference: Magnetic Fields and Oscillations, ed. B. Schmieder, A. Hofmann & J. Staude, ASP Conf. Ser., 184 (ASP: San Francisco), 181
Secchi, A. 1877, Le Soleil (Gauthier-Villars: Paris)
Schmieder, B., Gunár, S., Heinzel, P., & Anzer, U. 2007, Solar Phys., in press
Schmieder, B., Lin, Y., Heinzel, P., & Schwartz, P. 2004, Solar Phys., 221, 297
Stellmacher, G., & Wiehr, E. 2005, A&A, 431, 1059
Tandberg-Hanssen, E. 1995, The Nature of Solar Prominences (Kluwer: Dordrecht)
van Ballegooijen, A.A. 2004, ApJ, 612, 519
Vial, J.-C. 1982, ApJ, 254, 780
Vial, J.-C. 1998, in Proc. IAU Coll. 167, New Perspectives on Solar Prominences, ed. D. Webb, D. Rust, & B. Schmieder, ASP Conf. Ser., 150, 175
Vial, J.-C. 2006, Proc. SOHO 17 – 10 years of SOHO and Beyond, ESA SP-617 (CD-ROM)
Vial, J.-C., Ebadi, H., & Ajabshirizadeh, A. 2007, Solar Phys., in press
Vial, J.-C., Rovira, M., Fontenla, J., & Gouttebroze, P. 1989, in Proc. IAU Coll. 117, Hvar Obs. Bull. 13, 347
Wiehr, E., Stellmacher, G., & Hirzberger, J. 2007, Solar Phys., in press
Wiik, J.E., Dammasch, I.E., Schmieder, B., & Wilhelm, K. 1999, Solar Phys., 187, 405
Yakovkin, N.A., & Zel'dina, M. Yu. 1975, Solar Phys. 45, 319
Zharkova, V.V. 1989, in Proc. IAU Coll. 117, Hvar Obs. Bull., 13, 331
Zirker, J.B., & Koutchmy, S. 1990, Solar Phys., 127, 109
Zirker, J.B., & Koutchmy, S. 1991, Solar Phys., 131, 107
Zirker, J.B., Engvold, O., & Martin, S.F. 1998, Nature, 396, 440

The Physics of Chromospheric Plasmas
ASP Conference Series, Vol. 368, 2007
Petr Heinzel, Ivan Dorotovič and Robert J. Rutten, eds.

Unveiling the Magnetic Field Topology of Prominences

A. López Ariste[1] and G. Aulanier[2]

[1] *THEMIS/CNRS, La Laguna, Spain*
[2] *LESIA, Observatoire de Paris, Meudon, France*

Abstract. A renewed effort is being dedicated to infer magnetic fields in prominences through spectropolarimetry of emission lines like the He D_3 and 10830 Å lines. We will briefly review those present observational efforts pointing at how do they improve or disregard past attempts to measure magnetic fields in prominences and at how they try to answer some of the standing questions from theoretical models. A brief and gentle introduction to the Hanle effect and other subtle quantum phenomena is given, as they are key to present diagnostic techniques and, finally, an overview of future observational goals and wishes is presented.

1. Introduction

Triggered by the development of new spectropolarimeters in the last decades of the XXth century, and taking advantage of a better knowledge of the physics of the formation of polarized spectral lines and of the outcome of new fast and reliable techniques for data handling, a renewed effort is being dedicated to the diagnostics of magnetic fields in solar prominences. This review aims at bringing forward recent results on the observational techniques and in the interpretation of the spectropolarimetric data as well as at shedding some light on past diagnostic errors from the standpoint of present knowledge. Furthermore, we shall review what questions arising from theoretical modeling of prominences have been addressed by recent measurements or are yet left unanswered.

The first sound attempts at measuring the magnetic field in prominences can be traced back to the 1970's, but the field was particularly active in the 1980's. About half of the published works dating back to those years refer to the use of Zeeman techniques over the circular polarization signal of spectral lines seen in emission in prominences like Hα, but particularly in the He D_3 line. As we shall see on the next section all these measurements can be disregarded from present knowledge, since quantum-mechanical processes are known for those lines which are able to produce circular polarization not due to the Zeeman effect. Such processes were unknown at the time and the unexpected signals were either fully interpreted as purely Zeeman if filter-like instruments were observing, or disregarded as instrumental spurious polarization in the rare cases in which spectrographs were used. Around the same time a second group of researches tried to use resonance scattering polarization and Hanle effect to diagnose the magnetic fields. Most of that work was done by Leroy, Bommier and colleagues at Pic du Midi (France) while a second group, in strong contact with the first one, used the Evans coronagraph at Sacramento Peak with the Stokes I and II

polarimeters. Despite the added difficulties of using a physical phenomenon like the Hanle effect, these are the only results that are still fully acceptable today and they stand up as the very first strong constraints to the physical modeling of prominences still at use today.

Since the two groups stopped work on prominences in the early 1990's, no measurement was performed for about 10 years. The arrival of both THEMIS, with its multiline polarization-free spectrograph, and the Advanced Stokes Polarimeter (Elmore et al. 1992) at Sacramento Peak provided a new suite of powerful spectropolarimeters able to improve over past work. A third instrument joined those ones: the Tenerife Infrared Polarimeter (TIP, Martínez Pillet et al. 1999) taking advantage of the He I line at 10830 Å and opening a completely new diagnostic domain not only into prominences but also into filaments, observed against the solar disk.

In the meantime a new set of techniques had arisen to automatically infer magnetic fields from the observed Stokes profiles. Particularly successful was the application of Principal Component Analysis (PCA) to the fit of Stokes profiles and the subsequent determination of the magnetic field vector. The robustness and speed of such techniques allowed the reconstruction of 2-dimensional maps of the magnetic field over the prominence (as compared to a few points scattered over it) which revealed a much richer structure and finer details than previous measurements.

2. The Hanle Effect and the He D_3 Line

Hanle effect has been a promise for diagnostic of weak and turbulent magnetic fields in the Sun for the last 20 years. But very few actual results have actually come out outside its use in prominences. The reasons are easy to unveil although they should not justify any disregarding of this powerful technique.

When measuring magnetic fields in the photosphere, the Zeeman effect is called upon systematically. The Zeeman effect consists in the separation in energy of the magnetic sublevels involved in a given transition. For a field strong enough the separation can be such as to clearly split the spectral line, but this is not common in the solar photosphere. More often one makes use of the fact that each magnetic sublevel has a tendency to emit photons polarized in a deterministic manner. At zero field, the magnetic sublevels are degenerated in energy and the emitted photon cannot carry any particular polarization. The observation of line polarization gives a direct indication of the energy separation and of the magnetic field involved. Most solar photospheric lines can be adequately explained with very simple LS-coupling under which the splitting in energy is linear with the field strength. The only dependence of the resulting Stokes profile with the atom at its origin is a single scalar, the Landé factor. All this makes the Zeeman effect extremely simple to understand at first order and extraordinarily general and independent of the actual atom and spectral line observed. In the opposite world sits the Hanle effect, whose actual spectral signatures depend on the intricacies of the atomic system that includes the transition corresponding to the observed line, but also many others which have a strong influence on the observation, despite being attached to unobserved lines.

For the Hanle effect, every newly observed line is a new problem that should be handled from scratch.

But in order to consider any physics from the Hanle effect, one needs first a source of polarization. The Hanle effect does not create polarized photons as the Zeeman effect does, but it is limited to a modification of the pre-existent polarization of the atom. A common source of polarization is the use of atoms scattering light at great angles. Prominences, illuminated by the photosphere a few thousand kilometers below, re-emit light towards us at an angle approaching 90 degrees. Such scattering results in polarized light in a similar manner to Rayleigh or Mie scattering, altough here it is the atom itself, rather than big molecules or dust, that constitutes the scattering center. To enter in more details, a given atomic level (characterized by its total angular momentum J) with degenerated magnetic sublevels (characterized by their $M = -J \ldots + J$ value) will have a tendency to distribute the electrons evenly among those sublevels. Actually, in quantum terms, one can say that every single electron will have an equal probability of being in each one of the sublevels. If the atom is illuminated anisotropically, the incoming photons from privileged directions will carry angular momentum that will try to force the atom to change that even distribution of population among the sublevels. Characteristically an atom in the solar atmosphere illuminated by the cone of light from the photosphere below will have a tendency to create an imbalance among the $M \neq 0$ sublevels and the $M = 0$ ones. This imbalance is called *atomic alignment* an it is usually measured through a component of the σ^K_Q spherical tensor density matrix of the atom with $K = 2$. The actual amount of alignment σ^2_Q will now be dependent on the particular level of the atom we are looking at, but also on the net balance of electrons transferred from and to other atomic levels, aligned in their own terms and trying to pump alignment in and out our particular level. To compute the alignment of the atomic level of interest there is no other path than to compute the equilibrium of the full atomic system, with its distribution of levels illuminated at particular wavelengths by the underlying photosphere. This is the main source of complication in the use of the Hanle effect: the fact that each atomic system will reach equilibrium in a completely different state than any other, in processes highly-coupled throughout the atom.

Once a given level is aligned, a transition into or out of that level will carry the information on the population imbalance in the form of linear polarization observable if the geometry of the scattering is adequate. In the case of the $\mathrm{He\,D_3}$ line, the atomic system generally computed can be seen in Fig. 1. It contains 5 levels and 6 spectral lines (although many of those lines are formed by several transitions, as the $\mathrm{He\,D_3}$ one, made of 6 different transitions among levels with differring values of J). The equilibrium for such system is searched by computing the Liouville equation of the density matrix of the system, with its time derivatives set to zero. An example of the resulting linear polarization can be found in Fig. 1.

As soon as the atom is embedded in a external magnetic field, its atomic levels start to split because of the Zeeman effect. If the splitting is smaller than or comparable to the natural width of the levels, however, any alignment introduced by anisotropic illumination of the atom will survive and the magnetically induced splitting will modify it in one or another manner. It is common to simplify

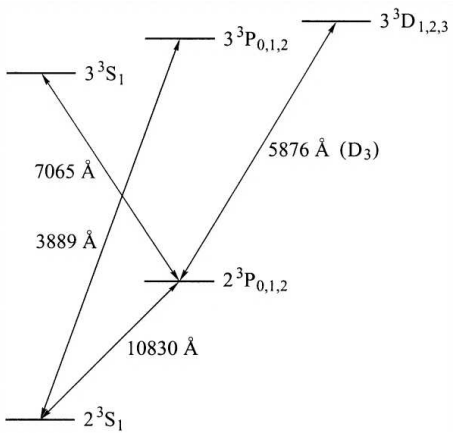

Figure 1. Atomic model of the He triplet system for the computation of the D_3 and 10830 Å lines of interest in prominence magnetometry.

the description of the ensuing phenomena by saying that the total amount of polarization will be decreased and the plane of polarization will turn. It is however dangerous to take those simplified behaviors as a general rule. Actually the atom will once more behave as to reach equilibrium among all its levels in the particular geometry imposed by both the direction in which it is illuminated and the direction of the magnetic field. The high dependence on the geometry results in a new element of complication when compared to the Zeeman effect.

Furthermore there are two new phenomena coming into play that should not be disregarded. The first one is Zeeman effect itself: as the field increases we should observe a continuous transition from the kind of Stokes profiles typical of scattering polarization and Hanle effect to the profiles typical of Zeeman effect. An atomic system properly modelled should be able to produce such transition naturally, as the atom itself does.

But also, as the atomic levels split it may occur that sublevels belonging to different levels start approaching each other too much as compared to their natural widths and new atomic coherences and population imbalances will appear, not inside the original level, but among different levels. Such new coherences can alter the amount of alignment in the levels but also, under appropriate circumstances, can result in a new kind of atomic coherence called *atomic orientation* in which the populations of positive M are imbalanced respect to those of negative M. Atomic orientation is measured with another component of the spherical tensor density matrix, that of $K = 1$ and immediately results in the emission of circular polarization. Because of its origin, such phenomena is often referred to as the *alignment-to-orientation transfer mechanism*. An example of circular polarization in the He D_3 line due to this effect can be seen in Fig. 2. Such source of circular polarization will nevertheless compete with the Zeeman effect, and the Stokes V profile for circular polarization will show a mixture of both characteristic profiles (see Fig. 3). Casini & López Ariste (2003) produced a plot of the contributions of Zeeman vs. alignment-to-orientation effects in the He D_3 line under typical fields and geometries found in prominences (Fig. 4) that reveals how important it is to consider all these quantum phenomena in the in-

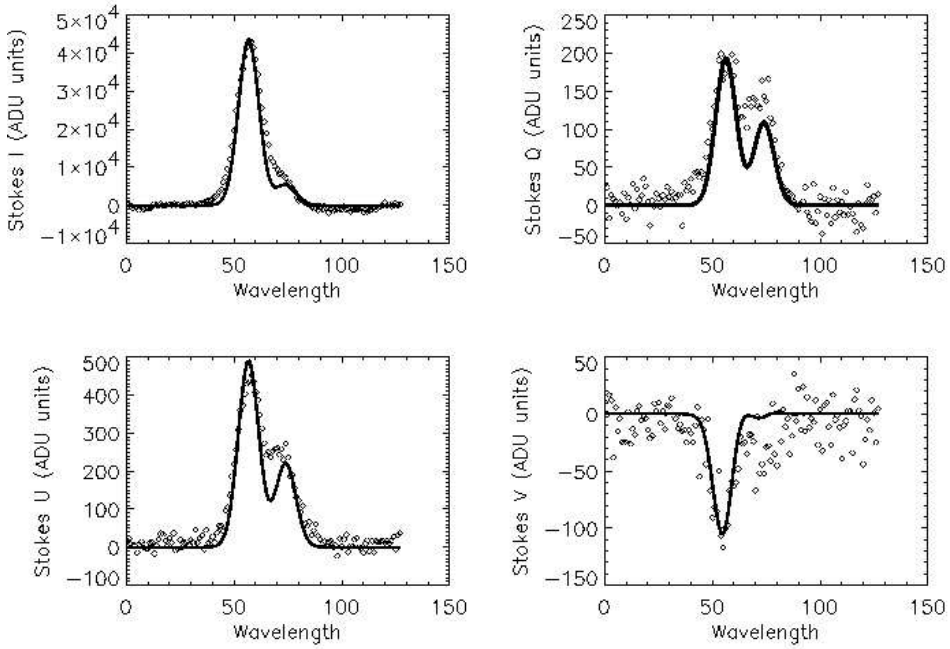

Figure 2. Observational example (diamonds) from THEMIS, fit by theory (continuous line) of the He D_3 line in prominences. The alignment-to-orientation mechanism dominates the Stokes V profile (bottom right).

terpretation of the polarization signals It is now plain evident how wrong can be to interpret the circular polarization amplitude of Fig. 3 as due to Zeeman effect alone. Brown et al. (2003) made such a test and produced a database of typical He D_3 Stokes V profiles and interpreted them as if seen through a magnetogram as done in the 1980's. The plot of true longitudinal field vs. inferred longitudinal field shows a perfect ball of no-correlation for the typical fields found in prominences (Fig. 5). The He D_3 can be interpreted under the longitudinal Zeeman effect alone only for fields around and higher than 100 G, much stronger than those found in prominences. Such result is enough to disregard all results from the past based upon Zeeman effect alone.

3. Past Measurements, Models and Standing Questions

The main results of previous measurements using Hanle effect diagnostics were the determination of an average field strength in quiescent prominences of 10-20 G with the magnetic field vector at a pitch or shear angle of 20° with the body axis of the prominence. Leroy, Bommier and coworkers also determined that 75% of their promineces presented a topological configuration known as *inverse*, in which the magnetic polarity accross the prominence body was opposite to the polarity accross the photospheric neutral line underlying the prominence. The other 25% was determined to be of *normal* polarity. Leroy and Bommier always used coronagraphs for their measurements, thus being limited to a min-

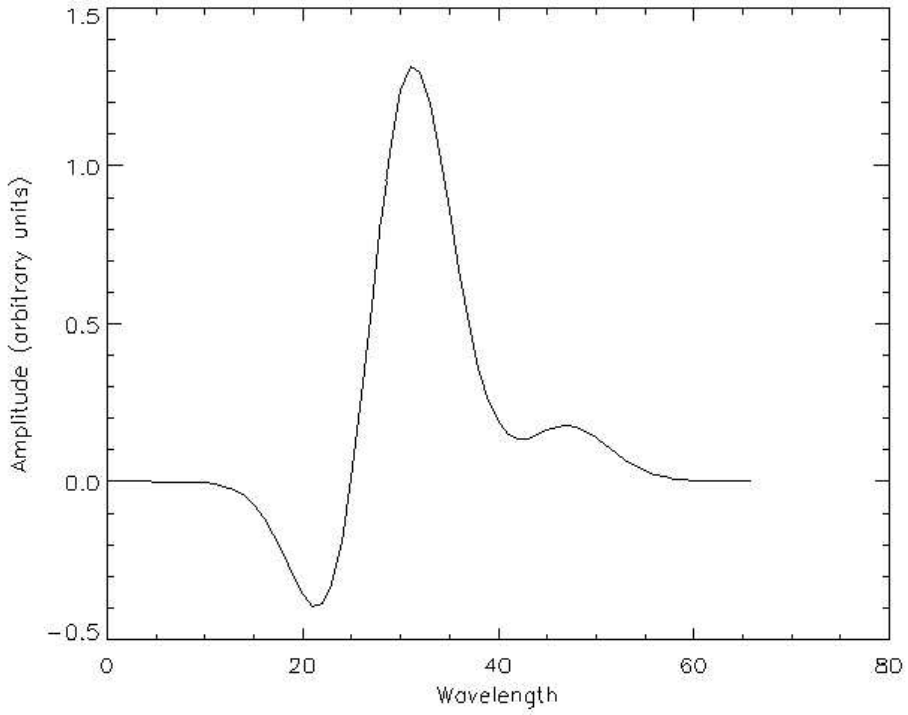

Figure 3. Example of a Stokes V profile of the $He\,D_3$ line with similar contributions from the Zeeman effect and the alignment-to-orientation mechanism.

imum height above the solar limb of roughly 20 arcsec (or 14 Mm). From the distribution in height of inverse and normal polarity prominences they made the hypothesis that low-lying prominences, the ones they could not observe, could majoritarily be of normal polarity, as to complete a 50-50 distribution of topologies among the two main configurations. Were such hypothesis confirmed,it would result in most of the active region prominences (low-lying highly dynamical prominences sitting upon neutral lines inside active regions) showing a normal polarity configuration, while inverse polarity will be chosen by the very stable quiescent promineces.

The horizontality of the magnetic field in the prominence body set the frame for the theoretical work in the modeling of prominences in the 90's. While some models still claim for vertical fields constrained in current sheet (curtain models, Osherovich 1989; Jensen 1990; Pécseli & Engvold 2000) based on the observation at certain wavelengths of vertical structures, most of the present models are based on flux tubes that posses some degree of twist, sometimes with much less than one full turn, whose main axis is roughly parallel to the photosphere(van Ballegooijen & Martens 1989; Antiochos et al. 1994; Priest 1990; Amari et al. 1999). A few of those, referred to as wire models, see such arcade as the only one present and the plasma is transported continuously along the field fields into the photosphere in a dynamical pseudo-equilibrium (Martin et al. 1994; Zirker

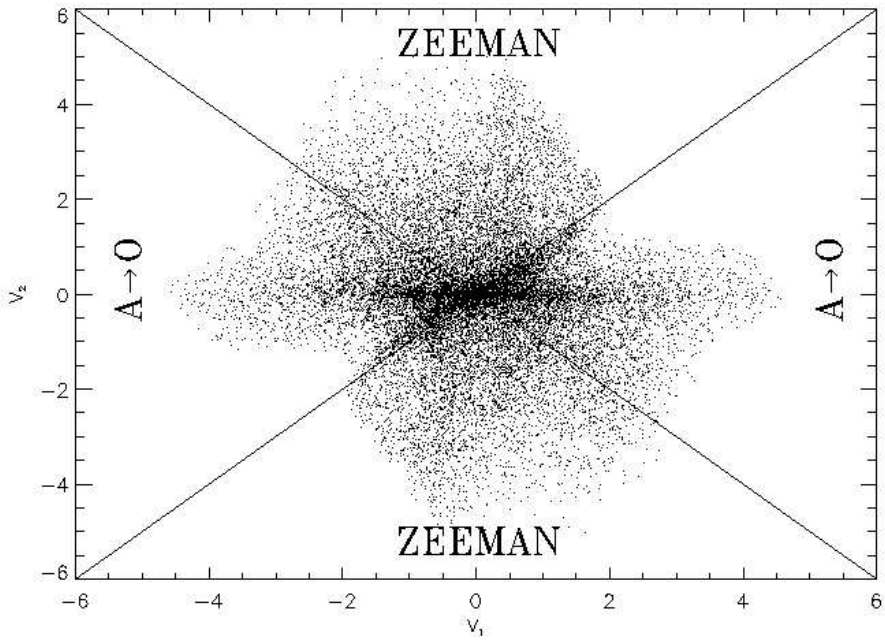

Figure 4. Distribution of the contributions of the Zeeman effect and the alignment-to-orientation mechanisms to the Stokes V profile of the He D_3 line.

et al. 1998). In such models out of the prominence body, the field turns into vertical and the theoretical prediction is that prominence feet or barbs should depart from the horizontality.

But the most successful models are those in which a flux rope is stabilized by a magnetic arcade ceiling in different manners. The flux rope naturally presents dips were plasma can accumulate in a stable manner. Such dips appear in the prominence body but also on other parts of the flux rope under the perturbation of parasitic magnetic concentrations in the photosphere, in particular in the prominence's feet or barbs (see the illustrative Fig. 6 for an example of the magnetic topology and the dip-filling plasma in such models). These models have been successful in explaining many of the observational constraints on prominences and the research has deepen into the detailed description of the magnetic topology of the flux rope. As the flux rope is still anchored in the photosphere, field extrapolations have been used to predict its shape as a function of the observed photospheric field. Magnetohydrostatic models, non-linear force-free fields extrapolations or full magnetohydrodynamical extrapolations have been used with weakly twisted flux ropes (less than or about one twist from one end to the other in the photosphere). The observed inverse or normal configurations of prominences have been seen to correspond in the theory to different scenarios of the same theory and furthermore the shearing of a sufficiently twisted flux rope can lead to a flux rope presenting simultaneously normal and inverse configuration when looking at different heights (Aulanier & Démoulin 1998; DeVore

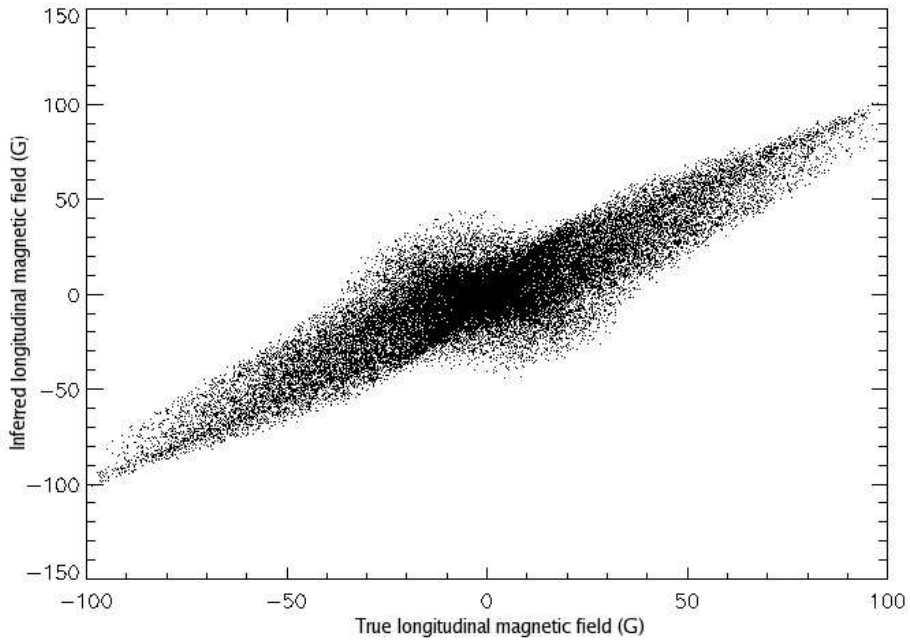

Figure 5. Inferred magnetic fields after use of the magnetograph formula over the $He\,D_3$ circular polarization. The measured values show no correlation, even in sign, for the most typical values of 10–20 G.

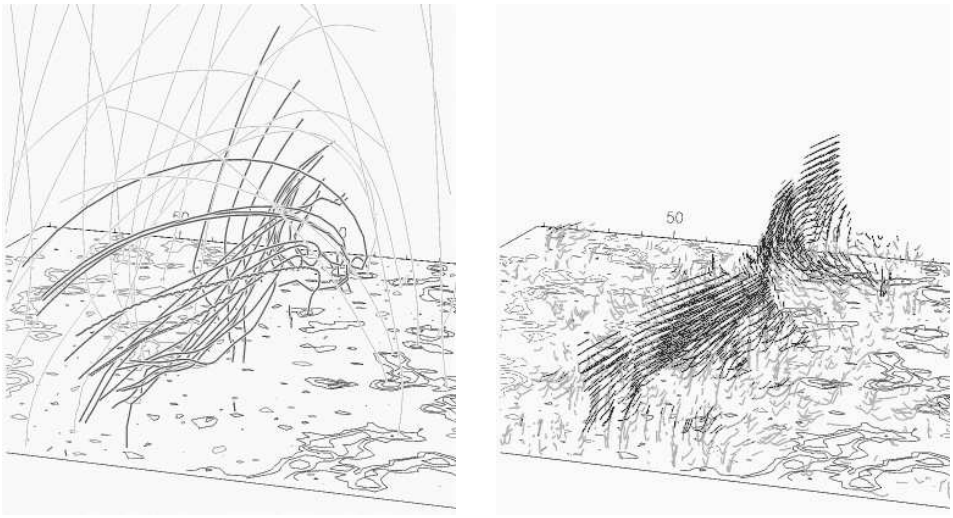

Figure 6. Example of modeling of a filament magnetic topology (left) and the location of the plasma-filled dips in the weakly-twisted flux tube. Adapted from Aulanier & Schmieder (2002).

& Antiochos 2000; Aulanier & Démoulin 2003), a theoretical prediction that has yet to be confirmed by observations.

The brief sketch of the theory of prominence modeling given above puts forward a few key questions to be answered by observations:

- Is the magnetic field in the prominence's feet mostly vertical (as in the wire models) or mostly horizontal (as in the dip models)?
- Is the mixture of inverse polarity and normal polarity configurations observed in the same prominence as predicted.
- Can observations of the magnetic field vector provide a measurement of the ratio of the perpendicular and parallel components to the prominence axis, and therefore of the number of twists in the flux rope?

How observations are trying to tackle those questions will be described in the following sections.

4. New Instruments, New Techniques and New Results

By the end of the 90's a new generation of instruments opened new possibilities. THEMIS, the French-Italian solar telescope at the Observatorio del Teide was the first to show the possibility of performing full Stokes spectropolarimetry in the He D_3 line, including Stokes V measurements (Paletou et al. 2001). Over the same spectral line, a slight modification of the Advanced Stokes Polarimeter (ASP) on the DST at Sacramento Peak resulted in the first spatial scanning of a prominence also with full Stokes measurements (Casini et al. 2003). Almost simultaneously the Tenerife Infrared Polarimeter (TIP, Martínez Pillet et al. 1999) on the German VTT showed the diagnostic potential of the He I line at 10830 Å (Trujillo Bueno et al. 2002) in prominences. This line had also proved interesting in the study of filaments (Lin et al. 1998) although the diagnostic capabilities await further work (Casini et al. 2005).

The better and more abundant data also required new techniques for data analysis. As in the case of the photospheric Zeeman diagnostic techniques, we are able to solve the forward problem but not the inverse. That is, given a magnetic field topology and a scattering geometry for the He atom, we are able to compute the emergent Stokes profiles. But given a set of four Stokes profiles, we are unable to compute the magnetic field in which the emitting atom was embedded. One is left with inversion techniques which, in one way or another, are based on comparison of the observed profiles with synthetic ones computed under known parameters. Often, the comparison procedure is plug into some trial–and–error algorithm that can guide the user in the modification of the initial parameters until an acceptable match is found between the observations and the synthetic profiles. Least-squares fitting falls under such description and has been widely used in the diagnostic of photospheric magnetic fields through Zeeman effect. The technique may nevertheless be very unstable, particularly in the cases we are handling where the presence of many local minima and physical ambiguities are known to exist. In order to address the problem with some guarantee of success new techniques were put to work. Rees et al. (2000) proposed the use of Principal Component Analysis to reduce the dimensionality of the observed data set to the point at which a simple search in a pre-computed database was feasible. López Ariste & Casini (2003) applied the technique to the He D_3 line in prominences and proved that it performed as expected with error bars of 2–3 G

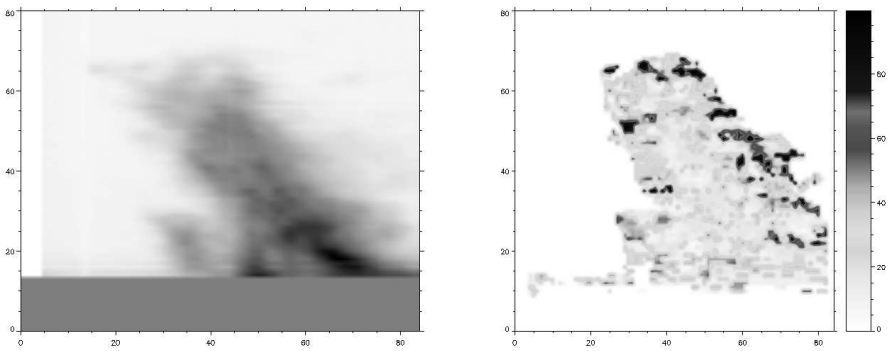

Figure 7. *Left:* Negative of the intensity emission of the observed prominence. *Right:* Magnetic field strength (in G) inferred after inversion of the $\mathrm{He\,D_3}$ line.

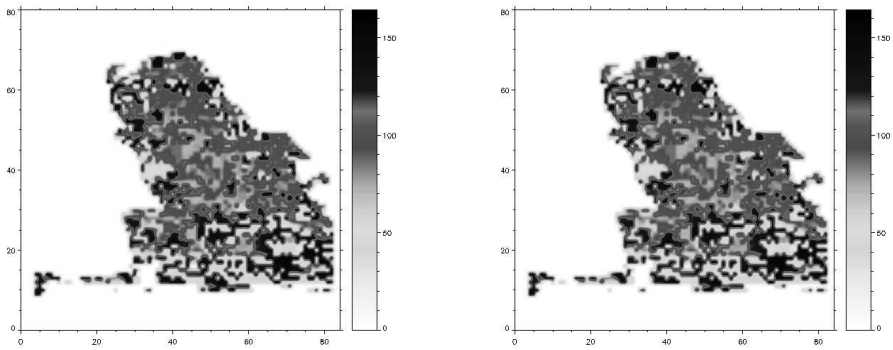

Figure 8. *Left:* Inclination of the magnetic field respect to the local vertical (90° meaning a horizontal field). *Right:* Inclination of the magnetic field respect to the observer's line of sight (0° meaning a field vector pointing towards the observer).

in the field strength and a few degrees in both the inclination and the azimuth of the magnetic field under very general conditions. The technique was successfully applied to real data from the ASP instrument by Casini et al. (2003) resulting in the first map of the magnetic field in a prominence. The results can be seen in Figs. 7 and 8. The average values of the three magnetic parameters shown in those figures coincide nicely with the average values measured by Leroy and Bommier in the 80's: a field strength of 20 G, mostly horizontal (90° respect to the local vertical in the figure) and a field vector pointing 20 to 30 degrees off the prominence axis (seen in the figure of the inclination respect to the line of sight which, for this particular prominence coincided for the data of the observation with the prominence axis).

But also unexpected results were obtained. The most intriguing one is the presence of localized regions in the prominence body with field strengths of up to 80 G. Such fields could not be seen by Leroy and Bommier in the 80's because of the absence of circular polarization in their data sets, unavailable for their instrument. Hanle effect saturates for the $\mathrm{He\,D_3}$ at about 40 G and the linear

polarization signals carry no information of field strengths at and above that threshold. From the point of view of linear polarization therefore a field of 35, 40 or 80 G shows the same signals. The only way left to tell apart those cases is Zeeman effect in circular polarization. As soon as Stokes V was made available by THEMIS and the ASP, we could detect fields as high as 80 G as shown in the figures of this particular prominence. The localized situation of these strong fields, nevertheless, points to interesting dynamics and is perhaps related to the fine structure of the prominence. Such strong fields will also have destabilizing tendencies that need to be further investigated.

A second finding was the slow turn of the field vector away of the prominence axis as the rim of the prominence is approached. In the body core Fig. 8 shows a shear of 30° that increases up to 60^circ off axis towards the rim. Is this due to a true torsion of the magnetic flux rope on its sides? or rather just a simple projection effect for this prominence?

But the map also produced negative results: with the measuring of the strong field spots here and there in the prominence body, it is impossible to determine any statistically sound gradient with height of the magnetic field. It is obvious that if any gradient is present at all, it is hidden behind the more important effects of fine structure.

5. The Magnetic Topology of Prominence Barbs or Feet

One of the standing questions discriminating among different models of prominences relates to the topology of the magnetic field in the so-called prominence feet or barbs. Summarizing, one family of models views prominence feet as lateral magnetic dips able to support plasma against gravity in the same manner as the main prominence flux rope, and therefore the plasma on them would be embedded also in a dominantly horizontal field. Such dips on the sides of the main flux rope would be due to the interaction of the main magnetic arcade with the actual magnetic distribution at small scales in the photosphere. In consequence, below each one of those feet one should find a photospheric magnetic dipole and a magnetic dip extending up from the photosphere into the chromosphere and lower corona.

A second family of models, on the other side, views feet as field lines anchoring into the photosphere. The plasma in the feet would be embedded in a mostly vertical field and down in the photosphere a one-polarity region should be found.

The direct measurements of magnetic fields in the prominence plasma have been repeatedly hindered by the low height over the solar limb of these features and by the strong dynamical processes occurring in the plasma, revealed in the anomalous non-thermal broadening of the spectral lines (Casini et al. 2003; Trujillo Bueno et al. 2005; López Ariste & Casini 2005). In part because of these reasons some of us started looking for signatures in the photospheric proxy. In observations performed with THEMIS in 2004, López Ariste et al. (2006) measured the photospheric field in a filament channel with high polarimetric sensitivity and found bipolar structures which, after a careful analysis of the geometry of the Zeeman effect that allowed a resolution of the 180° ambiguity, were proven to belong to a convex or loop-topology when found at the end

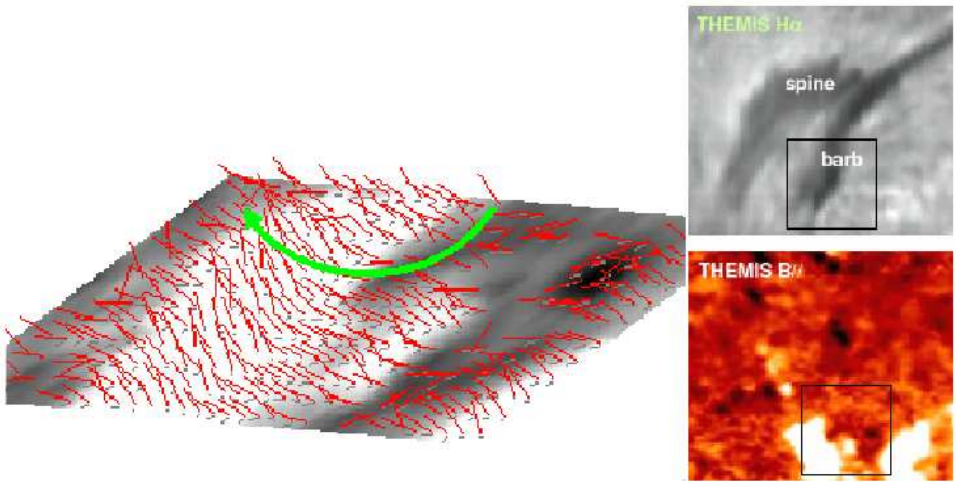

Figure 9. Summary of the observations at THEMIS confirming the presence of a concave (dip) magnetic topology in the photosphere under a filament barb. The barb, seen inside the square frame in the Hα image on the top right image, stands upon a small parasitic polarity (black) next to the a big region of the dominant polarity (white) in the magnetograph of the bottom right image. The vector magnetic field representation on the left image unveils the concave topology pointed by the curved overlying arrow.

point of the filament and a concave or dip-topology when found below a barb (see Fig. 9), thus confirming both the influence of the photospheric magnetic structures on the flux rope supporting the filament and the presence of lateral magnetic dips supporting filament feet and barbs.

6. Next Observational Goals

From the observational point of view, the near future goes in two well determined directions: to extend the magnetic field diagnostics to filaments (i.e. prominences observed against the solar disc) and to incorporate multi-line diagnostics to the magnetic field determination.

Filaments are easier to spot than prominences, in particular for the low-lying active region filaments, difficult to observe over the limb since hidden in the forest of chromospheric spicules during the short period of time in which they are geometrically visible. However filaments can only be seen in spectral lines optically deep enough through the filament plasma as to absorb a non-negligible amount of photons from the background continuum. The He D$_3$ line used for prominence diagnostics is barely detectable in filaments, therefore making its measurement difficult. The dark Hα and Hβ lines on the other hand are subject to too many physical phenomena that get entangled, even in polarization (López Ariste et al. 2005), with any spectral signature of the magnetic field, thus discarding them from the list. A spectral line simple enough in its formation to believe in the inferrement of magnetic fields, but optically deep enough to be visible in filaments is the He I line at 10830 Å. This is the line that has been used most to open the path to a reliable diagnostic (Lin et al. 1998; Trujillo Bueno

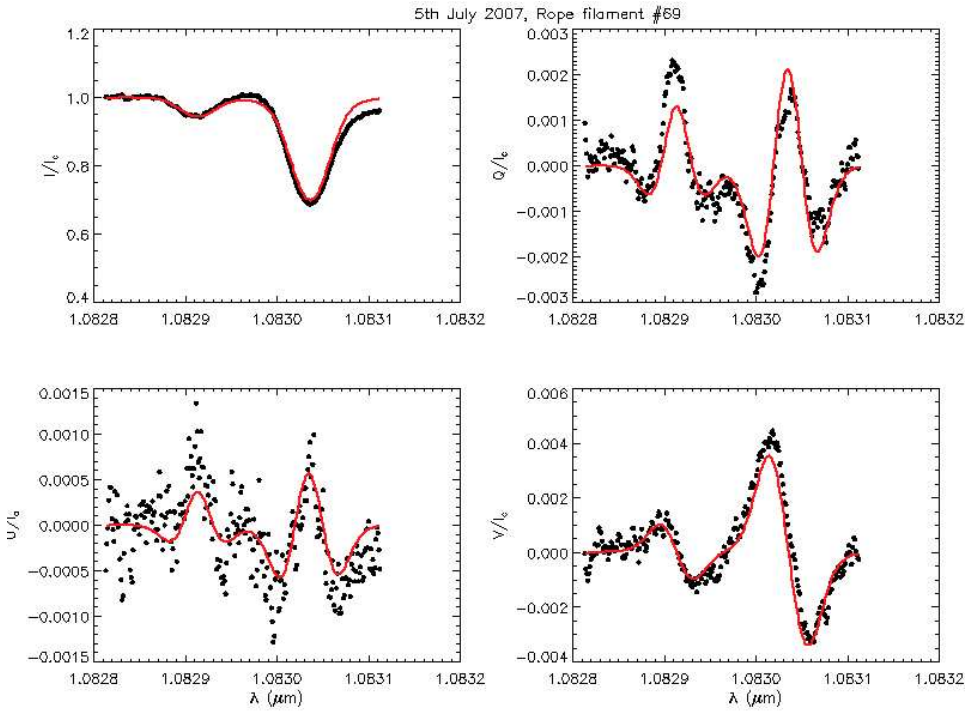

Figure 10. Measured Stokes profiles of the He line at 10830 Å with TIP over a filament in an active region. The continuous line shows a fit based on a Milne-Eddington model with a longitudinal field of 52 G and a transverse field of 522 G. Courtesy of V. Martínez Pillet (IAC).

et al. 2002). Recently measurements made with the TIP instrument (see Fig. 10) have shown that fields attaining hundreds of G can be found in active region filaments (Martínez Pillet et al. 2007). Such field strengths are well beyond any previous measurement but the clear Zeeman signatures are unmistakable, and the environment in which such filaments are found can be well in agreement with those values.

The line of He I at 10830 Å is also visible in emission in prominences and since formed in the same atomic model as the D_3 line, the simultaneous observation of both lines would shed light on the influence of prominence self-illumination on the outcoming Stokes profiles. It is the case today that every emitting He atom is considered as isolated and illuminated exclusively by the background photosphere. This approximation makes computation of the anisotropy of the radiation field very easy. But it is obvious that in many prominences the amount of light emitted by the prominence itself and illuminating other parts of the prominence cannot be neglected. Such radiation field would change the anisotropy of the radiation field illuminating any given atom and the initial amount of alignment introduced in the atom by the radiation field. The amount of observables found in the Stokes profiles of the He D_3 atom is nevertheless not sufficient to accept the introduction of new parameters in the model taking into account the changes in the anisotropy of the radiation field. If

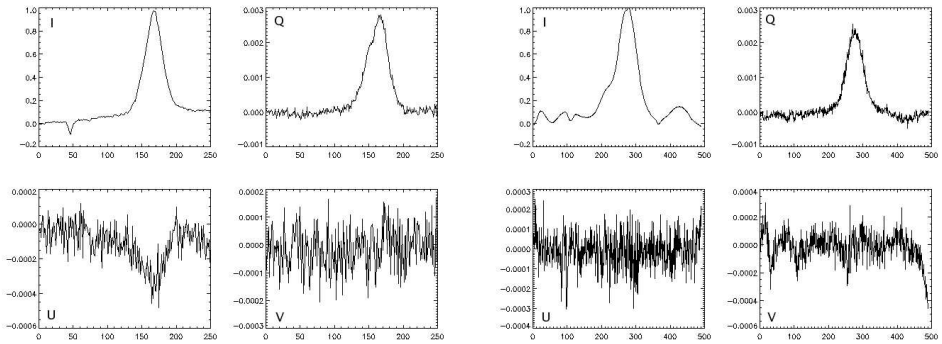

Figure 11. Simultaneous spectropolarimetry of the He D_3 (left) and 10830 Å (right) lines performed by THEMIS in October, 2006.

such phenomena is to be integrated in our models we need further observables, and the He line at 10830 Å seems the right choice for that.

Because of those reasons, instrumental efforts have been done to measure both spectral lines simultaneously with high spectral resolution and sensitive polarimetry. Such efforts have to overcome the problem of the 5000 Å separating both lines in the spectra and imposing changes in detectors or optical treatments. Those efforts have been made mostly at two places: the Evans facility at Sacramento Peak and THEMIS. In Fig. 11 we see the first successful profiles of both lines measured simultaneously in THEMIS and opening the path towards such improved diagnostics.

7. Conclusion

The recent efforts made to measure magnetic fields in prominences and filaments are starting to pay out with new measurements improving over the pioneering observations of Leroy and Bommier in the 1980's. However the 20-year gap in observational results has resulted in a separation between the outstanding questions from the theoretical models of prominence support and the richness of the measured spectra. While further observations will improve our understanding on how to answer many of those questions through an improved statistics of cases but also through a better understanding of the polarized line formation in such solar regions, it is also clear that theories should start incorporating the newly obtained results: the bigger field strengths found and the spatial and temporal variability of fields on the prominence bodies, among others.

References

Amari T., Luciani J. F., Mikic Z., Linker J., 1999, ApJ 518, L57
Antiochos S. K., Dahlburg R. B., Klimchuk J. A., 1994, ApJ 420, L41
Aulanier G., Démoulin P., 1998, A&A 329, 1125
Aulanier G., Démoulin P., 2003, A&A 402, 769
Aulanier G., Schmieder B., 2002, A&A 386, 1106

Bommier V., Landi Degl'Innocenti E., Leroy J.-L., Sahal-Bréchot S., 1994, Sol. Phys. 154, 231
Brown A., López Ariste A., Casini R., 2003, Sol. Phys. 215, 295
Casini R., Bevilacqua R., López Ariste A., 2005, ApJ 622, 1265
Casini R., López Ariste A., 2003, ASP Conf. Series, 307, 109
Casini R., López Ariste A., Tomczyk S., Lites B. W., 2003, ApJ Lett. 598, L67
DeVore C. R., Antiochos S. K., 2000, ApJ 539, 954
Elmore D. F., Lites B. W., Tomczyk S., Skumanich A. P., Dunn R. B., Schuenke J. A., Streander K. V., Leach T. W., Chambellan C. W., Hull H. K., 1992, in D. H. Goldstein, R. A. Chipman (eds.), Polarization analysis and measurement, 22
Jensen E., 1990, in V. Ruzdjak, E. Tandberg-Hanssen (eds.), Dynamics of Quiescent Prominences, IAU Colloq. 363, 129
Landi degl'Innocenti E., Landolfi M., 2004, Physics of Solids and Liquids
Leroy J. L., 1962, Annales d'Astrophysique 25, 127
Leroy J.-L., 1981, Sol. Phys. 71, 285
Leroy J. L., Bommier V., Sahal-Bréchot S., 1983, Sol. Phys. 83, 135
Leroy J. L., Bommier V., Sahal-Bréchot S., 1984, A&A 131, 33
Leroy J. L., Ratier G., Bommier V., 1977, A&A 54, 811
Lin H., Penn M. J., Kuhn J. R., 1998, ApJ 493, 978
López Ariste A., Aulanier G., Schmieder B., Sainz Dalda A., 2006, A&A 456, 725
López Ariste A., Casini R., 2003, ApJ Lett. 582, L51
López Ariste A., Casini R., 2005, A&A 436, 325
López Ariste A., Casini R., Paletou F., Tomczyk S., Lites B. W., Semel M., Landi Degl'Innocenti E., Trujillo Bueno J., Balasubramaniam K. S., 2005, ApJ 621, L145
Martin S. F., Bilimoria R., Tracadas P. W., 1994, in R. J. Rutten, C. J. Schrijver (eds.), Solar Surface Magnetism, 303
Martínez Pillet V., Collados M., Sánchez Almeida J., González V., Cruz-Lopez A., Manescau A., Joven E., Paez E., Diaz J., Feeney O., Sánchez V., Scharmer G., Soltau D., 1999, in T. R. Rimmele, K. S. Balasubramaniam, R. R. Radick (eds.), High Resolution Solar Physics: Theory, Observations, and Techniques, ASP Conf. Ser. 183, 264
Martínez Pillet V., Centeno R., Shimizu T., Collados M., 2007, A&A, in preparation
Osherovich V. A., 1989, ApJ 336, 1041
Paletou F., López Ariste A., Bommier, V. and Semel M., 2001, A&A 375, L39
Pécseli H., Engvold O., 2000, Solar Phys. 194, 73
Priest E. R., 1990, in V. Ruzdjak, E. Tandberg-Hanssen (eds.), IAU Colloq. 117: Dynamics of Quiescent Prominences, 150
Rees D., López Ariste A., Thatcher J., Semel M., 2000, A&A 355, 759
Trujillo Bueno J., Landi Degl'Innocenti E., Collados M., Merenda L., Manso Sainz R., 2002, Nat 415, 403
Trujillo Bueno J., Merenda L., Centeno R., Collados M., Landi Degl'Innocenti E., 2005, ApJ 619, L191
van Ballegooijen A. A., Martens P. C. H., 1989, ApJ 343, 971
Zirker J. B., Engvold O., Martin S. F., 1998, Nat 396, 440

Giuseppe Severino and Vincenzo Andretta

Marta Rovira, Juan Fontenla, Jean-Claude Vial

The Physics of Chromospheric Plasmas
ASP Conference Series, Vol. 368, 2007
Petr Heinzel, Ivan Dorotovič and Robert J. Rutten, eds.

Radiative Transfer in Prominence Fine Structure as a Multi-Component Atmosphere

A. Ajabshirizadeh[1,2] and H. Ebadi[1,2,3]

[1] *Tabriz University, Faculty of Physics, Tabriz, Iran*
[2] *Research Institue for Astronomy and Astrophysics, Maragha, Iran*
[3] *Instititut d'Astrophysique Spatiale, Unité Mixte, Orsay, France*

Abstract. We used Ambartsumian's method of the addition of layers to show that the various problems of radiative transfer in a plane-parallel inhomogeneous atmosphere may be reduced to the solution of Cauchy problems for linear differential equations. The idea of this approach is that we start with determining the reflection and transmission coefficients of an atmosphere by solving the initial-value problem for a set of linear differential equations of the first order. Then, the internal radiation field is found immediately without solving any new equation. This leads to pressure to develop a suitable theory of radiative transfer through a multi-component atmosphere.

1. Introduction

In many astrophysical problems, the necessity arises to interpret the radiation emitted by inhomogeneous media. The commonly used assumption of homogeneity simplifies the problem to a great extent and makes it possible to estimate some characteristics of the radiating medium averaged in some sense. Such attempts were made by a number of authors (see e.g., Jefferies et al. 1988, Gu et al. 1977, Meinkohn et al. 2002, as well as Nikoghossian et al. (2000) and Nikoghossian (2004). The linearity of the fundamental obtained equations suggests a simple analytical procedure for the addition of layers. The determination of the reflection and transmission of an atmosphere permits to find the radiation field in atmosphere with arbitrary distributed sources. These standard problems of astrophysical interest are reducible to the solution of the initial-value problems. Solar prominences consist of a number of fine-structure elements such as threads, knots, blobs, etc. The dimensions of these components vary throughout the prominence, and the smallest are generally supposed to be less than the spatial resolution of the instruments. One of the main problems of solar prominence is to determine the geometry and the physical properties of the fine structures, which is difficult, sometimes impossible, to establish directly by observations, because of the small sizes of the elements and their superposition along the line of sight. Because of such structures along the line of sight the emerging intensity has fluctuations. Thus, the determination of these fluctuations makes the study of these structures a necessity. To this end the most famous authors have used theoretical methods. The theory of the statistical properties of the line radiation emerging from a stochastic multi-component atmosphere such as

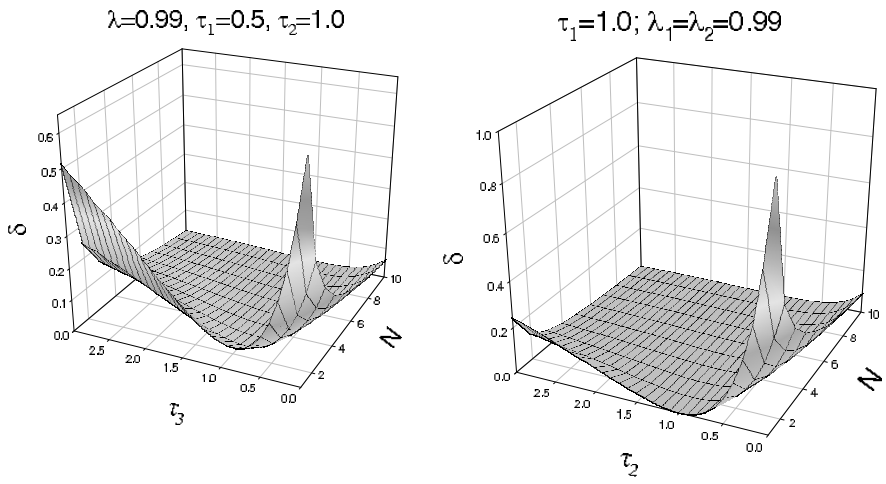

Figure 1. The Rel-MSD for the Non-LTE (left) and the multi-component atmosphere (right).

solar prominences was developed. The methods can be found in the papers by Adjabshirizadeh et al. (2005, 2007).

2. Intensity Fluctuations in the Non-LTE Atmosphere

The Non-LTE atmosphere differs significantly from that in LTE due to multiple scattering which establish coupling between various volumes of the medium. Now the averaging can no longer be performed by parts as for LTE, since the mean intensity of radiation emerging from any part of an atmosphere is altered when adding a new element to it. Then the Rel-MSD will have the following form:

$$\delta_N = \frac{\delta(B)}{N}\left[1 + \frac{N^2-1}{3}\left(\frac{\tau}{N\tau+2}\right)^2\right], \qquad (1)$$

where $\delta(B)$ is the Rel-MSD (fluctuation) of B. Figure 1 shows a plot of Rel-MSD in this case.

3. Multi-component Atmosphere

The multi-component atmosphere is an atmosphere composed of a single type of structural elements differing in their optical and geometrical characteristics. However, the formation of resonant and optically thick lines is controlled, in general, by multiple scattering effects which makes the theory complex. Allowance for random variations of the structural pattern needed in studying some non-stationary phenomena leads to further complications. We start with considering the diffuse reflection and transmission problem for an atmosphere consisting of N structural elements, each of which is described by its optical thickness τ_i and

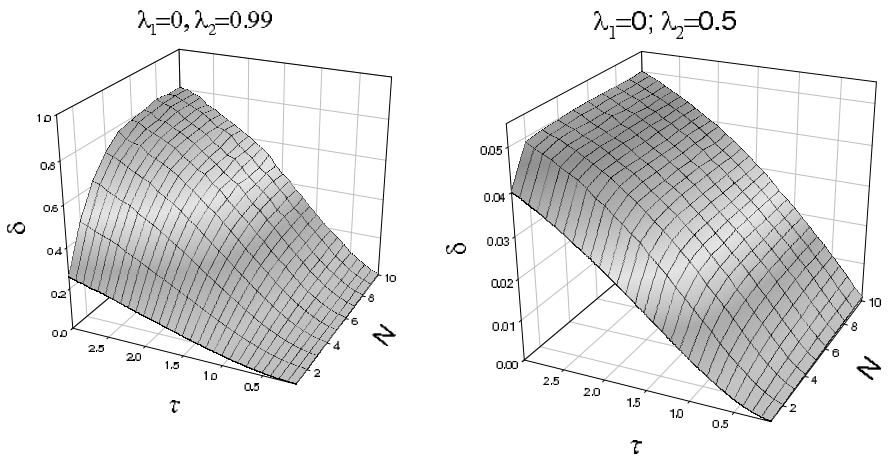

Figure 2. The Rel-MSD for the multi-component atmosphere with two different choices for the scattering albedo: $\lambda_1 = 0$, $\lambda_2 = 0.99$ (left), $\lambda_1 = 0, \lambda_2 = 0.5$ (right).

the value λ_i of the single-scattering albedo. Let us agree to designate by T_M the total optical thickness of M elements (beginning from the first). Observing that $T_N = T_{N-1} + \tau_N$, then we will have the following form:

$$P(T_N) = a(\tau_N)P(T_{N-1}) - b(\tau_N)S(T_{N-1}) \tag{2}$$

$$S(T_N) = b(\tau_N)P(T_{N-1}) + a(\tau_N)S(T_{N-1}), \tag{3}$$

where $a(\tau_N) = P(\tau_N)$, $b(\tau_N) = S(\tau_N)$, $c(\tau_N) = (1 - b^2(\tau_N))/a(\tau_N)$ and $P(\tau_0) = 1/(q(\tau_0))$ and $S(\tau_0) = r(\tau_0)/q(\tau_0)$ in which r and q are the reflectance and transmittance coefficients of the atmosphere respectively. Equations (2) and (3) with conditions $P(T_0) = 1$, $S(T_0) = 0$ represent the recurrence formula, which readily allow one to determine the reflection and transmission capacities for any kind of multi-component atmosphere. The main advantage of these equations is their linearity which is especially important in treating atmospheres with randomly varying optical characteristics. Knowing the reflection and transmission coefficients make it possible to determine emerging intensities from multi-component atmospheres and to calculate Rel-MSD. We did this and show the results in Figs. 1 and 2.

4. Results and Discussions

In the LTE atmosphere the fluctuations increased by an increase in the optical depth and a decrease in the number of structures in the line of sight. But in such kind of atmospheres when the internal sources are equal to each other, and the optical depth can vary, the treatments are different. As is clear from Fig. 1, the smaller the optical depth and the number of structures, the larger the intensity fluctuations. They vanish at large optical depth and for more fine

structures. The variations in the Non-LTE atmosphere with the varying optical depth is very similar to the LTE case. The only difference is that it increases with optical depth variations. This means that the structures should have different optical depth. The multi-component atmosphere when the elements are pure scattering, is similar to the Non-LTE atmosphere, but when the elements can be pure scattering or absorbing, it seems to be near to reality. As Fig. 2 shows, the larger the number of structures and their optical thickness, the larger the intensity fluctuations. This means that LTE or Non-LTE atmospheres are not a realistic case, and that we should study the structural elements as a multi-component atmosphere.

Acknowledgments. We would like to thank the CSPM organisers for a very good meeting and the editors for extensive revisions.

References

Jefferies J. T., Lindsey C., 1988, ApJ 335, 372
Meinkohn E., Richling S., 2002, A&A 392, 827
Gu Y., Lindsey C., Jefferies J. T., Avrett E. H., 1977, ApJ 484, 960
Nikoghossian A. G., 2004, A&A 422, 1059
Nikoghossian A. G., Mouradian Z., 2000, A&A 360, 1086
Ajabshirizadeh A., Ebadi H., 2005, JQSRT, 95, 127
Ajabshirizadeh A., Nikoghossian A. G., Ebadi H., 2007, JQSRT, 103, 351

The Physics of Chromospheric Plasmas
ASP Conference Series, Vol. 368, 2007
Petr Heinzel, Ivan Dorotovič and Robert J. Rutten, eds.

Polarimetric Properties of the D_2 Lines of Alkali Atoms

L. Belluzzi[1], E. Landi Degl'Innocenti[1] and J. Trujillo Bueno[2,3]

[1] *Dipartimento di Astronomia, Università degli Studi di Firenze, Italy*
[2] *Instituto de Astrofísica de Canarias, La Laguna, Spain*
[3] *Consejo Superior de Investigaciones Científicas, Spain*

Abstract. We present a theoretical investigation on the influence of a deterministic magnetic field on the linear and circular polarization of the Na I, K I, and Ba II D_2 lines. We describe the three ions by means of a three-level atomic model, and we take into account the hyperfine structure which is shown by some isotopes. We focus on the "solar prominence case", in which an optically thin slab of chromospheric plasma, situated 7000 km above the visible solar "surface", and permeated by a magnetic field of given strength and orientation, is illuminated from below by the continuum photospheric radiation field.

1. Introduction

The development of new spectropolarimetric instrumentation, able to reach high polarimetric sensitivity with high spectral and spatial resolution, is offering the chance of performing polarimetric measurements in spectral lines, within individual solar plasma structures. It is therefore worthwile to carry out theoretical investigations on the magnetic sensitivity of the polarization signals shown by diagnostically interesting spectral lines, in the presence of magnetic fields of various configurations and intensities (e.g., Trujillo Bueno et al. 2002; Belluzzi et al. 2006). For example, the observation and theoretical modeling of the polarization signals that the joint action of the Hanle and Zeeman effects produce in the Ba II D_2 line provides a novel diagnostic window on the investigation of the magnetic fields of the solar photoshere and chromosphere (see Belluzzi et al. 2006). In this work we extend our attention to the Na I and K I D_2 lines, which can be described through the same atomic model adopted for the Ba II ion. We apply the quantum theory of polarization described in Landi Degl'Innocenti & Landolfi (2004) (hereafter LL04), through which we can investigate within a general and rigorous physical approach the role of resonance scattering and magnetic fields on the polarimetric properties of these lines. We consider an optically thin slab model, through which we are able to investigate in a rigorous way the essential physical mechanisms involved (resonance polarization, Zeeman, Paschen-Back and Hanle effects), avoiding complications due to radiative transfer effects.

2. Formulation of the Problem

We consider an optically thin slab of chromospheric plasma at 6000 K, located 7000 km above the $\tau_{5000} = 1$ photospheric level. We assume the slab to be illuminated from below by the photospheric continuum radiation (i.e. by an

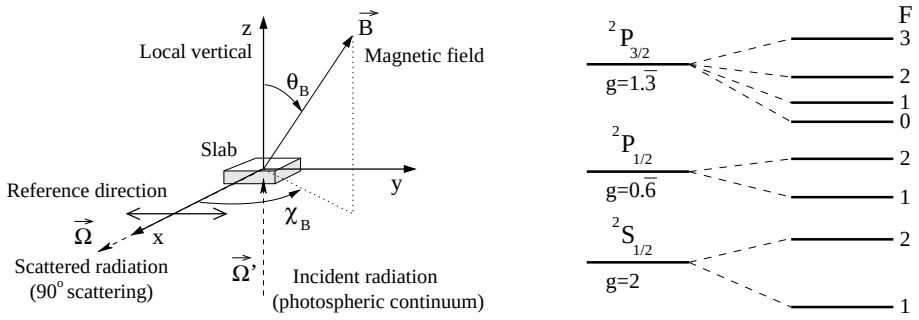

Figure 1. *Left:* geometry of the scattering process. *Right:* Grotrian diagram for the isotopes with nuclear spin $I = 3/2$. With the letter F we indicate the quantum number associated to the total (electronic plus nuclear) angular momentum operator, with the Landé factor g.

anisotropic, unpolarized radiation field, with cylindrical symmetry around the local vertical, without spectral structure (flat) over the typical width of the lines considered). The radiation field entering the Statistical Equilibrium Equations (SEEs), whose expression for an atomic system with hyperfine structure (HFS) can be found in Sect. 7.9 of LL04, is therefore known a priori. We calculate the intensity and the anisotropy factor of the photospheric continuum incident on the slab, at the frequencies of the lines under investigation, following Sect. 12.3 of LL04, and using the values for the disk-center intensities and limb-darkening coefficients given by Pierce (2000). Once the SEEs have been solved numerically, because of the optically thin slab assumption, the Stokes parameters of the radiation at frequency ν, scattered in the direction $\vec{\Omega}$, can be simply found by the equation

$$S(\nu, \vec{\Omega}) = k\varepsilon_S(\nu, \vec{\Omega}) \ , \tag{1}$$

where $S = I, Q, U, V$, ε_S is the corresponding emission coefficient, and k is a constant. The expressions of the emission coefficients for an atomic system with HFS can be found in Sect. 7.9 of LL04. In this work we will investigate the radiation scattered at 90° with respect to the local vertical, in the presence of a deterministic magnetic field of given orientation and strength. The reference direction for positive Q is assumed to be parallel to the limb (see the left panel of Fig. 1).

3. The Atomic Model

To describe the three ions under investigation, we adopt a three-level model consisting of the ground level ($^2S_{1/2}$), the upper level of line D_1 ($^2P_{1/2}$) and the upper level of line D_2 ($^2P_{3/2}$). The abundance, nuclear spin, isotope shifts, and HFS constants of the various isotopes considered in this work are listed in Table 1. A Grotrian diagram describing qualitatively the HFS levels splitting for an isotope with nuclear spin $I = 3/2$ is shown in the right panel of Fig. 1.

Table 1. Isotopes considered in this work

Isotope	Abund. (%)[a]	I	Isotope Shifts (MHz)[1]		HFS Constants (MHz)		
			D_1	D_2	$^2S_{1/2}$ $\mathcal{A}$	$^2P_{1/2}$ $\mathcal{A}$	$^2P_{3/2}$ $\mathcal{A}$ $\mathcal{B}^2$
^{23}Na	100	3/2	reference isot.		885.8130644[b]	94.3[c]	18.65[d] 2.82[d]
^{39}K	93.2581	3/2	reference isot.		230.8598602[e]	27.80[f]	6.13[g] 2.72[g]
^{41}K	6.7302	3/2	235.27[f]	236.15[f]	127.0069350[e]	15.19[f]	3.40[g] 3.34[g]
^{130}Ba	0.106	0	355.3[h]	372.3[h]			
^{132}Ba	0.101	0	278.9[h]	294.9[h]			
^{134}Ba	2.417	0	222.6[i]	234.6[i]			
^{135}Ba	6.592	3/2	348.6[h]	360.7[h]	3591.67[j]	664.6[k]	113.0[k] 59.0[k]
^{136}Ba	7.854	0	179.4[h]	186.9[h]			
^{137}Ba	11.232	3/2	271.1[h]	279.0[h]	4018.87[j]	743.7[k]	127.2[k] 92.5[k]
^{138}Ba	71.698	0	reference isot.				

[1]A positive I.S. means that the line is shifted to higher frequencies with respect to the reference isotope. [2]The HFS constant $\mathcal{B}$ is defined according to the convention of the american literature. [a]NIST on-line database; [b]Beckmann et al. (1974); [c]Hartmann (1970); [d]Schönberner & Zimmermann (1968); [e]Fueller (1976); [f]Bendali et al. (1981); [g]Ney (1969); [h]Wendt et al. (1984); [i]Wendt et al. (1988); [j]Becker et al. (1981); [k]Villemoes et al. (1993).

4. The Role of the Magnetic Field

In the presence of a magnetic field, each HFS level (or fine structure level, if the isotope is devoid of HFS) splits up into its magnetic sublevels. We describe this splitting within the framework of the general Paschen-Back effect theory (see LL04 Sect. 3.5).

As shown in Fig. 2, it is possible to distinguish three regimes: Zeeman effect regime (magnetic interaction weak with respect to the HFS interaction), incomplete Paschen-Back effect regime (magnetic and HFS interaction of the same order of magnitude) and complete Paschen-Back effect regime (HFS interaction weak with respect to the magnetic interaction). Note that the various regimes are reached by each of the three atomic systems under investigation for different magnetic field strengths. Hereafter, regardless of the particular regime, any polarization signal that originates from the splitting among the magnetic sublevels, will be referred to as Zeeman effect. The Zeeman effect produces in general elliptical polarization, which degenerates into linear polarization if the magnetic field lies on the plane perpendicular to the line-of-sight (LOS), and into circular polarization if the magnetic field lies along the LOS. The Zeeman effect dominates the polarization of the scattered radiation if the splitting among the magnetic sublevels is of the same order of magnitude or larger than the Doppler width ($\Delta\lambda_D$) of the line. For the ions under investigation, this gives the follow-

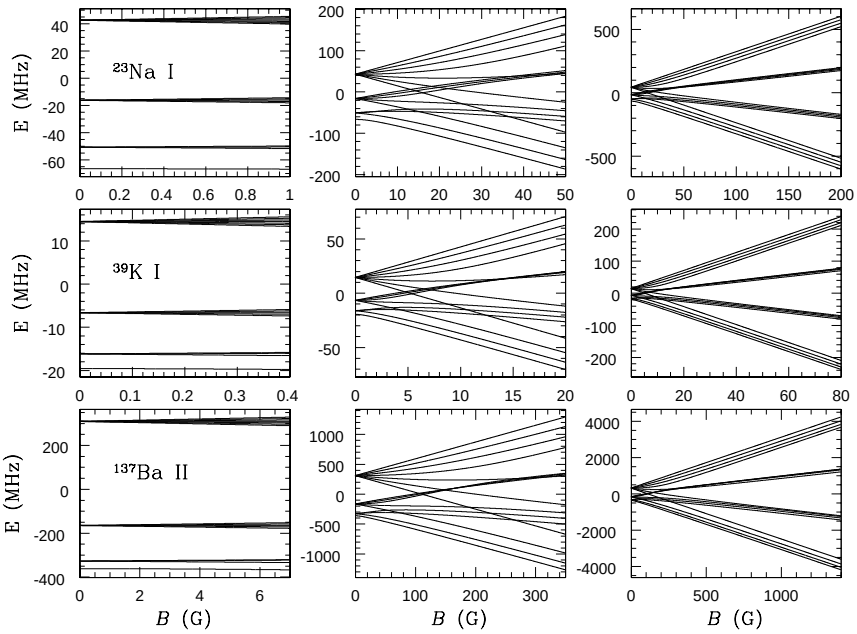

Figure 2. Splitting of the magnetic sublevels originating from the upper level of the D_2 line of three different isotopes with HFS, in the Zeeman effect regime (left column), incomplete Paschen-Back effect regime (central column and complete Paschen-Back effect regime (right column). The zero of the energy scale is taken at the energy of the corresponding fine structure J-level.

ing critical values: 2500 G for Na I ($\Delta\lambda_D$=41 mÅ), 1500 G for K I ($\Delta\lambda_D$=41 mÅ) and 1300 G for Ba II ($\Delta\lambda_D$=13 mÅ).

However, if the magnetic field is not too weak, and if there are no other mechanisms that dominate the polarization, it is possible to identify Zeeman effect signatures on the Stokes profiles even for intensities much smaller than the critical one. It is well known that polarization signals can be produced through scattering processes (without the need of a magnetic field), whenever the atomic system is anisotropically excited, and the geometry of the scattering event has no remarkable symmetries. If an atomic system is anisotropically excited, the various magnetic sublevels are no longer evenly populated and are characterized by well defined phase relations (or interferences). The atomic system is then said to be polarized. It can be demonstrated that a magnetic field is able to modify the atomic polarization (more precisely the interferences among the magnetic sublevels), and therefore the polarization of the scattered radiation (Hanle effect). Depending on the configuration of the magnetic field and on the polarization state of the atomic system, interferences between different magnetic sublevels are modified, and different signatures of the Hanle effect are produced on the polarization profiles of the scattered radiation. An atomic system is sensitive to the Hanle effect for magnetic fields much smaller than the ones needed for the Zeeman effect to be appreciable. In particular, it can be demonstrated that the atomic polarization of a given level is significantly modified by the Hanle effect when the Zeeman splitting is of the same order of magnitude as the inverse

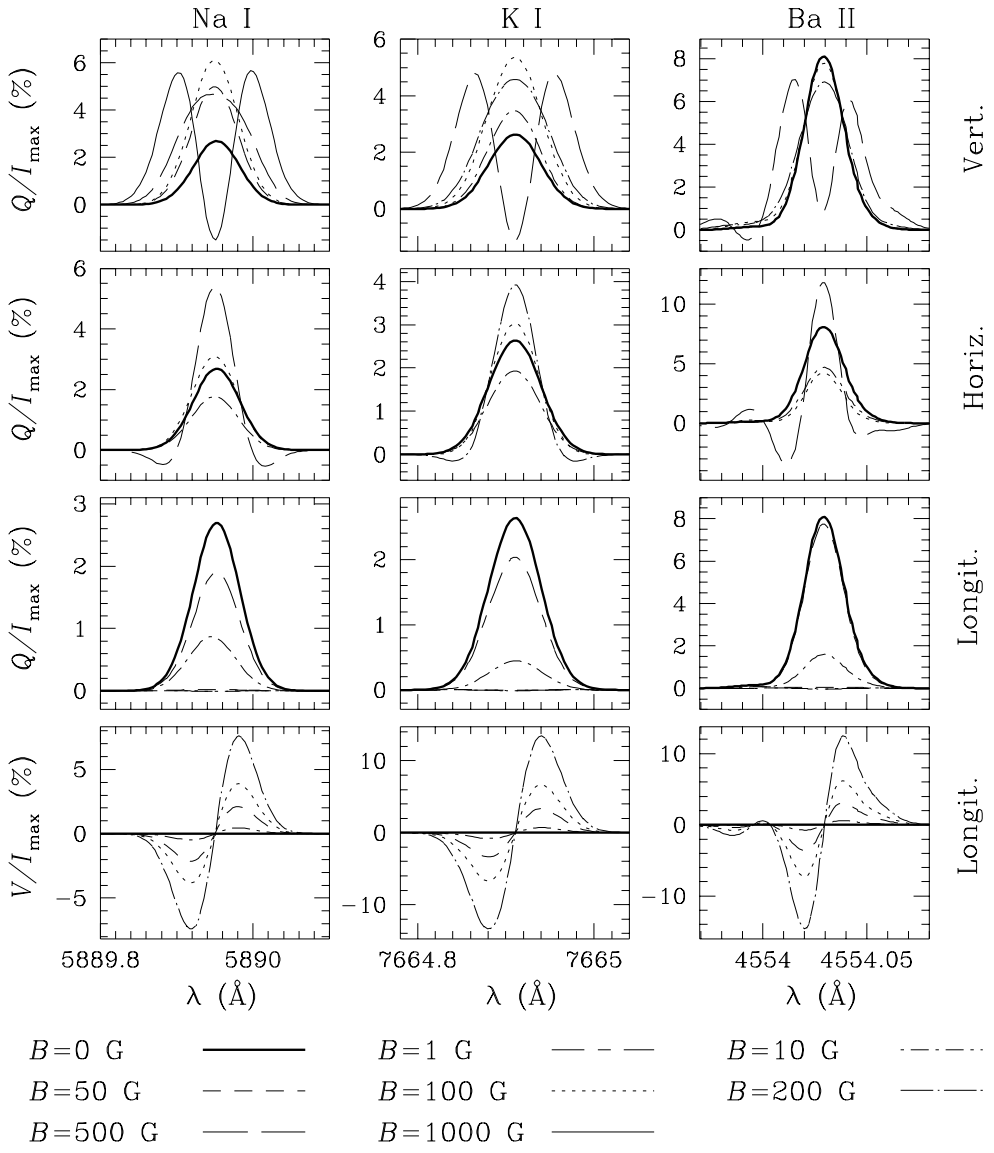

Figure 3. Theoretical Stokes profiles obtained in the presence of a vertical field (top row), of a horizontal field perpendicular to the LOS (second row) and of a horizontal field directed along the LOS (third and fourth rows). Note the non-zero linear polarization signals obtained in the absence of magnetic fields, and the modification towards the well known transverse Zeeman effect profiles for increasing magnetic fields. Note also that in each panel only the profiles corresponding to the more significative values of B are plotted.

lifetime of the level. For the ions we are considering, this gives a Hanle effect sensitivity of the D_2 line upper level (which is much more polarized than the ground level) for magnetic fields between 0.5 and 50 G for Na I, between 0.3 and 30 G for K I, and between 10 and 100 G for Ba II.

5. Results and Conclusions

In the presence of a vertical magnetic field, the isotopes with HFS produce an enhancement of the linear polarization (see Trujillo Bueno et al. 2002). This is due to a special manifestation of the Hanle effect, usually referred to as "Anti-Level-Crossing effect" (see Bommier 1980). Obviously, in the "solar prominence case" considered here, this enhancement of scattering polarization by a vertical field is much smaller for the case of barium, given the large abundance (82%) of isotopes without HFS (see top row of Fig. 3). However, it is important to emphasize that for the case of on-disk observations the "Anti-Level-Crossing effect" in the 18% of the barium isotopes endowed of HFS may produce a differential magnetic sensitivity of the three-peaks Q/I profile observed in the D_2 line, which could be of great interest for the detection of vertical magnetic fields in quiet regions of the solar atmosphere (see Belluzzi et al. 2006). As the magnetic field strength increases, the transverse Zeeman effect becomes more important, and finally dominates the polarization of the scattered radiation as the critical intensity is approached. In the presence of a horizontal magnetic field, perpendicular to the LOS, or of a longitudinal magnetic field, both the isotopes with and without HFS are sensitive to the Hanle effect, which produces a decrease of the linear polarization (see second and third rows of Fig. 3). In the former case the Zeeman effect superimposes to the Hanle effect, in the latter it does not affect the linear polarization, but produces circular polarization as shown by the Stokes V antisymmetric profiles (see last row of Fig. 3). We point out that in the presence of a longitudinal field the Hanle effect produces even a rotation of the plane of linear polarization, and therefore a non zero signal for the Stokes U parameter (not shown here).

Acknowledgments. This work is part of the European Solar Magnetism Network.

References

Becker, W., Blatt, R., & Werth, G., 1981, J. Phys. Coll. 42, C8-339
Beckmann, A., Böklen, K. D., & Elke, D., 1974, Z. Phys. 270, 173
Belluzzi, L., Trujillo Bueno, J. & Landi Degl'Innocenti, E., 2006, in R. Casini & B.W. Lites (eds.), *Solar Polarization Workshop 4*, ASP Conference Series, in press
Bendali, N., Duong, H. T., Vialle, J. L., 1981, J. Phys. B 14, 4231
Bommier, V., 1980, A&A 87, 109
Fueller, G. H., 1976, J. Phys. Chem. Ref. Data 5, 835
Hartmann, W., 1970, Z. Phys. 240, 323
Landi Degl'Innocenti, E., & Landolfi, M., 2004, Polarization in Spectral Lines, (Dordrecht: Kluwer)
Ney, J., 1969, Z. Phys 223, 126
Pierce, K., 2000, in Allen's Astrophysical Quantities, 4th ed., (Springer: New York)
Schönberner, D., & Zimmermann, D., 1968, Z. Phys. 216, 172
Trujillo Bueno, J., Casini, R., Landolfi, M., Landi Degl'Innocenti, E., 2002, ApJ 566, L53
Villemoes, P., Arnesen, A., Heijkenskjöld, F., & Wännström, A., 1993, J. Phys. B 26, 4289
Wendt, K., Ahamad, S. A., Buchinger, F., Mueller, A. C., Neugart, R., & Otten, E. W., 1984, Z. Phys. A 318, 125
Wendt, K., Ahamad, S. A., Ekström, C., Klempt, W., Neugart, R., & Otten, E. W., 1988, Z. Phys. A 329, 407

The Physics of Chromospheric Plasmas
ASP Conference Series, Vol. 368, 2007
Petr Heinzel, Ivan Dorotovič and Robert J. Rutten, eds.

Prominence Parameters from 2D Modeling of Lyman Lines Measured with SUMER

Stanislav Gunár[1,2,3], Petr Heinzel[1,2], Brigitte Schmieder[4] and Ulrich Anzer[2]

[1]*Astronomical Institute AS, Ondřejov, Czech Republic*
[2]*Max-Planck-Institut für Astrophysik, Garching, Germany*
[3]*Astronomical Institute, Charles University, Prague, Czech Republic*
[4]*Observatoire de Paris, Meudon, France*

Abstract. We present SOHO/SUMER observations of a solar prominence in the hydrogen Lyman series lines and compare the line profiles with the synthetic ones obtained using our 2D prominence modeling. The observations contain the Ly-β, Ly-γ, and Ly-δ lines on 25 May 2005.

In order to derive the prominence parameters we used our 2D fine structure models of vertical threads in magnetohydrostatic (MHS) equilibrium. By varying the input model parameters (central temperature, boundary pressure, magnetic field, central column mass and turbulent velocity) we obtained a model having the synthetic Lyman line profiles in good agreement with the observed ones. In this way we are able to determine the structure of the magnetic dip and the thermodynamical parameters in the observed prominence.

1. Introduction

In the last decade the SUMER UV spectrograph (Solar Ultraviolet Measurements of Emitted Radiation) on board of SOHO (SOlar and Heliospheric Observatory) provided us with a big amount of observations which give important insights into the properties of the solar atmosphere. A unique ability of SUMER to observe the whole hydrogen Lyman series leads to considerable amount of spectral data devoted to solar quiescent prominences and these data allow major steps towards our understanding of their structure and physical parameters. Some of the data and their analysis can be found in Schmieder et al. (1998, 1999, 2003), Heinzel et al. (2001) and Stellmacher et al. (2003); see also the review of SOHO prominence observations by Patsourakos & Vial (2002).

SUMER spectroscopic data provide an important constraint on prominence modeling. In order to interpret them properly one has to use highly sophisticated models with complex non-LTE radiative transfer computations. Such models of the prominence fine structure were recently presented by Heinzel & Anzer (2001) and Heinzel et al. (2005).

2. Observations

The SUMER instrument (Wilhelm et al. (1995)) on board SOHO is a stigmatic spectrograph equipped with two photon-counting detectors (A and B). Both

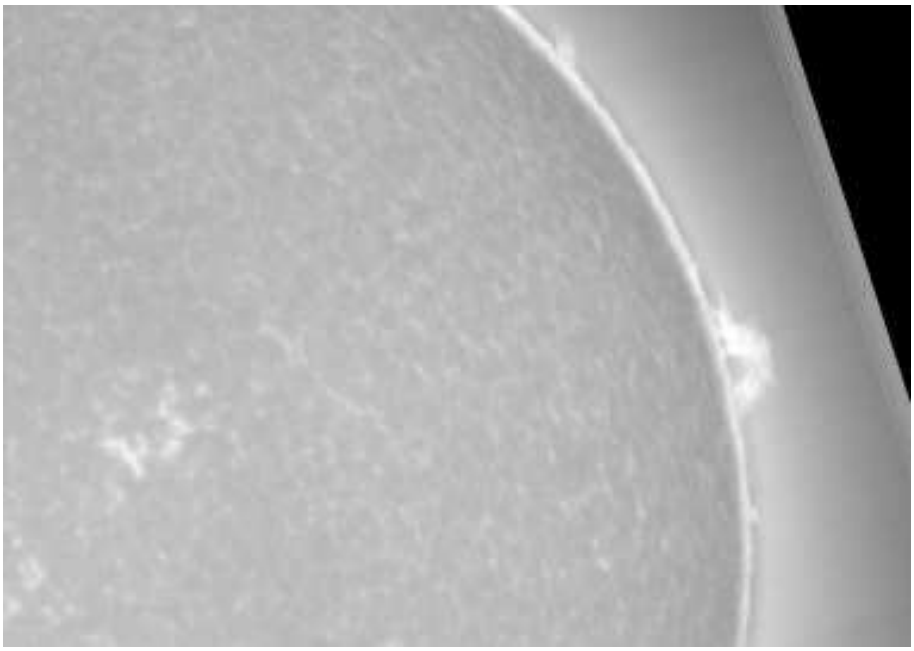

Figure 1. Hα image of a quiescent prominence observed on May 25 2005 by the Meudon Observatory.

detectors have 1024 spectral columns and 360 spatial rows. Since May 2004 the detector A has been showing a deterioration of the electronics responsible for the readout in the y direction (y-ADC), affecting the spatial (along the slit) information, while the x-ADC is working correctly, leading to correct spectral information.

Our study consists of the limb prominence observations in the Ly-β, Ly-γ, and Ly-δ lines on May 25 2005. Figure 1 shows the Hα image of the prominence obtained by the Meudon Observatory. The SUMER slit ($0.3'' \times 120''$) was pointed at coordinates $X = 972''$ and $Y = 168''$. The observation of Ly-β began at 19:12:23 UT and that of Ly-γ and Ly-δ at 19:14:32 UT, both with exposure times of 115 seconds. Each data set consists of 120 pixels along the slit, but only the pixels 6 to 60 are useful. For the analysis of the Lyman line profiles, and for their comparison with the synthetic ones obtained by the modeling we need profiles with symmetrical shape. Such profiles occur in the observational data in a small clustered locations (3 pixels close to each other) and they ensure us that there are no differential velocities in the observed areas. For the comparison of the observed data with our models we took averaged profiles over these small areas with three symmetrical profiles clustered in nearby pixels. It means for Ly-β the averaged profile over pixels 13 to 15, for Ly-γ over 15 to 17 and for Ly-δ the averaged profile over pixels 14 to 16. These profiles are shown in Fig. 2 (dashed black lines).

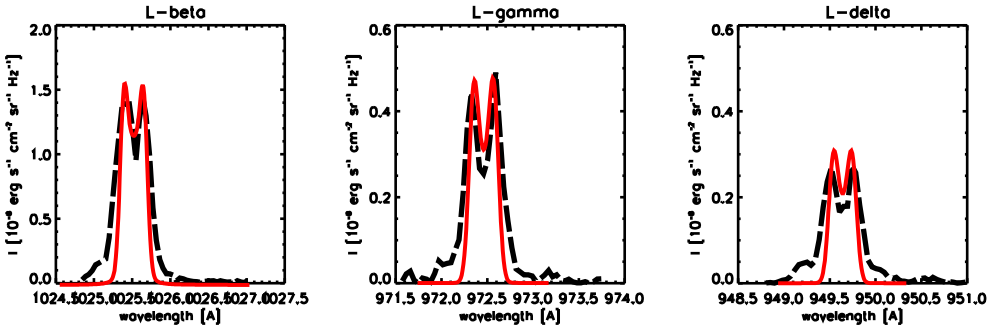

Figure 2. Ly-β, Ly-γ and Ly-δ observed profiles (dashed black lines) in comparison with the synthetic profiles (full orange lines).

3. Comparison with the Synthetic Spectra

In order to obtain synthetic spectra of the Lyman lines we use here prominence models presented by Heinzel & Anzer (2001). They consist of two-dimensional vertically infinite threads in MHS equilibrium with empirically prescribed temperature structures. Two-dimensional prominence thread models provide us with different synthetic profiles when the orientation of the line-of-sight is along or across the magnetic field lines, respectively (Heinzel et al. (2005)). As was shown in Heinzel et al. (2005), synthetic profiles seen across the field lines exhibits self-reversal shape even for higher Lyman lines. The observed Ly-β to Ly-δ lines show the same self-reversal behaviour and therefore we focus on this line-of-sight orientation in our comparison.

Synthetic line profiles of the Lyman lines show rather big shape and intensity variation at different positions along the length of the prominence thread. In order to find the best agreement between the synthetic and the observed profiles we use in our analysis all of the synthetic profiles along the length of the thread. By varying the model input parameters (central temperature, boundary pressure, magnetic field, central column mass and turbulent velocity) we obtain the model with the synthetic profiles which are in good agreement with all of the observed Lyman line profiles. Figure 2 shows the comparison between the observed profiles (dashed black lines) and the synthetic profiles (full orange lines).

This solution is unique in the way, that one cannot find any other model elsewhere in the parameter space with a similar agreement with all three lines. However, it is possible to find a slightly better fit by very small variations of the input parameters around the values of the current model. The input parameters of the resulting model are the central (minimum) temperature $T_0 = 7000\,\mathrm{K}$, maximum column mass in the center of the thread $M_0 = 1.1 \times 10^{-4}\,\mathrm{g\,cm^{-2}}$, horizontal field strength in the middle of the thread $B_x(0) = 6\,\mathrm{G}$ and the coronal pressure $p_0 = 0.015\,\mathrm{dyn\,cm^{-2}}$.

4. Conclusions

The observed profiles of the Ly-β, Ly-γ, and Ly-δ are well reproduced by the synthetic profiles from the same place of our resulting 2D model. The difference in the line wings, where the synthetic profiles are narrower than the observed ones can be explained by a multi-thread approach. In such a case one has more randomly distributed prominence threads along the line-of-sight. While the center and the self-reversal peaks of the line originate from the first thread (the thread is optically thick), the line wings are optically thin and the resulting wing intensity is the sum from more threads along the line-of-sight.

The previous comparison between the observed Lyman lines and the synthetic ones by Heinzel et al. (2001) was based on 1D prominence models prescribed in Anzer & Heinzel (1999). With such 1D slab models were the authors able to reproduce the observed Ly-β line, but the higher lines were more intense than the observed ones for both analyzed prominences. With usage of two dimensional models we are capable of fitting also higher Lyman lines. We are therefore able to estimate the thermodynamical parameters of the observed prominence.

Acknowledgments. This work was supported by ESA-PECS project No. 98030. SOHO is a space mission of international cooperation between the European Space Agency (ESA) and the National Aeronautic and Space Administration (NASA). The SUMER instrument and its operation are financed by the Deutsches Zentrum für Luft und Raumfahrt (DLR), the Centre National d'Etudes Spatiales (CNES), NASA and ESA's PRODEX programme (Swiss contribution).

References

Anzer U., Heinzel P., 1999, A&A 349, 974
Heinzel P., Anzer U., 2001, A&A 375, 1082
Heinzel P., Anzer U., Gunár S., 2005, A&A 442, 331
Heinzel P., Schmieder B., Vial J. C., Kotrč P., 2001, A&A 370, 281
Patsourakos S., Vial J. C., 2002, Solar Phys. 208, 253
Schmieder B., Heinzel P., Kucera T., Vial J. C., 1998, Solar Phys. 181, 309
Schmieder B., Heinzel P., Vial J. C., Rudawy P., 1999, Solar Phys. 189, 109
Schmieder B., Tziotziou K., Heinzel P., 2003, A&A 401, 361
Stellmacher G., Wiehr E., Dammasch I. E., 2003, Solar Phys. 217, 133
Wilhelm K., Curdt W., Marsch E., and 13 coauthors, 1995, Solar Phys. 162, 189

The Physics of Chromospheric Plasmas
ASP Conference Series, Vol. 368, 2007
Petr Heinzel, Ivan Dorotovič and Robert J. Rutten, eds.

Imaging of the He D_3/Hβ Emission Ratio in Quiescent Solar Prominences

J. Hirzberger[1], E. Wiehr[2] and G. Stellmacher[3]

[1]*MPI für Sonnensystemforschung, Katlenburg-Lindau, Germany*
[2]*Institut für Astrophysik, Göttingen, Germany*
[3]*Institute d'Astrophysique Paris, France*

Abstract. Quiescent solar prominences have been observed simultaneously in profile-integrated He D_3 and Hβ emission with the SST on La Palma. The two-dimensional ratio maps of the He D_3 and Hβ intensities are used to study temporal variations of intrinsic prominence parameters. Sub-areas with substantial variation of the intensity distribution indicate the evolution of prominence structures. When the emission ratio remains unchanged, the evolving threads are of largely equal physical state. Other regions which show a temporal varying emission ratio indicate substancial evolution of the intrinsic physical conditions. We propose that distance variation between the threads affects different penetration of the EUV irradiation required for populating of the He triplet system.

1. Introduction

Taking the ratio of the integrated intensity of prominence emission lines represents a good diagnostics for the physical conditions in prominences. The observation of emission ratios does not require the use of spectrographs with correspondingly long exposure times and thus limited spatial resolution. Stellmacher & Wiehr (2000) showed that prominence emission exhibits distinct maxima indicating a variable number of prominence structures ("threads") along the line-of-sight (LOS). They did not find a close correlation of those maxima in the Ca II 8542 Å/Hβ ratio map with the intensity structure in the corresponding images. This may fit computations by Gouttebroze & Labrosse (2002) which indicate that the Ca II 8542 Å/Hβ ratio is rather insensitive to the physical state of the prominence.

In contrast, Labrosse & Gouttebroze (2001) obtained from one-dimensional slab models a substantial sensitivity of the He D_3/Hβ emission ratio to the gas pressure and, to some extent, also to the temperature and the slab width. Spectral analysis of this ratio by Stellmacher & Wiehr (1995) shows a "branching" of this ratio which also occurs in the He 3889 Å/H_8 3888 Å emission ratio (Stellmacher & Wiehr 1994) and indicates strong dependence on the thermal line broadening. De Boer et al. (1998) find such different ratio values also within a single prominence, indicating the presence of regions with distinct physical state.

A more detailed investigation of the intrinsic thread physics, however, is hardly possible from spectra due to their limited spatial resolution. We therefore study well-resolved prominence images taken in the He D_3 and the Hβ lines.

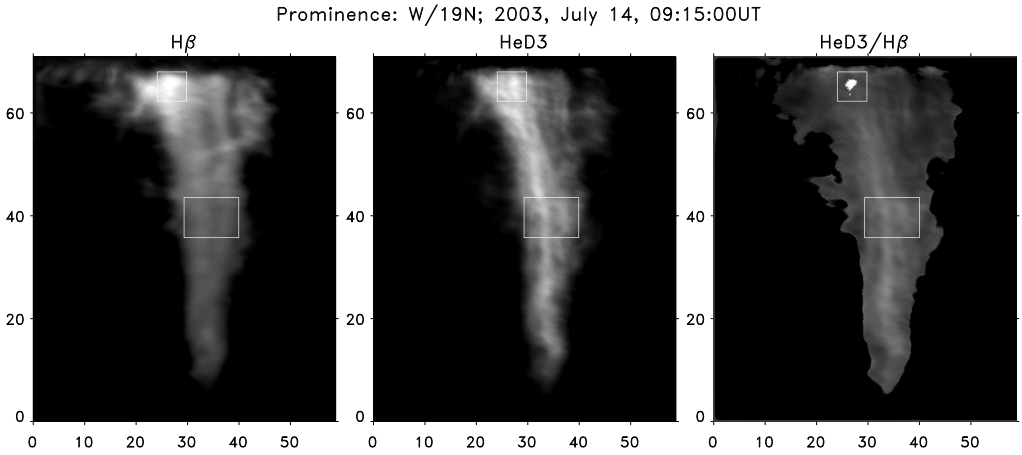

Figure 1. Prominence at W/19N in the integrated light of the Hβ (left) and the He D$_3$ emissions (middle) together with their brightness ratio map (right). Rectangles mark sub-regions with substantial evolution of the ratio.

2. Observations

We observed on July 14 and 15, 2003 with the Swedish 1-m Solar Telescope (SST) on La Palma several quiescent prominences, simultaneously in He D$_3$ and Hβ using a dichroic beam splitter and about 2 Å wide filters. The exposure time was between 0.1 s and 0.25 s, accounting for the individual prominence brightness. Image motion was minimized using the correlation tracker of the SST, set to a nearby white light limb facular grain as lock point. The raw images were corrected for the dark and the gain matrices; the underlying aureole was determined from the neighborhood of the respective prominence and subtracted.

3. Results

The final images and the corresponding ratio maps allow spatial and a temporal analysis. Since the spatial behaviour was discussed in Wiehr et al. (2007) we concentrate here on the temporal evolution. Figure 1 shows the prominence at W/19N observed during 12.3 min.

In Fig. 2 we show a scatterplot of the emission ratio versus the integrated intensities of He D$_3$ and Hβ, respectively. Also shown are the corresponding histograms obtained by integration of the scatterplots along the abscissa (ratio histograms) and along the ordinate (emission histograms). It can be seen that during the 12.3 min of evolution, the maximum of the He D$_3$ brightness increased from 310 to 380 counts, whereas the minimum of the Hβ brightness decreased from 400 to 300 counts.

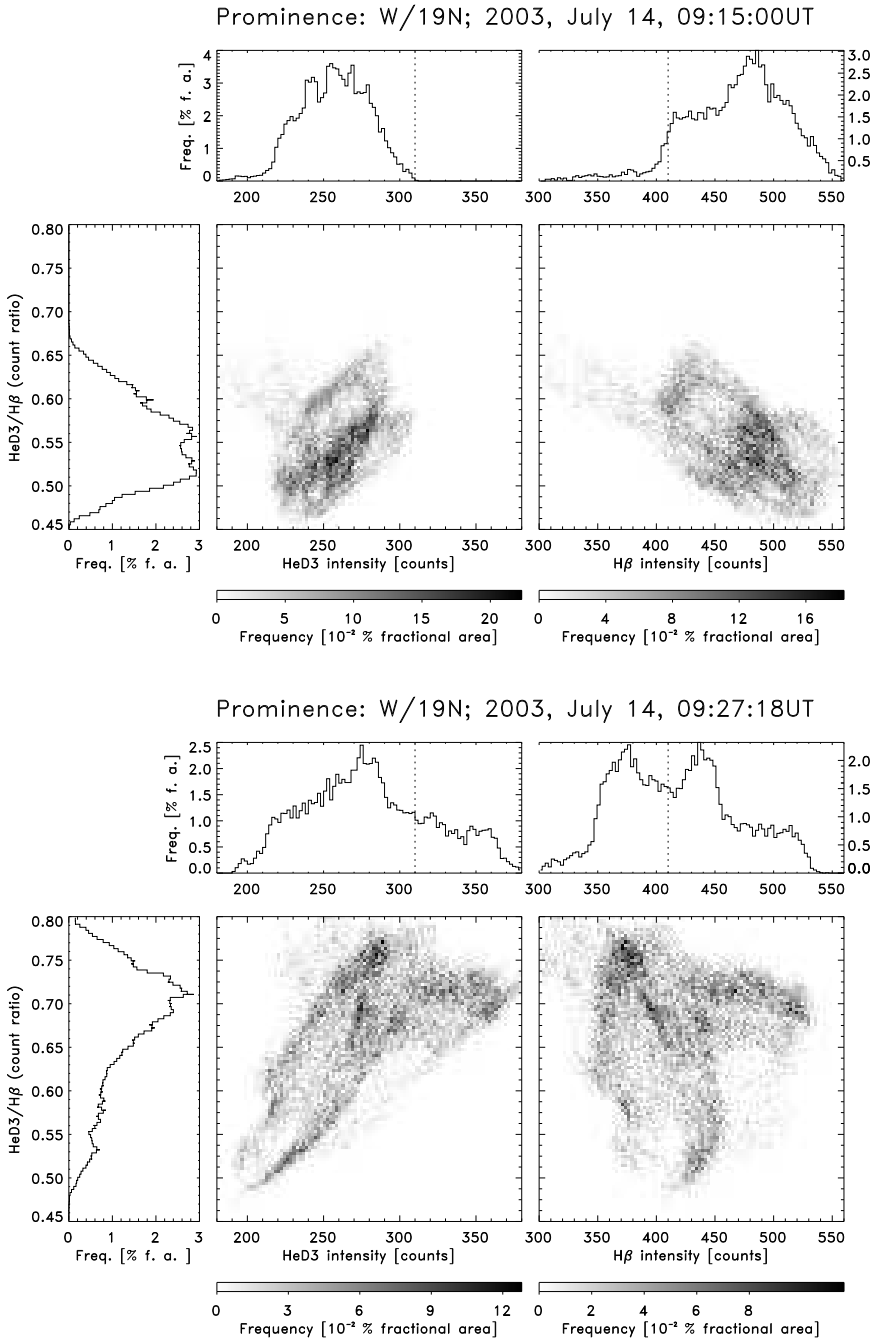

Figure 2. Scatterplot of the He D$_3$/Hβ ratio versus the total emission of He D$_3$ (middle) and Hβ (right panels) for the sub-region of the prominences at W/19N on July 14, 2003 (marked by the upper rectangle in Fig. 1). Left: ratio histograms obtained by integration of the scatterplots along the abscissa. Top panels: intensity histograms from integration along the ordinates.

4. Conclusion

In the context of the hypothesis of varying thread numbers along the line-of-sight (LOS) as the origin of the "structured" intensity histograms, the observed temporal variation of the histogram maxima indicates a "re-arrangement" of threads along the LOS as, e.g., described by Engvold (1998). For prominence regions where intensity variations are accompanied by such substantial changes of the emission ratio as seen in Fig. 2, the various superposing threads will have substantially different intrinsic physical state. The physical parameters responsible for various observed He D_3/Hβ emission ratios have been discussed by Labrosse & Gouttebroze (2001) from one-dimensional slab models which show that the ratio mostly depends on the gas pressure, less on slab width and temperature.

The rather fast temporal changes and, in particular, those with opposite brightness evolution as in Fig. 2, can hardly be explained by fast variations of these parameters. We therefore suggest a change of the spatial density of the substructures within each thread. Larger separations between them (i.e., smaller packing density) allow a deeper penetration of ionizing EUV radiation which affects the population of the He I triplet system and thus the amount of He D_3 excitation. Such a mechanism might be checked by simultaneous observations of the He ionizing EUV radiation (i.e., near 504 Å).

The complete discussion of these observations will appear in *Solar Physics*.

Acknowledgments. We thank the SST staff for help with the observations. The Swedish 1-m Solar Telescope is operated by the Swedish Academy of Science at the Spanish Observatorio del Roque de los Muchachos (IAC). This project has been supported by the European Commission through the Instituto de Astrofísica de Canarias to fund the European Northern Observatory in the Canary Islands.

References

De Boer C. R., Stellmacher G., Wiehr E., 1998, A&A 334, 280
Engvold O., 1998, in D. Webb, D. M. Rust, B. Schmieder (eds.), ASP Conf. Ser. 336: New Perspectives on Solar Prominences, 23
Gouttebroze P., Labrosse N., 2002, A&A 380, 323
Labrosse N., Gouttebroze P., 2001, A&A 380, 323
Stellmacher G., Wiehr E., 1994, A&A 286, 302
Stellmacher G., Wiehr E., 1995, A&A 299, 921
Stellmacher G., Wiehr E., 2000, Solar Phys. 196, 375
Wiehr E., Stellmacher G., Hirzberger J., 2007, in F. Kneer, K. G. Puschmann, A. D. Wittmann (eds.), Modern Solar Facilities - Advanced Solar Science, Göttingen 2007 (in press)

The Physics of Chromospheric Plasmas
ASP Conference Series, Vol. 368, 2007
Petr Heinzel, Ivan Dorotovič and Robert J. Rutten, eds.

White-Light Emission of Solar Prominences

S. Jejčič[1] and P. Heinzel[2]

[1] *University of Ljubljana, Department of Physics, Ljubljana, Slovenia*
[2] *Astronomical Insitut AS, Ondřejov, Czech Republic*

Abstract. Using an extended grid of prominence models we compute the prominence white-light (WL) emission due to Thomson scattering and compare it with that in Hα. The ratio of the WL emission and the total emission can explain the color of prominences as observed during the total eclipses and can tell us whether the pink color of prominences is due to their intrinsic white-light emission or due to coronal contribution at the prominence location. We also show how this ratio depends on the prominence electron density, temperature and thickness.

1. Prominences Observed During Total Solar Eclipses

Solar prominences are cool (6 000 – 10 000 K) and dense ($10^{-14} - 10^{-13}$ g cm^{-3}) plasma structures suspended in the solar corona, well visible above the solar limb during total solar eclipses. They are called filaments when seen against the solar disk. The strongest emission of the hydrogen Hα line gives them the red color, but during eclipses the prominences observed in white light are typically visible in pink color. The purpose of this investigation is to understand the nature of the prominence color.

2. Prominence Models

We use a set of 140 prominence models (Gouttebroze et al. 1993) to compute the theoretical WL emission. The prominences are modeled as 1-D slabs located 10000 km above the solar surface. These isothermal and isobaric slabs stand vertically above the solar disk. Each model is defined by its kinetic temperature, gas pressure and the geometrical thickness of the slab. The model set includes 7 different values for the gas pressure: 0.01, 0.02, 0.05, 0.1, 0.2, 0.5, and 1 dyn cm^{-2}, 6 different geometrical thicknesses: 200, 500, 1000, 2000, 5000, and 10000 km as well as 3 different temperatures: 6000, 8000, and 10000 K used for all models and two extreme temperatures 4300 and 15000 K used only for the thickness of 5000 km. This gives us 140 models. By solving the radiative transfer problem under the non-LTE conditions, the electron density ($n_{\rm e}$) at the center of the slab and the total energy emitted in the Hα line ($E_{\rm H\alpha}$) were calculated (Gouttebroze et al. 1993).

Figure 1. Total solar eclipse in 2001 observed by the Úpice Observatory Expedition. *Left:* composite coronal image processed by the method of Druckmüller et al. (2006). *Right:* detail of prominences on the limb.

3. White Light Emission

The WL emission of prominences is due to Thomson scattering of the disk radiation on free electrons in the prominence plasma. For simplicity we assume an *isotropic* and *coherent* scattering and neglect the effect of limb darkening.

The Thomson cross section is

$$\sigma_{\rm T} = \frac{8\pi}{3}\left(\frac{e^2}{m_{\rm e}\,c^2}\right)^2 = 6.65\cdot 10^{-25}{\rm cm}^2\ , \tag{1}$$

where e is the electron charge, $m_{\rm e}$ the mass of the electron and c the speed of light. The emission coefficient for coherent and isotropic scattering at a given prominence location is (Rybicki & Hummer 1994)

$$j(\nu) = n_{\rm e}\ \sigma_{\rm T}\ J(\nu)\ , \tag{2}$$

where $n_{\rm e}$ is the electron density. $J(\nu)$ is the mean intensity of the radiation incident from the solar surface.

If we neglect the limb darkening then $J(\nu)$ is equal to the intensity $I_0(\nu)$ emitted from the solar disk multiplied by a dilution factor W.

$$J(\nu) = I_0(\nu)W\ . \tag{3}$$

We take $W = 0.416$ which corresponds to the height of 10000 km (Gouttebroze et al. 1993).

The integrated WL emission due to Thomson scattering on free electrons in the slab is then

$$E_{\rm WL} = D\cdot\int_\nu j(\nu)\ d\nu = n_{\rm e}\ \sigma_{\rm T}\ I_{\rm tot}\ W\ D \propto n_{\rm e}\ D\ , \tag{4}$$

where D is the thickness of the slab and

$$I_{\rm tot} = \int_\nu I_0(\nu)\ d\nu = 1.2723\cdot 10^{10}\ {\rm erg\ sr^{-1}\ cm^{-2}\ s^{-1}}\ . \tag{5}$$

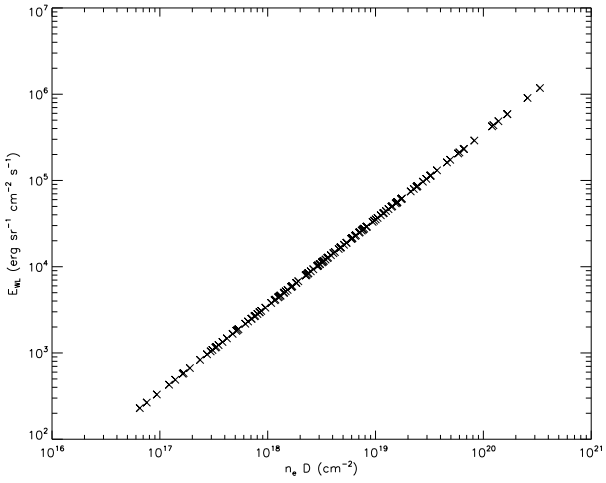

Figure 2. The WL emission as a function of the electron density multiplied by the geometrical thickness.

Here we assumed a constant electron density equal to that at the center of the slab. To compute $I_{\rm tot}$ we used the continuum intensities between 3700 Å and 8000 Å given by Allen (1973).

The integrated energy emitted in the Hα line is

$$E_{\rm H\alpha} \propto n_{\rm e}^2 \; D \; , \tag{6}$$

which is only weakly dependent on the temperature (Heinzel et al. 1994). Finally, $E_{\rm tot}$ is defined as $E_{\rm tot} = E_{\rm WL} + E_{\rm H\alpha}$.

4. Results

For all 140 models the WL emission of prominences was calculated, together with the ratio of the WL emission and the total emission $E_{\rm WL}/E_{\rm tot}$. The results of the computations are displayed in the following plots.

Figure 2 shows the WL emission intensity due to Thomson scattering as a linear function of the electron density and thickness for all 140 models with different temperatures and gas pressures. This naturally follows from previous equations.

Figure 3 shows that integrated emission in the Hα line for all models is a linear function of the emission measure for small line-center optical thicknesses ($\tau \leq 1$) where Hα emission is lower than 10^5 erg sr^{-1} cm^{-2} s^{-1} and it saturates for values which are larger than that.

Figure 4 shows that for optically thin prominences up to the electron density around 10^{10} cm^{-3}, where $\tau \sim 1$, the ratio of the WL emission and the total emission decreases with the increasing electron density for all temperatures and thicknesses as follows from the ratio

$$\frac{E_{\rm WL}}{E_{\rm tot}} \propto \frac{1}{1 + \varepsilon \; n_{\rm e}} \; , \tag{7}$$

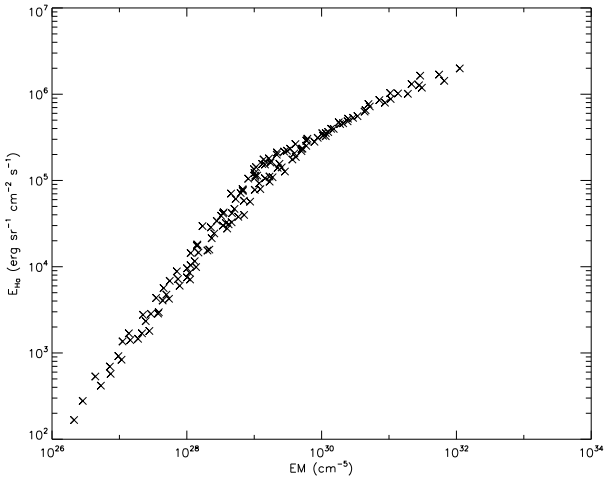

Figure 3. Integrated intensity emitted in the Hα line as a function of the emission measure $EM = \int n_\mathrm{e}^2 \, \mathrm{d}z = n_\mathrm{e}^2 \, D$. Here n_e is again the central electron density.

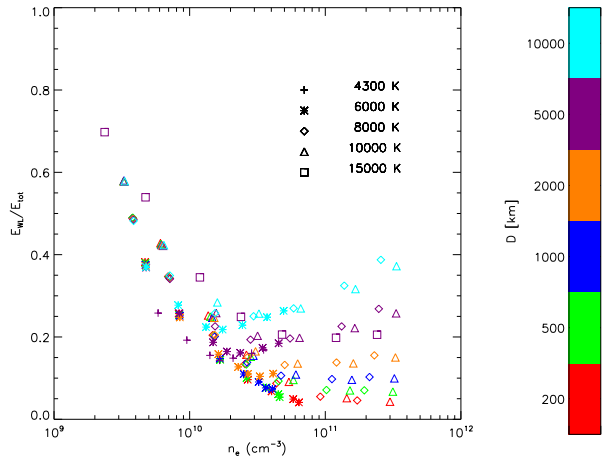

Figure 4. The ratio of the WL emission and the total emission as a function of electron density for different temperatures and different thicknesses.

where ε is of the order of n_e^{-1}.

However, for optically thick prominences ($\tau \geq 1$ and $n_\mathrm{e} \geq 10^{10}$ cm^{-3}), the total energy emitted in the Hα line starts to saturate, so at a given electron density the ratio of the WL emission and the total emission becomes dependent on the thickness of the slab. With increasing thickness its value also increases. The distribution of all 140 models shows that the pink color of prominences can indeed be explained by Thomson scattering on free electrons in prominences. In the limits of very low density and high temperatures the WL emission strongly dominates the Hα one.

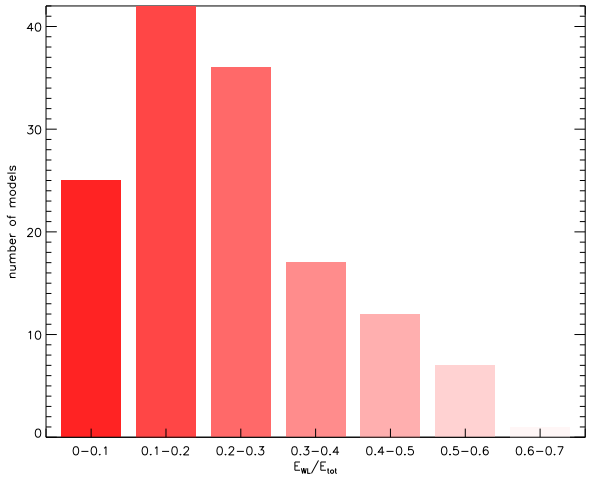

Figure 5. Number of models as a function of the ratio between the WL emission and the total emission.

The histogram in Fig. 5 represents the number of models as a function of the ratio of the WL emission and the total emission. The color of each column is marked according to this ratio value, where red (darker) color means dominant Hα emission, while white (lighter) color corresponds to dominant WL. The peak of the histogram is between 0.2 and 0.3 for about half of models. In optically thin prominences this ratio is larger compared to optically thick prominences as follows from Fig. 4.

5. Conclusions

In this study we have found that the WL emission of most solar prominences which is due to Thomson scattering on prominence electrons is large enough to explain the pink color of prominences as frequently seen during the eclipses (i.e., the mixture of the red Hα and WL radiation). The true color may, however, depend on some other factors. First, the WL emission of the corona in front and behind the prominence is in general superimposed on the prominence emission. Second, in the blue region the hydrogen Hβ line can also contribute to the total optical radiation. Actually, $E_{\mathrm{H}\beta}$ can be of the same order as the WL, i.e., 10–30% of $E_{\mathrm{H}\beta}$ (Gouttebroze et al. 1993).

References

Allen, C. W., 1973, Astrophysical Quantities, The Athlone Press
Druckmüller, M., Rušin V., Minarovjech M., 2006, Contr. Astron. Obs. Skalnaté Pleso, in press
Gouttebroze, P., Heinzel, P., Vial, J. C., 1993, A & AS 99, 513
Heinzel, P., Gouttebroze, P., Vial, J. C., 1994, A & A 292, 656
Rybicki, G. B., Hummer, D. G, 1994, A & A 290, 553

Javier Trujillo Bueno and Eberhard Wiehr

Emulation of solar granulation in Coimbra

The Physics of Chromospheric Plasmas
ASP Conference Series, Vol. 368, 2007
Petr Heinzel, Ivan Dorotovič and Robert J. Rutten, eds.

Old and New Aspects of Prominence Physics from Coronal Observations

Serge Koutchmy[1], Boris Filippov[2] and Philippe Lamy[3]

[1]*Institut d'Astrophysique de Paris, Paris, France*
[2]*Pushkov Institute of Terrestrial Magnetism, Ionosphere and Radio Wave Propagation, Russian Academy of Sciences, Russia*
[3]*Laboratoire d'Astronomie Spatiale, Marseille, France*

Abstract. Classical W-L eclipse observations at typical spatial resolution of 10 arcsec show dark cavities surrounding prominences. Images at higher spatial resolution processed with a spatial filter reveal small dynamical cool clouds moving inside the inner corona around prominences. More recently EIT/SoHO observations taken using the 304 Å channel showed He^+ prominences sometimes not seen in cooler lines. TRACE movies of the Fe IX and XI emissions where prominences are seen in absorption also bring appreciable informations on the dynamical surrounding of prominences, without showing obvious correlations between prominence and coronal structures. Accordingly, we re-examine the significance of the cavity and propose a possible interpretation as magnetic interlaced 3-D flux ropes and loops evacuating the corona, in addition to twisted flux ropes where the prominence plasma is condensing. Future space missions like ASPIICS should pay more attention to cavities and emptiness, to coronal dynamics around prominences, in order to resolve the long-standing problem of the origin of prominences and perhaps, perform a new diagnostic of the erupting process responsible for many CMEs.

1. Introduction

Coronal cavities (CCa) are known for a long time thanks to coronal W-L observations taken at time of solar total eclipses (see e.g. Saito & Tanberg-Hanssen 1973 for a quantitative analysis of the phenomenon). Figure 1 shows a recent eclipse image with several cases of CCa. They are mainly identified at the base of a large coronal streamer system where a prominence (P) is inserted. The suggestion was made that the total depletion of coronal material corresponds to the mass of cool plasma in the prominence, as a result of the so-called radiative instability process. Usually, the depletion of coronal density is rather impressive supporting this rather naive assumption. However the classical evaluation of the corresponding "missing" coronal mass showed that it is not found sufficient to explain the amount of plasma accumulated in the underlying prominence. Interestingly enough good radial gradient compensated images of the W-L corona show other locations where a depletion of density is found, see Fig. 1; they are then called emptiness. In addition the mass replenishment of the corona is a highly dynamical process whereas the mass storage in a quiescent prominence is a process of accumulation. A snapshot cannot be used to discuss the balance of masses.

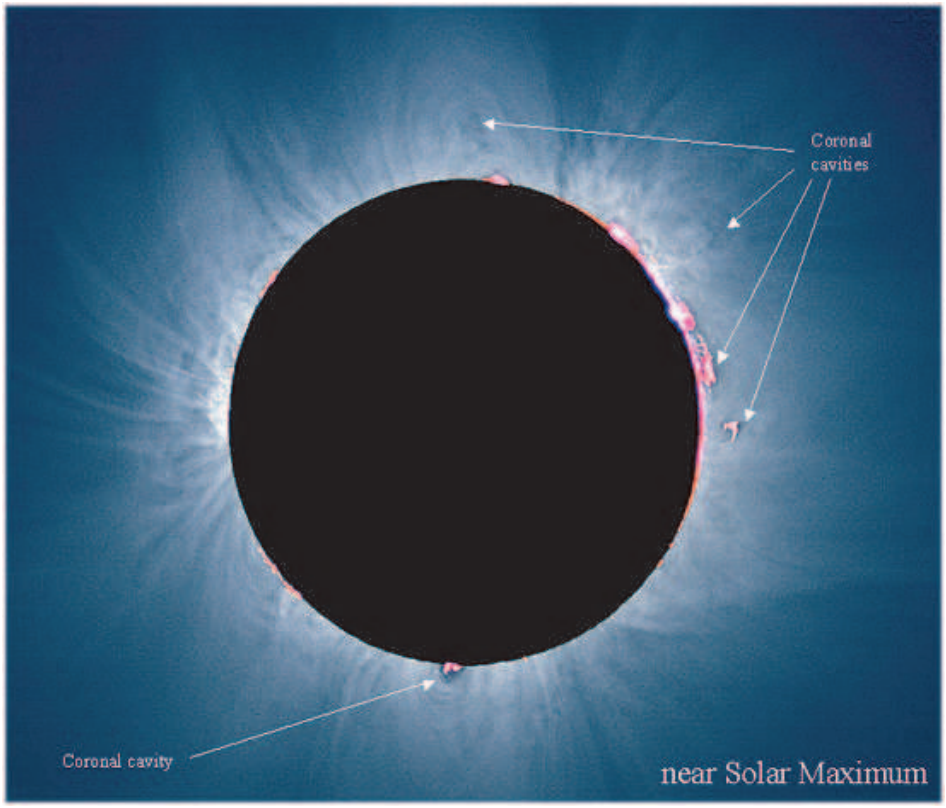

Figure 1. A W-L processed (to remove the radial gradient) eclipse 1999 image of the corona by M. Druckmüller. Several dark cavities are identified near the prominences producing Hα emissions, as well as higher in the corona.

To correctly evaluate the mass balance CCa/P, the prominence mass should be known and it cannot be well done because the ionization degree is poorly known and because indeed several distinct parts of the prominence should be considered: i) the quiescent and more massilve parts, usually optically thick in Hα, and ii) the dynamical hotter and less massive parts surrounding the prominence which is also called the prominence - corona (P-C) interface. Mass determination coming from eclipse W-L photometry of prominences usually provides smaller numbers (see Koutchmy 1983) then what is found from prominence spectroscopy.

The origin of the cool gas filling the magnetic structure of the prominence is still a matter of debate. It is probably related to the type of magnetic structure which is considered: a more open toward the corona structure, like in the Kuperus-Raadu model, would certainly be more appropriate to describe the relation cavity/prominence.

The apparent relation CCa/P is strongly suggesting that in 3D the space surrounding a filament channel could be a key to explain observations (see e.g. Heinzel et al. 2003). Eclipse observations needed to compute the coronal density depletion are not capable to tell very much about the 3D morphology nor about their dynamical aspects. However, the highest resolution W-L observa-

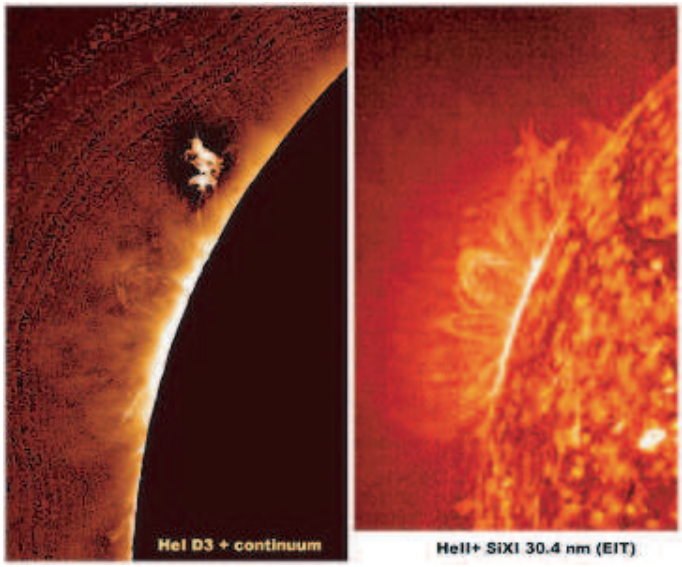

Figure 2. Partial frames to show the region of a coronal cavity observed on the E-limb of the eclipse 2001 corona. At left: from a filtergram taken using a 1 nm width filter put in the far wing (−3 nm) of the He I D3 line in order to have the coronal continuum recorded together with the prominence emission of D3. The radial gradient is removed and the contrast is enhanced. At right: the same field observed simultaneously in space using the 304 Å channel (He II) of EIT/SoHO.

tions obtained with the CFHT in 1991 (see Koutchmy et al. 1994), did show that at least in one case a CC could be resolved in overlapping along the l.o.s. dark loops. The lack of spatial resolution would then just result in a relative darkening around the prominence.

There is little doubt that some parts of the coronal plasma are evacuated inside those dark loops (see November & Koutchmy 1996). Then, the question of the surrounding the prominence magnetic structure should be considered to explain this critical observation, including the evacuation process.

2. Recent Observations

The most interesting observations are coming from the comparison of W-L eclipse observations with simultaneously obtained EUV images, including data from the EIT/SoHO spaceborne experiment. EUV disk observations are also rather valuable to look at filament channels and overlying the chromosphere cool plasma.

Figure 2 shows a comparison of what is seen during the eclipse 2001 observed from Angola using a broad band filter which includes the D3 line of He I with what is seen in the same region simultaneously observed with EIT using the 304 Å channel of the He II line. The CCa around the cool prominence (He I) is emphasized by image processing. We clearly see that the He II prominence material is surrounding the He I more compact structure and, in addition, loop

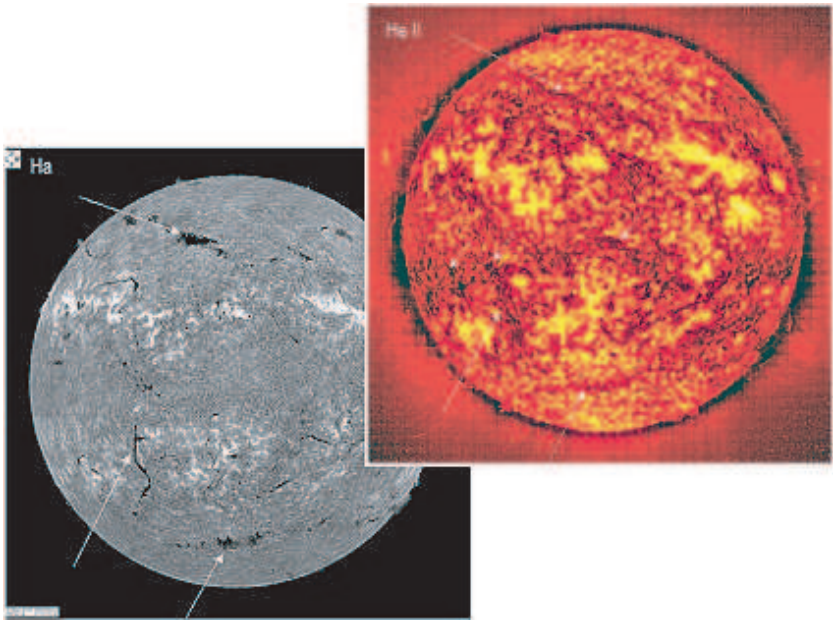

Figure 3. Comparison of 2 filtergrams taken on June 14, 2000 in a cool and in a hot chromospheric lines. At left, in Hα from the BBSO and at right from the 304 Å channel (He II) of EIT/SoHO. Arrows show absorbing features which are (at left) and are not (at right) correlated

structures exists in H II without any counterparts in He I. A movie was also obtained (observation by D. Crussaire) using the eclipse images. Its duration of 3 min permits to show several small W-L + He I clouds flying around and going downward with proper motions of order of 20 to 50 km/s. It suggests a condensation process going on. The dynamical aspects of the P-C interface surrounding a prominence was also well illustrated by an excellent broad band Hα 90 min speckle reconstructed movie taken with the DOT on July 9, 2000. It is quite convincing in showing a lot of very faint threads and clouds flying around a compact prominence, a phenomenon which is often referred to as a "turbulent" P-C interface.

EIT observations in 304 Å, compared to Hα solar disk filtergrams, are very interesting in revealing a lot of disk features inserted in the low corona. Figure 3 shows a comparison of almost simultaneous full disk processed images taken in Hα at BBSO (left) and in space with the 304 Å (He II) channel of EIT. The usual filament channels are readily identified (arrows on the left) and many absorbing in He II features (see the arrows on the right) are seen, including near the center of the disk, without any counterpart in the cool line Hα of H I. This analysis shows that the cool material of a classical prominence should now include the part at higher temperatures, as seen in He II (and in other TR lines like C IV) in order to understand its origin and its relationships with the corona.

Sometimes CCa-s show a rather perfect round shape as it is presented at right panel of Fig. 4. An absorbing polar crown prominence visible above the limb is stretched along the East-West line, so on the limb we look along the

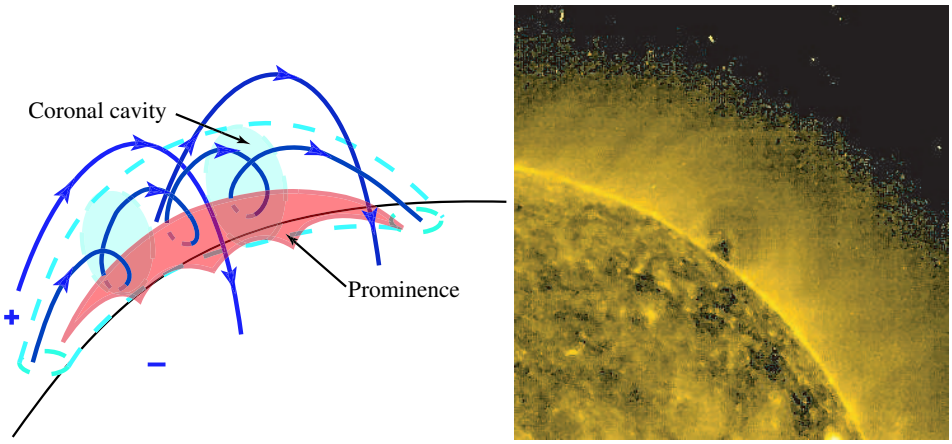

Figure 4. A sketch of the 3D geometry of the magnetic flux rope with a coronal cavity and a prominence inside (left) and EIT/SoHO Fe XV 284 Å image on 28 February 2005 showing a round dark cavity around and above an absorbing prominence on the limb (right).

prominence axis. We suggest that the 3D shape of the cavity is nearly a cylinder. In the well known flux rope model (Fig. 4, left), the cylindrical volume of depleted coronal material arises due to the additional magnetic field pressure of the coronal electric current in the equation of the gas pressure balance. Field lines of the current have the form of helices (or the form of circles in the cross section perpendicular to the prominence axis). This defines the perfect round shape of the dark region in Fig. 4. Circular lines around the top of a prominence are also seen in Fig. 5. Helical magnetic field tubes of the flux rope serve as magnetic traps in the gravitation field. Dense plasma could flow and be collected near the bottom parts of the helical tubes forming prominences or filaments.

3. Discussion and Conclusions

New observations show the striking behaviour of regions surrounding prominences, including what was called a cavity. CCa is convincingly seen only in W-L. The high resolution TRACE coronal movies do not show a clear evidence of cavities. Accordingly, W-L high resolution observations are needed to progress on this topic and, preferably, long time sequences are needed in order to take into account dynamical phenomena. This is one of the priority of the scientific program proposed for the ASPIICS mission (see the poster paper by Lamy et al. at this conference). This artificial eclipse experiment will permit many W-L images to be taken at high cadence during long uninterrupted time sequences. Their processing will reveal the structure of cavities and together with EUV and Hα images will permit to resolve the dynamical aspects of the P-C interface. Figure 5 shows an example of what will be available from the ASPIICS mission. Not only the P-C interface and the cavity region will be understood in 3D during the rotation of the Sun, but important dynamical aspects related to the physics of coronal streamers, including the analysis of the prominence

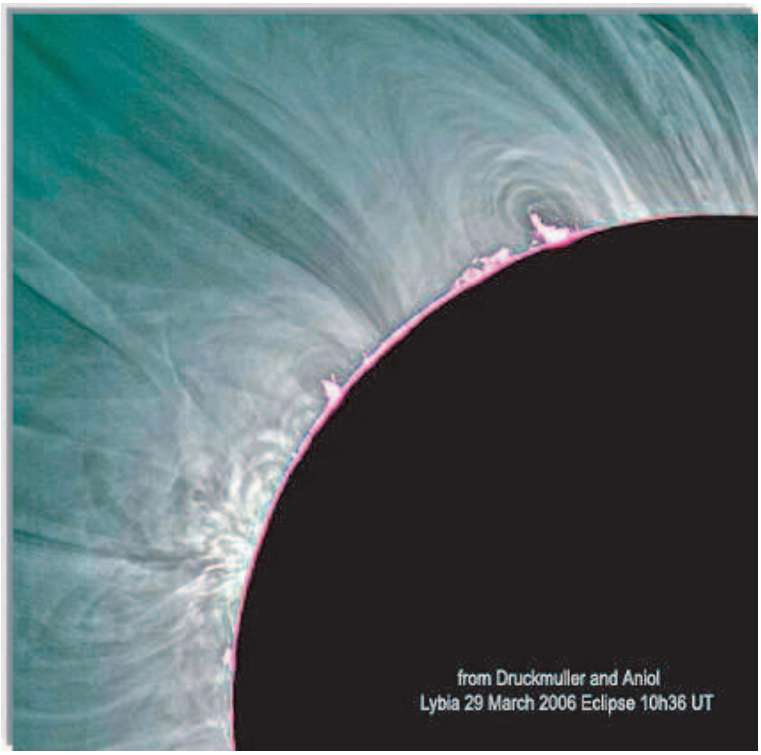

Figure 5. Partial frame from the best resolution W-L reconstructed and processed image of the eclipse corona on 29 March 2006. The processing permits to make clear the morphology of the corona inside the cavities surrounding 2 prominences at the NE limb. The prominence at the top is surrounded by many loops and, further out, by a large and extended streamer presumably streched out by the wind.

eruptions and CMEs, will be tackled out.

Acknowledgments. We thank the CSPM organisers for a fruitful and efficient meeting.

References

Heinzel P., Anzer U., Schmeider B., Schwartz P., 2003, in A. Wilson (ed.), Solar Variability as an Input to the Earth's Environment, ESA SP-535, 447
Koutchmy S., Lebecq C., Stellmacher G., 1983, A&A 119, 261
Koutchmy S. et al., 1994, A&A 281, 249
November L., Koutchmy S., 1996, ApJ 466, 512
Saito K., Tanberg-Hanssen E. 1973, Solar Phys. 31, 105

The Physics of Chromospheric Plasmas
ASP Conference Series, Vol. 368, 2007
Petr Heinzel, Ivan Dorotovič and Robert J. Rutten, eds.

Spectral Diagnostics of Active Prominences

Nicolas Labrosse[1], Pierre Gouttebroze[2] and Jean-Claude Vial[2]

[1]*Institute of Mathematical and Physical Sciences, Aberystwyth, UK*
[2]*Institut d'Astrophysique Spatiale, Orsay, FR*

Abstract. Active prominences exhibit plasma motions, resulting in difficulties with the interpretation of spectroscopic observations. These solar features being strongly influenced by the radiation coming from the solar disk, Doppler dimming or brightening effects may arise, depending on which lines are observed and on the velocity of the plasma. Interlocking between the different atomic energy levels and non local thermodynamic equilibrium lead to non-trivial spectral line profiles, and this calls for complex numerical modeling of the radiative transfer in order to understand the observations. We present such a tool, which solves the radiative transfer and statistical equilibrium for H, He I, He II, and Ca II in moving prominences where radial plasma motions are taking place. It is found that for isothermal, isobaric prominence models, the He II resonance lines are very sensitive to the Doppler effect and thus show a strong Doppler dimming. The Ca II lines Doppler effect for the prominence models considered here. We illustrate how the code makes it possible to retrieve the plasma thermodynamic parameters by comparing computed and observed line profiles of hydrogen and helium resonance lines in a quiescent prominence. This new non-LTE radiative transfer code including velocities allows us to better understand the formation of several lines of importance in prominences, and in conjunction with observations, infer the prominence plasma thermodynamic properties and full velocity vector.

1. Introduction

The main motivation of our modeling work is to contribute to building realistic prominence models. For this, we need an accurate knowledge of thermodynamic quantities (temperature, densities, ...), level populations (useful, e.g., to infer the magnetic field properties from spectro-polarimetric observations), velocity fields, energy budget. However these quantities still have large uncertainties associated with them. Observations of several different lines from different atoms/ions allow us in theory to measure these parameters. Among these lines, the H and He lines are important as they are strong and largely contribute to the radiative losses. However the prominence plasma being out of LTE and optically thick in H and He resonance lines, the interpretation of line spectra or intensities in radially moving prominences is a non-trivial task. Therefore, non-LTE radiative transfer calculations including velocity fields are needed to build realistic prominence models. Here we present such calculations and preliminary results.

2. Modeling Procedure

The prominence is represented by a 1D plane-parallel slab standing vertically above the solar surface. Each prominence model is defined by a set of free parameters: the temperature T, the gas pressure p, the slab thickness L (or the total column mass), the height of the slab above the limb H, the microturbulent velocity, and the radial speed. For this preliminary study we consider isothermal and isobaric prominences, although the code allows for inclusion of a transition region between the cold prominence and the hot corona. We first solve the pressure equilibrium, the ionization equilibrium, and the coupled statistical equilibrium (SE) and radiative transfer (RT) equations for a 20 levels H atom. Then the SE and RT equations are solved for other elements: He I (29 levels) and He II (4 levels), and Ca II (5 levels). More details on the modeling of the hydrogen, calcium, and helium spectra in quiescent prominences can be found in Gouttebroze & Labrosse (2000); Gouttebroze & Heinzel (2002); Labrosse & Gouttebroze (2004) respectively, and references therein.

For the modeling of active and eruptive prominences, we use a velocity-dependent incident radiation as boundary conditions for the RT equations. It has already been shown by Heinzel & Rompolt (1987) in the case of the hydrogen lines that the Doppler effect induces a frequency shift of the incident profile relative to the rest case, and also a distortion of the incident profile due to the variation of the Doppler shift with the direction of the incident radiation. It is also the case for the helium (Labrosse et al. 2006) and calcium incident radiation.

3. Diagnostics of Radial Velocities

3.1. Integrated intensities

We reproduce the results of Gontikakis et al. (1997a,b) who computed the hydrogen radiation emitted by a radially moving prominence, using partial redistribution in frequency (PRD) for the Lyman lines. We obtain the same variation of the relative intensities (intensities normalised to the line intensities when the prominence is at rest) and the same line profiles for Lyα, Lyβ, and Hα. The main result is that there exists an important coupling between Lyβ and Hα which causes these lines to be first Doppler brightened, and then Doppler dimmed, with increasing velocity, while there is only a Doppler dimming effect on Lyα.

Figure 1 presents relative intensities as a function of velocity for the He I 584 Å, He II 304 Å, and He I 10830 Å lines (left panel) and Ca II K and Ca II 8542 Å lines (right panel) at two different temperatures (8000 K and 15000 K).

The He I 10830 Å line does not show any sensitivity to the Doppler effect, which is mainly due to the very weak incident absorption line. The He I 584 Å line is quite sensitive to the Doppler effect. Its Doppler dimming is more important at low temperature. The He II resonance lines are the most sensitive to the radial velocity of the plasma (the relative intensity of the He II 256 Å line, not shown, exhibits a similar variation as He II 304 Å), and the Doppler dimming is strong at the temperatures considered in this study. Such a result was expected since the main mechanism of formation at these temperatures for these lines is the scattering of the incident radiation (Labrosse & Gouttebroze 2001). Let us

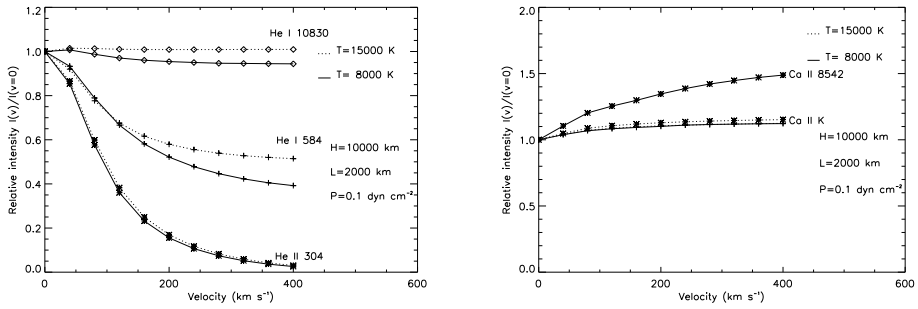

Figure 1. Relative intensities (intensities normalized to the line intensity at rest) as a function of velocity at 8000 K (solid lines) and 15000 K (dotted lines) for left: He I 10830 Å (diamonds), He I 584 Å (plus), and He II 304 Å (stars); right: Ca II K (plus) and Ca II 8542 Å (stars).

stress that in this preliminary study we have not included a transition region between the cold prominence and the hot corona (PCTR). The presence of a hotter plasma in the PCTR may somehow decrease the sensitivity of the He II resonance lines to the Doppler effect as collisions will become more important in the formation processes of these lines. This will be investigated in a future work.

The right panel of Fig. 1 indicates that there is no strong Doppler effect on the Ca II resonance lines, while we observe some Doppler brightening of the 8542 Å line (and indeed of the other two infrared lines at 8498 and 8662 Å, not shown) at low temperature.

3.2. Line profiles

If spectroscopic observations of erupting prominences are available, then a comparison between computed and observed line profiles can be made. We show in Figs. 2 and 3 the line profiles for the same helium and calcium lines considered in Fig. 1 at two different temperatures (solid line: 8000 K, dashed line: 15000 K), at four different velocities (from top to bottom: 0, 80, 200, and 400 km s^{-1}).

The Doppler dimming effect is well observed in the helium resonance lines at 584 Å and 304 Å as the radial velocity is increased (Fig. 2). We can observe asymmetries in the line profiles of these lines when the prominence plasma is moving radially, with some intensity enhancement which is especially visible in the red wing of the He I 584 Å line at low temperature. This is explained as follows. The radiation emitted by the disk center in our code is represented by symmetrical line profiles. When the prominence is at rest, the incident radiation illuminating the prominence slab is symmetrical; however when the prominence plasma is moving radially the incident line profile becomes distorted and shifted towards the red. As we used the PRD standard approximation in our calculations of the resonance lines of helium, the resulting line profiles are asymmetrical. This would not have been the case if we had considered complete redistribution in frequency (CRD) instead of PRD. The line asymmetry is more visible for the He I 584 Å line as its wings are fairly bright, while the wing intensities of the He II 304 Å line are low. Despite the fact that the line asymmetry increases

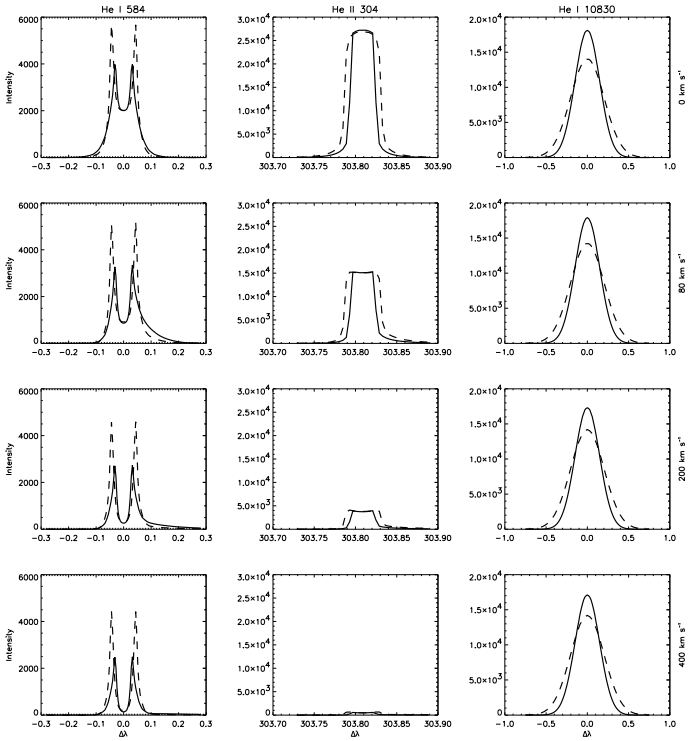

Figure 2. Line profiles for $T = 8000\,\mathrm{K}$ (solid line) and $T = 15\,000\,\mathrm{K}$ (dashed line), with $p = 0.1$ dyn cm^{-2}, and $L = 2000$ km, at different velocities: 0, 80, 200, and 400 km s^{-1} from top to bottom. Abscissa is $\Delta\lambda$ in Å and vertical axis is specific intensity in erg s^{-1} cm^{-2} sr^{-1} Å^{-1}. From left to right: He I 584 Å, He II 304 Å, and He I 10830 Å.

with speed for both lines, it is more visible at low speeds (when the intensity in the wing is high enough). Finally, it is more pronounced at low temperatures because the scattering of the incident radiation is relatively more important as compared to collisional processes than it is at higher temperatures.

Figure 3 shows that the intensities of the Ca II lines are lower at 15 000 K than at 8000 K, an effect of Ca II to Ca III ionization (Gouttebroze & Heinzel 2002).

4. Diagnostics of Thermodynamic Parameters

We show here how the non-LTE radiative transfer calculations can help us to infer the thermodynamic properties of a prominence observed by the SUMER spectrometer on SOHO. This prominence was actually a rather quiet prominence and we have not included any velocity fields in these calculations. It was observed during the 13th MEDOC campaign held at IAS in June 2004. We select a few pixels in the SUMER slit which cut across the prominence and average the line profiles there. We consider the line profiles of two H resonance lines (Lyβ and Lyϵ) and the He I resonance line at 584 Å. For the comparison between

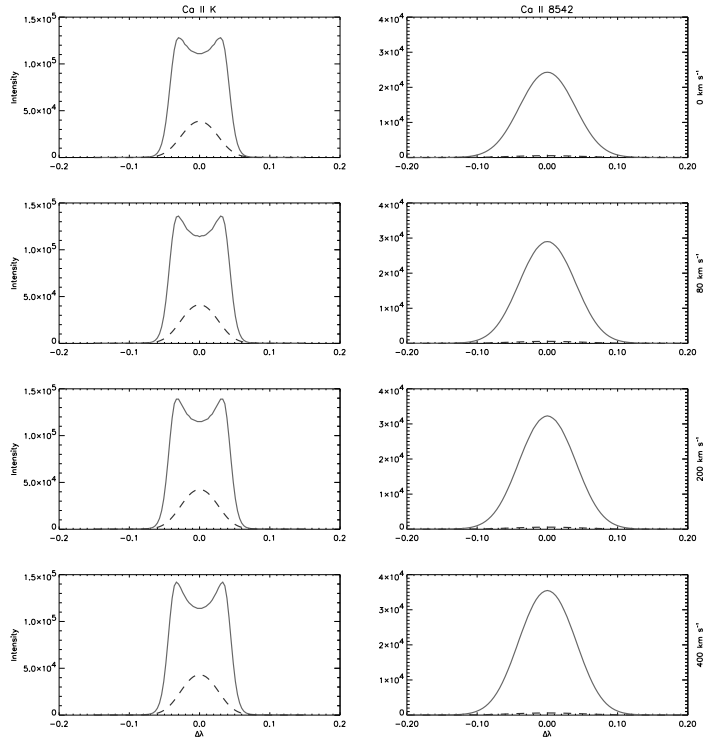

Figure 3. Same as in Fig. 2 for Ca II K and Ca II 8542 Å lines.

computed and observed line profiles we now include the presence of a PCTR. The temperature variation between the cold prominence core and the corona suggested by Anzer & Heinzel (1999) has been adopted for this study. By a trial and error process we selected the temperature profile shown in Fig. 4. The other prominence parameters are $p = 0.023$ dyn cm^{-2}, $L = 194$ km (total column mass $2.4\,10^{-7}$ g cm^{-2}), $H = 113722$ km, and the microturbulent velocity $\xi = 18$ km s^{-1}.

We obtain a very good agreement between the computed profiles (convoluted with the SUMER instrumental profile) and the observed profiles, as shown in Fig. 5. It is worth noting that fitting hydrogen *and* helium resonance lines simultaneously places strong constraints on the parameter space, and it was not possible to find another set of parameters for the prominence that would be significantly different than what is given above and that would lead to a satisfactory fit of the observed profiles.

5. Conclusions

The non-LTE radiative transfer modeling that we are developing is a key tool for interpreting observations and constructing realistic prominence models. The combination of lines from hydrogen, helium, and calcium, places strong constraints on the models. Imaging and spectroscopy must be used for comparisons with calculations to determine thermodynamic parameters and velocities. The

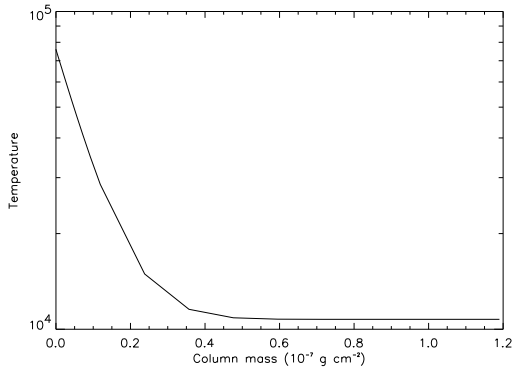

Figure 4. Temperature as a function of the column mass in one half of the prominence slab.

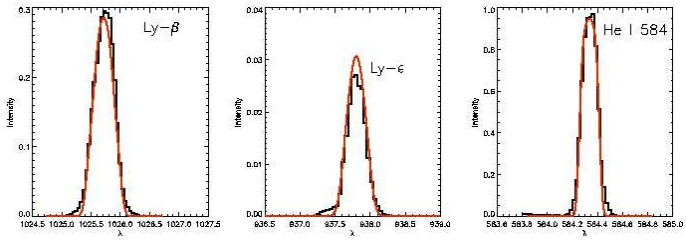

Figure 5. Observed (histograms) and computed (curves) lines profiles for Lyβ (left), Lyϵ (middle), and He I 584 Å (right).

radial velocity determined from the comparison between observed and computed line profiles, in combination with line-of-sight velocities, should allow us to infer the full velocity vector of the prominence plasma. In a future work we will compare our model results with simultaneous observations of, e.g., Hα and He II 304 Å.

Acknowledgments. N. L. acknowledges financial support from the organisers of the Coimbra Solar Physics Meeting, the University of Wales through the Gooding Fund, and PPARC through grant PPA/G/O/2003/00017.

References

Anzer U., Heinzel P., 1999, A&A 349, 974
Gontikakis C., Vial J.-C., Gouttebroze P., 1997a, A&A 325, 803
Gontikakis C., Vial J.-C., Gouttebroze P., 1997b, Solar Phys. 172, 189
Gouttebroze P., Heinzel P., 2002, A&A 385, 273
Gouttebroze P., Labrosse N., 2000, Solar Phys. 196, 349
Heinzel P., Rompolt B., 1987, Solar Phys. 110, 171
Labrosse N., Gouttebroze P., 2001, A&A 380, 323
Labrosse N., Gouttebroze P., 2004, ApJ 617, 614
Labrosse N., Vial J. C., Gouttebroze P., 2006, Solar Active Regions and 3D Magnetic Structure, 26th IAU GA, JD 3, 47, 3

The Physics of Chromospheric Plasmas
ASP Conference Series, Vol. 368, 2007
Petr Heinzel, Ivan Dorotovič and Robert J. Rutten, eds.

Modeling the Hemispheric Pattern of Solar Filaments

D. H. Mackay[1] and A. A. van Ballegooijen[2]

[1]*School of Mathematics and Statistics, St. Andrews, Scotland*
[2]*Harvard-Smithsonian Centre for Astrophysics, Cambridge, USA*

Abstract. New results in modeling the hemispheric pattern of solar filaments are presented. The simulations consider what type of chirality forms along the Polarity Inversion Line (PIL) lying in between two magnetic bipoles as they interact. The results demonstrate not only the origin of the dominant hemispheric pattern, but also why exceptions to it occur. The dominant hemispheric pattern may be attributed to the dominant range of bipole tilt angles and helicities in each hemisphere (Wang & Sheeley 1989; Pevtsov et al. 1995). Exceptions to the hemispheric pattern occur in cases of no initial helicity or for helicity of the minority type in each hemisphere, when large positive bipole tilt angles are used. As the simulations show a clear dependence of the chirality on observational quantities, this may be used to check the validity of the results.

1. Introduction

Solar filaments form over a wide variety of latitudes on the Sun. In recent years, it has been shown that the dominant axial magnetic fields (Leroy et al. 1983, 1984; Bommier & Leroy 1998) that thread through solar filaments display an unusual hemispheric pattern (Martin et al. 1994). In the northern/southern hemisphere at mid- to high-latitudes, dextral/sinistral filaments dominate although exceptions do occur. A dextral/sinistral filament, is one in which, when standing on the positive polarity side of the PIL and looking towards the main body of the filament the axial magnetic field points to the right/left.

The aim of this paper is to consider what type of chirality of the magnetic field is produced through the interaction of two magnetic bipoles, using a mixture of magnetic flux transport and magneto-frictional relaxation simulations. Such configurations of interacting bipoles are important for filaments as observations by Tang (1987) show that the majority of filaments form in between bipoles (Type-B) rather than within a single bipole (Type-A).

2. Model and Initial Setup

To determine the origin of the hemispheric pattern, we use a magnetic flux transport and magnetofrictional model (van Ballegooijen et al. 2000). The Sun's magnetic field $\mathbf{B}(= B_r, B_\theta, B_\phi) = \nabla \times \mathbf{A}$ is evolved by the induction equation. At the photosphere the magnetic field is subject to large-scale advection due to differential rotation and meridional flows. In addition to these global flows, the field is also subject to surface diffusion (see Equations 14 and 15 of van Ballegooijen et al. 2000).

In the coronal region the magnetic field evolves through the non-ideal induction equation,

$$\frac{\partial \mathbf{A}}{\partial t} = \mathbf{v} \times \mathbf{B} - \eta_{\rm c}\mathbf{j}, \tag{1}$$

where $\mathbf{v}(\mathbf{r}, t)$ is the plasma velocity, $\mathbf{j} = \nabla \times \mathbf{B}$ and $\eta_{\rm c}$ the coronal diffusion.

To ensure that the coronal field evolves through a series of force-free states a magneto-frictional method is employed (Yang et al. 1986) where,

$$\mathbf{v} = \frac{1}{\nu}\frac{\mathbf{j} \times \mathbf{B}}{B^2} + v_o \, {\rm e}^{-(2.5R_\odot - r)/r_w}\hat{\mathbf{r}}. \tag{2}$$

The first term on the right hand side represents the fact that in the corona the Lorentz force is dominant. The second term represents a radial outflow velocity which is imposed to ensure that the field lines remain radial at the source surface ($r = 2.5R_\odot$). Full details of the numerical method, boundary conditions and form of differential rotation and meridional flow can be found in van Ballegooijen et al. (2000)

The purpose of the present paper is to understand how bipolar magnetic regions interact for different initial helicities and tilt angles. To do this we consider a region in the northern hemisphere where the production of dextral magnetic fields is required to match observations. A typical initial configuration of the bipoles can be seen in Fig. 1(a).

Flux transport effects are then allowed to act on the magnetic field for a period of 54 days. Three sets of simulations with different initial conditions are considered. In the first set, the initial fields of both bipoles are given a small negative twist or helicity ($\beta = -0.2$ in non-dimensionalised units, Mackay & van Ballegooijen 2005), in the second set they are untwisted ($\beta = 0$) and in final set a small positive twist or helicity ($\beta = 0.2$) is used. These initial helicities only produce a small shear in the bipole and do not result in helically twisted coronal field lines. For each of these three cases the initial tilt angles (α) of both bipoles are varied from -30° to $+40^\circ$ where positive tilt angles are consistent with Joys Law.

3. Results of the Simulations

The results of the simulations can be seen in Fig. 2. Each graph shows the fraction of dextral (stars), sinistral (diamonds) or weak skew (squares) produced along the PIL lying in between the two bipoles as a function of the initial bipole tilt angle (α).

It is clear from Figs. 2(a)-(c) that on day 2 for all bipole tilt angles weak skew dominates and very similar results are obtained in all three cases. The reason for this is that when the bipoles are twisted, the twist, is mainly added to the inner parts of the bipole and the outer parts remain mainly untwisted. In the initial days of the simulation only the outer parts of the bipoles interact to produce field lines over the PIL, hence similar results are found for each case. A typical example of the field lines lying over the PIL between the two bipoles can be seen in Fig. 1(a) for the negative twist case and $\alpha = 10^\circ$.

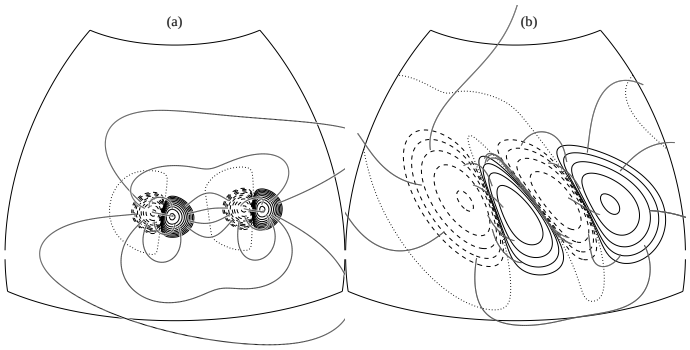

Figure 1. Field line structure for two bipoles interacting in the Northern Hemisphere for $\beta = -0.2$ and $\alpha = 10°$. Figure (a) shows the field structure on day 2 after the bipoles have made cross connections, and (b) the field after 46 days of evolution. In each case solid lines represent positive flux, dashed lines negative flux and the dotted line the PIL. The solid lines connecting positive and negative flux represent the field lines.

The results are however very different for each of the three cases after 46 days of evolution. Over this period differential rotation extends the bipoles in an East-West sense, meridional flow pushes them poleward and the two bipoles converge due to the combined effects of differential rotation and surface diffusion (Fig. 1(b)). Surface diffusion plays a key role in cancelling flux between the bipoles and transporting the twisted field lines from the inner parts of the bipoles to the PIL lying in between the bipoles. In Fig. 1(b) it can be seen that a strong dextral axial field, consistent with the hemispheric pattern forms above the PIL in between the two bipoles.

In Figs. 2(d)-(f) the full results can be seen for each set of simulations. For the negative twist case (Fig. 2(d)) it is clear that dextral skew (stars) dominates over the entire range of bipole tilt angles. It should be noted that observations by Wang & Sheeley (1989) show that 80% of bipoles emerge with tilt angles ranging between $-10° : 30°$. Therefore, by considering both the dominate range of bipole tilt angles (Wang & Sheeley 1989) and dominant helicities (Pevtsov et al. 1995) the dominant hemispheric pattern may be reproduced. The results are however more mixed for the zero and positive twist cases (Figs. 2 (e) and (f)). Dextral skew is once again dominant for tilt angles ranging from $-30°$ to $10°$. However, outside this range for the more extreme values of positive bipole tilt angles ($\alpha > 20°$), sinistral skew forms. Although this does not match the hemispheric pattern it does show how exceptions to the pattern may occur around the tail end of the dominant positive bipole tilt angles when the bipoles either have no twist or are twisted with the minority type of helicity for their hemisphere.

4. Discussion

In this paper magnetic flux transport simulations have been used to consider the origin of the hemispheric pattern of filaments. The results clearly demonstrate how the dominant chirality of Type-B filaments may be a result of the dominant

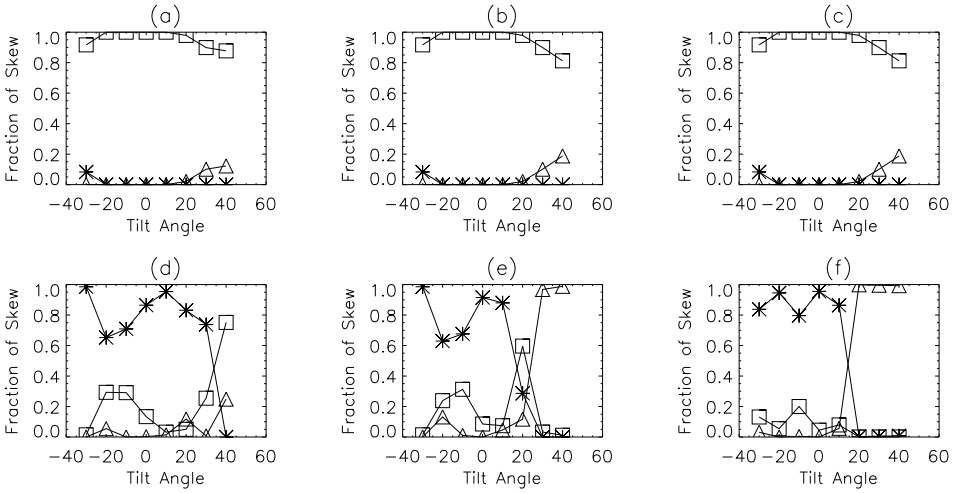

Figure 2. Fraction of skew along the PIL between the two bipoles as a function of the initial bipole tilt angle. Graphs (a)-(c) are for day 2 of the simulations and (d)-(f) day 46 where (a) and (d) correspond to the negative twist case, (b) and (e) zero twist and (c) and (f) positive twist. In each graph stars represent dextral skew, diamonds sinistral skew and squares weak skew.

bipole tilt angles and dominant helicity in emerging bipoles. Along with this exceptions to the hemisphere pattern may occur in a natural way near the tail end of dominant positive tilt angles, when the bipoles have either no twist or the minority type for their hemisphere.

The results show a clear dependence of the hemispheric pattern (and exceptions to it) on observable quantities such as bipole tilt angles and helicity. Such a dependence may in principle be checked through a detailed comparison of theory and observations.

Acknowledgments. D. H. M. would like to thank the UK Particle Physics and Astronomy Research Council for financial support. The simulations were carried out on a SHRIF/PPARC funded supercomputer located in St. Andrews.

References

Bommier, V. & Leroy, J. L. 1998, ASP Conf. Ser. 150, IAU Colloq. 167, New Perspectives on Solar Prominences, 150, 434

Leroy, J. L., Bommier, V., & Sahal-Brechot, S. 1983, Solar Phys. , 83, 1

Leroy, J. L., Bommier, V., & Sahal-Brechot, S. 1984, A&A, 131, 33

Mackay, D. H. & van Ballegooijen, A. A. 2001, ApJ, 560, 445

Mackay, D. H. & van Ballegooijen, A. A. 2005, ApJ, 621, L77

Martens, P. C. & Zwaan, C. 2001, ApJ, 558, 872

Martin, S. M., Bilimoria, R., & Tracadas, P. W. 1994, in Solar Surface Magnetism, ed. R. J. Rutten & C. J. Schrijver (New York: Springer-Verlag), 303-338

Pevtsov, A. A., Canfield, R. C., & Metcalf, T. R. 1995, ApJ, 440, L109

Tang, F. 1987, Solar Phys. , 107, 233

van Ballegooijen, A. A., Priest, E. R., & Mackay, D. H. 2000, ApJ, 539, 983

Wang, Y.-M. & Sheeley, N. R., Jr. 1989, Solar Phys. 124, 81

Yang, W. H., Sturrock, P. A., & Antiochos, S. K. 1986, ApJ, 309, 383

The Physics of Chromospheric Plasmas
ASP Conference Series, Vol. 368, 2007
Petr Heinzel, Ivan Dorotovič and Robert J. Rutten, eds.

A Magnetic Map of a Solar Filament

Laura Merenda[1], Javier Trujillo Bueno[1,2] and Manuel Collados[1]

[1] *Instituto de Astrofísica de Canarias, La Laguna, Spain*
[2] *Consejo Superior de Investigaciones Científicas, Spain*

Abstract. One of the most useful diagnostic tools for the detection of inclined magnetic fields in solar chromospheric and coronal structures is that based on the fact that the Hanle effect in forward scattering at the solar disk center creates linear polarization in some spectral lines, such as those of the He I 10830 Å multiplet. Here we show the preliminary results of an ongoing investigation on the magnetic field of a solar filament, based on the inversion of spectropolarimetric observations obtained with the Tenerife Infrared Polarimeter.

1. Introduction

Solar filaments (or prominences) are clouds of plasma, which are suspended above the solar surface by magnetic forces. Although there are many theoretical models on the magnetic field vector that confines the plasma of solar filaments (or prominences), many questions about their formation and evolution are still open. The empirical determination of a complete 2D map of the strength and geometry of the magnetic field in solar filaments would provide fundamental data useful to discern between different magnetic configurations, which in turn would provide clues about its evolution.

2. Observations and Results

The spectropolarimetric observations of a filament, located near the center of the solar disk, were obtained on 11 September 2003 using the Tenerife Infrared Polarimeter (TIP; see Martínez Pillet et al. 1999) attached to the Vacuum Tower Telescope at the Teide observatory. TIP allowed us to observe the full Stokes vector in a spectral range including the photospheric Si I 10827.1 Å line and the filament He I 10830 Å, multiplet with a high degree of polarimetric sensitivity. We took three scans of different parts of the filament, with the spectrograph slit parallel to the main axis of the filament (in its central part) and scanning along the direction perpendicular to it with the help of a correlation tracker. Similar observations have been presented by Collados et al. (2003).

The maps in Fig. 1 show where the absorption in the He I 10830 Å multiplet is maximum. To infer the magnetic field vector we compare the observed Stokes profiles with theoretical ones included in a database. We compute the theoretical Stokes profiles within the framework of the quantum theory of the Hanle effect, in the same way described in Trujillo Bueno et al. (2002), where it is demonstrated that the Hanle effect in forward scattering creates measurable

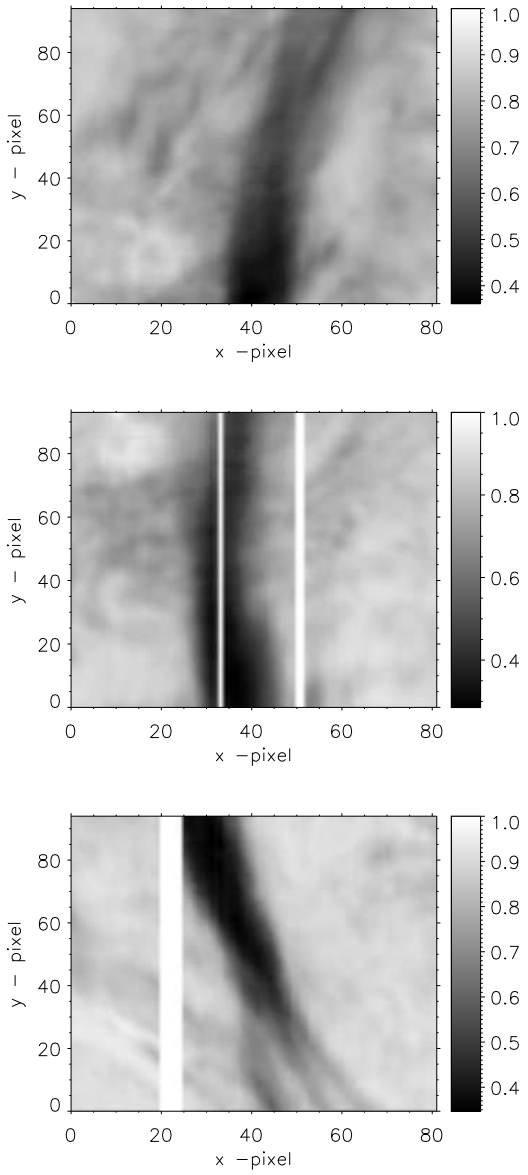

Figure 1. Intensity maps of the three scans of the observed filament. The values reported here correspond to the minimum of the red blended component of the He I 10830 Å multiplet after normalizing the intensity to the continuum value. The white vertical lines correspond to observational gaps due to errors in the tracking. We have rejected these data in our analysis.

linear polarization signals in the He I 10830 Å multiplet. In this preliminary work we restrict ourselves to the saturated Hanle effect regime, which for the He I 10830 Å multiplet ranges approximately from 10 to 100 G. In this magnetic field regime the linear polarization is only sensitive to the direction of the

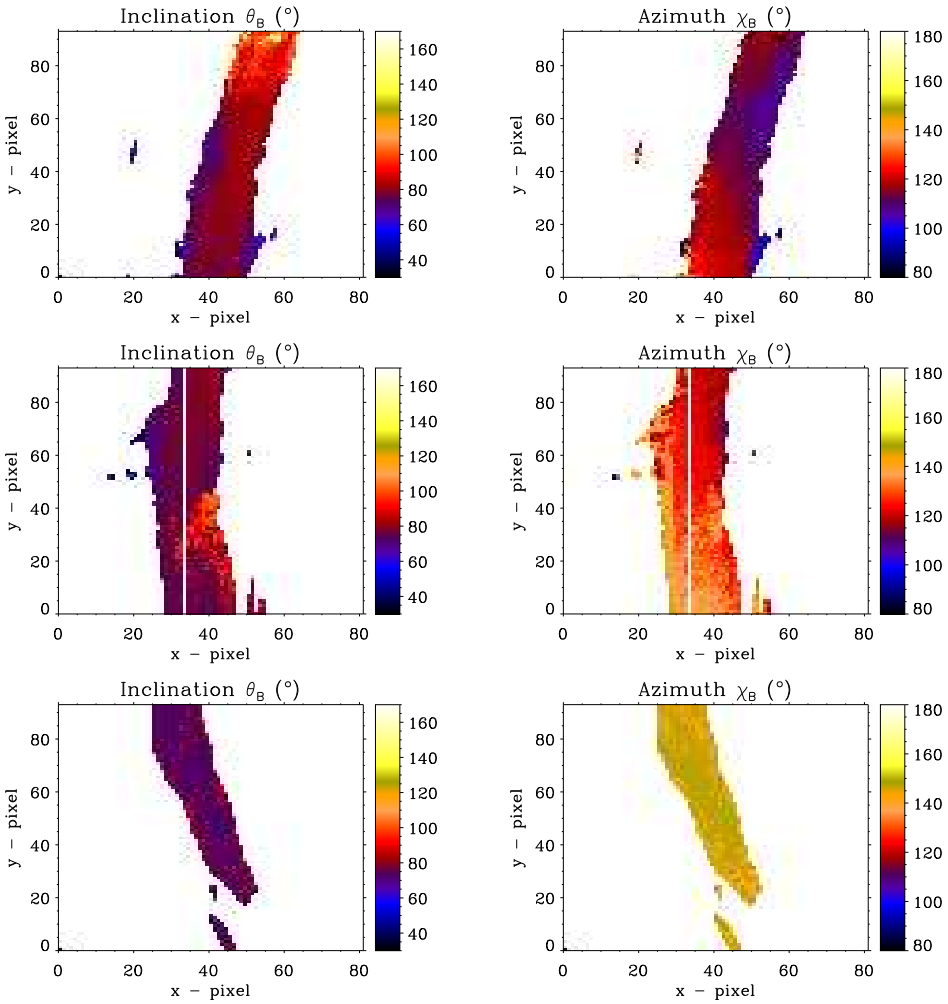

Figure 2. Results of the inversion of the observed Stokes profiles coming from the filament. θ_B is the inclination angle of the magnetic field vector with respect to the local solar vertical and χ_B is the azimuth angle, counted counterclockwise from $\chi_B = 0°$ (chosen as the radial direction to the nearest solar limb). The slit direction (y axis) forms an angle of $\approx 30°$ (clockwise) with the nearest limb. For this preliminary inversion we have assumed that the filament was located 5 arcsec above the solar visible surface.

magnetic field and does not change with intensity variations. Fig. 2 shows the results of the application of our Stokes inversion strategy, which we have applied previously to the case of polar-crown prominences (Merenda et al. 2006). We note that the inclination of the magnetic field changes along the filament and is almost horizontal is its central part, whereas its azimuth changes according to the changes in the orientation of the main axis of the filament.

3. Future Work

We have shown here an example of the high diagnostic potential of our inversion method, which we have applied to observations of the Hanle effect in the He I 10830 Å multiplet. This preliminary work has been based on two approximations. The first one is that we have made use of a database created for the saturated Hanle effect regime. Actually, at some filament points we have observed a strong circular polarization signal that could indicate the presence of a magnetic field stronger than 100 G. In the future we will relax this $10 \leq B \leq 100$ G assumption using a more complete database. The second one is that we have assumed that the filament was located 5 arcsec above the solar surface. As we cannot know the real height of this filament, we will have to investigate how this hypothesis affects the final result.

Acknowledgments. This work has been supported by the Spanish Ministerio de Ciencia y Tecnología through project AYA2004-05792 and by the European Commission via the European Solar Magnetism Network (ESMN).

References

Collados M., Trujillo Bueno J., Asensio Ramos A, 2003, in *Solar Polarization 3*, eds. J. Trujillo Bueno, & J. Sanchez Almeida, ASP Conf. Series Vol. 307, 468

Martínez Pillet V., Collados M., Sánchez Almeida J. et al., 1999, in *High Resolution Solar Physics: Theory, Observations and Techniques*, eds. Rimmele, T.R., Balasubramaniam, K.S. & Radick, R. R., ASP Conf. Series Vol. 183, 264

Merenda L., Trujillo Bueno J., Landi Degl'Innocenti E. & Collados M., 2006, ApJ, 642, 554

Trujillo Bueno J., Landi Degl'Innocenti E., Collados M., Merenda L. & Manso Sainz R. 2002, Nature, 415, 403

The Physics of Chromospheric Plasmas
ASP Conference Series, Vol. 368, 2007
Petr Heinzel, Ivan Dorotovič and Robert J. Rutten, eds.

Coronagraphic Broad-Band Hα Observations 1998 – 2000

Nadège Meunier[1], Jacques-Clair Noëns[1], David Romeuf[2], Serge Koutchmy[3], Raphaël Jimenez[1], Odile Wurmser[4], Serge Rochain[4] and the O.A. team[4]

[1] *Laboratoire d'Astrophysique de l'Observatoire Midi-Pyrénées, France*
[2] *Centre de Ressources Informatiques, Université Lyon, Lyon, France*
[3] *Institut d'Astrophysique de Paris, France*
[4] *Observateurs Associés FIDUCIAL (www.astrosurf.com/oa)*

Abstract. Broad-band full-limb Hα images of the inner corona were obtained since the beginning of the solar cycle 23 using one of the Pic-du-Midi coronagraph. We developed a tool to process the complete set of stored images and to automatically extract the properties and evolutions of the observed cold H I coronal structures over a large range of sizes and light fluxes, from small jets and/or spikes to large prominences. The paper describes the recognition techniques implemented in our software and discusses its use. Then we present some new results following a statistical analysis of the occurrence of structure parameters applied to a large sample of observations. It illustrates the capabilities of this software when applied to our database. Strong activity-asymmetries over the solar poles are shown, confirming similar results from elsewhere. We also discuss the distribution of relative light fluxes of these structures over a wide range of sizes. See also `http://bass2000.bagn.obs-mip.fr`.

1. Introduction

Since 1994, the 15 cm coronagraph of Pic-du-Midi Observatory (Niot & Noëns 1997) usually called "HACO" (H Alpha COronagraph), has been used to perform a daily survey of the evolution of the cool structures in the inner corona. Cool coronal structures were episodically studied in the past but no systematic quantitative analysis seems to exist. Our full limb coronagraphic Hα images are collected using a broad-band filter, with a time cadence which depends on the observed events. This program has provided a database of more than 185000 images covering the solar cycle XXIII. It was therefore necessary to build a special software in order to extract useful information about the H I structures and their time evolutions from this long time series. The difficulty comes from the non-uniform distribution of the background intensity produced by the sky brightness and seeing effects, convolved with instrumental background and the bright ring produced in the inner parts by the occulting system of the coronagraph. Here we describe briefly the software and the first results. More details can be found in Romeuf et al. (2006).

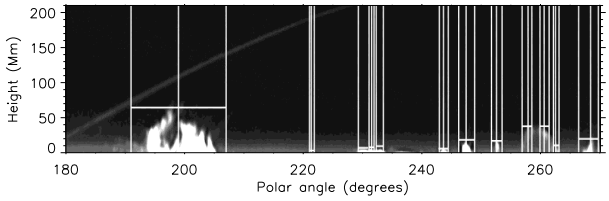

Figure 1. Example showing the height determination (limits of the structure, as well as the location of the center of the detection of each structure, and the height).

2. Data Processing

We have developped a software, SCANPROTU, with the objective of providing calibrated images of the limb as well as a list of structures identified on the limb together with some of their properties. It must produce series of calibrated images in relative units, corrected from the instrumental and seeing defaults as well as informations about the positions of the detected structures, in addition to their brightness and geometric properties. It must be able to show the time evolution of these parameters, and must give an indication about the activity in the detected regions at the time of observations. After flat-field correction and a photometric calibration which takes into account the filters and the variation of atmospheric transparency during the day, we perform the following steps:

- find the disk center and the solar radius in arbitrary units;
- transform into polar coordinates;
- computate the wavelet planes;
- suppress the artefacts and parasitic fringes created by the occulting disk;
- determine an average profile around the limb and filtering processing;
- perform a "pyramidal" analysis;
- computate a calibrated image;
- analyze the properties of each detected structure.

The properties of each structure for each detection (i.e. corresponding to each image, see Fig. 1 for an illustration) is included in a SQL archive[1]. The data can be retrieved in several ways. First, a simple form can be filled to provide the requested variables owing to various criteria (date, size, etc.). A large ascii file containing the list of structures and their properties can then be retrieved for subsequent analysis. Second, ready-to-use codes are also available. They use the database, make simple computations and provide results such as histograms, time evolution of structure location (coronagram), average value of a given parameter versus the polar angle, etc.

[1] `http://bass2000.bagn.obs-mip.fr/New2003/Pages/Coro/interro\_scanprotu.html`

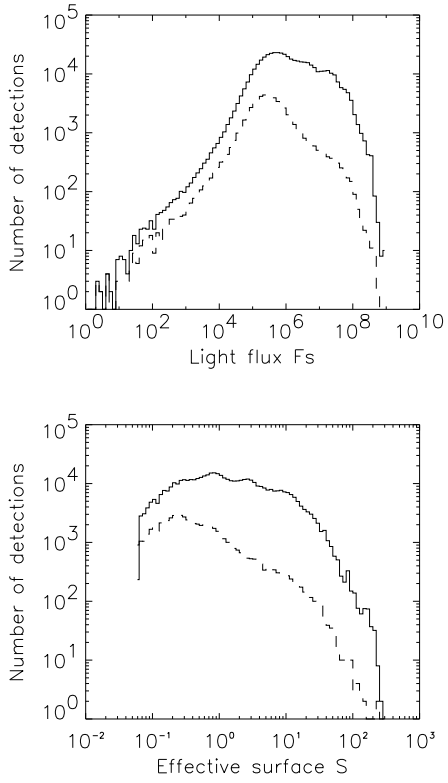

Figure 2. *Upper panel*: distribution of light fluxes F_S for all structures (solid lines) and the maximum light flux per structure after the selection (dashed line), with F_S expressed as a fraction of $10^{-11} F_\odot$, during the period 1998–2000. *Lower panel*: distribution in effective surface S for all structures (solid lines) and the maximum total light flux per structure after the selection (dashed line), with S expressed as a fraction of $10^{-5} S_\odot$.

3. First Results

A subset of data, covering 3 years, have been analysed using this technique. We have obtained a certain number of results concerning the relationship between the light fluxes F_S and effective surfaces S of structures, the distribution of these parameters, and the latitudinal distribution of the structures, including very small ones (Fig. 2). Effective surfaces are evaluated as a fraction of $10^{-5} S_\odot$ (with $S_\odot$ the surface of the solar disk). Three different regimes can be observed in the light fluxes and effective size distribution. Furthermore, the relationship between light fluxes and effective surfaces is found to be approximately linear on a log-log scale over almost three orders of magnitude. It corresponds to a power law with a slope of 5/4. For larger structures the flux is smaller than expected from the linear fit. There are in fact two regimes in the linear domain, with two distinct slopes below an effective surface of 1 (slope of 1.108 ± 0.003) and above it (slope of 1.312 ± 0.001). The slope is in general larger than 1, showing that in the linear regime, larger structures have a larger flux per square pixel than

smaller ones. The exception is for small structures, with a slope consistent with 1, indicating a constant flux per square pixel for S up to 1. Finally, we have studied the latitudinal distribution of structures for various categories of sizes (Romeuf et al. 2006). For all structures, we observe small gaps in activity at the equator and just above the activity belt, as well as a strong asymmetry between hemispheres, especially close to the poles. Very small features are definitely more present at the poles. The gap at intermediate latitudes could be related to the fact that it has been difficult to establish a connexion between the high latitude branch of solar activity (observed in the corona and using filaments as tracers) and the low latitude one (activity belt), as illustrated for example in Leroy & Noëns (1983). This is of great interest to the solar dynamo theories as it provides some constraints on the behavior of the dynamo waves. The North-South asymmetry may also be related to the dynamo action.

4. Conclusion

The software we have developped allows the detection of structures over a wide range of sizes, from small jets to large prominences. The preliminary results indicate interesting properties over this wide range of light fluxes, i.e. over almost eight orders of magnitude and over more than three orders of magnitude in effective surfaces. This database can therefore potentially be used to study in detail the parameters of small-scale structures, such as their spatial distribution in latitude, their lifetime distribution, as well as the variation of their properties over the solar activity cycle and the relationship with the closest active regions, eruptions, etc., taking into account the difference between the Northern and Southern hemisphere distributions. This software is currently being applied to the whole time series of HACO data (covering more than one solar cycle), as well as to the data from the new Pic du Midi Coronagraph, CLIMSO, which should start operating next spring. All the results will be available on the BASS2000 (Meunier et al. 2006) web site (`http://bass2000.bagn.obs-mip.fr`).

Acknowledgments. Living expenses of the large number of associated observers (O.A.) and most of the new equipment have been supported by FIDUCIAL. Observations are also supported by PNST of CNRS and INSU, Observatoire Midi-Pyrénées, Laboratoire d'Astrophysique of OMP and Institut d'Astrophysique de Paris, CNRS and UPMC. We thank the BASS2000 technical staff as well as the technical teams of the Pic du Midi Observatory for their help.

References

Leroy, J.-L. & Noëns, J.-C. 1983, A&A, L1

Meunier, N., Lafon, M., Maeght, P., Grimaud, F., & Roudier, T. 2006, SF2A-2006: Semaine de l'Astrophysique Francaise, F. Casoli, T. Contini, J.M. Hameury and L. Pagani eds., EdP-Sciences, Conference Series, in press

Niot, J. M., & Noëns, J.-C. 1997, Sol. Phys., 173, 53

Romeuf, D., Meunier, N., Noëns, J.-C., Koutchmy, S., Jimenez, R., Wurmser, O., Rochain, S., and the "Observateurs Associés" Team, 2006, Astron. Astrophys., in press

The Physics of Chromospheric Plasmas
ASP Conference Series, Vol. 368, 2007
Petr Heinzel, Ivan Dorotovič and Robert J. Rutten, eds.

Chromospheric Filament Network and Coronal Streamers

Teodor Pintér[1], Milan Rybanský[1] and Ivan Dorotovič[1,2]

[1]*Slovak Central Observatory, Hurbanovo, Slovak Republic*
[2]*Observatório Astronómico (GAUC, FCTUC), Coimbra, Portugal*

Abstract. We searched the anchoring distribution of coronal streamers as recorded by the LASCO C2 and C3 instruments of SOHO, using synoptic maps of filaments. Synoptic maps of the inner corona based on measurements of the intensity of the coronal emission line at 530.3 nm and synoptic maps of solar magnetic fields have been used as well. We suggest that the determinative condition for the formation of a stable streamer is a strong magnetic field.

1. Introduction

Coronal rays belong to the most characteristic objects that we can observe in the corona. Already by a quick review of coronal images one finds that they have various shapes and also have different lifetimes. The initial knowledge came from coronal observations during total solar eclipses, but these were substantialy extended by observations using space-borne coronagraphs, onboard Skylab, OSO 7, SMM, and especially SOHO (Fig. 1).

Stable coronal rays extend to large distances and rotate together with the solar surface. We can observe them at a particular location even during a full rotation period. No detailed investigation of their lifetimes has yet been carried out.

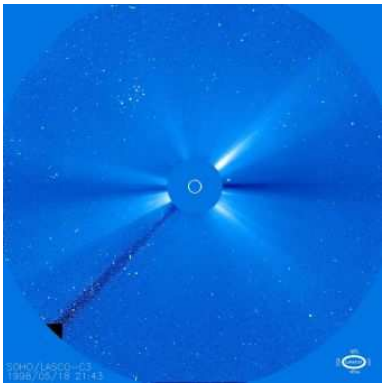

Figure 1. Coronal streamers observed by the LASCO C3 instrument onboard SOHO on 18 May, 1998 (courtesy of SOHO/LASCO consortium. SOHO is a project of international cooperation between ESA and NASA (`http://sohowww.estec.esa.nl/`).

We concentrate only on stable, long-lived (more than 5 days) coronal streamers in this contribution. We try to estimate where these streamers are anchored on the solar surface and what their relation is to other objects characterizing solar activity.

The physics of streamers and the processes maintaining their state are largely unknown. From our review of the observational material it seems that they are concentrated streams of coronal matter, oriented approximately perpendicularly to the surface. During individual eclipses they have been observed to extend out to 50 solar radii. It is not clear whether they are cylindrical or tubular bodies, or, on the contrary, thin differently oriented sheets. Sometimes coronal mass ejections (CMEs) arise at the location of a streamer with a typical speed of $300 - 2000$ km s^{-1}. After the CME formation streamers usually regenerate at their borders.

2. Method

Our main aim was to estimate the heliospheric coordinates of streamers. The kinematic properties of projection of a streamer to the plane of the sky during its rotation were used for this purpose, as illustrated in Fig. 2.

A radial coronal streamer moves during solar rotation along the surface of a cone. Projections of such streamers rotate clockwise if the streamer is in front of the solar disk on the Northern hemisphere, and counterclockwise if a streamer is in front of the disk on the Southern hemisphere. If a streamer is behind the disk, the rotational motion of the projection is the opposite.

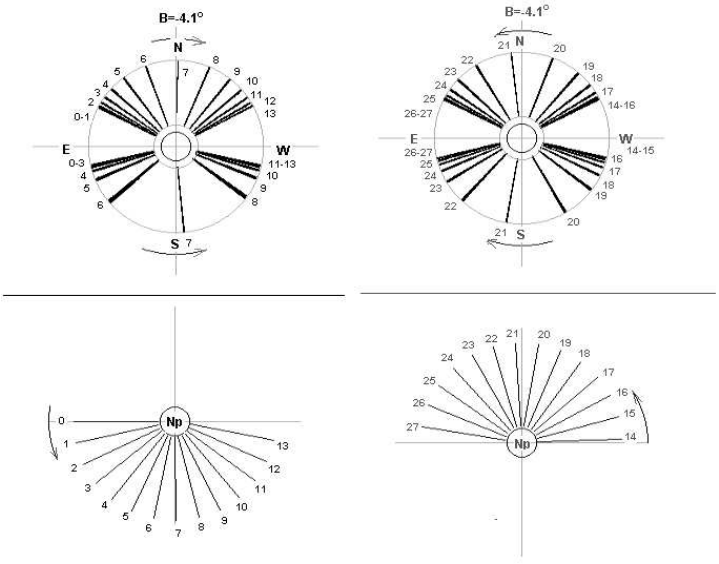

Figure 2. Explanation of the projection of a coronal streamer to the plane of the sky during the rotation of the Sun. On the Northern hemisphere a streamer with $b = 30°$ is shown, on the Southern one a streamer with $b = -15°$. Np denotes the North pole of the Sun.

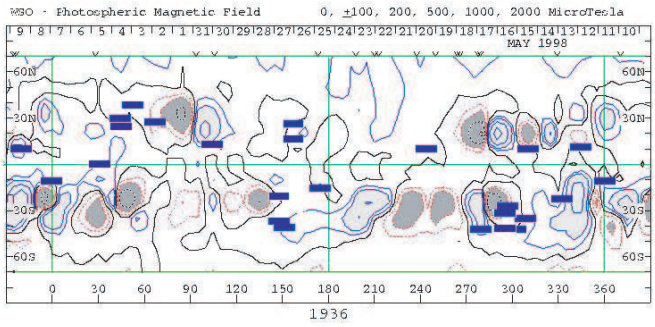

Figure 3. Synoptic map of magnetic field from Wilcox Solar Observatory together with position of identified streamers depicted by rectangles (`http://quake.stanford.edu/`).

Essential observational material for our analysis were movies combining frames of LASCO's C2 and C3 instruments from May 1998 (C2_may98sm.mpeg and C3_may98sm.mpeg). The first file contains 1273 frames, the second 733 frames. By analyzing the motion of the projection of a streamer from consecutive frames we estimate heliographic latitude b as a minimal apparent width of streamer's projection. At a specific location we estimate also its heliographic longitude l as one at the limb.

3. Results and Conclusions

Using this method we succeeded satisfactorily (although not completely convincingly) to estimate the positions of 23 stable streamers with a precision in latitude of $\pm 5°$, in longitude of $\pm 15°$. The uncertainty is caused mainly by two reasons. The first one is the occurence of transients (36 larger CMEs were observed during May 1998). The second is the fact that sometimes streamers in front of the disk and behind it are projected to the same location. We could not estimate the heliographic longitude of 8 streamers which were projected to the equatorial zone. The position of the identified streamers is plotted in the synoptic magnetic-field map in Fig. 3.

Table 1. Distance ρ to which we can observe rays (anchored at a latitude b above the poles). Note: C2 instrument is able to observe corona from $\rho = 1.5$ and C3 from $\rho = 3.0$.

b	5°	10°	15°	20°	30°	40°
ρ (LASCO C2)	17.2	8.6	5.8	4.4	3.0	2.3
ρ (LASCO C3)	34.4	17.3	11.6	8.8	6.0	4.7

We may state the following facts about the identification of coronal streamers:

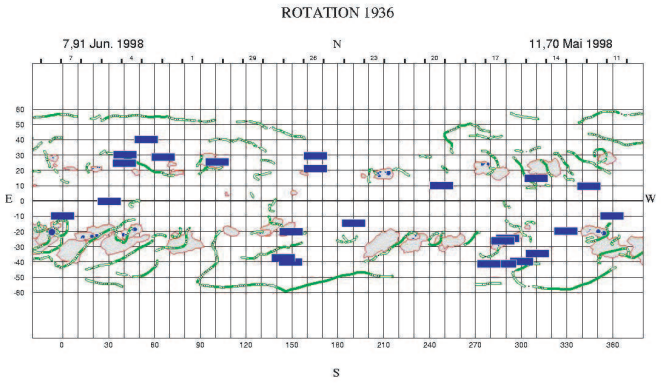

Figure 4. Synoptic map of filaments from the Meudon Observatory together with depicted position of coronal streamers (`http://bass2000.obspm.fr/`).

1. None is anchored at latitudes larger than 40°. The apparent polar rays are in fact projections of more distant parts of rays at lower latitude, which occur in front or behind the Sun. In the case of rays anchored at a latitude b we observe above the poles rays to a distance of ρ (in solar radii) as specified in Table 1.

2. The majority of the identified streamers is anchored in active regions, near localities of strong magnetic fields and not in localities of filaments as it was supposed initially. Figure 4 shows streamer positions superimposed on a synoptic filament map from Meudon Observatory, France.

3. It is possible that at $(b, l) = (30°, 55°)$, $(-20°, 155°)$, and $(-38°, 290°)$ we observe a only a single streamer with a lifetime longer than 20 days.

4. The largest intensities of green coronal line 530.3 nm (Rybanský et al. 2005) occurred in Carrington rotation No. 1936 in the same localities as the identified coronal streamers, in accordance with statements 2 and 3 above.

However, these conclusions do not need to be general because they are derived from data of a single month (May 1998) when the solar activity was in the rising phase two years before acticity maximum.

Acknowledgments. This work was partially supported by grant POCTI-SFA-2-675 from FCT, MCTES, Lisbon (I. D.).

References

Rybanský, M., Rušin, V., Minarovjech, M., Klocok, L., Cliver, E.W., 2005, J. Geoph. Res., 110, A088106

The Physics of Chromospheric Plasmas
ASP Conference Series, Vol. 368, 2007
Petr Heinzel, Ivan Dorotovič and Robert J. Rutten, eds.

Non-LTE Analysis of Lyman-Line Observations of a Filament with SUMER

P. Schwartz[1], B. Schmieder[2] and P. Heinzel[1]

[1]*Astronomical Institute AS, Ondřejov, Czech Republic*
[2]*Observatoire de Paris, Section Meudon, LESIA, Meudon, France*

Abstract. We present non-LTE diagnostics of the filament observed by SOHO/SUMER on May 27, 2005 in the whole Lyman series. The filament was situated close to the disk center. The Lα observations were carried out with normal voltage of detector A. The slit was placed at the central part of the detector – outside the Lα attenuator. Therefore, the observed profiles of this line could be calibrated reliably.

1. Introduction

In previous works (Schwartz et al. 2006a,b) we made the non-LTE modeling of the profiles of Lβ and higher hydrogen Lyman lines observed in EUV filaments by SoHO/SUMER on October 15, 1999 and May 5, 2000. For the latter EUV filament we had also observations of the Hα profiles from THEMIS/MSDP. In Schwartz et al. (2006a) it was found that estimates the of temperature in the filament interior need not be reliable if there are temperatures lower than 10 000 K in the filament interior and rather hot PCTRs (prominence-corona transition regions) with temperatures above 20 000 K at the same time. These problems occur especially for the Hα filaments. This problem can be solved by constraining the models with the profile of the Hα line that is not sensitive to the high temperature plasma of PCTRs (Schwartz et al. 2006b). Therefore its shape represent well the temperature structure of the cool filament interior. However, the problem is to find suitable Hα observations with the same position of the slit and made at the same time, as the SoHO/SUMER observations. The optically thick cores of the Lyman lines are formed in the top PCTRs while the optically thick parts of the wings are formed deeper. Wavelength intervals where the profiles of Lβ and higher Lyman lines are optically thick, are small ($\sim \pm 0.2$ Å or even smaller). Outside these interval the filament is transparent. Therefore the wings of these lines do not map the temperature structure of filament much deeper then the top PCTR. The profile of the Lα line could be much more sensitive to the cooler hydrogen plasma deeper in the filament than higher Lyman lines. Its is because of the wide wavelength interval ($\sim \pm 0.3$ – 1.4 Å or even larger) of the optically thick part of the profile, possibly spreading far into the wings.

In this work we are modeling profiles of the Lyman lines, Lyman continuum and Hα line observed in the Hα filament using the 1D-slab non-LTE model (Heinzel et al. 1997). As the results of a such diagnostics we obtain the temperatures, the gas pressure, plasma densities, ionization degree etc.

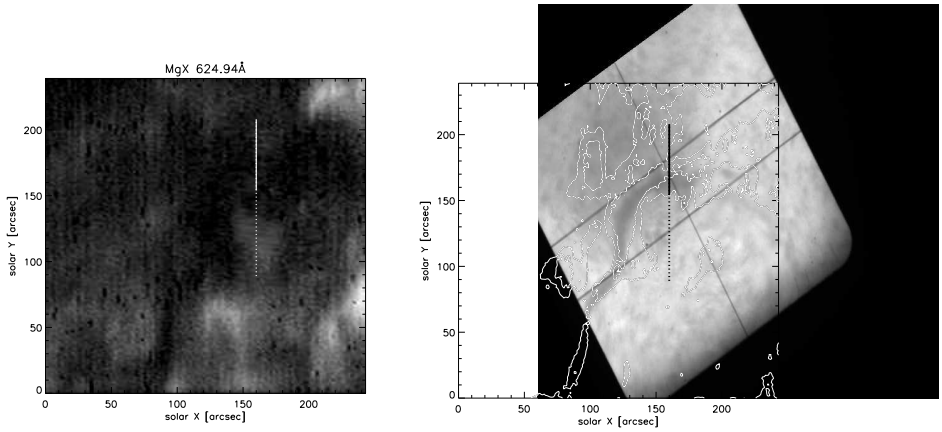

Figure 1. CDS observations of the EUV filament in the Mg X 624.94 Å line are shown in the left panel. In the right panel the slit-jaw of Hα observations of HSFA2 spectrograph are shown. The slit-jaw is co-aligned with the CDS observations of the He I 584 Å line represented by contours. The inclined hair crossed perpendicularly with two other hairs shows the position of the spectrograph slit during the observations of the Hα line. Vertical bar in both panels shows the position of the SUMER slit during the observations of the Lyman line series. Full-line part of the bar marks working part of the SUMER detector A.

2. Observations

A filament close to the solar disk (μ=0.9) was observed on May 27, 2005 (during the 15th MEDOC observing campaign), in EUV spectral lines by the CDS (Coronal Diagnostic Spectrometer) (Harrison et al. 1995) and SUMER (Solar Ultraviolet Measurements of Emitted radiation) (Wilhelm et al. 1995) both on-board of SoHO (Solar and Heliospheric Observatory) and in the Hα line by HSFA2 multicamera spectrograph at Ondřejov observatory. The SUMER observations of the filaments and prominences during this observing campaign are unique because the Lα line was placed on the bare part of the detector A (outside the attenuator) for the first time during any filament/prominence observations and thus it was possible to make a reliable calibration of the observed Lα profiles.

Observations with CDS and SUMER were carried out between 17:14 and 18:07 UT. CDS observed the EUV filament in three coronal EUV lines Mg X 624.94 Å, Ca X 557.77 Å and Mg IX 368.07 Å, two transition-region EUV lines O V 629.73 Å and Ne VI 562.80 Å and one chromospheric line He I 584.33 Å.

Position of the center of CDS rasters is 248″, −67″ (S 5 W 15 in Carrington coordinates) and their dimensions are 244″×240″. CDS observations in the Mg X 624.94 Å line are shown in the left panel of Fig. 1.

The Hα observations were carried out with the HSFA2 multicamera spectrograph of the Ondřejov observatory at 7:14 UT. The slit-jaw co-aligned with the CDS observations is shown in right panel of Fig. 1. The slit positions of HSFA2 and SUMER spectrographs are crossing the filament in different directions and the times of observations of HSFA2 and SoHO differs. However, since

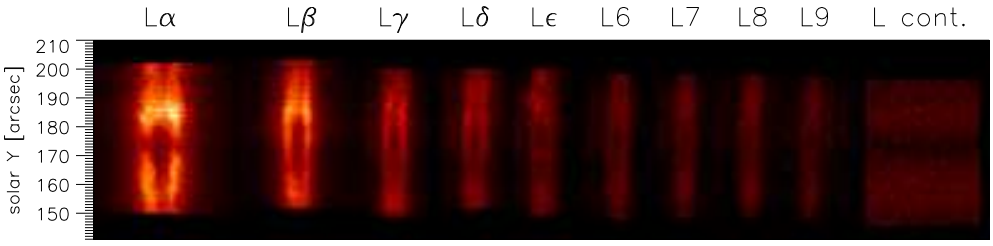

Figure 2. Spectra of the hydrogen Lyman lines Lα – L9 plus Lyman continuum observed by SUMER with detector A. The slit was positioned across the EUV filament as it is shown in the left panel of Fig. 1. Only 59″ of the spectra were obtained because only a part of the detector was working.

the filament seemed to be rather stable and compact, the HSFA2 observations of Hα could be used as additional data in our non-LTE modeling.

SUMER observed the EUV filament in a wide wavelength range so that the whole hydrogen Lyman line series is present. The spectra of Lyman lines Lα – L9 plus Lyman continuum are shown in Fig. 2. We do not use the lines L10 and L11 because with a 12-level model hydrogen atom our calculated populations of levels 11 and 12 are rather unprecise. Position of the SUMER slit during observation of the Lyman series is shown in Fig. 2. Only a part of the detector A was working therefore we obtained spectra from this part of the slit only (marked by full-line part of vertical bar in both panels of Fig. 1). This part of the slit is crossing almost only the darkest part of the EUV filament – the Hα filament.

3. Non-LTE Model of the Filament

A filament is approximated by the 1D horizontal isobaric slab (Heinzel et al. 1997) with temperature symmetrically decreasing from PCTRs to the interior. The radiative transfer is solved using MALI method (Heinzel 1995; Paletou 1995) and a 12-level model of the hydrogen atom. We used χ^2 minimization method proposed in Schwartz et al. (2006a) for fitting the observed profiles with synthetic ones. For reconstruction of Lyman line profiles emitted from beneath the filament (background irradiation) we used the method developed in Schwartz et al. (2006a) – the profiles of the background irradiation are identical with profiles from the filament in the optically thin wings. The optically thick cores of Lβ – L9 lines were reconstructed using the quiet-Sun profiles published by Warren et al. (1998). For Lα line the average profiles from the quiet-Sun observations carried out on April 14, 2005 between 13:26 and 14:26 UT were used (Dammasch 2006). During these observations the raster scan in the quiet-Sun area was made and the Lα line was placed at various positions on the bare part of the detector A. There was a problem with the reconstruction of the background--irradiation profiles of the Lα line because the width of the wavelength interval of optically thick central part of its profile is much more sensitive to optical thickness in the line center than it is for higher Lyman lines. Therefore only those optically thick parts of profiles of this line were modeled which transmit no radiation from below the filament.

4. Results and Conclusions

We obtained similar plasma properties as for other two Hα filaments studied in Schmieder et al. (2003) and Schwartz et al. (2006a) – temperatures around 6 000 K and 20 000 K in the filament interior and PCTRs, respectively. PCTRs both occupy less than 30 % of the geometrical thickness of the filament, plasma densities are 10^{-14}– 10^{-13} g cm^{-3}, electron densities around 10^{10} cm^{-3} and the hydrogen ionization degree is lower than 0.5 in the filament interior. Only the estimated gas pressure ~ 0.4 dyn cm^{-2} is about 3 times lower than that estimated for two other filaments.

We compared results of our modeling when fitting profiles of the whole Lyman series plus Lyman continuum without Hα and results obtained with the Hα line but without Lα and found similar plasma properties in both cases. But when fitting only Lyman lines without Lα the temperatures in the filament interior were underestimated. From our analysis of the dependence of the contribution function (computed using Eq. (13) of Heinzel et al. 2005) on the geometrical depth we found that the core of the Lyman lines is formed at the top of PCTR, in contrast with the Hα line profile that is formed almost completely in the cool interior. However, due to large optical thickness of Lα, its near wings are formed in cool parts of the Hα filament and this helps to determine the temperature of the filament interior. Using the Hα line gives a similar result.

Acknowledgments. This work was partly supported by grants A3003203 and 1QS300120506 of the Grant Agency of the Academy of Sciences of the Czech Republic, institutional project AV0Z10030501, by ESA-PECS project No. 98030 and by the European Solar Magnetism Network (ESMN-HPRN-CT-2002-00313). SoHO is a space mission of international cooperation between ESA and NASA. The SUMER data have been reduced with the intensity calibration procedure developed at MPI Lindau and the wavelength calibration procedure of M. Carlsson. All observations were obtained during the 15th MEDOC observing campaign.

References

Dammasch I. E., 2006, private communication
Harrison R. A., Sawyer E. C., Carter M. K., et al., 1995, Solar Phys. 162, 233
Heinzel P., 1995, A&A 299, 563
Heinzel P., Anzer U., Gunár S., 2005, A&A 442, 331
Heinzel P., Schmieder B., Vial J.-C., 1997, in A. Wilson (ed.), ESA SP-404: Fifth SOHO Workshop: The Corona and Solar Wind Near Minimum Activity, 427
Paletou F., 1995, A&A 302, 587
Schmieder B., Tziotziou K., Heinzel P., 2003, A&A 401, 361
Schwartz P., Heinzel P., Schmieder B., Anzer U., 2006a, A&A 459, 651
Schwartz P., Schmieder B., Heinzel P., 2006b, in H. Lacoste (ed.), ESA SP-617: Proc. SOHO17: 10 Years of SOHO and Beyond, published on CDROM
Warren H. P., Mariska J. T., Wilhelm K., 1998, ApJS 119, 105
Wilhelm K., Curdt W., Marsch E., et al., 1995, Solar Phys. 162, 189

Part V

Chromospheric Flares

The Physics of Chromospheric Plasmas
ASP Conference Series, Vol. 368, 2007
Petr Heinzel, Ivan Dorotovič and Robert J. Rutten, eds.

Chromospheric Flares

Hugh S. Hudson

Space Sciences Laboratory, University of California, Berkeley

Abstract. In this topical review I revisit the "chromospheric flare". This should currently be an outdated concept, because modern data seem to rule out the possiblity of a major flare happening independently in the chromosphere alone, but the chromosphere still plays a major observational role in many ways. It is the source of the bulk of a flare's radiant energy – in particular the visible/UV continuum radiation. It also provides tracers that guide us to the coronal source of the energy, even though we do not yet understand the propagation of the energy from its storage in the corona to its release in the chromosphere. The formation of chromospheric radiations during a flare presents several difficult and interesting physical problems.

1. Introduction

Solar flares first revealed themselves as visual perturbations of the solar atmosphere ("white light flares") and hence immediately were construed as a photospheric process. With the invention of spectroscopic techniques, though, it became clear that chromospheric emission lines such as Hα revealed flare presence much more readily. This led to the concept of the "chromospheric flare" and to a great deal of observational material on Hα flares and eruptions, as reviewed by Smith & Smith (1963), Zirin (1966), or Švestka (1976), for example. At some point, prior to the discovery of coronal flare effects, the misinterpretations of the Hα line profile even led to the incorrect idea that a flare was a sudden *cooling* of the solar atmosphere. In any case, a perturbation of the lower solar atmosphere violent enough to affect the solar luminosity itself ("white light") implies a large energy content.

Our view of flares now emphasizes the high temperatures and non-thermal effects seen in the corona, and we generally believe the chromospheric effects themselves to be secondary in nature. This may be true, but nonetheless the modern observations confirm the fact that the lower solar atmosphere dominates the radiant energy budget of a flare via the UV and white-light continua. Somehow, therefore, the energy stored in the solar corona rapidly focuses down into regions visible in chromospheric signatures; this accounts for the high contrast of flare effects there. Thus the "chromospheric flare" remains essential to our understanding of the overall processes involved.

The chromosphere nowhere exists as a well-defined layer with a reproducible height structure. In this paper I use the term interchangeably with "lower solar atmosphere," embracing the phenomena of the visible photosphere through the transition region. During flares the structure of these "layers" and the physical conditions within them may change drastically. The changes generally

happen so fast and on such small spatial scales that we cannot observe them comprehensively. Understanding the impulsive phase in the chromosphere may therefore seem like something of a lost cause from the the point of view of theory, especially in view of our inability to understand the *quiet* chromosphere any better than we do. The data repeatedly reveal that we simply have not yet resolved the spatial or temporal structures involved in the impulsive phase, and that without knowing the geometry of the physical structure, we cannot really comprehend its physics. The TRACE (Handy et al. 1999) and RHESSI (Lin et al. 2002) observations have provided more than one recent breakthrough, however, and it may be that we are beginning to understand the *gradual* phase of a flare at least.

This review is organized around several topics involving the behavior of the chromosphere during a flare. These include the process of "chromospheric evaporation" (Section 4), flare energetics (Section 5), the mechanisms of flare continuum emission (Section 6), and the inference of flare structure from the morphology of the chromospheric flare (Section 7 and Section 9). In Section 2 and Section 3 we give an overview of the history of chromospheric flares and show a cartoon to establish a working model of a solar flare. Sections 8 and 11 discuss large-scale magnetic reconnection and theoretical ideas, and Section 10 presents a γ-ray mystery.

2. Historical Development

Although it was the white-light continuum that initially revealed the existence of solar flares, the advent of spectroscopy (e.g., Hale 1930) allowed their regular observation via the Hα line (see Švestka 1966 for a discussion of the historical development of these observations). This strong absorption line actually becomes an emission line during bright flares, and Hα limb observations frequently show prominences and eruptions. Hα observers came to recognize a particular flare morphology, the so-called two-ribbon flare. Bruzek (1964) described the patterns followed by these events, which provided strong evidence that the solar corona had to play a major role in flare development. Figure 1 reproduces one of Bruzek's sketches, and then illustrates in a cartoon (due to Anzer & Pneuman 1982) how this morphology led to our standard magnetic-reconnection scenario that tries to embrace the X-ray observations and the coronal mass ejections (CMEs) as well as the chromospheric ribbon structures.

In this standard picture a solar flare develops in a complicated manner that involves restructuring of the coronal magnetic field in such a way as to release energy. The immediate effects of this energy release are to produce broad-band "impulsive phase" emissions and to drive chromospheric gas up into coronal magnetic loops, the process we term "chromospheric evaporation." A part of the field magnetic structure may actually erupt and open out into the solar wind, in the sense that the field lines stretch out past the Alfvé n critical point of the flow. This opening may consist of rising loops which then take the form of a coronal mass ejection (CME), or it may involve interactions with previously open field (a process often termed "interchange reconnection" nowadays; see Heyvaerts et al. 1977). If a CME does accompany the flare, as it almost invariably does for flares of GOES class X or greater, the energy involved in mass motions may

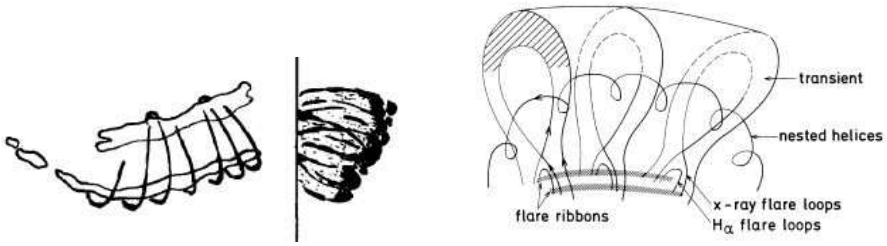

Figure 1. Left: one of Bruzek's (1964) sketches, showing a flare with ribbons on the disk and its equivalent Hα "loop prominence system" over the limb. This key observational pattern led directly to the formation of our standard flare model (right), in the form presented by Anzer & Pneuman (1982).

be comparable to the luminous energy (e.g., Emslie et al. 2005). Generally the observations are limited in resolution, both temporal and spatial, and especially in spectral coverage. Thus we often resort to a cartoon that serves to identify how the essential parts of a flare relate to one another.

Soft X-ray observations show hot loops in the gradual phase of a flare. These result from the material "evaporated" from the chromosphere and have anomalously high gas pressure (but still low plasma β; but see Gary 2001). Whereas the pressure at the base of the corona normally is of order 0.1 dyn cm^{-2}, a bright flare loop can achieve 10^3 dyn cm^{-2}. This over-dense and over-hot coronal loop gradually cools, and in its final stages the remaining plasma returns to a more chromospheric state and suddenly becomes visible in Hα (Goldsmith 1971). The loops that have reached this state then form Bruzek's Hα loop prominence system (Fig. 1).

During the ribbon expansion another important phenomenon occurs: hard X-ray emission appears at the footpoints of the coronal loops that are in the process of being filled by chromospheric evaporation (Hoyng et al. 1981). The hard X-rays show that a substantial part of flare energy appears in the form of non-thermal electrons (Kane & Donnelly 1971; Lin & Hudson 1976; Holman et al. 2003). The hard X-ray signature (and hence the energetic dominance of these electrons) is present whether or not the flare develops the two-ribbon morphology or has a CME association.

The hard X-ray emission occurs in the impulsive phase of the flare, contemporaneously with the period of chromospheric evaporation that fills the coronal loops and with the acceleration phase of the associated CME (Zhang et al. 2001). In Section 5 we describe this phase of the flare with the thick-target model (Kane & Donnelly 1971) which Hudson (1972) identified with the energy source of white-light flare continuum.

3. The Flare Spectrum

A (major) flare can be observed at almost any wavelength in a fast-rise/slow-decay time profile, with some (e.g., the white-light continuum) having a more impulsive variability, and others (e.g., the Balmer lines) having a more gradual pattern (Fig. 2, right). We generally describe a flare as consisting of a foot-

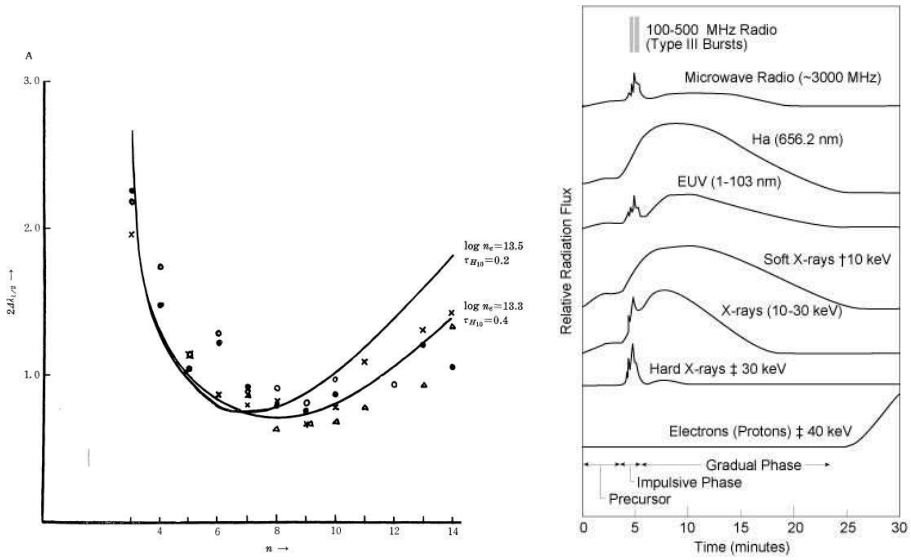

Figure 2. *Left*: Line widths of the Balmer-series lines, from the classic paper by Suemoto & Hiei (1959). The inferred densities added to the curves are $\log n_{\rm e} = 13.5$ and 13.3; the inferred filling factor is small, suggesting either filamentary structure or thin layering. *Right*: Typical time series of flare radiations, distinguishing the impulsive phase from the gradual phase (see Kane & Donnelly 1971).

point and ribbon structures in the lower atmosphere, coronal loops, and various kinds of ejecta. The impulsive phase is typically associated with the footpoint structures, and the gradual phase with the flare ribbons. Nowadays imaging spectroscopy in principle allows us to study these regions independently.

Flare spectroscopy began with the observation of the Balmer series, which shows broad lines tending towards emission profiles as the flare gets more energetic. Early observations of the higher members of the sequence allowed the inference of a relatively high density and of a small filling factor (Suemoto & Hiei 1959; see the left panel of Fig. 2). Such observations refer to what we would now call the *gradual phase* of the flare (see the right panel of Fig. 2 for a sketch of the temporal development of a flare). In the *impulsive phase* the continuum appears in emission, as noted originally by Carrington and by Hodgson independently. The weak photospheric metallic lines may also go weakly into emission (or are filled in by continuum) and the recent observations of Xu et al. (2004) show that flare effects can appear even at the "opacity minimum" region of the spectrum, where one would expect much higher densities. In fact a single density could never properly describe such a heterogeneous structure, but each spectral band provides its own clues. At the time of writing no proper analysis of spectroscopic "response functions" (e.g., Uitenbroek 2005) for any of the signatures has yet been attempted, so our inference of flare structure from the spectroscopy alone is weak.

The continuum radiation seen in white light and the UV constitutes the bulk of flare radiated energy (Kane & Donnelly 1971; Woods et al. 2006). TRACE imaging of this emission component shows it to consist of unresolved, intensely

bright fine structures (Hudson et al. 2006). The thick-target model invokes fast electrons (energies above about 10 keV) to transport coronal energy into the chromosphere. Here collisional losses provide the heating and footpoint emissions that accompany the hard X-ray bremsstrahlung. The thick-target model does not explain the particle acceleration, nor show how the footpoint sources can be so intermittent. We return to this question in Section 7.

The spectra emitted at the footpoints of the flaring coronal loops have contributions over an exceptionally broad wavelength range, as sketched in the right panel of Fig. 2. The prototypical observable is the hard X-ray flux, which imaging observations show to be concentrated at the footpoints (Hoyng et al. 1981), but impulsive footpoint emissions also occur in many spectral windows ranging from the microwaves (limited presumably by opacity) to the γ-rays (limited presumably by detection sensitivity). There is a large body of work on the Hα line alone, both observation and theory. Berlicki (2007) reviews the Hα spectroscopic material in detail on p. 387 ff in these proceedings. A strong absorption line forms across a wide range of continuum optical depths, and in principle this single line might provide sufficient information to infer the physical structure of the flare everywhere. In practice the complexities of the radiative transfer and of the flare motions, especially in the impulsive phase, make this information ambiguous (see Berlicki 2007).

4. Chromospheric Evaporation

The motions most directly relevant to the chromosphere are often called "chromospheric evaporation," even though the direct Doppler signatures of this motion are normally found in lines formed at higher temperatures (but see Berlicki et al. 2005). That this process occurs (even if it is not "evaporation" strictly speaking) was suggested by the early observations of loop prominence systems (e.g., Bruzek 1964) with their "coronal rain," and Neupert (1968) established its association with non-thermal processes such as bursts of microwave synchrotron radiation. The thermal microwave spectrum (e.g., Hudson & Ohki 1972) made it particularly clear that the gradual phase of a solar flare involves the temporary levitation of chromospheric material into the corona, as opposed to the process that might be imagined from the earlier term "sporadic coronal condensation" (e.g., Waldmeier 1963). The flows involved in chromospheric evaporation are along the field direction and serve to create systems of coronal loops with relatively high gas pressure and therefore higher (but still probably low) plasma beta.

The early observational indications of chromospheric evaporation actually came from blueshifts in EUV and soft X-ray lines (e.g., Antonucci et al. 1982; Acton et al. 1982) such as those from Fe XXV or Ca XIX. Figure 3 shows an image-resolved view of Doppler shifts in an evaporative flow (Czaykowska et al. 1999). The chromospheric effects are more subtle and in fact the impulsive-phase evaporation is difficult to disentangle from other effects (Schmieder et al. 1987). The high-temperature blueshifts correspond to upward velocities of some hundreds km/s and seldom appear in the absence of a stationary emission line; in other words, hot plasma has already accumulated in coronal loops as the process continues. Based on theory and simulations (Fisher et al. 1985) one can

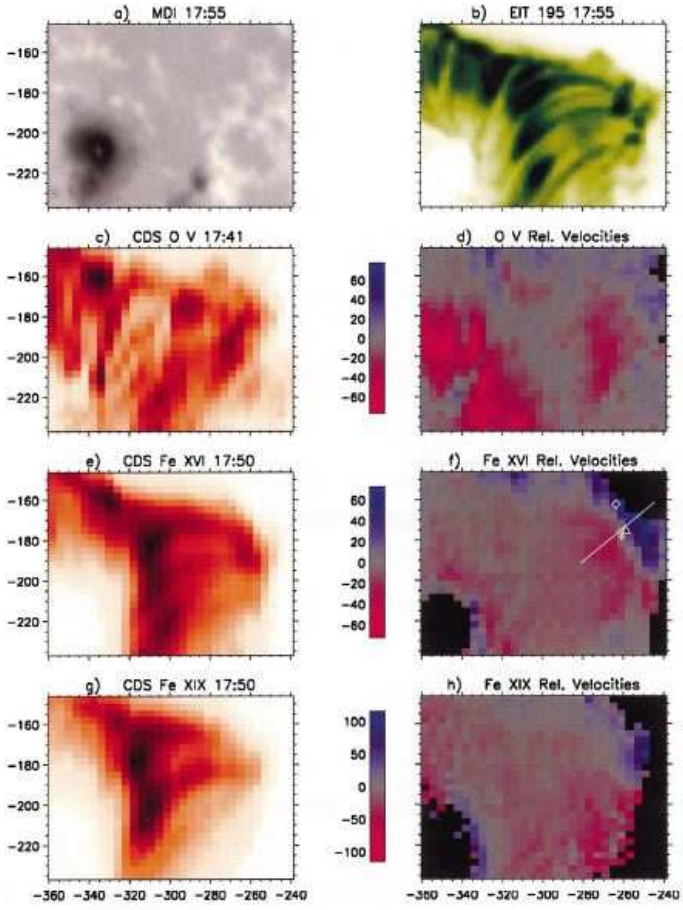

Figure 3. Imaging spectroscopy from SOHO/CDS of EUV emission lines in the gradual phase of a two-ribbon flare, showing the clear signature of blueshifted upflows in the expected locations along the flare ribbons. This is "gentle" evaporation not associated with strong hard X-ray emission (from Czaykowska et al. 1999). Note that CDS produces images by scanning in one spatial dimension, so that each image (while monochromatic) is not instantaneous.

distinguish "explosive" and "gentle" evaporation, depending upon the physics of energy deposition (e.g., Abbett & Hawley 1999). In explosive evaporation, driven hypothetically by an electron beam, one has the additional complication of a "chromospheric condensation" that produces a redshift as well. Schmieder et al. (1987) and Berlicki et al. (2005) survey our overall understanding. It would be fair to comment that the explosive evaporation stage remains ill-understood, even though it principle it describes the key physics of sudden mass injections into flare loops.

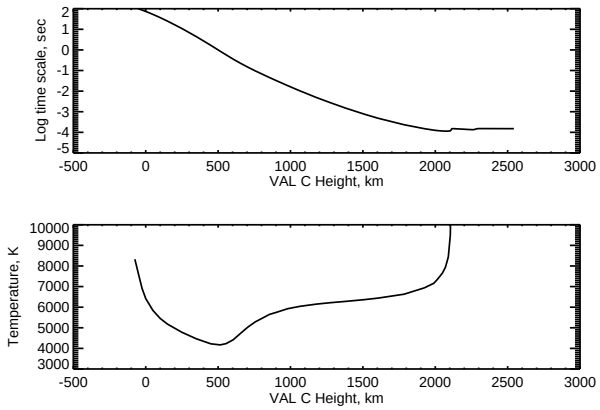

Figure 4. Characteristic radiative cooling time (upper) as a function of height in the VAL-C model, crudely estimated as described in the text. The lower panel shows the temperature in this model.

5. Energetics and Magnetic Field

We can use the standard VAL-C model (Vernazza et al. 1981), as discussed further in the Appendix, to discuss the energetics. First we establish that the chromosphere and the rest of the lower solar atmosphere (i.e., that for which $\tau_{5000} < 1$) have negligible heat capacity and limited time scales. Figure 4 shows an estimate of the radiative time scale in the VAL-C model (Vernazza et al. 1981). This shows $3\sigma(z)kT/\mathcal{L}_\odot$, where σ is the surface density as a function of height about the $\tau_{5000} = 1$ layer, and $\mathcal{L}_\odot$ the solar luminosity. The time scale decreases below 1 sec only above $z \sim 515$ km, near the temperature minimum in the VAL-C model. Above this height any energy injected into the system will tend to radiate rapidly, resulting in a direct energy balance between input and output energy, rather than a local storage and release. At lower altitudes we would not expect to see rapid variability.

The model also allows us to ask whether the chromosphere itself can store energy comparable to that released in a major flare or CME. Table 1 gives some order-of-magnitude properties for a chromospheric area of 10^{19} cm^2, showing both possible sources (bold) and sinks (italics) of energy. For the magnetic field we simply assume 10 or 1000 G as representative cases. Using the total magnetic energy in this manner is an upper limit, since the actual free energy would depend on its degree of non-potentiality. We find that magnetic energy storage limited to the volume of the chromosphere will not suffice, unless unobservably small-scale fields there somehow dominate. The gravitational potential energy also will not suffice. Estimates of this sort confirm the idea that the flare energy must reside in the corona prior to the event.

The estimate of gravitational potential energy is somewhat more ambiguous. The Table shows the value needed to displace the entire atmosphere by its total thickness, the equivalent of roughly $3''$ in the VAL-C model. There does not seem to be any evidence for such a displacement, although I am not aware of any searches. It is likely that the stresses that store energy in the coronal field

have their origin deeper in the convection zone, rather than in the atmosphere (McClymont & Fisher 1989). Actually the observable changes of gravitational energy are even of the wrong sign, given that we normally observe only outward motions, (against gravity) during a flare.

Table 1. Properties of a chromospheric volume of area $10^{19}\,\mathrm{cm}^2$

Parameter	VAL-C	VAL-C above $T_{\min}$
Mass	$4{\times}10^{19}$ g	$5{\times}10^{17}$ g
Magnetic energy	$1{\times}10^{28}$ erg	$8{\times}10^{27}$ erg (10 G)
Magnetic energy	$1{\times}10^{32}$ erg	$8{\times}10^{31}$ erg (10^3 G)
Gravitational energy[a]	$3{\times}10^{32}$ erg	$3{\times}10^{30}$ erg
Thermal energy	$2{\times}10^{31}$ erg	$3{\times}10^{29}$ erg
Kinetic energy	$3{\times}10^{29}$ erg	$3{\times}10^{27}$ erg
Ionization energy	$4{\times}10^{32}$ erg	$6{\times}10^{30}$ erg

[a]Potential energy for a vertical displacement of 2.5×10^8 cm

From Table 1 one concludes that the chromosphere probably does play a dominant role in the energetics of a solar flare, at least as described by a semi-empirical model such as VAL-C. This just restates the conventional wisdom, namely that the flare energy needs to be stored magnetically in the corona, rather than in the chromosphere where the radiation forms. Note that this is backwards from the relationship for steady emissions: the requirement for chromospheric heating is *larger* than that for coronal heating, so it is possible to argue that the steady-state corona actually forms as a result of energy leakage from the process of chromospheric heating (e.g., Scudder 1994).

We can make a similar estimate for energy flowing up from the photosphere. The Alfvén speed at $\tau_{5000} = 1$ ranges from 3 to $30\,\mathrm{km\,s^{-1}}$, depending on the field strength, in the VAL-C model (see Appendix). Below the surface of the Sun v_A drops rapidly because of the increase of hydrogen ionization. Thus chromospheric flare energy cannot have been stored just below the photosphere, since it could not propagate upwards rapidly enough (McClymont & Fisher 1989). This again supports the conventional wisdom that flare energy resides in the corona prior to the event.

To drive chromospheric radiations from coronal energy sources requires efficient energy transport, which is normally thought to be in the form of non-thermal particles (the "thick target model", Brown 1971; Hudson 1972) or in the form of thermal conduction as in the formation of the classical transition region. Both of these mechanisms provide interesting physical problems, but the impulsive phase of the flare (where the thick-target model usually is thought to apply) certainly remains less understood. Section 11 comments on models.

The magnetic field in the chromosphere is decisively important but ill-understood. The plasma beta is generally low (see Appendix), so just as in the corona the dynamics depends more on the behavior of the field itself than to the other forces at work. Generally we believe that the subphotospheric field exists in fibrils, implying the existence of sheath currents that isolate the flux tubes from their unmagnetized environment. On the other hand, the dominance of plasma pressure in the chromosphere as well as the corona implies that the field must rapidly expand to become space-filling. Longcope & Welsch (2000)

discuss the physics involved in this process as flux emerges from the interior. The effect of the flux emergence must be to create current systems linking the sources of magnetic stress below the photosphere, with the non-potential fields containing the coronal free energy. A full theory of how this works does not exist, and we must add to the uncertainty the possibilty of unresolved fields (e.g., Trujillo Bueno et al. 2004). Their suggested factor of 100 in B^2 would clearly affect the estimate of magnetic energy given in Table 1 and perhaps change everything. We note in this context that the "impulse response" flares (White et al. 1992) have scales so small that one could argue for an entirely chromospheric origin.

6. Energetics and the Formation of the Continuum

The formation of the optical/UV emission spectrum of a solar flare has from the outset presented a special challenge, since (a) it represents so much energy, and (b) it appears in what should be the stablest layer of the solar atmosphere. The recent observations of rapid variability and spatial intermittency make this all the more interesting, and these observations – now from space – also help to intercompare events; previous catalogs of white-light flares (e.g., Neidig 1989 and references therein) had to be based on spotty observations made with a wide variety of instruments. Observationally, the continuum appears to have two classes, with most events ("Type I" spectra) showing evidence for recombination radiation via the presence of the Balmer edge and sometimes the Paschen edge as well. A few events (e.g., Machado & Rust 1974) show spectra with weak or unobservable Balmer jumps, implicating H^- continuum as observed in normal photospheric radiation. The spectra in the latter class ("Type II") suggests a relationship to Ellerman bombs (Chen et al. 2001). However, the physics of Ellerman bombs appears to be quite different from that of solar flares (e.g., Pariat et al. 2004), though.

The strong suggestion from correlations is that non-thermal electrons physically transport flare energy from the corona, where it had been stored in the current systems of non-potential field structures, into the radiating layers. The hard X-ray bremsstrahlung results from the collisional energy losses of these particles, and other signatures (such as the optical/UV continuum) depends on secondary effects. Proposed mechanisms include direct heating, heating in the presence of non-thermal ionization, and radiative backwarming. In some manner these effects (or others not imagined) must provide the emissivity ϵ_ν, to support the observed spectrum. Note that the emissivity is often expressed in terms of the source function $S_\nu = \epsilon_\nu/\kappa_\nu$ via the opacity κ_ν. In a steady state one would have energy balance between the input (e.g., electrons) and the continuum. Fletcher et al. (2007) have now shown that this implies energy transport by low-energy electrons, below 25 keV, as opposed to the 50 keV or higher suggested by some earlier authors. Such low-energy electrons have little penetrating power and could not directly heat the photosphere itself from a coronal acceleration site. Thus either the continuum arises from altered conditions in the chromosphere, or some mechanism must be devised to link the chromosphere and photosphere not involving the thick-target electrons.

"Radiative backwarming" – for example Balmer and Paschen continuum excited in the chromosphere and then penetrating down to and heating a deeper

layer – could in principle provide a vertical step between energy source and sink. One problem with this is that the weaker backwarming energy fluxes might not cause appreciable heating in the denser atmosphere, and thus not be able to contribute to the observed continuum excess, because of the short radiative time scale. This idea is a variant of the mechanism of non-thermal ionization originally proposed by Hudson (1972) in the "specific ionization approximation," which involves no radiative-transfer theory and simply assumes ion-electron pairs to be created locally at a mean energy ($\sim$30 eV per ion pair). Finally, the rapid variability observed in the continuuum, even at 1.56 μm (Xu et al. 2006) provides a clear argument that the continuum forms at the temperature minimum or above (see Section 5, especially Fig. 4).

Early proponents of particle heating as an explanation for white-light flares also considered protons as an energy source (Najita & Orrall 1970; Švestka 1970). This made sense, because protons at energies even below those characteristic of γ-ray emission-line excitation can penetrate more deeply than the electrons that produce hard X rays. It makes even more sense now that we have the suggestion that ion acceleration in solar flares may rival electron acceleration energetically (Ramaty et al. 1995). Simnett & Haines (1990) suggest that particle acceleration in solar flares involves a neutral beam, implying that the major energy content (and hence the optical/UV continuum) would originate in the ion component. This idea does not appear to explain the apparent simultaneity of the footpoint sources (Sakao et al. 1996), and at present we do not understand the plasma physics of the particle acceleration and propagation well enough even to identify the location of the acceleration region.

7. Flare Structures Inferred from Chromospheric Signatures

The continuum kernels may move systematically for perhaps tens of seconds and generally have short lifetimes. We illustrate this in Fig. 5 (from Fletcher et al. 2004). This shows the motions of individual UV bright points within the flare ribbon structure. Such motions are only apparent motions, as in a deflagration wave, because they exceed the estimated photospheric Alfvén speed (see Section 4 and the Appendix). Figure 6 (from Hudson et al. 2006) makes the same point for a different flare, using TRACE white-light observations. The basic picture one gets from such observations is that the white light/UV continuum of a flare appears in compact structures that are essentially unresolved in space and in time within the present observational limits. These bright points contain enormous energy and thus must map directly to the energy source. We do not know if the fragmentation (intermittency) results from this mapping or is intrinsic to the basic energy-release mechanism.

How do the small chromospheric sources map into the corona, where the flare energy must reside on a large scale before its release? A strong literature has grown up regarding this point, interpreting the ribbon motions as measures of flux transfer in the standard magnetic-reconnection model (Poletto & Kopp 1986; see also literature cited, for example, by Isobe et al. 2005). The flux transfer in the photosphere is taken to measure the coronal inflow into the reconnecting current sheet, which appears to correlate with the radiated energy as seen in hard X-rays, UV, or Hα. Figure 1 (right) shows the assumed geometry

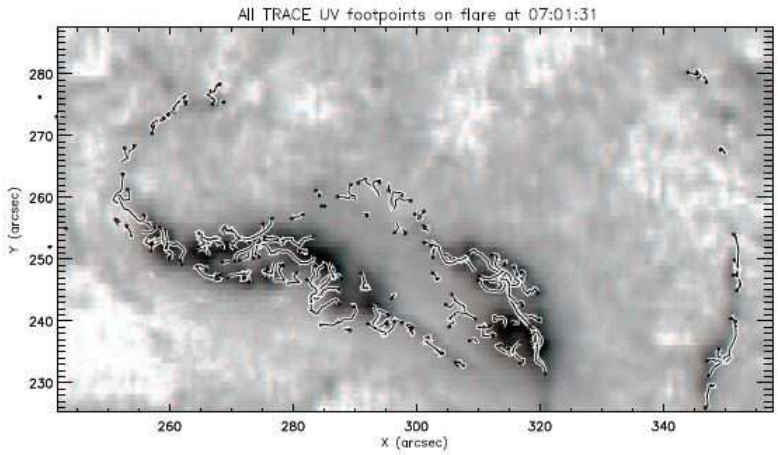

Figure 5. Flare footpoint apparent motions deduced from TRACE UV observations. Each squiggle represents the track of a bright point visible for several consecutive images at a few-second cadence, with the black dot showing the beginning of each track (Fletcher et al. 2004).

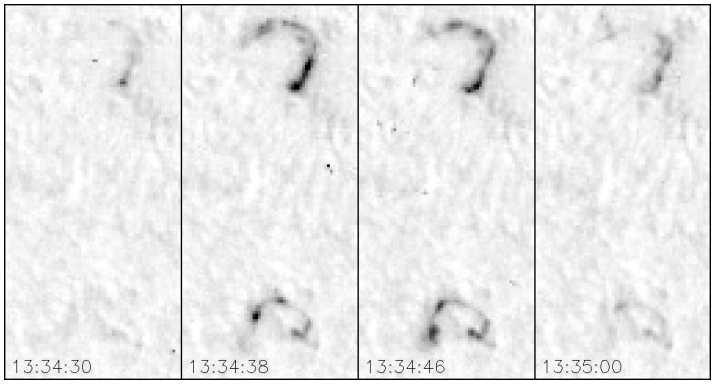

Figure 6. Intermittent structure seen in TRACE white-light images of an M-class flare on July 24, 2004. The individual frames have dimensions $32'' \times 64''$. Note the presence of bright features consistent with the TRACE angular resolution, and which change from frame to frame over the 30-second interval. These observations do not appear to resolve the fluctuations either in space or in time (Hudson et al. 2006).

linking the chromosphere and corona. The analysis extends to the multiple simultaneous UV footpoints apparently moving within the ribbons as they evolve, as noted in Fig. 5 above. The analyses suggest a strong relationship between energy release and the inferred coronal Alfvén speed.

8. Dynamics and Magnetic Reconnection

To release energy from coronal magnetic field in a largely "frozen-field" plasma, a flare must involve mass motions. We often do observe apparent motions,

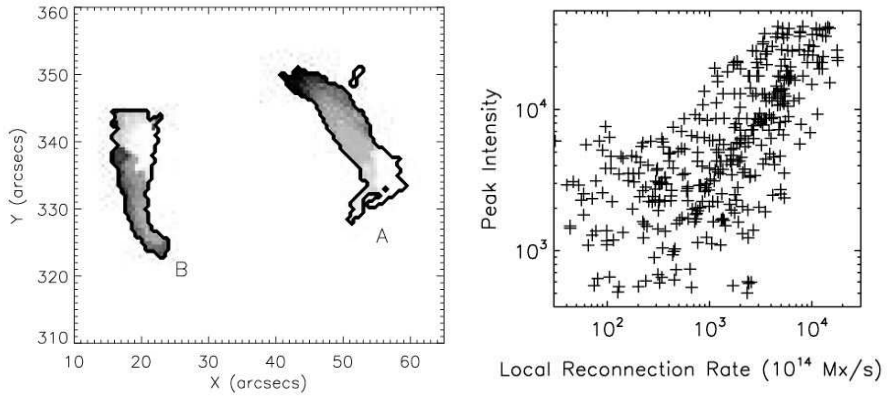

Figure 7. *Left:* UV ribbons (TRACE observations) from a flare of November 23, 2000. The gray scale shows the time sequence of brightening. *Right:* Correlation between pixel brightness in Ribbon A and the inferred reconnection rate (from Saba et al. 2006).

both parallel and perpendicular to the field as indicated by the image striations ("loops"). Most of the observable motions are outward, leading to the idea of a "magnetic explosion" (e.g., Moore et al. 2001). Motions apparently perpendicular to the magnetic field may become coronal mass ejections (CMEs) and contain a great deal of energy (e.g., Emslie et al. 2005). These perpendicular motions also are involved in flare energy release; for example the large-scale magnetic reconnection involved in many flare models (Fig. 1, right panel) necessarily involve "shrinkage" (e.g., Švestka et al. 1987; Forbes & Acton 1996). Note that this process is more of a magnetic implosion than a magnetic explosion (Hudson 2000).

The motion of flare footpoints and ribbons is (we believe) only apparent, because of the low Alfvén speed $v_{\rm A}$ in the photosphere, where the field is temporarily anchored ("line-tied"). For B =1000 G and $n = 10^{17}\,{\rm cm}^{-3}$ we find $v_A \sim 6\,{\rm km\,s}^{-1}$; observations often suggest motions an order of magnitude faster (e.g., Schrijver et al. 2006). The motions therefore represent a wave-light conflagration moving through a relatively fixed magnetic-field structure. It is natural to imagine that this sequence of field lines links to the coronal energy-release site, which the standard model identifies with a current sheet that mediates large-scale magnetic reconnection.

Figure 7 shows one example of the result of an analysis of the apparent motion of a flare ribbon (Saba et al. 2006). This and other similar analyses reveal a tendency for the "reconnection rate" to correlate with the pixel brightness. The reconnection rate is the rate at which flux is swept out in the ribbon motion, often expressed as an electric field from $\mathbf{E} = \mathbf{v}\times\mathbf{B}$ (the so-called "reconnection electric field"). In this picture the flare ribbons are identified with "quasi-separatrix structures" where magnetic reconnection can take place most directly.

9. Surges, Sprays, and Jets

Chromospheric material also appears in the corona in the form of surges and sprays, which may have a close relationship to the flare process (e.g., Engvold 1980). In addition, of course, we observe filaments and prominences in chromospheric lines, and these also have a flare/CME association, but too tangential for discussion in this review.

Surges and sprays are Hα ejecta, rising into the corona as a result of chromospheric magnetic activity. The literature traditionally distinguishes them by apparent velocity, with the faster-moving sprays taken to have stronger flare associations. Surges often appear to return to the Sun, while sprays accelerate beyond the escape velocity and do not return. Both appear to move along the magnetic field lines, but unlike the evaporation flow the surges and sprays incorporate material at chromospheric temperatures.

Modern soft X-ray and EUV data (Yohkoh, SOHO, and TRACE) have had sufficient time resolution to reveal the phenomenon of X-ray jets (Shibata et al. 1992); see also the UV observations of Dere et al. 1983. These tightly-collimated structures at X-ray temperatures have a strong correlation with surges and sprays, and indeed presumably lead to the jet-like CMEs seen at much greater altitudes (Wang & Sheeley 2002). These events have a strong association with emerging flux, and indeed the X-ray jets invariably have an association with microflares and originate in the chromosphere near the microflare loop(s) (Shibata et al. 1992). As Zirin famously remarked, most emerging flux emerges within active regions, and that is where the jets preferentially occur. The site is frequently in the leading part of the sunspot group. Figure 8 (Canfield et al. 1996) shows the sequence of events in an explanation of these phenomena invoking magnetic reconnection to allow chromospheric material access to open fields. Note that this scenario imposes two requirements on the chromosphere: there must be open and closed fields juxtaposed, and a large-scale reconnection process must be able to proceed under chromospheric conditions. The Canfield et al. (1996) observations strongly imply that this process requires the presence of vertical electric currents supporting the observed twisting motions.

The surges, sprays, and jets, not to mention flares and CMEs, underscore the time dependence and three-dimensionality characterizing what is often characterized as a thin time-independent layer for convenience. The subject of spicules is outside the scope of this review, but we note that they represent a form of activity that occurs ubiquitously outside the magnetic active regions.

10. A Chromospheric γ-ray Mystery

The γ-ray observations of solar flares have begun, as did the radio and X-ray observations before them, to open new windows on flare physics. Share et al. (2004) have made a discovery that is difficult to understand and which involves chromospheric material. They report observations of the line width of the 0.511 MeV γ-ray emission line formed by positron annihilation (Fig. 9). This emission requires a complicated chain of events: the acceleration of high-energy ions, their collisional braking and nuclear interactions in the solar atmosphere, the emission of secondary positrons by the excited nuclei, the collisional braking of these

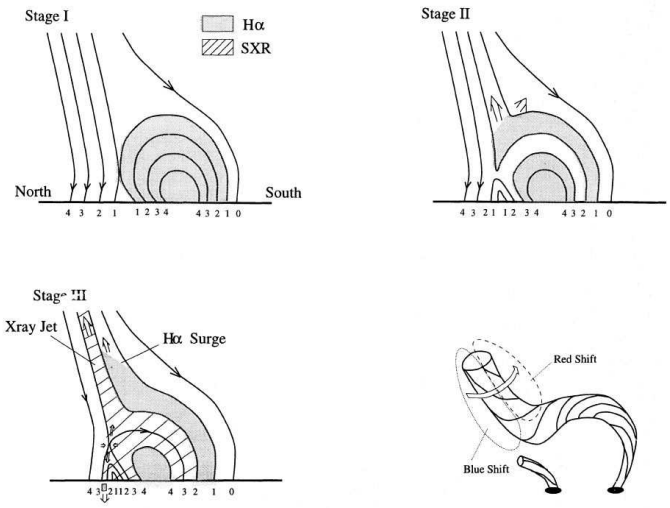

Figure 8. A mechanism for jet/surge formation involving emerging flux (upper left), with magnetic reconnection against already-open fields (upper right), which may lead to a high-temperature ejection (the jet) entraining chromospheric material (the surge). The cartoon at lower right describes the observations of (Canfield et al. 1996), who find a spinning motion suggesting that the process must occur in a 3D configuration rather than that of the cartoons left and above.

energetic positrons in turn, and finally their recombination with ambient electrons to produce the 0.511 MeV γ-rays. Because the γ-ray observations are so insensitive, this process requires an energetically significant level of particle acceleration that is possibly distinct from the well-known electron acceleration in the impulsive phase.

The mystery comes in the line width of the emission line. Surprisingly the pioneering RHESSI observations of Share et al. (2004) showed it to be broad enough to resolve. The likeliest source of this line broadening is Doppler motions in the positron-annihilation region. This requires the existence of a large column density (of order $\mathrm{g\,cm^{-2}}$) at transition-region temperatures; the transition region under hydrostatic conditions would be many orders of magnitude thinner (see also Fig. 11). According to Schrijver et al. (2006), the excitation of the footpoint regions during the the time of intense particle acceleration only continues for some tens of seconds at most. This would represent the time scale for the apparent motion of a foopoint source across its diameter. The γ-ray observations, on the other hand, require minutes of integration for a statistically significant line-profile measurement.

We therefore are confronted with a major problem. What is the structure of the flaring atmosphere that permits the formation of the broad 0.511 MeV γ-ray line? Recent spectroscopic observations of the impulsive phase in the UV, as viewed off the limb (Raymond et al. 2007) make a conventional explanation difficult.

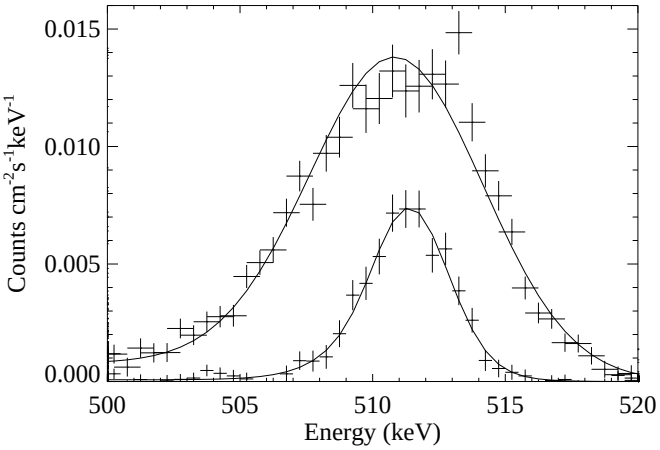

Figure 9. RHESSI γ-ray observations of the 0.511 MeV line of positron annihilation (Share et al. 2004). The two line profiles are from different integrations in the late phase of the X17 flare of 28 October 2003; for the broader line the authors suggest thermal broadening, which would require a large column depth of transition-region temperatures during the flare.

11. Theory and Modeling

To understand the chromospheric spectrum of a solar flare we must understand the formation of the radiation and its transfer in the context of the motions produced by (or producing) the flare. The representation of the spectrum by a "semi-empirical model" represents one shortcut; in such an approach (e.g., the standard VAL model that we use in the Appendix) one attempts to construct a model atmosphere capable of describing the spectrum even if it may not be physically self-consistent. Such descriptions may however be sufficient in the gradual phase of a flare when the flare loops no longer have energy input and simply evolve by cooling and draining. Even here, however, we do not have a good understanding of the "moss" regions that form at the footpoints of these high-pressure loops (but see Berger et al. 1999). So far as I am aware there is no literature specifically on "spreading moss," the similar structure that appears in association with flare ribbons.

A more complete approach to the physics comes from "radiation hydrodynamics" physical models, most recently those of Allred et al. (2005); see Berlicki (2007) for a fuller description. Such models solve the equations of hydrodynamics and radiative transfer simultaneously and can thus deal with chromospheric evaporation and the formation of the high-pressure flare loops. This framework is necessary if we are to be able to understand the flare impulsive phase (e.g., Heinzel 2003). Even these models do not have sufficient realism, though, since they work currently in one dimension and thus cannot follow the time development of the excitation properly; the high-resolution observations of UV and white light by TRACE clearly show that the energy release has unresolved scales. Further, as pointed out by Hudson (1972), the ionization of the chromosphere (and hence the formation of the continua) cannot be described by a fluid

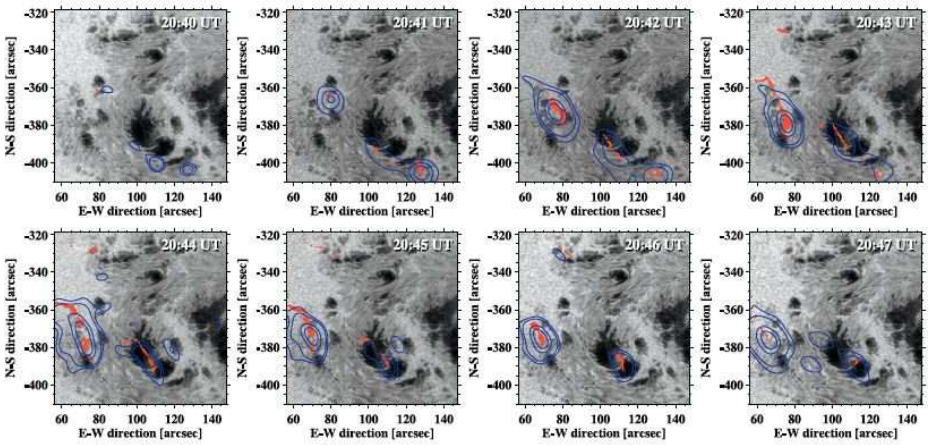

Figure 10. Continuum emission in the near infrared (1.56 μm, the "opacity minimum" region) during an X10 flare (Xu et al. 2004). Red shows the IR emissions, contours show the RHESSI 50-100 keV X-ray sources. The IR contrast relative to the preflare photosphere reached ∼20% in this event.

approximation, or even by non-LTE radiative transfer that assumes a unique temperature.

At present there has been little effort to create an electrodynamic theory of chromospheric flare processes, even though non-thermal particles are widely thought to provide the dominant energy in at least the impulsive phase. In the gradual phase there is interesting physics associated with heat conduction because the transition region would have to become so steep that classical conductivity estimates have difficulty (Shoub 1983). A more complete theory would have to take plasma effects into account and would probably contain elements of theories of the terrestrial aurora that are now largely missing from the solar lexicon. This lack of self-consistency in the modeling probably means that we have major gaps in our understanding of, for example, the evaporation process as it affects the fractionation of the elements and of the ionization states of the flare plasma. The Appendix gives estimates of the ranges of some the key plasma parameters in the chromosphere.

12. Conclusions

This article has reviewed chromospheric flare observations from the point of view of the newest available information – Yohkoh, SOHO, TRACE and RHESSI, for example, but not Hinode or STEREO (already launched), nor much less FASR or ATST (not launched yet at the time of writing). spite of the high quality of the data prior to these missions, we still find major unsolved problems:

- How does the chromosphere obtain all of the energy that it radiates?
- How can flare effects appear at great depths in the photosphere?
- How is the anomalous 0.511 MeV line width produced?
- What are the elements of an electrodynamic theory of chromospheric flares?

In my view the solution of these problems cannot be found in chromospheric observations alone, because the physical processes involve much broader regions of the solar atmosphere. Even providing answers to these specific questions may not reveal the plasma physics responsible for flare occurrence, which may involve spatial scales too fine ever to resolve. But we can hope that new observations from space and from the ground, in wavelengths ranging from the radio to the γ-rays, will enable us to continue our current rapid progress, and can speculate that eventually numerical tools will supplement the theory well enough for us to achieve full comprehension of the important properties of flares. To get to this point we will need to deal with the chromosphere, as messy as it is.

One important task that is probably within our grasp now is the computation of response functions for physical models of flares. At present these are restricted to very limited numerical explorations of the radiative transfer within the framework of one-dimensional radiation hydrodynamics (e.g., Allred et al. 2005). The energy transport in these models has been restricted to simplistic representations of particle beams for energy transport, and do not take account of complicated flare geometries, waves, or various elements of plasma physics. Future developments of chromospheric flare theory will need to complete the picture in a more self-consistent manner.

Acknowledgments. This work has been supported by NASA under grant NAG-5-12878 and contract NAS5-38099. I thank W. Abbett for a critical reading. I am also grateful to Rob Rutten for LaTeX instruction, and to Bart de Pontieu for meticulous keyboard entry.

Appendix: Plasma Parameters

The lower solar atmosphere marks the transition layer between regions of striking physical differences, and as one goes further up in height the tools of plasma physics should become more important. This Appendix evaluates for convenience several basic plasma-physics parameters for the conditions of the staple VAL-C atmospheric model (Vernazza et al. 1981)[1]. This is a "semi-empirical model" in which interprets a set of observations in terms of the theory of radiative transfer, but without any effort to have self-consistent physics. Such a model can accurately represent the spectrum but may or may not provide a good starting point for physical analysis. Because the optical depth of a spectral feature is the key parameter determining its structure, one often sees the model parameters plotted against continuum optical depth τ_{5000} evaluated at 5000 Å. Just for illustration, Fig. 11 shows the VAL-C temperature separately as a function of height, column mass, and optical depth. Note that features prominent in one display may appear to be negligible in another

The VAL-C model is an "average quiet Sun" model, and like all static 1D models, it cannot describe the variability of the physical parameters that theory and observation require (see e.g., Carlsson's review on p. 49 ff in these proceedings). Thus we should regard the plasma parameters estimated here as order-of-magnitude estimates only and note especially that the vertical scales, which depend in the model on the inferred optical-depth scale, may be systematically displaced.

The VAL-C model explicitly does not represent a chromosphere perturbed by a flare. Vernazza et al. (1981) and many other authors give more appropriate models

[1]The VAL-C parameters are available within SolarSoft as the procedure VAL_C_MODEL.PRO.

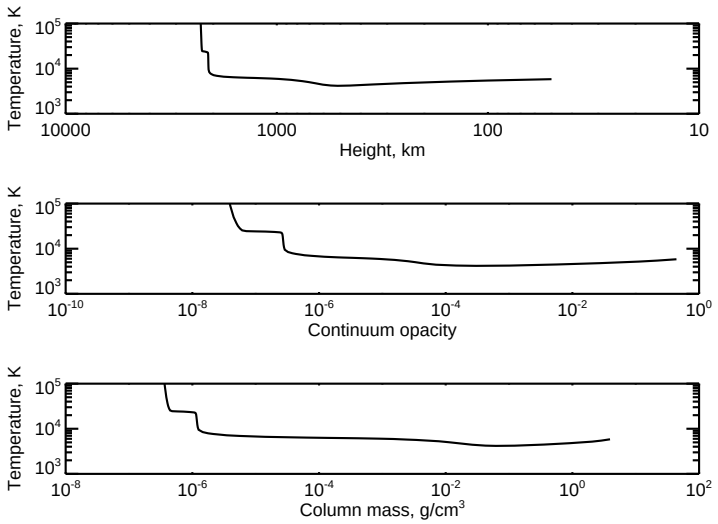

Figure 11. Illustration of the structure of a semi-empirical model, using three different independent variables: the VAL-C temperature plotted against height, optical depth, and column mass.

derived by similar techniques for flares as well as other structures. As the discussion of the γ-ray signatures in Section 10 suggests, though, a powerful flare may be able distort the lower solar atmosphere essentially beyond all recognition (especially in the impulsive phase). To estimate representative plasma parameters I have therefore chosen just to start with the basic VAL-C model, and we simply assume constant values of B at 10 G and 1000 G. The actual magnetic field may vary through this region (the "canopy") but the details are little-understood. The γ-ray literature usually uses a parametrization of the magnetic field strength $B \propto P_g^\alpha$ (Zweibel & Haber 1983), where P_g is the gas pressure.

The most complicated behavior of the plasma parameters happens preferentially near the top of the VAL-C model range (for example, Fig. 12 shows that the collision frequency decreases below the plasma and Larmor frequencies) above the helium ionization level (or even below this level for strong magnetic fields). Because VAL-C ignores time dependences and 3D structure, and assumes $T_\mathrm{e} = T_\mathrm{i}$, we can expect that it has diminished fidelity as one approaches the unstable transition region; thus one should be especially careful not to take these approximations too literally. The following notes correspond to each panel of the figure. Most of the plasma-physics formulae used in this Appendix are from Chen (1984).

Temperature: The VAL-C model, like all of the semi-empirical models, sets $T_\mathrm{e} = T_\mathrm{i}$. It therefore cannot support plasma processes dependent upon different ion and electron temperatures, or more complicated particle distribution functions (e.g. Scudder 1994).

Densities: Total hydrogen density, electron density, and densities of He I and He II.

Dimensionless parameters: We approximate the plasma beta as

$$\beta = \frac{2(n_\mathrm{H} + 2n_\mathrm{e})\, kT}{B^2/8\pi}$$

with n_H the hydrogen density, n_e the electron density. Figure 12(c) gives the number of electrons in a Debye sphere as the "plasma parameter" Λ.

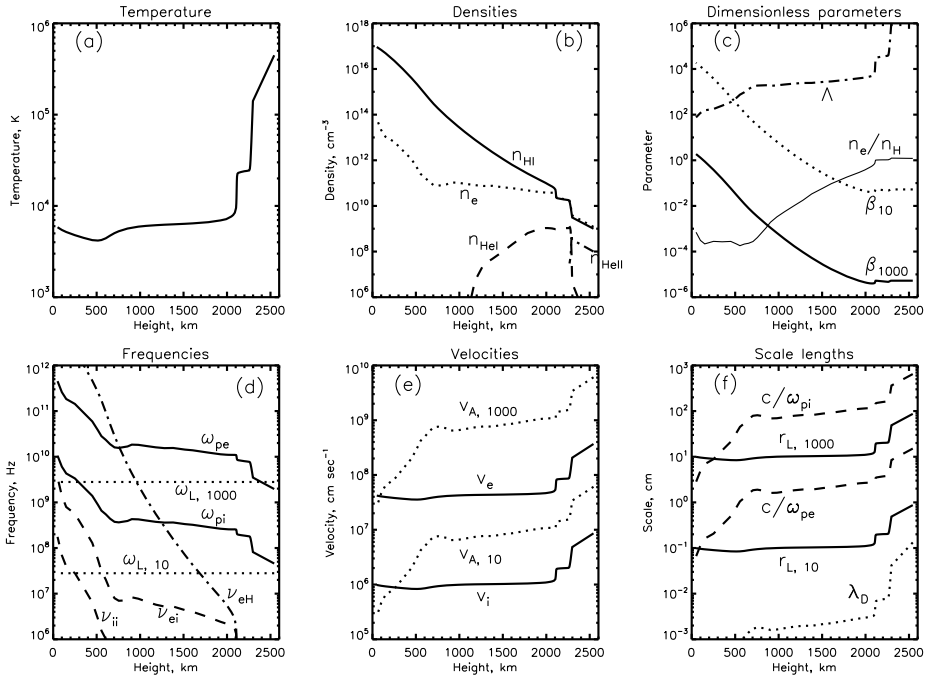

Figure 12. Various plasma parameters in the VAL-C model. We have assumed representative B values of 10 G and 1000 G. The different panels show the following, left to right and top to bottom: (a) Temperature. (b) Densities: solid, total hydrogen density; dotted, electron density; dashed, He I density; dash-dot, He II density. (c) Plasma beta: solid, for 1000 G; dotted, for 10 G; light solid, electron density as a fraction of total hydrogen density; dash-dot, the plasma parameter. (d) Frequencies. Solid, electron and ion plasma frequencies; dotted, electron gyrofrequencies for 10 and 1000 G; dashed, electron and ion collision frequencies; dash-dot, electron/neutral collision frequency. (e) Velocities: Solid, electron and ion thermal velocities; dashed, Alfvén speeds for 10 and 1000 G. (f) Scale lengths: solid, electron Larmor radii for 10 G and 100 G; dotted, Debye length; dashed, ion and electron inertial lengths.

Frequencies: The plasma frequency, the electron and proton Larmor frequencies, and the electron and ion and collision frequencies

$$\nu_{\rm ei} = 2.4 \times 10^{-6} n_{\rm e} \ln\Lambda / T_{\rm eV}^{3/2}; \quad \nu_{\rm ii} = 0.05 \times 4\nu_{\rm ei}; \quad \nu_{\rm eH} = (n_{\rm H}/n_{\rm e})\nu_{\rm e}$$

with $n_{\rm e}$ in cm^{-3}, $T_{\rm eV}$ the temperature in eV, using $Z = 1.2$ and the Coulomb logarithm $\ln\Lambda = 23 - \ln(n_{\rm e}^{0.5} T_{\rm eV}^{-1.5})$ (Chen 1984; De Pontieu et al. 2001).

Note that the collision frequencies are small compared with the plasma and Larmor frequencies above about 1000 km in this model. This means generally that plasma processes must have strong effects on the physical parameters of the atmosphere in this region.

Velocities: Electron and proton thermal velocities; Alfvén speeds $v_{\rm A}$ for 10 and 1000 G.

Scale lengths: Electron Larmor radii for 10 and 1000 G, the ion inertial length $c/\omega_{\rm pi}$, the electron inertial length $c/\omega_{\rm pe}$, and the Debye length $\lambda_{\rm D}$. The inertial lengths determines the scale for the particle demagnetization necessary for magnetic reconnection.

For VAL-C parameters the ion inertial length increases to about 100 m in the transition region.

References

Abbett W. P., Hawley S. L., 1999, ApJ521, 906
Acton L. W., Leibacher J. W., Canfield R. C., Gunkler T. A., Hudson H. S., Kiplinger A. L., 1982, ApJ263, 409
Allred J. C., Hawley S. L., Abbett W. P., Carlsson M., 2005, ApJ630, 573
Antonucci E., Gabriel A. H., Acton L. W., Leibacher J. W., Culhane J. L., Rapley C. G., Doyle J. G., Machado M. E., Orwig L. E., 1982, Solar Phys. 78, 107
Anzer U., Pneuman G. W., 1982, Solar Phys. 79, 129
Berger T. E., de Pontieu B., Fletcher L., Schrijver C. J., Tarbell T. D., Title A. M., 1999, Solar Phys. 190, 409
Berlicki A., Heinzel P., Schmieder B., Mein P., Mein N., 2005, A&A430, 679
Berlicki A., 2007, in P. Heinzel, I. Dorotovič, R. J. Rutten (eds.), The Physics of Chromospheric Plasmas, ASP Conf. Ser. 368, 387
Brown J. C., 1971, Solar Phys. 18, 489
Bruzek A., 1964, ApJ140, 746
Canfield R. C., Reardon K. P., Leka K. D., Shibata K., Yokoyama T., Shimojo M., 1996, ApJ464, 1016
Chen F. F., 1984, *Introduction to plasma physics, 2nd edition*, New York: Plenum Press, 1984
Chen P.-F., Fang C., Ding M.-D., 2001, Chinese Journal of Astronomy and Astrophysics 1, 176
Czaykowska A., de Pontieu B., Alexander D., Rank G., 1999, ApJ521, L75
De Pontieu B., Martens P. C. H., Hudson H. S., 2001, ApJ558, 859
Dere K. P., Bartoe J.-D. F., Brueckner G. E., 1983, ApJ 267, L65
Emslie A. G., Dennis B. R., Holman G. D., Hudson H. S., 2005, Journal of Geophysical Research (Space Physics) 110, 11103
Engvold O., 1980, in M. Dryer, E. Tandberg-Hanssen (eds.), IAU Symp. 91: Solar and Interplanetary Dynamics, p. 173
Fisher G. H., Canfield R. C., McClymont A. N., 1985, ApJ289, 434
Fletcher L., Pollock J. A., Potts H. E., 2004, Solar Phys. 222, 279
Forbes T. G., Acton L. W., 1996, ApJ459, 330
Gary G. A., 2001, Solar Phys. 203, 71
Goldsmith D. W., 1971, Solar Phys. 19, 86
Hale G. E., 1930, ApJ71, 73
Handy B. N. et al., 1999, Solar Phys. 187, 229
Heinzel P., 2003, Advances in Space Research 32, 2393
Heyvaerts J., Priest E. R., Rust D. M., 1977, ApJ216, 123
Holman G. D., Sui L., Schwartz R. A., Emslie A. G., 2003, ApJ595, L97
Hoyng P. et al., 1981, ApJ246, L155
Hudson H. S., 1972, Solar Phys. 24, 414
Hudson H. S., 2000, ApJ 531, L75
Hudson H. S., Ohki K., 1972, Solar Phys. 23, 155
Hudson H. S., Wolfson C. J., Metcalf T. R., 2006, Solar Phys. 234, 79
Isobe H., Takasaki H., Shibata K., 2005, ApJ632, 1184
Kane S. R., Donnelly R. F., 1971, ApJ164, 151
Lin R. P., et al., 2002, Solar Phys. 210, 3
Lin R. P., Hudson H. S., 1976, Solar Phys. 50, 153
Longcope D. W., Welsch B. T., 2000, ApJ545, 1089
Machado M. E., Rust D. M., 1974, Solar Phys. 38, 499
McClymont A. N., Fisher G. H., 1989, in J. H. Waite Jr., J. L. Burch, R. L. Moore (eds.), Solar System Plasma Physics, p. 219

Moore R. L., Sterling A. C., Hudson H. S., Lemen J. R., 2001, ApJ552, 833
Najita K., Orrall F. Q., 1970, Solar Phys. 15, 176
Neidig D. F., 1989, Solar Phys. 121, 261
Neupert W. M., 1968, ApJ 153, L59
Pariat E., Aulanier G., Schmieder B., Georgoulis M. K., Rust D. M., Bernasconi P. N., 2004, ApJ614, 1099
Poletto G., Kopp R. A., 1986, in *The Lower Atmosphere of Solar Flares*, p. 453
Ramaty R., Mandzhavidze N., Kozlovsky B., Murphy R. J., 1995, ApJ455, L193
Raymond J. C., Holman G., Ciaravella A., Panasyuk A., Ko Y. ., Kohl J., 2007, ArXiv Astrophysics e-prints 1359
Saba J. L. R., Gaeng T., Tarbell T. D., 2006, ApJ641, 1197
Sakao T., Kosugi T., Masuda S., Yaji K., Inda-Koide M., Makishima K., 1996, Advances in Space Research 17, 67
Schmieder B., Forbes T. G., Malherbe J. M., Machado M. E., 1987, ApJ317, 956
Schrijver C. J., Hudson H. S., Murphy R. J., Share G. H., Tarbell T. D., 2006, ApJ650, 1184
Scudder J. D., 1994, ApJ427, 446
Share G. H., Murphy R. J., Smith D. M., Schwartz R. A., Lin R. P., 2004, ApJ615, L169
Shibata K., et al., 1992, PASJ44, L173
Shoub E. C., 1983, ApJ266, 339
Simnett G. M., Haines M. G., 1990, Solar Phys. 130, 253
Smith H. J., Smith E. V. P., 1963, *Solar flares*, New York: Macmillan, 1963
Suemoto Z., Hiei E., 1959, PASJ11, 185
Trujillo Bueno J., Shchukina N., Asensio Ramos A., 2004, Nat430, 326
Uitenbroek H., 2005, AGU Spring Meeting Abstracts
Švestka Z., 1966, Space Science Reviews 5, 388
Švestka Z., 1970, Solar Phys. 13, 471
Švestka Z., 1976, *Solar Flares*, Dordrecht: Reidel, 1976
Švestka Z. F., Fontenla J. M., Machado M. E., Martin S. F., Neidig D. F., 1987, Solar Phys. 108, 237
Vernazza J. E., Avrett E. H., Loeser R., 1981, ApJS45, 635
Waldmeier M., 1963, Zeitschrift fur Astrophysik 56, 291
Wang Y.-M., Sheeley, Jr. N. R., 2002, ApJ575, 542
White S. M., Kundu M. R., Bastian T. S., Gary D. E., Hurford G. J., Kucera T., Bieging J. H., 1992, ApJ 384, 656
Woods T. N., Kopp G., Chamberlin P. C., 2006, Journal of Geophysical Research (Space Physics) 111, 10
Xu Y., Cao W., Liu C., Yang G., Jing J., Denker C., Emslie A. G., Wang H., 2006, ApJ641, 1210
Xu Y., Cao W., Liu C., Yang G., Qiu J., Jing J., Denker C., Wang H., 2004, ApJ607, L131
Zhang J., Dere K. P., Howard R. A., Kundu M. R., White S. M., 2001, ApJ559, 452
Zirin H., 1966, *The solar atmosphere*, Blaisdell: Waltham, Mass., 1966
Zweibel E. G., Haber D. A., 1983, ApJ264, 648

Jan Klimeš, Georgia Tsiropoula, Kostas Tziotziou

Pavol Schwartz, Stanislav Gunár, Michal Sobotka

The Physics of Chromospheric Plasmas
ASP Conference Series, Vol. 368, 2007
Petr Heinzel, Ivan Dorotovič and Robert J. Rutten, eds.

Observations and Modeling of Line Asymmetries in Chromospheric Flares

Arkadiusz Berlicki

Astronomical Institute, Wrocław University, Wrocław, Poland

Abstract. For many years various asymmetrical profiles of different spectral lines emitted from solar flares have been frequently observed. These asymmetries or line shifts are caused predominantly by vertical mass motions in flaring layers and they provide a good diagnostics for plasma flows during solar flares. There are many controversial results of observations and theoretical analysis of plasma flows in solar chromospheric flares. The main difficulty is the interpretation of line shifts or asymmetries. For many years, methods based on bisector techniques were used but they give a reliable results only for some specific conditions and in most cases cannot be applied. The most promising approach is to use the non-LTE techniques applied for flaring atmosphere. The calculation of synthetic line profiles is performed with the radiative transfer techniques and the assumed physical conditions correspond to flaring atmosphere. I will present an overview of different observations and interpretations of line asymmetries in chromospheric flares. I will explain what we have learnt about the chromospheric evaporation in the frame of hydrodynamical models as well as reconnection models. A critical review will be done on the classical methods used to derive Doppler-shifts for optically thick chomospheric lines. In particular, details on the new approach for interpreting chromospheric line asymmetries based on the non-LTE techniques will be presented.

1. Introduction

Spectroscopic observations of solar chromospheric flares show that the line profiles emitted by the flaring plasma almost always exhibit asymmetries or shifts. These features are surely due to the chromospheric plasma motion and the resulting Doppler-shifts effects. Interpretation of the shape of line profiles allows us to understand the nature of plasma flows during solar flares. Plasma flows in the chromosphere are important in the analysis of dynamics and energetics of solar flares as well as these phenomena supply matter to the coronal parts of flares in the process of chromospheric evaporation. Understanding of the mechanisms which generate flows is necessary for complete description of solar flares.

Spectral line asymmetries arise only because of the line-of-sight component of plasma velocity which due to the Doppler-shift is responsible for the modification of spectral line profiles. Therefore, for the flares located on the solar disk center we are able to analyze flows oriented perpendicular to the solar surface. For simplicity, the theoretical analysis of line asymmetries often assume that the emitting region is located on the solar disk center and only vertical flows are present.

Unfortunately, the interpretation of the shape of line profiles is not trivial and to determine the velocity field we must use advanced methods based on

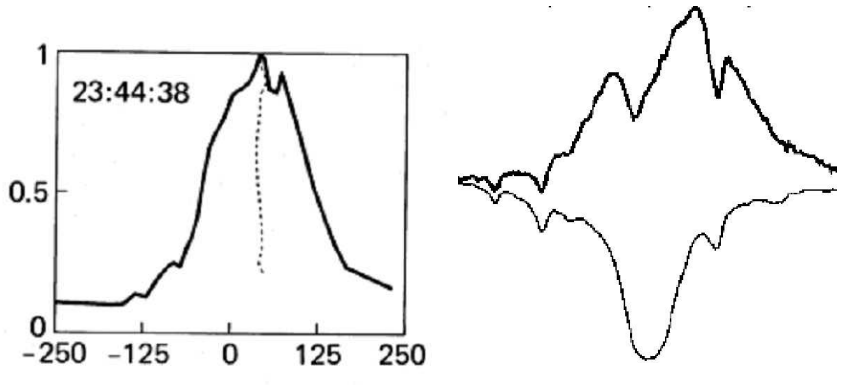

Figure 1. Two examples of the Hα line profiles observed during solar flares. *Left:* shifted profile – the Doppler velocity may be determined from the shift of the whole line. *Right:* complicated asymmetric profile – it is impossible to determine the Doppler velocity from such line profile using bisector methods.

hydrodynamical and radiative transfer techniques. There are some rare cases when the interpretation of line asymmetries is relatively simple. When the flow of the whole flaring region is homogeneous then the shape of the line is not disturbed compared to the static symmetric line profile, but the whole line is just shifted towards longer or shorter wavelengths (Fig. 1 – left). We can measure this shift and using a simple Doppler formula calculate specific value of the line-of-sight velocity. Unfortunately, in most cases the line profiles of solar flares exhibit much more complicated structure (Fig. 1 – right) which suggests that the velocity field is not homogeneous and different parts of the flare move in different way.

There are two main approaches to the modeling of chromospheric line asymmetries. One is based on the hydrodynamics calculations, where the time evolution of the solar flare atmosphere is calculated and the radiative transfer formulae are used to calculate the radiation from this evolving atmosphere. Another approach is based on semiempirical models of solar flares.

In this paper I will present a short review on observation and interpretation of the chromospheric line asymmetries observed during solar flares. The term chromospheric lines is commonly used to describe all spectral lines formed in the solar chromosphere, where the temperature is around 10^4 K. These lines are formed in strong non-LTE conditions and complicated radiative transfer calculations are necessary to describe the formation of these lines. Strong chromospheric lines are usually optically thick what means that the optical thickness of the plasma in these lines is very large ($\tau >> 1$).

There is a wide literature concerning this topic and I provide the readers some references contained the most important results. I will concentrate on chromospheric parts of solar flares where the emission comes from cool (10^4 K) plasma. This emission is produced mostly in strong resonance lines of hydrogen, calcium or magnesium (Hα, Hβ, Hδ, Ca II H, K, etc.) Since the most spectroscopic observations performed during past years concern Hα line, the interpretation of these results will take considerable part of this review.

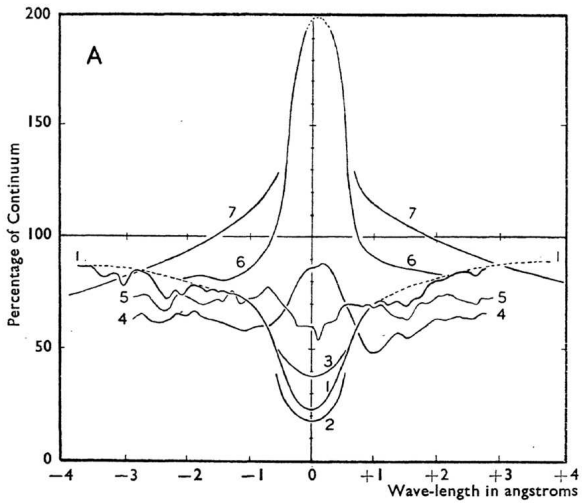

Figure 2. Examples of the observed Hα asymmetric line profiles. Profiles 4, 5, and 6 correspond to the flare emission (Ellison 1949).

2. Early Observations and Interpretations

Asymmetries of chromospheric lines emitted by the flaring plasma have been observed for more than half of the century. After the solar spectrographs were developed in order to produce the solar spectrum with sufficient spectral resolution, observers noticed that the line profiles emitted during solar flares are not symmetric (Fig. 2). It was clear from the beginning that these kinds of modifications of the spectral lines are due to the mass motion driven during solar flares. However, the mechanisms which could drive the plasma flows were not known yet at those days.

The first analysis of the line asymmetries were concentrated on statistical description of the behaviour of lines. Švestka et al. (1962) presented a qualitative analysis of 244 Hα and Ca II K spectra of 92 flares. They found that the blue asymmetry (blue wing enhancement) occurs mainly in the early phase of flares, before flare maximum. However, only 23% of flares contain at least one region with blue asymmetry. 80% of flares exhibit the red asymmetry which dominates during and after the maximum of flare. It is worth to notice that only 5% of flares shows blue asymmetry exclusively. However, because not all flares were observed from their beginning, the occurrence of blue asymmetry may be missed for many flares. In Fig. 3 the time evolution of the asymmetry is presented. Similar analysis was performed by Tang (1983). By inspection of off-band filtergrams of 60 flares obtained in ± 1 and ± 2 Å from the Hα line center he found that 92% of flares show red asymmetry and only 5% show blue asymmetry.

Early statistical analysis gave us an qualitative idea about the line asymmetry but the physical interpretation of the shape of line profiles is not considered. The asymmetric line profile contains an information about the velocity field in the region where the observed line is formed. Therefore, the first problem which needs to be solved is to determine this velocity field using the observed line pro-

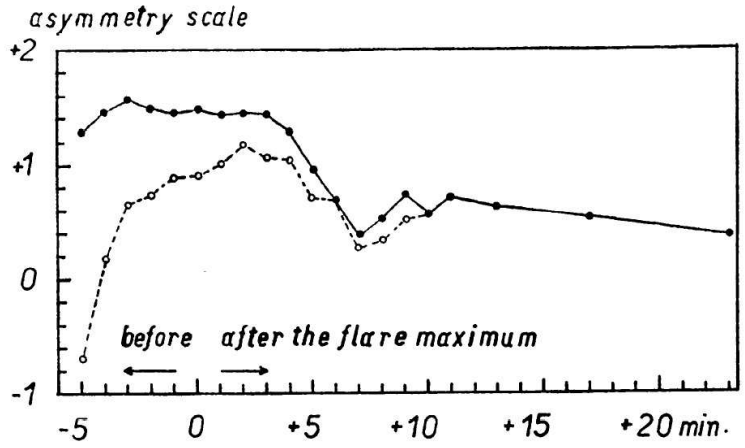

Figure 3. Absolute mean value of the asymmetry of the Hα line profiles as a function of time development of flares (solid line). Dashed curve takes positive and negative signs into account. Time of flare maximum = 0 (Švestka et al. 1962).

file. Secondly, we have to answer the question why do we observe such a flow of plasma, what can generate the flows?

Determination of the velocity from the observed profiles of the chromospheric lines is not a trivial task due to the complicated processes of line formation and complex velocity field in the chromosphere. Strong chromospheric lines are optically thick and the radiation observed at different parts of the line profile comes from different height z across the chromosphere (Mihalas 1978). The core of strong chromospheric lines (hydrogen Balmer lines, Ca lines) is formed much higher than the wings of these lines. Therefore, the asymmetry of the specific line depends on the relation between the height z of formation of given part of the line profile and the value of the velocity at this height. This means that if the function describing the velocity across the height in the chromosphere is complicated, the emergent line profile has also very complicated shape.

Despite of all difficulties with determining correctly the velocity from the line profile shape, many authors tried to use Hα, Ca II and other lines to find the velocity in the flaring chromosphere. All these determinations were based on the measurements of Doppler-shifts of the line cores or, more commonly, on the bisector technique.

Using the shift of the line core to obtain the velocity may be misleading and the determined velocity is not correct when the velocity gradient in the chromosphere is significant (Athay 1970). Unfortunately, the estimation of the Doppler-shift obtained with the bisector technique can also give wrong results. The Doppler-shift of the line profile correspond to the shift of the central point of the bisector connecting the two wings of the spectral line. Since the different parts of the spectral line are formed at different height in the chromosphere, using bisectors connecting the wings observed at different frequency, we can estimate the line-of-sight velocity at different layers of the chromosphere. However, because the radiation of specific frequency within the spectral line does

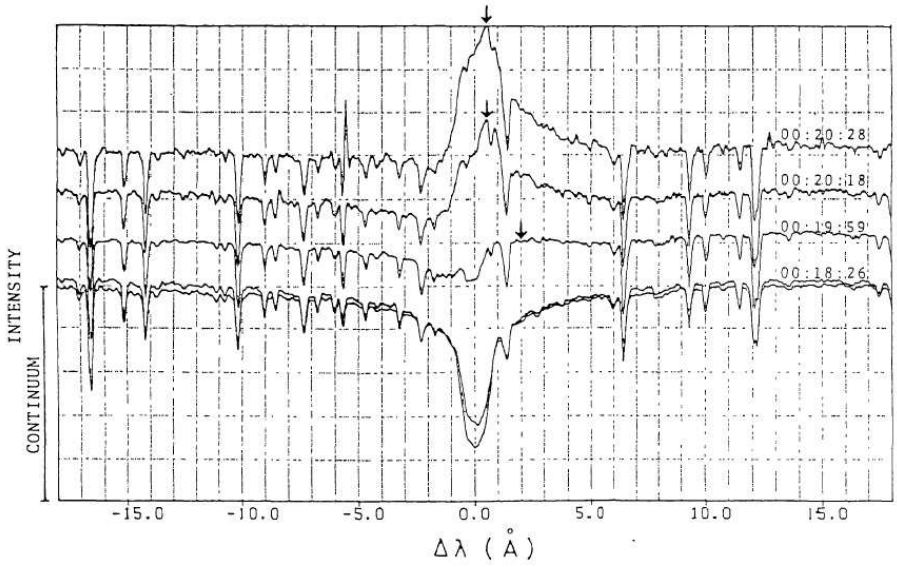

Figure 4. Temporal variation of the Hα line profiles observed during solar flare. The black arrow indicates the peak of asymmetric lines. The bottom profile represents the emission of the quiet-Sun area (Ichimoto & Kurokawa 1984).

not come from one narrow layer of the chromosphere but rather from geometrically thick region, we cannot say that the Doppler velocity determined form given bisector correspond to plasma flow at given height in the chromosphere. Moreover, if the velocity gradient in the chromosphere is large then the bisector method cannot be used because the Doppler-shift of any bisector results from a superposition of many shifts due to the motion of plasma with different velocity along line-of-sight. In spite of this the bisector technique was commonly used for many years until it was replaced by more advanced, complicated but much more precise non-LTE radiative transfer techniques with velocity field included.

One of the first interpretation of chromospheric line asymmetry observed during flare was presented by Acton et al. (1982). The authors postulated that these asymmetries are due to chromospheric evaporation driven by accelerated electrons or thermal conduction. Neupert (1968) was probably the first who realise that chromospheric plasma heated during solar flare may evaporate. This evaporated plasma provides material for loop prominences often observed as the so-called post-flare loops (Kopp & Pneuman 1976; Antiochos & Sturrock 1978). For more complete review of chromospheric evaporation see Hudson paper in this book. Acton et al. (1982) postulated that in the analysed flare the non-thermal electrons heat the chromosphere mainly during the impulsive phase, while thermal conduction from the hot coronal plasma heated earlier dominates during the late, thermal phase. Both mechanisms drive upflow of the cool plasma. The authors stress that for the first time they observed chromospheric evaporation in Hα line.

Contradictory results were published by Ichimoto & Kurokawa (1984) who suggested that during the impulsive phase of solar flares the downflow of the

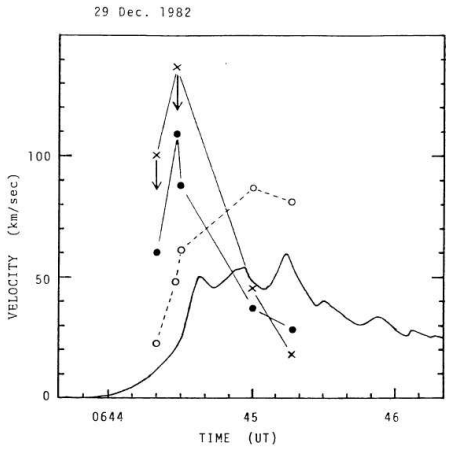

Figure 5. An example of temporal variation of the downflow velocity observed in flaring region. Filled circles correspond to the values obtained from the shift of the Hα far wings, while crosses to the values obtained from the shift of the line peak. Open circles represent the time evolution of the Hα intensity. The microwave emission at 3750 MHz is also shown (Ichimoto & Kurokawa 1984).

cool chromospheric plasma is present. These results are based on the large red asymmetry of the Hα line observed during the impulsive phase of many solar flares (Fig. 4). The downward motion increases at the onset of a flare to its maximum velocity of 40 to 100 km s^{-1} shortly before the impulsive peak of microwave emission, and rapidly decreases before the Hα reaches its maximum (Fig. 5). The red asymmetry of the Hα line may be also explained by the attenuation of the blue wing by the rising plasma over the flare but the authors exclude this case because the optical thickness of a rising cloud is too small to explain the emission deficit of the blue wing of Hα line. Also the high temporal resolution spectroscopic observations of Hα line performed by Wuelser (1987) confirm the existence of red asymmetry during the impulsive phase of solar flares. The largest asymmetry is observed during the maximum of microwave emission what confirms the earlier results that the plasma downflow is driven by the accelerated non-thermal electrons.

3. Hydrodynamic Modeling of the Flows

The downflow of cool plasma in the form of chromospheric condensations observed during solar flares was predicted theoretically by Fisher et al. (1985a). If a region of the chromosphere heated by non-thermal electrons is thick enough, then the rapid temperature increase produces an enhanced pressure in the heated region. This overpressure, besides the evaporation, also drives downward moving cool and dense chromospheric condensations (Fisher et al. 1985b) which seem to be responsible for red asymmetry of the Hα line profiles reported by many authors. Fisher et al. (1985b) modeled the hydrodynamic and radiative response of the atmosphere to short impulsive injections of non-thermal electron beams

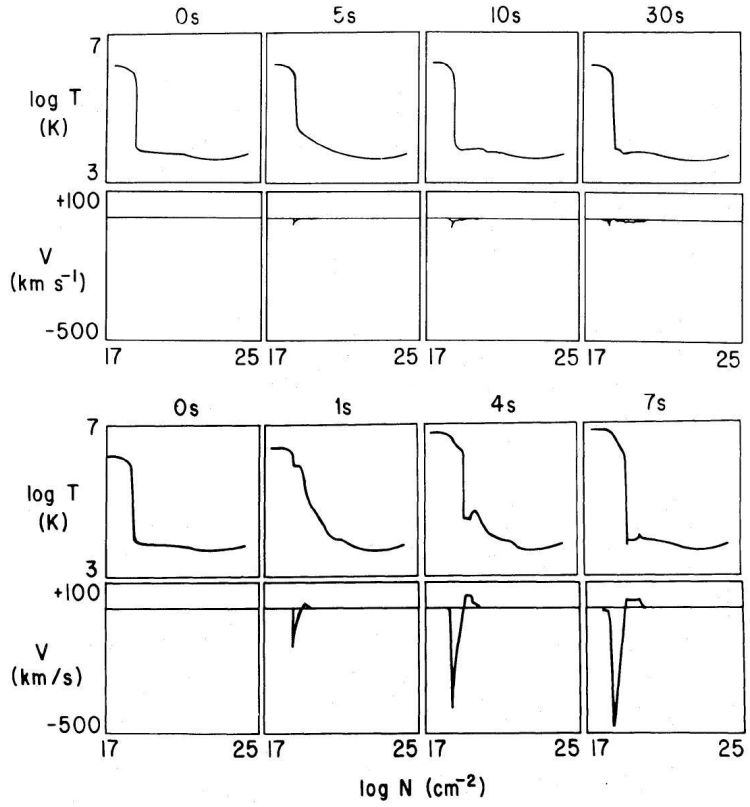

Figure 6. Time evolution of the temperature and velocity in the loop atmosphere heated by the low (upper two panels) and the high (lower two panels) flux of non-thermal electrons. In the first case the upflow with the low velocity in the transition region and in the chromosphere is present (gentle evaporation). For the strong flux of non-thermal electrons the high-velocity upflow (up to $-500\,\mathrm{km\,s^{-1}}$) in the high temperature region is obtained (explosive evaporation) and downflow (up to $+40\,\mathrm{km\,s^{-1}}$) is observed in the chromosphere (chromospheric condensations). For more details see the paper of Fisher et al. (1985a).

(Fig. 6). They showed that a high-energy flux of non-thermal electrons drives explosive evaporation accompanied by the formation of cool chromospheric condensations in the flare chromosphere. A different situation occurs when the flux associated with non-thermal electrons is very low. Then only a weak chromospheric evaporation takes place. This kind of evaporation is referred to as gentle evaporation (Antiochos & Sturrock 1978; Schmieder et al. 1987) and it can be observed in chromospheric spectral lines like Hα or in Ca II 8542 Å. Antiochos & Sturrock (1978) suggested that the gentle chromospheric evaporation may also occur after the primary energy release, when the non-thermal electron flux is stopped. This evaporation could be driven by the large conductive heat flux from a high temperature flare plasma contained in magnetic tubes above the chromosphere. Such physical conditions may appear during the gradual phase of solar flares, when there is no significant flux of non-thermal electrons. In the

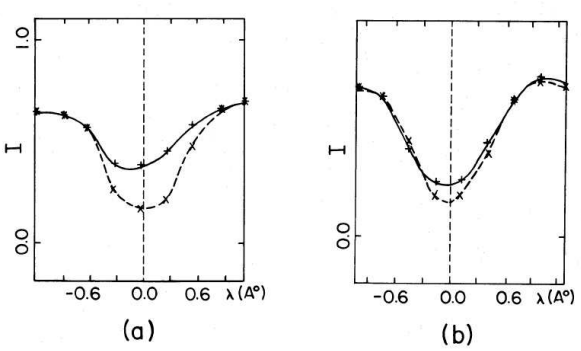

Figure 7. Hα line profiles observed during the gradual phase of a solar flare (solid lines). Weak blue-shift of these lines suggests slight upflow of the plasma with the velocity of a few $\mathrm{km\,s^{-1}}$ interpreted as gentle evaporation. Dashed lines represent the reference line profiles of the quiet Sun area (Schmieder et al. 1987).

Forbes et al. (1989) model for flare-loop formation by magnetic reconnection the conduction of the thermal energy generated at the slow-mode shocks drives a gentle evaporative upflow from the ribbons.

Schmieder et al. (1987) observed small but long-lasting blue-shifts in flare ribbons in the Hα line during the gradual phase of three solar flares and interpreted them as due to upflows with velocities less than $10\,\mathrm{km\,s^{-1}}$ (Fig. 7). These upflows were believed to be caused by gentle chromospheric evaporation driven by the heat conduction along the field lines connecting the chromosphere with a reconnection site in the corona.

The downflow of cool chromospheric plasma during the impulsive phase of solar flares predicted in the theoretical calculations was reported by many authors. Zarro et al. (1988) observed large red asymmetry of the Hα line during the period of hard X-ray burst (Fig. 8). These asymmetries were used to determine the downward velocities estimated from the maximum shift of the centroid of the bisectors. The averaged over all red-shifted pixels during the impulsive phase velocity was of the order of $60 \pm 10\,\mathrm{km\,s^{-1}}$. The downflow analysed in the Hα data and the upflow observed in the X-ray lines allows the authors to analyze the momentum balance of the flow. They conclude that the momenta of upflowing and downflowing plasma are approximately equal. Zarro & Canfield (1989) conclude that the downflow velocity measured from red wing enhancement can be used as a diagnostics of impulsive solar flare heating conditions (Fig. 9).

The work of Ding et al. (1995) shows that the velocity of chromospheric downflows deduced from the red asymmetry of Hα line is around $30 - 40\,\mathrm{km\,s^{-1}}$ with the lifetime of the order of 2 – 3 minutes. There are two major problems found by the authors: Why is the line center nearly not shifted while the line wing shows great asymmetries? The second problem concerns the life time of the downflow which is considerably longer than the life time predicted in Fisher (1989) simulations. Recent hydrodynamic and radiative transfer simulations may now explain these two problems.

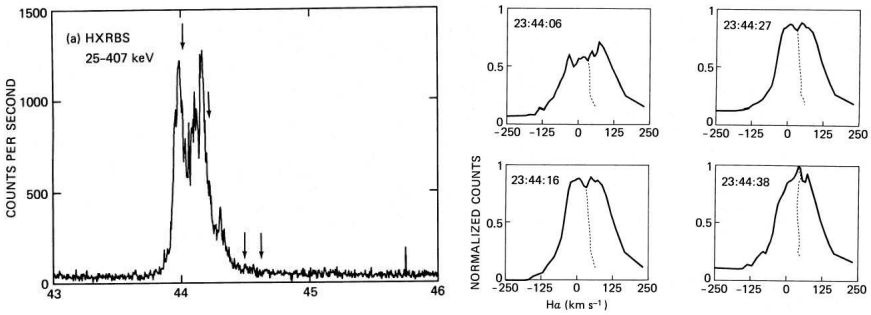

Figure 8. The hard X-ray emission (left) and the Hα excess line profiles (right) observed during the impulsive phase of a solar flare. Dashed lines mark the centroids of the profile. The obtained downward velocities are around $50\,\mathrm{km\,s^{-1}}$. The numbers on the X-axis of left panel represent minutes after 23 UT and the arrows – the times of Hα observed line profiles (Zarro et al. 1988).

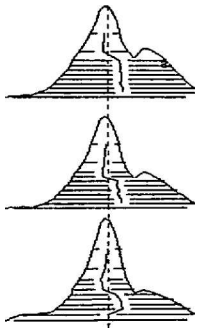

Figure 9. An example of the Hα line profiles observed during the impulsive phase of a solar flare. The red wing enhancement is observed at the same time as strong hard X-ray emission. Note that the central part of the line is slightly blue-shifted (Zarro & Canfield 1989).

There are more papers presenting the observations of the red asymmetry related to the chromospheric condensations driven during the impulsive phase of solar flares (e.g., Wuelser & Marti (1989) – Fig. 10). All of them determine more or less consistent observational picture of the chromospheric flows during the impulsive phase of flares. This picture is based on many spectroscopic observations of the chromospheric line profiles. An important step was done when it became possible to calculate theoretical line profiles and compare them with observations.

Canfield & Gayley (1987) computed time-dependent Hα line profiles for the dynamic model atmosphere of Fisher et al. (1985a). They simulate the effects of power-law electron beam heated chromosphere. Solving the radiative transfer equations for one-dimensional model atmosphere the evolution of Hα line profile was estimated. The time of the electron beam heating was 5 s and for detailed description of other parameters and computational methods see Canfield & Gayley (1987). In Fig. 11 the time sequence of the Hα line profile is presented. During the non-thermal heating, the red-shifted component is present but after

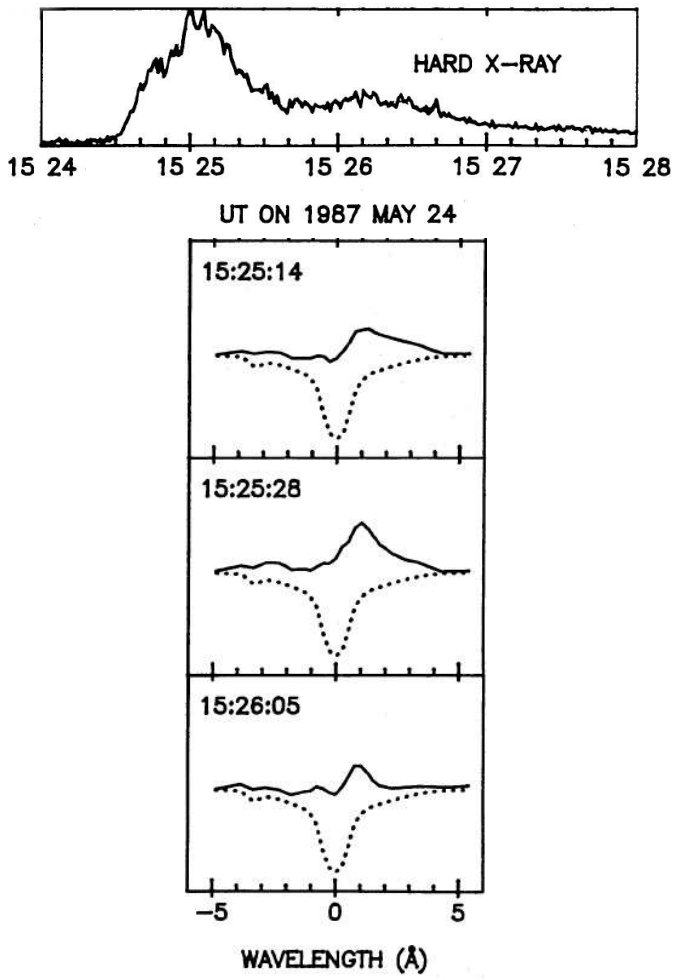

Figure 10. The hard X-ray emission (top) and the Hα line profiles with the red asymmetry (bottom) observed during the impulsive phase of a solar flare. Dotted lines mark the reference quiet Sun profile (Wuelser & Marti 1989).

the heating was stopped, the Hα line exhibit the blue asymmetry although the central absorption feature is shifted towards longer wavelengths. This behaviour is explained by downflow of the chromospheric condensation. It is also worth to notice that the response of the Hα emission to the non-thermal electron beam is very fast (less than second).

Similar but more precise simulations of the dynamics and radiation in a solar flare loop was presented by Abbett & Hawley (1999). Except the non-thermal heating of the chromosphere, they took into account the thermal heating by the soft X-ray irradiation within 1 – 250 Å range. Carlsson & Stein (1997) radiative-hydrodynamic code was used to analyze the response of the lower atmosphere at the footpoint of a flare loop. In the radiative transfer calculations the important transitions of hydrogen, helium and singly ionized calcium and magnesium

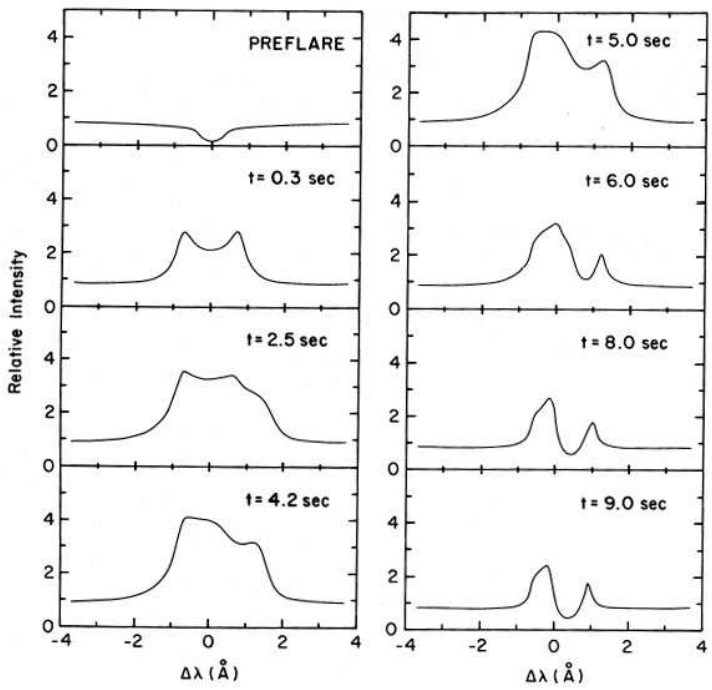

Figure 11. Time evolution of the calculated Hα line profiles for the electron beam heated model atmosphere of Fisher et al. (1985a) (Canfield & Gayley 1987).

were treated in non-LTE. One-dimensional atmospheric model was used in the calculations.

As a starting models the authors took two different cases PF1 and PF2. The temperature and electron density stratifications of both preflare atmospheres are shown in Fig. 12. Three levels of the non-thermal heating was considered which correspond to weak (F9), moderate (F10), and strong (F11) non-thermal flare heating. The PF1 atmosphere is heated for 70 s with the F9 and F10 fluxes, and the PF2 atmosphere is heated for a shorter, 4 s burst but with strong F11 heating.

Figure 13 presents the time evolution of emergent Hα and Ca II K line profiles. For the Hα line separated blue-shifted component is clearly visible while Ca II line exhibit red-shifted component. The contribution function calculated for these two lines explain why we observe such a two-components and asymmetric profiles (Fig. 14).

This analysis shows that the evolution of non-thermally heated chromosphere progresses through two distinct dynamic phases (Abbett & Hawley 1999): a gentle phase, where the non-thermal energy input of the flare is essentially radiated away into space, and an explosive phase, where the flare energy rapidly heats the atmosphere and drive large amounts of chromospheric material up into the corona, and down toward the photosphere. During the explosive phase, there is significant plasma motion and there are steep velocity gradients. More-

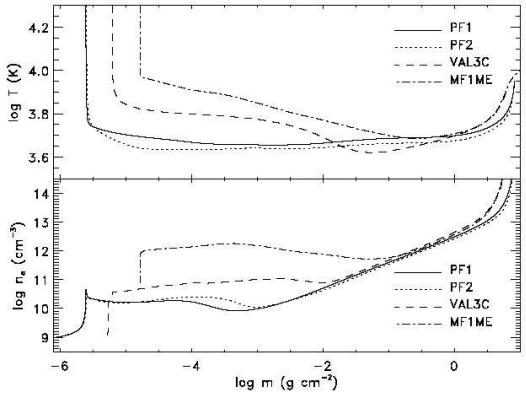

Figure 12. The temperature and electron density stratifications of both preflare atmospheres PF1 and PF2 compared to the standard semiempirical VAL3C chromospheric model of Vernazza et al. (1981) and to the semiempirical active atmosphere MF1ME of Metcalf (1990) (Abbett & Hawley 1999).

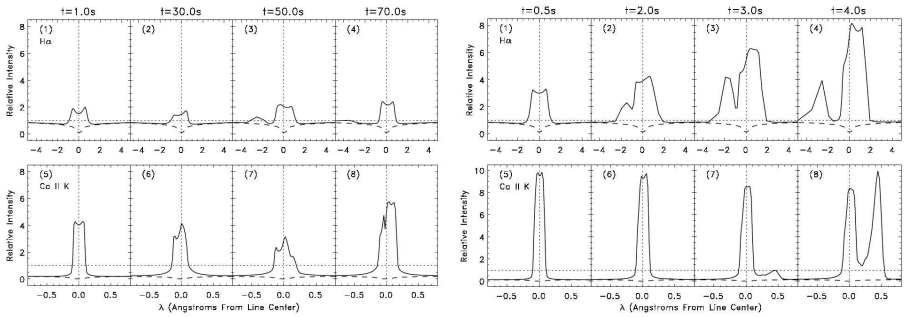

Figure 13. *Left:* Time evolution of the Hα and Ca II K line profiles for moderate heating of the atmosphere by non-thermal electrons (model F10). In each panel, the vertical axis represents relative intensity with respect to the continuum level and the horizontal axis denotes the wavelength from the line centre. The dashed lines in each panel represent the preflare line profile. *Right:* Time evolution of the Hα and Ca II K line profiles but calculated for strongly heated atmosphere (model F11) (Abbett & Hawley 1999).

over, the effects of thermal X-ray heating of the chromosphere remain negligible compared to the non-thermal heating in the impulsive phase.

Similar, but much more extended calculations were presented by Allred et al. (2005). The basics of computational methods are similar to those described by Abbett & Hawley (1999) but there are some significant improvements. The authors include the double power-law electron beam energy distributions recently observed in solar flares with the Reuven Ramaty High-Energy Solar Spectroscopic Imager (RHESSI) satellite. Additionally, the effects of XEUV heating from a large number of high-temperature lines was taken into account using results from the CHIANTI and ATOMDB databases and a wide range 1 – 2500 Å was used for direct thermal heating of the chromosphere. Figure 15

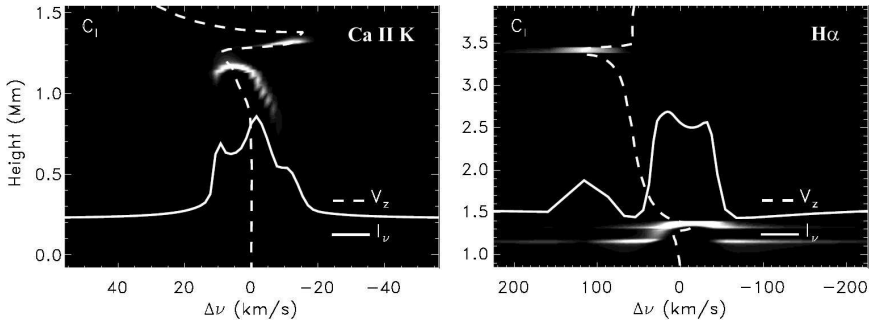

Figure 14. The approximate formation height of different parts of the spectral line profile may be described by contribution function. This figure presents components of the intensity contribution function for Ca II K (left) and Hα (right) lines after 50 s of flare heating in model F10. Line frequencies are in velocity units. Atmospheric velocities (dashed lines) are taken to be positive toward the corona. Thus, negative velocities associated with downward-moving material correspond to red-shifts in the profile (Abbett & Hawley 1999).

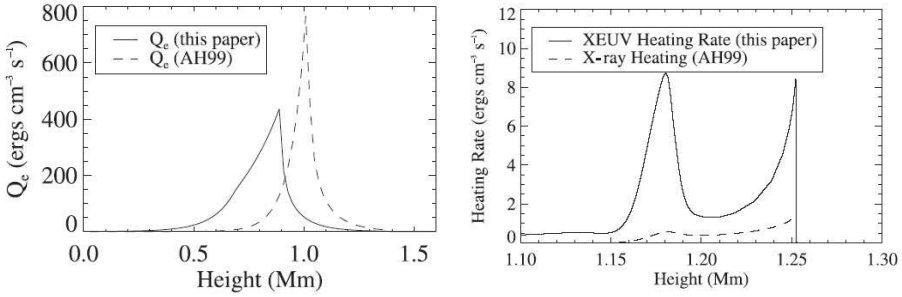

Figure 15. *Left:* Comparison of the electron beam heating rate in the preflare atmosphere for the F10 flare model. The solid line shows the heating rate used in the paper of Allred et al. (2005), and the dashed line shows the initial beam heating rate of Abbett & Hawley (1999). *Right:* Solid line – thermal XEUV heating used in Allred et al. (2005), dashed line – soft X-ray heating rate used previously by Abbett & Hawley (1999).

present the comparison of the heating rates used by Abbett & Hawley (1999) and Allred et al. (2005).

These new calculations confirmed the previous results. However, the line profiles evolution differs from the Abbett & Hawley (1999) calculations – the line asymmetry is not so significant and the blue and red components of the Hα and Ca II K lines, respectively, are not observed separately. Instead, the lines are asymmetric with blue or red wing enhancement (Fig. 16). As in Abbett & Hawley (1999), the authors found that the impulsive flare naturally divides into two phases, an initial gentle phase followed by a period of explosive increases in temperature, pressure and velocity.

There are more papers which treat the problem of plasma flows in the non-thermally heated chromosphere (Mariska et al. 1989; Emslie et al. 1998; Karlický

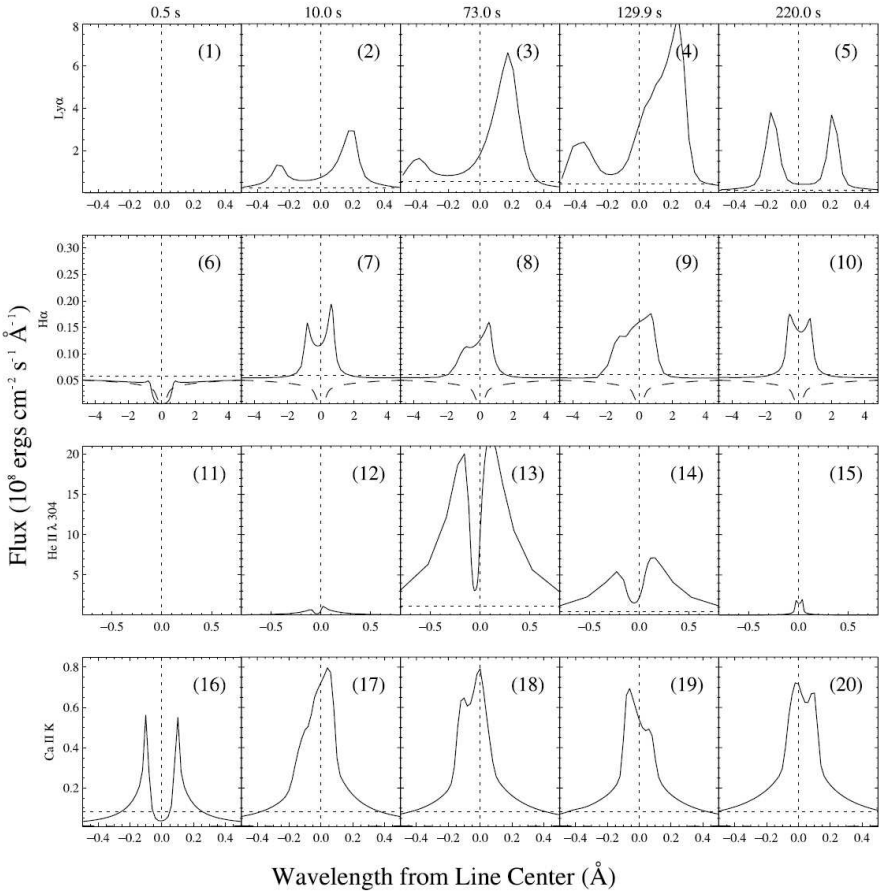

Figure 16. Time evolution of the synthetic line profiles of Ly-α, Hα, He II 304 Å, and Ca II K lines for the moderate level of non-thermal heating (model F10). Times are indicated at the top of each column. The dotted lines indicate the level of the continuum close to the line center, while the dashed line is the preflare line profile (Allred et al. 2005).

& Hénoux 1992; Gan & Fang 1990; Gan et al. 1991). All these hydrodynamic simulations predict an upflow of the hot coronal plasma due to the enhanced pressure in the region heated by non-thermal electrons or protons. This upflow is associated with downflow of chromospheric condensations, but with much lower velocities (Fig. 17). These condensations disturb the line profiles emitted from the chromosphere and cause significant asymmetries observed e.g., in Hα line.

The calculated line profiles emerging from flaring atmosphere show roughly similar behaviour than the observed ones but unfortunately, the appearance and the time evolution of the calculated line profiles was not compared to the spectroscopic observations of particular flares. The validity of the modeling summarized in this chapter was not confirmed observationally up to now.

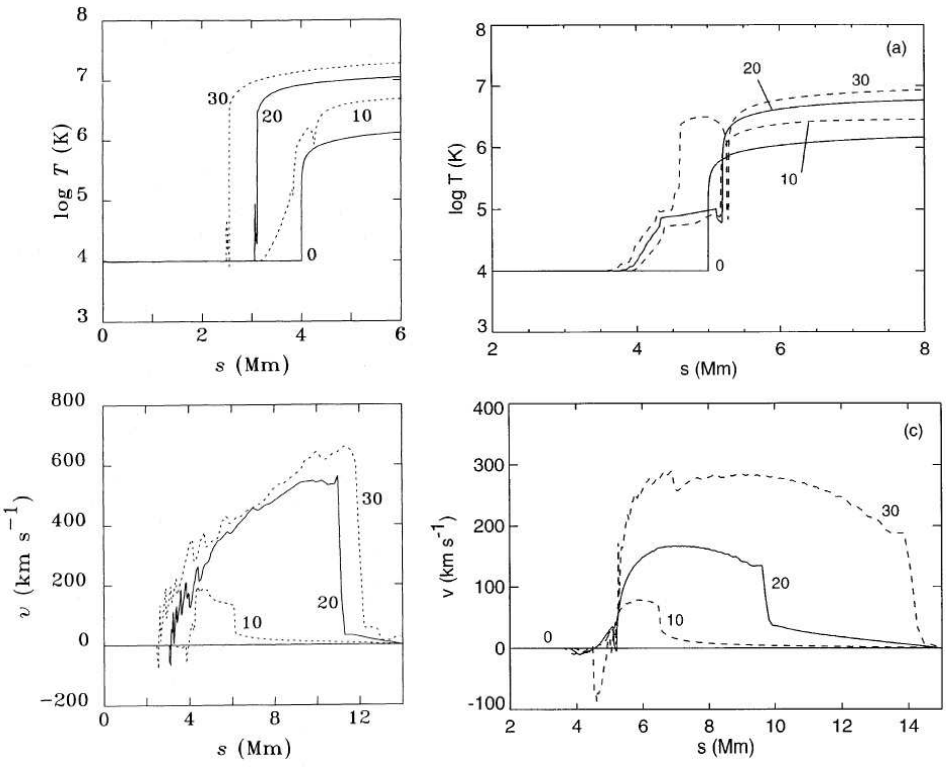

Figure 17. Left panels: Hydrodynamic response of the temperature and velocity to the non-thermal electron beam heating (Mariska et al. 1989) and to the non-thermal proton beam heating (right panels) (Emslie et al. 1998). Positive values of the velocity correspond to upward motion of the plasma. Labels 10, 20, and 30 are the times in seconds after start of non-thermal heating.

4. Velocity Field in Semiempirical Models of the Flare Atmosphere

Asymmetries observed in chromospheric line profiles are also modeled using semiempirical flare models. This approach is based on the idea that the temperature stratification of the atmosphere is determined empirically in the way to reproduce the calculated spectrum in the best agreement with observations. This means that the energy-balance equation is not considered. Many spectral lines and continua are used to construct such kind of models. Initially, static semiempirical models were developed for a quiet-Sun atmosphere (Vernazza et al. 1981) and then for the static flaring atmosphere (Machado et al. 1980). These models were constructed under assumption of 1-dimensional geometry and hydrostatic equilibrium (Fig. 18). They are static however the time sequence of many semiempirical models can be used to describe the evolving atmosphere but this method is valid only for slowly-evolving atmospheres. More detailed description of semiempirical models can be found in the paper of Mauas in this book.

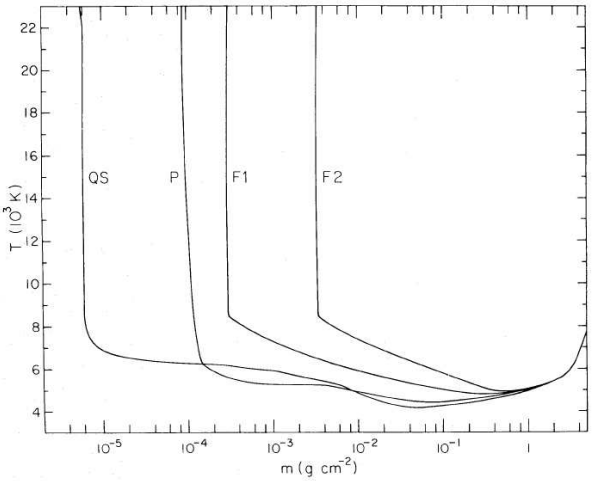

Figure 18. Temperature as a function of column mass for the flare models F1 and F2, for the quiet-Sun QS (VAL-C) model of Vernazza et al. (1981) and for the plage (P) model of Basri et al. (1979) (from Machado et al. 1980).

Non-LTE radiative transfer methods applied to semiempirical models allows us to calculate the spectrum emerging from the atmosphere. In particular, the profiles of the chromospheric optically thick lines may be calculated in details (Heinzel et al. 1994). It is also possible to reproduce asymmetric line profiles solving the transfer equation for a dynamic atmosphere with velocity field, using previously calculated level populations for static model (Berlicki et al. 2005). However, this approach is justified only for relatively small velocities ($V \leq 10$ km s^{-1}) which do not significantly affect the level populations of the static model (Nejezchleba 1998). It cannot be used for impulsive phase of flares to model the chromospheric condensations which move quite fast. Therefore, such simplified calculations are used to model e.g., the gradual phase of solar flares, when the velocities in the chromosphere are low.

One of the first semiempirical modeling of chromospheric flows was performed by Gan et al. (1993). Using the Hα line profiles observed for two flares the authors constructed the series of semiempirical models with chromospheric condensations. It was shown that chromospheric condensations are responsible not only for the red asymmetry of the Hα line, but also for the blue asymmetry of the line with central reversal (Fig. 19). Chromospheric condensations were assumed to be homogeneous with constant velocity. The most important conclusion of this paper is that the properties of chromospheric condensations seem to be consistent with the results of hydrodynamical models of solar flares. Comparison of calculated Hα line profiles with real observations present also a valuable part of this paper.

An interesting work was presented by Nejezchleba (1998) who simulate the influence of the velocity field on the Hα line profiles. The calculations were performed using non-LTE model of plane-parallel solar flare atmosphere with stationary velocity field. This velocity field was applied to different layers of the solar atmosphere and the emergent Hα line profiles were calculated for two mod-

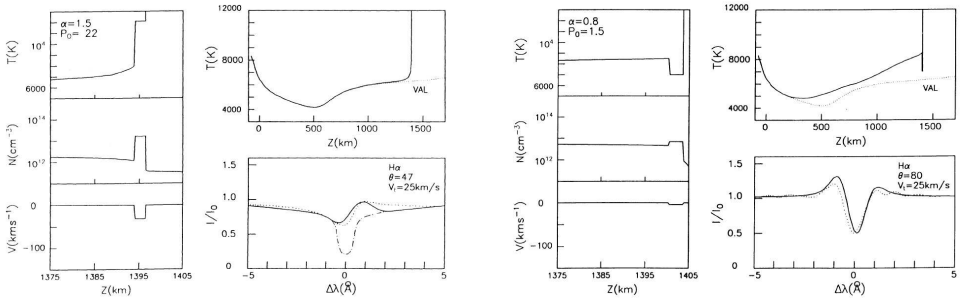

Figure 19. Two examples of semiempirical models of the chromosphere with cool condensation. Left three panels correspond to the condensation which is responsible for the red asymmetry of the Hα line while right three panels presents condensation producing Hα line with blue asymmetry. Temperature, electron density and velocity stratification is presented for both cases (negative sign of the velocity corresponds to downflow). The calculated Hα line profiles are plotted with solid line, observed ones – with dotted line (Gan et al. 1993).

els of solar flare F1 and F2 (Machado et al. 1980). Figure 20 present an example of asymmetric line profiles calculated for a weak-flare model atmosphere F1 and for different velocity fields. The main conclusion of this work is that the velocity field affects the level populations via the increase of the downward radiation. Nevertheless, for velocities that do not exceed the thermal velocity of plasma, one can use the static populations for the formal solution of radiative transfer equation including the velocity to reproduce the observed line asymmetries. Other important point is that application of the bisector method would lead in some cases to reverse velocity, in others to underestimation of the velocity. It includes, besides the part of the profile directly affected by the moving material, also a "static" part of the profile. To use the bisector in terms of Doppler-shift the static part should be somehow eliminated. This remark makes questionable all estimations of the Doppler velocity obtained with the bisector method applied to self-reversed or emission chromospheric lines observed in solar flares.

The conclusions of Nejezchleba (1998) suggest that deducing the velocity from flare line profiles is rather difficult and cannot be done only by searching for Doppler-shifts with the bisector method. Chromospheric line profiles suggest that the flare atmosphere is highly dynamic and stratified with rather complicated plasma motion. These lines are optically "thick" and the only reliable way to analyze the flows is to use the non-LTE radiative transfer codes, which enable us to compute the chromospheric models with velocity fields. Resulting synthetic line profiles can then be compared with the observed ones.

The direct comparison of the observed and synthetic line profiles was presented in the paper of Falchi & Mauas (2002). They study the chromospheric structure of a small flare and construct 5 semiempirical models for different times, which reproduce the profiles of the Hδ, Ca II K, and Si I 3905 Å lines during the flare evolution. In order to reproduce the asymmetry of the lines the velocity fields were introduced in the line profile calculations. The modeling was done using the non-LTE Pandora code of Avrett & Loeser (1984). The trial-and-error method was used to reproduce the observed line profiles by the synthetic ones. Figure 21 (upper panels) present an example of the observed and fitted Hδ

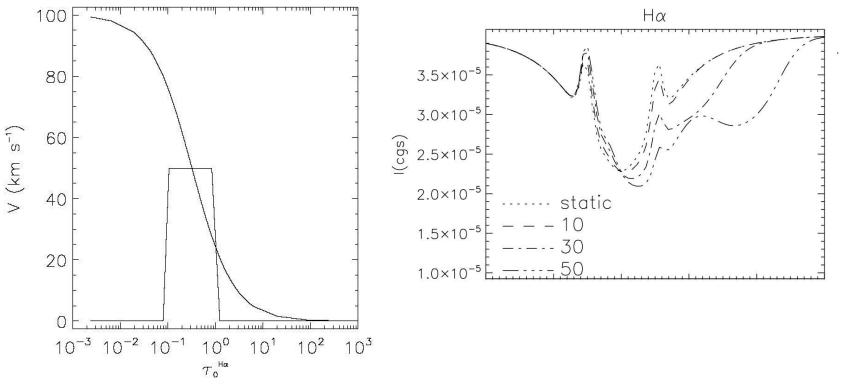

Figure 20. *Left:* Models of the velocity field in the chromosphere used in the non-LTE calculations (positive sign of the velocity corresponds to downflow). *Right:* Some examples of synthetic Hα line profiles calculated for a static and dynamic atmosphere with different velocities 10, 30, and 50 km s^{-1} (Nejezchleba 1998).

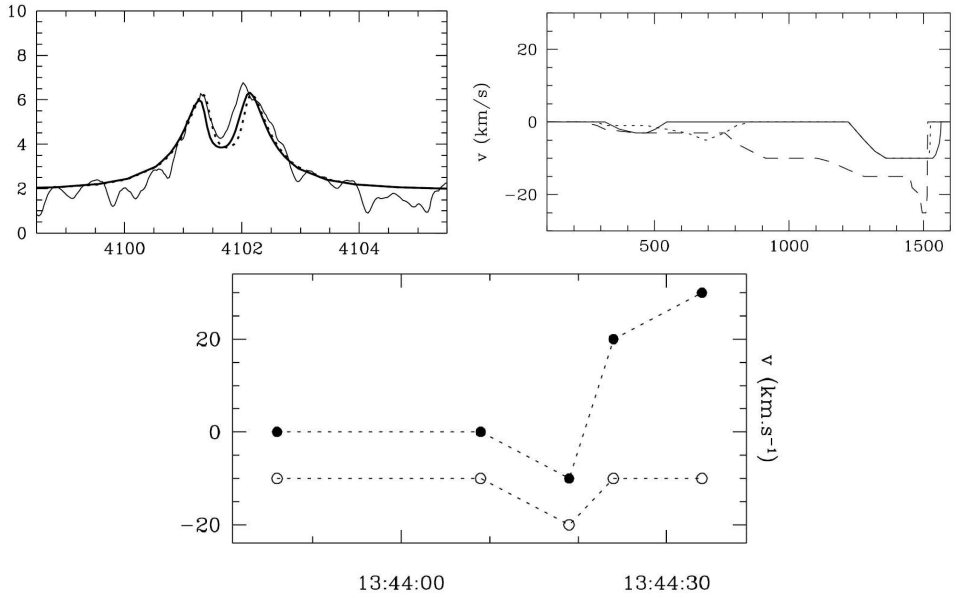

Figure 21. An example of the observed (thin line) and fitted (thick line) Hδ line profiles and determined velocity field across the atmosphere. Negative value indicates an upward velocity. In the lower panel the time evolution of the velocity value at two different heights in the atmosphere is presented. Filled circles refer to the height $\approx$ 900 and open circles to the height $\approx$ 1400 km (Falchi & Mauas 2002).

line profiles and determined velocity field across the atmosphere. In the lower panel of Fig. 21 the time evolution of the velocity value at two different heights in the atmosphere is presented. The presence of an upward motion in the flaring

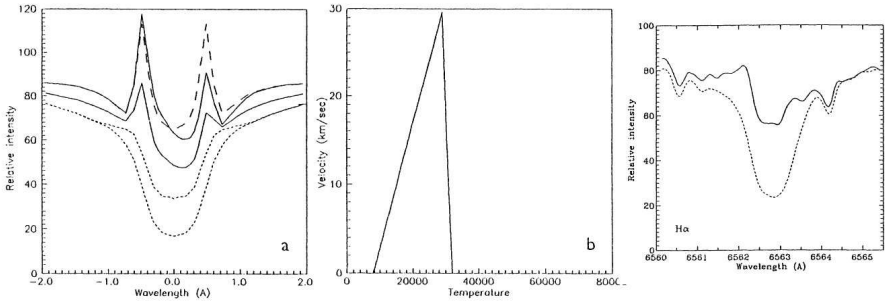

Figure 22. Left: Simulation of the influence of the downward velocity field on the emergent Hα line profile emitted from flaring model atmosphere F1 of Machado et al. (1980). In the middle panel the velocity used in the modeling as a function of temperature is shown (positive sign of the velocity indicates downflow). Also an example of the observed Hα line with red asymmetry is presented (for details see Heinzel et al. (1994)).

atmosphere at 1400 km, might be a signature of the chromospheric evaporation observed at chromospheric levels. It is interesting to notice that around 13:44:30 UT the downflow is observed at the height of 900 km, while the upward motion is evident at 1400 km above the photosphere. One possible explanation is that chromospheric evaporation together with condensations is observed. In this case chromospheric evaporation is observed at chromospheric levels and not, as more common, at coronal levels.

Using the semiempirical F1 model of a weak flare (Machado et al. 1980), Heinzel et al. (1994) showed that the blue asymmetry of Hα line profile is observed due to the downflow of chromospheric plasma. It is interesting to notice that the blue asymmetry is associated with the red-shift of the central absorption feature. Similar results was shown by Gan et al. (1993). The structure of the velocity field used in the non-LTE simulations of Heinzel et al. (1994) was qualitatively consistent with the concept of downward-moving chromospheric condensations (Fig. 22). These calculations were performed using the non-LTE code developed by Heinzel (1995) and modified for flare conditions. The code uses a 1D plane-parallel geometry and the atmosphere is in hydrostatic equilibrium. Hydrogen excitation and ionization equilibrium have been computed by solving simultaneously the radiative transfer equations, the equations of statistical equilibrium for a five-level plus continuum atomic model of hydrogen and the equations of particle and charge conservation. The equations of statistical equilibrium have been preconditioned according to Rybicki & Hummer (1991). The preconditioning is based on the lambda-operator splitting technique, where the exact lambda operator is expressed as an approximate operator plus the correction. Then the correction is iteratively applied to a lagged source function by using the so-called Accelerated Lambda Iterations (ALI) method. For multilevel atoms this method is referred to as MALI – Multilevel Accelerated Lambda Iterations (Rybicki & Hummer 1991). The preconditioned equations are then linearized with respect to the atomic level populations and electron density and solved iteratively (Heinzel 1995).

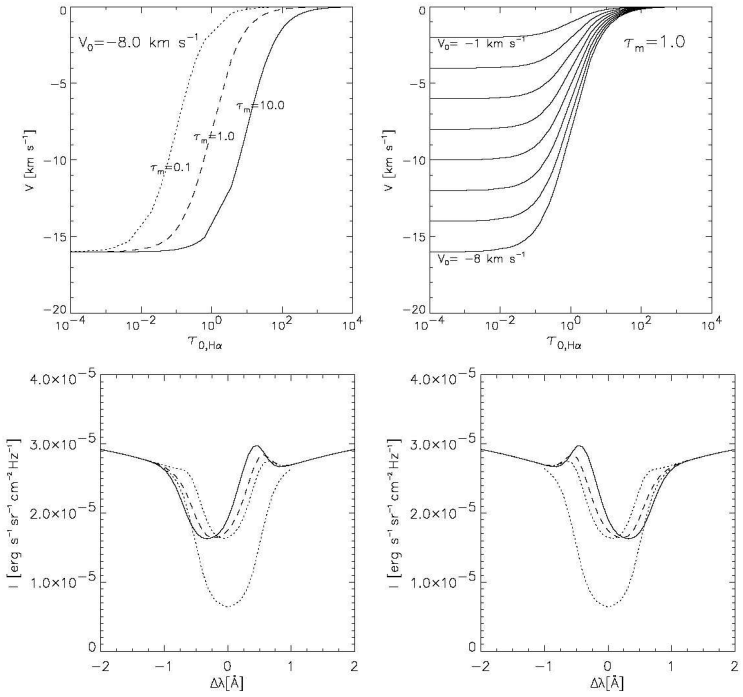

Figure 23. The Hα line-centre optical depth distribution of the velocity field used in the modeling plotted for different values of $\tau_{\rm m}$ and for $V_0 = -8$ km s^{-1} (upper left panel) and for different values of V_0 and for $\tau_{\rm m} = 1.0$ (upper right panel). In the lower panels the influence of the velocity field on Hα line profiles emitted from flare is presented (upflow defined by $V_0 = -8$ and downflow $V_0 = +8$ km s^{-1} for three values of $\log \tau_{\rm m} = 0.1, 1.0$, and 10.0 (dotted, dashed and continuous lines, respectively) (Berlicki et al. 2005).

This non-LTE code was also used in Berlicki et al. (2005) to analyse the time evolution of the line asymmetry observed during the gradual phase of the solar flare on October 22, 2002. In this paper for the first time the evaporative flows in the gradual phase are studied quantitatively by using a non-LTE radiative transfer code and spectroscopic observations of the flare ribbons. First the authors analyse the influence of different velocity fields on the emergent Hα line profile. Again, it was shown that the downflow of flaring plasma causes blue asymmetry of the self-reversed line while upflow – red-asymmetry (Fig. 23). For the modeling of the observed line asymmetry except the changes of the value of the velocity, also the height of the velocity field in the atmosphere was different. The procedure of fitting the Hα line profiles was performed using a grid of many models by varying different parameters. Each observed profile was fitted by the least-square technique to a closest synthetic profile from the grid and the model with the velocity field was found for each analysed line profile.

In the analysis the MSDP (Multichannel Subtractive Double Pass) spectrograph (Mein 1991) coupled to the VTT telescope working at the Teide Observatory (Tenerife, Canary Islands) was used. 36 Hα line profiles (six areas at six different times) observed during the M1.0 flare on October 22, 2002 were

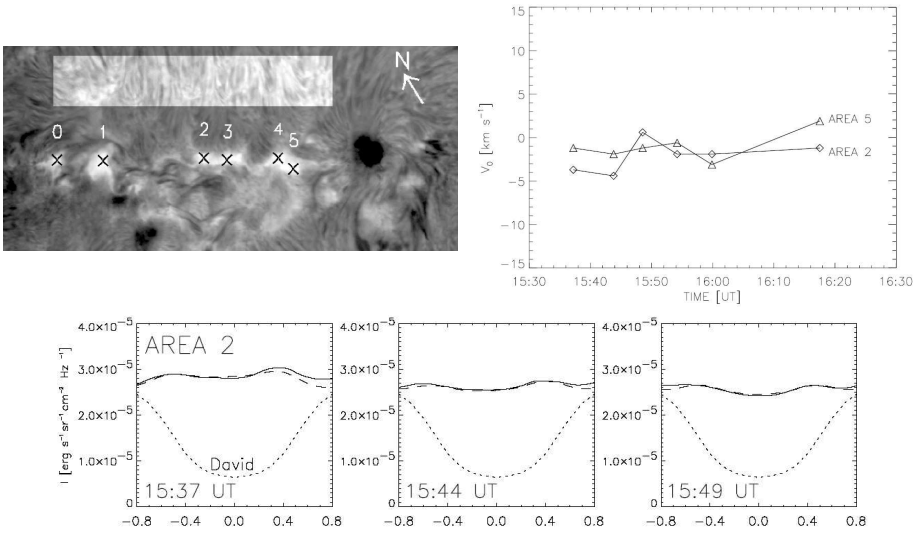

Figure 24. The image of the flare on October 22, 2002 used in the analysis of Berlicki et al. (2005) and the observed (continuous lines) and fitted (dashed lines) Hα line profiles (upper and lower left panels). 0 – 5 are the areas used in the analysis. The time evolution of the velocity in the chromosphere deduced from line asymmetries is plotted for two analysed areas in the right panel. Negative velocities correspond to upflow (Berlicki et al. 2005).

taken for the analysis (Fig. 24 – upper left panel). As an example we present in Fig. 24 (lower panel) some profiles observed in chosen area at three times. These observed profiles (solid lines) are fitted with the synthetic ones (dashed lines) obtained from the grid. In the right panel of Fig. 24 the temporal evolution of the velocity field is presented for two different areas of the flare.

The authors interpret the upflows found in the flare ribbons in terms of the Antiochos & Sturrock (1978) model for gentle evaporation. This process may occur during the gradual phase of solar flares and it can be driven by conductive heat flux from the high-temperature flare plasma contained in magnetic flux tubes above the photosphere. In the future it would be interesting to use more spatial points at more times and to use the spectra obtained within a wider range of wavelengths. Other distributions of the velocity field in the chromosphere should also be tested. In addition, to perform non-LTE modeling of the flare structure it would be useful to have other spectral lines formed at different levels of the chromosphere.

5. Summary

In this review I presented some interesting papers concerning plasma flows observed during solar flares in cool chromospheric layers. These flows are directly responsible for the line-asymmetries and/or line-shifts often observed in chromospheric lines emitted by the flaring plasma.

An important work was done to understand the flows and their mechanisms. In order to determine the plasma velocity and flow direction the bisector method was applied for line profiles. Unfortunately, as we could see, this method leads in some cases to misleading estimations of the velocity. Recently, the direct comparison of the observed and synthetic line profiles gives more valuable information about velocity fields in the chromosphere. All the data support the evaporative model of solar flares where explosive chromospheric evaporation of the hot plasma is associated with the chromospheric condensations observed in "cool" chromospheric lines. In the late phases of flares the gentle evaporation may be observed in chromospheric lines.

For the future it is necessary to use large and dense grids of the chromospheric models computed with hydrodynamic and non-LTE codes. They may help us to understand the flows and give more realistic description of the physical processes during the flares, particularly the heating mechanisms and their role at different phases of the flare evolution.

Finally, really good spectral observations of flares are needed. They have to be co-spatial, simultaneous and obtained in different spectral ranges (X-ray, EUV, UV, optical, IR). Such observations would be very helpful to construct the full picture of the plasma flows during flares. There are some data concerning the flows observed in soft X-ray and EUV but they are extremely rare and almost never cospatial nor simultaneous with the observations in chromospheric lines.

Acknowledgments. This research was supported by the European Commission through the RTN programme (European Solar Magnetism Network, contract HPRN-CT-2002-00313. The author also would like to thank P. Heinzel for helpful comments and valuable remarks.

References

Abbett W. P., Hawley S. L., 1999, ApJ 521, 906
Acton L. W., Leibacher J. W., Canfield R. C., Gunkler T. A., Hudson H. S., Kiplinger A. L., 1982, ApJ 263, 409
Allred J. C., Hawley S. L., Abbett W. P., Carlsson M., 2005, ApJ 630, 573
Antiochos S. K., Sturrock P. A., 1978, ApJ 220, 1137
Athay R. G., 1970, Solar Phys. 12, 175
Avrett E. H., Loeser R., 1984, Line transfer in static and expanding spherical atmospheres, 341–379, Methods in Radiative Transfer
Basri G. S., Linsky J. L., Bartoe J.-D. F., Brueckner G., van Hoosier M. E., 1979, ApJ 230, 924
Berlicki A., Heinzel P., Schmieder B., Mein P., Mein N., 2005, A&A 430, 679
Canfield R. C., Gayley K. G., 1987, ApJ 322, 999
Carlsson M., Stein R. F., 1997, ApJ 481, 500
Ding M. D., Fang C., Huang Y. R., 1995, Solar Phys. 158, 81
Ellison M. A., 1949, MNRAS 109, 3
Emslie A. G., Mariska J. T., Montgomery M. M., Newton E. K., 1998, ApJ 498, 441
Falchi A., Mauas P. J. D., 2002, A&A 387, 678
Fisher G. H., 1989, ApJ 346, 1019
Fisher G. H., Canfield R. C., McClymont A. N., 1985b, ApJ 289, 434
Fisher G. H., Canfield R. C., McClymont A. N., 1985a, ApJ 289, 414
Forbes T. G., Malherbe J. M., Priest E. R., 1989, Solar Phys. 120, 285

Gan W. Q., Fang C., 1990, ApJ 358, 328
Gan W. Q., Rieger E., Fang C., 1993, ApJ 416, 886
Gan W. Q., Zhang H. Q., Fang C., 1991, A&A 241, 618
Heinzel P., 1995, A&A 299, 563
Heinzel P., Karlický M., Kotrč P., Švestka Z., 1994, Solar Phys. 152, 393
Ichimoto K., Kurokawa H., 1984, Solar Phys. 93, 105
Karlický M., Hénoux J.-C., 1992, A&A 264, 679
Kopp R. A., Pneuman G. W., 1976, Solar Phys. 50, 85
Machado M. E., Avrett E. H., Vernazza J. E., Noyes R. W., 1980, ApJ 242, 336
Mariska J. T., Emslie A. G., Li P., 1989, ApJ 341, 1067
Metcalf T. R., 1990, Ph.D. thesis, AA(California Univ., San Diego.)
Mihalas D., 1978, Stellar atmospheres /2nd edition/, San Francisco, W. H. Freeman and Co., 1978. 650
Nejezchleba T., 1998, A&AS 127, 607
Neupert W. M., 1968, ApJ 153, L59
Rybicki G. B., Hummer D. G., 1991, A&A 245, 171
Schmieder B., Forbes T. G., Malherbe J. M., Machado M. E., 1987, ApJ 317, 956
Tang F., 1983, Solar Phys. 83, 15
Švestka Z., Kopecký M., Blaha M., 1962, Bulletin of the Astronomical Institutes of Czechoslovakia 13, 37
Vernazza J. E., Avrett E. H., Loeser R., 1981, ApJS 45, 635
Wuelser J.-P., 1987, Solar Phys. 114, 115
Wuelser J.-P., Marti H., 1989, ApJ 341, 1088
Zarro D. M., Canfield R. C., 1989, ApJ 338, L33
Zarro D. M., Canfield R. C., Metcalf T. R., Strong K. T., 1988, ApJ 324, 582

Welcome reception in the Old Cathedral's Cloister

Fado de Coimbra

The Physics of Chromospheric Plasmas
ASP Conference Series, Vol. 368, 2007
Petr Heinzel, Ivan Dorotovič and Robert J. Rutten, eds.

The Spotless Flare of March 16, 1981

Aleksander V. Borovik and Daniel Yu. Myachin

Institute of Solar-Terrestrial Physics, SD RAS, Russia

Abstract. This paper examines morphological features of the development of the 16 March 1981 spotless flare, temporal variations in the area of flare ribbons, near and far flare mottles and their relationships with the longitudinal component of magnetic field.

1. Introduction

The spotless flare of 16 March 1981 emerged away from spots and plage areas, 10° from the nearby active regions AR 512, AR 514, and AR 523, at 07:53 UT (Borovik and Myachin 2002). Its coordinates were N09W22, its lifetime about 1.5 hours. It was classed as a two-ribbon flare. This paper relies on Baikal Astrophysical observatory data as well as on those from other observatories.

2. The Flare Onset

The flare onset was characterized by the emergence of two groups of bright mottles (ribbons) A1, A2, and B1 – B4 on the opposite sides of the polarity inversion line (PIL) of the longitudinal magnetic field component. These groups were 110″ (80 000 km) apart (Fig. 1a). The sizes of the initial mottles in the lefthand ribbon were: 3.5″ for A1; 5.5″ for A2. The distance between the mottle centers was 10″ (7 000 km). The sizes for the righthand ribbon: mottle B1 5″, B2 4″, B3 3.5″, B4 6.5″. The distance between B1 and B2 was 14″ (10 000 km), between B2 and B3 8″ (6 000 km), and between B3 and B4 8″ (6 000 km).

The initial mottles of the flare were 35″ (40 000 km) away from the PIL, very close to hills with strong magnetic field (Fig. 1b). In particular, the distance between A1 and the 137 G magnetic field hill was 8″ (6 000 km); between A2 and the 204 G magnetic field hill, 4″ (3 000 km). The distance between mottle B1 and the -83 G hill was 4″(3 000 km); between B2 and the -96 G hill, 3″(2 000 km); between B3 and the -139 G hill, 8″ (6 000 km); between B4 and the -178 G hill, 7″ (5 000 km).

3. The Flare Development Stages

The character of the changes makes it possible to distinguish three periods in the flare development (Fig. 2). All periods are approximately similar in duration (10–12 minutes) and begin identically, with a sharp reduction in the area of ribbons and a simultaneous increase in flare brightness. During the first two stages, the ribbon areas change almost synchronously, but in the third stage,

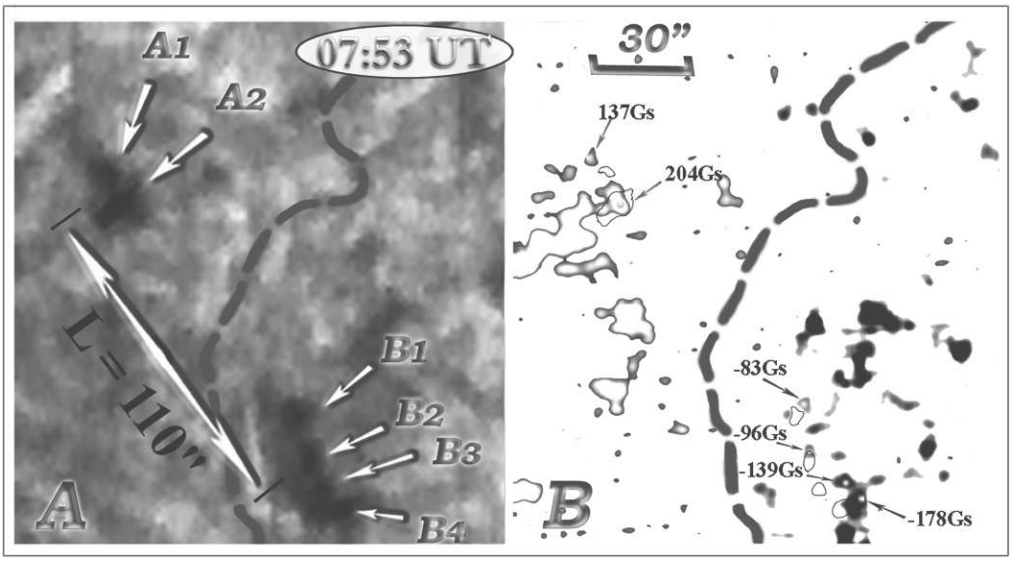

Figure 1. a) Spotless flare onset in the Hα-line at 07:53 UT (inverse image). b) Kitt Peak magnetogram. The contours of the magnetic field are shown for values over 80 G.

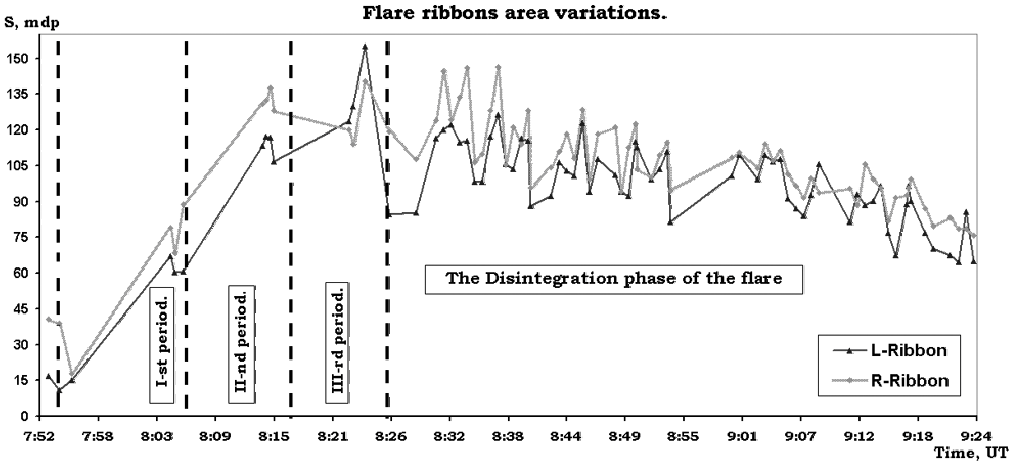

Figure 2. Flare ribbon area variations.

near the flare maximum, the simultaneity is broken: the change of ribbon areas becomes anti-phase relative to each other. In our opinion, this may indicate the beginning of the flare disintegration phase. Each of the periods is characterized by a new development of the ribbons and by the emergence of mottles both near and very far from the flare. The average sizes of flare mottles were 4″. As a rule, the brightest parts of flare ribbons as well as the flare mottles are located near magnetic hills with high values of magnetic field intensity, from 80 to 380 G (mean H is about 150 G). The average distances from mottles to magnetic field hills are 4″. The diffuse parts of the ribbons are above the areas

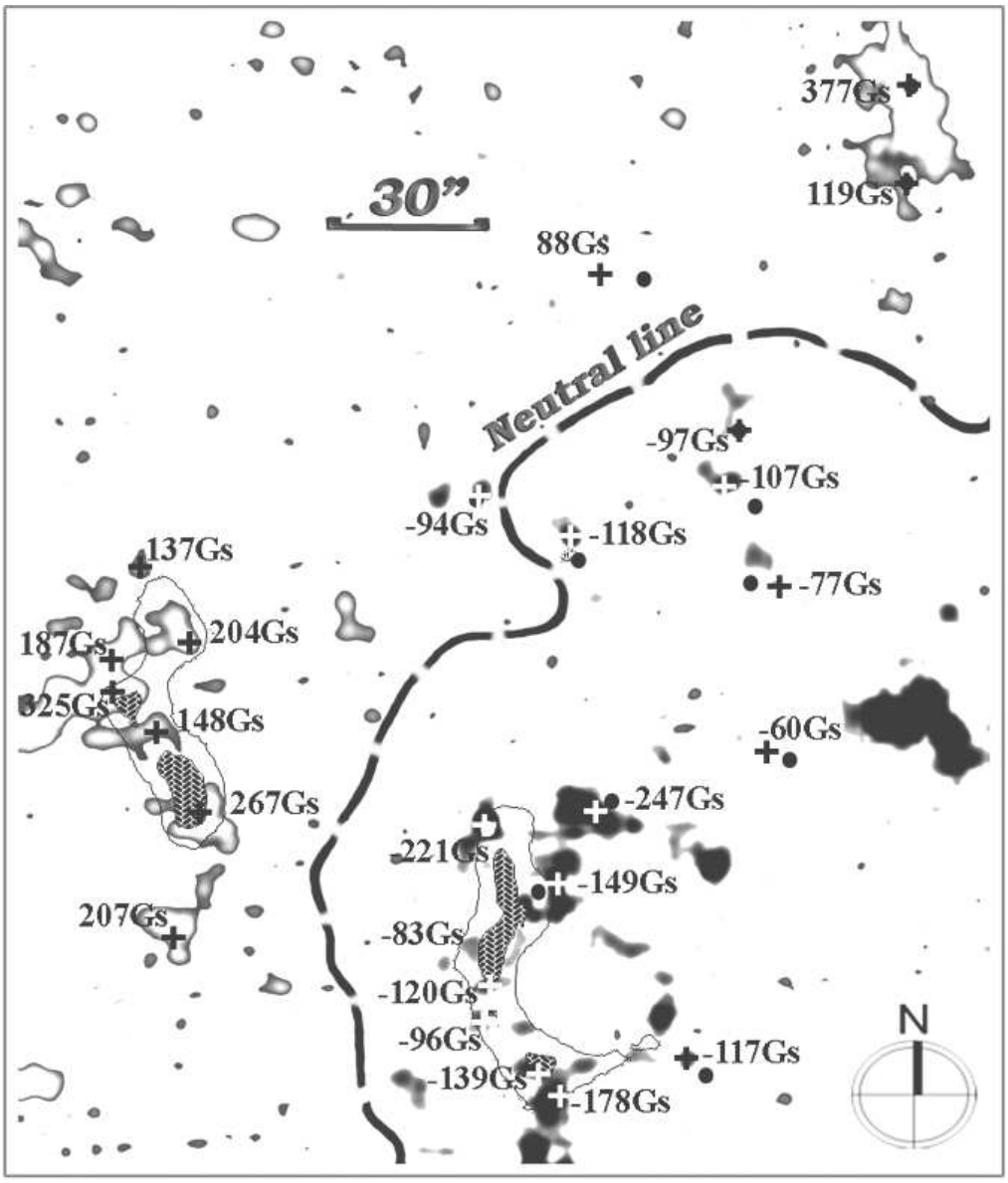

Figure 3. Schematic location of flare ribbons and mottles. Flare mottles are shown by dots; magnetic field hills in the flare area are marked by crosses.

with magnetic field intensity not exceeding 50 G. (Fig. 3). The ribbons generally develop towards the nearest hills of magnetic field as follows: the bright mottle appears near the magnetic field hill and then it merges with the body of the flare ribbons (by means of loops). As a result, by the moment of the flare maximum development, the flare process has covered regions over 18 000 000 km^2 (Fig. 4).

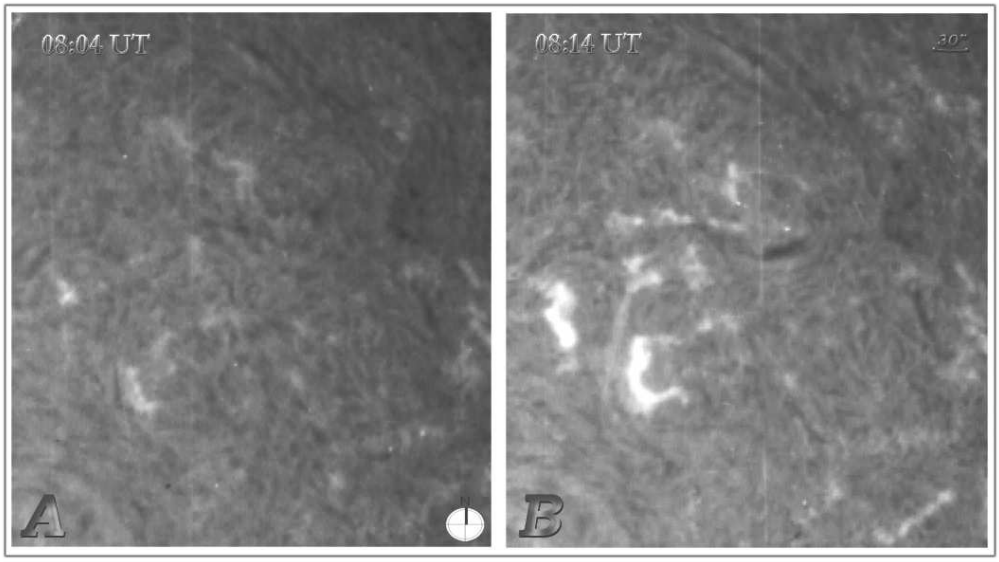

Figure 4. Spotless flare in the Hα-line. a) flare onset at 08:04 UT. b) maximum flare development at 08:14 UT.

4. Conclusions

After analysing the 16 March, 1981 flare, we have made the following conclusions concerning the features of the spotless flare:

- slow development until maximum, lasting about 30 minutes;
- close relationship with magnetic field hills with high intensities;
- significant remoteness of flare ribbons from the polarity inversion line;
- the absence of divergence of ribbons, typical for two-ribbon flares.

Both in the preflare (Borovik A.V and Myachin D.Yu., 2002) and flare period, disturbances engulfed regions reaching far beyond the flare events proper.

References

Borovik A. V., Myachin D. Yu., 2002, Solar Phys. 205, 105

The Physics of Chromospheric Plasmas
ASP Conference Series, Vol. 368, 2007
Petr Heinzel, Ivan Dorotovič and Robert J. Rutten, eds.

Radio Observations of the December 20, 2002 Flares

Germán Cristiani[1], Igor de Benedetto e Silva[2],
Carlos G. Giménez de Castro[2], Cristina H. Mandrini[1],
Marta G. Rovira[1] and Pierre Kaufmann[2,3]

[1] *Instituto de Astronomía y Física del Espacio, Buenos Aires, Argentina*
[2] *Centro de Rádio Astronomia e Astrofísica Mackenzie, São Paulo, Brazil*
[3] *CSC, Universidade Estadual de Campinas, Campinas (SP), Brazil*

Abstract. Solar flare observations at mm-λ and submm-λ are an important diagnostic tool of particle acceleration processes and energy release (White & Kundu 1992). In that spectral range, gyrosynchrotron from mildly relativistic electrons and thermal bremsstrahlung are the main emission mechanisms. Gyrosynchrotron emission analysis allows to infer the physical conditions in flaring regions. As X-ray emission, it may be used to derive the electron distribution function, althought unlike X-ray emission, gyrosynchrotron emission is also a sensitive function of the magnetic field.

Early observations showed that some flares have an aparent spectral flattening at mm-λ. Kaufmann et al. (1986) tried to explain that flattening with an additional high frequency spectral component. Ramaty & Petrosian (1972) argued that free-free absorption of the non-thermal gyrosynchrotron emission can explain this flatness. Chertok et al. (1995) showed a few more examples of flat spectra. They adhered to the free-free model, and argued that chromospheric evaporation could be responsible for the local density increase that absorbed the gyrosynchrotron emission.

In this work we analyze a sequence of two solar flares ocurred on December 20, 2002. The events took place in the active region AR10226 (S26 W32) at 13:16 UT and 13:18 UT. Radio data at 1-405 GHz frequency range were obtained from the Solar Submillimeter Telescope (SST), Radio Solar Telescope Network (RSTN) and the patrol radiotelescopes of the Bern University, one of them working as a null interferometer at 89.4 GHz. Images from the Hα Solar Telescope for Argentina (HASTA) were used to identify the possible emission sources.

The microwave emission during the peak time of the first flare shows the classical gyrosynchrotron spectrum shape due to a population of accelerated power law electrons in a homogeneous ambient (Ramaty 1969) with a turnover frequency around 12 GHz. The second flare has a microwave spectrum with a flat region of about one decade length (between 2 GHz and 14 GHz approximately). We used a homogeneous model to fit the gyrosynchrotron emission (Ramaty et al. 1994) which gave us, for the first flare, $B = 310$ G, $A = 9''$, $n = 5 \times 10^8$ cm^{-3} and $\delta = 2.9$, for the magnetic field strength, emitting area, number density and electron index respectively. A fitting to the spectrum of the second flare yielded the following results: $B = 310$ G, $A = 18''$, $n = 1.4 \times 10^9$ cm^{-3} and $\delta = 3.8$. In addition, the flux density observed at 212 GHz could indicate the presence of a high frequency second component, as has been observed in other events (see e.g., Kaufmann et al. 2004).

Hα images reveal the presence of three kernels which flare at different times. One of them peaks simultaneously with the first radio bursts, while the brightening of the other two, are coincident with the second burst.

Taking into account the results derived from the fittings, wich showed very different electron populations, we conclude that a loop-loop interaction occurred which changed significantly the medium where the second burst took place. In order to better support this hypothesis we will analyze in detail the AR magnetic field evolution and a coronal magnetic field model will be built to identify the interacting coronal structures.

References

Chertok I. M., Fomichev V. V., Gorgutsa R. V., Hildebrandt J., Kruger A., Magun A., Zaitsev V. V., 1995, Solar Phys. 160, 181

Kaufmann P., Correia E., Costa J. E. R., Zodi Vaz A. M., 1986, A&A 157, 11

Kaufmann P., Raulin J. P., de Castro C. G. G., Levato H., Gary D. E., Costa J. E. R., Marun A., Pereyra P., Silva A. V. R., Correia E., 2004, ApJ 603, L121

Ramaty R., 1969, ApJ 158, 753

Ramaty R., Petrosian V., 1972, ApJ 178, 241

Ramaty R., Schwartz R. A., Enome S., Nakajima H., 1994, ApJ 436, 941

White S. M., Kundu M. R., 1992, Solar Phys. 141, 347

The Physics of Chromospheric Plasmas
ASP Conference Series, Vol. 368, 2007
Petr Heinzel, Ivan Dorotovič and Robert J. Rutten, eds.

The Origin of Solar White-Light Flares

M. D. Ding

Department of Astronomy, Nanjing University, Nanjing, China

Abstract. It is believed that solar white-light flares (WLFs) originate from the lower atmosphere. In particular, some recently observed WLFs show a very large continuum enhancement at 1.56 μm where the opacity reaches minimum. Therefore, it is important to make clear how the energy is transferred to the very low layers responsible for the production of WLFs. We study the possible mechanisms that may directly or indirectly help increase the continuum emission. We make calculations of model atmospheres and compare the results with observations.

1. Introduction

Solar white-light flares (WLFs) are usually among the most energetic flare events. The origin of the continuum emission in WLFs has attracted much attention in last decades. It is generally believed that the white-light continuum originates from either the lower chromosphere through recombinations of hydrogen atoms, or the upper photosphere through emissions from negative hydrogen ions, or both. Correspondingly, semi-empirical models of WLFs require either a heated and condensed layer in the chromosphere or a temperature increase in the photosphere in order to reproduce the observed continuum increase (e.g., Avrett et al. 1986; Mauas et al. 1990; Ding et al. 1994).

Therefore, one of the most important questions is how the lower atmosphere gets heated during the occurrence of WLFs. Up to now, there have been proposed many heating mechanisms that can deposit energy in the temperature minimum region (TMR) and the upper photosphere. These include heating by a non-thermal electron beam (e.g., Hudson 1972; Aboudarham & Hénoux 1986) or a proton beam (Machado et al. 1978), soft X-ray irradiation (e.g., Hénoux & Nakagawa 1977), EUV irradiation (e.g., Poland et al. 1988), dissipation of Alfvén waves (Emslie & Sturrock 1982), return current instability (Matthews et al. 1998), and chromospheric radiative backwarming (Machado et al. 1989; Metcalf et al. 1990; Gan & Mauas 1994). However, most heating mechanisms, if working alone, are shown to be insufficient in producing the heating extent to explain observations (e.g., Machado et al. 1978; Emslie & Machado 1979; Gan et al. 2000).

Observations of WLFs have been greatly advanced since the launch of recent spacecrafts like Yohkoh, TRACE, and RHESSI. There arises more and more evidence showing a close relationship between the white-light emission and the hard X-ray emission, both in space and in time (Hudson et al. 1992, 2006; Neidig et al. 1993a; Metcalf et al. 2003; Matthews et al. 2003; Chen & Ding 2005, 2006;

Fletcher et al. 2006). This suggests that the non-thermal electrons, responsible for the hard X-ray emission, are the main energy supply for powering the WLFs.

The association between the continuum emission and hard X-ray emission has been further investigated quantitatively. Chen & Ding (2005) found that, while the continuum emission and the hard X-ray emission are closely related, the continuum enhancement is not simply proportional to the electron beam flux deduced from the hard X-ray spectra. There are other factors, like the coronal pressure, that can influence the heating of the lower atmosphere. Chen & Ding (2006) found further a motion of the white-light footpoint during the development of the WLF, in roughly the same tendency of the motion of the hard X-ray source. However, the hard X-ray spectrum in this WLF is very soft with a power index of 7. Fletcher et al. (2006) studied the energetics of 9 WLFs and found that the energy required by the enhanced white-light continuum is comparable to the electron beam energy to produce the hard X-ray emission only if the low energy cut-off of the beam is less than 25 keV. These facts suggest that the heating energy in WLFs can reside in lower energy electrons.

Hudson et al. (2006) made a survey of TRACE/RHESSI WLFs and found that white-light continuum emission can appear in weak flares, the weakest of which has an importance of only C1.6. This seems to support the conclusion of Neidig (1989) that white-light continuum occurs in essentially all flares. The fact is only that most of them are out of the detection limit of the current instruments.

On the other hand, observations of WLFs have been extented to longer wavelengths, like the near-infrared (Liu et al. 2001; Xu et al. 2004, 2006). In particular, Xu et al. (2004, 2006) reported two WLFs in 1.56 μm, the wavelength of opacity minimum. Note that the opacity unity at 1.56 μm is about 50 km deeper than that at 5000 Å. For this WLF, strong hard X-ray emission, up to 500 keV, was detected spatially and temporally coincident with the white-light emission.

While it is clear that the electron beam is the chief energy supply to produce most WLFs (except for those termed as Type II WLFs), it is still an unresolved problem to quantitatively reproduce the very strong white-light emission like those observed by Xu et al. (2004, 2006). In this paper, we investigate the origin of WLFs in the framework of electron beam heating plus radiative backwarming. We discuss another possible effect of lateral expansion of flaring plasma. We show that in some special conditions, the observed continuum contrast can be explained.

2. Numerical Method

The basic model for WLFs discussed here can be summarized as follows. At first, the electron beam deposits energy in the chromosphere. The chromospheric material gets heated and results in an enhanced radiation that can be transported below. Then, the photosphere and the TMR are heated indirectly through absorbing more radiation from the chromosphere.

Denote by H the energy deposition rate by an electron beam and by Φ the radiative cooling rate. The former can be calculated using the formulae given in Emslie (1978), while the latter is evaluated through non-LTE calculations

of the model atmosphere. With electron beam heating, the lower atmosphere gets heated through backwarming. This is reflected by a decrease of the radiative cooling rate there. Therefore, to retain the energy balance, a temperature increase is required, that is,

$$H = \Phi_{\rm NT}(T) - \Phi_{\rm T}(T_0), \tag{1}$$

where $\Phi_{\rm NT}$ and $\Phi_{\rm T}$ are radiative cooling rates in the non-thermal and thermal cases, respectively. The temperature in the lower atmosphere rises from T_0 to T, which is the main contributor to the white-light emission. The temperature structure that meets the requirement of Eq. (1) refers to the case of fully heating, which requires a timescale of seconds to tens of seconds in deeper layers.

As was done in Ding et al. (2003), we start from a preflare atmosphere, taken as the F1 model (Machado et al. 1980). We then derive the new temperature distribution of the atmosphere when an electron beam bombards it. This is achieved through numerical calculations. Since the problem is highly non-local. We usually need a large number of iterations to get the final solution of Eq. (1).

Besides, we propose that the lateral expansion of the heated plasma can also help produce WLFs. Heating in the lower atmosphere results in an enhanced gas pressure there; the plasma then expands laterally leading to a dilution of the mass density. This redistributes the energy deposition of the electron beam and also affects the backwarming process. To make an evaluation of the plasma expansion processes, we assume that the gas pressure is nearly a constant during the expansion. Then, the plasma density varies simply anti-proportional to the temperature.

3. Results and Discussions

Using the above method, we have calculated the continuum emission at both the visible wavelength 5000 Å and the near-infrared wavelength 1.56 μm for the model atmospheres heated by various electron beams. We plot in Fig. 1 the continuum contrast, defined as the relative enhancement of the continuum intensity to the non-heated case, against the energy flux of the electron beam (in the case of $\mu = \cos\theta = 1$). Figure 2 shows the variation of the continuum contrast at different positions of the flare site (the energy flux of the electron beam is 3×10^{11} erg cm^{-2} s^{-1}). In the figures, the solid and dashed lines are for the cases without and with considering the plasma expansion effect, respectively.

Figures 1 and 2 show that the plasma expansion effect may play an important role in the production of WLFs. We find that the model that includes electron beam heating, radiative backwarming, and plasma expansion effect can explain the very energetic WLFs observed by Xu et al. (2004, 2006), as long as the electron beam is strong enough. This is supported by the hard X-ray observations for these WLFs.

3.1. The center-to-limb variation

The results show that, the same atmospheric condition and the electron beam yield a bigger continuum contrast in cases close to the limb than close to the disk center. This is an expected result. The reason is that in limb cases, the continuum emission is formed in higher layers that are easier to heat. However,

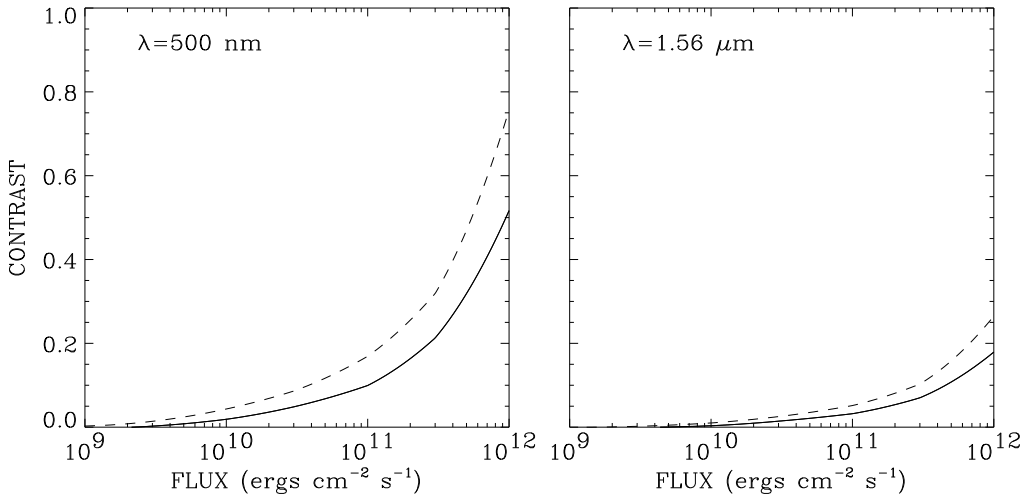

Figure 1. Continuum contrast at 5000 Å and 1.56 μm in dependence on the energy flux of the electron beam (in the case of $\mu = 1$). Solid and dashed lines are for the cases without and with considering the plasma expansion effect, respectively.

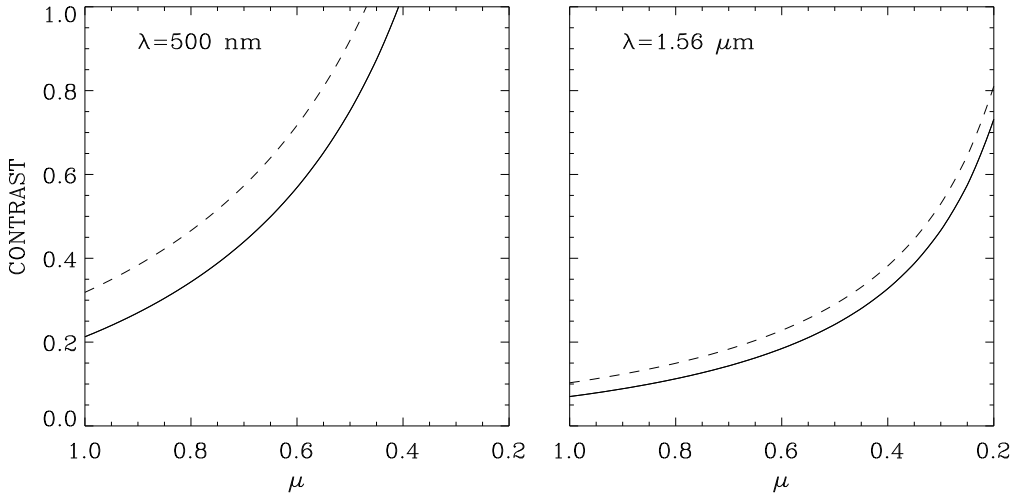

Figure 2. Continuum contrast at 5000 Å and 1.56 μm in dependence on the flare site (the energy flux of the electron beam is 3×10^{11} erg cm^{-2} s^{-1}). Solid and dashed lines are for the cases without and with considering the plasma expansion effect, respectively.

distribution of the occurrence rate of WLFs is not simply a monotonic function of the angular distance. It may be rather complicated, because solar activity is usually concentrated in preferred latitude belts, and in lime cases, some WLFs are occulted by the solar disk. A detailed discussion on this issue can be found in Neidig et al. (1993b).

3.2. WLFs and ordinary flares

In observations, most of the flares are found to be associated with non-thermal electrons. One then asks a practical question: do all flares show more or less white-light continuum emission? Judging from the calculation results, we find that the continuum increase is actually very unconspicuous when the electron beam is weak. Therefore, if we set a detection threshold for the continuum contrast, say 5%, we then need a fairly strong electron beam to produce detectable WLFs in observations, in particular in cases close to the disk center. This may answers why WLFs are usually among the most energetic flares. However, the real situation may be more complex than a simple electron beam heating model. If there are other heating mechanisms, as mentioned in Sect. 1, we may detect white-light continuum emission in weaker flares. We can also say that, with the sensitivity of observing instruments improved, more and more WLFs should be observed; correspondingly, the fraction of detected WLFs will be increased.

3.3. Type I and Type II WLFs

According to Machado et al. (1986), WLFs can be classified into two categories. Type I WLFs show a Balmer/Paschen jump in the continuum spectra, strong Balmer line emission, and associated hard X-ray emission (see also Fang & Ding 1995). The majority of WLFs belong to this type. However, there is a small fraction of WLFs, the so-called Type II WLFs, showing only weak chromospheric line emission and no obvious Balmer/Paschen jump. Thus the canonical picture cannot work well in this case.

Energy release through magnetic reconnection in lower layers has been proposed as a possibility for Type II WLFs. In particular, Chen et al. (2001) performed numerical simulations showing that although the magnetic reconnection in a lower layer is less efficient than in corona, it can still heat the atmosphere to the extent that produces white-light continuum enhancement. Under the assumption that energy release occurs in the TMR, Ding et al. (1999) studied the response of the atmosphere subject to both electron beam heating and radiative heating, and computed the continuum output in different time stages during the flare evolution. The results show that in the final stage, when the atmosphere is fully heated and the electron beam ceases to exist, the continuum spectrum is quite similar to a Type II WLF spectrum.

Acknowledgments. This work was supported by National Natural Science Foundation of China (NSFC) under grants 10221001, 10333040, and 10673004, and by NKBRSF under grant 2006CB806302.

References

Aboudarham, J., Hénoux, J.-C. 1986, A&A, 168, 301
Avrett, E. H., Machado, M. E., & Kurucz, R. L. 1986, in The Lower Atmosphere in Solar Flares, ed. D. F. Neidig (Sunspot, NM: National Solar Observatory), 216
Chen, P. F., Fang, C., & Ding, M. D. 2001, ChJAA, 1, 176
Chen, Q. R. & Ding, M. D. 2005, ApJ, 618, 537
Chen, Q. R., & Ding, M. D. 2006, ApJ, 641, 1217
Ding, M. D., Fang, C., Gan, W. Q., & Okamoto, T. 1994, ApJ, 429, 890
Ding, M. D., Fang, C., & Yun, H. S. 1999, ApJ, 512, 454

Ding, M. D., Liu, Y., Yeh, C.-T., & Li, J. P. 2003, A&A, 403, 1151
Emslie, A. G. 1978, ApJ, 224, 241
Emslie, A. G. & Machado, M. E. 1979, Solar Phys., 64, 129
Emslie, A. G. & Sturrock, P. A. 1982, Solar Phys., 80, 99
Fang, C. & Ding, M. D. 1995, A&AS, 110, 99
Fletcher, L., Hannah, I. G., Hudson, H. S., & Metcalf, T. R. 2006, ApJ, in press
Gan, W. Q. & Mauas, P. J. D. 1994, ApJ, 430, 891
Gan, W. Q., Hénoux, J. C., & Fang, C. 2000, A&A, 354, 691
Hénoux, J.-C. & Nakagawa, Y. 1977, A&A, 57, 105
Hudson, H. S. 1972, Solar Phys., 24, 414
Hudson, H. S., Acton, L. W., Hirayama, T., & Uchida, Y. 1992, PASJ, 44, L77
Hudson, H. S., Wolfson, C. J., & Metcalf, T. R. 2006, Solar Phys., 234, 79
Liu, Y., Ding, M. D., & Fang, C. 2001, ApJ 563, L169
Machado, M. E., Emslie, A. G., & Brown, J. C. 1978, Solar Phys., 58, 363
Machado, M. E., Avrett, E. H., Vernazza, J. E., & Noyes, R. W. 1980, ApJ, 242, 336
Machado, M. E. et al. 1986, in The Lower Atmosphere of Solar Flares, ed. D. F. Neidig (Sunspot, NM: National Solar Observatory), 483
Machado, M. E., Emslie, A. G., & Avrett, E. H. 1989, Solar Phys., 124, 303
Matthews, S. A., Brown, J. C., & van Driel-Gesztelyi, L. 1998, A&A, 340, 277
Matthews, S. A., van Driel-Gesztelyi, L., Hudson, H. S., & Nitta, N. V. 2003, A&A, 409, 1107
Mauas P. J. D., Machado M. E., & Avrett E. H. 1990, ApJ, 360, 715
Metcalf, T. R., Canfield, R. C., & Saba, J. L. R. 1990, ApJ, 365, 391
Metcalf, T. R., Alexander, D., Hudson, H. S., & Longcope, D. W. 2003, ApJ, 595, 483
Neidig, D. F. 1989, Solar Phys., 121, 261
Neidig, D. F., Kiplinger, A. L., Cohl, H. S., & Wiborg, P. H. 1993a, ApJ, 406, 306
Neidig, D. F., Wiborg, P. H., & Gilliam, L. B. 1993b, Solar Phys., 144, 169
Poland, A. I., Milkey, R. W., & Thompson, W. T. 1988, Solar Phys., 115, 277
Xu, Y., Cao, W., Liu, C., Yang, G., Qiu, J., Jing, J., Denker, C., & Wang, H. 2004, ApJ, 607, L131
Xu, Y., Cao, W., Liu, C., Yang, G., Jing, J., Denker, C., Emslie, A. G., & Wang, H. 2006, ApJ, 641, 1210

The Physics of Chromospheric Plasmas
ASP Conference Series, Vol. 368, 2007
Petr Heinzel, Ivan Dorotovič and Robert J. Rutten, eds.

Energy Deposition in White Light Flares with TRACE and RHESSI

Lyndsay Fletcher[1,2], Iain G. Hannah[2], Hugh S. Hudson[2]
and Thomas R. Metcalf[3]

[1] *Department of Physics and Astronomy, University of Glasgow, UK*
[2] *Space Sciences Laboratory, University of California Berkeley, USA*
[3] *NWRA/Colorado Research Associates, Boulder, USA*

Abstract. In Fletcher et al. (2007) we investigated the white light (WL) continuum during solar flares and its relationship to energy deposition by electron beams. In 9 flare events, spanning GOES classifications from C4.8 to M9.1, we have high cadence TRACE WL and RHESSI hard X-ray observations, and compare the WL radiative power output with that provided by flare electrons. Under the thick–target model assumptions, we find that the electron beam must extend down to 15–20 keV, and the energy input to the chromosphere should occur within the collisional stopping depth of these electrons - approximately 2×10^{-4} g cm^{-2}. In this short paper, we discuss some ideas on flare WL emission, summarise the results of the Fletcher et al. (2007) study and discuss their implications for chromospheric heating and white light flare emission.

1. Introduction

The earliest recorded flare observations were of white light flares (WLFs), yet the physical mechanism for the generation of this broadband emission remains unknown. The fact that WLFs can outshine the surrounding photosphere (and in fact in some large flares are observable against the entire visible photosphere, e.g., Woods et al. 2004) demonstrates that they involve colossal energy deposition. Direct imaging shows that this deposition occurs in very small surface patches. The problem of generating the WL continuum enhancement is intimately related to the problem of heating around the chromospheric temperature minimum region during flares, as inferred from observations of flare line emission (Machado & Linsky 1975).

An excellent overview of possible modes of WL generation during flares was presented by Metcalf et al. (1990). We concentrate here on WL generation mechanisms involving particle beams. The earliest such theories (e.g., Najita & Orrall 1970) held that WL emission was caused by direct excitation of the photosphere by beams of electrons or protons from the corona, which led to heating and ionization. Both processes would increase the white-light yield, through an increase in the blackbody intensity and in the H^- opacity. However, to penetrate to the photosphere, electrons of hundreds of keV are required (Aboudarham & Henoux 1986a estimate 350 keV), which - given that we know from hard X-ray observations that electrons have a roughly power-law distribution in energy - requires orders of magnitude more energy at tens of keV energy. This is not energetically feasible. The proton penetration energy to the photosphere is on the

order of 15 MeV. However, to have a reasonable energy budget for the flare, and explain the WL emission, one would require all protons to be at $\approx 10 - 20$ MeV (Machado et al. 1978), inconsistent with inferences from γ-ray observations.

Brown (1973) studied the effect of localised heat input by electron beams, finding significant temperature increases in relatively narrow layers of the solar chromosphere. Machado & Linsky (1975) point out that Brown's analytic results are similar, in terms of temperature as a function of column depth, to their semi-empirical modeling, especially when correction for Brown's over-estimate of radiative losses is made. However models relying solely on beam heating are unable to provide the temperature minimum region enhancement. Machado & Linsky (1975) and Machado et al. (1978) comment that excitation by an electron beam cannot, for reasonable beam energies, produce the upper-photospheric temperature increase, deduced from spectral line observations of the Ca II lines, of ≈ 100 K at mass column densities down to about 0.3 g cm^{-2}.

The effect of collisional over-ionization in the context of WLFs was first discussed by Hudson (1972), who investigated the free-bound continuum generated following direct collisional ionization of the deep chromosphere by electron beams. Later models of WL generation, known as "chromospheric backwarming" models, studied the radiative heating and excitation of deep layers by the free-bound Balmer-Paschen continuum (e.g., Aboudarham & Henoux 1987, Aboudarham & Henoux 1989). Since the temperature minimum region of the deep chromosphere produces the ultraviolet continuum, it should also absorb and be heated by these wavelengths. Other backwarming models have invoked optically thin ultraviolet lines (Machado et al. 1978), extreme UV (Emslie & Machado 1979) or soft X-rays (Somov & Syrovatskii 1974, Machado 1978), which produces photoionization of heavy elements and enhancement of H^- emission. But to be effective, such models require very compact (≈ 100 km) and intense sources, within a few hundred kilometers of the temperature minumum region (e.g., Emslie & Machado 1979, Metcalf et al. 1990). Conceivably, observations in the 1550 Å filter of TRACE could help assess whether this is reasonable; at the time of these earlier studies it was considered to be unlikely.

2. Chromospheric Backwarming

Following a detailed study of 5 solar flares Metcalf et al. (1990) concluded that chromospheric backwarming by Balmer-Paschen continuum was the most likely WL generation mechanism. The Balmer-Paschen models require excitation at a depth with sufficient neutral hydrogen to provide the Balmer-Paschen emissivity. In Aboudarham & Henoux (1986b) and Aboudarham & Henoux (1989) the effect of collisional ionization only becomes significant at column masses above a few times 10^{-3} g cm^{-2}, or column depths of a few times 10^{21} cm^{-2}; the bulk of the Paschen continuum is also generated at such values. A study of a TRACE and Yohkoh Hard X-ray Telescope event by Metcalf et al. (2003) concluded that sufficient energy existed in electrons above 20 keV to generate the Balmer-Palmer continuum required to explain the backwarming, and also that the beam ionization leading to the enhanced continuum and ultimately the WL emission was formed at an electron density of about 9×10^{12} cm^{-3}. In a semi-empirical flare model atmosphere, such as that of Machado et al. (1980), 20 keV

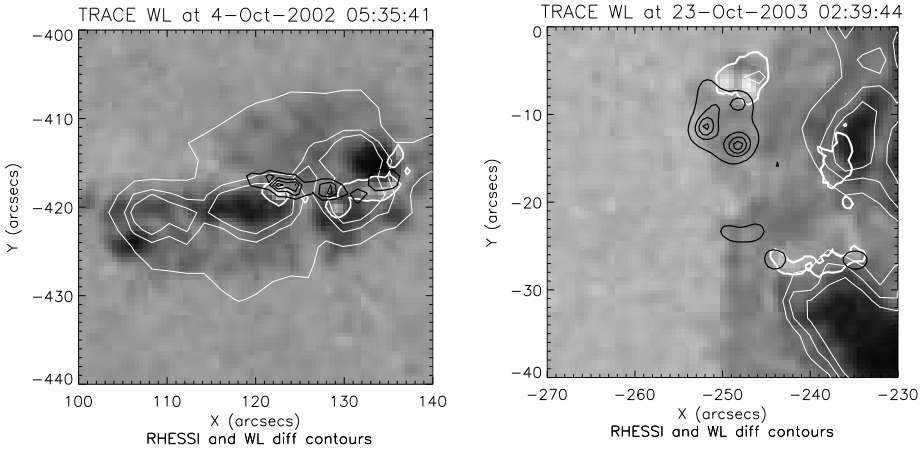

Figure 1. Two examples of RHESSI/TRACE flares from the sample in Fletcher et al. (2007). On the left is a case in which the HXR 25-50 keV contours (black contours, calculated using Pixons) aligns well with the maxima in the TRACE WL difference images (thick white contours). On the right, the alignment is not so good though the spatial distribution of the strong features is the same. The contours are superposed on the nearest WL image to HXR maximum.

electrons can readily penetrate to such densities but this is not true of pre-flare atmospheres, in which the bulk of the electrons would be stopped in targets of insufficient optical depth to produce the required UV continuum. So the question of whether chromospheric backwarming can indeed produce the WL enhancement depends on the model used for the chromospheric density distribution. As the WL enhancement (like the HXR enhancement) is an impulsive-phase phenomenon, there is justification for using quiet sun models, such as the Model "C" of Vernazza et al. (1981), rather than the flare models of Machado et al. (1980), since these latter are based primarily on spectral observations made after the Hα flare maximum. This is most certainly also after the flare impulsive phase, once the atmosphere has had time to respond dynamically to the flare energy input. WL and HXR emission is an impulsive-phase phenomenon.

3. Summary of the TRACE White Light and RHESSI Flare Study

In our recent study (Fletcher et al. 2007) we used joint RHESSI and TRACE white light observations to investigate the energetics of WLF production. The RHESSI hard-X-ray and TRACE WL sources correlate well in space (within pointing errors) and time (with peaks coinciding within the ≈ 10 s time cadence). Examples of the HXR and WL co-alignment are shown in Fig. 1, and of time profiles in Fig. 2. The interested reader is referred to the full Journal paper for more detail.

By calculating the WL luminosity and comparing it with the energy content of the electron beam implied by the HXR emission, we can arrive at an

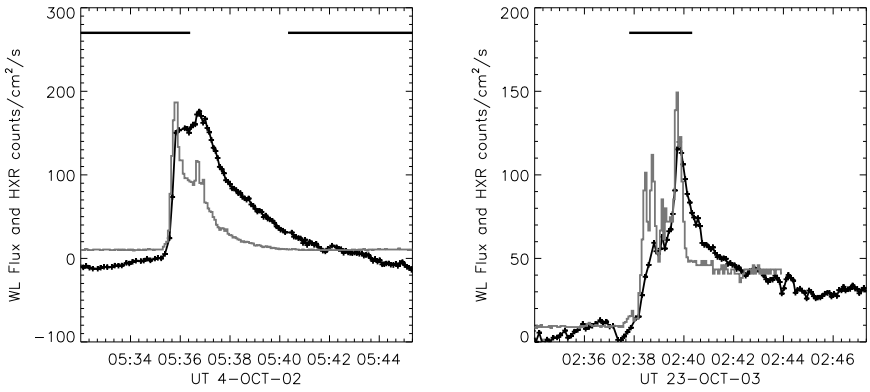

Figure 2. The light curves corresponding to the flares in Fig. 1. Black shows the RHESSI 25-50 keV light curve, and grey the TRACE WL light curve. The horizontal black bars show the times during which the RHESSI thin attenuator is in. TRACE WL includes a strong UV response; when this is subtracted (see Metcalf et al. 2007 in prep.) the "true" WL peaks map extremely well onto the HXR peaks.

upper limit for the energy down to which the beam must extend to balance the WL luminosity. Since we do not have any substantial WL spectral information we can only do this approximately. However, the TRACE observation sequence interleaves broadband WL emission with images taken through the 1700 Å filter, so we do have a filter ratio value. We proceeded under two different assumptions: firstly that the WL (and 1700 Å) enhancement is increased blackbody radiation due to photospheric heating; secondly that the emission is Balmer-Paschen continuum emission but not at an increased temperature (c.f. Metcalf et al. 2003), rather at the photospheric colour temperature of 5300 K. We are confident that the first assumption provides an upper limit to the WL power, since we use an increased temperature of 25,000 K, commensurate with the observed ratio of 1700 Å to broadband WL emission. The second assumption provides a lower limit, since by taking a temperature of 5300 K we are neglecting the enhanced UV component.

The electron beam power can be calculated by invoking the collisional thick-target model Brown (1971), in which an electron beam radiates HXR radiation as it decelerates (and heats) in the dense chromospheric plasma. The collisional thick-target model provides the link between the observed properties of the HXR photon spectrum and the parameters of the parent electron spectrum. The beam power can be deduced straightforwardly knowing the slope of the HXR spectrum in its power-law regime, the intensity, and assuming a "cut-off" electron energy, below which there are no more beam electrons.

The result of this study can be summarised as follows: The lower limit to the WL enhancement implies that the HXR and WL power budgets are compatible, but that the parent electron spectrum must extend to 15-20 keV to provide the required power. In Table 1 we give the white-light luminosity assuming the Balmer-Paschen model (lower limit); the photon spectral index; the electron

beam cut-off energy (E_c) required to match the power budgets for each flare – see below.

Table 1. TRACE and HXR flare parameters

Date	Time	GOES	$P_{WL}/10^{27}$[a]	γ	E_c(keV)
2002-07-26	19:59:28	M1.0	12	7.4	15.1
2002-10-04	05:35:41	M4.0	42	4.4	18.9
2002-10-05	10:41:58	M1.2	8.8	4.7	13.5
2002-11-12	18:15:49	C9.9	8.3	4.8	17.8
2002-06-12	01:22:59	M7.3	23	7.3	19.9
2003-10-23	02:39:42	M2.4	33	5.9	22.9
2004-01-09	01:39:42	M3.2	13	6.0	20.9
2004-07-22	00:29:42	M9.1	140	5.6	15.7
2004-07-24	13:34:47	C4.8	32	4.3	15.0

[a] WL power assuming Balmer-Paschen at $T = 5.3 \times 10^3$ K, in erg s^{-1}

The electron beams are typically fairly steep power-laws (with index given by $\gamma + 1$ in a fully-ionised thick target) so the majority of the beam energy resides in the lower energy part of the spectrum. So, if the beam is "injected" at the top of the chromosphere it cannot penetrate very deep, and the excitation that leads ultimately to the WL enhancement must also occur relatively high in the atmosphere. From Emslie (1978) we have (for electrons)

$$\frac{dE}{dN} = -\frac{2\pi e^4}{\mu E}\left(x\Lambda + (1-x)\Lambda'\right) \tag{1}$$

where E is the electron energy, N the column depth, μ the pitch-angle cosine of the beam electrons (which we take to be 1), e the electronic charge, Λ the Coulomb logarithm for charged-particle interactions, Λ' the effective Coulomb logarithm for electron-neutral interactions, and x the ionization fraction (see Emslie (1978) for details). This can be used to calculate the stopping depth of an electron in a target of arbitrary ionization fraction. Electrons at the values of E_c we find have a collisional stopping depth of $\approx 10^{20}$ cm^{-2}, or 2×10^{-4} g cm^{-2}. Using a background VAL-C chromospheric model Vernazza et al. (1981), Fig. 3 compares this stopping depth with the model estimates from Aboudarham & Henoux (1987) for the depth at which the Balmer-Paschen continuum is produced, and of the backwarmed layer.

The penetration depth of those electrons in which the bulk of the beam energy resides is significantly smaller than that typically required by the UV radiative backwarming models.

4. Discussion

Clearly the vertical density structure of the pre-flare chromosphere in the region where the beam interacts is critical in this discussion, as it determines whether the Balmer-Paschen continuum can be excited in a region of sufficiently high density. We have adopted a non-flaring chromosphere since the

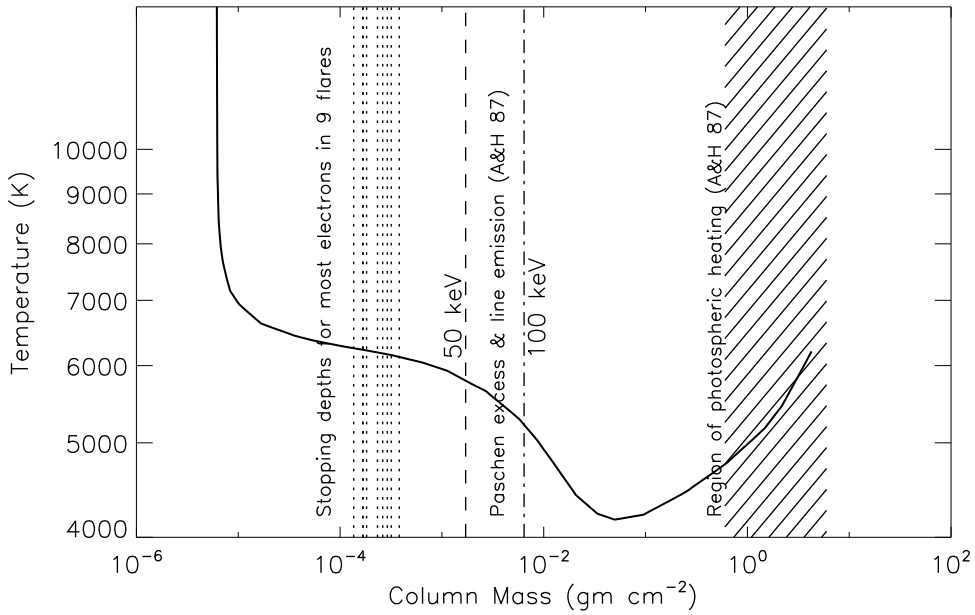

Figure 3. VAL-C model temperature as a function of mass column density. Superposed are (dotted lines) the stopping depths of the majority of electrons in the 9 flares studied; (dash, dot-dash) stopping depths for 50 keV and 100 keV electrons (with the excess Paschen continuum and UV lines generated in this range, Aboudarham and Henoux 1987); (hatched area) the location of photospheric heating (ibid).

WL events that we observe are impulsive phase phenomena and the combination of the HXR time profiles and the motion of the WL and HXR sources from one spot to another during the flare suggest that an electron beam will enter essentially undisturbed chromosphere. However this should be studied in detail using lower-energy RHESSI channels to search for pre-flare activity, or TRACE UV to search for pre-flare chromospheric brightenings in the regions which are later illuminated by the WL and HXR emission.

Although we have not calculated them here, our observations of flare WL footpoint areas, combined with inferred beam parameters, lead us to extremely high electron beam numbers and number fluxes (on the order of $10^{19}\,\mathrm{cm}^{-2}\,\mathrm{s}^{-1}$) which are problematic for the collisional thick target model involving beams accelerated in the corona; firstly the total number of electrons required appears to be in excess of what the flaring corona can supply; secondly, even invoking the involvement of a large coronal volume still requires the electrons to be focussed into a small number of tiny footpoints; thirdly, the beam density in the corona appears to be beyond what can be supported in a stable beam – return current system. Added to this, recent observations of disturbances in the photospheric magnetic field during flares (Sudol & Harvey 2005) and evidence that the electron distribution in the chromosphere is nearer isotropic than beam-like (Kontar & Brown 2007) leads us to suggest that perhaps now it is time

for theoretical models of chromospheric flare heating and particle acceleration to move away from ideas of coronal beams, and concentrate on chromospheric processes, involving large-scale disturbances to the magnetic field (akin to the auroral electron acceleration in the Earth's magnetosphere/ionosphere system) - for example revisiting the work of Emslie & Sturrock (1982) on Joule dissipation of Alfvénic disturbances.

Acknowledgments. I am very grateful for travel support provided by the British Council in Portugal. I am also indebted to Rob Rutten for providing this LaTeX style file. This work was carried out under NASA contract NNG05GG17G.

References

Aboudarham J., Henoux J. C., 1986a, A&A 156, 73
Aboudarham J., Henoux J. C., 1986b, A&A 168, 301
Aboudarham J., Henoux J. C., 1987, A&A 174, 270
Aboudarham J., Henoux J. C., 1989, Solar Phys. 121, 19
Brown J. C., 1971, Solar Phys. 18, 489
Brown J. C., 1973, Solar Phys. 31, 143
Emslie A. G., 1978, ApJ 224, 241
Emslie A. G., Machado M. E., 1979, Solar Phys. 64, 129
Emslie A. G., Sturrock P. A., 1982, Solar Phys. 80, 99
Fletcher L., Hannah I. G., Hudson H. S., Metcalf T. R., 2007, ApJ, in press
Hudson H. S., 1972, Solar Phys. 24, 414
Kontar E. P., Brown J. C., 2007, ApJ, in press
Machado M. E., 1978, Solar Phys. 60, 341
Machado M. E., Avrett E. H., Vernazza J. E., Noyes R. W., 1980, ApJ 242, 336
Machado M. E., Emslie A. G., Brown J. C., 1978, Solar Phys. 58, 363
Machado M. E., Linsky J. L., 1975, Solar Phys. 42, 395
Metcalf T. R., Alexander D., Hudson H. S., Longcope D. W., 2003, ApJ 595, 483
Metcalf T. R., Canfield R. C., Saba J. L. R., 1990, ApJ 365, 391
Najita K., Orrall F. Q., 1970, Solar Phys. 15, 176
Somov B. V., Syrovatskii S. I., 1974, Solar Phys. 39, 415
Sudol J. J., Harvey J. W., 2005, ApJ 635, 647
Vernazza J. E., Avrett E. H., Loeser R., 1981, ApJS 45, 635
Woods T. N., Eparvier F. G., Fontenla J., Harder J., Kopp G., McClintock W. E., Rottman G., Smiley B., Snow M., 2004, Geophys. Res. Letts. 31, 10802

Joana Morais, Joana Rebocho, Arek Berlicki

Pieter Thijssen, Arek Berlicki, Duncan Mackay, Lyndsay Fletcher, Alan Title, Rob Rutten, Hugh Hudson, Godelieve Hammerschlag-Hensberge, Rob Hammerschlag

The Physics of Chromospheric Plasmas
ASP Conference Series, Vol. 368, 2007
Petr Heinzel, Ivan Dorotovič and Robert J. Rutten, eds.

Balmer-Line Diagnostics of Accelerated Particles

L. K. Kashapova[1,2], P. Kotrč[3] and Yu. A. Kupryakov[3,4]

[1]*Institute of Solar-Terrestrial Physics, Irkutsk, Russia*
[2]*Physical Faculty, Irkutsk State University, Irkutsk, Russia*
[3]*Astronomical Institute AS, Ondřejov, Czech Republic*
[4]*GAISH MGU, Moscow, Russia*

Abstract. Preliminary results of empirical study of a non-thermal electron effect on Hα/Hβ line intensity ratio in solar flares are presented. Analysis of spectral observations of the 26 June 1999 flare revealed some peculiarities of the Hα/Hβ line intensity ratio (the "sidelobes") in the emission kernels associated with radio bursts and HXR emission that could be considered as an indirect evidence of accelerated non-thermal particle beams. According to our conclusions they appeared due to non-thermal electron beam effects. Consequently, the obtained results confirmed the theoretical predictions and bore a first witness for a detection of the spatial and temporal presence or absence of the non-thermal electron beams in optical spectra. However, as a more statistically probative evidence was needed, we extended our analysis on two flares where presence of non-thermal mechanisms of excitation was verified by HXR data. The obtained results are quite promising as concerns of diagnostics of the energy release and transfer mechanisms during the flare.

1. Introduction

Diagnostics of the lower atmosphere response to the particle beams still remains an unsolved problem of the solar flare physics. Up to the recent time the measurements of linear polarization caused by a particle beam bombardment has been considered as a perspective method of non-thermal processes detection. However, the late observations showed cases when appearance of HXR sources was followed by absence of any linear polarization (Bianda et al. 2005; Hanaoka 2003). Even more difficulties appeared when theoretical simulations revealed a dependency of the linear polarization value on inclination of magnetic field lines (Zharkova & Kashapova 2005). So, necessity of an additional and independent method of the particle beam diagnostics in optical spectra becomes evident.

Kobylinskii & Zharkova (1996) calculated radiative energy losses for the Balmer series lines. A comparison of energy release distribution by atmospheric density shows that in case of non-thermal electron beam influence the maximum of energy release shifts to deeper layers. Looking for diagnostic tools suitable for comparison of theoretical line profiles with the observed ones, Kašparová & Heinzel (2002) suggested to use the line profile intensity ratios. Authors considered the intensity ratio at 0.4 Å from the Hα line center and revealed a difference in cases of only thermal and non-thermal beam excitation.

From the theoretical simulations of the physical mechanisms is well known that line profiles are formed in different layers of solar atmosphere. When com-

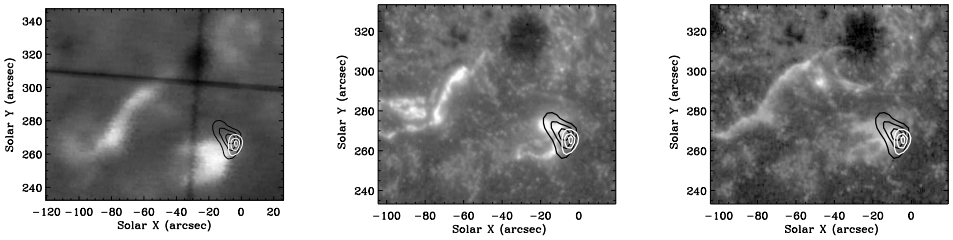

Figure 1. Position of HXR source obtained by Yohkoh Hard X-ray Telescope (from 07:17:12.214 to 07:17:39.714 UT) as projected on the Hα slit-jaw image of the flare taken by MFS at 07:23:18 UT (left) and images in 1600 Å band at 07:17:15 UT and 07:28:45 UT. The L band (13.9–22.7 keV) and the M1 band (22.7–32.7 keV) are marked by black and white lines, correspondingly.

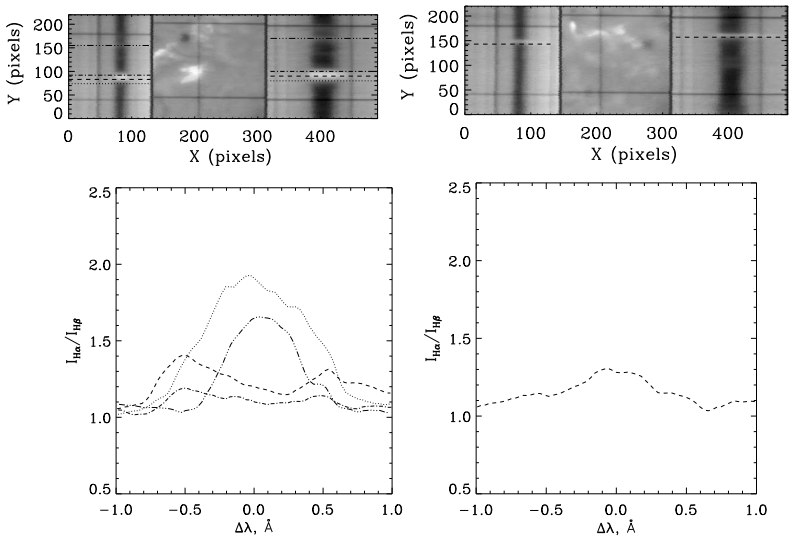

Figure 2. *Left*: The top image is composed of the Hβ spectrogram, Hα slit-jaw filtergram and Hα spectrogram (from left to right) taken by MFS at 07:23:42 UT. The ratios of the Hα to Hβ intensity profiles are in the bottom. A line style corresponds to a scan position as marked on the top panel. *Right*: The same as in the left panel but at 07:40:37 UT.

pared with the thermal mechanism effects in a standard chromosphere model, the non-thermal electron beams result in shift of the energy release maximum to deeper layers and a difference origin in intensity ratio profiles of Balmer series lines. The aim of current contribution is to look for peculiarities of the Hα/Hβ line intensity ratio in the flare emission kernels associated with an indirect evidence of accelerated non-thermal particle (mainly the HXR emission) and to analyze results for applicability of theoretically obtained parameters.

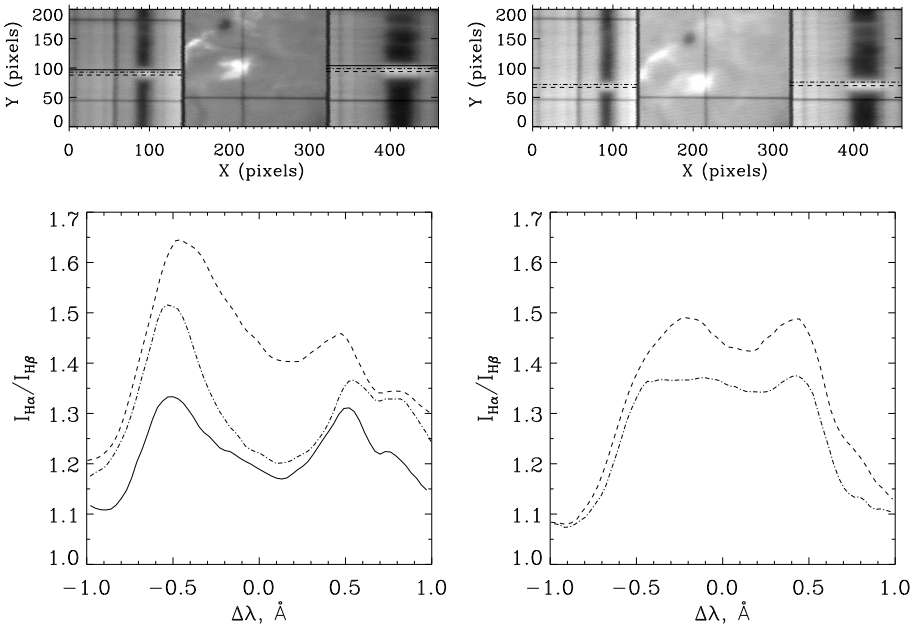

Figure 3. Evolution of the Hα to Hβ intensity ratio profiles. *Left*: The same as in Fig. 2 but at 07:23:41 UT. *Right*: The same as in Fig. 2 but at 07:35:21 UT.

2. Observational Evidence

The first flare, which we analyzed, was the solar flare on 26 June 1999. It consisted of three subsequent phases. All of them were followed by events of quite different types (Kotrč et al. 2004). Only the second phase of the flare was accompanied by radio bursts and HXR emission that could be considered as an indirect evidence of accelerated non-thermal particle beams. Moreover, polarization observations of the third phase obtained by the Large Solar Vacuum Telescope (LSVT) revealed no substantial linear polarization. The observation of all the three different phases obtained by the Ondřejov Multichannel Flare Spectrograph (MFS) gave us an unique opportunity to test a possible effect of electron beams on the intensity of Balmer series spectral lines as was predicted by Kašparová & Heinzel (2002). As can be seen at 1600 Å image in Fig. 1 the emission kernel associated with HXR source was compact and bright at 07:17:15 UT which corresponded to the moment of HXR flux maximum. But at 07:28:45 UT the whole intensity of the kernel decreased and the structure became diffused. We can see only one bright point in this kernel. Possibly, this point corresponds to the real location of HXR source of electron beam with energy more than 22 keV. But in any case, this emission kernel could be chosen as arisen by non-thermal beam effect. In the flare kernel we found that the Hα/Hβ line intensity ratios demonstrated a very specific form (Fig. 2). It substantially differs from those ones obtained in "thermal" kernels (occurring in the first and in the third flare phases). This effect can be characterized by presence of specific "sidelobes" occurring in the ratio of profiles (Kashapova

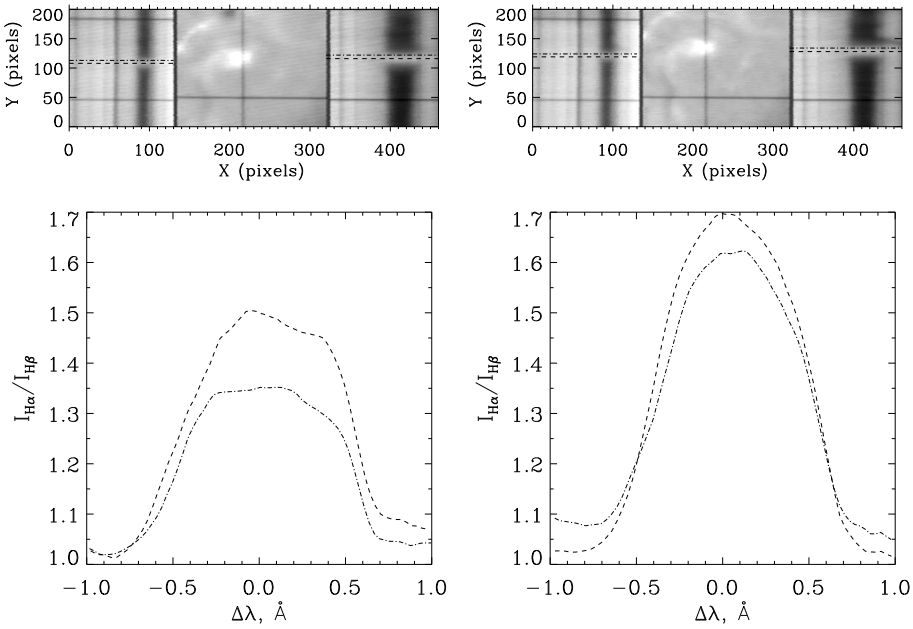

Figure 4. Evolution of the Hα to Hβ intensity ratio profiles. *Left*: The same as in Fig. 2 but at 07:45:35 UT. *Right*: The same as in Fig. 2 but at 07:54:43 UT.

et al. 2005). It is important to point out that the "sidelobes" on the Hα/Hβ line intensity ratio coincided in position and in time only with the occurrence of HXR source.

Effect should follow the occurrence of the particle beams in time and then decay more rapidly then flare emission. We traced the evolution and the possible decay of the sidelobes effect (Figs. 3, 4). The effect was not visible till the end of the emission in this kernel, i.e. a strong emission was still visible after about 40 minutes from the kernel rise, but the "sidelobes" on the profiles ratio had already disappeared after 25 minutes.

For a more statistically probative evidence we extended our analysis on two flares where presence of non-thermal mechanisms of excitation was verified by HXR data. The flare on 13 July 2000 attracted our attention even over its location nearby the solar limb and visibility of two HXR sources that most possibly corresponded to the loop footpoints (see Fig. 5). Its spectrum was little bit softer than the previous flare. The sidelobes effect was detected for both emission kernels and position of peculiarities also coincided. The central part of the profiles was also slightly disturbed. The next flare was the flare on 24 April 2001. Although, this two-ribbon flare was the important (M2.1/N1), the contribution of non-thermal electrons was less then influence of thermal electrons with energies lower 23 keV (see Fig. 6). As it could be seen in Fig. 7, the "sidelobes" effect was detected only in the flare ribbon associated with influence of harder electron beams.

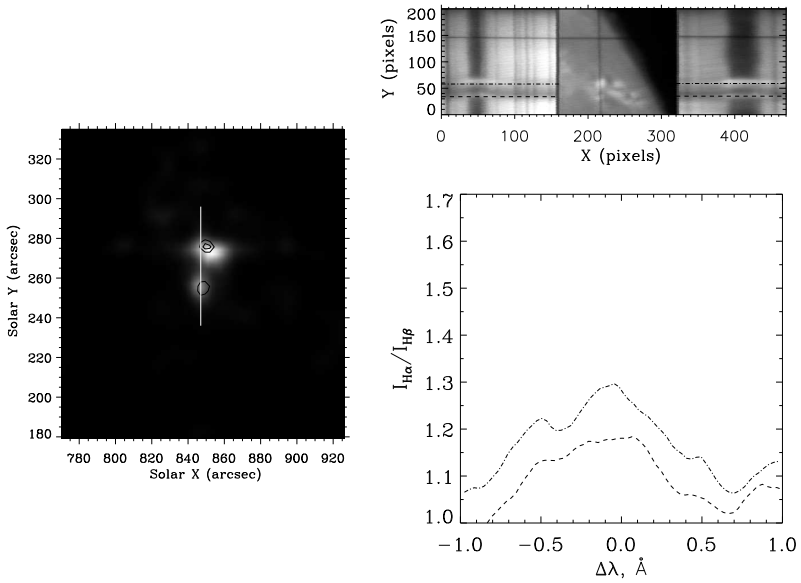

Figure 5. C7.1/SF flare on 13th July 2000. *Left*: Image of HXR source obtained by Yohkoh HXT in the L band overlaid by the M2 HXR-source and position of MSF spectrograph slit. *Right*: The same as in Fig. 2 but at 06:12:58 UT on 13th July 2000.

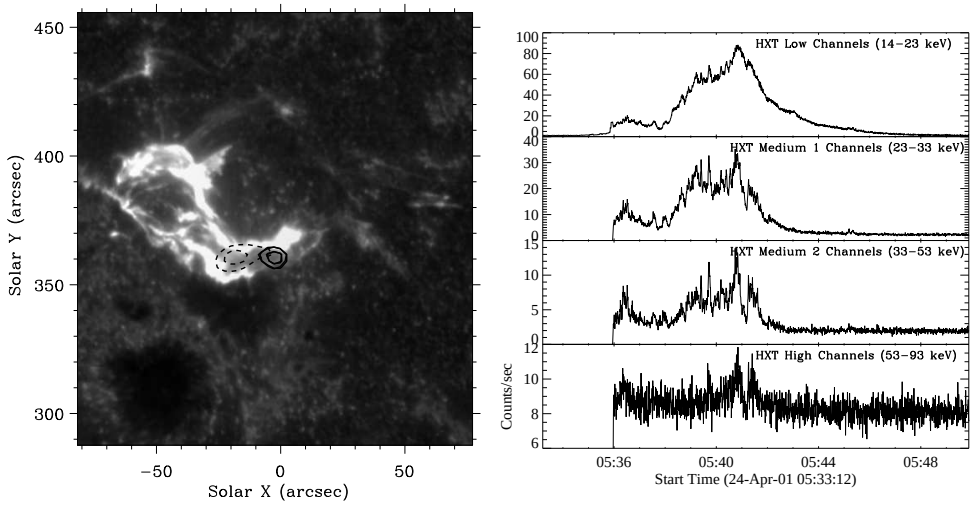

Figure 6. M2.1/1N flare on 24th April 2001. *Left*: Position of HXR sources obtained by Yohkoh HXT (L and M2 bands, dashed and solid lines, correspondingly) overlaid on images in 1600 Å band at 05:38 UT. *Right*: Temporal variation of HXR bands − L, M1, M2, and H registered during the flare.

3. Brief Conclusions

The predicted and now also observed effect of "sidelobes" is found in three flares. As it was expected the effect depends on HXR source location and temporal

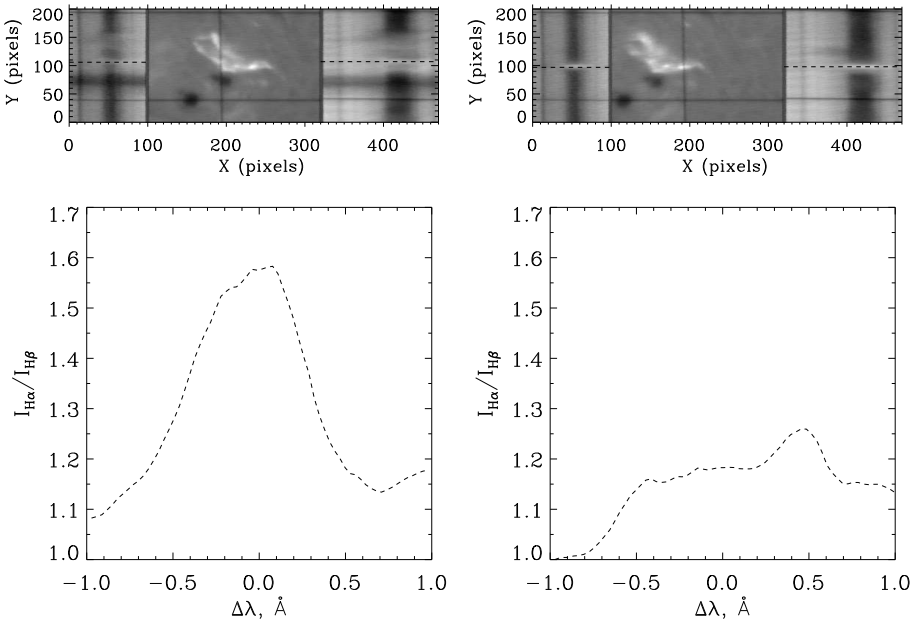

Figure 7. M2.1/1N flare on 24th April 2001. *Left*: The same as in Fig. 2 but at 05:37:33 UT. *Right*: The same as in Fig. 2 but at 05:38:12 UT.

occurrence. We could suppose that importance of the effect depends on the electron beam parameters as power index of HXR spectrum. Thus, theoretical calculations of thermal mechanisms coupled with accelerated electron beams in flares showed that the Hα/Hβ line intensity ratio could be a possible indicator whether a mechanism of non-thermal excitation was present or absent. The obtained results are quite promising as concerns of diagnostics of the energy release and transfer mechanisms during the flare.

Acknowledgments. We are grateful to the Yohkoh, SOHO and TRACE teams who provided free access to their results. LKK would like to thank the Program of Basic Investigations of RAS No 30, grant 06-02-27287-z of RFBR and the CSPM organizing committee for support. PK appreciates grant A3003203 of the Academy of Sciences of the Czech Republic, the project AV0Z10030501 of the Astronomical Institute of the Academy of Sciences of the Czech Republic and the project No 95 of the Czech–Slovak cooperation.

References

Bianda M., Benz A. O., Stenflo J. O., Küveler G., Ramelli R., 2005, A&A 434, 1183
Hanaoka Y., 2003, ApJ 596, 1347
Kashapova L. K., Kotrč P., Kupryakov Y. A., Kašparová J., 2005, in ESA SP-600: The Dynamic Sun: Challenges for Theory and Observations
Kašparová J., Heinzel P., 2002, A&A 382, 688
Kobylinskii V. A., Zharkova V. V., 1996, Advances in Space Research 17, 129
Kotrč P., Kashapova L. K., Kupryakov J. A., 2004, in A. V. Stepanov, E. E. Benevolenskaya, A. G. Kosovichev (eds.), IAU Symposium, 463
Zharkova V. V., Kashapova L. K., 2005, A&A 431, 1075

The Physics of Chromospheric Plasmas
ASP Conference Series, Vol. 368, 2007
Petr Heinzel, Ivan Dorotovič and Robert J. Rutten, eds.

Signatures of High-Energy Particles in Hα Emission Before the Solar Flare of August 16, 2004

L. K. Kashapova[1], V. V. Zharkova[2] and V. V. Grechnev[1]

[1] *Institute of Solar-Terrestrial Physics, Irkutsk, Russia*
[2] *The School of Informatics, University of Bradford, Bradford, UK*

Abstract. We study multi-spectral chromospheric and coronal emissions that appeared during the impulsive event occurring before the flare on 16 August 2004 observed by RHESSI, Large Solar Vacuum Telescope (Irkutsk), and Nobeyama Radioheliograph (NoRH, 17 and 34 GHz). There are three separate sources detected: 1 in hard X-rays (RHESSI), two in microwaves (NoRH) (1 of which coincides with HXR) and one in Hα emission (3). The emission in all sources reveals a close (within 1 s) temporal correlation that can be only associated with precipitation of high-energy particles. Possible scenarios of particle precipitation and its effect on the observed signatures are discussed.

1. Observational Data

According to RHESSI observations, the impulsive event on 16 August 2004 started at 03:28:20 UT in AR 10656. Figure 1 shows the locations of 3–100 keV X-ray sources at $(677'', -250'')$ (hereafter arc seconds from the solar disk center). Note that the higher-energy HXR source is extended in the NE–SW direction. Also there are two compact impulsive microwave sources (FWHM $\simeq 6$ s) observed with NoRH at 17 and 34 GHz from 03:28:18 to 03:28:31 UT (Fig. 2). The eastern source (E) coincides with the HXR source (Fig. 3). The other, a weaker western source (W), is located at $(764'', -250'')$. The maximum brightness temperature of E source is 1.4 MK at 17 GHz and 1 MK at 34 GHz, while its maximum flux density is 6.7 sfu at 17 GHz. The maximum brightness temperature of the W source is 1 MK at 17 GHz and 60 000 K at 34 GHz. The microwave flux of the W source lags behind the E source by ≈ 1 s at 17 GHz (Fig. 2, right panel). Both sources are in average positively polarized by 40% (E) and 20% (W), while the degree of circular polarization in the E source has a slope in the NE–SW direction from 20% to 50%.

There is also the Hα line emission observed with broad (up to 2 Å) wings and the maximum occurring at 03:28:22 UT that is close (within a few seconds) to the HXR spike ('dash–three dots' line in Fig. 1). However, the Hα source is the third source that is located on the west $(760'', -269'')$ from the HXR source but on the south from the east E source observed in microwaves. The linear polarization in the center of the Hα line does not exceed 2%. The origin of this Hα emission is not yet clear, but it is important to establish, because a powerful flare occurred from 03:30 UT onwards just at the same location. The TRACE 171 Å image (Fig. 3, right) shows the bright features corresponding to the position of the HXR source. There is also a small bright loop-like structure

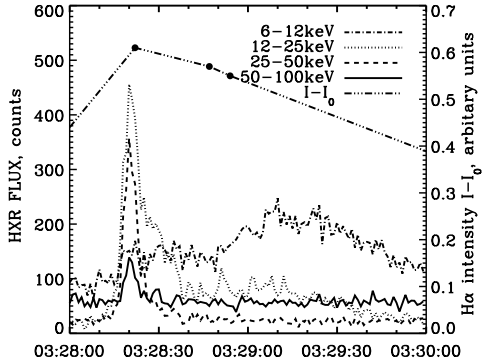

Figure 1. Time profiles of hard X-ray flux (RHESSI) and Hα intensity.

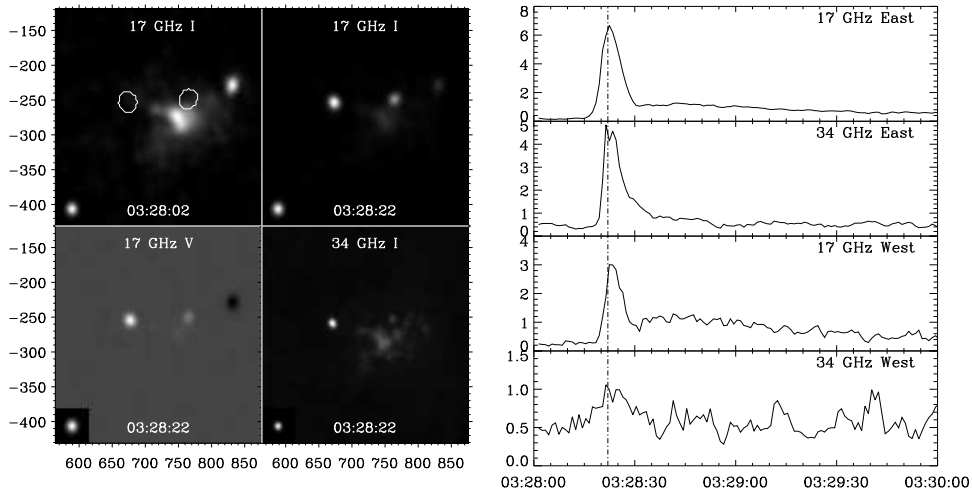

Figure 2. The microwave I and V images (left) with the contours of the E and W sources, whose time profiles (1 s sampling) are shown in the right panel. The NoRH beam is shown in the lower left corners of each image.

corresponding to the microwave source E and the extended HXR source. The other two bright features are related to the microwave source W and the Hα emission. A SOHO/MDI magnetogram shows that the SW end of the extended eastern site is in the North-polarity area, while its NE end and the remote western region are in South-polarity areas.

2. Parameters of Non-thermal Electrons

The spectra and polarization of the both microwave (MW) sources show that their emission is the gyrosynchroton one from high-energy electrons. The well-correlated temporal profiles in both MW sources prove their connection by a closed loop. With a semi-circular shape of the loop, from microwave images in Fig. 2 and taking into account a spherical shape of the solar surface, its length is estimated to be about 1.1×10^5 km. The delay of $\simeq 1$ s can only be

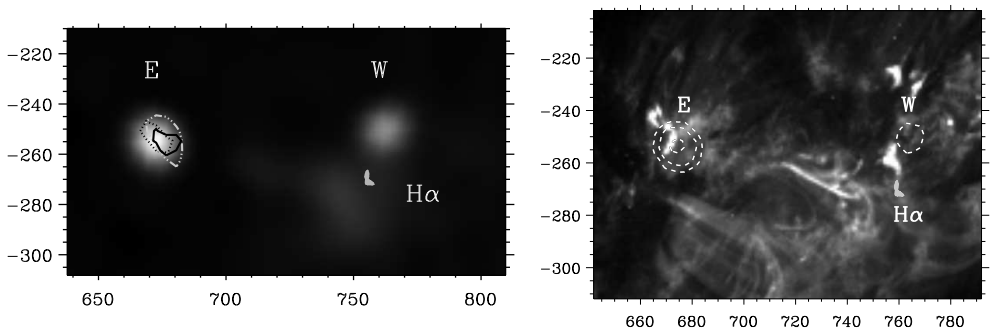

Figure 3. *Left*: The NoRH 17 GHz images overlaid by 50% contours of the X-ray sources for 6–12 keV (solid black), 12–25 keV (dotted black), and 25–50 keV (light gray) bands. The solid gray contour shows Hα source. *Right*: TRACE 171 Å image (03:28:22) with the white dashed contours of the microwave sources and the gray contour of the Hα source.

caused by the fast electron travel time between the two footpoints. Thus, the electron energy is roughly estimated to be ∼150–200 keV assuming a beam-like pitch-angle anisotropy for this burst. From the NoRH images observed at 17 and 34 GHz, the electron power-law index δ is $2.3 - 3.1$ in the E source and $\delta \simeq 4.1 - 4.6$ in the W source. The microwave W source and Hα-emitting feature are associated with different sides of a bright feature visible in a soft X-ray GOES/SXI image. The observations with the Siberian Solar Radio Telescope (SSRT) also show the E source at 5.7 GHz.

In order to estimate the parameters of non-thermal electrons from X-ray observations, we fitted two X-ray spectra computed from the RHESSI data. One of them is an instantaneous mean RHESSI spectrum obtained using OSPEX software, another spectrum was computed for the isolated HXR source. This spectrum was accumulated from a set of 1–100 keV images observed from 03:28:20 through 03:28:24 UT reconstructed with the Pixon method. Hence, we obtain the total flux from the latter spectrum of $3.26 \times 10^9\,\mathrm{erg\,s^{-1}\,cm^{-2}}$ and the photon spectral index $\gamma = 2.88$. The electron index δ is related to γ as $\delta = \gamma + 1.5$ for thick-target X-ray bremsstrahlung and $\delta = \gamma - 0.5$ for thin-target case. In order to pick the correct model, let us discuss the temporal variations of the HXR and MW emissions. There is a discrepancy between $\delta_{\mathrm{MW}} \simeq 2.3 - 3.1$ estimated from the microwaves and $\delta_{\mathrm{HXR}} = 4.4$ from the HXR emission. A well-known trapping effect could be employed to interpret a difference up to $\delta_{\mathrm{MW}} = \delta_{\mathrm{HXR}} - (0.5 - 2)$. However, in this flare the microwave time profiles do not exhibit any manifestations of trapping being as short as the HXR ones that rules out magnetic trapping as the explanation. On the other hand, the absence of pronounced soft X-ray emission in the main eastern flare site suggests that the precipitating electrons penetrated into deeper atmospheric layers and deposited only a part of their energy in the chromosphere. Then this HXR emission in the E source can be considered closer to the thin-target emission that co-ordinates the spectral indices δ_{MW} and δ_{HXR}.

3. Discussion and Conclusions

The flare configuration mainly consisted of three loops: a compact one shown by the X-ray and TRACE 171 Å images, located at the main, eastern flare site and two longer asymmetric ones connecting the main flare site with the remote western site of South polarity. The compact loop's SW end had magnetic North polarity, while the NE end had South polarity, corresponding to the slope of the microwave polarization. The hardest-spectrum electrons were present in the small eastern loop, where both HXR and MW emissions were observed. In the longer loop, at whose western end the microwave emission was observed, electrons had a softer spectrum. The Hα-emitting region where no microwave or HXR emissions were detected likely represents the western end of the third long loop.

The microwave flux from the W source at 17 GHz was only twice smaller than that one from the E source. This fact and the absence of high energy electrons in the third source implies the Hα emission to be caused by precipitation of protons rather than electrons that is also consistent with the wide wing emission in the Hα line. The quasi-thermal origin of the emission in this region is also confirmed by TRACE 171 Å and SXR GOES/SXI images.

Correlation of all light curves in the sources points out to their common origin in the main flare site (E-site) related to energy release. Presumably, this is reconnection of magnetic fluxes with subsequent energy transport by accelerated electrons and/or protons, from the reconnection site to lower atmospheric layers. TRACE 171 Å images taken on 16 August 2004 (20 hr after the event) and presented at the Web site `http://zorak.lmsal.com/ar/` for active regions with the restored coronal magnetic field lines extrapolated from magnetograms clearly show the magnetic connections between the discussed 3 flaring sites. The highlighted differences in MW and HXR fluxs and spectral indices can be caused by a number of reasons: magnetic mirroring, electron deceleration in self-induced electric field or other agents of transport (protons). Magnetic mirroring because of stronger magnetic field in the source W could be a good explanation of the difference between MW and HXR indices. However, in the previous section we ruled this option out because of the same temporal profiles of the HXR and MW emissions. Then these differences can be related to different accelerated particles precipitating into different loops (protons in the Hα loop and electrons in MW loop). This can be combined with the electron deceleration in a self-induced electric field (in the microwave-emitting loop) or energization of the ambient thermal electrons by precipitating protons causing the observed Hα emission (in the loop with Hα).

The quantitative interpretation of HXR, MW and Hα emission excited by the protons in the full non-LTE approach is the scope of a future study.

Acknowledgments. L. K. and V. Z. thank the Royal Society, UK, for a short-term visiting grant that expedited the study and to the University of Bradford for hospitality and facilities provided. V. G. also wishes to thank the colleagues from NRO/NAO, Japan, for their help and hospitality.

The Physics of Chromospheric Plasmas
ASP Conference Series, Vol. 368, 2007
Petr Heinzel, Ivan Dorotovič and Robert J. Rutten, eds.

Hα with Heating by Particle Beams

J. Kašparová[1], M. Varady[1,2], M. Karlický[1], P. Heinzel[1] and Z. Moravec[2]

[1] *Astronomical Institute AS, Ondřejov, Czech Republic*
[2] *Department of Physics, J. E. Purkinje University, Czech Republic*

Abstract. Using 1D NLTE radiative hydrodynamics we model the influence of the particle beams on the Hα line profile treating the beam propagation and the atmosphere evolution self-consistently. We focus on the influence of the non-thermal collisional rates and the return current. Based on our results, we propose a diagnostic method for determination of the particle beam presence in the formation regions of the Hα line.

1. Introduction

Some of the flare models assign a fundamental role to the high energy particle beams in the flare energy transport. As the beams interact with the ambient plasma, their energy is dissipated and transformed mainly into the thermal energy of the transition region and chromosphere plasma. Several models studied electron and proton beams as heating agents (e.g., Mariska et al. 1989; Emslie et al. 1998) as well as their influence on spectral line profiles (e.g., Allred et al. 2005). The propagation of electron beams is inevitably connected with the so-called return current (RC, van den Oord 1990) which also contributes to the beam energy dissipation. Besides the heating, the beams influence atomic level populations of the ambient plasma via collisional excitation and ionization. The work presented here concentrates on these two effects which are commonly neglected in the flare modeling and assesses their importance on the formation of Hα line in solar flares.

2. Model

The beam propagation and energy deposition is modelled by a test particle approach consistently with the hydrodynamics of the atmosphere and NLTE radiative transfer in the transition region, chromosphere, and photosphere. Details of the model and the methods used are described in Kašparová et al. (2005).

We study the response of quiet Sun atmosphere (VAL C from Vernazza et al. 1981) to beam pulses of short duration, 1 s with sinus-like time modulation, and power-law energy spectrum with $\delta = 3$.

3. Hydrodynamics and Beam Propagation

The model takes into account Coulomb collisions of the beam with ambient neutrals and electrons, scattering of beam electrons, and optionally RC for the

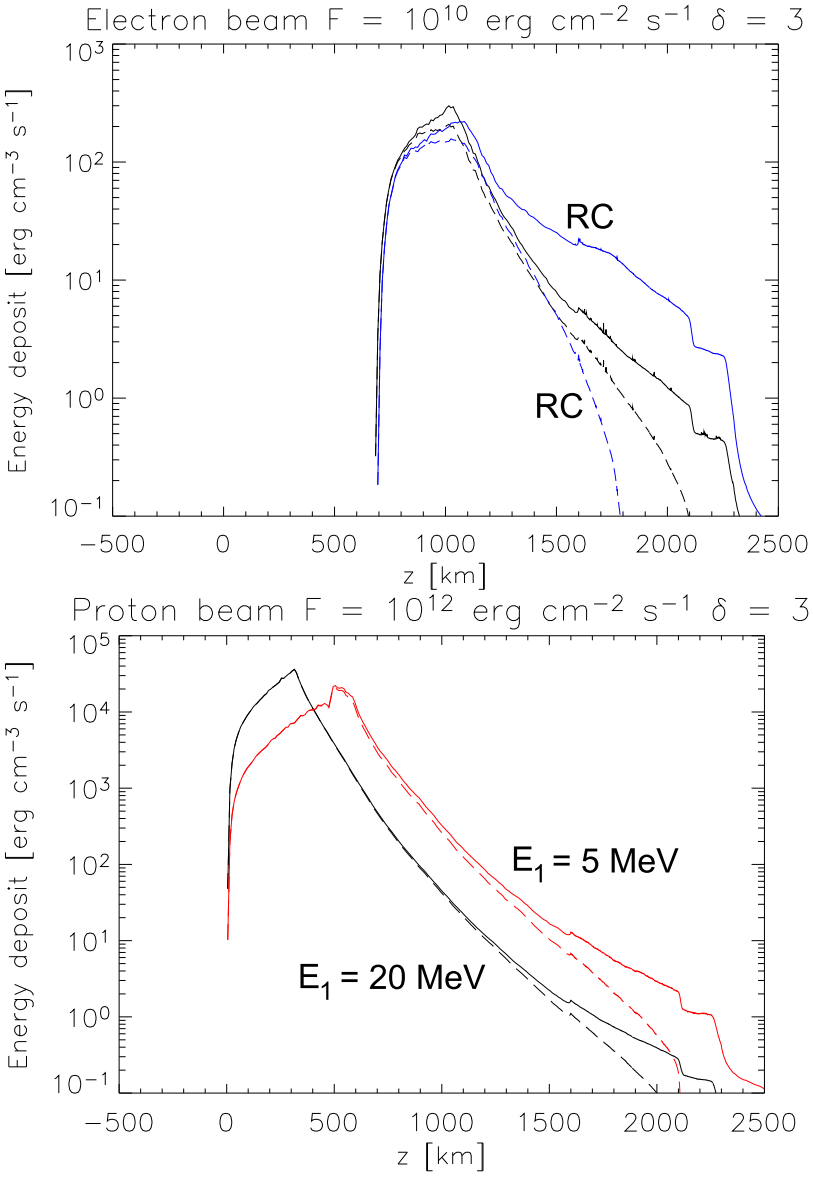

Figure 1. Total energy deposit (solid) and energy deposit to hydrogen (dashed) at beam flux maximum. *Top*: electron beam with and without RC included. *Bottom*: proton beam with $E_1 = 5$ MeV and $E_1 = 20$ MeV.

case of an electron beam (return current is a factor of E_e/E_p lower for protons carrying the same power as electrons (Brown et al. 1990) and is neglected). The return current is included in a runaway approximation assuming $\alpha = 0.1$, i.e. 10% of ambient electrons carry RC. For details and other approximations of RC in solar atmosphere conditions see Varady et al. (2005, 2007).

Figure 1 shows that RC significantly increases the energy deposit of electron beams at heights > 1500 km leading to corresponding increase of the tempera-

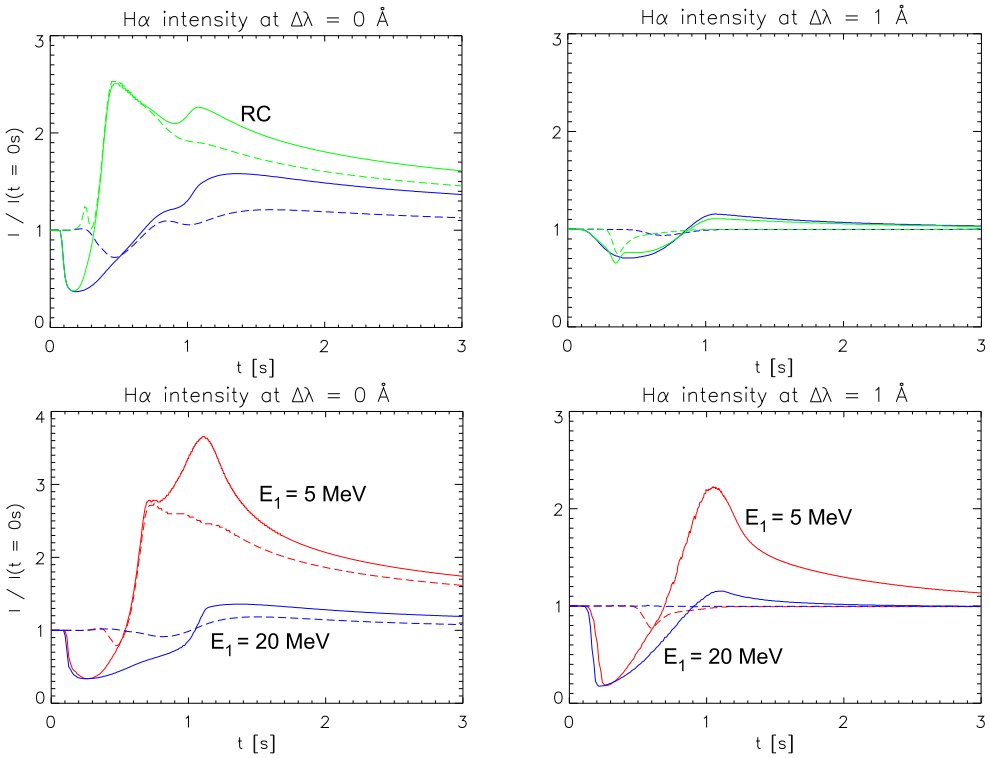

Figure 2. Time evolution of the Hα line center (left column) and wing (right column) intensities. *Top*: electron beam for $F = 10^{10}$ erg cm^{-2} s^{-1} and $\delta = 3$ with and without RC. *Bottom*: proton beam for $F = 10^{12}$ erg cm^{-2} s^{-1}, $\delta = 3$, and $E_1 = 5,\ 20$ MeV. The solid curves refer to cases with $C^{\rm nt}$ included, dashed lines to cases without $C^{\rm nt}$.

ture and ionization. The atmospheric response to proton beams was modelled for two different values of the low-energy cutoff $E_1 = 5,\ 20$ MeV. Note that deka-MeV protons produce approximately the same amount of hard X-rays as deka-keV electrons (Emslie & Brown 1985). Figure 1 illustrates that proton beams deposit their energy into deeper layers than electron beams (Emslie et al. 1996). The energy deposit of proton beams with lower value of E_1 peaks at higher atmospheric layers and is larger at heights above in comparison with a proton beam of $E_1 = 20$ MeV. Consequently, the temperature at these layers is substantially increased.

4. Hα Line Profiles

The hydrogen level populations are affected also by non-thermal collisional ionization and excitation. The corresponding rates $C^{\rm nt}$ are directly proportional to the beam's energy deposit on hydrogen (see Fang et al. 1993 for electron beams, and Hénoux et al. 1993 for proton beams). Their influence on the temporal evolution of the Hα profile was studied for electron beams by Heinzel (1991); Kašparová et al. (2005). Here, we describe in detail their effect for proton beams

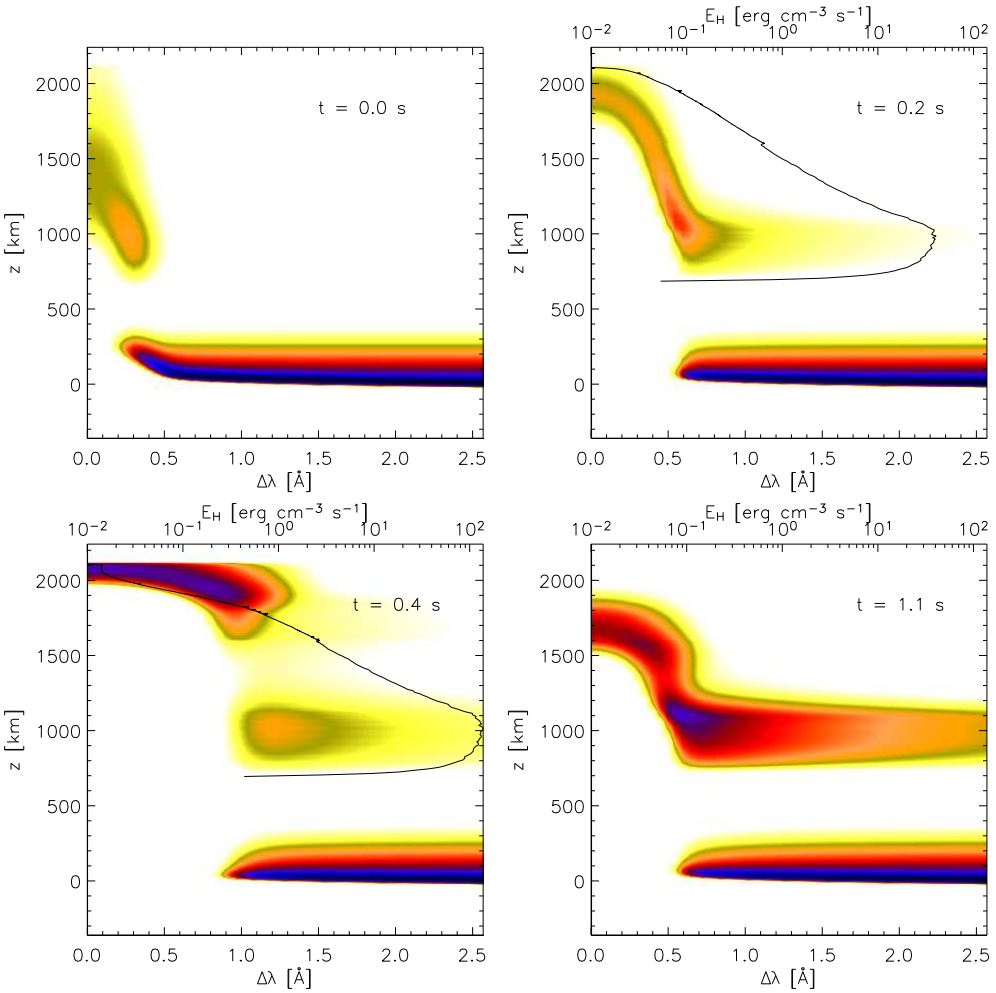

Figure 3. Hα contribution function CF for an electron beam. RC and $C^{\rm nt}$ were included. Solid curve: energy deposit on hydrogen.

and the influence of RC for electron beams. The temporal evolution of the Hα line-center ($\Delta\lambda = 0$ Å) and wing ($\Delta\lambda = 1$ Å) intensities are shown in Fig. 2. As discussed in Heinzel (1991) and Kašparová et al. (2005) for the case of electron beams, $C^{\rm nt}$ cause a decrease of the line-center intensity at the very start of the beam propagation and enhance the wing intensity later on (mainly for fluxes $\gtrsim 10^{11}$ erg cm^{-2} s^{-1}). The line behaviour can be understood in terms of contribution functions CF to the outgoing intensity given by $I_\lambda = \int CF_\lambda \, {\rm d}z$, where z is the height.

Figure 3 shows the evolution of Hα CF for the case of an electron beam with RC and $C^{\rm nt}$ included. A decrease of the line center intensity is caused by an increase of opacity due to $C^{\rm nt}$ (see CF at 0.2 s). Later on, a new region of wing formation occurs at the layers where the energy deposit peaks (see CF at 0.4 s). Such a layer is not formed if $C^{\rm nt}$ are not considered. Since RC causes heating of the top parts of the atmosphere, it is responsible for the increase

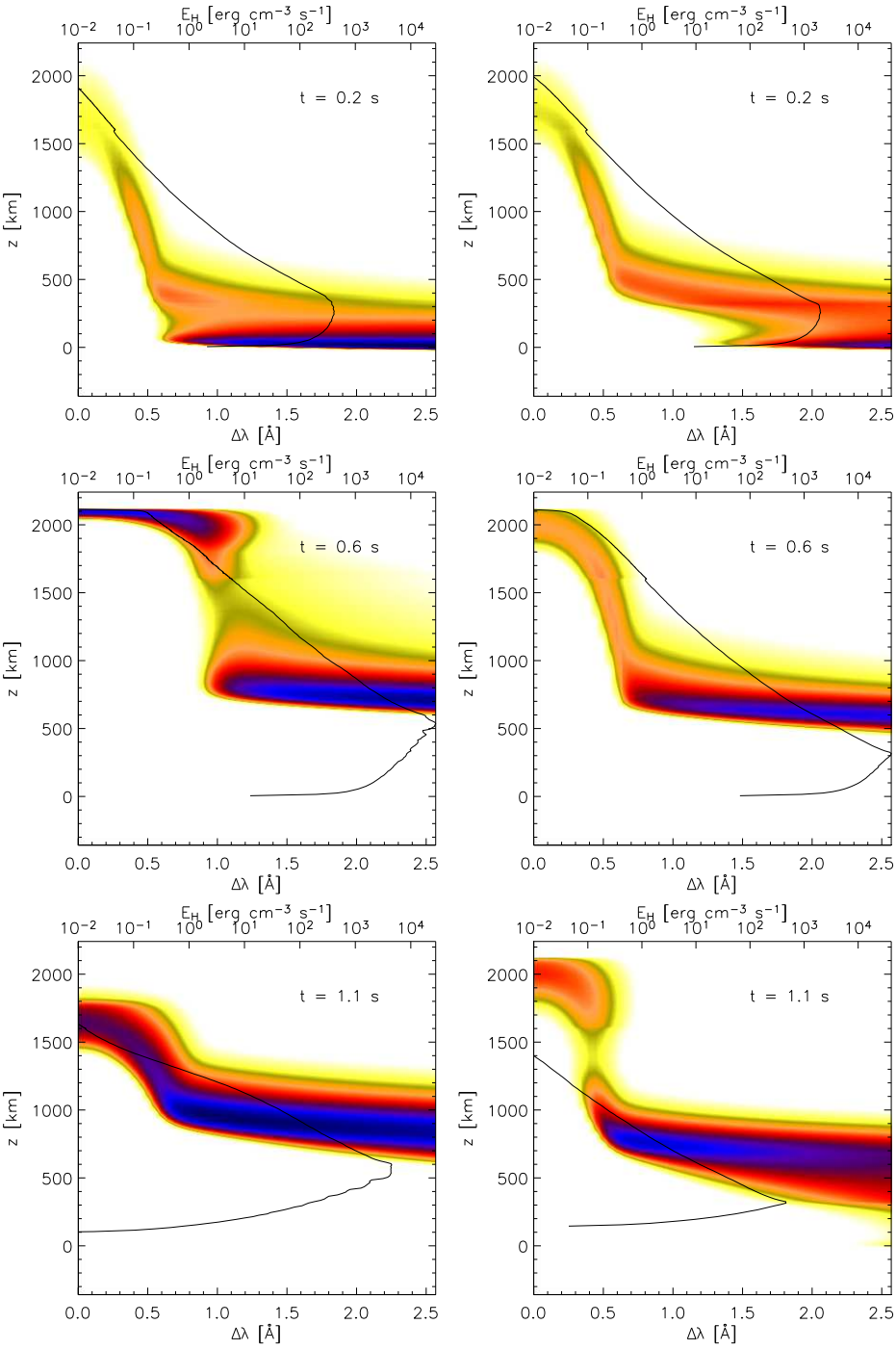

Figure 4. Comparison of Hα contribution function CF for proton beams with $E_1 = 5$ MeV (first column) and $E_1 = 20$ MeV (second column). $C^{\rm nt}$ were included.

of the line center intensity at 0.4 s (see Fig. 2) forming in a narrow region at ~ 2000 km (see Fig. 3).

The situation for a proton beam is shown in Fig. 4. In the case of $E_1 = 20$ MeV, the beam energy is deposited in regions where the line wings are formed. If $C^{\rm nt}$ are included, they cause increase of opacity which leads to a drop of both the wing and the line-center intensities (see CF at 0.2 s). Later on, a new wing region occurs. Neglecting $C^{\rm nt}$, the line intensity does almost not change because the temperature structure is not significantly affected by the beam propagation.

However, for a proton beam of $E_1 = 5$ MeV, the temperature increase is large enough to form a new region of the line center intensity, as in the case of RC for an electron beam. Also, the energy deposit is large enough to create a new layer of strong wing intensity (see CF at 0.4 and 1.1 s and Fig. 2). The second peak of the line center intensity at about 1.1 s is due to broadening of the formation region. Similarly to the electron beams, the line wings are not changed if $C^{\rm nt}$ are not considered.

5. Conclusions

The Hα line is influenced by temperature structure resulting from the beam propagation and return current as well as the non-thermal collisional rates. We propose to use the decrease of Hα line-center intensity as diagnostic indicating the presence of particle beams. We also predict that proton beams with deka-MeV low-energy cutoffs produce only *decrease* of the Hα in comparison with quiet-sun intensities.

Acknowledgments. This work was mainly supported by the grants 205/04/0358 and 205/06/P135 (GA CR), partially by grants IAA3003202, IAA3003203 (GA AS), and by the key project AV0Z10030501 (AI AS).

References

Allred J. C., Hawley S. L., Abbett W. P., Carlsson M., 2005, ApJ 630, 573
Brown J. C., Karlický M., MacKinnon A. L., van den Oord G. H. J., 1990, ApJS 73, 343
Emslie A. G., Brown J. C., 1985, ApJ 295, 648
Emslie A. G., Henoux J.-C., Mariska J. T., Newton E. K., 1996, ApJ 470, L131
Emslie A. G., Mariska J. T., Montgomery M. M., Newton E. K., 1998, ApJ 498, 441
Fang C., Hénoux J.-C., Gan W. Q., 1993, A&A 274, 917
Heinzel P., 1991, Sol. Phys. 135, 65
Hénoux J.-C., Fang C., Gan W. Q., 1993, A&A 274, 923
Kašparová J., Varady M., Karlický M., Moravec Z., Heinzel P., 2005, in ESA SP-600: The Dynamic Sun: Challenges for Theory and Observations
Mariska J. T., Emslie A. G., Li P., 1989, ApJ 341, 1067
van den Oord G. H. J., 1990, A&A 234, 496
Varady M., Karlický M., Kašparová J., 2005, in ESA SP-600: The Dynamic Sun: Challenges for Theory and Observations
Varady M., Karlický M., Kašparová J., 2007, in P. Heinzel, I. Dorotovič, R. J. Rutten (eds.), The Physics of Chromospheric Plasmas, ASP Conf. Ser. 368, 473
Vernazza J. E., Avrett E. H., Loeser R., 1981, ApJS 45, 635

The Physics of Chromospheric Plasmas
ASP Conference Series, Vol. 368, 2007
Petr Heinzel, Ivan Dorotovič and Robert J. Rutten, eds.

Spectroscopic Properties of Solar Flares in Different Lines

Hui Li and Jianqi You

Purple Mountain Observatory, Nanjing, China

Abstract. Using the data from the Multi-channel Infrared Solar Spectrograph (MISS) at Purple Mountain Observatory (PMO), we studied the spectroscopic properties of solar flares in the Hα, Ca II, and He I lines in different phases of flares, in diverse layers of flaring atmosphere, and in various locations of flares on the Sun. Our results show that the Hα line displays red-shift only and no wide-wing in the initial phase of a flare. Large broadening of the Hα line are observed in few minutes after flare onset within small regions of $3-5''$ in both disk and limb flares with/without non-thermal process. Far wings similar to those with damping broadening appear not only in the Hα line but in the He I line as well in flares with non-thermal process. We sometimes detect weak far wings in the Ca II line in disk flares. Such large broadenings are observed in both the footpoints and the tops of flare loops, and possibly result from strong turbulence and/or macroscopic motion. Therefore, the so-called non-thermal wing of Hα profile is not a sufficient condition to distinguish whether a non-thermal electron process exists in a flare. The Ca II line shows lower intensity on the loop-tops and higher intensity in the parts of loops close to the solar surface. Emissions larger than continuum in the He I line are detected only in small regions with strong X-ray emissions and away from sunspot umbrae. Meanwhile, the He I line is sensitive to the structure of flare plasma. Therefore, this line is suitable for discriminating the X-ray emission in regions above flring plasma and valuable in profile simulations.

1. Introduction

Solar flare spectral analysis is one of the most important diagnostic tools of the physical states in solar flares. Early study of flare spectra revealed that broadenings in disk flares were only observed in hydrogen lines in the visible wavebands. The broadenings of hydrogen lines in disk flare were generally ascribed to the Stark effect. Canfield and Gayley (1987) computed the Hα profiles in the first few seconds when the chromosphere was heated by non-thermal electron beams. So one can determine a flare is of thermal properties or non-thermal properties from its spectral profiles even though a chromospheric flare is just a secondary response to a coronal explosion. Many solar flares were observed in the He I line during the 22nd solar cycle and in the Hα, the Ca II, and the He I lines during the 23rd solar cycle with the Multi-channel Infrared Solar Spectrograph (MISS) (Li et al. 1999, 2002) at Purple Mountain Observatory (PMO). We are puzzled by the fact that in many flares, especially in many limb flares, the He I profiles presented very large broadenings with damping wings as the Hα profiles did, which can be well simulated by Stark broadening instead of Doppler broadening, requiring unrealistic high electron density of $>10^{17}\mathrm{cm}^{-3}$ (You et al. 1998;

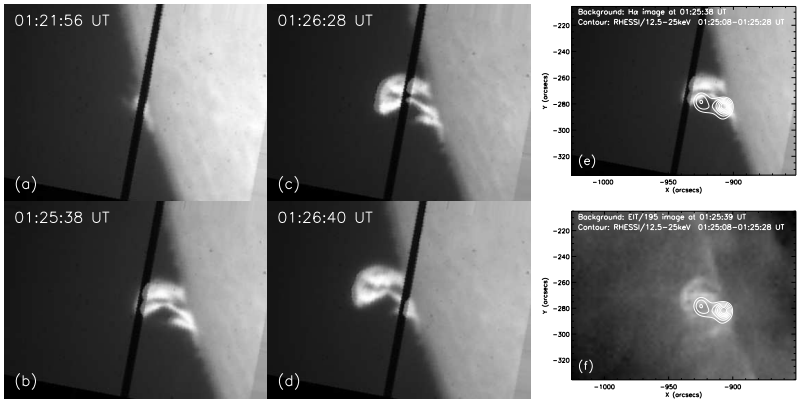

Figure 1. (a) – (d) Slit-jaw Hα images of the 2003 August 1 limb flare at 01:21:56 UT, 01:25:38 UT, 01:26:28 UT, and 01:26:40 UT, respectively; (e) slit-jaw Hα image at 01:25:38 UT and (e) EIT/195Å image at 01:25:39 UT are overlaid with contours of RHESSI 12 – 25 keV image at 01:25:08 UT. The thick dark line in the Hα image indicates the entrance slit of MISS.

Li and You 2001). We will summarize the spectroscopic properties of solar flares in different chromospheric lines based on our study of selected 30 flares. We will examine the reasonability to determine whether the chromosphere is heated by non-thermal electrons by scrutinizing the profile shapes of the Hα line wings.

2. Observations and Data

The spectral data used in this paper were obtained by MISS. The observations consist of spectra in the Hα, Ca II, He I, and Hα images obtained simultaneously by the slit-jaw system. The spectral dispersions for the three lines are 0.05453 Å, 0.05113 Å, and 0.04776 Å per pixel, respectively. The spatial resolution is 1.34″ along the slit after 4-row binning, while the temporal resolution is about 2.8 s. For more information about MISS, please refer to the above references. The observed spectral data are corrected for the dark-current, the flat-field, the scattered light, and the instrumental profile, and absolutely calibrated. We will present our results from two representative flares: the limb flares of 2003 August 1 and the disk flares of 2001 September 9.

3. Results

3.1. The 2003 August 1 (C5.6) limb flare

This C5.6 flare occurred at 01:19 UT, peaked at 01:26 UT and ended at 01:32 UT when AR 10424 was at the east solar limb. We obtained a complete set of data for this flare (Li et al. 2005). Selected slit-jaw Hα images, EIT/195 Å image with contours of RHESSI image in 12 – 25 keV are shown in Fig. 1. Retrieved profiles are presented in Fig. 2. This flare is of thermal property, i.e., no significant non-thermal emission was detected by RHESSI (Li et al. 2005).

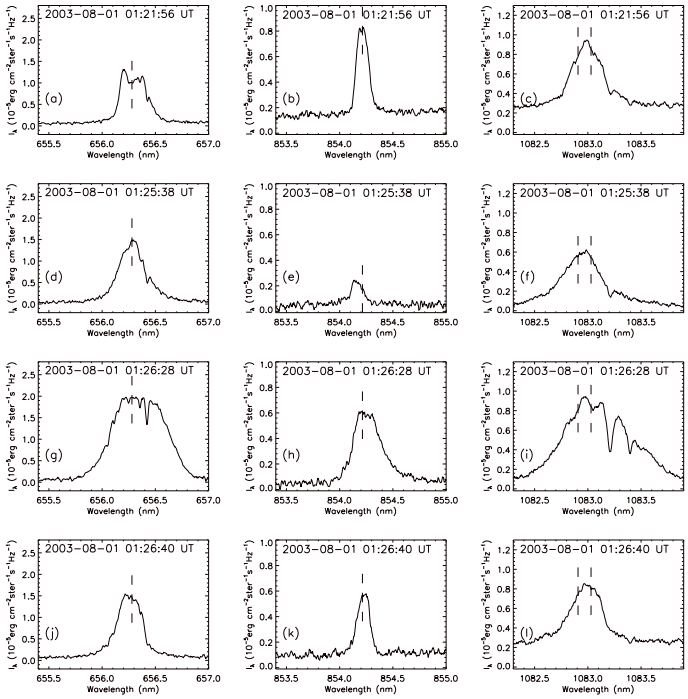

Figure 2. The widest Hα (*left*), Ca II (*middle*), and He I (*right*) profiles along the slit in Fig. 1. The dashed vertical bars indicate the rest wavelengths of Hα, Ca II, and the I_{12} and I_3 components of the He I line. The observation times are shown in each plot.

Just after the flare onset, the Hα profile did not show large intensity but displayed "flat-top" structure in the line-center part, suggestive of saturated emission due to large optical thickness (Fig. 2, the first row). All the three lines were slightly broadened. Then the Hα flare developed into loop systems. A bright thin arc connected the two footpoints of the loops (Fig. 1(b)). The Ca II line intensity in the Hα loop-top region was low and the Hα and the He I lines displayed wide damping wings (Fig. 2).

The maximum broadenings of all the three lines were detected in this bright arc-like area between the two loops (Fig. 2, the third row). However, the Hα profile at this time did not show wide damping wings but large full width at half maximum (FWHM) and saturated line-center. The Ca II lines also showed saturated line-center and increased width. The He I line showed proportionally increased width to the increase in the Hα line and more significant damping wing. The target area at 01:26:40 UT showed moderately enhanced EUV 195 Å emission and X-ray emission in 12 – 25 keV (Figs. 1(e) and (f)). During the flare process, all the three lines displayed consistent shift velocities.

3.2. The 2001 September 9 (2B/M1.9) disk flare

This flare was a confined disk flare close to disk center (S24E26) and had only one bright area. YOHKOH/HXT detected hard X-ray (HXR) emission only below 53 keV. This flare has been studied by Li et al. (2006). Therefore, we

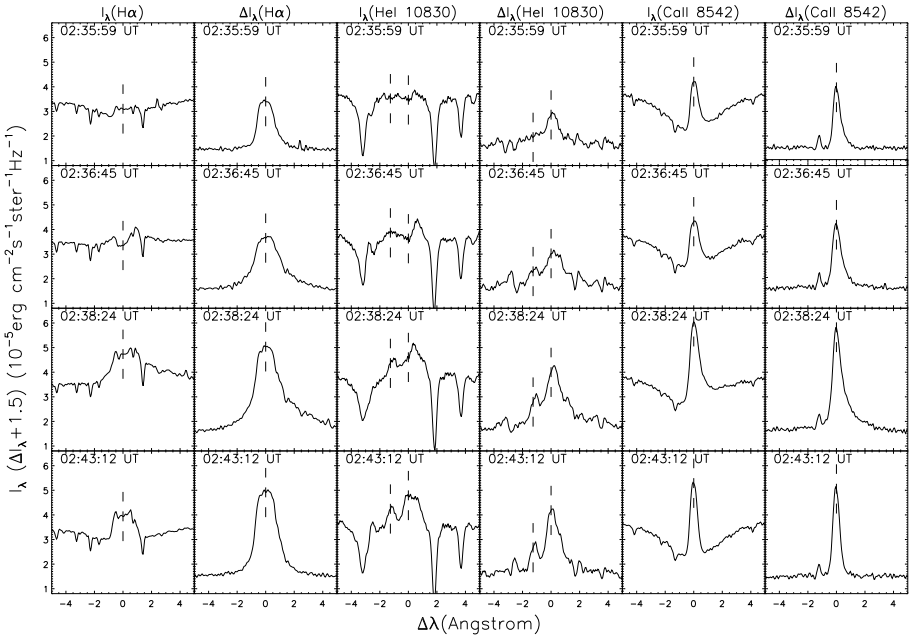

Figure 3. The selected Hα original (first column) and excess (second column) profiles observed during the 2001 September 9 2B/M1.9 by MISS. The He I original and excess profiles are plotted in columns 3 and 4, respectively, while those for Ca II line in columns 5 and 6, respectively. The dashed bars indicate the unshifted line centers. The observation times are shown in each plot. Please note that in the plot we added 1.5×10^{-5}erg cm^{-2}s^{-1}ster^{-1}Hz^{-1} to the intensities in the excess profiles in order to show them properly.

just refer to their results in this subsection. Just after its onset, at 02:35:59 UT, this flare showed similar spectral properties to the 2003 August 1 limb flare (Fig. 3). The He I profile appeared as slight absorption while the Ca II line showed obviously enhanced emission (Fig. 3). Later on, the Hα line wing gradually became apparent and a dip was observed in the center part (Fig. 3) due to the absorption of stationary material above the chromosphere (Li et al. 2006). It was slightly discernible in the main component of the He I line but not visible in the weak component and the Ca II line. This absorption disappeared around the flare maximum and the Hα profile again showed "flat-top" structure with broadened line wings (Fig. 3). All the three lines showed enhanced red-wings up to $4-5$ Å.

Computation of the velocity of the flare plasma showed that for the same profile the velocities derived by different methods had different values and temporal variations (Li et al. 2006). Meanwhile, the three lines gave different velocities at a given time for the same position. This can be explained by the existence of velocity gradient along the LOS (Li et al. 2006). In limb flares, we measure the velocities in the lateral direction from Doppler shifts, which can be the same. Our results reveal that the velocity derived from the excess profiles can more effectively reflect the motions in the lower flare plasma.

4. Spectral Characteristics of Solar Flares

4.1. The Ca II line

The distribution of bright areas of disk flares in the Ca II line is similar to that in the Hα line (You et al. 2001). The Ca II line shows stronger emission in the early and late phases of solar flares than the Hα line, but it generally does not display "flat-top" (saturated) structure in the line-center (Li et al. 2006). It is relatively stronger near the solar limb. It is also broadened in limb flares but its half-width increases slower than the Hα and the He I lines, which is different from the Ca II H and K lines. Measured line-center shift velocity from the Ca II line in disk flares is smaller than those from the Hα line and the main component of the He I line (Li et al. 2006). But they are comparable in limb flares.

4.2. The He I line

Spectral properties of the He I line is related to both the selected flare and the location of the studied point in the flare. Most of the flares has one or more small areas ($3-10''$) where the He I line showed emissions larger than nearby continuum. Such areas spatially correspond to the Hα flare kernels (You et al. 1993). In Hα bright pathes out of the kernels the He I line appeared as absorption, which is consistent with Rust and Bridges III (1975) and has been confirmed by our later observations. Our estimation shows that one may detect emissions greater than nearby continuum in the He I line in disk flares only when the GOES 1 – 8Å X-ray level of the flare is larger than about C6. Otherwise, the He I line only shows absorption in regions where the Hα line shows emission. Furthermore, in the impulsive phases of solar flares the He I line often shows significant broadenings with damping wings. The two components (I_{12} and I_3) begin to be separated after the flare maximum. Such profiles cannot be simulated by Doppler broadening with a uniform flare model, even though it can reproduce the profiles of prominence, post-flare loops and surges observed during flare process.

Generally bright regions of solar flares in the He I line are much smaller than in the Hα and the Ca II lines with some exceptions (You et al. 2001). On the one hand, the emission regions of solar flares in the He I line tend to be in the penumbrae of sunspots, similar to that in the Hα and the Ca II lines. On the other hand, different from the Hα and the Ca II lines, we have not found any case, in which the He I line bright patches extend into sunspot umbrae.

5. Summary

Our results are partially consistent with (Švestka 1976) but we obtained more details about the Hα, the Ca II, and the He I line profiles in flares. Moreover, our results indicate that different flares may have quite different spectroscopic characteristics. These differences are mainly manifested in the He I line. In the initial phase of solar flares the Hα line shows asymmetries and most of the asymmetries are red-asymmetry. The Hα line-center part often shows a "flat-top" structure, indicating that the flare plasma where the Hα line is formed is already optically thick. Then the line is broadened and increased emissions are detected in the two line-wings. Meanwhile, the line-center part shows a reversed

profile, which disappears at the flare maximum while the broadening reaches its largest value.

During the flare process, one can always find a region in all the flares where the Hα line is significantly broadened, no matter whether there exists a non-thermal process in the flares or not. We also detected large damping-like broadenings in the He I line profiles. Therefore, the "non-thermal" wide wing in the Hα line profile is not sufficient condition to conclude that the flare chromosphere is heated by non-thermal electrons instead of thermal conduction. The time difference between the Hα maximum broadening and the GOES 1 – 8 Å X-ray peak may be a better indicator of the flare chromosphere is heated by non-thermal electrons or thermal conduction (Li et al. 2006). Yet this needs to be confirmed by more observational data.

The large broadenings of the Hα line observed in most of the disk flares and the loop-tops of limb flares are of the same origin: strong turbulence and/or large macroscopic motions associated with the flares. The velocity derived from the Ca II profiles is much smaller than that from the Hα profiles for disk flares but comparable for limb flares. The He I line shows unique spectral properties in solar flares. Its intensity is not associated with the area of the flare and the Hα line intensity but with the X-ray intensity only. Therefore, the He I line can reflect the X-ray emission strength in the corona above a flare and provide observational data to diagnose the excitation mechanisms of helium lines. Moreover, it is much more difficult to simulate the observed He I triplet profiles than the Hα and the Ca II lines. The He I line can also be used to diagnose the structure of flare plasma.

Acknowledgments. This work was supported by the National Natural Science Foundation of China (NSFC, grant number 10333040 and 10573038) and National Basic Research Priorities Project of China (grant number 2006CB806302).

References

Canfield R.C., Gayley K.G., 1987, ApJ 322, 999
Kosugi T. et al., 1991, Solar Phys. 136, 17
Li H., You J.Q., 2001, A&A 374, 1121
Li H., Fan Z.Y., You J.Q., 1999, Solar Phys. 185, 69
Li H., You J.Q., Du Q.S., 2006, Solar Phys. 235, 107
Li H., You J.Q., Wu Q.D., Yu X.F., 2002, Chinese Phys. Letters 19, 742
Li H., You J.Q., Du Q.S., Yu X.F., 2005, Solar Phys. 225, 75
Rust D.M., Bridges III C.A., 1975, Solar Phys. 43, 129
Švestka Z., 1976, Solar Flares, D. Reidel Publ. Co., Dordrecht, the Netherlands
You J.Q., Wang C.J., Fan Z.Y., 1993, in G.X. Ai et al. (eds.), Proceedings of the First China-Japan Seminar on Solar Physics, Kunming Tondar Institute, 148
You J.Q., Wang C.J., Fan Z.Y., Li H., 1998, Solar Phys. 182, 431
You J.Q., Li H., Fan Z.Y., Sakurai T., 2001, Solar Phys. 203, 107

The Physics of Chromospheric Plasmas
ASP Conference Series, Vol. 368, 2007
Petr Heinzel, Ivan Dorotovič and Robert J. Rutten, eds.

Comparison of Hα and Ca II K from Flares

Jan Klimeš and Eva Marková

Observatory Úpice, Czech Republic

Abstract. The Sun has been observed in the spectral lines Hα (6563 Å) and Ca II K (3934 Å) at the Observatory Úpice since 1997. In this contribution we address the visibility of chromospheric explosion events in both spectral lines and the interpretation of the results obtained from our observations.

1. Introduction

We have observed a great amount of active chromospherical events with the reconstructed solar telescope at our observatory since 1997. A concise history of the solar observation on the Observatory is presented in Marková et al. (2000) and some details about the used telescope are given in Klimeš et al. (1999). A very important part of this telescope is a system of Šolc's birefringent filters for the Hα and Ca II K lines. Synchronous scanning of the solar disk in both spectral bands gives a chance for more valuable observations and detailed exploration of such scanned events. At the start of our new observations the opinion that in the Ca II lines only a few events occur during of the maximum phase of flares, and only rarely at that, was widely spread. This opinion is corrected in this paper, since our observations give incontestable evidence that the situation is the reverse.

2. Data Used

The events that we selected for this paper have the following attributes: a chromospheric flare on the solar disk or limb, an active prominence/filament, and the best observing conditions. Our data collection contains also one case with shock wave propagation on the solar surface. Some of the events are illustrated in Figs. 1 and 2. All the events are summarized in Table 1. A brief description is given below:

15.05.2000 quiet prominence on the eastern limb, afterwards flare behind the limb and it change to active state of prominence (Figs. 1 and 2)
11.06.2000 flare on the disk
21.06.2000 flare on the disk
19.09.2000 flare on the disk
28.03.2001 series of flares on the disk following by propagation of the shock waves on the solar surface
2.04.2001 flare on the western limb with active prominence
24.04.2001 flare on the disk

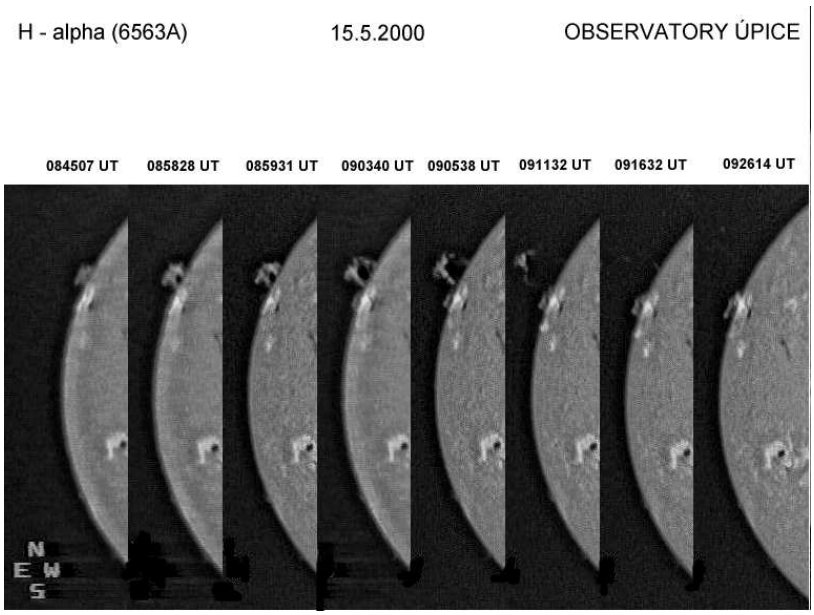

Figure 1. The active event on the solar limb, 15 May 2000, Hα line

13.06.2001 flare on the disk
15.06.2001 flare on the disk
4.01.2002 active prominence with flare on the eastern limb
18.03.2002 flare on the disk
19.03.2203 flare on the disk
9.06.2003 flare on the disk with active filament
10.06.2003 flare on the disk with active filament
23.10.2003 active prominence with flare on the eastern limb
27.04.2004 flare on the disk
18.08.2004 flare on the disk
17.01.2005 flare on the disk

3. Results

In Table 1 the duration of any event is computed for both the spectral bands and represents width of the observational window. In the next column the difference between duration of in Hα and in Ca II K shows length of the overlapping interval. We have made some evaluations of Table 1. In accordance with the remarks and global characteristics per event in Table 1 we find these results:

a) All the events were always observed in both ranges, from starting phase over maximum to the end.

b) Duration in Ca II K was always shorter then that in Hα – from 28 s to 57 min. The distribution of duration is shown in Table 2.

c) Better coincidence between Hα and Ca II K occurs during dynamic situations on the solar disk.

Table 1. Chronologic listing of the events.

Date	Maximum		Duration		Diff.	Note
	Hα	Ca II K	Hα	Ca II K	Hα-Ca II K	
00-05-15	09:26:14	09:27:50	$2^h\ 4^m\ 44^s$	$1^h\ 15^m\ 36^s$	$49^m\ 8^s$	
00-06-11	10:46:08	10:47:22	$45^m\ 2^s$	$46^m\ 36^s$	$-1^m\ 18^s$	1
00-06-21	10:20:45	10:19:05	$5^h\ 2^m\ 22^s$	$4^h\ 56^m\ 27^s$	$5^m\ 55^s$	
00-09-19	08:27:30	08:26:04	$3^h\ 16^m\ 48^s$	$3^h\ 13^m\ 57^s$	$2^m\ 51^s$	1
	07:35:39	07:36:45	$52^m\ 16^s$	$26^m\ 37^s$	$25^m\ 39^s$	
01-03-28	09:13:30	09:12:41	$34^m\ 19^s$	$31^m\ 3^s$	$3^m\ 16^s$	2
	09:50:09	09:49:08	$28^m\ 3^s$	$16^m\ 35^s$	$11^m\ 28^s$	
	09:30:28	09:29:38	$1^h\ 29^m\ 13^s$	$1^h\ 15^m\ 11^s$	$14^m\ 2^s$	
01-04-02	10:19:26	10:18:16	$46^m\ 38^s$	$35^m\ 9^s$	$10^m\ 59^s$	3
	11:18:00	11:18:54	$17^m\ 10^s$	$16^m\ 58^s$	$12^m\ 0^s$	
01-04-24	07:03:10	07:02:00	$21^m\ 40^s$	$19^m\ 7^s$	$2^m\ 33^s$	
	12:57:06	12:56:25	$37^m\ 17^s$	$29^m\ 7^s$	$8^m\ 10^s$	
01-06-13	11:40:08	11:42:52	$57^m\ 22^s$	$56^m\ 54^s$	28^s	4
01-06-15	10:20:27	10:19:23	$1^h\ 4^m\ 26^s$	$54^m\ 36^s$	$9^m\ 50^s$	
02-01-04	09:15:02	09:16:42	$1^h\ 22^m\ 30^s$	$25^m\ 22^s$	$57^m\ 8^s$	5
02-03-18	11:50:10	11:49:08	$58^m\ 25^s$	$46^m\ 18^s$	$12^m\ 7^s$	
03-03-19	09:59:06	09:56:35	$1^h\ 0^m\ 32^s$	$34^m\ 54^s$	$25^m\ 38^s$	
03-06-09	08:50:03	08:49:07	$19^m\ 52^s$	$13^m\ 47^s$	$6^m\ 5^s$	
	11:28:46	11:28:00	$22^m\ 28^s$	$17^m\ 1^s$	$5^m\ 27^s$	
03-06-10	08:39:02	08:38:10	$1^h\ 15^m\ 11^s$	$1^h\ 0^m\ 31^s$	$14^m\ 40^s$	
	11:11:16	11:12:03	$50^m\ 56^s$	$30^m\ 15^s$	$20^m\ 41^s$	
03-10-23	08:46:15	08:47:09	$1^h\ 25^m\ 10^s$	$1^h\ 4^m\ 38^s$	$20^m\ 38^s$	
04-04-27	07:20:22	07:21:02	$55^m\ 54^s$	$46^m\ 58^s$	$8^m\ 56^s$	
04-08-18	10:47:09	10:46:21	$16^m\ 29^s$	$11^m\ 49^s$	$4^m\ 40^s$	
05-01-17	09:58:04	09:50:40	$2^h\ 27^m\ 48^s$	$1^h\ 51^m\ 10^s$	$36^m\ 38^s$	6

Legend:

1 – broad interval of maximum in Hα
2 – the selection of all the events on the disk
3 – between second and third presented event another one flare in the same region in Hα was observed
4 – start of the event is prominent in Ca II K before the one in Hα, but the end is as usually in Hα
5 – the whole interval is in Hα, in Ca II K only maximal phase of the active prominence
6 – times of maximal phases in Hα and in Ca II K are strong different

Table 2.

Difference of durations	Number of events
0 – 9 min	12
10 – 29 min	10
30 – 59 min	3

d) When an active prominence is situated on the Sun, we can observe it in the Ca band whenever a nearby flare is located on the limb. However, in the opposite case the prominence is not alway seen.

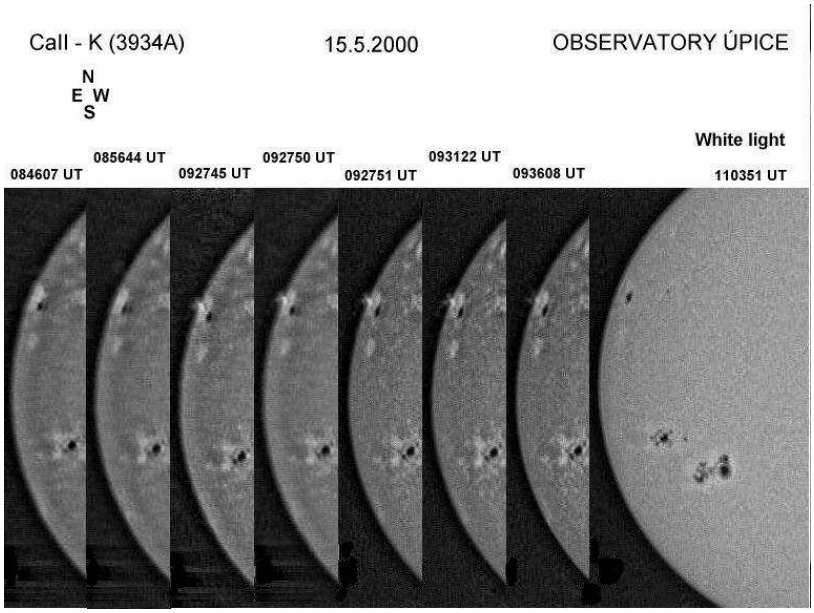

Figure 2. The active event on the solar limb, 15 May 2000, Ca II K line

4. Conclusion

Our results show that we can see most dynamic events in the Ca II K line too. We are aware of the limitation posed by the small amount of data discussed here. However, a very large amount of observational data where we can see dynamics events in both lines is archived at the Observatory Úpice. We chose only those whose quality fulfilled stringent conditions for the reliable determination of temporal details.

The maximum of events occurs approximately at the same time for both spectral bands. In our case the differences found between the times of maxima are encumbered by methodical errors imposed by the optical system with exchangeable filters which does not allow exactly simultaneous scanning in both spectral bands.

References

Marková E., Bělík M., Klimeš J. sr., & Klimeš J. jr. 2000, Proc. 1^{st} Solar & Space Weather Euroconference, ESA SP-463

Klimeš J. jr., Bělík M., Klimeš J. sr., & Marková E. 1999, Proc. 8^{th} SOHO Workshop, ESA SP-446, 375

The Physics of Chromospheric Plasmas
ASP Conference Series, Vol. 368, 2007
Petr Heinzel, Ivan Dorotovič and Robert J. Rutten, eds.

Line Profile Asymmetries in Records from the Multichannel Flare Spectrograph

Tomáš Prosecký

Astronomical Institute AS, Ondřejov, Czech Republic
Charles University, Faculty of Mathematics and Physics, Prague, Czech Republic

Abstract. The archive of the Ondřejov Multichannel Flare Spectrograph (MFS) contains video records of several hundreds of flares observed between 1995 and 2004. This contribution shows preliminary results of basic statistical processing on a sample of 50 flares observed in the Hα line between May, 1999 and May, 2001. No significant differences between occurrence of red and blue asymmetries for different flare importance and X-ray classes were found. For the decay phase of a flare no visible asymmetry or faint blue asymmetry seems to be typical.

1. Introduction

Spectral line profiles of solar flares may indicate so-called line profile asymmetries, which originate due to vertical mass motions in flaring atmosphere. Detailed analysis of asymmetries observed in different spectral lines can provide information about motions of flaring atmosphere and/or its vertical velocities. For a detailed review of the topic see the keynote contribution of Berlicki in these proceedings (p. 387 ff).

2. Data

The MFS had been in operation since 1958 till June 2004; a description of the device can be found in Kotrč (1997). An example of MFS record is given in Fig. 1. In the given period (May, 1999 – May, 2001) all flare records with $\mu \geq 0.3$ and good seeing conditions have been selected and processed. Eventually we so got 50 flares: 30 flares of class S, 15 of class 1, 4 of class 2 and 1 of class 3 (source: NGDC web page[1]). According to GOES, 35 flares were of class C, 11 of class M and 2 of class X. For 2 flares no record had been found in GOES archive. There were multiple kernels in several flares. As a result, 292 profiles of the Hα line taken in different times and 68 different places have been processed.

The total emissivity in Hα was estimated for each of the profiles from the difference of the flaring and the appropriate quiet-Sun profile in the wavelength range ± 1.6 Å around line center. The phase of each flare (impulsive or gradual) was estimated for each profile according to the GOES data. Finally, qualitative

[1] `http://www.ngdc.noaa.gov/stp/SOLAR/flareint.html`

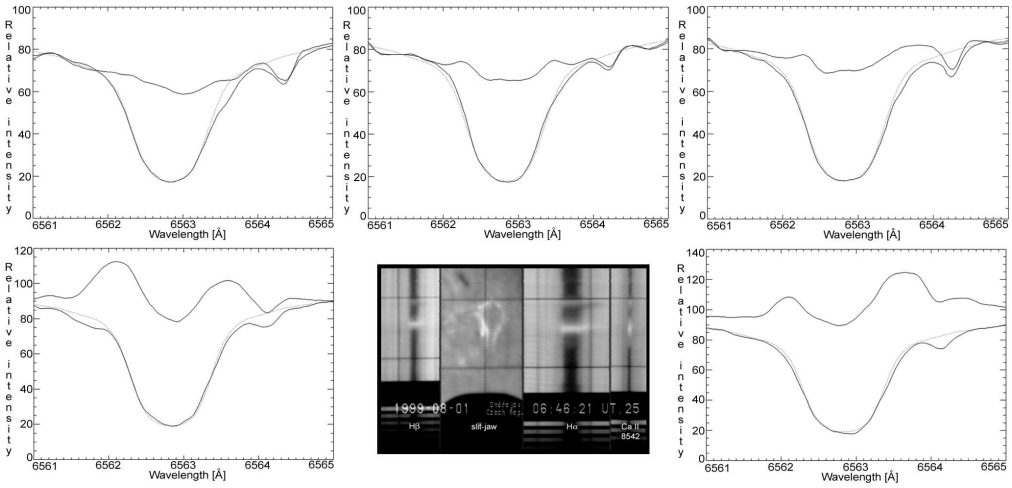

Figure 1. Sample images of different categories of asymmetry profiles as defined previously; images are composed of flaring and quiet Sun profiles (solid lines) and reference quiet Sun profile (dotted line, David (1961)) — blue (*lower left* image, flare NOAA 9393, April 2, 2001, 11:07:17 UT), blue faint (*upper left* image, NOAA 8552, May 31, 1999, 13:03:57 UT), without asymmetry (*upper center*, NOAA 8602, June 23, 1999, 07:13:09 UT), red faint (*upper right*, NOAA 8651, July 30, 1999, 08:53:45 UT), red (*lower right*, NOAA 9393, April 2, 2001, 10:09:40 UT).
Lower center: Sample image of the flare (NOAA 8645, August 1, 1999) from our data set taken by the MFS device that recorded Hβ, slit-jaw, Hα, and Ca II 8542 Å images simultaneously.

attributes of asymmetries were investigated. All profiles were divided into 5 categories: profiles without significant asymmetry (differences in intensity between the red and blue wings $< 1\%$ of the relative intensity), profiles with faint blue or red asymmetry (differences $\geq 1\%$ and $\leq 5\%$ of the relative intensity) and profiles with blue or red asymmetry (differences $> 5\%$ of the relative intensity). Examples of various asymmetries can be found in Fig. 1.

3. Results and Conclusions

The possible dependence of occurrence on total emissivity, estimated phase of a flare, importance and X-ray class has been investigated in these data sets for each category of asymmetries. For results see Fig. 2 – Fig. 5.

In 68 different flare kernels only the red asymmetry in 27 cases (40%) was observed, only the blue asymmetry in 22 cases (32%), no asymmetry in 6 cases (9%) and a change from red into blue (or to the contrary) during flare evolution in 13 cases (19%) has been observed.

No significant differences between occurrence of red and blue asymmetries in different importance and X-ray classes of flares were found. However, the studied set of flares is mainly for class M and X and importance 2 and 3 too small. It is necessary to investigate more observations of other flares.

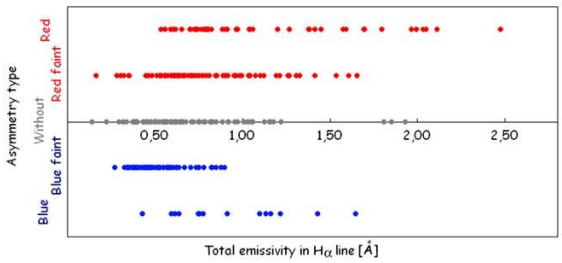

Figure 2. Occurrence of different types of asymmetry in the Hα line vs. total emissivity (defined as an equivalent width of the Hα line). It can be seen that for the lower emissivity no asymmetry or only the faint one is more frequent.

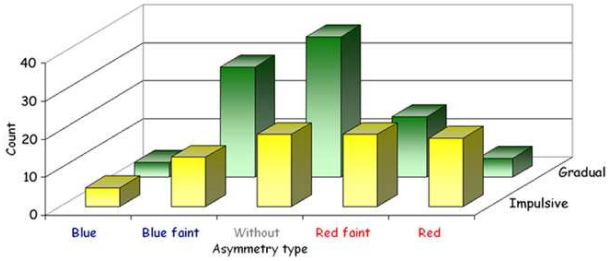

Figure 3. Occurrence of different types of asymmetry in the Hα line during estimated impulsive and gradual phases of selected flares. For impulsive phases of flares there are no significant differences, on the other hand no visible asymmetries or faint blue ones are more frequent for a decay phase of a flare.

No significant asymmetry or a faint blue asymmetry seems to be the most common phenomena for gradual phase of a flare. According to simulations and results in Schmieder et al. (1987), Berlicki et al. (2005), Prosecký et al. (2006) a faint asymmetry can be interpreted as a motion with velocities of about $\pm$ 10 km/s. However, it is necessary to make more sophisticated non-LTE simulations for clear determination of velocities and their direction. According to the simulations of Berlicki et al. (2005) it seems that mainly a faint red asymmetry should appear during the gradual phase of a flare, whether a scenario of gentle evaporation (Antiochos & Sturrock 1978) is primary during this kind of a phase. However, the red asymmetry was observed only in 18% of cases in our data set, whereas the blue one was observed in 32%.

4. Future Outline

As the next stage in this work we plan to reduce more cases of flares recorded with the MFS device during 2001 and 2004. We intend to take into account other spectral lines recorded with the MFS (Hα, Ca II 8542 Å). Processing of new observations obtained by our modern HSFA 2 device (see the contribution by Kotrč on p. 559 ff) is also planned. It is also necessary to obtain a quantitative data description (to determine vertical velocity fields) via radiation transfer

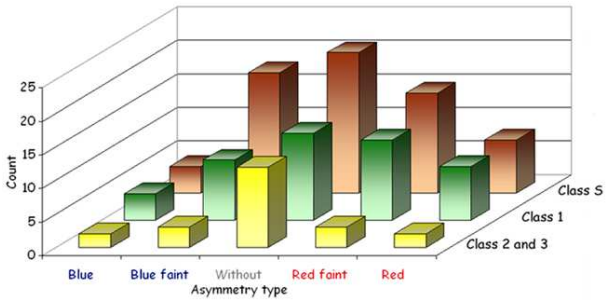

Figure 4. Occurrence of different types of asymmetry in the Hα line in various classes of selected flares. No significant differences between red and blue asymmetry can be seen.

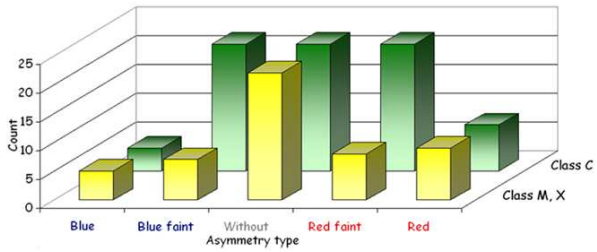

Figure 5. Occurrence of different types of asymmetry in the Hα line in various X-ray classes of selected flares. No significant differences between red and blue asymmetry can be seen.

modeling in a flaring atmosphere and comparison of observed and synthetic non-LTE profiles. As a first step we will follow the approach of Berlicki et al. (2005).

Acknowledgments. The author thanks the CSPM organisers for a very good meeting and P. Heinzel and P. Kotrč for helpful discussion and suggestions. The author acknowledges support by grant No. 3203 of the Grant Agency of the Academy of Sciences of the Czech Republic and Institutional Project AV0Z10030501.

References

Antiochos S., Sturrock P., 1978, ApJ 220, 1137
Berlicki A., Heinzel P., Schmieder B., Mein P., Mein N., 2005, A&A 430, 679
David K. H., 1961, Zeitschrift für Astrophysik 53, 37
Kotrč, P., 1997, Hvar obs. Bull. 21, 97
Prosecký T., Kotrč P., Berlicki A., 2006, Cent. Eur. Astrophys. Bull. 30, 31
Schmieder B., Forbes T.G., Malherbe J.M., Machalo M.E., 1987, ApJ 317, 956

The Physics of Chromospheric Plasmas
ASP Conference Series, Vol. 368, 2007
Petr Heinzel, Ivan Dorotovič and Robert J. Rutten, eds.

Multiwavelength Study of the May 13, 2005 Flare Event

Marta G. Rovira[1], Stanislava Šimberová[2], Marian Karlický[2],
M. Luisa Luoni[1] and František Fárník[2]

[1]*Instituto de Astronomía y Física del Espacio, Buenos Aires, Argentina*
[2]*Astronomical Institute AS, Ondřejov, Czech Republic*

Abstract. A global view to the flare evolution via the image data of various parts of electromagnetic spectra is introduced. Data from the ground-based observations in Hα (HASTA, El Leoncito, Argentina) and radio spectra in the 1-2-4.5 GHz range (Radiospectrographs, Ondřejov, Czech Republic) have been analyzed. As to the space observations, there were involved data of the event from SoHO (MDI, EIT, LASCO C2) and RHESSI (X-ray sources). Some results of possible relations among various layers of the Sun's atmosphere and following astrophysical interpretation are presented.

1. Introduction

The subject of interest (see Fig. 1) in the active region (AR) NOAA 10759 was classified as 2N in Hα and GOES M8. According to the SGD (Solar Geophysical Data) the spot group was recognized on May 5, 2005 at N12 E61. In this area there were registered an one 2N flare on May 11, another 2N on May 13, the four class 1 flares and many subflares during their passage through the disk. The positive polarity is preceding the active region (AR) with a leading round spot. On the other side, the negative polarity presents a uniform shape. The AR is classified as b-g configuration (2005/05/13).

2. Image Data Processing and Event Analysis

2.1. Two ribbon flare in Hα

Hα observations were made by the HASTA solar telescope, Argentina, see Bagalá et al. (1999). In the initial phase (16:35 UT, Fig. 2a) it is possible to recognize two kernels (A,B) that would be identified as a part of the ribbons during the flare evolution, described e.g., by Švestka (1976). The equipotentials of the longitudinal magnetic field MDI ($\pm$100 G, 1000 G) over each Hα image correspond (+ white, − black) to 16:03 UT in a) and b), and 17:00 UT in c). The maximum of brightening appears at 17:00 UT in b). We can identify two ribbons: one of them, the east sided has an L shape. The width and the distance between them are increasing during the event evolution. At 17:37 UT in c) the flare occurs in its gradual phase.

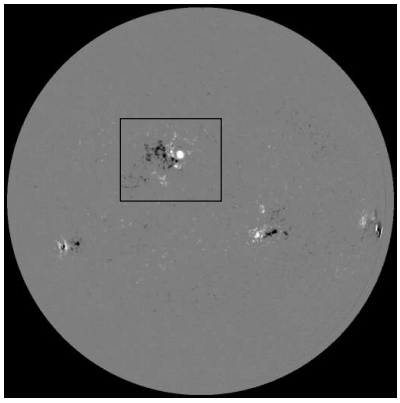

Figure 1. Area of the event on May 13, 2005.

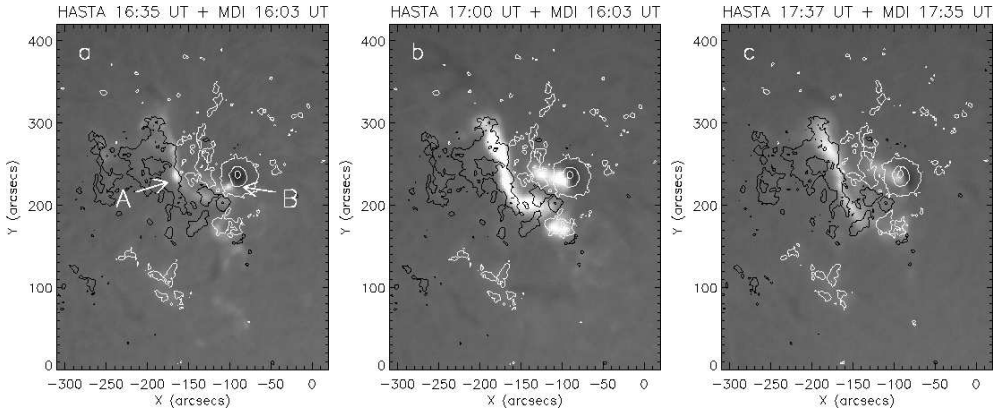

Figure 2. The flare evolution in Hα.

2.2. RTO – radio observations

Radio observations were made by the Ondřejov radiospectrograph, Jiřička et al. (1993). In the 0.8–2.0 GHz radio range the event started at 16:32 UT. It had three maxima (at 16:34, 16:47 and 17:05 UT) and dismissed at about 17:12 UT (Figs. 3 and 4). A detailed analysis shows that the first maximum is connected with the zebra pattern in the 1.6–1.8 GHz range at 16:33:30-16:33:43 UT and narrowband drifting pulsating structures (DPSs) in 0.8–1.3 GHz at 16:33–16:40 UT. The frequency drifts of this DPS are about $-1\,\mathrm{MHz\,s^{-1}}$. This first DPS which is observed during the rising phase of the hard X-ray emission we interpret as radio manifestation of the plasmoid ejection as in the papers by Kliem et al. (2000) and Karlický (2004).

The second maximum for 1.4 GHz corresponds in the spectrum (Fig. 3) to the broad band continuum in 1.3–2.0 GHz. The smooth character of this continuum indicates that this radio emission is generated by the gyro-synchroton emission mechanism. It is interesting to see that the maximum of this gyro-emission is delayed of about 5 minutes behind the maximum of the 25-50 X-ray flux (Fig. 4).

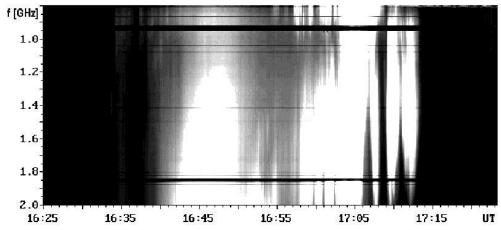

Figure 3. The 1–2 GHz Ondřejov radio spectrum.

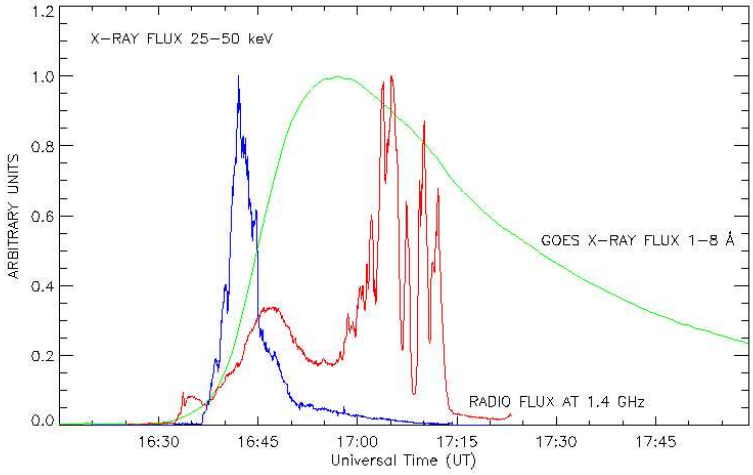

Figure 4. Superposition of X-Ray flux 25–50 keV, GOES X-Ray flux 1–8 Å, and radio flux at 1.4 GHz.

The radio emission in the interval close to the third maximum (17:05 UT) looks to be generated by the plasma emission mechanism because it is rapidly variable and on the spectrum (Fig. 3) we can recognize the frequency drifts of individual bursts. Some of them have the positive frequency drift indicating a downwards motion. The whole group of the bursts are drifting towards lower frequencies (the radio sources move globally to higher heights in the solar atmosphere) with the frequency drift of about $-0.7\,\mathrm{MHz\,s^{-1}}$. This drifting structure (16:50 – 17:12 UT) is observed after the hard X-ray maximum, i.e. at the phase of the growing flare loops arcade. Therefore we propose that this drifting structure is generated at the top of this loop arcade. Namely, the plasma density at the loop top decreases with time and thus the radio burst drifts towards lower frequencies. The termination shock may also be present at the top of this loop arcade and contribute to the radio emission as proposed by Auras & Mann (2004).

2.3. Magnetic field evolution and RHESSI observation

The magnetic field (SoHO/MDI) evolution during the day is in Fig. 5. In a) we can see a cloud of negative polarities surrounding the positive leading spot at 9:39 UT. A small point of the negative polarity appears at the North, see the

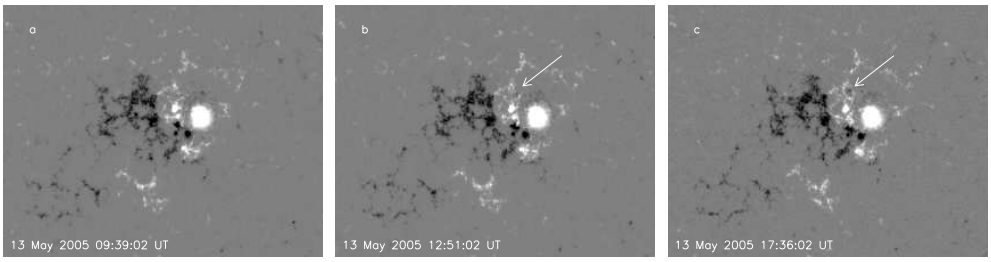

Figure 5. The magnetic field evolution.

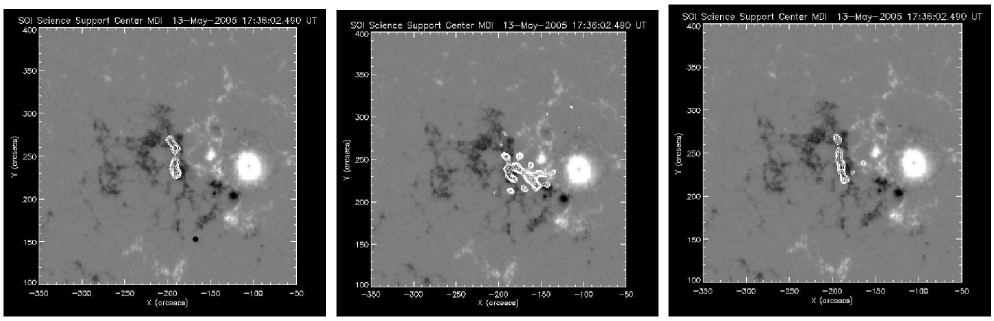

Figure 6. The magnetic field topology and X sources.

white arrow in b). At 17:36 UT the negative spot reached its maximum size, see c). This behavior of the magnetic field topology can be understood as a new emergence flux to originate the flare and perturbation of two filaments in the AR.

Superpositions of the RHESSI X-sources (from left to right, 25-50 keV at 16:42 UT; 12-25 keV at 16:44 UT, and 25-50 keV at 16:44 UT) over the MDI magnetic field (17:36 UT) are presented in Fig. 6. There is no X-ray source close to the leading spot, which indicates that electrons are reflected at the magnetic mirror in the strong magnetic field. It looks as the X-ray sources are located at the flare footpoints opposite to those anchored near the leading sunspot.

2.4. TRACE, SoHO-MDI, and HASTA observations

In order to analyze an evolution of the magnetic field we consider an image at the beginning of the flare (16:08 UT, TRACE). The coronal loops present a potential behavior according to the levels of the longitudinal magnetic field ($\pm$100 G, 1000 G), MDI, see Fig. 7a). In Fig. 7b, c there are evident the postflare loops. In Fig. 7b HASTA contours (17:46 UT) overplot the TRACE (18:45 UT), and vice versa in Fig. 7c, the TRACE contours over the HASTA image are displayed at the same time. In both cases it is possible to see that the footpoints of the loops coincide with the Hα ribbons.

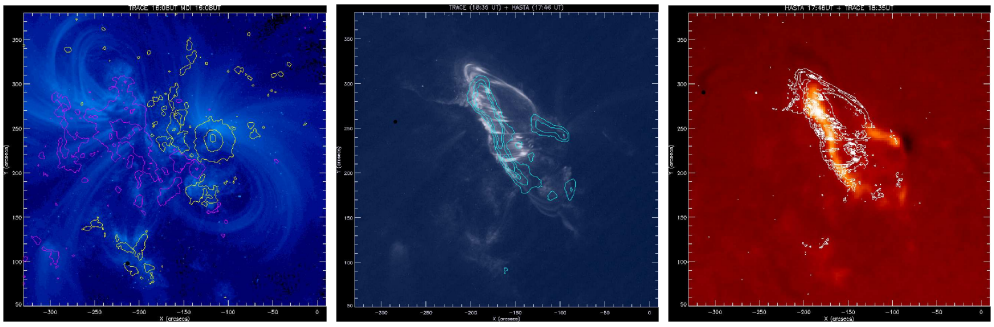

Figure 7. Example of coaligned images from TRACE, MDI, and HASTA.

3. Conclusions

An analysis of the multiwavelength ground-based and satellite observations of the solar event is presented.

The two ribbon flare was observed and described in X-rays, EUV, white light, Hα and radio wavelengths. There were studied relations to a bright full halo CME. The event was first seen in SoHO/LASCO C2 at 17:22 UT. It looks brighter above the NE limb. Unfortunately, the LASCO electronic box failed afterward and there are no more C2 images until 23:22 UT. For the same reason there is a C3 data gap. Evolution of the magnetic field and an emergence of the magnetic flux before the flare appeared are remarkable.

There was processed a huge amount of HASTA data in the big filament area appeared north-west from the flare. We were searching for some Hα intensity variations in the three independent subregions around the filament. Unfortunately only the small variations had been recognized in those areas during the 16:50 – 17:15 UT interval while the intensity variation of the second drifting pulsation structure was observed in radio. Obtained results in Hα intensity variations are comparable in all independent subregions and are close to the limit of HASTA resolution and the additive noise in the image.

Acknowledgments. This research was supported by bilateral project CONICET Argentina/AV ČR R.No. 2354/05 and partially by the grant GAČR 102/04/0155 and AV ČR project 1QS300120506. M.R. is member of the Carrera del Investigador Científico. SOHO is a joint ESA-NASA program.

References

Aurass, H. & Mann, G. 2004, ApJ, 615, 526
Bagalá, L.G., Bauer, O.H., Fernández Borda, R., Francile, C., Haerendel, G., Rieger, R., & Rovira, M.G. 1999, Proc. 9th European Solar Physics Meeting, ESA SP-448, 469
Jiřička, K., Karlický, M., Kepka, O., & Tlamicha, A. 1993, Solar Phys., 147, 203
Karlický, M. 2004, A&A, 417, 325
Kliem, B., Karlický, M., & Benz, A.O. 2000, A&A, 360, 715
Švestka, Z. 1976, Solar Flares, Reidel, Dordrecht

Excursion to the Old Cathedral of Coimbra

Mats Carlsson, Han Uitenbroek, Anna Pietarila, Bart De Pontieu, Hossein Ebadi, Oskar Steiner

The Physics of Chromospheric Plasmas
ASP Conference Series, Vol. 368, 2007
Petr Heinzel, Ivan Dorotovič and Robert J. Rutten, eds.

Full-Stokes Observations and Analysis of He I 10830 Å in a Flaring Region

Clementina Sasso[1], Andreas Lagg[1], Sami K. Solanki[1],
Regina Aznar Cuadrado[1] and Manuel Collados[2]

[1] *MPI für Sonnensystemforschung, Katlenburg-Lindau, Germany*
[2] *Instituto de Astrofísica de Canarias, La Laguna, Spain*

Abstract. We present observations of the full Stokes vector in a flaring region, taken in the chromospheric He I 10830 Å multiplet. The data were recorded with the new Tenerife Infrared Polarimeter (TIP 2) at the German Vacuum Tower Telescope (VTT) during May 2005. The He profiles during the flare are extraordinary, showing extremely broad Stokes I absorption and very complex and spatially variable Stokes V signatures. We give first results on the line-of-sight velocities and the magnetic field vector values in the chromosphere for one observed Stokes profile by applying an inversion code to the He I lines.

1. Introduction

The He I 10830 Å multiplet is a powerful diagnostic of the solar chromospheric magnetic and velocity field. The components of the He I multiplet are sensitive to the Zeeman effect and therefore these lines are suitable for spectropolarimetric measurements of the magnetic field vector in the upper chromosphere, where they are formed (Trujillo Bueno et al. 2002; Solanki et al. 2003).

The He I 10830 Å multiplet originates between the atomic levels 2^3S_1 and $2^3P_{2,1,0}$. It comprises a "blue" component at 10829.09 Å with $J_u = 0$ (Tr1), and two "red" components at 10830.25 Å with $J_u = 1$ (Tr2) and at 10830.34 Å with $J_u = 2$ (Tr3), which are blended at solar chromospheric temperatures.

2. Observations

The data we present here were recorded with the German Vacuum Tower Telescope (VTT) with the new Tenerife Infrared Polarimeter (TIP 2; Collados et al. 2007) at the Teide Observatory in Tenerife. During observations on 2005 May 18, a flare of GOES class C2.0 erupted in the west part of the active region NOAA 10763, located at 24° W, 14° S on the solar disc. The active region was covered by scanning in steps of 0.35″ perpendicular to the slit orientation from 14:38:29 to 15:02:26 UT. In the scanned region a filament and the flare ribbons were visible in the Hα slit jaw camera images. The spectral dispersion of the instrument is 15 mÅ per pixel. The spectral window (10825 – 10836 Å) contains four photospheric lines of Si I at 10827.1 Å, Ca I at 10829.3 and 10833.3 Å and Na I at 10834.8 Å, the chromospheric He I multiplet and two telluric blends at

10832.1 Å and 10833.9 Å. Figure 1 displays Stokes I maps for the observed region in the continuum and in the core of the "red" components of the He I lines.

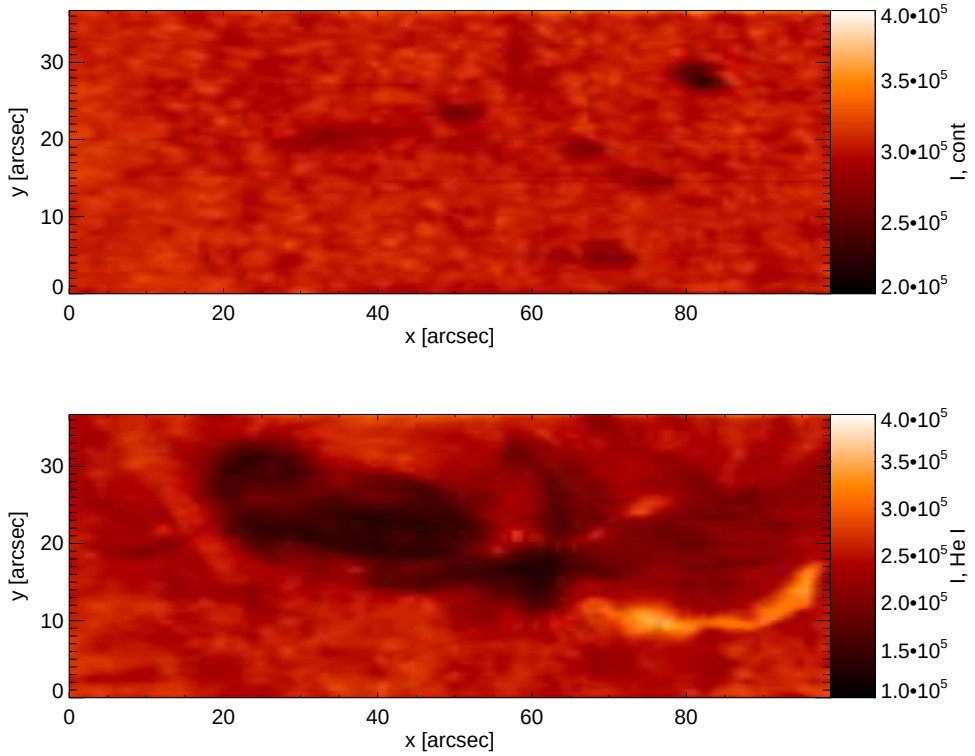

Figure 1. Intensity maps of the active region NOAA 10763 (24° W, 14° S) obtained at different wavelength regions. *Top*: Continuum. *Bottom*: He I line core of the "red" component.

From the lower map of Fig. 1 the presence of a strong absorption in the He lines is clearly visible during the central part of the scan. At the end of the scan, the lines show a completely different behaviour and show less absorption then in the quiet sun, at $y \approx 8'' - 15''$ ($65'' < x < 98''$). The analysis of the He Stokes profiles observed during the scan reveals huge differences in the profile shape. In Fig.2 we present some examples of observed Stokes I profiles at different pixel positions. In all the profiles we can notice the presence of different atmospheric components for the He lines (see Sect. 3) which are blue- or redshifted, implying upflows or downflows. In some profiles of Fig. 2, e.g., (b) and (c), blueshifted and redshifted components of the He multiplet coexist. Another example is shown in Fig. 3 (black lines) the Stokes vector at pixel position $x = 64''$, $y = 15''$ of Fig. 1. The spectra are binned over four spectral pixels and eight spatial pixels in order to increase the signal-to-noise level. The I profile shows a very broad absorption affecting the wavelength range 10829 Å to 10835 Å and in the Stokes V profile we see the signature of several magnetic components within this range. We observe an unusually wide range of Stokes profiles at several locations of the scan.

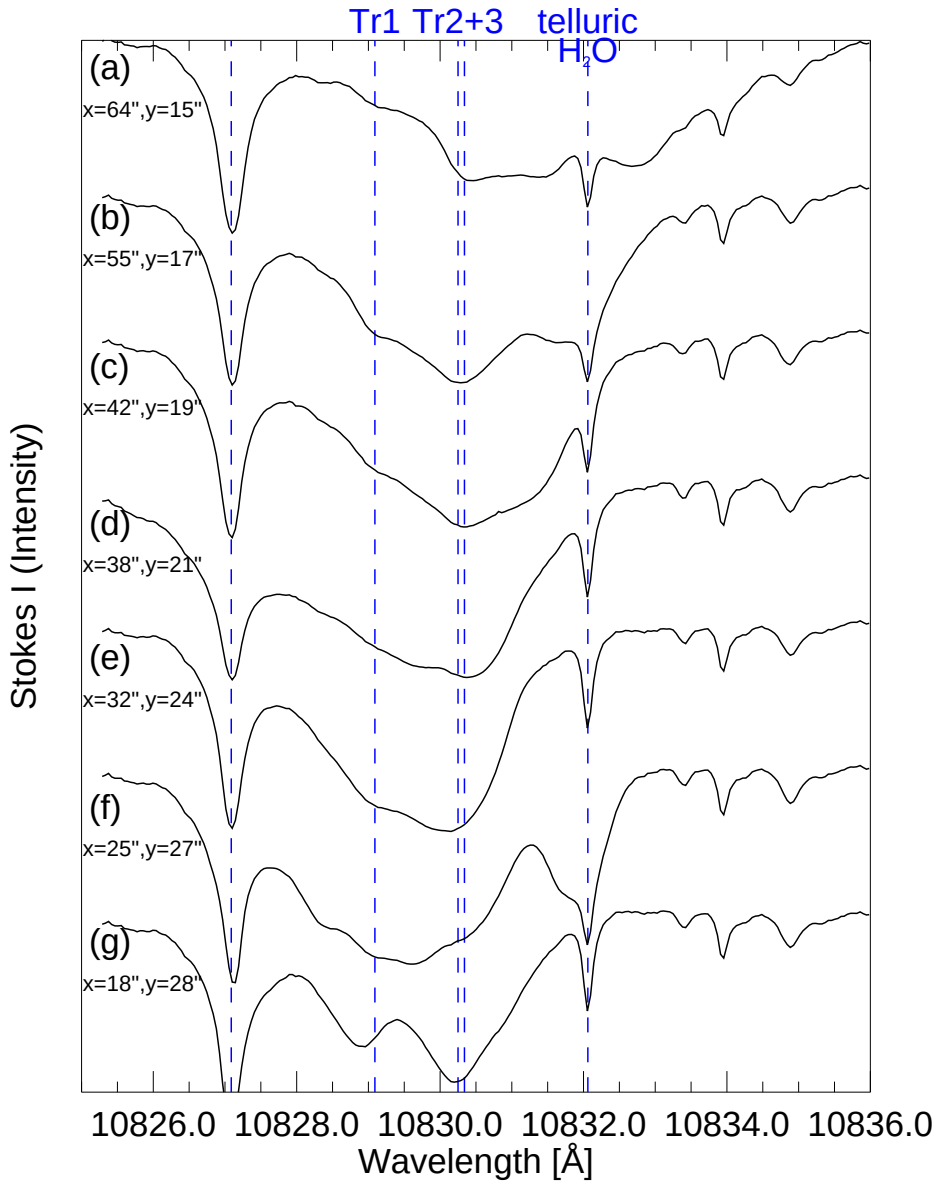

Figure 2. Examples of the observed Stokes I profiles, with their pixel positions marked on their left side.

3. Inversions of the Stokes Vector

In order to retrieve the full magnetic field vector and the velocity along the line-of-sight, we analyze the chromospheric He I lines with an inversion involving the forward calculations of the four Stokes profiles. The He I lines show a complex non-LTE formation but due to their optical thinness, their narrowness and the absence of any significant photospheric contributions, these lines can be used to deduce the magnetic field vector and the line-of-sight velocity at the height of

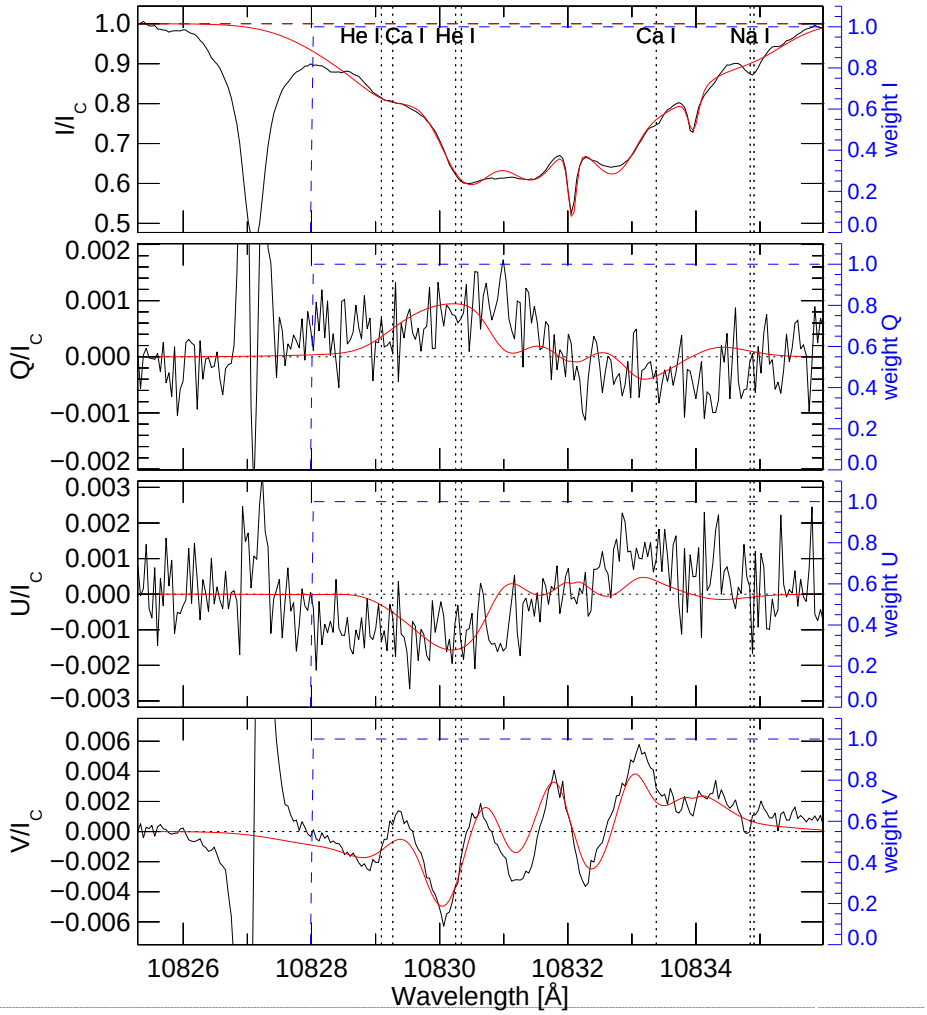

Figure 3. Inversions of the Stokes I, Q, U and V at position $x = 64''$, $y = 15''$ of Fig. 1. The black thick lines are the observed profiles while the thin (red in the electronic version) lines are the fits obtained considering, as input to the inversion code, three coupled magnetic components of the He I lines.

formation without the need to understand the details of their formation (Rüedi et al. 1995).

We apply to the spectropolarimetric data the numerical code for the synthesis and inversion of Stokes profiles in a Milne-Eddington atmosphere described by Lagg et al. (2004). This inversion method was extended to take into account the effect of incomplete Paschen-Back splitting following Socas-Navarro et al. (2005) and Sasso et al. (2006). Here we present, in particular, the inversion of the full Stokes vector in the He I 10830 Å multiplet, at pixel position $x = 64''$, $y = 15''$ of the maps in Fig. 1. In order to obtain a good fit to the observations, we had to consider 3 different atmospheric components for the He I lines. The

components have the same magnetic field vector, but different velocities along the line-of-sight. The best fit shown in Fig. 3 reproduces the observed Stokes vector reasonably well. A sufficient good 3-component fit of these profiles is obtained for a single magnetic component with a ≈ 380 G, an inclination to the vertical of 116° and an azimuth of 60°. The different components do show strongly different line shifts, however. The fit identifies a component almost at rest and two fast components with supersonic velocities of 36 and 64 km/s. Such profiles displaying 3 atmospheric components are reasonably common and we have even found cases which require 4 atmospheric components to be reproduced.

4. Discussion

From the analysis of the observed profile discussed in Sect. 3, and of other profiles not presented in this paper, we have evidence for the presence of different unresolved atmospheric components for the He lines, coexisting in the same resolution element. Multiple unresolved atmospheric components are also found in non-flaring regions (Lagg et al. 2006), but they are more common and in particular three or more components are often needed. Some times supersonic upflows and downflows of the He I lines appear in the same pixel. We have also evidence of different He components showing emission and absorption within the same profile. The shifts for most of the profiles are associated with supersonic velocities. In particular, we measure upflows with velocities up to 40 km/s and downflows with velocities up to 64 km/s.

In addition to completing the inversion of the whole map we plan to investigate the connection between the flare, happening at coronal heights, and what we observe at chromospheric levels.

References

Collados M., Lagg A., Díaz García J. J, Hernández Suárez E., López López R., Páez Mañá E., Solanki S. K., 2007, in P. Heinzel, I. Dorotovic, R. J. Rutten (eds.) The Physics of Chromospheric Plasmas, ASP Conf. Series, these proceedings

Lagg A., Woch J., Krupp N., Solanki S. K., 2004, A&A 414, 1109

Lagg A., Woch J., Solanki S. K., Krupp N., 2006, A&A, in press

Rüedi I., Solanki S. K., Livingston W. C., 1995, A&A 293, 252

Sasso C., Lagg A., Solanki, S. K., 2006, A&A 456, 367

Socas-Navarro H., Trujillo Bueno J., Landi Degl'Innocenti E., 2005, ApJS 160, 312

Solanki S. K., Lagg A., Woch J., Krupp N., Collados M., 2003, Nat 425

Trujillo Bueno J., Landi Degl'Innocenti E., Collados M., Merenda L., Manso Sainz R., 2002, Nat 415, 403

Adriana Garcia at spectroheliograph

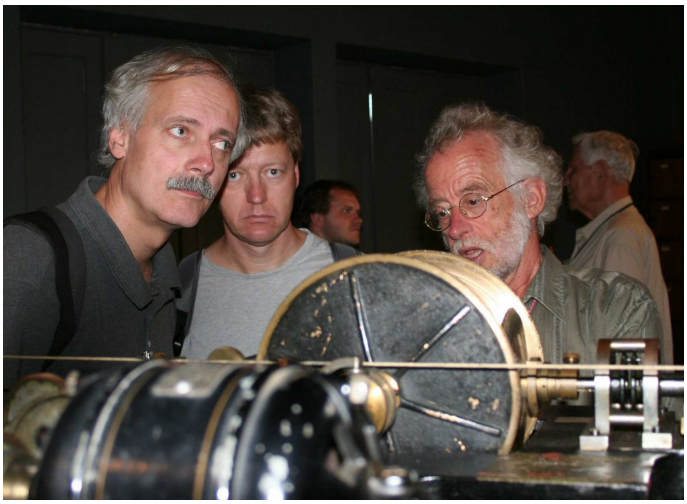

Mats Carlsson, Torben Leifsen, Peter Gömöry, Rob Rutten, Václav Bumba

The Physics of Chromospheric Plasmas
ASP Conference Series, Vol. 368, 2007
Petr Heinzel, Ivan Dorotovič and Robert J. Rutten, eds.

Return Current and Energy Deposit in Flares

Michal Varady[1,2], Marian Karlický[2] and Jana Kašparová[2]

[1]*Department of Physics, Faculty of Natural Sciences, Purkinje University, Ústí nad Labem, Czech Republic*
[2]*Astronomical Institute AS, Ondřejov, Czech Republic*

Abstract. The return current (RC) related effects represent in flares one of the possible mechanisms of conversion of the kinetic energy of electron beams into the thermal energy of flare plasma. Using a 1-D current-in-cell model, details of formation and properties of the RC driven by monoenergetic electron beams are calculated. Based on results of the simulations, the influence of the RC on the energy deposit in flares is discussed.

1. Introduction

According to the standard flare model the flare energy is released in the corona due to the reconnection of coronal magnetic fields and consequently transported by energetic beams of charged particles along the magnetic fieldlines downwards to the transition region, chromosphere and photosphere where the bulk of the beam kinetic energy is converted into the thermal energy of the flare. Due to the diagnostics of non-thermal hard X–ray bremsstrahlung emitted by flares, the electron beams are the best studied agents transporting energy in flares. The propagation of electron beams with power–law spectra and energies in the range from $\approx 15\,\mathrm{keV}$ to several $100\,\mathrm{keV}$ and energy fluxes from $\approx 10^{10}$ erg cm^{-2} s^{-1} to almost 10^{12} erg cm^{-2} s^{-1} observed in flares is inevitably connected with an origin of enormous electric currents which according to the Maxwell's theory have to be *exactly balanced* by RCs created by the plasma background electrons (Knight & Sturrock 1977, Hoyng et al. 1978, van den Oord 1990).

RCs in flares are powered by electric field originating as a result of the beam current injection into the ambient plasma in the solar atmosphere. According to the majority of RC models, the induced electric field accelerates the background electrons, generates the RC and the accelerated RC electrons then via collisions with ions contribute to the flare heating of the ambient plasma. At the same time the induced electric field tends to decelerate the beam electrons and besides the Coulomb collisions it thereby contributes to the dissipation of the electron beam kinetic energy. Although the contribution to the flare heating from the Coulomb collisions is fairly known (Emslie 1978) the contribution from the RC remains unclear and the conclusions obtained by various models are rather controversial, depending on the considered mode of propagation of the RC. The models using the Ohm's law in connection with either the classical (Emslie 1980) or anomalous (Emslie 1981, Duijveman et al. 1981, Cromwell et al. 1988, Matthews et al. 1996) electrical conductivity attribute an important role to the flare heating due to the RC, whereas other models (e.g., Rowland & Vlahos 1985) based on detailed

theoretical considerations of kinetic collective effects related to the RC formation conclude that the bulk of the plasma background electrons is trapped and the RC is carried only by a small population of fast, supra-thermal (runaway) electrons. Collisional losses of such electrons are due to their high velocities substantially reduced and therefore the effects of the RC on the flare heating function as well.

In this contribution we concentrate on a microscopic modeling of the formation of the RC generated by a monoenergetic electron beam in a typical chromospheric plasma. Using a 1-D current-in-cell code we calculate the distribution functions of electrons carrying the RC. We follow evolution of the electric field powering the RC from the transient, unstable state towards a stationary state. The final mean values of the stationary field driving the RC are compared with the electric field which would correspond to the field obtained from the Ohm's law and the classical Spitzer conductivity for the same current.

2. Model Description

We consider a 1-D system of numerical background plasma electrons whose charge is neutralized by static protons. The simulations are initiated by a penetration of a beam of numerical electrons from one side of the computational domain. The details concerning of the code, adopted methods and physical approach are given in Varady et al. (2005).

3. Results

All the simulations were carried out for *monoenergetic* electron beams and as a typical value of plasma density in the chromosphere was taken $n_\mathrm{e} = 10^{12}$ cm^{-3}. To see all the details of the RC formation, the time step of the code had to be shorter than the period of the electron plasma oscillations, i.e. $\Delta t = 5 \times 10^{-13}$ s. Three distinct models have been calculated:

1. Model A: RC formation at the very onset of the interaction of cold chromospheric plasma $T = 0\,\mathrm{K}$, ($v_{T_\mathrm{e}} = 0$ cm s^{-1}) with the electron beam.
2. Model B: RC formation for a constant beam flux propagating through chromospheric plasma, $T_\mathrm{e} = 10^4\,\mathrm{K}$. Model includes only Coulomb collisions, collective effects are *not* taken into account.
3. Model C: RC formation for a constant beam flux propagating through chromospheric plasma $T_\mathrm{e} = 10^4\,\mathrm{K}$. Model includes both the Coulomb collisions and the collective plasma effects.

3.1. Model A: initial phases of the beam injection – cold plasma

Several runs with different densities of the electron beam and with different numbers of numerical electrons (20000 and 200000) were carried out. The real densities were simulated by weighting of the numerical electrons. In the initial state of the system with length 100 cm the background plasma electrons were uniformly distributed into 1000 grid cells in order to resolve the collective plasma effects. Then the beam electrons with velocity $v_\mathrm{b} = -10^{10}$ cm s^{-1} were continuously injected into the domain at its right boundary (i.e. at the position

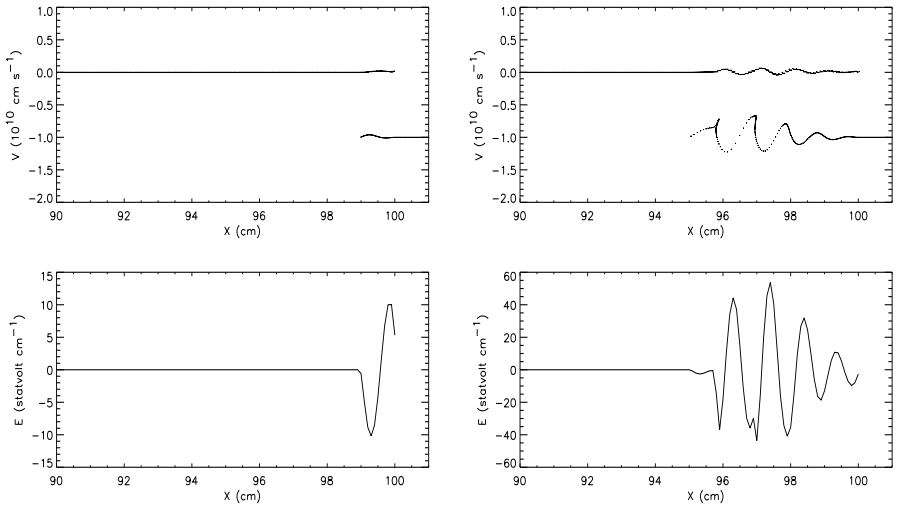

Figure 1. *Left:* The state of the system at 1×10^{-10} s. Upper panel: The distribution of electrons in the phase-space. The initial velocity of background and beam electrons is zero and -10^{10} cm s^{-1}, respectively. Bottom panel: The electric field generated along the beam path. *Right:* The state of the system at 5×10^{-10} s. Upper: The distribution of electrons in the phase-space. Bottom: The electric field generated along the beam propagation.

100 cm). The result of the simulation with $n_\mathrm{b} = 10^{10}$ cm^{-3} at t=10^{-10} s, i.e. immediately after the beam injection when the beam penetrates only 1 cm into the system, is shown on the left side in Fig. 1. The magnitude of the electric field formed at the beam front corresponds to the value analytically derived by van den Oord (1990)

$$E = 4\pi j_\mathrm{b}/\omega_\mathrm{p} \quad , \tag{1}$$

where j_b is the electron beam current and ω_p is the plasma frequency. The corresponding wavelength L of plasma oscillations is (from the relation $k = 2\pi/L = \omega_\mathrm{p}/v_\mathrm{b}$, where v_b is the beam velocity) $L = 1.11$ cm which in agreement with the simulation. Moreover, the mean velocity of the accelerated background electrons times their density equals to the initial electron beam velocity times n_b, i.e. the beam current is equal to the RC.

In the following times, e.g., at $t = 5 \times 10^{-10}$ s (see the right side of Fig. 1) the amplitude of the oscillations grows due to the two-stream instability. The analytical expression for the growth rate of the instability is (Michajlovskij 1975)

$$\gamma = \omega_\mathrm{p} \frac{\sqrt{3}}{2^{4/3}} \left(\frac{n_\mathrm{b}}{n_\mathrm{e}} \right)^{1/3} \quad , \tag{2}$$

which gives $\gamma = 0.148\ \omega_\mathrm{p}$. The theoretical value is again in a good agreement with the value given by the model.

As a consequence of the growing electric field the beam electrons are getting trapped in the generated electrostatic wave. The trapping process leads to the

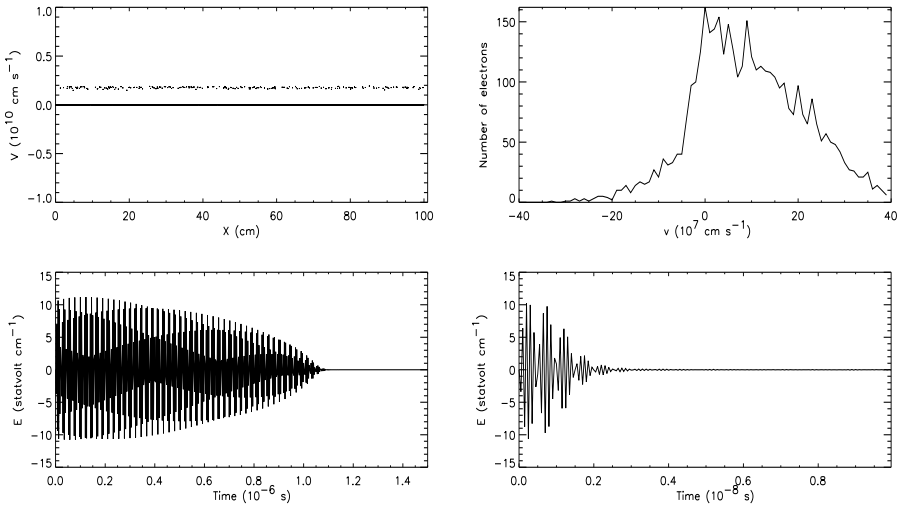

Figure 2. *Left:* Results of Model B. Upper: Phase-space diagram showing two parts of background plasma electrons at 10^{-6} s. The RC is carried by electrons with a mean velocity 1.69×10^9 cm s^{-1}. Bottom: The time evolution of the electric field. *Right:* Results of Model C: Upper: The distribution function of the background plasma at 10^{-8} s. Bottom: The evolution of the mean electric field in the system.

saturation of the two-stream instability. The energy level of the saturation can be estimated by Birdsall & Langdon (1985)

$$W_s = \frac{\mid E \mid^2}{8\pi} = \frac{1}{2} n_\mathrm{b} m_\mathrm{e} v_\mathrm{b}^2 \left(\frac{R}{2}\right)^{1/3} \quad , \tag{3}$$

where $R = n_\mathrm{b}/n_\mathrm{e}$, which gives $E = 44.3$ statvolt cm^{-1} at time $t = 5 \times 10^{-10}$ s.

3.2. Model B: RC including collisions only

The model is almost identical with Model A. The only changes are that the boundary conditions are now periodic in space and there is no spatial grid. The consequence of the latter change results in elimination of the collective plasma processes (e.g., RC instability) from the system, so only the global electric field and the collisional deceleration of electrons are considered. The beam having an arbitrary distribution in the velocity space is always represented by a constant electron flux (current) so this is a good approximation of power-law beams commonly used in the interpretation of hard X-ray emission. The initial distribution function of the background plasma is Maxwellian with temperature $T_\mathrm{e} = 10^4$ K. The RC formation for electron flux $n_\mathrm{b} v_\mathrm{b} = 10^{20}$ cm^{-2} s^{-1} is shown on the left side in Fig. 2. From the figure it is also apparent that due to the collisions, the background plasma electrons are divided into two populations: a) a bulk of electrons with zero velocity; b) a population of fast electrons carrying the RC. The ratio of their densities is $n_\mathrm{RC}/n_\mathrm{bulk} = 5.98 \times 10^{-2}$. The mean velocity of the electrons forming the RC is 1.69×10^9 cm s^{-1}, i.e. the RC again balances

the beam current. During the simulation electric field in the system oscillates with gradually decreasing amplitude and finally (after $\approx 1.1 \times 10^{-6}$ s) a weak and constant electric field driving the RC is formed. The final electric field $E_{\rm final}$ is much less than the electric field calculated from the Ohm's law using the classical conductivity and the same electric current (see Table 1). Similar calculations have been carried out also for beam flux $n_{\rm b}v_{\rm b} = 10^{19}$ cm^{-2} s^{-1} and results are listed in Table 1.

3.3. Model C: RC including collisions and collective effects

The model remains again almost the same as Model B only the computational domain has been divided into 1000 grid cells. The consequence is inclusion of the RC instabilities (i.e. plasma collective effects). The formation of the RC for the electron beam flux $n_{\rm b}v_{\rm b} = 10^{20}$ cm^{-2} s^{-1} is shown on the right panel in Fig. 2. The formation of a stationary RC is much shorter than in Model B due to the waves generated by the instability of the RC. The resulting distribution function has an extended tail for $v > 0$ and strongly deviates from the Maxwellian. The extended tail formed from the background plasma electrons carries the RC. The final, stationary electric field is higher than that in the Model B, but still lower than the Ohm's electric field calculated for the same electric current. Similar calculations have been made also for beam flux $n_{\rm b}v_{\rm b} = 10^{19}$ cm^{-2} s^{-1} and results are listed in Table 1.

Table 1. A comparison of the RC parameters obtained from Model B and Model C. The values $n_{\rm RT}$ and $n_{\rm bulk}$ are the densities of the RC and the bulk populations, $\overline{v_{\rm RT}}$ is the mean velocity of the electron population carrying the RC, $E_{\rm final}$ is the final stationary electric field and $E_{\rm Ohm}$ is the corresponding electric field calculated from the Ohm's law and the classical conductivity.

Electron flux [cm^{-2} s^{-1}]	$n_{\rm RC}/n_{\rm bulk}$	$\overline{v_{\rm RC}}$ [cm s^{-1}]	$E_{\rm final}$ [statvolt cm^{-1}]	$E_{\rm Ohm}$ [statvolt cm^{-1}]
		Model B		
10^{20}	5.98×10^{-2}	1.69×10^{9}	-1.42×10^{-4}	-5.19×10^{-2}
10^{19}	2.01×10^{-2}	4.97×10^{8}	-1.76×10^{-4}	-5.19×10^{-3}
		Model C		
10^{20}	—	—	-6.32×10^{-3}	-5.19×10^{-2}
10^{19}	—	—	-2.08×10^{-3}	-5.19×10^{-3}

4. Conclusions

Using a simple model based on a 1-D current-in-cell code describing the formation of the RC on microscopic scales, we were able to reproduce several important aspects of the RC formation which have been earlier found analytically. All the presented models, in accordance with theory, produced RCs which exactly balanced the beam current. The oversimplified model with cold background plasma (Model A) successfully mimics the magnitude of the electric field formed at the beam front and the properties of the current instabilities (generation of

the plasma waves with the expected parameters, correct grows of two-stream instability, etc.) which are generated immediately after the beam enters the plasma. Model B and Model C showed that the distribution function of the background electrons are strongly non–Maxwellian. Considering only Coulomb collisions and neglecting the collective effects, Model B gives two populations of background electrons: standing bulk and a fast population of background electrons carrying the RC. At this point our the results resemble the results of Rowland & Vlahos (1985). A more realistic Model C taking into account both, collisions and collective effects gives distribution functions which strongly deviate Maxwellian and the RC is here carried by the electrons from an extended tail of the distribution. So the RC is not formed by a simple velocity shift which is the same for all background plasma electrons as sometimes assumed. An obvious consequence is that due to the considerable velocities of the electrons forming the RC their collisional frequency decreases (see Eq. 4 in Varady et al. 2005). Consequently, the electric field which powers the RC and dissipates the kinetic energy of the beam decreases as well (relative to the electric field obtained for the same current using the Ohm's law and classical conductivity). The main conclusion is that according to our simulations, the RC related flare heating calculated using the Ohm's law and classical conductivity overestimates the role of the RC contribution in the calculations of flare heating.

Acknowledgments. This work was supported by grants 205/04/0358 of the Grant Agency of the Czech Republic (GAČR) and 1ET400720409 of the Grant Agency of Academy of Sciences of the Czech republic (GAAV ČR).

References

Birdsall Ch.K., Langdon A.B., 1985, Plasma physics via computer simulations, McGraw-Hill, New York
Cromwell D., McQuillan P., Brown J.C., 1988, Solar Phys. 115, 289
Duijveman A., Hoyng P., Ionson J.A., 1981, ApJ245, 721
Emslie A.G., 1978, ApJ 224, 241
Emslie, A.G. 1980, ApJ 235, 1055
Emslie A.G. 1981, ApJ 249, 817
Hoyng P., Knight J.W., Spicer D.S., 1978, Solar Phys. 58, 139
Knight J.W., Sturrock P.A., 1977, ApJ 218, 306
Matthews S.A., Brown J.C, Melrose D.B., 1996, A&A 305, L49
Michajlovskij A.B., 1975, Teorija plazmennych neustojchivostej, Atomizdat, Moskva
van den Oord G. H. J., 1990, A&A 234, 496
Rowland H.L., & Vlahos L., 1985, A&A 142, 219
Spicer D.S., 1982, Space Sci. Rev. 31, 388
Varady M., Karlický M., Kašparová J., 2005, in: Proceedings of the 11th European Solar Physics Meeting (ESA SP-600), Leuven, Belgium. Editors: D. Danesy, S. Poedts, A. De Groof and J. Andries, 146.1

Part VI

Long-term Solar Variations

The Physics of Chromospheric Plasmas
ASP Conference Series, Vol. 368, 2007
Petr Heinzel, Ivan Dorotovič and Robert J. Rutten, eds.

Solar Cycle Variation of Chromospheric Radiation

S. K. Solanki

MPI für Sonnensystemforschung, Katlenburg-Lindau, Germany

Abstract. Radiation emitted by the Sun's chromospheric gas displays a significant cyclic variation. The magnitude of this variability and the shape of the light curve differs from that exhibited by photospheric radiation, or total solar irradiance. The amplitude of the cyclic variation of chromospheric radiation is larger and less affected by the contribution of sunspots. Consequently, the influence of small-scale magnetic features forming plage and the network dominates. Here a brief introduction is given to the solar cycle variation of chromospheric radiation, its connection with the magnetic field, its quantitative modeling and related questions, such as the solar cycle variability of the quiet Sun chromosphere and its cause. Finally, some thoughts on the possible secular change of chromospheric (and total) irradiance are presented.

1. Introduction

Most solar phenomena are found to vary over the solar cycle. As the cycle progresses the number of features such as sunspots, faculae, plage, coronal loops or active regions change, as does the solar surface area covered by such features. In addition, global solar properties, such as the total or spectral solar irradiance, also evolve in phase with the solar activity level. Irradiance is the solar radiative flux measured above the Earth's atmosphere (normalized to a mean distance of 1AU from the Sun). The irradiance in a restricted wavelength range is called the spectral irradiance, while integrated over the whole spectrum it is termed the total irradiance.

Along with the radiation from other layers of the atmosphere, the radiation from the chromosphere varies over the activity cycle. The cause of this variation, at all scales, is thought to be localized in individual concentrations of the Sun's magnetic field: As the number of facular elements (magnetic elements) increases, so does their combined output at chromospheric wavelengths. Together, these local contributions add up to a change in the global chromospheric radiative output, i.e. chromospheric irradiance.

In this paper I provide an overview of the change in the chromospheric radiation (both local and global) and how it is related to the underlying magnetic field.

2. Solar Irradiance Variations: Different Atmospheric Layers

Figure 1 shows the variation of solar irradiance in different wavelength bands reflecting different layers of the solar atmosphere. The total solar irradiance

(TSI), the Mg II core-to-wing index and the F10.7 cm flux are plotted along with two activity indicators, the sunspot number, R_Z, and sunspot area, A_S.

Although the TSI gets contributions from all emitting layers of the solar atmosphere, the lion's share comes from the photosphere ($> 95\%$, Solanki & Unruh 1998). Hence the TSI indicates variations of the photospheric contribution to irradiance (although these variations are dominated by the contributions of the spectral lines, Mitchell & Livingston 1991; Unruh et al. 1999). Plotted is the PMOD composite due to Fröhlich (2005), which has been put together from measurements recorded by instruments flying on different satellites. TSI composites that deviate to a lesser or larger degree from the plotted one have been published by Willson & Mordvinov (2003) and DeWitte et al. (2004). They differ partly in the data sets used and in particular in the applied corrections for degradation of instrumental sensitivity etc.

The relative amplitude of the TSI variation over the solar cycle is only 0.1% and there is a qualitative difference between the daily (dotted) and monthly running mean values (solid). The daily values show individual strong downward excursions lasting typically around a week, while the excursions in the positive direction are significantly weaker. The monthly averages are much more symmetric as far as short-term variations are concerned. These fluctuations are restricted mainly to the periods around the maximum of the activity cycle. The downward excursions are due to the passage of sunspots over the solar disk (they do not last quite 2 full weeks because of foreshortening effects and because the faculae surrounding sunspots are increasingly bright near the limb where they increasingly compensate the sunspot darkening. The upward excursions are due to faculae. They appear when active regions are close to the solar limb, where the faculae actually dominate over the spots, but are partly due to older, decaying active regions whose sunspots have decayed so that the active regions are composed entirely of faculae.

The Mg II core-to-wing ratio or Mg-index is, as the name suggests, the ratio of the irradiance in the cores of the Mg II h and k lines relative to the irradiance in their wings (Heath & Schlesinger, 1986; Deland & Cebula 1998; Viereck & Puga 1999; Viereck et al. 2001). Taking the ratio between the irradiance at two wavelengths that lie relatively close to each other has the advantage that, the instrumental degradation at both wavelengths being roughly the same, this quantity is nearly independent of instrumental degradation. Since the variation in the chromospheric Mg II h and k line core is much larger than in the wings of these lines (formed in the photosphere), this index mainly represents the chromospheric excess radiation relative to the photosphere. Note the much larger relative variation (roughly 6–7%) compared to the TSI and the fact that the daily points are relatively symmetrically distributed around the monthly curve. Not surprisingly, the correlation coefficient between the daily Mg II index and the TSI is rather low, with a correlation coefficient of $r_c = 0.52$. However, the monthly running means correlate rather well ($r_c = 0.80$). The difference in behaviour to the TSI light curve is mainly because the sunspots do not contribute significantly to the Mg index.

The 10.7 cm radio flux (Tapping, 1987; Tapping & Detracey 1990) has a coronal source. Here the flux (irradiance) varied by a factor of roughly 2.5 over the last three cycles. Although the general shape of the cyclic changes is similar to that shown by the Mg II index, the short term fluctuations (around cycle

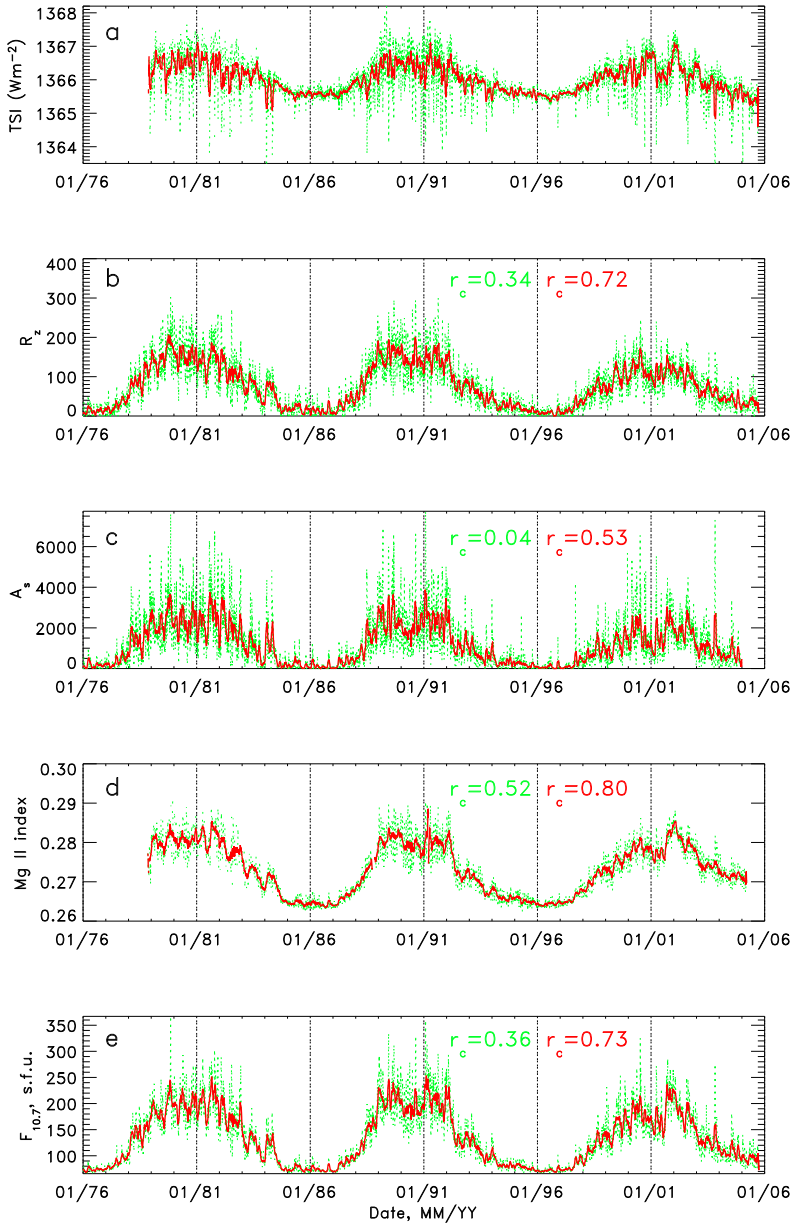

Figure 1. a) Total solar irradiance (TSI) vs. time. The dotted (green in the electronic version) line represents daily measurements, the solid (red) line, monthly averages. b) Sunspot number, R_Z. Correlation coefficients between the plotted curves and the total irradiance are given (the number on the left refers to daily values, the one on the right to monthly means). c) Sunspot area, A_S, i.e. the area covered by all sunspots in ppm of the solar disk. d) Mg II k core-to-wing ratio (Mg II index). e) F10.7, i.e. flux at 10.7 cm. Figure kindly provided by N. A. Krivova.

maxima) are considerably larger. Consequently the correlations of both the daily and the monthly smoothed time series with the corresponding TSI time series are lower ($r_c = 0.36$ and 0.73, respectively) than for the Mg index.

3. Irradiance and Magnetic Field

There is strong evidence that the changes in the irradiance arising from all atmospheric layers are due to the evolution of magnetic features on the solar surface. Magnetic features can lead to either a local brightening roughly cospatial with the magnetic field (bright points forming faculae in the photosphere, plage in the chromosphere and the network), or a local darkening at the solar surface (pores, sunspots). Quite instructive is to consider the dependence of the brightness emanating from different layers on the magnetogram signal (longitudinal magnetic field strength averaged over the spatial resolution element). Already the early work by Frazier (1971), illustrated in Fig. 2, showed just how different this dependence is for the photosphere and the chromosphere. The upper frame (b) shows the Ca II K core contrast (the relative difference between the intensity at a given magnetogram level and the quiet Sun intensity, i.e. the intensity at null magnetogram signal) plotted vs. magnetogram signal, while in the lower frame (a) the contrast of the continuum intensity in the green part of the solar spectrum is plotted. The dots are individual positions on the solar disk, while the solid lines are trend curves. Both sets of measurements refer to the center of the solar disc.

Clearly, whereas in the photosphere the contrast initially increases slightly with magnetogram signal, reaching a maximum contrast of roughly 0.035 at around 200 G and then decreases again to the extent that above 500 G it becomes negative (i.e. the magnetic features are darker than the quiet photosphere). This is not unexpected, since the largest magnetogram signals are shown by pores and sunspot umbrae, both of which are dark. Indeed it has recently been shown that sunspot umbrae are darker for increasing area of the magnetic structure (see Mathew et al. 2007). This basic behaviour is also revealed by newer studies (e.g., Topka et al. 1997; Ortiz et al. 2002), although closer to the solar limb the turnover point where the contrast starts decreasing again moves to increasingly higher magnetogram signals. Thus, small pores are dark at disk cemtre, but can appear bright near the limb.

The contrast of the chromospheric radiation, however, shows no sign of decreasing again for large magnetogram signals, although the rise slows (cf. Schrijver et al. 1989; Solanki et al. 1991). Schrijver et al. found that they could describe the dependence on the field of the Ca II K core contrast by a power law of the form $\langle B \cos\theta \rangle^{0.6}$. Cores of photospheric spectral lines lie in between the two extreme behaviours illustrated above.

4. Influence of Magnetic Features on Brightness

The dependence of the brightness or contrast on magnetic flux in the resolution element can be at least qualitatively understood by considering the sketch shown in Fig. 3, which has been adapted from a figure in Zwaan (1978). It shows a schematic magnetic flux tube (the boundaries or side walls of the flux tube are

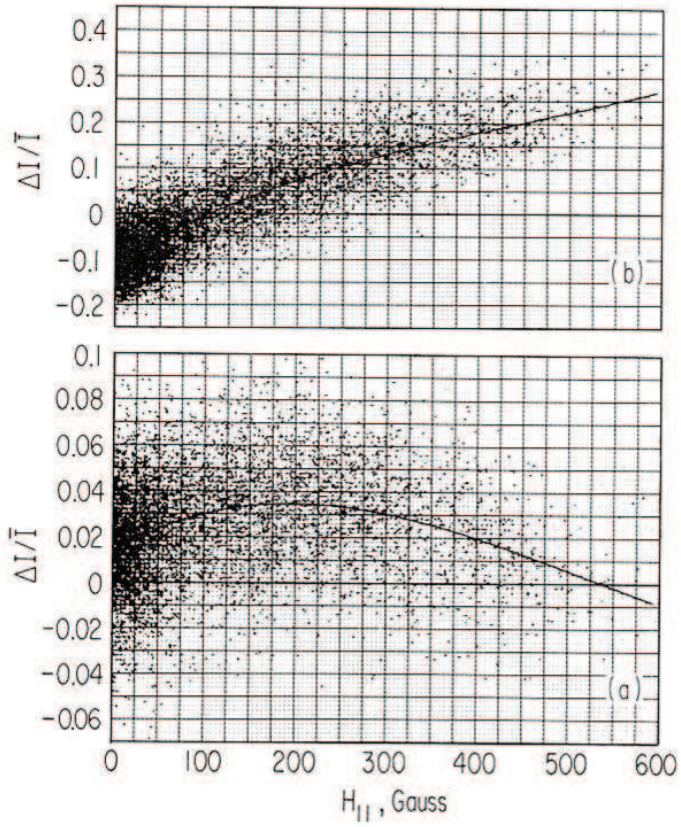

Figure 2. Intensity contrast, $\Delta I/\langle I\rangle = (I(H_{||}) - I(H_{||} = 0))/\langle I(H_{||}\rangle$, vs. magnetogram signal $H_{||}$. Upper panel (b): Ca II K line core. Lower panel (a): continuum in the green part of the solar spectrum. Figure adapted from Frazier (1971).

represented by the curved, nearly vertical lines) passing through the solar surface (indicated by the thick horizontal lines, with the solar surface lying at a lower level in the flux tube due to its evacuation). In the subphotosphere the magnetic field leads to a reduction in the efficiency of convection (heat blocking), indicated in Fig. 3 by the vertical (red) arrows (internal vertical energy flux $F_i \ll F_e$). This is compensated by the lateral inflow of radiation into the flux tube (F_r) through the walls at a level lying above the internal $\tau = 1$ surface and the external $\tau = 1$ surface, indicated by the upper horizontal (yellow) arrows. For a strong field that almost completely blocks the internal convective transport, to first order the amount of heating depends on the ratio of the wall area to the area of the flux tube's cross section (although other factors, such as the properties of the surrounding gas also play a role; cf. Deinzer et al. 1984a,b; Vögler et al. 2005). If the flux tube is small, then the inflowing radiation can more than compensate the blocked vertical energy flux, leading to a positive contrast of the magnetic features. This simple model also, at least qualitatively, explains the centre-to-limb behaviour of the contrast, in particular the brightening seen

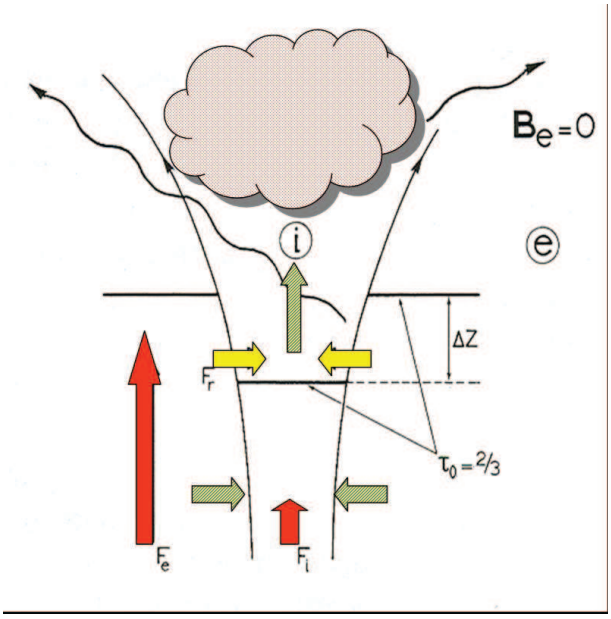

Figure 3. Sketch of a magnetic flux tube and the processes leading to excess radiation emerging from it in the photosphere and the chromosphere. See text for details. Adapted from Zwaan (1978).

away from disk centre, as the hot walls become visible (indicated in Fig. 3 by the long wavy arrow leaving the right wall towards the upper left).

For the chromospheric radiation the underlying physics is expected to be significantly different, and has been worked out in less detail than the simpler photospheric case. The classical picture is that in addition to radiation, mechanical energy is laterally introduced into the magnetic feature by the turbulent medium in which it is embedded. This buffetting by the neighbouring convection cells is clearly seen in the 2-D numerical simulations of Steiner et al. (1996), although it is likely that the effect is exaggerated somewhat in 2-D, since the granular flows cannot work their way round the flux tube, which is the case in 3-D. Convection excites different MHD wave modes that travel up along the field (e.g., Huang et al. 1995). These can be longitudinal, tube waves (e.g., Roberts & Webb 1978; Musielak et al. 2000), transverse modes (Musielak and Ulmschneider 2002) or torsional Alfvén waves (Noble et al. 2003). See e.g., Narain and Ulmschneider (1996); Roberts and Ulmschneider (1997), Carlsson & Hansteen (2005) for overviews. The energy input by the granular buffeting is indicated in Fig. 3 by the lower pair of horizontal (green) arrows.

These waves carry a given energy flux into the chromosphere, indicated by the upper vertical (green) arrow. In the case of the magneto-acoustic tube mode the energy can be dissipated in the chromospheric layers through the formation of shocks (Herbold et al. 1985; Fawzy et al. 1998). The dissipation region is indicated by the shaded cloud (representing a cloud of heated gas) in Fig. 3. This heated cloud radiates at wavelengths typical of the chromosphere. Clearly, since it is relatively optically thin, this cloud radiates in all directions, which

qualitatively explains why, e.g., the contrast of magnetic features in Ca II K is equally large at all locations on the solar disc.

The increase in the contrast with magnetic flux or magnetogram signal seen in Fig. 2b at small $H_{||}$ is explained by the increasing density of magnetic flux tubes as the magnetic flux increases (Solanki et al. 1991; Fawzy et al. 1998) and the saturation at large $H_{||}$ by a decreased excitation rate of waves as a large density of flux tubes starts affecting the granules around them (Title et al. 1989). However, unlike in the photosphere, the chromospheric brightness does not decrease with increasing B (outside of sunspots).

So far much of the theoretical work on flux-tube waves suffers from the fact that the computations are restricted to 1-D models. Recent 2-D simulations, as described by Carlsson and Hansteen (2005), as well as planned 3-D simulations, show considerable promise for significant progress in this field.

Sunspots are dark in the photosphere and the lower chromosphere, while in the upper chromosphere and the transition region they are either neutral (i.e. at a similar brightness as the quiet Sun), or are bright (in particular the penumbrae). This suggests that although in the photosphere the large surface area of the sunspots relative to their circumference is the dominent reason for sunspot darkness (the quenching of the convective energy transport can be only partly compensated by the inflow of radiation through the side walls), in the chromosphere the magnetic heating mechanisms appear to work for them as well, although not with the same efficiency as in the magnetic elements.

Using the above information we can now attempt to explain the qualitative solar cycle behaviour shown by the irradiance from different atmospheric layers in Fig. 1. Basically, the difference is due to the fact that the photospheric radiation gets enhanced contributions from the magnetic elements, and depressed contributions from the sunspots. The fact that the sunspot contrast is much larger than the contrast of magnetic elements leads to the strong downward deflection of the TSI. In the chromosphere the influence of the magnetic elements is enhanced (stronger contrast in the chromosphere) and the influence of the sunspots is small (even neutral), leading to a larger variation of the chromospheric irradiance, with most of the variations being due to the plage regions. Finally, the corona shows a similar behaviour as the chromosphere, but with some differences due to the fact that coronal loops, whose heating mechanism is different again, contribute to a large extent, which explains the even lower correlation with the TSI.

The increased correlation between TSI and the other indicators for the running monthly means is due to the fact that the darkening due to a particular spot or a group of sunspots usually lasts a week or less, whereas the plages within active regions firstly display a brightening for the full two weeks that they remain visible per solar rotation (the enhanced contrast near the limb roughly compensates for the smaller projected area, etc.), and, secondly, they live for a much longer time. Consequently, the same patches of plage will in general be visible over multiple cycles. Finally, plage is distributed much more homogeneously over the solar surface than sunspots. All these effects work to smooth out the short-term irradiance variations due to plage compared to those due to sunspots. At longer time scales, therefore, both photospheric and chromospheric irradiance are dominated by the influence of plages.

5. Quantitative Reconstruction of Irradiance: SATIRE Models

Models aiming to quantitatively reproduce solar irradiance variations can be divided into two classes. The first class contains those models that use the correlation between the irradiance to be modelled and one or more activity indicators as the basis for the reconstruction. The second class of models employs model atmospheres of different types of magnetic features to compute their spectra. These spectra are then combined according to the area covered by each type of feature to get the irradiance.

The Spectral And Total Irradiance REconstrution (SATIRE) model (Fligge et al. 2000; Krivova et al. 2003) is a successful example of the second type of model. The results obtained by other models that use model atmospheres to compute the spectral irradiance have been published by Fontenla et al. (2004); Haberreiter et al. (2005); Fontenla and Harder (2005) and Harder et al. (2005).

These models have in common that they divide the solar surface into features (components), which are assumed to have universal properties (e.g., all sunspot umbrae and penumbrae are assumed to be well-described by the same time-independent model atmosphere). The number of such atmospheric components differs from model to model. In the case of the SATIRE models, 4 atmosphere components are deemed sufficient: sunspot umbrae, sunspot penumbra, quiet Sun and faculae (the network elements are described by the same atmospheric parameters, although this is known not to be strictly correct; e.g., Solanki & Stenflo 1984; Solanki 1986). The evolution of these components is deduced from the observed evolution of the magnetic field at the solar surface (from magnetograms in the case of SATIRE, from brightness images in the case of other models). More details can be found in Fligge et al. (2000), Krivova et al. (2003), Krivova & Solanki (2005), Wenzler et al. (2006).

The SATIRE model has successfully reconstructed the TSI over 3 decades. E.g., it is found that over 90% of the TSI variations in cycle 23, for which the best data are available, are due to the magnetic field at the solar surface.

In spite of this success there are a few important shortcomings of the SATIRE models. Firstly, there is a free parameter that can be adjusted in order to obtain a good match to the TSI data. Secondly, and more importantly for chromospheric irradiance variability, the spectra computed in the context of SATIRE are in LTE, since it is mainly aimed at reproducing the photospheric signature of irradiance variations.

An overview of the important NLTE-based work in this field is given by Fontenla (2007). Whereas in LTE all strong lines display a large amplitude of the solar cycle variation, the measurements show that the lines actually behave rather differently. Two extreme examples are the Mg I 285.21 nm and the Mg II h and k resonance lines. Whereas the emission core of the latter varies strongly over the cycle (to the extent that the Mg II core-to-wing ratio is used as a standard indicator for solar activity; see Fig. 1), the core of the Mg I resonance line shows very little variation. This behaviour has been explained and reproduced by the non-LTE computations of Uitenbroek and Briand (1995). SATIRE reproduces the Mg II variability, but not that of the Mg I resonance line due to the restriction of the model to LTE (Unruh et al. in preparation).

This implies the need for an empirical extension of SATIRE in order to reproduce the variability at shorter wavelengths. This can be achieved by mak-

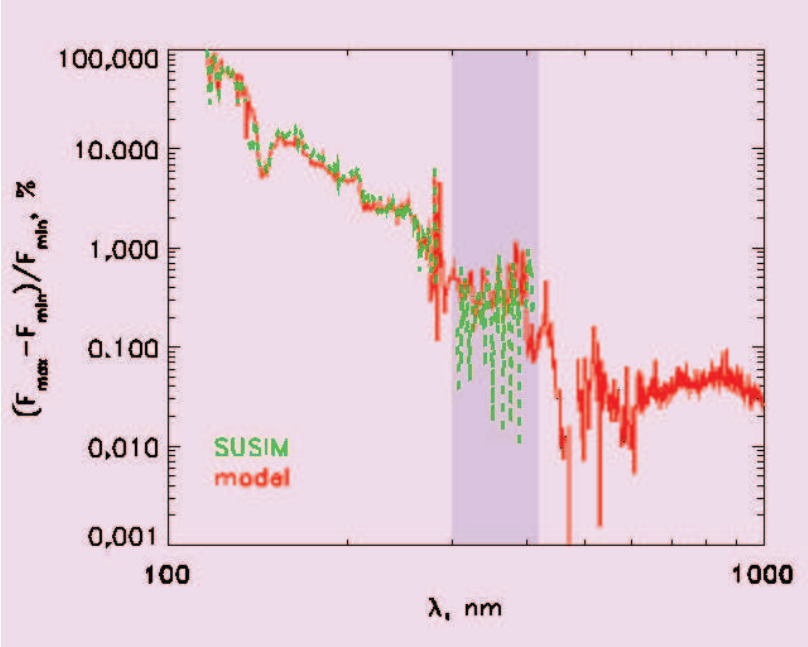

Figure 4. Relative difference between the spectral irradiance at solar activity maximum (averaged over a two month period, April-May 2000) and at solar activity minimum (October-November 1996). Plotted are the results obtained by the SUSIM instrument (dashed curve; green in the electronic version) and computed by the SATIRE model, including its empirical extension to shorter wavelengths (solid curve; red in the electronic version). Figure adapted from Krivova et al. (2006).

ing use of the good correlation between SATIRE and, e.g., SUSIM (Vanhoosier et al. 1981) data at individual wavelengths (e.g., Mg II core or the continuum around 220-240 nm), as well as the good correlation between the irradiance at different SUSIM wavelengths. Together these relationships allow us to use magnetograms to reconstruct the spectral irradiance variations down to Ly-α wavelengths (Krivova et al. 2006). In Fig. 4 we show the relative difference between the maximum and minimum of solar cycle 23 as measured by SUSIM and as computed by SATIRE (including its empirical extension to shorter wavelengths). Note the logarithmic wavelength scale. The uncertainties in the SUSIM data are larger than the relative variability at $\lambda > 300$ nm and it generally underestimates the variability there. Clearly, for the wavelengths at which SUSIM does give reliable data, both model and reconstruction agree relatively well with each other. We stress that these reconstructions were carried out with the same value of the SATIRE free parameter as used for the TSI reconstructions.

Of particular interest for the upper atmosphere of the Earth is the irradiance variability of the Ly-α line, since its radiation is absorbed by NO_x in layers above the stratosphere. Consequently, considerable work has been done to reconstruct the variations in this line. These have culminated in the composite of Ly-α variations (Woods et al. 2000) based on measurements from SOLSTICE (SOLar Stellar Irradiance Climate Experiment; Rottman et al. 1993) on the

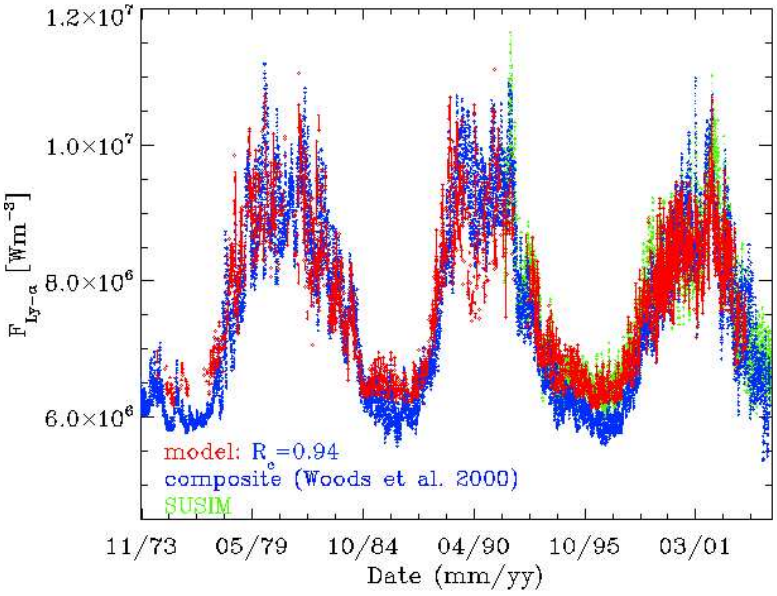

Figure 5. Composite of Ly-α irradiance (blue curve in electronic version) based on UARS/SOLSTICE and other satellite measurements, as well as proxy models, compared with the reconstruction of Ly-α irradiance reconstructed using the empirically extended SATIRE model (red curve) and the UARS/SUSIM measurements (green curve). The correlation coefficient between the synthetic SATIRE-based Ly-α irradiance and the composite is indicted. Figure kindly provided by N. A. Krivova.

UARS spacecraft, other instruments and proxy models (used to fill in the gaps and extend the time series further back in time). In Fig. 5 this composite is plotted (in blue in the electronic version). Also plotted (in green) are the SUSIM data and (in red) the SATIRE reconstruction. Once again, the same value of the free parameter was used as for the TSI reconstructions. It is noticeable that although the general agreement between the model and the composite is very good, the amplitude of the solar cycle variation is underestimated by roughly 5% by the SATIRE model. However, the agreement with the SUSIM data, which was originally used to calibrate and extend the model to shorter wavelengths is far better.

This success of modeling the variability of chromospheric irradiance bodes well for long-term reconstructions of this quantity. By combining the extended SATIRE reconstruction method with computations of the evolution of the magnetic field, it should be possible to deduce the Ly-α irradiance back to 1611, the start of telescopic observations of the Sun.

6. Evidence for Pumping between Mg II and Mn I?

W. Livingston has been regularly measuring disk integrated spectra of a series of visible lines for 3 decades (e.g., Livingston et al. 2006). A number of these

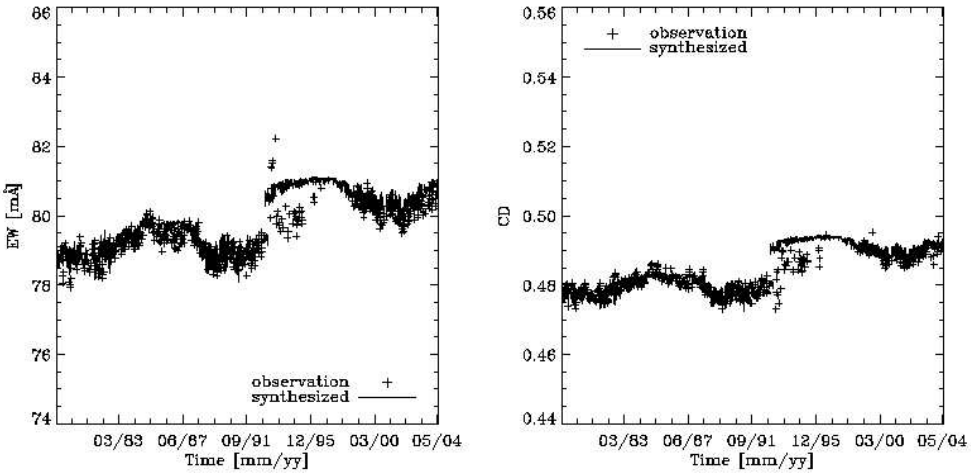

Figure 6. Equivalent width (EW, left panel) and line depth (LD, right panel) of the Mn I 5394 Å line vs. time. The crosses refer to values measured by W. Livingston, the solid curve to the synthesized EW and LD obtained from the SATIRE model. Figure adapted from Danilovic et al. (2007).

lines display a cyclic behaviour in their equivalent widths (EW), with the most prominent such behaviour being shown by the Ca II K line core. In general the photospheric lines display a strongly reduced cyclic variation. Some lines, such as Fe I 5395 Å hardly shows any variation at all. In contrast, the Mn I 5394 Å line, which is formed in the photosphere, displays a very clear cyclic signature. Its EW decreases during periods of high activity, i.e., it varies in antiphase with the sunspot number or Mg II k core-to-wing ratio. The measured Mn I EW and line depth are plotted vs. time in Fig. 6. They are represented by the crosses. Changes were made to the spectrograph in 1992, which led to an offset in the measured EW and line depth. Trials with the new instrument lasted until 1996, so that only the data prior to 1992 and after 1996 should be considered for any subsequent analysis (Livingston, private communication).

The uncharacteristically large variability of the Mn I lines at 5394 and 5432 Å led Doyle et al. (2001) to propose that these Mn I lines are very sensitive to optical pumping by the Mg II k line. An alternative explanation may be due to a particularly large temperature sensitivity of these lines. This was first pointed out by Elste (1985, 1987).

Using SATIRE it is possible to distinguish between these two alternative scenarios by carrying out computations of the Mn I 5394 Å line assuming LTE, but taking into account the influence of the evolving surface magnetic field. In Fig. 6 the synthetic Mn I EW and line depth values are represented by the solid lines. The effects of the change in instrumental parameters are taken into account in a simple way. This introduces a free parameter, which basically influences the magnitude of the offsets in these two quantities between 1992 and 1996, but does not significantly influence the amplitude of the solar cycle variation seen in the parameters of this line. Note that the free parameter of the

SATIRE model is, once more, fixed to the value given by the TSI reconstruction. The fact that the variation of the parameters of the synthetic Mn I line agrees relatively well with the measured values, although the former were computed entirely in LTE suggests that optical pumping does not play a dominant role in explaining the behaviour of this line. More details on this work can be found in Danilovic et al. (2007).

An alternative approach to tackling this question has been taken by Vitas et al. (2007). They explicitly include the pumping and compare its influence compared to other processes.

7. Does the Quiet Sun Change over the Solar Cycle at Chromospheric Layers?

An intriguing question, in particular for the understanding of the secular variation of solar irradiance, is whether the quiet Sun changes over the solar cycle. For the photosphere, after some false alarms (e.g., Kuhn et al. 1988) which have recently been defused (Woodard & Libbrecht 2003), there is no definite evidence of a strong cyclic variation of the quiet Sun. This may, however, be different in the chromosphere, where a much smaller fraction of the total solar irradiance is emitted, so that it is energetically not so challenging to produce a variation of the quiet Sun emission from these layers.

Intriguingly, Schühle et al. (2000) found that the radiance of a quiet Sun region near disk center does increase significantly from solar activity minimum towards maximum in UV lines measured by the SUMER instrument. The analysed lines are formed in the chromosphere, transition region and corona. There is also some, although somewhat less strong, evidence for a change in quiet Sun millimeter wavelength radiation (Loukitcheva 2005), which implies a change in chromospheric thermal structure.

Pauluhn and Solanki (2003) showed that the amount of magnetic flux in the quiet Sun regions studied by Schühle et al. (2000) evolves significantly with time with a good correlation between the radiance and the amount of magnetic flux. Figure 7 illustrates the correspondence between the magnetic flux and the radiance of the He I 504 Å line averaged over the considered quiet Sun regions. It seems that absolutely quiet Sun can hardly be found near the equator of the Sun at the time around activity maximum. The decaying active regions keep feeding the seemingly quiet Sun with additional magnetic flux faster than it can be transportrd away. This build up of magnetic flux in the quiet Sun is the main reason for any observed changes in radiation coming from there. Note that the large patches of unipolar field resulting from the decay of active regions decay far more slowly than the mixed polarity network maintained by the emergence of ephemeral active regions (Harvey 1993; Hagenaar et al. 2003).

In summary, changes in chromospheric radiance of the quiet Sun over cycle 23 are coupled with the evolution of the magnetic field and thus with the evolution of photospheric radiance.

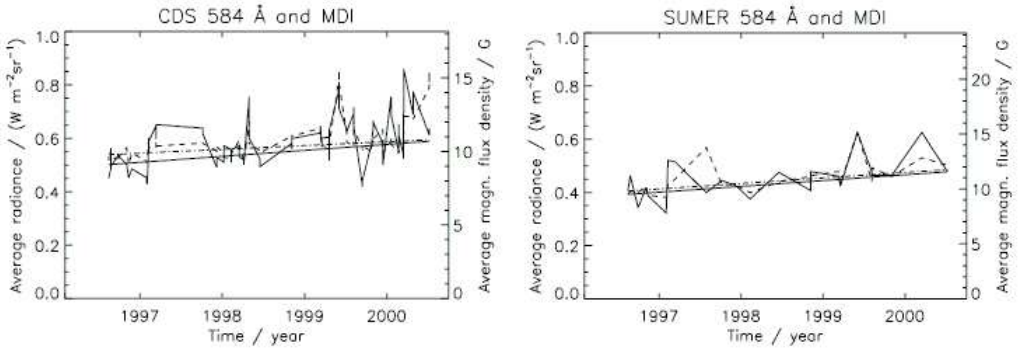

Figure 7. Time series of the spatially averaged radiances of the He I 584 Å line and corresponding MDI/SOHO magnetic fluxes. The radiances were obtained by the CDS and SUMER spectrometers on SOHO. The solid lines represent the radiance data and their linear fits, the dashed and dot-dashed lines refer to the MDI data and their corresponding fits. The plotted fits indicate an increase between 15% (MDI in CDS sampling) and 22% (SUMER) within the four years from June 1996 to June 2000. Figure taken from Pauluhn and Solanki (2003).

8. Steps towards Determining Secular Variations of Solar Chromospheric Irradiance

The question of whether there is a secular variation of chromospheric irradiance is closely related to the similar one whether total solar irradiance also shows a secular change. This is because significant secular change in the irradiance can only be due to a change in the quiet Sun contribution to it (since the active region contribution all but disappears at the time of activity minimum) and variations of the chromospheric radiance of the quiet Sun are related to photospheric variations, as argued in the previous section. Similarly, we expect secular changes in the chromospheric radiation to depend on such changes in the magnetic field, although we cannot rule out other causes as well (e.g., variations in the "basal flux" of chromospheric radiation; e.g., Schrijver et al. 1989).

Only measurements that are available over a long period of time can be used for estimating secular change of the Sun's irradiance (including the chromospheric contribution). The direct solar measurements that have so far mainly been used to consider this question are measurements of sunspot number and area. These are, on their own, insufficient to give a proper answer to this question. Indirect evidence is provided by the reconstruction of the interplanetary magnetic field (which is a good proxy of the Sun's open magnetic flux according to measurements by the Ulysses spacecraft) by Lockwood et al. (1999). The reconstruction shows that the open flux has doubled over the last century. Does this doubling imply also an increase of total magnetic flux and consequently irradiance?

The basic idea to explain this doubling of open flux makes use of the concept of overlapping solar activity cycles, which follows from the extended solar cycle postulated by Wilson et al. (1988). Such an overlap can be produced by the long lifetime (decay time) of magnetic flux. In general, it is magnetic flux having the same polarity on large spatial scales, which usually corresponds to open magnetic

flux, which has a long lifetime (Solanki et al. 2000; Solanki & Schüssler 2005). A second process that can lead to an overlap between cycles is if magnetic flux belonging to the new cycle starts appearing while there is still active region flux belonging to the old cycle present at the solar surface. Ephemeral active regions have been shown to have an emergence cycle which lasts longer and may be shifted in phase relative to the cycle of the normal active regions (Harvey 1992; 1993; Hagenaar et al. 2003). In this case, since ephemeral regions contribute very significantly to the total amount of flux emerging at the solar surface, the total magnetic flux could also show a secular change (Solanki et al. 2002; Baumann et al. 2004; Solanki & Schüssler 2005).

However, there is still considerable uncertainty regarding the magnitude of the secular variation of the total magnetic flux. Different recent estimates lie widely apart from each other.

Historical records of images made in the cores of strong chromospheric lines have the potential to help resolve some of these open questions. In particular, spectroheliograms in the cores of the Ca II K line, as have been recorded over many decades at different observatories including Kodaikanal, Mt. Wilson, Arcetri and, last but not least, Coimbra. For a more complete list see Ermolli et al. (2007).

The spectroheliograms were recorded on film which has an *a priori* unknown non-linear blackening curve and they also suffer from other artifacts. Unfortunately, these images have either no calibration information associated with them, or this information is inadequate (in particular for the older and hence more valuable images).

There are two approaches to utilizing these data: Foukal (1996) and Foukal & Milano (2001) have neglected all problems and have simply taken the images at face value. Although this approach is straightforward and simple, it is at best limited to drawing qualitative conclusions.

I. Ermolli, A. Tlatov and others have, in contrast, put great care into determining the calibration as best as possible and into removing as many of the artifacts as possible prior to carrying out any analysis of these data. The latter approach, which, in a first step, is being applied to Kodaikanal, Arcetri and Mt Wilson data, promises superior results, but is still in the process of being developed. It is clear that the Coimbra archive will play an important role in this effort, once these data are digitized. Only a careful intercomparison between images obtained at different locations can uncover all the artifacts and validate the results obtained from Ca II K spectroheliograms (e.g., by catching often undocumented changes in the instrumentation, or picking out images degraded strongly by poor seeing). See the paper by Ermolli et al. (2007) for more details. Furthermore, the so far considered data sets contain many gaps, so that the availability of a further data set is very valuable to fill these. The Coimbra dataset will thus play an important role in answering the question of the magnitude of the secular change of solar total and spectral irradiance. It will in particular also help to determine the chromospheric contribution to such change.

9. Conclusion

The cyclic and secular variation of chromospheric radiation is of considerable importance for a variety of questions related to the physics of magnetic elements, to the evolution of solar magnetism and activity, and to the variation of total and spectral solar irradiance. Radiation from the chromosphere, due to its large variability (compared to the photospheric radiation) and due to the ease of measurement (compared to transition region and coronal emission), often serves as a useful proxy of solar activity, magnetism or total solar irradiance. In many ways chromospheric radiation is superior to the generally used sunspot number or area records employed to reconstruct activity and irradiance further back in time. The availability of historical records of chromospheric radiation (basically spectroheliograms of Ca II K core intensity) reaching back to the early part of the 20th century is exciting and holds the promise to answer the fundamental question regarding the secular variation of solar activity and irradiance: how strong were these changes? The data set recorded in Coimbra will surely play an important role in such an effort.

Acknowledgments. Many people helped to make this paper become a reality. My thanks go to the organizers for their kindness and to the editors for their patience, to N. Krivova and S. Danilovic for providing figures prior to publication, and to B. Wieser, P. Daly and B. Podlipnik for technical help.

References

Baumann, I., Schmitt, D., Schüssler, M., & Solanki, S. K. 2004, A&A, 426, 1075
Carlsson, M., & Hansteen, V. 2005, in Chromospheric and Coronal Magnetic Fields, Eds. Innes, D. E., Lagg, A. & Solanki, S. K., ESA SP-596
Danilovic S., Solanki S.K., Krivova N.A., & Livingston W. 2007, in Modern Solar Facilities – Advanced Solar Science, Eds. F. Kneer et al., Universitätsverlag Göttingen, in press
Deinzer, W., Hensler, G., Schuessler, M., & Weisshaar, E. 1984a, A&A, 139, 426
Deinzer, W., Hensler, G., Schussler, M., & Weisshaar, E. 1984b, A&A, 139, 435
Deland, M. T., & Cebula, R. P. 1998, Solar Phys., 177, 105
Dewitte, S., Crommelynck, D., Mekaoui, S., & Joukoff, A. 2004, Solar Phys., 224, 209
Doyle, J. G., Jevremović, D., Short, C. I., Hauschildt, P. H., Livingston, W., & Vince, I. 2001, A&A, 369, L13
Elste, G. 1985, in Theoretical Problems in High Resolution Solar Physics, Ed. H.U. Schmidt, Max Planck Inst. f. Astrophys., 185
Elste, G. 1987, Solar Phys., 107, 47
Ermolli et al. 2007, in P. Heinzel, I. Dorotovič, R. J. Rutten (eds.), The Physics of Chromospheric Plasmas, ASP Conf. Ser. 368, 533
Fawzy, D. E., Ulmschneider, P., & Cuntz, M. 1998, A&A, 336, 1029
Fligge, M., Solanki, S. K., & Unruh, Y. C. 2000, A&A, 353, 380
Fontenla, J. 2007, in P. Heinzel, I. Dorotovič, R. J. Rutten (eds.), The Physics of Chromospheric Plasmas, ASP Conf. Ser. 368, 499
Fontenla, J., & Harder, G. 2005, Mem. Soc. Astron. It., 76, 826
Fontenla, J. M., Harder, J., Rottman, G., Woods, T. N., Lawrence, G. M., & Davis, S. 2004, ApJ Lett., 605, L85
Foukal, P. 1996, Geophys. Res. Lett., 23, 2169
Foukal, P., & Milano, L. 2001, Geophys. Res. Lett., 28, 883
Frazier, E. N. 1971, Solar Phys., 21, 42

Fröhlich, C. 2005, Mem. Soc. Astron. It., 76, 731
Haberreiter, M., Krivova, N. A., Schmutz, W., & Wenzler, T. 2005, Adv. Space Res., 35, 365
Hagenaar, H. J., Schrijver, C. J., & Title, A. M. 2003, ApJ, 584, 1107
Harder, J., Fontenla, J., White, O., Rottman, G., & Woods, T. 2005, Mem. Soc. Astron. It., 76, 735
Harvey, K. L. 1992, The Solar Cycle, in ASP Conf. Ser., Vol. 27, 335
Harvey, K. L. 1993, Ph.D. Thesis, Magnetic Dipoles on the Sun, University of Utrecht, Utrecht
Heath, D. F., & Schlesinger, B. M. 1986, J. Geophys. Res., 91, 8672
Herbold, G., Ulmschneider, P., Spruit, H. C., & Rosner, R. 1985, A&A, 145, 157
Huang, P., Musielak, Z. E., & Ulmschneider, P. 1995, A&A, 297, 579
Krivova, N. A., & Solanki, S. K. 2005, Mem. Soc. Astron. It., 76, 834
Krivova, N. A., Solanki, S. K., Fligge, M., & Unruh, Y. C. 2003, A&A, 399, L1
Krivova, N. A., Solanki, S. K., & Floyd, L. 2006, A&A, 452, 631
Kuhn, J. R., Libbrecht, K. G., & Dicke, R. H. 1988, Science, 242, 908
Livingston, W., Wallace, L., White, O. R., & Giampapa, M. S. 2006, ApJ, in press
Lockwood, M., Stamper, R., & Wild, M. N. 1999, Nature, 399, 437
Loukitcheva, M. 2005, The structure and dynamics of the solar chromosphere from observations at millimeter wavelengths, Ph.D. thesis, Saint-Petersburg University, Russia.
Mathew S., Martínez Pillet V., Solanki S.K., & Krivova N.A. 2007, A&A, in press
Mitchell, W. E., Jr., & Livingston, W. C. 1991, ApJ, 372, 336
Musielak, Z. E., & Ulmschneider, P. 2002, A&A, 386, 606
Musielak, Z. E., Rosner, R., & Ulmschneider, P. 2000, ApJ, 541, 410
Narain, U., & Ulmschneider, P. 1996, Space Sci. Rev., 75, 453
Noble, M. W., Musielak, Z. E., & Ulmschneider, P. 2003, A&A, 409, 1085
Ortiz, A., Solanki, S. K., Domingo, V., Fligge, M., & Sanahuja, B. 2002, A&A, 388, 1036
Pauluhn, A., & Solanki, S. K. 2003, A&A, 407, 359
Roberts, B. & Ulmschneider, P. 1997, European Meeting on Solar Physics, Eds. Simnett, G. M., Alissandrakis, C. E. & Vlahos, L., Lecture Notes in Physics, Vol. 489, 75
Roberts, B. & Webb, A. R. 1978, Solar Phys., 56, 5
Rottman, G. J., Woods, T. N., & Sparn, T. P. 1993, J. Geophys. Res., 98, 10667
Schrijver, C. J., Cote, J., Zwaan, C., & Saar, S. H. 1989, ApJ, 337, 964
Schühle, U., Wilhelm, K., Hollandt, J., Lemaire, P., & Pauluhn, A. 2000, A&A, 354, L71
Solanki, S. K. 1986, A&A, 168, 311
Solanki, S. K., & Stenflo, J. O. 1984, A&A, 140, 185
Solanki, S. K., & Schüssler, M. 2005, Mem. Soc. Astron. It., 76, 781
Solanki, S. K. & Unruh, Y. C. 1998, A&A, 329, 747
Solanki, S. K., Steiner, O., & Uitenbroeck, H. 1991, A&A, 250, 220
Solanki, S. K., Schüssler, & M., Fligge, M. 2000, Nature, 408, 445
Solanki, S. K., Schüssler, M., & Fligge, M. 2002, A&A, 383, 706
Steiner, O., Grossmann-Doerth, U., Schussler, M., & Knolker, M. 1996, Solar Phys., 164, 223
Tapping, K. F. 1987, J. Geophys. Res., 92, 829
Tapping, K. F., & Detracey, B. 1990, Solar Phys., 127, 321
Title, A. M., Tarbell, T. D., Topka, K. P., Ferguson, S. H., Shine, R. A., & SOUP Team 1989, ApJ, 336, 475
Topka, K. P., Tarbell, T. D., & Title, A. M. 1997, ApJ, 484, 479
Uitenbroek, H., & & Briand, C. 1995, ApJ, 447, 453
Unruh, Y. C., Solanki, S. K., & Fligge, M. 1999, A&A, 345, 635
Vanhoosier, M. E., Bartoe, J.-D. F., Brueckner, G. E., Prinz, D. K., & Cook, J. W. 1981, Solar Phys., 74, 521

Viereck, R. A., & Puga, L. C. 1999, J. Geophys. Res., 104, 9995
Viereck, R., Puga, L., McMullin, D., Judge, D., Weber, M., & Tobiska, W. K. 2001, Geophys. Res. Lett., 28, 1343
Vitas, N., Vince, I., Danilović, S., & Andriyenko, O. 2007, in P. Heinzel, I. Dorotovič, R. J. Rutten (eds.), The Physics of Chromospheric Plasmas, ASP Conf. Ser. 368, 543
Vögler, A., Shelyag, S., Schüssler, M., Cattaneo, F., Emonet, T., & Linde, T. 2005, A&A, 429, 335
Wenzler, T., Solanki, S. K., Krivova, N. A., & Fröhlich, C. 2006, A&A, 460, 583
Wilson, P. R., Altrock, R. C., Harvey, K. L., Martin, S. F., & Snodgrass, H. B. 1988, Nature, 333, 748
Willson, R. C., & Mordvinov, A. V. 2003, Geophys. Res. Lett., 30, 3
Woodard, M. F., & Libbrecht, K. G. 2003, Solar Phys., 212, 51
Woods, T. N., Tobiska, W. K., Rottman, G. J., & Worden, J. R. 2000, J. Geophys. Res., 105, 27195
Zwaan, C. 1978, Solar Phys., 60, 213

Javier Trujillo Bueno, Petr Heinzel, Július Koza

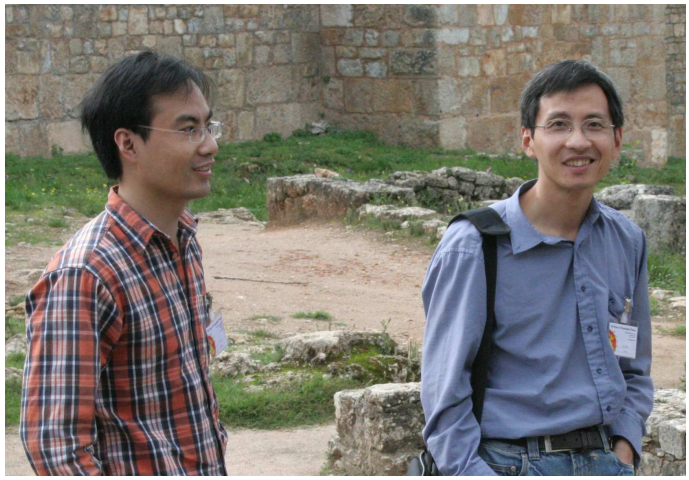

Jianping Li and Mingde Ding

The Physics of Chromospheric Plasmas
ASP Conference Series, Vol. 368, 2007
Petr Heinzel, Ivan Dorotovič and Robert J. Rutten, eds.

Chromospheric Heating and Low-Chromosphere Modeling

J. M. Fontenla[1], K. S. Balasubramaniam[2] and J. Harder[1]

[1]*LASP - University of Colorado, Boulder, USA*
[2]*National Solar Observatory, Sunspot, USA*

Abstract. Updated modeling of the "quiet" Sun low chromosphere based on existing observations show that at least all the data we examined in detail is consistent with a single model that has a very low temperature minimum and a sharp temperature increase above it. Such a model explains simultaneously the deep CO lines observed on the disk and off the limb, as well as the UV and radio continua and thus solves the controversy regarding the minimum temperature without resorting to "bifurcation". This results simply from considering both: the spatial extent of the intensity contribution functions, and non-LTE. The model also shows that the structure of the low-chromosphere cannot be unambiguously inferred from any simple diagnostic but rather needs to be examined by forward modeling with consideration of full-NLTE radiative transfer and observations at many wavelengths. In addition, the characteristics of this model are consistent with the magnetic heating of the chromosphere. The mechanism proposed consists of small scale magnetic fields and sudden triggering of their free-energy dissipation by a plasma instability starting at the base of the chromospheric plateau. As a result of such a mechanism a complex spatial structure would result in the upper chromosphere that can hardly be explained in terms of shocks but instead shows magnetic patterns.

1. Introduction

Observations of the CO lines have been discussed in the literature often and are usually explained in terms of "bifurcated" models, e.g. Ayres et al. (1986), in which at the same altitude two atmospheres exist. One of these models has a very low temperature minimum set to explain the CO line intensities, e.g. Ayres et al. (2006) and another that has a higher temperature minimum to explain the UV and radio continuum, e.g. Fontenla et al. (1993). The high temperature models have also been invoked for explaining the Ca II line wings, e.g. Avrett and Loeser (1981). However, there is no observational evidence that confirms such "bifurcated" models because even at the highest resolution the material in the low chromosphere seems to be almost homogeneous with small fluctuations in space and time, e.g. Ayres and Rabin (1996).

Here, as part of our ongoing revision of the set of one-dimensional steady state models for the solar atmosphere at medium resolution (1–2″) we discuss a new model of the low chromosphere in network cell centers. Our study finds that such a "bifurcated" model is not required by any of the existing observations and that instead a single model can explain them all. We briefly explain why the new model can explain such disparate observations and discuss a physical mechanism that could be responsible for the model structure.

Of course we do not argue that a one-dimensional model is able to explain all the observations because it is clear that the upper chromosphere has a remarkable spatial structure and dynamics (e.g. elsewhere in these proceedings).

Moreover, the chromospheric heating mechanism we propose (see Fontenla 2005) leads naturally to strongly inhomogeneous and fluctuating upper chromospheric structure very different from the much smaller fluctuations at the low chromosphere that relate to the photospheric granulation. The one-dimensional model we show here may not be a bad approximation for the low chromosphere but is just a first or initial approximation for the upper chromosphere where "realistic" 3-dimensional models with magnetic fields and consistent heating need to still be developed.

2. The Model

Figure 1 shows the new model compared with the previous FAL model C. The new model essentially coincides with the previous model up to about 500 km (where the previous model reached a minimum temperature) but the new model temperature continues to decrease above this height and reaches a much lower temperature minimum of about 3800 K (set to explain the off-limb CO observations). Unlike the old model, the new model has a very steep temperature increase above the temperature minimum height (at about 800 km above the $\tau_{5000} = 1$ layer) and reaches a very shallow temperature plateau at we designate as the chromospheric plateau. The upper chromospheric portion of the model is still somewhat undefined but we believe that it can be better defined by using UV observations (e.g. Avrett in these proceedings). Although a one-dimensional model may be somewhat crude for the chromospheric plateau it would be able to produce useful data for more sophisticated calculations.

3. Discussion

Characteristics and findings in the new model are:

1. Recent low abundances of C, N, and O are able to explain not only photospheric but also low chromospheric lines when NLTE is considered. We slightly adjusted these abundance values basing on observed lines that also include molecular species. Thus, no significant elemental separation occurs between the photosphere and the low chromosphere, and any FIP effect (if present) occurs elsewhere. Since similar values were used by Avrett (in these proceedings) for the upper chromosphere and transition region in order to match UV lines, it may very well be that there is no significant FIP effect and only that the older high abundances were not realistic.
2. Our calculations show that the controversy about the value of the temperature minimum is not justified, and that "bifurcated" models are not needed for explaining the observations. We find that a single model can explain all the observations ranging from the CO lines to the UV and radio continua. Further calculations are in progress and based on these we believe this model (perhaps with some modifications in the upper chromospheric layers) can also explain the Ca II and Mg II line wings, the Mg I lines, and probably all others.

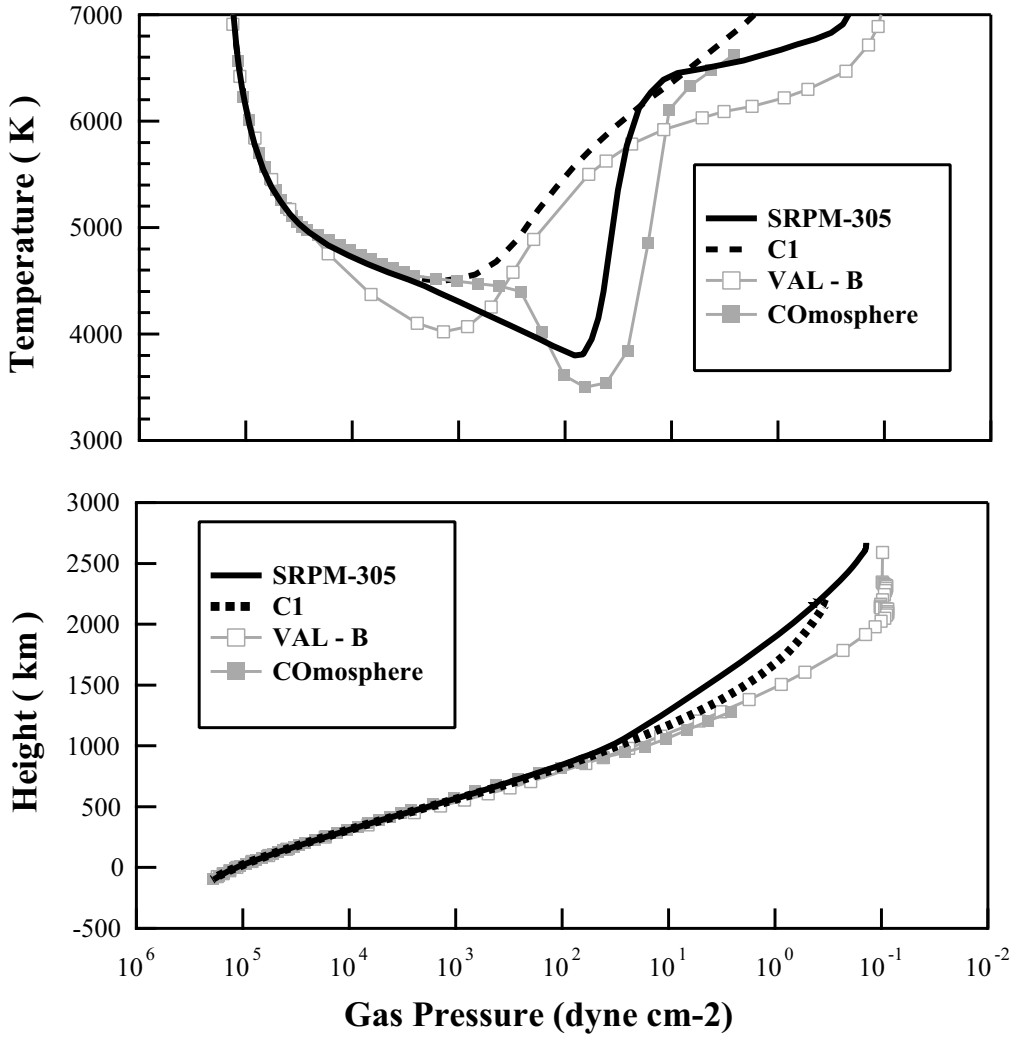

Figure 1. The new model (B305) compared with the previous FAL model C (C1), with the VAL3 model B, and with the COmosphere from Ayres et al.

3. The above occurs essentially because of the combination of two factors:

   (a) The most important factor is the finite extent of the intensity contribution function that includes layers above that of τ=1 at any given wavelength. Therefore, when the optical depth unity occurs at the $T_{\rm min}$ and a sharp temperature rise occurs above it, the higher temperature layers mask the emission from those at $T_{\rm min}$ and even in LTE the emitted radiation brightness temperature can be well above the value of $T_{\rm min}$. The situation is different in molecular lines because they are not dependent on the slowly varying electron density, but also because these species depend on the square of the hydrogen density and inversely on the temperature. Thus, molecular species quickly disappear above the $T_{\rm min}$ layer and are not affected by the chromospheric plateau.

(b) Not only is the emitted intensity at many wavelengths affected by the chromospheric plateau, but also the mean intensity at the $T_{\rm min}$ layers is larger than in LTE due to the photons originating at the base of the plateau. As a consequence of this illumination important over-ionization and NLTE effects cause the source function in many transitions to be above that of LTE at the layers around that of $T_{\rm min}$. This effect, and the previous, were minimized in the previous models because the value of $T_{\rm min}$ was higher and located at higher pressure, and because the chromospheric temperature was assumed to smoothly rise in the layers above $T_{\rm min}$. Most conclusions about the approximate validity of LTE in certain transitions at certain locations are far from general and only rested on the particulars of the models chosen. In our new model most atomic transitions are importantly affected by NLTE effects at the $T_{\rm min}$ layers.

4. A secondary issue is that in our model we change the previous scheme for parametric departures from hydrostatic equilibrium. We now discard the use of the "turbulent pressure velocity" and instead use a "non-gravitational acceleration". The parameter in our new scheme can be chosen to describe not only velocity effects that were described in the previous formulation, but also can describe the effects of Lorentz forces. Thus this new more general formulation is used to extend the pressure height-scale at and around the layers of $T_{\rm min}$ in such way as to match the observed emission in CO lines above the continuum limb. However, this issue is not essential for the simultaneous matching off the CO lines and the UV and radio continua but is only critical to models for matching the off-limb data which indicates a larger extension than that resulting from hydrostatic equilibrium. Because of the combined changes in the temperature structure and pressure stratification our new model has a pressure stratification in the chromospheric plateau that departs considerably from our previous models. Eclipse, off-limb, or space observations should be carried at several wavelengths and comparing such with models should be carried to establish better the chromospheric height scale. Stereo observations at critical wavelengths can also help in this.

4. Conclusions

Modeling must resort to all wavelengths including molecular lines in order to resolve the inherent ambiguity of interpretation of observations due to line and continua formation in the chromosphere.

One-dimensional modeling may be a reasonable approach for the lower chromospheric structure where fluctuations in space and time are not too large. However, for the upper chromosphere more sophisticated 3-dimensional models are needed and probably time-dependent as well. Such models must consider magnetic effects and magnetic heating in order to be able to explain the observed spatial structure of the upper chromosphere. While more sophisticated models are produced, one-dimensional semi-empirical ones would provide first estimates about the chromospheric structure that can help the more sophisticated ones.

The one-dimensional model presented here is just a representative one of a range of variations existing in the solar atmosphere. Such variations occur at the

medium resolution scale we consider, e.g. supergranular structure or even structure observed within a supergranule cell interior (e.g., Fontenla et al. 2007). The existence of these variations does not invalidate the one-dimensional approach as long as the radiative interaction between them is small compared with the interaction within the resolution element addressed. This approach can be called "in-pixel" modeling, and may not be completely valid in the upper chromosphere but it still is a good first approximation for estimating radiation effective parameters and the spectrum observed at medium (1–2″) angular resolution. Also, temporal variations on time-scales that are long compared with those characteristic of ionization do not significantly affect the modeling.

However, if large spatial variations occur within a resolution element then one-dimensional modeling of separate components would not be adequate because it would not consider the radiative interaction between these components. Furthermore, if very rapid strong temporal variations occurred, the chromosphere elemental ionization would not be able to reach equilibrium and would not be properly computed by an instantaneous statistical equilibrium. Because of these reasons, and the lack of observational evidence for medium-scale strong temporal or spatial variations in the CO lines, we believe the "bifurcated" models that have been proposed are not physical meaningful. However, small scale structure obviously exist, as can be seen in several papers in these proceedings, and should be modeled using more sophisticated 3D time-dependent codes that consider MHD and plasma processes.

Acknowledgments. JMF thanks the CSPM organizers for inviting him to this very good meeting. Fontenla and J. Harder work that was presented here was supported by NASA contract NAS5-97045 at the University of Colorado. K. Balasubramaniam was supported by NSO.

References

Vernazza, J.E., Avrett, E.H., & Loeser, R., 1981, ApJS 45, 635, VAL
Ayres, T.R., Testerman, L., & Brault, J.W., 1986, ApJ 304, 542
Ayres, T.R., Plymate, C., & Keller, C.U., 2006, ApJS 165, 618
Ayres, T.R., & Rabin, D., 1996, ApJ 460, 1042
Fontenla, J.M., Avrett, E.H., Loeser, R., 1993, ApJ 406, 319, FAL3
Fontenla, J.M., 2005, A&A 442, 1099
Fontenla, J.M., Curdt, W., Avrett, E.H., & Harder, J., 2007, A&A, in press

Brigitte Schmieder, Horst Balthasar, Arturo López Ariste

Rob Rutten, Sami Solanki, Boris Filippov, Brigitte Schmieder, Zadig Mouradian

The Physics of Chromospheric Plasmas
ASP Conference Series, Vol. 368, 2007
Petr Heinzel, Ivan Dorotovič and Robert J. Rutten, eds.

Automation of Meudon Synoptic Maps

Jean Aboudarham[1], Isabelle Scholl[1,2], Nicolas Fuller[1],
Morgan Fouesneau[3], Maud Galametz[3], François Gonon[3],
Antonin Maire[3] and Yann Leroy[3]

[1] *LESIA, Observatoire de Paris, Meudon, France*
[2] *International Space University, Strasbourg, France*
[3] *ENSPS, Strasbourg, France*

Abstract. Thanks to the automatic solar features detection developed in the frame of the European EGSO (European Grid of Solar Observations) project, an important part of the automation of Meudon Synoptic Maps is achieved. Nevertheless, the tracking of these solar structures over time has still to be done to synthesize their evolution during a Carrington rotation. A new approach to track filaments, based on image segmentation and intersection of regions of interest, gives successful results, This is a major step to move towards a fully automatic building of Meudon Synoptic Maps of Solar Activity.

1. Introduction

The first series of "Cartes Synoptiques de la Chromosphere Solaire" was published in 1928 by L. d'Azambuja. The strong usefulness of those maps comes from their ability to present at a glance a comprehensive view of the solar activity during one rotation. These maps were manually completed prior to 1998[1]. Data used to produce these maps are obtained from Meudon spectroheliograms, weather permitting, with gaps filled in using Coimbra observations, since both instruments are very similar. Filaments are extracted from Hα observations, faculae from Ca II K, and sunspots from Ca II K1. Prominences are obtained with Ca II K3 observations overexposed with an absorbing mask on the disk.

These solar features were copied out from solar images to synoptic maps. At a later stage, the synthesis was realized on a full Carrington rotation leading to the Meudon maps. Since 1998, the outline of solar structures was obtained using a graphics tablet, and, once the synthesis was made, the plot of the synoptic map was automatically realized. In 2003, after the person in charge of synoptic maps production retired, this activity stopped.

The only realistic way to resume this activity and therefore to continue providing the community with this powerful tool, is to fully automate this process right after the data acquisition. The first step is then to detect automatically the relevant solar features. This process is detailed in Section 2. Section 3 is devoted to remind the global functioning of these synoptic maps. In conclusion,

[1]Recent synoptic maps are available in the BASS 2000 Meudon archive (`http://bass2000.obspm.fr/home.php`), from Carrington rotation 1824 to rotation 2008 (i.e. from 1989/12/19 to 2003/09/26).

new perspectives deduced from this work are mentioned as well as the current plans to achieve the automatic production of solar synoptic maps.

2. Solar Features Detection

EGSO, the European Grid of Solar Observations, (Bentley et al. 2004)[2] is a program funded by European Community within the 5th Framework. Its goal was to build a virtual solar observatory with strong added values. In order to achieve this latter objective, a work package was fully devoted to solar feature recognition. The sizeable effort made in this field has been successful and codes have been developed that automatically detect filaments (Fuller et al. 2005), sunspots (Zharkov et al. 2004), faculae (Benkhalil et al. 2006) and prominences (Fuller & Aboudarham, 2005, private communication). For the purpose of this paper, only the filament detection is presented. This processing consists in two steps reminded hereafter: image cleaning (Zharkova et al. 2003) followed by the filament detection itself (Fuller et al. 2005).

2.1. Image cleaning

As original images may contain many defects, a cleaning process must be applied to them in order neither to detect false features nor to miss faint features. The first process consists in limb fitting to apply geometrical correction to the solar shape. It corrects the distortion due to pixels that are not exact squares. It also helps to center the sun on the image. Then, intensity normalization can be applied which consists in two steps: correction of center-to-limb darkening, and correction of sky transparency variations. As spectroheliograms are obtained by scanning the Sun, some faint clouds may darken the image obtained in some places. To avoid as much as possible errors during the detection, it is essential to be very cautious with intensity variations on the solar disk.

2.2. Filament detection

Filaments are structures characterized by their elongated shape, leading to a specific cleaning process to be applied before the detection itself. Since grains of dust may occasionally settle on the slit, those effects appear on images as very thin straight and faint lines, which have to be removed during the processing. After this extra cleaning process, the real detection may begin. First, the image is enhanced using a Laplacian filter. Then, seeds of filaments are detected thanks to a local image thresholding, followed by a region growing process. Finally, a morphological closing helps to recover fainter parts of filaments. As a result, a complete geometrical description of the filament is obtained. An exhaustive list of the detected characteristics can be seen in Aboudarham & Zharkov 2004. Figure 1 shows an example of filament detection obtained from a Meudon Hα spectroheliogram.

[2] `http://www.egso.org/`

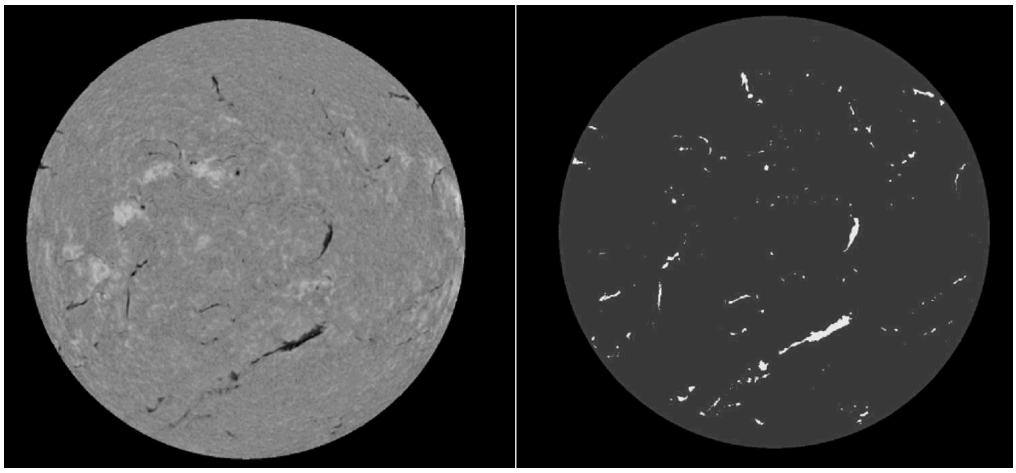

Figure 1. Example of automatic filament detection. Left image is the original Meudon Hα spectroheliogram. Right image shows detected filaments.

3. Synoptic Maps

Meudon Synoptic Maps of Solar Activity provide a powerful synthesis of the visible solar activity during one Carrington rotation. Moreover, a set of such maps gives a quick overview of its evolution over time. Looking at those maps, interesting periods can be easily detected during a rotation: for instance, maximum of activity for faculae, periods of stability or instability for filaments. Some studies based on synoptic maps are described in Mouradian 1998: examples are about detection of "pivot-points" and emerging sunspots in pre-existing plages.

3.1. Overall description

On Meudon Synoptic Maps of Solar Activity (see Fig. 2), the behavior of plages, sunspots and filaments is plotted. It is critical to notice that the actual plot does not correspond to the actual position of solar features, however it is a synthesis of its behavior. Synoptic maps represent one solar rotation plotted on a graph with latitude as ordinate and Carrington longitude, and time as abscissa. On those maps, available in the BASS2000 database[3], plages are indicated in red, sunspots in blue and filaments in green. Too scattered plages and one-day filaments are not represented. Moreover, only sunspots above 2000 km can be detected on images and therefore are the only ones that appear on synoptic maps. In an active region, plages are separated using magnetic polarity of sunspots and faculae. Active centers (i.e. sunspots and faculae) are plotted at the maximum of their evolution, corresponding to the maximum of their spotted area. Plages without any spots are plotted at the maximum of their surface whereas filaments are plotted at their maximum extension. The drawing corresponds to their mean position during the considered rotation (see Section 3.2 for details). Hachures complete the description of features on synoptic maps:

[3] `http://bass2000.obspm.fr/home.php` choose 'For the synoptic maps' in the left panel

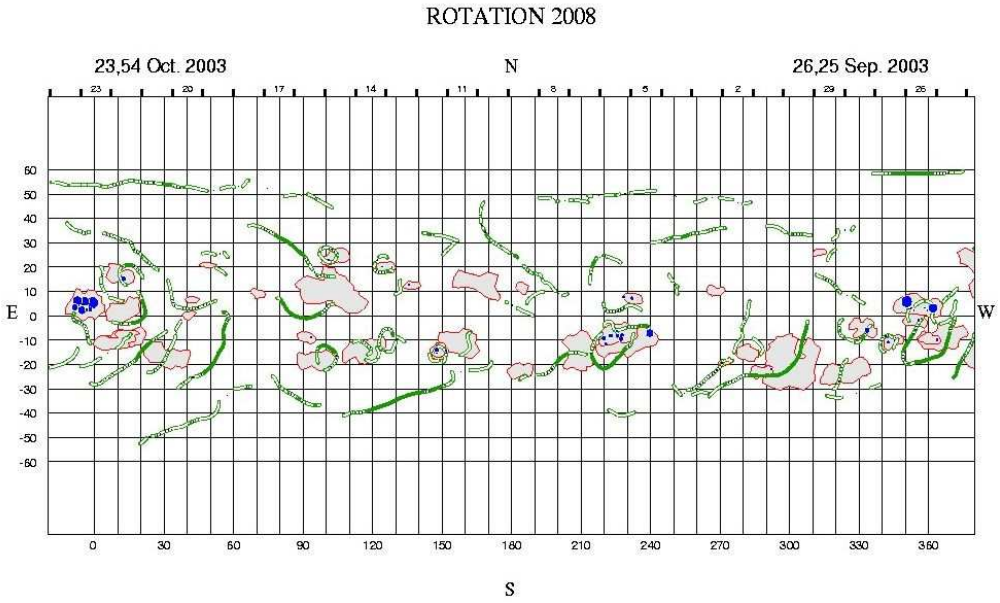

Figure 2. Example of a Meudon Synoptic Map of Solar Activity.

tight hachures for faculae indicate a very bright feature whereas it indicates stability for filaments (i.e. number of days the filament stayed at the same place). Finally, blue dots represent sunspots with a size proportional to their diameter.

3.2. Dedicated filaments map

On those maps (see the example in Fig. 3), daily tracks of filaments are plotted. The more tracks at the same position, the steadier the filament. This information leads to a synthesized filament appearing on the Synoptic Maps of Solar Activity, as described in the previous section.

4. Automation and Conclusion

The main difficulty to convert a filaments map into a Synoptic Map of Solar Activity, containing the synthesis of a Carrington rotation, comes from the tracking of filaments over time. Since their shape may change, their position may vary, sky transparency interfere, automatically keeping track of a filament during a rotation is not an obvious task. Therefore, to solve this difficulty an original approach has been adopted. Starting from the daily tracks of filaments, each group of filaments on the dedicated synoptic map is isolated using standard techniques of feature detection. Then, each group is fitted with a regression curve, giving a general behavior of the filament during one rotation. Afterwards, discretizers are defined perpendicularly to the regression curve, knowing that the number of intersections of each discretizer with a filament gives an indication of its stability. The whole process is shown in Fig. 4.

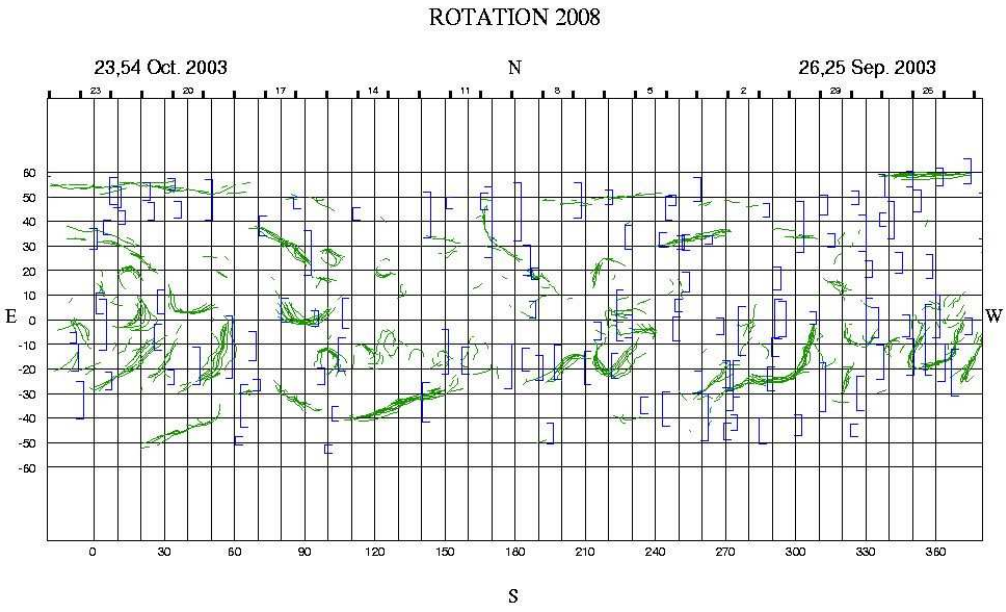

Figure 3. Example of a Meudon Synoptic Map dedicated to filaments. The blue square brackets correspond to prominences which are out of the scope of this paper.

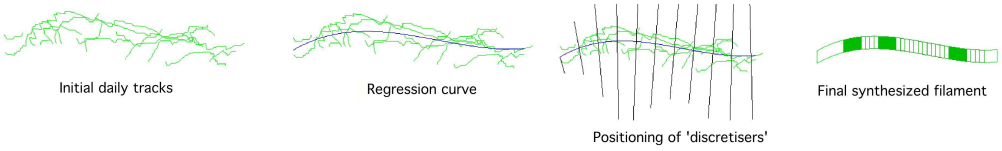

Figure 4. Four-step method for the synthesis of filament behavior.

This method has actually been tested only on a few maps to compare a full automatic plot versus a manual plot. It has still to be applied to more set of data to estimate its reliability not only for the synthesis, but also regarding the accuracy of filaments group detection. A very interesting extension of this method to complete the tracking, is the possibility to reverse the process to identify afterwards filaments on their daily plot from the group detection.

References

Aboudarham, J. and Zharkov, S., 2004, Features Parameters Description and Organization, EGSO-WP5-IR3-2.3 (`http://www.egso.org/documents/Features_ParametersV2.3.pdf`)

Benkhalil A., Zharkova V., Ipson S., Zharkov S., 2006, Solar Phys. 231, 87

Bentley R.D., Csillaghy A., Scholl I., 2004, SPIE 5493, 170

Collin, B. and Nesme-Ribes, E., 1992, in Dame, L. and Guyenne, T.-D. (eds.), Solar Physics and Astrophysics at Interferometric Resolution, 145

Fuller N., Aboudarham J., Bentley R.D., 2005, Solar Phys. 227, 61

Mouradian, Z. and Zlicaric, G., 1998, in Observatoire de Paris (eds.), Cartes Synoptiques de l'Activité Solaire, 8

Mouradian, Z. , 1998, in Balasubramaniam, K. S. and Harvey, J. and Rabin, D. (eds.), Synoptic Solar Physics, ASP Conf. Ser. 140, 197

Semel, M., Mouradian, Z., Soru-Escaut, I., Maltby, P., Rees, D., Makita, M., & Sakurai, T. 1991, Solar interior and atmosphere, University of Arizona Press, 1991, 844

Zharkov, S.I., Schetinin, V., Zharkova, V.V., 2004, 35th COSPAR Scientific Assembly, 2331

Zharkova, V. V., Ipson, S. S., Zharkov, S. I.,Benkhalil, A., Aboudarham, J., & Bentley, R. D. 2003, Solar Phys. 214, 89

The Physics of Chromospheric Plasmas
ASP Conference Series, Vol. 368, 2007
Petr Heinzel, Ivan Dorotovič and Robert J. Rutten, eds.

Regularities in the Distribution of Solar Magnetic Fields

V. Bumba[1], M. Klvaňa[1] and A. Garcia[2]

[1] *Astronomical Institute AS, Ondřejov, Czech Republic*
[2] *Observatorio Astronomico, Universidade de Coimbra, Portugal*

Abstract. We examined the distribution and concentration of the solar magnetic fields from the Wilcox observatory synoptic charts for the whole period of their existence (May 1976 – February 2006). We divided them into four latitudinal zones, studying the changes of their various structures, density, etc. These sets of maps demonstrate striking regularities in the photospheric magnetic field distribution with time, continuous existence of characteristic longitudes of magnetic field concentration and their longitudinal shift with three main rotational periods of 26.8, 28.2, and 27.14 days. They show formation of specific structures of background weaker fields, connected with the development of activity complexes, polarity alternation, etc. We mention the possible sources of found regularities in the solar activity modulation.

1. Introduction

Chromospheric activity does not only map the distribution of solar, as well as stellar magnetic fields, its most energetic events manifest processes, in which the magnetic field plays the most important role. During my several stays in Coimbra I examined hundreds of spectroheliograms (especially taken in the K line of Ca II) brought together in its plate vault. They reflect the true spreading out of the magnetic fields over the solar surface and best of all solar phenomena demonstrate the short and long-term changes and the dynamics of their development.

2. Distribution of the Magnetic Fields over the Solar Surface and its Changes with Time

If we align synoptic charts of the Stanford Wilcox Solar Observatory photospheric magnetic field into chronological series, we get successions of mainly longitudinally formed magnetic patterns, demonstrating as long-lasting, stable regularities, as well as fast changing structures.

To get better understanding of reasons how and why such magnetic field features vary, we cut individual (Carrington) synoptic charts into different latitudinal strips and only than we organized them in the chronological order. We used four main latitudinal zones: $\pm 20°, \pm(20° - 40°), \pm 40°$, and $\pm 60°$.

Due to the measuring method and lower resolution of the Wilcox Observatory, its synoptic charts represent above all the background, weaker, already more integrated magnetic fields. As yet, they present 402 Carrington rotations (Since No. 1641 in May 1976 till No. 2043 in May 2006).

The main mark of the global distribution of the equatorial $\pm 20^\circ$ background magnetic field are the characteristic patterns formed from tens of rotations lasting negative and positive polarity strips inclined in the Carrington rotation system in and slightly around the main direction represented by the rotational period of 26.8 days (Fig.1). The strips with slightly slower or faster rotational periods are the source of deviations in the statistical estimations of rotational periods for individual background magnetic field structural features. Often we observe bipolarity of the global background magnetic field distribution. The influence of the local magnetic fields with higher field intensities on these topological patterns is suppressed. Surprisingly, the general character of this longitudinal distribution of the equatorial background magnetic field polarities and concentrations does not change with the cycle phase.

Local activity develops successively in longitudinal steps: its gradual beginnings are shifted with time in longitude in such a way that they lie on an imaginary line shifting from one rotation to the next with a rotational period of 26.8 days. But the developed activity centers stay in an approximately same longitude, or their shift is substantially smaller (with the rotational periods close to 27.14 days). The life-time of such activity centers is very often longer then one year.

Consequently, the photospheric magnetic field penetrates the solar atmosphere in such a manner that it forms a complicated magneto-hydrodynamical system, not only controlling the global magnetic field distribution, but also bringing itself very fast into an equilibrium condition.

The same construction of succession of strips from Stanford magnetic maps representing the latitudinal zones between 20° and 40°, separately for both solar hemispheres, presents similar results: The magnetic field distribution in form of strips of both polarities shapes similar system of long-lasting chains or streams like in the equatorial zone. But their inclination is reversed, they rotate slower than the Carrington system, their rotational period is close to 28.2 days. The activity chains or streams start on both hemispheres in the same heliographic longitudes, although their polarity can be different.

Although succession of broader equatorial zones $\pm 40^\circ$ represents combination of both preceding successions, character of the background magnetic field structures is different. Separated polarity chains are more compact, demonstrating more often the apparent bipolarity of the global magnetic field. All three inclinations of individual polarity strips visible on the two previous successions are visible too, but they are encoded in other way in the magnetic features. Also the local stronger fields are in these broader zones more outstanding. The inclination with faster 26.8 days rotational period can be found during the whole length of succession, but there are periods during the ascension of new cycles, when they are almost lost, and the opposite direction with slower rotational period of 28.2 days is more pronounced. And again during the periods of the highest activity the chains rotating almost with the Carrington's rotation velocity (27.14 days) can be recognized.

On the succession of the whole synoptic charts (latitudinal range $+60^\circ - 60^\circ$) we can recognize periodical formation of sometimes badly recognizable large-scale features of one or of both polarities. They are expressed by accumulation in certain longitudinal interval of areas of one polarity to the disadvantage of the other polarity. During the period of their best visibility, the accumulated

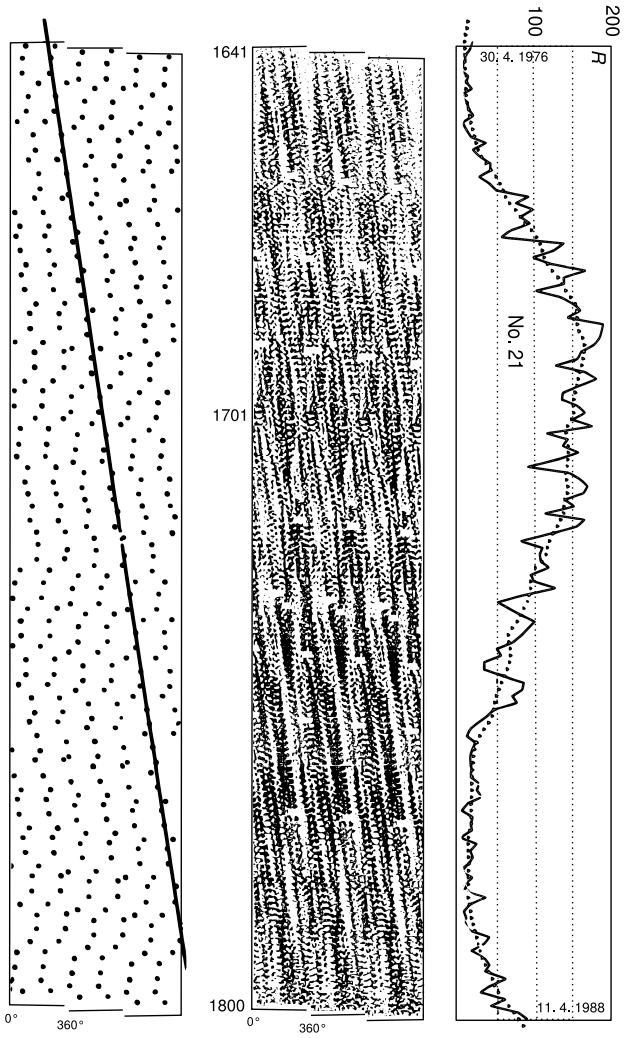

Figure 1. Comparison of the equatorial magnetic field longitudinal distribution (in the middle) with the projection of conjunctions and oppositions of the Earth and Mercury in the same Carrington system (for C. Rs. Nos. 1641–1800) (on the left; on the right monthly means of the relative number).

one polarity areas are organized into large drop-shaped figures, occupying often more than half of the solar longitudinal extent.

Mostly, each polarity has its own giant structure. They can be clearly separated in longitude, in such case the Sun is practically bipolar, but they can partly or fully overlap each other, and then it is difficult to recognize them. There are periods of time they are dominating the magnetic synoptic charts, and intervals we can hardly find them. The periodicity of described changes is close to 1.6 year.

3. Discussion and Conclusion

Already in 1968, Švestka obtained similar graphs of the distribution of proton-flares in time and on the solar surface with similar rotational periods. In 1975, Svalgaard & Wilcox published graphs of the interplanetary magnetic field polarity distribution for cycles 16 – 20. They demonstrated that the sectors of the negative polarity form long-lasting strips, existing through the whole period of time. The main strip repeats its central meridian passage with the period of 26.84 days, the second one of 27.14 days and the third one of 29 days. In the same year we compiled results of more than 10 authors studying active longitudes in various types of solar activity occurrence and constructed a summary graph of all of them (Bumba & Hejna 1991). We got the graphical distribution of as yet found active longitudes in succession of the Carrington rotations. The median values of rotational periods of two main active longitudes were: 26.84 and 27.14 days.

Recently, Stenflo and his coworkers (for example, Knaack et al., 2005, or Knaack & Stenflo, 2005), as well as other authors published values of rotational periods found by statistical investigations of various solar activity regularities. Again the values of 28.2, 26.8, and 29, eventually 25.0 – 25.5 days, are frequently registered.

How to explain the found magnetic field regularities? The regularities in the background magnetic field temporal and spacial distribution do exist. As yet, we do not see other explanation than action of some kind of a feedback between the heliosphere and the solar atmosphere and its activity. This idea is supported by our final graphs: if we draw into our series of successions of the magnetic field distribution in individual latitudinal zones the successions of dots into which the conjunctions and oppositions of planetary pairs are projected in the same Carrington longitudinal system, we see the parallelism of both systems of successions. More than that, we can follow different behavior of conjunction and opposition lines in the network of opposite polarity strips, polarity variation, etc. The periodicity of 26.8 days is connected with meetings of the Earth and Mercury (Fig. 1), periodicity of 28.2 days with meetings of Venus and Jupiter, period of 27.14 days with Mercury and Jupiter, and period of 1.6 year with meetings of the Earth and Venus.

Acknowledgments. This work could be realized by the efficient support of the grant project Czech Science Foundation (GAČR) 205/04/2129 and the Research plan AV0Z10030501.

References

Bumba V., Hejna L., 1991, Bull. Astron. Inst. Czechosl. 42, 76
Knaack R., Stenflo J. O., 2005, A&A 438, 349
Knaack R., Stenflo J. O., Berdyugina S. V., 2005, A&A 438, 1067
Svalgaard L., Wilcox J. M., 1975, Solar Phys. 41, 461
Švestka Z., 1968, Solar Phys. 4, 18

The Physics of Chromospheric Plasmas
ASP Conference Series, Vol. 368, 2007
Petr Heinzel, Ivan Dorotovič and Robert J. Rutten, eds.

Synoptic Observing at Big Bear Solar Observatory

C. Denker[1,2], M. Naqvi[1], N. Deng[1], A. Tritschler[3]
and W. H. Marquette[4]

[1]*New Jersey Institute of Technology, Newark, U.S.A.*
[2]*Astrophysikalisches Institut Potsdam, Potsdam, Germany*
[3]*National Solar Observatory, Sunspot, U.S.A.*
[4]*Helio Research, La Crescenta, U.S.A.*

Abstract. Synoptic solar observations in the chromospheric absorption lines Ca II K and Hα have a long tradition at Big Bear Solar Observatory (BBSO). The advent of the New Solar Telescope (NST) will shift the focus of BBSO's synoptic observing program toward high-resolution observations. We present an overview of the telescopes and instrumentation and show some of the most recent results. This includes Ca II K data to track solar irradiance variations, Hα full-disk data to monitor eruptive events, Dopplergrams from two-dimensional spectroscopy, as well as image restorations of diffraction-limited quality.

1. Introduction

One of the unique characteristics of BBSO is its location. The observatory is located on a small island in Big Bear Lake (Fig. 1), which is connected to the northern shore of the lake by a 300 m causeway. The lake with a surface area of 12 km^2 follows the east-west orientation of Big Bear Valley in the San Bernardino Mountains of Southern California. The observatory was established in 1969 as the result of a comprehensive site survey conducted in 1965 (Zirin and Mosher 1988) by California Institute of Technology. The survey concluded that the best seeing conditions were encountered in the proximity of lakes or close to oceans. The water acts as a heat reservoir and provides a natural temperature inversion, which effectively suppresses air turbulence and ground-layer seeing. These findings are also supported by the recent site survey (Hill et al. 2004, 2006) for the Advanced Technology Solar Telescope (ATST, Rimmele et al. 2005; Wagner et al. 2006).

Historically, BBSO has conducted synoptic observations of solar activity. The almost flat seeing profile from sunrise to sunset with a median Fried-parameter r_0 exceeding 6 cm makes this lake-site observatory ideal to monitor solar active regions for solar eruptive phenomena such as flare, filament and prominence eruptions, and signatures of Coronal Mass Ejections (CMEs). These types of events are important in the context of space science and space weather forecasting (Gallagher et al. 2002a). An early implementation of a flare prediction system was "Bearalerts" (Zirin and Marquette 1991), an electronic mail system, which reported the rapid development of certain active regions based on magnetic field topology and Hα morphology. The Active Region Monitor (ARM, Gallagher et al. 2002b) was developed at BBSO as the web-based successor of

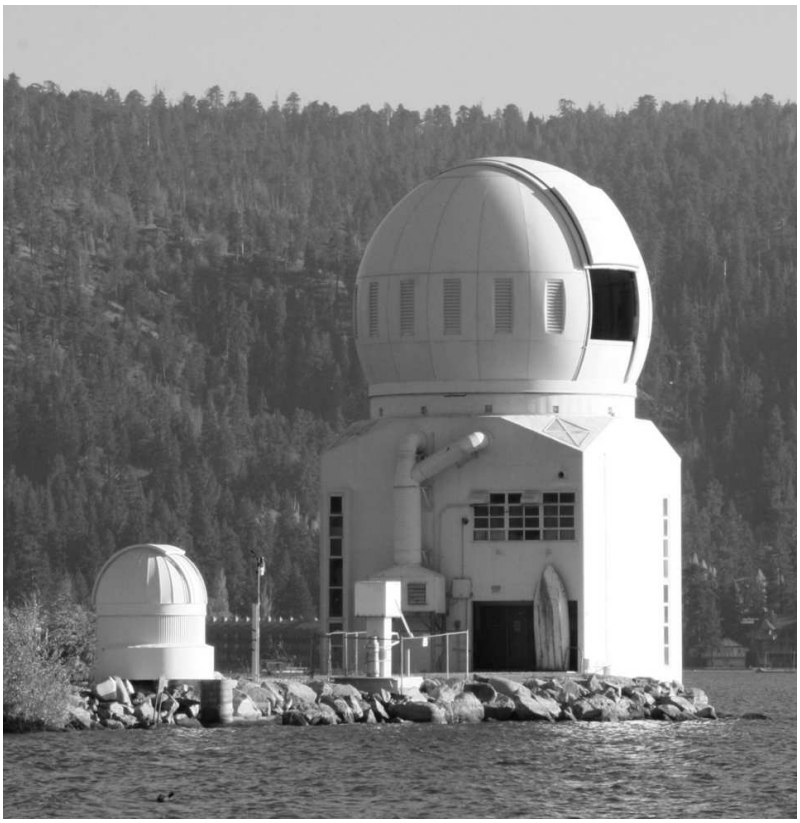

Figure 1. Big Bear Solar Observatory.

Bearalerts and is now operated independently (`http://solarmonitor.org`) at NASA Goddard Space Flight Center's Solar Data Analysis Center (SDAC).

In the following sections, we will describe the individual telescopes at BBSO and their science objectives. A cluster of telescopes (65 cm vacuum reflector, 25 cm reflector, Singer Hα full-disk telescope, photometric full-disk telescope, and Earthshine telescope) share the same equatorial mount. However, the 65 cm and 25 cm telescopes can be individually pointed. An overview of the synoptic observing and instrumentation program at BBSO was previously presented in Goode et al. (2003b).

2. Hα Full-Disk Telescope

The Hα full-disk telescope was built by Boller and Chivens under contract to Singer-General Precision in Binghamton, New York. Hence, it was called the Singer telescope. It consists of a 22 cm singlet lens, which is stopped down to 15 cm to deliver an unvignetted image of the Sun through Lyot filter manufactured by Halle in Berlin, Germany. A special coating of the singlet lens restricts the transmitted sunlight to a 30 nm spectral window centered at Hα. A narrow-band interference filter selects the correct order of the Lyot filter, which has a bandpass of 0.05 nm. The birefringent filter can be manually tuned to

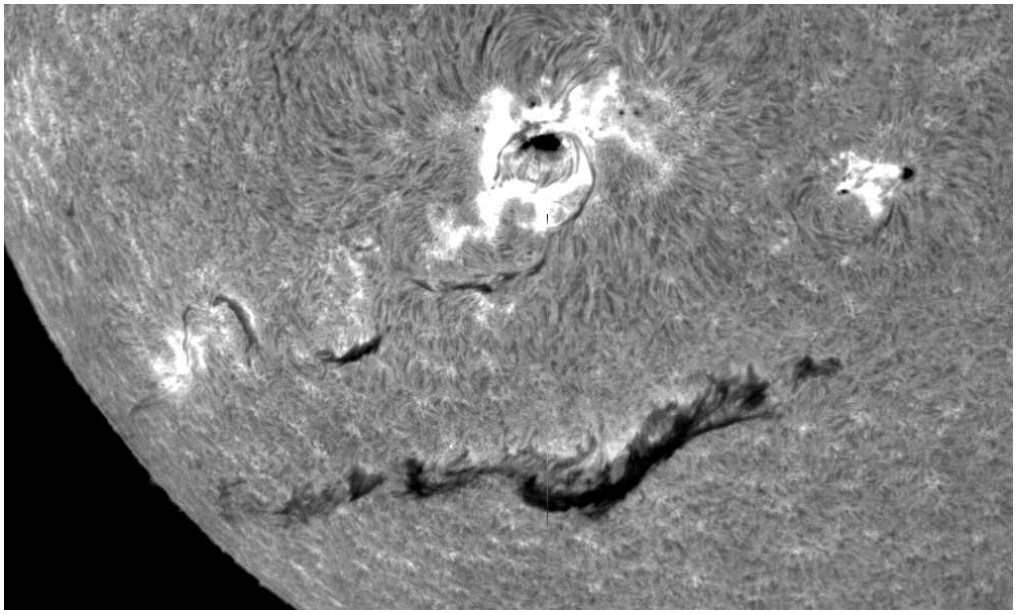

Figure 2. Partial view of an Hα full-disk filtergram showing a filament eruption on June 11, 2003.

Hα $\pm$ 0.1 nm so that Hα line wing images can be taken in dedicated observing runs (e.g., Moreton waves). A weak field lens in front of the Lyot filter and a re-imaging lens after the filter provide an 18 mm solar full-disk image at the final focus.

Digital data was taken with this system since 1996. First with a Kodak 4.2 CCD camera and later with an Apogee KX4 CCD camera. However, the detector characteristics are very similar. In both cases, the images have 2k $\times$ 2k pixel and the imaging cadence is typically one minute. Considering the good and stable seeing conditions at BBSO, the full-disk images usually have a spatial resolution close to the nominal 2″ (see Fig. 2). All data are carefully calibrated and a limb-darkening function is computed to provide contrast-enhanced full-disk images (Denker et al. 1998). The data processing has been standardized for all BBSO full-disk images. Sample images and movies are posted on a daily basis on the world wide web (`http://www.bbso.njit.edu`).

A detailed description of the Singer Hα full-disk telescope and the data processing is given in (Denker et al. 1998). The Singer telescope is also part of the Global Hα Network (GHN, Steinegger et al. 2000), which is a collaboration between BBSO, Observatoire de Paris in France, Kanzelhöhe Solar Observatory in Austria, Catania Astrophysical Observatory in Italy, Yunnan Astronomical Observatory in China, and Huairou Solar Observatory in China.

3. Photometric Full-Disk Telescope

The photometric full-disk telescope is a simple refractor with an aperture of 12.5 cm diameter (stopped down to 6.5 cm). Full-disk images in Ca II K line at

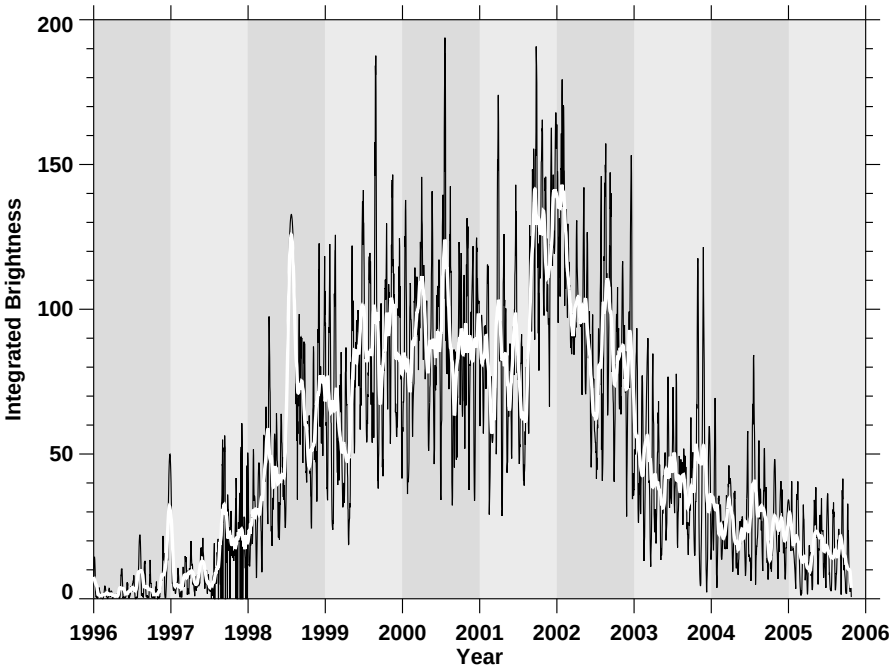

Figure 3. Ca II K brightness index for solar cycle No. 23.

393.3 nm and green continuum at 520 nm are taken once a day. Occasionally, G-band full-disk images are taken as well. A Daystar filter restricts the bandpass of the Ca II K line images to 0.15 nm. Ca II K full-disk filtergrams were observed at BBSO since 1981. Digital data acquisition started in 1996. A blue-sensitive, Lumigen coated Kodak 1.4i MegaPlus CCD camera record 1k × 1k pixel filtergrams.

Based on these filtergrams, daily indices are computed (Johannesson et al. 1995, 1998) to track the solar irradiance variability, which can be attributed to bright magnetic features (Lean et al. 1998). In Fig. 3, we show one of these brightness indices covering solar cycle No. 23 from 1996 until the end of 2005. Ca II K observations allow us to monitor ultraviolet irradiance variability of the Sun (Warren et al. 1996) and can reproduce other irradiance indices (e.g., Ly-α), which would otherwise only be accessible from space (Johannesson et al. 1995, 1998). Since the data coverage is more than 25 years, the BBSO Ca II K data presents a valuable reference point for ground- and space-based observations of solar irradiance variability. Since a continuation of this program beyond 2006 seems unlikely, we are currently preparing a summary of the observations and a description of the data products, which will be published in a forthcoming paper (Naqvi et al. 2007).

4. Digital Vector Magnetograph

The main instrument on the 25 cm refractor is the Digital Vector Magnetograph (DVMG, Spirock et al. 2001). In addition, a computer controlled mirror system can direct the light to two side benches with Lyot filters, which typically observed

the Sun in the chromospheric absorption lines Hα and Ca II K. All camera system have a field-of-view (FOV) of about $300'' \times 300''$ and 512×512 pixel. The cadence for active region observations is typically one minute.

First attempts to convert the now obsolete video magnetograph system (Varsik 1995) to a digital system were described in Wang et al. (1998). This also includes a discussion of image selection, alignment and restoration, and other techniques to improve the sensitivity and spatial resolution of magnetograms. The current system uses a combination of ferro-electric crystal and nematic liquid crystals to obtain vector magnetograms in the Ca I line at 610.3 nm. The DVMG is a filter-based magnetograph using a Lyot filter with a bandpass of 0.025 nm. Images in different polarization states are accumulated at a rate of 30 Hz with a 12-bit Dalsa 1M15 CCD camera to minimize seeing-induced cross-talk. Typically, 100 are integrated for longitudinal magnetograms of active regions. This number increases to 1000 for quiet Sun observations or measurements of transverse fields.

5. High-Resolution Observations

High-resolution observations, in particular two-dimensional imaging spectro-polarimetry, are the domain of ground-based solar observatories. This holds even more true in an era with 0.5-meter telescopes flying in space such as Hinode (Shimizu et al. 2004) and the next generation of synoptic space missions preparing for launch such as the Solar Dynamics Observatory.

Adaptive optics (AO) is a necessity to achieve a spatial resolution close to the diffraction limit of today's meter-class solar telescopes. Future large-aperture solar telescope would not even be possible without AO. The high-order AO system at the 65 cm reflector was developed by the National Solar Observatory (Rimmele et al. 2004) in collaboration with BBSO. Most of the hardware is identical to the twin system at the Dunn Solar Telescope in New Mexico. Only the optical design differs taking into account the equatorial mount of the Gregorian reflector and space limitations at BBSO (Didkovsky et al. 2003; Ren et al. 2003). A performance evaluation of the BBSO AO system is presented in Denker et al. (2007).

Even with AO correction, some high-order aberrations remain, which can be compensated with post-facto image restoration (e.g., Denker et al. 2005). In Denker et al. (2001), we have shown that speckle masking imaging in combination with distributed computing is capable to deliver restored images on time-scales comparable to the evolution time-scale on the Sun (about one minute). Furthermore, the image restoration techniques can be applied to two-dimensional spectro-polarimetry. Considering this fact and the superior photon efficiency, Fabry-Pérot based spectro-polarimeters are the first choice for modern solar telescopes. Two imaging spectro-polarimeters, one for the visible and one for the near infrared, have been developed at BBSO (Denker et al. 2003a,b). First science data have been obtained (see Fig. 4) and are currently being prepared for publication. The FOV of the instruments is about $80'' \times 80''$, which is sufficiently large to cover a sunspot. The spectral resolution is better than 0.01 nm and a typical wavelength scan takes about 20 s. These imaging instruments are ideally suited for solar activity studies.

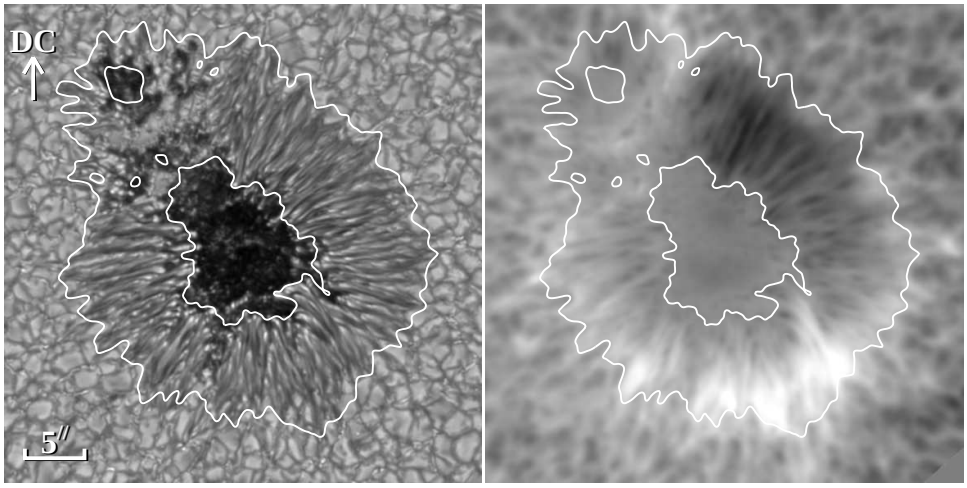

Figure 4. Image restoration using the speckle masking technique and corresponding Dopplergram obtained with two-dimensional spectroscopy. The white contour lines indicate the penumbra boundaries and the white arrow points toward disk center (DC).

6. New Solar Telescope

The New Solar Telescope (NST) project is a collaboration among BBSO, the Korean Astronomical Observatory (KAO) and Institute for Astronomy (IfA) at the University of Hawai'i (Goode et al. 2003a; Denker et al. 2006). The current telescope cluster will be replaced by a 1.6-meter aperture, off-axis Gregorian telescope with an open design. The telescope is currently under construction and all major contracts have been placed. A new 5/8-sphere dome has already been installed to accommodate the larger NST. The old telescopes will be removed in early 2007 and the telescope pier will be modified in preparation for the installation of NST in August 2007. Full operation is expected in 2008.

7. Conclusions

The operation of NST significantly shifts the focus of BBSO's synoptic observing program. At the moment, there is no funding to replace the capabilities of the full-disk telescopes and the 25 cm refractor, which provided context information with moderate spatial resolution. Some of these capabilities exist at other observatories or on space missions such as the Solar and Heliospheric Observatory, Hinode, and the Solar Dynamics Observatory. Therefore, synoptic high-resolution observations and Earthshine observations (Pallé et al. 2004) will take precedence in the future. All high-resolution instruments described in the previous section can be adapted to fit NST. AO-corrected, two-dimensional spectropolarimetry in the visible and near infrared wavelength regions will become the main data source for solar activity and space weather studies at BBSO. These data will be complemented by high-resolution imaging using image restoration techiques such as speckle masking imaging.

Acknowledgments. This work was supported by NSF under grants ATM 00-86999, ATM 02-36945, IIS ITR 03-24816, and AST MRI 00-79482 and by NASA under grant NAG 5-12782.

References

Denker, C., Tritschler, A., Rimmele, T. R., and 3 co-authors, 2007, PASP, submitted
Denker, C., Goode, P. R., Ren, D., and 17 co-authors, 2006, Proc. SPIE 6267, 62670A
Denker, C., Mascarinas, D., Xu, Y., and 5 co-authors, 2005, Solar Phys. 227, 217
Denker, C., Didkovsky, L., Ma, J., and 5 co-authors, 2003a, Astron. Nachr./Astron. Not. 324, 332
Denker, C., Ma, J., Wang, H., and 4 co-authors, 2003b, Proc. SPIE 4853, 223
Denker, C., Yang, G., Wang, H., 2001, Solar Phys. 202, 63
Denker, C., Johannesson, A., Marquette, W. H., and 3 co-authors, 1998, Solar Phys. 184, 87
Didkovsky, L. V., Dolgushyn, A., Marquette, W. H., and 10 co-authors, 2003, Proc. SPIE 4853, 630
Gallagher, P. T., Denker, C., Yurchyshyn, V., and 4 co-authors, 2002a, Ann. Geophys. 20, 1105
Gallagher, P. T., Moon, Y.-J., Wang, H., 2002b, Solar Phys. 209, 171
Goode, P. R., Denker, C., Didkovsky, L. I., and 2 co-authors, 2003a, J. Korean Astron. Soc. 36, 125
Goode, P. R., Denker, C., Wang, H., 2003b, Astrophys. Space Sci. Lib. 288, 137
Hill, F., Beckers, J., Brandt, P., and 18 co-authors, 2006, Proc. SPIE 6267, 62671T
Hill, F., Beckers, J., Brandt, P., and 17 co-authors, 2004, Proc. SPIE 5489, 625
Johannesson, A., Marquette, W. H., Zirin, H., 1998, Solar Phys. 177, 265
Johannesson, A., Marquette, W. H., Zirin, H., 1995, Solar Phys. 161, 201
Lean, J., Cook, J., Marquette, W. H., Johannesson, A., 1998. ApJ 492, 390
Naqvi, M. H., Denker, C., Marquette, W. H., Tritschler, A., 2007, Solar Phys. , in preparation
Pallé, E., Goode, P. R., Montañés-Rodríguez, P., Koonin, S. E., 2004 Science 304, 1299
Ren, D., Hegwer, S. L., Rimmele, T. R., and 2 co-authors, 2003, Proc. SPIE 4853, 630
Rimmele, T. R., Keil, S. L., Wagner, J., and 8 co-authors, 2005, Proc. SPIE 5901, 41
Rimmele, T. R., Richards, K., Hegwer, S., and 10 co-authors, 2004, Proc. SPIE 5171, 179
Shimizu, T., 2004, ASP Conf. Ser. 325, 3
Spirock, T., Denker, C., Chen, H., and 6 co-authors, 2001, ASP Conf. Proc. 236, 65
Steinegger, M., Denker, C., Goode, P. R., and 9 co-authors, 2000, ESA Conf. Proc. SP-463, 617
Varsik, J. R., 1995, Solar Phys. 161, 207
Wagner, J., Rimmele, T. R., Keil, S. L., and 12 co-authors, 2006, Proc. SPIE 6267, 626709
Wang, H., Denker, C., Spirock, T., and 7 co-authors, 1998, Solar Phys. 183, 1
Warren, H. P., Mariska, J. T., Lean, J., and 2 co-authors, 1996, Geophys. Res. Lett. 23, 2207
Zirin, H., Marquette, W. H., 1991, Solar Phys. 131, 149
Zirin, H., Mosher, J., 1988, Solar Phys. 115, 77

Conference dinner in the Palácio São Marcos

Daniel Myachin, Pavel Kotrč, Larisa Kashapova, Boris Filippov

The Physics of Chromospheric Plasmas
ASP Conference Series, Vol. 368, 2007
Petr Heinzel, Ivan Dorotovič and Robert J. Rutten, eds.

COSIS: Coimbra Observatory Solar Information System

Ivan Dorotovič[1,2,3], João Fernandes[1], José M. Fonseca[2], André Mora[2], Carlos Moreira[2] and Rita A. Ribeiro[2]

[1] *Observatório Astronómico, Coimbra, Portugal*
[2] *UNINOVA, Caparica, Portugal*
[3] *Slovak Central Observatory, Hurbanovo, Slovak Republic*

Abstract. Since 1926 full-disk spectroheliograms have been routinely taken in Coimbra Observatory in the Ca II K line (K_1 and K_3) and in 1990 regular observations in the Hα line have also started. These observations are preformed by a spectroheliograph, a twin of the spectroheliograph operated at the Observatoire de Meudon. In 2002 we started to digitalize our collection of more than 30 000 solar images. In 2005 we started the project COSIS (Coimbra Observatory: Solar Information System). The purpose of COSIS[1] is to develop a software tool for automatic image processing and feature recognition of sunspots (K_1), chromospheric plages (K_3), and filaments (Hα) for usage by astronomers and other interested parties. At this stage of the project only automatic image processing of sunspot is being performed and the first results are presented in this contribution. However, we intend in the future to extend the automatic feature recognition process to chromospheric spectroheliograms (K_3 and Hα) as well.

1. Historical Background

Since 1926 full-disk spectroheliograms have been routinely taken in Coimbra Observatory in the Ca II K line (K_1 and K_3). In 1990 started regular observations in the Hα line. In 2002 began the digitalization (backwards) of our collection of more than 30 000 solar images and also the collaboration of A. Garcia with M. Klvaňa (Ondřejov) to install a CCD camera as the recording device. In 2005 began project COSIS (the Coimbra Observatory Solar Information System). In 2007 regular observations with the video spectroheliograph of the OAUC in Coimbra will begin.

2. Objectives

The main objectives of the project are: *(i)* to develop a software tool for automatic image processing and feature recognition of sunspots (Ca II K_1), chromospheric plages (Ca II K_3), and filaments (Hα) for usage by astronomers and other interested parties; *(ii)* to process the huge amount of existing images to enable studies of the temporal evolution of solar activity, and *(iii)* to compare

[1]Financed by FCT, MCTES, Lisbon, Portugal: POCTI-CTE-AST/58333/2004

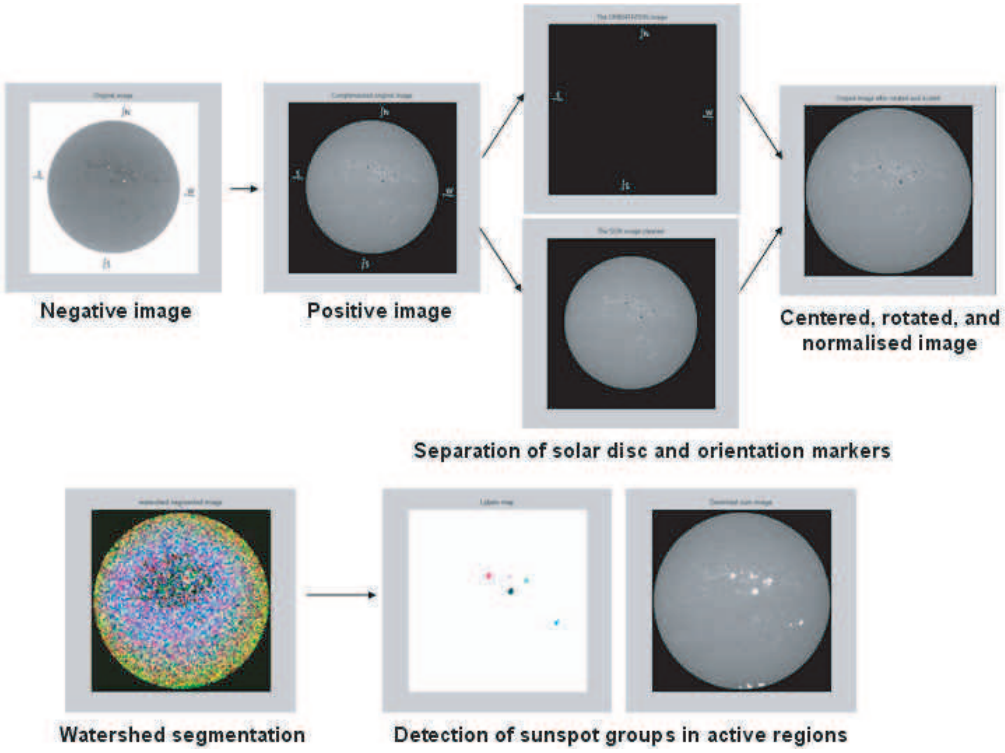

Figure 1. An example of detection and area estimation.

criteria for feature recognition with other standards (possibly also the creation of a special standard).

The overall expected result for this project is to create a data center at the Coimbra Astronomical Observatory for the storage and manipulation of solar data extracted from the rich heritage of existing images.

The COSIS prototype to be developed integrates the following key computing technologies:

- decision-support oriented database;
- image/feature recognition techniques.

3. Automatic Detection of Active Regions and Individual Features in Solar Images

3.1. Example of detection and area estimation

At this stage of the project (up to December 2006) only automatic image processing of sunspots is being performed (Fig. 1).

3.2. Watershed-based color image segmentation

Image segmentation is an essential process for most sub-sequent image analysis tasks. Watershed transform is built by implementing a flooding process on the solar gray-tone image that identifies the most active areas on the solar image and

delimits the area that is related with each sunspot. Because this segmentation process often produces significant over segmentation we developed a merging algorithm that combines compatible areas in the watershed segmented image reducing the number of false splitting borders. The selection of the areas found on the segmented image is done based on a set of rules that weight different factors such as area, gray level and form factor in order to find only the relevant spots and discard all the non-significant areas found by the watershed process.

The software is divided in three steps. The first step consists of a pre-processing analysis of the images in order to create a standard orientation and dimension of the solar images, to achive a centered, rotated, and normalised image. The second step starts with a standard solar image and creates an image with the sunspots highlighted on it. The third step consists on counting and maping all the detected sunspots. After the solar image normalization the next step is the sunspots detection. The software detects individual sunspots (not sunspot groups) and total area of umbra and penumbra (U+P) is estimated. The watershed transform divides the solar image into small areas. These areas receive a label depending on its grey level, meaning that the darkest areas are possible sunspots. The areas are labelled from 1 to a maximum of areas defined (the area with the darkest grey level is labelled with 1). For each identified sunspot its position, area in pixels and in MSH (millionths of the solar hemisphere) is determined and available at the webpage. The area (in pixels) is multiplied by mean greyscale intensity of corresponding watershed label. This resulting value is used in further tresholding process. The darkest and considerably large areas are set to 1 (black), identifying a possible sunspot. The area in MSH is corrected for foreshortening (sphere-to-plane projection). We decided to omit the spots of corrected sunspot area being smaller than 6 MSH to avoid the possible consideration of large pores as tiny spots.

3.3. COSIS dialog page

The COSIS interface (Fig. 2) is available at `http://cosis.uninova.pt`. In this page one can choose particular observation for certain limits of date and hour (initial/end date or hour), sunspots number, position, area of sunspots. The second level page (resulting page) shows then available observational material for the selected criteria such as number of results (how many images fulfill the criteria), date of the photo, time of the photo, number of sunspots in photo. Clicking on "Click here for image details" it will open the 3rd level page with processed images including also information on group number, X/Y position, area (MSH), area (pixels). The resulting images for the specific date of 2 June, 1981 are shown in Fig. 3.

Besides the sunspots features a file containing information on solar image (name, format, date and hour of the image) is generated as well.

The project team also started cooperation with the Virtual Observatory Alliance (`http://www.ivoa.net`) and the Sunspot Index Data Center (SIDC) – Solar Weather Browser project at the Royal Observatory of Belgium (`http://sidc.oma.be/`). This site already includes some images from the Coimbra archive.

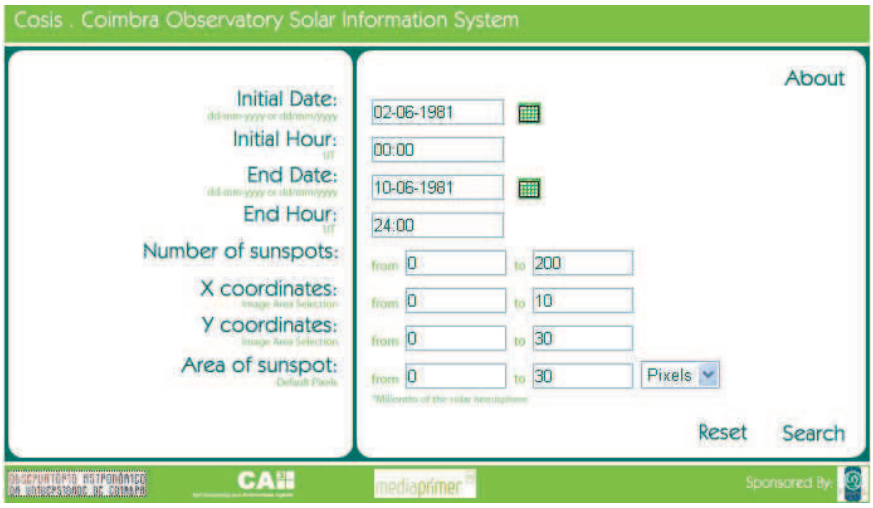

Figure 2. Interface of the COSIS webpage.

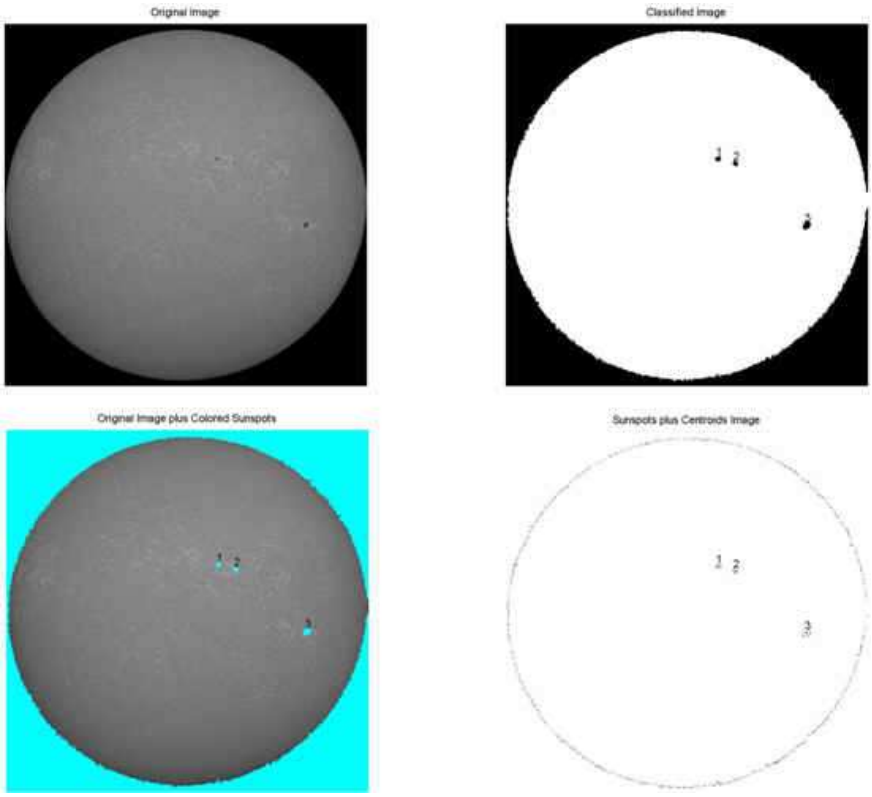

Figure 3. Four types of images are presented for each selected observational day in the image details. *Upper left:* Original spectroheliogram. *Lower left:* Recognized sunspots – original image plus colored sunspots. *Upper right:* Classified image – sunspots. *Lower right:* Sunspots and centroids image: 2 June, 1981.

The Physics of Chromospheric Plasmas
ASP Conference Series, Vol. 368, 2007
Petr Heinzel, Ivan Dorotovič and Robert J. Rutten, eds.

North-South Asymmetry of Ca II K Plages

Ivan Dorotovič[1,2,3], Patrice Journoud[1,4], Ján Rybák[5]
and Július Sýkora[5]

[1] *Observatório Astronómico (GAUC, FCTUC), Coimbra, Portugal*
[2] *UNINOVA, Caparica, Portugal*
[3] *Slovak Central Observatory, Hurbanovo, Slovak Republic*
[4] *Observatoire de Paris, Meudon, France*
[5] *Astronomical Institute, SAS, Tatranská Lomnica, Slovak Republic*

Abstract. The level and evolution of solar activity is not identical in the northern and southern Sun's hemispheres. This fact was repeatedly confirmed in the past by analysis of a number of long-term observations of various solar activity indices. Presently, it seems that the north-south (N−S) asymmetry represents quite specific, independent and very promising tool to advance in analysis of the long-term solar activity variations. This paper is focused to give a software tool for estimation of the N−S asymmetry in the area of bright chromospheric plages, as measured on the Ca II K_3 spectroheliograms registered since 1926 in the Observatório Astronómico da Universidade de Coimbra, Portugal. In fact, studies of the N−S asymmetry of just this phenomenon are rare, namely due to absence of technique allowing reliable quantitative estimations of the Ca II K_3 plages parameters. Our algorithm is also partially limited, it provides the area of bright Ca II K_3 emission structures, but it does not perceive differences in the brightness of individual chromospheric features. As for the N−S asymmetry of the chromospheric plages alone, we present here a sample of its estimation only. Its behavior during the first half of 2000 year is provided to illustrate application of the software developed. A comparison and cross-correlation with the N−S asymmetries found for the sunspots and corona green line brightness is added. We intend to discuss the results of more extensive analysis of the chromospheric plages N−S asymmetry as soon as a sufficiently long time series of the Ca II K_3 Coimbra spectroheliograms will be digitized and processed.

1. Introduction

Non-identity in the level and time variations of solar activity on the northern and southern Sun's hemispheres has been revealed by analysis of a number of solar indices characterizing different long-term aspects of solar activity. Numerous properties of the north-south (N−S) asymmetry have been revealed during the last several decades. For example, Temmer et al. (2002, 2006) have investigated the significance of the N−S asymmetry, together with the differences in rotation separately at the both solar hemispheres, based on the hemispheric sunspot numbers (Kanzelhöhe Solar Observatory, Austria, and Skalnaté Pleso Observatory, Slovakia − KSO/SPO). Badalyan et al. (2005, 2006) estimated and discussed a number of features in the mutual correlativness of the N−S asymmetry of different indices (coronal green line brightness − CGLB, total sunspot area, total sunspot number) characterizing solar activity at various lev-

els of the solar atmosphere. Badalyan et al. (2003, 2006) revealed and examined convincing quasi-biennial oscillations in the N−S asymmetries of four studied solar activity indices.

A software tool to estimate the N−S asymmetry of the area of bright chromospheric features (ABCHF), as derived from the Ca II K_3 spectroheliograms taken in the Observatório Astronómico da Universidade de Coimbra (OUAC), Portugal (henceforth called AKFEAT tool: N−S Asymmetry Index of the Area of Ca II K Emission FEATures), is presented in this paper. Similar technique of solar feature identification have been developed, e.g., by Worden et al. (1998), and Preminger et al. (2001).

2. Data and Method of Processing

Digitalized spectroheliograms obtained in the Ca II K_3 spectral line at the OAUC (`http://www.mat.uc.pt/~obsv/obsv/solar.html`) were used as an input data to investigate the ABCHF N−S asymmetry. These spectroheliograms were continuosly recorded in the OAUC since 1926. Now, the photographic films with spectroheliograms are being digitalized backwards starting from the year 2000 (maximum phase of the cycle 23) and at this moment (September 2006) the last twenty years are already completed.

We have developed the software tool to determine automatically the AKFEAT of the ABCHF from the spectroheliograms. The software starts with determination of the quiet-Sun center-to-limb variation (CLV) using a method presented by Brandt and Steinegger (1998). Their method makes possible reliable day-to-day comparison of the spectroheliograms obtained under different weather conditions (sky transparency) and, therefore, using different exposure times. Similarly to the cited authors, we divided the solar disk into 20 rings centered to the solar disk center and covering the same area. In each ring the "quiet Sun" intensity was calculated. The set of the quiet Sun intensities creates then the center-to-limb darkening profile. The algorithm continues further by calculation of the ABCHF as a sum of pixels area above the corresponding local quiet-Sun intensity separately in individual rings. The total ABCHF is a sum of subtotal area values from all rings. Finally, the algorithm estimates the real area of bright chromospheric features, i.e., it transforms the area from the plane back to the sphere. The interface of the AKFEAT tool for estimation of the ABCHF is illustrated in Fig. 1.

Recently, Ballester et al. (2005) pointed out that the normalization that is commonly used when calculating the N−S asymmetry index could give misleading results for a periodical analysis. Therefore, we have accepted their proposal and now define the north-south asymmetry A of the ABCHF simply as $A = N\text{-}S$, where N and S are the ABCHF determined for the northern and southern hemispheres, correspondingly (as percentage of the area of the pertinent hemisphere).

To compare the N−S asymmetry of the Ca II plages with the same phenomenon of some other solar indices the "Catalogue of the hemispheric sunspot numbers (1945-2004)" of Temmer et al. (2006), the SIDC data on sunspots (Brussels) and our own "Database of the Coronal Green Line Brightness (1939-2001)" (Sýkora and Rybák 2005, and references therein) have been used. An

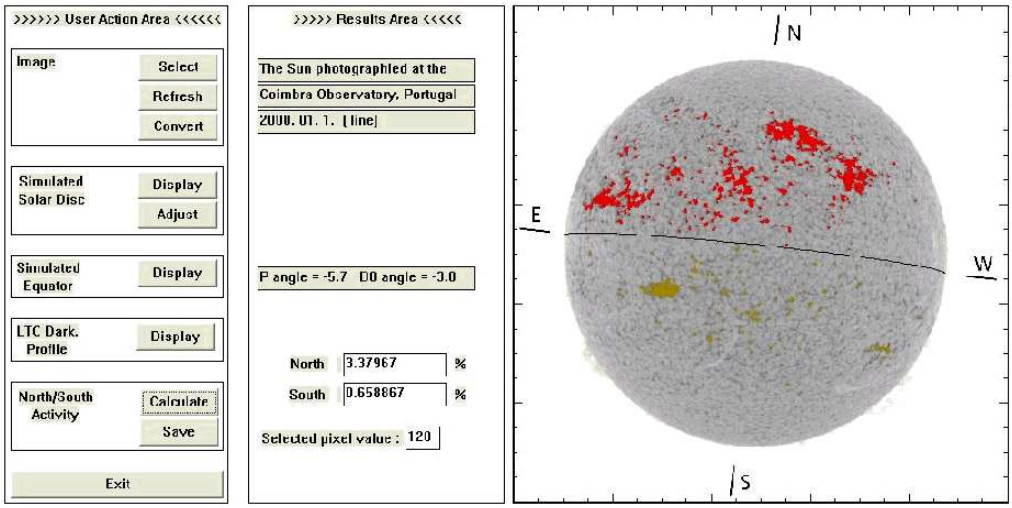

Figure 1. Interface of the AKFEAT tool for estimation of the ABCHF. It is capable to browse an image, for the selected image to calculate the solar disk and position of the equator, CLV darkening profile, and north/south ABCHF, respectively (lefthand panel). In the middle panel is information on image acquisition date, positional and B_0 angle of the solar rotational axis, and the calculated activity index. The righthand panel is a preview window for the processed solar image.

important advantage of the CGLB data comes from their spatial resolution since they are created from measurements performed daily along the solar limb, thus providing resolution of 5° in solar latitude and ∼13° in solar longitude). This permits, for example, a unique opportunity to investigate the N−S asymmetry phenomenon considering arbitrarily chosen latitudinal zones, symmetrically situated with regard to the solar equator.

3. Results

(a) Understandably, the principal result of this contribution consists in developing of a software tool to estimate quantitatively area of the Ca II plages recorded on the spectroheliograms and gathered in the Coimbra (Portuguesse) Observatory from 1926. The algorithm used determines an area of bright Ca II K_3 emission, it does not distinguish individual bright chromospheric features (plages, enhanced network structures, etc.), because it incorporates each pixel above the corresponding local level of the quiet Sun intensity. Moreover, the tool does not accurately account for the borders of chromospheric structures.

(b) Evolution of the daily N−S asymmetry derived from actual distribution of the bright chromospheric features found on the Coimbra spectroheliograms is shown in the upper panel of Fig. 2 for a relatively short period of time (the first 150 days in 2000). This panel pnly illustrates the effectiveness of our method to estimate the area of chromospheric plages. However, already a clear 27-day periodicity and marked predominance of Ca-plage activity on the southern solar

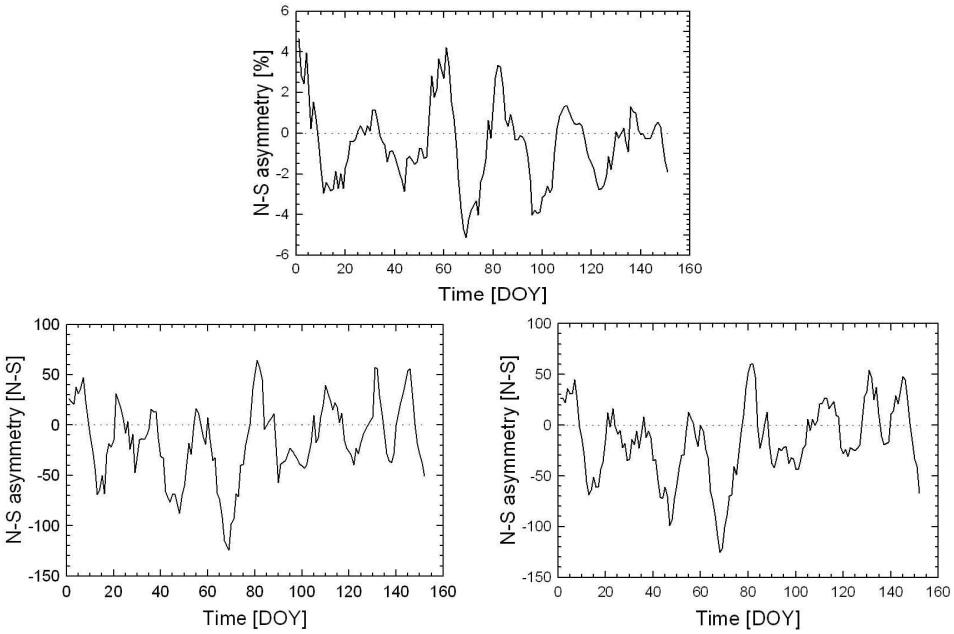

Figure 2. *Upper panel*: evolution of the hemispheric N−S asymmetry NSA of the corrected (plane-to-sphere projection, CLV) area of chromospheric plages. *Lower left panel*: N−S asymmetry of the hemispheric sunspot number (Temmer et al. 2006). *Lower right panel*: N−S asymmetry of the SIDC sunspot number (Van der Linden and the SIDC team, `http://www.sidc.be/sunspot-data`). Time span: January 1 – May 31, 2000.

hemisphere are visible. It is intended to digitize successively the whole Coimbra set of spectroheliograms and process these with the techniques described here. Then, much more of the large-scale and long-term properties in the distribution of Ca II bright features can be investigated. For a visual comparison of the Ca-plage N−S asymmetry with that of sunspots see the lower graphs in Fig. 2 drawn from the SIDC and KSO data, respectively. Cross-correlations in the mathematical sense are discussed under (d).

(c) As mentioned in Section 2, the coronal green line brightness (CGLB) is measured daily pole-to-pole at the solar limb with step of 5° in solar latitude. That is why, we are able to calculate the CGLB N−S asymmetry separately for each of these latitudes (see Fig. 3). Understandably, these "latitudinal" CGLB asymmetries are, on one hand, much less smoothed than those obtained from the whole-Sun Ca-plages and the sunspot indices (Fig. 2). On the other hand, the CGLB are measured at different points above the sun's limb and, therefore, they are correspondingly smoothed due to line of sight integration of "signal" in comparison with the sun's disk observations of the Ca plages and sunspots. Anyhow, combination of the both circumstances results in appearance of Fig. 3. The 27−day variations in the CGLB N−S asymmetry are preserved also here, though more smashed. There seems to exist a certain tendency of left-to-right shifting of the N−S asymmetry curves when advancing from higher to the low

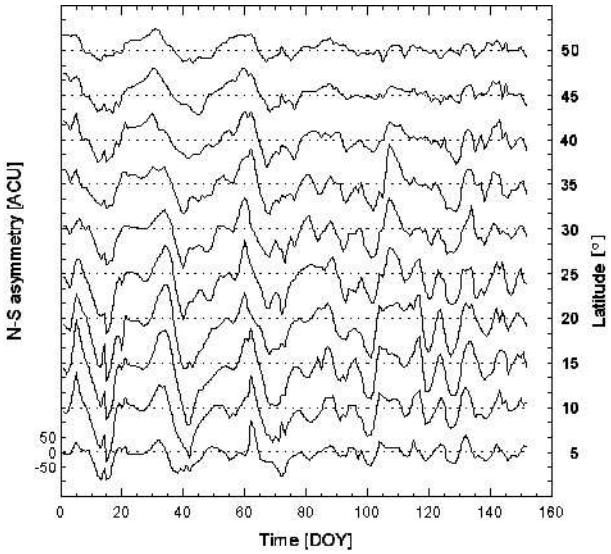

Figure 3. Evolution of the N−S asymmetry of the coronal green line brightness; ACU = Absolute Coronal Unit (scale on the left) for latitudinal zones from ± 5° to ± 50° (Sýkora & Rybák, 2005): January 1 – May 31, 2000.

solar latitudes. This practically represents some delaying of the CGLB N−S asymmetry at the low latitudes in comparison to that at the higher latitudes. Cross-correlations of a more smoothed zonal CGLB N−S asymmetries with the Ca-plages are described below.

(d) Although the treated period of data is rather short (150 days only) the cross-correlation coefficients (CC) of the N−S asymmetries, as presented in Fig. 4, are enough informative. Figure 4 (at left) displays CC = +0.65 between the Ca-plages and the sunspot number (SN) N−S asymmetries (thick and thin lines are for the SIDC and KSO sunspot data, correspondingly). Clearly, the maximum cross-correlation occurs at about one-day lag of the correlated data. This, in fact, means that the Ca-plages N−S asymmetry is delayed for about one day in comparison with the N−S asymmetry of sunspots. The "centre of gravity" of the cross-correlation graph evoke even larger than one-day displacement from lag zero. Correspondingly, two minima of the cross-correlation curves are situated asymmetrically from lag zero vertical dotted line (they are approximately at lag −11.5 and lag +14.0) and, understandably, the negative CC at two minima of the cross-correlation curves are close to −0.55 and −0.60.

The righthand panel of Fig. 4 shows the CC curves between the Ca-plages and the CGLB N−S asymmetries, when the CGLB is considered separately for three chosen zones of solar latitude. Again, the cross-correlation is enough high reaching up to CC = +0.70 for the highest latitude zone. In this case only inexpressive right-sided shifting of the curves maxima is visible (the largest for the close-to-equator 5° – 15° zone) indicating only small delay of the coronal N−S asymmetry in comparison with the chromospheric Ca-plages N−S asymmetry. However, it is well noticeable that this delay increases advancing from the higher to low solar latitudes.

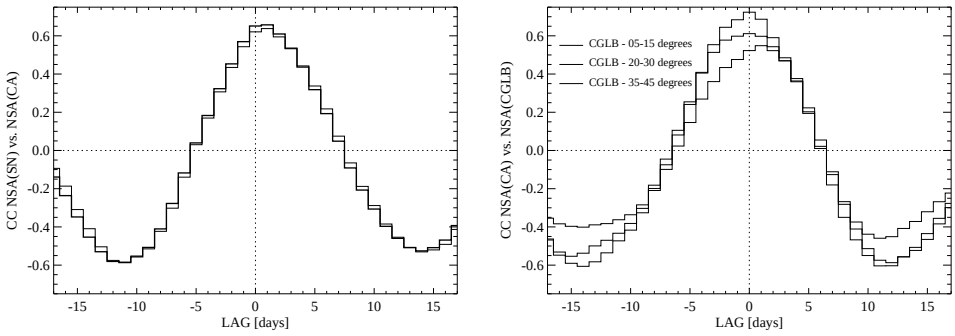

Figure 4. *Left*: cross-correlations between the SIDC sunspot number NSA and the Coimbra Ca NSA (thick curve), and between the KSO NSA and the Coimbra Ca NSA (thin curve). *Right*: cross-correlations between the CGLB NSA and the Coimbra Ca NSA for latitude zones ± 5° – 15°, ± 20° – 30°, and ± 35° – 45°.

(e) We should emphasize once more that the analysis discussed here treats the N−S asymmetry of solar indices and not the indices themselves. In any case it seems that the N−S asymmetry represents a basic global phenomenon of solar activity. Further investigation of it may help to understand the long-term and large-scale properties and variability of solar activity. When having more digital Ca-plage data, it will be possible to elaborate the trends in N−S asymmetry displayed above, in particular to explain its progression from the lower to the upper layers of the solar atmosphere and from higher latitudes towards the solar equator.

Acknowledgments. This work was supported by grant SFRH/BPD/14628/2003, partially by POCTI–SFA–2–675 from Fundação para a Ciência e Tecnologia, MCTES, Lisbon, Portugal (I.D. and P.J.), and by the Slovak VEGA Grant Nos. 2/7012/27 (J.S.) and 2/6915/26 (J.R.). This research was part of the European Solar Magnetism Network (EC/RTN contract HPRN–CT–2002–00313).

References

Badalyan, O. G., Obridko, V. N., & Sýkora, J. 2005, in D. Danesy, S. Poedts, A. De Groof, & J. Andries (eds.), Procs. 11th European Solar Physics Meeting, ESA SP-600 (CD)

Badalyan, O. G., Obridko, V. N., & Sýkora, J. 2006, Solar Phys., in press

Badalyan, O. G., Obridko, V. N., Rybák, J., & Sýkora, J. 2003, in A. Wilson (ed.), Proc. International Solar Cycle Studies Symposium, ESA SP-535, 63

Ballester, J. L., Oliver, R., & Carbonell, M. 2005, A&A, 431, L5

Brandt, P.N. & Steinegger, M. 1998, Solar Phys., 177, 287

Preminger, D.G., Walton, S.R., & Chapman, G.A. 2001, Solar Phys., 202, 53

Sýkora & J. and Rybák, J. 2005, Adv. Space Res., 35, 393

Temmer, M., Veronig, A., & Hanslmeier, A. 2002, A&A, 390, 707

Temmer, M., Rybák, J., Bendík, P., Veronig, A., Vogler, F., Otruba, W., Pötzi, O., & Hanslmeier, A. 2006, A&A, 447, 735

Worden, J.R., White O.R., & Woods, T.N., 1998, ApJ, 496, 998

The Physics of Chromospheric Plasmas
ASP Conference Series, Vol. 368, 2007
Petr Heinzel, Ivan Dorotovič and Robert J. Rutten, eds.

Solar Activity and Irradiance Studies with Ca II Spectroheliograms: Potential and Problems

Ilaria Ermolli[1], Andrey Tlatov[2], Sami K. Solanki[3], Natalie A. Krivova[3] and Jagdev Singh[4]

[1]*INAF Osservatorio Astronomico di Roma, Italy*
[2]*Pulkovo Observatory, Kislovodsk Solar Station, Russia*
[3]*MPI für Sonnensystemforschung, Katlenburg-Lindau, Germany*
[4]*Indian Institute of Astrophysics, Koramangala, Bangalore, India*

Abstract. Various observatories around the globe carried out synoptic full-disk observations of the Sun since the beginning of the 20th century. The archives created by these observations, especially those including Ca II spectroheliograms, have the potential of providing far more detailed information on solar activity than the indices usually used to study activity variations, solar cycle and irradiance changes. However, these data suffer significantly from various problems including numerous defects in the photographic plates, missing or inaccurate calibration of the blackening curve, changes in the positioning of the exit slit with respect to the spectral line and variable seeing. Here we discuss the quality of images obtained by the digitization of three historic Ca II K time series, specifically those stored by the Arcetri, Kodaikanal and Mt Wilson Observatories. The aim of this work is to evaluate the potential value of these data for studies of solar activity and variability. It also shows the importance of the detailed and accurate image processing technique, in order to obtain uniform and trustable results from images coming from different historic archives.

1. Introduction

The most widely used indicators of solar activity are the number and the area of sunspots observed on the solar surface. This is because they make the longest continuous series of measured activity indicators. However, these numbers alone do not fully characterize the solar variability. In fact, solar activity is driven by the temporally and spatially varying distribution of the magnetic flux in the solar atmosphere. It covers phenomena occurring at all atmosphere levels and at all the time-scales.

High resolution observations show that magnetic features are composed of clusters of flux-tube elements. The density of these elements determines the apparent magnetic field strength measured with magnetographs, as well as the brightness of the magnetic features when observed in the strong resonance Ca II K line. Full-disk synoptic observations in this line were regularly performed at several observatories since the beginning of the last century. The archives of these observations have thus the potential of storing detailed information on solar magnetism, with moderate spatial and temporal resolution.

The analysis of these observations should permit insight to be gained into many topics of solar activity and should prove useful for variability studies. For

Figure 1. Examples of the Arcetri (left), Kodaikanal (middle) and Mt Wilson (right) analyzed images (January 9, 1958.)

instance, the cyclic evolution of the magnetic field in quiet Sun regions, studied by Harvey (1994) using full-disk magnetograms, would deserve further investigations on longer time-scales (Lockwood et al. 1999). Since such magnetograms are only available for the last three cycles, these investigations can only be addressed with the historic Ca II K observations. Another important application of these data concerns long term irradiance changes. In fact, the success of the recent models (Krivova et al. 2003; Penza et al. 2003; Wenzler et al. 2005) in reproducing the directly measured irradiance variations suggests that also past irradiance changes can be evaluated with significant precision, given accurate distributions of the solar surface magnetic features which may be gathered from these historic observations.

In the last few years the increasing interest in such early observations and the availability of new hardware resources led to the initiation of projects to digitize existing solar photographic archives. For instance, Arcetri, Kodaikanal and Mt Wilson archives have been already fully digitized (Ulrich et al. 2004; Makarov et al. 2004; Marchei et al. 2006). Similar projects are now ongoing at several observatories, for example in Coimbra.

Here we present examples of the three digitized Ca II K archives and describe the main problems affecting these data. This work was carried out in order to evaluate the potential value of these data for solar activity and irradiance studies. It also shows the importance of the accurate image processing technique, in order to obtain uniform and trustable results from images coming from different historic archives.

2. Data

We analyzed images obtained by the digitization of the photographic Ca II K spectroheliograms stored in the archives of the Arcetri, Kodaikanal and Mt Wilson Observatories. The plates stored in these archives have different dimensions and content. They also were digitized using different devices and criteria. Figure 1 shows examples of these data, taken at the three sites on January 9, 1958, although the observing time differs by more than 16 hours due to the site locations. Note that the intensity pattern of both Arcetri and Kodaikanal digitized data was reversed, in order to show the brightness pattern usually observed in the intensity images of the solar disk.

The first set of the spectroheliograms analyzed here was recorded at the G.B. Donati tower of the INAF Arcetri Astrophysical Observatory in Florence from 1931 to 1974. The spectroheliograph used for these observations (Godoli & Righini 1950; Gasperini et al. 2004) had a grating of 600 lines/mm and a ruled area of 100 mm × 110 mm, with a dispersion of 0.33 mm/Å at 3934 Å. The size of the solar disk on most of the plates is ≈ 6.5 cm; the image scale is thus about 0.033 mm/arcsec. The spectral window for these observations was 0.3 Å, centered in the line core. It is worth noting that several instrumental changes occurred during the about fifty years that the spectroheliograph was utilized. These include the use of additional lens and changes of the slits positions, which improved the image definition and monocromaticity, as well as decreased the stray light level. The problem of discontinuities marked by instrumental changes is common among most, if not all, the existing long time series of synoptic observations. The digitization of the Arcetri archive was performed by the CVS project at the Rome Astronomical Observatory (Centrone et al. 2005; Giorgi et al. 2005; Marchei et al. 2006). The work was carried out through a commercial scanner, used with the setting 1200 × 1200 dpi and 16 bit greyscale significant data. From these data, which are saved in the TIF format, 2040 × 2720 pixels 16 bit FITS images for each solar observation were singled out. Information about the plate acquisition noted in the observation logbooks were included in the file headers. The size of the solar disk in these images is about 1550 pixels; the pixel scale due to the digitization is thus 1.2 arcsec/pixel. The digital archive of Ca II K Arcetri observations contains 5976 spectroheliograms obtained on 5042 observing days. The instrumentation used to acquire these observations is no longer available.

The second set of spectroheliograms used here is that recorded at the Kodaikanal Observatory of the Indian Institute of Astrophysics in Bangalore from 1907 to 1999. In brief, the spectrograph used (Evershed 1911; Bappu 1967) is a two prism instrument, with a dispersion of 0.14 mm/Å near 3930 Å. The 70 μm exit slit of the instrument corresponds to a 0.5 Å bandpass, which includes K_{232}. The size of the solar disk on most of the plates is ≈ 6 cm; the image scale is thus about 0.031 mm/arcsec. The full set of Ca II K observations was digitized using a linear array of 900 pixels Makarov et al. (2004). The original observations were stored as ≈ 1.8k × 1.8k, 8 bit greyscale JPEG images. The solar disk in the digitized images has a radius of about 710 pixels; the pixel scale due to the digitization is thus 1.3 arcsec/pixel. The digital archive of Ca II Kodaikanal observations contains 26640 spectroheliograms obtained on 26620 observing days. The instrument used to acquire these observations is still available.

The third set of spectroheliograms studied is that taken at the Mt Wilson Observatory from 1915 to 1985. The spectroheliograph used at the beginning of these observations (Hale 1915) had a grating with 567 lines/mm and a ruled area of 74 × 92 mm. The 80 μm exit slit admits the passage of a band of about 0.2 Å centered on the Ca II K line core at 3933 Å. The size of the solar disk on most of the plates is ≈ 5 cm; the image scale is thus about 0.026 mm/arcsec. The Mt Wilson observations were digitized in the framework of a project (Ulrich et al. 2004; Lefebvre et al. 2005) carried out at UCLA Division of Astronomy, by using a commercial scanner providing images with the setting 1200 × 1200 dpi and 16 bit greyscale significant data. From these data, 2601 × 2601 16 bit TIF images

were singled out, in which intensity values are stored as positive integers. The solar disk in these images has a radius of about 1000 pixels, the pixel scale due to the digitization is thus about 1 arcsec/pixel. At present, some information about plate dimensions and content are available on the project webpage. The Mt Wilson Ca II K digital archive contains about 40000 images recorded on over 22000 observing days. The images we analyze are the reduced-size (800 $\times$800 pixels) science quality FITS files posted for distribution on the project webpage. The solar disk in these images has a radius of about 350 pixels, the pixel scale in these images is thus reduced to 2.7 arcsec/pixel. The file headers contain information about the acquisition of the original plate and its digitization, as well as measurements of the disk horizontal and vertical radii and an evaluation of the plate quality.

Although the Arcetri archive contains a rather small number of plates with respect to the other ones, more than 65% of the plates in the archive contain exposure wedges for the calibration of the non-linear response of the photographic emulsion. By contrast, most of both Mt. Wilson and Kodaikanal plates (75 and 55 %, respectively), do not include wedge calibrations.

3. Data Quality

The analyzed data show some specific artifacts originating from the instrument used at the time of observations, as well as some effects of the observing and storing procedures. For example, sometimes local darkenings due to the passage of clouds during observations are seen on the solar disk. The resolution may also vary over the disk within one image, which is due to changes of the atmospheric turbulence during the observation.

Some images also show dark lines across the solar disk, which were produced by dust particles on the optical components of the instrument used to get these observations. Scratches and holes found in the plate emulsion are mostly due to the handling and storage of the plates.

Some of the plates display intensity patterns over the solar disk, which are likely due to chemical effects during the plate development. Large scale intensity patterns, which are clearly seen outside the solar disk but also affect the solar images, are mostly due to scattered light by instrumental components (dispersion grating, entrance slit).

Finally, another frequent problem of these historic observations is the difference in the velocity setting of the driving motors which translate the input solar image and the photographic plate, or the spectrograph slits. This results in geometric distortions on the solar image stored on the plates. In particular, the resulting image is elliptic, the axes of the ellipse being parallel and perpendicular to the slit. Note that the differential refraction of the atmosphere also resulted in an oblateness of the solar disk.

Figures 2 and 3 show some of the artifacts described above. Visual inspection of the analyzed images shows that the Kodaikanal time series is on average less affected by plate defects, such as scratches, rows and geometrical distortions, than both the Arcetri and Mt Wilson series. It might be due to the fact that the digital archive of the Kodaikanal Observatory contains only plates with the best quality. Quantitative measurements of the level of intensity in-

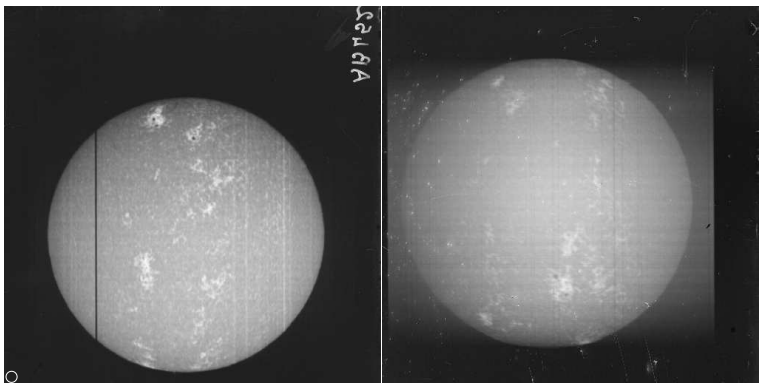

Figure 2. Examples of artifacts affecting the analyzed plates: scratches (left) and holes (right) in the emulsion pattern.

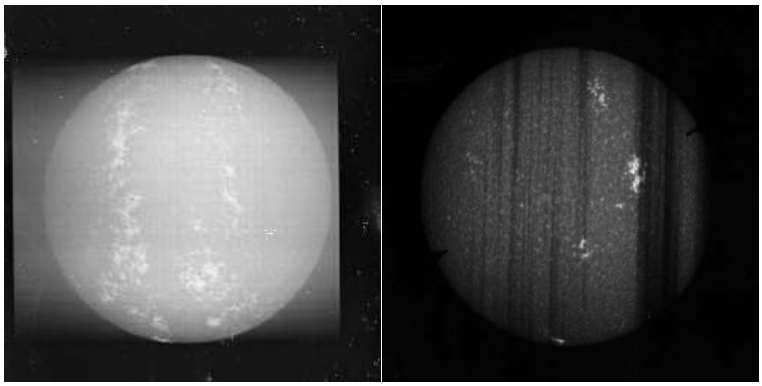

Figure 3. Examples of artifacts affecting the analyzed plates: scattered light by the optical components (left) and intensity in-homogeneities over the solar image (right).

homogeneities over and outside the solar disk, as well as of the spatial resolution on solar images extracted from the three time series confirm the findings of the visual inspection of the data (Ermolli et al. 2006).

It is worth noting that the plate problems listed above affect a rather small portion of the data in the three analyzed time series. Moreover, most of these artifacts can be compensated by applying a proper image processing technique. Finally, the number of images available in two of the three analyzed time series allows the selection and further analysis of only best quality images, without introducing significant losses of the data available for studies focusing on solar variations on daily to multi-decadal time scales.

4. Conclusions

We analyzed images extracted from three digital archives of Ca II K full-disk observations obtained at the Arcetri, Kodaikanal and Mt Wilson Observatories. These images (as also all others coming from similar archives) store detailed spa-

tial and temporal information about solar magnetism during the last century. However, these data suffer significantly from various problems originating from the observational technique, the data storage and the subsequent digitization process. Some of these problems, especially those concerning plate defects, can be solved through the development and further application of a proper image processing technique. For example, the solar disk ellipticity can be compensated by a proper re-sizing of the analyzed images before their processing. On the other hand, effects of the multiple changes that occurred in the instrumentation used during the several decades of observations are more difficult to account for. Such instrumental changes are seen as temporal variation of the results obtained by the analysis of these observations. They can be singled out from solar temporal variations only with the inter-calibration of the data coming from different archives. The main challenge remains the photometric calibration of the data, however.

Acknowledgments. The authors thank the Arcetri, Kodaikanal, Mt Wilson and Rome Solar Groups for having given the chance of working with their digital archives. This work was partly supported by the CVS (Regione Lazio) and by the Deutsche Forschungsgemeinshaft, DFG project SO-711/1-1.

References

Bappu, M. K. V. 1967, Solar Phys. , 1, 151
Centrone, M., Ermolli, I.,& Giorgi, F. 2005, Mem. SAIt., 76, 941
Ermolli I. et al. 2006, in preparation
Evershed, W. 1911, MNRAS, 71, 719
Gasperini, A., Mazzoni, M., & Righini, A. 2004, Giornale di Astronomia, 3, 23
Giorgi, F., Ermolli, I., Centrone, M., & Marchei, E. 2005, Mem. SAIt., 76, 977
Godoli, G. & Righini, A. 1950, Mem. SAIt., 21, 4
Hale, G. E. 1915, PASP, 27, 161, 233
Harvey, K. 1994, IAU Coll. 143, 217
Krivova, N. A., Solanki, S. K., Fligge, M. & Unruh, Y. C. 2003, A&A, 399, L1
Lefebvre, S., Ulrich, R. K., Webster, L. S., Varadi, F., Javaraiah, J., Bertello, L., Werden, L., Boyden, J. E. & Gilman, P. 2005, Mem. SAIt., 76, 862
Lockwood, M., Stamper, R. & Wild, M. N. 1999, Nature, 399, 437
Makarov, V. I., Tlatov, A. G., Singh, J. & Gupta, S. S. 2004, IAU Symp. 223, 125
Marchei, E., Ermolli, I., Centrone, M., Giorgi, F., & Perna, C. 2006, Mem. SAIt. S., 9, 51
Penza, V., Caccin, B., Ermolli, I., Centrone, M., & Gomez, M.T. 2003, ESA-SP 535, 299
Righini, A. 2003, Mem. SAIt., 74, 556
Ulrich, R. K., Webster, L. S., Varadi, F., Javaraiah, J., Lefebvre, S., & Gilman, P. 2004, AGU Fall Meeting Abstracts, A3+
Wenzler, Th., Solanki, S. K., & Krivova, N. A. 2005, A&A, 432, 1057

The Physics of Chromospheric Plasmas
ASP Conference Series, Vol. 368, 2007
Petr Heinzel, Ivan Dorotovič and Robert J. Rutten, eds.

North–South Asymmetry of Solar Activity during Cycle 23

B. Joshi[1], P. Pant[1], P. K. Manoharan[2] and K. Pandey[3]

[1]*ARIES, Nainital, India*
[2]*Radio Astronomy Centre, TIFR, Ooty, India*
[3]*Department of Physics, Kumaun University, Nainital, India*

Abstract. In this paper, we have made a statistical analysis of solar Hα flares that occurred during the period 1996 to 2005 to investigate their spatial distribution with respect to northern and southern hemispheres of the Sun. The analysis includes a total of 21608 single events. The study shows a significant N−S asymmetry which is persistent with the evolution of the solar cycle. The flare activity favors the northern hemisphere in general during the rising and maximum phase of the solar cycle (i.e., in 1997, 1999, and 2000), while the declining phase (i.e., from 2001 to 2005) shows a southern dominance. Further, the monthly N−S asymmetry index for flares, sunspot numbers and sunspot areas suggests similar variations for these phenomena with the progress of solar cycle. We also find that in terms of asymmetric behavior of solar flares, cycle 23 seems to act quite differently from cycle 22 but comparably to cycle 21.

1. Introduction

The occurrence of various features of solar activity is not symmetric considering their manifestation in the northern and southern hemispheres of the Sun. This phenomena, known as North−South (N−S) asymmetry, has been studied using several solar activity indices such as flares, sunspot numbers, sunspot areas, prominences & filaments, magnetic flux, coronal intensity, etc. by various authors (Newton & Milson 1955; Howard 1974; Roy 1977; Vizoso & Ballester 1987; Garcia 1990; Verma 1993; Ataç & Özgüç 1996; Li et al. 1998; Temmer et al. 2002; Joshi & Joshi 2004; Knaack et al. 2004; Brajša et al. 2005; Temmer et al. 2006). These studies reveal the existence of a real N−S asymmetry that has bearing with the solar dynamo mechanism (Ossendrijver 1996).

In this paper a detailed analysis of N−S asymmetry has been performed with solar Hα flares that occurred during solar cycle 23. The study covers almost full solar cycle 23 (1996−2005) and is an extension of our earlier analysis (Joshi & Pant 2005). In Section 2, the pattern of flare occurrence is studied with respect to heliographic latitudes and the significance of observed N−S asymmetry is evaluated using binomial probability distribution. The study also throw light on the evolution of flare activity with the progress of solar cycle. Further, the comparison of asymmetric behavior of flare activity is made with sunspot numbers and areas which is presented in Section 3. The results of the study are discussed in the final section.

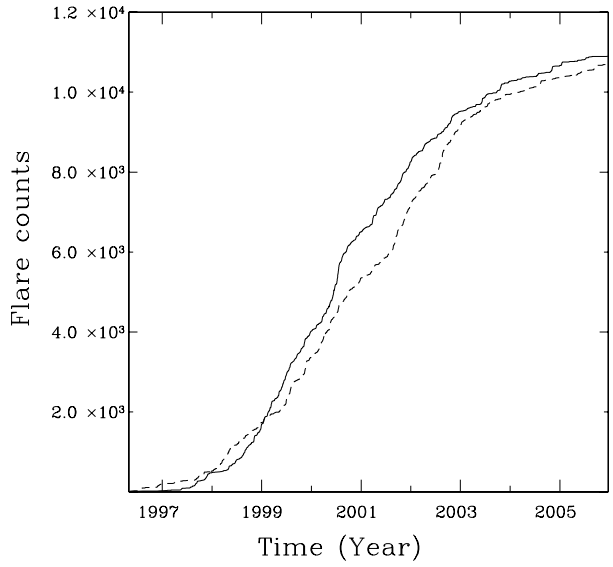

Figure 1. Cumulative counts of flares occurring in the northern (solid line) and southern hemispheres (dashed line).

2. N−S Distribution and Asymmetry of Solar Flares

The data used in the present study have been collected from Hα flare lists published in the SGD (Solar Geophysical Data) from 01 May 1996 to 31 December 2005, covering 10 years of solar cycle 23. Out of 21620 flares, 21608 events are selected for the study for which complete information about the heliographic location (latitude and longitude) was available. To study the latitudinal distribution of flares with solar cycle evolution, we compute the yearly flare counts in 10° latitudinal bands (within ±50° latitudes, flares above 40° latitudes being very small) in the northern and southern hemispheres from 1996 to 2005 (Table 1). We find that the yearly flare counts in the northern and southern hemispheres show an asymmetry (column 8 of Table 1). To evaluate the statistical significance of observed asymmetry we have used binomial probability distribution (see Joshi & Pant 2005 and references therein). The cumulative binomial probability of getting more flares in one of the hemispheres and consequently the dominant hemisphere is also given in the table (see columns 9 and 10). In Fig. 1, N−S asymmetry has been presented by plotting the cumulative counts of flares in the northern (solid line) and southern (dashed line) hemispheres during cycle 23. The vertical distance between solid and dashed lines is a measure of northern/southern excess up to that time. To compare the N−S asymmetry observed in flares with sunspot areas and numbers, we plot the monthly absolute asymmetry index ($\Delta = N_{\rm N} - N_{\rm S}$; see Ballester et al. 2005) for all these phenomena in Fig. 2.

Table 1. Number of Hα flares at different latitude bands in the northern (N) and southern (S) hemispheres are tabulated for each year. The binomial probability (Prob.) and the dominant hemisphere (DH) is given for all the years as well as for all the latitudinal bands. A dash (−) specifies that the probability is not significant. Flares occurring exactly at the equator have been excluded.

Years		Number of flares							Prob.	DH
		0-10°	10-20°	20-30°	30-40°	40-50°	> 50°	Total		
1996	N	21	2	0	1	0	0	24	1.107×10^{-33}	S
	S	112	53	21	2	0	0	188		
1997	N	39	160	230	20	0	0	449	5.641×10^{-6}	N
	S	5	103	199	18	1	1	327		
1998	N	13	635	503	54	1	1	1207	0.428	–
	S	3	366	807	31	9	0	1216		
1999	N	169	1240	811	105	11	0	2336	7.017×10^{-30}	N
	S	71	874	644	38	0	0	1627		
2000	N	463	1327	633	55	1	2	2481	8.712×10^{-14}	N
	S	248	1288	373	79	1	0	1989		
2001	N	503	978	262	5	1	0	1749	0.058	S
	S	449	1062	282	42	8	0	1843		
2002	N	250	746	255	6	0	0	1257	1.329×10^{-35}	S
	S	675	1006	272	4	0	0	1957		
2003	N	407	315	14	3	0	0	739	0.069	S
	S	222	475	83	17	0	0	797		
2004	N	231	159	0	0	0	0	390	0.123	–
	S	165	254	4	0	0	0	423		
2005	N	56	176	1	0	0	1	234	9.054×10^{-6}	S
	S	219	117	0	0	0	0	336		
Total	N	2152	5738	2709	249	14	4	10866	0.134	–
	S	2169	5598	2685	231	19	1	10703		
Prob.		0.398	0.095	0.371	0.205	0.189	0.0625	0.134	–	
DH		–	N	–	–	–	–			

3. Results and Conclusions

1. We find a significant N−S asymmetry in solar flare occurrence during cycle 23 which is persistent during the course of the solar cycle. The activity dominates the northern hemisphere in general during the rising and maximum phase of the solar cycle (i.e., in 1997, 1999, and 2000), while the declining phase (i.e., from 2001 to 2005) shows southern dominance.

2. The cumulative flare counts show a southern excess in the rising phase of the cycle (1997 to 1999), while after 1999 northern excess prevails. The northern excess first increases till mid 2001 and then decreases continuously till 2003. After 2003, we find a small but constant northern excess (cf. Fig. 1). In terms of asymmetric behavior of solar flares, cycle 23 seems to act quite differently from the previous cycle (i.e. cycle 22) but is comparable to cycle 21 (see Temmer et al. 2001 for N−S flare asymmetry during cycles 21 and 22). The different behavior of odd and even numbered cycles may be interpreted as the two parts of the basic 22-year solar periodicity (Švestka, 1995).

3. We find similar variations in N−S asymmetry of solar flares, sunspot areas and sunspot numbers during solar cycle evolution (cf. Fig. 2). However, the amplitude of N−S asymmetry, determined by the absolute asymmetry index (Δ), for different months varies between various solar activity phenomena.

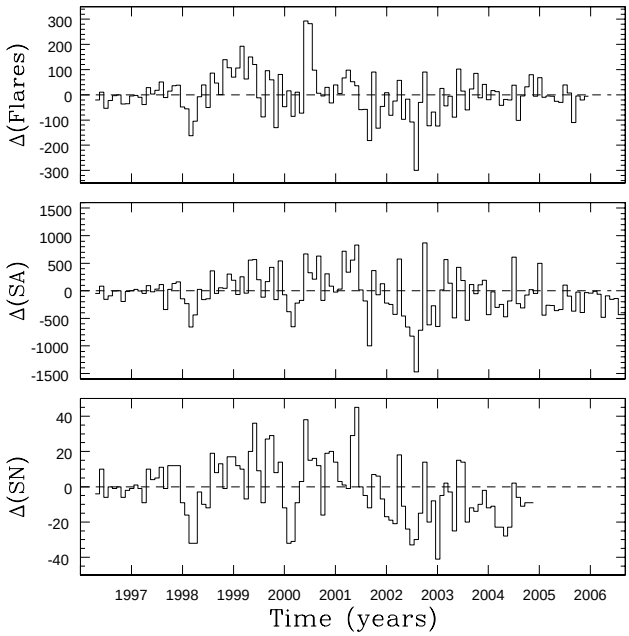

Figure 2. Monthly values of absolute asymmetry index ($\Delta = N_N - N_S$) during solar cycle 23. The figure shows the plots of asymmetry index for monthly flare counts, monthly mean sunspot areas (SA) and monthly mean sunspot numbers (SN) (from top to bottom panel).

Acknowledgments. B. Joshi thanks the organizers for an excellent conference that led to many fruitful discussions.

References

Ataç, T. & Özgüç, A. 1996, Solar Phys., 166, 201
Ballester, J. L., Oliver, R., & Carbonell, M. 2005, A&A, 431, L5
Brajša, B., Wöhl, H., Vršnak, B., et al. 2005, Solar Phys., 231, 29
Garcia, H. A. 1990, Solar Phys., 127, 185
Howard, R. 1974, Solar Phys., 38, 59
Joshi, B. & Joshi, A. 2004, Solar Phys., 219, 343
Joshi, B. & Pant, P. 2005, A&A, 431, 359
Newton, H. W. & Milson, A. S. 1955, MNRAS, 115,398
Knaack, R., Stenflo, J. O. & Berdyugina, S. V. 2004, A&A, 418, L17
Li, K. J., Schmieder, B. & Li, Q. Sh. 1998, A&A, 131, 99
Ossendrijver, A. J. H., Hoyng, P. & Schmitt, D. 1996, A&A, 313, 938
Roy, J.-R. 1977, Solar Phys., 52, 53.
Švestka, Z. 1995, Adv. Space Res., 16(9), 27
Temmer, M., Veronig, A., Hanslmeier, A., Otruba, W., & Messerotti, M. 2001, A&A, 375, 1049
Temmer, M., Veronig, A., Hanslmeier, A. 2002, A&A, 390, 707
Temmer, M., Rybák, J., Bendík, P., et al. 2006, A&A, 447, 735
Verma, V. K. 1993, ApJ, 403, 797
Vizoso, G. & Ballester, J. L. 1987, Solar Phys., 112, 317

The Physics of Chromospheric Plasmas
ASP Conference Series, Vol. 368, 2007
Petr Heinzel, Ivan Dorotovič and Robert J. Rutten, eds.

Is the Mn I 539.4 nm Variation with Activity Explained?

Nikola Vitas[1,2] and Ištvan Vince[2,3]

[1] *Sterrekundig Instituut, Utrecht University, The Netherlands*
[2] *Department of Astronomy, Faculty of Mathematics, Belgrade, Serbia*
[3] *Astronomical Observatory, Belgrade, Serbia*

Abstract. The photospheric Mn I 539.4 nm line in the solar spectrum shows unusual variability with the solar cycle in that its depth decreases with increasing activity. Doyle et al. (2001) claimed that this phenomenon is due to interlocking between the chromospheric Mg II h & k lines and an overlapping Mn I multiplet. In this contribution we test this hypothesis by synthesizing Mn I 539.4 nm line including these interlocking lines for a range of standard solar models and then combining resulting profiles without and with interlocking to emulate the full-disk profile variation. We find that the interlocking gives only a minor contribution; the largest one comes from different temperature stratifications in the photospheric layers of the various models.

1. Introduction

The Mn I 539.4 nm line in the solar spectrum is a photospheric one but it shows a significant variation with the 11-year activity cycle of the Sun (Livingston & Wallace 1987). Vince & Erkapić (1998) synthesized the line from different solar models but without finding the observed level of sensitivity to activity. However, at this meeting Solanki (2007) reported work by Danilović (2007) showing that LTE 1.5D modeling with an appropriate set of model atmospheres indeed mimics the observed behavior of the Mn line. In an earlier paper, Doyle et al. (2001) claimed that the unusual behavior is caused by coupling between the Mn I line and the Mg II k line. In this report we combine the two approaches by synthesizing the line for a range of standard solar models including interlocking with Mg II k.

2. Calculations

The Mn I 539.4 nm line is an intercombination transition from the Mn I ground state (multiplet 1, $a^6S \rightarrow z^8P^o$). The line is broadened considerably by hyperfine splitting. In the solar spectrum it appears as a relatively weak feature with an unusually broad core and visible substructure. It is mostly formed in the photosphere (Vitas 2005). The computed line strongly depends on the temperature stratification of the model atmosphere (Vitas & Vince 2005). Thackeray (1937) already pointed out that the Mn I 539.4 nm line shares the ground level with the UV1 multiplet of Mn I (279.482, 279.827, 280.106 nm, $a^6S \rightarrow y^6P^o$) which overlaps with the Mg II h & k lines (280.270 and 279.553 nm), see Fig. 1. The blue component of the UV1 multiplet is close to the emission core of Mg II k while the

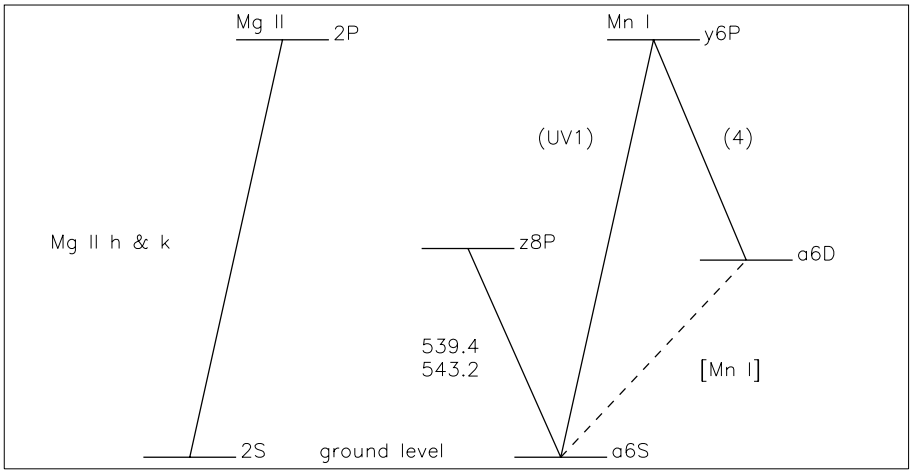

Figure 1. A partial Grotrian diagram of Mg II and Mn I. Mn I multiplet 4 is expected to show behavior opposite to multiplet 1 (539.4, 543.2 nm). The transition $a^6S \rightarrow a^6D$ is forbidden. Its appearance as an emission line in the spectra of Mira's was attributed to optical pumping between Mg II and Mn I already by Thackeray (1937).

other two components are located in the absorption dip between h & k. Doyle et al. (2001) suggested that (*i*) the low "local continuum"of the UV1 multiplet due to the absorption in Mg II k causes overpopulation of the Mn I ground level and increases the absorption coefficient in the Mn I 539.4 nm line, and that (*ii*) the increase of the emission in the Mg II k core with solar activity depopulates the ground level of Mn I, causing weakening of the Mn I line. The numerical results of Doyle et al. supported these conclusions qualitatively. However, they neglected the hyperfine structure of Mn I and assumed that the variation of the Mn I 539.4 nm line with activity can be modeled by varying a single 1D atmospheric model in somewhat arbitrary fashion, rather than using multiple models with appropriate filling factors.

To test the interlocking hypothesis we employ the Mn I model atom specified in Vitas (2005) and a Mg model atom supplied by Jevremović (2003). The set of 1D semi-empirical model atmospheres of Fontenla et al. (1999) was selected to represent six types of structures on the solar disk[1]. The evolution of these features with the cycle is not considered here, but their average filling factors at solar minimum and maximum as specified by Fontenla et al. (1999) are taken into account. The radiative transfer computation was done with MULTI 2.2 (Carlsson, 1992). The radiation field in the Mg II h & k lines was computed first, and then it was used as a pumping radiation field in the lines of Mn I.

We find that the central depth r of the computed Mn I 539.4 nm line profile depends strongly on the specific feature represented by the various models. In the hotter models, the line is weaker; in the cooler models it is stronger than in the quiet sun. Moreover, the effect of the Mg II k interlocking also depends on

[1]The sunspot model is not considered because of its small filling factor (0.3 – 0.4% in the maximum of activity) and difficulties in Mg II h & k modeling with it.

the selected model. In plage it produces depopulation of the Mn I ground level and weakens the Mn I 539.4 nm line. On the contrary, in the quiet sun model the effect is larger population of the ground level and a stronger line. The relative change of the Mn I central depth ($\delta = r'/r$) when the optical pumping is taken into account (r') is given in Table 1 for each of the models. The table also specifies the average filling factors Fontenla et al. (1999).

Model	Quiet Sun (q)	Active Sun Small Plages (a_1)	Active Sun Large Plages (a_2)	δ
A	0.10	0.09	0.08	1.138
C	0.77	0.70	0.67	1.065
E	0.10	0.09	0.10	1.026
F	0.03	0.06	0.07	1.007
H	0.00	0.05	0.05	0.995
P	0.00	0.007	0.026	0.977
S	0.00	0.003	0.004	...

Table 1. Average filling factors of the models of Fontenla et al. (1999) and the computed relative change of the Mn I central depth (δ) when the optical pumping is taken into account.

Linear combination of the parameters of the profiles computed from the different models with their corresponding filling factors describing quiet and active sun with large coverage by plage ($a \equiv a_2$) gives an estimate of the maximum line depth variation during the activity cycle, ρ:

$$\rho = \frac{r_{\rm active}}{r_{\rm quiet}} = \frac{\sum_m a_m\, r_m}{\sum_m q_m\, r_m} = 0.970,$$

where r_m is the central depth in model m, q_m and a_m are the corresponding filling factors for quiet and active sun (Table 1), and $m \in (A, C, E, F, H, P)$. When the optical pumping mechanism is taken into account, its effect can be taken as a correction (δ) to the calculated line profile, and this correction will depend on the model:

$$\rho_{\rm corr} = \frac{r_{\rm corr,active}}{r_{\rm corr,quiet}} = \frac{\sum_m a_m\, \delta_m\, r_m}{\sum_m q_m\, \delta_m\, r_m} = 0.963.$$

If active sun with small coverage by plage is considered ($a \equiv a_1$), the estimated variation is smaller ($\rho = 0.981$, $\rho_{\rm corr} = 0.975$). The overall effect of optical pumping to the variation of the Mn I 539.4 nm line is about 20% of the effect of the coverage variation.

An additional numerical experiment was designed to test the importance of the wavelength coincidence between the Mg II k emission peak and the blue component of the UV1 multiplet. Namely, if the hypothesis of Doyle et al. is valid, then the optical pumping should be more effective when blue UV1 component lies closer to the emission peak. To check this, we artificially changed the energy of the y^6P^0 level to change the wavelength of the blue UV1 component in the range between 279.466 and 279.681 nm. The calculations were repeated for each value. Practically no variation of the Mn I 539.4 nm line profile is produced

in this way. We can conclude that the Mn I resonance multiplet 1 is actually insensitive to the photons emitted in the core of Mg II h & k.

3. Conclusions

Doyle et al. (2001) suggested that absorption in Mg II k as a quasi-continuum influences the Mn I populations. This is not likely to occur in the photosphere. On the other side, the variation of the Mn I 539.4 nm line with activity is more likely to be dominated by variable coverage of the solar disk by various activity features (Vince & Erkapić 1998, Danilović 2007). Our modeling supports this hypothesis and shows that the interlocking between the Mg II h & k lines and the UV1 multiplet of Mn I is insufficient to explain the observed variation. However, a much more detailed approach is necessary to confirm this conclusion. In particular, Mg II h & k should be synthesized including the effects of incomplete frequency redistribution.

Acknowledgments. It is pleasure to thank Olga Atanackovic-Vukmanović and Mats Carlsson for critical and constructive discussions. We thank Darko Jevremović for providing the magnesium model atom. The paper was improved by critical reading by Rob Rutten. The Ministry of Science and Environmental Protection of Serbia partially supported this research (project "Stellar and solar physic"). Nikola Vitas is presently part of the USO Graduate School for Solar Physics on a Marie Curie Early Stage Research Training Fellowship of the European Community's Sixth Framework Programme under contract number MEST-CT-2005-020395

References

Danilović S., 2007, in preparation
Doyle J. G., Jevremović D., Short C. I., Hauschildt P. H., Livingston W., Vince I., 2001, A&A 369, L13
Fontenla J., White O. R., Fox P. A., Avrett E. H., Kurucz R. L., 1999, ApJ 518, 480
Jevremović D., 2003, private communication
Livingston W., Wallace L., 1987, ApJ 314, 808
Solanki S., 2007, in P. Heinzel, I. Dorotovič, R. J. Rutten (eds.), The Physics of Chromospheric Plasmas, ASP Conf. Ser. 368, 481
Thackeray A. D., 1937, ApJ 86, 499
Vince I., Erkapić S., 1998, in F.-L. Deubner, J. Christensen-Dalsgaard, D. Kurtz (eds.), IAU Symp. 185: New Eyes to See Inside the Sun and Stars, p. 459
Vitas N., 2005, Memorie della Societa Astronomica Italiana Supplement 7, 164
Vitas N., Vince I., 2005, Memorie della Societa Astronomica Italiana 76, 1064

Part VII

Solar Physics Instrumentation

The Physics of Chromospheric Plasmas
ASP Conference Series, Vol. 368, 2007
Petr Heinzel, Ivan Dorotovič and Robert J. Rutten, eds.

The Modernized Spectroheliograph at Coimbra

M. Klvaňa[1], A. Garcia[2] and V. Bumba[1]

[1] *Astronomical Institute AS, Ondřejov, Czech Republic*
[2] *Observatório Astronómico, Universidade de Coimbra, Portugal*

Abstract. Application of CCD chips in astronomical instruments constructed for the registration of measured data on a photographic emulsion brings some special issues. The problems increase, if we need to digitize the whole solar disk. The spectroheliograph of the Coimbra university has been constructed for registration of the full-disk spectroheliograms on a photographic emulsion. Its construction is mechanically highly precise. Among others, it perfectly compensates the spectral line curvature in such a way that the resulting monochromatic solar disk is without any deformation. The compensation requires an adjustment of the entrance and exit slits, which are both curved.

The fact that during the transition from the photographic to the CCD registration it was necessary to preserve the original function of data registration on a photographic emulsion brings a whole number of specific problems. It was necessary to change the parameters of the optical system, to remove brightness and shape deformations of the solar disk, originating from the recording medium change. In this paper we analyze the mentioned issues and we describe how to treat them. We also present alternative spectroheliograph usages, for example for measuring Doppler velocities.

1. Statement of the Problem

Solar observations using spectroheliograms have a long-lasting tradition at the Astronomical institute of Coimbra university. A very close collaboration with the Meudon observatory enabled to inaugurate in Coimbra a classical spectroheliograph taking quality photographic spectroheliograms in several spectral wavelengths just eighty years ago.

Recently it was neccessary to substitute the photographic emulsion by a CCD element. The main reason is the gradual narrowing of assortment of the produced photographic materials. Tests made during the preceding years (Klvaňa et al. 2005) demonstrated that the classical CCD cameras (although their cost is higher) are for astronomical purposes indisputably more suitable compared to the cheaper video-systems.

2. Parameters of the Spectroheliograph

The telescope is fed by two planar coelostat mirrors. The objective lens of the horizontal telescope has a focal length of 4060 mm and a diameter of 250 mm. The maximum diameter of the solar disk on the entrance slit of the spectrograph is 38.5 mm. The optical system of the spectrograph consists of a collimator with focal length 1300 mm and diameter 150 mm, a camera objective lens with focus

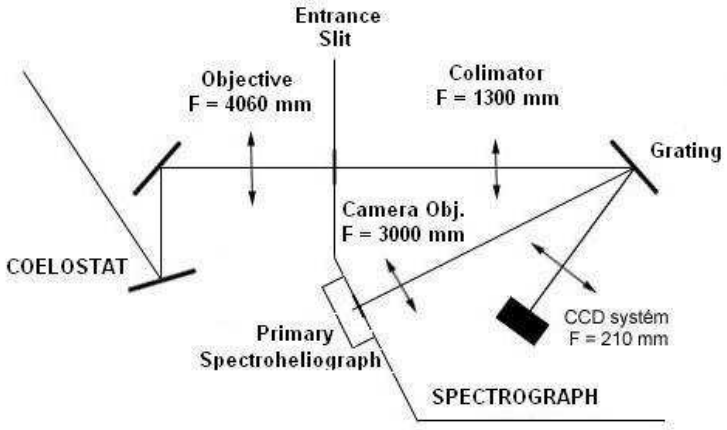

Figure 1. Original optical system of the Coimbra telescope and spectroheliograph with the installed CCD system

3000 mm and diameter 132 mm, and a reflecting diffraction grating with 300 grooves per mm (Lobo da Costa 1929).

The spectroheliograph is made very precisely. All factors connected with the full-disk imaging are compensated (Silva Simoes 1968). The spectroheliograph is projected in such a way that without modification of the grating's position one can expose successively spectroheliograms in the lines Hα, Ca II K_3 and Ca II K_1, changing only two colour filters.

3. Particularities of the CCD Elements Application

In classical astronomical instruments proposed originally for work with a photographic emulsion, application of CCD cameras generally leads to the necessity to change parameters of the optics. The main reason is in the chip's dimension. The spatial resolution of a chip is approximately of the same order as of photographic emulsion, but its size is substantially smaller. If we need to register a sufficiently large area, we have to choose a trade-off that will enlarge the size of the measured region at the cost of the resolving power.

The next important factor influencing the adjustment of an astronomical instrument is the fact that the greatest part of classical instruments mostly did not use the whole resolution of photographic emulsion. The image size on their output was much larger than requested by the resolution of the emulsion.

If an instrument, originally used for work with a photographic emulsion, is adapted for the use of a CCD chip, the necessary change of the image size on its exit is appreciable. In our case, we have to decrease the original output image almost 15 times.

4. Criteria for the Instrument Adjustment

In order to maintain continuity of observations with the spectroheliograph we decided to:

a) keep as much as possible of the present construction, without substantial changes due to the necessary minimization of the expenses;

b) keep the possibility to use the instrument also for photographic work;

c) keep operational flexibility of the instrument, this means the possibility to get spectroheliograms in short time intervals between clouds;

d) do not adjust the software for the spectroheliogram processing to a particular construction of the spectrograph (curvature of input slit, position of the objective with a CCD camera in the spectrograph), but keep it flexible. It must allow to remove the disturbing phenomena independently of the setting and adjustment of the optical system.

The chosen technical solution is a trade-off between the image quality of the resulting spectroheliogram and the acquisition prices of the objective and the CCD camera. The optical system of the telescope allows theoretical image resolution better than $1''$. However, the local observational conditions influenced by the telescope site do not allow to archieve such resolution. Therefore we decided to use a cheaper CCD camera with the chip size of 1280×1024 pixels, which allows the best resolution of $3''$ in the resulting spectroheliogram. This resolution is still better than the average quality of the seeing in the place of observation. In the case of extraordinarily good observational conditions it is possible to use the classical spectroheliograph.

On the basis of such criteria we placed a new optical arm with a front-end filter, an objective with an adjustable focal length (200 – 240 mm) and a CCD Camera CCD-1300LN from VDS Vosskuehler GmbH (see) into the spectrograph (Fig. 1).

5. Mode of Spectra Digitization

Spectra evaluated in form of spectroheliograms are digitized during the shift of the solar image in the direction perpendicular to the spectrograph entrance slit. The shift is ensured by an original scanning mechanism of the spectroheliograph – by the motion of the telescope objective. To get the required registration velocity of the spectroheliogram, the digitization of spectra must be made in an asynchronous mode. During 80 s we obtain about 3000 frames of spectra.

6. The Curvature of Spectral Lines

If we want to get the spectrum of the whole solar disk, we have to count with the fact that in the spectrograph the spectral lines will be appreciably curved. During the photographic registration this curvature is corrected by the curvature of both the entrance and exit slits. When using CCD camera the original

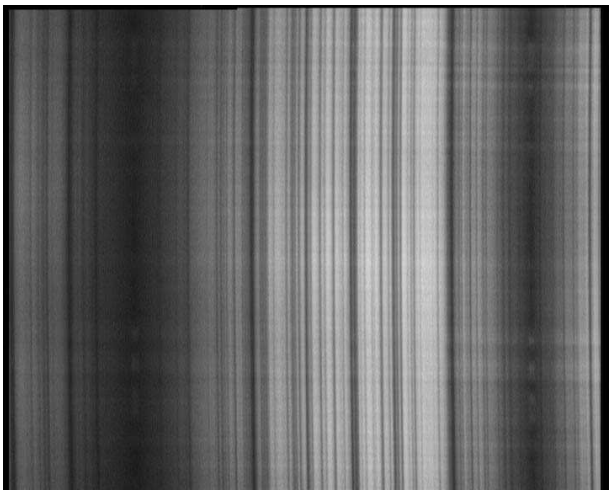

Figure 2. Example of one from a series of almost thousand spectra used in the selected spectral wavelength for construction of a spectroheliogram. On the left the Ca II K and on the right Ca II H spectral lines.

optical system is used only partially (the compensation of the shape of the spectroheliogram with the exit slit is not used). So, the curvature of the spectral lines fundamentally influences the further evaluation of spectra.

The spectral line curvature is estimated by the fitting of the spectral line profile and by the interpolation of a smooth curve through the profile minima. The method needs longer operating time. We used therefore the following modified method:

As the first step we find the brightness minima in three points of the spectral line (close to the upper an lower end of the line and in its middle). We fit a parabola to these three points.

As the second step we find the optimum curvature of the parabola following the principle of minimization of the sum of the subpixel interpolated brightness of the spectral line in all points of the parabola.

7. Adjustment of Spectra

First we remove the spectral inhomogeneities caused by the dirt and defects in the optical path and on the CCD chip. Especially in spectroheliograms the dirt on the spectrograph entrance slit forms thin, but distinctly visible horizontal lines. The flat field correction removes such defects in a digitized spectrum.

7.1. Flat-field correction

Dark current recording: we perform the dark current registration through digitization of about 50 spectra obtained with the closed spectrograph entrance slit. All obtained spectra we average into one picture of the dark current $DC(x, y)$.

Flat field recording: we make the registration of the flat field using the digitization of about 50 spectra during the motion of the solar disk image on

the slit. If the solar disk diameter is smaller than the slit height, we shift the solar disk vertically outside the slit and we shift it uniformly along the slit into a symmetrical position on the opposite side of the slit. During the disk motion we digitize the spectra, which are all averaged into one flat field $FF_2(x, y)$.

7.2. Flat fielding of digitized spectra

From the flat field recording $FF_2(x, y)$, which contains also the dark current recording, we firstly subtract the dark current $DC(x, y)$ and we obtain the flat field without the dark current:

$$FF_1(x, y) = FF_2(x, y) - DC(x, y). \tag{1}$$

Next we average vertically all columns of the flat field spectrum $FF_1(x, y)$ into the curve $K(x)$. If the spectral lines are curved we must first find the shape of this curvature and remove it. After that we can average vertically all columns of the flat field spectrum into the curve $K(x)$.

The situation is even more complicated if the spectral lines have different curvatures in different parts of the digitized spectrum. In our case we therefore apply the flat field only for the part of the spectrum in which the wavelength of our spectroheliogram is situated and for which we exactly know the line curvature.

All rows of the flat field spectrum we divide by the corresponding values of the curve $K(x)$ and in this way we obtain the standardized flat field spectrum:

$$FF(x, y) = FF_1(x, y)/K(x). \tag{2}$$

Following this we must correct the position of the curve $K(x)$ in the axis x for the curvature of the spectral line.

The corrected spectra $SP(x, y)$ we obtain from the original ones $SP_1(x, y)$ using the relation:

$$SP(x, y) = [SP_1(x, y) - DC(x, y)] / FF(x, y), \tag{3}$$

where $SP_1(x, y)$ are registrations of individual spectra, digitized for the specroheliogram construction.

7.3. Missing flat field data

If the flat field of the measurement is not suitable (for example due to presence of clouds etc.), it is possible to use a flat field calculated from the adjacent measurements. When even this possibility does not make satisfactory results, one can use the software correcting the horizontal structures. The result of such correction is shown in Fig. 3.

8. Construction of the Spectroheliogram

An individual step of the spectroheliogram construction depends on the entrance slit, as well as on the spectral line shape, because they can deform the solar disk shape quite irregularly. It also depens on the velocity of spectra digitization, which changes the ratio of the horizontal and vertical diameters of the disk.

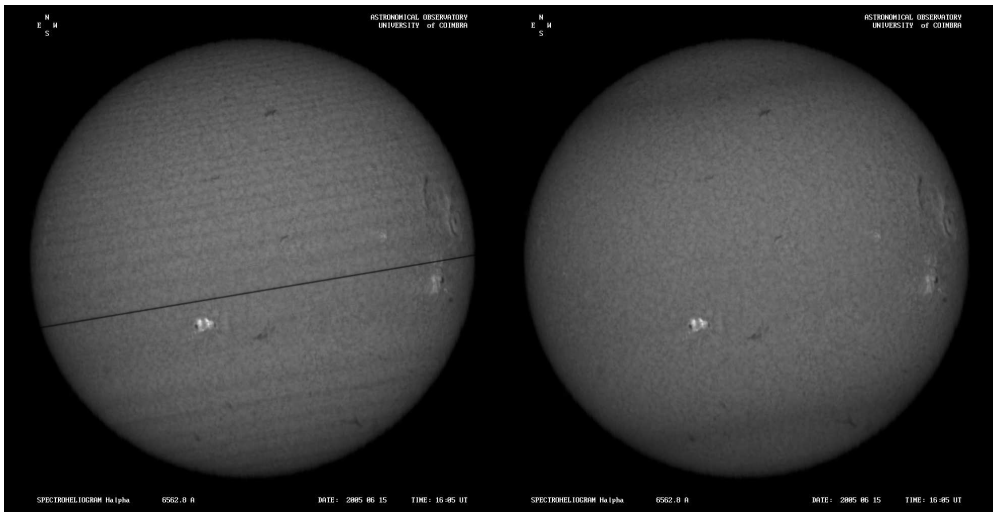

Figure 3. *Left:* Hα spectroheliogram including interference strips, a guiding fibre and a dirt on the input slit. Originally horizontal structures were inclined due to the orientation of spectroheliogram. *Right:* The same spectroheliogram after the removal of disturbing structures. It can be seen that also the guiding fibre was removed.

For the given spectral wavelength we construct the classical spectroheliogram lining up the segments of the corrected spectrum of this wavelength chronologically. With a non curved spectral line and with a straight entrance slit of the spectrograph these segments have a form of an rectangle and the selection is simple. The individual segments we get from the pictures of the digitized spectra selecting the points corresponding by their position in the spectrum to the given wavelength.

The spectrograph entrance slit curvature is in our case projected into the form of the spectral line already deformed by the optical system. To make the form of a spectral line linear, we have to remove both deformations simultaneously.

First we remove the deformation of the spectral line by the same procedure demonstrated in Sect. 7.2. In the case we draw the spectroheliogram usign the classical method, the curved spectrograph entrance slit causes that the rows are mutually shifted following the curvature of the entrance slit. Because the shift is constant for the whole row, it is more simple to draw the spectroheliogram by the classical method and to corrected the deformation of the spectroheliogram row by row (see Sect. 8.2).

8.1. The speed of spectra digitization

The optimum speed of the spectra digitization helps to hold the same length of the horizontal and vertical diameters of the solar disk in the spectroheliogram. But mostly, the speed of digitization and the velocity of the solar disk shift on the spectrograph entrance slit, as well as the width of the drawn segment, do not permit to get the same length of the disk diameters. It would be necessary to resample the spectroheliogram in one direction.

We found that an asynchronous mode of spectra digitization does not make possible an equidistant sampling of the solar disk. The number of spectra is three times larger than it is necessary. Every set of the digitized spectrum stored in the DIG format includes the time of digitization with an accuracy of 0.001 s. From the vertical diameter of the disk on a spectroheliogram we find the number of spectra needed for the spectroheliogram construction and following the time of digitization we select those spectra which best fit the condition of a the equidistant sampling. In this way we remove the problem of a spectroheliogram deformation due to an uneven solar disk sampling. At the same time we get the identification of its horizontal and vertical diameters.

8.2. Removal of solar disk deformation

After a setting up of a spectroheliogram, the solar disk is deformed due to the curvature of the spectral line and the spectrograph entrance slit. The deformation we remove by finding the deviations from a circular line of individual row ends of the disk image and we shift them to compensate the deviation. The correction for deformation is made according to the following algorithm:

a) We assemble a histogram of the spectroheliogram intensities.

b) From the histogram we determine the intensity limit corresponding to the total number of pixels of the solar disk (this number of pixels we calculated from the known disk diameter).

c) We make an image segmentation of the disk limb around the found intensity limit and we estimate the horizontal deviations of the disk limb from a circle in the individual rows of the spectroheliogram.

d) Through these deviation points we draw a parabola describing the solar disk deviation in individual rows. By the shifts of these rows read on the parabola we compensate the disk deformation.

8.3. Orientation and solar disk position

If we correct the spectroheliogram with the described method and if we draw it, with high probability the solar disk will be placed outside the image center and the rotational axis of the Sun will not be vertical.

Therefore the further transformation consists of the shift of the solar disk to the image center and of the turning (eventually flipping) of the disk around it to get the north up, the east to the left and the solar rotational axis vertical. This way we assure the homogenity of the whole series of spectroheliograms.

8.4. Minimization of loss of spatial resolution

All shifts and transformations lead toward the necessity of the spectroheliogram points interpolation. If we take every described operation separately, we have to interpolate several times. Every interpolation reduces the image space resolution, so that we should make the described procedures simultaneously with only one interpolation.

9. Spectroheliogram Visualization

Brightness j in spectra is measured linearly and digitized in 12 bits, it means discretely from 0 to 4095. Before the measurement it is necessary to adjust the chip illumination in such a way that we have the whole digitized spectrum in this range of values. A spectroheliogram taken in a spectral line darker than continuum will be too dark.

During the spectroheliogram construction we try to use the whole density scale we have to our disposal. Therefore in the given spectroheliogram we find first the maximum intensity $j_{\max}$ and all measured intensities we normalise into the range of values 0.0 – 4095.0:

$$j_{\text{norm}} = 4095 j / j_{\max} \tag{4}$$

The usually applicable range for printing or visualization on the display device is eight bits, it means a range of 256 values. The obtained values we transform into this range without information losses (they are real numbers, not integer values, their resolution therefore corresponds to twelve bits):

$$j_{8\text{b}} = j_{\text{norm}}/16 \tag{5}$$

To visualise a larger range of brightness different conversion curves between the measured and visualized values different conversion curves are used. The conversion curves enlarge the contrast in a specific image zone and in this way they improve the resolution of structures located there.

The following five curves transferring the measured brightness from the 12-bit to the 8-bit range have been tested for the spectroheliogram construction. They are ordered following the resulting brightness of the spectroheliogram. The classical exponential and logarithmic functions were not used to increase the speed of computation.

These curves are used in dependence on the phenomenon we want to highlight on the spectroheliogram (activity, the whole disk, prominences) and also depending on the spectroheliogram mode (Hα, Ca II K$_3$, Ca II K$_1$, continuum). In Fig. 4 one can see examples of spectroheliograms after application of proposed corrections:

The curve W (White disk):

$$j_{\text{W}} = 64 \sqrt[4]{j_{8\text{b}}} \tag{6}$$

The curve P (Prominence):

$$j_{\text{P}} = 16 \sqrt{j_{8\text{b}}} \tag{7}$$

The curve N (Normal):

$$j_{\text{N}} = j_{8\text{b}} \tag{8}$$

Curve D (Dark disk):

$$j_{\text{D}} = (j_{8\text{b}}/16)^2 \tag{9}$$

Curve B (Black disk):

$$j_{\text{B}} = 4\,(j_{8\text{b}}/64)^3 \tag{10}$$

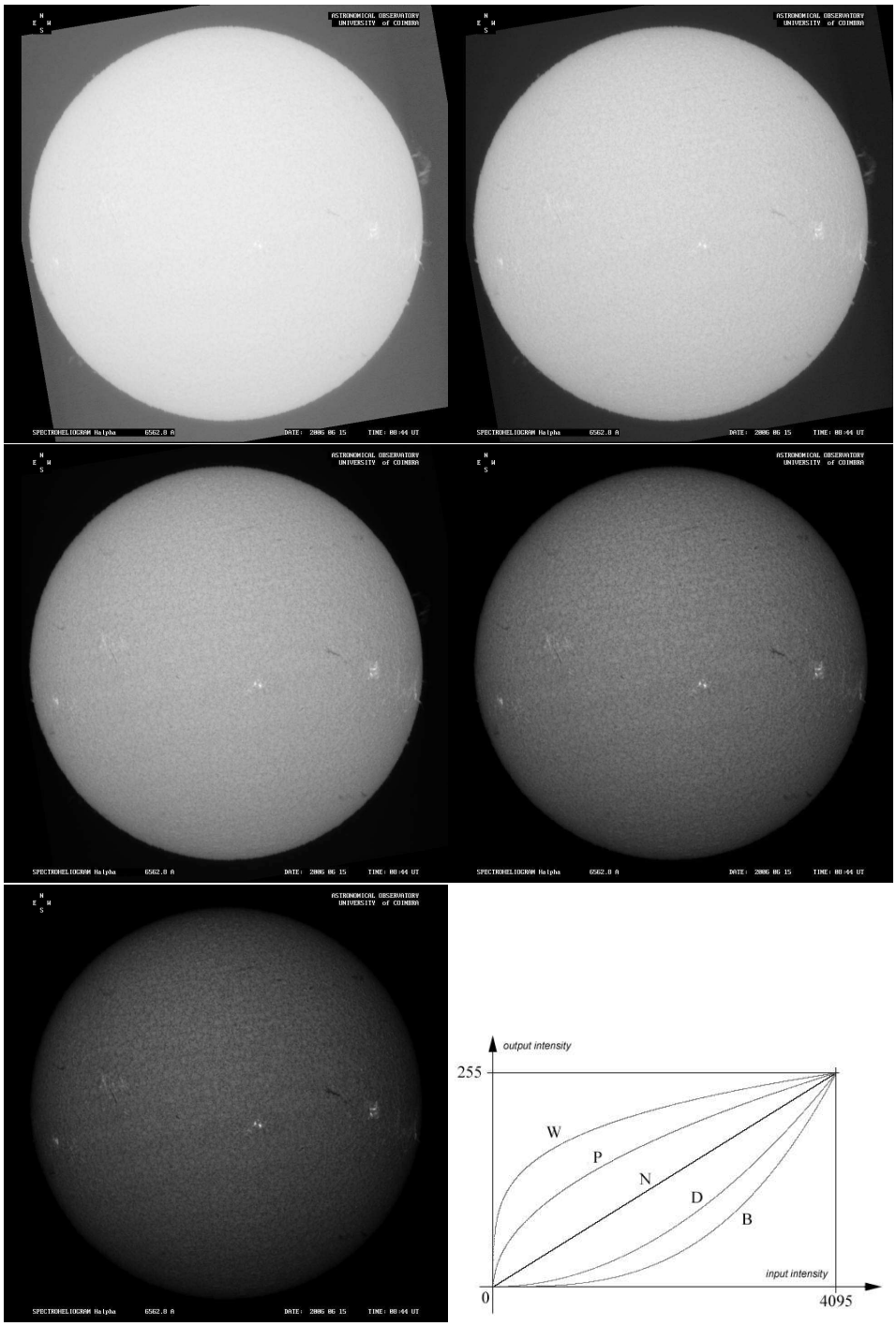

Figure 4. Hα spectroheliogram transformed using different conversion curves: *Upper left*: curve W, *upper right*: curve P, *middle row, left*: curve N, *middle row, right*: curve D, *bottom left*: curve B, *bottom right*: the form of the conversion curves used for visualization of the resulting spectroheliograms. The horizontal axis represents the input brightness.

10. Storage of Spectroheliograms

The eight-bit formats PNG and BMP, responding to the display capability of usual monitors and printers, satisfy fully for the display and print. The described conversion curves can be applied to enhance important parts of the image (prominences, resolving of intensive emission structures on the disk). For digital evaluation we have to use maximal information of all twelve bits without the conversion curves. For this purpose we use the format FITS. Every spectroheliogram in the image directory has its text file, describing the parameters of measurement, mode of its evaluation and containing other data.

11. Conclusions

At the present time, a new CCD-spectroheliograph is tested in a pilot run at the Astronomical institute of Coimbra university. In its development we gained much experience described in this contribution.

Spectroheliograms of the whole disk compared with the spectroheliograms of solar disk segments need more attention, due to the existence of the described effects. As we can see from the presented examples, all these effects can be compensated to obtain spectroheliograms of good quality.

Spectra obtained during full-disk observations allow the imaging of the solar disk in different wavelengths and also computation of the velocity fields using various methods. One possible method which we are going to test with Coimbra Spectroheliograph data is described by Druckmüller et al. (2006).

Acknowledgments. This work could be realized by the efficient support of the grant projects of the Czech Science Foundation (GAČR) 205/04/2129, the Research Plan of the Academy of Sciences of the Czech Republic AV0Z10030501 and a grant project GRICES, Proc. 4.1.1 Ac. Rep. Checa.

References

Klvaňa M., Bumba V., & Garcia A. 2005, Zborník referátov z 17.celoštátného slnečného seminára, I. Dorotovič (ed), Slov. ústred. hvezdáreň Hurbanovo, 207–211 (in Czech)

Lobo da Costa, F. M. 1929, Anais do Observatório Astronómico da Universidade de Coimbra, Tomo I, 7-19

Silva Simoes, A. 1968, Pub. Obser. Astro. Univ. Coimbra, No 4

Technical documentation by Vosskuhler GmbH, Weiss & Breite 7, D-410084 Osnabruck, BRD

Druckmüller, M., Klvaňa, M., Druckmüllerová, Z. 2006, Cent. Eur. Astrophys. Bull, in press

The Physics of Chromospheric Plasmas
ASP Conference Series, Vol. 368, 2007
Petr Heinzel, Ivan Dorotovič and Robert J. Rutten, eds.

The Modernized Solar Spectrograph at Ondřejov

P. Kotrč

Astronomical Institute AS, Ondřejov, Czech Republic

Abstract. The spectrograph of one of the two medium-size horizontal solar telescopes ϕ 500/34850 mm has recently been changed from Czerny-Turner to a multicamera system. Change of the diffraction grating from Bausch & Lomb to a Richardson one enabled to use 4 high speed CCD cameras working simultaneously in 4 diagnostically important spectral lines (Hα, Hβ, He I D3, and Ca II H or K). In addition, the Hα slit-jaw imaging system has been improved and equipped with an identical CCD camera. Another CCD camera operating in white light was implemented to provide information necessary for the observer. Full-disk image taken in Hα is also provided. The VDS Vosskühler CCD cameras (1280 × 1024 pxs, 12 bits) can sample several spectra and filtergrams per second. Data are stored, archived and reduced in an off-line regime. The observing room has been moved from the primary focus to the basement of the pavilion to minimize possible interferences of the sensitive optical device. The observation system is flexible enough with respect to observations of dynamic phenomena of solar activity (flares, prominences, filaments, etc.). Therefore, the observational program is scheduled for any active phenomenon momentarily occurring at the solar disk or limb. The only limitation is weather and season of the year. The program is open for cooperations with other ground based and space born instruments in the frame of existing and future projects. Examples of the data and description of the solar optical spectrograph can be found at `http://www.asu.cas.cz/~pkotrc/index5.html`. Experience obtained during the two years of its initial operation is mentioned. Technical details and scientific plans of the spectrograph are outlined and discussed.

1. Introduction

The beginning of solar optical spectrography at the Ondřejov observatory can be dated 1958 when a Multichannel Flare Spectrograph (MFS) was put into operation (Valníček et al. 1959). The MFS detected spectra of solar flares and prominences on photographic plates sized 13 × 18 cm in seven spectral regions. They encompassed spectral bands from Hα line through D3, Hβ, Hγ, Ca II H and K and the higher members of the Balmer series up to the Balmer limit. The device was modernized several times, as concerns its control (from electronic tubes to the integrated circuits) and the detector changes (from photographic plates through 35 mm film to first analog and then digital CCD video cameras), (see Kotrč et al. 1993; Kotrč 1997). Both the photographic and the video archive of the MFS observations are still a valuable source of solar activity spectra, see the above-mentioned web page. As the MFS was located on the second floor of the rather busy solar department building, its stability was influenced by undesirable disturbances such as frequent vibrations of the sensitive optical system and by medium local seeing conditions. Therefore it was continuously

Figure 1. The HSFA2 telescope is located in a new part of the Ondřejov Observatory, surrounded by forest at altitude of 500 m above sea level. To the left is the coelostat tower, to the right the telescope. The spectrograph pavilion is on the first floor and the controlling room in the basement.

frequently discussed to perform solar spectral observations using other Ondřejov facilities.

In the 1960s a prototype of solar horizontal telescope with a rotating spectrograph was developed and put into operation in a site 50 m west of the solar department building where the MFS was still in use. Its main purpose was to measure solar magnetic fields both using the photoelectric magnetograph and the photographic methods of detecting Zeeman effects (Bumba et al. 1976). Because there were serious problems with the mechanical stability of the rotating spectrograph, it stayed in a fixed position but even so the device has shown itself to be useful. First for the magnetic measurements and secondly for developing a more sophisticated horizontal telescope and spectrograph called the HSFA (abbreviation from the German expression Horizontal Sonnen Forschungs Anlage, i.e. Horizontal Device for Solar Investigations) devices.

A small series of five HSFA telescopes was designed by the Carl Zeiss Jena company according to the experience with the Ondřejov spectrograph and delivered to Czechoslovakia in 1980s. While 2 almost identical devices were built in Slovakia and 1 device sent through Moscow University into Kazakhstan Moun-

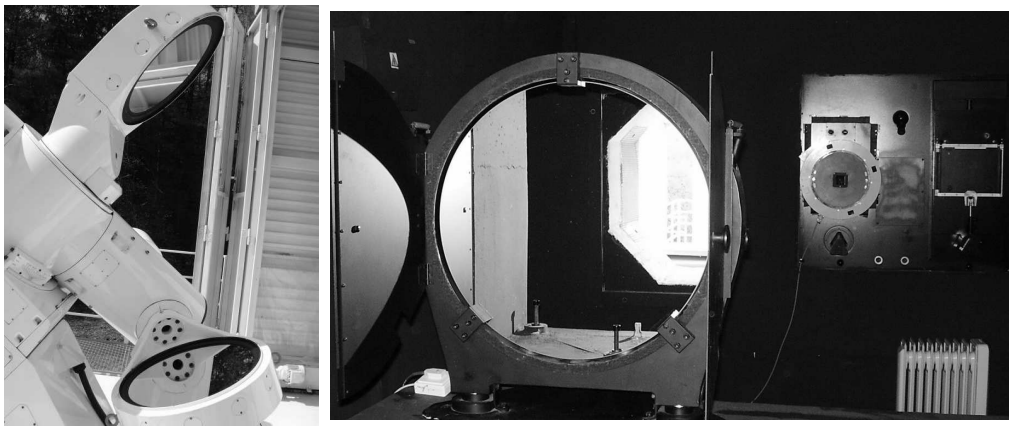

Figure 2. Left: The Jensch-type coelostat consisting of two 60 cm flat mirrors is located $4-6$ m above the ground and is covered by a moving metallic shelter. Right: the main objective has a 50 cm parabolic mirror and 35 m focal length. To the right is the entrance slit of the spectrograph with the rectangular reflecting mirror for the slit-jaw system.

tain Station, another two of the series (i.e. the HSFA1 which was used more or less as magnetograph, while the HSFA2 was dedicated to classical solar spectroscopy with high spectral resolution) were located in the new part of the Ondřejov observatory at about 700 m north of the solar department building. Some parameters of the HSFA2, including the instrumental profile, have been measured by Sobotka & Kotrč (1987). The device was used for optical spectroscopy but also for near-infrared spectroscopy of quiescent prominences (see Heinzel et al. 1986). For a general view of the HSFA2 facility see Fig. 1. The Jensch coelostat and the main objective as well as the slit with the slit-jaw reflective mirror can be seen in Fig. 2.

After two decades of using the two large horizontal solar telescopes with spectrographs at Ondřejov, both the HSFA1 and the HSFA2 underwent important reconstruction. The original designation of the two instruments was mostly preserved. The telescope/spectrograph HSFA1 continues to be used for the measurement of solar magnetic and velocity fields, while HSFA2 would be rebuilt to a multichannel spectrograph equipped with CCD cameras. The reconstruction of the electronic control systems was the most important task. The up-to-date electronic equipment enables remote control of numerous functions of the instruments. It also offers a large amount of automated procedures and it is resistive to disturbances caused by atmospheric electricity. While the previous system needed a full operator's assistance, the new telescope/spectrograph control system is designed to reduce and simplify the observer's work as much as possible. A concept for the reconstruction of the electronic control systems of the two large horizontal solar telescopes with spectrographs has been described by Klvaňa et al. (2001).

It has to be pointed out that in the same period when the two HSFA devices were built, used and then reconstructed and modernized, the theoretical

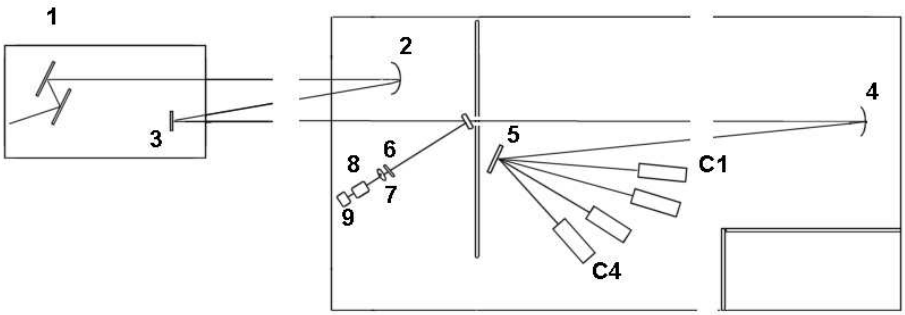

Figure 3. Optical schema of the telescope and spectrograph. 1 - ϕ 60 cm coelostat mirrors, 2 - main objective ϕ 500 mm / f 34850 mm, 3 - secondary flat mirror ϕ 320 mm, 4 - collimator ϕ 250 mm / f 10000 m, 5 - diffraction grating, C1 ... C4 are the CCD cameras for individual spectral regions. Slit-jaw system: 6 - broad band filter, 7 - objective, 8 - narrow band Hα filter Day Star, 9 - CCD camera.

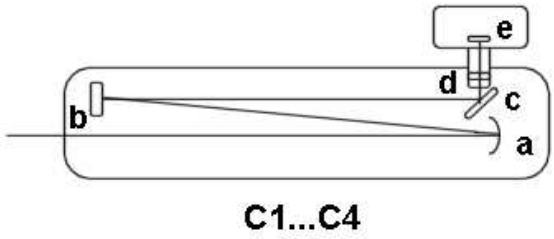

Figure 4. Imaging systems for each of the four CCD cameras C1 ... C4 in the spectrograph: a = main objective mirror ϕ 200 mm / f 2500 mm, b = flat mirror, c = elliptical flat mirror, d = slab for correction of astigmatism and coma, e = CCD camera.

capability in Ondřejov grew substantially as well. It enabled to interprete solar spectra on a qualitatively higher level for better understanding.

2. Technical Parameters

The spectrograph was rebuild from the Czerny-Turner configuration to the multicamera version, see Fig. 3. The goal of the rebuilding was to enable simultaneous spectral observations in several diagnostically important lines with the best possible spectral and temporal resolutions. We had to respect the limited depth of the building. Therefore we carried out optimization of the imaging optics for CCD cameras with small chips for various options of the current and for a different diffraction grating (Kotrč & Kschioneck 2003). We suggested optical schema with a folded pattern of beams, (the main camera mirror ϕ 200 mm, f 2500 mm) and put it in practice, see Figs. 3, 4, and 6.

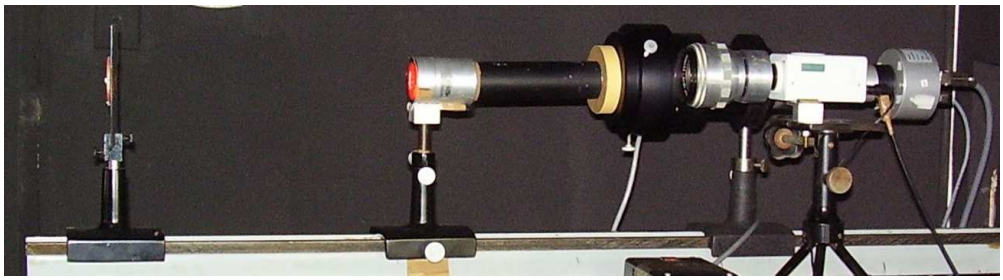

Figure 5. A detailed view on the slit-jaw system with a monochromatic filter in the Hα line. In the foreground to the right is located an auxiliary telescope with a video camera or providing information about position of the solar image in the slit plane.

The lines were selected considering their diagnostic importance as well as their location in the spectrograph: Hα (6563 Å), D3 (5875 Å), Hβ (4861 Å), Ca II K resp. Ca II H (3934 resp. 3968 Å). Unfortunately, the Ca II IR 8542 Å is so close to the Hα line, that both of them can not be observed simultaneously. In addition, the used CCD chip would have rather small sensitivity (less then 10% in the near IR) which would complicate the regime of exposures. Then, instead of the one large photographic detector in the former Czerny-Turner spectrograph we now have 5 CCD cameras. Four of them are placed at these lines and the fifth is part of the new slit-jaw system, see Fig. 5.

The former diffraction grating from Bausch & Lomb with $C = 632.1$ mm^{-1}, width $W = 206$ mm, height $H = 154$ mm, angle of incidence $\varphi = 51°$, and with maximum intensity concentrated into the 4th order was replaced by the Richardson grating, $C = 1200$ mm^{-1}, width $W = 206$ mm, height $H = 154$ mm, blaze angle $\varphi = 17.5°$, and with maximum light concentrated into the 1st order. Therefore, after the grating replacement the spectral resolving power decreased from 521 000 to 247 000. Thus, the spectral resolution $\Delta\lambda$ for the Hα line is 26 mÅ while for Ca II H or Ca II K the spectral resolution is 16 mÅ. These values in combination with new small size detectors mean that the results are quite satisfactory.

The fast CCD cameras VDS Vosskühler CCD-1300LN have pixel size 6.7μm $\times$6.7μm, chip size $s = pH \times pV = 1280(H) \times 1024(V)$ pixels and are combined with Matrix Vision grabbers. They are 12 bits and each camera has its own controlling PC. All the PCs are linked to a local network connected with the telescope/spectrograph controlling server, see Fig. 7.

The cameras can operate either in full chip resolution s or with binning $s1 = pH \times pV = 1280(H) \times 512(V)$. They can be handled either with an asynchronous or synchronous shutter, have exposure range of 1/10 000 till 10 s, reading noise ≤ 14 e, saturation at > 25000 e. The grabber contains a digital 12-bit output RS-644, the chip quantum efficiency reaches up to 50% in the region from 4800 Å till 5500 Å and then slowly decreases to near IR wave bands. The dynamic range is 1 : 2000.

As compared with the MFS (Kotrč 1997), the HSFA2 device brought several advantages as it was our first professionally-made instrument with better optics

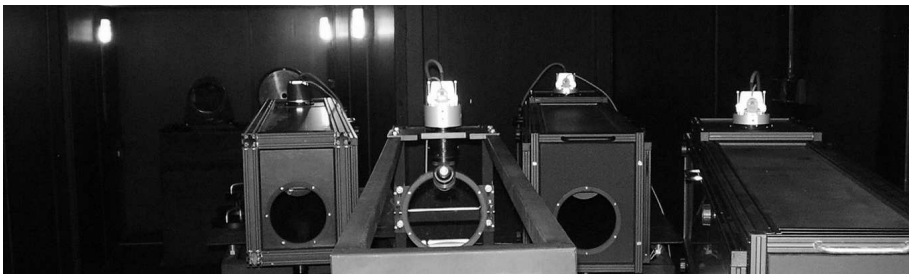

Figure 6. Imaging objectives of individual spectral cameras. The main camera mirror ϕ 200 mm, f 2500 mm can be seen through the open construction. At the top the four Vosskühler CCD cameras are situated.

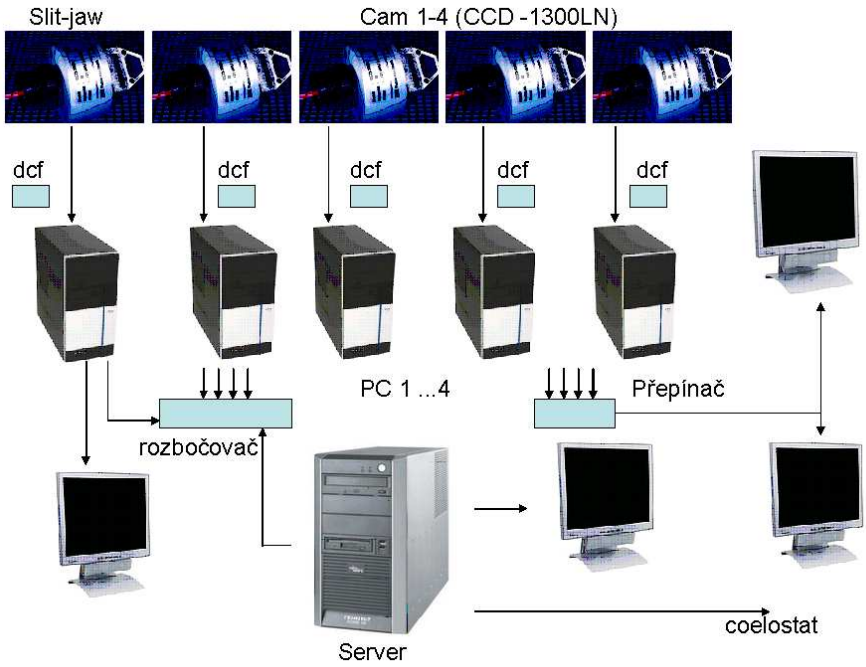

Figure 7. Interconnection of the CCD cameras, time signal DCF and other spectrograph technical parts. The term *rozbocovac* means a hub, while *Prepinac* stands for a switch of monitors.

and electronics, and placed into better seeing conditions with minimal external disturbances, etc. As concerns the weaker points, the short depth of the pavilion can be mentioned as well as a limited usage when the outdoor temperature is less than 0° C due to oil viscosity in the hydraulic bearings as the Jensch coelostat is laid on oil seal.

The solar image at the primary focus has a diameter of 35 cm. When this large size is combined with small CCD chip, fast orientation over the solar disk is difficult. Therefore the full solar disk is additionally observed with a small

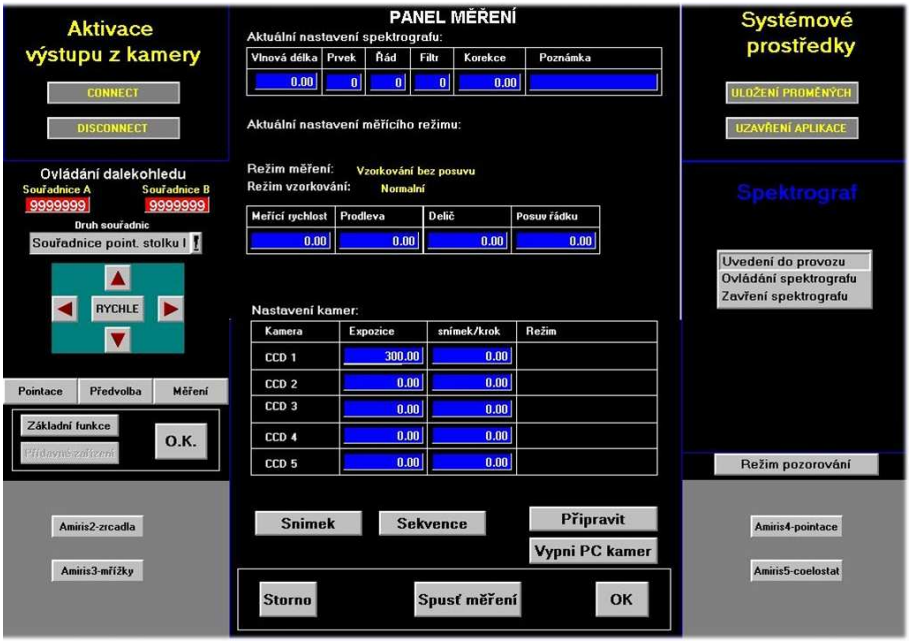

Figure 8. The controlling code of the main server gets information and provides all operations from only one access point by clicking the mouse on the screen.

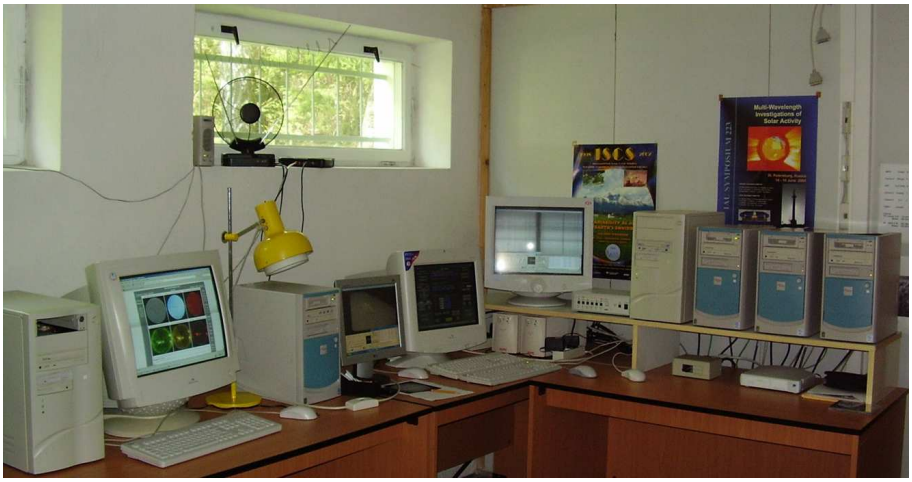

Figure 9. Before the reconstruction the observer controlled the spectrograph and telescope with a handbox near the entrance slit. Now his working place is a comfortable room in the basement of the pavilion to minimize man-made vibrations and heating.

auxiliary telescope of 1 m focus through a Hα Coronado filter. Thus the observer has complete information what is going on at the solar disk.

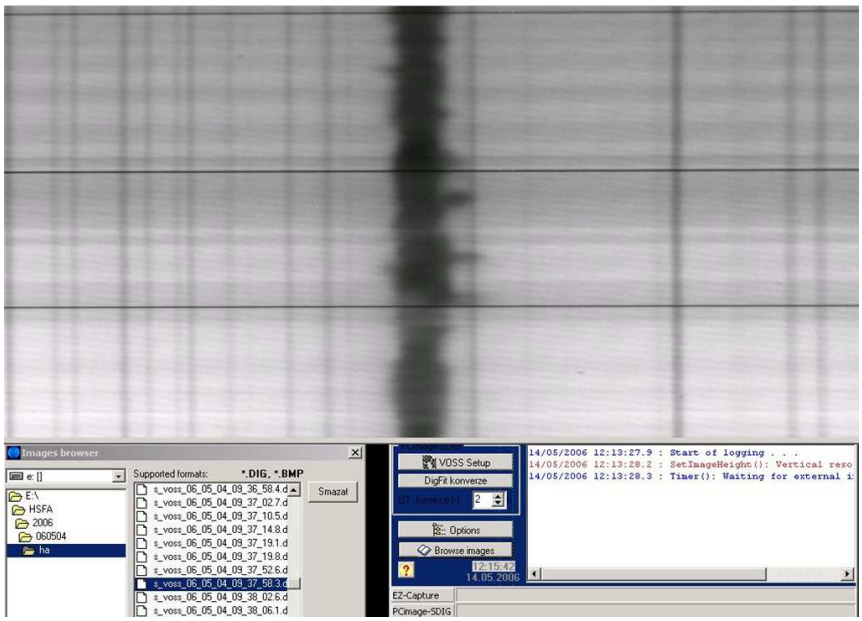

Figure 10. The observer has information about the quality of the spectrum (Hα in this case) on the same monitor where the list of recorded files is displayed.

Then, for more convenient work with the archive data, a linux server is connected to the data-aquisition PCs and daily observations are converted from internal *.dig files into *.fts files and moved to a disk field memory for further processing. It also performs dark frames subtraction and flat-fielding.

3. Conclusions

When we compare spectra and filtergrams of the MFS with those of the HSFA2 we notice a substantial improvement in almost all parameters, especially in spatial and spectral resolution. The dynamical range of the detected signal has improved from 8 to 12 bits. Though the temporal resolution has decreased from 25 to about 5 frames per second, it is still a satisfactory cadence when we take into account the high spectral resolution and dispersion, see Fig. 12. A key advantage of the HSFA2 is its continual readiness and availability for observations at the selected spectral lines anytime whenever the scientific interest needs it, e.g. when an ephemeral solar activity phenomenon appears on the Sun. The only limitations for observation are the weather, time of the day and season. A substantial improvement is also the decreased level of scattered light in the spectrograph and in the slit-jaw telescope, see the example in Fig. 11 and monitoring of the full solar disk in Hα filter.

There are still many plans to be realized, e.g., improving the quality of the spectral images, installation of better entrance slit, a better handling and automation processing of the data. After improving and finishing these projects

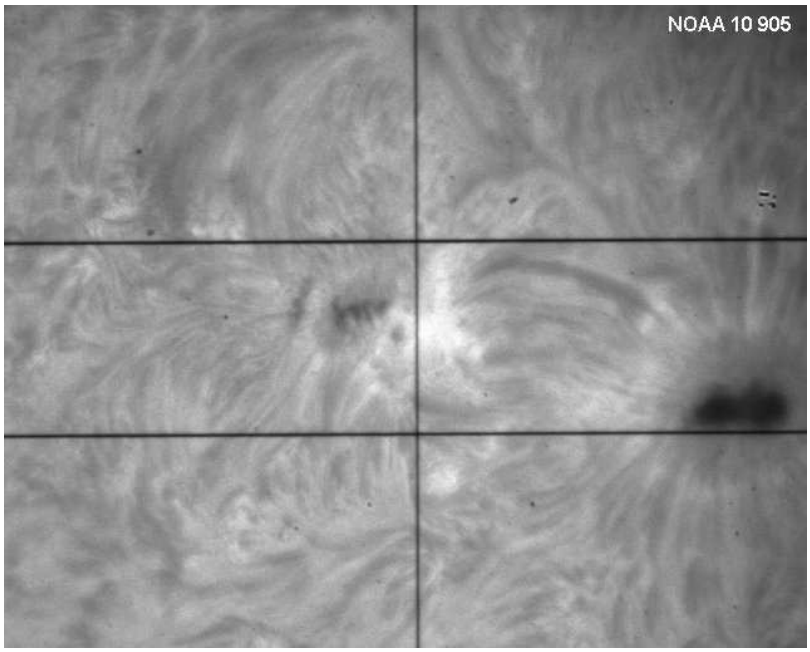

Figure 11. The NOAA 10905 active region on 24th August 2006 at 08:10:06 UT as observed through slit-jaw Hα filter (Day Star 0.5 Å University Series).

we would like to share all the data on the web on demands. However, it needs more time and funds. Nevertheless, when one compares the spectra obtained at the beginning of the HSFA2 testing operations with the latest images, see `http://www.asu.cas.cz/~pkotrc/2006.html`, quite a good progress in many aspects has been achieved.

Taking into account that the HSFA2 is competitive in its availability, offers a high temporal and relatively good spectral resolution, as well as the availability of other optical and radio observatings at the Ondřejov observatory (see Kotrč et al. 1995; Ambrož & Kotrč 2002), we consider the main HSFA2 targets as follows:

- long-sequence observation of ephemeral solar activity phenomena like flares, eruptive prominences, surges, filaments etc. with high temporal and quite good spectral resolution;
- getting special observations for advanced spectral diagnostics and modeling of solar phenomena;
- participation in international coordinated observing campaigns;
- ground based observations for support of space missions like Hinode etc.;
- education and practical training of undergraduate and graduate students in spectroscopy;
- testing of new observation and detection technics.

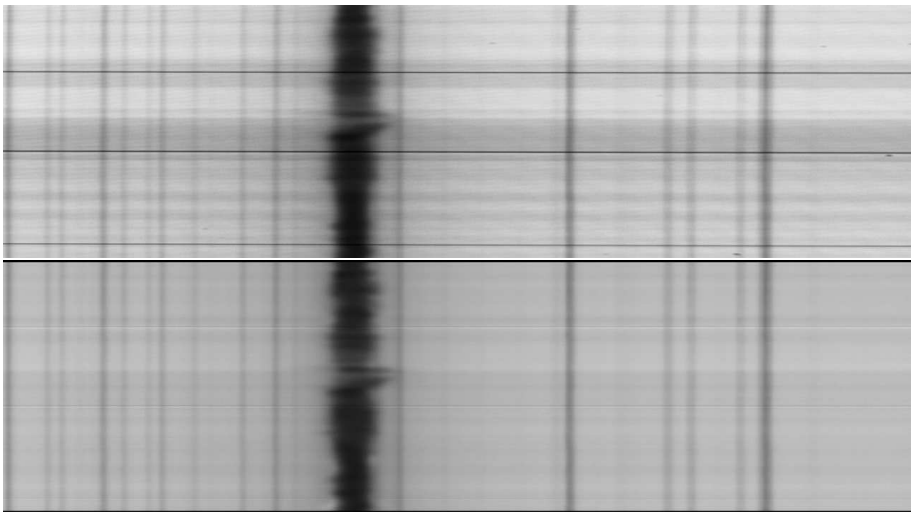

Figure 12. Top: A raw Hα spectrum of the NOAA 10905 active region before flat fielding. Bottom: The same after flat fielding.

Acknowledgments. This work was partly supported by grants A3003203 of the Grant Agency of the Academy of Sciences of the Czech Republic, institutional project AV0Z10030501, the project No. 95 of the Czech - Slovak cooperation and the European Solar Magnetism Network (ESMN-HPRN-CT-2002-00313). The author would like to express his gratitude to the HSFA2 observers, namely Yu. A. Kuprjakov and J. Leško for their precise work as concerns observations and for many ideas that steadily improve the parameters of the device. The snapshots were taken by I. P. Pavlenko.

References

Ambrož P., Kotrč P., 2002, in A. Kučera (ed.), Joint Organization for Solar Observations, Annual Report 2001/2002, 50

Bumba V., Klvaňa M., Macák P., 1976, Bulletin of the Astronomical Institutes of Czechoslovakia 27, 257

Heinzel P., Kotrč P., Sobotka M., Zloch F., Scherbakova Z. A., 1986, Contributions of the Astronomical Observatory Skalnaté Pleso 15, 171

Klvaňa M., Kotrč P., Knížek M., Sobotka M., Heinzel P., 2001, Astronomische Nachrichten 322, 371

Kotrč P., 1997, Hvar Observatory Bulletin 21, 97

Kotrč P., Heinzel P., Karlický M., Knížek M., Jiřička K., 1995, in M. Saniga (ed.), Joint Organization for Solar Observations, Annual Report 1994, 196

Kotrč P., Heinzel P., Knížek M., 1993, in A. von Alvensleben (ed.), Joint Organization for Solar Observations, Annual Report 1992, 114

Kotrč P., Kschioneck K., 2003, in A. Wilson (ed.), ESA SP-535: Solar Variability as an Input to the Earth's Environment, 717

Sobotka M., Kotrč P., 1987, Bulletin of the Astronomical Institutes of Czechoslovakia 38, 272

Valníček B., Letfus V., Blaha M., Švestka Z., Seidl Z., 1959, Bulletin of the Astronomical Institutes of Czechoslovakia 10, 149

The Physics of Chromospheric Plasmas
ASP Conference Series, Vol. 368, 2007
Petr Heinzel, Ivan Dorotovič and Robert J. Rutten, eds.

Hα Observations at Modra-Piesok

Alena Kulinová, Elena Dzifčáková, Dušan Kalmančok and Pavol Zigo

Faculty of Mathematics, Physics and Informatics, Comenius University, Bratislava, Slovak Republic

Abstract. We describe the Hα solar telescope of the Astronomical and Geophysical Observatory (AGO) in Modra-Piesok in Slovakia. The instrument is a refractor with $f = 304$ cm and $D = 8$ cm and equipped with a broadband interference Hα filter. Its width has the advantages that coalignment with photospheric images is easier and that Dopplershifted features such as prominence legs do not shift out of the passband. The field of view is approximately 6×4 arcmin^2. The daily observations are recorded on videotapes. The digitalized images are planned to be put on AGO webpage.

1. Introduction

The Astrophysical and Geophysical Observatory (AGO) in Modra-Piesok belongs to the Department of Astronomy, Physics of the Earth and Meteorology at the Faculty of Mathematics, Physics and Informatics of Comenius University in Bratislava, Slovak Republic. Modra-Piesok is situated about 50 km to northwest from Bratislava, in the Little Carpathian mountains. The observatory is located at an altitude of 535 meters with geographical coordinates: lon 17.274E, lat 48.373N.

2. Telescope and Equipment

The telescope used for Hα observation of solar flares, active regions and prominences is a refractor on a parallactic mount with a Zeiss objective of 20 cm in diameter and a focal length of $f = 304$ cm. The scheme of the observing assembly is depicted in Fig. 1. Actually, in the Hα observations the entrance aperture is reduced to $D = 8$ cm by the blocking pre-filter which was part of previously used prominence Hα filter set. Another blocking filter is an interference filter (Andover Corporation) with FWHM = 9.91 Å and central wavelength 6564 Å. The Hα filter itself has FWHM = 1.43 Å centered on 6563 Å. It is also a metallic interference filter produced by Andover Corporation. The transmission of both filters is shown in Fig. 2. The Hα filter is maintained at its working temperature 23° C; the wavelength can be tuned by changing the inclination of the filter with respect to the light beam. The stray light in the system is minimized by aperture stops. To register the image a commercial 8-bit TV CCD camera with 1/3 inch chip (795×596 pixels) is used. The field of view is approximatelly 6×4 arcmin^2.

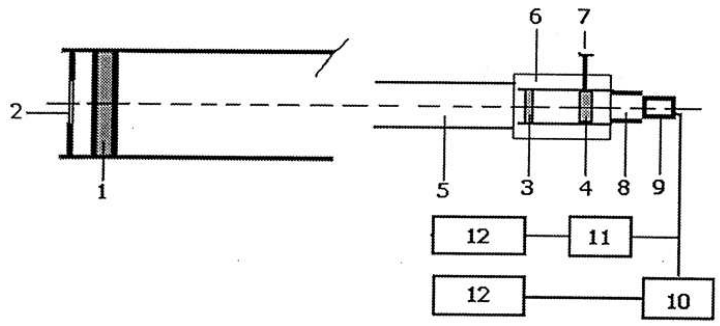

Figure 1. The scheme of the AGO, Modra-Piesok Hα telescope: 1 – objective, 2 – blocking pre-filter, 3 – red blocking filter, 4 – Hα filter, 5 – aperture minimalising the stray light, 6 – filter thermalising assembly (working temperature is 23°), 7 – filter tuning, 8 – focusing and iris aperture, 9 – TV CCD camera, 10 – VHS videorecorder, 11 – grabber, 12 – PCs.

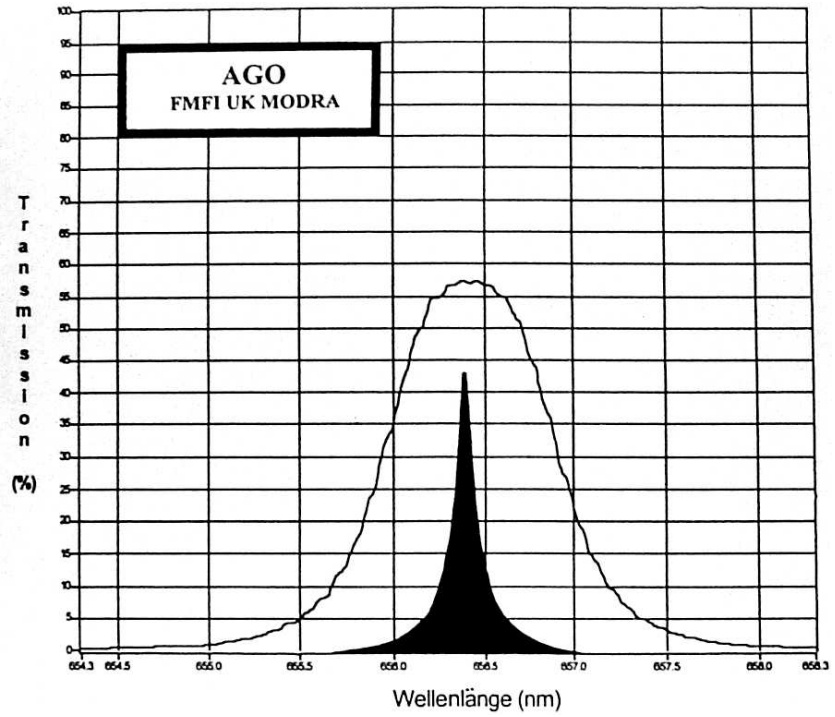

Figure 2. Transmission of the blocking filter (black curve) and the rather wide Hα filter (dark shading).

3. Observations

The daily observations are recorded on VHS videotapes. After finishing an observing day the tapes are inspected, and in case of interesting event and good

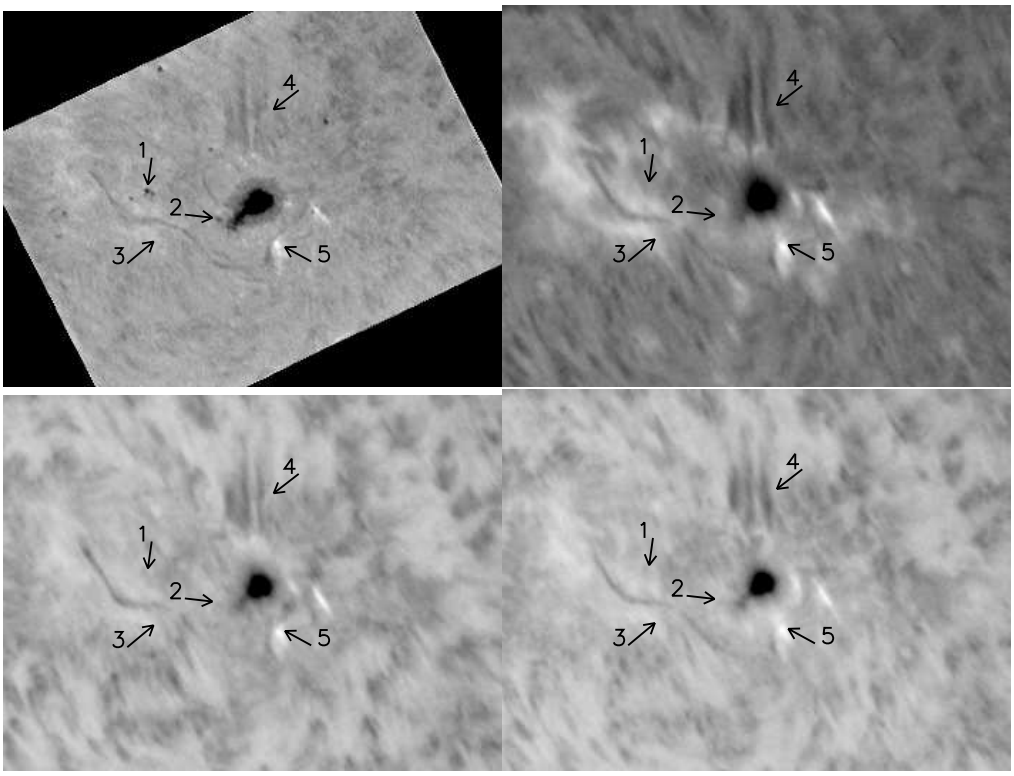

Figure 3. This set of images consists of a Hα filtergram from AGO and three images obtained with the Meudon Spectroheliograph on March 31, 2004 about 08:54:36 UT. The original fits file from Meudon included 5 full-disk images. We present here image 3 (central Hα) and images 1 & 5 taken in the wings of the Hα line (blue and red, respectively). For comparison the approximately the same field of view is shown. The arrows mark the position of the five structures in the AGO image and refer to the same positions at other images.

weather conditions (seeing) the events are digitalized by commercial software. The field of view of CCD camera is approximately 6×4 arcmin^2; the full-resolution digitalized image measures 640×480 pixels. When digitalizing the tape one can usually find two to three images with good seeing within one second. However, the seeing conditons are often moderate.

An example of our data can be found in Fig. 3. The first image is from AGO while the other three are from the Meudon Spectroheliograph. The second image in Fig. 3 was obtained in the center of Hα, the bottom two in the wings of Hα. The arrows 1 and 2 in AGO image mark well-observed small sunspots which are not visible at the center of the Hα line in the Meudon spectroheliogram. On the contrary, the plage under the filament (arrow 3) is not as bright as it is in the center of the Hα line. This is due to the higher continuum contribution in our filtergrams. Dark filaments and structures are visible in all four images. Bright structures (arrow 5) are well observed in all images too.

Good visibility of small sunspots is very useful when coaligning with white-light data from other instruments. Due to our wider filter we are also able to

observe moving structures without tuning the filter, and usually we observe at once all parts of a filament vissible in the center and both the wings of Hα. However, we have smaller contrast in our images.

The observations are provided daily depending on weather conditions. Internet archiving is not available yet but is planned for the future. Some examples of our observations are available at `http://cyril.fmph.uniba.sk/~AGO/`.

Acknowledgments. We thank the CSPM organisers for a very good meeting. ED and AK would like to thank the Solar Department of Ondrejov Observatory for supporting us to take part in the conference. This work was supported by the Scientific Grant Agency VEGA, Slovakia, grant No. 1/2026/05. The Meudon spectroheliograph data were obtained from the archive at `http://bass2000.obspm.fr/home.php`.

The Physics of Chromospheric Plasmas
ASP Conference Series, Vol. 368, 2007
Petr Heinzel, Ivan Dorotovič and Robert J. Rutten, eds.

Aperture Increase Options for the Dutch Open Telescope

R. H. Hammerschlag, F. C. M. Bettonvil, A. P. L. Jägers and R. J. Rutten

Sterrekundig Instituut, Utrecht University, The Netherlands

Abstract. This paper is an invitation to the international community to participate in the usage and a substantial upgrade of the Dutch Open Telescope on La Palma (DOT, `http://dot.astro.uu.nl`).

We first give a brief overview of the approach, design, and current science capabilities of the DOT. It became a successful 0.2-arcsec-resolution solar movie producer through its combination of *(i)* an excellent site, *(ii)* effective wind flushing through the fully open design and construction of both the 45-cm telescope and the 15-m support tower, *(iii)* special designs which produce extraordinary pointing stability of the tower, equatorial mount, and telescope, *(iv)* simple and excellent optics with minimum wavefront distortion, and *(v)* large-volume speckle reconstruction including narrow-band processing. The DOT's multi-camera multi-wavelength speckle imaging system samples the solar photosphere and chromosphere simultaneously in various optical continua, the G band, Ca II H (tunable throughout the blue wing), and Hα (tunable throughout the line). The resulting DOT data sets are all public. The DOT database (`http://dotdb.phys.uu.nl/DOT`) now contains many tomographic image sequences with 0.2-0.3 arcsec resolution and up to multi-hour duration. You are welcome to pull them over for analysis.

The main part of this contribution outlines DOT upgrade designs implementing larger aperture. The motivation for aperture increase is the recognition that optical solar physics needs the substantially larger telescope apertures that became useful with the advent of adaptive optics and viable through the DOT's open principle, both for photospheric polarimetry at high resolution and high sensitivity and for chromospheric fine-structure diagnosis at high cadence and full spectral sampling.

Our upgrade designs for the DOT are presented in an incremental sequence of five options of which the simplest (Option I) achieves 1.4 m aperture using the present tower, mount, fold-away canopy, and multi-wavelength speckle imaging and processing systems. The most advanced (Option V) offers unblocked 2.5 m aperture in an off-axis design with a large canopy, a wide 30-m high support tower, and image transfer to a groundbased optics lab for advanced instrumentation. All five designs employ adaptive optics. The important advantages of fully open, wind-transparent and wind-flushed structure, polarimetric constancy, and absence of primary-image rotation remain. All designs are relatively cheap through re-using as much of the existing DOT hardware as possible.

Realization of an upgrade requires external partnership(s). This report about DOT upgrade options therefore serves also as initial documentation for potential partners.

1. Introduction

During the late 1990s the Dutch Open Telescope (DOT, Fig. 1 and `http://dot.astro.uu.nl`) was the pioneering demonstrator of the open-telescope technology now pursued in the German GREGOR and BBSO NST projects and inspirational to the US ATST project. These projects capitalize on the advents in wavefront restoration through adaptive optics (AO) and numerical image processing which now enable meter-class image sharpness, far beyond the best Fried-parameter values at any site, and so require telescope technology beyond the 1-m evacuated-telescope technology limit realized by the Swedish 1-m Solar Telescope (SST). In the meantime the 45-cm DOT became an outstanding supplier of solar-atmosphere movies sampling the photosphere and chromosphere simultaneously at up to 0.2 arcsec resolution (Section 2). The resulting image sequences are publicly available for analysis (Section 3).

The major science drivers for aperture increase beyond the SST are:

1. *Photosphere*: precise, deep, and complete Stokes polarimetry at high angular resolution, preferably combining visible and infrared lines in 2-D mapping. Targets: umbrae, penumbrae, pores, plage and network magnetic elements, internetwork fields, etc.
2. *Chromosphere*: high to very high cadence profile-sampled narrow-band imaging in chromospheric lines, in particular Ca II H&K with spectral sampling throughout the extended line wings in order to follow dynamic phenomena with height throughout the upper photosphere and low chromosphere, and the Ca II infrared lines and the Balmer lines with full profile mapping in order to disentangle the complex opacity, source function, and Doppler sensitivities that make the chromosphere such a rich scene in these lines. Targets: filaments, active regions, mottles/fibrils/spicules, Ellerman bombs, flares, wave patterns, shock dynamics, etc.

For both, sufficient photon collection is the principal large-aperture motivation. To freeze the seeing no exposure should exceed 10 ms, also for narrow-band diagnostics. Multi-frame image collection for MOMFBD restoration (van Noort et al. 2005) or many-frame collection for speckle reconstruction must be completed within the solar-change time per resolution element, including spectral profile sampling as necessary. The change time becomes shorter for larger angular resolution and can be much shorter than the sound-speed crossing time, as demonstrated by the recent 1-s-cadence Hα movies of van Noort & Rouppe van der Voort (2006).

These science motivations plus the fact that the 50-cm SOT onboard Hinode duplicates many current DOT capabilities at a much higher duty cycle (no bad seeing, no bad weather, no nights during its non-eclipse seasons) led us to the larger-aperture designs discussed below. In Section 4 we outline how conversion of the 45-cm DOT into a larger solar telescope is not only feasible but actually a relatively cheap venue to meter-class angular resolution through using existing parts where possible. We focus on 1.4-m and 2.5-m strawman designs in a sequence of options ranging from minimum cost to maximum science capability.

We cannot realize such DOT upgrades on our own; they require external support. At present the DOT is run on a budget of about 250 kEuro/year covering salaries (excluding the first and last author who are academic staff), travel

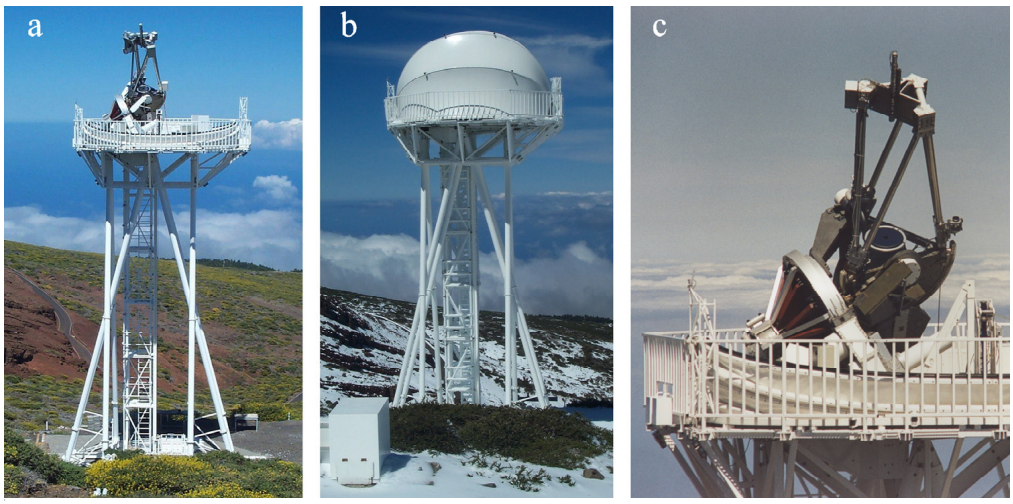

Figure 1. The existing DOT with 45-cm primary mirror at 2350 m altitude on La Palma.
(a) The DOT in operation. The 15-m tower and the telescope are sufficiently transparent to not disturb the wind which maintains temperature homogeneity in and around the telescope. At sufficient wind strength (7 km/h can be enough depending on the wind direction) the larger temperature fluctuations occurring near ground level do not reach the telescope. The special tower geometry keeps the platform parallel to the ground even under strong wind loads. The clam-shell canopy is opened completely for observations.
(b) When not in operation the telescope is protected by closing the folding canopy. It is made of strong tensioned polyester cloth with an outer PVDF coating on which snow and ice do not stick. The canopy can be opened and closed within a few minutes in winds up to 100 km/h. When closed it can withstand much stronger winds, and has already survived storms of 200 km/h.
(c) The telescope close-up. The primary mirror and the optical beam to the primary focus are fully open to wind. The DOT was the first telescope showing that such an open air path can permit diffraction-limited resolution. Note that the primary mirror is located well above the declination axis of the equatorial mount. It sticks out high above the platform into full wind flushing.

to La Palma and equipment, plus an additional allocation of up to 3000 man-hours/year of Utrecht University workshop effort encompassing mechanical design and fabrication as well as electronics and software development in very close collaboration with the DOT team. Our present funding covers these costs up to 2008, but not beyond that date while a larger budget is required to realize and operate a larger telescope (Section 5). This paper is therefore intended as initial documentation for potential partners.

2. DOT Technical Overview

The DOT performs so well thanks to the combination of *(i)* its wind-swept oceanic mountain site at the Observatorio del Roque de los Muchachos on the Canary Island La Palma, *(ii)* minimum obstruction to the wind by the very open tower, the very open telescope, and the fully-folding canopy, *(iii)* effective

wind-flushing of the open telescope, *(iv)* short-exposure speckle imaging, and *(v)* the consistent application of speckle restoration in an on-site processor farm.

The DOT design and construction are characterized by rigorous adherence to its open principle and large emphasis on mechanical stability. The open tower, fold-away canopy, and equatorial telescope mount are highly transparent to the fairly laminar Northern trade winds that bring the best seeing at the Roque de los Muchachos. They don't spoil the seeing; in addition, the wind flushes the telescope interior faster than internal turbulence can develop. The remaining higher-layer wavefront aberrations are corrected through speckle processing. Its advantages are that it restores the full field of observation in equal measure and that it delivers rather good results already at relatively poor seeing. It requires a large amount of post-processing but this has been remedied with the parallel DOT Speckle Processor in a nearby building. The complete system delivers 0.2 arcsec diffraction-limited image quality whenever the seeing is reasonable, already at Fried-parameter values of order 6-10 cm. At La Palma such seeing sometimes occurs during multiple hours.

During the past years the DOT has been equipped with an elaborate multi-wavelength imaging system harboring six identical speckle cameras that register wide-band continua in the blue and red, the G band at 4305 Å, Ca II H with an interference filter that can be tuned per speckle burst through the blue line wing, and narrow-band Hα using a 250 mÅ FWHM Lyot filter that can also be tuned per speckle burst. Two-channel speckle reconstruction following Keller & von der Lühe (1992) permits the registration of multi-wavelength Hα movies at 20-30 s cadence or single-wavelength Hα movies at much faster cadence.

The DOT is usually manned from early spring until late autumn, usually with the first author taking care of the telescope operation and P. Sütterlin in control of all observing and speckle processing. A typical two-week campaign delivers on average 5–6 days with good data. Thanks to the parallel processing the data now become available soon after the campaign.

More detail is given in Hammerschlag (1981) for the original DOT design description, Rutten et al. (2004a, 2004b) for general overviews, Hammerschlag et al. (2006a) for the tower design, Bettonvil et al. (2006) for the multi-wavelength imaging, Snik et al. (2007) for ongoing work on Ba II 4554 polarimetry, and Bettonvil et al. (2004) for an earlier description of a DOT upgrade to 1.4 m aperture. All DOT papers are available at `http://dot.astro.uu.nl`.

3. DOT Database

All DOT data are public. The DOT has collected high-resolution movies of the sun since the autumn of 1999 in an increasing number of spectral diagnostics. The yearly harvest increased markedly in 2005 with the advent of the large-volume parallel DOT Speckle Processor. The DOT database resides at ftp site `ftp://dotdb.phys.uu.nl/` and has a user-friendly graphical interface at `http://dotdb.phys.uu.nl/DOT/` which for every day with worthwhile data serves a thumbnail pictorial index of what was collected. It also specifies the target, observing mode, time of observation, cadence, solar disk location, average seeing quality (Fried parameter r_0), a link to the pertinent Mees active region map, a burst-by-burst plot of the Fried parameter, and a "Get data" link to the

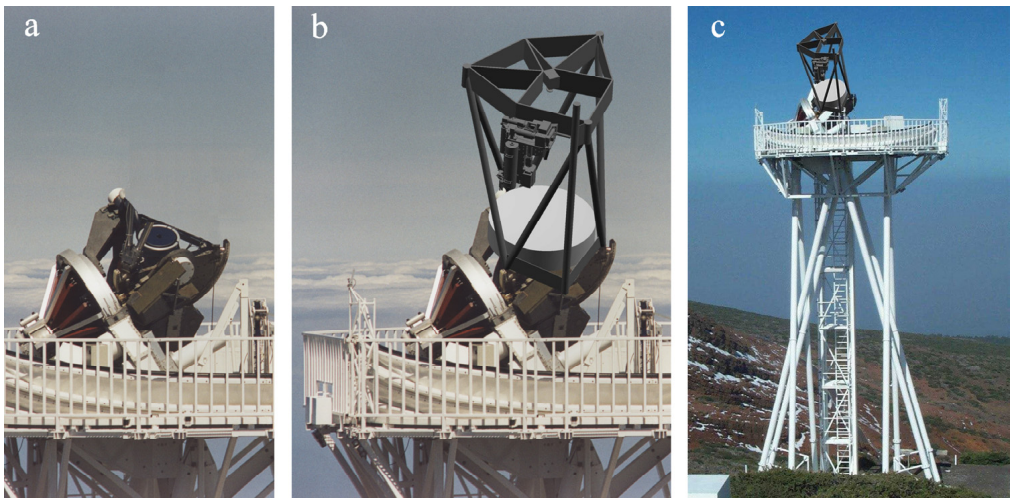

Figure 2. Option I: DOT upgrade to 1.4-m aperture.
(a) Remove the existing telescope top.
(b) Place a new mirror with a new mirror support on the existing equatorial mount, add a new telescope top, relocate the existing multi-channel imaging system to its side, and add a new prime-focus optics package. The optical scheme is shown in Fig. 3.
(c) The result – in observing position – on top of the existing tower. At a focal length of $f = 2.3\,\mathrm{m}$ the telescope can still be parked within the existing 7-m canopy.

corresponding directory in the DOT database. The basic DOT data product consists of FITS files per speckle-reconstructed image, but for many runs the data base also serves processed and aligned image sequences as data cubes.

You are welcome to use any DOT data for detailed analysis. Explanation and IDL reading instruction is given under "DOT data" at `http://dot.astro.uu.nl`. Questions should go to P.Suetterlin@astro.uu.nl.

We plan to integrate the DOT data base into the Virtual Solar Observatory (`http://sdac.virtualsolar.org`) and to add more search capability as well as other user commodities.

4. DOT Upgrade Designs

In the remainder of this contribution we present a range of options to increase the DOT aperture to meterclass size, in order of increasing gain in science capability and cost.

4.1. Option I: upgrade to 1.4-m aperture

The simplest, Option I, is to upgrade the existing DOT with 45-cm primary mirror shown in Fig. 1 to 1.4-m aperture by removing the existing telescope top, placing a new mirror support with a new 1.4-m mirror with focal length $f = 2.3\,\mathrm{m}$ (opening ratio $f/1.64$) on the existing telescope mount, adding a new prime-focus optics package (secondary parabolic mirror, two flat mirrors

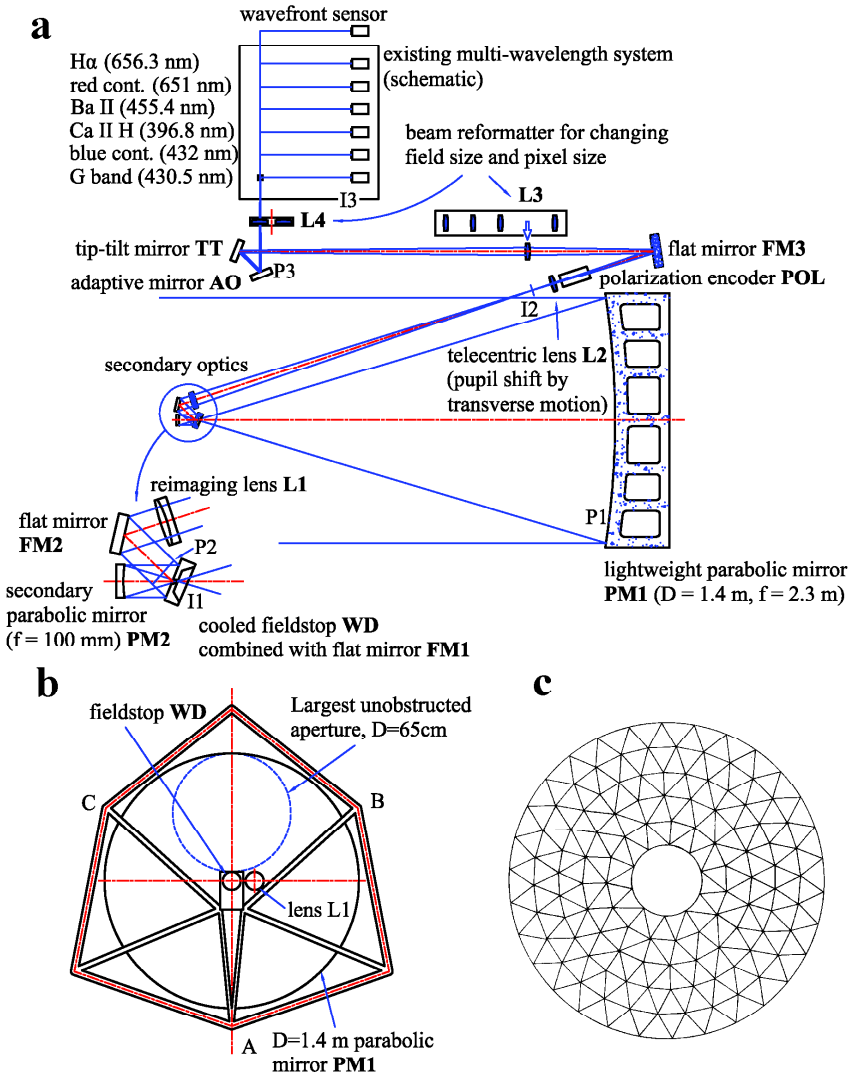

Figure 3. Optical layout of Option I with 1.4-m primary mirror. *(a)* Side view. The parabolic primary and secondary mirror together are coma-free to produce diffraction-limited quality over the full field of view. L1 produces an enlarged image I2 near the field lens L2. The ensembles of interchangeable lenses L3 and L4 produce user-selectable choice between angular resolution and field size whereas transverse translation of telecentric field lens L2 offers transversal pupil shift.
(b) Top view of the aperture = primary mirror with spider shadow. Transversal pupil shift allows obstruction-free apertures up to 65 cm (circle in the upper part). The inclined flat mirrors FM1 and FM2 reflect the light in perpendicular directions to compensate partial polarization. *(c)* Alternative spider design using very thin plates gradually spreading in all directions to obtain a diffraction pattern without pronounced ghosts. Such spider geometry can be optimized together with the AO layout.

and re-imaging lens) and adaptive optics, and constructing a new telescope-top support structure (Figs. 2 and 3). Re-used are the existing tower, the platform, the folding canopy, the equatorial mount, the multi-wavelength imaging system, and the image acquisition and processing computers in the nearby SST and Automatic Transit Circle (ATC) buildings. We call this simplest and cheapest upgrade Option I here. It was called DOT^{++} in a proposal detailed in Bettonvil et al. (2004) and is summarized here.

The optical layout is shown in Fig. 3. Both the primary and secondary mirrors are parabolic because two parabolic mirrors in cascade leave no coma, making the whole field diffraction limited. The two 20° inclined flat mirrors FM1 and FM2 reflect in mutually perpendicular directions compensating their partial polarization. The layout includes a tip-tilt mirror and an adaptive-optics mirror. The spider construction may be optimized commensurate with the AO pupil geometry (Fig. 3c).

This optical design permits a flexible near-instantaneous user choice between angular resolution and field size, achieved with the sets of interchangeable "zoom-out" lenses L3 and L4 and maintaining the photon flux per pixel. Transversal pupil shift is possible through translation of telecentric field lens L2 and enables selection of obstruction-free apertures up to 65 cm. See Bettonvil et al. (2004) for detail.

An advantage of the equatorial mount is that there are no image rotations relative to the AO-system for the optics system on the pointed telescope structure. Combination of AO with post-detection numerical wavefront restoration is possible and desirable.

4.2. Option II: upgrade to 2.5-m aperture

The existing canopy has a diameter of 7 m which limits the focal length of the primary mirror to 2.3 m. This limits the aperture diameter to 1.4 m because a faster opening ratio brings too severe optical and thermal problems.

However, the existing equatorial DOT telescope mount and drives are sufficiently stable, stiff, and large to harbor a 2.5 m diameter mirror with appropriate mirror support and prime-focus support structures without modification. Fig. 4 shows photographs of the extraordinary stable DOT mount and gears. They were considerably overdimensioned in the original design to ensure strict rigidity and enable the option of installing a larger mirror later. The equatorial mount has a declination gear wheel with pitch circle diameter 174 cm, pitch 2.5 cm and teeth width 7 cm and an hour-angle gear wheel with pitch circle 190 cm, pitch 3.1 cm and teeth width 11 cm. The DOT drives are not only overdimensioned but also employ self-aligning pinions invented, developed, and tested during the DOT construction. Their principle is illustrated in Fig. 4d; more details are given in Hammerschlag (1983). These pinions achieve line contact between meshing teeth over the whole tooth width under typical telescope loads. The latter are small compared with standard mechanical practice. Under such small loads teeth contact in classical drives occurs only over a part of the tooth width, reducing the structural stiffness. Large preloads are no remedy since they would produce stick-slip irregularities in the very slow motion needed to follow targets. These self-aligning pinions turned out to work exceptionally well, so that

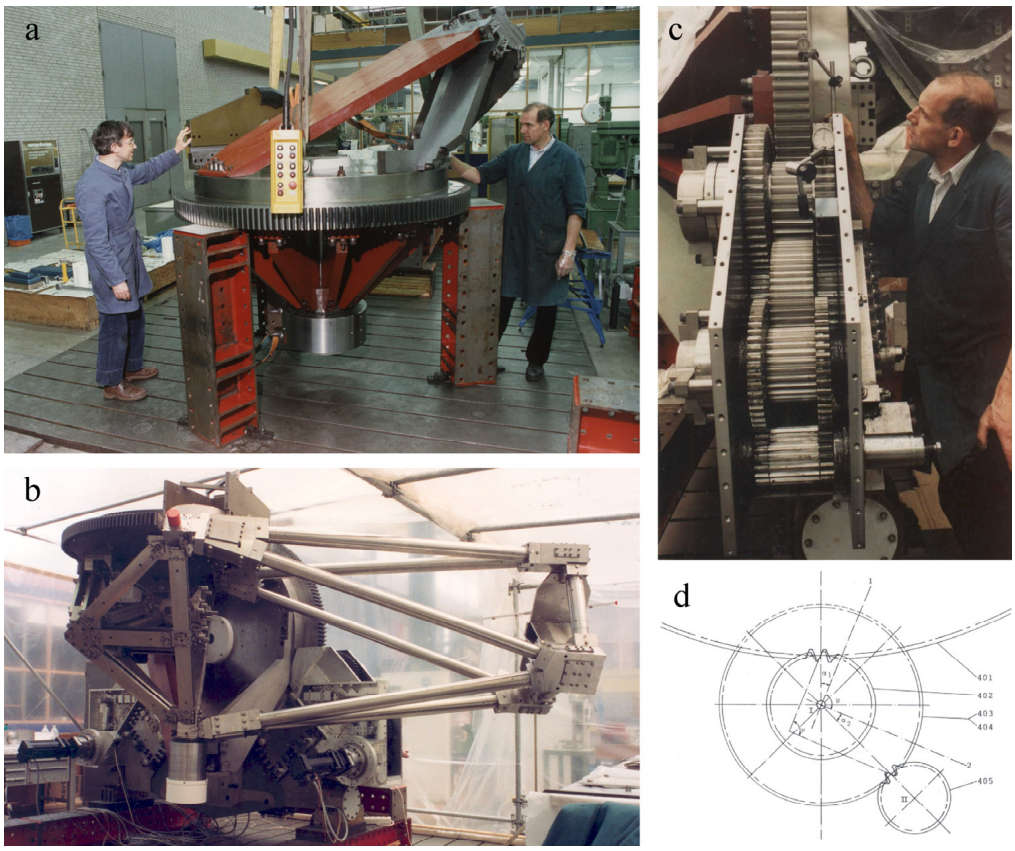

Figure 4. Fabrication of the exceedingly stable DOT mount and drives.
(a) Hour-angle gear wheel (190 cm diameter) with above the teeth the roller raceway for the radial support. The fork is in construction above the raceway. Below, near the floor, is the large double-row spherical roller bearing which was custom-made by SKF to minimize clearance. It has a large central hole to permit beam passage to an optional optics lab.
(b) The mount and drives fully assembled in the workshop, with the hour-angle axis oriented horizontally. The mount permits pointing in all directions.
(c) One of the two hour-angle gears. All gears have self-aligning pinions. This special design, a DOT invention to minimize the risk of stick-slip, achieves line contact between the meshing teeth over the whole tooth width even under the relatively small loads used here.
(d) Principle of the self-aligning pinions. On both sides of a pinion is a gear of the next stage. This pair of gears is fixed with a ring of screws to the pinion. It forms a single block, which is supported by a single double-row spherical roller bearing. This bearing permits rotation around three axes: the normal rotation around axis I perpendicular to the drawing plane, and two perpendicular axes 1 and 2 in the plane of the drawing. Rotations of the block around axis 1 provide line contact of the pinion with the large gear wheel whereas rotation around axis 2 provides line contact between the gears of the next stage (pinion II). The two half parts of the next gear were ground together for optimum matching.

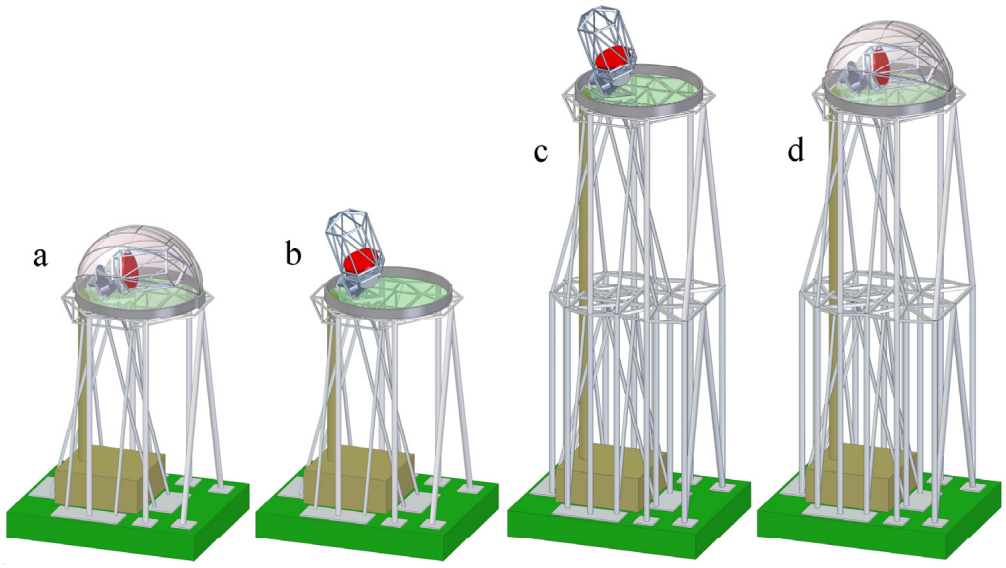

Figure 5. Options II and III with 2.5-m primary mirror.
(a) Option II: enlarged 15-m tower and platform, carrying 9 m canopy with 2.5-m mirror on the existing mount.
(b) Option II with open canopy and telescope in operating position.
(c) Option III: the Option II tower with platform, telescope and canopy put on top of an secondary base structure of 15-m height, bringing the telescope to 30 m above the ground. The added base structure also has a geometry which maintains parallel motion of the platform relative to the ground under varying wind loads. Such parallel motion combines well with the geometry of the upper tower with separated base points of the triangles (see text for further explanation).
(d) Option III with telescope in parked position and closed canopy.

the gears are actually much stiffer than the design tolerance of deformations ≤ 0.07 arcsec at wind speeds 0–10 m/s set by the DOT diffraction limit.

Thus, for an upgrade to a 2.5-m mirror the DOT mount can simply stay but a larger canopy is needed for bad-weather telescope protection. A telescope with 4.1 m focal length will just fit within a canopy of 9 m diameter as illustrated in Fig. 5a. This is the size of the canopy for the GREGOR telescope on Tenerife which was installed by us in 2004 and already survived an exceedingly strong storm with gusts of 245 km/hr. More detail is given in Hammerschlag et al. (2006b).

Such size increase also requires an enlargement of the platform including additional support from the ground to make the enlarged platform stiff enough against wind loading. The latter support is shown in Fig. 5a,b. It consists of an isosceles triangle on the north side and four vertical posts – two on the east side and two on the west side. Like the already existing 4 isosceles triangles of the present DOT tower, the additional elements provide a geometry that keeps the platform parallel to the ground at the small but inevitable leg deformation under wind load. More information about geometries for such parallel motion

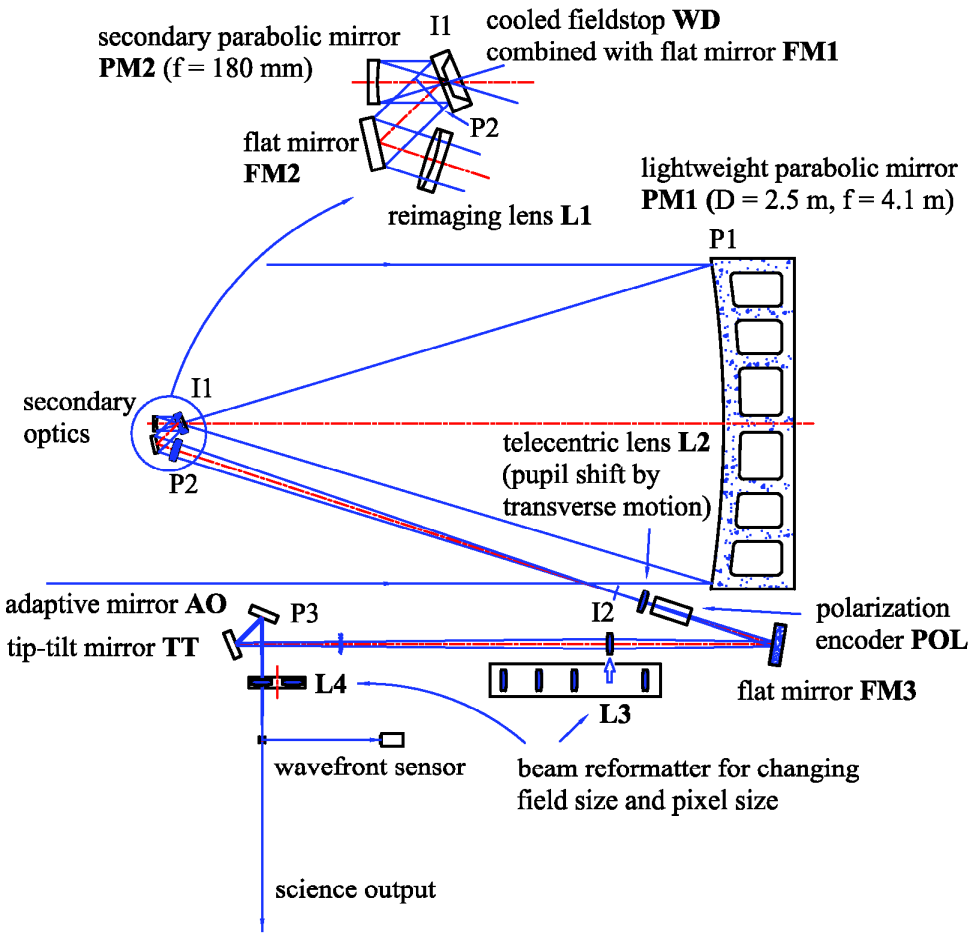

Figure 6. Optical layout for the options II to IV with 2.5-m mirror, similar to the 1.4-m upgrade with the same advantages.

is given by Hammerschlag et al. (2006a). The additional triangle also increases the stiffness against platform rotations around a vertical axis.

The diameter of the additional tubes is set at 406.4 mm, whereas the diameter of the tubes making up the existing tower is 244.5 mm. The choice of a larger diameter over the same free distance of 15 m prevents sensitivity to vortex oscillations (Karman eddies). Consequently, the additional tubes need no rubber dampers as the ones presently mounted between the existing tubes. The additional triangle and two of the four vertical posts require together four additional concrete foundation blocks of 1.5×1.5 m^2 surface. The other two vertical posts rest on the existing foundation blocks.

The optical layout of the Option II setup ($D = 2.5$ m, $f = 4.1$ m) is shown in Fig. 6 and is similar to Option I ($D = 1.4$ m, $f = 2.3$ m). Both designs have an opening ratio $f/1.64$. The 2.5 m version has the same important advantages: no coma due to the use of two parabolic mirrors in cascade, low polarization, user-selectable choice between angular resolution and field size, possibility of

transversal pupil shift and accompanying choice of obstruction-free aperture, in this case up to 116 cm.

The existing telescope mount has a central hole through its hour-angle shaft. In the Option II design we propose to let the secondary beam pass through it to a mirror which reflects the beam into a vertical shaft to an optical lab on the ground. In such a transfer system we suggest to use a tandem AO system: the first to correct seeing-imposed wavefront deformations and remaining tip-tilt fluctuations due to the telescope structure, the second for the beam part along the hour-angle axis, through the vertical shaft and in the optical lab. An alternative is to split the AO into a system for instrumentation mounted on the telescope and an independent system for instrumentation in the optical lab.

In the vertical shaft the light should travel parallel over the whole length of the shaft, or large parts of it, in order to eliminate image motion from wind-induced parallel translations between the platform and the ground, which are of the order of 0.1 mm. What remains are small transversal shifts of the optical surfaces following wind gusts and thus slow compared with the seeing motions. Such small pupil shifts do not disturb the AO correction. In order to accommodate a parallel beam over the whole shaft length without use of relay optics, the minimum shaft diameter is $d = \sqrt{2\ell\ D\ \alpha} = 330$ mm when a pupil image is located at the middle of the shaft for the following parameter values: transfer length $\ell = 15000$ mm, primary mirror diameter $D = 2500$ mm, field of view $\alpha = 5\pi/(180 \times 60)$ rad $= 5$ arcmin, and pupil diameter $d/2 = 165$ mm. For a pupil image at one end of the shaft, the diameters of shaft and pupil become $\sqrt{2}$ times larger, 467 and 234 mm respectively. We propose to evacuate the vertical shaft using entrance and exit windows to minimize the internal seeing. The above quantification shows that windows of only 50-cm diameter permit transfer of a diffraction-limited image with $5'$ field of view without requiring relay optics in the shaft.

There are other optical setups possible that avoid image motion from parallel translation between platform and the ground level. An example is one-to-one image transfer from the top to the bottom with a relay lens halfway up the shaft which shifts over half the value of the platform translation. This can be realized with a passive mechanical construction. The minimum shaft diameter then becomes two times smaller, 165 mm instead of 330 mm. Such a setup may fit better in the overall optics layout.

The relay optics on top of the vertical shaft can and should be connected to the inner platform of the DOT tower in a very stiff way. The inner platform is an important complementary part to the equatorial mount. Fig. 7a shows this inner platform during its assembly at the university workshop in Delft. There are three connection plates for the telescope mount: one on the corner point on the left side, the two others are where the hoist eyebolts are placed on the diagonal from the front to the back in this photograph. This inner platform transforms in an extremely stiff way all forces and moments from the telescope mount to direct forces without moments in its corner points, to which the long downward tower tubes are connected directly.

Another very important mechanical part is the support of the primary mirror. In the open concept, the support has to give stability against the varying wind load on the primary mirror. For the 45-cm primary of the present DOT

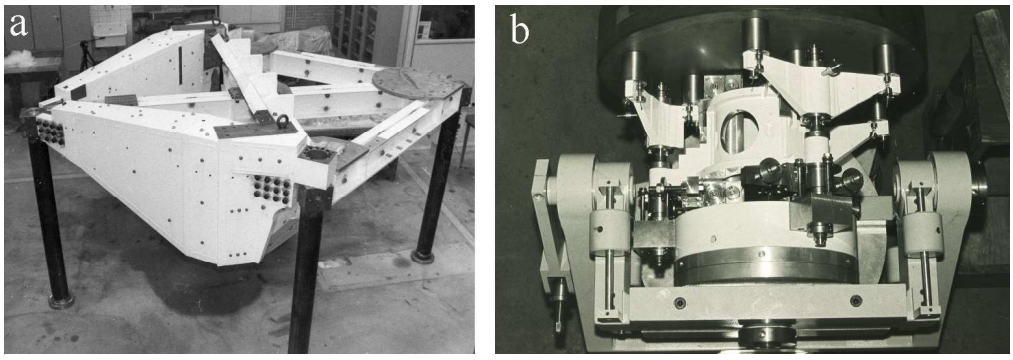

Figure 7. DOT inner platform and mirror support.
(a) The existing inner platform of the DOT is an important complementary part to the equatorial mount and can be re-used together with the mount, also in the broader tower of Options IV & V. This inner platform is shown here during the assembly at the TU workshop in Delft.
(b) DOT mirror with its support in test mount. The 3-dimensional design of the whiffle-trees provides high stability against the varying wind load.

a support system was developed that gives extreme stability using only passive means. A key aspect is the 3-dimensional design of its individual support elements, including the whiffle trees seen in Fig. 7b. This support system is actually much stiffer than was required for the 45-cm mirror. A 2.5-m mirror support can consist of many more support units of similar design. The mirror will be a classical thick mirror, but hollow with a honeycomb structure with triangular cavities for high stiffness. Such honeycomb structures can be realized in common mirror materials like Zerodur, Cervit or ULE, or a new material like Cesic (SiC). The stiff whiffle tree design avoids deformations by variable gravity and wind loads to the extent that the wind pressure is homogeneous over the mirror surface. Only wind inhomogeneities smaller than the mirror diameter, set by shear in the wind field, cause moments that are not carried off by the whiffle trees. These moments are at most a few tens of Nm and are carried by the thick mirror structure. The thickness of the mirror will be larger than the diameter of the AO sub-apertures projected to the primary mirror. Consequently, the deformations by the wind-field shear are small for the AO system due to the high bending stiffness of the thick mirror.

Of course, many variants are possible for the optical layout. The use of focal-plane instrumentation directly on the pointed telescope structure itself remains possible as well. In fact, the existing DOT multi-wavelength imaging system could represent the initial instrument package to start observing as in Fig. 3a, retaining its advantages of absence of image rotation and a relatively simple optical scheme with few components.

4.3. Option III: upgrade to 2.5-m aperture on doubled tower

Option III doubles the DOT tower in height in order to improve the best-seeing occurrence frequency. At La Palma the frequency of excellent seeing observations increases with the telescope height above ground, roughly doubling at double height. This was ascertained in the ATST site selection surveys including La

Palma under the supervision of M. Collados (IAC). Details are given in the final report of the ATST Site Survey Working Group[1]. The DOT is situated eleven meters lower than the SST. This is not a disadvantage because the ATST test measurements show that what counts is not the absolute height but the height above the local terrain; the ground-layer turbulence follows its slope. The DOT indeed experiences closely similar seeing to the only slightly higher SST and its SVST predecessor.

The tower height doubling is accomplished in Option III by placing Option II (the existing tower with enlarged platform and additional support carrying a 2.5-m telescope and a GREGOR-copy 9-m canopy) as "upper" tower on top of a new "lower" one. The latter is again an open steel framework with a geometry which maintains parallel platform motion. Fig. 5c,d illustrates this doubling to 30-m height with the telescope in observing and parked position, respectively.

The principle of maintaining parallel platform motion in strong-wind buffeting works as follows. A horizontal wind load on the top platform causes at the "first floor" level between the upper and lower parts a horizontal force of the same strength and in the same direction, plus a moment given by the force multiplied by the height (15 m) of the upper part. The direction of the moment is horizontal and perpendicular to the direction of the wind force. The four original DOT-tower triangles and the fifth triangle added through Option II transfer this horizontal force and moment to the intermediate first-floor level at which a complete network of steel triangles ensures stiffness between the foot points of the five upper-part triangles and four vertical posts.

The proposed lower-part framework between the base at ground level and the first floor consists of five isosceles triangles with exactly the same geometry as in the upper part. In addition, each foot point of the upper-part triangles and vertical posts is connected by a vertical post to the ground level. The diameter of these fourteen posts is the same as for the four in the top part, viz. 406.4 mm. The five lower-part triangles transfer the horizontal load downward from the first floor to the base while keeping these two parallel to each other. The moment caused by the horizontal force on the top platform is transported downward from the first-floor level by the vertical posts attached to the foot points of the triangles of the upper part of the tower. Each moment-component consists of a tensile force and a compressive one of equal value at the two foot points of an isosceles triangle of the top part of the tower. The elongation and shortening of the two vertical posts under the two foot points are equal in value. Consequently, the top point of the isosceles triangle in the upper tower part moves horizontally, maintaining the parallel motion of the top platform.

Elongation and shortening, respectively, of the two lower-part vertical posts under the foot points of an upper-part triangle tilt the latter at the first-floor level. However, such tilts do not influence the top platform because the upper-part triangles have separate endpoints at the first floor. All connections in this

[1] ATST Project Documentation Report #0021 Revision A, available at `http://atst.nso.edu/site/reports/` in file `RPT-0021.pdf`; in particular Appendix "La Palma Height Comparison" in files `A13.11_LaPalmaHtComp_Final.pdf` and `twoheight_r0.pdf`. The second file provides additional data to the first one.

floor are horizontal, perpendicular to the vertical posts in the lower part. These connections cannot transport a significant vertical force from one post to another because the bending stiffness is much smaller than the tensile and compressive stiffness.

The vertical component of a wind force on the top platform is transported in a very stiff manner to the first floor by the triangles and posts in the upper tower part. The fourteen posts in the lower tower part transmit these forces directly and hence also in an extremely stiff way to the foundation at ground level.

The horizontal wind forces on the first floor are brought downward by the five isosceles triangles of the lower tower part while keeping the first floor parallel to the ground floor, as explained above.

All together, the top platform remains parallel to the ground under wind loads on the tower. The existing concrete foundation can be maintained while doubling the tower height to 30 m because its 2-m deep concrete blocks are heavy enough to withstand the moments imposed by any storm. In addition, their configuration with the lower-part triangles anchored in separate blocks also favors holding the first floor and top platform parallel to the ground.

The setup with an instrument lab at ground level fed by a vertical vacuum tube remains as in Option II. In the case of parallel-beam image transport, the doubling of the tube length necessitates increase of the pupil and shaft diameters with $\sqrt{2}$, see above. The parallel translations increase from 0.1 mm to about 0.4 mm but this increase can be reduced through larger wall thickness for the lower-part tubes. One-to-one imaging from the top to the bottom can be realized by two relay lenses, midway between platform and the first level and midway between the latter and the ground level, with an intermediate image with field lens located at the first level. This setup offers the possibility of passive mechanical relay lens translation to cancel the image motion at the ground level. The minimum diameter of the shaft then remains 165 mm.

The existing electric elevator can be extended over the full height and then connects the optical lab directly with the platform. The needed space is available in the lower part while the upper part retains the existing open elevator shaft. Further options are closing the cage, or possibly the whole elevator shaft, for easier platform access in bad weather.

Note that a 30-m high tower of concrete cannot meet the stringent demand on absence of platform tilt under large wind loads unless it is much wider than this open-tower design employing tilt cancelation through special geometry. A wide concrete building would present a severe obstacle to the ambient flow and jeopardize the seeing quality at the telescope height. The concrete SST tower is relatively slender (narrower than its platform) and puts the SST imaging element (its 1-m objective) high up in the wind. In this sense even the evacuated SST is an open telescope.

4.4. Option IV: upgrade to 2.5-m aperture with wide 30-m tower

In Option IV the existing equatorial DOT mount and inner platform are to be placed on a new 30-m tower with a larger platform and a folding canopy of 12 m diameter (Fig. 8a) in order to gain working space around the telescope.

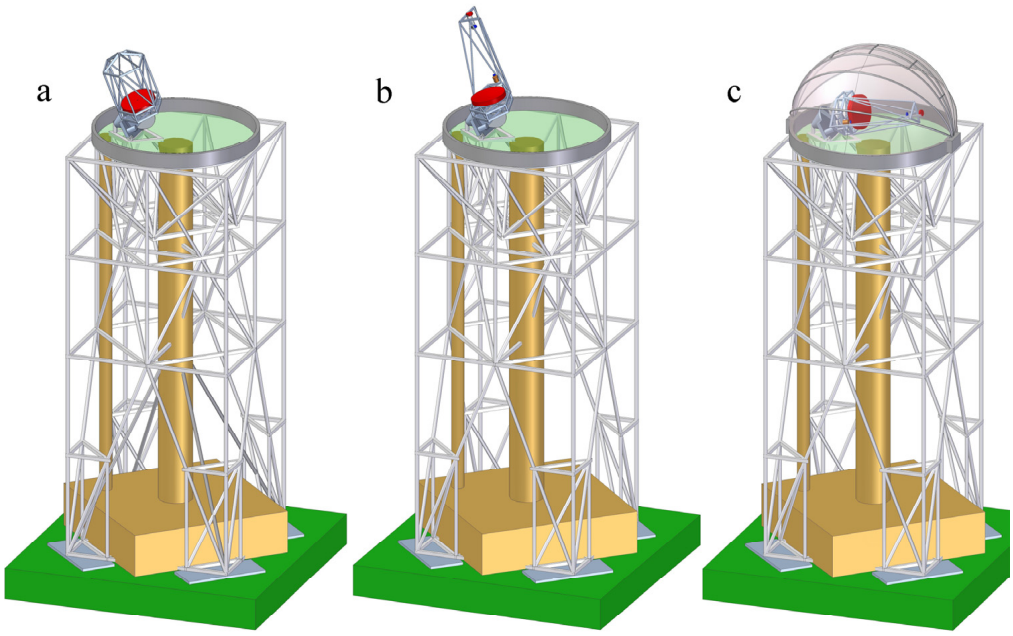

Figure 8. Options IV and V with 2.5-m primary mirror.
(a) Option IV: new 30-m tower with the 2.5-m telescope of Options II and III. The canopy has a diameter of 12 m. The design for parallel motion of the platform is based on the principle of an outer and inner tower, see text.
(b) Option V: 2.5-m telescope with off-axis primary mirror on the new tower.
(c) Option V with closed canopy.

The broader 30-m tower is again designed in a geometry which keeps the top platform parallel to the ground under varying wind loads. This version is based on the principle of having an outer and inner double tower. The outer tower consists of four 30-m vertical posts holding the top platform parallel to the ground. The inner tower consists again of triangle framework providing high translational stiffness as well as stiffness against rotations around a vertical axis. All connections between the inner and outer tower are horizontal and hence perpendicular to the four outer posts so that they do not disturb the parallel motion. The inner telescope platform is connected to the four post tops with a separate framework hanging free of the inner tower. A more detailed description of this tower design is given in Hammerschlag et al. (2006a). Its characteristics were checked through simulations with finite-element analysis (program ANSYS, Lanford et al. 2006).

The post-focus beam travels down through an evacuated shaft to an optical lab on the ground, similar to the Option-III design. In the center of the tower an elevator shaft can be placed as indeed added in Fig. 8. The 12-m canopy would be a further development of the 9-m GREGOR canopy. The tower can be placed on a foundation of 4 blocks of concrete, each with a surface of 3 × 5 m.

The tower shown in Fig. 8a–c implements the concept for a 30-m tower. The design principle of an outer tower to hold the platform parallel and an

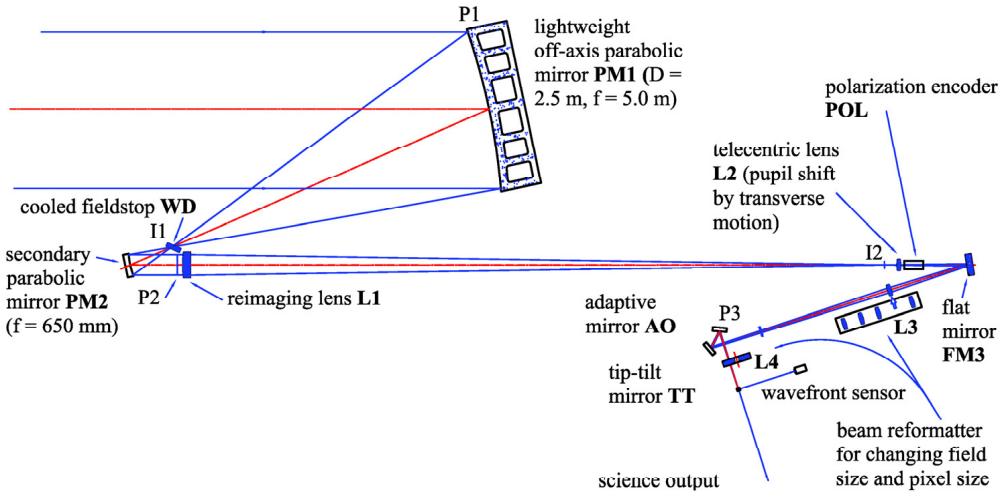

Figure 9. Optical layout of Option V with 2.5-m off-axis primary mirror.

inner tower for stiffness remains suitable for yet higher towers: the shown four-level geometry is suitable for heights up to 60 m, while larger height requires more stories.

4.5. Option V: upgrade to 2.5-m off-axis aperture on 30-m tower

In this final and most expensive option an off-axis parabolic primary mirror is purchased to obtain a fully clear aperture. Figure 8b,c shows such a telescope placed on the new 30-m tower of Option IV, in observing position and in parked position with the folding canopy closed. Figure 9 shows the optical layout. The focal length of the primary mirror is 5 m. The distance between the optical axis and the nearest rim of the primary mirror is one third of its diameter, hence 0.833 m. A user-selectable choice between angular resolution and field size and the possibility of transversal pupil shift are again incorporated with a system similar to that in the on-axis design. For the off-axis design the transversal pupil shift provides the option to use a smaller pupil close to the optical axis to reduce partial polarization.

The choice between on-axis and off-axis design has many aspects and tends to invite many different opinions. Mechanically, both are possible. Figure 10a,b shows in more detail how also in an off-axis setup the mechanical structure of the telescope top can be designed to guarantee stiff support of the secondary mirror. Optically, the off-axis design requires extremely precise alignment between the primary and the secondary mirrors transverse to the optical axis because otherwise the coma correction becomes incomplete.

5. Cost Estimates

Table 1 gives our cost estimates of the various upgrade options. These do not include the purchase of the primary mirror, nor the cost of post-focus instrumentation, nor the effort and running costs of the DOT team.

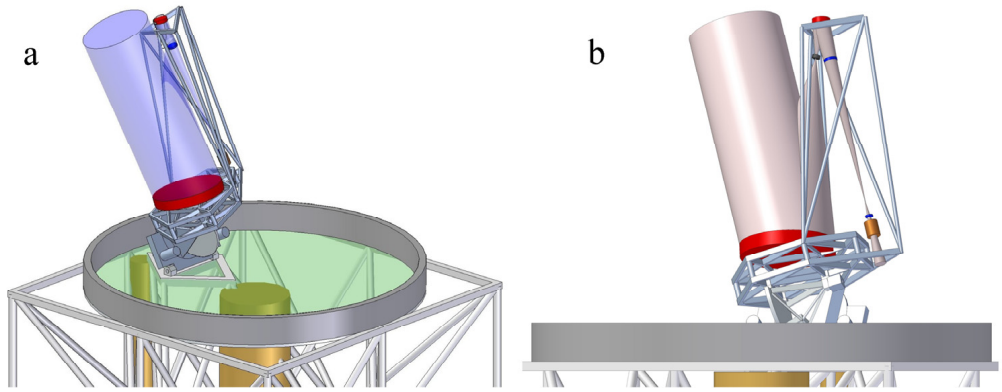

Figure 10. Off-axis design with stiff geometry of the framework supporting the secondary mirror in the telescope top.
(a) View from above.
(b) View from behind, showing the framework geometry more clearly. The optical beams are drawn as cylinders and cones. The beam from the primary mirror to the primary focus passes under the diagonal tube in the framework.

The price of a primary mirror depends on market constraints such as the order book and capacity of the few firms capable of fabrication of large optics, for example the availability of a blank, the occupancy of large polishing machines, etc. We note that although SiC is the preferential mirror material for large solar telescopes particularly because of its excellent thermal conductivity (60 times higher than Zerodur), the fully open designs proposed here can live with Zerodur because their mirror flushing becomes sufficiently effective already at medium wind speeds. The larger weight of Zerodur poses no problem in these designs because the DOT mount, re-used in all of them, is sufficiently over-dimensioned (see above).

The cost of post-focus instrumentation obviously ranges from low (re-usage of the existing DOT multi-camera multi-wavelength imaging system) to large (the image lab at ground level harboring many instruments). We envisage emphasis on high-cadence line-profile sampling with LC polarimetry for large fields of view and two-dimensional multi-line spectrometry including spectropolarimetry with phase-diverse MOMFBD restoration using a fiber field-of-view reformatter from two-dimensional to slit geometry (cf. Rutten 1999).

The DOT team is indispensable in the proposed upgrades not only because the latter use bits and pieces of the present DOT but yet more because of the team's expertise in tower and telescope open-design principles, computational verification of these, hardware solutions, and the La Palma environment. In addition, the teams would supply the intensive contacts with the university workshops (at Utrecht and Delft) whose contributions are budgeted separately in the next-to-last column in Table 1. A rough estimate of the DOT-team manpower, management, and operational costs to undertake the proposed upgrades ranges from 250 kEuro/year (the present DOT operations budget) to 500 kEuro/year.

The costs listed in Table 1 under "Optics" cover the prime-focus and subsequent packages. "Telescope structure" includes a new mirror support. The University workshops are needed for design work on the telescope structure,

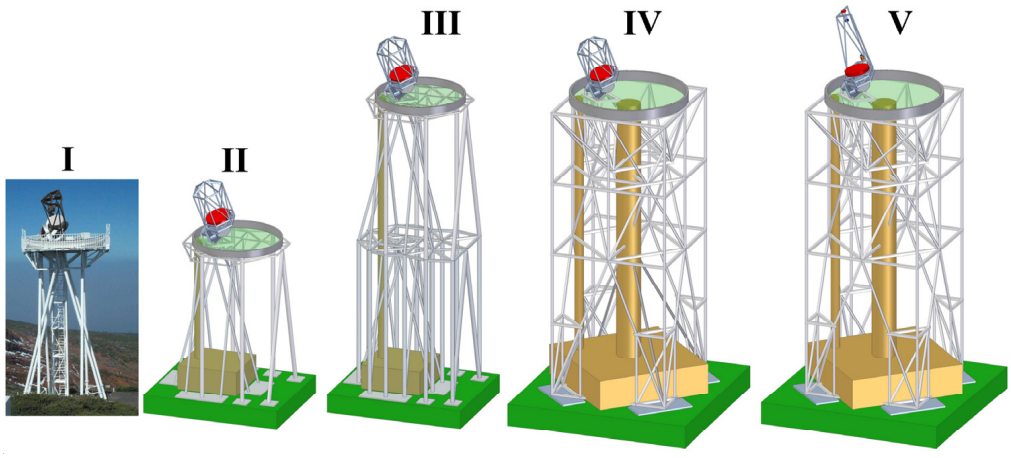

Figure 11. Overview of the five options. I: upgrade of the present DOT to 1.4-m aperture. II–IV: 2.5 m aperture with increasing tower height and platform width. V: 2.5 m off-axis version.

Table 1. Cost estimates in kEuro, excluding the primary mirror, post-focus instrumentation, and DOT-team effort.

Option*	Optics	Telescope structure	Tower+ platform	Canopy	University workshops	Total
I	200	300			300	800
II	300	400	300	600	300	1900
III	400	400	900	600	600	2900
IV	400	400	3200	1100	600	5700
V	600	400	3200	1100	600	5900

* I 1.4-m aperture with existing 7-m canopy and existing 15-m tower
II 2.5-m aperture with 9-m GREGOR-like canopy and widened 15-m tower
III 2.5-m aperture as Option II with a doubled 30-m tower
IV 2.5-m aperture with 12-m canopy and new, wide 30-m tower
V the same as Option IV with a 2.5-m off-axis primary mirror

tower and platform, in addition to the industrial manufacturing costs listed in the respective columns. Special small parts and test equipment must also be produced in these workshops. The increase in workshop costs from Option II to Option III reflects additional design work for the higher towers, in particular the far-from-trivial joints in the corner points, the beam transfer tube, and the elevator. The joints need very careful designing in order to maintain the high stiffness of the overall geometry, and will need complex special parts that are best manufactured in-house.

Figure 11 shows a pictural overview of the five options. In summary: without inclusion of the DOT team, the primary mirror, and post-focus instrumenta-

tion, Option I takes roughly 1 MEuro, Option II 2 MEuro, Option III 3 MEuro, and options IV and V 6 MEuro. The latter two options are costlier due to their new tower and foundation.

These various options may be realized in overlapping phases with continued observing. For instance, the Option-II platform and canopy enlargements can be realized keeping the DOT in operation, with fast subsequent upgrading of the telescope. The Option-III tower doubling may follow on the Option II aperture upgrade. In Options III–V the higher tower may be realized first and tested with the existing telescope before the latter is replaced. Other variants and option combinations are also possible.

6. Conclusion

The DOT telescope and tower combine rigorously open design with extraordinary stiff construction. This combination was achieved through the application of special geometries and the careful attention to the design of joints and drives that is necessary to indeed realize the geometrical stiffness. The excellent DOT high-resolution observations have amply proven both the open concept and the DOT's pointing stability.

We would like to enlarge the DOT and profit fully from its concept. Only relatively moderate investments are needed through re-using existing DOT parts, in particular the equatorial mount and drives which are indeed oversized for the present 45-cm primary mirror. In this paper we have outlined strawman designs for upgrades to 1.4-m and 2.5-m aperture, optionally adding a groundbased post-focus lab and 30-m tower height to double the frequency of super-seeing. Even with a 2.5-m primary mirror diffraction-limited pointing stability can be reached without compromising the rigorously open construction of both the telescope and the tower.

We welcome partners to share in DOT operation and the realization of one of these upgrades.

Acknowledgments. We thank the CSPM organisers for a very good meeting. The DOT is presently operated by Utrecht University at the Spanish Observatorio del Roque de los Muchachos of the Instituto de Astrofísica de Canarias with funding from Utrecht University and the Netherlands Graduate School for Astronomy NOVA. A. P. L. Jägers is supported by the Netherlands Technology Foundation STW. R. J. Rutten acknowledges travel support from the Leids Kerkhoven-Bosscha Fonds and the European Solar Magnetism Network.

References

Bettonvil F. C. M., Hammerschlag R. H., Sütterlin P., Rutten R. J., Jägers A. P., Snik F., 2004, in J. Oschmann (ed.), Astronomical Telescopes and Instrumentation, Procs. SPIE 5489, 362

Bettonvil F. C. M., Hammerschlag R. H., Sütterlin P., Rutten R. J., Jägers A. P. L., Sliepen G., 2006, in I. S. McLean, M. Iye (eds.), Ground-based and Airborne Instrumentation for Astronomy, Procs. SPIE 6269, paper 62690E

Hammerschlag R. H., 1981, in R. B. Dunn (ed.), Solar Instrumentation: What's Next?, Proc. Sacramento Peak Nat'l Obs. Conf., Sunspot, New Mexico, 547

Hammerschlag R. H., 1983, Procs. SPIE 444, 138

Hammerschlag R. H., Bettonvil F. C. M., Jägers A. P. L., 2006a, in E. Atad-Ettedgui, J. Antebi, D. Lemke (eds.), Optomechanical Technologies for Astronomy, Procs. SPIE 6273, paper 62731O

Hammerschlag R. H., Bettonvil F. C. M., Jägers A. P. L., Sliepen G., Snik F., 2006b, in Spatial Structures, Procs. IASS, paper 108

Keller C. U., von der Lühe O., 1992, A&A 261, 321

Lanford E., Swain M., Meyers C., Muramatsu T., Nielson G., Olson V., Ronsse S., Vinding Nyden E., Hammerschlag R., Little P., 2006, in Monnier, John D., Schöller, Markus, Danchi, William C. (eds.), Advances in Stellar Interferometry, Procs. SPIE 6268, paper 626814

Rutten R. J., 1999, in T. R. Rimmele, K. S. Balasubramaniam, R. R. Radick (eds.), High Resolution Solar Physics: Theory, Observations, and Techniques, Procs. 19th NSO/Sacramento Peak Summer Workshop, ASP Conf. Ser. , Vol. 183, 296

Rutten R. J., Bettonvil F. C. M., Hammerschlag R. H., Jägers A. P. L., Leenaarts J., Snik F., Sütterlin P., Tziotziou K., de Wijn A. G., 2004a, in A. V. Stepanov, E. E. Benevolenskaya, A. G. Kosovichev (eds.), Multi-Wavelength Investigations of Solar Activity, Procs. IAU Symposium 223, Cambridge University Press, 597

Rutten R. J., Hammerschlag R. H., Bettonvil F. C. M., Sütterlin P., de Wijn A. G., 2004b, A&A 413, 1183

Snik F., Bettonvil F. C. M., Jägers A. P. L., Hammerschlag R. H., Rutten R. J., Keller C. U., 2007, in B. W. Lites, R. Casini (eds.), Procs. 4th Solar Polarization Workshop, ASP Conf. Ser. , in press

van Noort M., Rouppe van der Voort L., Löfdahl M. G., 2005, Solar Phys. 228, 191

van Noort M. J., Rouppe van der Voort L. H. M., 2006, ApJ 648, L67

The Physics of Chromospheric Plasmas
ASP Conference Series, Vol. 368, 2007
Petr Heinzel, Ivan Dorotovič and Robert J. Rutten, eds.

THEMIS Instrumentation and Strategy for the Future

Bernard F. Gelly

CNRS-UPS 853 THEMIS, La Laguna, Tenerife, Islas Canarias, Spain

Abstract. Imaging of the solar surface from ground based telescopes has achieved to be diffraction limited almost ten years ago, while diffraction-limited spectropolarimetry is, for obvious reasons of available flux, far from being reachable nowadays. Among the 1-meter class solar telescope currently in operation, THEMIS is the most specifically devoted to high-precision spectropolarimetry with an appealing level of specifications, some of them hardly to be find in any other telescopic installation. We shall discuss in this paper the recent evolution of this telescope toward more polarimetric efficiency and the use of modern detectors, in order to push further its possibilities in and hopefully contribute to open the path of a future large size solar European facility.

1. Introduction

THEMIS is a joint operation from France (CNRS) and Italy (CNR) national research agencies. It is a 90 cm solar telescope, currently the third larger in the world, located at Izaña, 2400 m, within the Teide Observatory from the Instituto de Astrofísica de Canarias, on Tenerife (Canary Islands, Spain), and started operating in 1999. Its specific design for high-quality polarimetry includes an alt-az mounting, a helium filled telescope tube, a Stokes polarimeter located at the prime focus, and a multi-mode spectrograph. THEMIS delivers routinely vector polarimetry with an accuracy of 10^{-4} and up to 10^{-6} in some special configurations. The spectrograph design allows the observation of up to 10 wavelengths simultaneously, opening the possibility to perform 3D inversions of the magnetic field structure in the solar atmosphere.

2. New Image Stabilizer for Spectropolarimetry

Besides its polarimetric capabilities and multi-line spectrograph, THEMIS was designed to attain the $0.2''$ resolution so as to explore the small spatial scales of the solar magnetic field. The benefit to correct for atmospheric turbulence when aiming at high resolution *and* high accuracy spectropolarimetry has been recently addressed in Judge et al. 2004, resulting in the evidence that '*even the lowest order AO correction (just tip and tilt) is essential for accurate spectropolarimetric measurements [...] below 0.3 arcsec*'. This is very exactly the issue we wanted to address. Several solar image stabilizers have been developed in the late 90' (Von der Luehe et al. 1989, Rimmele et al. 1991, Ballesteros et al. 1996), most of them to evolve into adaptive optics system as hardware was becoming more affordable for small telescopes. Building an all purpose digital image sta-

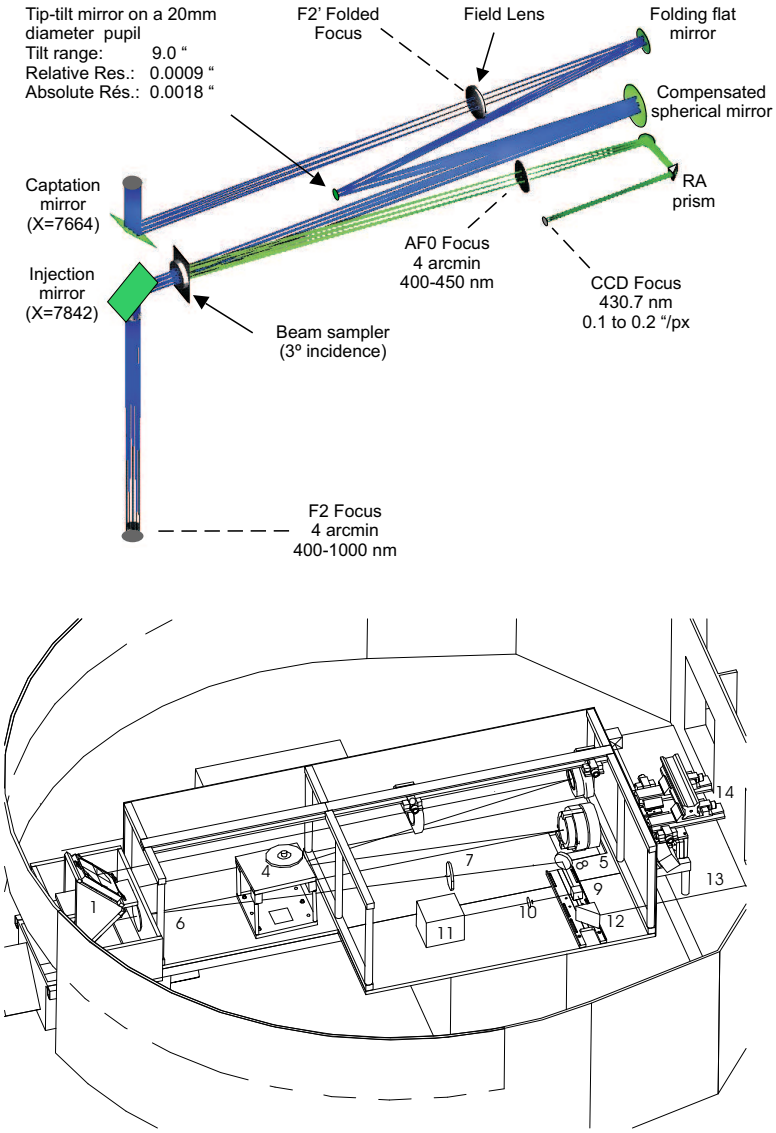

Figure 1. Top: tip-tilt detour optical layout. Bottom: Corresponding mechanical CAD design

bilizer nowadays is not so much of a challenge, except in the case of THEMIS, as we shall see below.

The decision to build an image stabilizer (hereafter IS) was taken in January 2004, on the basis of an existing local project document, contributed by previous references like Molodij et al. (1996), Aulanier et al. (2003), Cruvellier (2003). The IS was commissioned in 2005 and 2006 and went into service in 2006. The scientific specifications of the device were: **i)** a complete compatibility with all the observing modes (currently 3 observing modes, with or without polarimetric analysis, are possible at THEMIS, each of them with a significantly different

pre-slit configuration), **ii)** the stabilizer cannot use a significant fraction of the photons of the current science channels and **iii)** the stabilizer must work on all typical solar objects, e.g., granulation, spots and limb. This broad picture has been translated into functional and technical requirements like:

- the IS can work with the mostly unused blue part of the spectrograph bandwidth, below 450 nm
- the correlation algorithm shall be TDB accurate over low contrast scenes (3% rms at worst) at this wavelength
- the closed loop frequency cutoff shall be at least 60 Hz (from Ballesteros (1996)), expecting no mechanical high frequencies from the telescope or the building
- the stabilization must interact with the general command-control to allow the possibility to scan the solar surface while stabilizing at the same time

And to these requirement we can add two comments: using the blue part of the spectrum actually enhances somewhat the granulation contrast, but also, a large provision must be made for important variations (1 to 100) in the available flux that may occur due to the instrumental settings when changing the observing setup.
The final optical layout of the tip-tilt is shown on Fig. 2 top. The original F2 focus is sent to a re-imaging doublet to obtain a 20mm pupil on the agile mirror. A flat folding mirror is required to keep inside the available volume. The piezo platform works in the pupil plane and its axes can match exactly the axes of the camera and of the slit in F2 by using a small rotation stage. A spherical mirror and an injection mirror send the F2 focus to its original destination. On the way out, the beam crosses a semi-transparent plate that picks up 12% of the beam intensity for wavelengths below 450 nm. This light goes through a 45° mirror to a 50/50 beam splitter which is simultaneously feeding the motion detection camera and the alternate feed for our slit-jaw camera.

This design was first checked with an optical software package, then the actual layout went through a static qualification once implemented in the telescope. The conclusions are that the tip-tilt additional optics preserve the optical quality of the telescope at F2 ($0.22''$ at worst) over a field of $140''$at least, and without noticeable chromatic shift.

After testing a classical fast CCD camera, we decided to use an 8 bits CMOS camera with a resolution of 0.15"/px, allowing the readout of a 72x72 pixels area at 2000 fps. Image motions are detected using the "Sum-Absolute Difference" (SAD) function (Vassiliadis et al. 1998). The SAD of 2 identical images is zero at the origin and positive elsewhere. When applied to astronomical (solar) images randomly displaced by atmospheric turbulence, it is minimum at the (x, y) location of the displacement value. The estimation of the image motion is then translated in finding the minimum of a SAD function. The SSE2 assembly instructions included in the latest Intel processor allow to compute the SAD function over 128 bits words, or rather blocks of 16 x 8 bits pixels, hence speeding up very significantly the result. For a real-time application, it is a nice alternative to FFT based correlation functions reputedly slower if not used with a specific hardware. Our code (SAD2006) computes the SAD function in 16 pixels chunks over 2304 (48x48) pixels inside a 5184 (72x72) pixel (reference

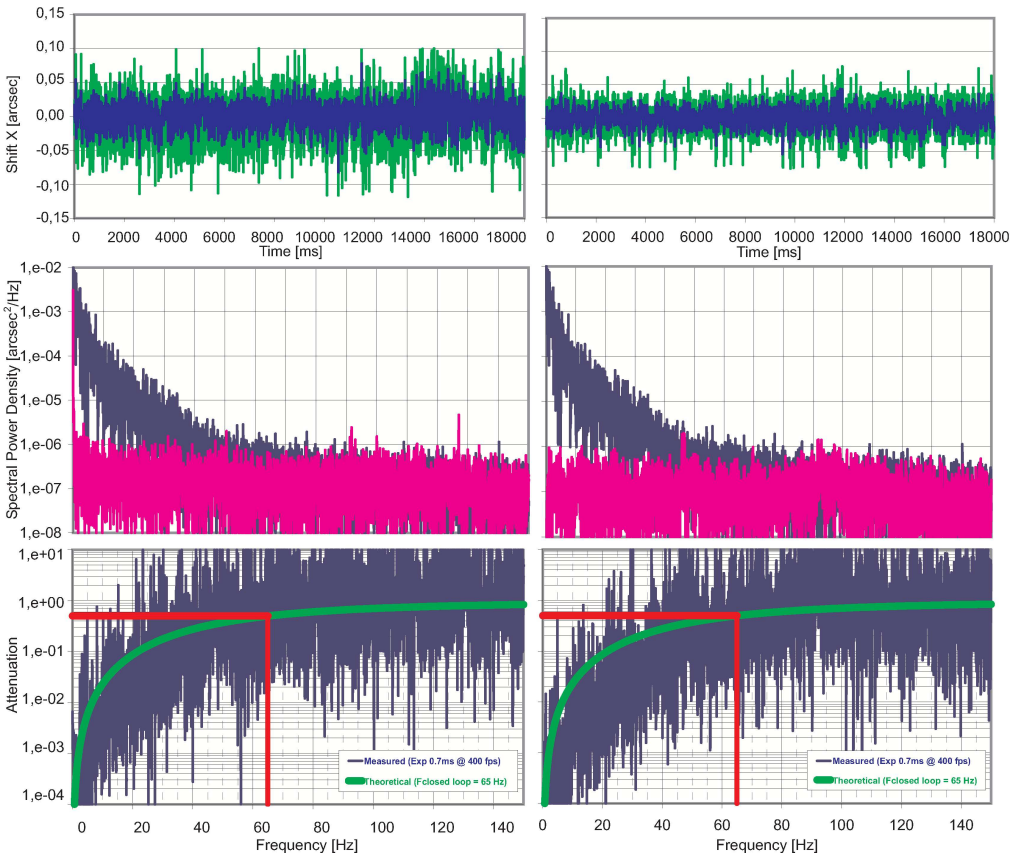

Figure 2. Results of the qualification run over a sunspot in April 2006. Left column are results from measurements during BAD seeing conditions and right column during GOOD seeing conditions. Top to bottom are: (a)the temporal behavior of the image motion residuals over 18 secs, the light gray is at nominal rate and the dark gray is smoothed to a 10 ms equivalent, (b)the power spectra of image motions with (light gray) and without (dark gray) stabilization, and their ratio (e.g., the transfer function), with an overplot of the crossover frequency estimation

image, and estimates its minimum in 0.3 msec on a 2.0 GHz PIV processor. Given the typical parabolic shape of the SAD function, a simple barycenter computation add sub-pixel precision to the result. We estimate the accuracy of this algorithm in real life to perform nicely to $1/5^{th}$ of a pixel taking noise and seeing into account.

To test the quality of the stabilizer on several solar scenes and actually measure the transfer function of the system, we setup a second identical CMOS camera, making sure that the temporal sampling of the stabilized image exceed the speed of the actuation, so as to avoid temporal frequency aliasing in the result. Images were acquired in consecutive bursts of 8000 frames stabilized and non-stabilized. Motion detection over raw images and relative to a time origin

Table 1. Stabilizer device qualification results on various solar scenes

	Limb	Spot		Granulation	
Date	March 06	April 06			
Image size (px)	256x32 or 32x256	200x200			
Exp. time (ms)	0.5	0.5			
Fps	543 (1.84 ms)	400 (2.50 ms)			
Analysis cutoff freq. (Hz)	270	200			
Seeing during measurements	bad	bad	good	bad	good
rms residual image motion ($''$)	0.074	0.031	0.020	0.052	0.036
ν_c (-3dB) cross. freq. (Hz)	50	65	65	65	65

are computed using the same SAD algorithm than for the IS, then a Fourier analysis is performed.

Table 1 summarizes both the setup conditions and the main results of the tests. Middle and bottom plots on Fig. 2 are showing example spectra and transfer functions in the above mentioned conditions. The crossover frequency at -3dB establishes at about 65 Hz, which is the current system status. We do not see on these plots any evidence for high-frequencies that would indicate some mechanical vibrations inside the instrument or building. This is quite important in the perpectice of a possible evolution of this system toward a full adaptive optics design.

3. New Cameras for the MTR Mode

MTR is the multiline spectropolarimetric mode of THEMIS that has been designed to observe up to 10 spectral lines simultaneously (Rayrole et al. 1998). The combination of that many possible lines with the option to have one camera per Stokes component resulted in THEMIS needing a maximum pool of 20 cameras to run. For a refurbishing of this ageing system, it has been decided that only 6 wavelengths at once will be available for the future. This lower number still allows a nice set of chromospheric/photospheric and magnetic/non-magnetic lines to be observed (and still no other telescope allows it). Similarly, it has been approved that the main interest of having one camera per Stokes component is the access to a wider field. However, a faster camera can do the job as well in the same time, even with a higher polarimetric accuracy. Hence the new pool of camera will have only 6 units. The selected camera is a commercial off-the-shelf product from Andor Technologies using an E2V L3 vision

Table 2. Main specifications of the new MTR camera

Foundry	Thinned back-illuminated (QE > 90% (500 nm)
Format	512x512 px (16 μm square)
Well-Depth	200 000 $\bar{e}$
Frequency	10 MHz, 35 msec readout (28.5 fps)
On chip amplification	1 to 1000
Converter	14 bits
Cooling	-80°C (dark < 0.005 $\bar{e}$ /px/s)

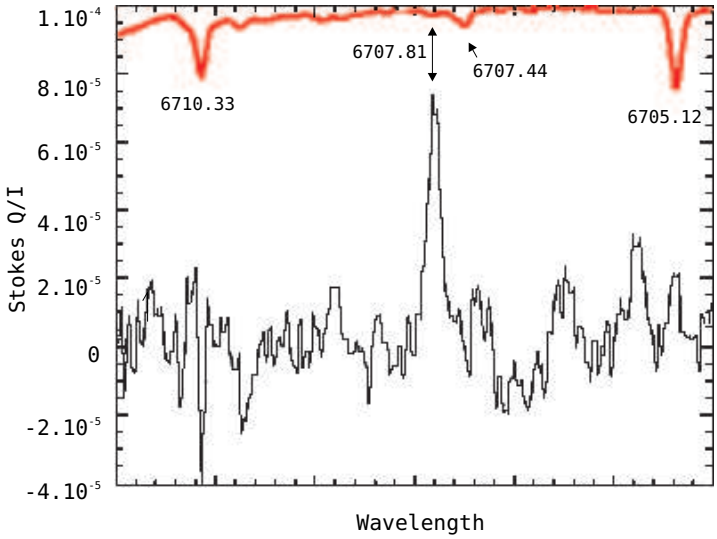

Figure 3. Linear Q/I polarization of the Li 670.78 nm over the quiet Sun. Top thick line is the reference intensity. The unprecedented quality of this result is also largely coming from the stabilization of the spectra.(Data courtesy López Ariste and Themis).

chip, whose main features are summarized in the Tab. 2. We expect the on-chip amplification feature to be very useful in smoothing the spectrograph output efficiency over several decades from 400 to 650 nm. Also, the improved quantum efficiency allows to observe lines like HeI 1083 nm, which was impossible before.

A nice example of the additional quality brought by only one camera is visible on Fig. 3 which shows the Li 6708 line over the quiet Sun. The understanding of Lithium surface abundance of solar type stars remains a difficult topic with huge implications from the history of the star angular momentum and mixing to the existence of internal gravity waves, to the diagnosis of extrasolar planets on solar type stars (Charbonnel et al., 2006). While this light element is barely distinguishable in intensity and a very difficult target (Brault & Mueller 1975), its linear polarized spectra is well above our noise level which in this case was only a few 10^{-6}. Indeed THEMIS is now much better than its original specification of 10^{-3} relative accuracy.

The complete acquisition system for MTR2 is sketched on Fig. 3. Each camera is connected to a proximity computer, to ensure a full acquisition speed in parallel to that point. The rest of the architecture is based on 3 main buses: data (1/10 Gb concentrator), command (1 Gb), and for convenience the video bus for real time control is implemented in hardware rather than software. The system shall be operational in early 2007.

4. New Cameras for the MSDP Mode

Unlike the MTR, the MSDP mode is not affected by a convolution of the image with a narrow slit. The slicing of the field of view given by the (mandatory)

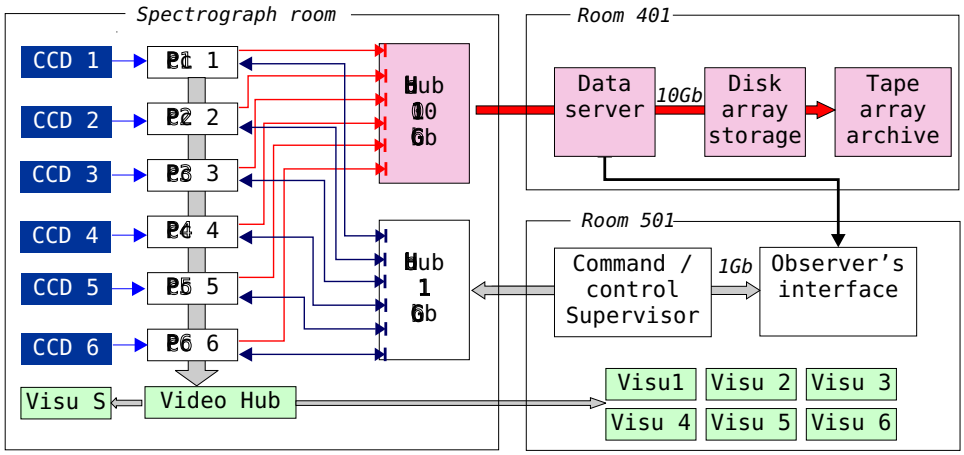

Figure 4. Sketch of the full acquisition system for the MTR2. The physical distances to bridge when connecting the 3 rooms are about 50 meters and there is a large cable winding drum to cross due to the alt-azimuth mount.

grid shaped pre-slit is handled by the data analysis software which rebuilds the entire field in the 2 simultaneous wavelengths (Mein 2002). Improving the duty cycle speed and spatial resolution have been the main issues of our renewing of the MSDP. In principle the MSDP can maintain the spatial resolution of the telescope at F2 (0.22″), but the minimum exposure times are typically of 300 ms, consequently the pixel size needed should be rather 0.2″ than less. It does not require very big CCD full-well capacities because images can be averaged off-line to give the required SNR (even more so with a tip-tilt), but, for reasons of beam aperture at the output, the pixel size must be 10 μm at least. The acquisition should handle 2 to 3 i/s, compatible with the exposure times, and with the maximum acceptable duration of a complete scan over a field of 5′ (typically 3 min). Further trade-off between the size of the field and the duration of the scan is an observer's decision.

Following this analysis, the THEMIS team made a selection over available commercial products at the fall of 2004. The preferred chip was a 1500x1000 Kodak KAF 1603ME (microlensed version), with square 9 μm pixels, QE ranging from 45 to 77% across our spectrograph bandwidth, and a readout speed of 10 MHz allowing for 8 i/s at most. The project was completed in summer 2005.

Fig 5 shows the results of the study of NOAA 0808 from Sep 12th, 2005 18:12UT using this new system. THEMIS MSDP allows the simultaneous observation of 2 lines (in this case H_α and NaD1). Given to the spectral slicing made by the prism boxes, several wavelengths are available along the line profile at once. Full-Stokes polarimetry is possible and vector magnetic maps have been computed for the first time in 2006 (Mein et al. 2006), soon to be checked against the same MTR maps. For its moderate accuracy in polarimetry and its speed faster than any other instrument, the MSDP may become a challenging instrument to tunable filters for the mapping of large magnetic regions.

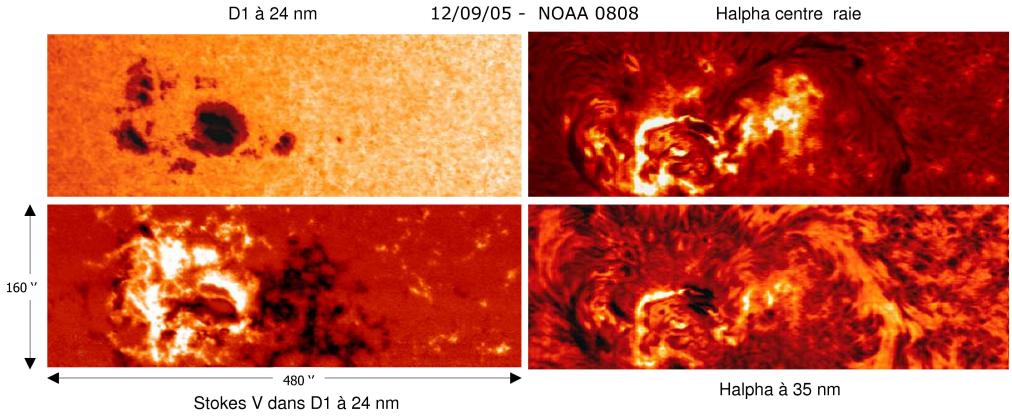

Figure 5. Left: Top NaD1 map of NOAA 0808 at 24nm from line center. Bottom: Stokes V of the above map. Right: Same map in the chromosphere at H_α line center (top) and H_α at 35 nm from line center. All maps are simultaneous. (Picture courtesy B. Schmieder & P. Mein)

5. THEMIS Data and Analysis Software

THEMIS instruments are producing large volume of not-user-friendly raw data. A typical good observing day can yield 200 - 500 Gb, the unit base item being either a MTR spectrum (which most of the time is only a part of a scan and has little value as is), or an MSDP raw frame which is also a complex product, that need to be properly handled by a dedicated software and reconstructed for wavelength and field. It is out of the scope of this paper to discuss the details of these processes. However at management level, some tidying of the analysis tools was necessary in order to speed up the obsrvation/data analysis/publication cycle of the THEMIS observers. This has been done at THEMIS for the MTR processing and at BASS 2000 (the French solar national database for non-spatial instruments) for the MSDP processing. Since 2005, THEMIS is making available at the telescope and also as off-line software two data analysis packages: SQUV and INVTOOLS.

- SQUV is a package of IDL developed functions to handle the raw MTR data. It accepts data from any configuration of the MTR sub-modes (3 are possible), and apply the typical reduction steps, flat and dark corrections, line curvature de-slanting, demodulation of the Stokes parameters, and construction of the Stokes maps from the initial scan data. The operations are controlled using a widget-based interface, and once the critical choices have been checked by the scientist, the program can be left running without further attention. This 'automatic' batch mode is saving a lot of time.
- INVTOOLS is a mixed fortran/IDL package that plugs into the output of the SQUV program. It contains a set of tools intended to help the user analyze the results he has just observed. They are mostly organized around an inversion code able to retrieve the magnetic field vector from the doublet of Fe photospheric lines at 630 nm. The first tool handles the data files created by the SQUV package and allows the user to create maps of the scanned region

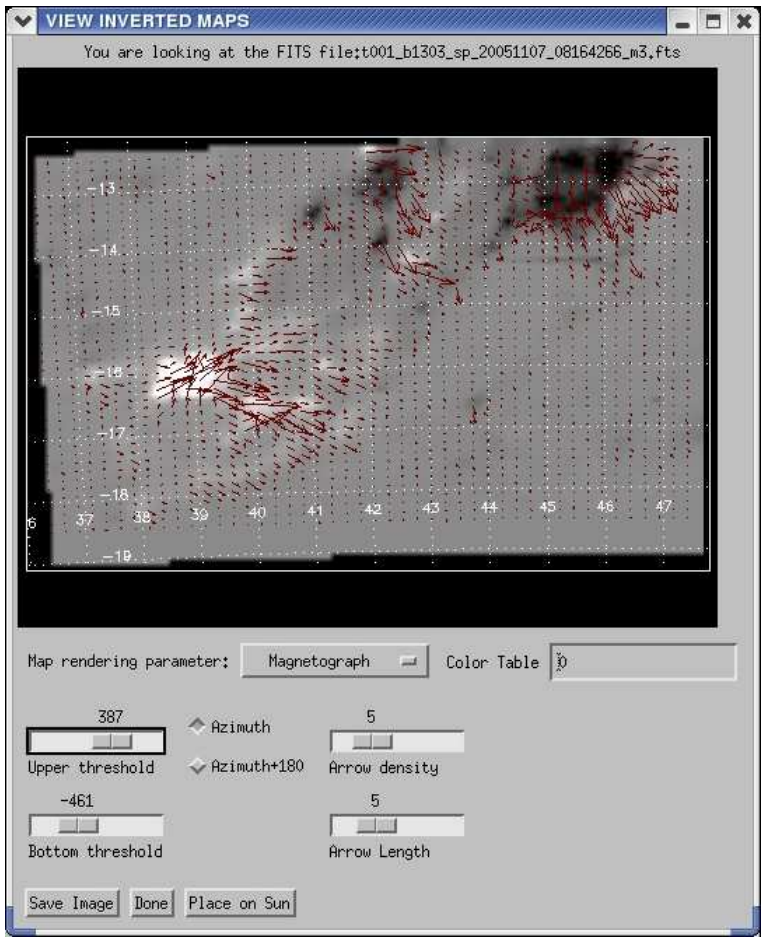

Figure 6. Example of the analysis tool of the INVTOOLS package. The image shows the scanned solar region in terms of longitudinal flux with arrows representing the field vector overplotted. The data arises from the inversion code included in the package. Note the visualization options and the 'fundamental ambiguity switch'

in the wavelength of choice and for all Stokes parameters. The resulting maps can be saved, or projected against the solar disk with an overlying of solar coordinates, to give a few examples of its capabilities. The second tool is an inversion code for the Fe doublet at 630 nm. These two lines are well known for their high sensitivity to the photospheric magnetic fields.It is based on a Principal Component Analysis (PCA) algorithm. PCA techniques have been probed for their robustness and speed. A typical THEMIS photospheric scan is inverted in 5 to 10 minutes. With such performance the code can be safely been put to work by any user during the observation and the vector field is inferred in almost real time. This capability is unique to THEMIS to this day. More tools are also provided to check and visualize the inversion results.

In conclusion, to measure and map the vector field has been many times put forward as one of our top goals. THEMIS becomes thus the first solar telescope ever to provide the vector magnetic field in real time thanks to this code.

6. Planned Changes for the Near Future

To complement the above set of new features, we are currently studying the speeding up of the polarimetric analysis duty cycle so as to match the improved speed of the detectors and decrease the seeing induced cross-talk. TTL driven achromatic LCD retarders combinations are now being considered as replacements for our mechanically driven quartz/MgF2 units. The CAD drawing phase for the mechanical parts is ready and a test bench for the qualification of Meadowlark retarder plates is being designed for 2007. Such a device would be available by mid-2008.

Recently, on the grounds of a preliminary study of wavefront measurement made during the summer 2006, the Themis Board authorized the qualification of a deformable mirror as a first step toward the evolution of the stabilizer device toward an AO system by the same home team; This qualification will start in early 2007 with an OKO mirror using 48 actuators. Our broad picture is to propose a correction for the first 20 Zernike polynomials using the same ingredients that we put in the stabilizer, and reusing the same optical bench. The device may be in operation by the end of 2008, early 2009.

7. 2012 and Beyond, OPTICON, European Perspective

So far, high quality spectropolarimetry has been greatly improved by the stabilization of the images. The full exploitation has only started, helped by the availability of suitable reduction codes, and boosted also by the arrival of modern cameras for both the MTR and MSDP observing modes. In this framework, plans are crafted to extend the lifetime of this installation so as to continue its scientific exploitation. 2012 is for us a minimum threshold to reach, even at the expense of changing the current operational model for another more economical one. However, the complexity of the various THEMIS subsystems for the instrumental setups, the handling of the observation, the cold water production, the periodic changes of the helium content of tube, etc, will possibly prevent forever its successful use by non-trained personnel only.

The Canary Islands are providing a very appropriate test bench for lots of European collaboration in solar astronomy. European countries are currently operating there 4 world-class major solar facilities, soon to be 5: the 1m NSST operated by Sweden (RSAS), the 60 cm DOT operated by the University of Utrecht, the 60 cm VTT operated by the Kiepenheuer Institute für Sonnenphysics from Freiburg and the 90 cm THEMIS operated by CNRS/CNR. First light of the 1.5 m GREGOR from KIS is planned for 2008. All these solar telescopes participate to the OPTICON I3 European program, and among them THEMIS has been particularly active in the 'Access Program' providing 'access units' (e.g., days of observations) to not-by-the-law users (Opticon access office, 2004-2006). This action shall continue into the FP7 program.

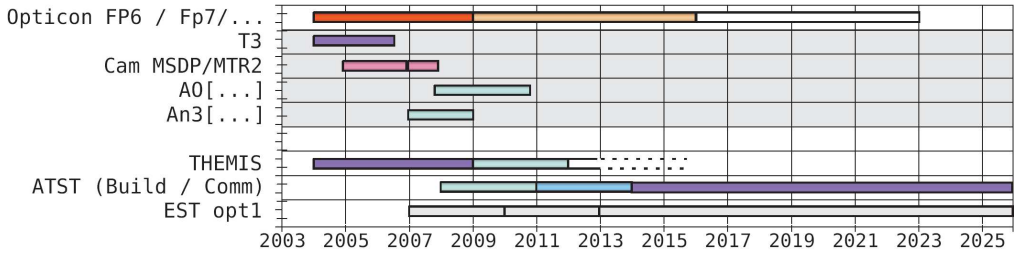

Figure 7. THEMIS current and planned technical developments are indicated over a gray shaded area. The building of the An3 analyzer has been approved as of Dec. 06 and the in-house qualification of a deformable mirror for the adaptive optics will start in 2007. Themis operations at the current funding level will possibly not extend after 2009, however the scientific yield of today's technical improvement are expected to deliver results until about 2012, the minimum delay allowing to reasonably exploit an updated THEMIS.

While these meter class telescopes are currently handled at national or university levels, the underlying scientific community, if properly federated, has obviously the expertise and size to conduct and successfully achieve much larger projects than just the upgrading its present facilities. A couple of recent meetings are just stating this, like the "Mondragone resolution" (see ESF exploratory workshop (2006)) *(i)An organization shall be established at the European level with the task to define and to co-ordinate the effort necessary to ensure access of European solar astronomers to, and promote creation of, worldwide leading ground based observing facilities. (ii) The Undersigned shall seek national and European funding for a viable and active partnership in the design, construction and operation of the ATST*[1]

This meeting was followed by a brainstorming session of telescope operators in Freiburg leading to the creation of a consortium structure (EAST)[2] whose mission is defined like: *[...] ensuring access of European solar astronomers to world-class observing facilities. In order to achieve this goal, EAST shall : (i) develop, construct and operate a next-generation large aperture European Solar Telescope (EST) in the Canaries (ii) co-ordinate the operation and scientific use of optical solar facilities in Europe, (iii) co-ordinate and facilitate efforts of its members to participate in other solar facilities such as the Advanced Technology Solar Telescope*

It is out of the scope of this paper to discuss the pro and cons of the many paths that extend in front us. However, Fig. 7 indicates an agenda for THEMIS technical improvements, and his exploitation time-line; The 2012 horizon for THEMIS is possibly not very different of the lifetimes of the already existing other Canarian solar telescopes. If we do not believe that only one ATST will fullfil the needs of both the US and EU community after 2015, we better start

[1] Advanced Technology Solar Telescope: see Keil et al. (2003)

[2] European Association for Solar Telescopes

immediately planning for the EST.

Acknowledgments. THEMIS is operated on the Island of Tenerife by the Centre National de la Recherche Scientifique (CNRS, France), the Institut National des Sciences de l'Univers (INSU, France) and the Consiglio Nazionale delle Ricerche (CNR, Italy) in the Spanish Observatorio del Teide of the Instituto de Astrofísica de Canarias.

References

Aulanier G., Gigan P., Malherbe J.-M., Molodij G., 2003, Projet de stabilisation d'image pour le télescope THEMIS, Technical proposal, Report to the THEMIS Scientific Advisory Council

Ballesteros E., 1996, Ph.D. thesis, Universidad de La Laguna

Ballesteros E., Collados M., Bonet J. A., Lorenzo F., Viera T., Reyes M., Rodriguez Hidalgo I., 1996, A&AS 115, 353

Brault J. W., Mueller E. A., 1975, Solar Phys. 41, 43

Cruvellier P. e. a., 2003, THEMIS adaptive optics, Technical proposal, Report to the THEMIS Scientific Advisory Council

ESF exploratory workshop, 2006, in 'New Generation Large Aperture Solar Telescopes: Science Drivers, Observational Strategies and Perspectives', Villa Mondragone, Monte Porzio Catone (Roma)

Judge P. G., Elmore D. F., Lites B. W., Keller C. U., Rimmele T., 2004, Appl. Optics 43, 3817

Keil S. L., Rimmele T., Keller C. U., Hill F., Radick R. R., Oschmann J. M., Warner M., Dalrymple N. E., Briggs J., Hegwer S. L., Ren D., 2003, in S. L. Keil, S. V. Avakyan (eds.), Innovative Telescopes and Instrumentation for Solar Astrophysics. Edited by Stephen L. Keil, Sergey V. Avakyan . Proceedings of the SPIE, Volume 4853, pp. 240-251 (2003)., 240

Mein P., 2002, A&A 381, 271

Mein P., Mein N., Schmieder B., Bommier V., 2006, in V. Bommier (ed.), Proceedings of the Solar Magnetism and Dynamics & THEMIS users meeting, Paris Observatory, Nov 2006, to appear

Molodij G., Rayrole J., Madec P. Y., Colson F., 1996, A&AS 118, 169

Rayrole J., Mein P., Schmieder B., 1998, in C. E. Alissandrakis, B. Schmieder (eds.), ASP Conf. Ser. 155: Three-Dimensional Structure of Solar Active Regions, 260

Rimmele T., von der Luehe O., Wiborg P. H., Widener A. L., Dunn R. B., Spence G., 1991, in M. A. Ealey (ed.), Active and adaptive optical systems; Proceedings of the Meeting, San Diego, CA, July 22-24, 1991 (A93-39451 15-74), 186-193., 186

Vassiliadis S., Hakkennes E. A., Wong J., Pechanek G. G. (eds.), 1998, The Sum-Absolute-Difference Motion Estimation Accelerator

Von der Luehe O., Widener A. L., Rimmele T., Spence G., Dunn R. B., 1989, A&A 224, 351

The Physics of Chromospheric Plasmas
ASP Conference Series, Vol. 368, 2007
Petr Heinzel, Ivan Dorotovič and Robert J. Rutten, eds.

GREGOR: the New German Solar Telescope

H. Balthasar[1], O. von der Lühe[2], F. Kneer[3], J. Staude[1], R. Volkmer[2], T. Berkefeld[2], P. Caligari[2], M. Collados[5], C. Halbgewachs[2], F. Heidecke[2], A. Hofmann[1], M. Klvaňa[4], H. Nicklas[3], E. Popow[1], K. Puschmann[3], W. Schmidt[2], M. Sobotka[4], D. Soltau[2], K. Strassmeier[1] and A. Wittmann[3]

[1] *Astrophysikalisches Institut Potsdam, Germany,*
[2] *Kiepenheuer-Institut für Sonnenphysik, Freiburg, Germany,*
[3] *Institut für Astrophysik, Universität Göttingen, Germany,*
[4] *Astronomical Institute AS, Ondřejov, Czech Republic,*
[5] *Instituto de Astrofísica de Canarias, La Laguna, Spain*

Abstract. GREGOR is a new open solar telescope with an aperture of 1.5 m. It replaces the former 45-cm Gregory Coudé telescope on the Canary island Tenerife. The optical concept is that of a double Gregory system. The main and the elliptical mirrors are made from a silicon-carbide material with high thermal conductivity. This is important to keep the mirrors on the ambient temperature avoiding local turbulence. GREGOR will be equipped with an adaptive optics system. The new telescope will be ready for operation in 2008. Post-focus instruments in the first stage will be a spectrograph for polarimetry in the near infrared and a 2-dimensional spectrometer based on Fabry-Pérot interferometers for the visible.

1. Introduction

Magnetic features on the sun are rather small or have an internal fine structure with typical scales of the order of 50 – 100 km. Variations occur on short time scales of a few minutes. To collect the required number of photons, large telescopes are needed to investigate such features. Such a telescope must have good polarimetric properties in order to enable high precision polarimetric measurements. A German consortium consisting of the Kiepenheuer-Institut für Sonnenphysik, the Institut für Astrophysik in Göttingen and the Astrophysikalisches Institut Potsdam presently builds a new solar telescope with an aperture of 1.5 m, GREGOR. International partners in the construction are the Astronomical Institute Ondřejov (Czech Republic) and the Instituto de Astrofísica de Canarias (Tenerife, Spain). GREGOR replaces the previous 45-cm Gregory-Coudé-telescope on Tenerife. Reports on the progress in constructing this telescope can be found in Volkmer et al. (2005), Volkmer et al. (2006) and Volkmer (2007).

GREGOR is designed as an open telescope, so the air can flow freely through the telescope. Problems with plane-parallel entrance windows of the required size are avoided this way, but now one has to care for the absorbed heat at the surfaces which are exposed to the full sunlight. Roughly 2000 W of radiation fall

on a primary mirror of 1.5 m diameter, and with a coating of aluminum about 10% will be absorbed. Therefore, active cooling of the primary mirror is required to keep it at the ambient temperature. If the material of the mirror body has a high thermal conductivity, it is sufficient to blow cold air onto the backside of the mirror. This is the reason why we decided not to use a standard glass-ceramic. Instead, the main mirror and the two following ones will be made from a silicon-carbide material. Besides its high thermal conductivity, this material has also the advantage of a quite high stiffness, so that the mirror is less bent due to the changing orientation during the day. In addition, the mirror mount is designed to minimize the influence of gravitational forces on the mirror. On the other hand it is very difficult to produce a mirror of this size fulfilling the optical requirements. More details can be found in Krödel et al. (2006).

The telescope has an alt-azimuthal mounting, thus the telescope structure is very compact and mechanical problems are reduced to a minimum. To realize the concept of an open telescope, and in order to make room for the 1.5 m telescope, the dome of the GCT had to be removed. It was replaced by a foldable tent of the same type as that of the Dutch Open Telescope on La Palma. Since the erection of this new dome several strong storms passed Tenerife which the dome resisted. The telescope structure was mounted at the site in 2004 and is shown in Fig. 1. The movements of the telescope are computer-controlled guaranteeing a precise basic guiding. The fine tracking is done by an adaptive optics system.

The telescope is designed for the wavelength range 380 nm through 12 μm.

The operation of the telescope and the control of the post-focus instruments will be done from a separate room in the third floor of the building. Graphical interfaces give access to all instruments and sensors.

2. The Optical Path

A scheme of the optical path is displayed in Fig. 2. The optical concept is that of a double-Gregory Coudé telescope. This telescope has an effective focal length of 55 m. The first three mirrors are aligned along the same optical axis to keep instrumental polarization to a minimum until the secondary focus.

The primary mirror M1 has a diameter of 1.5 m, is shaped parabolically, and has a focal width of 2.5 m. Cold air will be blown into pockets on the back side of the body of the mirror to keep temperature differences to the ambient below 0.3 K, sufficient to avoid heat-driven air turbulence at the front surface of the mirror. The temperature of the cooling air is adjusted according to the prevailing air temperature.

At the primary focus F1 there is a field stop which allows a circular field of 150 arcsec diameter to pass, alternatively a wider hole with 300 arcsec width can be inserted. The rest of the light (more than 97%!) is deflected out of the telescope. Because of the concentrated light at this location, this field stop needs active cooling by a water circulation, which is realized in two circuits. This way, the temperature difference to the surrounding air will be kept below 5 K.

The secondary mirror M2 is an elliptical one with a diameter of 42 cm. The two focal lengths are 67 cm and 2.3 m. This mirror will absorb 6 W, therefore passive cooling is enough to avoid temperature differences of more than 2 K. The alignment of this mirror with respect to M1 is extremely crucial for the optical

Figure 1. The mechanical structure of the telescope on top of the building. The dome is folded down. The Vacuum Tower Telescope is seen in the background.

performance of the telescope. M2 will be mounted on a hexapod permitting the needed degrees of freedom for movements. These movements will be done under control of the adaptive optics system (AO).

Little space is available near the secondary focus F2, nevertheless there is the possibility to introduce a linear polarizer (a Marple-Hess prism) and one of two achromatic quarter-waveplates (380 – 800 nm and 750 – 1600 nm, respectively). All these elements can be rotated with a step width of 0.1 degrees allowing the instrumental calibration of the instrument and a proper measurement of the circular polarization. For alignments, also a grid target or a pinhole can be inserted here. A more detailed report on polarimetry with GREGOR is given by Hofmann (2006).

The tertiary mirror M3 is used to focus the telescope. It is again an elliptical mirror with a diameter of 36 cm. The focal lengths of this mirror are 1.6 m and 10.1 m. Passive cooling is sufficient for this mirror too.

M3 reflects the light beam to flat mirror M4 which is located at the intersection of the optical axis of the telescope and the elevation axis. M4 reflects the light into the elevation axis. From there the beam passes three more flat mirrors (M5 – M7), and is finally reflected into the azimuth axis of the telescope. Heat absorption is not a problem for these mirrors, so they are made from ZERODUR. For the case that turbulence occurs in this part of the optical

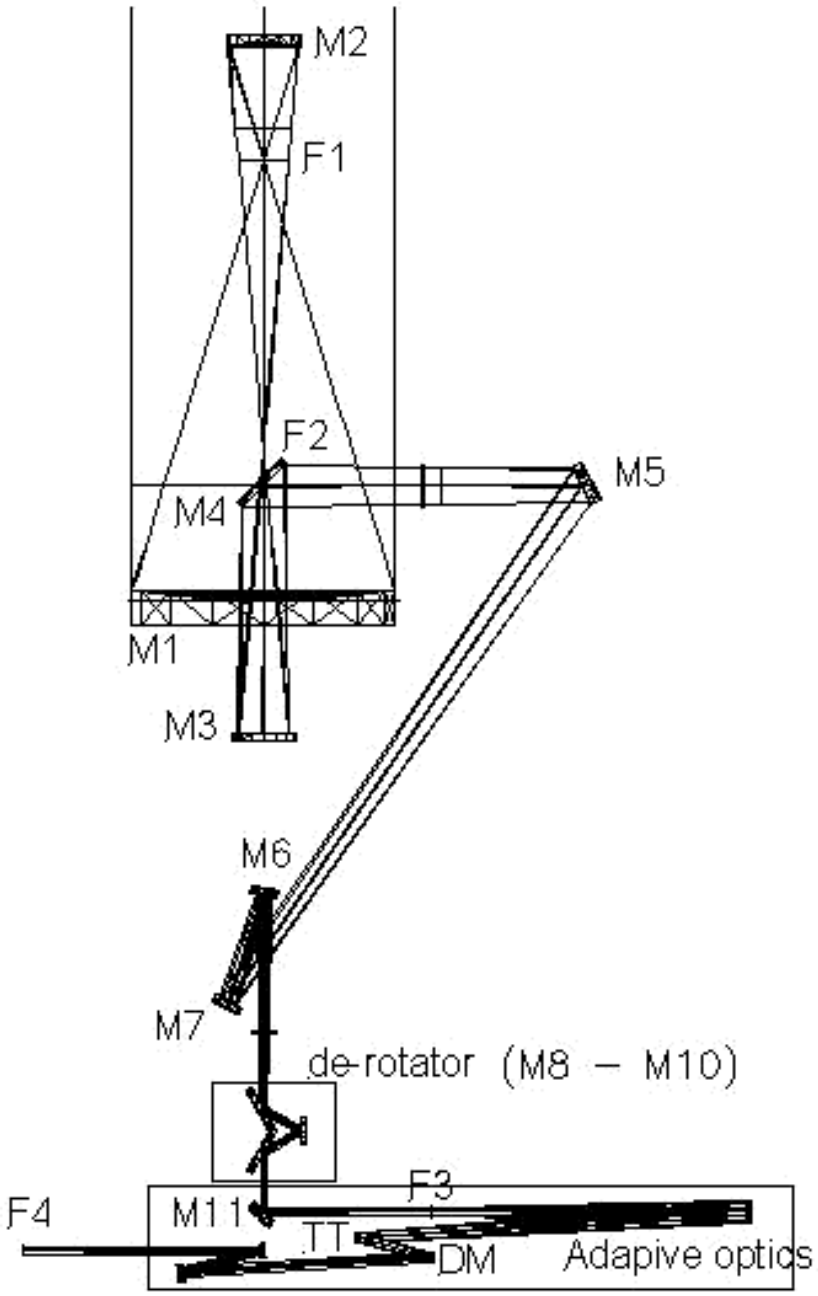

Figure 2. Optical scheme of the telescope.

path, glass plates are introduced between M4 and M5 and after M7, and the tube inbetween can be evacuated. For observations at wavelengths longer than 2.5 μm, these plates must be removed.

A disadvantage of the alt-azimuthal mounting is the rotation of the final image. This will be compensated by a de-rotator consisting of three flat mirrors M8 – M10. In addition, the de-rotator can be used to change the orientation of the image with respect to the post-focus instruments, e. g. the spectrograph slit. The de-rotator can be removed from the optical beam.

Mirror M11 reflects the light into the AO system. A filter wheel is placed at the tertiary focus F3; different field stops, a pinhole, a target, and a cover for dark exposures can be inserted here. Then the light passes the collimator M12, the tip-tilt mirror TT, the deformable mirror DM and the camera mirror M15, before mirror M16 sends the light to the requested post-focus instrument. M11 and M16 can be removed to bypass the AO. The deformable mirror DM has 80 electrodes and a free aperture of 55 mm. Each post-focus instrument will have its own wavefront sensor of Shack-Hartmann type. The wavefront sensors will have 78 usable sub-apertures. One sub-aperture will be covered by 24 × 24 pixel, and one pixel will correspond to 0.5 arcsec. Further details about the AO-system can be found in Soltau et al. (2006).

3. Post-focus Instruments

In the first stage GREGOR will be equipped with a 2D-spectrometer and a slit spectrograph together with an infrared polarimeter. Most post-focus instruments are placed in the optical laboratory in the fifth floor of the building, just below the telescope. The entrance slit and the polarimetry unit of the spectrograph are placed here too, then the light is reflected down to the fourth floor where stable conditions are guaranteed for the spectrograph.

The 2D-spectrometer is an upgrade of the Göttingen Fabry-Pérot spectrometer which was operated successfully for many years at the Vacuum Tower Telescope (VTT). It is based on two new tunable Fabry-Pérot interferometers (FPI) which have a diameter of 70 mm. The FPIs are placed in the collimated beam near the telescope pupil. The usable wavelength range is 530 – 870 nm, and the resolving power is of the order of 250000.

The slit spectrograph of Czerny-Turner type is optimized for the near infrared to be used with the Tenerife Infrared Polarimeter (TIP 2, Collados et al. 2007), which was operated at the VTT before. The heart of the spectrograph is the grating previously used at the GCT. The focal lengths of both, collimator and camera mirrors of the new spectrograph are 6 m. At 1.1 μm it has a resolving power of 525000, and the dispersion corresponds to 52 pm/mm. The spectrograph can be used for any single wavelength range in the visible too, only the dispersion is not well adapted to the pixel size of modern CCD-detectors. A few combinations of two visible ranges to be observed simultaneously are possible. A detailed description of the spectrograph is given by Collados et al. (2006).

Our plans also foresee to move the Polarimetric Littrow Spectrograph (POLIS) from the VTT to GREGOR as soon as GREGOR is ready. A description of this instrument was published by Beck et al. (2005).

One free optical table is available for experimental setups or guest experiments.

On a longer time scale, GREGOR will also be used for stellar astronomy, the Astrophysical Institute Potsdam plans a special spectrograph to obtain stellar spectra over the whole visible range. This spectrograph will be placed in the fourth floor.

4. Conclusion

With its aperture of 1.5 m and equipped with an adaptive optics system, GREGOR will be the most powerful solar telescope for high resolution spectroscopy in the range from 380 nm through 2200 nm for the near future. GREGOR has good polarimetric properties and will be equipped with a polarimeter for the infrared and the visible spectral range (TIP and POLIS).

First light and commissioning are expected to occur in 2008.

Acknowledgments. This report benefits from the ESMN (European Solar Magnetism Network) supported by the European Commission under contract HPRN-CT-2002-00313.

References

Beck C., Schmidt W., Kentischer T., Elmore D., 2005, A&A 437, 1159

Hofmann A., 2006, SUN and GEOSPHERE, (in press)

Collados M., Lagg A., Solanki S. K., 2007, in P. Heinzel, I. Dorotovič, R. J. Rutten (eds.) The Physics of Chromospheric Plasmas, ASP Conf. Ser. 368, 611

Collados M., Díaz J. J., Hernández E., López R., Páez, E., 2006, in Proc. Sociedad Española de Astronomia: Barcelona, September 2006, (in press)

Krödel M. R., Luichtel G., Volkmer R., 2006, in E. Atad-Ettegui, J. Antebi, D. Lemke (eds.) Proc. SPIE 6273: Optomechanical Technologies for Astronomy, 22

Soltau D., Berkefeld T., Volkmer R., 2006, in L. M. Stepp (ed.) Proc. SPIE 6267: Ground-based and Airborne Telescopes, 34

Volkmer R., 2007, in F. Kneer, K. G. Puschmann, A. D. Wittmann (eds.) Proc.: Modern Solar Facilities – Advanced Solar Science, Universitätsverlag Göttingen, (in press)

Volkmer R., von der Lühe O., Kneer F., Staude J., Berkefeld T., Caligari P., Halbgewachs C., Schmidt W., Soltau D., Nicklas H., Wittmann A., Balthasar H., Hofmann A., Strassmeier K., Sobotka M., Klvaňa M., Collados M., 2005, in S. Fineschi, R. A. Viereck (eds.) Proc. SPIE 5901: Solar Physics and Space Weather Instrumentaition, 75

Volkmer R., von der Lühe O., Kneer F., Staude J., Berkefeld T., Caligari P., Halbgewachs C., Heidecke F., Schmidt W., Soltau D., Nicklas H., Wittmann A., Balthasar H., Hofmann A., Strassmeier K., Sobotka M., Klvaňa M., Collados M., 2006, in L. M. Stepp (ed.) Proc. SPIE 6267: Ground-based and Airborne Telescopes, 29

The Physics of Chromospheric Plasmas
ASP Conference Series, Vol. 368, 2007
Petr Heinzel, Ivan Dorotovič and Robert J. Rutten, eds.

Tenerife Infrared Polarimeter II

M. Collados[1], A. Lagg[2], J. J. Díaz García[1], E. Hernández Suárez[1], R. López López[1], E. Páez Mañá[1] and S. K. Solanki[2]

[1] *Intituto de Astrofísica de Canarias, La Laguna, Spain*
[2] *MPI für Sonnensystemforschung, Katlenburg-Lindau, Germany*

Abstract. Since May 2005 the Tenerife Infrared Polarimeter II (TIP-II) has been operational at the Vacuum Tower Telescope on Tenerife. The core of the polarimeter is a 1024×1020 pixel infrared camera allowing for high precision measurements of the full Stokes vector with a pixel size of 0.18″, corresponding to the diffraction limit of the telescope at 1 μm. The polarimeter is able to reach a polarimetric accuracy of a few times 10^{-4}, covering a wavelength range of 1 to 1.8 μm. With an upgrade in July 2006, the slit size has been increased to 77″ allowing most active regions to be covered with a single scan. Here we present the technical details of the polarimeter and the camera. We also show some data illustrating the power of this new instrumentation.

1. Introduction

The Tenerife Infrared Polarimeter (TIP, Martínez Pillet et al. 1999) has been operating at the German VTT of the Observatorio del Teide since 1999, as a common use instrument. It is based on a pair of ferroelectric liquid crystals (FLCs) followed by a polarizing beamsplitter. Depending on an applied external voltage, the FLCs alternate the orientation of their fast axis between two orientations, separated by an angle close to 50 degrees at ambient temperatures. The four different orientation combinations allowed by the two FLCs give rise to four independent linear combinations of the Stokes parameters. As demonstrated by Collados (1999), del Toro Iniesta & Collados (2000), and Collados (2007), very good efficiencies can be obtained with this type of polarimeter. The polarizing beamsplitter generates two beams that, when combined, allow to minimize the crosstalk from intensity to the other Stokes parameters (Collados 1999). As shown by Collados (2007), a single pair of FLCs only have good efficiencies in a range about ±15% of the central wavelength. For this reason, TIP uses two different sets of FLCs to cover the full wavelength range from 1 to 1.8 μm.

Up to now, the most used and successful observed spectral ranges are those centered at 1.083 μm and 1.565 μm. The first one includes several photospheric lines and the chromospheric He I triplet, making possible the study of chromospheric magnetism (Trujillo Bueno et al. 2002, Solanki et al. 2003, Sasso et al. 2007) and its relation to photospheric phenomena (Centeno et al. 2006, Bloomfield et al. 2007). The second spectral range includes the highly magnetically sensitive $g = 3$ Fe I 1.5648 μm line, that allows for the study of weak magnetic field strengths (Khomenko et al. 2003) or its small fluctuations (Bellot Rubio et al. 2000).

Sensor	Rockwell TCM-8600 HgCdTe
Size	1024 × 1020 px
Pixel	18 μm (sq.)
Well depth	320000 e^-
Gain	20 e^-/ADU
Max. fr. rate	36 fr/s
Quantum effic.	$> 55\%$
Wavel. range	0.9-2.5 μm
Read noise	80 e^-
Dark current	220 e^-/s

Filter	Jlow	Jhigh	H
Maximum transmission	70%	82%	90%
$\lambda_{\rm center}(\mu{\rm m})$	1.105	1.265	1.635
FWHM(μm)	0.15	0.19	0.29

Table 1. Properties of the detector used in TIP-II (left table) and of the filters located inside the dewar to isolate the adequate diffraction order (right table).

In a collaboration between IAC and MPS, the system has been upgraded to a second version, named TIP-II (Tenerife Infrared Polarimeter II). To that aim, the detector and the polarization beamsplitter have been changed, which provides three major advantages: (i) the spatial sampling is reduced to match the value required to reach the diffraction limit of the VTT at 1 μm; (ii) the observed spectral range is increased, allowing more spectral lines to be observed. This may be useful for a better recovery of the magnetic and thermodynamical conditions of the observed regions using appropriate inversion codes; (iii) the spatial coverage along the slit has been doubled, making possible the coverage of large active regions with a single scan. The detector change was implemented during the 2005 observing campaign (with the old beamsplitter), while the new beamsplitter was installed in 2006.

In the following, the properties of the new elements are described. The performance of TIP-II at the VTT is given, together with its expected capabilities at GREGOR (Volkmer et al. 2006, Collados et al. 2007). The comparison with TIP operating at the VTT is also shown. Finally, some example data are presented.

2. Detector

The properties of the new detector are summarized in Table 1. The sensor is placed inside a cryostat that keeps it at liquid N_2 temperature (77 K). A filter wheel inside the cryostat permits the selection of the appropriate grating order for wavelength selection. Presently three filters are available (see the right part of Table 1). The filter wheel still has three unused positions for potential new filters.

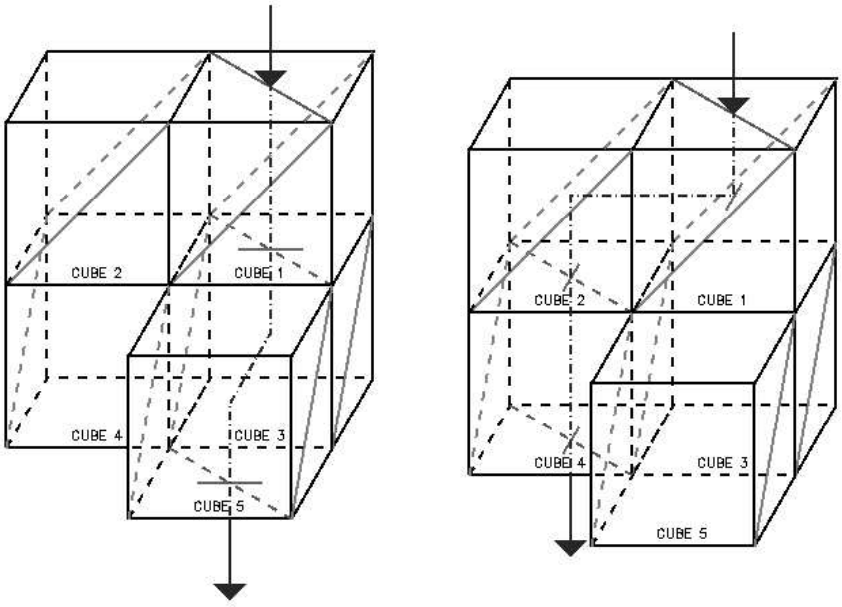

Figure 1. Diagrams showing the optical path followed by the beams. At the exit, two images of the input slit are formed with perpendicular linear polarization and very good polarization purity.

	TIP at VTT (1998)	TIP-II at VTT (2005)	TIP-II at GREGOR (2008)
Spatial sampling	0.36″/px	0.18″/px	0.135″/px
Spatial coverage	36″	77″	60″
Spectral sampling			
1.08 μm	29.6 mÅ/px	11.6 mÅ/px	21.1 mÅ/px
1.56 μm	29.4 mÅ/px	15.6 mÅ/px	44.9 mÅ/px
Spectral coverage			
1.08 μm	7.6 Å	11.8 Å	21.7 Å
1.56 μm	7.5 Å	15.9 Å	45.9 Å
Spectral dispersion			
1.08 μm	1.35 mm/Å	1.55 mm/Å	0.85 mm/Å
1.56 μm	1.36 mm/Å	1.16 mm/Å	0.40 mm/Å

Table 2. Characteristic parameters of TIP-II operating at the VTT. For comparison, the same parameters are given for TIP operating at the VTT and TIP-II at GREGOR.

3. Beamsplitter

Two new beamsplitters with the same optical principles have been installed. One comes from Meadowlark, and uses Versalight material for the separation of the p and s components. The properties of Versalight makes the device valid from 400 nm up to 2 μm. The second unit, from Fichou, uses dielectric coatings for the separation and can be used from 1.0 to 1.3 μm. Both beamsplitters

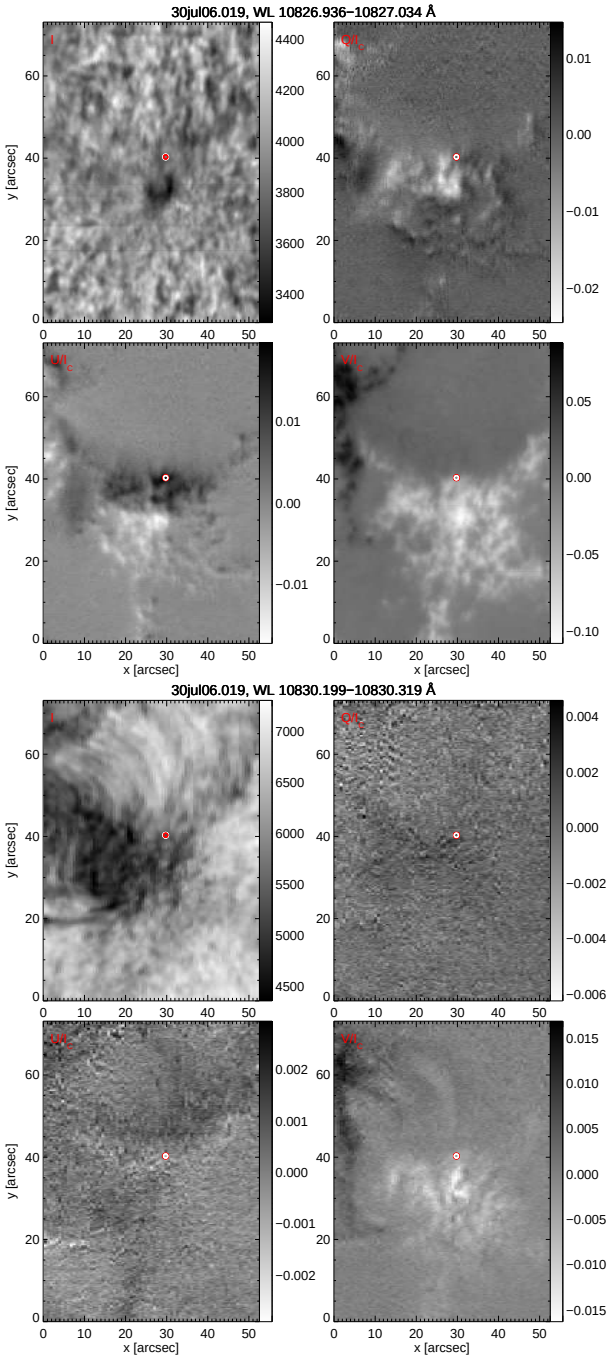

Figure 2. Stokes I, Q, U, and V map of an active region containing a small pore close to the the core of the Si I 10827 Å line (upper four images) and the He I 10830 Å line (lower four images). The images are composite maps of the individual slit spectra for the wavelength ranges given in the image titles.

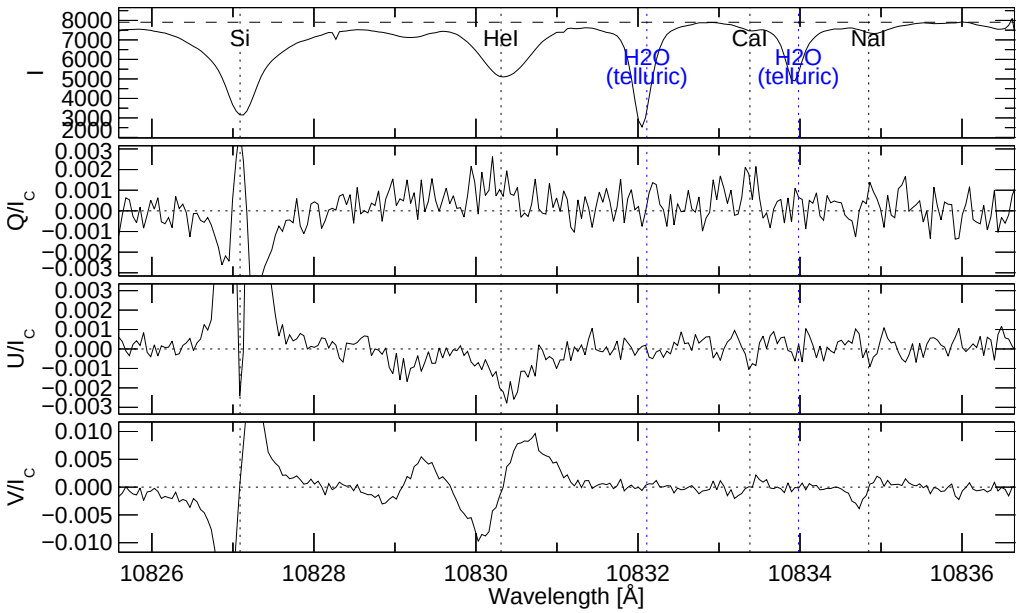

Figure 3. Stokes profiles for position $x = 30''$, $y = 40''$ in Fig. 2 (indicated by red dot), demonstrating the large spectral range and the polarization sensitivity achievable with TIP-II.

are composed by five individual cubes of 20 mm sides, adequately oriented to produce an excellent polarization purity of both beams (see Fig. 1). The optical path length for both beams is absolutely identical.

The beamsplitter is placed together with the FLCs just after the entrance slit of the spectrograph. The longitudinal separation of the beams is 28 mm, which, after the demagnifying factor 2 of the spectrograph camera mirror, become 14 mm. This is larger than the size of half the detector (9.2 mm). A set of prisms located in front of the entrance window of the cryostat make both beams fall onto the detector. This way, the field of view has been increased from $35''$ (TIP) to $77''$ (TIP-II).

4. Comparative performance

Table 2 gives the comparative performance of the systems TIP and TIP-II operating at the VTT, as well as that expected for TIP-II at GREGOR.

5. TIP-II Data

To demonstrate the capabilities of TIP-II we show a scan of an active region recorded during the first observing campaign when the full field of view of $77''$ was available. Figure 2 shows Stokes I, Q, U, and V maps of an active region in the photospheric Si I 10827 Å line and the chromospheric He I 10830 Å line at the solar position 35°W, 9°N. The inclination angle of the solar vertical to the line-of sight was 35°. The region of $52''\times77''$ was scanned in 150 scanning steps

from UT 18:33 until 19:05 on July 30 2006. The exposure time per slit position was 10 s, resulting in a signal to noise ratio of ≈1000 (RMS-noise). The image was stabilized using the Kiepenheuer Adaptive Optic System (KAOS, von der Lühe et al. 2003), the estimated spatial resolution of the image was limited by the seeing to ≈1.5″. Standard data reduction routines as provided by the IAC have been used to calibrate the images and to remove instrumental crosstalk.

Figure 3 shows a sample spectrum arbitrarily selected from the map in Fig. 2, binned over four wavelength bins. The spectral region contains 4 major solar spectral lines (Si I, He I triplet, Ca I and Na I) and two telluric H_2O blends. The Q, U, and V signal of the photospheric Si I line is cropped to emphasize the polarization sensitivity and the signal to noise ratio achievable with TIP-II.

Acknowledgments. Part of this research has been funded by the Spanish Ministerio de Educación y Ciencia through project AYA2004-05792. We would also like to thank the observers R. Aznar, C. Sasso and S. Bloomfield.

References

Bellot Rubio L. R., Collados M., Ruiz Cobo, B., Rodríguez Hidalgo, I., 2000, ApJ 534, 989.

Bloomfield D. S., Lagg A., Solanki S. K., 2007, in P. Heinzel, I. Dorotovič, R. J. Rutten (eds.), The Physics of Chromospheric Plasmas, ASP Conf. Ser. 368, 239

Centeno R., Collados M., Trujillo Bueno J., 2006, ApJ 640, 1153.

Collados M., 1999, in B. Schmieder, A. Hofmann, J. Staude (eds.) ASP Conf. Ser. 184: Advances in Solar Physics Euroconf. III. Magnetic fields and oscillations, 3.

Collados M., 2007 in Proc. Modern solar Facilities - Adavanced Solar Science, Goettingen, September 2006 (in press).

Collados M., Díaz García J. J., Hernández E. López López R., Páez Mañá E., 2007, in Proc.Sociedad Española de Astronomía, Barcelona, September 2006 (in press).

Khomenko E. V., Collados M., Solanki S. K., Lagg A., Trujillo Bueno J., 2003, A&A 408, 1115.

von der Lühe O., Soltau D., Berkefeld T., Schelenz T., 2003, in S. L. Keil, S. V. Avakyan (eds.), Innovative Telescopes and Instrumentation for Solar Astrophysics. Edited by Stephen L. Keil, Sergey V. Avakyan . Proceedings of the SPIE, Volume 4853, pp. 187-193 (2003)., 187

Martínez Pillet V., Collados M., Sánchez Almeida J. et al., 1999, in T.R. Rimmele, K. S. Balasubramaniam, R. R. Radick (eds.) ASP Conference Ser. 183: High Resolution Solar Physics: Theory, Observations, and Techniques, 264. .

Sasso C., Lagg A., Solanki S. K., Aznar Cuadrado R., Collados M., 2007, in P. Heinzel, I. Dorotovič, R. J. Rutten (eds.), The Physics of Chromospheric Plasmas, ASP Conf. Ser. 368, 467

Solanki S. K., Lagg A., Woch J., Krupp N., Collados M., 2003, Nature 425, 692

del Toro Iniesta J. C., Collados M., 2000, Appl. Opt. 39, 1637.

Trujillo Bueno J., Landi degl'Innocenti E., Collados M., Merenda L., Manso Sainz R. 2002, Nature 415, 403.

Volkmer R., von der Lühe O., Kneer F. et al., 2006, in L.M. Stepp (ed.) Proc. of the SPIE, 6267: Ground-based and Airborne Telescopes.

The Physics of Chromospheric Plasmas
ASP Conference Series, Vol. 368, 2007
Petr Heinzel, Ivan Dorotovič and Robert J. Rutten, eds.

Simulation of Magneto-Optical Filter Transmission Profiles

Giuseppe Severino[1], Maurizio Oliviero[1]
and Egidio Landi Degl' Innocenti[2]

[1]*INAF-Osservatorio Astronomico di Capodimonte, Napoli, Italia*
[2]*Dip. di Astronomia e Scienza dello Spazio, Università di Firenze, Italia*

Abstract. We present a numerical simulation of a potassium Magneto-Optical Filter (MOF) enabling to compute the filter transmission. The results of the simulation are compared with experimental transmission profiles at different heating temperatures, measured with a diode laser system. The comparison reveals a significant amount of agreement but also shows some important differences.

1. Introduction

Magneto-Optical Filters (MOF) are widely used in astronomy as well as in other fields of research because of their characteristics which include: narrow passband ($\sim$ 50 mÅ at transmission peaks); high transmission (max. 50% for incoming unpolarized light); high out-of-band rejection (10^5); large field of view, which makes them suitable for imaging; absolute wavelength reference and, hence, spectral stability. Therefore, it would be worthwhile to implement a theoretical simulation of the filter which enables to make reliable predictions of the filter transmission as a function of the two main parameters controlling the filter performances, i.e. the temperature at which the cell is heated and the external magnetic field in which the cell is embedded.

2. Method

Experimental cell transmission profiles for several heating temperatures and different magnetic fields are measured with a diode laser system. The diode laser by Sacher Lasertechnik works in Littman configuration. Its central wavelength is 769.45 nm; the full wavelength range is $>$ 10 nm; the fine tuning range is $>$ 30 GHz, i.e. 600 mÅ at 770 nm; the present resolution is 0.33 mÅ at 770 nm. The sensors are two PMTs with a dynamical range of 10^7. A portable PC controls the whole measurement procedure with a software running on a LabView platform.

On the track of the pioneering work of Cacciani et al. (1994), we carried out a numerical simulation of a potassium MOF which can compute the filter transmission, taking into account: spatial variations of temperature, potassium density and magnetic field inside the cell, line broadening induced by the buffer gas, and hyperfine structure of the K I D_1 resonance line, including isotopic shifts between the ^{39}K and ^{41}K isotopes.

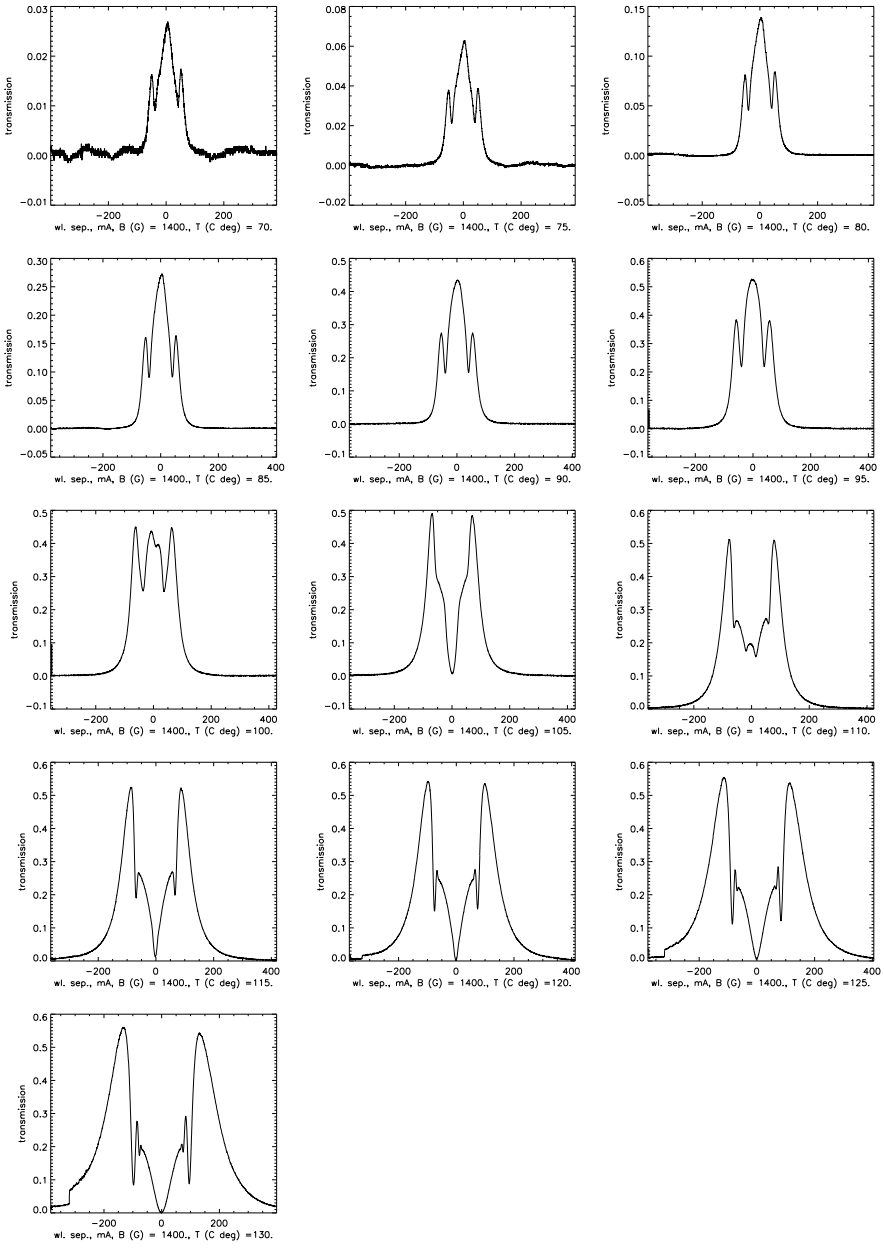

Figure 1. Experimental transmission profiles for several temperatures in the interval from 70°C to 130°C. The magnetic field at the center of the cell holder is 1400 G.

The temperature T inside the vapour cell satisfies a Laplace equation for thermal conduction with constant conductivity:

$$\nabla^2 T = 0\,. \tag{1}$$

The gas is a binary mixture, the potassium vapour being a minor constituent respect to the buffer gas. The number density of potassium N solves a steady-

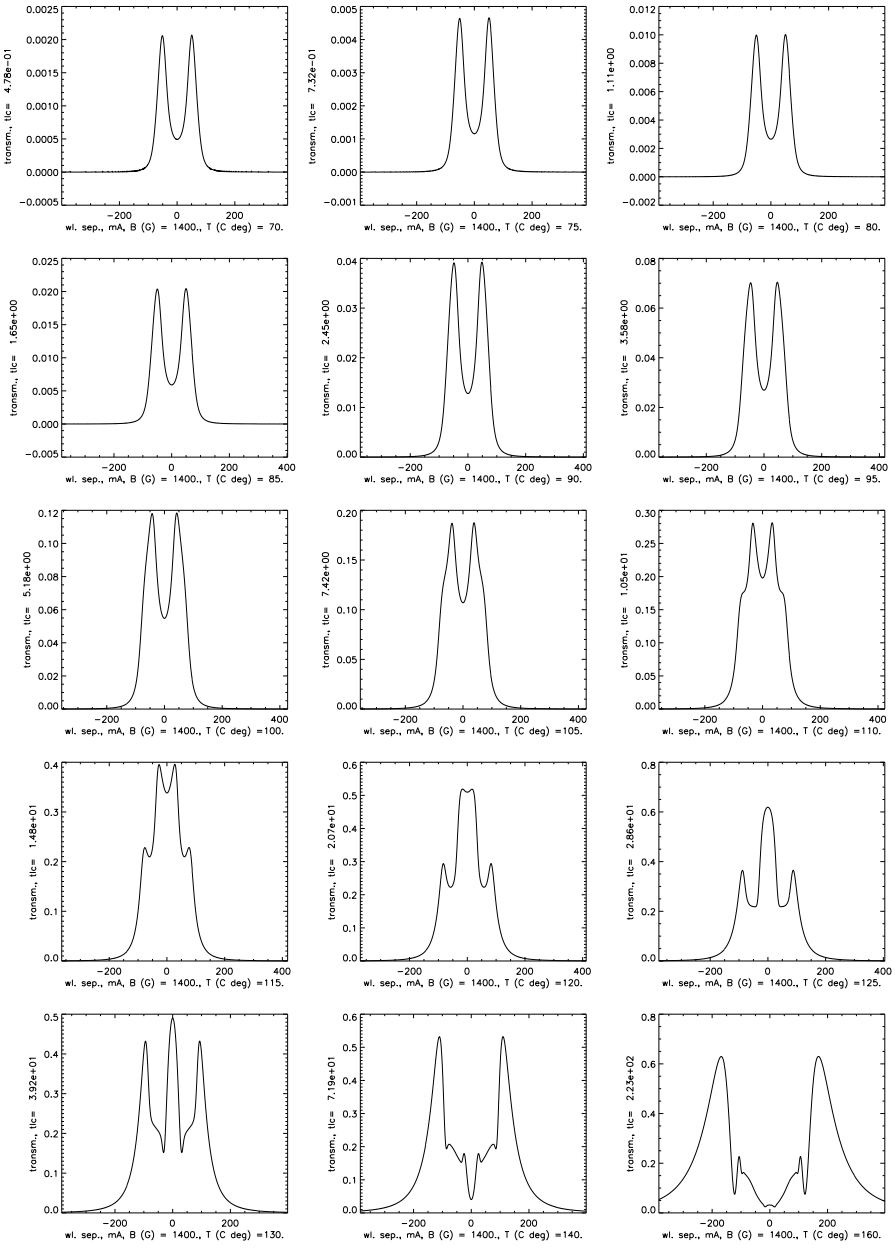

Figure 2. Results of the simulation for several temperatures in the range from 70°C to 160°C and for a central magnetic field of 1400 G.

state diffusion equation:

$$\nabla \cdot (D \nabla N) = 0\,, \tag{2}$$

where D is the diffusion coefficient. Both T and N distributions are found analytically in terms of the temperature on the cell boundary and of the vapour pressure of potassium at the liquid-gas interface.

The variation of the magnetic field along the cell axis was assumed as due to four "monopoles" located at the stem sides, the top charges being of opposite

sign with respect to the bottom ones. Stokes parameters inside the cell are the solution of the LTE transfer equations for polarized light, which are integrated numerically with the fourth-order Runge-Kutta method (Landi Degl'Innocenti 1975, Beckers 1969). Note that the K I D_1 line hyperfine structure includes isotopic shifts between the ^{39}K and ^{41}K isotopes (Landi Degl'Innocenti 1978, Bendali et al. 1981, Fricke-Begemann 2004). Moreover K I D_1 line broadening induced by the buffer gas (argon) is based on experimental data and the 6-8-12 theory (Andretta et al. 1991).

3. Results and Conclusions

The results of the simulation are compared with experimental transmission profiles acquired at different heating temperatures and measured with the diode laser system (Figs. 1 and 2). The comparison reveals that:

(i) for lower heating temperatures (slightly above the potassium fusion point), a definite discrepancy appears: experimental transmission has a central peak; this peak is missing in the simulation which shows only the expected Righi bandpass at the wavelengths of the two Zeeman components.

(ii) for higher heating temperatures, there is a significant amount of agreement, provided that suitable simulation heating temperatures are selected to best fit the experimental transmission profiles.

Particular care was taken to make the experimental data reliable. The three-peak transmission profiles at low heating temperatures are confirmed by measurements at various magnetic fields ($B_{\max}$=1100, 1400, and 2200 G) and with different cells. The unexpected central peak should not be due to the Macaluso-Corbino effect, since the whole bandpass changes by similitude when the heating temperature or the magnetic field are varied. We conclude that a significant difference between experimental and current theoretical MOF transmission profiles at low heating temperatures does exist and deserves further work to be fully explained, also from the theoretical side.

Acknowledgments. This work was supported by the Italian Department for University and Research (MIUR) with the contract PRIN-2004 c.r.a. 1.06.02.06.

References

Andretta V., Gomez M. T., Severino G., 1991, Solar Phys. 131, 1
Beckers J. M., 1969, Solar Phys. 9, 372
Bendali N., Duong H. T., Valle J. L., 1981, J. Phys. B: At. Mol. Phys., 14, 431
Cacciani A., Rosati P., Ricci D., Egidi A., Appourchaux T., Marquedant R. J., Smith E. J., 1994, in JPL internal report #D11900: Theoretical and Experimental Study of the Magneto-Optical Filter
Fricke-Begemann C., 2004, in IAP Nr. 10/2004: Lidar Investigations of the Mesopausa Region: Temperature Structure and Variability
Landi Degl'Innocenti E., 1975, A&A 45, 269
Landi Degl'Innocenti E., 1978, A&AS 33, 157

The Physics of Chromospheric Plasmas
ASP Conference Series, Vol. 368, 2007
Petr Heinzel, Ivan Dorotovič and Robert J. Rutten, eds.

Šolc Birefringent Filter for Various Interesting Lines

Radek Melich, Zbyněk Melich and Ivan Šolc

Institute of Plasma Physics AS, Turnov, Czech Republic

Abstract. In this paper there is described a Šolc birefringent chain narrow-bandpass filter that allows observation in more than 30 interesting spectral lines (Hα, Ca II K, Hβ, Hγ, D_1, D_3 etc.). A solar spectrographic telescope meeting demands for constant solar image scale in wavelength from 380 nm to 760 nm is also presented. This telescope equipped with the proposed filter is designed as a unit providing a top quality imaging.

1. Introduction

Observing the Sun chromosphere with the polarization interference filters has an advantage of their long lasting and high stability (Šolc 1997; Yariv & Yeh 2003). Such filters are mainly constructed for just one spectral line (e.g., Hα). Construction of a filter for more spectral lines (Kustal & Skomorovski 2000; Šolc 1976) or tunable via wider spectral range is much more difficult, however, such a solution is theoretically possible. In Kustal & Skomorovski (2000) we can find a description of Lyot type filter recently used for observing in Hα and He I lines. A fully tunable filter working in a wide spectral range was realized by Title, but his unique concept (Title & Rosenberg 1979) consists of a very complicated construction.

Scientific workers of Solar Department of Astronomical Institute of Academy of Sciences of the Czech Republic required manufacturing of several pieces of narrow-band filters for professional solar chromosphere observation at minimum price. The filter set should provide an observation in astronomically interesting lines such as Hα, Ca II K, Hβ, Hγ, D_1, D_3 and if possible even more.

After thorough analysis it has been stated that fulfilling of these requirements is possible using a Šolc birefringent chain filter. An appropriately chosen plates construction will suit filter transparency in required lines. During the observation only one line will be used and the others will be cut off by pre-filters (Melich 2005).

2. Filter Design

In the theoretical part of filter design it has been concluded that the filter cannot be accomplished as a simple spectral element. However, the filter can be built up using a combination of several interdependent optical elements in the way shown in Fig. 4.

The first barrier element of the filter is implemented as a dielectric filter set (DF) placed in a carousel. The second barrier element (SF1) of the filter is

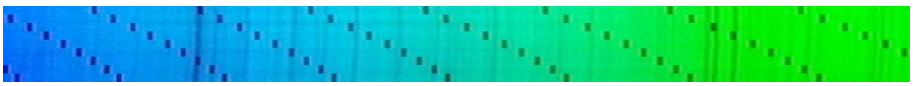

Figure 1. Tuning of barrier sub-filter transmitting spectrum maxima by its inclination. Each line represents the inclination of 1°. As a result we can see tuning of the filter maxima. (Transmittance of the sub-filter is negative in this Fig.)

realized as Šolc filter built up of birefringent obliquely cut plates (not parallel cut to optical axis of a crystal as usual) (Melich et al. 2005). Such a sub-filter is tunable in a wide spectrum range with a simple inclination (see Fig. 1). Behind the barrier sub-filters in an optical path there is placed a main sub-filter (SF2) that is designed as a quartz element built up of 26 plates.

The design of a filter that should be working at a wavelength λ is projected with respect to the equation

$$d = kM(\lambda, t), \tag{1}$$

where d is a thickness of a plate, M is a unit thickness (established by Šolc; has a dimension of length and has meaning of a plate thickness when a path difference of ordinary and extraordinary waves is equal to λ) and k is an order of the plate $(0.5, 1.5, 2.5, \ldots)$ (Šolc 1976). The filter transmits the required wavelength when thickness of its plates satisfies the condition (1). A proportion is valid for a filter: the smaller plate thickness d, the higher the distance between maxima of the filter channel spectrum. The full width in a half maximum (FWHM) of one filter maximum is proportional to a total length of the filter Σd. The bigger is Σd, the thinner is the FWHM.

The design of a filter for 2 spectral lines can be found in Šolc (1976). We applied this method in connection with other numerical methods to obtain such the plate thickness that provides transmittance of the filter for astronomically interesting spectral lines as much as possible. In addition, we have employed the fact that the unit thickness $M(\lambda, t)$ depends on temperature (Šolc 1984), what causes an increase of the number of observable lines. The number of lines listed in Fig. 2 has been observed with SF2 sub-filter. An acceptable temperature range of $10 - 60$°C is used to tune the filter to the desired line. From several proposed thicknesses d of the main sub-filter SF2, 11.4000 mm with an optical diameter of 32 mm has been chosen. The main sub-filter has the FWHM equal to 1 Å in the Hα region.

To decrease the FWHM of the entire filter a next Šolc type sub-filter (SF3) is placed in the optical path. This one is contrary to other sub-filters (made from quartz) made from calcite. Such a solution using for instance 6 pieces of plates with $d = 4.0000$ mm leads to FWHM of 0.4 Å in the Hα region. All the sub-filters are separated by polarizers P1, ..., P4.

The idea of birefringent barrier sub-filters is based on the fact that each sub-filter has a different plate thicknesses and therefore it transmits slightly different wavelengths. However, it is possible to choose such plate thicknesses that after several maxima of the first sub-filter (cut off by the second sub-filter), the coincidence of both filter maxima occurs and such a wavelength is transmitted by both filters (Šolc 1971).

Element	Lambda [A]	Tw[C]	Element	Lambda [A]	Tw[C]	Element	Lambda [A]	Tw[C]	Element	Lambda [A]	Tw[C]
Ca	6499.654	16.98	Cr Fe	5208.432	34.11	Fe	4920.514	41.22	Fe	4260.486	48.42
Fe	5914.213	20.30	Fe	4325.775	34.11	Fe	4191.437	42.12	Ca Cr	4289.729	49.11
Fe Ba2	6496.908	21.65	Fe	5139.473	34.60	Mn	4762.375	42.17	Fe	5369.974	49.17
Mg – 3	5167.327	23.77	He D3	5875.625	34.61	Fe	5442.060	42.21	Fe	6633.758	51.21
Fe	6494.994	24.46	Mn	4823.514	34.68	Fe	4415.135	42.50	Fe	4118.555	52.81
Fe	5142.936	27.32	H-γ	4340.475	34.86	Fe	4383.551	42.85	Fe	6592.926	52.88
H-δ	4101.748	28.30	Ni	6643.638	35.62	Fe	4233.612	43.24	Na D1	5895.940	52.97
Fe	5074.753	29.27	Fe	5302.307	36.32	Ca-H	3968.492	43.29	Fe	4187.047	53.02
Fe	4404.761	29.61	Mo2 Fe	4250.797	36.56	Fe	5227.192	43.39	Fe	4132.067	53.16
Fe	6003.022	30.40	Mg – 1	5183.619	37.08	Mg	4351.921	43.58	Fe	5269.550	53.45
Ni	4786.542	31.00	Fe	4152.176	37.19	Mn	4030.763	43.66	Fe	5367.476	53.82
Fe	5232.952	31.46	Fe	4235.949	37.28	Cr	5298.283	43.97	Fe2	5316.620	56.27
Fe	5429.706	31.59	Fe	4071.749	37.86	Fe	4005.254	44.85	Fe	5987.070	58.74
Fe	4153.906	31.89	Mn	4783.424	38.22	Fe	4918.998	45.05	Fe	5364.880	58.76
Fe	5816.380	32.14	H-β	4861.342	38.29	Fe	4938.820	45.68	Mg-2	5172.698	59.39
Mg	4167.277	32.68	Fe	5137.393	38.55	Fe Ni	5371.501	45.98	Al	3961.535	61.54
Ti2	4805.099	32.68	Ca-K	3933.682	38.90	Fe	4134.438	47.44	Na D2	5889.973	63.73
Fe	5328.051	33.72	Fe	4045.825	39.00	Fe	5110.435	47.69	Ca	5857.459	67.01
			H-α	6562.808	39.16				Fe Dy2	4957.613	69.75

Figure 2. Table of spectral lines observable with the main Šolc sub-filter SF2. T_w is working temperature used for the main Šolc sub-filter to be tuned on a proper line.

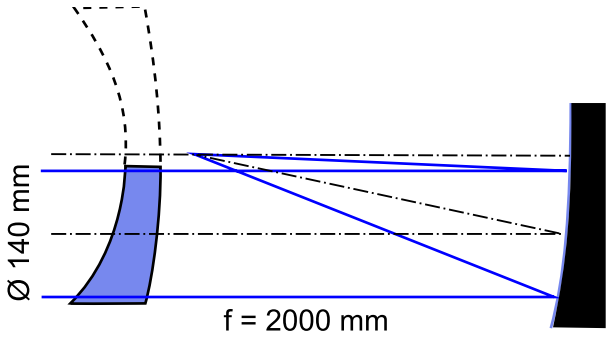

Figure 3. Scheme of Maksutov off-axis system. It uses an eccentric meniscus and a spherical mirror.

3. Imaging System

For observing of the Sun it is necessary to use a high-quality objective that provides a sufficient resolution of observed chromosphere details. In the Czech Republic the seeing reaches a value in order of seconds, rarely and only at good observation posts it decreases under one second. Considering the observation of the entire Sun disk and using our experience with similar telescopes design, the objective of optical diameter $d = 140$ mm and image focal length $f' = 2000$ mm has been chosen. Hence, the primary image of the Sun has a diameter about 19 mm. A theoretical resolution of this mentioned objective is 0.7 second of arc.

A criterion for the objective design quality is a low value of a longitudinal chromatic aberration. The best results regarding the correction of a spherical aberration, coma and modulation transfer function are obtained using the off-axis version of Maksutov system (see Fig. 2) where there is no shading of the

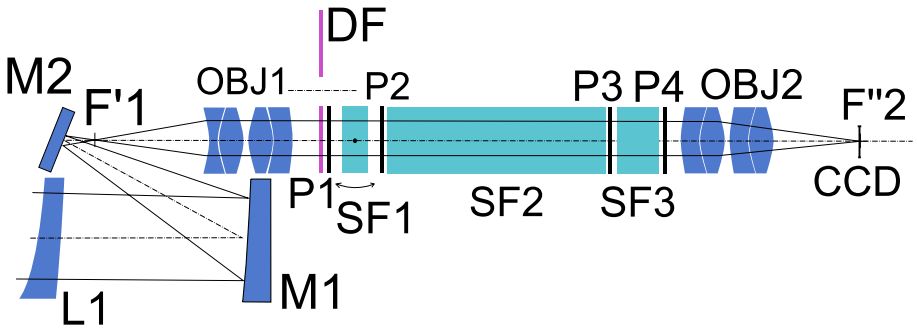

Figure 4. An optical scheme of chromospheric telescope. Elements L1, M1 and M2 form the entrance objective, OBJ1 is the collimating objective, elements DF, P1, ..., P4, SF1, SF2 and SF3 create the filter and OBJ2 is the objective focusing light to the CCD element.

primary mirror. Spherochromatic abberation of our objective reaches a value of only $ds' = 0.03\,\mathrm{mm}$ for a spectral range 380 – 760 nm. Geometrical images in a view field of a Sun disk size are smaller than diffraction patterns of $20\,\mu$m diameter (Rail et al. 2006).

The entire optical system can be seen in Fig. 4. The optics of collimation objective OBJ1 and image objective OBJ2 is currently under construction. The entire system, including the imaging system and the filter, is optimized as a unit. As a sensor we use a CCD camera SoftHard Technology with a 2/3 inch chip (SONY ICX285AL, 10.2×8.3 mm with matrix of 1376×1038 pixels, one pixel has $6.5 \times 6.5\,\mu$m).

4. Conclusion

The paper describes the design of original narrowband-pass birefringent filter. The filter is designed in a way that transmits more that 30 astronomically interesting spectral lines (only one is chosen for observation). The special objective based on off-axis Maksutov optical system meeting high demands on aberrationless imaging in a spectral region 380 – 760 nm has been developed for the filter. The field tests with the entire system are expected to be done in the next year. Astrophysicists will get a unique new device that helps to extend the knowledge of the Sun characteristics.

Acknowledgments. This work is supported by project 1SQ100820502 of the "Support of purposeful programme of the Czech Academy of Sciences".

References

Kustal G., Skomorovski V., 2000, Journal of Optics 6, 99

Melich Z., 2005, Support of purposeful programme of Czech Academy of Sciences project 1SQ10085050 (in Czech), Technical report, Academy of Sciences of the Czech republic

Melich Z., Klimes J., Šolc I., 2005, in Procs. Úpice Obs. Conf. "The man in his terrestrial and cosmic neighbourhood", 30

Rail Z., Jares D., Ledl V., 2006, in Procs. Úpice Obs. Conf. "The man in his terrestrial and cosmic neighbourhood"
Šolc I., 1971, Fine Mechanics and Optics 159–161
Šolc I., 1976, Fine Mechanics and Optics 21, 279
Šolc I., 1984, Fine Mechanics and Optics 2, 43
Šolc I., 1997, in Procs. Úpice Obs. Conf. "The man in his terrestrial and cosmic neighbourhood"
Title A., Rosenberg W., 1979, Research on Spectroscopic Imaging, Lunar and Planetary Programs, Technical report, NASA Headquarters
Yariv A., Yeh P., 2003, Optical Waves in Crystals, John Wiley & Sons, Inc., Hoboken, New Jersey

Serge Koutchmy and Renzo Ramelli

Thanks. . . !

The Physics of Chromospheric Plasmas
ASP Conference Series, Vol. 368, 2007
Petr Heinzel, Ivan Dorotovič and Robert J. Rutten, eds.

Measurement of the Polarization of the Flash Spectrum during a Total Solar Eclipse

Alex Feller[1], Renzo Ramelli[2], Jan O. Stenflo[1,3] and Daniel Gisler[1]

[1]*Institute of Astronomy, ETH Zurich, Switzerland*
[2]*Istituto Ricerche Solari Locarno, Switzerland*
[3]*Faculty of Mathematics & Science, University of Zurich, Switzerland*

Abstract. Total solar eclipses offer the unique opportunity for a clean observation of the light emitted by different chromospheric layers without being disturbed by photospheric stray light, since the moon is operating as a sharp knife edge. During the 29th March 2006 total solar eclipse we thus performed a pioneering measurement of the polarization of the flash spectrum from UV to the near IR with a spectral resolution of order 0.6 nm. The measurement has been obtained with a dedicated instrument composed of an 8-inch Dall-Kirkham type telescope and a slitless spectropolarimeter. The complete flash phase at the second contact was observed with a cadence of 25 frames per second corresponding to a height resolution of about 20 km in the solar atmosphere. We could nicely register the dramatic transition from an absorption-line spectrum to an emission spectrum dominated by the strong chromospheric resonance lines. At the third contact we recorded the opposite transition with a variable frame rate reaching up to 75 frames per second.

1. Introduction

The chromospheric emission spectrum, called flash spectrum, has already been recorded successfully during multiple eclipse expeditions (Cillié and Menzel 1935; Mitchell 1947; Dunn *et al.* 1968; Shen *et al.* 1981). The mentioned authors have compiled catalogues itemizing the calibrated absolute fluxes of more than a thousand emission lines in the range 300 to 910 nm. The spectra of Dunn *et al.* (1968) cover 4500 km on the Sun with a height resolution of 100 km in the direction of lunar movement. Although these data lack polarization information, they have been very helpful for the design of our instrument, allowing us to narrow down the required sensitivity range.

In terms of polarimetry we know of two past eclipse observations, which allowed to set an upper limit of 5% for the Ca II K line (Hanson *et al.* 1976) and a general upper limit of 10% estimated by eye for the whole optical spectrum (Stokley 1948).

The flash spectrum is extremely difficult to observe outside an eclipse. The steep intensity decrease at the extreme limb of the Sun makes a coronagraph very vulnerable to stray light caused by the earth's atmosphere and by the optics of the instrument itself. The main challenge here is the occulting disc. It must not exceed the solar disk by more than a fraction of an arcsecond, to properly isolate the thin chromospheric layer from the photosphere while still leaving it uncovered. Another serious drawback of out-of-eclipse observations

is the spatial resolution of current solar telescopes, which is limited to about 100 km. In contrast, as the eclipsing Moon is moving at a relative speed of about 350 km/s, a height resolution of order 10 km on the Sun can already be achieved with a moderate rate of 50 frames/s.

The lunar limb is somewhat serrated, but the corresponding height variations can be easily accounted for (Espenak and Anderson 2004) since our spatial resolution is about $5''$ in the limb direction.

The scientific rationale of our observations is described in detail by Stenflo (2006). A theoretical reference has been developed by Chandrasekhar (1950) in terms of an idealized model for a plane-parallel purely scattering atmosphere. The conditions at the extreme limb of the Sun are approaching this Chandrasekhar limit, but the real polarization can nevertheless be significantly influenced by different physical processes: the relative importance of different opacities, collisions, deviation from plane-parallel stratification (spherical geometry at the limb, small scale inhomogeneities), atomic physics (quantum interference, optical pumping), radiative-transfer physics and magnetic fields (Hanle effect). These processes affect the individual spectral lines in different ways. By recording a large part of the spectrum, we may be able to untangle and quantify them with the help of differential diagnostics.

2. Instrument

2.1. Sensitivity

When designing a polarimeter one has to make a trade-off between spatial, spectral, and time resolution and polarimetric sensitivity. The chromospheric sickle is not resolved in practice in the direction of lunar movement, because of the steep intensity drop with height.

The huge dynamic range between the strongest (Hα) and the weak lines of interest cannot be handled by the camera at once. At maximum frame rate the instrument has to be sensitive enough to just saturate in the weak lines at the beginning of the flash phase. The stronger lines will then drop into the sensitivity range later on. It is important to have a CCD with an anti-blooming factor of at least 1000 $\times$ saturation, to avoid any crosstalk from the strong lines during the saturated phase. As we were able to obtain a very fast F/2.8 spectrograph, we can adequately expose the camera with a modest and easily transportable 8-inch telescope (see Fig. 1).

Close to saturation the intensity signal to noise ratio, given by photon-statistics, is about 250. This meets the requirements on polarimetric precision and is adequately sampled with a 10 bit A/D conversion (cf. Table 1). At less than 0.1 $\times$ saturation the readout noise begins to dominate. Dark current is negligible. For a more detailed discussion see Feller et al. (2006).

2.2. Telescope and spectropolarimeter unit

The telescope is an 8-inch Dall-Kirkham Cassegrain reflector. The imaging is nearly diffraction limited within our small field of view and the Cassegrain design is virtually free of instrumental polarization.

A scaled drawing and a close-up photograph of the spectropolarimeter unit are shown in Fig. 1. To keep the optical efficiency high and chromatic aberrations

spectral range	340 - 870 nm
spectral sampling	0.21 nm/pixel
time resolution	13 - 40 ms
spatial sampling	5″/pixel
field of view	150″
sampling	50 e^-/count, 10 bit
anti-blooming factor	1000

Table 1. Main instrument characteristics.

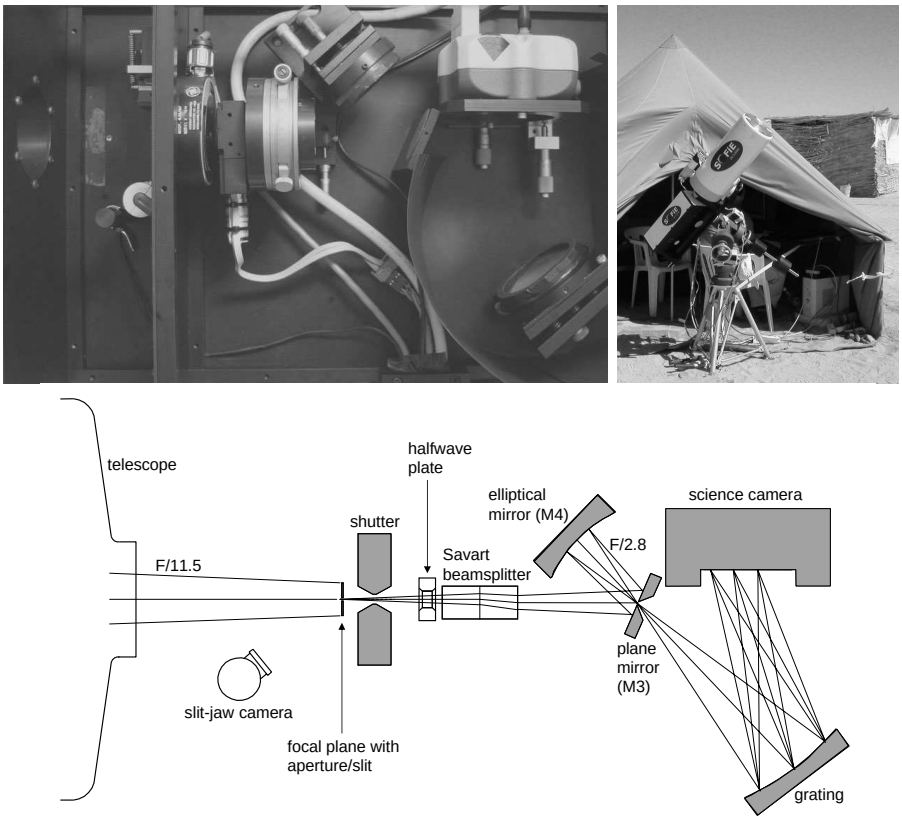

Figure 1. *Bottom:* optical setup. *Top left:* top view of the spectropolarimeter unit. *Top right:* overview of the setup at the eclipse site near Waw an Namos, Libya. The spectropolarimeter unit is mounted behind the telescope. In the background one can see the tent which is used as work place and protection for the electronic equipment. The electrical power of the whole setup (150 – 200 W) is provided by fuel generators and secured with a UPS.

at a minimum, the use of glass in the beam path is avoided, except for the half wave plate and the beam splitter. At the telescope focus one can choose between a 50 μm slit of length 1.6 mm and an aperture of 1.6 mm × 1.6 mm. With the slit we record calibration spectra of the solar disk or a spectral lamp. The aperture is used for the actual observation of the flash spectrum. This slitless mode has

some important advantages: it allows the imaging of extended solar structures and relaxes the tolerances on guiding and pointing of the telescope. Then again we observed disadvantages like aberrations caused by an off-axis position of the sickle or the smearing of nearby spectral lines.

In terms of polarimetry we opt for a Savart beam splitter. It is installed in the slower F/11.5 beam to keep its aberrations below the size of a pixel. The disadvantage of this position is the need of rather thick calcite elements. We have 2×22.8 mm, giving us a beam separation between 3.40 and 3.76 mm, depending on wavelength. To eliminate the effect of the polarization dependent grating efficiency, the beam splitter has to be turned so that the polarization direction of both beams is oriented $\pm 45°$ to the grooves of the grating. A half wave plate is needed in this context to realign the Moon's limb with the direction of Stokes $+Q$. We renounce the use of true beam exchange because of the intricacies of getting an adequate fast-switchable and achromatic half wave plate. Instead the retarder is turned mechanically by 45° one single time between the two flash phases of second and third contact.

After the Savart plate the two beams are deflected by a plane mirror (M3) with a circular hole of 2.5 mm diameter, reduced by an elliptical mirror (M4) to F/2.8 and then focused through the hole in M3 into the spectrograph.

The spectrograph consists of an aberration corrected holographic concave grating with 405 grooves/mm, serving as both the dispersive and focussing element. Operated in first order it provides a practically linear dispersion of 0.21 nm/pixel over the whole wavelength range. The grating efficiency varies between about 45% (393 nm) and 23% (866 nm). We find however a significant residual astigmatism, clearly dominating the total aberrations of the instrument. As a trade-off we adjust the grating and camera position to align the detector plane as good as possible with the spectral focal plane, but accepting therefore a strong wavelength dependent spatial defocussing.

Both the telescope and the spectropolarimeter unit are assembled on a parallactic mounting with computer-controlled stepping motors on both axes. The guiding and pointing accuracies in the hour axis are limited by the worm gear which has a period of about 12 minutes at guiding speed and a mean amplitude of some $40''$. Due to their periodicity, the hour axis errors can at least be partly compensated with the guiding software. The guiding and pointing accuracies in the declination axis are of order $1''$/minute and $10''$ respectively and can be neglected for our purpose. The knowledge of the pointing accuracies is crucial for the eclipse observations as the telescope has to be moved blindly to the opposite limb during totality. It defines the minimum size of the aperture in the spectropolarimeter unit.

Our observing spot is located near Waw an Namos in the Sahara of southern Libya (24:28:03 N, 17:57:52 E), on the center line of the eclipse path and close to the point of maximum duration of totality. The center-line position is necessary to avoid sickle movements during the flash phases and it has the advantage that the sickles of second and third contact are parallel.

2.3. Instrument control and observing procedure

The science camera and shutter as well as the rotation of the half wave plate are controlled with software developed in-house and optimized for the particular requirements of the eclipse observation.

The time server is providing UTC with an accuracy of about 10 ms, which corresponds to the time resolution of the instrument.

For accurate pointing on the Sun a special guiding software has been developed in-house which uses the solar limb as reference frame. Before the first contact the pointing position is determined by scanning the solar disk in the two axis directions with the spectropolarimeter in slit-mode, and determining the limb position by the corresponding inflection point in the measured intensity. First contact is used to check the positioning and orientation of the spectropolarimeter. Measurements started 30 seconds before second contact at a fixed rate of 25 frames per second and lasted for more than one minute. The third contact was observed with variable rates between 25 and 75 frames per second, based on a visual evaluation of the flash intensity. After the eclipse dark and flat calibration where performed. In addition the reference spectrum of a Rb I lamp was recorded.

3. Conclusions and Outlook

The instrument described here has been developed and built from scratch within one year for the 29 March 2006 eclipse. The observing location in the desert, hundreds of km away from any infrastructure, called for robust, compact, reliable and completely autonomous equipment as well as elaborate logistics.

Despite all these challenges the equipment was running faultlessly. The eclipse was passing under ideal weather conditions and we were able to measure both flash phases of second and third contacts, on opposite solar limb positions.

Our requirements were however not entirely satisfied. The main drawback of the instrument is the residual aberrations caused by the grating, in particular the differential effects between the two beams (cf. Fig. 2). They have been discovered only during the tests of the final instrument, and we were not able to fully resolve them in due time. On the other hand the slitless mode has proven to be an advantage for isolated spectral lines like Hα, allowing to image extended structures like a prominence, but a disadvantage for adjacent lines like He I D_3, Na I D_1 and D_2.

The data reduction is still ongoing, and the results as well as the reduction techniques will be discussed in detail in a later publication. The main challenge is to study and model the aberrations in order to determine the cospatial regions in both images and to improve the spatial resolution in some parts of the spectrum.

Finally we are already thinking of incorporating our experiences for a second generation eclipse experiment. The key enhancements we will be working on are the replacement of the slitless mode with an array of optical fibers, the use of an échelle grating, and a true achromatic beam exchange.

Acknowledgments. Financial support for this work has been obtained through grants Nos. 200020-101603 and 200020-109159 from Swiss Nationalfonds. We would like to thank the technical staff at the Institute of Astronomy of ETH Zurich as well as Michele Bianda and Evio Tognini from the Istituto Ricerche Solari Locarno for helping

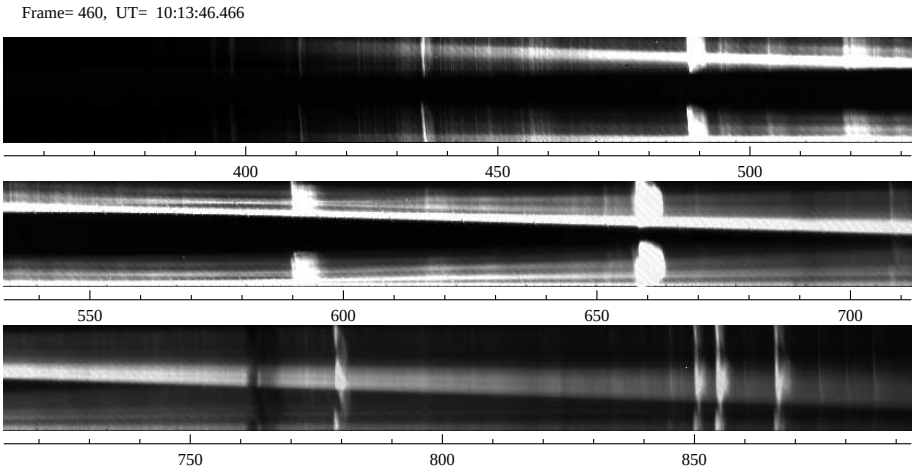

Figure 2. Sample frame from the flash phase at second contact, representing the raw data (only corrected for bias and flat field). The scale gives the wavelength in nm. The two orthogonally polarized spectra are imaged above each other. Since the separation between them is strongly wavelength dependent, they are well separated in the UV (so well that vignetting is severe), while they significantly overlap in the infrared. While some strong lines, like Hβ, the He I D3 lines, and Hα, are still saturated in this particular frame, the Ca II H and K lines in the UV are already quite faint. The almost horizontal bright band represents the remaining part of the photospheric sickle. In this frame one can discern the main instrumental problems: vignetting, overlap, and aberrations, in particular the differential effects between the two spectra.

with the development of the instrument and the control software and for handling the time pressure so calmly. We are also grateful to the Specola Solare Ticinese in Locarno, for having made available to us a very convenient testing environment, and to Osama Shalabiea and the Sebha University for their kind support in Libya.

References

Chandrasekhar, S.: 1950, *Radiative Transfer*, Clarendon Press, Oxford
Cillié, G.G. and Menzel, D.H.: 1935, *Harvard College Obs. Circ.*, **410**, 1
del Toro Iniesta, J.C. and Collados, M.: 2000, *Appl. Opt.* **39**, 1637
Dunn, R.B., Evans, J.W., Jefferies, J.T., Orrall, F.Q., White, O.R., and Zirker, J.B.: 1968, ApJS, **15**, 275
Feller, A., Stenflo, J. O., Gisler, D., and Ramelli, R.: 2006, in R. Ramelli, O. Shalabiea, I. M. Saleh, and J. O. Stenflo (eds.), Proceedings of the International Symposium on Solar Physics and Solar Eclipses, Sebha University publ., Sebha, Libya
Espenak, F. and Anderson, J.: 2004, *NASA Technical Paper No.* **212762**
Hanson, T., Stenholm, B., Söderhjelm, S.: 1976, *Reports from the Observatory of Lund, No.* **8**
Mitchell, S.A.: 1947, ApJ, **105**, 1
Shen L., Li, Q., Yu, J., Sun, R.: 1981, *Chin.* A&A, **5**, 388
Stenflo, J. O.: 2006, in R. Ramelli, O. Shalabiea, I. M. Saleh, and J. O. Stenflo (eds.), Proceedings of the International Symposium on Solar Physics and Solar Eclipses (SPSE2006), Sebha University publ., Sebha, Libya
Stokley, J.: 1948, AJ, **53**, 117

The Physics of Chromospheric Plasmas
ASP Conference Series, Vol. 368, 2007
Petr Heinzel, Ivan Dorotovič and Robert J. Rutten, eds.

Chromospheric Science with the STEREO Mission

Angelos Vourlidas

Solar Physics Branch, Naval Research Laboratory, USA

Abstract. The STEREO mission, launched in October 2006 comprises two spacecraft drifting at opposite directions from Earth. STEREO carries a suite of solar telescopes to provide, for the first time, stereoscopic views CMEs and of the corona including the cool, upper chromospheric line of He II at 304 Å. In my talk, I give an overview of the mission and its science objectives and discuss the areas where STEREO can provide important contributions to chromospheric science questions.

1. Introduction

On October 26, 2006, the Solar TErrestrial RElations Observatory (STEREO) was launched into space from Cape Canaveral. The main objectives of the mission are to investigate the physical mechanisms behind the initiation and evolution of coronal mass ejections (CMEs) and to follow the propagation of CMEs through the heliosphere. STEREO will also study the mechanisms and sites of energetic particle acceleration and develop 3D time-dependent models of the magnetic topology, temperature, density and velocity of the solar wind between the Sun and Earth. To accomplish these goals, STEREO employs the unique strategy of imaging the solar corona and heliosphere simultaneously with identical telescope suites located on two spacecraft (Fig. 1, left). One spacecraft leads and the other one trails the Earth with a separation rate of about 22 deg/year (Fig. 1, right). The two vantage points permit the use of stereoscopic techniques to estimate the 3D morphology of solar structures (e.g., loops, streamers, CMEs) and the increasing separation will allow the employment of the techniques to structures of varying scales (small loops at the beginning and CMEs at latter stages of the mission). Each STEREO spacecraft carries four experiments which together will characterize the space environment from the Sun's corona to the Earth's vicinity using both remote sensing and in-situ measurements.

The In situ Measurements of Particles and CME Transients (IMPACT) experiment (Luhmann et al. 2005) is a collection of in-situ sensors to measure the interplanetary magnetic field, thermal and suprathermal solar wind electrons, and energetic electrons and ions.

The PLAsma and SupraThermal Ion Composition (PLASTIC) experiment is another in-situ package to measure protons, alpha particles, and heavy ions. It focuses on measurements of the mass and charge state composition of heavy ions and can discriminate the CME plasma from ambient coronal plasma.

The STEREO/WAVES (S/WAVES) instrument is a radio spectrometer that observes the generation and evolution of traveling radio disturbances from

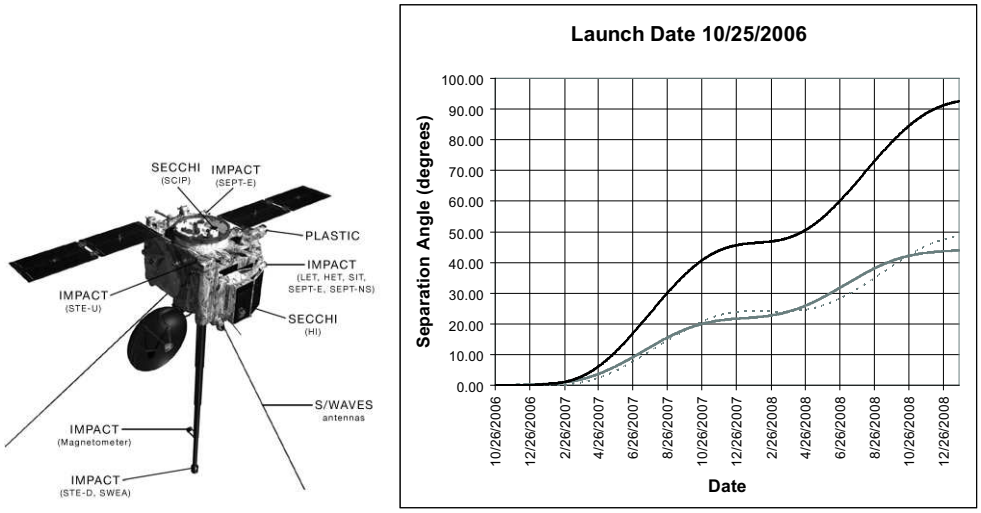

Figure 1. *Left:* The four instrumental suites (SECCHI, IMPACT, PLASTIC, and SWAVES) comprise the science payload of each STEREO spacecraft. Most of the synergies with the chromosphere are provided by the SECCHI telescopes. *Right:* Plot of the angular separation between the two STEREO spacecraft (solid black line) for the duration of the primary mission (2 years). The separations between Earth and STEREO-A (gray line) and Earth and STEREO-B (gray dotted line) are also shown.

the Sun to the orbit of Earth. It is an evolution of the WAVES instrument aboard the Wind satellite.

The Sun-Earth Connection Coronal & Heliospheric Investigation (SECCHI) experiment (Howard et al. 2002) is a suite of optical telescopes that observe the entire inner heliosphere from the solar surface out to the vicinity of Earth. SECCHI carries an EUV Imager (EUVI) that observes the full solar disk in four EUV passbands including the He II line at 304 Å. This telescope offers some very exciting opportunities for chromospheric science that we will outline later.

2. The SECCHI Experiment

2.1. Science objectives

The primary objective of the STEREO mission is to understand the CME phenomenon. CMEs were discovered in 1971 and have been observed by coronagraphic instruments on five missions, most recently the NASA/ESA Solar and Heliospheric Mission (SOHO). But, STEREO is the first mission whose primary objective is to elucidate the CME itself. Accordingly, the primary science objectives of SECCHI reflect this emphasis: (1) Determine the 3D properties of CMEs, (2) determine the timing of physical properties involved in the CME initiation, (3) determine the critical forces controlling CME propagation in the corona and heliosphere, and (4) determine the 3D structure of coronal loops, streamers, and large-scale structures.

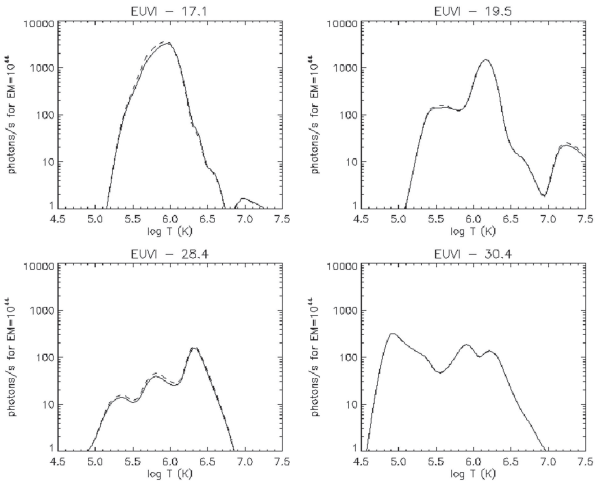

Figure 2. The temperature response of the EUVI wavelength bands. The solid lines are for the EUVI-A(head) and the dashed lines for the EUVI-B(ehind) telescopes.

2.2. Instruments

The SECCHI telescopes are arranged in two packages (Fig. 1, left). The Sun-Centered Imaging Package (SCIP) consists of the EUVI telescope observing the corona and upper chromosphere out to 1.7 $R_{\rm sun}$, two white light coronagraphs (COR1 & COR2) viewing the corona from 1.5 to 15 $R_{\rm sun}$ and a guide telescope. The Heliospheric Imager Package (HI) consists of two wide-field imagers that observe the heliosphere between the Sun and the Earth (from 12 to $>$ 215 $R_{\rm sun}$). We anticipate that SECCHI will provide pioneering observations of other solar structures, such as loops, plumes, streamers, comets, etc., using stereo deconvolution techniques. Specifically, the four wavelength bands of the EUVI telescope will provide high resolution observations of the solar atmosphere in a variety of temperatures (Fig. 2).

2.3. Operations plan

Unlike SOHO, where the majority of the observations are conducted through specialized Joint Observing Programs (JOPs), SECCHI, and STEREO overall, will be run as a synoptic instrument. The main driver for this operational mode is the need to obtain *simultaneous* observations of CMEs from both spacecraft. Simultaneity is essential for the successful use of deconvolution algorithms to obtain the 3D structure information. We recognize that special observations can greatly enhance the science return from the mission. For this reason, 20% of the SECCHI telemetry is allocated to special observing programs. The rest is devoted to a synoptic program designed to address the primary science of the SECCHI program (Table 1). As can be seen, the synoptic program alone will provide $\sim$ 1000 full disk EUV images per day. This is an increase of more than a factor of 5 over the current EIT observations.

Table 1. Typical SECCHI Synoptic Program

Telescope	No of Images & Size (pixels)	Cadence (minutes)	Images (Day)	Compression Factor	Mbits (Day)
EUVI	1 2k × 2k	2.5	552	36.0	900.4
	1 2k × 2k	3.75	360	36.0	587.2
	4 2k × 2k	60	90	18.0	313.2
COR1	3 1k × 1k	7.5	576	10.0	845.6
COR2	3 2k × 2k	60	72	10.0	422.8
	3 1k × 1k	15	216	10.0	317.1
HI1	1 1k × 1k	30	48	2.5	422.8
HI2	1 1k × 1k	60	24	2.5	211.4
Total			1944		4020.4

3. SECCHI and the Chromosphere

Although STEREO is not specifically designed to address problems of the solar atmosphere, its mission design and instrumental capabilites give the SECCHI instruments some interesting advantages: (1) Views of the upper chromosphere/corona *away* from the Sun-Earth line, (2) *simultaneous* views of chromospheric/coronal structures from two viewpoints, (3) full disk observations with $\sim$ 3.5 arcseconds resolution, and (4) high cadence ($\sim$ 2 min) observations of He II emission.

These capabilities should allow insights into the physics and geometry of filaments and prominences and their associated cavities, the atmospheric structure from photosphere to corona, and the filament heating during eruptions. Let us take a look at some examples.

Filament studies Filaments have been studied extensively for decades using ground-based Hα observations. However, these observations record only the cool ($\sim$ 10 K) component of these structure. Since the *Skylab* He II 304 Å prominence observations, it is known that the prominence can exist in many temperatures. This has prompted the construction of various models such as multi-thermal strand models (Schmahl & Orrall 1986). However, it is still unclear how the multi-thermal plasma reaches coronal heights and how it is distributed in space.

Originally, it was thought that the appearance of prominences was similar in Hα and He II images. Recent results show differences between the two. Generally speaking, He II emission tends to come from the top and the outer part of the prominence while Hα tends to concentrate at the bottom and inner parts of these structures. He II prominences are taller ($\sim 3-4$ Mm) and longer (Martin 2002). They also exhibit larger mass flows ($10-70$ km/s) compared to $5-20$ km/s in Hα (Wang 1999; Zirker et al. 1998).

The upcoming SECCHI observations in He II will establish whether the above conclusions are correct. They will also help on areas where the reduced EIT cadence has prevent us from making solid progress. For example, can we have a He II prominence without Hα emission and vice versa? Under what conditions and why? Do He II barbs end in opposite polarity regions (Wang 2001)?.

Atmospheric structure The temperature structure of the solar atmosphere as a function of height is also an area of intense research. Numerous studies have investigated this question using multiband observations of loop structures on the disk or on the limb. But controversy has plagued the results because the true 3D configuration of the structures is uncertain. The SECCHI suites will provide observations in several temperatures from two additional viewpoints. When combined with the observations from Solar-B, SOHO, TRACE and ground-based observatories, these images will provide important spatial and temperature constraints. Note that the ability to observe a coronal loop simultaneously from both the top and from the side has never been available before. Tthe SECCHI observations will give us the ability to study the morphology of spicules, surges and prominences. The 3D information will be invaluable to theoretical modeling of the structures, for coronal magnetic field extrapolations and for the understanding the physics of formation of optically thick lines, such as He II.

Eruptions This is the most straightforward connection between the chromosphere and the SECCHI objectives. Disappearing prominences and filaments have been one of the earliest indicator of ejections from the Sun (Pettit 1940). Thanks to the numerous ground-based Hα observations since, an enormous amount of literature has been accumulated on the subject. The most recent and relevant to our discussion have been studies of eruptive prominences in the EUV passbands of the EIT and Hα (Wang 2001; Jing et al. 2004). These studies have demonstrated a strong connection between prominence eruptions and CMEs. However, the correlation is not always one-to-one. One of the problems is that some prominences might be visible in the EUV but not show Hα emission at all biasing any Hα-CME statistics. Unfortunately, the low EIT cadence in He II does not allow us to examine whether the He II line is a better indicator for an erupting prominence.

The SECCHI/EUVI observations could contribute significantly in this and other questions: Do eruptive He II prominences correlate better than Hα prominences with white light CMEs? Is the prominence activation observed in He II? Does it come before of after the Hα activation? What are the dynamics of the structure lift-off in He II relative to Hα? Are the heating profiles different? What fraction of the mass in each wavelength erupt? How are surges and sparys in He II and Hα relate?

4. How to Get Involved?

The default NASA policy dictates that all data from space missions be publicly available when the science phase of the mission starts. For STEREO, science data will become available in mid-January 2007. The STEREO data is donwlinked once a day, five days a week and the transfer and processing of the raw SECCHI telemetry takes about a day. Therefore the full resolution science images will be available online within about 1.5 days after their acquisition on board the spacecraft. The SECCHI images can be accessed from either the STEREO Science Center (`http://stereo.gsfc.nasa.gov`) or the SECCHI website (`http://secchi.nrl.navy.mil`) where additional data products (e.g., Carrington maps) will be available. Mirror sites will be available in Europe

(e.g., MEDOC) and other places. The latest information will be available at the SECCHI website. This is also the place where special observing programs can be submitted for consideration by the SECCHI operations team, at least a month before the desired observations date. All observing schedules will be available on the SECCHI site. Interested parties can contact the SECCHI team through the Operations Scientist (`simon.plunkett@nrl.navy.mil`), the Mission Scientist (`vourlidas@nrl.navy.mil`) or the PI (`russ.howard@nrl.navy.mil`).

Acknowledgments. I thank the SOC for inviting me to present the SECCHI instrument capabilities, and the local organizers for putting together a very good meeting in a beautiful place. My work at NRL is supported by various NASA and ONR grants.

References

Howard R. A., Moses J. D., Socker D. G., Dere K. P., Cook J. W., 2002, Advances in Space Research 29, 2017

Jing J., Yurchyshyn V. B., Yang G., Xu Y., Wang H., 2004, ApJ 614, 1054

Luhmann J. G., Curtis D. W., Lin R. P., Larson D., Schroeder P., Cummings A., Mewaldt R. A., Stone E. C., Davis A., von Rosenvinge T., Acuna M. H., Reames D., Ng C., Ogilvie K., Mueller-Mellin R., Kunow H., Mason G. M., Wiedenbeck M., Sauvaud A., Aoustin C., Louarn P., Dandouras J., Korth A., Bothmer V., Vasyliunas V., Sanderson T., Marsden R. G., Russell C. T., Gosling J. T., Bougeret J. L., McComas D. J., Linker J. A., Riley P., Odstrcil D., Pizzo V. J., Gombosi T., Dezeeuw D., Kecskemety K., 2005, Advances in Space Research 36, 1534

Martin S. F., 2002, in Bulletin of the American Astronomical Society, p. 684

Pettit E., 1940, PASP 52, 172

Schmahl E. J., Orrall F. Q., 1986, in A. I. Poland (ed.), Coronal and Prominence Plasmas, p. 127

Wang Y.-M., 1999, ApJ 520, L71

Wang Y.-M., 2001, ApJ 560, 456

Zirker J. B., Engvold O., Martin S. F., 1998, Nat 396, 440

The Physics of Chromospheric Plasmas
ASP Conference Series, Vol. 368, 2007
Petr Heinzel, Ivan Dorotovič and Robert J. Rutten, eds.

Chromospheric and Prominence Physics with the ASPIICS Formation Flying Coronagraph

Philippe Lamy[1], Sébastien Vivès[1], Serge Koutchmy[2] and Jean Arnaud[3]

[1]*Laboratoire d'Astrophysique de Marseille, France*
[2]*Institut d'Astrophysique de Paris, France*
[3]*Laboratoire d'Astrophysique de Toulouse et Tarbes, France*

Abstract. Classical externally-occulted coronagraphs are presently limited in their performances by the distance between the external occulter and the front objective. The diffraction fringe from the occulter and the vignetted pupil which degrades the spatial resolution prevent observing the inner corona inside typically 2–2.5 solar radii ($R_\odot$). Formation flying opens new perspectives and allow to conceive giant, externally-occulted coronagraphs using a two-component space system with the external occulter on one spacecraft and the optical instrument on the other spacecraft. ASPIICS (Association de Satellites Pour l'Imagerie et l'Interférométrie de la Couronne Solaire) is a mission proposed to ESA in the framework of the PROBA-3 program of formation flying which is presently under study, to exploit this technique for coronal observations. ASPIICS is composed of a single coronagraph which performs high spatial resolution imaging of the corona as well as 2-dimensional spectroscopy of several emission lines (in particular the forbidden line of Fe XIV at 530.285 nm) from the coronal base out to 3 $R_\odot$. The classical design of an externally occulted coronagraph is adapted to the detection of the very inner corona, and the addition of a Fabry-Pérot interferometer. By tuning the position of the occulter spacecraft, it will be possible to reach the chromosphere and the upper part of the spicules. Filtergrams on the helium D3 line or even better, the hydrogen Hβ line (which is optically thin contrary to Hα) will give access to the "cold corona", and could allow measuring the chromospheric prolateness.

1. Introduction

After 40 years of space coronagraphy, the lower corona (defined here as extending from the solar limb to a solar elongation of approximately 2.5 $R_\odot$) remains practically unobserved. The only available images are those obtained with the SOHO/LASCO-C1 coronagraph (Brueckner et al. 1995) before it failed following the temporary loss of control of the SOHO spacecraft. Although these images were obtained in the bright green line of Fe XIV, their contrast remains rather limited because of the high level of instrumental stray light. Routine images of the lower corona are obtained with ground-based coronagraphs (e.g., Mk III and IV in Hawaii) but their quality is affected by seeing and atmospheric conditions, and their useful fields of view rarely exceed a few tenth of solar radii. The SECCHI suite of instruments aboard the STEREO dual spacecrafts includes a Lyot coronagraph, and it will be interesting to see the expected white light images of the inner corona in the coming months when it will start operating.

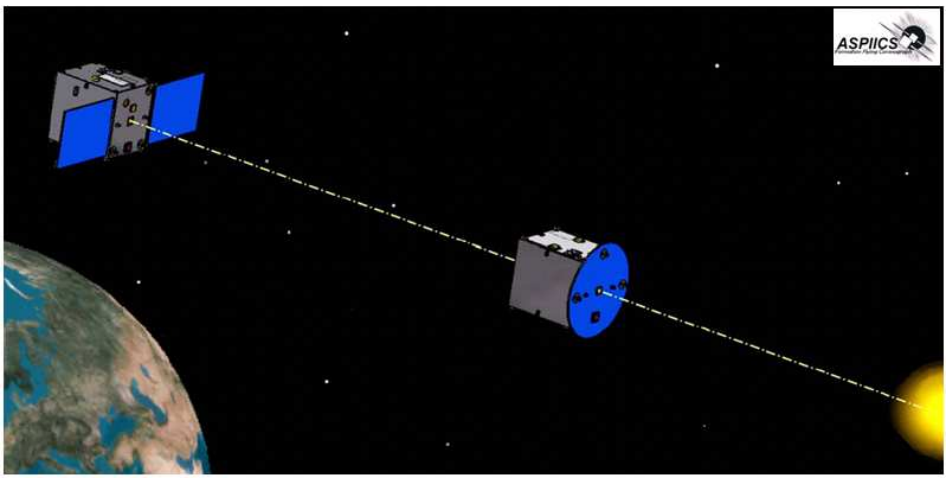

Figure 1. ASPIICS on a two-component space system with the external occulter on one spacecraft and the optical instrument on the other spacecraft at 150 m from the first one. Formation flying configuration studied by ESA (2006).

For completeness, we mention the images taken on the occasions of (rare) total solar eclipses whose quality remains unsurpassed.

Formation flying opens the possibility to conceive and deploy giant coronagraphs in space that are not affected by the above limitations. Basically, the idea of "formation flying" is to coordinate a cluster of platforms that acts as a single virtual instrument or as a single mission spacecraft for coordinated observations or in situ measurements. This technique allows to reconcile the demand for increased instrumental performances with spacecraft and launcher limitations. The PROBA-3/ASPIICS (standing for "Association de Satellites Pour l'Imagerie et l'Interférométrie de la Couronne Solaire") mission is composed of two platforms separated by about 150 m and forming a giant coronagraph: the external occulter is supported by one satellite while the second satellite hosts the optical system (Fig. 1).

2. The ASPIICS Instrument

2.1. Optical concept and design

ASPIICS is an externally occulted coronagraph entirely protected from direct sunlight by remaining in the shadow of the external occulter hosted by another spacecraft. The classical design of an externally occulted coronagraph is adapted to both the detection of the very inner corona as close as 1.02 $R_\odot$ from the Sun center with high spatial resolution (5 arcsec), and the addition of a Fabry-Pérot interferometer. The current optical design (Fig. 2) is a combination of reflective (basically a three-mirror anastigmat) and a refractive optical systems as such solution presents major technical advantages: a natural front baffle, protection of the first optics against contamination and thermal variations, a design naturally folded (reducing the overall length).

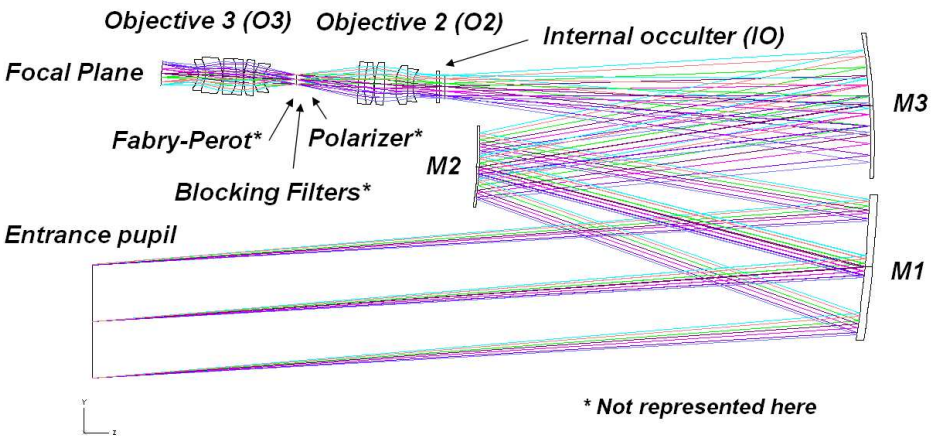

Figure 2. Optical layout of the ASPIICS coronagraph.

The external occulter (EO) blocks the light from the solar disk while the coronal light passes through the circular entrance aperture (140 mm diameter). A Three-Mirror Anastigmat (TMA) system forms the image of the EO onto the internal occulter with reduced geometric and chromatic aberrations to provide more efficient inner occultation. The internal occulter blocks the bright diffraction fringe surrounding the EO. The amount of over-occultation results from the compromise between the stability of the formation, the attitude of the spacecraft hosting the coronagraph, and the vignetting which determines the spatial resolution in the inner part of the corona. The second objective (O2) forms a collimated beam and produces a real image of the entrance pupil at the Lyot stop with a magnification of 10. The narrow-bandpass Fabry-Pérot (F-P) interferometer and a set of blocking filters plus polariser plates are mounted on a double wheel located in this collimated beam. Each blocking filter selects a specific emission line spectral interval, and blocks all but a single transmitted interferometer order. A large band filter allows to transmit several orders thus yielding polychromatic images. To improve the signal-to-noise ratio of polychromatic images and their image quality, the F-P could be removed from the beam in that case. The final image is formed by a telephoto lens system on a detector located behind a mechanical shutter. The layout is such that a circular field of view with a radius of 3 $R_{\odot}$ forms an inscribed circle on the 2k $\times$ 2k pixels CCD detector where one pixel subtends 2.8 arcsec in the corona.

2.2. The "etalon" Fabry-Pérot interferometer

Various instrumental solutions have been considered to perform spectral measurements in the corona. Conventional slit spectrographs have the disadvantage that they give 1-D information, i.e., along the slit. All or part of the instrument must be rotated to map the corona (e.g., SOHO/UVCS). This requires bulky mechanisms on the one hand, and a fairly long time to perform 2-D observations (several hours in the case of UVCS) on the other hand, both aspects being incompatible with the practical constraints of the contemplated demon-

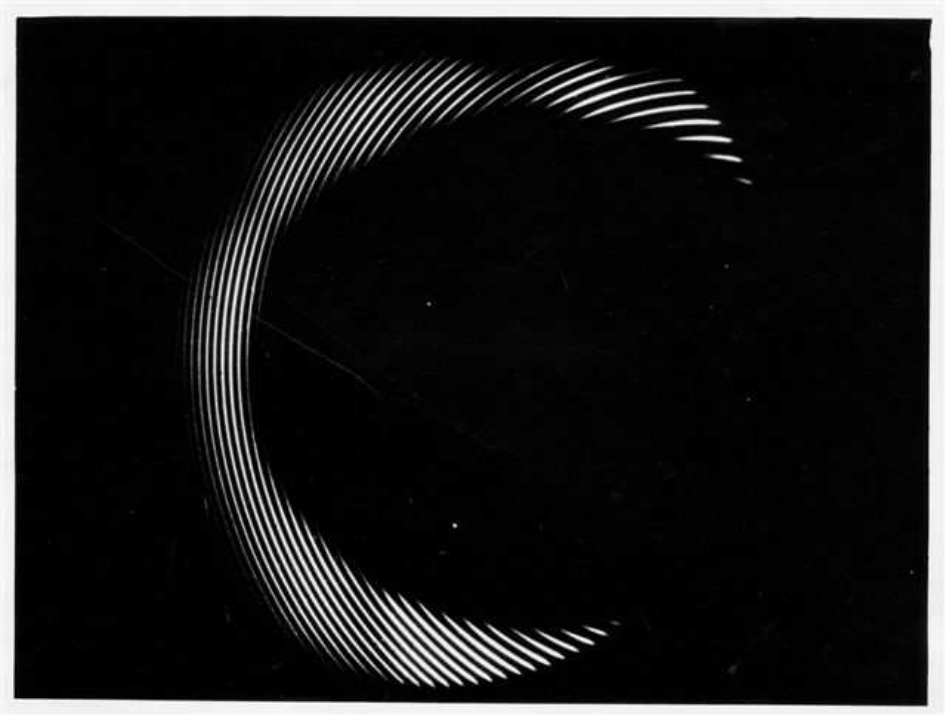

Figure 3. Fabry-Pérot interferogram obtained by Desai et al. during the solar eclipse on February 1980 (Desai et al. 1982). Note that their interferometer was so tilted (center on the solar disk) that only 2/3 of the corona was covered by the fringe network. The fringes at the bottom (south) are not broadened but actually splitted.

stration of formation flying. The optical concept best suited to our problem is the Fabry-Pérot (F-P) interferometer. Two possibilities exist: the tunable F-P incorporating a scanning mechanism and the solid "etalon" F-P. For ASPIICS, we propose the second solution which does not require any internal adjustments. Indeed, the F-P interferometer cavity length and parallelism directly affect the filter passband central wavelength and shape, respectively. Significant cavity length drift results in variations of the central wavelength of the passband, and a lack of parallelism reduces the instrument finesse, and consequently broadens the transmission profile. These problems are avoided using a solid etalon. Furthermore, a tunable F-P needs a combination of several images to reconstruct the line profile at any point of the field of view that requires perfect tuning of the F-P at each position, and this requires extensive in-fligth adjustements.

The method consists in analyzing the bi-dimensional distribution of line profiles by a set of quasi concentric fringes generated by the etalon. This method has already been used by Desai et al. (1982) during the solar eclipse on February 1980 (Fig. 3). The fringes have an instrumental profile of typically 0.05 nm, narrower than the width of the line (0.1 nm for Fe XIV) so that the observed profiles are not significantly affected by the instrumental function and directly give the real profiles of the coronal emission line to a very good accuracy. The free spectral range will be approximately 0.4 nm, a compromise between the

expected shifts and the rejection of the continuum corona, leading to a finesse of about 20. The set of fringes can be centered on the Sun or decentered, even outside the solar disk. In the former case, the analysis is axially symmetric but the F-P works in low orders thus limiting the spatial resolution. In the latter case, it works in high orders producing dense fringes thus resulting in a higher spatial resolution. The etalon will be mechanically tilted to displace the set of fringes and increase the resolution. The interferogram may be viewed as resulting from a multislit spectrograph: all the spectral information is contained in the image, and there is no need to combine several images as in the scanning F-P to reconstruct the spectra.

To perform a precise line profile analysis far enough out in the corona, the strongest emission line available, the forbidden line of Fe XIV at 530.285 nm, is the prime choice. This truly coronal emission line formed at temperature $T = 1.8 \times 10^6$ K is not sensitive to the so-called Doppler dimming effect, such that its profile is directly reflecting line-of-sight velocities inside the corona. In addition, it has been established a long time ago (Allen 1946) that the line is measurable in the corona all along large radial distances (beyond at least 3 $R_\odot$ from the solar center). Furthermore, this line is linearly polarized thus giving access to the direction of the coronal magnetic field. The iron lines are also much more appropriate to resolve the turbulence inside the corona, including the higher corona were the lines are no more collisionally dominated but are radiatively dominated. Additional emission lines will be included to better address different coronal regions, in particular the helium D3 line and the hydrogen Hβ line (which is optically thin contrary to Hα) will give access to the "cold corona", and could allow measuring the chromospheric prolateness. Finally, a broad spectral channel will image the white light corona so as to derive electron densities.

3. Formation Flying Requirements

The optimal inter-satellite distance is approximately 150 m (Vivès et al. 2006). This essentially results from a compromise between both the limitation of the vignetting by the external occulter (so as to preserve the spatial resolution as close as possible to the solar limb), and the compensation of the steep gradient of intensity of the inner corona by vignetting the field of view up to 1.1-1.15 $R_\odot$. As an example, for two spacecrafts separated by 150 m, the unvignetted field of view extends from 1.15 $R_\odot$ and the diameter of the occulter is about 1.5 m.

The stability of the formation is directly linked to the high level requirement of keeping the pupil in the shadow of the occulter. As a baseline, the lateral positioning is about $\pm$2.5 mm while lthe ongitudinal positioning is about $\pm$250 mm. These specifications allow to observe the corona down to 1.01$\pm$0.0075 $R_\odot$. There is a coupling between lateral/longitudinal positionings, and the absolute attitude of the spacecraft hosting the coronagraph ($\pm$20 arcsec on transverse axes) since the fringe diffracted by the occulting disk has to be blocked by the internal occulter. It is interesting to note that the attitude of the satellite hosting the occulting disk is not strongly constrained by science as a tilt of its axis will result in a slightly ellipsoidal projected shadow. For instance, a tilt of 2 degrees implies a difference of only 0.001 $R_\odot$ between the two axes of the ellipse.

4. Conclusion

Formation flying offers the outstanding opportunity to conceive giant, externally-occulted coronagraphs capable of observing from the very inner corona up to several solar radii with high spatial resolution. This article presents the implementation of such a coronagraph for the formation flying demonstration PROBA-3 of ESA. The ASPIICS coronagraph will perform high spatial resolution imaging of the corona as well as two-dimensional spectroscopy of several emission lines in order to address key questions of coronal physics. By tuning the position of the occulter spacecraft, it will be possible to reach the chromosphere and the upper part of the spicules. Filtergrams on the helium D3 line or even better, the hydrogen Hβ line will give access to the "cold corona", and could allow measuring the chromospheric prolateness.

Acknowledgments. We thank the CSPM organisers for a fruitful meeting.

References

Allen C. W., MNRAS, 106, 137 (1946)
Brueckner G. E. et al., 1995 Solar Physics, 162, 357
Desai J. N., Chandrasekhar T., & Angreji P. D., 1982, Journal of Astrophysics and Astronomy, 3, 69
Vivès S., Lamy P. et al., 2006 Proc. SPIE, Vol. 6265

The Physics of Chromospheric Plasmas
ASP Conference Series, Vol. 368, 2007
Petr Heinzel, Ivan Dorotovič and Robert J. Rutten, eds.

Solar Orbiter: A Mission Update

Richard G. Marsden and Bernhard Fleck
ESA, ESTEC, Noordwijk, The Netherlands

Abstract. The Solar Orbiter Mission will study the Sun in greater detail than ever before due the close proximity of the spacecraft as it orbits the Sun. At its closest point, Solar Orbiter will be about 0.22 AU from the Sun, closer than any other satellite to date. In addition to providing high-resolution images of the solar surface, perihelion passes at these distances occur in near co-rotation with the Sun, allowing the instruments to track features on the surface for several days. The mission profile also includes a high-latitude phase that will allow observations from up to 35° above the solar equator. The combination of near-Sun, quasi-heliosynchronous and high-latitude observations by remote-sensing and in-situ instruments makes Solar Orbiter a unique platform for the study of the links between the Sun and the inner heliosphere.

1. Introduction

The Solar Orbiter mission will provide the next major step forward in the exploration of the Sun and the heliosphere and will address many of the fundamental problems remaining in solar and heliospheric science. It incorporates both a near-Sun and a high-latitude phase. The near-Sun phase of the mission enables the Orbiter spacecraft to approach the Sun as close as 48 solar radii (≈0.22 AU) during part of its orbit, thereby permitting observations from a quasi-helio-synchronous vantage point (so-called co-rotation.). At these distances, the angular speed of a spacecraft near its perihelion approximately matches the rotation rate of the Sun, enabling instruments to track a given point on the Sun surface for several days. During the out-of-ecliptic phase of the mission, the Orbiter will reach intermediate solar latitudes (up to 35° in the extended phase), making possible detailed studies of the Sun's polar caps by the remote-sensing instruments.

1.1. Background

In 2000, the Solar Orbiter mission was submitted to ESA and selected by ESA's Science Programme Committee (SPC) to be implemented as a flexi-mission, with a launch envisaged in the 2008-2013 timeframe (after the BepiColombo mission to Mercury). In November 2003, the SPC agreed to begin an Assessment Study of Solar Orbiter, and in 2004 confirmed the place of Solar Orbiter in the Cosmic Vision programme with the objective of a launch no later than May 2015.

Delta studies in industry were performed between April and July 2005, focusing on the interfaces between the spacecraft and instruments and a chemical propulsion option.

At its meeting in February 2006, the SPC requested a work plan for key technology developments and other preparatory activities that would maintain the possibility of a launch of Solar Orbiter in 2015. A Call for Letters of Intent to propose instruments for the payload of Solar Orbiter was issued on 11 July 2006. Twenty-three Letters of Intent were received in response to this Call. The technical and scientific information provided in these Letters (augmented by further iterations with the respondents) will be used as input to the next round of industrial studies that will focus on heat shield technology developments.

2. Science Goals

The Sun's atmosphere and the heliosphere represent uniquely accessible domains of space, where fundamental physical processes common to solar, astrophysical and laboratory plasmas can be studied under conditions impossible to reproduce on Earth or to study from astronomical distances. The results from missions such as Helios, Ulysses, Yohkoh, SOHO, TRACE and RHESSI have advanced significantly our understanding of the solar corona, the associated solar wind and the three-dimensional heliosphere. Further progress is to be expected with the next generation of missions, including the recently launched Hinode (Solar-B), STEREO, and the first of NASA's Living With a Star (LWS) missions, the Solar Dynamics Observatory (SDO). Each of these missions has a specific focus, being part of an overall strategy of coordinated solar and heliospheric research. An important element of this strategy, however, has yet to be implemented. We have reached the point where further in-situ measurements, now much closer to the Sun, together with high-resolution imaging and spectroscopy from a near-Sun and out-of-ecliptic perspective, promise to bring about major breakthroughs in solar and heliospheric physics. The Solar Orbiter will, through a novel orbital design and an advanced suite of scientific instruments, provide the required observations. The unique mission profile of Solar Orbiter will, for the first time, make it possible to:

- Explore the uncharted innermost regions of our solar system;
- Study the Sun from close-up;
- Fly by the Sun tuned to its rotation, examine solar surface and space above from a co-rotating vantage point;
- Provide images and spectral observations of the Sun polar regions from out of the ecliptic.

Within the framework of the global strategy outlined above, the top-level scientific goals of the Solar Orbiter mission are to:

- Determine the properties, dynamics and interactions of plasma, fields and particles in the near-Sun heliosphere;
- Investigate the links between the solar surface, corona and inner heliosphere;
- Explore, at all latitudes, the energetics, dynamics and fine-scale structure of the Sun's magnetized atmosphere;
- Probe the solar dynamo by observing the Sun's high-latitude field, flows and seismic waves.

The scientific objectives of the mission are discussed in detail in Marsch *et al.* (2001, 2005) and Marsden & Fleck (2003).

3. Reference Payload

The actual scientific payload for the Solar Orbiter mission will be selected on a competitive basis, following an Announcement of Opportunity that will be open to the international scientific community. The reference payload described in this paper has been used in order to progress with the mission definition before selection of actual instruments and comprises instruments (in-situ and remote-sensing measurements) defined on the basis of input received from the scientific community. In order to maintain compatibility with the boundary conditions of a medium-size mission, a resource-effective payload is required (e.g., a maximum total allocated mass of 180 kg, including maturity margins).

A summary of the Solar Orbiter reference payload is provided in Table 1. The reference payload can be grouped into three main categories: a) In-Situ instruments; b) Remote-Sensing instruments, constrained to follow a ∼1 arcsec, 1 meter philosophy (representing the spatial resolution and maximum allowed envelope for the largest units; c) Payload Support Elements (e.g., boom, doors and windows, etc.). The table refers to the core payload complement, reflecting the science prioritization given by the Science Definition Team. All figures reported in the table include design maturity margins (depending on heritage). Detailed descriptions of the reference instruments are given in the Payload Definition Document (ESA-ESTEC, SCI-A/2004/175/AO). The scientific requirements for the payload are given in the Science Requirements Document (Marsden & Marsch, 2005).

Instrument	**Mass [kg]**	**Power [W]**
a) In-Situ instruments		
Solar Wind Plasma Analyzer (SWA)	16.5	15.5
Radio and Plasma Wave Analyzer (RPW)	13.0	7.0
Magnetometer (MAG)	2.1	1.5
Energetic Particle Detector (EPD)	9.0	8.5
Dust Particle Detector (DPD)	1.8	6
Neutron Gamma ray Detector (NGD)	5.5	5.5
Remote-Sensing instruments		
Visible Imager & Magnetograph (VIM)	30.4	35
EUV Spectrometer (EUS)	18.0	25
EUV Imager (EUI)	20.4	28
Coronagraph (COR)	18.3	30
Spectrometer Telescope Imaging X-rays (STIX)	4.4	4
c) Payload Support Elements (PSE)	**28.4**	**4**
TOTAL	**167.8**	**170.0**

Table 1. The Solar Orbiter Reference Payload as given in the Payload Definition Document.

4. Mission Profile

Obtaining an orbit that reaches both high solar latitude and low perihelion distance requires high-energy transfers. This can only be done with conventional propulsion systems by making use of gravity assist manoeuvres (GAM). In the case of Solar Orbiter, Venus GAMs will be employed to obtain orbital inclinations allowing the spacecraft to reach latitudes of 35° with respect to the Sun's equator at the end of the mission.

To accomplish this, Solar Orbiter will be placed in a resonant orbit with respect to Venus, making it possible to perform regular GAMs to raise the inclination. A trade-off between the time needed to achieve the required inclination (which ideally should be as short as possible) and the maximum tolerable thermal load on the spacecraft resulted in a decision that the final science orbits should be in 3:2 resonance with Venus (three ≈150-day spacecraft orbits for every two Venus orbits), giving a minimum perihelion distance of about 0.22 AU.

Several mission design approaches were investigated during the assessment phase. A common constraint for all investigated alternatives was that that they would need to be compatible with a launch on a Soyuz-Fregat 2-1B launch vehicle from Centre Spatial Guyanais (CSG). The alternatives included the use of Solar Electric Propulsion (SEP), chemical propulsion or hybrid solutions. As a hybrid solution utilizing both chemical and electric propulsion would add both complexity and cost it was decided in an early phase to discard this option. The chemical option and the SEP option were therefore studied in detail. Although attractive from the point of view of offering a shorter cruise time than the chemical option, the SEP option was found to be both a higher risk and higher cost solution, and is therefore no longer considered for Solar Orbiter. That being the case, we focus here on the chemical option.

Using chemical propulsion and a launch on Soyuz-Fregat, the minimum cruise time to reach the nominal science orbit is about 3.4 years. In this scenario, the spacecraft will execute a Venus-Earth-Earth-Venus gravity assist trajectory before insertion. The current baseline is for a launch in May 2015, with a back up in January 2017. The characteristics of the trajectory for a launch in 2015 are shown in Figs. 1-4. Of particular interest is Fig. 4, which shows the ecliptic projection of the trajectory in a coordinate system that is fixed with respect to the Sun-Earth line. It can be seen that the full range of solar longitudes is covered during the mission, including a number of "far-side" perihelion passages. This will provide excellent opportunities for coordinated observations, in particular with near-Earth observing platforms. It is also envisaged to have close coordination between Solar Orbiter and the NASA Living With a Star Sentinels programme whose Inner Heliospheric Sentinel spacecraft will have trajectories that are similar to the near-ecliptic orbits of Solar Orbiter.

5. Programmatic Issues

The Solar Orbiter mission concept described here is the one that has been studied extensively during the assessment phase, and as such remains the focus of the current round of parallel industrial studies. This concept has also been considered to date to be implemented as an "ESA-only" mission (with the exception

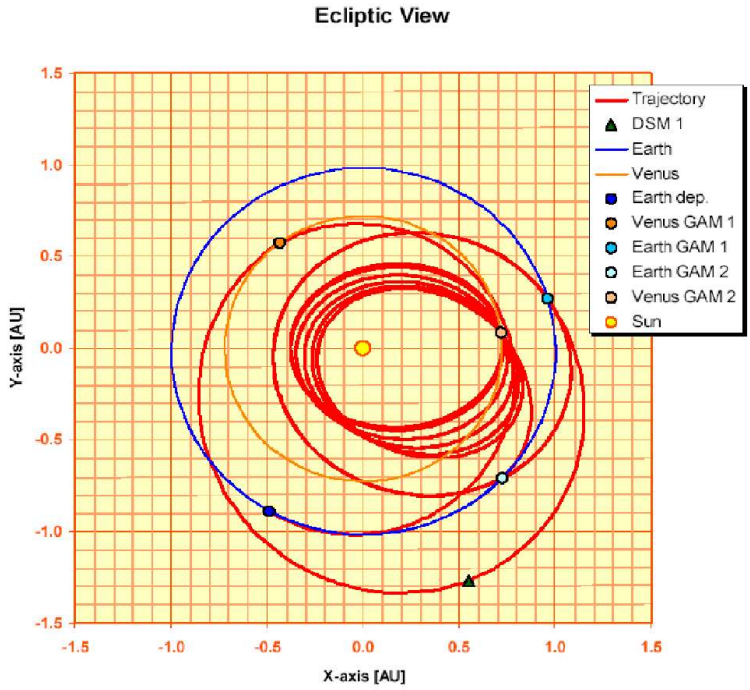

Figure 1. Ballistic trajectory (2015 launch opportunity, ecliptic plane projection).

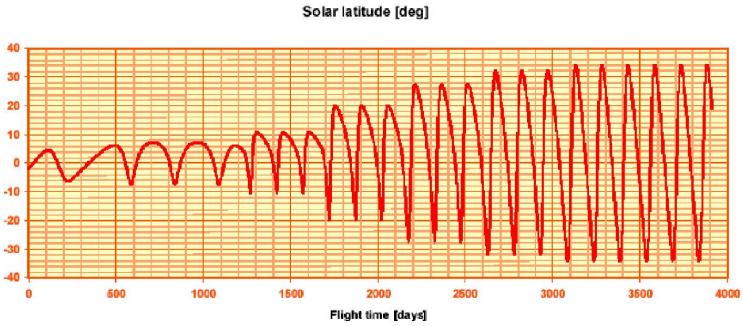

Figure 2. Solar latitude vs. flight time (2015 launch opportunity).

of the scientific payload, where contributions from non-ESA member states are envisaged). Nevertheless, discussions are ongoing concerning the possibility of joining Solar Orbiter and NASA's Solar Sentinels to form a single collaborative programme. This would have potential benefits for both missions, not only from a cost point of view, but also scientifically, as there are clear synergies between the two projects. An element of the proposed collaboration is a joint launch provided by NASA. A detailed technical evaluation has yet to be made, however, and until this has been done, no firm decision can be taken.

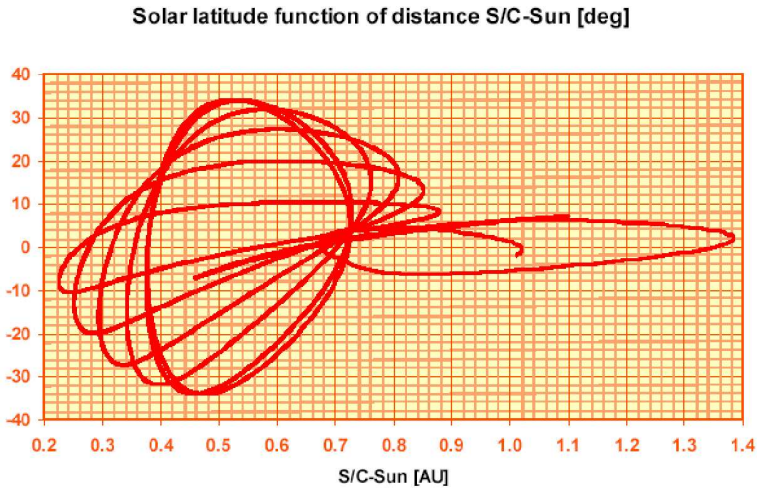

Figure 3. Solar latitude vs. S/C-Sun distance (2015 launch opportunity).

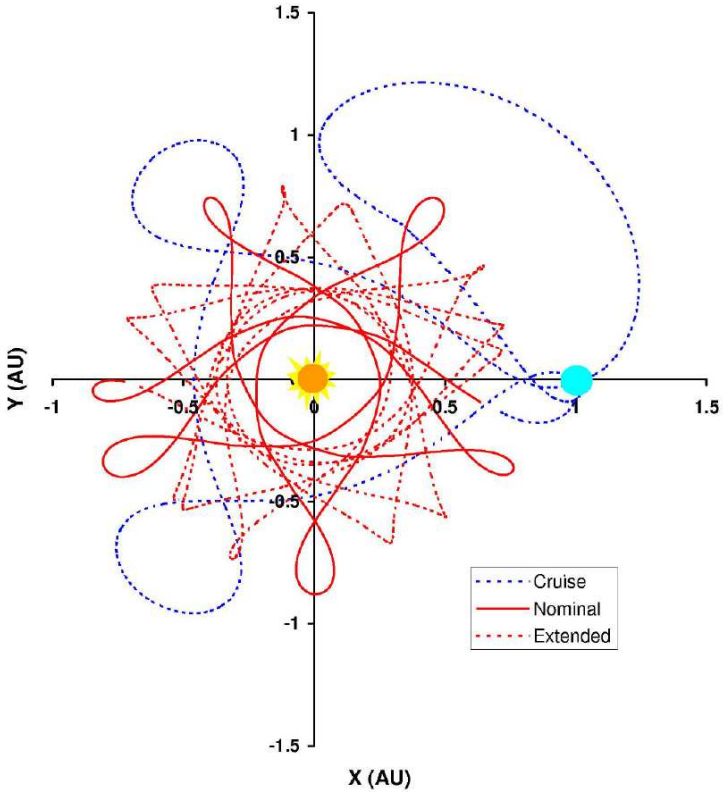

Figure 4. Spacecraft trajectory (cruise, nominal and extended phases) plotted in a coordinate system with the Sun-Earth line fixed (2015 launch opportunity).

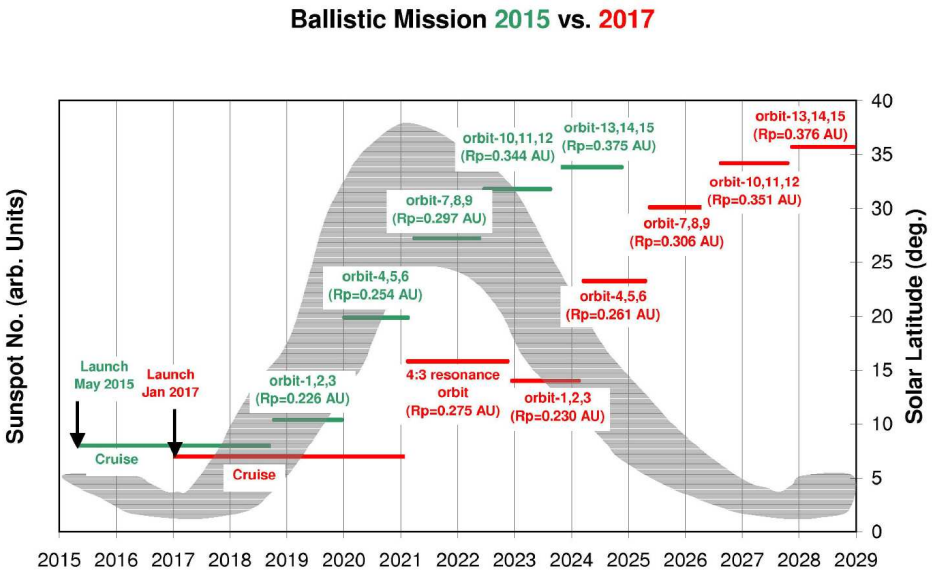

Figure 5. Mission phases vs. solar cycle. See text for details.

When discussing the possible launch date for Solar Orbiter, two issues to be considered (in addition to any programmatic/cost constraints) are:

– Venus launch opportunities, which occur every 19 months and drive the mission delta-V requirement and the cruise duration;

– The solar cycle (predicted maxima in 2010 and 2021).

Concerning the former, opportunities exist in May 2015 and January 2017. If programmatic constraints dictate that the window in 2017 becomes the baseline, a backup exists in 2018, albeit with poorer overall performance. Regarding the solar cycle, the situation is less clear-cut. For certain of the scientific goals, a phasing of the mission such that the polar regions of the Sun are viewed from the highest achievable latitudes when well-developed polar coronal holes are present, i.e. near solar minimum, would be advantageous. On the other hand, the polar field reversal is also of great interest, and this, like many of the near-Sun studies, would benefit from a relatively active Sun. Taken overall, the earliest practical launch opportunity (2015) is to be preferred. Nevertheless, it should be stressed that first-class science will be achieved by the Solar Orbiter independent of the exact point in the solar activity cycle at which these mission phases occur. In Fig. 5, we show a comparison of the two launch opportunities in terms of their phasing with respect to the solar cycle. The "steps" indicate the increase in inclination following each Venus gravity assist for the various science orbits. Also shown is the corresponding perihelion distance. The solar cycle is represented by a simple curve with some uncertainty in both phase and amplitude.

6. Next Steps

6.1. Heat shield / system technology studies

The major objective of these studies is to consolidate critical heat shield technologies and to advance system design. In addition, they will confirm the feasibility of the mission, refine the costs and the schedule, and prepare for the November 2007 SPC meeting to seek approval to proceed to the Definition Phase. Two parallel studies will be performed by industrial contractors, with a view to obtaining different heat shield concepts, together with breadboard models. The contractors will also study accommodation issues and refine interface details, particularly the heat shield interfaces (apertures, thermal aspects, baffles, doors, etc.). It is planned to start the contracts in November 2006 for a 12-month activity.

6.2. Recent planning assumptions

The following summarises the key project milestones as presently envisaged for a launch in 2015:

- Nov 2007: Consolidated mission work plan to be presented to SPC;
- Dec 2007: AO release (TBC);
- Jan 2008: Start of definition phase (16 months);
- Nov 2008: SPC approval of payload;
- Jan 2010: Start of implementation phase (TBC);
- May 2015: Launch.

Acknowledgments. The authors would like to thank N. Rando and his team for their support to the mission during the assessment phase. F. Jubineau (Alcatel Space) and F. Faye and P. Regnier (Astrium Toulouse) are also acknowledged for their contribution to the work done in the framework of the industrial activities during the Solar Orbiter assessment.

References

Marsch, E., Martinez-Pillet, V., Fleck, B., & Marsden, R.G. (Eds.) 2001, Solar Encounter, Procs. First Solar Orbiter Workshop, ESA SP-493

Marsch, E., Marsden, R.G., Harrison, R.A., Wimmer-Schweingruber, R., & Fleck, B. 2005, Adv. Space Res., 36, 1360

Marsden, R.G. & Fleck, B. 2003, Adv. Space Res., 32, 2699

Marsden, R.G. & Marsch, E. (Eds.) 2005, Solar Orbiter science requirements document, ESA-ESTEC

SOC (almost complete): Ivan Dorotovič, Jean-Claude Vial, Han Uitenbroek, Rob Rutten, Werner Curdt, Petr Heinzel, Mats Carlsson, Carsten Denker

Editorial office in Ondřejov